Published in Journals: GeoHazards, Land,
Remote Sensing, Sustainability and Water

Topic Reprint

Natural Hazards and Disaster Risks Reduction

Volume II

Edited by
Stefano Morelli, Veronica Pazzi and Mirko Francioni

mdpi.com/topics

MDPI

Natural Hazards and Disaster Risks Reduction—Volume II

Natural Hazards and Disaster Risks Reduction—Volume II

Editors

Stefano Morelli
Veronica Pazzi
Mirko Francioni

MDPI

Basel • Beijing • Wuhan • Barcelona • Belgrade • Novi Sad • Cluj • Manchester

Editors

Stefano Morelli
University of Urbino "Carlo Bo"
Urbino
Italy

Veronica Pazzi
University of Firenze
Firenze
Italy

Mirko Francioni
University of Urbino "Carlo Bo"
Urbino
Italy

Editorial Office
MDPI
St. Alban-Anlage 66
4052 Basel, Switzerland

This is a reprint of articles from the Topic published online in the open access journals *GeoHazards* (ISSN 2624-795X), *Land* (ISSN 2073-445X), *Remote Sensing* (ISSN 2072-4292), *Sustainability* (ISSN 2071-1050), and *Water* (ISSN 2073-4441) (available at: https://www.mdpi.com/topics/Natural_Hazards_Disaster_Risks_Reduction).

For citation purposes, cite each article independently as indicated on the article page online and as indicated below:

Lastname, A.A.; Lastname, B.B. Article Title. *Journal Name* **Year**, *Volume Number*, Page Range.

Volume II
ISBN 978-3-7258-0323-1 (Hbk)
ISBN 978-3-7258-0324-8 (PDF)
doi.org/10.3390/books978-3-7258-0324-8

Set
ISBN 978-3-7258-0319-4 (Hbk)
ISBN 978-3-7258-0320-0 (PDF)

Contents

About the Editors . . . . . **ix**

Preface . . . . . **xi**

Hyuck-Jin Park, Kang-Min Kim, In-Tak Hwang and Jung-Hyun Lee
Regional Landslide Hazard Assessment Using Extreme Value Analysis and a Probabilistic Physically Based Approach
Reprinted from: *Sustainability* **2022**, *14*, 2628, doi:10.3390/su14052628 . . . . . **1**

Zhu Liang, Wei Liu, Weiping Peng, Lingwei Chen and Changming Wang
Improved Shallow Landslide Susceptibility Prediction Based on Statistics and Ensemble Learning
Reprinted from: *Sustainability* **2022**, *14*, 6110, doi:10.3390/su14106110 . . . . . **18**

Jiakai Lu, Chao Ren, Weiting Yue, Ying Zhou, Xiaoqin Xue, Yuanyuan Liu and Cong Ding
Investigation of Landslide Susceptibility Decision Mechanisms in Different Ensemble-Based Machine Learning Models with Various Types of Factor Data
Reprinted from: *Sustainability* **2023**, *15*, 13563, doi:10.3390/su151813563 . . . . . **39**

Hu Jiang, Qiang Zou, Bin Zhou, Zhenru Hu, Cong Li, Shunyu Yao and Hongkun Yao
Susceptibility Assessment of Debris Flows Coupled with Ecohydrological Activation in the Eastern Qinghai-Tibet Plateau
Reprinted from: *Remote Sens.* **2022**, *14*, 1444, doi:10.3390/rs14061444 . . . . . **88**

Marco Loche, Luigi Lombardo, Tolga Gorum, Hakan Tanyas and Gianvito Scaringi
Distinct Susceptibility Patterns of Active and Relict Landslides Reveal Distinct Triggers: A Case in Northwestern Turkey
Reprinted from: *Remote Sens.* **2022**, *14*, 1321, doi:10.3390/rs14061321 . . . . . **112**

Wubiao Huang, Mingtao Ding, Zhenhong Li, Jianqi Zhuang, Jing Yang, Xinlong Li, et al.
An Efficient User-Friendly Integration Tool for Landslide Susceptibility Mapping Based on Support Vector Machines: SVM-LSM Toolbox
Reprinted from: *Remote Sens.* **2022**, *14*, 3408, doi:10.3390/rs14143408 . . . . . **126**

Zijin Fu, Fawu Wang, Jie Dou, Kounghoon Nam and Hao Ma
Enhanced Absence Sampling Technique for Data-Driven Landslide Susceptibility Mapping: A Case Study in Songyang County, China
Reprinted from: *Remote Sens.* **2023**, *15*, 3345, doi:10.3390/rs15133345 . . . . . **148**

Junjie Ji, Yongzhang Zhou, Qiuming Cheng, Shoujun Jiang and Shiting Liu
Landslide Susceptibility Mapping Based on Deep Learning Algorithms Using Information Value Analysis Optimization
Reprinted from: *Land* **2023**, *12*, 1125, doi:10.3390/land12061125 . . . . . **182**

Chun Liu and Hongjun Liao
Buffer Capacity of Steel Shed with Two Layer Absorbing System against the Impact of Rockfall Based on Coupled SPH-FEM Method
Reprinted from: *Sustainability* **2022**, *14*, 13680, doi:10.3390/su142013680 . . . . . **204**

Guodong Liu, Zhijun Zhou, Shiqiang Xu and Yuanmeng Cheng
Post Evaluation of Slope Cutting on Loess Slopes under Long-Term Rainfall Based on a Model Test
Reprinted from: *Sustainability* **2022**, *14*, 15838, doi:10.3390/su142315838 . . . . . **217**

Mabkhoot Alsaiari, Basil Onyekayahweh Nwafor, Maman Hermana, Al Marzouki Hassan H. M. and Mohammed Irfan
Understanding the Mechanisms of Earth Fissuring for Hazard Mitigation in Najran, Saudi Arabia
Reprinted from: *Sustainability* **2023**, *15*, 6006, doi:10.3390/su15076006 . . . . . **243**

Edris Alam, Fahim Sufi and Abu Reza Md. Towfiqul Islam
A Scenario-Based Case Study: Using AI to Analyze Casualties from Landslides in Chittagong Metropolitan Area, Bangladesh
Reprinted from: *Sustainability* **2023**, *15*, 4647, doi:10.3390/su15054647 . . . . . **265**

Heni Masruroh, Soemarno Soemarno, Syahrul Kurniawan and Amin Setyo Leksono
A Spatial Model of Landslides with a Micro-Topography and Vegetation Approach for Sustainable Land Management in the Volcanic Area
Reprinted from: *Sustainability* **2023**, *15*, 3043, doi:10.3390/su15043043 . . . . . **285**

Xichun Jia, Wei Zhang, Xinghan Wang, Yuhao Jin and Peitong Cong
Numerical Analysis of an Explicit Smoothed Particle Finite Element Method on Shallow Vegetated Slope Stability with Different Root Architectures
Reprinted from: *Sustainability* **2022**, *14*, 11272, doi:10.3390/su141811272 . . . . . **311**

Yu Zhang, Jierui Feng, Longhuan Du, Peng Zhao, Jiao Peng, Chen Yang, et al.
Numerical Investigation of the Dynamic Response of a Sand Cushion with Multiple Rockfall Impacts
Reprinted from: *Sustainability* **2023**, *15*, 3554, doi:10.3390/su15043554 . . . . . **335**

Xianzheng Zhang, Chenxiao Tang, Yajie Yu, Chuan Tang, Ning Li, Jiang Xiong and Ming Chen
Some Considerations for Using Numerical Methods to Simulate Possible Debris Flows: The Case of the 2013 and 2020 Wayao Debris Flows (Sichuan, China)
Reprinted from: *Water* **2022**, *14*, 1050, doi:10.3390/w14071050 . . . . . **356**

Wenpeng Ning and Hua Tang
Dynamic Response Law and Failure Mechanism of Slope with Weak Interlayer under Combined Action of Reservoir Water and Seismic Force
Reprinted from: *Water* **2023**, *15*, 1956, doi:10.3390/w15101956 . . . . . **379**

Qing Guo, Lianzi Tong and Hua Wang
A Monitoring Method Based on Vegetation Abnormal Information Applied to the Case of Jizong Shed-Tunnel Landslide
Reprinted from: *Remote Sens.* **2022**, *14*, 5640, doi:10.3390/rs14225640 . . . . . **403**

Jiahao Yan, Yichen Zhang, Jiquan Zhang, Yanan Chen and Zhen Zhang
Study on the Source of Debris Flow in the Northern Scenic Spot of Changbai Mountain Based on Multi-Source Data
Reprinted from: *Remote Sens.* **2023**, *15*, 2473, doi:10.3390/rs15092473 . . . . . **423**

Zhixing Deng, Wubin Wang, Tengfei Yan, Kang Xie, Yandong Li, Yangyang Liu and Qian Su
In Situ Experimental Study of Natural Diatomaceous Earth Slopes under Alternating Dry and Wet Conditions
Reprinted from: *Water* **2022**, *14*, 831, doi:10.3390/w14050831 . . . . . **443**

Lidu Zhao, Xiaping Ma, Zhongfu Xiang, Shuangcheng Zhang, Chuan Hu, Yin Zhou and Guicheng Chen
Landslide Deformation Extraction from Terrestrial Laser Scanning Data with Weighted Least Squares Regularization Iteration Solution
Reprinted from: *Remote Sens.* **2022**, *14*, 2897, doi:10.3390/rs14122897 . . . . . **461**

Yajing Yan, Yongshuai Yan, Guizhang Zhao, Yanfang Zhou and Zhoufeng Wang
Combined ERT and GPR Data for Subsurface Characterization of Weathered Hilly Slope: A Case Study in Zhejiang Province, Southeast China
Reprinted from: *Sustainability* **2022**, *14*, 7616, doi:10.3390/su14137616 . . . . . **487**

Collin Cronkite-Ratcliff, Kevin M. Schmidt and Charlotte Wirion
Comparing Root Cohesion Estimates from Three Models at a Shallow Landslide in the Oregon Coast Range
Reprinted from: *GeoHazards* **2022**, *3*, 428–451, doi:10.3390/geohazards3030022 . . . . . **507**

Yiwei Zhang, Jianping Chen, Qing Wang, Yongchao Li, Shengyuan Song, Feifan Gu and Chen Cao
Sequence Analysis of Ancient River Blocking Events in SE Tibetan Plateau Using Multidisciplinary Approaches
Reprinted from: *Water* **2022**, *14*, 968, doi:10.3390/w14060968 . . . . . **531**

Fumeng Zhao, Wenping Gong, Tianhe Ren, Jun Chen, Huiming Tang and Tianzheng Li
Permafrost Stability Mapping on the Tibetan Plateau by Integrating Time-Series InSAR and the Random Forest Method
Reprinted from: *Remote Sens.* **2023**, *15*, 2294, doi:10.3390/rs15092294 . . . . . **550**

Yuming Wu and Hengxing Lan
Study on the Deformation of Filling Bodies in a Loess Mountainous Area Based on InSAR and Monitoring Equipment
Reprinted from: *Land* **2022**, *11*, 1263, doi:10.3390/land11081263 . . . . . **578**

Jian Wang, Yuming Wang, Yueli Li and Xiaotao Huang
Fast Displacement Estimation of Multiple Close Targets with MIMO Radar and MUSICAPES Method
Reprinted from: *Remote Sens.* **2022**, *14*, 2005, doi:10.3390/rs14092005 . . . . . **595**

About the Editors

Stefano Morelli

Stefano Morelli has been a professor at the Department of Pure and Applied Sciences (DiSPeA) of the University of Urbino in Physical Geography and Geomorphology since 2021. Previously, from 2005 to 2021, he carried out research activities at the Department of Earth Sciences of the University of Florence, where he was a fixed-term Researcher in Engineering Geology (2016–2019), a short-term Research Fellow (2005–2008) and a Research Assistant (2008–2016 and 2016–2109). He obtained a research doctorate in Geomorphology in 2010. His interests include the geomorphological evolution of river environments and methods for characterizing hydraulic risk in order to improve knowledge of the most effective methodologies and technologies to implement a national monitoring system. At the same time, his interests are oriented toward the protection, safeguarding and sustainable management of natural and anthropic territories and cultural heritage from slope instability risks via the synergistic use of new technologies and traditional methods. His main experiences in this research field relate to his participation in national and international projects (EU-founded and others) on landslides and slope stability analysis under both ordinary and emergency conditions. In particular, he has applied his experience in developing areas of the world, in some UNESCO sites, in national initiatives with the Italian Civil Protection system and in activities dealing with the improvement of resilience for populations threatened by harmful geological events. He is a permanent member of the Editorial Board of Geoenvironmental Disasters as an Editor. He has participated in some Special Issues as Lead Guest Editor, and he is the author or co-author of 40 peer-reviewed international publications (SCOPUS), several book chapters and conference proceedings in the field of geo-hydrological natural hazards (100 works from Scholar sources).

Veronica Pazzi

Veronica Pazzi received her M.Sc. degree in Environmental Engineering (with a thesis on geophysical methods applied to geo-archaeological problems) and her Ph.D. degree in Civil and Environmental Engineering (with a thesis on geophysical methods applied to environmental problems) from the University of Firenze (Florence, Italy) in 2007 and 2011, respectively. From 2011 to 2021, she was a Postdoctoral Researcher at the Department of Earth Sciences at the University of Florence. She also collaborates with the Centre for the Civil Protection of the University of Firenze, a Centre of Competence of the National Department of Civil Protection of the Italian Government for geo-hydrological hazards. From 2021 to 2024, she was a Researcher at the University of Trieste. Since 2024, she has been an Associate Professor in Applied Geophysics at the University of Firenze. Her research interests are focused on the many aspects of engineering geology and applied seismology. These mainly include geophysical investigations, especially electrical resistivity and passive seismic methods, applied to slope instability and the characterization of local seismic effects. Moreover, her field of application is in the development of methods for hazard, vulnerability, risk, and resilience assessment, with special attention to buildings and cultural heritage sites. She is a member of the SEG, EAGE, EGU, IAEG Italian Section, AIGEO and AIGA societies. She is the Editor of *NHESS*, *Landslides*, the *International Journal of Disaster Risk Reduction* and the *International Journal of Geophysics*, as well as many Special Issues in different journals. She has authored about 50 papers (source SCOPUS) and is a reviewer for many international peer-reviewed journals. Since 2022, she has been the Scientific Officer of the EGU NH3—Landslides and Avalanches subdivision.

Mirko Francioni

Mirko Francioni is a professor of Engineering Geology at the University of Urbino, Carlo Bo (Italy). His research mainly involves the combined use of remote sensing, GIS and numerical simulations for the study of natural and engineering slopes. During his academic career, he received his Ph.D. in Engineering Geology at the University of Siena. After obtaining his Ph.D., he worked in Canada (Simon Fraser University) as a post-doctoral researcher, in the UK as a lecturer (University of Exeter) and in Italy as a research fellow and senior researcher (University of Chieti and University of Urbino, respectively). Over the course of these years, he developed new methods for the use of remote sensing/GIS data for conventional and numerical slope analyses. He has participated in several international projects in Africa, Canada, the UK and Italy. Mirko has been the PI of two national (at the University of Exeter and the University of Urbino) and one international project (at the University of Urbino). He has collaborated and performed field work with many universities around the world and has also worked as a consultant for geological engineering and exploration companies in Canada and Italy. He currently serves on the scientific committee of the Italian Association of Engineering Geology and Environment. In 2018, he was appointed as an Honorary Lecturer in Mining Engineering at the University of Exeter, and in the same year, he was awarded by the American Association of Environmental and Engineering Geologists (AEG) with a Publication Award (the best paper from the last four issues of Environmental and Engineering Geoscience). In 2020, Mirko received the Italian National Scientific Habilitation for full professorship.

Preface

This reprint is the second of three volumes that collect articles on the topic of Natural Hazards and Disaster Risks Reduction. It focuses on slope instability and landslides hazard demonstrating how endogenous and exogenous environmental processes that regulate the Earth's system can lead, in some cases, to the formation of sudden and violent natural occurrences, with uneven impacts on the Earth. Climate change and human actions can worsen these phenomena. These events can threaten human life and community safety, especially when they interact with inhabited areas. The unregulated development of human activities has made society increasingly vulnerable and in need of intervention. The content of these works provides a useful compendium for supporting scientists engaged in the study of the discussed phenomena and the search for implementing specialized solutions. Additionally, thanks to the applicative characteristics of the content, it is useful for public administration technicians who intend to work on security in areas subject to such natural adversities that are in pursuit of sustainable development.

Stefano Morelli, Veronica Pazzi, and Mirko Francioni
Editors

sustainability

MDPI

Article

Regional Landslide Hazard Assessment Using Extreme Value Analysis and a Probabilistic Physically Based Approach

Hyuck-Jin Park [1,*], Kang-Min Kim [2], In-Tak Hwang [1] and Jung-Hyun Lee [1]

[1] Department of Energy Resources and Geosystem Engineering, Sejong University, Seoul 05006, Korea; intak999@gmail.com (I.-T.H.); jhlee6086@gmail.com (J.-H.L.)
[2] Department of Geography, Kyung Hee University, Seoul 02453, Korea; kmkim0208@khu.ac.kr
* Correspondence: hjpark@sejong.ac.kr; Tel.: +82-2-3408-3965

Abstract: The accurate assessment of landslide hazards is important in order to reduce the casualties and damage caused by landslides. Landslide hazard assessment combines the evaluation of spatial and temporal probabilities. Although various statistical approaches have been used to estimate spatial probability, these methods only evaluate the statistical relationships between factors that have triggered landslides in the past rather than the slope failure process. Therefore, a physically based approach with probabilistic analysis was adopted here to estimate the spatial distribution of landslide probability. Meanwhile, few studies have addressed temporal probability because historical records of landslides are not available for most areas of the world. Therefore, an indirect approach based on rainfall frequency and using extreme value analysis and the Gumbel distribution is proposed and used in this study. In addition, to incorporate the nonstationary characteristics of rainfall data, an expanding window approach was used to evaluate changes in the mean annual maximum rainfall and the location and scale parameters of the Gumbel distribution. Using this approach, the temporal probabilities of future landslides were estimated and integrated with spatial probabilities to assess and map landslide hazards.

Keywords: temporal probability; spatial probability; landslide hazard; physically based model; extreme value analysis

Citation: Park, H.-J.; Kim, K.-M.; Hwang, I.-T.; Lee, J.-H. Regional Landslide Hazard Assessment Using Extreme Value Analysis and a Probabilistic Physically Based Approach. *Sustainability* **2022**, *14*, 2628. https://doi.org/10.3390/su14052628

Academic Editors: Stefano Morelli, Veronica Pazzi and Mirko Francioni

Received: 26 January 2022
Accepted: 22 February 2022
Published: 24 February 2022

1. Introduction

Landslides occur frequently, not only in Korea but also around the world, and cause severe damage to human lives and property. To prevent or reduce damage, injuries, and death caused by landslides, there is a need for landslide hazard analysis, which estimates the probability of a potential landslide occurrence within a given period of time and over a specific area [1,2]. That is, the spatial and temporal probabilities of landslide occurrence should be analyzed to determine landslide hazards. The spatial probability of landslide occurrence, which is also known as landslide susceptibility, predicts where a landslide may occur. A large number of studies have been conducted on landslide susceptibility using a variety of approaches. Landslide susceptibility analyses are generally either statistically or physically based [3–6]. Statistical approaches acquire knowledge of susceptibility obtained through the statistical analysis of the relationship between landslide occurrences and various conditioning factors [5,7–13]. However, when applied to a wide area, statistical analysis requires considerable data on both landslide distribution and conditioning factors. In addition, statistical analysis considers the statistical relationship between landslides and conditioning factors exclusively without the consideration of slope failure mechanisms [14]. Therefore, in recent years, physically based analysis, which incorporates the physical processes and mechanisms of landscape occurrence, has been used with a physical slope model to estimate the spatial probability of landslide occurrence independent of its occurrence history [14–32]. This is, therefore, a very promising approach

to shallow landslide susceptibility analysis [33]. Moreover, a grid-based analytical structure provides a convenient framework for wide-area coverage in a geographic information system (GIS) environment [34].

In contrast, temporal landslide probability predicts when landslides may occur. Relative to landslide susceptibility analysis, few temporal probability studies have been conducted. In general, temporal probability has been evaluated using the statistical analysis of landslide frequency through long-period multitemporal landslide inventory [35–41]. However, considerable time and effort are required to construct the necessary multitemporal landslide inventory and, accordingly, these data are not available in most areas. An indirect approach based on the frequency of landslide-triggering events (i.e., earthquake or rainfall events) is, therefore, proposed. In this approach, recognizing that landslides are mainly caused by rainfall events, the temporal probability of such rainfall events is adopted as the temporal probability of landslide occurrence [42–49]. A rainfall threshold for landslide occurrence is determined and then historical rainfall data are analyzed to derive the probability that the rainfall threshold will be exceeded by a certain rainfall event (the exceedance probability). The rainfall exceedance probability is observed as an effective surrogate for temporal landslide probability [37,42,43,45,46,48]. The advantages of this approach are that a complete multitemporal inventory is not required and that temporal probability can be estimated wherever historical rainfall records, which can be easily obtained from rainfall gauges, are available.

In this research, temporal landslide probability was estimated using historical rainfall records. Then, landslide hazard was calculated by combining temporal probability with the spatial probability obtained by conducting a physically based analysis. This approach was adopted in the Jinbu region of Gangwon-do, Korea, where many landslides occurred in July 2006 as a result of extreme rainfall. This approach can also help to solve a global social issue. Achour [50] noted that landslide hazard analysis is one of the significant measures necessary for land use planning and disaster risk reduction, supporting target 15.3 ("By 2030, combat desertification, restore degraded land and soil, including land affected by desertification, drought and floods, and strive to achieve a land degradation-neutral world") of the United Nations 2030 Sustainable Development Goals (SDGs). Our approach will, therefore, contribute to the achievement of the UN's SDGs, especially goals 13 ("Take urgent action to combat climate change and its impacts") and 15 ("Sustainably manage forests, combat desertification, halt and reverse land degradation, halt biodiversity loss").

2. Materials and Methods

2.1. Study Area

The Jinbu area was selected for testing the proposed approach because it experienced an extreme rainfall event from 14 to 16 July 2006, with numerous landslides being reported (Figure 1). The study area is at latitude 37°33′20″ N–37°39′26″ N and longitude 128°29′49″ E–128°36′36″ E and is mostly mountainous, with an average altitude of about 660 m. The predominant lithological units are Triassic Nokam formation and Imgye granite (Figure 2). These are located on a Precambrian biotite gneiss. The Nokam formation is mostly fine sandstone and sandy shale, and the Jurassic Imgye granite, which occurs as batholiths, consists of granite with syenite and diorite. Ordovician limestone, with a small amount of sandstone and shale, is also distributed across the area. The region was extensively intruded by granitoids during the Daebo Orogeny, which lasted from the Jurassic to the Cretaceous periods [14,51].

To construct a landslide inventory, landslide locations were identified by conducting the comparison of 0.5 m resolution aerial photographs, obtained from the National Geographic Information Institute (Suwon, Korea), taken before and after the 2006 event. A total of 1310 landslides were identified (Figure 1). This is the only landslide record for this study area, given that no other landslide occurrence, either before or after the 2006 event, has been reported. The identified landslides in this area were translational shallow landslides. Their length and width ranged from 30 to 1200 m and from 4 to 20 m, respectively. Their

depth to failure plane ranged from 0.5 to 3 m. They started as translational shallow slides and became flow-type landslides as they moved downward. Rainfall data from 1973 to 2017 were obtained from the Sangjinbu rainfall station (latitude 37°39′32″ N and longitude 128°34′41″ E), which is the most reliable rainfall station in the area.

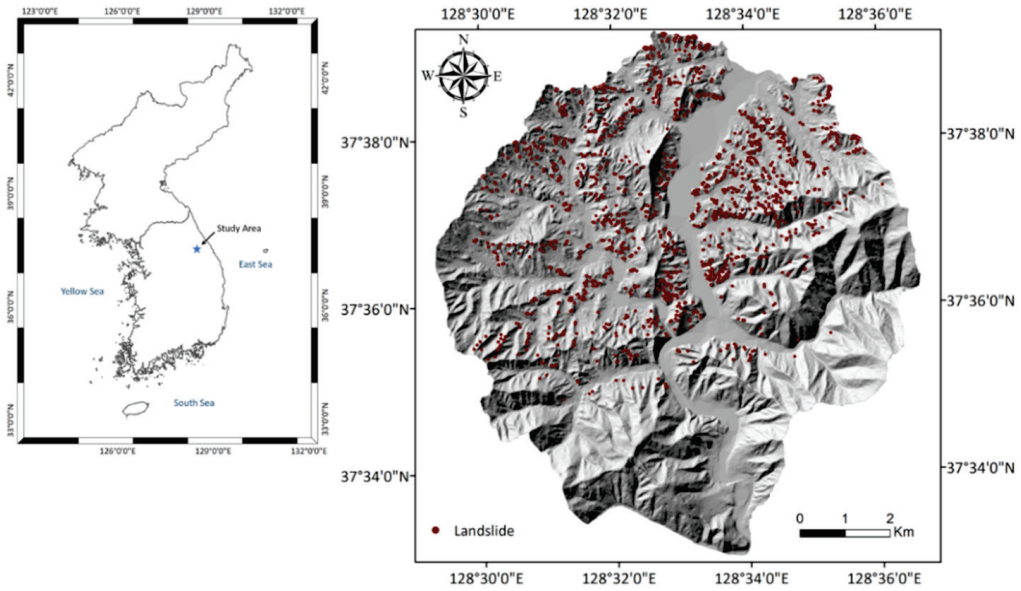

Figure 1. The study area and location of the landslides.

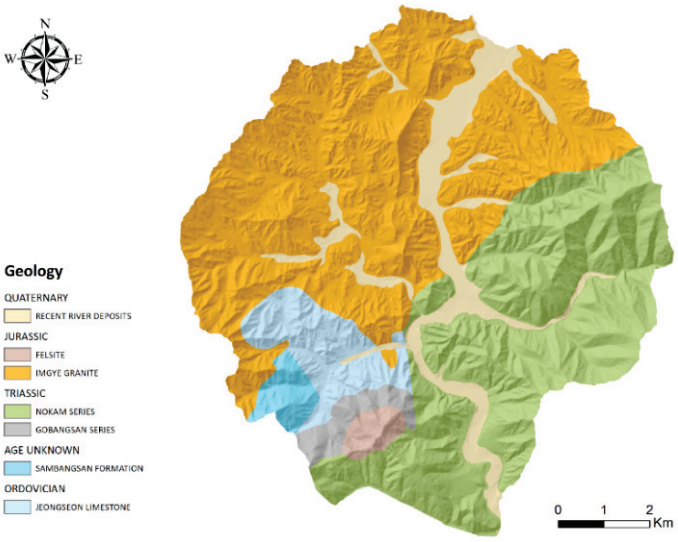

Figure 2. Geology of the study area.

2.2. Evaluation of Temporal Probability

2.2.1. Extreme Value Analysis

In this study, an indirect approach to the evaluation of the temporal landslide probability was adopted. Specifically, the temporal probability of a landslide-triggering rainfall event was evaluated by conducting statistical analysis on historic rainfall data, and the probability of such a rainfall event was adopted as the temporal probability of a landslide occurring. A rainfall threshold, the minimum rainfall required to initiate landslides [48], was first determined. Based on rainfall records and the literature, the rainfall threshold in this area was estimated as 227 mm over a 24 h time period; in July 2006, this threshold was reached and triggered landslides [52]. Once this threshold was determined, its exceedance probability could be calculated. In previous studies, exceedance probabilities have been

evaluated using a binomial or Poisson distribution model [37,42,45,46,53–55]. However, the use of these models requires an estimate of the mean recurrence interval for the periods between landslide-triggering events. Where no recurrent landslide event has been recorded, such as in this study area, it is impossible to estimate the recurrence interval [56]. Therefore, extreme value analysis, which is able to infer the probabilities of future extremes using past records, was used to evaluate the exceedance probability. This can be applied even in areas where no recurrent landslide-triggering rainfall has been observed. Extreme value analysis is recognized as appropriate for the analysis of the temporal probability of shallow landslides caused by intense rainfall [48]. Therefore, it has been widely used in the context of extreme hydrological events. In extreme value analysis, the maximum rainfall event in a given year, the annual maximum (AM), is considered to follow a generalized extreme value (GEV) distribution [56,57]. Among various GEV distributions, the Gumbel distribution (extreme value type I) has been adopted to estimate the temporal probability of rainfall-induced landslides [39,46,48,49,58–63]. In addition, the Gumbel distribution has been applied to determine the frequency of extreme rainfall events in Korea [64]. The cumulative Gumbel distribution is evaluated by the following:

$$F_{GUM}(x) = exp\left\{-exp\left(-\frac{x-u}{\alpha}\right)\right\}, -\infty < x < \infty, \quad (1)$$

where u is the location parameter and α is the scale parameter. Subsequently, the exceedance probability of a rainfall event for a specific year is evaluated by the following.

$$p = 1 - F_{GUM}(x) = 1 - exp\left\{-exp\left(-\frac{x-u}{\alpha}\right)\right\} \quad (2)$$

To evaluate the exceedance probability by adopting the Gumbel distribution, Gumbel parameters (i.e., location and scale parameters) must be estimated. The method of moments, which assumes the equality of population and sample moments, has commonly been applied to estimate the parameters for a given probability model [39,62]. In this study, the method of moments was used to estimate Gumbel parameters.

2.2.2. Nonstationary Approach

Previously, extreme value analysis assumed processes to be stationary, which means that historical rainfall data are invariant over extended time periods. However, increases in extreme rainfall frequency and intensity caused by climate change have been reported by many recent studies. The stationary assumption, with unchanging AM values and Gumbel parameters, is therefore not valid. A nonstationary model should respond to changes in AM rainfall and consequent changes in Gumbel parameters. Zeng et al. [65] proposed an expanding window approach to analyze nonstationarity in AM rainfall. The expanding window begins with a given minimum size at a fixed starting point, but as the analysis progresses into the time series, the window expands to include each new data value rather than only a finite and constant widow size [66]. Initially, a 20-year window of historical data, as suggested previously [67], was used to evaluate the mean AM and Gumbel parameters. Next, the period window was expanded to include 21 years. This procedure was repeated until all the data years were included. In this study, rainfall data from 1973 to 2017 were available, and the mean AM rainfall and Gumbel parameters were initially calculated from 1973 to 1992. Using the expanding window, the means and parameters were then obtained for 1973 to 1993, etc. This approach is able to reveal any nonstationary trend in mean and statistical parameters.

2.3. Evaluation of Spatial Probability

Spatial probability was calculated using a physically based approach. As recent landslides triggered by heavy rainfall are mainly shallow, the infinite slope model, which is widely used for shallow-depth slope failure, was used as the physical model. Previously,

the infinite slope model has mainly been used to assess the stability of individual slopes. With the rapid development of GIS-based analysis, the infinite slope model can now be used to analyze shallow landslide susceptibility over broad areas.

The infinite slope model evaluates a factor of safety (FS) based on the concept of limit equilibrium. It analyzes the equilibrium of a potentially unstable mass by comparing the driving force, the force tending to slide along the failure plane, with the resisting force, which is the shear strength. If the groundwater height is assumed to be z_w above the sliding plane (Figure 3), the equation used for calculating FS using the infinite slope model is as follows:

$$\mathrm{FS} = \frac{c + (\gamma D - \gamma_w z_w)\cos^2 \alpha \tan \phi}{\gamma D \sin \alpha \cos \alpha} \quad , \tag{3}$$

where c and ϕ are the cohesion and effective friction of the slope materials; γ and γ_w are the unit weights of the slope materials and water, respectively; D is the vertical depth to the failure surface; z_w is the groundwater level; and α is the angle of the slope.

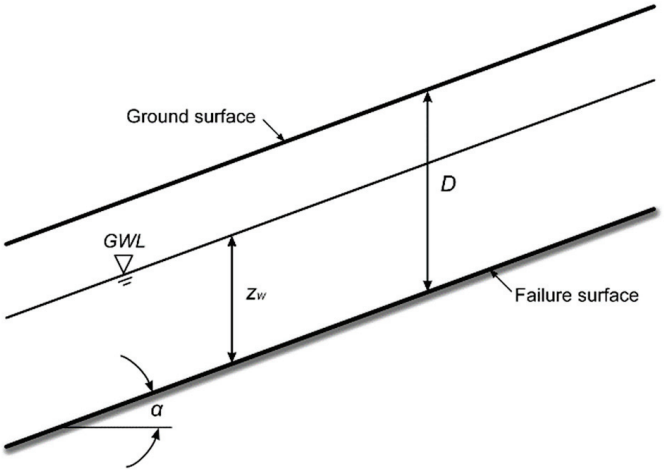

Figure 3. The infinite slope model.

A transient hydrological model was used to estimate z_w. The transient infiltration model is a process used for estimating pore pressure changes during rainfall infiltration. This was used in conjunction with a grid-based regional slope stability model (Transient Rainfall Infiltration and Grid-Based Regional Slope-Stability Model, TRIGRS) [68], which estimates shallow landslide occurrence by combining the transient pressure increases caused by rainfall and infiltration [69]. The infiltration model was based on Iverson's [70] solution, which provides a theoretical background to the influence of hydrologic processes on landslide locations and occurrence times derived using the Richards' equation [18,27]. This evaluates transient infiltration by modeling pore water pressure. TRIGRS was coupled with Monte Carlo simulation (MCS) for the spatial probability assessment carried out in this study. In MCS, the values of predictive variables are randomly generated according to their probability density functions (PDFs). This technique is widely used for probabilistic analysis because of its robustness and conceptual simplicity. Here, FS values were calculated from sets of these randomly generated input values. After numerous iterations, the failure probability was evaluated from the repeated FS values. This calculation was carried out for all pixels throughout the study area, and the results were mapped as the spatial distribution of landslide probability.

2.3.1. Construction of a Spatial Database of Input Parameters

The physical slope model requires input parameters such as geometric characteristics and strength parameters for the slope materials. Geometric input parameters can be obtained from topographic data and strength parameters can be acquired from field investigation and laboratory tests. A digital elevation model (DEM) was constructed to

obtain the geomorphic attributes of the study area using digital topographic maps acquired from the National Geographic Information Institute. Then, a thematic map for the slope angle (Figure 4) was created using DEM. In addition, soil thickness, which is the depth to the failure surface, was acquired from digital soil maps obtained from the National Institute of Agricultural Science (NIAS, Jeollabuk-do, Korea). The obtained map was converted into a grid-based (raster) layer, providing a thematic map of soil thickness with a 10 m resolution (Figure 5).

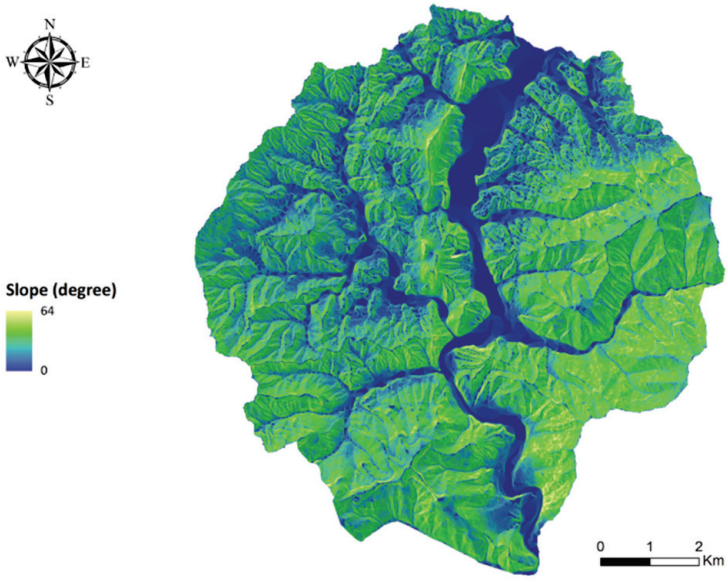

Figure 4. Distribution of slope angle.

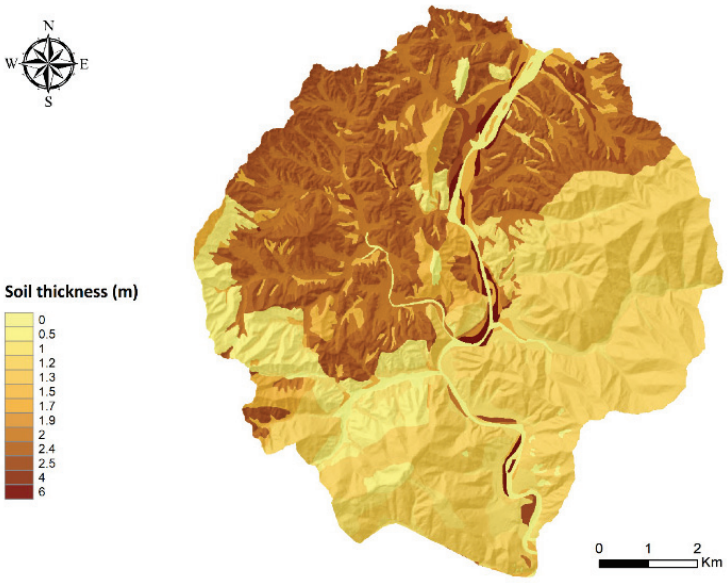

Figure 5. Distribution of soil thickness.

The calculation of spatial probability using a physically based method (Equation (3)) requires strength parameters (cohesion and friction angle), unit weight, and the hydraulic conductivity of slope materials, since these are indispensable input parameters in physically based analyses [71]. These parameters should be obtained from laboratory tests of soil samples collected from the field. Twenty soil samples were collected from the study area. The geotechnical parameters were obtained from direct shear tests conducted on the slope materials. Other laboratory tests (such as permeability tests) were carried out to obtain

the hydraulic conductivities and unit weights of the soils. These were considered as deterministic parameters.

Slope material is composed of soils developed from underlying rocks, and soil properties such as geotechnical and hydrological parameters are strongly affected by the rock type involved. The soil samples used for laboratory tests were, therefore, collected from areas with different underlying rock types. The geotechnical and hydrological parameters listed in Table 1 are linked to the underlying rock type. While the mean values of the strength parameters were calculated using test data, there was substantial uncertainty because the quantity of test data was limited compared with the size of the study area. Therefore, high values for their coefficients of variation (COV) (namely, 30% for cohesion and 15% for friction angle) were used in this analysis. To estimate the groundwater height using the hydrological model, hourly rainfall data were acquired from Sangjinbu automatic weather station (Figure 6). The landslides began around 10:00 on 15 July, and 227 mm (in the previous 24 h) was considered as the landslide-triggering rainfall threshold [52].

Table 1. Input parameters for the physically based model.

Geological Formation	Friction Angle (°)		Cohesion (kPa)		Unit Weight (kN/m^3)	Hydraulic Conductivity (m/h)
	Mean	COV (%)	Mean	COV (%)		
Felsite	20.8	15	17.5	30	17.8	0.171
Quartzite in Sambangsan	40.6	15	8.0	30	19.3	0.096
Imgye granite	35.2	15	3.8	30	23.2	0.089
Jeongseon limestone	28.4	15	4.4	30	17.9	0.019
Sandstone in Nokam	40.2	15	10.4	30	18.4	0.090
Sandstone in Gobangsan	37.1	15	7.8	30	18.7	0.084

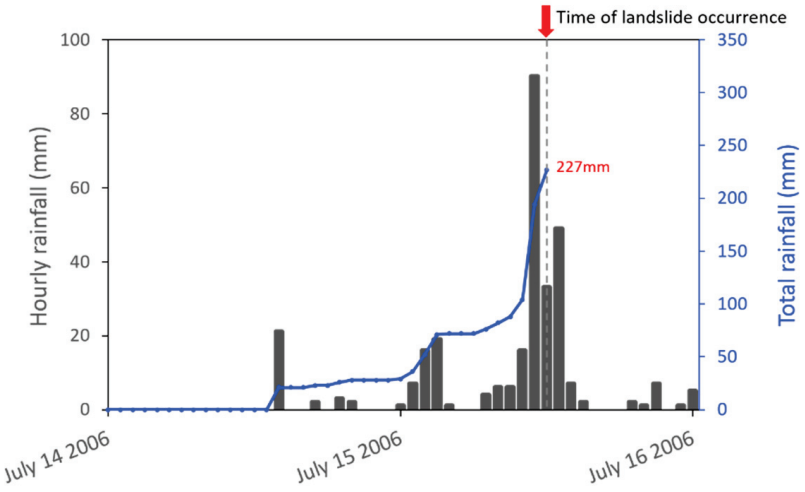

Figure 6. Hourly rainfall, 14–16 July 2006.

2.3.2. Monte Carlo Simulation

In probabilistic analyses, using MCS, cohesion and friction angle, the major sources of uncertainty as a consequence of limited sampling and spatial variability, were considered as random variables. Their statistical properties, as required for MCS, were based on a normal PDF, as previous studies have suggested [21,72–80]. Their assigned means and COVs are shown in Table 1. In the MCS process, uniformly distributed random numbers between zero and one were generated, then random values for each input variable were calculated using the generated random numbers corresponding to the cumulative normal distribution function for each input variable. The generated parameters were used, in combination with the deterministic input data, to calculate 5000 individual FS values for

each pixel. Then, the failure probability, or the proportion of cases in which FS was less than 1, was determined. This process was conducted for all pixels in the study area to produce a landslide probability distribution map.

3. Results

3.1. Temporal Probability of Landslide Occurrence

The Sangjinbu rainfall time series from 1973 to 2017 were used to determine the nonstationary character of the local rainfall data using the expanding window approach. The maximum 24 h rainfall value for each year was calculated from hourly rainfall data and designated as the AM rainfall for that year. Then, the mean AM values and Gumbel parameters were calculated for the first 20 years of data (1973–1992). By adding rainfall data for each year to the initial 20 years of data, new mean AM and Gumbel parameters were then derived. Table 2 shows the mean AM and location and scale parameters for different time periods under this method.

Table 2. Mean AM rainfall and the parameters of the Gumbel distribution using an expanding window.

No.	Data Period	Location Parameter	Scale Parameter	Mean of AM Rainfall
1	1973–1992	110.42	50.12	140.4
2	1973–1993	109.38	50.91	138.8
3	1973–1994	106.18	50.40	135.6
4	1973–1995	109.10	50.01	138.5
5	1973–1996	111.02	50.46	140.0
6	1973–1997	113.05	49.37	141.7
7	1973–1998	115.45	49.85	144.0
8	1973–1999	118.18	49.97	147.1
9	1973–2000	116.54	49.98	145.2
10	1973–2001	116.88	49.73	145.1
11	1973–2002	119.60	50.49	148.7
12	1973–2003	120.84	49.87	149.6
13	1973–2004	120.57	50.19	148.9
14	1973–2005	121.34	50.31	149.2
15	1973–2006	123.82	50.77	153.1
16	1973–2007	122.81	50.35	151.9
17	1973–2008	124.10	50.94	152.9
18	1973–2009	126.16	50.33	155.3
19	1973–2010	126.28	50.81	155.0
20	1973–2011	128.40	50.59	157.9
21	1973–2012	125.95	51.43	155.7
22	1973–2013	126.25	50.86	155.6
23	1973–2014	125.42	50.59	154.6
24	1973–2015	122.44	51.02	152.1
25	1973–2016	124.28	51.21	154.4
26	1973–2017	122.87	51.13	153.1

Linear regression was then used to check for temporal trends in the mean AM and Gumbel parameters to estimate the AM values and Gumbel parameters for future years. Figure 7 shows the results of the linear regression for mean AM. The linear regression equation used was as follows:

$$Mt = (0.7677 \times N_t) - 1390.2, \quad (4)$$

where Mt is the mean AM for the year N_t. Using this equation, the mean AM for future target years can be estimated. The Gumbel parameters were estimated, for future years, using linear regressions between the mean AM values and the location and scale parameters (Figures 8 and 9). Equation (5) is the linear regression equation used for estimating location

from the mean AM, while Equation (6) is the regression equation used for the scale and mean AM:

$$u_T = 0.9863 \times Mt - 27.077, \quad (5)$$

$$\alpha_T = 0.0215 \times Mt + 47.231, \quad (6)$$

where u_T is the location parameter, Mt is the mean AM, and α_T is the scale parameter for the target year. Using these equations, the mean AM and the scale and location parameters of the Gumbel function for each of the next N_i years from the final year of rainfall data, 2017, were estimated for N_i = 10, 50, 100, and 150 (Table 3). From these values, future exceedance probabilities can be calculated using the Gumbel distribution function, and these values can be considered as the temporal probability of landslide occurrence. Table 4 shows the temporal landslide probabilities over the four analyzed time periods.

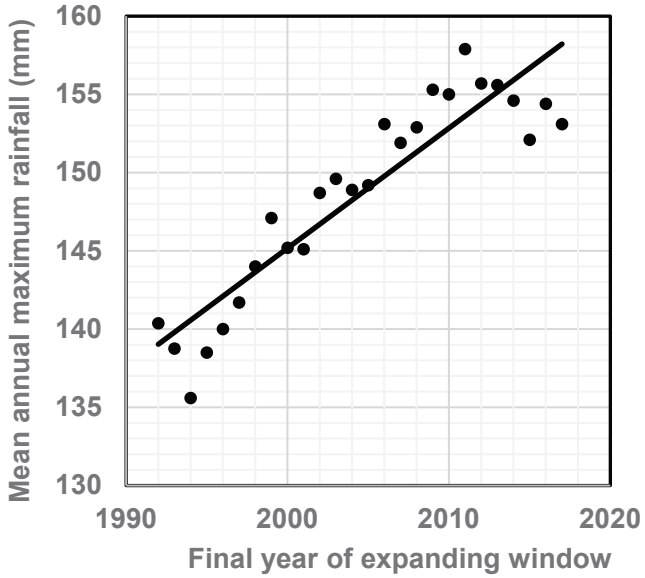

Figure 7. Relationship between the mean annual maximum (AM) rainfall and time using an expanding window.

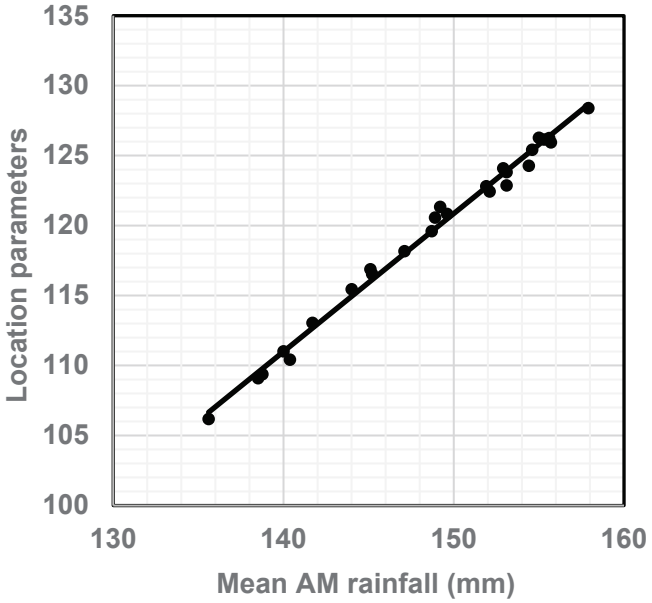

Figure 8. Relationship between the mean annual maximum (AM) rainfall and location parameters.

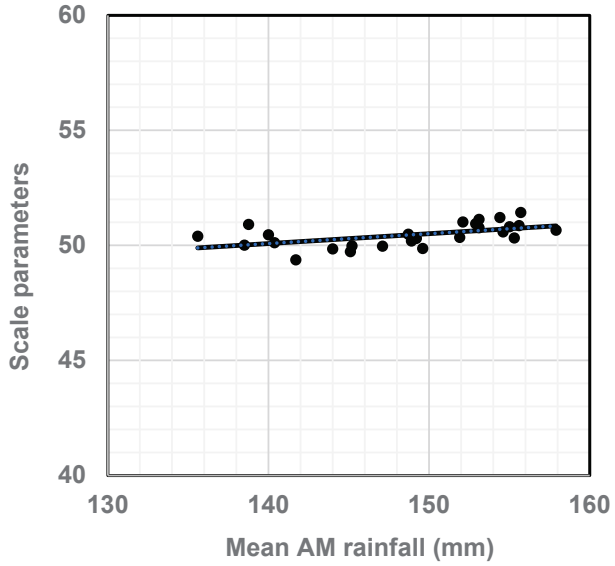

Figure 9. Relationship between the mean annual maximum (AM) rainfall and scale parameters.

Table 3. Mean AM and statistical parameters of the Gumbel distribution over the next N_i years.

Period N_i (Years)	Mean AM	Location Parameter	Scale Parameter
10	160.6	131.35	50.69
50	191.3	161.64	51.35
100	229.7	199.50	52.17
150	268.1	237.35	53.00

Table 4. Temporal probability of landslide occurrence over the next N_i years.

Period N_i (Years)	Temporal Probability
10	0.2197
50	0.3659
100	0.6145
150	0.8575

3.2. Spatial Probability of Landslide Occurrence

Figure 10 maps the distribution of the spatial landslide probability. A receiver operating characteristics (ROC) graph was used to evaluate model performance. In the analysis, true class (landslide occurrence) is compared with modeled class (landslide prediction) using a confusion matrix [3]. Here, the analyzed grid cells (i.e., modeled class) were classified as unstable or stable for comparison with the landslide occurrence (i.e., true class). In previous studies [27,30,33,77,81–83], a landslide probability greater than 10% has been used as the criterion for an unstable area; hence, a grid cell with a probability greater than 10% was classified here as unstable. It was found that 71.3% of the observed landslide locations were classified as unstable. That is, the true positive rate (TPR; the number of correctly predicted landslide pixels over the total number of landslide occurrence pixels) was 0.713. In addition, 27.4% of the nonlandslide pixels were mapped as unstable; that is, the false positive rate (FPR) was 0.274. Model performance was evaluated as 71.9% on the basis of the area under the curve (AUC) value.

3.3. Landslide Hazards

Landslide hazard was evaluated by multiplying the temporal probability of landslide, obtained from extreme value analysis, by spatial probability, which was obtained using a physically based model and MCS. The landslide hazards for four future time periods (10,

50, 100, and 150 years) were calculated (Table 5) and are mapped in Figure 11. As expected, the landslide hazard values increased as the time period increased. In the 10-year-period landslide hazard map, no pixels had landslide hazard values of over 0.2. Moreover, for the 10- and 50-year periods, all pixels were less than 0.5, which means that there was a low landslide hazard area. When the landslide hazard maps for 10 and 50 years were compared with the spatial probability map, landslide hazards were substantially lower than the spatial probability of landslide occurrence. This is because the temporal probabilities that were multiplied by the spatial probabilities to obtain the landslide hazards over the 10- and 50-year periods were small: 22.0% and 36.6%, respectively.

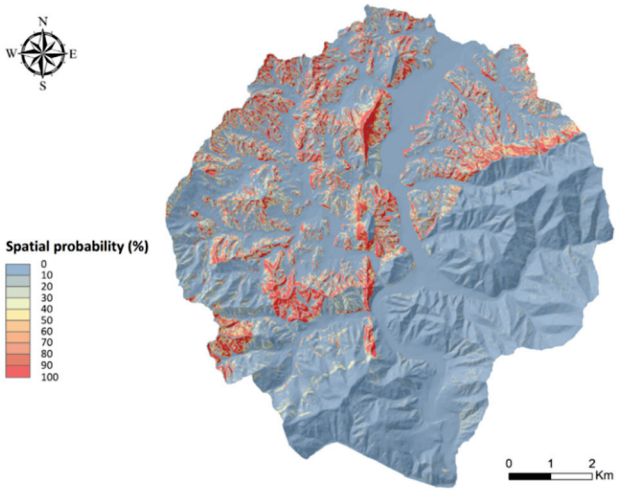

Figure 10. Spatial probability of landslide occurrence.

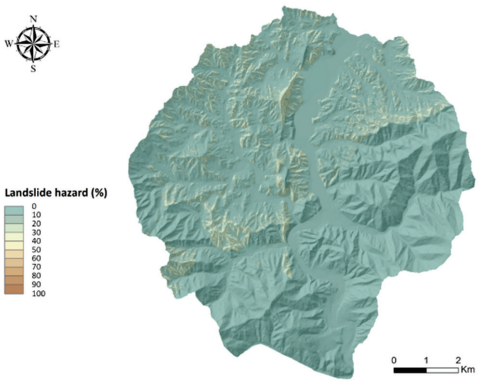

(**a**)

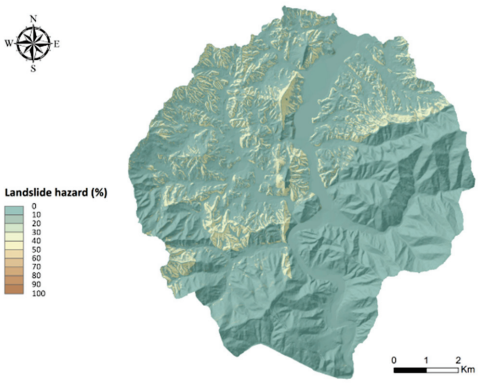

(**b**)

Figure 11. *Cont.*

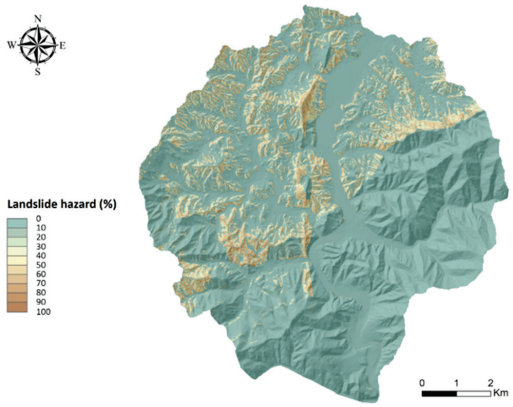

(**c**)

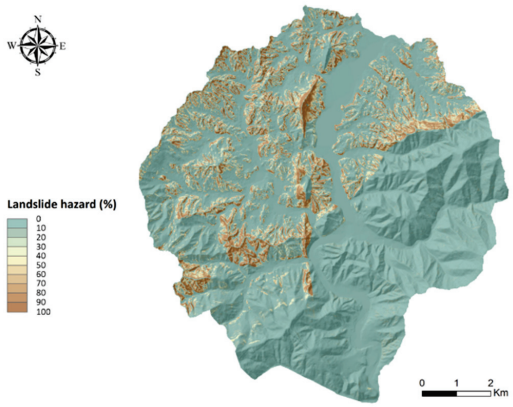

(**d**)

Figure 11. Landslide hazard maps. (**a**) 10 years; (**b**) 50 years; (**c**) 100 years; (**d**) 150 years.

Table 5. Proportion (%) of landslide hazard values.

Time Period (Years)	Landslide Hazard									
	0–0.1	0.1–0.2	0.2–0.3	0.3–0.4	0.4–0.5	0.5–0.6	0.6–0.7	0.7–0.8	0.8–0.9	0.9–1.0
10	85.90	9.21	4.89							
50	82.02	5.76	5.31	6.91						
100	78.02	5.23	3.36	2.98	3.19	5.66	1.56			
150	74.47	6.26	3.01	2.37	2.14	2.11	2.30	3.22	4.12	

The landslide hazard values for the 100- and 150-year periods were, as expected, larger than those in the 10- and 50-year periods. The proportion of high-hazard pixels (hazard value > 0.5) in the 100- and 150-year periods was greater: for 100 years, 7.22%, and for 150 years, 11.75%. This is because of the greater temporal probabilities found for the 100- and 150-year periods: 61.5% and 85.8%, respectively.

4. Discussion and Conclusions

We proposed a process to estimate temporal landslide probability using extreme value analysis and spatial probability using a physically based model. In previous studies, temporal probability was estimated by using frequency analysis of historical landslide occurrences or, indirectly, of rainfall events that triggered landslides. For this, sufficient data on repetitive landslides or recurrent rainfall events are required. However, in many cases it is practically impossible to obtain sufficient data on either landslide occurrence or recurrent landslide-triggering rainfall events. Therefore, this study adopted extreme

value analysis to evaluate temporal probability. This approach can be applied in areas where a multitemporal inventory is not available or where a single landslide event has occurred. Extreme value type I distribution, also known as the Gumbel distribution, was used to analyze time series rainfall data and estimate the triggering threshold exceedance probability. Moreover, to accommodate the nonstationary character of rainfall records in a time of climate change, the expanding window method was adopted, and changes in AM rainfall and the Gumbel parameters were estimated. Rainfall data from 1973 to 2017 were used and AM rainfall and Gumbel parameters for four future periods (10, 50, 100, and 150 years hence) were estimated using linear equations derived by the expanding window method. The temporal probabilities of landslide occurrence for the next 10, 50, 100, and 150 years were calculated, and their values were 0.2197, 0.3659, 0.6145, and 0.8575, respectively. Spatial probabilities were evaluated using a physically based approach and the infinite slope model, in conjunction with probabilistic analysis. Input parameters were obtained from laboratory tests and a DEM, with the strength parameters considered as random variables because of their uncertainty and variability. Subsequently, MCS, known as the most complete probabilistic method, was used to account for the uncertainty and estimate the spatial probabilities. Finally, temporal and spatial probabilities were combined to estimate the landslide hazard for future periods.

The proposed approach overcomes the shortcomings of previous studies that determined temporal probability from the frequency analysis of recurrent events. When a multitemporal inventory of historical landslide data is not available or no recurrent landslide events have occurred in an area, as in our case, the existing approach cannot estimate temporal probability. Therefore, an extreme value model (based on the Gumbel distribution) was used to obtain temporal probabilities from available time series rainfall data for the study area. This approach can be used when the conventional approach is impossible. In addition, our approach estimated nonstationary temporal probability, which previous stationary extreme value analyses could not calculate, by using an expanding analytical window. In this manner, the temporal probabilities of landslide occurrence for several different periods were obtained and combined with spatial probabilities, obtained from the probabilistic physically based approach, to evaluate landslide hazard. In previous work, spatial probabilities were estimated using statistical analysis or machine learning methods. However, it has been argued that translating the results of statistical analysis into spatial probabilities may not be appropriate, since the landslide susceptibility index from statistical analysis could not be replaced directly with spatial probability [84]. Therefore, this study used a more appropriate approach by estimating, in combination with probabilistic analysis, physically based spatial probabilities.

However, our proposed approach has some limitations. In this study, only the strength parameters of slope materials were considered as random variables in the MCS in order to limit computational time and effort. However, uncertainty and variability also could be involved in hydrological parameters and the unit weight of soil, and these could also be considered as random variables in future research. In addition, climate change and its influence on landslide occurrence can vary substantially, even over small distances [85]. In our experience, rainfall in this study area has a nonstationary trend, but other rainfall gauges located some distance from the study area suggest a more stationary character. Therefore, it is critical to carefully scrutinize stationarity in rainfall data. Finally, since information about elements at risk and their vulnerability was not available for our study area, it was not possible to fully assess landslide risks—that is, the accurate assessment of threat to life and property. To reduce or prevent the damages and fatalities caused by landslide occurrences effectively, landslide risk should be evaluated in future studies.

Author Contributions: Conceptualization, H.-J.P. and K.-M.K.; methodology, K.-M.K. and I.-T.H.; software, J.-H.L.; validation, J.-H.L.; formal analysis, K.-M.K. and I.-T.H.; investigation, J.-H.L.; resources, J.-H.L.; data curation, J.-H.L.; writing—original draft preparation, H.-J.P.; writing—review and editing, H.-J.P.; visualization, I.-T.H.; supervision, H.-J.P.; project administration, H.-J.P.; funding acquisition, H.-J.P. All authors have read and agreed to the published version of the manuscript.

Funding: This research was supported by a National Research Foundation of Korea (NRF) grant funded by the Korean government (MSIT) (NRF-2021R1A2C1003540).

Institutional Review Board Statement: Not applicable.

Informed Consent Statement: Not applicable.

Data Availability Statement: Not applicable.

Conflicts of Interest: The authors declare no conflict of interest.

References

1. Varnes, D.J. *Landslide Hazard Zonation: A Review of Principles and Practice*; UNESCO Press: Paris, France, 1984; p. 63.
2. Van Westen, C.J.; Van Asch, T.W.J.; Soeters, R. Landslide hazard and risk zonation—Why is it still so difficult? *Bull. Eng. Geol. Environ.* **2006**, *65*, 167–184. [CrossRef]
3. Aleotti, P.; Chowdhury, R. Landslide hazard assessment: Summary review and new perspectives. *Bull. Eng. Geol. Environ.* **1999**, *58*, 21–44. [CrossRef]
4. Guzzetti, F.; Carrara, A.; Cardinali, M.; Reichenbach, P. Landslide hazard evaluation: A review of current techniques and their application in a multi-scale study, Central Italy. *Geomorphology* **1999**, *31*, 181–216. [CrossRef]
5. Corominas, J.; Van Westen, C.J.; Frattini, P.; Cascini, L.; Malet, J.P.; Fotopoulou, S.; Catani, F.; Van den Eeckhaut, M.; Mavrouli, O.C.; Agliardi, F.; et al. Recommendations for the quantitative analysis of landslide risk. *Bull. Eng. Geol. Environ.* **2014**, *73*, 209–263. [CrossRef]
6. Chae, B.G.; Park, H.J.; Catani, F.; Simoni, A.; Berti, M. Landslide prediction, monitoring and early warning: A concise review of state-of-the-art. *Geosci. J.* **2017**, *21*, 1033–1070. [CrossRef]
7. Galli, M.; Ardizzone, F.; Cardinali, M.; Guzzetti, F.; Reichenbach, P. Comparing landslide inventory maps. *Geomorphology* **2008**, *94*, 268–289. [CrossRef]
8. Van Westen, C.J.; Castellanos, E.; Kuriakose, S.L. Spatial data for landslide susceptibility, hazard, and vulnerability assessment: An overview. *Eng. Geol.* **2008**, *102*, 112–131. [CrossRef]
9. Achour, Y.; Boumezbeur, R.A.; Hadji, R.; Chouabbi, A.; Cavaleiro, V.; Bendaoud, E.A. Landslide susceptibility mapping using analytic hierarchy process and information value methods along a highway road section in Constantine. *Arab J. Geosci.* **2017**, *10*, 194. [CrossRef]
10. Sezer, E.A.; Nefeslioglu, H.A.; Osna, T. An expert-based landslide susceptibility mapping (LSM) module developed for Netcad Architect Software. *Comput. Geosci.* **2017**, *98*, 26–37. [CrossRef]
11. Reichenbach, P.; Rossi, M.; Malamud, B.D.; Mihir, M.; Guzzetti, F. A review of statistically-based landslide susceptibility models. *Earth-Sci. Rev.* **2018**, *180*, 60–91. [CrossRef]
12. Kocaman, S.; Tavus, B.; Nefeslioglu, H.A.; Karakas, G.; Gokceoglu, C. Evaluation of Floods and Landslides Triggered by a Meteorological Catastrophe (Ordu, Turkey, August 2018) Using Optical and Radar Data. *Geofluids* **2020**, *2020*, 8830661. [CrossRef]
13. Pham, Q.B.; Achour, Y.; Ali, S.A.; Parvin, F.; Vojtek, M.; Vojteková, J.; Al-Ansari, N.; Achu, A.L.; Costache, R.; Khedher, K.M.; et al. A comparison among fuzzy multi-criteria decision making, bivariate, multivariate and machine learning models in landslide susceptibility mapping. *Geomat. Nat. Hazards Risk* **2021**, *12*, 1741–1777. [CrossRef]
14. Park, H.J.; Lee, J.H.; Woo, I. Assessment of rainfall-induced shallow landslide susceptibility using a GIS-based probabilistic approach. *Eng. Geol.* **2013**, *161*, 1–15. [CrossRef]
15. Zhou, G.; Esaki, T.; Mitani, Y.; Xie, M.; Mori, J. Spatial probabilistic modeling of slope failure using an integrated GIS Monte Carlo simulation approach. *Eng. Geol.* **2003**, *68*, 373–386. [CrossRef]
16. Xie, M.; Esaki, T.; Zhou, G. GIS-based probabilistic mapping of landslide hazard using a three-dimensional deterministic model. *Nat. Hazards* **2004**, *33*, 265–282. [CrossRef]
17. Chen, C.Y.; Chen, T.C.; Yu, F.C.; Lin, S.C. Analysis of time varying rainfall infiltration induced landslide. *Environ. Geol.* **2005**, *48*, 466–479. [CrossRef]
18. Salciarini, D.; Godt, J.W.; Savage, W.Z.; Conversini, P.; Baum, R.L.; Michael, J.A. Modeling regional initiation of rainfall-induced shallow landslides in the eastern Umbria Region of central Italy. *Landslides* **2006**, *3*, 181–194. [CrossRef]
19. Huang, J.C.; Kao, S.J.; Hsu, M.L.; Liu, Y.A. Influence of specific contributing area algorithms on slope failure prediction in landslide modeling. *Nat. Hazards Earth Syst. Sci.* **2007**, *7*, 781–792. [CrossRef]
20. Godt, J.W.; Baum, R.L.; Savage, W.Z.; Salciarini, D.; Schulz, W.H.; Harp, E.L. Transient deterministic shallow landslide modeling: Requirements for susceptibility and hazard assessments in a GIS framework. *Eng. Geol.* **2008**, *102*, 214–226. [CrossRef]
21. Liu, C.N.; Wu, C.C. Mapping susceptibility of rainfall-triggered shallow landslides using a probabilistic approach. *Environ. Geol.* **2008**, *55*, 907–915. [CrossRef]
22. Simoni, S.; Zanotti, F.; Bertoldi, G.; Rigon, R. Modelling the probability of occurrence of shallow landslides and channelized debris flows using GEOtop-FS. *Hydrol. Process.* **2008**, *22*, 532–545. [CrossRef]
23. Ho, J.Y.; Lee, K.T.; Chang, T.C.; Wang, Z.Y.; Liao, Y.H. Influences of spatial distribution of soil thickness on shallow landslide prediction. *Eng. Geol.* **2012**, *124*, 38–46. [CrossRef]

24. Alvioli, M.; Guzzetti, F.; Rossi, M. Scaling properties of rainfall induced landslides predicted by a physically based model. *Geomorphology* **2014**, *213*, 38–47. [CrossRef]
25. Anagnostopoulos, G.G.; Fatichi, S.; Burlando, P. An advanced process-based distributed model for the investigation of rainfall-induced landslides: The effect of process representation and boundary conditions. *Water Resour. Res.* **2015**, *51*, 7501–7523. [CrossRef]
26. Alvioli, M.; Baum, R.L. Parallelization of the TRIGRS model for rainfall-induced landslides using the message passing interface. *Environ. Model. Softw.* **2016**, *81*, 122–135. [CrossRef]
27. Lee, J.H.; Park, H.J. Assessment of shallow landslide susceptibility using the transient infiltration flow model and GIS-based probabilistic approach. *Landslides* **2016**, *13*, 885–903. [CrossRef]
28. Salciarini, D.; Fanelli, G.; Tamagnini, C. A probabilistic model for rainfall—induced shallow landslide prediction at the regional scale. *Landslides* **2017**, *14*, 1731–1746. [CrossRef]
29. Salvatici, T.; Tofani, V.; Rossi, G.; D'Ambrosio, M.; Tacconi Stefanelli, C.; Masi, E.B.; Rosi, A.; Pazzi, V.; Vannocci, P.; Petrolo, M.; et al. Application of a physically based model to forecast shallow landslides at a regional scale. *Nat. Hazards Earth Syst. Sci.* **2018**, *18*, 1919–1935. [CrossRef]
30. Park, H.J.; Jang, J.Y.; Lee, J.H. Assessment of rainfall-induced landslide susceptibility at the regional scale using a physically based model and fuzzy-based Monte Carlo simulation. *Landslides* **2019**, *16*, 695–713. [CrossRef]
31. Marin, R.J.; Velásquez, M.F. Influence of hydraulic properties on physically modelling slope stability and the definition of rainfall thresholds for shallow landslides. *Geomorphology* **2020**, *351*, 106976. [CrossRef]
32. Keles, F.; Nefeslioglu, H.A. Infinite slope stability model and steady-state hydrology-based shallow landslide susceptibility evaluations: The Guneysu catchment area (Rize, Turkey). *Catena* **2021**, *200*, 105161. [CrossRef]
33. Fell, R.; Corominas, J.; Bonnard, C.; Cascini, L.; Leroi, E.; Savage, W.Z. Guidelines for landslide susceptibility, hazard and risk zoning for land use planning. *Eng. Geol.* **2008**, *102*, 85–98. [CrossRef]
34. Sorbino, G.; Sica, C.; Cascini, L. Susceptibility analysis of shallow landslides source areas using physically based models. *Nat. Hazards* **2010**, *53*, 313–332. [CrossRef]
35. Brabb, E.E. Innovative approaches to landslide hazard and risk mapping. In Proceedings of the International Landslide Symposium, Tokyo, Japan, 23–31 August 1985.
36. Guzzetti, F.; Malamud, B.D.; Turcotte, D.L.; Reichenbach, P. Power-law correlations of landslide areas in Central Italy. *Earth Planet Sci. Lett.* **2002**, *195*, 169–183. [CrossRef]
37. Guzzetti, F.; Reichenbach, P.; Cardinali, M.; Galli, M.; Ardizzone, F. Probabilistic landslide hazard assessment at the basin scale. *Geomorphology* **2005**, *72*, 272–299. [CrossRef]
38. Guzzetti, F.; Galli, M.; Reichenbach., P.; Ardizzone, F.; Cardinali, M. Landslide hazard assessment in the Collazzone area, Umbria, Central Italy. *Nat. Hazards Earth Syst. Sci.* **2006**, *6*, 115–131. [CrossRef]
39. Jaiswal, P.; Van Westen, C.J.; Jetten, V. Quantitative estimation of landslide risk from rapid debris slides on natural slopes in the Nilgiri hills, India. *Nat. Hazards Earth Syst. Sci.* **2011**, *11*, 1723. [CrossRef]
40. Das, I.; Stein, A.; Kerle, N.; Dadhwal, V.K. Probabilistic landslide hazard assessment using homogeneous susceptible units (HSU) along a national highway corridor in the northern Himalayas, India. *Landslides* **2011**, *8*, 293–308. [CrossRef]
41. Motamedi, M.; Liang, R.Y. Probabilistic landslide hazard assessment using copula modeling technique. *Landslides* **2014**, *11*, 565–573. [CrossRef]
42. Jaiswal, P.; Van Westen, C.J. Estimating temporal probability for landslide initiation along transportation routes based on rainfall thresholds. *Geomorphology* **2009**, *112*, 96–105. [CrossRef]
43. Jaiswal, P.; Van Westen, C.J.; Jetten, V. Quantitative landslide hazard assessment along a transportation corridor in southern India. *Eng. Geol.* **2010**, *116*, 236–250. [CrossRef]
44. Nefeslioglu, H.A.; Gokceoglu, C. Probabilistic risk assessment in medium scale for rainfall-induced earthflows: Catakli catchment area (Cayeli, Rize, Turkey). *Math. Prob. Eng.* **2011**, *2011*, 280431. [CrossRef]
45. Tien Bui, D.; Pradhan, B.; Lofman, O.; Revhaug, I.; Dick, Ø.B. Regional prediction of landslide hazard using probability analysis of intense rainfall in the Hoa Binh province, Vietnam. *Nat. Hazards* **2013**, *66*, 707–730. [CrossRef]
46. Afungang, R.N.; Bateira, C.V. Temporal probability analysis of landslides triggered by intense rainfall in the Bamenda Mountain Region, Cameroon. *Environ. Earth Sci.* **2016**, *75*, 1032. [CrossRef]
47. Dikshit, A.; Sarkar, R.; Pradhan, B.; Jena, R.; Drukpa, D.; Alamri, A.M. Temporal probability assessment and its use in landslide susceptibility mapping for eastern Bhutan. *Water* **2020**, *12*, 267. [CrossRef]
48. Lee, J.H.; Kim, H.; Park, H.J.; Heo, J.H. Temporal prediction modeling for rainfall-induced shallow landslide hazards using extreme value distribution. *Landslides* **2021**, *18*, 321–338. [CrossRef]
49. Kim, H.; Lee, J.H.; Park, H.J.; Heo, J.H. Assessment of temporal probability for rainfall-induced landslides based on nonstationary extreme value analysis. *Eng. Geol.* **2021**, *294*, 106372. [CrossRef]
50. Achour, Y.; Saidani, Z.; Touati, R. Assessing landslide susceptibility using a machine learning-based approach to achieving land degradation neutrality. *Environ. Earth Sci.* **2021**, *80*, 575. [CrossRef]
51. Geological Society of Korea. *Changdong–Hajinburi Geological Map Sheet*; Korea Institute of Geoscience and Mineral Resources: Daejeon, Korea, 1962.

52. NIDP (National Institute for Disaster Prevention). *A Study on the Monitoring and Detection of Slope Failure (III)*; Research Report NIDP-2006-01; NIDP: New Delhi, India, 2006.
53. Coe, J.A.; Michael, J.A.; Crovelli, R.A.; Savage, W.Z. *Preliminary Map Showing Landslide Densities, Mean Recurrence Intervals, and Exceedance Probabilities as Determined from Historic Records, Seattle, Washington*; US Geological Survey Open-File Report; USGS: Seattle, WA, USA, 2000.
54. Crovelli, R.A. *Probability Models for Estimation of Number and Costs of Landslides*; US Geological Survey Open-File Report; USGS: Seattle, WA, USA, 2000.
55. Romeo, R.W.; Floris, M.; Veneri, F. Area-scale landslide hazard and risk assessment. *Environ. Geol.* **2006**, *51*, 1–13. [CrossRef]
56. EI Adlouni, S.; Ouarda, T.B.; Zhang, X.; Roy, R.; Bobée, B. Generalized maximum likelihood estimators for the nonstationary generalized extreme value model. *Water Resour. Res.* **2007**, *43*, W03410. [CrossRef]
57. Coles, S.; Bawa, J.; Trenner, L.; Dorazio, P. *An Introduction to Statistical Modeling of Extreme Values*; Springer Press: London, UK, 2001.
58. Finlay, P.J.; Fell, R.; Maguire, P.K. The relationship between the probability of landslide occurrence and rainfall. *Can. Geotech. J.* **1997**, *34*, 811–824. [CrossRef]
59. Zêzere, J.L.; Garcia, R.A.C.; Oliveira, S.C.; Reis, E. Probabilistic landslide risk analysis considering direct costs in the area north of Lisbon (Portugal). *Geomorphology* **2008**, *94*, 467–495. [CrossRef]
60. Frattini, P.; Crosta, G.; Carrara, A. Techniques for evaluating the performance of landslide susceptibility models. *Eng. Geol.* **2010**, *111*, 62–72. [CrossRef]
61. Nefeslioglu, H.A.; Gokceoglu, C.; Sonmez, H.; Gorum, T. Medium-scale hazard mapping for shallow landslide initiation: The Buyukkoy catchment area (Cayeli, Rize, Turkey). *Landslides* **2011**, *8*, 459–483. [CrossRef]
62. Martha, T.R.; Van Westen, C.J.; Kerle, N.; Jetten, V.; Kumar, K.V. Landslide hazard and risk assessment using semi-automatically created landslide inventories. *Geomorphology* **2013**, *184*, 139–150. [CrossRef]
63. Lee, S.; Won, J.S.; Jeon, S.W.; Park, I.; Lee, M.J. Spatial landslide hazard prediction using rainfall probability and a logistic regression model. *Math. Geosci.* **2015**, *47*, 565–589. [CrossRef]
64. ME (Ministry of Environment). *Standard Guidelines for Design Flood Estimation*; Ministry of Environment: Sejong, Korea, 2019.
65. Zeng, Z.; Lai, C.; Wang, Z.; Chen, X.; Zhang, Z.; Cheng, X. Intensity and spatial heterogeneity of design rainstorm under nonstationarity and stationarity hypothesis across mainland China. *Theor. Appl. Climatol.* **2019**, *138*, 1795–1808. [CrossRef]
66. Nielsen, A. *Practical Time Series Analysis: Prediction with Statistics and Machine Learning*; O'Reilly Media Press: Sebastopol, CA, USA, 2019.
67. Kwon, Y.M.; Park, J.W.; Kim, T.W. Estimation of design rainfalls considering an increasing trend in rainfall data. *KSCE J. Civil Eng.* **2009**, *29*, 131–139.
68. Baum, R.L.; Savage, W.Z.; Godt, J.W. *TRIGRS—A Fortran Program for Transient Rainfall Infiltration and Grid-Based Regional Slope-Stability Analysis*; U.S. Geological Survey Open-File Report; USGS: Seattle, WA, USA, 2002; Volume 424, p. 38. Available online: http://pubs.usgs.gov/of/2002/ofr-02-424 (accessed on 21 February 2022).
69. Baum, R.L.; Savage, W.Z.; Godt, J.W. *TRIGRS—A Fortran Program for Transient Rainfall Infiltration and Grid-Based Regional Slope-Stability Analysis, Version 2.0*; U.S. Geological Survey Open-File Report; USGS: Seattle, WA, USA, 2008. [CrossRef]
70. Iverson, R.M. Landslide triggering by rain infiltration. *Water Resour. Res.* **2000**, *36*, 1897–1910. [CrossRef]
71. Coduto, D.P.; Yeung, M.R.; Kitch, W.A. *Geotechnical Engineering: Principles and Practices*, 2nd ed.; Pearson: New York, NY, USA, 2010.
72. Vanmarcke, E.H. Probabilistic modeling of soil profiles. *J. Geotech. Eng. Div.* **1977**, *103*, 1227–1246. [CrossRef]
73. Mostyn, G.R.; Li, K.S. Probabilistic slope analysis-state of play. In Proceedings of the Conference on Probabilistic Methods in Geotechnical Engineering, Canberra, Australia, 10–12 February 1993; pp. 89–109.
74. Lacasse, S.; Nadim, F. Uncertainties in characterizing soil properties. In *Uncertainty in the Geologic Environment: From Theory to Practice*; ASCE Geotechnical Special Publication: Madison, WI, USA, 1996; pp. 49–75.
75. Terlien, M.T.J. Modelling Spatial and Temporal Variations in Rainfall-Triggered Landslides: The Integration of Hydrologic Models, Slope Stability Models and Geographic Information Systems for the Hazard Zonation of Rainfall-triggered Landslides with Examples from Manizales (Colombia). Ph.D. Thesis, Ultrecht University, Ultrecht, The Netherlands, 1996.
76. Nilsen, B. New trend in rock slope stability analysis. *Bull. Eng. Geol. Environ.* **2000**, *58*, 173–178. [CrossRef]
77. Pathak, S.; Nilsen, B. Probabilistic rock slope stability analysis for Himalayan conditions. *Bull. Eng. Geol. Environ.* **2004**, *63*, 25–32. [CrossRef]
78. Zolfaghari, A.; Heath, A.C. A GIS application for assessing landslide hazard over a large area. *Comput. Geotech.* **2008**, *35*, 278–285. [CrossRef]
79. Wang, Y.; Cao, Z.; Au, S.K. Efficient Monte Carlo simulation of parameter sensitivity in probabilistic slope stability analysis. *Comput. Geotech.* **2010**, *37*, 1015–1022. [CrossRef]
80. Melchiorre, C.; Frattini, P. Modelling probability of rainfall-induced shallow landslides in a changing climate, Otta, Central Norway. *Clim. Chang.* **2012**, *113*, 413–436. [CrossRef]
81. Priest, S.D.; Brown, E.T. Probabilistic stability analysis of variable rock slopes. *Trans. Inst. Min. Metall.* **1983**, *92*, A1–A2.
82. AGS, Landslide Risk Management Concepts and Guidelines. *Aust. Geomech. J.* **2000**, *35*, 49–92.

83. Silva, F.; Lambe, T.W.; Marr, W.A. Probability and risk of slope failure. *J. Geotech. Geoenviron. Eng.* **2008**, *134*, 1691–1699. [CrossRef]
84. Lee, C.T. Multistage statistical landslide hazard analysis: Rain-induced landslides. In *Landslide Science for a Safer Geo-Environment*; Springer: Berlin/Heidelberg, Germany, 2014; Volume 3, pp. 291–298.
85. Ho, K.K.S.; Lacasse, S.; Picarelli, L. Preparedness for Climate Change Impact on Slope Safety. In *Slope Safety Preparedness for Impact of Climate Change*; CRC Press: Boca Raton, FL, USA, 2017; p. 571.

sustainability

MDPI

Article

Improved Shallow Landslide Susceptibility Prediction Based on Statistics and Ensemble Learning

Zhu Liang [1,2,3], Wei Liu [2,3], Weiping Peng [2,3], Lingwei Chen [2,3] and Changming Wang [4,*]

[1] College of Construction Engineering, South China University of Technology, Guangzhou 510641, China; liangzhu19@mails.jlu.edu.cn
[2] Guangzhou Urban Planning & Design Survey Research Institute, Guangzhou 510060, China; liuwei@gzpi.com.cn (W.L.); pengweiping@gzpi.com.cn (W.P.); lingweichen@163.com (L.C.)
[3] Guangdong Enterprise Key Laboratory for Urban Sensing, Monitoring and Early Warning, Guangzhou 510060, China
[4] College of Construction Engineering, Jilin University, Changchun 130012, China
* Correspondence: wangcm@jlu.edu.cn; Tel.: +86-135-0441-8751

Abstract: Rainfall-induced landslides bring great damage to human life in mountain areas. Landslide susceptibility assessment (LSA) as an essential step toward landslide prevention has attacked a considerate focus for years. However, defining a reliable or accurate susceptibility model remains a challenge although various methods have been applied. The main purpose of this paper is to explore a comprehensive model with high reliability, accuracy, and intelligibility in LSA by combing statistical methods and ensemble learning techniques. Miyun country in Beijing is selected as the study area. Firstly, the dataset containing 370 landslide locations inventories and 13 conditioning factors were collected and non-landslide samples were prepared by clustering analysis. Secondly, random forest (RF), gradient boosting decision tree (GBDT), and adaptive boosting decision tree (Ada-DT) were selected as base learners for the Stacking ensemble method, and these methods were evaluated using measures like area under the curve (AUC). Finally, the Gini index and frequent ratio (FR) were combined to analyze the major conditioning factors. The results indicated that the performance of the Stacking method was enhanced with an AUC value of 0.944 while the basic classifiers also performed well with 0.906, 0.910, and 0.917 for RF, GBDT, and Ada-DT, respectively. Regions with a distance to a stream less than 2000 m, a distance to a road less than 3000 m, and elevation less than 600 m were susceptible to the landslide hazard. The conclusion demonstrates that the performance of LSA desires enhancement and the reliability and intelligibility of a model can be improved by combining binary and multivariate statistical methods.

Keywords: landslide susceptibility; statistical methods; ensemble techniques; GIS

Citation: Liang, Z.; Liu, W.; Peng, W.; Chen, L.; Wang, C. Improved Shallow Landslide Susceptibility Prediction Based on Statistics and Ensemble Learning. *Sustainability* **2022**, *14*, 6110. https://doi.org/10.3390/su14106110

Academic Editors: Stefano Morelli, Veronica Pazzi and Mirko Francioni

Received: 3 May 2022
Accepted: 13 May 2022
Published: 18 May 2022

1. Introduction

Landslides are a common natural phenomenon and may cause unpredictable damage to human beings and property worldwide, especially in China where geohazards are enormously occurring and widely distributed [1]. Generally, damages can be decreased or mitigated by predicting the area prone to landslides [2,3]. Therefore, landslide susceptibility mapping (LSM), which predicts the spatial distribution of the likelihood of a landslide occurring, is significant and worthwhile for the reduction of hazards.

How to improve the quality of a model is always the focus of attention and discussed by researchers although related studies have been conducted on improving the predictive accuracy [4,5]. The effectiveness of LSM depends greatly on the models adopted [6], which can be roughly divided into knowledge-based and data-driven methods [7]. Conventional knowledge-based methods as a heuristic, are subjective and limited to be applied in small-scale areas. Conventional statistical methods, like logistic regression (LR) and principal component analysis, are popular due to their simplicity. Nevertheless, the mechanism of a

landslide is complicated and usually involves multiple factors. Nevertheless, conventional statistical methods fail to deal with nonlinear problems [8,9]. Geographic information systems (GIS) and computing techniques are increasingly developing so that machine learning techniques (MLT) translated from statistical methods have achieved promising performance for LSM [10]. However, the inductive preference is inevitable for MLT and the performance of different MLT fluctuates as the data change. Besides, the performance of a model will be affected by the purity of the samples. Accordingly, controversy continues over which method is the best and which is feasible for further improvement [11]. A single classifier applied to form an ensemble is called the "base learner". Base learners are not limited to homogeneous but also can be heterogeneous. Bagging and boosting are two of the most popular ensemble techniques of homogeneous and have been applied to LSM by some researchers [12]. While the stacking ensemble method, which is heterogeneous, has seldom been applied to LSM and needs more exploration [13].

Data-driven methods are binary classification processes and are sensitive to the quality of training data, which require a data set consisting of an equal amount of both disaster presence and absence observations in LSM [14]. In terms of landslide presence data, it is obtained from the landslide inventory, which was achieved through historical records, remote sensing technology, and extra field investigations. While absence samples were not available, they are usually selected randomly or subjectively from the "safe area" based on the acknowledgment and experience of the experts [15]. Nevertheless, it is controversial and difficult to implement especially for a large area. We could not identify the area with low susceptibility based on the historical records because these landslide-free areas may contain locations prone to landslides, which have not been recorded in the past. Unreliable sampling strategies may bring the noise to the data and eventually, a false assessment of the models. This study applies clustering analysis to improve the quality of samples and the performance of models [16]. Two initial landslide susceptibility maps are made by k-means clustering and Fuzzy c-means (FCM) and the reasonability of the initial maps are compared and finally determined the better one. Accordingly, the non-landslide samples are selected from the very low susceptibility area.

Previous studies have emphasized the importance of accuracy and regarded it as the only indicator for evaluating a model. However, emphasizing accuracy is not enough for the requirement of prevention and control. Communication between theory and practice can be improved through a better understanding of major variables. The bivariate statistical method as FR is commonly applied to explore the relationship between conditioning factors and the occurrence of landslides by calculating the FR values of factors in a certain interval [17]. While the bivariate statistical method fails to determine the relative importance among different factors and Gini index (the larger the value indicates the greater the contribution to the occurrence of landslides) makes up for it [18].

The current study aims to explore a model with high reliability, accuracy, and intelligibility on LSM. Three ensemble techniques were evaluated by 5-fold cross-validation according to the Receiver Operating Characteristic (ROC) curve and statistical indexes. RF, GBDT, and Ada-DT are selected as the candidate base learners of the stacking method and LR as the meta-learner. The stacking method is explored as a potential application to LSM and is compared to other ensemble methods. The purity of the samples is improved by selecting the non-landslide samples in a more reliable way. The Gini index and FR were combined to identify and analyze the major conditioning factors to improve intelligibility. Miyun country, China, where shallow landslides occurred frequently, was selected as the study area and a comparison of the ensemble methods above was made.

2. Materials

2.1. Study Area

Miyun country located in Beijing, China, extends from longitudes of 116°39′ E to 117°30′ E and latitudes of 40°13′ N to 40°47′ N (Figure 1). It has a population of more than 470,000 and occupies an area of about 2229.45 km^2, which is composed of mountainous

areas (82.9%), cultivated land (8.3%), and reservoirs, roads, and villages (collectively 9.8%). The average annual precipitation is 663.1 mm (1981–2012) mainly concentrated in summer (76.4%) and it is a continental monsoon semi-arid climate.

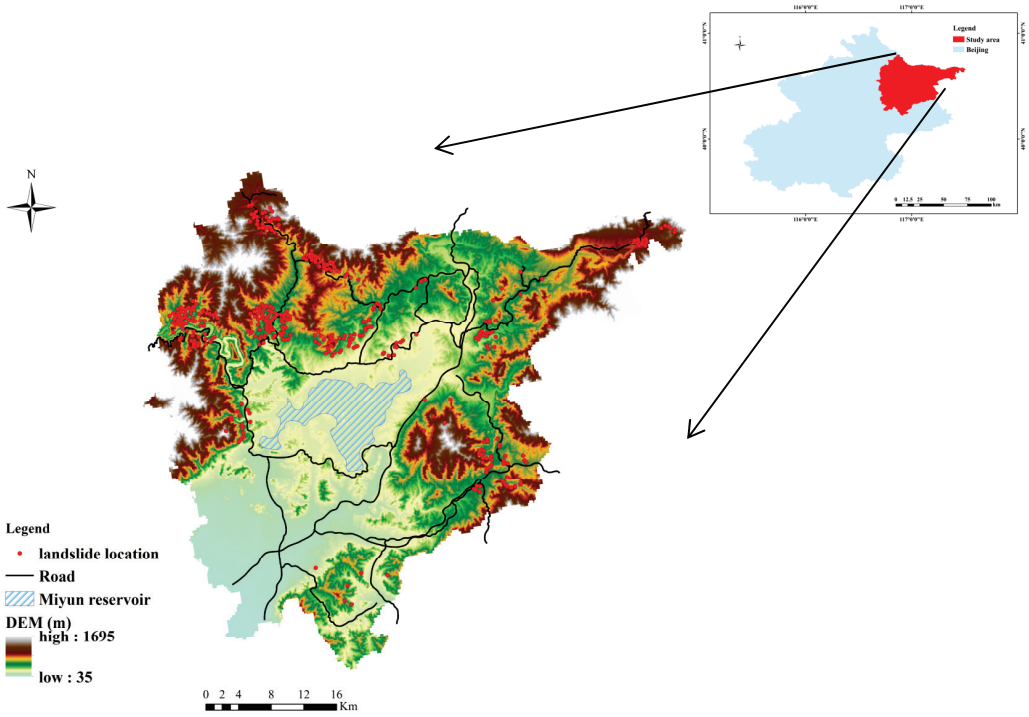

Figure 1. Location map of the study area showing landslide inventory.

The study area is part of the transition zone between the North China Plain and the Yanshan mountains, which leads to a series of large fold and fault structures. The faults are large in scale and widely distributed, mainly in the Northeast and north-south directions. The elevation ranges from 45 m to 1750 m above mean sea level with a slope angle between 10–45°. The strata are mainly composed of Archaean (Ar), Proterozoic (Pt), Mesozoic Jurassic (J), and Quaternary (Q). Three types of lithology are usually exposed in our investigation: gneiss from Middle Archean (ArXdgn), dolomites from Proterozoic (Pt22w), and siltstone from Mesozoic Jurassic (J2z). Magmatic intrusive rocks are widely distributed, accounting for nearly one-third of the total area and are exposed discontinuously in the northeast direction.

Road traffic is developed, and human activities are intensive in the study area, involving mining, reservoir, and power station projects. The disasters are various and frequent, mainly rain-induced landslides, which has affected the normal life of the local villagers.

2.2. Data Preparation

2.2.1. Landslide Inventory

The statistically based models follow a crucial assumption: future landslides have more chances to occur again in the places with the conditions which cause the landslides once and present [18,19]). Accordingly, the landslide inventory map as the initial source is essential and was depicted according to related records (from 1970–2010), field surveys (from 2016–2017) (Figures 2 and 3), and Google Earth satellite images interpretation (May 2018) (Figure 4). Ultimately, 620 landslide locations were identified, including soil slides (370), rockslides (6), and falls (244) [18]. It is accepted that different type of landslides has a different mechanism of occurrence. Soil slides were only considered in our work and were represented as points shown in Figure 1. Landslides occurred during or after heavy rainfall. Based on field investigation, remote sensing interpretation and relevant records, the scale of landslides in the study area is generally small, accounting for about 80%. The area of

landslides ranges from 3.6 km^2 to 300 m^2 while the depth of most landslides is less than 4 m, belonging to shallow landslides.

(**a**) (**b**)

Figure 2. Field investigation photos. (**a**) shallow landslide in Lama Gate South gully; (**b**) falls in Lama Gate South gully.

(**a**) (**b**)

Figure 3. Field investigation photos. (**a**) early debris-flow deposits in Dawa gully; (**b**) Partial enlargement.

Figure 4. Stereo remote sensing map of landslides in Duitaizi county (Chen et al., 2016).

2.2.2. Choice of Mapping Units

The selection of mapping units should be determined in advance for LSM [20]. Another piece of literature discussed and compared the difference among mapping units, such as grid cells and slope units [21]. To better predict or identify the locations of landslides, slope units were applied in our work, which describes the topographic and geomorphic conditions of landslides integrally. Finally, the area was divided into 8736 slope units using the hydrologic analysis tool in ArcGIS and indispensable artificial corrections according to remote sensing images. Detailed division steps and discussion can be referred to in other literature [22].

2.2.3. Conditioning Factors

Factors responsible for a landslide are various and there is no consensus on the choice of number and types of factors. It is commonly accepted that landslide is controlled by topographical, geological, and triggering factors. However, data availability, reliability, and accuracy should be given priority [23] and finally, 13 conditioning factors were selected. Detailed information on conditioning factors is shown in Table 1 and Figure 5a–m. A brief description of each controlling factor is given below.

Table 1. Landslide conditioning factors in this study.

Category	Conditioning Factors	Type	Data Source	Values
Topographical	Elevation (m)	Continuous	SRTM	(1) <200; (2) 200–400; (3) 400–600; (4) 600–800; (5) >800
	Plan curvature	Continuous	SRTM	(1) <0; (2) 0–0.01; (3) 0.01–0.02; (4) 0.02–0.03; (5) >0.03
	Profile curvature	Continuous	SRTM	(1) <0; (2) 0–0.01; (3) 0.01–0.02; (4) 0.02–0.03; (5) >0.03
	Slope angle (°)	Continuous	SRTM	(1) <10; (2) 10–20; (3) 20–30; (4) >30
	TWI	Continuous	SRTM	(1) <6.5; (2) 6.5–7; (3) 7–7.5; (4) 7.5–8; (5) 8–8.5; (6) >8.5
	MED (m)	Continuous	SRTM	(1) <100; (2) 100–200; (3)200–300; (4) 300–400; (5) 400–500; (6) >500
	Slope aspect	Categorical	SRTM	(1) north; (2) northeast; (3) east; (4) southeast; (5) south; (6) southwest; (7) west; (8) northwest
Geological and Geomorphological	Distance to faults (m)	Continuous	Geological map	(1) <1000; (2) 1000–2000; (3) 2000–3000; (4)3000–4000; (5) >4000
	Distance to streams (m)	Continuous	DNRB	(1) <1000; (2) 1000–2000; (3) 2000–3000; (4)3000–4000; (5) >4000
	Lithology	Categorical	Geological map	(1) Gneiss; (2) Dolomites; (3) Siltstone (4) Granite;(5) Limestone; (6) Conglomerate
Triggering factors	Maximum 24 h rainfall (mm)	Continuous	BHM	(1) <270; (2) 270–280; (3) 280–290; (4) >290
	Maximum 7 days rainfall (mm)	Continuous	BHM	(1) <320; (2) 320–330; (3) 330–340; (4) >340
	Distance to roads (m)	Continuous	DNRB	(1) <1000; (2) 1000–2000; (3) 2000–3000; (4)3000–4000; (5) >4000

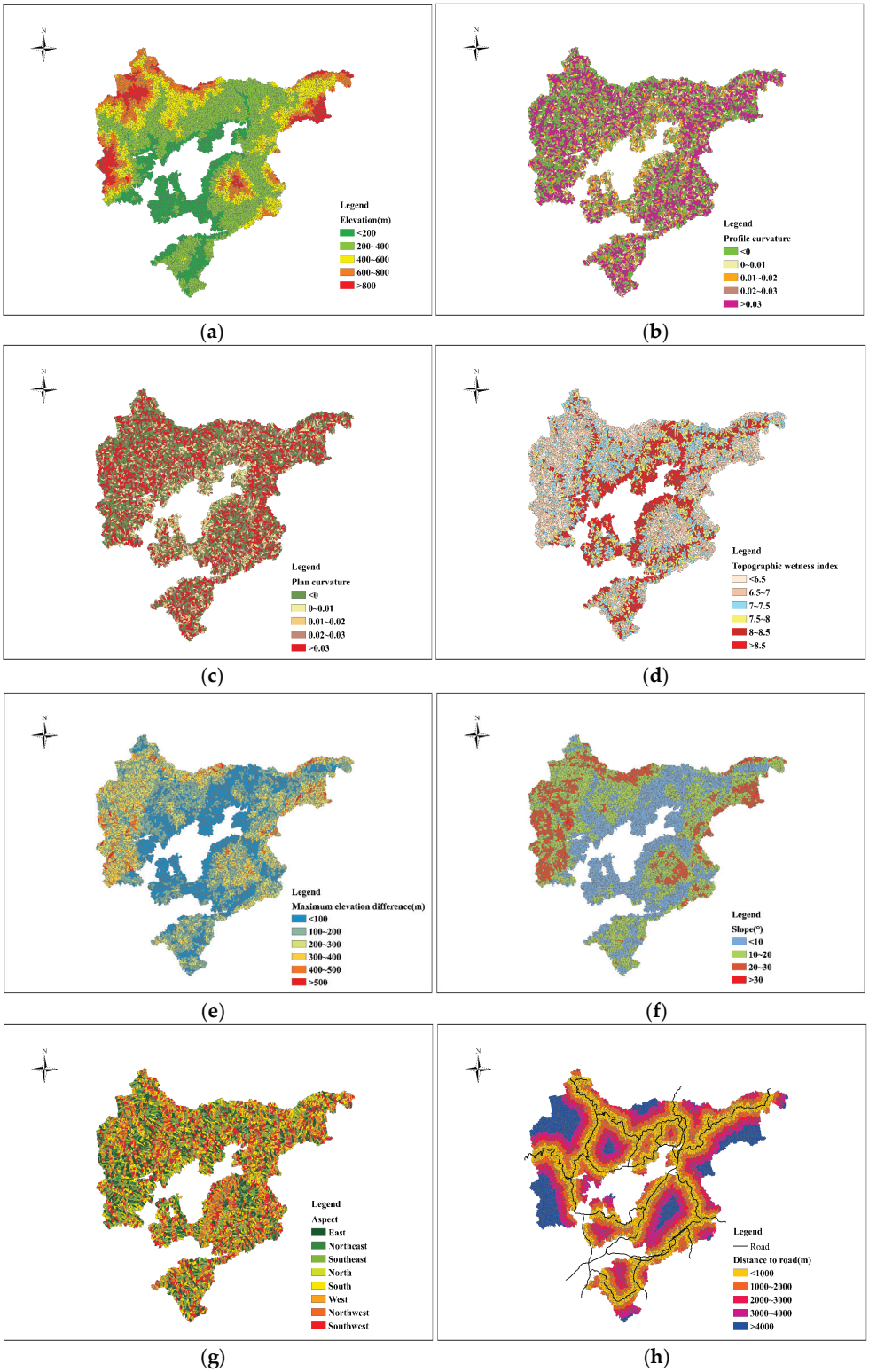

Figure 5. *Cont.*

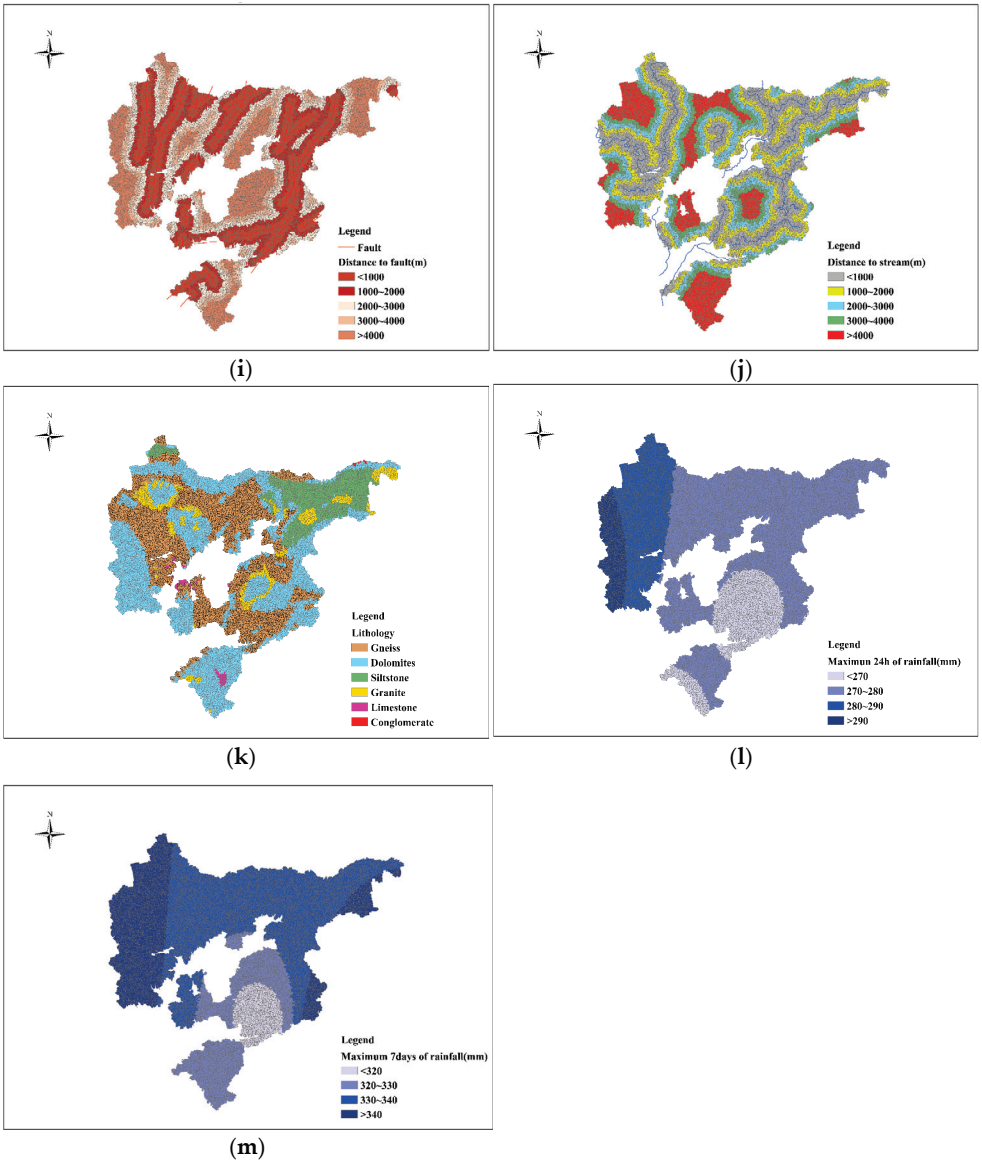

Figure 5. Study area thematic maps: (**a**) Elevation; (**b**) Plan curvature; (**c**) Profile curvature; (**d**) TWI; (**e**) MED; (**f**) Slope; (**g**) Aspect; (**h**) DTR; (**i**) DTF; (**j**) DTS; (**k**) Lithology; (**l**) Maximum 24 h Rainfall; (**m**) Maximum seven days Rainfall.

Topographic-related factors were derived from the DEM (Digital Elevation Model) with a resolution of 30 m (http://www.gscloud.cn, accessed on 4 April 2022) originally sourced from the Shuttle Radar Topography Mission (SRTM) data. Elevation affects slope instability and precipitation properties and was frequently applied to LSM [24,25]. Landslides are likely to occur as slopes become steep and vice versa [26]. Maximum elevation difference (MED) reflects the potential energy of a slope and was calculated in ArcGIS [27]. Topographic wetness index (TWI) and Curvature reflect topographic relief [28]. TWI was reclassified into six classes (Figure 5g) and the related algorithm is as follows:

$$\mathrm{TWI} = \ln\left(\frac{\mathrm{A_S}}{\tan\beta}\right) \quad (1)$$

where, A_s is the specific catchment area, β is the slop angle.

The plan curvature (Figure 5g) and profile curvature (Figure 5g) are both the most extensively used predisposing factors, which reflect the changes in terrain [29]. The slope aspect map was reclassified into eight classes according to the eight cardinal directions (Figure 5g).

Fault information (Figure 5i) was collected from a geological map of which the ratio was 1:50,000. Faults decrease the rock strength, which acts as potential weak planes in slopes. It was produced by the spatial distance analysis tool in ArcGIS. Similarly, the distance to roads (Figure 5h) and distance to rivers (Figure 5j) were both constructed based on the data from the Department of Natural Resources of Beijing (DNRB).

Shallow landslides are mainly caused by heavy or continuous rainfall [30]. Consequently, both the maximum 24 h rainfall (Figure 5l) and maximum seven days of rainfall (Figure 5m) were selected based on the data (1981–2000) from Beijing Hydrology Manual (BHM) using the kriging interpolation coordinated with elevation in ArcGIS and 11 precipitation stations nearby were taken as reference. Rainfall was regarded as the natural trigger while the distance to the road was the human factor.

Factors were reclassified into four to eight classes and the mean value was regarded as the statistic value of slope units.

3. Methods

3.1. Sampling Strategy

3.1.1. K-Means Clustering

K-means comes out to be a well know clustering method due to its efficiency and feasibility [31]. It is applied to divide n observations into k clusters, where each sample is allocated to the cluster based on the closest Euclidean distance, thus considered as the centroid of the cluster [32]. The procedure is then repeated until the change of the cluster seed from one stage to the next is negligible. The main equation involved in k-means is as follows:

$$\frac{|u_{n+1} - u_n|}{u_{n+1}} \leq \varepsilon \tag{2}$$

where u_{n+1} represents the sum of squares of distances from each point to the cluster center after the nth clustering; ε represents the precision value.

3.1.2. FCM Algorithm

The fuzzy c-means method is a soft clustering method developed by Dunn [33] and it is different from K-means (hard clustering). It has been widely used for statistical analysis of geological problems because of its flexibility and rationality [34]. Its core idea is to assign the objects to the corresponding clusters according to the degree of membership. The function of the FCM clustering is defined by the equation:

$$C_i = \sum_{j=1}^{n} \mu_{ij}^m x_j / \sum_{j=1}^{n} \mu_{ij}^m \tag{3}$$

$$J = \sum_{j=1}^{N} \sum_{i=1}^{C} \mu_{ij}^m d^2(X_j, V_i) \tag{4}$$

$$\mu_{ij} = 1 / \sum_{k=1}^{C} \left(\frac{d_{ij}}{d_{kj}} \right)^{2/(m-1)} \tag{5}$$

where C_i represents the cluster centers, C represents the number of centers, u_{ij} represents the membership matrix; m represents the degree of fuzziness; J is the objective function and n is the number of objects in the database; d^2 is the Euclidean distance between the ith clustering center and the jth sample [35].

Two parameters as m and C are required to determine in advance. C is determined by the cluster validity function [36] and m is equal to 2 referred to in most applications in this study.

Machine learning methods need both positive and negative datasets. Three-hundred-seventy positive samples (that is, landslide locations) were set as "1" and the same number of negative samples with the value of "0", which were selected based on the result of

K-means and FCM in this study. As the purity of absent samples increases, it is more likely to reflect the characteristics of non-landslide areas. Accordingly, the critical value of the model results distinguishing landslides and non-landslides is 0.5.

3.1.3. Frequency Ratio

The equation for determining the FR value of a certain level of conditioning factor is defined below [16]:

$$\mathrm{FR}_i = \frac{\frac{\mathrm{landslide\_\_cell}_{s_i}}{\mathrm{landslide\_\_cell}_{s_{tot}}}}{\frac{\mathrm{total\_\_cell}_{s_i}}{\mathrm{total\_\_cell}_{s_{tot}}}} \quad (6)$$

where i indicates the i-th class for each variable considered.

An FR_i greater than 1 manifest that there exists a close relationship between landslide occurring and variable class, and if the values are less than 1 then a weak correlation is reflected. Continuous variables are required to be reclassified into classes before application, as Table 1 showed.

3.2. Modeling Landslide Susceptibility

3.2.1. LR Model

LR establishes a non-linear probability function model, trying to find appropriate regression coefficients to express the correlation between the independent variable and the dependent variable [37]. The LR model is constructed as the equation below:

$$p = \frac{1}{1 + e^{-y}} \quad (7)$$

where p is the probability of a landslide occurring; y is a linear combination function as Equation (7).

$$y = b_0 + b_1 x_1 + b_2 x_2 + b_3 x_3 + \ldots b_n x_n \quad (8)$$

where b_0 is the constant value, and b_1, b_2, . . . , b_n refer to each significant input variable (x_1, x_2,..., $x_{n)}$ causing the landslide.

The forward7 stepwise method was adopted to screen variables during LR modeling in SPSS software.

3.2.2. RF

RF belongs to a family of ensemble methods based on the decision tree and Bagging technique and it was first introduced by Breiman [17]. The bagging technique, which is also called bootstrap aggregation, is applied to selecting variables and samples randomly as the training data for modeling. Unused observations are applied to calculate the classification error. Consequently, there are two powerful ideas of RF: random feature selection and Bagging [38]. More details about RF can be found in Breiman [17]. RF was modeled in Python 3.7 using the scikit-learn package [39]. The number of trees (k) and the number of predictive variables (n) are required tuning before modeling [40].

3.2.3. GBDT

GBDT forms weak classifiers (DT) iteratively based on Gradient Boosting [41]. The parameter of the weak classifier defaults to the direction of the. The GBDT was applied in Python 3.7 using the GBDT class library of scikit-learn.

3.2.4. AdaBoost-DT

AdaBoost (known as adaptive boosting) is another boosting algorithm, which was invented by Freund and Schapire [42]. Unlike gradient boosting, AdaBoost assigns incorrectly classified samples with modified weights after each iteration. The final classifier is constructed by combining all weak classifiers. AdaBoost-DT is also applied in Python 3.7 using the AdaBoost class library of scikit-learn.

3.2.5. Gini Index

The split method tree-based classifiers adopt is the minimum principle of Gini and thus Gini index is applied to calculate the relative importance of conditioning factors. The relevant formula is as follows:

$$\text{Gini}(T) = 1 - \sum_{j=1}^{N} P_j^2 \tag{9}$$

where T expresses the training set, N is the number of categories, and P is the probability of a sample that is classified into the kth class.

3.2.6. Stacking

The stacking ensemble consists of base-classifiers and meta-classifier. Stacking takes the results predicted by the base-classifiers as the input attributes and the meta-classifier merges the different predictions into the final prediction. It is believed that stacking performs better than any basic classifiers [43]. Figure 6 shows the structure of the Stacking. The basic classifiers of Stacking were three ensemble learning machines that have been showing great performance in statistical analysis: RF, GBDT, and AdaBoost-DT. LR model was used as the combiner. To avoid over-fitting of the meta-classifier, the dataset is divided into two disjoint subsets: one for training base-classifiers and the other for testing. To train the meta-level classifier, 5-fold cross-validation is applied to construct the meta-levels for all combining methods.

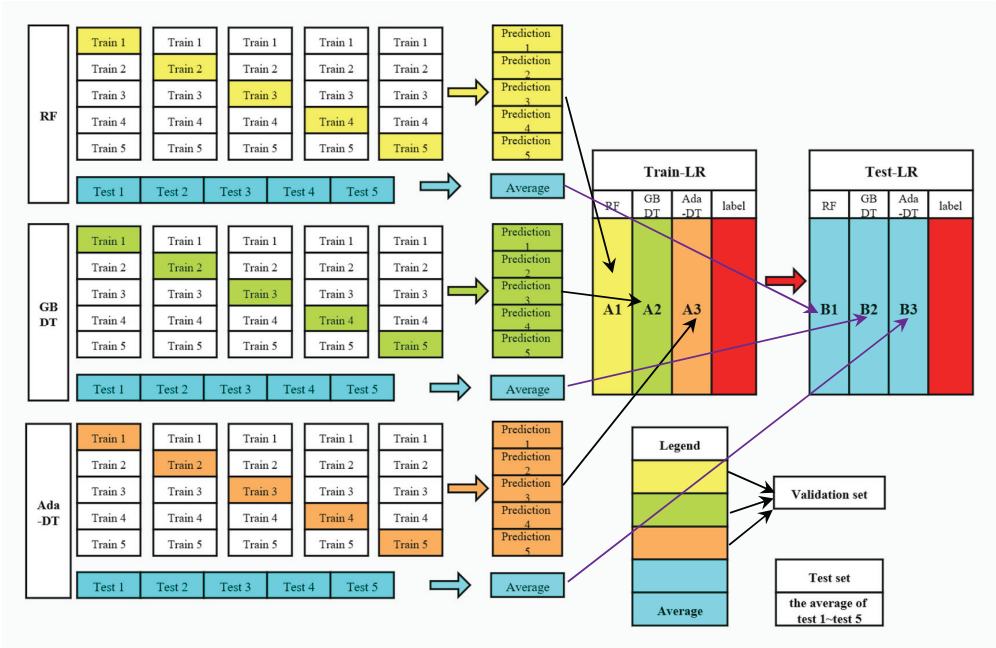

Figure 6. The structure of Stacking.

3.3. Evaluating Model Performance

Models need a reliable evaluation and/or validation process [44]. The capacity of a model to classify was evaluated by a 5-fold cross-validation procedure, where the data is divided into five independent groups, one at a time for testing and the remaining four groups for training [45].

Accuracy, sensitivity, and specificity were three statistical indexes evaluating the performance [13]:

$$\text{Accuracy} = \frac{\text{TP} + \text{TN}}{\text{TP} + \text{TN} + \text{FP} + \text{FN}} \tag{10}$$

$$\text{Sensitivity} = \frac{\text{TP}}{\text{TP} + \text{FN}} \tag{11}$$

$$\text{Specificity} = \frac{\text{TN}}{\text{FP} + \text{TN}} \tag{12}$$

where True Positive (TP) refers to the number of landslide samples with correct classification, True Negative (TN) refers to the number of non-landslide samples with correct classification, False Positive (FP) refers to the number of landslide samples with incorrect classification and False Negative (FN) refers to the number of non-landslide samples with incorrect classification.

AUC is a metric commonly used to assess the quality of the model and it varies from 0.5 to 1. The higher the AUC value shows the stronger the predictive ability [46].

Non-parametric models need to be optimized by tuning related hyperparameters before application [47]. The involved parameters for modeling utilized in this study were shown in Table 2 and the flowchart of methods involved was shown in Figure 7.

Table 2. The optimized parameters of methods utilized in this study.

Methods	Parameters
DT	Criterion = 'gini'; max_features = None; max_depth = 20; min_samples_split = 2; min_samples_leaf = 1; max_leaf_nodes = None; class_weight = None
RF	n_estimators = 500; criterion = 'gini'; max_depth = None; max_features = 'sqrt';
GBDT	n_estimators = 100; learning_rate = 0.1; max_depth = 2; verbose = 1; subsample = 0.7; max_leaf_nodes = None
AdaBoost-DT	base_estimator = None; n_estimators = 100; learning_rate = 1.0; algorithm = 'SAMME.R'; random_state = None

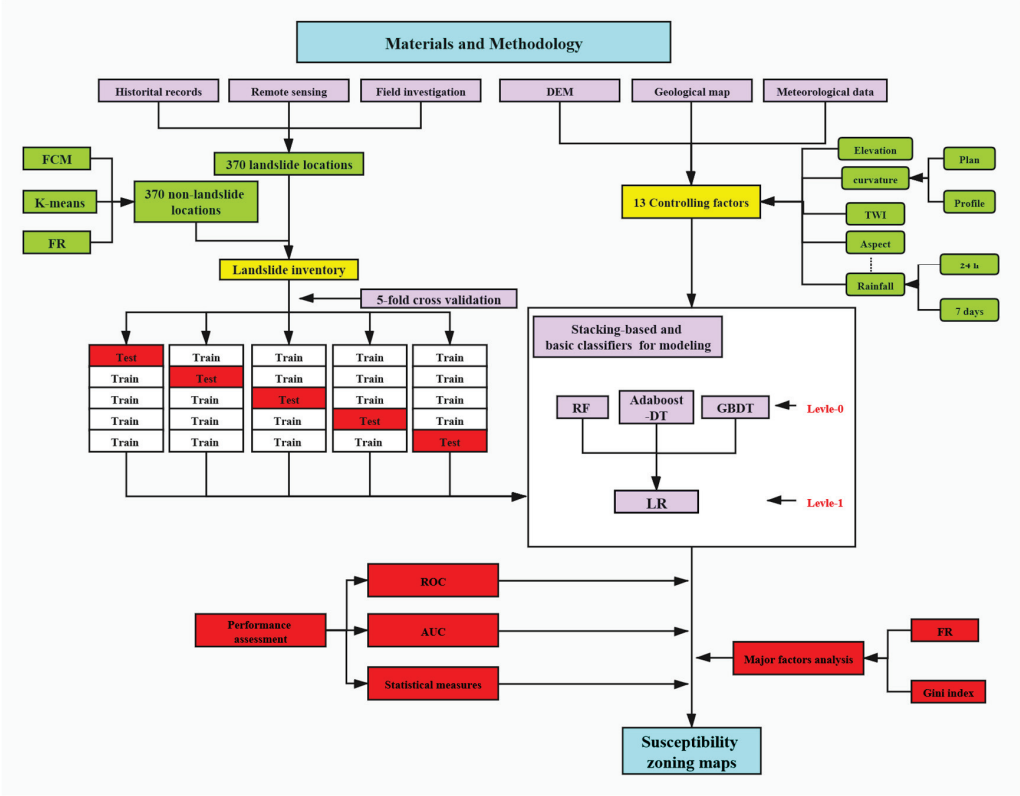

Figure 7. Flowchart of the methodology followed in this study.

4. Results and Verification

4.1. Non-Landslide Samples Selected by FCM and K-Means

LSM generated based on cluster analysis does not need to identify the positive and negative labels of the samples in advance. Based on the curve of the clustering effectiveness

index Vcs (Figure 8), the preferred value is five. Consequently, the study area was reclassified into five areas based on the FR values, which were very low, low, moderate, high, and very high. The proportions of each area are: very low (15.97%), low (23.25%), moderate (19.29%), high (33.5%) and very high (8%). Among them, the very-low area accounted for 15.97% of the whole study area with only 3.24% of landslide locations and an FR value of 0.2. Besides, the high or very-high area accounted for 41.5% of the study area with more than 55% of landslide locations and the FR values were both greater than 1.

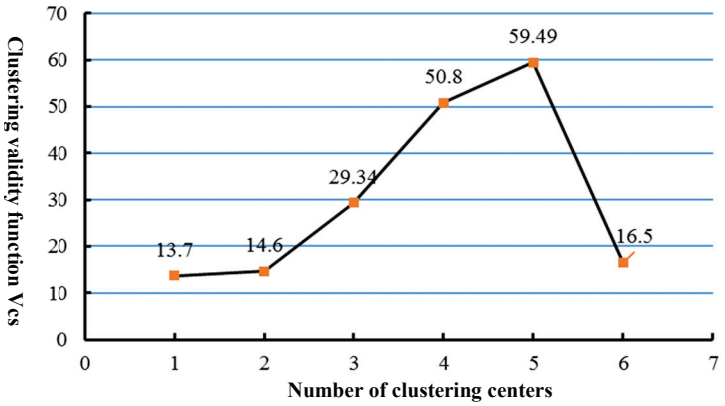

Figure 8. Clustering validity function Vcs.

Similarly, the results constructed by K-means were shown in Table 3. The proportions of each area are: very low (11.66%), low (22.30%), moderate (18.71%), high (39.16%), and very high (8.17%). The very-low area accounted for only 1.62% of landslide locations with an FR value of 0.14. The high or very-high area accounted for 47.33% of the study area with more than 55% of landslide locations.

Table 3. Frequency ratios of five susceptibility classes assessed with FCM and K-means.

Method	Class	Landslide Ratio (%)	Area Ratio (%)	FR
FCM	Very low	3.24	15.97	0.20
	Low	19.73	23.25	0.85
	Moderate	21.35	19.29	1.11
	High	40.00	33.50	1.19
	Very high	15.68	8.00	1.96
k-means	Very low	1.62	11.66	0.14
	Low	15.41	22.30	0.69
	Moderate	15.57	18.71	0.83
	High	48.11	39.16	1.22
	Very high	17.30	8.17	2.11

Compared to the results obtained by FCM, the area with low or very low class predicted by K-means occupied a smaller area (5.26%) while a bigger area (5.83) with high or very high class. The zoning maps should follow two rules: (1) the recorded landslides should appear in high-susceptibility areas as many as possible and (2) the high-susceptibility area should occupy a small proportion (Bui et al., 2012). Therefore, the results obtained by FCM were more reasonable. Selecting the non-landslide samples in a more reliable area is the main purpose and it means that the bigger the very-low class area, the easier the sampling will be. Meanwhile, 370 non-landslides samples were collected from the area with very-low susceptibility predicted by FCM.

4.2. Evaluation and Comparison of Different Models

To highlight the performance of the Stacking model, three basic classifiers were also applied for modeling. Analyses of the statistical measures using the training set were shown in Table 4. The Stacking showed the best performance in terms of classifying landslides (sensitivity = 91.89%), followed by the GBDT model (sensitivity = 86.97%), the Ada-DT model (sensitivity = 85.66%) and RF model (sensitivity = 79.93%). In terms of the classification of non-landslides zones, Stacking model also performed best (specificity = 91.84%), followed by the GBDT model (specificity = 85.67%), the Ada-DT model (specificity = 82.26%) and the CART model (specificity = 83.16%). Besides, the Stacking model also had the highest accuracy (91.84%). It was noticed that the Stacking model achieved an AUC of 0.963, while RF was 0.920, GBDT was 0.957 and Ada-DT was 0.959 (Table 5). The standard errors were less than 0.05 and the probability estimation was negligible.

Table 4. Models' performance using training dataset.

Metrics	RF	GBDT	Ada-DT	Stacking
TP (%)	82.46	84.88	81.29	91.22
TN (%)	76.80	87.67	86.44	92.20
FP (%)	17.54	15.12	18.71	8.78
FN (%)	23.2	12.37	13.56	7.80
Sensitivity (%)	79.93	86.97	85.66	91.89
Specificity (%)	83.16	85.67	82.26	91.78
Accuracy (%)	81.56	86.29	83.87	91.84

Table 5. ROC analysis of the four models using training data.

Models	AUC	Standard Error	95% Confidence Interval
RF	0.920	0.011	0.899–0.941
GBDT	0.957	0.008	0.942–0.973
Ada-DT	0.959	0.009	0.942–0.976
Stacking	0.963	0.006	0.950–0.975

The predictive capacity needs to be evaluated using validation data. The results confirmed that the Stacking model perform the best as the values of sensitivity, specificity, accuracy and AUC were highest (Tables 6 and 7), which was 91.78%, 90.54%, 91.16% and 0.944, respectively, followed by Ada-DT (sensitivity = 86.96%, specificity = 82.19%, accuracy = 85.13% and AUC = 0.917), GBDT (sensitivity = 86.11%, specificity = 84.00%, accuracy = 85.03% and AUC = 0.910), and RF (sensitivity = 81.33%, specificity = 75.34%, accuracy = 78.38 and AUC = 0.906) (Figure 9).

Table 6. Models' performance using verification dataset.

Metrics	RF	GBDT	Ada-DT	Stacking
TP (%)	77.22	86.30	83.54	90.54
TN (%)	79.71	83.78	86.96	91.78
FP (%)	22.78	13.70	16.46	9.46
FN (%)	20.29	16.22	13.04	8.22
Sensitivity (%)	81.33	86.11	86.96	91.78
Specificity (%)	75.34	84.00	82.19	90.54
Accuracy (%)	78.38	85.03	85.13	91.16

Table 7. ROC analysis of the models using validating data.

Models	AUC	Standard Error	95% Confidence Interval
RF	0.906	0.027	0.853–0.959
GBDT	0.910	0.026	0.859–0.962
Ada-DT	0.917	0.021	0.877–0.958
Stacking	0.944	0.018	0.908–0.980

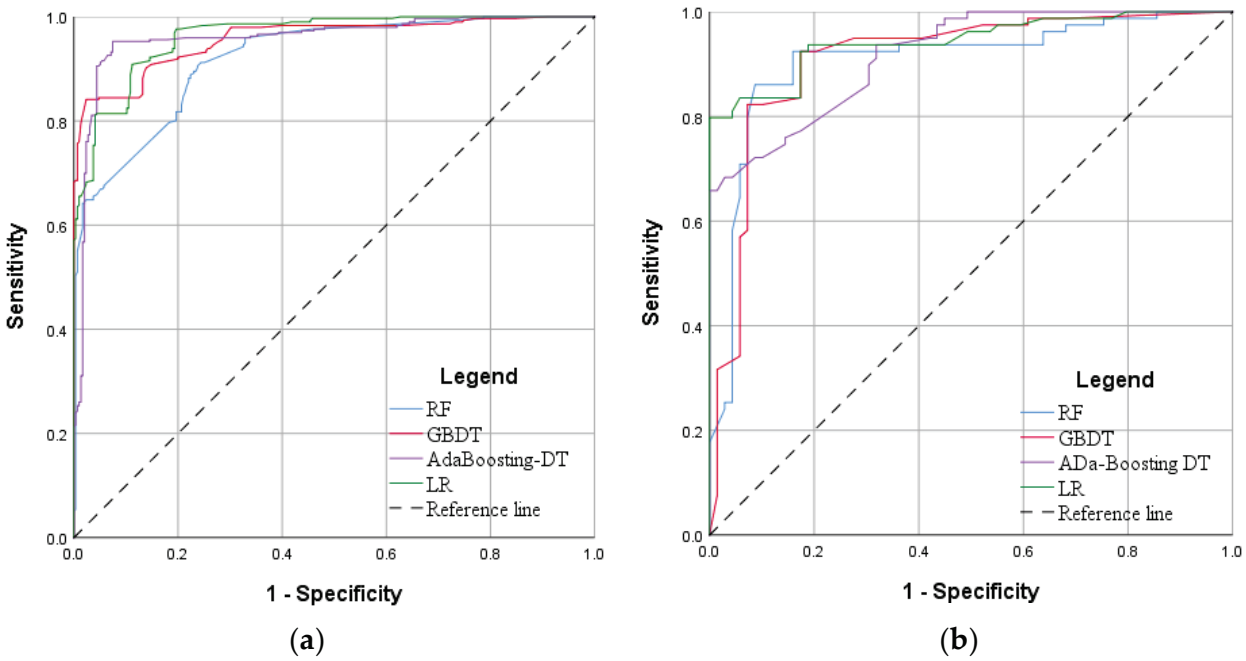

Figure 9. Analysis of ROC curve for the landslide susceptibility map: (**a**) Success rate curve of landslide using the training dataset; (**b**) Prediction rate curve of landslide using the validation dataset.

The Stacking model exhibited the best both in training and validation data compared to the other three ensemble learning methods, which indicated ideal goodness-of-fit to modeling and generalization capability. The performance of GBDT and Ada-DT was similar, and the RF model performed the worst but was still satisfactory. The gaps in performance between training and validation data were not obvious among the models. Compared to the RF model, the application of the Stacking model enhanced the performance significantly and was regarded as the most suitable model for LSM in this study.

4.3. Application of Stacking Method for LSM

The above analysis proves that the Stacking method has superior ability in LSM compared with the other three models. Therefore, the probability of landslides occurring was calculated for all mapping units in the whole study area. The LSM was also constructed with five susceptible classes, which were very low (0–0.2), low (0.2–0.4), moderate (0.4–0.6), high (0.6–0.8), and very high (0.8–1) (Figure 10). Table 3 showed the distribution ratio of each level. The very low susceptible level occupied 26.04% of the area while low, moderate, high, and very high susceptible levels represented 15.31%, 15.46%, 32.45%, and 10.74%, respectively (Figure 11). It was noticed that LSM has the smallest area percentage in very high susceptibility levels while the largest is in high. Landslide locations were mostly distributed in the red areas. Meanwhile, most of the non-landslide samples screened by FCM clustering appeared in blue areas.

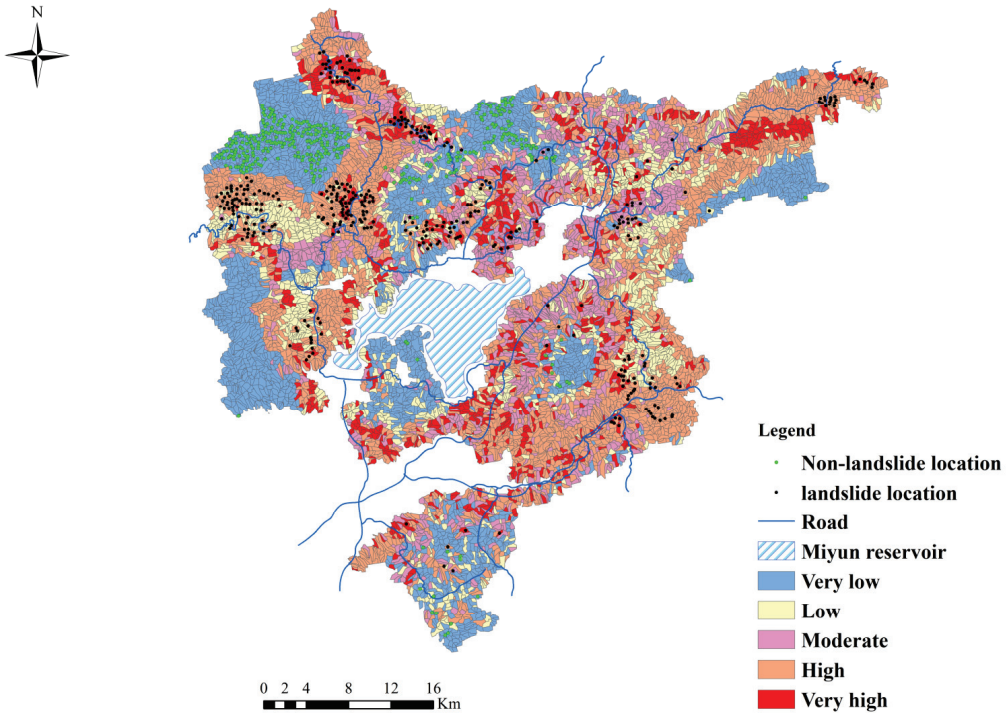

Figure 10. Landslide susceptibility map using the Stacking model.

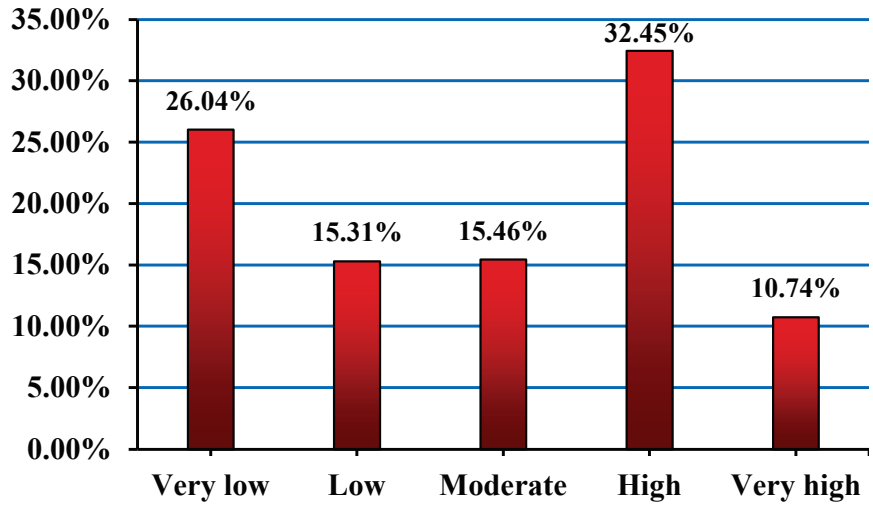

Figure 11. The distribution of susceptible classes on landslide susceptibility maps.

The high or very-high susceptibility areas are mainly distributed closed to streams or provincial highway, which runs through three townships including Fanzipai Town, Sihetang Town, and Fengjiayu Town in the study area. These areas are densely populated.

The landslide susceptibility class ranged from very low to very high around the Miyun reservoir. It is noteworthy that once a landslide occurs in this area, a series of disaster chains may be induced.

4.4. Analysis of Major Conditioning Factors

The stacking method performed the best in terms of accuracy, but the results had a poor analysis of the occurrence of landslides, which was confusing. Understanding the major factors that have a significant contribution to landslides occurring helps in the prevention and treatment of landslides. Based on the Gini index, ten major parameters were selected and normalized as shown in Table 8, including DTS, DTR, elevation, slope

angle, TWI, maximum 24 h rainfall, lithology, MED, maximum seven days of rainfall, and profile curvature. Among them, DTS, DTR, and elevation have a significant impact on the occurrence of landslides (Figure 12), the weight values of which were 0.37, 0.34, and 0.16, respectively. While the weight values of lithology, MED, maximum seven days rainfall, and profile curvature were close to 0.01, which had a limited contribution. The weight values of slope angle, TWI, and maximum 24 h rainfall were close to 0.04, 0.03, and 0.02, respectively.

Table 8. Conditioning factors assigned by the Ada-DT.

Method	DTS	DTR	Elevation	Slope Angel	TWI	Maximum 24 h Rainfall	Lithology	MED	Maximum 7 Days Rainfall	Profile Curvature
GBDT	0.37	0.34	0.16	0.04	0.03	0.02	0.01	0.01	0.01	0.01

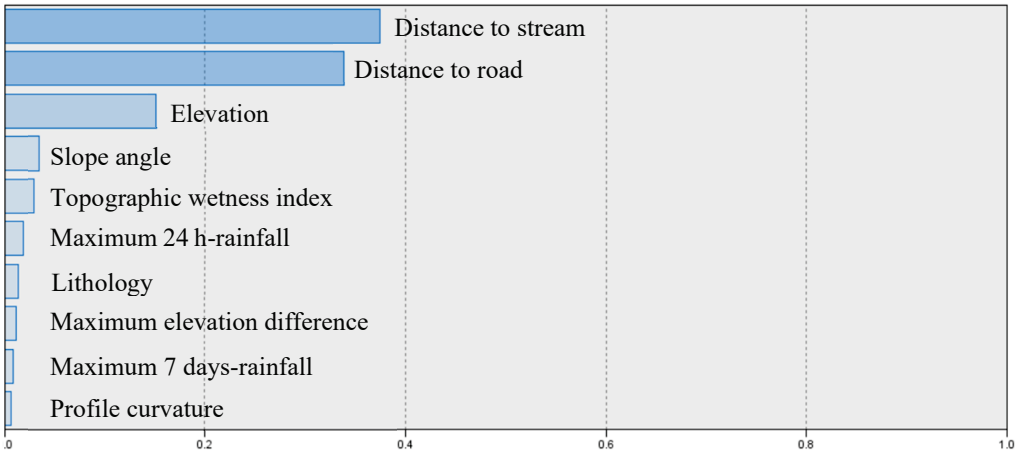

Figure 12. Parametric importance graphics obtained from Ada-DT.

Therefore, three conditioning factors, namely DTS, DTR, and elevation, were considered the major factors responsible for the landslide. Rivers are an important factor affecting the occurrence of landslides. On the slopes closer to the river, the toe of the slope is easily soaked by the river water, which reduces the strength of the rock and makes landslides more likely. Road development and construction are important tasks in mountainous area construction. However, unreasonable road excavation is a common human factor that induces geological disasters. Road construction often produces a large number of slopes, which destroy the stability of the slope and finally, lead to the occurrence of landslides.

The relationship between the major factors and landslides was further explored by calculating the FRi of each parameter (Table 9). As for DTS, the percentages of landslide area of the first two classes (<1000 m and 1000–2000 m) were 46.99% and 24.43% with the FR values of 49.3 and 173.29, accounting for more than 70% of the landslides area. Similarly, DTS showed a positive correlation in the first three classes (<1000 m, 1000–2000 m, and 2000–3000 m) with FR values greater than 1. Regarding elevation also a positive correlation in the first three classes (<200m, 200–400 m, and 400–600 m) with values of FR gradually decreasing with altitude and a negative relationship in the last two classes (>600 m).

The selection and analysis of major factors by combining basic machine learning and bivariate methods made up for the defects of stacking, thereby ensuring the integrity of geological hazard assessment.

Table 9. Spatial relationship between landslide conditioning factors and landslides using frequency ratio.

Conditioning Factor	Zone	Landslide (%)	Non-Landslide (%)	FR
DTS(m)	<1000	46.99%	0.95%	49.30
	1000–2000	24.43%	0.14%	173.29
	2000–3000	14.33%	6.63%	2.16
	3000–4000	5.33%	15.72%	0.34
	>4000	8.91%	76.69%	0.12
DTR(m)	<1000	56.06%	7.13%	7.87
	1000–2000	23.02%	7.13%	3.23
	2000–3000	15.59%	9.29%	1.68
	3000–4000	3.95%	11.51%	0.34
	>4000	1.37%	66.79%	0.02
Elevation(m)	<200	4.36%	2.08%	2.09
	200–400	53.76%	12.29%	4.37
	300–600	30.36%	23.70%	1.28
	400–800	10.06%	34.52%	0.29
	>800	1.46%	27.41%	0.05

5. Discussion

5.1. Ensuring the Reliability of Models

5.1.1. Internal and External Cross-Validation

The basic classifiers used in our work have several hyperparameters that control the behavior and performance. In some cases, reasonable "guesses" are available (e.g., *n* tree = 500 in RF), in other cases classifiers are very sensitive to the parameters, which means that default hyperparameter settings fail to guarantee optimal performance of machine-learning techniques. Therefore, hyperparameters need to be tuned before application and inner cross-validation should be used for this [48].

On the other hand, external cross-validation was also essential. One can find an "excellent model" using the method "Leave-One-Out" because of the randomness in the sampling scheme, the results of which are unconvincing. Only by implementing a more rigorous k-fold (or other types) cross-validation scheme can one infer the actual capacity of a model to learn the functional relationships between landslides and causative factors as well as the variability that the models and the susceptibility estimates exhibit [45,48].

While various machine-learning algorithms have been recognized in recent years due to their powerful capabilities of data processing and generalization, there are several practical challenges related to bias-reduced assessment of a model's predictive power and some researchers often ignore them, which leads to an unreliable or uncertain result. Single hold-out model performance measures were popular [49]. However, statistically based landslide susceptibility models desire a more credible validation and assessment before generalization.

5.1.2. The Selection of Non-Landslide Samples

A complete disaster inventory map is emphasized in a multitude of studies, which consists of the locations and number of a certain disaster [9]. The quality of landslide presence samples is more convincing compared to that of landslide absence because non-landslide samples are selected randomly or subjectively although quite a few methods or principles will be adopted. Seldom do studies consider or discuss the noise and influence of the absence of data bring to data-driven models [50]. Non-landslide points need to be selected from low-prone areas as far as possible, which is arduous to implement by selecting randomly. Clustering analysis help solve the problem by combining with the bivariate methods. FR was calculated to judge the area with low susceptibility based on the results of FCM and K-means in this study and the non-landslide samples were generated from it, which improved the quality of non-landslide records and the performance of models logically.

5.2. Increasing the Accuracy of LSM

How to achieve an accurate landslide susceptibility zoning map is always a hot topic and the main concern of researchers. However, determining the most suitable model is challenging because the performance varies according to the study area and methods applied. Actually, related studies have applied various methods and compared their performance based on the value of AUC to obtain the best method for a given region [51,52]. Yet, it is controversial that we claim a model to be better than the other according to the decimal places down the line (AUC). Therefore, it is necessary to explore new methods for significant improvement and ensemble techniques are considered in our study, which have also been proven to be an excellent solution [53–55]. A detailed comparison among three ensemble techniques in LSM, namely bagging, boosting, and stacking was implemented. Bagging and boosting are two algorithms commonly used in LSM while stacking have rarely been applied. The results proved that the ensemble of the GBDT-Adaboost-DT-RF-LR had the ability to enhance the predictive performance and the improvement was obvious. This enhancement originates from reducing both bias and variance and avoiding over-fitting problems [56,57]. It is believed that the stacking technique and its comparison will guarantee a better result for further studies [58].

5.3. Maintain the Integrity of Geological Hazard Assessment

An optimal model should not only focus on accuracy, especially for geological hazard assessment [50]. An outstanding model should also require communication skills, that is, make it easy for researchers to understand, accept and apply, especially for natural disasters [59]. The capacity of communicating model behavior is another valuable quality for LSA, which is arduously achieved by machine learning methods because of the "black box" nature. Stacking performed the best in terms of accuracy while it had a low capacity for recognizing the importance of the variables. Gini index and FR were combined to determine the major conditioning factors and analyze the individual landslide-related factors in each interval and the relative importance among them, which improved the readability of the stacking model.

6. Conclusions

LSM is the basis of supplementary analyses, such as land use and hazard prevention. Meanwhile, this field of geomorphology has become an empty shell with no research question on whether a model can be evaluated in an unreliable sampling strategy and focus only on accuracy. Therefore, a more reliable and accurate landslide susceptibility map is urgently needed through further comparison and application of different methods. In the present study, three ensemble learning machines were compared in terms of the performance of LSM in Miyun County, Beijing, China. Non-landslide samples were determined in a more reliable way with the use of FCM and K-means clustering. Statistical indexes and AUC were combined to assess the accuracy performance of the models. The major conditioning factors were determined and analyzed based on the Gini index and FR. The following conclusions can be drawn from the present study:

1. The performance of different ensemble techniques varies, but achieved satisfactory results as a whole. Stacking was considered the most suitable model with obvious improvement in terms of accuracy compared to the basic classifiers.
2. The combination of the bivariate statistical method and Gini index helps better explore the major conditioning factors and improve the integrity of ensemble techniques.
3. The non-landslide samples selected by FCM are more representative and improved the quality of samples. Overall, improvement of sample quality and selection of advanced methods help improve the practicability of LSM.

Author Contributions: Z.L. writing—original draft, methodology, and software; W.L., W.P. and C.W., review and validation; L.C. reviewing and editing. All authors have read and agreed to the published version of the manuscript.

Funding: This work was supported by Key-Area Research and Development Program of Guangdong Province (Grant No. 2020B0101130009) and Guangdong Enterprise Key Laboratory for Urban Sensing, Monitoring and Early Warning (No. 2020B121202019) and The Science and Technology Foundation of Guangzhou Urban Planning & Design Survey Research Institute (Grant No. RDI2210204140, RDI2210204146).

Institutional Review Board Statement: Not applicable.

Informed Consent Statement: Informed consent was obtained from all subjects involved in the study.

Data Availability Statement: The related code of machine learning applied in the study is available at https://github.com/Liangzhu-mz, accessed on 6 April 2022.

Acknowledgments: The authors would like to thank the Editors and anonymous reviewers for their valuable comments, which improve this paper.

Conflicts of Interest: The authors declare no conflict of interest.

References

1. Huang, X.; Guo, F.; Deng, M.; Yi, W.; Huang, H. Understanding the deformation mechanism and threshold reservoir level of the floating weight-reducing landslide in the Three Gorges Reservoir Area, China. *Landslides* **2020**, *17*, 2879–2894. [CrossRef]
2. Sun, X.; Chen, J.; Li, Y.; Rene, N.N. Landslide Susceptibility mapping along a rapidly uplifting river valley of the Upper Jinsha River, Southeastern Tibetan Plateau, China. *Remote Sens.* **2022**, *14*, 1730. [CrossRef]
3. Kim, J.C.; Lee, S.; Jung, H.S.; Lee, S. Landslide susceptibility mapping using random forest and boosted tree models in Pyeong-Chang, Korea. *Geocarto Int.* **2018**, *33*, 1000–1015. [CrossRef]
4. Safran, E.B.; O'Connor, J.E.; Ely, L.L.; House, P.K.; Grant, G.; Harrity, K.; Jones, E. Plugs or flood-makers? The unstable landslide dams of eastern Oregon. *Geomorphology* **2015**, *248*, 237–251. [CrossRef]
5. Zhu, A.X.; Miao, Y.; Wang, R.; Zhu, T.; Deng, Y.; Liu, J.; Hong, H. A comparative study of an expert knowledge-based model and two data-driven models for landslide susceptibility mapping. *Catena* **2018**, *166*, 317–327. [CrossRef]
6. Ayalew, L.; Yamagishi, H. The application of GIS-based logistic regression for landslide susceptibility mapping in the Kaku-da-Yahiko Mountains, Central Japan. *Geomorphology* **2005**, *65*, 15–31. [CrossRef]
7. Jiao, Y.; Zhao, D.; Ding, Y.; Liu, Y.; Xu, Q.; Qiu, Y.; Liu, C.; Liu, Z.; Zha, Z.; Li, R. Performance evaluation for four GIS-based models purposed to predict and map landslide susceptibility: A case study at a World Heritage site in Southwest China. *Catena* **2019**, *183*, 104221. [CrossRef]
8. Shi, M.; Chen, J.; Song, Y.; Zhang, W.; Song, S.; Zhang, X. Assessing debris flow susceptibility in Heshigten Banner, Inner Mongolia, China, using principal component analysis and an improved fuzzy C-means algorithm. *Bull. Eng. Geol. Environ.* **2016**, *75*, 909–922. [CrossRef]
9. Liang, Z.; Wang, C.M.; Zhang, Z.M.; Khan, K.U.J. A comparison of statistical and machine learning methods for debris flow susceptibility mapping. *Stoch. Environ. Res. Risk Assess.* **2020**, *34*, 1887–1907. [CrossRef]
10. Lian, C.; Zeng, Z.; Yao, W.; Tang, H. Extreme learning machine for the displacement prediction of landslide under rainfall and reservoir level. *Stoch. Environ. Res. Risk Assess.* **2014**, *28*, 1957–1972. [CrossRef]
11. Merghadi, A.; Abderrahmane, B.; Tien Bui, D. Landslide susceptibility assessment at Mila Basin (Algeria): A comparative as-sessment of prediction capability of advanced machine learning methods. *ISPRS Int. J. Geo-Inf.* **2018**, *7*, 268. [CrossRef]
12. Tien Bui, D.; Ho, T.C.; Revhaug, I.; Pradhan, B.; Nguyen, D.B. *Landslide Susceptibility Mapping Along the National Road 32 of Vietnam Using GIS-Based J48 Decision Tree Classifier and Its Ensembles[M]//Cartography from Pole to Pole*; Springer: Berlin/Heidelberg, Germany, 2014; pp. 303–317.
13. Hu, X.; Zhang, H.; Mei, H.; Xiao, D.; Li, Y.; Li, M. Landslide susceptibility mapping using the stacking ensemble machine learning method in Lushui, Southwest China. *Appl. Sci.* **2020**, *10*, 4016. [CrossRef]
14. Bennett, G.L.; Miller, S.R.; Roering, J.J.; Schmidt, D.A. Landslides, threshold slopes, and the survival of relict terrain in the wake of the Mendocino Triple Junction. *Geology* **2016**, *44*, 363–366. [CrossRef]
15. Du, J.; Glade, T.; Woldai, T.; Chai, B.; Zeng, B. Landslide susceptibility assessment based on an incomplete landslide in-ventory in the Jilong Valley, Tibet, Chinese Himalayas. *Eng. Geol.* **2020**, *270*, 105572. [CrossRef]
16. Lee, S.; Min, K. Statistical analysis of landslide susceptibility at Yongin, Korea. *Environ. Earth Sci.* **2001**, *40*, 1095–1113. [CrossRef]
17. Breiman, L. Random forests. *Mach. Learn.* **2001**, *45*, 5–32. [CrossRef]
18. Varnes, D.J. Landslide types and processes. *Landslides Eng. Pract.* **1958**, *24*, 20–47.
19. Furlani, S.; Ninfo, A. Is the present the key to the future? *Earth-Sci. Rev.* **2015**, *142*, 38–46. [CrossRef]
20. Guzzetti, F.; Galli, M.; Reichenbach, P.; Ardizzone, F.; Cardinali, M.; Galli, M. Estimating the quality of landslide susceptibility models. *Geomorphology* **2006**, *81*, 166–184. [CrossRef]
21. Guzzetti, F.; Galli, M.; Reichenbach, P.; Ardizzone, F.; Cardinali, M. Landslide hazard assessment in the Collazzone area, Umbria, Central Italy. *Nat. Hazards Earth Syst. Sci.* **2006**, *6*, 115–131. [CrossRef]

22. Sun, X.L.; Zhao, Y.G.; Wang, H.L.; Yang, L.; Qin, C.Z.; Zhu, A.X.; Li, B. Sensitivity of digital soil maps based on FCM to the fuzzy exponent and the number of clusters. *Geoderma* **2012**, *171*, 24–34. [CrossRef]
23. Van Westen, C.J.; Castellanos, E.; Kuriakose, S.L. Spatial data for landslide susceptibility, hazard, and vulnerability assessment: An overview. *Eng. Geol.* **2008**, *102*, 112–131. [CrossRef]
24. Feizizadeh, B.; Blaschke, T.; Nazmfar, H. GIS-based ordered weighted averaging and dempster—Shafer methods for landslide susceptibility mapping in the Urmia Lake Basin, Iran. *Int. J. Digit. Earth* **2012**, *7*, 688–708. [CrossRef]
25. Hong, H.; Pradhan, B.; Xu, C.; Bui, D.T. Spatial prediction of landslide hazard at the Yihuang area (China) using two-class kernel logistic regression, alternating decision tree and support vector machines. *Catena* **2015**, *133*, 266–281. [CrossRef]
26. Magliulo, P.; Di Lisio, A.; Russo, F.; Zelano, A. Geomorphology and landslide susceptibility assessment using GIS and bivariate statistics: A case study in southern Italy. *Nat. Hazards* **2008**, *47*, 411–435. [CrossRef]
27. Liang, Z.; Wang, C.; Han, S.; Khan, K.U.J.; Liu, Y. Classification and susceptibility assessment of debris flow based on a semi-quantitative method combination of the fuzzy C-means algorithm, factor analysis and efficacy coefficient. *Nat. Hazards Earth Syst. Sci.* **2020**, *20*, 1287–1304. [CrossRef]
28. Evans, I.S. An integrated system of terrain analysis and slope mapping. *Z. Geomorphol.* **1980**, *36*, 274–295.
29. Camilo, D.C.; Lombardo, L.; Mai, P.M.; Dou, J.; Huser, R. Handling high predictor dimensionality in slope-unit-based landslide susceptibility models through LASSO-penalized generalized linear model. *Environ. Model. Softw.* **2017**, *97*, 145–156. [CrossRef]
30. Dou, J.; Yamagishi, H.; Xu, Y.; Zhu, Z.; Yunus, A.P. *Characteristics of the Torrential Rainfall-Induced Shallow Landslides by Typhoon Bilis, in July 2006, Using Remote Sensing and GIS[M]//GIS Landslide*; Springer: Tokyo, Japan, 2017; pp. 221–230.
31. Anil, K. Data clustering: 50 years beyond K-Means. *Pattern Recogn. Lett.* **2010**, *31*, 651–666.
32. Hartigan, J.; Wong, M. Algorithm AS 136: A K-means clustering algorithm. *J. R. Stat. Soc. C.* **1979**, *28*, 100–108. [CrossRef]
33. Dunn, J.C. A fuzzy relative of the ISODATA process and its use in detecting compact well-separated clusters. *J. Cybern.* **1973**, *3*, 32–57. [CrossRef]
34. Bezdek, J.C. *Pattern Recognition with Fuzzy Objective Function Algorithms*; Springer Science & Business Media: Berlin/Heidelberg, Germany, 2013.
35. Wang, J.; Chen, J.; Yang, J. Application of distance discriminant analysis method in classification of surrounding rock mass in highway tunnel. *J. Jilin Univ.* **2008**, *38*, 999–1004.
36. Chen, J.; Pi, D. A cluster validity index for fuzzy clustering based on non-distance. In Proceedings of the 2013 International Conference on Computational and Information Sciences, Yongzhou, China, 21–23 June 2013; pp. 880–883.
37. Neter, J.; Wasserman, W.; Kutner, M.H. *Applied Linear Statistical Models*; Irwin: Chicago, IL, USA, 1996.
38. Fernández-Delgado, M.; Cernadas, E.; Barro, S.; Amorim, D. Do we need hundreds of classifiers to solve real world classification problems? *J. Mach. Learn. Res.* **2014**, *15*, 3133–3181.
39. Pedregosa, F.; Varoquaux, G.; Gramfort, A.; Michel, V.; Thirion, B.; Grisel, O.; Blondel, M.; Prettenhofer, P.; Weiss, R.; Dubourg, V.; et al. Scikit-learn: Machine learning in Python. *J. Mach. Learn. Res.* **2011**, *12*, 2825–2830.
40. Youssef, A.M.; Pradhan, B.; Jebur, M.N.; El-Harbi, H.M. Landslide susceptibility mapping using ensemble bivariate and multivariate statistical models in Fayfa area, Saudi Arabia. *Environ. Earth Sci.* **2014**, *73*, 3745–3761. [CrossRef]
41. Wang, Y.; Feng, L.; Li, S.; Ren, F.; Du, Q. A hybrid model considering spatial heterogeneity for landslide susceptibility mapping in Zhejiang Province, China. *Catena* **2020**, *188*, 104425. [CrossRef]
42. Freund, Y.; Schapire, R.E. A decision-theoretic generalization of online learning and an application to boosting. *J. Comput. Syst. Sci.* **1997**, *55*, 119–139. [CrossRef]
43. Džeroski, S.; Ženko, B. Is combining classifiers with stacking better than selecting the best one? *Mach. Learn.* **2004**, *54*, 255–273. [CrossRef]
44. Chung, C.J.F.; Fabbri, A.G. Validation of spatial prediction models for landslide hazard mapping. *Nat. Hazards* **2003**, *30*, 451–472. [CrossRef]
45. James, G.; Witten, D.; Hastie, T.; Tibshirani, R. *An Introduction to Statistical Learning*; Springer: New York, NY, USA, 2013.
46. Green, D.M.; Swets, J.A. *Signal Detection Theory and Psychophysics*; Wiley: New York, NY, USA, 1966.
47. Schratz, P.; Muenchow, J.; Iturritxa, E.; Richter, J.; Brenning, A. Hyperparameter tuning and performance assessment of statistical and machine-learning algorithms using spatial data. *Ecol. Model.* **2019**, *406*, 109–120. [CrossRef]
48. Duarte, E.; Wainer, J. Empirical comparison of cross-validation and internal metrics for tuning SVM hyperparameters. *Pattern Recognit. Lett.* **2017**, *88*, 6–11. [CrossRef]
49. Bengio, Y. Gradient-based optimization of hyperparameters. *Neural Comput.* **2000**, *12*, 1889–1900. [CrossRef] [PubMed]
50. Reichenbach, P.; Rossi, M.; Malamud, B.D.; Mihir, M.; Guzzetti, F. A review of statistically-based landslide susceptibility models. *Earth-Sci. Rev.* **2018**, *180*, 60–91. [CrossRef]
51. Ciurleo, M.; Cascini, L.; Calvello, M. A comparison of statistical and deterministic methods for shallow landslide susceptibility zoning in clayey soils. *Eng. Geol.* **2017**, *223*, 71–81. [CrossRef]
52. Liu, R.; Yang, X.; Xu, C.; Wei, L.; Zeng, X. Comparative study of convolutional neural network and conventional machine learning methods for landslide susceptibility mapping. *Remote Sens.* **2022**, *14*, 321. [CrossRef]
53. Dou, J.; Yunus, A.P.; Bui, D.T.; Merghadi, A.; Sahana, M.; Zhu, Z.; Chen, C.; Han, Z.; Pham, B.T. Improved landslide assessment using support vector machine with bagging, boosting, and stacking ensemble machine learning framework in a mountainous watershed, Japan. *Landslides* **2020**, *17*, 641–658. [CrossRef]

54. Di Napoli, M.; Carotenuto, F.; Cevasco, A.; Confuorto, P.; Di Martire, D.; Firpo, M.; Pepe, G.; Raso, E.; Calcaterra, D. Machine learning ensemble modelling as a tool to improve landslide susceptibility mapping reliability. *Landslides* **2020**, *17*, 1897–1914. [CrossRef]
55. Arabameri, A.; Chandra Pal, S.; Rezaie, F.; Chakrabortty, R.; Saha, A.; Blaschke, T.; Thi Ngo, P.T. Decision tree based ensemble machine learning approaches for landslide susceptibility mapping. *Geocarto Int.* **2021**, 1–35. [CrossRef]
56. Li, W.; Fang, Z.; Wang, Y. Stacking ensemble of deep learning methods for landslide susceptibility mapping in the Three Gorges Reservoir area. China. *Stoch. Environ. Res. Risk Assess.* **2021**, 1–22. [CrossRef]
57. Chen, W.; Xie, X.; Wang, J.; Pradhan, B.; Hong, H.; Bui, D.T.; Ma, J. A comparative study of logistic model tree, random forest, and classification and regression tree models for spatial prediction of landslide susceptibility. *Catena* **2017**, *151*, 147–160. [CrossRef]
58. Dietterich, T.G. An experimental comparison of three methods for constructing ensembles of decision trees: Bagging, boosting, and randomization. *Mach. Learn.* **2000**, *40*, 139–157. [CrossRef]
59. Youssef, A.M.; Pourghasemi, H.R. Landslide susceptibility mapping using machine learning algorithms and comparison of their performance at Abha Basin, Asir Region, Saudi Arabia. *Geosci. Front.* **2021**, *12*, 639–655. [CrossRef]

sustainability

MDPI

Article

Investigation of Landslide Susceptibility Decision Mechanisms in Different Ensemble-Based Machine Learning Models with Various Types of Factor Data

Jiakai Lu [1], Chao Ren [1,2,*], Weiting Yue [1], Ying Zhou [1], Xiaoqin Xue [1], Yuanyuan Liu [1] and Cong Ding [1]

[1] College of Geomatics and Geoinformation, Guilin University of Technology, 319 Yanshan Street, Guilin 541006, China; 2120222009@glut.edu.cn (J.L.); yueweiting@glut.edu.cn (W.Y.); zhouying01@glut.edu.cn (Y.Z.); 2120222038@glut.edu.cn (X.X.); liuyuanyuan@glut.edu.cn (Y.L.); dc3050367@gmail.com (C.D.)
[2] Guangxi Key Laboratory of Spatial Information and Geomatics, 319 Yanshan Street, Guilin 541006, China
* Correspondence: renchao@glut.edu.cn

Abstract: Machine learning (ML)-based methods of landslide susceptibility assessment primarily focus on two dimensions: accuracy and complexity. The complexity is not only influenced by specific model frameworks but also by the type and complexity of the modeling data. Therefore, considering the impact of factor data types on the model's decision-making mechanism holds significant importance in assessing regional landslide characteristics and conducting landslide risk warnings given the achievement of good predictive performance for landslide susceptibility using excellent ML methods. The decision-making mechanism of landslide susceptibility models coupled with different types of factor data in machine learning methods was explained in this study by utilizing the Shapley Additive exPlanations (SHAP) method. Furthermore, a comparative analysis was carried out to examine the differential effects of diverse data types for identical factors on model predictions. The study area selected was Cenxi, Guangxi, where a geographic spatial database was constructed by combining 23 landslide conditioning factors with 214 landslide samples from the region. Initially, the factors were standardized using five conditional probability models, frequency ratio (FR), information value (IV), certainty factor (CF), evidential belief function (EBF), and weights of evidence (WOE), based on the spatial arrangement of landslides. This led to the formation of six types of factor databases using the initial data. Subsequently, two ensemble-based ML methods, random forest (RF) and XGBoost, were utilized to build models for predicting landslide susceptibility. Various evaluation metrics were employed to compare the predictive capabilities of different models and determined the optimal model. Simultaneously, the analysis was conducted using the interpretable SHAP method for intrinsic decision-making mechanisms of different ensemble-based ML models, with a specific focus on explaining and comparing the differential impacts of different types of factor data on prediction results. The results of the study illustrated that the XGBoost-CF model constructed with CF values of factors not only exhibited the best predictive accuracy and stability but also yielded more reasonable results for landslide susceptibility zoning, and was thus identified as the optimal model. The global interpretation results revealed that slope was the most crucial factor influencing landslides, and its interaction with other factors in the study area collectively contributed to landslide occurrences. The differences in the internal decision-making mechanisms of models based on different data types for the same factors primarily manifested in the extent of influence on prediction results and the dependency of factors, providing an explanation for the performance of standardized data in ML models and the reasons behind the higher predictive performance of coupled models based on conditional probability models and ML methods. Through comprehensive analysis of the local interpretation results from different models analyzing the same sample with different sample characteristics, the reasons for model prediction errors can be summarized, thereby providing a reference framework for constructing more accurate and rational landslide susceptibility models and facilitating landslide warning and management.

Citation: Lu, J.; Ren, C.; Yue, W.; Zhou, Y.; Xue, X.; Liu, Y.; Ding, C. Investigation of Landslide Susceptibility Decision Mechanisms in Different Ensemble-Based Machine Learning Models with Various Types of Factor Data. *Sustainability* **2023**, *15*, 13563. https://doi.org/10.3390/su151813563

Academic Editors: Stefano Morelli, Veronica Pazzi and Mirko Francioni

Received: 28 July 2023
Revised: 20 August 2023
Accepted: 28 August 2023
Published: 11 September 2023

Keywords: landslide susceptibility; explainable machine learning; Shapley additive explanations; conditional probability model; ensemble learning

1. Introduction

Landslides rank among the most devastating geological perils globally, characterized by their wide distribution, frequent occurrence, and high destructiveness [1]. The ecological environment incurs significant damage due to frequent geological disasters, and there are considerable losses to agricultural and industrial production and people's lives and property [2]. According to data released by the China Geological Survey, there were 4810 landslides in China during 2020, marking an increase of 590 compared to 2019. These landslides constituted 61.35% of the overall count of geological disasters [3]. Therefore, in light of the growing occurrence of landslide catastrophes, constructing accurate and reliable landslide susceptibility maps (LSMs) is essential for regional landslide susceptibility assessment and risk analysis [4,5]. An LSM generally refers to a model that accurately predicts the study area that determines the landslide susceptibility index (LSI) by examining the relationship between the location of known landslide areas and the factors that contribute to landslides. This analysis generates a probability map showing the likelihood of landslides occurring throughout the entire study area [6]. The LSI calculates the likelihood of a landslide happening in a particular area by using a nonlinear combination of various environmental factors. Thus, an LSM serves as the foundation for studying landslide risks and finds wide applications in urban planning, early disaster prevention, and other fields, providing a reliable theoretical basis for regional planning, disaster prevention, and mitigation.

Due to the ongoing advancements in computer science, as well as geographic information systems, remote sensing technology, and related disciplines, the approaches used for studying landslide susceptibility have transitioned from qualitative and semi-quantitative to quantitative analysis [7]. Abundant expert experience is typically required for qualitative and semi-quantitative analysis methods, such as expert scoring and the analytic hierarchy process (AHP), to determine the likelihood of a landslide event occurring [8,9]. Nevertheless, these approaches heavily depend on subjective prior knowledge, and in cases where expert opinions prove to be erroneous, the resulting calculations may diverge from objective reality [10]. Driven by data, methods of quantitative analysis are more practical for assessing susceptibility to landslide disasters. These methods primarily utilize physical–mechanical, conditional probability, and machine learning (ML) models to reflect the correlation between occurrences of landslides and the factors that contribute to them [11]. Physical–mechanical models calculate and analyze the mechanism of landslide occurrence based on geological and topographical parameters obtained through field investigations in landslide-prone areas [12]. They have the advantages of clear physical meaning and accurate analysis results. However, they require many geological and hydrological parameters and are only suitable for analyzing specific types of landslides on a small scale [13]. Common conditional probability models include frequency ratio (FR), information value (IV), certainty factor (CF), evidential belief function (EBF), and weights of evidence (WOE). Statistical algorithms enable these models to effectively demonstrate the connection between landslides and various attribute intervals of individual conditioning factors. They possess a simple computational nature but overly rely on the quality of samples and factors. The weight and correlation of each indicator factor cannot be accurately expressed, nor can the complex relationship between conditioning factors and landslide events be fully conveyed [14,15]. Landslide susceptibility assessment has seen widespread application of different machine learning models such as logistic regression, artificial neural network (ANN), naive Bayes, support vector machine (SVM), and random forest (RF) in recent years [16]. These models establish connections between landslide data and different conditioning factors; by emphasizing the nonlinear association between landslides and factors,

it is possible to achieve more precise predictive outcomes [17,18]. While the accuracy of various machine learning models for predicting landslide susceptibility may differ within a given location, it is widely recognized that ensemble-based machine learning models like random forest (RF) and extreme gradient boosting (XGBoost) consistently offer notable benefits over other machine learning models across all regions for landslide susceptibility modeling: higher modeling efficiency, better predictive performance, and superior ability to handle outliers [17,19,20].

In summary, different analysis methods have their advantages and limitations. Among them, conditional probability models have the advantages of simplicity, strong operability, and practicality. However, they only reflect the influence of landslides in various classification intervals of combined conditioning factors, without taking into account the correlations between these factors or the variations in their influence on landslide occurrence [21]. As for ML models, although they can effectively capture the intricate nonlinear connection between multiple conditioning factors and the occurrence of landslides, they are susceptible to overfitting or underfitting when there is insufficient data or when the factor types are too complex. Therefore, relying solely on a single prediction model cannot guarantee the accuracy of the prediction [22]. To fully leverage the strengths of both conditional probability models and ML models, many scholars have begun to adopt coupled models combining the two approaches to study landslide susceptibility [23–25].

In recent years, research on landslide susceptibility with the help of machine learning (ML) models has mainly focused on adopting superior algorithms or improving existing algorithms in order to increase the precision and reliability of predicting landslide susceptibility. However, such studies tend to ignore another essential characteristic of ML models: complexity. The complexity of a model is reflected in its structural complexity, which is affected by model characteristics and modeling data types. In landslide susceptibility studies, in addition to focusing on model prediction accuracy, it is more important to elucidate the impact of the factors within the model on landslide events, facilitating the analysis of causal factors and regional landslide characteristics [26]. Although some ML methods, such as the neural-network-based connection weighting method for hidden layers [27], average reduction accuracy in decision trees [28], and Gini index in random forests, have been widely used to explain the importance of model factors, the evaluation methods of different ML models are inconsistent. They can only reflect the relative influence of the factors on the prediction results. The Shapley Additive exPlanations (SHAP) method based on game-theoretic ideas can overcome this problem, explaining the contribution of factors to the decision outcome in global and local dimensions and clearly explaining the impact of complex interactions among factors on the prediction outcome. In the past few years, there have been advancements made in landslide susceptibility modeling using ML models, especially deep learning. However, the practical application of these models is limited due to their opacity. To address this problem, SHAP, an interpretable ML-based algorithm, was introduced to interpret model results. For example, Biswajeet Pradhan et al. investigated landslide susceptibility using a convolutional neural network model, which marked the first use of an interpretable ML model in landslide susceptibility modeling by demonstrating the process of elucidating the model to achieve a particular result through SHAP plots, showing the feature interactions at both landslide and non-landslide locations [29]. Ajaya Pyakurel et al. used a combination of ET-SHAP analysis and factor importance analysis to reveal the critical influencing factors, emphasizing the importance of earthquakes, terrain ruggedness, and slopes in causing landslides during earthquakes, highlighting the significance of SHAP in explaining model results and factor importance in geohazard research [30]. IBAN Muzaffer Can et al. utilized the SHAP method to examine in depth how conditioning factors impact the occurrence of avalanches [31]. Deliang Sun et al. utilized the SHAP technique to provide comprehensive explanations for the outcomes prediction by models in landslide studies [32]. Zhang Junyi et al. constructed a model that was developed to assess susceptibility to landslides using the SHAP-XGBoost algorithm. Their analysis focused on examining the attributes and variations in space of the factors

that impact landslides [33]. Ömer Ekmekcioğlu et al. applied a model agnosticism-based game-theoretic SHAP algorithm to analyze the prediction influenced by the factors of hazardous conditions of landslide and flood event outcomes [34]. Despite the extensive research on ML-based models for predicting susceptibility to landslides and the preliminary outcomes of utilizing the SHAP approach to interpret these models in terms of application, the current research mainly focuses on exploring the decision-making mechanisms of using the SHAP approach in explaining different ML models. It lacks the comparison and analysis of the internal decision-making differences of models constructed based on different factor data types. Therefore, exploring the internal decision differences of models in landslide susceptibility built on various types of factor data can help further explain the intricacy of models for predicting the likelihood of susceptibility to landslides.

In summary, this research is the first attempt to employ the SHAP method to explain landslide susceptibility models constructed based on different factor data types and the well-performing integrated ML method. Using 214 landslides in Cenxi as data samples, the comprehensive evaluation took into account the spatial distribution of landslides and identified 23 factors that contribute to the occurrence and mitigation of landslides. Next, by coupling the initial factor data and the factor data transformed by five conditional probability models (FR, IV, CF, EBF, and WOE) with two ensemble-based ML methods (RF and XGBoost), a total of 12 models were built to assess susceptibility to landslides, and the corresponding LSMs were generated. Then, various evaluation metrics were used to examine and contrast the similarities and differences of the models built using different ML methods and different types of factor data, and the best-performing model was selected. Finally, in addition to different ML methods, this study focused on providing comprehensive explanations using the SHAP method for landslide susceptibility models constructed based on distinct categories of factor data. A comparison was made between the impact of different data types on the internal decision mechanisms of the models, and the reasons why the coupled models obtained using conditional probability models and ML methods exhibited superior predictive performance were explored. By employing the SHAP interpretation method, this study achieved transparency and rationality in model interpretation, thoroughly dissecting the complexity of ML-based models.

In summary, the main contributions of this paper are presented as follows:

(1) This paper's innovation is to focus on two critical aspects of landslide susceptibility assessment: accuracy and complexity. The interplay between prediction accuracy and modeling complexity is emphasized. This dual focus is rare in the existing literature and highlights the need for highly accurate prediction and interpretable modeling.
(2) The innovation of the methodology in this paper is mainly reflected in data type and model interpretability. Since different types of factor data may have different effects on model predictions, different types of factor data are introduced, including initial factor data and transformed conditional probability model data. In addition, the SHAP method is used in this paper to explain the model predictions.
(3) The innovation of the experimental design and data analysis consists in its comprehensiveness and diversity. In this paper, two ensemble ML methods, random forest (RF) and XGBoost, were chosen to construct the landslide susceptibility model. In addition, this paper uses different data types and constructs multiple versions of the model for each type.
(4) The innovation in error analysis and prediction error interpretation is reflected in its in-depth analysis of prediction errors. Through local explanations and analysis, this paper delves into the interpretation of model predictions for error samples.

The remainder of this paper is structured as follows: Section 2 provides a comprehensive introduction to the research field and the specific data set used for modeling. Besides samples from landslides and non-landslides, the dataset also includes landslide conditioning factors. Section 3 introduces the methodology in detail. Section 3.1 introduces the process of assessing the independence of landslide adjustment factors, examined thoroughly and comprehensively; five commonly used conditional probability models are

introduced in Section 3.2. Section 3.3 provides a detailed description of the principles of two tree-structure-based ML algorithms (RF and XGBoost). Section 3.4 presents various evaluation criteria that are employed for assessing the performance of the model's prediction. Furthermore, the basic principle and application status of the SHAP method is explained in Section 3.5. Section 4 analyzes the test results of the independence of landslide condition factors, the structure and optimization results of different models, the LSMs and precision evaluation results generated by different models, and the decision-making mechanism of landslide susceptibility prediction results of different models using the SHAP method. Section 5 analyzes, in turn, the following: (1) The unique features and advantages of the SHAP method compared to traditional feature importance ranking methods; (2) the SHAP method being utilized to locally interpret different models using several typical samples. (3) local interpretation of samples incorrectly predicted in a model with the best prediction performance; and (4) a discussion of how the research results of this paper complement, confirm, and contradict the current state of SHAP research and an exploration of feature importance assessment for fused decision tree models. Finally, the concluding remarks are provided in Section 6.

2. Study Region and Data Overview

2.1. Study Region

The research area is Cenxi, Wuzhou City, Guangxi Zhuang Autonomous Region. Cenxi is located in the southeastern region of the Guangxi Zhuang Autonomous Region and shares its eastern border with Guangdong Province. The geographical coordinates range from 110°43′ to 111°22′ east longitude and 22°37′ to 23°13′ north latitude, with a combined surface area of approximately 2783 square kilometers (see Figure 1a,b). The elevation in the region ranges from 29 m to 1123 m; the southeast has elevated land while the northwest has lower land. Cenxi can be found in the Bobai–Cenxi fault zone in southeastern Guangxi and consists mostly of hilly and mountainous regions. Being abundant in mineral resources, it serves as a notable supplier of granite in China. The region serves as a convergence point between the Pearl River Delta Economic Zone and the southwestern region of China, playing a significant role in transportation and the economy. In recent years, the rapid expansion of urban areas has accelerated the deterioration of the fragile ecological environment. Cenxi has become more susceptible to landslide disasters due to the rise in human mining activities and the increasing occurrence of extreme weather events. The serious threat of landslides to people's lives and property demands our attention.

2.2. Data Acquisition

Having precise historical data on landslides is vital when examining and evaluating the potential for landslide catastrophes in a particular region [12]. The landslide inventory was created in this study using various methods such as Google Earth images, optical satellite images, and disaster news reports. Multiple data sources were utilized in this study to construct an inventory of historical landslides. First, the approximate locations where historical landslides occurred were identified through visual interpretation with the help of Google Earth software. Then, the location and extent of these landslides were further confirmed using optical remote sensing imagery, specifically, optical satellite imagery. These images provided high-resolution surface information that enabled more accurate identification and definition of landslide areas. In addition, disaster news reports and relevant literature were reviewed to obtain detailed information on historical landslide events, including the exact time, location, and number of occurrences. A total of 214 historical landslide areas were ultimately collected, providing essential data for interpreting the characteristics of landslides in the region and predicting their occurrence.

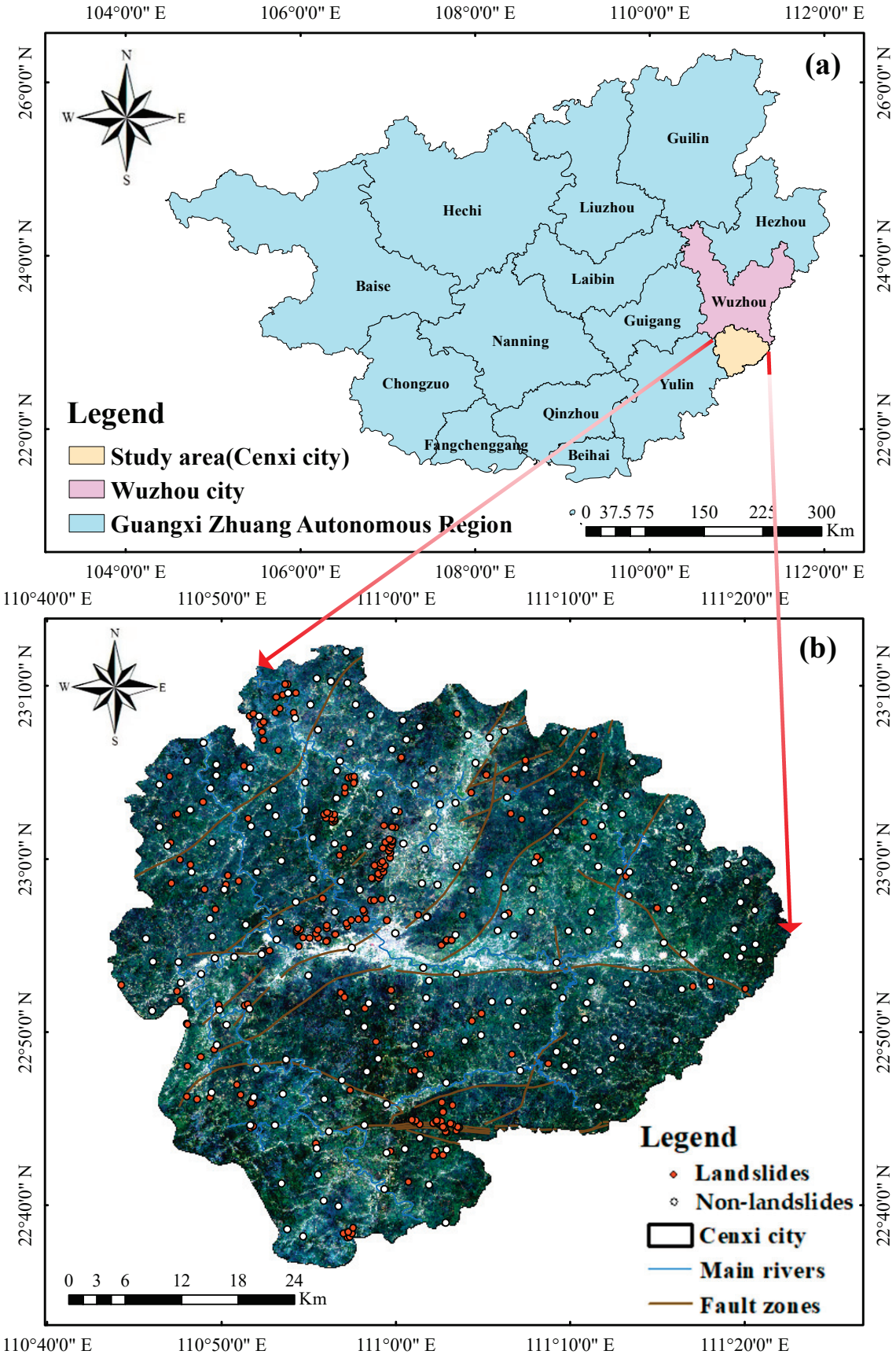

Figure 1. Location of the study area and landslide distribution. (**a**) The location of the research area in Guangxi; (**b**) the location of the study area and the distribution of landslides and non-landslides.

Landslide occurrences are typically the result of a combination of internal geological and topographic conditions within the slope and external environmental factors [35–37]. Therefore, the importance of choosing precise and suitable modeling data cannot be overstated when utilizing machine learning (ML) techniques to forecast landslide susceptibility. In this research, the conditions for the development of landslides in Cenxi were studied, which involved analyzing the geological and environmental information and the distribution status of historical landslides. The research area encompassed various aspects, including geological and soil information, topography, meteorological and hydrological conditions, land cover, soil conditions, and human activities, for a total of 23 factors selected to study the susceptibility to landslides. Table 1 provides the origins and explanations of these conditioning factors that contribute to landslides. Due to variations in coordinate systems and resolutions among different factors, the ArcGIS 10.2 software was used to project all factor data onto the UTM-Zone48 coordinate area based on the WGS1984 reference surface. All factors were transformed to a uniform spatial resolution of 30 m by generating a target raster using the Shuttle Radar Topography Mission (SRTM) data with a resolution of 30 m by 30 m.

Table 1. Sources and scale of conditioning factors data used in this study.

Major Data	Source	Data Layer	Scale/Resolution
SRTM DEM	https://gdex.cr.usgs.gov/gdex (accessed on 11 February 2020)	Elevation, slope, TWI, SPI, profile curvature, plane curvature, slope variation, slope direction	30 m × 30 m
Rainfall information	CHIRPS Pentad: Climate Hazards Group InfraRed Precipitation With Station Data	Total rainfall in 2020, number of days with heavy rainfall (rainfall for the day>25 in 2020)	0.05° × 0.05°
Soil moisture information	CLDAS Soil Volume Moisture Content Analysis Product V2.0 (http://data.cma.cn/data (accessed on 11 February 2020))	Average daily soil moisture in 2020	0.0625° × 0.0625°
Surface cover information	Landsat-8 Operational Land Imager (OLI) multispectral image (https://earthexplorer.usgs.gov/ (accessed on 11 February 2020))	NDVI, MNDWI	30 m × 30 m
Ground hydrological traffic information	National Catalogue Service For Geographic Information (in Chinese) (http://www.webmap.cn (accessed on 11 February 2020))	River density, road density	1:250,000
Soil information	Harmonized World Soil Database v 1.2 (HWSD) (http://www.fao.org/soils-portal (accessed on 11 February 2020))	Soil type, soil erodibility	1:5,000,000
Geological and geomorphological information	National Geological Archives Data Center (in Chinese) (http://dc.ngac.org.cn (accessed on 11 February 2020))	Mineral point density, fracture zone density, hydrogeology, thickness of weathering layer, type of landform	1:200,000
Human activity	WordPop Open Population Repository (WOPR) (http://hub.worldpop.org (accessed on 11 February 2020))	Population density	1 km × 1 km

2.3. Construction of the Modeling Dataset

The majority of landslides in the area typically happen on a limited scale, with the size of the slope altering before and after the occurrence of the landslide. Therefore, the landslide sample used for modeling was taken from the center raster of the landslide surface [38,39]. In selecting the non-landslide samples used for landslide susceptibility modeling, the following principles were fully considered in this study to ensure the reasonableness and representativeness of the sample selection:

(1) First, to avoid sampling in areas with similar geography to known landslides, areas beyond 100 m from historical landslides were chosen as the selection range. This helped to maintain sample diversity and avoid introducing unnecessary bias due to geographic similarities.

(2) Second, land areas that do not contain permanent bodies of water were extracted as the area for non-landslide samples. The consideration behind this principle is that landslide events do not usually involve areas of water bodies, ensuring that non-landslide samples were carefully selected; with an emphasis on this aspect, the selected samples were more geographically and geomorphologically similar to landslide events.

(3) Given that landslides typically occur on steep slopes possessing higher slope values, areas with slopes less than 30° were extracted as extraction areas for the non-landslide samples. This selection helps to maintain similarity to landslide events, as steep-slope areas are more prone to landslides. Through this principle, we pursued maintaining a reasonable match of geomorphic features in the sample selection process.

Based on the above principles, criteria for selecting non-landslide sample areas were delineated. A total of 214 non-landslide samples were selected at random, maintaining a ratio of 1:1 with the number of landslide samples. This ratio was chosen to help keep the samples balanced and to allow the modeling dataset to contain a sufficient quantity of positive and negative samples. A total of 428 samples were created by merging the chosen landslide samples (labeled as 1) with the non-landslide samples (labeled as 0) for modeling purposes. Eventually, the dataset containing all the relevant data was randomly split into a training set with 299 samples and a test set with 129 samples, maintaining a ratio of 7:3. The dispersion of sample points in the landslide moderator layer as shown in Figure 2a–i, Figure 3a–i, Figure 4a–e.

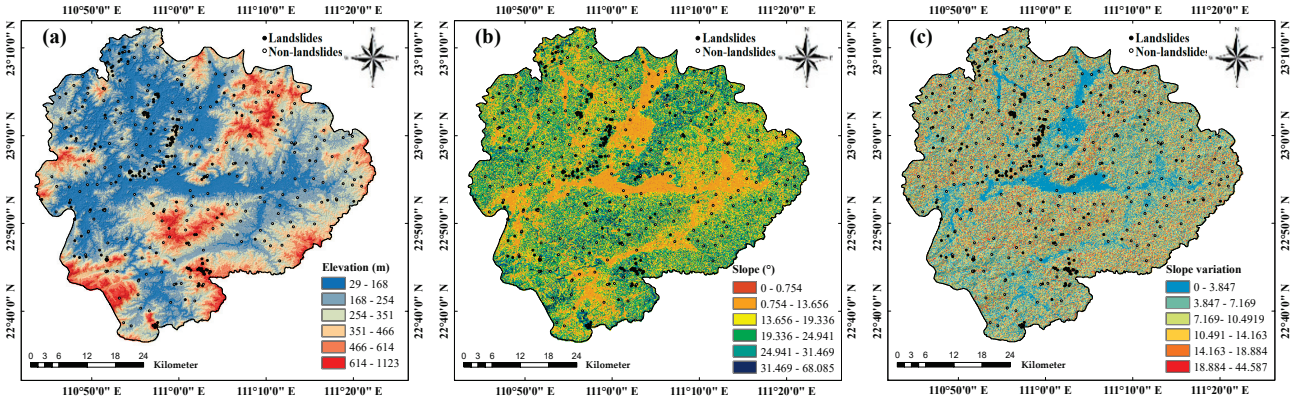

Figure 2. *Cont.*

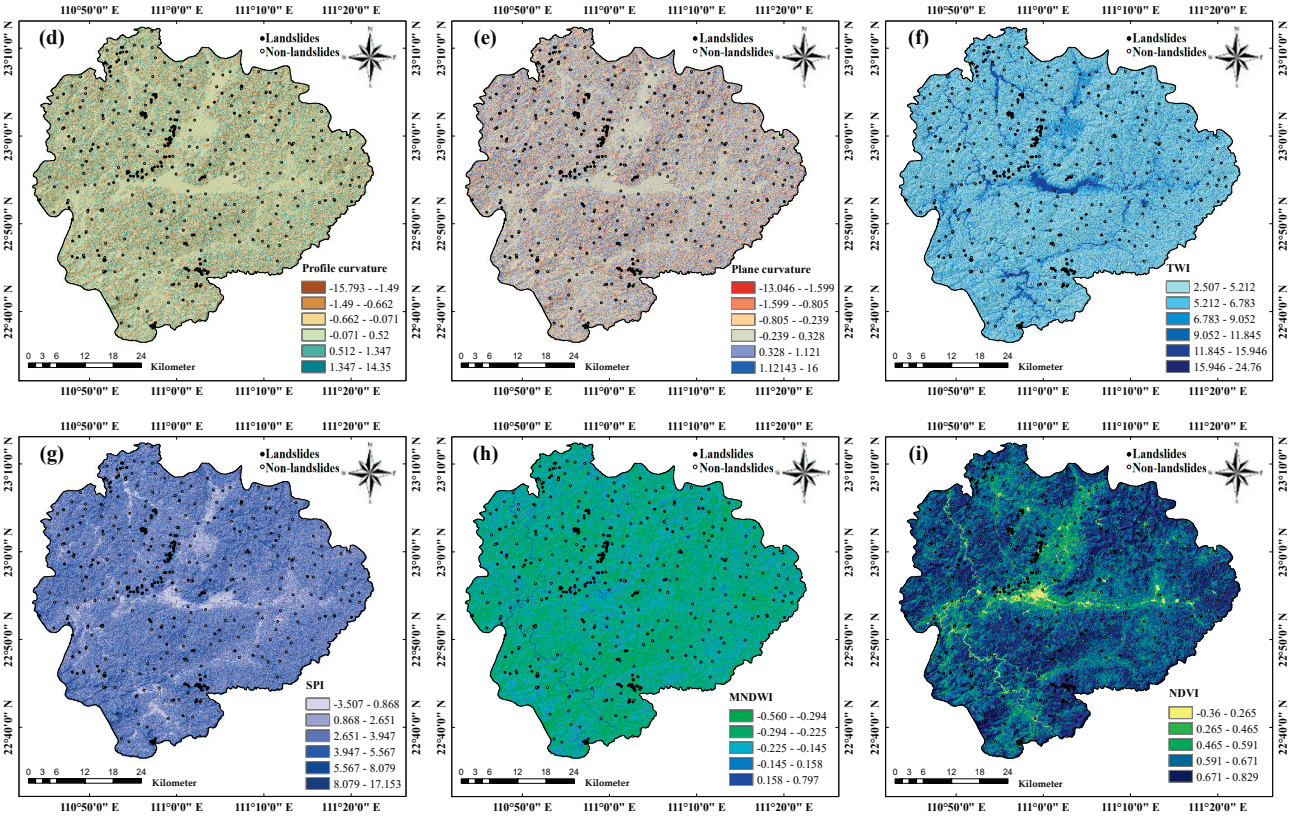

Figure 2. Landslide conditioning factors (I). (**a**) Elevation; (**b**) slope; (**c**) slope variation; (**d**) profile curvature; (**e**) plane curvature; (**f**) TWI; (**g**) SPI; (**h**) MNDWI; (**i**) NDVI.

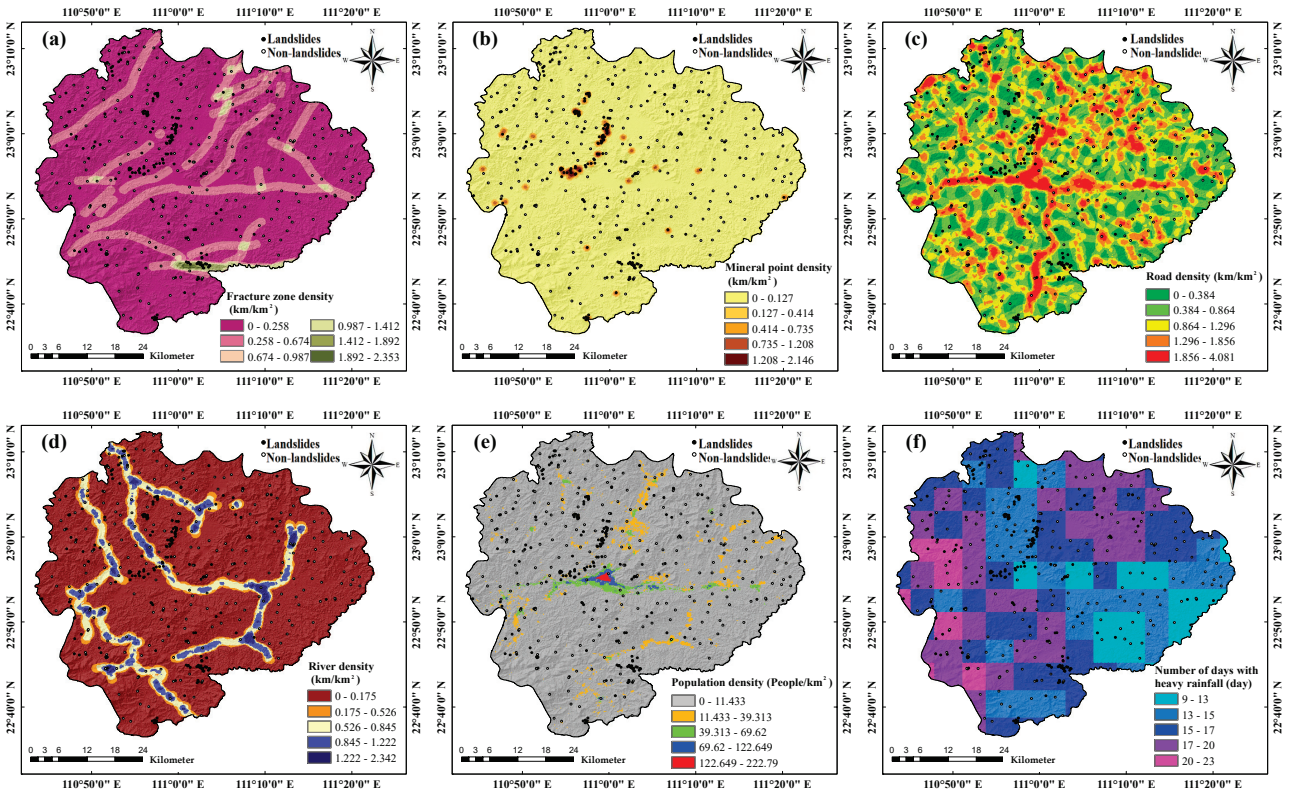

Figure 3. *Cont.*

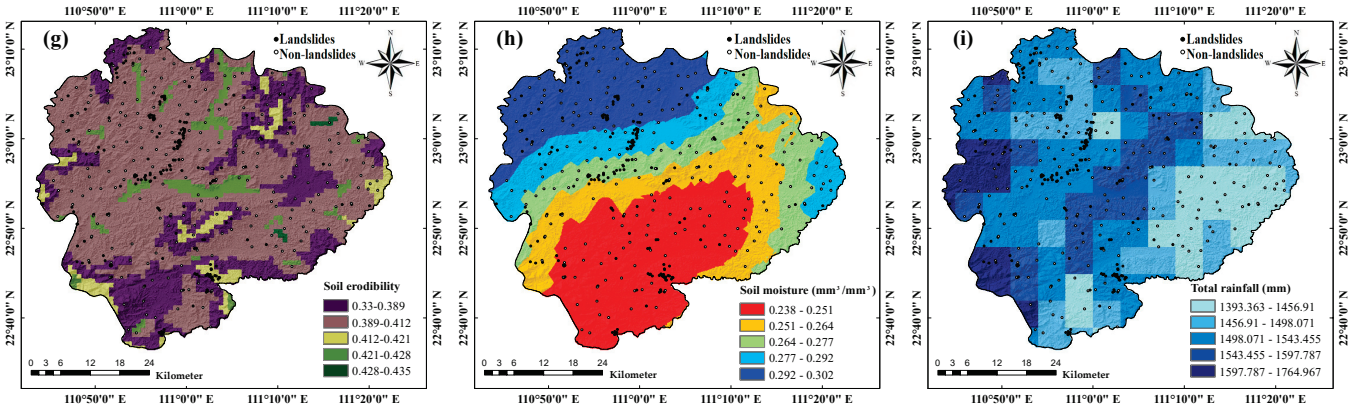

Figure 3. Landslide conditioning factors (II). (**a**) Fracture zone density; (**b**) mineral point density; (**c**) road density; (**d**) river density; (**e**) population density; (**f**) number of days with heavy rainfall; (**g**) soil erodibility; (**h**) soil moisture; (**i**) total rainfall.

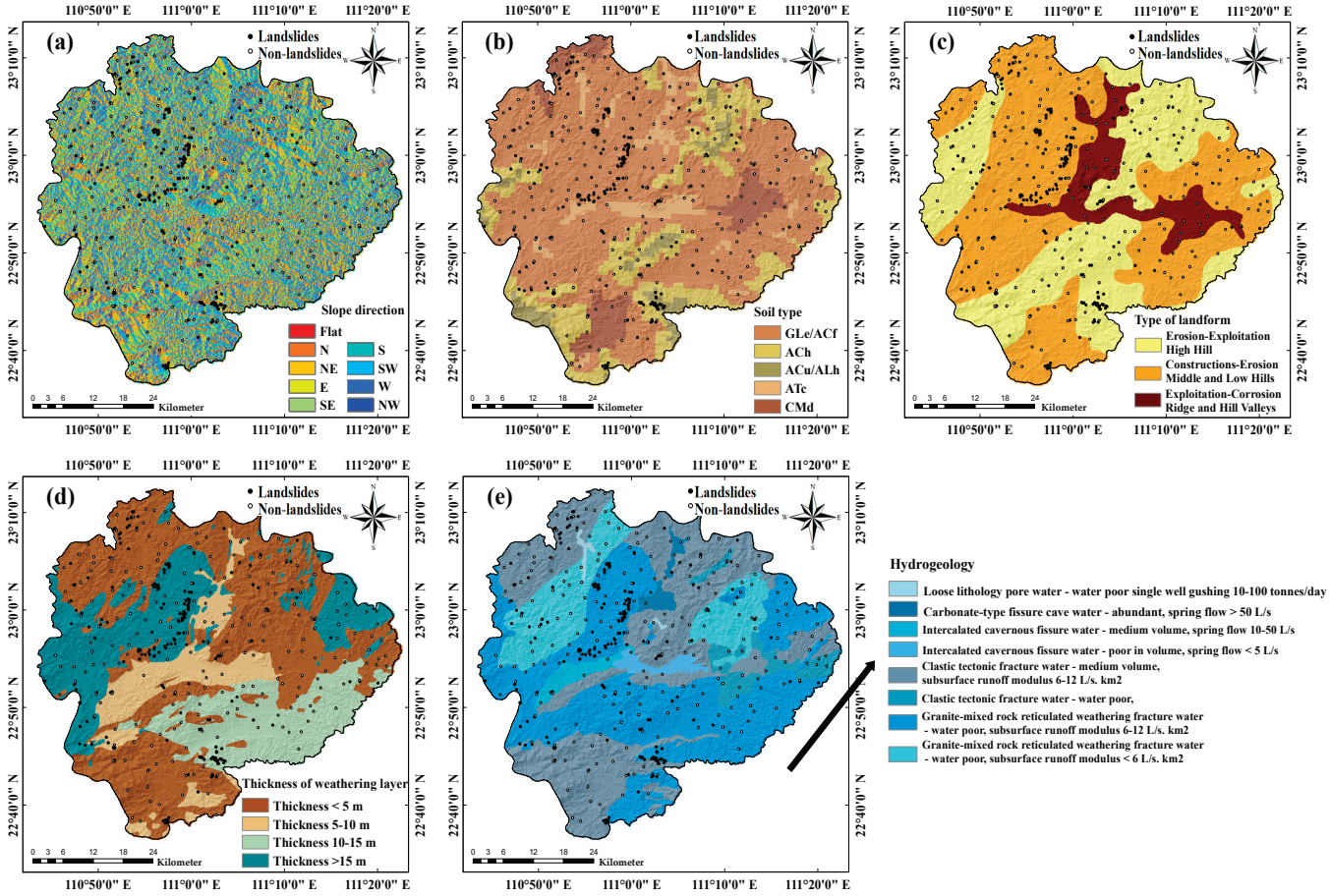

Figure 4. Landslide conditioning factors (III). (**a**) Slope direction; (**b**) soil type; (**c**) type of landform; (**d**) thickness of weathering layer; (**e**) hydrogeology.

3. Methods

The main objective of this research is to examine how various types of factor data affect the accuracy of landslide susceptibility models that rely on an ensemble machine learning framework. Additionally, the methodology of interpretability using SHAP is used to explain the influence of factors on data types, both globally and locally, in landslide susceptibility models to influence the decision mechanism of predictive results. The data

processing platform used in this study is ArcGIS 10.2, and the programming language utilized is Python. The research procedure encompasses the subsequent stages, as outlined in Figure 5.

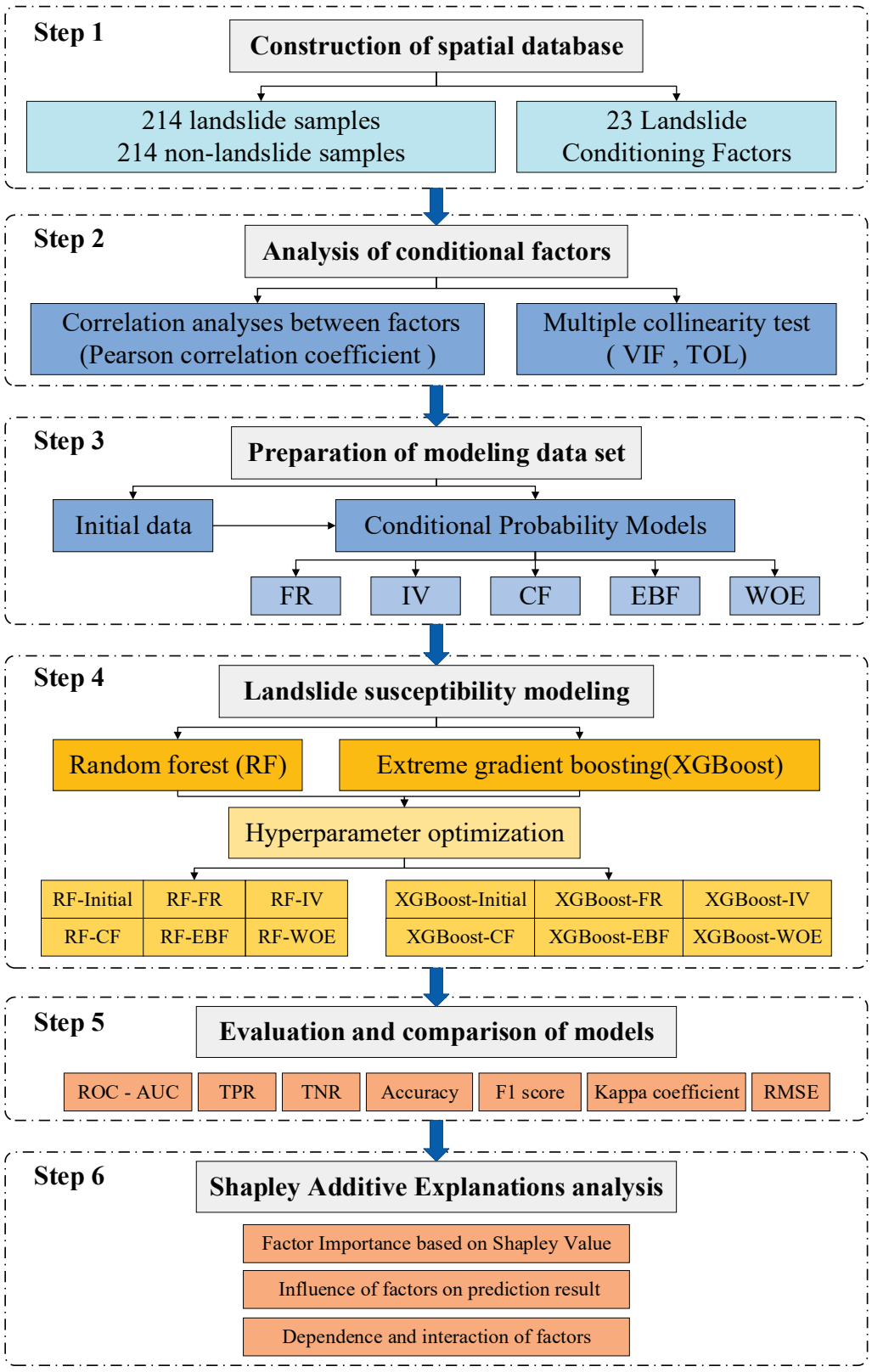

Figure 5. Flowchart of the study.

(1) The process involves preparing data and constructing a spatial database that includes both samples from landslides and non-landslides, as well as conditioning factors that contribute to landslides.
(2) Independence testing of landslide conditioning factors, including Pearson correlation analysis and multicollinearity diagnosis, is performed.
(3) Preparation of the modeling dataset. In order to partition and standardize the attribute intervals of each factor, five different conditional probability models were employed: frequency ratio, statistical index, certainty factor, evidential belief function, and weights of evidence. Afterward, the data of the initial and processed factors were extracted to the sample points, resulting in the creation of six modeling datasets.
(4) Landslide susceptibility modeling. Based on the six different modeling datasets, twelve landslide susceptibility prediction models were constructed using the random forest and extreme gradient boosting algorithms, and landslide susceptibility maps were generated.
(5) Evaluation of model predictive performance. The performance of the twelve models as compared and analyzed using different statistical methods, identifying the best-performing model.
(6) Shapley Additive exPlanations (SHAP) analysis. The influence of every factor on the models was investigated through the creation of SHAP models for all twelve landslide susceptibility models and the dependency relationship between the predictive results and features in models built using different machine learning methods and types of factor data.

3.1. Analysis of Conditioning Factors

Since landslides occur due to the combined effect of multiple adjustment factors, the diversity and complexity of the factors need to be fully considered [40]. Based on historical studies and expert experience, there may be statistical covariance among the initially selected landslide adjustment factors, which can lead to the inability of the landslide susceptibility model to accurately analyze the proper relationship between the evaluated factors and landslides [41].

Conducting a correlation analysis on the 29 identified moderating factors is necessary due to potential correlations among the indicator factors that may impact the accuracy of the landslide susceptibility model. The aim of this paper is to utilize the Pearson correlation coefficient (*PCC*) to evaluate the correlation between the layers of the factor. The calculation formula is described as Equation (1). A weak correlation between the factors is indicated if the *PCC* value is less than 0.6, and the opposite is also true. There is a significant correlation [42]. In addition, to ensure the independence of the data when building a multiple regression model, the degree of multivariate co-linearity of each factor was measured by calculating the tolerance (*TOL*) and variance inflation factor (*VIF*). Severe multicollinearity is indicated when the *VIF* value for a factor exceeds ten or the *TOL* value is below 0.1 between the factor and other factors, and the factor should be removed from the model The calculation formula is:

$$PCC = \frac{\sum_{i=1}^{n}(x_i - \overline{x})\sum_{i=1}^{n}(y_i - \overline{y})}{\sqrt{\sum_{i=1}^{n}(x_i - \overline{x})^2 \sum_{i=1}^{n}(y_i - \overline{y})^2}} \quad (1)$$

$$VIF = \frac{1}{TOL} = \frac{1}{(1 - R^2)} \quad (2)$$

where x_i and y_i denote the i-th variable between factor x and factor y; $\overline{x}$ and $\overline{y}$ are the means of all variables in factor x and factor y, respectively, and n is the number of variables in the factor; the coefficient of determination R^2 is utilized to measure how well the independent variable explains the variation in the dependent variable in regression analysis. Additionally, *TOL* and *VIF* are reciprocally related to each other.

3.2. Conditional Probability Models

When evaluating landslide susceptibility, the factors evaluated at all levels are not only characterized by high data volume but also exhibit inconsistency in magnitude, which may lead to overfitting or underfitting after inputting into the model. To avoid this effect, the conditional probability model can subdivide and standardize each factor to establish a preliminary link in the interaction between landslides and the factors that moderate them. The connection between the pre-existing probability of landslides for each factor under evaluation and the probability of landslides occurring in various classification states is established based on historical landslide data [43,44]. Therefore, in this study, the frequency ratio, statistical index, certainty factor, evidential belief function, and weights of evidence were selected to convert the initial data of landslide adjustment factors into values reflecting landslide susceptibility, and the ML model utilized the calculated results to generate maps indicating the susceptibility to landslides.

3.2.1. Frequency Ratio

The method of bivariate statistics known as the frequency ratio (*FR*) is straightforward. The likelihood of a landslide happening is calculated by the analytical model, which allows for a quantitative assessment of landslide susceptibility in different secondary classification intervals for each factor, combined with spatial data [45,46]. FR has been widely used in hazard probability assessment involving several geographic layers [47]. The formula for the calculation is as follows:

$$FR_{ij} = \frac{N_{ij}/N}{S_{ij}/S} \tag{3}$$

where FR_{ij} is the frequency ratio of the j-th secondary classification level of the i-th moderating factor. $FR_{ij} > 1$ means that the corresponding factor conditions are favorable for landslide occurrence; $FR_{ij} < 1$ indicates that the attributes of the factor interval are weakly related to landslide occurrence; $FR_{ij} = 0$ means that the factor i does not provide landslide development information in the state j. N_{ij} is the number of landslides occurring in the j-th secondary classification interval of factor i; S_{ij} is the quantity of rasters in the interval; N is the number of landslides; and S is the number of rasters in the interval.

3.2.2. Information Value

The derivation of information value (*IV*) involved the creation of a blend of statistical models and information theory. The assessment of geohazard susceptibility is performed using a statistical method that relies on informative values. This method transforms the distribution of landslides across various factors in the study area into quantifiable magnitudes that provide valuable information. By examining the amount and level of detail in the data pertaining to regions affected by landslides, we can determine the likelihood of landslides occurring in the research region. The formula for the calculation is as follows:

$$IV_{ij} = \ln\left(\frac{D_{ij}}{D}\right) = \ln\left[\left(\frac{N_{ij}/S_{ij}}{N/S}\right)\right] \tag{4}$$

where IV_{ij} represents the quantity of information at the j-th level of secondary classification for the i-th adjustment factor; D_{ij} is the landslide density in the j-th secondary classification interval of the i-th adjustment factor; and D is the landslide density in the whole area. The parameters of N_{ij}, S_{ij}, N, and S are the same as those in Section 3.2.1.

3.2.3. Certainty Factor

In 1975, Shortliffe and Buchanan proposed a segmented probability function called the Certainty Factor (*CF*). In 1986, the model was further improved by Heckerman to analytically study the sensitivity of factors affecting the occurrence of an event. The

statistical relationship is believed to determine the probability of landslide occurrence between known landslides and adjustment factors [48]. The representation is as follows:

$$CF_{ij} = \begin{cases} \frac{PP_{ij} - PP_s}{PP_s(1-PP_{ij})} & (PP_{ij} < PP_s) \\ \frac{PP_{ij} - PP_s}{PP_{ij}(1-PP_s)} & (PP_{ij} \geq PP_s) \end{cases} \quad (5)$$

where CF_{ij} indicates the certainty coefficient of landslide occurrence in the j-th secondary classification interval of the i-th factor and takes values in the range of [–1, 1]. When $CF > 0$, a more significant value indicates a higher probability of landslide; when $CF < 0$, a smaller value indicates a lower probability of landslide; when $CF = 0$, it is impossible to judge whether a landslide will occur. PP_s is the a priori probability of landslides occurring in the entire study area, expressed as the ratio of the total number of landslides in the whole study area to the total number of rasters in the study area. PP_{ij} is the conditional probability of landslides occurring in the j-th secondary classification interval of the i-th adjustment factor, which is usually expressed as the ratio between the number of landslides and the number of rasters in the factor classification used for the study.

3.2.4. Evidential Belief Function

The Evidential belief function (EBF) is a model that incorporates spatial integration and is rooted in the theory of the Dempster–Shafer evidence algorithm [49]. The EBF method has been widely adopted in numerous research domains and has yielded favorable outcomes when investigating susceptibility to landslides [50]. EBF has the benefit of being able to effectively process diverse incomplete data, resulting in outputs that specifically reflect belief (*Bel*), disbelief (*Dis*), uncertainty (*Unc*), and plausibility (*Pls*). There are four parameters that comprise the EBF model, which are calculated by the following equations:

$$WE_{ij} = \frac{\frac{N(L \cap Eij)}{N(L)}}{\frac{N(Eij) - N(L \cap Eij)}{N(A) - N(L)}} \quad (6)$$

$$Bel_{ij} = \frac{WE_{ij}}{\sum_{j=1}^{m} WE_{ij}} \quad (7)$$

$$\overline{W}E_{ij} = \frac{\frac{N(L) - N(L \cap Eij)}{N(L)}}{\frac{N(\mathrm{A}) - N(L) - [N(Eij) + N(L \cap Eij)]}{N(\mathrm{A}) - N(L)}} \quad (8)$$

$$Dis_{ij} = \frac{\overline{W}E_{ij}}{\sum_{j=1}^{m} \overline{W}E_{ij}} \quad (9)$$

$$Unc_{ij} = 1 - Dis_{ij} - Bel_{ij} \quad (10)$$

$$Pls_{ij} = 1 - Dis_{ij} \quad (11)$$

where Bel_{ij} is the degree of belief; Dis_{ij} is the degree of disbelief; Unc_{ij} is the degree of uncertainty; and Pls_{ij} is the degree of plausibility. The range of values is [0, 1]. $N(L \cap Eij)$ and $N(Eij)$ are the number of landslides and the number of rasters in the j-th secondary classification interval of the i-th factor, and $N(L)$ and $N(A)$ are the number of landslides and the number of rasters in the whole region, respectively. In this study, *Bel* was used as a factor importance evaluation index. A higher *Bel* indicates a higher probability of landslide occurrence, while a decrease in *Bel* indicates a decrease in the likelihood of landslides occurring, and when *Bel* is 0, it means that no landslide data are available to prove the probability of landslide occurrence.

3.2.5. Weights of Evidence

An event's likelihood of happening by combining different pieces of evidence can be estimated using the weights of evidence (WOE) approach, which is a quantitative method that employs a Bayesian criterion. It has been widely used by many scholars for multivariate information synthesis and spatial decision support systems [51,52]. Nowadays, many scholars use this model to assign weights to each landslide moderator to evaluate and analyze the landslide susceptibility of a district [51,53]. The weights, both positive and negative, along with the final combined weight, are calculated as follows:

$$W_{ij}{}^{+} = \ln \frac{P\left(\frac{B}{D}\right)}{P\left(\frac{B}{\overline{D}}\right)} \tag{12}$$

$$W_{ij}{}^{-} = \ln \frac{P\left(\frac{\overline{B}}{D}\right)}{P\left(\frac{\overline{B}}{\overline{D}}\right)} \tag{13}$$

$$C_{ij} = W_{ij}{}^{+} - W_{ij}{}^{-} \tag{14}$$

In the equation, $P\left(\frac{B}{D}\right)$ and $P\left(\frac{B}{\overline{D}}\right)$ represent the probabilities of landslide occurrence and non-occurrence, respectively, under the secondary classification level of a regulating factor; $P\left(\frac{\overline{B}}{D}\right)$ and $P\left(\frac{\overline{B}}{\overline{D}}\right)$ represent the probabilities of landslide occurrence and non-occurrence, respectively, in areas except for the secondary classification level of a regulating factor; within the second-level classification of this factor, B and D denote the count of landslides and non-landslides, respectively, and, except for the second-level classification of this factor, $\overline{B}$ and $\overline{D}$ correspond to the count of landslides and non-landslides; C_{ij} stands for comprehensive weight, the weight of the j-th secondary classification interval of the i-th factor to the landslide. The larger the value of C_{ij}, the more indicative the secondary classification level of the factor is of the probability of landslide occurrence. If $C_{ij} = 0$, it means that the secondary classification level of the factor does not indicate landslide occurrence; $C_{ij} > 0$ indicates a favorable condition for landslide occurrence; and $C_{ij} < 0$ indicates an unfavorable condition for landslide occurrence.

3.3. Tree-Based Machine Learning Models

3.3.1. Random Forest

An algorithm called random forest (RF) was proposed by Breiman to integrate multiple decision trees. It mainly extracts a plurality of samples from the initial dataset and proceeds to train these gathered samples using the decision tree algorithm, then derives the ultimate prediction outcome based on the combined decision tree results through a voting process [30]. The RF algorithm finds its utility in both classification and regression tasks. In contrast to conventional machine learning techniques like artificial neural networks, logistic regression, and support vector machines, RF prevents model overfitting through random sample selection and exhibits a level of resilience towards outliers. In addition, it has high accuracy, facilitating comprehensive data examination of high-dimensional feature data [19]. This research applies the RF algorithm within the Python 3.9 environment using the "sklearn. Encrypt" package.

3.3.2. Extreme Gradient Boosting

Chen T et al. introduced a technique called extreme gradient boosting (XGBoost) in 2016, representing a novel machine learning approach which can be used to scale up the tree boosting algorithm, a popular method for landslide susceptibility modeling prediction in recent years. Like RF, XGBoost is an integrated learner that uses decision trees as building blocks. However, unlike RF, XGBoost uses boosting in its integration learning process [54]. By utilizing weak decision trees as the foundational learner during training, it amalgamates

preferences to produce a robust collective evaluator. The algorithm effectively prevents the occurrence of overfitting. It improves the model accuracy by improving the boosting algorithm by adding a regularization term when addressing the loss function's extreme values. In addition, the convergence speed is faster and computational efficiency higher than other algorithms. The main practical function of XGBoost is shown in Equation (15). This research incorporates this technique within the Python 3.9 environment through utilization of the "XGBoost" Python package.

$$\hat{y}_i{}^{(t)} = \sum_{k=1}^{t} f_k(x_i) = \hat{y}_i{}^{(t-1)} + f_k(x_i) \tag{15}$$

where $\hat{y}_i{}^{(t)}$ represents the sample's predictive outcome i after the t-th iteration; $\hat{y}_i{}^{(t-1)}$ signifies the preceding predictive outcome of $t-1$ trees; $f_k(x_i)$ denotes the function associated with the t-th tree.

3.4. Model Evaluation Criteria

3.4.1. Receiver Operating Characteristic

The ROC curve is frequently utilized to assess the results of landslide susceptibility experiments in a qualitative manner [55]. The horizontal axis corresponds to the false positive rate (1-specificity), illustrating the accumulating percentage of terrain classified from high to low susceptibility. Meanwhile, the vertical axis signifies the true positive rate (sensitivity), indicating the accumulating percentage of landslide samples. The AUC value reflects the probability of a randomly chosen positive sample outranking a randomly chosen negative sample, and the model's effectiveness in accurately predicting landslide occurrence or absence is evaluated based on this metric [13]. In the case of $AUC > 0.5$, a higher AUC value signifies a superior model fit. The formula for the calculation is as follows:

$$AUC = \frac{(\sum TP + \sum TN)}{(P + N)} \tag{16}$$

where TP represents the count of accurately predicted landslide samples; TN represents the count of correctly predicted non-landslide samples; P represents the total count of landslide samples; and N represents the total count of non-landslide samples.

3.4.2. Confusion Matrix

When assessing the accuracy performance of a binary classification model for landslide susceptibility, a confusion matrix is often used [56]. The true positive (TP) in the confusion matrix indicates the number of accurately predicted landslide samples, whereas the false negative (FN) signifies the quantity of incorrectly predicted landslide samples. Additionally, the term "true negative" (TN) is used to describe the count of correctly predicted samples that are not landslides. An incorrect prediction of non-landslide samples is what is known as a false positive (FP). Using five statistical indicators, this study evaluated the accuracy of the landslide susceptibility model in predicting future occurrences, including true positive rate (TPR), true negative rate (TNR), accuracy (ACC), $F1$ score ($F1$), and kappa coefficient (KC). In detail, TPR represents the proportion of correctly classified landslide samples; TNR represents the proportion of correctly classified samples that are not landslides; Acc represents the proportion of accurately classified samples in the entire set; and the $F1$ value is capable of offering a thorough evaluation of the model's prediction performance for landslide samples. It quantitatively represents the degree of consistency between the predicted attributes of the samples and their actual attributes. The formula for the calculation is as follows:

$$TPR(True\ Positive\ Rate) = \frac{TP}{TP + FN} \tag{17}$$

$$TNR(True\ Negative\ Rate) = \frac{TN}{FP + TN} \tag{18}$$

$$Acc = \frac{TP + TN}{TP + FP + FN + TN} \tag{19}$$

$$F1 - score = \frac{2TP}{2TP + FN + FP} \tag{20}$$

$$KC = \frac{P_0 - P_e}{1 - P_e} \text{ where } P_0 = \frac{TP + TN}{TP + FN + FP + TN},\ P_e = \frac{(TP + FN)(TP + FP)(TN + FN)(FP + TN)}{(TP + FN + FP + TN)^2} \tag{21}$$

3.4.3. Root Mean Square Error between the Predicted and Actual Values of the Sample

To evaluate the precision of a model's prediction, the commonly used approach is to utilize the root mean square error (*RMSE*). A smaller *RMSE* value signifies that the prediction results of the sample data are more closely aligned with the actual attributes, and the model performs better [56]. In this research, the *RMSEs* for predicting the overall, landslide, and non-landslide samples with their corresponding true values are calculated in this paper. The results are named *RMSE*, *RMSE*-1, and *RMSE*-0, respectively.

$$RMSE = \sqrt{\frac{1}{N}\sum_{i=1}^{N}(Y_i - f(X_i))^2} \tag{22}$$

where N represents the number of samples within the specific category from which the calculation will be performed; Y_i represents the true value of the i-th sample; and X_i is the predicted value of the i-th sample after model operation.

3.5. Shapley Additive ExPlanations

Shapley Additive exPlanations (SHAP) was suggested by Lundberg and Lee in 2017 as a game theory-based approach to interpret any machine learning model. In detail, the term "Shapley" pertains to the calculation of the Shapley value for every characteristic variable in the model, for each sample. The term "Additive" indicates that, for each sample, the Shapley value of every characteristic variable can be combined. The term "exPlanation" refers to the explanation of how each characteristic variable influences the predictive value of the model for each individual sample. The Shapley value of each feature illustrates its contribution to the final outcome forecast in order to explain the difference between the actual and average predicted values [57,58]. The interpretability of features is provided by SHAP both globally and locally and considers the interaction synergy between variables while considering the impact of individual variables. Given the excellent interpretability of SHAP for ML models, it has seen extensive use in interpreting disaster susceptibility and ecological environment domains [59]. The purpose of this research was to develop a landslide susceptibility model utilizing the RF and XGBoost algorithms, which was then interpreted and analyzed using the Shapley value estimation method from the SHAP theory of treeSHAP. The implementation of SHAP utilized the Python 3.9 library version 0.39.0 for SHAP. The SHAP value can be calculated. The formula for the calculation is as follows:

$$\varphi_j(x) = \sum_{S \subseteq N \setminus \{j\}} \frac{|S|!(|N| - |S| - 1)!}{|N|!} \left[f\left(x_{S \cup \{j\}}\right) - f(x_S) \right] \tag{23}$$

where $\varphi_j(x)$ represents the SHAP value of the j-th feature, indicating the effect of that feature on the sample x; N is the total number of features; S is a subset of N with feature j removed; $f(x_S)$ represents the removal of features in j after removing the set of features x_S corresponding to the model predictions; $f\left(x_{S \cup \{j\}}\right)$ represents the model predictions

corresponding to the feature set $x_{S\cup\{j\}}$ after inclusion of feature j; $|S|$ denotes the size of the set S; and $|N|$ denotes the total number of features.

The average of the SHAP values is designed to measure the overall impact of the features in the sample set on the model predictions. With the formula for calculation as follows, we can calculate the average of the SHAP value.

$$I_j = \frac{1}{n}\sum_{k=1}^{n}\left|\varphi_j^{(k)}\right| \tag{24}$$

where I_j represents the average SHAP value of the feature j; n is the size of the sample set; and $\varphi_j^{(k)}$ represents the SHAP value of the feature j in the sample k.

4. Results

4.1. Landslide Conditioning Factors Analysis

In this paper, correlations between 23 landslide moderation factor layers were calculated using MATLAB R2022a software. After obtaining the correlation coefficients between the factors, we used the matplotlib.pyplot library in Python to visualize the correlation matrix. According to Figure 6, the positive correlation between the factors becomes stronger as the color gets lighter; the strength of the negative correlation between the factors increases as the color becomes darker. The results show that, among the 23 factors, the magnitude of the correlation coefficient between any pair of factors is below 0.6, indicating that the correlation between the evaluation factors is small. In addition, this paper used SPSS 20.0 software to analyze the factors for multicollinearity, and the results are shown in Table 2. All landslide adjustment factors had *TOL* values that were greater than 0.1; the *VIF* values were less than 10. Among them, the lowest *TOL* was 0.31, while the highest *VIF* was 3.24, indicating no multicollinearity among the factors. The combined analysis of the two indicators indicates that all factors satisfy the requirement of mutual independence and can be involved in landslide susceptibility modeling and evaluation [60].

Table 2. Collinearity diagnostic results of landslide conditioning factors.

Factor	*TOL*	*VIF*	Factor	*TOL*	*VIF*
MNDWI	0.8	1.25	Slope	0.31	3.21
NDVI	0.41	2.43	Slope variation	0.79	1.27
SPI	0.46	2.18	Slope direction	0.91	1.1
TWI	0.36	2.76	Profile curvature	0.61	1.65
Thickness of weathering layer	0.69	1.45	Number of days with heavy rainfall	0.6	1.67
Fracture zone density	0.67	1.5	Population density	0.71	1.4
Type of landform	0.55	1.82	Hydrogeology	0.66	1.52
Elevation	0.31	3.24	Soil erodibility	0.58	1.73
River density	0.74	1.36	Soil type	0.74	1.35
Mineral point density	0.45	2.2	Soil moisture	0.7	1.43
Road density	0.78	1.27	Total rainfall	0.63	1.59
Plane curvature	0.57				

4.2. Model Structuring and Optimization

Before constructing a landslide susceptibility model utilizing the ML method, the hyperparameters used for the different models need to be optimized [61]. After dividing the sample data randomly into training and test sets in the ratio of 7:3 (295:129), to improve the models' ability to generalize, the training set was used to train the models with 10-fold cross-validation. Additionally, the hyperparameters were optimized using the grid search method [62]. The optimized hyperparameter values were also substituted into the model for training to construct a model for determining the likelihood of a landslide. Table 3 displays the explanations and names of the hyperparameters that will be modified in the RF and XGBoost models used in this research. Furthermore, the hyperparameters of different

models that were optimized to obtain the optimal values using RF and XGBoost are listed in Tables 4 and 5, respectively. The results showed that, based on the same modeling method, the hyperparameter values varied when modeling using different factor data types. Compared with the default parameters, when the optimized hyperparameters were employed, the model showcased enhanced accuracy in both training and validation.

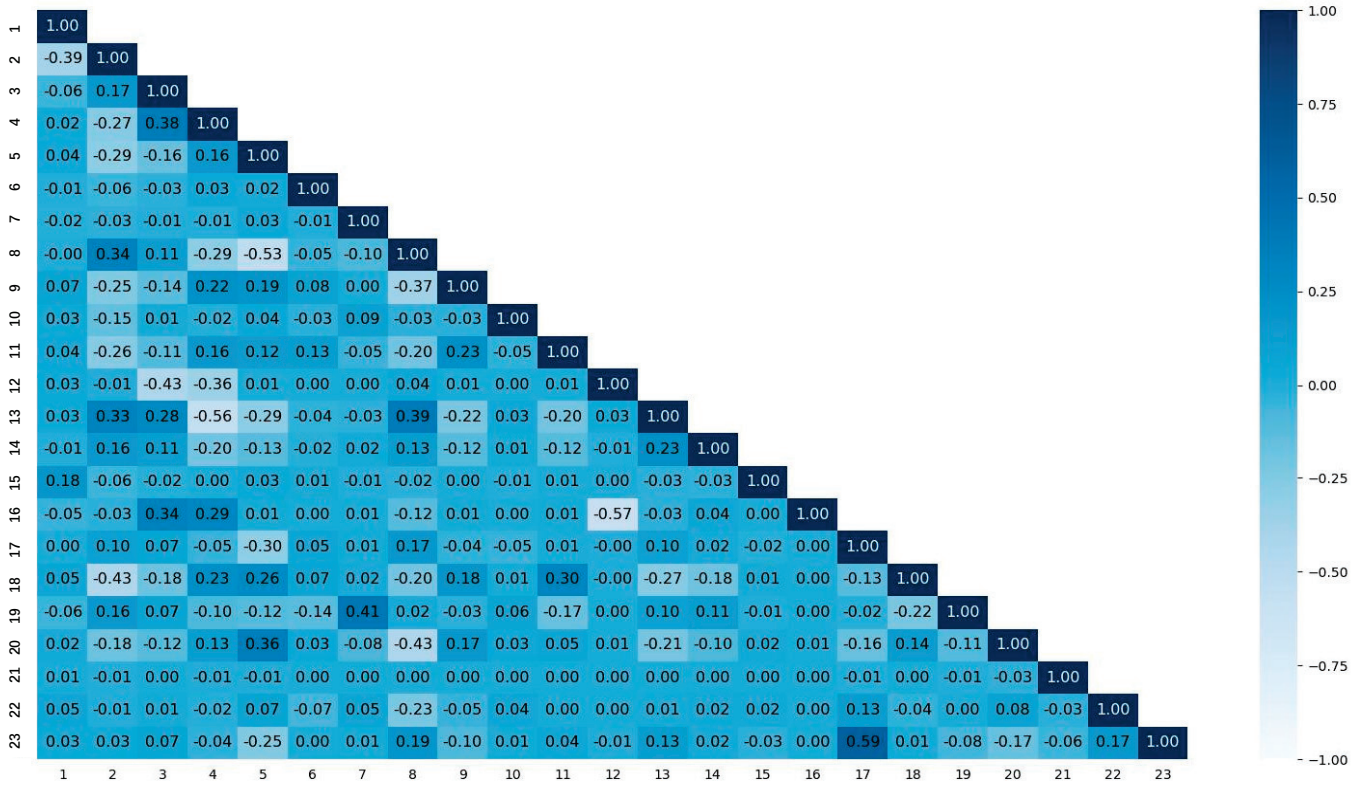

Figure 6. Correlation analyses between landslide conditioning factors. 1: MNDWI; 2: NDVI; 3: SPI; 4: TWI; 5: type of landform; 6: fracture zone density; 7: thickness of weathering layer; 8: elevation; 9: river density; 10: mineral point density; 11: road density; 12: plane curvature; 13: slope; 14: slope variation; 15: slope direction; 16: profile curvature; 17: number of days with heavy rainfall; 18: population density; 19: hydrogeology; 20: soil erodibility; 21: soil type; 22: soil moisture; 23: total rainfall.

Table 3. Interpretation of main hyperparameters of the RF and XGBoost models.

Methods	Hyperparameter	Definition and Explanation
XGBoost	n_estimators	Number of sub-models
	learning_rate	The weights of the model generated for each iteration
	max_depth	Maximum depth of the tree, often used to avoid over-fitting
	min_child_weight	The sum of the minimum leaf node sample weights, which can effectively control overfitting
	gamma	Specifies the minimum loss function descent value required for node splitting. The larger the value of this parameter, the more conservative the algorithm
	subsample	The proportion of subsamples used to train the model to the entire set of samples
	colsample_bytree	The proportion of features randomly sampled when building the tree
RF	n_estimators	The number of decision trees in the forest
	max_depth	Maximum depth of the tree
	max_features	Number of features to consider when finding the optimal segmentation

Table 4. Values of hyperparameters for XGBoost models based on different data types.

	XGBoost-Initial	XGBoost-FR	XGBoost-IV	XGBoost-CF	XGBoost-EBF	XGBoost-WOE
n_estimators	60	80	70	90	90	100
learning_rate	0.1	0.1	0.1	0.1	0.2	0.1
max_depth	10	10	10	10	10	10
min_child_weight	2	2	2	2	4	2
gamma	0.01	0.01	0.03	0	0.02	0.01
subsample	0.8	0.8	0.7	0.9	0.8	0.8
colsample_bytree	0.6	0.8	0.9	0.7	0.7	0.7

Table 5. Values of hyperparameters for RF models based on different data types.

	RF-Initial	RF-FR	RF-IV	RF-CF	RF-EBF	RF-WOE
n_estimators	70	80	80	80	80	80
max_depth	9	9	9	9	8	8
max_features	7	8	8	8	8	8

4.3. Landslide Susceptibility Maps for Different Models

This study constructed 12 landslide susceptibility prediction models using two ML methods (RF and XGBoost) combined with six-factor data types (Initial, FR, IV, CF, EBF, and WOE), respectively. Then, the LSIs for all raster cells in the study area were estimated. The estimated values cover a range of values [0, 1]. Finally, to generate the corresponding LSMs, the LSIs of all raster cells in the study area were visualized using ArcGIS10.2 software. In order to compare and analyze the zoning results of different landslide susceptibility models, it is necessary to unify the classification thresholds of susceptibility classes. Therefore, this study classified the LSMs in the study area into five landslide susceptibility classes: very low, low, medium, high, and very high susceptibility. This classification was based on the fixed threshold method using intervals of [0,0.20], (0.20,0.50], (0.50,0.90], (0.90,0.95], and (0.95,1.0]. As a result, six LSMs using the RF model (see Figure 7) and six LSMs using the XGBoost model (see Figure 8) were obtained.

Overall, on the premise of the same factor data type, the LSI distributions obtained using the RF and XGBoost models predictions are approximately the same, with significant differences in details. In addition, LSMs generated using factor data processed by different conditional probability models based on the same ML model have a high similarity in the scattering of LSIs across the region. Compared with the LSMs generated using initial factor data, there are fewer high-susceptibility areas, eliminating the spatially discontinuous anomalous areas and effectively improving the reasonableness of the prediction results of landslide susceptibility.

In order to conduct a quantitative analysis of the distribution of landslides across various areas classified by their susceptibility levels, the statistical analysis tools in ArcGIS10.2 were used to calculate the area, the quantity, and the frequency ratio of landslides in areas of distinct susceptibility grades (see Tables 6 and 7). The frequency ratios of all models are on the rise with an increase in the susceptibility level except the susceptibility level area with the frequency value of 0 (not statistically significant). Moreover, the frequency ratio exhibited by all models within the high-risk zone significantly surpasses that observed in the low-risk region. The LSMs generated in this study are all reasonable.

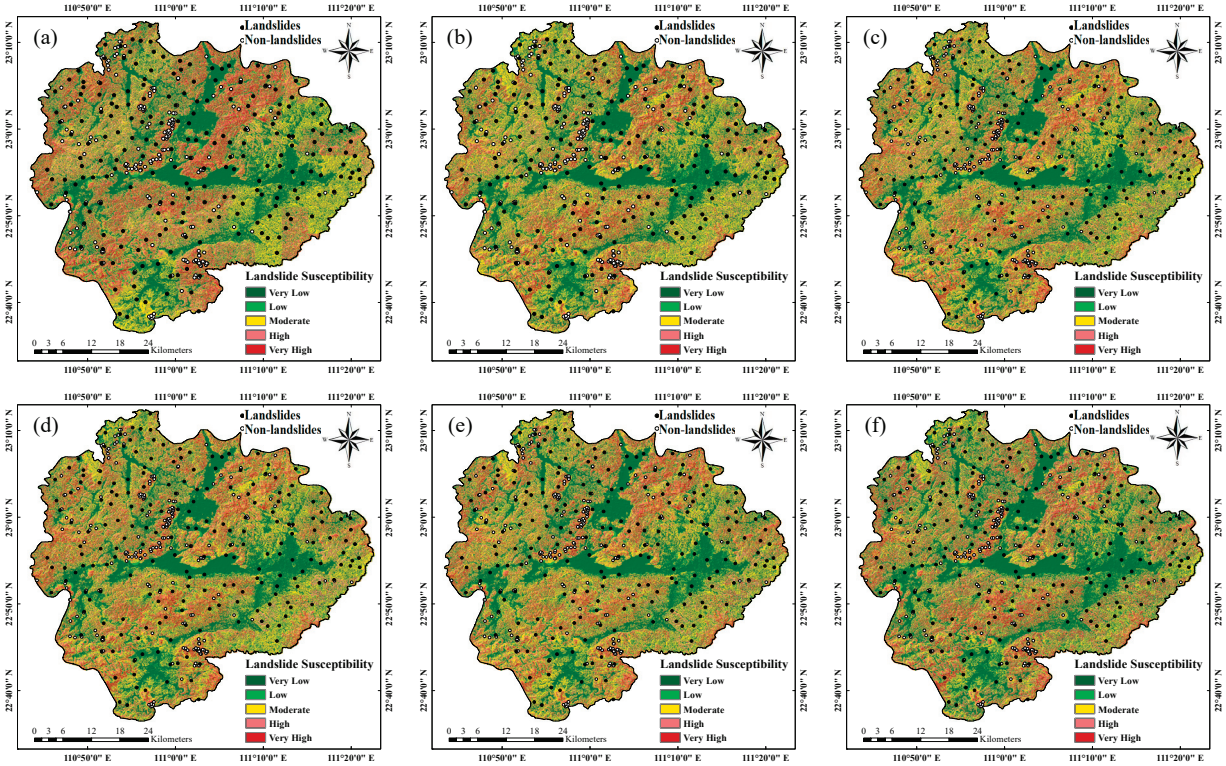

Figure 7. Landslide susceptibility maps based on different types of data using the RF model. (**a**) RF-Initial; (**b**) RF-FR; (**c**) RF-IV; (**d**) RF-CF; (**e**) RF-EBF; (**f**) RF-WOE.

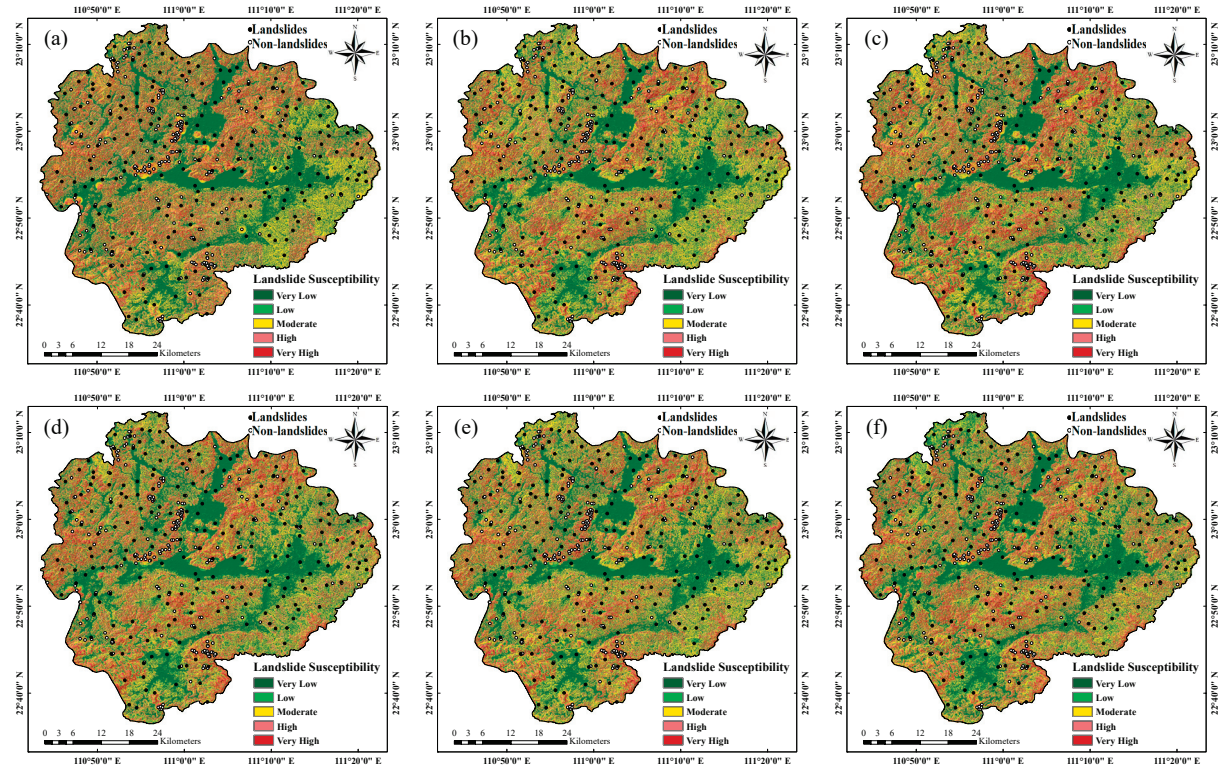

Figure 8. Landslide susceptibility maps based on different types of data using the XGBoost model. (**a**) XGBoost-Initial; (**b**) XGBoost-FR; (**c**) XGBoost-IV; (**d**) XGBoost-CF; (**e**) XGBoost-EBF; (**f**) XGBoost-WOE.

The main objective of evaluating regional landslide susceptibility prediction outcomes is to identify and be alert about areas at risk of landslides [63]. Therefore, in this study, the "extremely high + high" susceptibility areas of different landslide susceptibility models is mapped as the landslide risk area (see Figure 9). The statistical results show that, based on the same factor data type, LSMs generated by XGBoost have marked more landslide risk areas and have more landslide samples. However, the mapping of RF to the landslide risk area is insignificant. For the XGBoost model, LSMs generated by different types of factor data have different responses to landslide risk areas. With the exception of the XGBoost-Initial model, the XGBoost-CF model, determined by the CF values of factor data, encompasses a landslide risk region that constitutes 24.959% of the entire study area, encompassing 91.121% of all landslide samples across the study area. The XGBoost-CF model completely contains both landslide risk areas and those pertinent to landslide samples and has good zoning results.

Table 6. Results of landslide susceptibility partition analysis using RF models.

Models	Landslide Susceptibility Partition	Number of Rasters in Partition	Percentage of the Number of Rasters in Partition (%)	Number of Landslides in Partition	Percentage of the Number of Landslides in Partition (%)	Frequency Ratio
RF-Initial	very low	963,793	31.072	0	0	0
	low	399,163	12.869	1	0.467	0.036
	medium	966,350	31.155	30	14.019	0.450
	high	296,372	9.555	21	9.813	1.027
	very high	476,116	15.350	162	75.701	4.932
RF-FR	very low	985,601	31.775	1	0.467	0.015
	low	328,415	10.588	0	0	0
	medium	1,207,486	38.929	41	19.159	0.492
	high	255,378	8.233	35	16.355	1.987
	very high	324,914	10.475	137	64.019	6.112
RF-IV	very low	1,007,537	32.482	0	0	0
	low	306,201	9.872	2	0.935	0.095
	medium	1,152,358	37.151	37	17.290	0.465
	high	276,690	8.920	36	16.822	1.886
	very high	359,008	11.574	139	64.953	5.612
RF-CF	very low	987,481	31.836	1	0.467	0.015
	low	319,689	10.307	0	0	0
	medium	1,128,281	36.375	48	22.430	0.617
	high	267,800	8.634	25	11.682	1.353
	very high	398,543	12.849	140	65.421	5.092
RF-EBF	very low	951,642	30.680	0	0	0
	low	386,748	12.469	0	0	0
	medium	1,090,413	35.154	39	18.224	0.518
	high	279,600	9.014	41	19.159	2.125
	very high	393,391	12.683	134	62.617	4.937
RF-WOE	very low	970,618	31.292	0	0	0
	low	533,070	17.186	2	0.935	0.054
	medium	855,243	27.573	38	17.757	0.644
	high	305,781	9.858	27	12.617	1.280
	very high	437,082	14.091	147	68.692	4.875

Table 7. Results of landslide susceptibility partition analysis using XGBoost models.

Models	Landslide Susceptibility Partition	Number of Rasters in Partition	Percentage of the Number of Rasters in Partition (%)	Number of Landslides in Partition	Percentage of the Number of Landslides in Partition (%)	Frequency Ratio
XGBoost-Initial	very low	1,078,778	34.779	0	0	0
	low	315,682	10.177	1	0.467	0.046
	medium	883,914	28.497	13	6.075	0.213
	high	260,888	8.411	21	9.813	1.167
	very high	562,531	18.136	179	83.645	4.612
XGBoost-FR	very low	969,022	31.241	1	0.467	0.015
	low	359,445	11.588	0	0	0
	medium	1,050,424	33.865	18	8.411	0.248
	high	211,581	6.821	20	9.346	1.370
	very high	511,322	16.485	175	81.776	4.961
XGBoost-IV	very low	990,492	31.933	0	0	0
	low	336,805	10.858	2	0.935	0.086
	medium	968,651	31.229	28	13.084	0.419
	high	231,242	7.455	29	13.551	1.818
	very high	574,604	18.525	155	72.430	3.910
XGBoost-CF	very low	1,000,714	32.262	1	0.467	0.014
	low	391,725	12.629	0	0	0
	medium	935,183	30.150	18	8.411	0.279
	high	220,239	7.100	5	2.336	0.329
	very high	553,933	17.858	190	88.785	4.972
XGBoost-EBF	very low	943,278	30.411	0	0	0
	low	449,747	14.500	0	0	0
	medium	993,538	32.031	24	11.215	0.350
	high	200,146	6.453	28	13.084	2.028
	very high	515,085	16.606	162	75.701	4.559
XGBoost-WOE	very low	931,095	30.018	0	0	0
	low	480,175	15.481	1	0.467	0.030
	medium	900,990	29.047	18	8.411	0.290
	high	214,484	6.915	23	10.748	1.554
	very high	575,050	18.539	172	80.374	4.335

4.4. Model Accuracy Evaluation

The ROC curves express the correlation between the cumulative proportion of landslide occurrences and the landslide susceptibility index. They are used to evaluate the models' overall performance and generalization ability. Figure 10 displays the ROC curves for the different models, which were derived from the testing set; Figure 11 displays the ROC curves of the various models when considering the entire sample set. Figure 11 displays the AUC values for the RF model and the XGBoost model on the testing set and the full sample set, considering different types of factor data. The AUC values of both the RF and XGBoost models for the testing set and the full sample set are nearly equal to 1. This implies that there is strong generalization ability among all models, and there is no occurrence of overfitting or underfitting. In addition, for the same type of factor data, the AUC values of the XGBoost model exhibited greater significance compared to those of the RF model, which proves the superiority of the XGBoost model again.

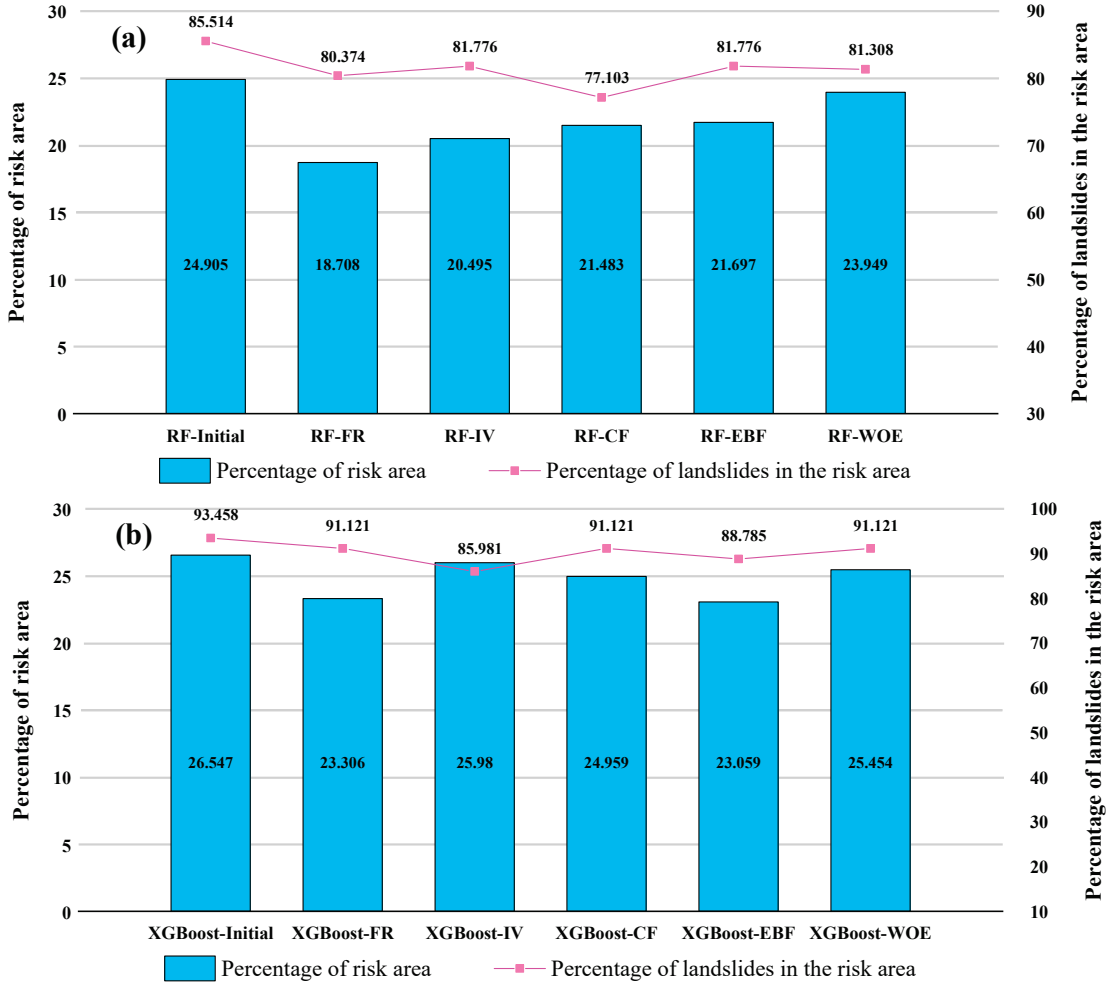

Figure 9. The statistical results of risk area. (**a**) RF models; (**b**) XGBoost models.

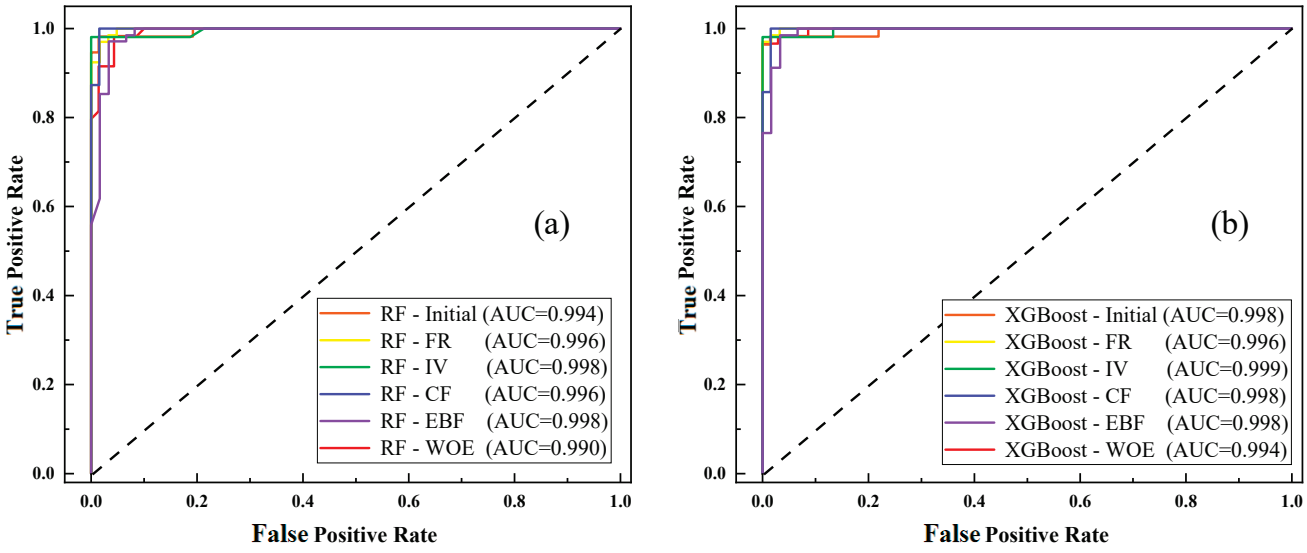

Figure 10. ROC curves of the seven models for the testing set. (**a**) RF models; (**b**) XGBoost models.

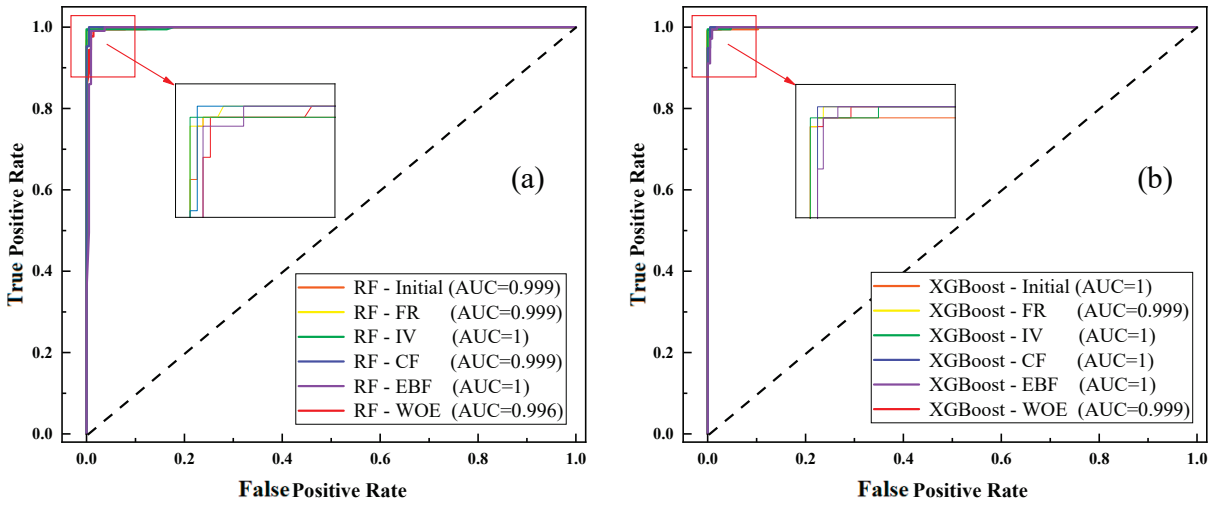

Figure 11. ROC curves of the seven models for the full sample set. (**a**) RF models; (**b**) XGBoost models.

In this study, the prediction accuracy and feasibility of different landslide susceptibility models were evaluated based on the confusion matrix and sensitivity, specificity, accuracy, F1 score, and kappa coefficient with the premise of validating the overall performance of the models. The accuracy evaluation of distinct RF models and XGBoost models, based on the complete sample dataset, is depicted in Tables 8 and 9, respectively. Overall, all models can provide an accurate representation of the landslide susceptibility in the study area. The maximum number of prediction errors for landslide samples is two; a maximum of five predictions can be made for non-landslide samples. In general, models built with XGBoost had higher prediction accuracy than RF models when using the same type of factor data for the samples. In addition, the LSMs generated using factor data processed by different conditional probability models have higher prediction accuracy than the initial factor data. Among them, RF-EBF and XGBoost-EBF models constructed based on EBF data for factors had the highest prediction performance. They have improved *TPR* by 0.467, *TNR* by 1.869, accuracy by 1.168, *F*1 score by 0.012, and kappa coefficient value by 0.023 compared to the RF-Initial and XGBoost-Initial models. The XGBoost-CF model and XGBoost-FR model each had a prediction error number of one for landslide and non-landslide samples, and the prediction performance of landslide susceptibility ranked second.

Table 8. Statistics of landslide susceptibility partition results based on RF models.

	TP	*FN*	*TN*	*FP*	*TPR*	TNR	*Acc*	*F*1	*KC*
RF-Initial	213	1	209	5	99.533	97.664	98.598	0.986	0.972
RF-FR	213	1	212	2	99.533	99.065	99.299	0.993	0.986
RF-IV	212	2	214	0	99.065	100	99.533	0.995	0.991
RF-CF	213	1	212	2	99.533	99.065	99.299	0.993	0.986
RF-EBF	214	0	213	1	100	99.533	99.766	0.998	0.995
RF-WOE	212	2	212	2	99.065	99.065	99.065	0.991	0.981

Table 9. Statistics of landslide susceptibility partition results based on XGBoost models.

	TP	*FN*	*TN*	*FP*	*TPR*	*TNR*	*Acc*	*F*1	*KC*
XGBoost-Initial	213	1	209	5	99.533	97.664	98.598	0.986	0.972
XGBoost-FR	213	1	213	1	99.533	99.533	99.533	0.995	0.991
XGBoost-IV	212	2	214	0	99.065	100	99.533	0.995	0.991
XGBoost-CF	213	1	213	1	99.533	99.533	99.533	0.995	0.991
XGBoost-EBF	214	0	213	1	100	99.533	99.766	0.998	0.995
XGBoost-WOE	213	1	212	2	99.533	99.065	99.299	0.993	0.986

The reliability of the model is crucial in the work of predicting landslide susceptibility. Suppose we only pay attention to the model's prediction accuracy and disregard its reliability and stability. Under these circumstances, the landslide susceptibility model will lose substantial application significance [64]. Therefore, this study examined the model's reliability and stability in addition to assessing its prediction performance. Figures 12 and 13 show the analysis of the scatter of target and output values of the sample data set based on different types of data types for the RF and XGBoost models, respectively. The RMSE values for the XGBoost model were lower than those for the RF model, including RMSE, RMSE-1, and RMSE-0, when using the same factor data, which were more stable and reliable models. Among them, the RMSE values were reduced by 0.0151–0.0305, RMSE-1 by 0.0077–0.0276, and RMSE-0 by 0.0163–0.0367.

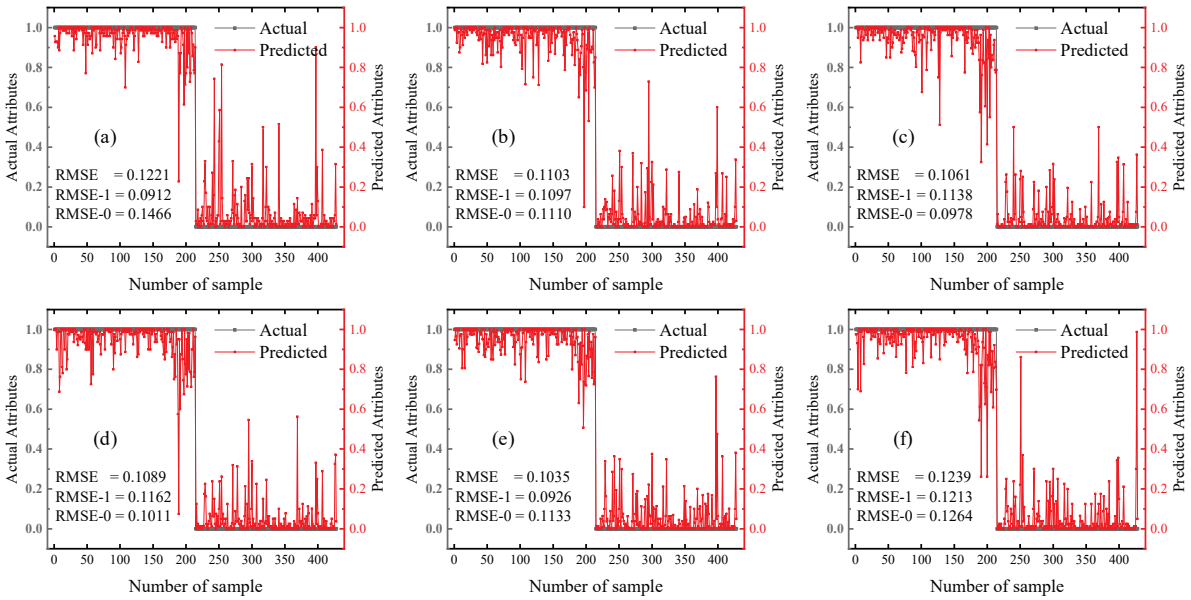

Figure 12. RMSE for RF models based on different data types. (**a**) RF-Initial; (**b**) RF-FR; (**c**) RF-IV; (**d**) RF-CF; (**e**) RF-EBF; (**f**) RF-WOE.

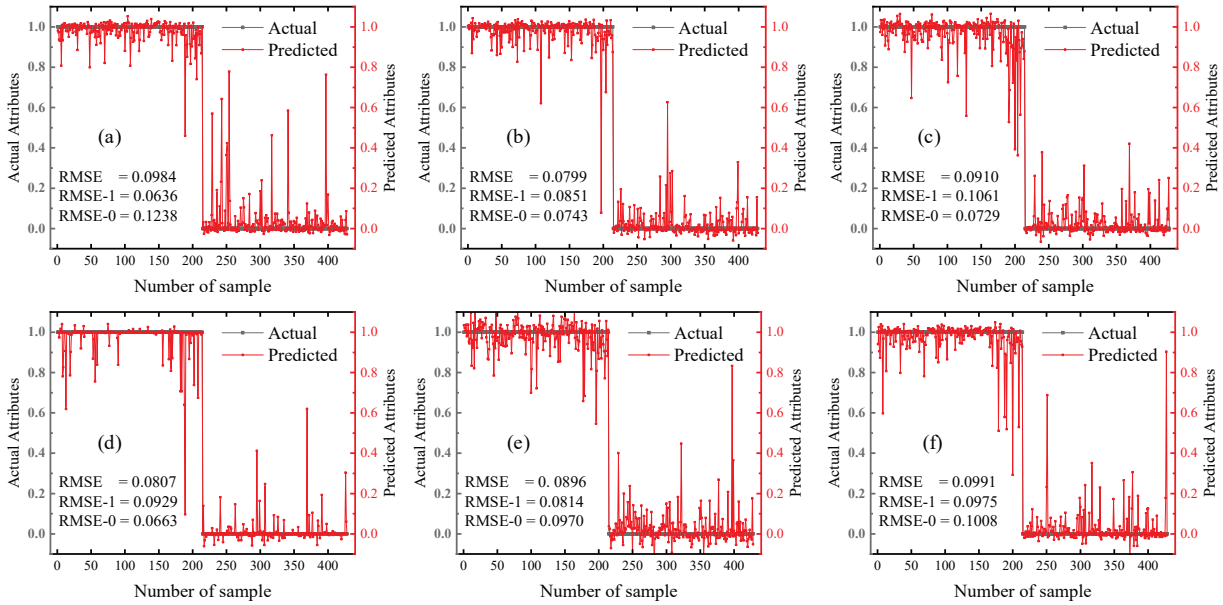

Figure 13. RMSE for XGBoost models based on different data types. (**a**) XGBoost-Initial; (**b**) XGBoost-FR; (**c**) XGBoost-IV; (**d**) XGBoost-CF; (**e**) XGBoost-EBF; (**f**) XGBoost-WOE.

In addition, the landslide susceptibility model built using the factor data obtained after conditional probability model processing exhibits a reduced RMSE for predictive reliability compared to the initial factor data for the same machine learning model. The RMSE values were reduced by 0.0074–0.0185 for the RF models except for RF-WOE. For the XGBoost models, the RMSE values were decreased by 0.0117–0.0186 except for XGBoost-WOE. The WOE model did not improve the performance of the other conditional probability models. The reason that the WOE model did not improve the model performance as much as other conditional probability models was that the weights of evidence for the secondary classification of the factors depended on the number of pixels of the landslides during the modeling process, and the method overestimates or underestimates the weights if the second level of classification for a factor is minimal and the landslides are not evenly distributed. Accordingly, instead of calculating the area of each landslide, the number of spaces where landslides occur was chosen as a modeling sample in this paper. Therefore, it is inevitable that the WOE model does not enhance or even reduce the performance of the landslide susceptibility prediction model in this study. From a comprehensive analysis, the above findings demonstrate that selecting a suitable conditional probability model has an essential influence on developing stable and reliable landslide susceptibility models. Moreover, among the 12 models, the XGBoost-CF model has the lowest RMSE value (RMSE = 0.0807, RMSE-1 = 0.0929, RMSE-0 = 0.0663) and the highest stability and reliability.

In summary, the XGBoost model effectively enhances the prediction performance of landslides compared with the RF model. Among them, the XGBoost-CF model stands out as an effective solution for enhancing the accuracy of predictions made by the model while ensuring the reasonableness of landslide susceptibility zoning results and has the highest stability and reliability among all models. Therefore, the XGBoost-CF model outperforms the other 11 models in this study, making it the most optimal choice.

4.5. Shapley Additive ExPlanations (SHAP) Analysis

4.5.1. Factor Importance Based on Shapley Value

To obtain a general understanding of which adjustment factors hold the greatest significance in relation to the landslide susceptibility model, this study uses the "summary_plot" function to draw the Shapley value of each adjustment factor for each sample, which shows which factors have the most critical influence on the landslide and their influence range on the data set. As shown in Figures 14 and 15, four landslide susceptibility models based on both Initial and CF types of factor data and using RF and XGBoost rank the factors according to the sum of Shapley values of all sample data and use Shapley values to show the influence distribution of each factor on the model output. The points in the figure represent the sample data, and the color indicates whether the factor value of each sample is high or low (red: high, blue: low). The color enables us to match how the change in factor eigenvalue affects the change in landslide susceptibility. The position on the horizontal axis is determined by each Shapley value. However, the overlapping points fluctuate in the vertical axis direction so that we can know the Shapley value distribution of each factor, and their importance sorts these features.

The outcomes showed that there was both uniformity and variability in the distribution and ranking of Shapley values across various landslide susceptibility models. The uniformity is demonstrated by the fact that slope, SPI, TWI, mineral point density, and elevation are all rated as the most influential factors in the different models. Among them, the slope has the highest Shapley value due to its extensive extension in the horizontal axis direction, so it is considered the factor with the highest importance and interaction in landslide susceptibility prediction. As for the several factors ranked lower in the different summary plots of SHAP, although their Shapley values are lower, they also impact the prediction performance of the model and are indispensable for constructing excellent and comprehensive landslide susceptibility models.

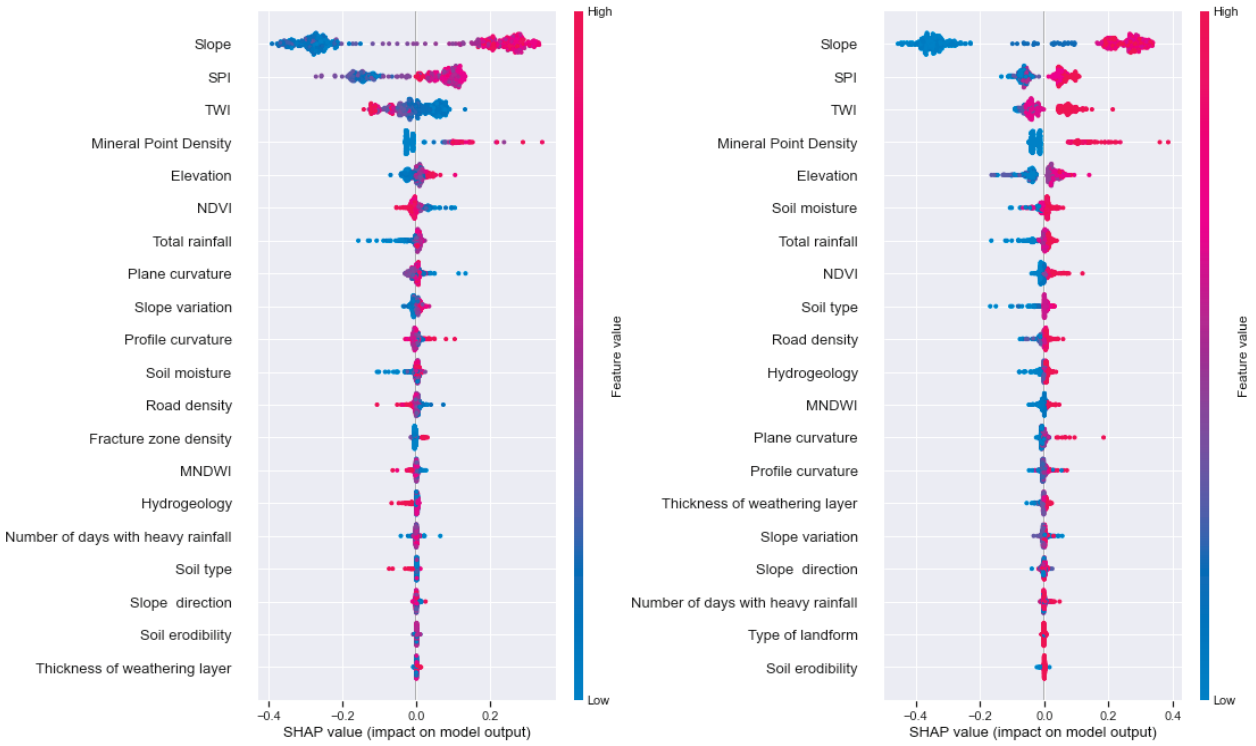

(a) RF - Initial **(b) RF - CF**

Figure 14. Summary plots of SHAP values derived from RF models (top 20). (**a**) RF-Initial; (**b**) RF-CF.

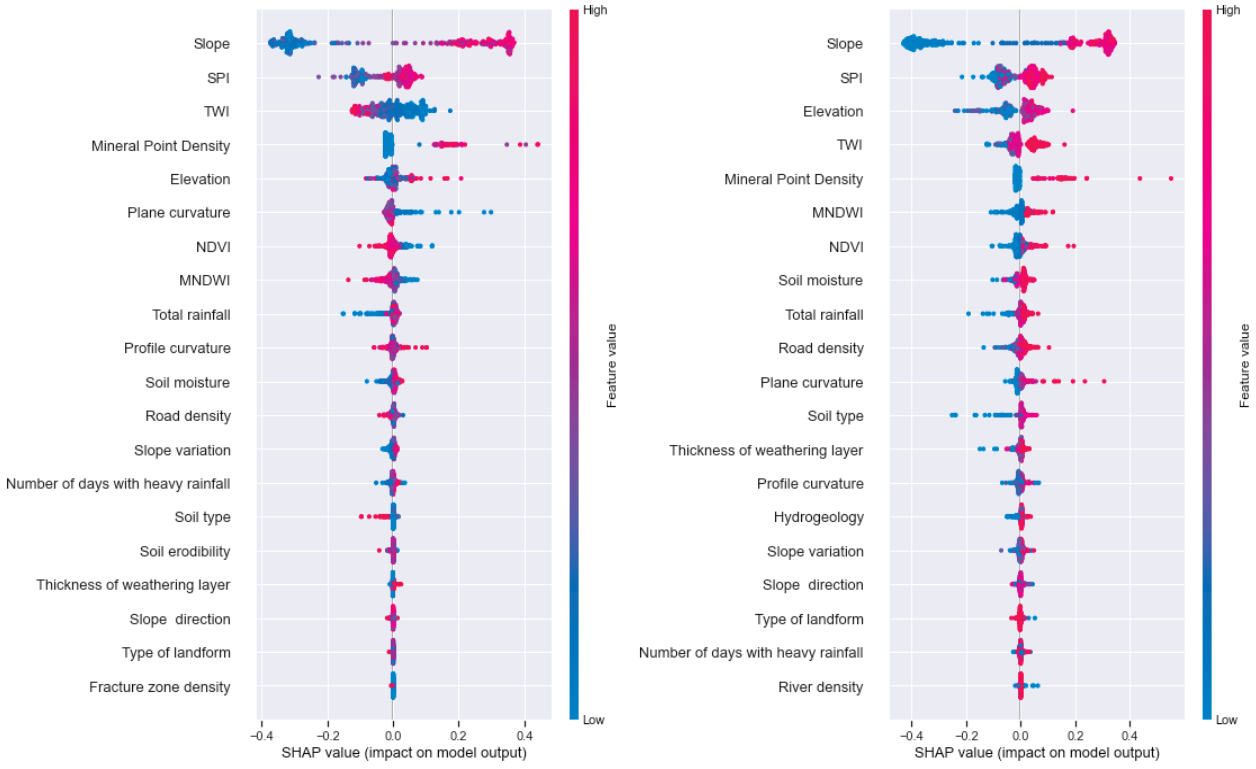

(a) XGBoost - Initial **(b) XGBoost - CF**

Figure 15. Summary plots of SHAP values derived from XGBoost models (top 20). (**a**) XGBoost-Initial; (**b**) XGBoost-CF.

The differences are mainly manifested in two aspects. Firstly, although different models have good performance in predicting landslides, the chosen models could improve the consistency of their decision-making mechanisms, causing variations in the distribution of Shapley values for the same factor across different models. Secondly, when founded on the initial factor data, the positive and negative correlations of different factors on landslide susceptibility prediction are different in the model. On the contrary, in the model constructed using the factor data obtained after the conditional probability model, almost all factors positively correlate with landslide prediction. For example, when using the initial data of factors, continuous factors such as TWI, NDVI, MNDWI, road density, and plane curvature and discrete factors such as hydrogeology and the occurrence of landslides are more favorable when the factor value is lower, indicating a negative correlation with soil type. However, the data processed by conditional probability models such as FR, IV, and CF positively correlate with landslide prediction. This is because the conditional probability model based on statistical thought can standardize the factors with landslide data, as when the factor value increases, the risk of landslide also increases. On the premise of improving the prediction accuracy, the significant influence of factors on landslide prediction can be expressed more clearly, and the interpretability of the model to factors and their data can be increased.

The above analysis results show that the integrity of landslide adjustment factors, the data types of factors, and the prediction performance of the landslide susceptibility model will be greatly influenced by the modeling methods.

The average of the absolute Shapley values for each sample in Figures 14 and 15 was computed in order to determine the individual significance of each feature in predicting landslides, and the factor importance was plotted using the "shap.plots.bar" function (Figures 16 and 17). The outcomes showed that the contribution and importance ranking of the main factors affecting landslide prediction (top nine) varied among the different landslide susceptibility models. However, among all the models, the five factors of slope, SPI, TWI, mineral point density, and elevation are in the top five positions and make the main contribution to the accurate prediction of landslides. The sum of average SHAP absolute values of the following 14 factors are in the range of [0.04, 0.12], which have less influence on landslide prediction. Secondly, compared to the RF model, the XGBoost model highlights the pronounced impact of the slope factor more.

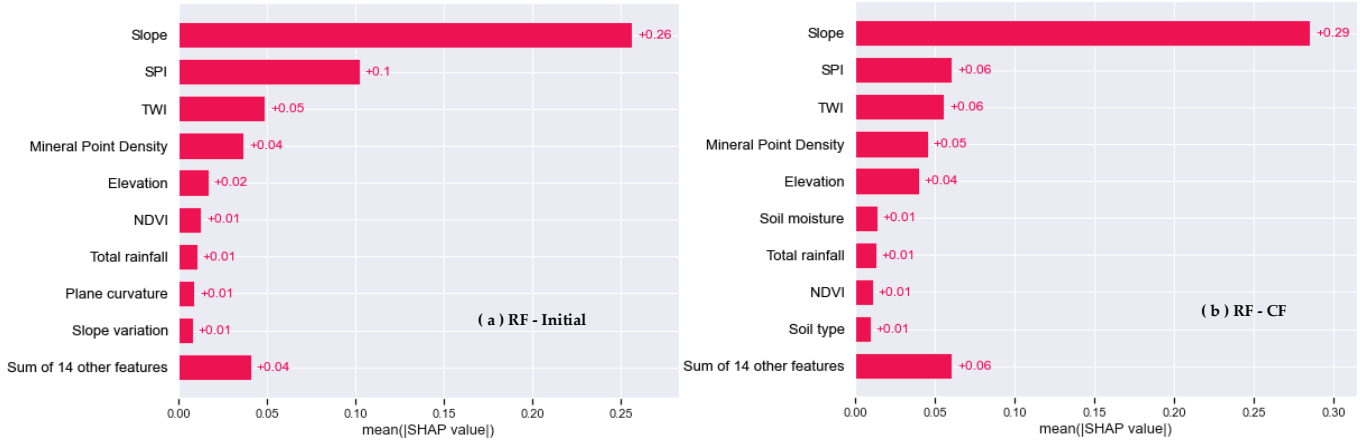

Figure 16. Factor importance plot derived from RF models. (**a**) RF-Initial; (**b**) RF-CF.

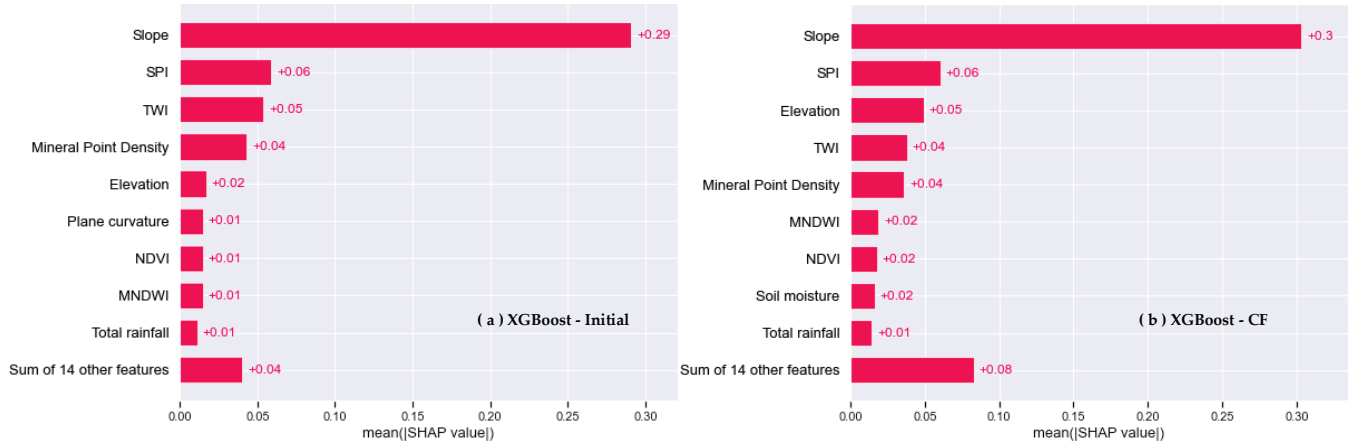

Figure 17. Factor importance plot derived from XGBoost models. (**a**) XGBoost-Initial; (**b**) XGBoost-CF.

4.5.2. Influence of Factors on Prediction Result

In order to systematically display the overall results of the sample data set in the model and the influence degree of the main features on the predicted values of the samples, the Shapley value matrix is transferred to the "Shapley. Plots. Heat Map" function, and the heat maps of the RF model and XGBoost model based on different types of factor data are drawn by this function (Figures 18 and 19). In the figure, the X axis is each sample, the ranking of samples is based on the hierarchical clustering method, and the samples are clustered by Shapley value. The Y axis is the influence of each factor on the sample. The color describes the impact of the factor on the sample. Above the color matrix is a curve formed by connecting the output values of the model. The bar chart on the right shows the global importance of each factor in the model.

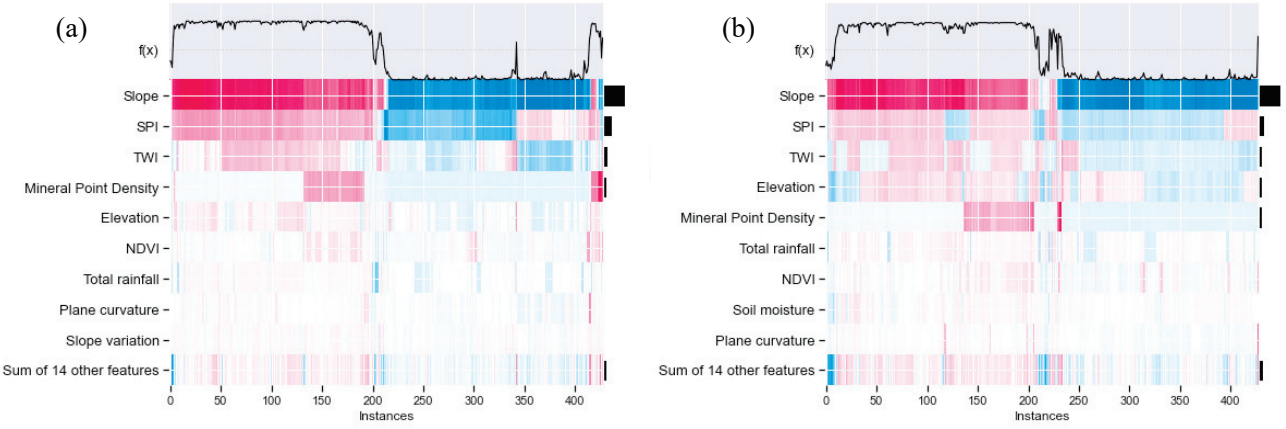

Figure 18. Heatmap plots derived from RF models. (**a**) RF-Initial; (**b**) RF-CF.

According to the analysis, the heatmap can clearly show how the landslide adjustment factors generate the predicted value of each sample through the stacking of factors. It also shows the direction and strength of a factors' influence on predicting landslide susceptibility, which achieves the interpretability and transparency of the model. In addition, for the same type of factor data, the heatmap's prediction curves indicate that the XGBoost model produces highly smooth prediction results, while the RF model's prediction results show relatively low smoothness. Among them, the XGBoost-CF model stands out among the others with its smooth prediction curve, as well as achieving the highest levels of prediction accuracy and stability. The findings of this research align with the analysis findings presented in Section 4.4, which again proves the superiority of the XGBoost-CF model.

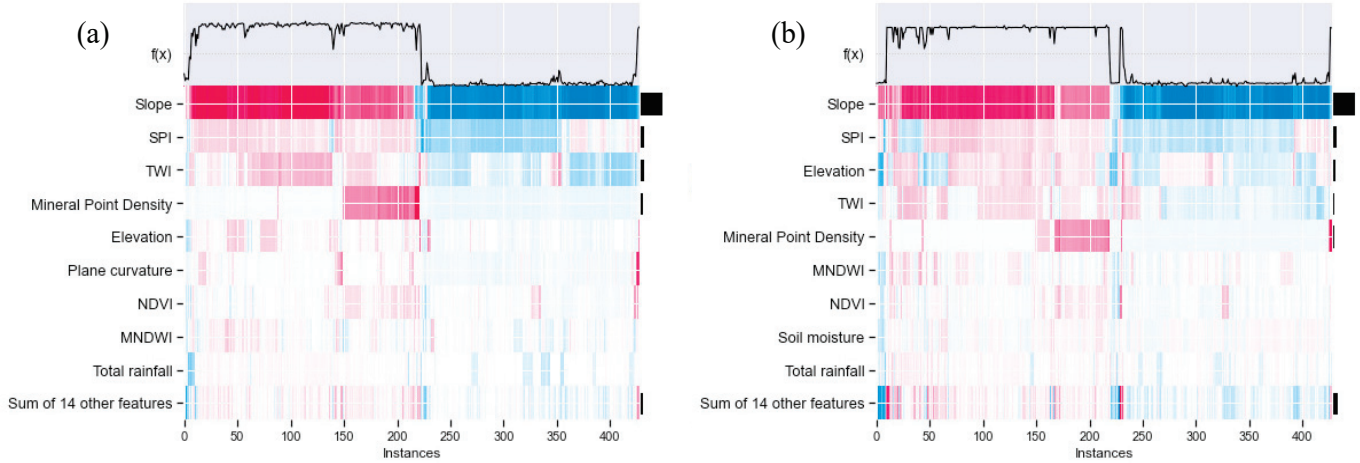

Figure 19. Heatmap plots derived from XGBoost models. (**a**) XGBoost-Initial; (**b**) XGBoost-CF.

4.5.3. Dependence and Interaction of Factors

Dependence plots show the marginal effect of one or two features on the predicted outcome of a landslide susceptibility model, and they can show whether the relationship between landslide moderators and predicted values is monotonic, non-monotonic, or more complex. Dependency plots of factors fall into two categories. One describes how a single factor affects the predicted outcome of landslide susceptibility across the entire dataset. The other describes the effect of variables from two factors on the predicted development under interaction [36,65].

Examples of models used in this study include XGBoost-Initial and XGBoost-CF, based on different types of factor data from the whole modeling dataset. The function "shap.dependence_plot" is utilized for plotting single-factor dependence plots and analyzing the impact of the primary influential factors in each model on the prediction outcomes. Every variable in the dataset is represented by a point on the dependence plot; the value of a specific factor in the dataset is plotted on the horizontal axis, while the Shapley value for each sample of that feature is plotted on the vertical axis. The Shapley value indicates the extent to which that feature influences the prediction outcomes of the model. Figure 20 shows the factor dependence plots of the top nine most important factors in the XGBoost-Initial model. Different factors have different relationships with the prediction results across the entire dataset. Firstly, taking the slope factor as an example, the slope and the prediction results are monotonic. When the slope is less than 10 or more than 20, the increase in slope does not obviously result in an increase in the probability of a landslide, which shows that this range is conducive to landslide detection. However, when the slope is in the range of [8,18], the model is insensitive to detecting landslides, and most of the prediction errors are in this range. Among them, when the slope is greater than 18, the occurrence of landslides benefits from a Shapley value that is greater than 0. Secondly, SPI is not monotonic with the predicted results, and Shapley's value changes sharply with the increase in SPI value. If the SPI value falls between 2 and 6, the Shapley value will be greater than 0 and the landslide risk will be elevated. Finally, the total rainfall is monotonic with the predicted results. If the total rainfall exceeds 1500 mm, then the Shapley value will be greater than 0, and landslide risk will be increased. The above analysis results of individual factors are in high agreement with the objective characteristics of landslides in this study area. Therefore, the dependence plots of a single factor based on the initial data can clearly show the complexity between factors and landslides and the interval and sensitivity of factors that affect the occurrence of landslides.

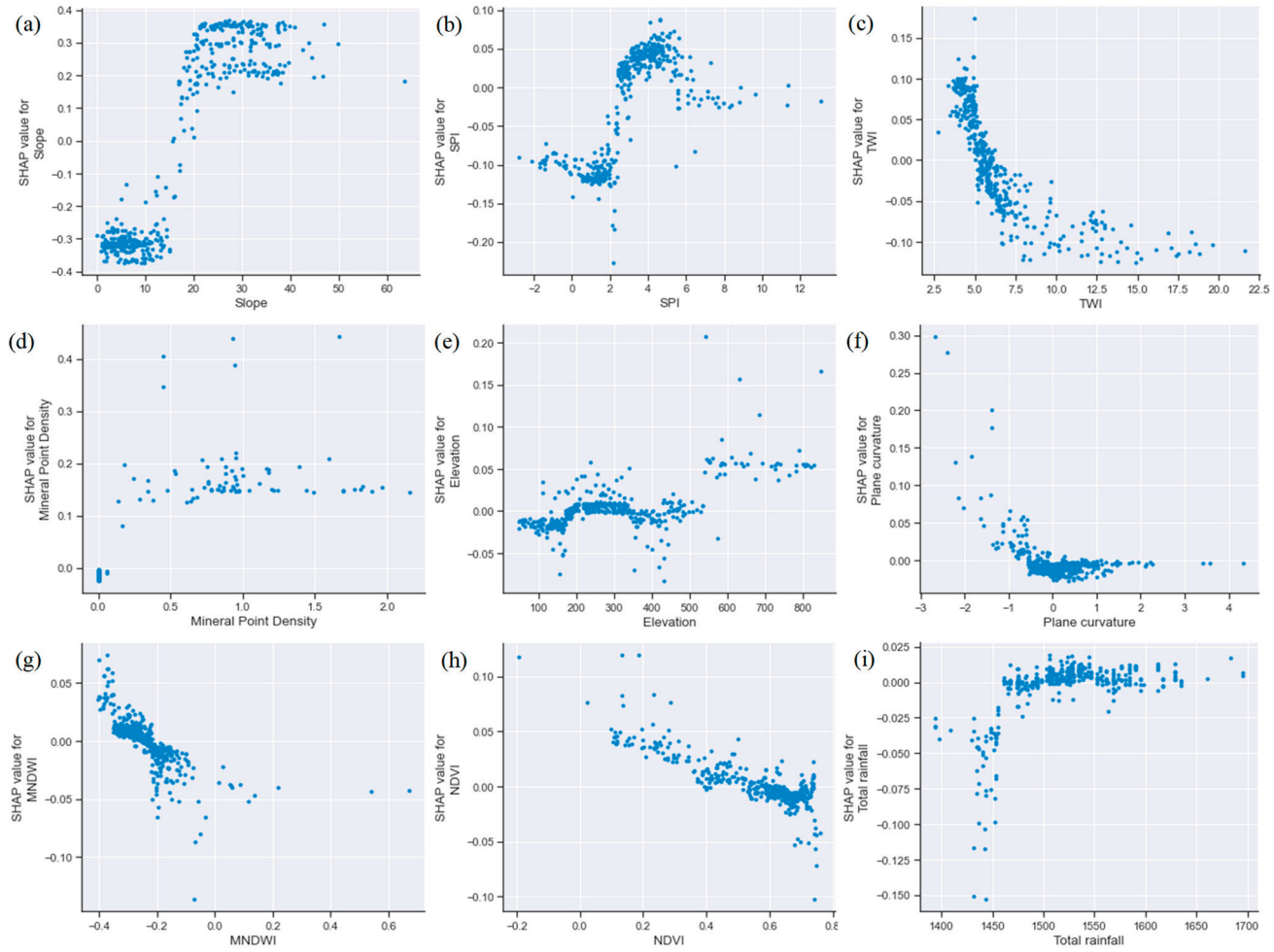

Figure 20. Single-factor dependence plots of the main factors based on the XGBoost-Initial model. (**a**) Slope; (**b**) SPI; (**c**) TWI; (**d**) mineral point density; (**e**) elevation; (**f**) plane curvature; (**g**) MNDWI; (**h**) NDVI; (**i**) total rainfall.

The dependence plot of the top nine factors in the importance ranking in the XGBoost-CF model is shown in Figure 21. Compared with the XGBoost-Initial model, the most obvious difference is that the scattering of the sample Shapley values does not have interval continuity; the scale value of the sample present on the horizontal axis is equal to the CF value of each secondary classification interval of the factor, and for the same factor data, the Shapley values of the samples of the secondary classification are scattered vertically along the vertical axis. The factor scatter's Shapley value increases as the CF value of the factor increases, showing a positive relationship with the prediction results.

According to the dependence relationship between the factors based on CF value and the outcome of the prediction, the inconsistency between the influence degree of the factors obtained by SHAP and the statistical results calculated by the CF model can be observed. For example, as the factor CF value increases, the dispersion interval of the Shapley value for the slope factor also increases. Additionally, when the CF value of the slope is greater than 0, all the Shapley values of the samples are greater than 0. Thus, the factor positively affects landslides. However, in the case where the slope's CF value equals −0.622, the Shapley value of certain samples exceeds 0, contradicting the statistical significance of the CF model. Likewise, when the CF value for the elevation factor surpasses 0, the Shapley values of all samples are greater than 0 as well. However, when the CF value is −0.034, it implies that the Shapley value of the samples in the secondary classification range of the

corresponding factor is positive, indicating that the factor also encourages the occurrence of landslides.

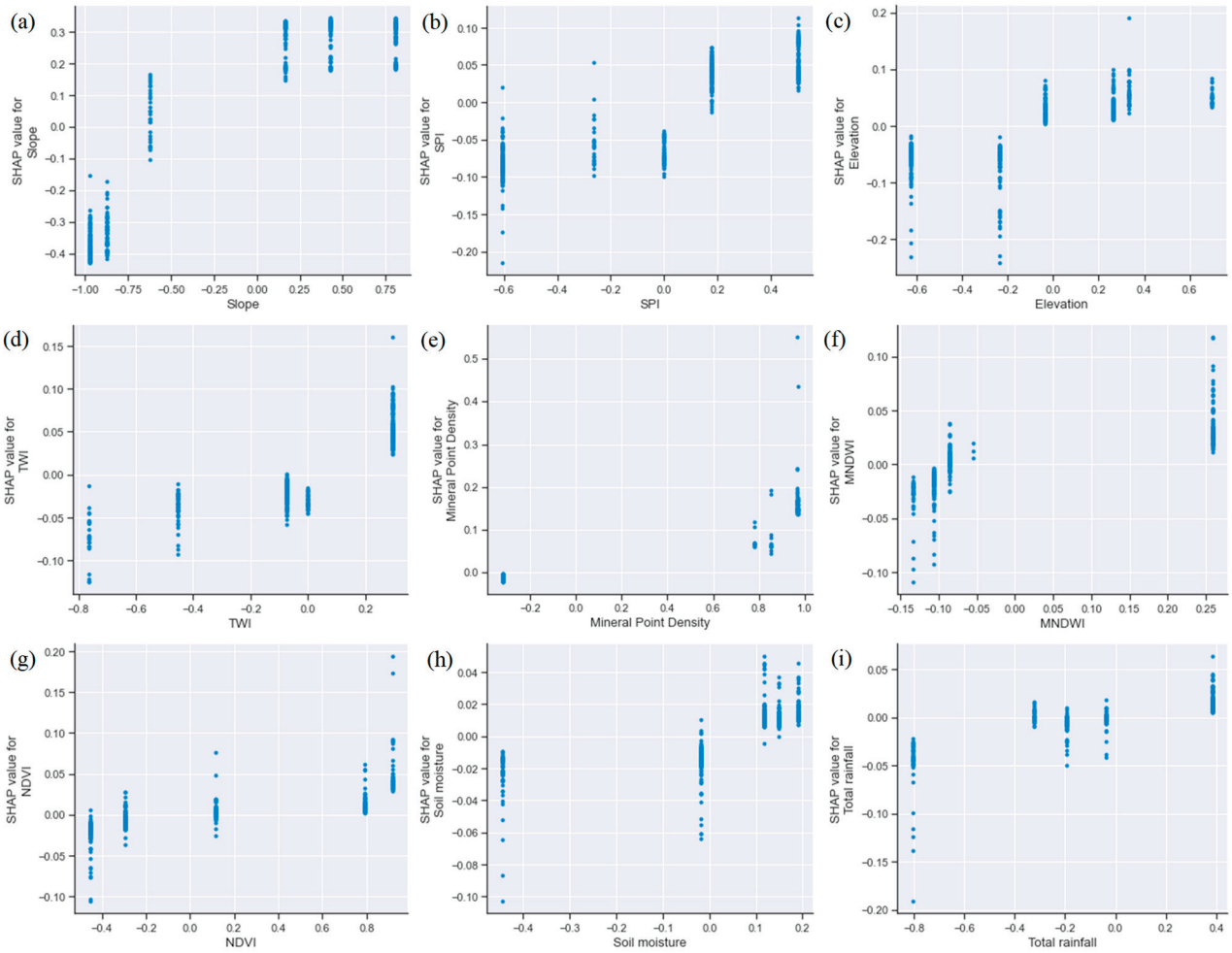

Figure 21. Single-factor dependence plots of main factors based on the XGBoost-CF model. (**a**) Slope; (**b**) SPI; (**c**) elevation; (**d**) TWI; (**e**) mineral point density; (**f**) MNDWI; (**g**) NDVI; (**h**) soil moisture; (**i**) total rainfall.

The statistical significance of the CF model will not be fully considered when using the XGBoost algorithm combined with the CF data of the factors for landslide susceptibility prediction. Instead, the optimization aims to enhance the prediction performance of the sample by optimizing the degree of influence of the CF values on the prediction results in a global manner. Therefore, a priori statistical results of the influence of the factors on landslides obtained using the conditional probability model and the impact of the factors on the predicted results obtained using the ML method possess a notable discrepancy. The coupled model is beyond the capabilities of a basic superposition calculation to analyze.

From the analysis results of the single-factor dependence of XGBoost-Initial and XGBoost-CF models, the influence of individual factors on landslide susceptibility prediction results can be more comprehensively explained by considering both the initial data of factors and the factor data processed by the conditional probability model, taking into account their characteristics together. It is evident that this approach yields a clearer understanding of the prediction of landslide susceptibility.

Landslide phenomena arise from the combined effect of various factors. Therefore, it is important to investigate the relationship of how a factor interacts with another factor to influence the prediction results of landslide susceptibility once the extent of influence

of a single factor regarding the outcome forecast has been analyzed. Figure 22 shows the double-dependence plot of the slope factor with the remaining main influencing factors in the XGBoost-Initial model.

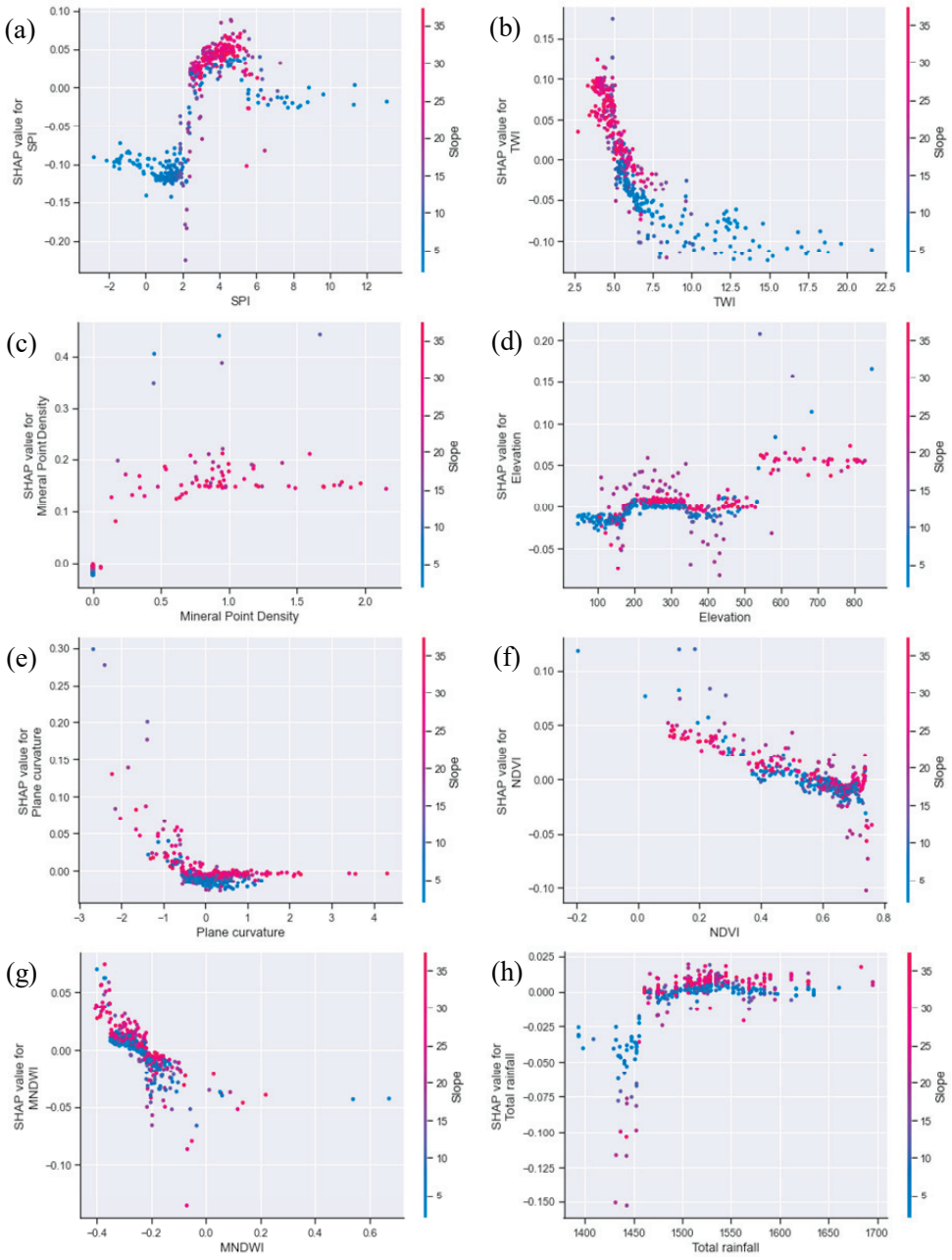

Figure 22. Plots of SHAP interaction effects based on the XGBoost-Initial model. (**a**) Slope and SPI; (**b**) slope and TWI; (**c**) slope and mineral point density; (**d**) slope and elevation; (**e**) slope and plane curvature; (**f**) slope and NDVI; (**g**) slope and MNDWI; (**h**) slope and total rainfall.

The points in the figure indicate the Shapley values for every factor in all samples. Except for slope, the horizontal coordinates represent the range of values for the factors that exert the greatest impact on landslides. The vertical coordinates indicate the corresponding Shapley values for each sample. The color analyzes the distribution of the slope factor in the process of other factor changes. Throughout the dataset, landslide-prone samples with higher slope values are overwhelmingly samples with larger Shapley values in the other factors. This suggests a strong positive interaction between slope and other factors that can

promote landslides. For example, for areas with SPI values at [2,6], the presence of larger slope values and Shapley values greater than 0 in the samples indicates a higher likelihood of landslides. Most sample points have larger slope values in the region where mineral point density is greater than 0, contributing to landslides. When the amount of rainfall surpasses 1500 mm, the majority of samples showing positive Shapley values tend to be found in regions characterized by steeper slopes. This demonstrates that the occurrence of landslides can either be enhanced or inhibited by the interaction between the factors and slope, which confirms that slope is the main influence of landslides in the region.

Based on Figure 23, in the XGBoost-CF model, if a factor's CF value is above 0, the CF value of the slope for the sample, which has a Shapley value greater than 0, tends to be significant rather than being 0. It can be seen that slope and other main influencing factors also have a positive mutual effect with landslide prediction. As with the single dependence of the XGBoost-CF model, the horizontal axis is not sorted by the order of the classification intervals but by the CF values corresponding to the different classification intervals of the factors from smallest to largest. After analysis, as the CF values of the main factors affecting the slope increase, the number of samples with CF values greater than 0 for the slope gradually increases. The findings indicate that the mutual effect of the slope and each factor significantly affects the accuracy of prediction of landslide susceptibility. Moreover, the efficacy of the conditional probability model in improving the model's performance is demonstrated.

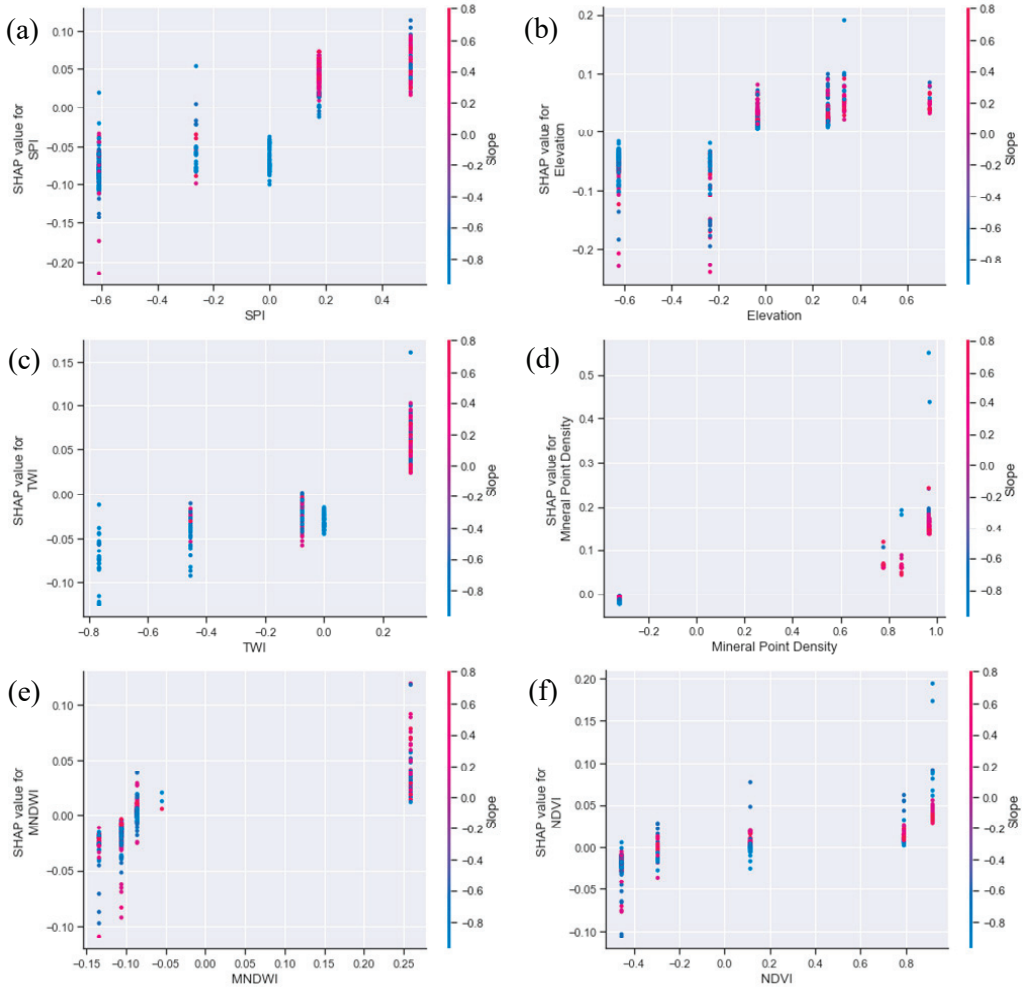

Figure 23. *Cont.*

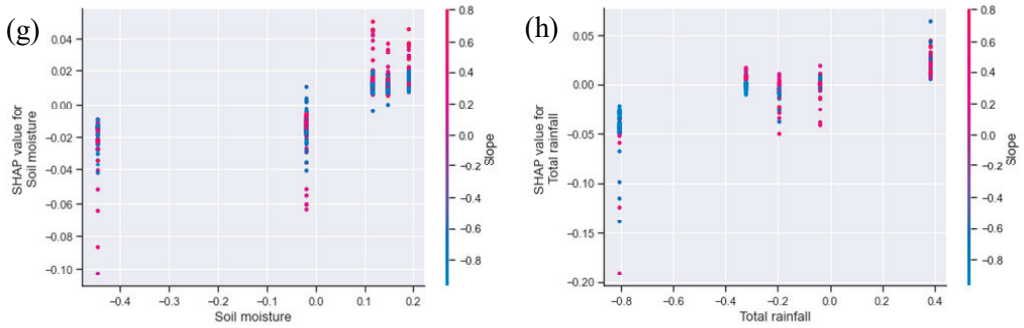

Figure 23. Two-factor dependence plots of main factors based on the XGBoost-CF model. (**a**) Slope and SPI; (**b**) slope and elevation; (**c**) slope and TWI; (**d**) slope and mineral point density; (**e**) slope and MNDWI; (**f**) slope and NDVI; (**g**) slope and soil moisture; (**h**) slope and total rainfall.

5. Discussion

5.1. Features and Advantages of SHAP

When using the ML method to predict landslide susceptibility, the metrics can only account for a portion of the outcomes that the model forecasts, such as accuracy, precision rate, and recall rate. The model's performance may fluctuate when various environmental factors change in the dimensions of time and space. Therefore, it is critical to understand how the model based on the ML method can make some decisions by modeling. To ensure the reliability, fairness, and transparency in the landslide susceptibility prediction model, the model's explanation should include three aspects:

1. An understanding of whether each feature's influence on the model's final decision-making result is positive or negative along with the explanations for the respective influence.
2. An ability to find the feature interactions in the model and analyze how the interactions between features affect the prediction results of the landslide susceptibility model.
3. A local decision evaluation of the typical sample data in the model besides the global interpretation of the model.

The above is of great significance in explaining how the adjustment factors of the input model affect landslide susceptibility.

The traditional feature importance-ranking method can reflect the importance of each feature to landslide development locally and intuitively and illustrate which characteristics exert a considerable influence on the final model. Still, it cannot clearly show how the features affect the outcome of the forecast. One of the key benefits of the Shapley value is its ability to accurately represent the impact of each feature on every sample. It shows the positive and negative impact of features on the target. As shown in Figure 24, taking XGBoost-Initial and XGBoost-CF models as examples, the ranking results of landslide susceptibility importance obtained by using three characteristic importance calculation methods (weight, gain, and cover) attached to XGBoost are different and have significant differences. However, using the SHAP method based on Mean (|Tree SHAP|) can effectively avoid this phenomenon and has a high degree of attribution consistency (see Figure 25).

It can be seen that, given the complexity of the landslide phenomenon, there are unique advantages to analyzing the decision-making results of landslide susceptibility by using the SHAP interpretable method of ML model: (1) In addition to addressing the issue of multicollinearity, SHAP also takes into account the impact of individual variables and the combined effect of variables on the prediction outcomes. (2) SHAP not only contains more feature information than the traditional feature importance-ranking method but also fully ensures the consistency of global features and local samples.

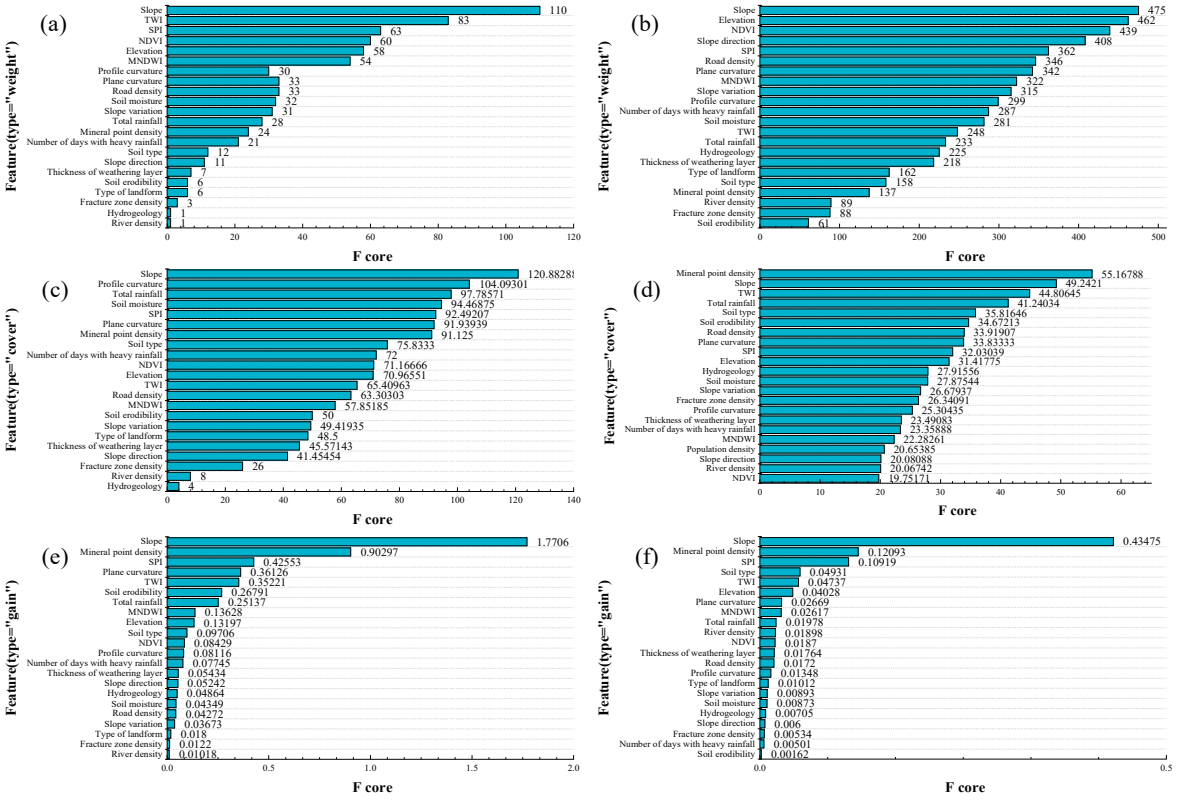

Figure 24. Global feature importance calculation in XGBoost. (**a**) XGBoost-Initial model (im portance_type = "weight"); (**b**) XGBoost-CF model (importance_type = "weight"); (**c**) XGBoost-Initial model (importance_type = "cover"); (**d**) XGBoost- CF model (importance_type = "cover"); (**e**) XGBoost-Initial model (importance_type = "gain"); (**f**) XGBoost-CF model (importance_type = "gain").

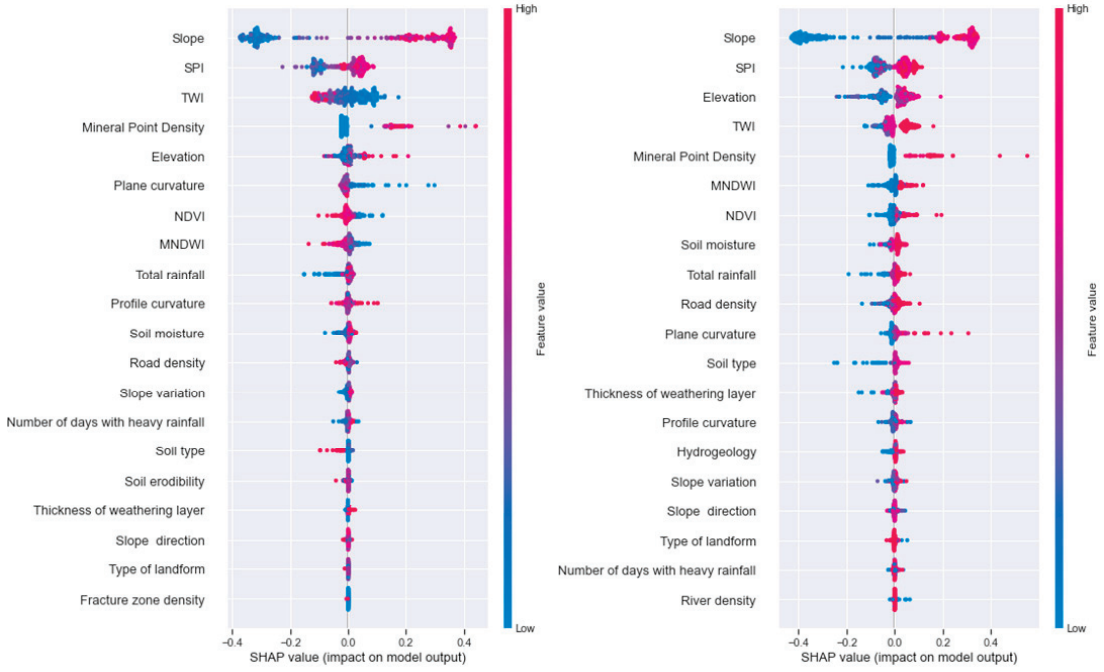

(a) XGBoost - Initial **(b) XGBoost - CF**

Figure 25. SHAP-based global feature importance calculation (top 20). (**a**) XGBoost-Initial model; (**b**) XGBoost-CF model.

It is important to note that this study exclusively utilizes SHAP to elucidate how various RF and XGBoost models, constructed with different types of factor data, generate predictions of landslide susceptibility. In doing so, it does not provide an objective explanation based on realistic principles. The RF and XGBoost models are developed using specific sample data, and thus any modification to the factors or samples may lead to alterations in the final decision regarding landslide susceptibility. Consequently, SHAP cannot be regarded as a straightforward causal model. To ensure that the explanatory results of the landslide susceptibility model closely align with objective reality, it is crucial to select a model with outstanding performance and ensure the accuracy of the sample data as well as the completeness of the adjustment factors.

5.2. Local Interpretation of Typical Samples

SHAP can explain the landslide prediction by landslide adjustment factors in the global dimension and analyze the influence of different factors in a single sample on landslide prediction to the local extent [40,41]. SHAP can visualize the contribution of factors to the n-th sample, find the explanation of the prediction results of a specific sample, and expose the model's decision-making process for this sample. This study uses the local interpretation function of samples based on SHAP to analyze the contribution of factors to landslide and non-landslide samples. The study area utilized the RF-Initial, XGBoost-Initial, RF-CF, and XGBoost-CF models to interpret and analyze the locality of two representative landslide samples and two non-landslide samples.

For Case 1 (Figure 26), the predicted values of the four models are 1.00, 1.02, 1.00, and 1.00, respectively, and the prediction results of all models are more accurate and judged to be landslides. Topographic factors such as slope, SPI, and elevation positively contribute to landslides, and their corresponding Shapley value sums are more significant than 0.4. Although total rainfall, MNDWI, and soil type also contribute positively to this landslide, the degree of contribution is more minor, and their Shapley values are all around 0.01. The analysis results are consistent with the objective facts.

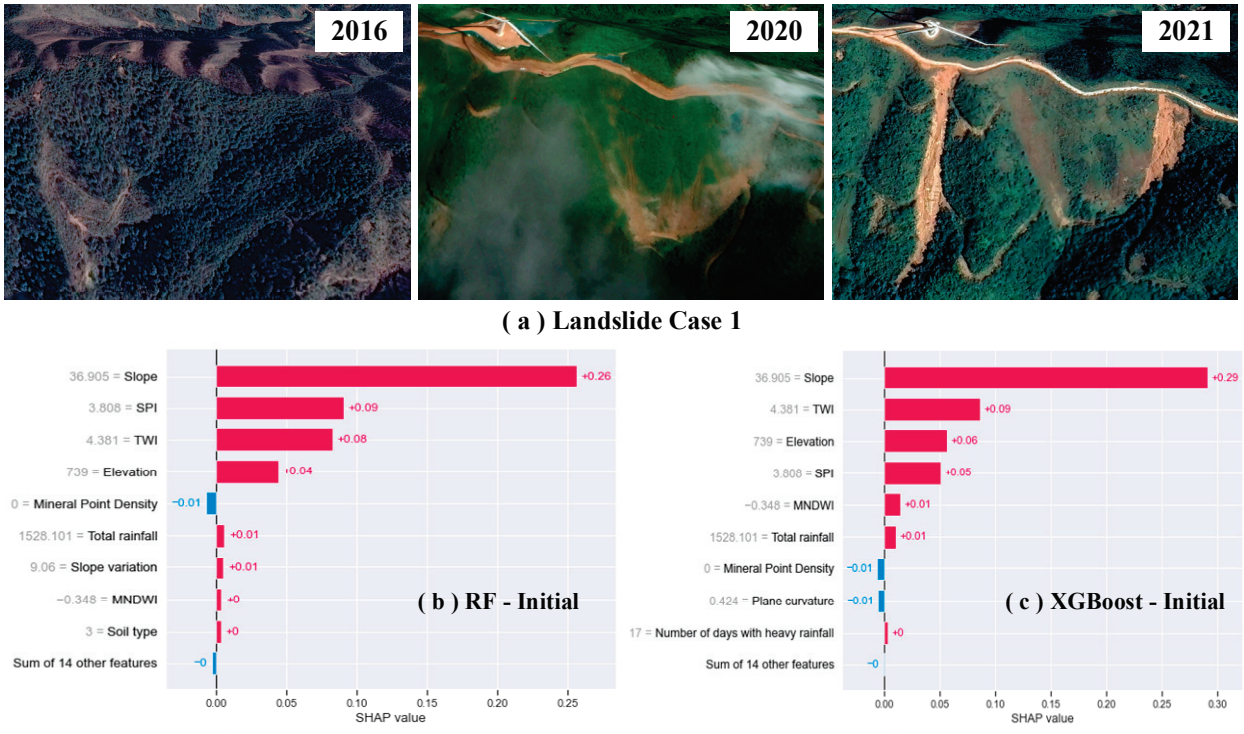

Figure 26. *Cont.*

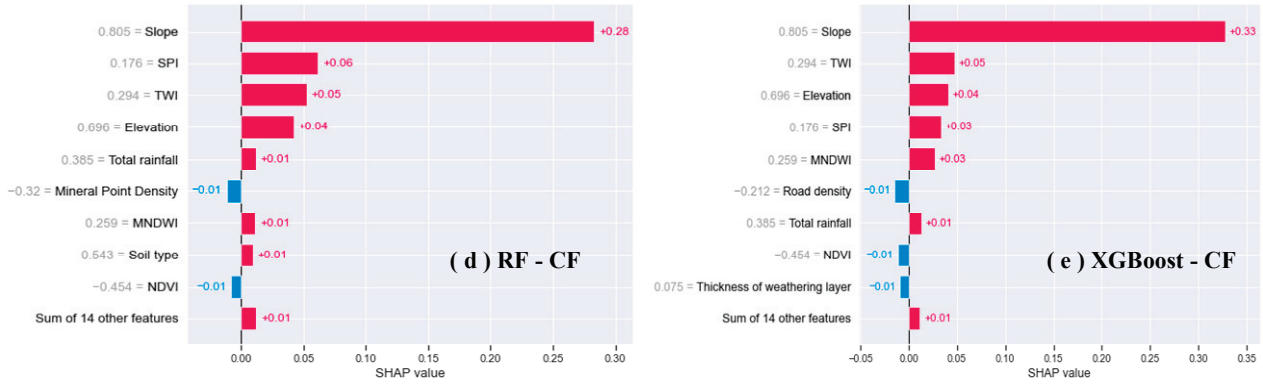

Figure 26. Local interpretation of the susceptibility of landslide Case 1. (**a**) Time sequence image of landslide area (from Google Earth); (**b**) RF-Initial; (**c**) XGBoost-Initial; (**d**) RF-CF; (**e**) XGBoost-CF.

For Case 2 (Figure 27), the four models made predictions with values of 1.00, 0.96, 0.99, and 1.00, respectively. The RF-CF and XGBoost-CF models were the most precise in assessing the occurrence of landslides. Alongside topographic factors like slope, SPI, elevation, and TWI, mineral point density also plays a notable role in causing landslides, as reflected by Shapley values of 0.1 and 0.15. Moreover, the lower vegetation cover (NDVI = 0.117) allows landslides to develop. The Shapley value was in the interval of [0.02, 0.05]. Thus, it can be seen that the human mining and engineering behavior disrupts the state of equilibrium of the original stresses within the slope's rock formation, destabilizing the rock and soil and leading to the landslide phenomenon. Therefore, slope is the primary condition factor of this landslide, and mineral point density is the main trigger factor. The analysis results are consistent with the objective facts.

(a) Landslide Case 2

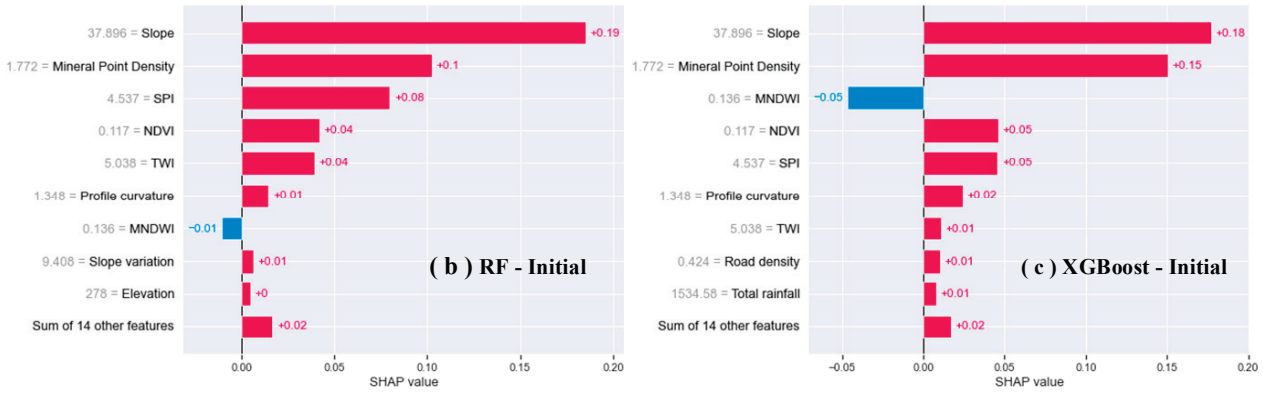

Figure 27. *Cont.*

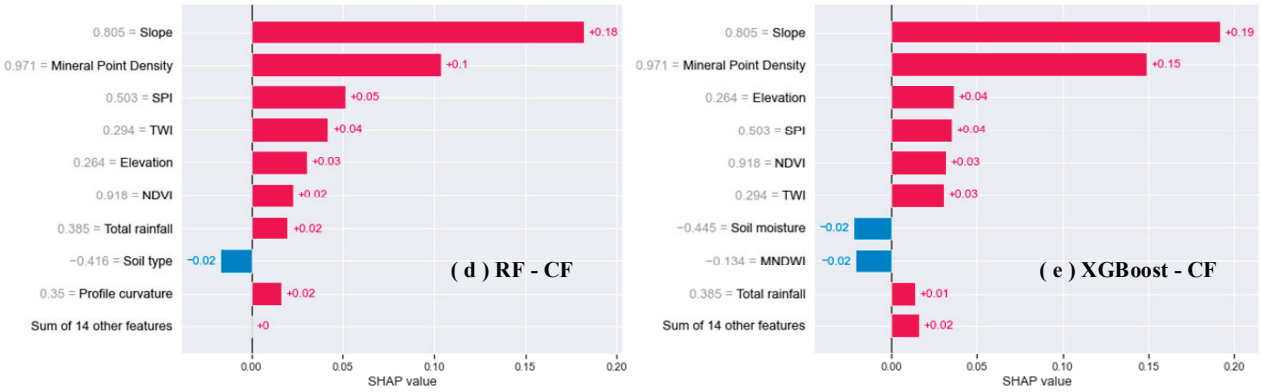

Figure 27. Local interpretation of the susceptibility of landslide Case 2. (**a**) Time sequence image of landslide area (from Google Earth); (**b**) RF-Initial; (**c**) XGBoost-Initial; (**d**) RF-CF; (**e**) XGBoost-CF.

For the typical non-landslide Case 1 (Figure 28), the predicted values of the four models were 0.23, 0.18, 0.38, and 0.01, respectively, and the XGBoost-CF model has the most accurate judgment result, and the judgment result is non-landslide. Although slope positively impacts landslides, TWI, SPI, MNDWI, soil texture, and road density are not conducive to landslides. The projected outcomes align with the objective facts.

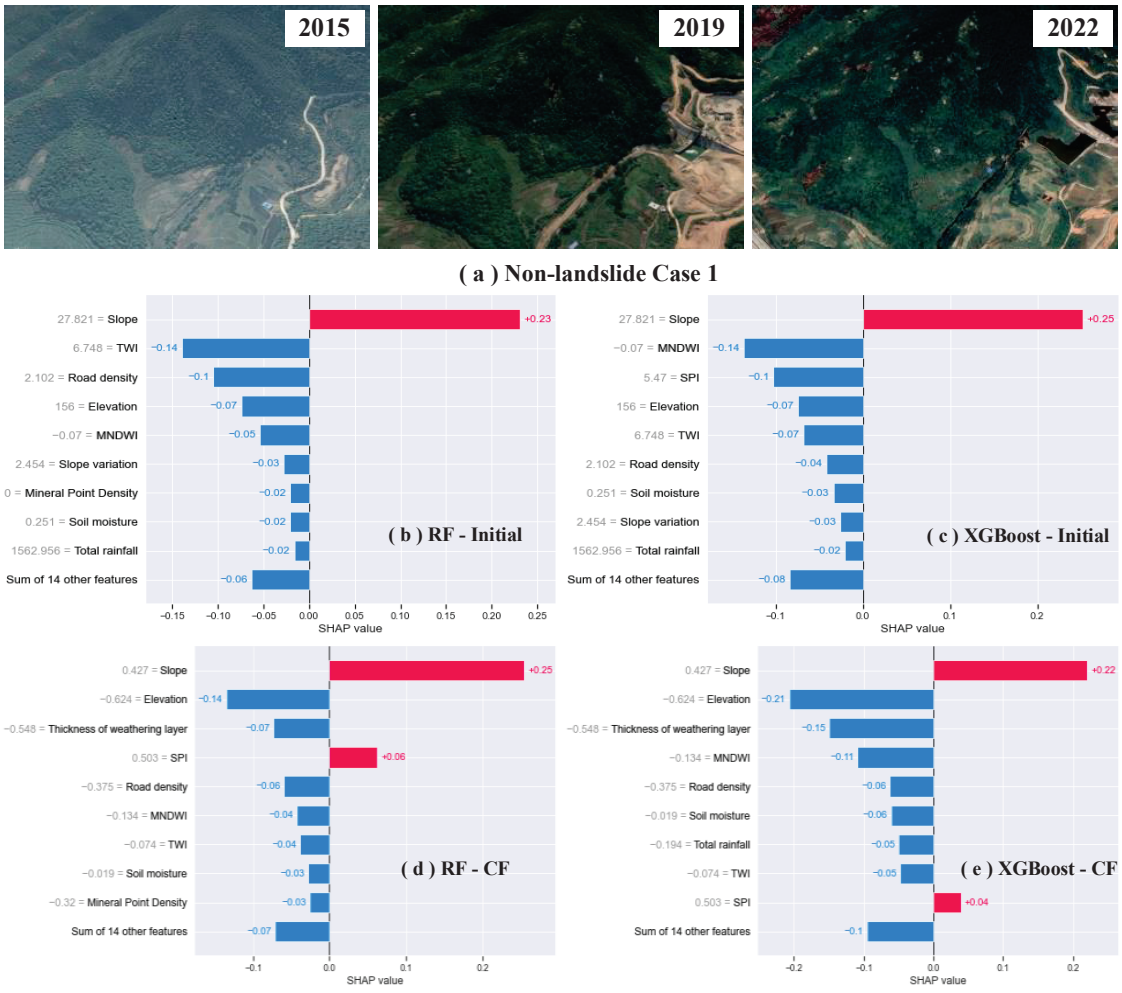

Figure 28. Local interpretation of the susceptibility of non-landslide Case 1. (**a**) Time sequence image of non-landslide area (from Google Earth); (**b**) RF-Initial; (**c**) XGBoost-Initial; (**d**) RF-CF; (**e**) XGBoost-CF.

In the case of non-landslide Case 2 (as shown in Figure 29), the four models had prediction values of 0.74, 0.64, 0.17, and 0.00, respectively. It is worth noting that the RF-Initial and RF-CF models made incorrect predictions, indicating a landslide occurrence. The XGBoost-CF model had the most accurate judgment result, and the judgment result was non-landslide, which was consistent with the objective facts.

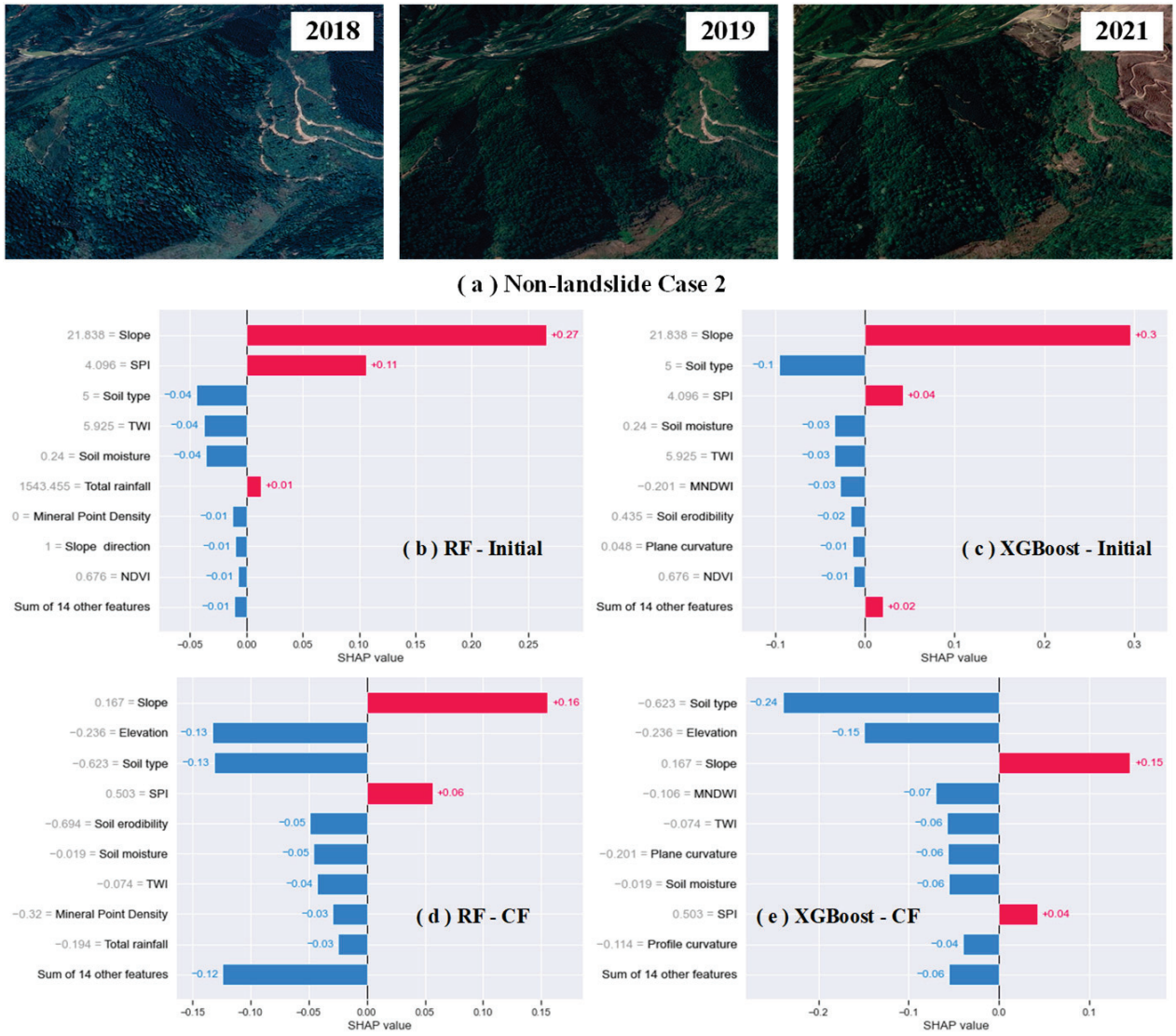

Figure 29. Local interpretation of the susceptibility of non-landslide Case 2. (**a**) Time sequence image of non-landslide area (from Google Earth); (**b**) RF-Initial; (**c**) XGBoost-Initial; (**d**) RF-CF; (**e**) XGBoost-CF.

According to the results of the local interpretation of typical samples using four models, the XGBoost-CF model of landslide susceptibility has the best prediction performance. The role of the slope factor is always of utmost importance when predicting landslides on both a global and local scale. Its contribution to the model is significantly higher than that of other factors. Furthermore, when compared to the RF algorithm, the landslide susceptibility model built with the XGBoost algorithm demonstrates greater accuracy in predicting samples. Moreover, the interpretation of factors using XGBoost is more reasonable and aligns better with objective facts.

5.3. Local Interpretation of Samples with Wrong Prediction

The XGBoost-CF model exhibited the highest prediction performance in this study, with a single prediction error for both landslide and non-landslide samples. Therefore, to analyze the prediction errors of the models, this study provides a local interpretation and analysis of the samples with prediction errors in the XGBoost-CF model based on four models, RF-Initial, XGBoost-Initial, RF-CF, and XGBoost-CF, in the two dimensions of model and data type.

In Figures 30 and 31, the images of the prediction error can see for both the landslide and non-landslide samples, as well as the local interpretation bar graphs, respectively. The Shapley value of each feature is represented on the horizontal axis. The vertical axis shows the factors that have the greatest influence on the prediction result of the sample, with the top factor being the most influential and the bottom factor being the least influential. The factor values of the sample are displayed on the left side. The color of the bar chart in the figure indicates the direction of influence of the factors on the prediction results, with red indicating a positive influence and blue indicating a negative influence. The length of the bars represents the degree of influence. Different models based on different decision mechanisms possess considerable differences in the interpretation of locality for the same samples. Figure 30a reveals a landslide sample with inaccurate prediction. The time series images clearly indicate that the sample exhibits evident signs of a landslide and falls into the category of a typical landslide sample. However, as seen in Figure 30b–e, the model mainly emphasizes the negative contribution of slope to landslide prediction. Compared with the positive effects of individual factors, the negative effects of slope, elevation, and other factors on landslide prediction are more significant, making the model output deviate from reality. We try to analyze the reasons for the prediction errors and conclude the following: Since the non-landslide samples in this study are mainly selected in areas with lower slopes, the number of samples with slope values less than 15° is as high as 197 out of 214 non-landslide samples, and the slope value of this landslide sample is 13.617°. Considering the conclusion that slope is the most influential factor in predicting landslides, this leads to an error in the model's prediction of the given sample, classifying it incorrectly as a non-landslide.

On the other hand, for non-landslide samples with incorrect predictions in the XGBoost-CF model, as can be seen in Figure 31a, the surface environment of the area where the sample is located has remained unchanged in the time series and does not meet the conditions for landslide occurrence. It belongs to a typical non-landslide sample. From the output of the model, the RF-Initial and XGBoost-Initial models based on the initial data of the factor predict this sample as a non-landslide sample, and the prediction results are correct. Based on the factorial CF data, the RF-CF and XGBoost-CF models incorrectly predicted this sample as a landslide sample. Analysis of the local interpretation of the different models shows that, in the RF-Initial and XGBoost-Initial models, even though factors such as TWI may have a positive effect on the occurrence of landslides, they are far from being able to offset the significant negative impact of SPI and slope, ensuring the stability of the sample properties. However, in the RF-CF and XGBoost-CF models, the influence of slope on this sample changed from negative to positive, and the number of factors that positively influenced the occurrence of landslides became larger. The combined effect of all factors tends to predict the landslide of this sample positively, deviating from the actual properties of the sample, and the prediction result is a landslide. The reason for this phenomenon is that, when converting factor data using the certainty factor model, the interval and number of secondary classifications will determine the reasonableness and accuracy of the factor CF values, which will positively or negatively affect the model's performance. For example, because the secondary slope classification in this study was not comprehensive enough, the non-landslide sample fell in the wrong interval. Hence, the influence of the slope factor on this sample was biased in both direction and strength, ultimately impacting the final decision of the model. However, when the model is built by utilizing the factor data processed by the conditional probability model, the secondary

classification of factors is served for for landslide samples, which cannot consider the function of displaying the classification characteristics of complex non-landslide samples. Therefore, this kind of error is inevitable.

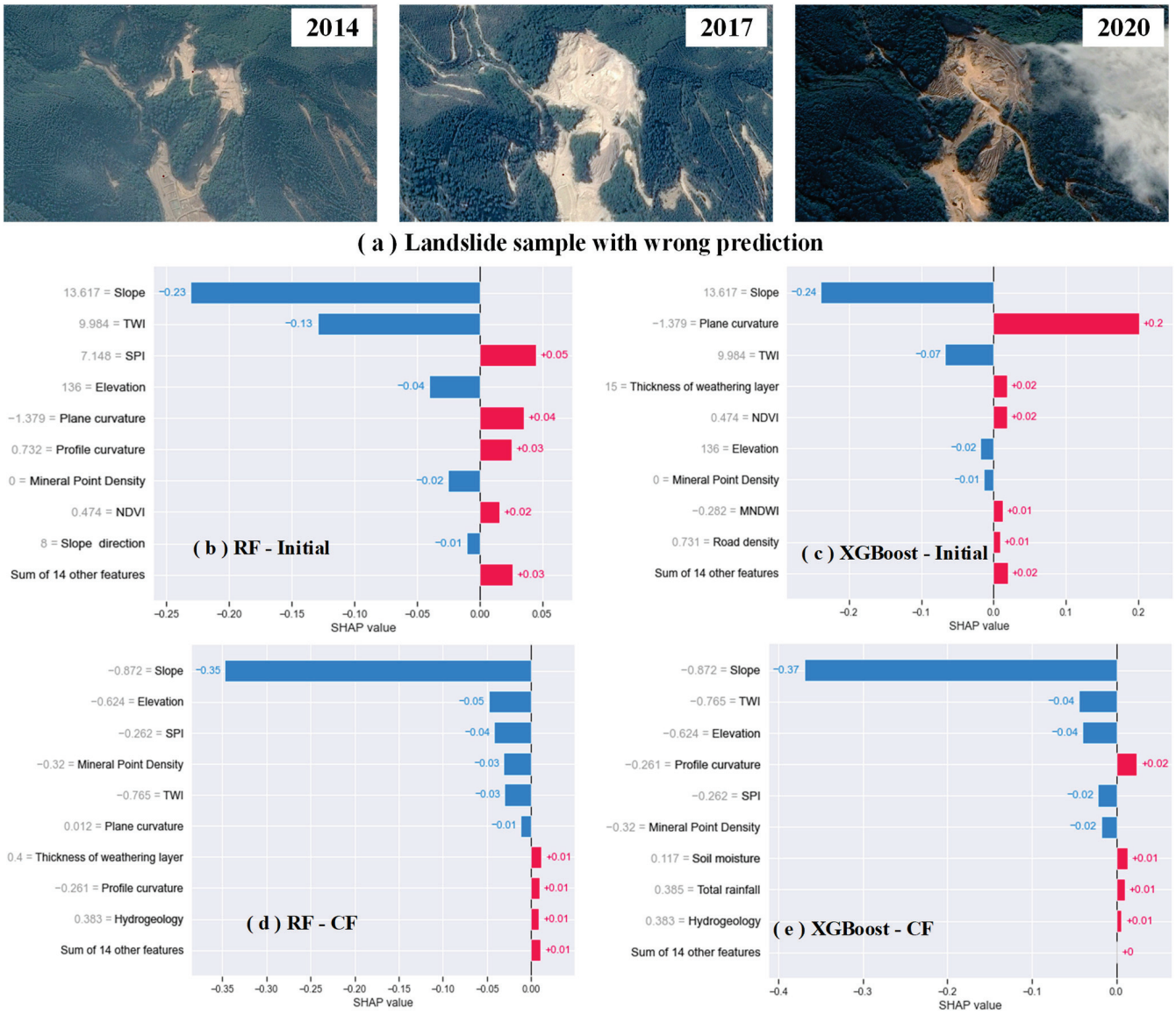

Figure 30. Local interpretation of the susceptibility of landslide sample with wrong prediction. (**a**) Time sequence image of landslide area (from Google Earth); (**b**) RF-Initial; (**c**) XGBoost-Initial; (**d**) RF-CF; (**e**) XGBoost-CF.

In summary, the landslide susceptibility model constructed by the XGBoost algorithm based on factorial CF data has excellent prediction performance. However, it also inevitably needs a better prediction for the sample data. After systematic analysis, to avoid the number of prediction errors to the maximum extent, the researcher improves the pre-processing process of data from two aspects: improving the rationality of non-landslide samples and the precision of the secondary classification status of factors.

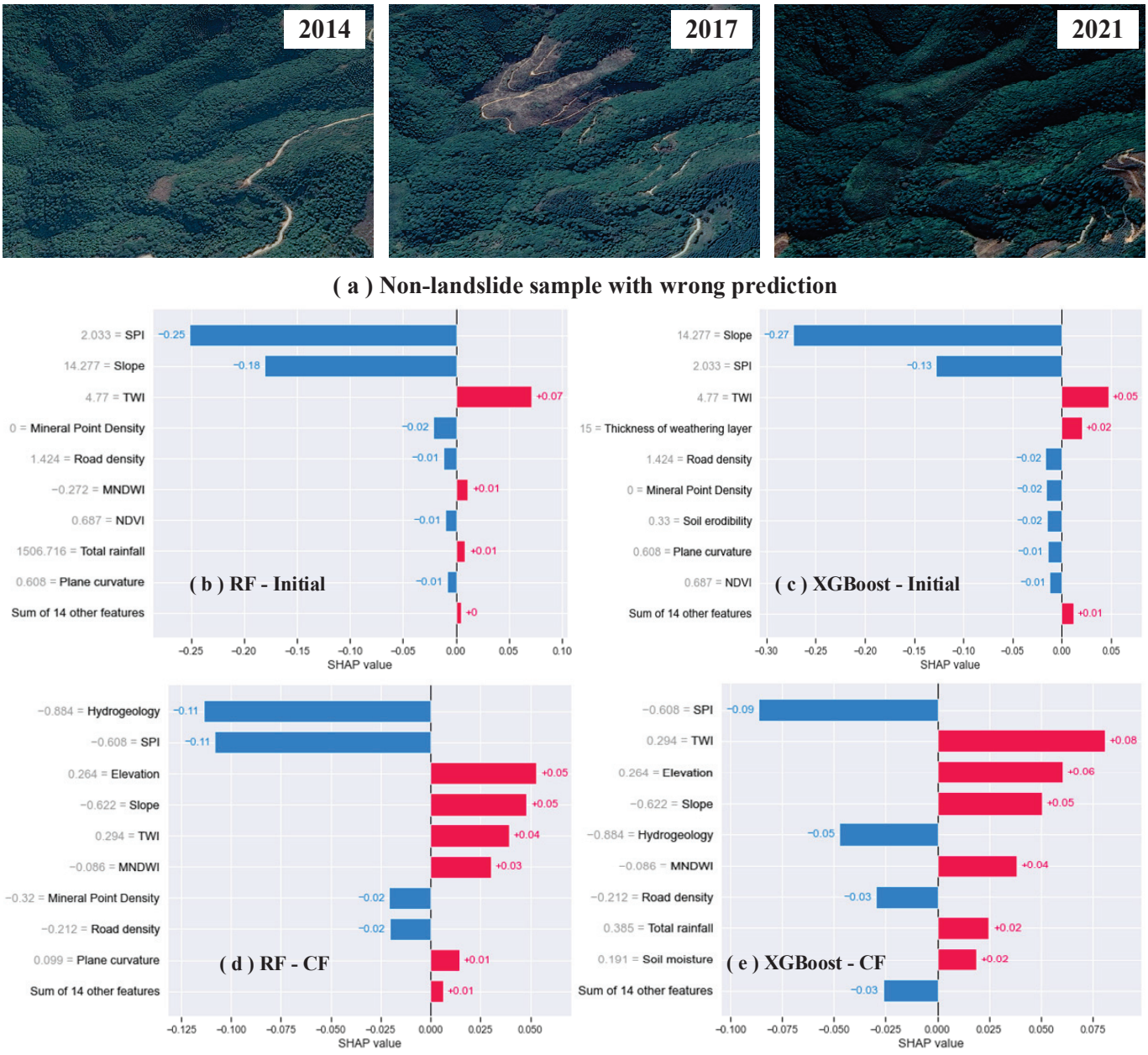

Figure 31. Local interpretation of the susceptibility of non-landslide sample with wrong prediction. (**a**) Time sequence image of non-landslide area (from Google Earth); (**b**) RF-Initial; (**c**) XGBoost-Initial; (**d**) RF-CF; (**e**) XGBoost-CF.

5.4. Post-Programming

5.4.1. Exploration and Discussion

This paper specifically examines how the model's internal decision-making process operates using the interpretable approach of SHAP. It is found that models constructed by different ML methods and factor data types have different decision-making mechanisms, and the same factor contributes to varying models with different directions, strengths, and interactions. The slope is the main factor that interacts with other factors to promote landslide occurrence. The proposed explainable landslide susceptibility model can explain the samples in local dimensions, which analyzes the causes of landslide occurrence and improves the prediction errors.

The research results in this paper further explore and apply the existing SHAP (Shapley Additive exPlanations) methodology, which adds significant value to the explanatory

analysis of modeling susceptibility to landslides. The following is a discussion of how the research results of this paper complement, confirm, or contradict the current state of SHAP research:

1. Exploration of different factor data types: Current landslide susceptibility research is mainly focused on exploring the interpretation of different ML models, whereas this paper's analysis introduces new dimensions in considering different factor data types, which are different from the present condition of research. This paper presents the initial effort to employ the SHAP method in elucidating landslide susceptibility models utilizing various types of factor data. This investigation introduces a fresh standpoint to clarify the impact of diverse factor data types on the decision-making process within the model.
2. Interpretability advantage: The research in this paper confirms the advantage of the SHAP method in interpreting landslide susceptibility models constructed based on the ML method. The internal decision-making mechanism of the model is thoroughly explained in this paper through the utilization of the SHAP method, which improves the transparency and interpretability of the model. Since existing studies have emphasized the importance of the SHAP method in providing model explanations [35], this is consistent with the current state of research.
3. Comparison and analysis of internal decision-making within models: The study in this paper compared and analyzed the differences in internal decision making within landslide susceptibility models constructed based on different types of factor data. This point, to some extent, contradicts the status quo that current research mainly focuses on exploring the interpretation of different ML models because the research in this paper focusing on the effect of factor data types on the decision-making process within the models is not limited to just selecting and interpreting the models.

In summary, this paper's findings offer a fresh perspective on the interpretation of landslide susceptibility models by adding to the existing body of research, confirming the interpretability advantages of the SHAP method, and comparing and analyzing the differences in model internal decision making across factor data types.

5.4.2. A Discussion of Feature Importance Assessment for Fused Decision Tree Models

The above study demonstrated the superior performance of five conditional probability models for landslide susceptibility prediction. However, as another class of commonly used machine learning methods, decision tree models have unique advantages in terms of interpretability and feature importance assessment. Decision tree models can provide intuitive decision paths that help us understand the prediction mechanism of the models under different feature conditions. To deepen the understanding of the role of decision tree models in landslide susceptibility prediction, we plan to introduce ranked feature importance analysis in future research work. Ranked feature importance analysis is a powerful tool to measure how much each feature affects the model performance. By randomly rearranging the feature values, we can observe the extent to which the features affect the accuracy of the predictions. Applying this method to our decision tree and other conditional probability models allows for further comparison of their differences in feature importance. This provides insights into how much attention different models pay to different features and reveals the impact of interactions between features on prediction results.

While the primary emphasis of this investigation was on five distinct models of conditional probability, recognizing the feature importance scores of decision tree models is crucial for model interpretation and understanding of prediction results. In future studies, we plan to incorporate decision tree models into the framework of the current research to comprehensively evaluate the performance of the different models in predicting landslide susceptibility and to further investigate the influence of feature importance on decision tree models.

In future research, the results of comparing the decision tree model with the five conditional probability models mentioned above, in terms of ranking feature importance

analysis, will be explored and integrated into the explanatory framework. By combining the feature importance scores of the different models with their decision paths, a more comprehensive explanation of the model's prediction mechanism for landslide susceptibility can be achieved. This will further enhance the comprehensiveness and explanatory nature of the study and provide more accurate landslide management and prevention recommendations to the regional authorities.

6. Conclusions

The objective of this study is to examine the variations among various types of factor data in the decision-making process of the landslide susceptibility model built using the integrated structure ML method. In this paper, we take 214 landslide samples from Cenxi as an example and construct 12 different models for assessing landslide susceptibility utilizing RF and XGBoost algorithms based on the initial factor data and five types of factor data converted by conditional probability model, and find the model with the best performance using multiple evaluation indices. In addition, we innovatively utilize a SHAP-based interpretable model to evaluate and analyze the internal decision-making mechanisms of models based on different types of factor data. The principal findings are as follows:

(1) The study successfully constructed 12 landslide susceptibility models, all of which performed exceptionally well. Among these models, the XGBoost-CF model, created using the XGBoost algorithm based on CF values, demonstrated superior stability and reliability in evaluating landslide susceptibility in the study area. It achieved an AUC value of 1, an accuracy value of 99.533, a kappa coefficient value of 0.991, and an RMSE value of 0.0807. The results from the XGBoost-CF model indicated that 91.121% of the landslides occurred within 24.959% of the high- and very-high-susceptibility zones, while only 0.467% of the landslides were located in 44.891% of the low- and very-low-susceptibility zones. This suggests that the model covers landslide risk areas comprehensively and exhibits specificity in the identification of landslide samples, thereby producing optimal zoning results.

(2) The utilization of SHAP as an interpretable approach enables a clear explanation of the correlation between factors and the forecasted outcomes of landslide susceptibility. The results demonstrate that landslide susceptibility models, which are constructed using various machine learning techniques and different types of factor data, employ diverse decision-making processes within the same study area. Specifically, the impact direction and strength of a particular factor vary across different models, and the interaction of the same factor has varying effects on the forecasted outcomes. Moreover, the type of factor data plays a significant role in shaping the decision-making process of the models. By taking into consideration the distinct characteristics of different types of factor data, a more comprehensive understanding of how factors influence the forecasted outcomes of landslide susceptibility can be attained.

(3) Using the interpretable method based on SHAP to analyze the factor importance and factor interaction in different models, it can be determined that the main factor causing landslides in this area is the slope, and it enhances the occurrence of landslides by interacting with other factors.

(4) The explainable landslide susceptibility model proposed in this paper can explain individual samples in the local dimension. It can not only explain and analyze the causes of the occurrence of typical landslides but also be used to test whether the selection of non-landslide samples is reasonable. Most importantly, by using this function to explain and analyze samples with incorrect predictions locally, the causes can be summarized and used to further improve the landslide susceptibility model.

In conclusion, in addition to different ML methods, the factor data type can seriously affect the model's decision results for individual samples. The reason for this analysis is that different data types of the same factor contribute to the direction and strength of the sample differently. It is evident that utilizing the factor data transformed by the conditional probability model effectively enhances the prediction accuracy of the model. However, it is

equally important to pay attention to the characteristics of the original factor data in order to provide a comprehensive and clear explanation of how these factors impact the model's prediction results. The interpretable landslide susceptibility model proposed in this study, based on various types of factor data, can offer substantial theoretical and technical support to regional authorities responsible for managing and preventing landslide hazards.

Author Contributions: Conceptualization, C.R.; methodology, J.L. and W.Y.; software, C.R. and Y.Z.; validation, J.L., X.X. and Y.L.; formal analysis, C.D.; investigation, J.L.; resources, C.D.; data curation, W.Y.; writing—original draft preparation, C.R., J.L. and W.Y.; writing—review and editing, J.L. and W.Y.; visualization, J.L.; supervision, W.Y.; project administration, C.R.; funding acquisition, C.R. All authors have read and agreed to the published version of the manuscript.

Funding: This research was funded by the National Natural Science Foundation of China (No. 42064003).

Institutional Review Board Statement: Not applicable.

Informed Consent Statement: Not applicable.

Data Availability Statement: Not applicable.

Conflicts of Interest: The authors declare no conflict of interest.

References

1. Kavzoglu, T.; Teke, A.; Yilmaz, E.O. Shared blocks-based ensemble deep learning for shallow landslide susceptibility mapping. *Remote Sens.* **2021**, *13*, 4776. [CrossRef]
2. Mandal, K.; Saha, S.; Mandal, S. Applying deep learning and benchmark machine learning algorithms for landslide susceptibility modelling in Rorachu river basin of Sikkim Himalaya, India. *Geosci. Front.* **2021**, *12*, 101203. [CrossRef]
3. Han, Y.; Wang, P.; Zheng, Y.; Yasir, M.; Xu, C. Extraction of Landslide Information Based on Object-Oriented Approach and Cause Analysis in Shuicheng, China. *Remote Sens.* **2022**, *14*, 502. [CrossRef]
4. Mustafa, K.; Zhang, B.; Cao, J.; Zhang, X.; Chang, J. Comparative Study of Artificial Neural Network and Random Forest Model for Susceptibility Assessment of Landslides Induced by Earthquake in the Western Sichuan Plateau, China. *Sustainability* **2022**, *14*, 13739.
5. Wang, H.; Zhang, L.; Luo, H.; He, J.; Cheung, R. AI-powered landslide susceptibility assessment in Hong Kong. *Eng. Geol.* **2021**, *288*, 106103. [CrossRef]
6. Yi, Y.; Zhang, Z.; Zhang, W.; Jia, H.; Zhang, J. Landslide susceptibility mapping using multiscale sampling strategy and convolutional neural network: A case study in Jiuzhaigou region. *Catena* **2020**, *195*, 104851. [CrossRef]
7. Wang, Z.; Liu, Q.; Liu, Y. Mapping landslide susceptibility using machine learning algorithms and GIS: A case study in Shexian county, Anhui province, China. *Symmetry* **2020**, *12*, 1954. [CrossRef]
8. Yang, C.; Tong, X.; Chen, G.; Yuan, C.; Lian, J. Assessment of seismic landslide susceptibility of bedrock and overburden layer slope based on shaking table tests. *Eng. Geol.* **2023**, *323*, 107197. [CrossRef]
9. Zou, Q.; Jiang, H.; Cui, P.; Zhou, B.; Jiang, Y.; Qin, M.; Liu, Y.; Li, C. A new approach to assess landslide susceptibility based on slope failure mechanisms. *Catena* **2021**, *204*, 105388. [CrossRef]
10. Chen, Y.; Dong, J.; Guo, F.; Tong, B.; Zhou, T.; Fang, H.; Wang, L.; Zhan, Q. Review of landslide susceptibility assessment based on knowledge mapping. *Stoch. Environ. Res. Risk Assess.* **2022**, *36*, 2399–2417.
11. Lima, P.; Steger, S.; Glade, T. Counteracting flawed landslide data in statistically based landslide susceptibility modelling for very large areas: A national-scale assessment for Austria. *Landslides* **2021**, *18*, 3531–3546. [CrossRef]
12. Reichenbach, P.; Rossi, M.; Malamud, B.D.; Mihir, M.; Guzzetti, F. A review of statistically-based landslide susceptibility models. *Earth-Sci. Rev.* **2018**, *180*, 60–91. [CrossRef]
13. Zhuo, L.; Huang, Y.; Zheng, J.; Cao, J.; Guo, D. Landslide Susceptibility Mapping in Guangdong Province, China, Using Random Forest Model and Considering Sample Type and Balance. *Sustainability* **2023**, *15*, 9024. [CrossRef]
14. Yuan, X.; Liu, C.; Nie, R.; Yang, Z.; Li, W.; Dai, X.; Cheng, J.; Zhang, J.; Ma, L.; Fu, X.; et al. A Comparative Analysis of Certainty Factor-Based Machine Learning Methods for Collapse and Landslide Susceptibility Mapping in Wenchuan County, China. *Remote Sens.* **2022**, *14*, 3259. [CrossRef]
15. Wang, Y.; Feng, L.; Li, S.; Ren, F.; Du, Q. A hybrid model considering spatial heterogeneity for landslide susceptibility mapping in Zhejiang Province, China. *Catena* **2020**, *188*, 104425. [CrossRef]
16. Raja, M.N.A.; Jaffar, S.T.A.; Bardhan, A.; Shukla, S.K. Predicting and validating the load-settlement behavior of large-scale geosynthetic-reinforced soil abutments using hybrid intelligent modeling. *J. Rock Mech. Geotech. Eng.* **2023**, *15*, 773–788. [CrossRef]
17. Merghadi, A.; Yunus, A.P.; Dou, J.; Whiteley, J.; ThaiPham, B.; Bui, D.T.; Avtar, R.; Abderrahmane, B. Machine learning methods for landslide susceptibility studies: A comparative overview of algorithm performance. *Earth-Sci. Rev.* **2020**, *207*, 103225. [CrossRef]

18. Chen, W.; Chen, Y.; Tsangaratos, P.; Ilia, I.; Wang, X. Combining evolutionary algorithms and machine learning models in landslide susceptibility assessments. *Remote Sens.* **2020**, *12*, 3854. [CrossRef]
19. Dou, H.; Huang, S.; Jian, W.; Wang, H. Landslide susceptibility mapping of mountain roads based on machine learning combined model. *J. Mt. Sci.* **2023**, *20*, 1232–1248. [CrossRef]
20. Sun, D.; Ding, Y.; Zhang, J.; Wen, H.; Wang, Y.; Xu, J.; Zhou, X.; Liu, R. Essential insights into decision mechanism of landslide susceptibility mapping based on different machine learning models. *Geocarto Int.* **2022**. [CrossRef]
21. Wang, Y.; Sun, D.; Wen, H.; Zhang, H.; Zhang, F. Comparison of random forest model and frequency ratio model for landslide susceptibility mapping (LSM) in Yunyang County (Chongqing, China). *Int. J. Environ. Res. Public Health* **2020**, *17*, 4206. [CrossRef] [PubMed]
22. Zhao, B.; Ge, Y.; Chen, H. Landslide susceptibility assessment for a transmission line in Gansu Province, China by using a hybrid approach of fractal theory, information value, and random forest models. *Environ. Earth Sci.* **2021**, *80*, 441. [CrossRef]
23. Zhao, Z.; Liu, Z.; Xu, C. Slope Unit-Based Landslide Susceptibility Mapping Using Certainty Factor, Support Vector Machine, Random Forest, CF-SVM and CF-RF Models. *Front. Earth Sci.* **2021**, *9*, 589630. [CrossRef]
24. Fan, H.; Lu, Y.; Hu, Y.; Fang, J.; Lv, C.; Xu, C.; Feng, X.; Liu, Y. A landslide susceptibility evaluation of highway disasters based on the frequency ratio coupling model. *Sustainability* **2022**, *14*, 7740. [CrossRef]
25. Arabameri, A.; Pradhan, B.; Rezaei, K.; Lee, C. Assessment of landslide susceptibility using statistical-and artificial intelligence-based FR–RF integrated model and multiresolution DEMs. *Remote Sens.* **2019**, *11*, 999. [CrossRef]
26. Kavzoglu, T.; Teke, A. Predictive Performances of ensemble machine learning algorithms in landslide susceptibility mapping using random forest, extreme gradient boosting (XGBoost) and natural gradient boosting (NGBoost). *Arab. J. Sci. Eng.* **2022**, *47*, 7367–7385. [CrossRef]
27. Huang, F.; Zhang, J.; Zhou, C.; Wang, Y.; Huang, J.; Zhu, L. A deep learning algorithm using a fully connected sparse autoencoder neural network for landslide susceptibility prediction. *Landslides* **2020**, *17*, 217–229. [CrossRef]
28. Arabameri, A.; Pal, S.C.; Rezaie, F.; Chakrabortty, R.; Saha, A.; Blaschke, T.; Di Napoli, M.; Ghorbanzadeh, O.; Ngo, P.T.T. Decision tree based ensemble machine learning approaches for landslide susceptibility mapping. *Geocarto Int.* **2022**, *37*, 4594–4627. [CrossRef]
29. Pradhan, B.; Dikshit, A.; Lee, S.; Kim, H. An explainable AI (XAI) model for landslide susceptibility modeling. *Appl. Soft Comput. J.* **2023**, *142*, 110324. [CrossRef]
30. Pyakurel, A.; Dahal, B.K.; Gautam, D. Does machine learning adequately predict earthquake induced landslides? *Soil Dyn. Earthq. Eng.* **2023**, *171*, 107994. [CrossRef]
31. Iban, M.C.; Bilgilioglu, S.S. Snow avalanche susceptibility mapping using novel tree-based machine learning algorithms (XGBoost, NGBoost, and LightGBM) with eXplainable Artificial Intelligence (XAI) approach. *Stoch. Environ. Res. Risk Assess.* **2023**, *37*, 2243–2270. [CrossRef]
32. Sun, D.; Chen, D.; Zhang, J.; Mi, C.; Gu, Q.; Wen, H. Landslide Susceptibility Mapping Based on Interpretable Machine Learning from the Perspective of Geomorphological Differentiation. *Land* **2023**, *12*, 1018. [CrossRef]
33. Zhang, J.; Ma, X.; Zhang, J.; Sun, D.; Zhou, X.; Mi, C.; Wen, H. Insights into geospatial heterogeneity of landslide susceptibility based on the SHAP-XGBoost model. *J. Environ. Manag.* **2023**, *332*, 117357. [CrossRef] [PubMed]
34. Ekmekcioğlu, Ö.; Koc, K. Explainable step-wise binary classification for the susceptibility assessment of geo-hydrological hazards. *Catena* **2022**, *216*, 106379. [CrossRef]
35. Al-Najjar, H.A. A novel method using explainable artificial intelligence (XAI)-based Shapley Additive Explanations for spatial landslide prediction using Time-Series SAR dataset. *Gondwana Res.* **2022**. [CrossRef]
36. Zhou, X.; Wen, H.; Li, Z.; Zhang, H.; Zhang, W. An interpretable model for the susceptibility of rainfall-induced shallow landslides based on SHAP and XGBoost. *Geocarto Int.* **2022**, *37*, 13419–13450. [CrossRef]
37. Lin, Q.; Lima, P.; Steger, S.; Glade, T.; Jiang, T.; Zhang, J.; Liu, T.; Wang, Y. National-scale data-driven rainfall induced landslide susceptibility mapping for China by accounting for incomplete landslide data. *Geosci. Front.* **2021**, *12*, 101248. [CrossRef]
38. Liu, Y.; Zhao, L.; Bao, A.; Li, J.; Yan, X. Chinese High Resolution Satellite Data and GIS-Based Assessment of Landslide Susceptibility along Highway G30 in Guozigou Valley Using Logistic Regression and MaxEnt Model. *Remote Sens.* **2022**, *14*, 3620. [CrossRef]
39. Pham, V.D.; Nguyen, Q.-H.; Nguyen, H.D.; Pham, V.-M.; Vu, V.M.; Bui, Q.-T. Convolutional neural network—Optimized moth flame algorithm for shallow lands.lide susceptible analysis. *IEEE Access* **2020**, *8*, 32727–32736. [CrossRef]
40. Gani, A.M.S.; Rahman, M.S.; Ahmed, N.; Ahmed, B.; Rabbi, M.F.; Rahman, R.M. Improving spatial agreement in machine learning-based landslide susceptibility mapping. *Remote Sens.* **2020**, *12*, 3347.
41. Chen, W.; Yan, X.; Zhao, Z.; Hong, H.; Dieu Tien, B.; Biswajeet, P. Spatial prediction of landslide susceptibility using data mining-based kernel logistic regression, naive Bayes and RBFNetwork models for the Long County area (China). *Bull. Eng. Geol. Environ.* **2019**, *78*, 247–266. [CrossRef]
42. Cheng, J.; Dai, X.; Wang, Z.; Li, J.; Qu, G.; Li, W.; She, J.; Wang, Y. Landslide Susceptibility Assessment Model Construction Using Typical Machine Learning for the Three Gorges Reservoir Area in China. *Remote Sens.* **2022**, *14*, 2257. [CrossRef]
43. Rohan, T.J.; Wondolowski, N.; Shelef, E. Landslide susceptibility analysis based on citizen reports. *Earth Surf. Process. Landf.* **2021**, *46*, 791–803. [CrossRef]

44. Chang, Z.; Du, Z.; Zhang, F.; Huang, F.; Chen, J.; Li, W.; Guo, Z. Landslide susceptibility prediction based on remote sensing images and GIS: Comparisons of supervised and unsupervised machine learning models. *Remote Sens.* **2020**, *12*, 502. [CrossRef]
45. He, W.; Chen, G.; Zhao, J.; Lin, Y.; Qin, B.; Yao, W.; Cao, Q. Landslide Susceptibility Evaluation of Machine Learning Based on Information Volume and Frequency Ratio: A Case Study of Weixin County, China. *Sensors* **2023**, *23*, 2549. [CrossRef] [PubMed]
46. Huang, F.; Cao, Z.; Guo, J.; Jiang, S.; Li, S.; Guo, Z. Comparisons of heuristic, general statistical and machine learning models for landslide susceptibility prediction and mapping. *Catena* **2020**, *191*, 104580. [CrossRef]
47. Mehrabi, M. Landslide susceptibility zonation using statistical and machine learning approaches in Northern Lecco, Italy. *Nat. Hazards* **2022**, *111*, 901–937. [CrossRef]
48. Wen, H.; Wu, X.; Ling, S.; Sun, C.; Liu, Q.; Zhou, G. Characteristics and susceptibility assessment of the earthquake-triggered landslides in moderate-minor earthquake prone areas at southern margin of Sichuan Basin, China. *Bull. Eng. Geol. Environ.* **2022**, *81*, 346. [CrossRef]
49. Saranya, T.; Saravanan, S. Assessment of groundwater vulnerability using analytical hierarchy process and evidential belief function with DRASTIC parameters, Cuddalore, India. *Int. J. Environ. Sci. Technol.* **2022**, *20*, 1837–1856. [CrossRef]
50. Ghosh, B. Spatial mapping of groundwater potential using data-driven evidential belief function, knowledge-based analytic hierarchy process and an ensemble approach. *Environ. Earth Sci.* **2021**, *80*, 625. [CrossRef]
51. Roy, J.; Saha, S.; Arabameri, A.; Blaschke, T.; Bui, D.T. A novel ensemble approach for landslide susceptibility mapping (LSM) in Darjeeling and Kalimpong districts, West Bengal, India. *Remote Sens.* **2019**, *11*, 2866. [CrossRef]
52. Goyes Peñafiel, P.; Hernandez Rojas, A. Landslide susceptibility index based on the integration of logistic regression and weights of evidence: A case study in Popayan, Colombia. *Eng. Geol.* **2021**, *280*, 105958. [CrossRef]
53. Ilinca, V.; Şandric, I.; Jurchescu, M.; Chiţu, Z. Identifying the role of structural and lithological control of landslides using TOBIA and Weight of Evidence: Case studies from Romania. *Landslides* **2022**, *19*, 2117–2134. [CrossRef]
54. Quevedo, R.P.; Maciel, D.A.; Uehara, T.D.T.; Vojtek, M.; Rennó, C.D. Consideration of spatial heterogeneity in landslide susceptibility mapping using geographical random forest model. *Geocarto Int.* **2021**, *37*, 8190–8213. [CrossRef]
55. Wang, Y.; Fang, Z.; Hong, H. Comparison of convolutional neural networks for landslide susceptibility mapping in Yanshan County, China. *Sci. Total Environ.* **2019**, *666*, 975–993. [CrossRef]
56. Xia, D.; Tang, H.; Sun, S.; Tang, C.; Zhang, B. Landslide Susceptibility Mapping Based on the Germinal Center Optimization Algorithm and Support Vector Classification. *Remote Sens.* **2022**, *14*, 2707. [CrossRef]
57. Lundberg, S.M.; Erion, G.; Chen, H.; DeGrave, A.; Prutkin, J.M.; Nair, B.; Katz, R.; Himmelfarb, J.; Bansal, N.; Lee, S.-I. From local explanations to global understanding with explainable AI for trees. *Nat. Mach. Intell.* **2020**, *2*, 56–67. [CrossRef]
58. Inan, M.S.K.; Rahman, I. Integration of Explainable Artificial Intelligence to Identify Significant Landslide Causal Factors for Extreme Gradient Boosting based Landslide Susceptibility Mapping with Improved Feature Selection. *arXiv* **2022**, arXiv:2201.03225.
59. Woo, K.Y.; Kim, T.; Shin, J.; Lee, D.; Park, Y.; Kim, Y.; Cha, Y. Validity evaluation of a machine-learning model for chlorophyll a retrieval using Sentinel-2 from inland and coastal waters. *Ecol. Indic.* **2022**, *137*, 108737.
60. Sonkoué, D.; Monkam, D.; Fotso-Nguemo, T.C.; Yepdo, Z.D.; Vondou, D.A. Evaluation and projected changes in daily rainfall characteristics over Central Africa based on a multi-model ensemble mean of CMIP5 simulations. *Theor. Appl. Climatol.* **2019**, *137*, 2167–2186. [CrossRef]
61. Wen, H.; Hu, J.; Zhang, J.; Xiang, X.; Liao, M. Rockfall susceptibility mapping using XGBoost model by hybrid optimized factor screening and hyperparameter. *Geocarto Int.* **2022**, *37*, 16872–16899. [CrossRef]
62. Zhang, Y.; Wen, H.; Xie, P.; Hu, D.; Zhang, J.; Zhang, W. Hybrid-optimized logistic regression model of landslide susceptibility along mountain highway. *Bull. Eng. Geol. Environ.* **2021**, *80*, 7385–7401. [CrossRef]
63. Feng, H.; Miao, Z.; Hu, Q. Study on the Uncertainty of Machine Learning Model for Earthquake-Induced Landslide Susceptibility Assessment. *Remote Sens.* **2022**, *14*, 2968. [CrossRef]
64. Panahi, M.; Rahmati, O.; Rezaie, F.; Lee, S.; Mohammadi, F.; Conoscenti, C. Application of the group method of data handling (GMDH) approach for landslide susceptibility zonation using readily available spatial covariates. *Catena* **2022**, *208*, 105779. [CrossRef]
65. Cha, Y.; Shin, J.; Go, B.; Lee, D.; Kim, Y.; Kim, T.; Park, Y. An interpretable machine learning method for supporting ecosystem management: Application to species distribution models of freshwater macroinvertebrates. *J. Environ. Manag.* **2021**, *291*, 112719. [CrossRef]

remote sensing

MDPI

Article

Susceptibility Assessment of Debris Flows Coupled with Ecohydrological Activation in the Eastern Qinghai-Tibet Plateau

Hu Jiang [1,2], Qiang Zou [1,2,3,*], Bin Zhou [1,2], Zhenru Hu [1,4], Cong Li [1,2], Shunyu Yao [2,5] and Hongkun Yao [1,2]

1 Key Laboratory of Mountain Hazards and Earth Surface Process, Institute of Mountain Hazards and Environment (IMHE), Chinese Academy of Sciences (CAS), Chengdu 610041, China; jianghu@imde.ac.cn (H.J.); zhoubin@imde.ac.cn (B.Z.); 2019050050@stu.cdut.edu.cn (Z.H.); licong@imde.ac.cn (C.L.); yaohongkun21@mails.ucas.ac.cn (H.Y.)
2 University of Chinese Academy of Sciences, Beijing 100049, China; yaoshunyu16@mails.ucas.edu.cn
3 China-Pakistan Joint Research Center on Earth Sciences, CAS-HEC, Islamabad 45320, Pakistan
4 College of Earth Sciences, Chengdu University of Technology, Chengdu 610059, China
5 Institute of Geographic Sciences and Natural Resources Research, Chinese Academy of Sciences, Beijing 100101, China
* Correspondence: zouqiang@imde.ac.cn

Abstract: The eastern margin of the Qinghai-Tibet Plateau is an extreme topography transition zone, and characterized by significant vegetation zonation, in addition to geographic features (such as enormous topographic relief and active tectonics) that control the occurrence of debris flows, which are rapid, surging flows of water-charged clastic sediments moving along a steep channel and are one of the most dangerous mountain hazards in this region. There is thus an urgent need in this region to conduct a regional-scale debris flow susceptibility assessment to determine the spatial likelihood of a debris flow occurrence and guarantee the safety of people and property, in addition to the smooth operation of the Sichuan-Tibet transport corridor. It is, however, a challenging task to estimate the region's debris flow susceptibility while taking into consideration the comprehensive impacts of vegetation on the occurrence of debris flows, such as the positive effect of root anchoring and the negative effect of vegetation weight loads. In this study, a novel regional-scale susceptibility assessment method was constructed by integrating state-of-the-art machine learning algorithms (such as support vector classification (SVC), random forest (RF), and eXtreme Gradient Boosting (XGB)) with the removing outliers (RO) algorithm and particle swarm optimization (PSO), allowing the impacts of vegetation on debris flow initiation to be integrated with the topographical conditions, hydrological conditions, and geotechnical conditions. This method is finally applied to assess the regional-scale susceptibility of debris flows in the Dadu River basin on the eastern margin of the Qinghai-Tibet Plateau. The study results show that (i) all hybrid machine learning techniques can effectively predict the occurrence of debris flows in the extreme topography transition zone; (ii) the hybrid machine learning technique RO-PSO-SVC has the best performance, and its accuracy (ACC) is 0.946 and the area under the ROC curve (AUC) is 0.981; (iii) the RO-PSO algorithm improves SVC, RF, and XGB performance (according to the ACC value) by 3.84%, 2.59%, and 5.94%, respectively; and (iv) the contribution rate of ecology-related variables is almost only one-tenth that of topography- and hydrology-related factors, according to the factor important analysis for RO-PSO-SVC. Furthermore, debris flow susceptibility maps for the Dadu River basin were created, which can be used to assess and mitigate debris flow hazards.

Keywords: debris flow susceptibility prediction; machine learning; the eastern margin of Qinghai-Tibet Plateau; ecohydrological activation

Citation: Jiang, H.; Zou, Q.; Zhou, B.; Hu, Z.; Li, C.; Yao, S.; Yao, H. Susceptibility Assessment of Debris Flows Coupled with Ecohydrological Activation in the Eastern Qinghai-Tibet Plateau. *Remote Sens.* **2022**, *14*, 1444. https://doi.org/10.3390/rs14061444

Academic Editors: Mirko Francioni, Stefano Morelli and Veronica Pazzi

Received: 21 January 2022
Accepted: 9 March 2022
Published: 17 March 2022

1. Introduction

The eastern margin of the Qinghai-Tibet Plateau is located at the junction of the Chengdu Plain and the Qinghai-Tibet Plateau, and this region features significant elevation

differences, active tectonics, and active ecological conditions [1–3], all of which contribute to the development of debris flows that endanger human lives and property in this area. Debris flows are rapid, surging flows of water-charged clastic sediments moving along a steep channel [4,5], and they are one of the most dangerous mountain hazards in this region. Examples of these events include: (1) on 25 July 2020, a debris flow broke out in Wujia gully, Zengda Township, causing damage to the houses at the mouth of the gully; (2) on 17 June 2020, a mountain disaster chain occurred in Meilong gully, Danba County, in which a debris flow broke out, blocking the Xiaojinchuan River and forming a barrier lake with a volume capacity of 100×10^4 m^3; then, a landslide occurred in Aniang Village due to intense erosion at the slope foot caused by the burst of the barrier dam, completely interrupting National Highway G350 and causing the deaths of two people and damage to houses; and (3) on 22 June 2019, a debris flow broke out in Shelong gully, Jinchuan County, with a volume of approximately 17×10^4 m^3, causing 300 m^2 of farmland and 14 houses to be damaged and interrupting traffic and power lines [6]. As a result, there is an urgent need in this region to perform a debris flow susceptibility assessment to determine the spatial likelihood of a debris flow occurring in an area depending on local conditions [7], and to ensure the safety of people and property, in addition to the smooth operation of the Sichuan-Tibet transport corridor.

Because of the unique environmental conditions, this region is characterized by significant vertical and horizontal vegetation zonation [8,9], and geographic features that control debris flow formation, such as enormous topographic relief and active tectonics, making it an ideal natural research site for investigating the relationship between eco-hydrological conditions and debris flow occurrence [9]. Many studies have been performed to improve the understanding of the physical mechanisms governing how the mechanics and hydrology of vegetation affect debris flow formation [10–12]. The comprehensive effects of vegetation on the occurrence of the landslide flows, such as the positive effect of root anchoring and the negative effect of vegetation weight loads, increase the complexity of debris flow environmental conditions [13–16], presenting a challenging task for accurately predicting the debris flow susceptibility in the extreme topography transition belt when the regional debris flow is going to occur [17,18].

Over the past several decades, scholars have proposed several strategies for predicting debris flow susceptibility, including the expert method, data-driven statistical methods, and deterministic approaches [19–21]. Among these methods, the expert method [22] is utilized early in the evaluation of the likelihood of a debris flow occurrence, in which the relationship between the occurrence of debris flows and causal factors is established directly based on experts' experience and background knowledge. This approach may be controversial since it can be difficult to objectively quantify or evaluate an outcome [23]. Data-driven statistical methods, including principal component analysis [24], logistic regression [25], and evidence weighting methods [19], are used to predict debris flow susceptibility by mathematically modeling the link between debris flow occurrence and disaster-causing factors [21,26]. As opposed to the expert technique, data-driven statistical methods are more objective [27]. Furthermore, deterministic approaches are utilized to investigate the physical mechanisms of debris flows and develop models to simulate debris flow susceptibility [28,29]. These physical methods are commonly restricted to the local scale and are challenging to use in regional-scale studies due to the need for sophisticated input data and parameter calibrations [30,31]. Overall, there are few regional debris flow susceptibility studies that look at the effects of vegetation on debris flow formation from the perspective of physical mechanisms [18,32].

In recent years, machine learning algorithms have been increasingly used in the prediction of debris flow susceptibility using remote sensing data [20,33,34]. The susceptibility of debris flows can be estimated using machine learning models by fitting the nonlinear correlations between debris flow occurrence and disaster-causing factors [35]. Many studies have demonstrated that common machine learning algorithms, including gradient boosting machines (GBMs) [35], support vector machines (SVMs) [36], and random forest

(RF) algorithms [33], can produce regional-scale susceptibility prediction results with high reliability. In addition, scholars generally perform debris flow susceptibility research by combining machine learning models with other parameter optimization strategies to obtain more accurate prediction results [37–39]. Due to the capabilities of automated parameter optimization and data pre-processing, the hybrid model generally outperforms the above common models in terms of accuracy of predicted outcomes and application in other areas.

The purpose of this study was to assess the occurrence likelihood of debris flows in the Dadu River basin, a typical extreme topography transition zone on the eastern margin of the Qinghai-Tibet Plateau, and to provide technical support for disaster prevention and mitigation. In this study, some novel hybrid machine learning approaches for assessing debris flow susceptibility were developed in collaboration with the removing outliers algorithm and the particle swarm optimization algorithm, to integrate topographical conditions, hydrological conditions, and geotechnical conditions with vegetation impacts on debris flow formation from the perspective of physical formation mechanisms. Finally, debris flow susceptibility mapping was performed based on these novel hybrid machine learning methods.

2. Study Area

The Dadu River basin is located on the eastern margin of the Qinghai-Tibet Plateau, at the transition zone between the Sichuan Plain and Qinghai-Tibet Plateau (Figure 1). Due to the uplift of the Qinghai-Tibet Plateau, this region has become a typical extreme topography transition with high mountains and deep valleys. Affected by enormous elevation differences, the climate in the northern part of the study area is different from that in the other regions. The northern part of the study area has a mountainous plateau climate with little rainfall throughout the year, the annual precipitation is 500–750 mm, with most precipitation falling as snow, and the snow accumulation period can last up to 5 months. The rest of the region has a monsoon climate with warm winters, hot summers, and humid and rainy characteristics, with an annual precipitation total of 1000 mm. The annual precipitation in Luding and Shimian Counties can reach 1200–1500 mm, and that in the downstream parts of the Dadu River region can reach 1400–1900 mm. Torrential rain is mainly concentrated in the middle and lower reaches of the Dadu River from May to September, and especially in July and August. Moreover, the spatial distribution of annual rainfall shows a trend of high in the south and low in the north, and the annual average temperature ranges from −19.1 to 18.2 °C. The vegetation has significant vertical zonality in this region due to the influence of the topographically extreme belt, especially in the alpine and gorge areas, where the vegetation types successively change with elevation and include broad-leaved forests, mixed coniferous and broad-leaved forests, coniferous forests, shrubs, and meadows.

Furthermore, the river system in this region is developed. From north to south, the Suomo River, Dajinchuan River, and Xiaojinchuan River converge to form the Dadu River, which turns to the east through Luding County and Shimian County and then flows into the Minjiang River south of Leshan City through Hanyuan County and Ebian County. There are 28 tributaries draining watershed areas greater than 1000 km^2 along the river, and the river network density is 0.39 [40].

Lithologically, according to the geological map of Sichuan Province [41], the main rock strata that outcrop along the Dadu River from north to south in the study area include Triassic sandstones, slates and late granitic intrusions, pre-Sinian granites and granitic gneiss, Paleozoic limestones, metamorphic rocks, sand shales, and basalts. Tectonically, the study area is located in three different geological tectonic units, namely, the Ganzi Aba fold belt, the Kangdiantai anticline, and the Emeishan block fault. In addition, the Y-shaped junction zone formed by the Longmenshan fault zone, the Xianshuihe fault zone and the Anninghe fault zone is also located in the study area, as shown in Figure 1. Intense tectonic activity leads to jointing and folding, and these activities facilitate the formation of debris flows in this region.

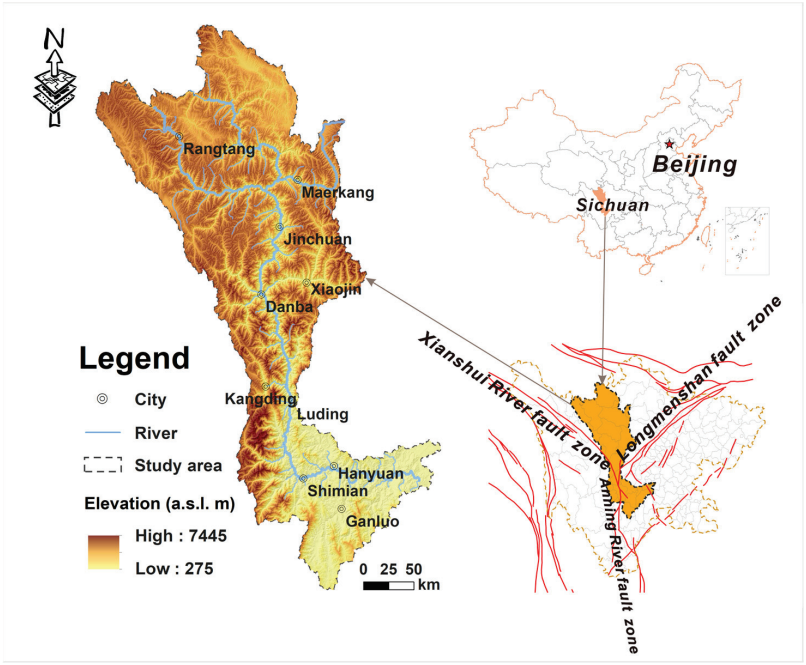

Figure 1. Location of the study area (Dadu River basin) and the distribution of faults.

3. Materials and Methods

This paper proposes new hybrid methods for assessing debris flow susceptibility coupled with ecohydrological activation from the perspective of debris flow formation, which includes several parts: parameter collection, indicator system construction, hybrid model generation, evolution calculation of model hyperparameters, model training, optimal model determining, and susceptibility assessment. Figure 2 depicts the flow chart that represents this process.

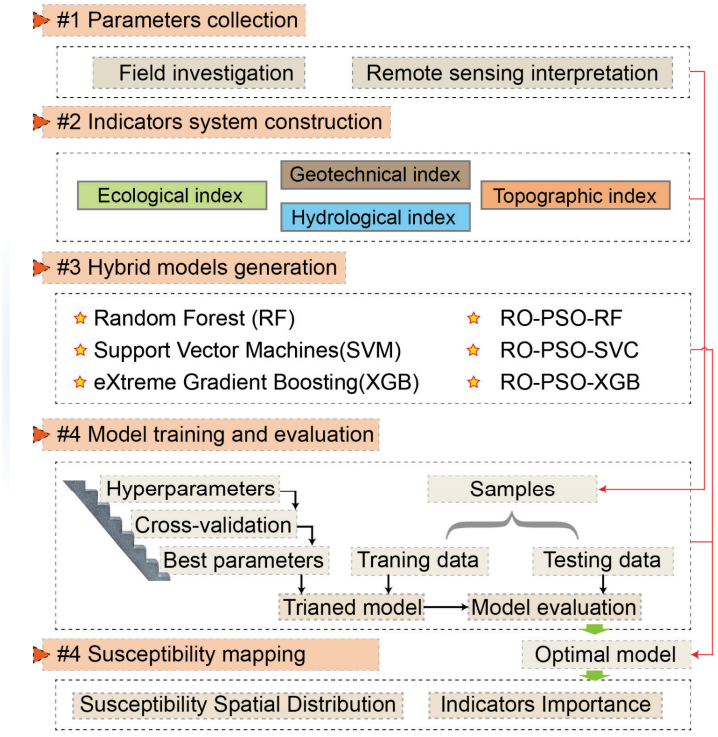

Figure 2. Methodological flow chart.

3.1. Catchment Boundaries Division

The catchment unit is a self-contained hydrological area, with the river serving as the mainline and the water division acting as the boundary [42]. Catchment units having more physical, geological, or geomorphological significance than grid cells are better suitable for predicting debris flow occurrence [21,43]. Furthermore, in terms of debris flow formation, activities such as material source initiation, debris flow movement, erosion, and deposition all occur within catchment units. As a consequence, catchments were selected as mapping units for this research. As illustrated in Figure 3, the Dadu river basin is divided into a total of 1780 catchments using GIS spatial analysis tools with the DEM (30 m resolution).

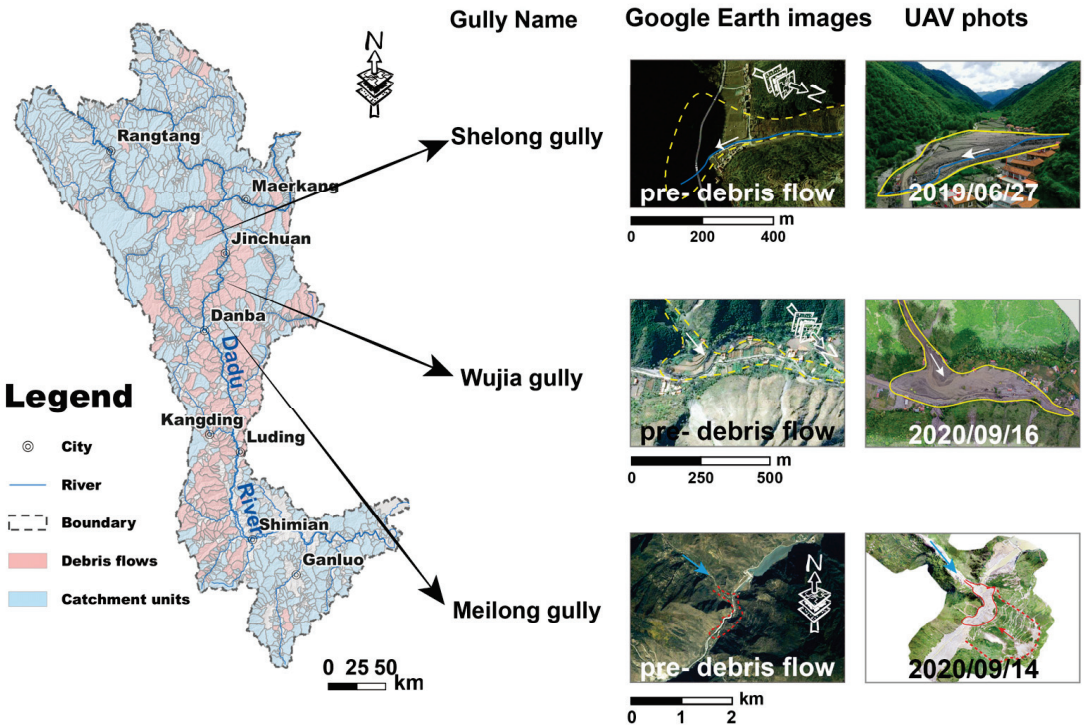

Figure 3. Catchment units in the Dadu River basin.

3.2. Inventory of Debris Flows

In recent years, several field investigations on debris flow disasters in the Dadu River basin have been conducted. However, due to its complex topographical conditions and massive area, it is hard to perform an investigation that spans the whole Dadu River basin. Given that remote sensing interpretations allow for flexibility and low labor costs [44], this study utilized high-resolution remote sensing images to perform visual interpretations, giving an abundance of data for model training. Distinguishing factors such as vegetation changes, landslide scar(s), and clear channel visibility were fully considered in this interpretation procedure to ensure the reliability of the interpretation outcomes [45]. Finally, 562 catchments were picked from the 1780 catchments to train the hybrid machine learning models, with a total of 281 catchments identified in the study area as being prone to debris flow (DFs), and the remaining 281 catchments as being not prone to debris flow (NDFs).

3.3. Establishment of an Indicator System Coupled with Ecohydrological Activation

The selection of predictor factors is crucial in predicting the susceptibility of debris flows [36,46]. The debris flow formation process can be split into several stages based on the physical formation mechanism, such as accumulation of loose materials, initiation driven by rainfall, dynamic movement controlled by terrain and channel conditions, and accumulation at the outlet [47–49]. Based on the aforementioned factors, this article presents a debris flow susceptibility indicator system coupled with ecohydrological activation from

the standpoint of physical mechanisms, taking into account the comprehensive effects of vegetation, such as the positive effect of root anchoring and the negative effect of vegetation weight loads, on the slope failure from the physical mechanism. Overall, the structure of this new indicator system (Figure 4) is designed based on the debris flow formation mechanism and general disaster-causing factors used in traditional debris flow susceptibility methods, and the indicator system consists of ecological indexes, hydrological indexes, geotechnical indexes, and topographic indexes. The processed data of this research and their sources are presented in Table 1. To ensure the consistency of spatial resolution among all data, the feasibility of parameter calculation, and the applicability of the accurate topography depicted in the DEM to the debris flow susceptibility assessment [50], all data from different sources were resampled to the same spatial resolution as the DEM (30 m) using the GIS platform's resampling tool. Due to the need for machine learning input parameter formats, the GIS platform's Zonal Statistics tools were then used to obtain the feature statistics (such as the mean or majority) of each catchment.

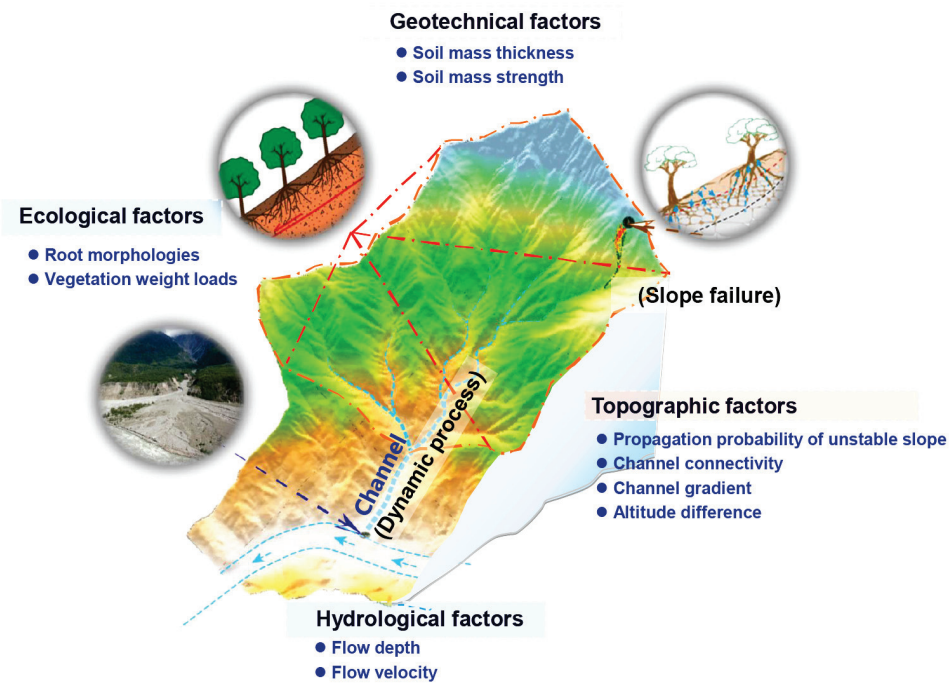

Figure 4. Susceptibility prediction index system sketch coupled with eco-hydrological activation.

Table 1. Employed information and their sources in the current research.

Information	Related Factor Maps or Parameters	Source	Scale/Resolution
Digital Elevation Model (DEM)	The Altitude Difference, Channel Gradient, Connectivity Index and Propagation Probability Index	DEM Dataset (GDEMV2) Downloaded from Geospatial Data Cloud	30 m
The Soil Thickness	The Soil Thickness and Soil Strength	Depth to Bedrock (DTB) Map of China [51]	100 m
Vegetation Types	Vegetation Weight Loads and Root Morphology	Environmental & Ecological ScienceData Center for West China, National Natural Science Foundation of China [52]	1:1,000,000
Precipitation	The Flow Depth and Runoff Velocity	The National Data Center of China for Meteorological Sciences	90 m

3.3.1. Ecological and Hydrological Indexes

(1) Vegetation weight loads (VWL) and root morphology (RM).

Vegetation is the producer in the food chain in terrestrial ecosystems; it transports materials and energy through the ecosystem and is directly tied to the creation of the natural environment [53]. The vegetation in the studied region has obvious vertical and horizontal zonality, which is assisted by the topographically extreme belt conditions; distinct vegetation species with differing vegetation weight loads and root morphologies are concentrated at different altitudes [54,55]. Given that root reinforcement and vegetation weight loads are important in the stability evaluation of vegetation-covered slopes [54,56], and that shallow landslides are one of the main material sources of debris flows, vegetation weight loads and root morphology are included as ecological indexes in the debris flow susceptibility assessment indicator system. The root morphological properties of various plant types in the research region were collected via field investigations (Table 2), and the quantitative techniques and details of the vegetation weight load calculations were found to be similar to those employed by Zou et al. (2021b) [8].

Table 2. Morphological parameters of different vegetation types.

Vegetation Type	Plant Diameter at Breast Height/cm	Root Depth/m	Plant Height/m
Trees	25.0	15.0	20.0
Shrub	1.0	0.5	0.5
Grassy marshland	0.1	0.4	0.4
Alpine sparse vegetation	0.4	0.4	0.4
Agricultural vegetation	6.0	5.0	5.0
Alpine swamp	0.1	0.4	0.4

(2) Flow depth (FD) and runoff velocity (RV).

Water is not only the main triggering factor of debris flow formation, but it is also a fundamental component of the debris flow; hence, hydrological conditions are important for debris flow formation. The flow depth and runoff velocity at a gully's mouth are the overall outcomes of a dynamic hydrologic process that involves rainfall, water storage, depression filling, overflowing within the slope area, and channel confluence [57,58]. To some degree, these characteristics reflect the catchment's topographic relief, the complexity of the gully morphology, and the roughness of the gully base. As a result, to represent the hydrodynamic properties of the runoff in the assessed river branches and channels, the flow velocity and runoff depth are included as hydrological indicators in the susceptibility indicator system. However, the study area is too large to use electronic equipment to monitor flow velocity and runoff depth in each catchment. To compensate for this deficiency, index values based on five assumptions were derived to substitute real flow velocity and depth measurements:

i. A constant rainfall intensity,
ii. The water input from rainfall is equal to the output in the catchment,
iii. The effect of potential energy is considered, and the work done by resistance is ignored,
iv. The influence of different water depths on potential energy is ignored, and
v. Water particles at the same elevation arrive at the gully mouth at the same time.

According to assumption 1, the rainfall per unit time is equal to the volume of water output from the basin and can be deduced as follows:

$$PA\mathrm{d}t = Q\mathrm{d}t, \quad (1)$$

where P is the rainfall intensity; A is the watershed area; Q is the discharge at the outlet; and $\mathrm{d}t$ is the unit of time.

Since resistance and the effect of the water depth on the potential energy are ignored, all gravitational potential energy is converted into kinetic energy. Therefore, the following formula is given for any particle:

$$mgh = \frac{1}{2}mv^2, \tag{2}$$

where m is the mass of the water particle; g is the acceleration of gravity; h is the height difference between the water particle and the point at the gully mouth; and v is the particle velocity at the gully mouth.

The initial potential energy of particles that flow to the gully mouth at the same time is calculated as follows:

$$\int mgh\mathrm{d}h = P\mathrm{d}t\int L(h)B(h)\rho gh\mathrm{d}h, \tag{3}$$

$$mgh = \int mg\mathrm{d}h = P\mathrm{d}t\int L(h)B(h)\rho g\mathrm{d}h, \tag{4}$$

where ρ is the density of water; *L(h)* is the length contour line where the relative height is h; and *B(h)* is the horizontal displacement of the contour line.

The average kinetic energy of particles that flow to the gully mouth at the same time is calculated using Formula (5):

$$\frac{1}{2}mv^2 = \frac{1}{2}PA\mathrm{d}t\rho v^2 = P\mathrm{d}t\int L(h)B(h)\rho g\mathrm{d}h, \tag{5}$$

The runoff velocity is calculated as follows:

$$v = \sqrt{\frac{2\int L(h)B(h)g\mathrm{d}h}{A}}, \tag{6}$$

The flow depth is calculated as follows:

$$H = S/b, \tag{7}$$

$$S = Q/v, \tag{8}$$

$$Q = PA, \tag{9}$$

where b is the average width of the wet crossing section and S is the area of the wet crossing section.

3.3.2. Geotechnical and Topographic Indexes

(1) Thickness (ST) and strength (SS) of the soil mass.

The direct reason for the formation of unstable slopes is that the impervious-layer soil shear strength is less than the sliding force of the soil mass, which contributes to the formation of landslide disasters [59,60]. Therefore, the soil shear strength and soil mass thickness, related to the depth of the impervious layer, are included as geotechnical indicators in the susceptibility prediction index system. Here, the soil shear strength refers to the ultimate strength of the soil mass against shear failure. According to the Mohr–Coulomb failure criterion [61], this variable is calculated using the following formulas:

$$\tau_f = c + \sigma\tan\varphi, \tag{10}$$

$$\sigma = \gamma z, \tag{11}$$

$$\tau_f = c + \gamma z\tan\varphi, \tag{12}$$

where τ_f and c are the shear strength (kPa) and cohesion (kPa) of the soil mass, respectively; φ and γ are the friction angle (°) and density (t/m^3) of the soil mass, respectively; σ is the

normal stress of the soil mass (kPa); and z is the elevation difference from the surface of the soil mass to the bedrock surface (m).

(2) Altitude difference (AD) and channel gradient (CG).

Topographical factors have a considerable impact on the initiation and dynamic process of debris flow formation [62,63]. The steep channel and enormous relief may give an abundance of potential energy conditions for debris flow formation [20]. As a consequence, general topographical characteristics such as altitude difference and channel gradient are included in this index system for assessing debris flow susceptibility. The altitude difference (AD) between the catchment's top and outflow shows the catchment's overall potential energy conditions [64]. The channel gradient (CG) reflects the channel's overall steepness and is computed by dividing AD by the channel length [65].

(3) Connectivity index (IC) and propagation probability index (PPI).

The formation of a debris flow requires not only an abundant water source and loose material conditions but also steep topographic conditions that are conducive to the movement of the debris flow [66]. The lower the stability of a slope with loose material in the source area, the higher the terrain connectivity from the source area to the gully mouth, and the more conducive the conditions to the formation of a debris flow. Therefore, the propagation probability index and connectivity index are incorporated as topographic indexes into the debris flow prediction index system.

The propagation probability index calculated by the Flow-R model [67] provides the probability of the unstable materials propagating to a point likely to be reached by debris flows. The Flow-R model's key input parameters are a digital elevation model (DEM) and the loose material source area. The procedure identifying the source area considers the mechanical anchoring effect of the root system and the vegetation weight loads on the slope covered with various vegetation types. Details and results of the propagation probability index computation can be acquired by referring to Zou et al. (2021b) [8].

The connectivity index was used in this study to represent the potential connectivity between the outlet and other parts of the catchment, and can be quantified by the spatial analysis tools in geographic information systems (GIS). According to Equation (13), its input parameters include land-use data (at a 30 m resolution) and a DEM (at a 30 m resolution) [68,69].

$$IC_k = \log_{10}\left(\frac{D_{up,k}}{D_{dn,k}}\right) = \log_{10}\left(\frac{\overline{W}\,\overline{S}\sqrt{A}}{\sum_i \frac{d_i}{W_i S_i}}\right), \quad (13)$$

where IC_k is the connectivity index; D_{up} is the potential of sediments moving from the upstream channel to the downstream channel; D_{dn} is the possibility of sediments reaching the outlet through the flow path; $\overline{W}$ is the average weight of the upslope catchment area determined by the land-use type; $\overline{S}$ is the average gradient of the upslope catchment area; $\sqrt{A}$ is the square root of the upslope catchment area; d_i is the length of the flow path from the debris source area to the ith unit; and W_i and S_i are the weight and the gradient of the ith unit in the watershed, respectively.

3.4. Parameter Preprocessing

3.4.1. Analysis of Selected Characteristics' Collinearity

Characteristics' collinearity in machine learning modeling indicates that two or more features contain similar information, i.e., there is a strong correlation between them, and that strong collinearity may cause model instability [20,35,38]. The Spearman correlation analysis technique was used to compute the correlation coefficients (Figure 5) in this research. There were two pairs of variables with strong relationships, with correlation coefficients of 0.83 for RM vs. VWL and 0.82 for ST vs. SS. As a result, RM and ST were eliminated.

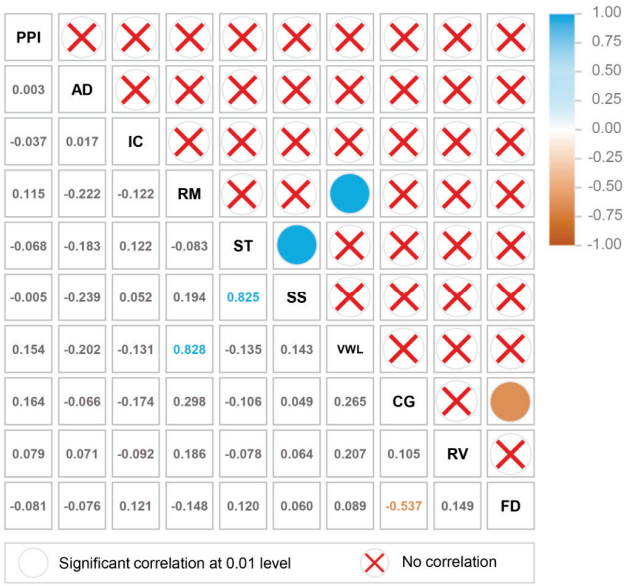

Figure 5. Correlation matrix among the predictor variables.

3.4.2. Data Standardization

The indexes involved in the index system can be quantified according to the calculation methods described above based on the field investigations and collected documentation. Furthermore, considering the direct use of data with different orders of magnitude and dimensions for training affects the accuracy of the model [70], these indexes were standardized using Formula (14) to accelerate model convergence and improve the model accuracy [20].

$$I_{final} = \frac{I - I_{min}}{I_{max} - I_{min}}, \tag{14}$$

where I_{final} is the index value after standardization; I is the index value before standardization; I_{min} is the minimum index value; and I_{max} is the maximum index value.

Finally, some quantified indexes involved in the index system are shown in Figure 6a–f.

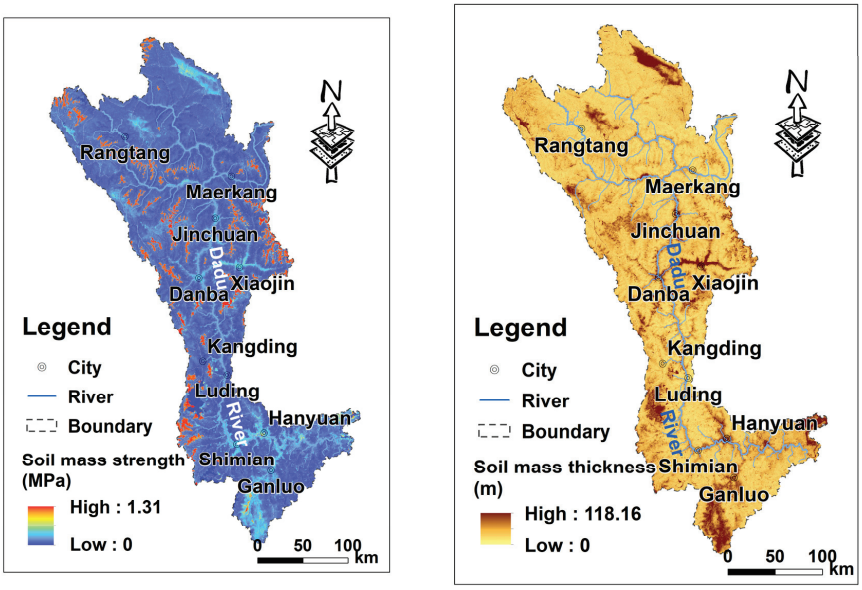

(**a**) (**b**)

Figure 6. *Cont.*

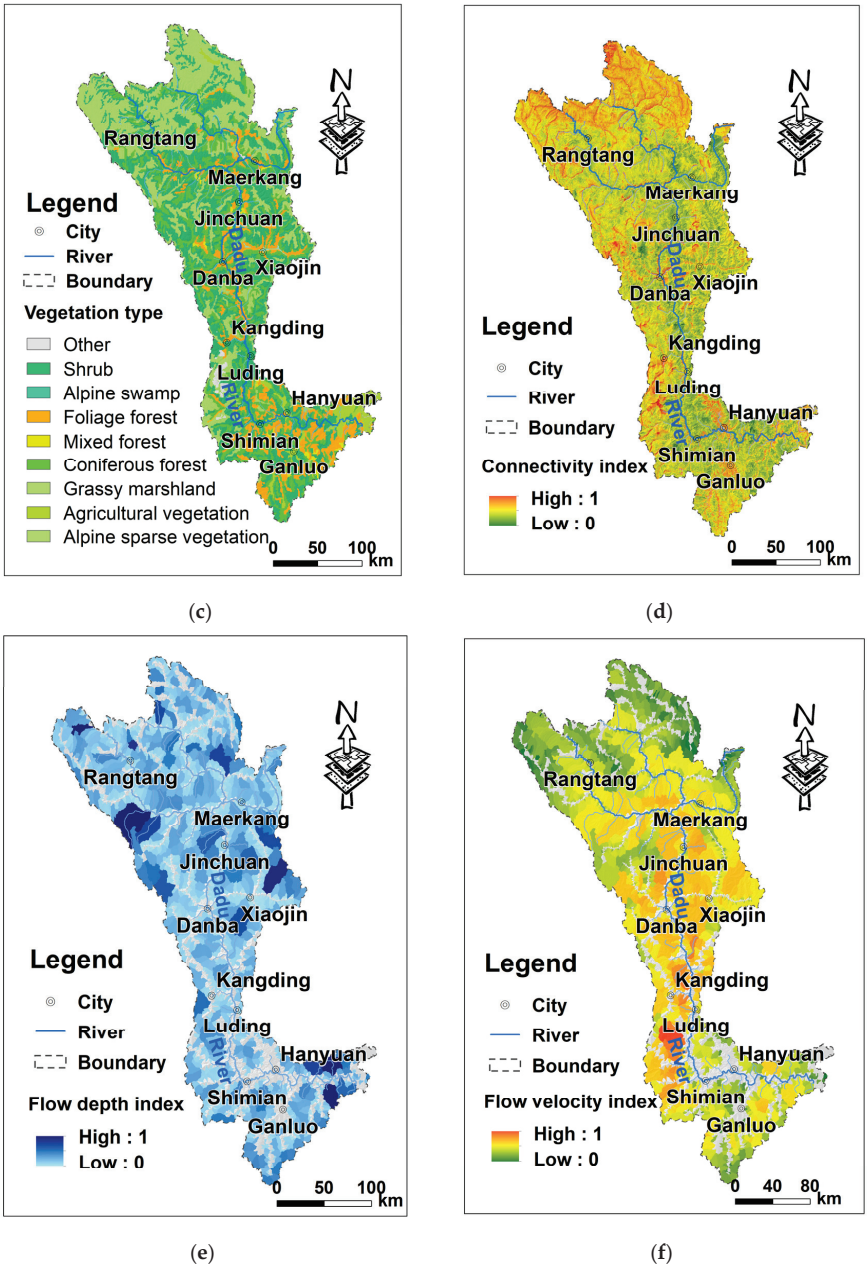

Figure 6. The data used for the susceptibility prediction: (**a**) the soil mass strength, (**b**) soil mass thickness, (**c**) vegetation types, (**d**) channel connectivity, (**e**) flow depth, and (**f**) runoff velocity.

3.4.3. Generating the Cross-Validation Dataset

There is still a chance of overfitting on the test set because the parameters may be changed until the estimator performs optimally when testing multiple settings ("hyper-parameters") for estimators, and the cross-validation algorithm in Scikit-learn was thus used to build the cross-validation dataset. As a consequence, the model may be trained with different subsets of training data before being tested with the test dataset, avoiding overfitting. In this work, 70% of the sample set was used to construct the cross-validation dataset (Figure 7), with the remaining 30% used for final model validation.

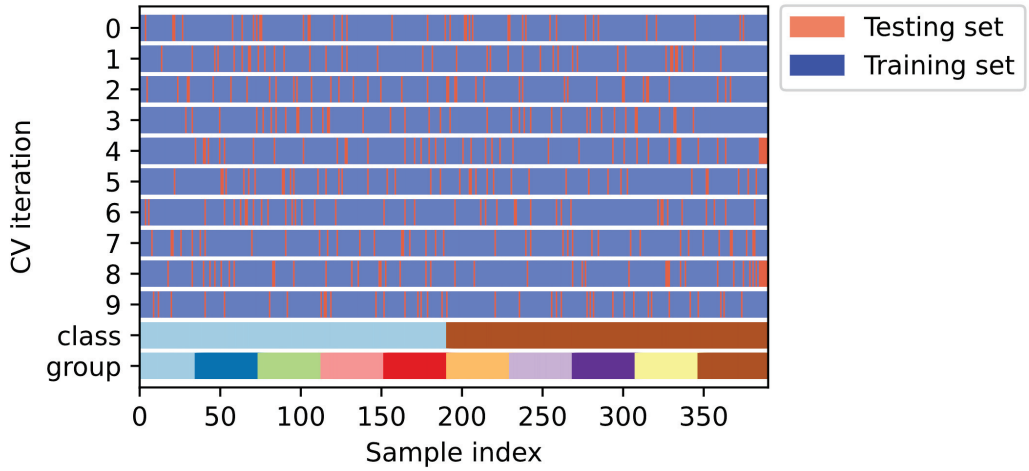

Figure 7. The composition structure of the cross-validation dataset.

3.4.4. Removing Outliers (RO)

Outliers are abnormal values in a dataset, and the goal of integrating the RO algorithm with the machine learning model in this study was to eliminate outliers from the input dataset since their existence is often caused by human errors caused by the data collection, recording, or input procedure, or to natural error. The removing outliers procedure improves the capacity to fit and mine the main relationships between debris flow occurrence and disaster-causing factors by reducing noisy data learning in the machine learning model [71,72]. As a consequence, the operation of removing outliers from the original data was performed in this study before training the hybrid machine learning models. According to the Pauta criteria [73], the process of removing outliers is separated into two steps:

Step 1: When the data obey a normal distribution, values outside 3δ from the mean are discarded since this is a small probability event.

Step 2: For the remaining data that do not obey a normal distribution, data outside x δ from the mean are determined to be outliers. The δ is the standard deviation, and the value of x needs to be decided depending on expert experience and the actual situation.

3.5. Machine Learning Algorithms

Due to the abundance of datasets available from remote sensing interpretations, the use of machine learning methods to interpret patterns or extract information from data [74] is increasing for mountain disaster prediction. These machine learning algorithms, such as support vector machines (SVMs), eXtreme Gradient Boosting (XGB), and random forest (RF) [33,35,36], were selected as the basis of hybrid machine learning methods and then combined in a hybrid with the RO algorithm and hyperparameter optimization algorithm.

3.5.1. Support Vector Machines (SVMs)

SVM is a general term for some classifiers that are used to solve the separation hyperplane with the maximum interval on the feature space, with interval maximization as the learning strategy [20,34]. The hyperplane is a linear subspace with the residual dimension equal to 1 in the n-dimensional Euclidean space and is used to split the feature space into two half-spaces [75]. In this study, support vector classification (SVC) was selected.

3.5.2. Random Forests (RF)

Random forest (RF) is one of the ensemble-learning approaches commonly used for assessing debris flow susceptibility [36]. This technique improves the decision tree algorithm by integrating numerous decision trees, the formation of which is based on samples chosen independently [33]. To be more specific, some samples are drawn at random from the original training sample set, and then a series of decision trees are created

to build the random forest based on the decision rules. Finally, the classification results of the new data are computed based on the number of votes cast by the decision trees. As a result of the random selection of features and samples during each decision tree training, random forest (RF) is distinguished by strong noise resistance and steady performance.

3.5.3. eXtreme Gradient Boosting (XGB)

XGB is a cutting-edge machine learning approach for debris flow susceptibility that quickly implements the Gradient Boosting Decision Tree (GBDT) algorithm and adds many refinements to it, integrating several tree models to construct a strong classifier [20]. The technique is several times quicker than conventional algorithms due to the massively parallel boosting tree, and it has superior computational accuracy since XGB conducts a second-order Taylor expansion on the loss function, whereas common algorithms only use a first-order Taylor expansion. XGB was thus chosen for this investigation.

3.6. Particle Swarm Optimization (PSO)

The particle swarm optimization (PSO) algorithm is a biological heuristic method in the realm of computer intelligence that is often used for intelligence optimization [38]. The PSO algorithm is inspired by the study of bird feeding behavior, and reflects an effective and easy method used by birds to hunt for food by looking in the area nearest the food. The particle is likened to a bird in that it decides its next move based on its own experience and the best experience of its companions. The progression of its movement is summarized in Equations (16) and (17).

$$V_{i\text{th}}^{m+1} = \omega V_{i\text{th}}^{m} + l_1 r_1 (Pbest_{i\text{th}}^{m} - X_{i\text{th}}^{m}) + l_2 r_2 (Gbest^{m} - X_{i\text{th}}^{m}), \quad (15)$$

$$X_{i\text{th}}^{m+1} = X_{i\text{th}}^{m} + V_{i\text{th}}^{m+1}, \quad (16)$$

where m is the number of current iterations, $V_{i\text{th}}^{m}$ and $X_{i\text{th}}^{m}$ are the position and velocity of ith particle in the mth iteration in the feature space, r_1 and r_2 are random number of values between 0 and 1, l_1 and l_2 are learning factors, ω is the inertial weight coefficient, $Pbest_{i\text{th}}^{m}$ is the personal best position of particle i in the mth iteration, and $Gbest^{m}$ is the best position of all particles.

3.7. Generating the Hybrid Machine Learning Models

In this study, the procedure of integrating each machine learning model with RO and PSO consists of two steps:

Step 1: The RO algorithm removes outliers from the input dataset because their presence is often attributable to human mistakes or to natural error. The goal of this step is to improve the capacity to fit and mine the main relationships between debris flow occurrence and disaster-causing factors by reducing noisy data learning in the machine learning model. As a result, the operation of removing outliers is important.

Step 2: The dataset that has been processed by the RO algorithm is then utilized to train the machine learning model. Some parameters, known as hyperparameters, must be artificially set in the traditional training process of machine learning models. The traditional hyperparameter debugging procedure cannot easily locate the optimal hyperparameters from all parameter groups due to time and labor costs, particularly when the hyperparameters can be parameters of the floating-point type. To address this shortcoming, the PSO algorithm is used to optimize the selection of hyperparameters. By integrating with the PSO algorithm, the computer can automatically calculate the optimal hyperparameters of machine learning algorithms, avoiding the intervention of human subjective factors.

Finally, hybrid machine learning models, including RO-PSO-SVC, RO-PSO-RF, and RO-PSO-XGB, were established by integrating the aforementioned machine learning algorithms with the remove outliers (RO) operation and the PSO algorithm, which boosts the model's fitting accuracy and stability. The efficacy of the RO operation in hybrid model

construction was evaluated further by comparing it to several hybrid models that just use PSO, such as PSO-SVC, PSO-RF, and PSO-XGB.

3.8. Model Training and Evaluation

The relationship between disaster-causing factors and debris flow occurrence can be quantified by model training with a set of weights and bias parameters of machine learning models. However, the hyperparameters of conventional machine learning models have to be artificially tuned, and the debugging process is subjective and highly dependent on the experience of experts. In this article, the particle swarm algorithm (PSO) is used to look objectively for the optimal super parameters for PSO-RF, PSO-SVC, PSO-XGB, RO-PSO-RF, RO-PSO-SVC, and RO-PSO-XGB, with mean squared error (*MSE*) and root mean squared error (*RMSE*) closest to 0 and prediction accuracy (*ACC*) (Formula (18)) scores closest to 1. Additionally, the spatial consistency of these debris flow susceptibility results produced by different models needs to be evaluated using Spearman's rank correlation coefficients, since a similar susceptibility result obtained by different approaches indicates that these results are reliable [36,76]. To assess the effectiveness of these six hybrid models, the *ACC*, *MSE*, *RMSE*, and the time consumed for hyperparameters optimization were recorded (Table 3). According to Table 3, RO-PSO-SVC has the greatest performance with a test data ACC of 0.946. The area under the curve (AUC) was also calculated to estimate the performance of the models using the receiver operating characteristic (ROC) curve [77,78], as shown in Figure 8. The higher the AUC value, the better the prediction performance of the model. The prediction accuracy (*ACC*) (Formula (3)) is a rate of correct assignment for test samples.

$$ACC = (TP + TN)/(TP + FN + FP + TN), \quad (17)$$

where *TP* and *TN* show the number of properly identified catchments, whereas *FP* and *FN* show the number of wrongly categorized catchments (Table 4).

Table 3. Final optimal super parameters of the models and consumed time (Note: for an explanation of each parameter and its role in the model adjustment, refer to the Scikit-learn website: https://scikit-learn.org, accessed on 20 February 2022).

No	Classifier Algorithm	Optimal Parameters	*ACC*	*AUC*	*MSE*	*RMSE*	Runtimes
1	SVC	Default	0.911	0.968	0.068	0.261	/
2	RF	Default	0.888	0.964	0.094	0.307	/
3	XGB	Default	0.893	0.952	0.158	0.397	/
4	PSO-SVC	'kernel' = 'rbf' 'C' = 7.5675 'gamma' = 0.0647 'probability' = True 'decision_fuction_shape' = 'ovo' 'criterion' = 'gini'	0.935	0.973	0.063	0.251	649 s
5	PSO-RF	' max_depth ' = 5 ' n_estimators ' = 159	0.893	0.967	0.077	0.278	3674 s
6	PSO-XGB	'learning_rate' = 0.0595 'max_depth' = 2 'n_estimators' = 35	0.905	0.955	0.084	0.291	1563 s
7	RO-PSO-SVC	'kernel' = 'rbf' 'C' = 64.6924 'gamma' = 0.0225 'probability' = True 'decision_fuction_shape' = 'ovo' 'criterion' = 'gini'	0.946	0.981	0.050	0.224	1103 s
8	RO-PSO-RF	' max_depth ' = 23 ' n_estimators ' = 665	0.911	0.972	0.073	0.270	8721 s
9	RO-PSO-XGB	'learning_rate' = 0.0604 'max_depth' = 30 'n_estimators' = 337	0.946	0.977	0.055	0.234	4352 s

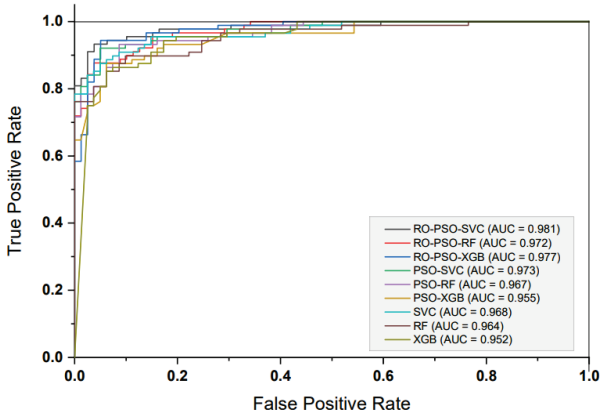

Figure 8. Receiver operating characteristic (ROC) curve and the AUC of different machine learning models.

Table 4. Confusion matrix.

		Predicted	
		Positive	**Negative**
Observed	Positive	True Positive (*TP*)	False Negative (*FN*)
	Negative	False Positive (*FP*)	True Negative (*TN*)

The *MSE* and *RMSE* are used for estimating the generalization error of the model, and can be expressed as follows:

$$MSE = \sum_{i=1}^{n} \left(x_{i,tru} - x_{i,pre}\right)^2 / n, \tag{18}$$

$$RMSE = \sqrt{\sum_{i=1}^{n} \left(x_{i,tru} - x_{i,pre}\right)^2 / n}, \tag{19}$$

where $x_{i,tru}$ represents the observed values in the training dataset or validation dataset, $x_{i,pre}$ represents the predicted values from the debris flow susceptibility models, and n is the total number of the samples in the training or validation datasets.

4. Results

Using the techniques described above for parameter optimization, optimal models with matching hyperparameters (Table 3) were identified and used to predict the susceptibility of debris flows. The spatial consistency of the debris flow susceptibility maps for the different optimal models noted above was thus analyzed using Spearman's rank correlation coefficients. The Pearson correlation coefficients range from 0.86 to 0.98 (Figure 9), indicating that the index system presented in this article can predict the occurrence of debris flows in the topographically extreme belt, and the results are reliable and effective. The outputs of the aforementioned hybrid or non-hybrid models were used to reclassify susceptibility levels into five groups (very low, low, medium, high, and very high) using the natural break classification technique [36]. Susceptibility maps were then generated on the GIS platform for visualization (Figure 10). The findings reveal that those catchments with high and very high debris flow susceptibility are most prevalent in the study area's central mountainous region, whereas the northern plateau areas with gentle topographical change have lower susceptibility. Compared with the distribution of the susceptibility maps (Figure 10) obtained by different models, the findings show that the catchments with different susceptibility levels tend to be clustered together with greater spatial continuity after integrating the machine learning models used in this article with the RO and PSO algorithms. This may be because the RO and PSO algorithms enhance the machine learning model's ability to fit and mine the major relationships between debris flow occurrence and disaster-causing factors by reducing noisy data learning and hyperparameter optimization.

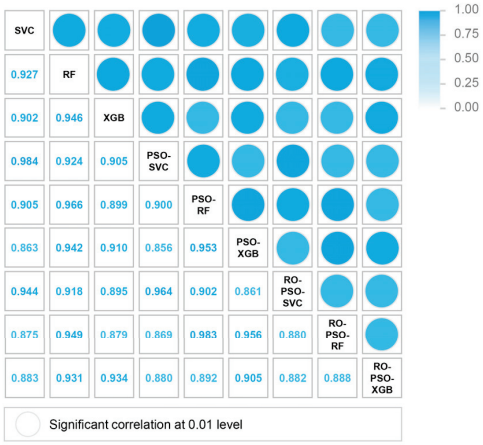

Figure 9. Spatial consistency matrix among the debris flow susceptibility maps.

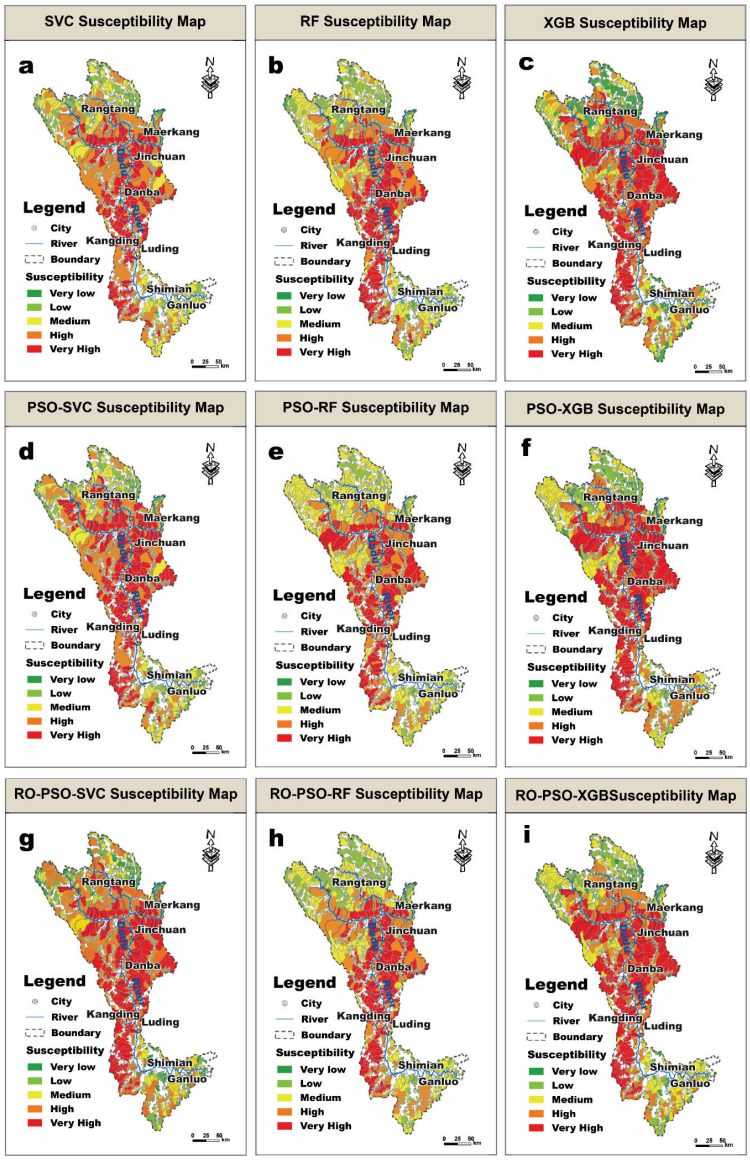

Figure 10. The debris flow susceptibility maps of the Dadu River based on the (**a**) SVC, (**b**) RF, (**c**) XGB, (**d**) PSO-SVC, (**e**) PSO-RF, (**f**) PSO-XGB, (**g**) RO-PSO-SVC, (**h**) RO-PSO-RF, and (**i**) RO-PSO-XGB models.

Figure 11 depicts the relative distribution of each model's different susceptibility levels. The high level has the highest percentage (28.99%) in the RO-PSO-SVC model, with the remaining 24.33%, 13.82%, 21.35%, and 11.51% of watersheds falling into the very low, low, medium, and very high susceptibility levels, respectively. The percentages of the total of low and very low for all of the above-mentioned models' debris flow susceptibility maps are quite close to 38.85%. Furthermore, the main classes in the research region include medium, high, and extremely high debris flow susceptibilities.

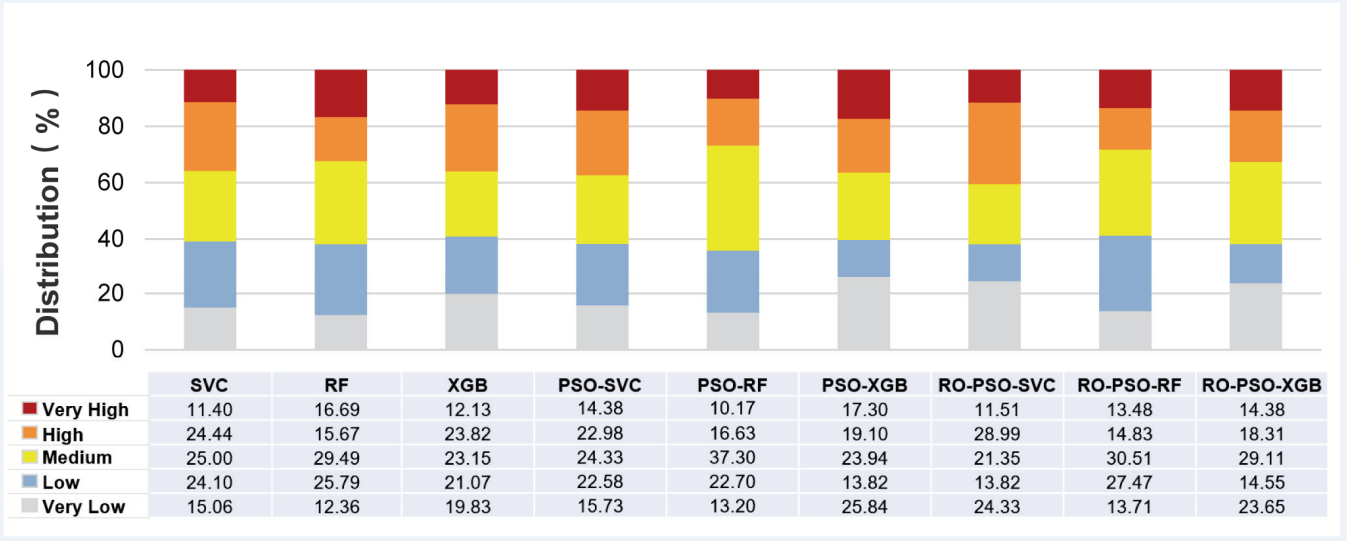

	SVC	RF	XGB	PSO-SVC	PSO-RF	PSO-XGB	RO-PSO-SVC	RO-PSO-RF	RO-PSO-XGB
Very High	11.40	16.69	12.13	14.38	10.17	17.30	11.51	13.48	14.38
High	24.44	15.67	23.82	22.98	16.63	19.10	28.99	14.83	18.31
Medium	25.00	29.49	23.15	24.33	37.30	23.94	21.35	30.51	29.11
Low	24.10	25.79	21.07	22.58	22.70	13.82	13.82	27.47	14.55
Very Low	15.06	12.36	19.83	15.73	13.20	25.84	24.33	13.71	23.65

Figure 11. Proportions of the different debris susceptibility levels among the hybrid or non-hybrid models.

5. Discussion

This study proposes new hybrid machine-learning approaches combined with the removing outliers (RO)algorithm and the particle swarm optimization (PSO) algorithm to predict the susceptibility of debris flows in the Dadu River basin, a typical extreme topography transition belt on the eastern margin of the Qinghai-Tibet Plateau. The PSO and RO algorithms were implemented in these hybrid models to identify the perfect hyperparameters for the machine learning model and to lessen the impact of noise on the model's convergence speed and prediction accuracy. The model performance evaluation analysis (ACC) revealed that machine learning models enhanced by the PSO and RO algorithms outperformed solo machine learning models. According to the ACC analysis, the RO-PSO optimization algorithms improved the performance of SVC, RF, and XGB by 3.84%, 2.59%, and 5.94%, respectively. The ACC value of SVC, RF, and XGB rose by 2.63%, 0.56%, and 1.34%, respectively, when only the PSO algorithm was used. Furthermore, the RO algorithm improved the performance of PSO-SVC, PSO-RF, and PSO-XGB by 1.21%, 2.03%, and 4.60%, respectively. The improvement in the performance of these machine learning models shows that the indicators can shed light on the physical mechanisms behind the debris flow formation, such as the physical failure mechanism on vegetation-covered slopes revealed by the index PPI. Another point worth noting is that the degree of RF improvement is not obvious after integrating only with the PSO algorithm. Results analysis showed that the PSO algorithm can significantly improve the performance of machine learning models with floating-point-type super parameters, such as SVC and XGB, since the PSO algorithm has a stronger parameter search capability for floating-point-type super parameters than for integer super parameters. The greater the number of floating-point-type super parameters in the model, the greater the performance benefit. As a result, the fact that the major super parameters for RF debugging in this study were all integer types restricts the PSO algorithm's ability to improve.

RO-PSO-SVC has the strongest spatial recognition capacity to identify debris flow hazards among all of the aforementioned models, as its total percentage of debris flow catchments

(Figure 12) with high and very high susceptibility is the biggest, accounting for 91.04%. Interestingly, we found that RO-PSO-SVC and RO-PSO-XGB result in fewer false alarms than RO-PSO-RF, with a lower total percentage (1.44%) of debris flow catchments with very low and low susceptibility levels. RO-PSO-XGB, by comparison, classifies more debris flow as medium susceptibility than RO-PSO-SVC. In this regard, RO-PSO-SVC is better able to minimize false alarms since the total percentage of debris flow catchments with very low, low, and medium susceptibility is 8.96%, compared to 11.47% for RO-PSO-XGB.

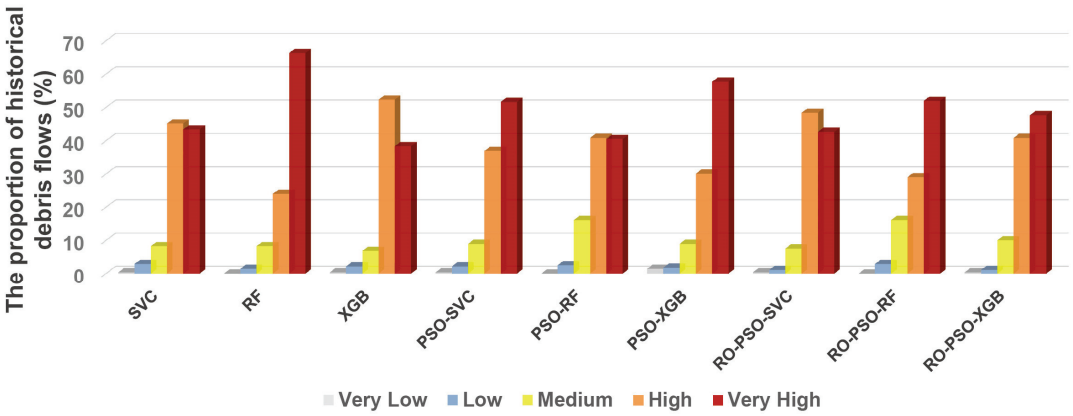

Figure 12. Proportions of the historical debris flow occurring at the catchments with different susceptibility levels among the different models.

RO-PSO-SVC also has the best performance for predicting debris flow susceptibility, according to the model performance evaluation analysis (*ACC*, *MSE*, and *RMSE*), and was thus chosen to interpret and diagnose the contribution of different predictor factors. SHAP (SHapley Additive exPlanations) [79], a game-theoretic technique to explain the output of any machine learning model, can quantify the relative importance of each causal factor. Figure 13 shows that runoff velocity (RV) is the most significant predictor variable in the RO-PSO-SVC model, with a relative importance value of 49.57%, and flow depth (FD), the associated predictor variable representing hydrological conditions, has a relative importance value of 8.45%. Topography-related factors such as AD, CG, IC, and PPI have a relative relevance of 11.08%, 9.05%, 4.26%, and 3.33%, respectively. Such results suggest that topography and hydrology play important roles in debris flow formation as general factors, which is consistent with previous research [34–36] in topographically extreme belts. Furthermore, the factor importance analysis shows that the ecology-related factor, vegetation weight loads (VWL), has a relatively low contribution to the debris flow occurrence, which is similar to the findings of previous studies [35,36] that revealed that ecology-related factors reflecting vegetation cover, such as Normalized Difference Vegetation Index (NDVI), contribute less to debris flow formation than topography- and hydrology-related factors, taking the Sichuan province as the study area.

The top three indicators with the greatest contribution according to Figure 13 were selected for further statistical analysis to investigate the impact of triggering factors on debris flow occurrence. Figure 14 depicts the proportion of catchments with different debris flow susceptibility (as predicted by RO-PSO-SVC) for each level of different triggering factors. This shows that there is an obvious positive correlation between the factors of runoff velocity and altitude difference with debris flow occurrence, because the catchments with high and very high susceptibility levels are concentrated in the catchments with a greater runoff velocity index and a greater altitude difference index. The performance of altitude difference is easy to understand since the enormous relief may provide an abundance of potential energy conditions for the formation of debris flows. After deep analysis, we attribute the strong sensitivity of the runoff velocity factor to the debris flow occurrence to the good ability of this index to represent the process of debris flow formation, which indicates that there is strong link between the physical movement mechanism used

in the derivation process of the runoff velocity index and the dynamic process of debris flow movement. The factor of channel gradient also plays an essential role, as implied in Figure 14. The total proportion of catchments with very high and high susceptibility in 100–200‰ of the channel gradient is 49.60%, the highest of all channel gradient levels. This result is consistent with the findings of Xiong et al. (2020) [36], who conducted debris flow susceptibility research in the Sichuan Province.

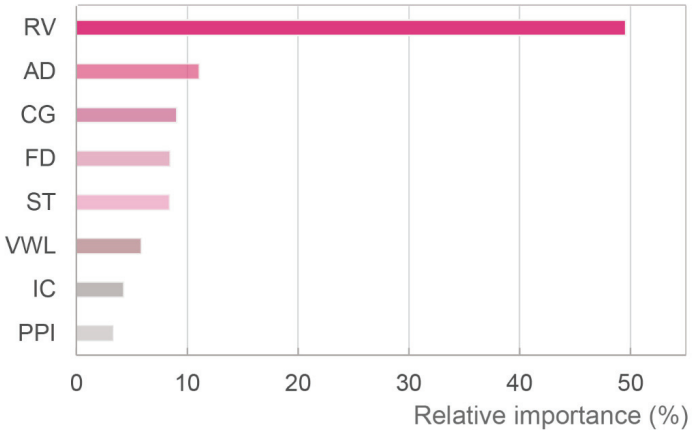

Figure 13. The relative importance of disaster-causing factors in the RO-PSO-SVC model. The relative importance is normalized so that they sum to 1.

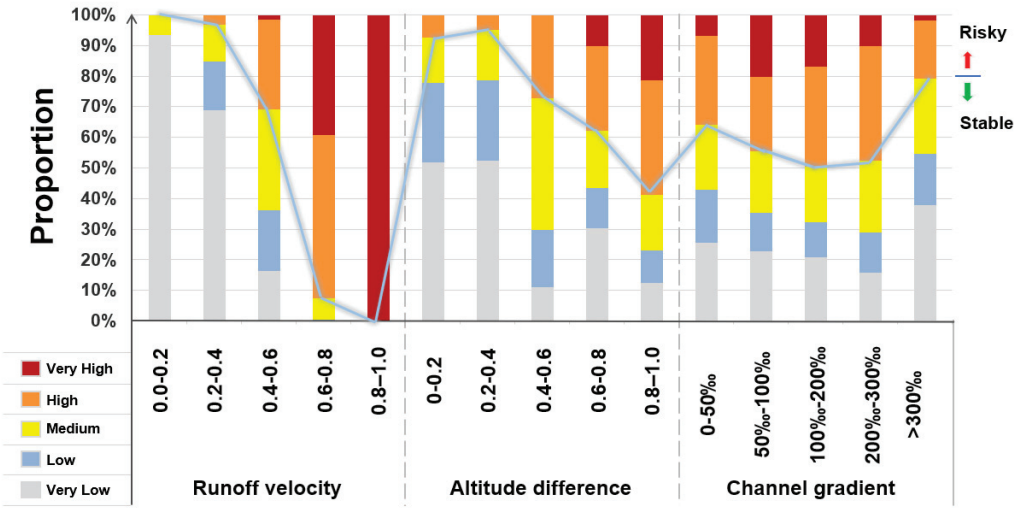

Figure 14. Proportions of the catchments with different debris flow susceptibility obtained by RO-PSO-SVC for each level of different triggering factors.

It is worth noting that the susceptibility classification results show that there is a high proportion of catchments with high and very high susceptibility in the study area, which is consistent with the study results of Xiong et al. (2020), who explain that this is because this region belongs to the transition belt, where the topography varies enormously, from the Qinghai–Tibet Plateau to the Sichuan Basin, and is coupled with dry valleys and fault zones. Another point of concern is that, although the study improved the performance of the debris flow susceptibility assessment by introducing some factors related to physical–mechanical mechanisms, the computation of these factors was time consuming, particularly for the PPI reflecting the physical failure mechanism on vegetation-covered slopes, which took nearly a month to compute with 26 computers. As a result, the next stage of the research will look for methods to lower the computing costs associated with introducing parameters related to physical–mechanical mechanisms at the regional scale.

It is well known that the physics behind the debris flow formation are closely related to the accumulation of loose materials, initiation driven by rainfall, the potential of dynamic movement controlled by terrain and channel conditions, and accumulation at the outlet. From the viewpoint of indicator selection, all indicators used in this research are focused on the physical mechanisms behind debris flow formation, such as the failure mechanisms of the vegetated slope and the dynamic processes of debris flows. As a result, the main contribution of this paper is to propose a regional-scale susceptibility index system for predicting the probability of debris flow occurrence in the Dadu River basin, a typical extreme topography transition belt on the eastern margin of the Qinghai-Tibet Plateau, from the perspective of the debris flow formation mechanism. This system takes into account not only the common geographic features (such as enormous topographic relief and active tectonics) that control the occurrence of debris flows, but also the comprehensive impacts of vegetation on the occurrence of debris flows, such as the positive effect of root anchoring and the negative effect of vegetation weight loads. In this respect, this study is innovative and essential for the development of regional-scale debris flow susceptibility evaluation. To ensure that the causal factors selected in this study stand up to scrutiny, these indicators were classified into different categories, as is commonly done in the traditional methodology. This was undertaken to ensure that the primary concept of constructing the indicator system in this article was based on three fundamental disaster-causing factors that control debris flow formation, namely, topographic condition, hydrological condition, and material condition. Furthermore, the novel hybrid models formed by integrating the machine learning model with RO and PSO algorithms were, for the first time, also used in the catchment-based assessment of regional-scale debris flow susceptibility. These hybrid models with good performance also provide a scientific reference for future regional-scale debris flow susceptibility assessments.

6. Conclusions

A novel hybrid machine learning approach combined with the RO and PSO algorithms is presented to assess the debris flow susceptibility in the Dadu River basin, a typical extreme topography transition zone on the eastern margin of the Qinghai-Tibet Plateau, taking into account the effects of vegetation on debris flow formation from the perspective of physical mechanisms. Some of the significant findings are as follows. Based on the index system coupled with ecohydrological activation, the hybrid machine learning technique RO-PSO-SVC can effectively predict the occurrence of debris flows in an extreme topography transition zone. The factor important analysis (for the RO-PSO-SVC method) reveals that the ecology-related factor, vegetation weight load (VWL), contributes to the occurrence of debris flows at a lower rate than topography- and hydrology-related factors, and the contribution rate of the ecology-related factor is one-tenth that of topography- and hydrology-related factors. Furthermore, according to the ACC value, the RO-PSO algorithm enhanced SVC, RF, and XGB performance by 3.84%, 2.59%, and 5.94%, respectively. The RO-PSO algorithm was included in the machine learning model, which provided the capacity to remove anomalous data and automatically optimize hyperparameters. Nonetheless, caution should be used when applying this model to determine debris flow susceptibility since performance varies among research locations. The given susceptibility results can offer scientific assistance to local governments for debris flow prevention and mitigation.

Author Contributions: Conceptualization, Q.Z. and H.J.; methodology, Q.Z. and H.J.; software, H.J.; validation, B.Z. and S.Y.; formal analysis, Z.H. and C.L.; investigation, C.L., B.Z., S.Y. and H.Y.; resources, B.Z.; writing—original draft preparation, H.J.; writing—review and editing, Q.Z.; visualization, H.J.; supervision, Q.Z.; project administration, Q.Z.; funding acquisition, Q.Z. All authors have read and agreed to the published version of the manuscript.

Funding: This research was supported by the National Nature Science Foundation of China (Grant No. 41790432), the Strategic Priority Research Program of the Chinese Academy of Sciences (Grant No. XDA23090303), the Second Tibetan Plateau Scientific Expedition and Research Program (STEP)

(Grant No. 2019QZKK0902), and the Sichuan Science and Technology Planning Program (Grant No. 2019YJ0006).

Institutional Review Board Statement: Not applicable.

Informed Consent Statement: Not applicable.

Data Availability Statement: Raw data were generated at the Institute of Mountain Hazards and Environment (IMHE), China. Derived data supporting the findings of this study are available from the corresponding author [Q.Z.] on request. The link below includes the code of this research and its related document of license. https://github.com/CodefromJiangHu/DebrisFlowSusceptibilityEvaluation, accessed on 20 February 2022.

Conflicts of Interest: The authors declare that there is no conflict of interest.

References

1. Zhong, X. *The Environment and Ecosystem in the Eastern Edge of Qinhai-Xizang Plateau*; Sichuan University Press: Chengdu, China, 2002.
2. Cao, J.; Zhang, Z.; Wang, C.; Liu, J.; Zhang, L. Susceptibility Assessment of Landslides Triggered by Earthquakes in the Western Sichuan Plateau. *Catena* **2019**, *175*, 63–76. [CrossRef]
3. Zhang, P.-Z. A review on active tectonics and deep crustal processes of the Western Sichuan region, eastern margin of the Tibetan Plateau. *Tectonophysics* **2013**, *584*, 7–22. [CrossRef]
4. Hungr, O.; Leroueil, S.; Picarelli, L. The Varnes classification of landslide types, an update. *Landslides* **2014**, *11*, 167–194. [CrossRef]
5. Jomelli, V.; Pavlova, I.; Eckert, N.; Grancher, D.; Brunstein, D. A New Hierarchical Bayesian Approach to Analyse Environmental and Climatic Influences on Debris Flow Occurrence. *Geomorphology* **2015**, *250*, 407–421. [CrossRef]
6. Zou, Q.; Cui, P.; Jiang, H.; Liu, Y.; Li, C.; Hu, S.; Zhou, B. Characteristics and Causes of the Debris Flow in Shelong Gully, China. In *Understanding and Reducing Landslide Disaster Risk. WLF 2020. ICL Contribution to Landslide Disaster Risk Reduction*; Springer: Cham, Germany, 2020; pp. 237–243.
7. Bertrand, M.; Liebault, F.; Piegay, H. Debris-flow Susceptibility of Upland Catchments. *Nat. Hazards* **2013**, *67*, 497–511. [CrossRef]
8. Zou, Q.; Jiang, H.; Cui, P.; Zhou, B.; Jiang, Y.; Qin, M.; Liu, Y.; Li, C. A New Approach to Assess Landslide Susceptibility Based on Slope Failure Mechanisms. *Catena* **2021**, *204*, 105388. [CrossRef]
9. Xia, L.; Wanze, Z.; Shouqin, S.; Shumiao, S.; Zheliang, S.; Jun, Z.; Ting, L.; Zhicai, Z. Influence of habitat on the distribution pattern and diversity of plant community in dry and warm valleys of the middle reaches of the Dadu River, China. *Biodivers. Sci.* **2020**, *28*, 117–127. [CrossRef]
10. Gonzalez-ollauri, A.; Mickovski, S.B. Hydrological Effect of Vegetation against Rainfall-induced Landslides. *J. Hydrol.* **2017**, *549*, 374–387. [CrossRef]
11. Gonzalez-ollauri, A.; Mickovski, S. Plant-soil Reinforcement Response under Different Soil Hydrological Regimes. *Geoderma* **2017**, *285*, 141–150. [CrossRef]
12. Bordoni, M.; Meisina, C.; Vercesi, A.; Bischetti, G.B.; Chiaradia, E.A.; Vergani, C.; Chersich, S.; Valentino, R.; Bittelli, M.; Comolli, R.; et al. Quantifying the Contribution of Grapevine Roots to Soil Mechanical Reinforcement in an Area Susceptible to Shallow Landslides. *Soil Tillage Res.* **2016**, *163*, 195–206. [CrossRef]
13. Zhang, B.; Zhang, S.; Zhou, W. Investigation and Assessment of Landslides and Debris Flows in Sichuan Province of China by Remote Sensing Technique. *Chin. Geogr. Sci.* **2006**, *16*, 223–228. [CrossRef]
14. Michelini, T.; Bettella, F.; D'agostino, V. Field Investigations of the Interaction between Debris Flows and Forest Vegetation in Two Alpine Fans. *Geomorphology* **2017**, *279*, 150–164. [CrossRef]
15. Shi, L.; Chen, N.; Yang, C. Relationships between Vegetation and Debris Flow in Well-vegetated Wawagou Valley. *Res. Soil Water Conserv.* **2008**, *15*, 96–99.
16. Bettella, F.; Michelini, T.; D'agostino, V.; Bischetti, G.B. The Ability of Tree Stems to Intercept Debris Flows in Forested Fan Areas: A Laboratory Modelling Study. *J. Agric. Eng.* **2018**, *49*, 42–51. [CrossRef]
17. Cui, P.; Lin, Y.; Chen, C. Destruction of Vegetation due to Geo-hazards and Its Environmental Impacts in the Wenchuan Earthquake Areas. *Ecol. Eng.* **2012**, *44*, 61–69. [CrossRef]
18. Phillips, C.; Hales, T.; Smith, H.; Basher, L. Shallow Landslides and Vegetation at the Catchment Scale: A Perspective. *Ecol. Eng.* **2021**, *173*, 106436. [CrossRef]
19. Chen, X.; Chen, H.; You, Y.; Chen, X.; Liu, J. Weights-of-evidence method based on GIS for assessing susceptibility to debris flows in Kangding County, Sichuan Province, China. *Environ. Earth Sci* **2016**, *75*, 70. [CrossRef]
20. Qing, F.; Zhao, Y.; Meng, X.; Su, X.; Qi, T.; Yue, D. Application of Machine Learning to Debris Flow Susceptibility Mapping along the China-Pakistan Karakoram Highway. *Remote Sens.* **2020**, *12*, 2933. [CrossRef]
21. Reichenbach, P.; Rossi, M.; Malamud, B.; Mihir, M.; Guzzetti, F. A Review of Statistically-based Landslide Susceptibility Models. *Earth-Sci. Rev.* **2018**, *180*, 69–91. [CrossRef]

22. Dahal, R.; Hasegawa, S.; Nonomura, A.; Yamanaka, M.; Masuda, T.; Nishino, K. GIS-based Weights-of-evidence Modelling of Rainfall-induced Landslides in Small Catchments for Landslide Susceptibility Mapping. *Environ. Geol.* **2008**, *54*, 311–324. [CrossRef]
23. Merghadi, A.; Yunus, A.; Dou, J.; Whiteley, J.; ThaiPham, B.; Bui, D.T.; Avtar, R.; Abderrahmane, B. Machine Learning Methods for Landslide Susceptibility Studies: A Comparative Overview of Algorithm Performance. *Earth-Sci. Rev.* **2020**, *207*, 103225. [CrossRef]
24. Wang, Q.; Kong, Y.; Zhang, W.; Chen, J.; Xu, P.; Li, H.; Xue, Y.; Yuan, X.; Zhan, J.; Zhu, Y. Regional Debris Flow Susceptibility Analysis Based on Principal Component Analysis and Self-organizing Map: A Case Study in Southwest China. *Arab. J. Geosci.* **2016**, *9*, 718. [CrossRef]
25. Bregoli, F.; Medina, V.; Chevalier, G.; Hürlimann, M.; Bateman, A. Debris-flow Susceptibility Assessment at Regional Scale: Validation on an Alpine Environment. *Landslides* **2015**, *12*, 437–454. [CrossRef]
26. Barella, C.F.; Sobreira, F.G.; Zêzere, J. A comparative analysis of statistical landslide susceptibility mapping in the southeast region of Minas Gerais state, Brazil. *Bull. Eng. Geol. Environ.* **2018**, *78*, 3205–3221. [CrossRef]
27. Wang, W.; He, Z.; Han, Z.; Li, Y.; Dou, J.; Huang, J. Mapping the susceptibility to landslides based on the deep belief network: A case study in Sichuan Province, China. *Nat. Hazards* **2020**, *103*, 3239–3261. [CrossRef]
28. Hutter, K.; Svendsen, B.; Rickenmann, D. Debris Flow Modeling: A Review. *Contin. Mech. Thermodyn.* **1994**, *8*, 1–35. [CrossRef]
29. Park, D.W.; Lee, S.R.; Vasu, N.N.; Kang, S.H.; Park, J.Y. Coupled Model for Simulation of Landslides and Debris Flows at Local Scale. *Nat. Hazards* **2016**, *81*, 1653–1682. [CrossRef]
30. Carrara, A.; Crosta, G.; Frattini, P. Comparing Models of debris-flow Susceptibility in the Alpine Environment. *Geomorphology* **2008**, *94*, 353–378. [CrossRef]
31. Stancanelli, L.M.; Peres, D.J.; Cancelliere, A.; Foti, E. A Combined Triggering-propagation Modeling Approach for the Assessment of Rainfall Induced Debris Flow Susceptibility. *J. Hydrol.* **2017**, *550*, 130–143. [CrossRef]
32. Dikshit, A.; Pradhan, B.; Alamri, A.M. Pathways and Challenges of the Application of Artificial Intelligence to Geohazards Modelling. *Gondwana Res.* **2021**, *100*, 290–301. [CrossRef]
33. Zhang, Y.; Ge, T.; Tian, W.; Liou, Y.-A. Debris Flow Susceptibility Mapping Using Machine-Learning Techniques in Shigatse Area, China. *Remote Sens.* **2019**, *11*, 2801. [CrossRef]
34. Zhao, Y.; Meng, X.; Qi, T.; Qing, F.; Xiong, M.; Li, Y.; Guo, P.; Chen, G. AI-based identification of low-frequency debris flow catchments in the Bailong River basin, China. *Geomorphology* **2020**, *359*, 107125. [CrossRef]
35. Di, B.; Zhang, H.; Liu, Y.; Li, J.; Chen, N.; Stamatopoulos, C.A.; Luo, Y.; Zhan, Y. Assessing Susceptibility of Debris Flow in Southwest China Using Gradient Boosting Machine. *Sci. Rep.* **2019**, *9*, 12532. [CrossRef]
36. Xiong, K.; Adhikari, B.R.; Stamatopoulos, C.A.; Zhan, Y.; Wu, S.; Dong, Z.; Di, B. Comparison of Different Machine Learning Methods for Debris Flow Susceptibility Mapping: A Case Study in the Sichuan Province, China. *Remote Sens.* **2020**, *12*, 295. [CrossRef]
37. Nguyen, V.; Pham, B.; Vu, T.; Prakash, I.; Jha, S.; Shahabi, H.; Shirzadi, A.; Ba, D.N.; Kumar, R.; Chatterjee, J.M.; et al. Hybrid Machine Learning Approaches for Landslide Susceptibility Modeling. *Forests* **2019**, *10*, 157. [CrossRef]
38. Qian, X.; Chen, J.; Xiang, L.; Zhang, W.; Niu, C.C. A Novel Hybrid KPCA and SVM with PSO Model for Identifying Debris Flow Hazard Degree: A Case Study in Southwest China. *Environ. Earth Sci.* **2016**, *75*, 991. [CrossRef]
39. Vasu, N.N.; Lee, S.-R. A hybrid feature selection algorithm integrating an extreme learning machine for landslide susceptibility modeling of Mt. Woomyeon, South Korea. *Geomorphology* **2016**, *263*, 50–70. [CrossRef]
40. Compilation of Sichuan Local History Compilation Committee. *Geography of Sichuan Province*; Chengdu Map Publishing House: Chengdu, China, 1996.
41. Sichuan Bureau of Geological Survey. *The Geological Map of Sichuan Province (Yanyuan Sheet)*; Geological Publishing House: Beijing, China, 1971.
42. Wang, P.F. *Encyclopedia of China: Hydrological Science*; Encyclopaedia of China Publishing Press: Beijing, China, 1998.
43. Guzzetti, F.; Carrara, A.; Cardinali, M.; Reichenbach, P. Landslide hazard evaluation: A review of current techniques and their application in a multi-scale study, Central Italy. *Geomorphology* **1999**, *31*, 181–216. [CrossRef]
44. Zhang, H.; Chi, T.; Fan, J.; Liu, T.; Wang, W.; Yang, L.; Zhao, Y.; Shao, J.; Yao, X. Debris-flows Scale Predictions Based on Basin Spatial Parameters Calculated from Remote Sensing Images in Wenchuan Earthquake Area. In *Iop Conference Series: Earth and Environmental Science Bristol*; IOP Publishing: Bristol, UK, 2014; Volume 17, pp. 22–26.
45. Chevalier, G.; Medina, V.; Hürlimann, M.; Bateman, A. Debris-flow Susceptibility Analysis Using Fluvio-morphological Parameters and Data Mining: Application to the Central-eastern Pyrenees. *Nat. Hazards* **2013**, *67*, 213–238. [CrossRef]
46. Dias, H.; Gramani, M.; Grohmann, C.; Bateira, C.; Vieira, B.C. Statistical-based Shallow Landslide Susceptibility Assessment for a Tropical Environment: A Case Study in the Southeastern Brazilian Coast. *Nat. Hazards* **2021**, *108*, 205–223. [CrossRef]
47. Cui, P.; Peng, J.; Shi, P.; Tang, H.; Ouyang, C.; Zou, Q.; Liu, L.; Li, C.; Lei, Y. Scientific Challenges of Research on Natural Hazard and Disaster Risk. *Geogr. Sustain.* **2021**, *2*, 216–223. [CrossRef]
48. Liu, M.; Zhang, Y.; Tian, S.-F.; Chen, N.-S.; Mahfuzr, R.; Javed, I. Effects of loose deposits on debris flow processes in the Aizi Valley, southwest China. *J. Mt. Sci* **2020**, *17*, 156–172. [CrossRef]
49. Zhang, Y.; Chen, N.; Liu, M.; Wang, T.; Deng, M.; Wu, K.; Khanal, B.R. Debris flows originating from colluvium deposits in hollow regions during a heavy storm process in Taining, southeastern China. *Landslides* **2019**, *17*, 335–347. [CrossRef]

50. Chang, K.; Merghadi, A.; Yunus, A.; Pham, B.T.; Dou, J. Evaluating Scale Effects of Topographic Variables in Landslide Susceptibility Models Using GIS-based Machine Learning Techniques. *Sci. Rep.* **2019**, *9*, 12296. [CrossRef] [PubMed]
51. Yan, F.; Shangguan, W.; Zhang, J.; Hu, B. Depth-to-bedrock Map of China at a Spatial Resolution of 100 meters. *Sci. Data* **2020**, *7*, 2. [CrossRef] [PubMed]
52. Hou, X. 1:1 Million Vegetation Map of China [DS]: National Tibetan Plateau Data Center 2019. Available online: https://data.tpdc.ac.cn/en/data/eac4f2cf-d527-4140-a35d-79992957f043/ (accessed on 20 February 2022).
53. Ling, H.; Yan, J.; Xu, H.; Guo, B.; Zhang, Q. Estimates of shifts in ecosystem service values due to changes in key factors in the Manas River basin, northwest China. *Sci. Total Environ.* **2018**, *659*, 177–187. [CrossRef] [PubMed]
54. Arnone, E.; Caracciolo, D.; Noto, L.; Preti, F.; Bras, R.L. Modeling the Hydrological and Mechanical Effect of Roots on Shallow Landslides. *Water Resour. Res.* **2016**, *52*, 8590–8612.
55. Ma, S.; Qiao, Y.; Wang, L.; Zhang, J.C. Terrain Gradient Variations in Ecosystem Services of Different Vegetation Types in Mountainous Regions: Vegetation Resource Conservation and Sustainable Development. *For. Ecol. Manag.* **2021**, *482*, 118856. [CrossRef]
56. Osinski, P.; Rickson, R.; Hann, M.; Koda, E. Assessment of Slope Stability Influenced by Vegetation Cover and Additional Loads Applied. *Ann. Wars. Univ. LifeSci. Land Reclam.* **2014**, *46*, 81–91. [CrossRef]
57. Wu, G.-H. *Physical Geography*, 4th ed.; Higher Education Press: Beijing, China, 2008.
58. Stancanelli, L.M.; Musumeci, R.E. Geometrical Characterization of Sediment Deposits at the Confluence of Mountain Streams. *Water* **2018**, *10*, 401. [CrossRef]
59. Asch, T.; Buma, J.; Beek, L. A View on Some Hydrological Triggering Systems in Landslides. *Geomorphology* **1999**, *30*, 25–32. [CrossRef]
60. Liu, B.; Li, S.; Zhang, L. Experimental and Discrete Element Numerical Analysis of Side Slope Instability Induced by Fissure Water Underlying Impervious Bed. *Sci. China Technol. Sci.* **2005**, *48*, 65–80.
61. Labuz, J.; Zang, A. Mohr-Coulomb Failure Criterion. *Rock Mech. Rock Eng.* **2012**, *45*, 975–979. [CrossRef]
62. Li, L.; Yu, B.; Zhu, Y.; Chu, S.; Wu, Y. Topographical factors in the formation of gully-type debris flows in Longxi River catchment, Sichuan, China. *Environ. Earth Sci* **2014**, *73*, 4385–4398. [CrossRef]
63. Kang, S.; Lee, S.; Vasu, N.N.; Park, J.Y.; Lee, D.H. Development of an Initiation Criterion for Debris Flows Based on Local Topographic Properties and Applicability Assessment at a Regional Scale. *Eng. Geol.* **2017**, *230*, 64–76. [CrossRef]
64. Zhou, W.; Tang, C.; Van Asch, T.W.; Chang, M. A Rapid Method to Identify the Potential of Debris Flow Development Induced by Rainfall in the Catchments of the Wenchuan Earthquake Area. *Landslides* **2016**, *13*, 1243–1259. [CrossRef]
65. Johnson, P.A.; Mccuen, R.H.; Hromadka, T.V. Magnitude and Frequency of Debris Flows. *J. Hydrol.* **1991**, *123*, 69–82. [CrossRef]
66. Wei, F.; Gao, K.; Hu, K.; Li, Y.; Gardner, J.S. Relationships between Debris Flows and Earth Surface Factors in Southwest China. *Environ. Geol.* **2008**, *55*, 619–627. [CrossRef]
67. Horton, P.; Jaboyedoff, M.; Rudaz, B.; Zimmermann, M. Flow-R, a Model for Susceptibility Mapping of Debris Flows and Other Gravitational Hazards at a Regional Scale. *Nat. Hazards Earth Syst. Sci.* **2013**, *13*, 869–885. [CrossRef]
68. Borselli, L.; Cassi, P.; Torri, D. Prolegomena to Sediment and Flow Connectivity in the Landscape: A GIS and Field Numerical Assessment. *Catena* **2008**, *75*, 268–277. [CrossRef]
69. Zou, Q.; Cui, P.; Jiang, H.; Wang, J.; Li, C.; Zhou, B. Analysis of Regional River Blocking by Debris Flows in Response to Climate Change. *Sci. Total Environ.* **2020**, *741*, 140262. [CrossRef]
70. Bisong, E. *Building Machine Learning and Deep Learning Models on Google Cloud Platform: A Comprehensive Guide for Beginners*; Apress: New York, NY, USA, 2019; pp. 215–229.
71. Debruyne, M. An Outlier Map for Support Vector Machine Classification. *Ann. Appl. Stat.* **2009**, *3*, 1566–1580. [CrossRef]
72. Liang, G.; Peng, W.; Ying, Z. Water Quality Forecast through Application of Bp Neural Network at Sifangtai. *J. Harbin Inst. Technol.* **2009**, *41*, 62–66.
73. Liu, J.; Zhu, L.; Ma, Y.; Liu, J.; Zhou, W.; Yu, D. Anomaly Detection of Hot Components in Gas Turbine Based on Frequent Pattern Extraction. *Sci. China Technol. Sci.* **2018**, *61*, 567–586. [CrossRef]
74. Dey, A. Machine Learning Algorithms: A Review. *Int. J. Comput. Sci. Inf. Technol.* **2016**, *7*, 1174–1179.
75. Ding, S.; Hua, X.; Yu, J. An Overview on Nonparallel Hyperplane Support Vector Machine Algorithms. *Neural Comput. Appl.* **2014**, *25*, 975–982. [CrossRef]
76. Dou, Q.; Qin, S.; Zhang, Y.; Ma, Z.; Chen, J.; Qiao, S.; Hu, X.; Liu, F. A Method for Improving Controlling Factors Based on Information Fusion for Debris Flow Susceptibility Mapping: A Case Study in Jilin Province, China. *Entropy* **2019**, *21*, 695. [CrossRef] [PubMed]
77. Chen, W.; Peng, J.; Hong, H.; Shahabi, H.; Pradhan, B.; Liu, J.; Zhu, A.-X.; Pei, X.; Duan, Z. Landslide susceptibility modelling using GIS-based machine learning techniques for Chongren County, Jiangxi Province, China. *Sci. Total Environ.* **2018**, *626*, 1121–1135. [CrossRef]

78. Peres, D.J.; Cancelliere, A. Derivation and Evaluation of Landslide-triggering Thresholds by a Monte Carlo Approach. *Hydrol. Earth Syst. Sci.* **2014**, *18*, 4913–4931. [CrossRef]
79. Lundberg, S.M.; Lee, S. A Unified Approach to Interpreting Model Predictions. In *Advances in Neural Information Processing Systems*; Curran Associates, Inc.: Red Hook, NY, USA, 2017.

remote sensing

MDPI

Technical Note

Distinct Susceptibility Patterns of Active and Relict Landslides Reveal Distinct Triggers: A Case in Northwestern Turkey

Marco Loche [1], Luigi Lombardo [2], Tolga Gorum [3], Hakan Tanyas [2] and Gianvito Scaringi [1,*]

[1] Institute of Hydrogeology, Engineering Geology and Applied Geophysics, Faculty of Science, Charles University, 12843 Prague, Czech Republic; marco.loche@natur.cuni.cz
[2] Faculty of Geo-Information Science and Earth Observation (ITC), University of Twente, 7514 Enschede, The Netherlands; l.lombardo@utwente.nl (L.L.); h.tanyas@utwente.nl (H.T.)
[3] Eurasia Institute of Earth Sciences, Istanbul Technical University, Istanbul 34469, Turkey; tgorum@itu.edu.tr
* Correspondence: gianvito.scaringi@natur.cuni.cz

Abstract: To understand the factors that make certain areas especially prone to landslides, statistical approaches are typically used. The interpretation of statistical results in areas characterised by complex geological and geomorphological patterns can be challenging, and this makes the understanding of the causes of landslides more difficult. In some cases, landslide inventories report information on the state of activity of landslides, adding a temporal dimension that can be beneficial in the analysis. Here, we used an inventory covering a portion of Northwestern Turkey to demonstrate that active and relict landslides (that is, landslides that occurred in the past and are now stabilised) could be related to different triggers. To do so, we built two landslide susceptibility models and observed that the spatial patterns of susceptibility were completely distinct. We found that these patterns were correlated with specific controlling factors, suggesting that active landslides are regulated by current rainfalls while relict landslides may represent a signature of past earthquakes on the landscape. The importance of this result resides in that we obtained it with a purely data-driven approach, and this was possible because the active/relict landslide classification in the inventory was accurate.

Keywords: landslide susceptibility; landslide inventory; controlling factor; slope unit; generalised additive model

Citation: Loche, M.; Lombardo, L.; Gorum, T.; Tanyas, H.; Scaringi, G. Distinct Susceptibility Patterns of Active and Relict Landslides Reveal Distinct Triggers: A Case in Northwestern Turkey. *Remote Sens.* **2022**, *14*, 1321. https://doi.org/10.3390/rs14061321

Academic Editor: Stefano Morelli

Received: 25 February 2022
Accepted: 4 March 2022
Published: 9 March 2022

1. Introduction

Data-driven models can be thought as empirical tools that extract functional relationships from past phenomena to estimate the expected behaviour of the same phenomena in a pre-defined (or ill-defined) future. This framework is commonly referred to as Hutton's uniformitarian principle, and is more commonly translated as *the past is the key to the future* [1–3]. Hutton first and subsequently Lyell helped to develop and spread the concept of *uniformitarianism*, replacing the then prevailing idea of *catastrophism*. Since then, this concept has formed the backbone of any landslide susceptibility study [3].

Landslide susceptibility models (LSM) can be used to predict the spatial occurrence of future landslides by assuming, consistently with the uniformitarian principle, that in any given area, slope failures will occur under the same circumstances and because of the same conditions that caused them in the past. However, this principle may not always hold true [4]. First-failure landslides and reactivations may have different controls, acting both on their triggers and kinematics: think of the peak and residual shear strengths, or the role of strong earthquakes as opposed to aftershocks or rainfall [5]. Changes in material properties also are reflected in morphological changes which, in turn, affect the process dynamics [6].

Uniformitarianism still represents a fundamental component of the literature [7–12], albeit the current climate change has led us to question its present-day validity [13]. In fact, data-driven models are generally built upon the effects of past events, which may

not inform on the slope response to events of different nature in the future. This topic is hardly addressed in the literature as it requires an understanding not only of the evolution of the triggers, but also of the predisposing or preparatory conditions. These may behave differently in time [4], reflecting changes in mechanical [14], hydrological and hydraulic [15], or thermal conditions [13,16].

Moreover, the complexity of a seismically active area does not help perform a straightforward analysis and interpretation of both the predisposing and triggering factors. This is true, for instance, in Turkey (Figure 1a), where the huge variability and complexity of the territory makes the modelling difficult to tackle. The capability and feature of an existing landslide inventory [17], able to discern relict (termed "inactive" in the inventory) from active landslides, comes to our aid as it could enable the distinction of different processes in place and their drivers. Moreover, especially for active landslides, the definition of the main triggering factors is crucial for the evaluation of economic costs related with the frequency and magnitude of disaster events [18].

Seismically active areas may contain many landslide bodies. The seismic shaking likely triggers their first movement, while subsequent remobilisations become increasingly related to different triggers and predisposing factors as time goes by [16,19]. Different triggers can also produce distinct patterns in space [20]. In Northwestern Turkey, which we took as our study area, we can discern two sub-areas: the North Anatolian fault region in the southwest, characterised by a higher density of relict bodies, and the region close to the Black Sea in the northeast, richer in active ones (Figure 1b,c). These sub-areas display an attitude of surface processes to be related to distinct triggers: seismicity and rainfall (Figure 1d,e). However, these differences may be difficult to discern in an inventory in which landslide types or activity states or stages are not classified.

The effect of biases in susceptibility modelling has been explored in the literature [21–23]. The necessity to operate with an unbiased area [24,25] led us to focus on a specific sector in Northwester Turkey, rich in landslides but not too tectonically complex, and sufficiently geologically and geomorphologically homogeneous.

In terms of modelling approaches, the literature offers many options. We opted for the Generalised Additive Model (GAM; [15,26]), which can explain the spatial distribution of landslides via a family of Bernoulli exponential functions, in which the influence of the covariates can be captured via linear and nonlinear relationships. As such, the approach allows us to display the uncertainties in the estimations, which are intrinsically part of a Bayesian framework [27]. This statistical implementation is utilised here for the first time to investigate relationships between two distinct models covering the same area but differing by a categorical entity (active/inactive landslide). Furthermore, we decided to use Slope Units (SUs) as they are geomorphologically-consistent subdivisions that can be linked with landslide processes and are thus preferrable to grid-based subdivisions [28–31].

2. Study Area

The geology and geomorphology of Turkey is unique and extremely complex, owing to both past and ongoing processes in place. Various studies exist [32–36], in which the national settings are dissected per geological history and geomorphological processes. Figure 1 displays the large-scale geomorphological and geological features.

The diversity of morphologies derives from a geodynamic environment that is still quite active and determines a variety in outcropping lithologies [35]. Three main landslide-dominated landscapes are recognised, corresponding to the tectonostratigraphically-distinct Western, Central, and Eastern Pontides [37]. The lithological units forming the Pontides vary along the belt, featuring west-east-oriented sub-parallel bands of sedimentary, metamorphic, and igneous rocks. While the western portion is richer in Triassic to Paleogene sedimentary and medium-grade metamorphic outcrops, the central zone comprises Eocene volcaniclastic and sedimentary rocks and Palaeozoic metamorphic rocks, and the eastern zone features Paleogene and Cretaceous plutonic and igneous formations underlying Eocene and Neogene sedimentary and volcanic formations [38].

The portion chosen as our study area (Figure 1) corresponds to the Zonguldak quadrangle in the Western Pontides. Here, the North Anatolian Fault System (NAFS) produced a landform dominated by mountain belts and plateaus. The NAFS is an over 1600 km long, right-lateral strike-slip, active transform fault running along Northern Anatolia in the E–W direction, that also separates the study area in a southern and a northern sector (Figure 1a).

Climatically, the area belongs to the *Black Sea climatic region* in the north and the *continental inner Anatolian climatic region* in the southeast [39]. The former receives rainfall throughout the year (>1000 mm mean annual precipitation, up to 2300 mm in its eastern portion) [39]. The north-facing slopes of the coastal mountain belt are comparatively wetter as they intercept the weather fronts, and this is reflected by a relative abundance of landslides (Figure 1e). Precipitation decreases southward, where the Palaeocene-Eocene flysch and Palaeocene-Middle Miocene volcanics are the most landslide-prone units [39].

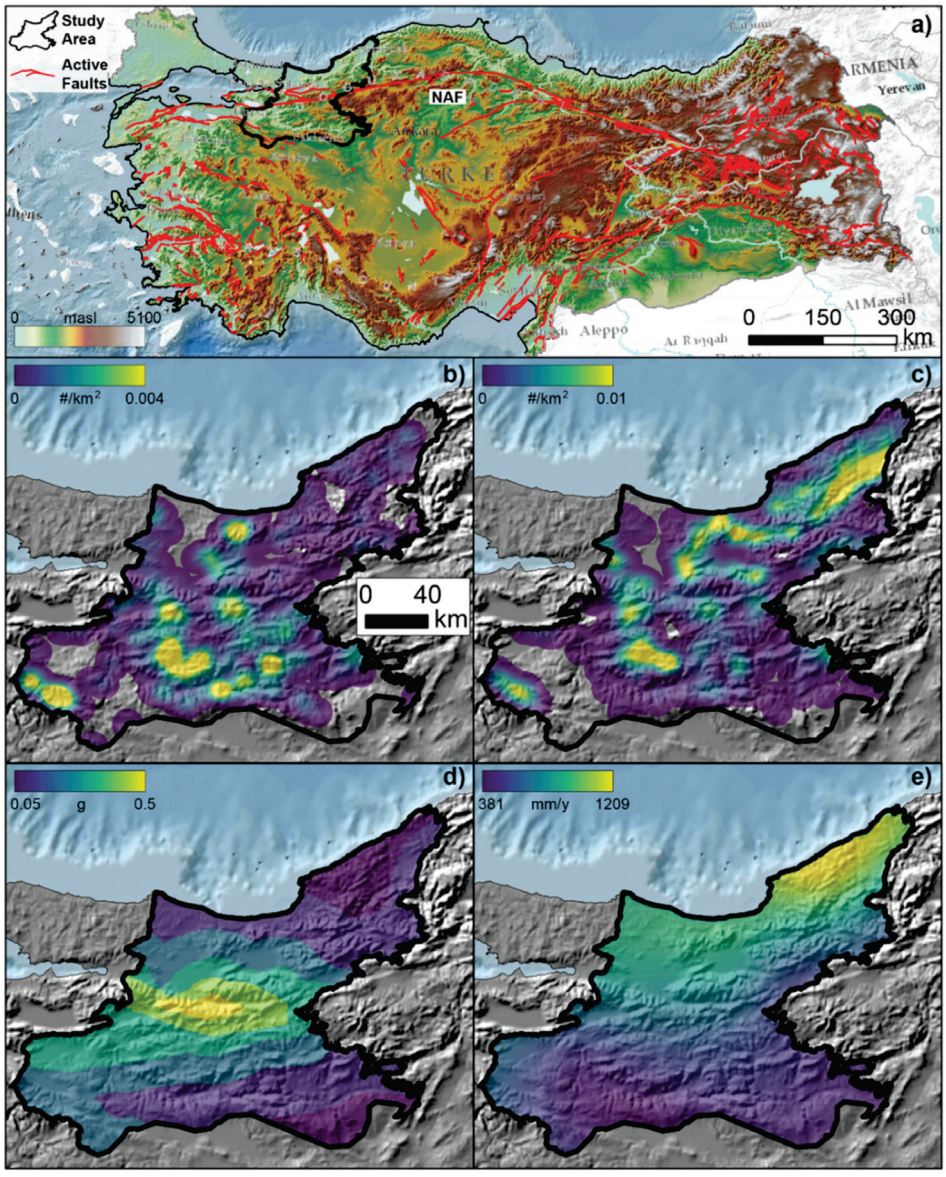

Figure 1. Identification of the study area in Turkey and the North Anatolian Fault (**a**); density maps of inactive (**b**) and active (**c**) landslides (see Section 2.2 for definitions); Peak Ground Acceleration map (**d**) from [40]; mean annual precipitation map (**e**) from [41].

2.1. Mapping Units

We used SUs as terrain partitions characterised by similar hydrological and geomorphological conditions [42]. Each SU has a distinct shape given by the interplay between lithotypes and morphometries, and thus offers morphological and lithological characteristics that can be analysed statistically. An SU-based subdivision is not the only possible choice. In fact, most contributions in the literature opt for a regular lattice or pixel-based subdivisions [3]. These, however, even though they can be expressed at a fine to very-fine resolution, do not reflect any natural characteristics. Conversely, SUs can, better than pixels, represent geomorphological processes (e.g., [43,44]) and, at the same time, reduce the computational burden, especially in models covering large areas (in our case, SU-based calculations are ~100 faster than pixel-based ones).

We used the r.slopeunits software [28]) to generate SUs. Specifically, we subdivided the study area into SUs [28–30,45]. We computed 50,104 SUs, covering ~24,000 km^2 out of ~29,400 km^2 of the study area as we excluded flat areas that are not prone to landslides (Figure 2) [31,46,47].

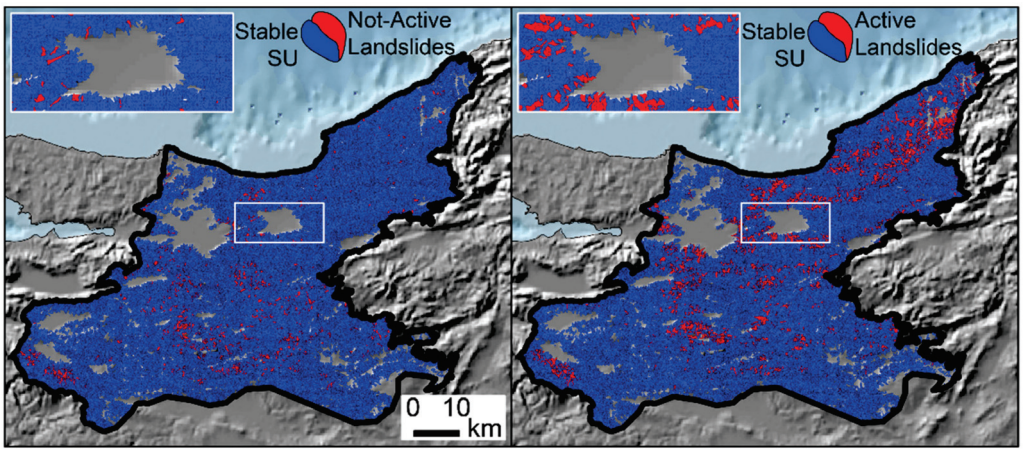

Figure 2. Slope Unit partition of the study area: SUs containing inactive (**left**) and active (**right**) landslides are shown. The sub-panels show a detail for a small region, in which it is possible to observe the flat areas excluded by the SU calculation (see Section 4.2 for explanation). The legend is valid for the whole area and zoomed panels.

2.2. Landslides

The landslide inventory was compiled by the General Directorate of Mineral Research and Explorations of Turkey (MTA) and published in 1:25,000 scale for the entire national territory (http://yerbilimleri.mta.gov.tr/, accessed on 1 February 2022). It is a general polygon-based-inventory that carries some complexities because the mapped phenomena are related to a plurality of causes. Thus, the identification of unstable areas should benefit from the use of as many variables as possible to discern the main factors affecting slope stability.

The catalogue [39], within our study area, comprises 4084 active landslides and 1140 inactive landslides. The former are those that were moving at the time of mapping (1997–2003), while the latter could be classified as relict according to the UNESCO Working Party on World Landslide Inventory (1993) [48]. Qualitatively, we notice an abundance of active phenomena in the northeastern area where the climatic influence of the Black Sea is stronger. A less dense but significant presence of landslides can be seen in the southwestern sector (Figure 2).

We extracted the highest point in the landslide polygon to better represent the source material and/or lithology [49,50]. Subsequently, separately for each model, we reported the count of active or inactive landslides within each SU, attributing the presence of landslides to those SUs containing at least one point. Finally, we identified 2822 SUs (X% of SUs) with active phenomena, and 983 (Y%) with inactive phenomena.

3. Modelling Strategy

In a binomial GAM, the data (y) are assumed to be conditionally independent given the linear predictor η:

$$y_i \mid \eta_i \sim \text{Binomial}\,(N_i, p_i) \tag{1}$$

$$\eta_i = p_i/(1-p_i) \tag{2}$$

where p_i is the binomial probability.

Here, we assume $N_i = 1$ for all $_i$ because we have binary data. The η_i as a function of p_i is called the link function, and we describe it using a logit, but we note that other link functions are possible. The linear predictor η is where we put the additive model:

$$\eta_i = \beta_{1x1,i} + ... + \beta_{mxm,i} + f(\text{Slope}) + f(\text{Precipitation}), \tag{3}$$

where β_j are the fixed (or linear) effects, with weak priors, describing the linear relationship of the covariates x_j. Each f represents a random (or nonlinear) effect with

$$f \sim N\,(0, \tau-1) \tag{4}$$

and τ is a constant. For the two f, we use a spline model, also referred to as Random Walk of the first order (RW1; [51])

A RW1 induces adjacent class dependence among mean slope and precipitation bins, respectively [52]. The whole implementation makes use of the INLA framework [46,47].

To quantitatively compare the inventories of active and inactive landslides, we relied on the effects of the selected covariates. Active and inactive phenomena should present distinct correlations with physical variables owing to changes in predisposing and triggering conditions as well as their values. For instance, active and inactive phenomena could be characterised by distinct distributions of slope angles or vegetation coverage. However, while morphological and climatic factors can change rather rapidly, geological, lithological, and structural factors are not expected to vary over human time scales (in absence of catastrophic events).

Possible multicollinearity issues among covariates (Figure S1) were eliminated by discarding those showing more than 0.75 collinearity with another covariate [53–55]. The final list of covariates is reported in Table 1. We preferred covariates that are well known in the literature [3,56], and analysed their linear effects in most cases. We investigated the nonlinear effect of slope and precipitation to better capture the role of gravitative-hydrological processes in landsliding.

For model fitting, we used the whole sets of active and inactive landslides (separately). For validation, we used a tenfold Cross Validation (CV) with mutually exclusive subsets, implying that no SUs are repeated across CV replicates, and thus, there is no autocorrelation [57]. We used the Area Under the Receiving Operating Characteristic Curve (AUC) and the confusion matrix to evaluate the model performance. This is not the only possibility. In fact, new articles suggest a spatial CV with connected packages [58–60]. However, this solution is still under discussion [61], which is why we preferred to use a pre-consolidated methodology.

Table 1. List of covariates. L and NL indicate that the linear and nonlinear effects were investigated, respectively. SD stands for standard deviation. All values are calculated within each SU.

Name	Abbreviation	Reference	Usage in the Inventory	
			Inactive	Active
Mean slope	Slope	[62]	NL	NL
SD of slope	Slopeσ	[62]	L	L
Mean Rainfall	Precipitation	[5]	NL	NL
Mean peak ground acceleration	PGAμ	[5]	L	L
Topographic relief	Reliefμ	[35]	L	L
Elongation of the SU	Elongation	[46]	L	L
Mean Eastness	ESTμ	[50]	L	L
Mean Northness	NRTμ	[50]	L	L
SD of Northness	NRTσ	[50]	L	L
SD of planar curvature	PLCσ	[63]	L	L
Mean profile curvature	PRCμ	[63]	L	L
Mean Relative slope position	RSPμ	[64]	L	L
SD of Relative slope position	RSPσ	[64]	L	L
Mean topographic wetness index	TWIμ	[64]	L	L
SD of topographic wetness index	TWIσ	[64]	L	L
Mean Stream power index	SPIμ	[65]	L	L
SD of Stream power index	SPIσ	[65]	L	L
Mean Distance to Fault	D2Fμ	[15]	L	L
SD of Distance to Fault	D2Fσ	[15]	L	L

4. Results

We report the outcomes of the so-called fitting (within sample) and cross-validation (out of sample) procedures. The former is used to interpret the patterns of the explanatory variables, while the latter is a tool for model validation. We then produce two susceptibility maps (that is, two spatial probability maps), one for the active landslides, and one for the relict landslides. These maps are compared with those of a number of explanatory variables, to seek common patterns. It should be stressed that the susceptibility maps are intended as descriptions of past/present phenomena and not as a temporal prediction tool.

4.1. Distinct Patterns of Explanatory Variables

The main tool that we can use to evaluate the extent to which the classification into inactive and active landslides relates to distinct controlling factors is the analysis of the effects of these factors, represented by sets of covariates in the statistical model. We believe, in fact, that inactive and active landslide phenomena should be spatially correlated with physical variables in a distinct way. Predisposing factors that cause landslides must be congruent in inactive as well as in active landslides. Hence, what should stand out the most is that the predisposing factors can change over time.

The posterior marginal distributions of the linear effects of each covariate in the models constructed with inactive and, separately, active landslides are displayed in Figure 3. Notably, about half of the covariates exhibit distinct effects in the two models, suggesting that the phenomena featured in the two classes may be controlled by different processes.

Geomorphologically, reasonable patterns are described. The role of Northness is consistent with the distribution of precipitation, which comes from the Black Sea, north of the study area (Figure 1). Negative values of RSPμ are observed in active landslides. Seemingly counterintuitively, PGAμ is positively correlated with inactive landslides. However, this is consistent with the observation [39] that these landslides may be related to historical earthquakes in the NAFS. The elongation of the SUs has a negative effect on both active and inactive landslides, as elongated slopes offer less room for large, deep-seated landslides to form. The average slope negatively correlates with the presence of active landslides, while no correlation is found with inactive ones. For active landslides, this suggests that phenomena on very steep slopes are unlikely; in fact, unstable bodies are quickly removed from steep slopes, while landslide inventories tend to better capture movements over more gentle slopes, which can remain active for a longer time. Hydrological covariates (TWIσ and SPIμ) seem to exert a negative effect in both active and inactive landslides, suggesting their preferential occurrence in the upper portions of catchments. The effect of lithology (Figure S2, Table S1) also shows some differences between the models. For

instance, granitoid areas are negatively correlated with active landslides, while the opposite holds true for carbonate rocks.

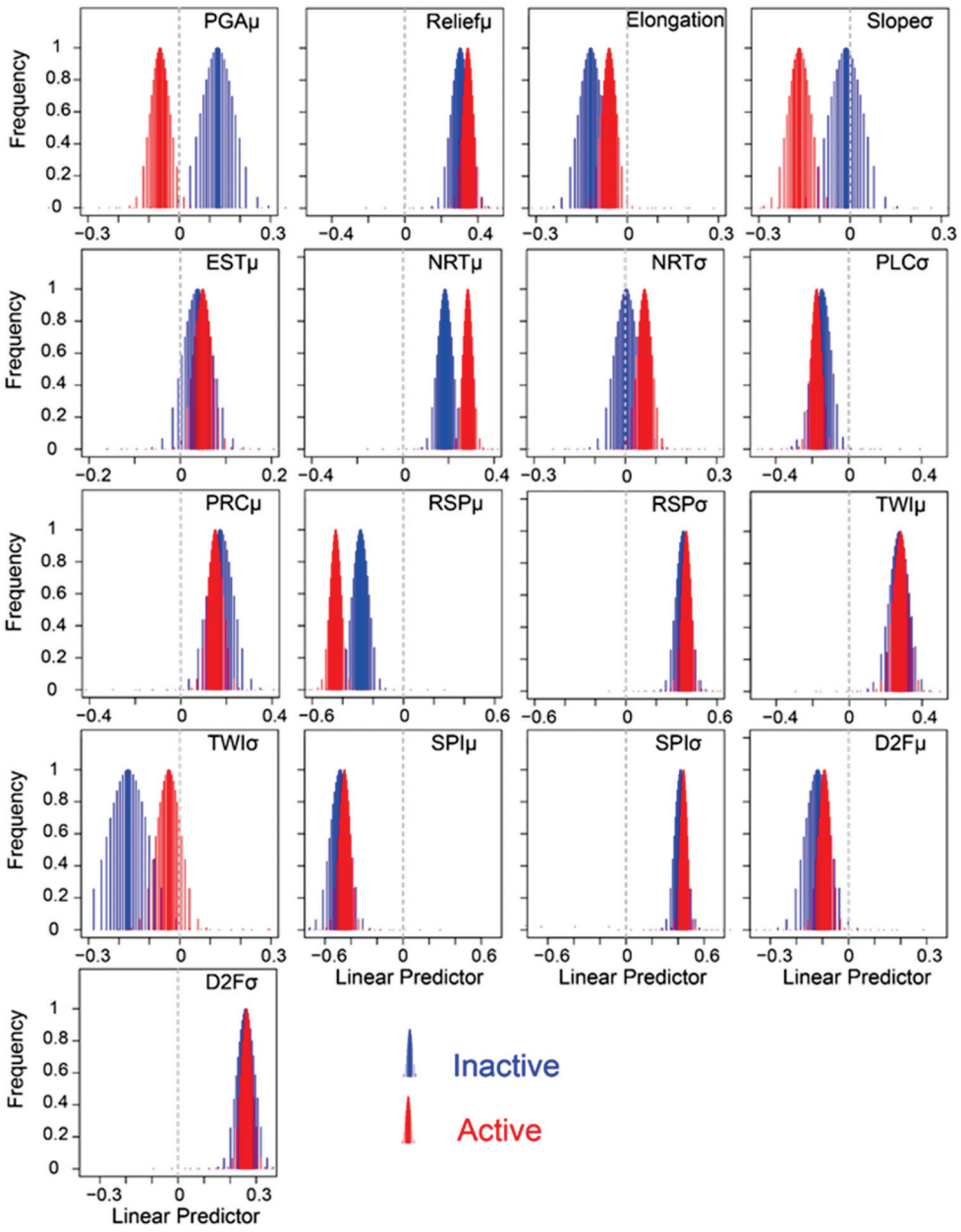

Figure 3. Fixed effects of geomorphological variables expressed as marginal distributions for inactive and active landslides.

4.2. Distinct Landslide Triggers

The behaviours of the nonlinear effects of covariates for inactive and active phenomena also are different, as shown in Figure 4. These nonlinear effects clearly point to distinct triggers for inactive and active landslides. In fact, for inactive landslides, neither slope nor precipitation exert significant effects (95% confidence level). For active landslides, positive effects are seen within a certain range of slope angles (10–20°) that could be related to specific materials capable of sustaining prolonged landslides, and for large amounts of annual precipitation (>800 mm/year), capable of frequently triggering or sustaining a variety of movements. On the contrary, in areas with less precipitation, the effect is slightly negative.

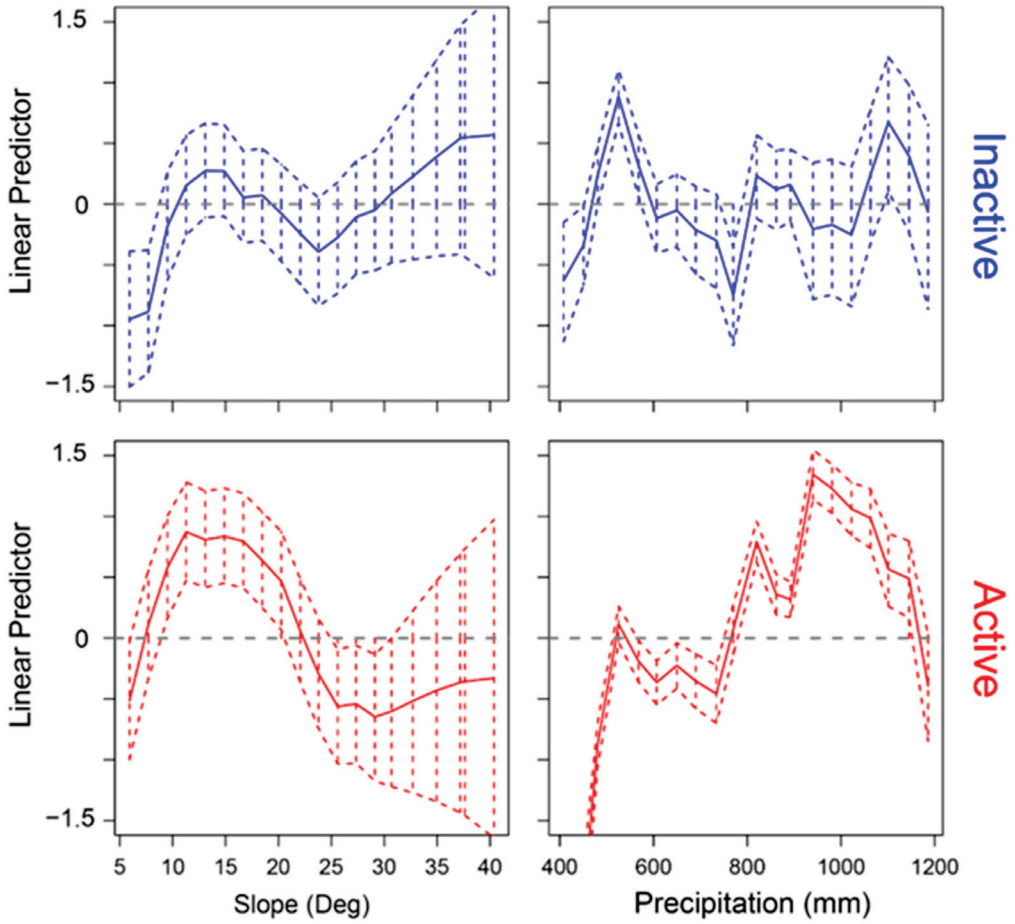

Figure 4. Nonlinear effects of slope (**left** column) and precipitation (**right** column) for inactive (**top** row) and active (**bottom** row) landslides. The effect is modelled as a random effect estimated over 20 classes with adjacent dependency. Thick coloured lines represent the posterior means whereas the coloured dashed lines indicate the posterior 95% credible interval. Dashed grey lines indicate the zero line along which coefficients play no role in the modelling outcome.

In order to validate the result, the out-of-sample performance of the model is investigated. This is done in two steps: the first one involves the use of AUC for each of the considered landslide classes, whereas the second one maintains the same structure but focuses on the summary metrics of confusion matrices.

Figure 5a shows the ROC curves and their AUC values for ten cross-validations for the active and inactive landslide models. The AUC values (~0.8) can be deemed satisfactory and are consistent across the replicates, indicating robustness of the model [66]. The figure (bottom row) also shows the confusion plots of the two models, which are rather similar in both the high ability to detect true positive cases (~90%) and the lower ability to identify the true negative ones (47–50%). Consequently, the error rate (bottom right) is also of similar magnitude (44–50%), and it seems to fail on the stable conditions, together with the ratio between Predicted True Negatives and Observed Negatives.

However, we should remind that the SUs had been calculated only for areas with slope topography, as we excluded the flat areas that are obviously not susceptible to gravitative movements. This could be interpreted as a weakness of the model, but actually facilitates its ability in recognising the instable areas.

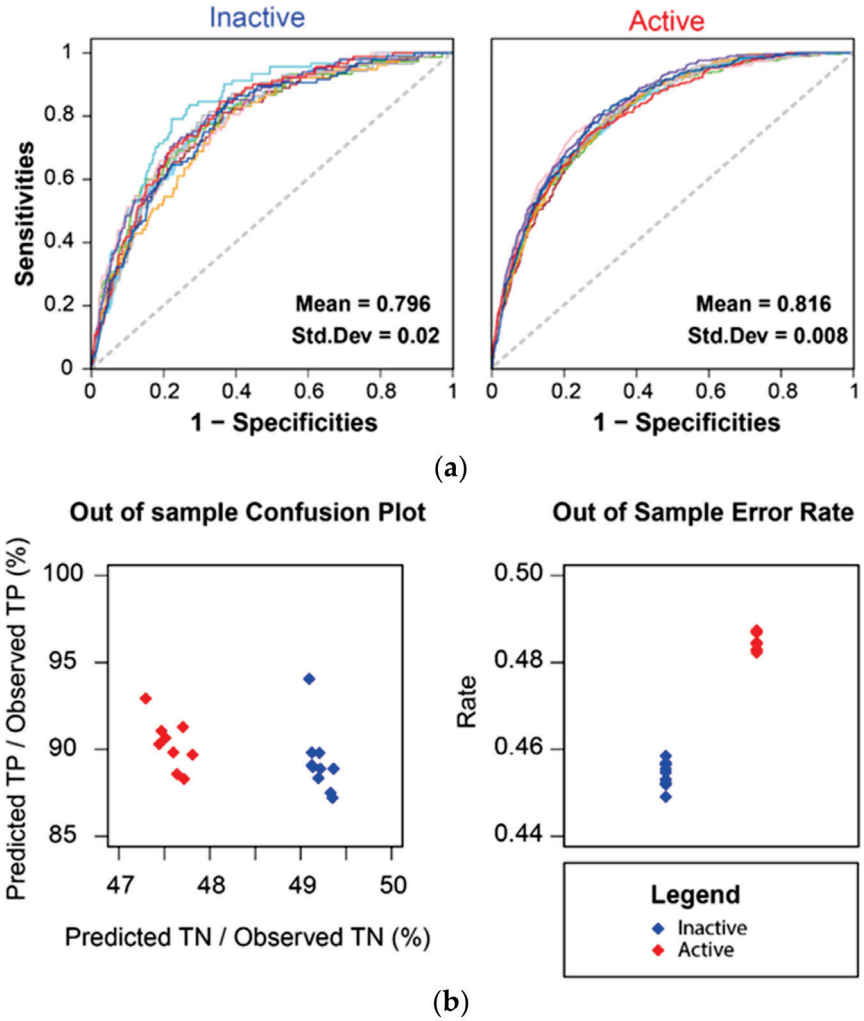

Figure 5. (**a**) ROC curves and their AUCs for ten cross-validations for the inactive (**left**) and active (**right**) landslide models. (**b**) Confusion plot (**left**) constructed via the percentage of Observed TP and fitted TP against the percentage of Observed TN and fitted TN (for each landslide type), and error rates (**right**), both have been obtained from a tenfold CV.

4.3. Distinct Susceptibility Maps

In Figure 6, we show the resulting susceptibility maps for the inactive and active landslides. The maps display markedly different spatial patterns that are consistent with the qualitative (Figure 1) and quantitative (Figures 3 and 4) observations that the distribution of active landslides better correlates with the annual precipitation and that the distribution of inactive landslides better correlates with the peak ground acceleration.

What is more, the two maps are not "one the negative of the other". The patterns that emerge are, in fact, distinct. Indeed, we do not observe a specular negative effect of precipitation in the distribution of inactive landslides (in fact, we do not observe a significant effect at all). However, we do see a negative effect of the peak ground acceleration in the distribution of active landslides, but the magnitude of this effect is smaller than that seen for inactive landslides.

The absence of correlation between the two maps is demonstrated quantitatively in Figure 6d, where the Pearson correlation shown is 0.5, indicating a random dependence. Similarities in the two maps mainly exist in areas with low density of landslides, independently of their state of activity, such as the northwestern and southernmost portions.

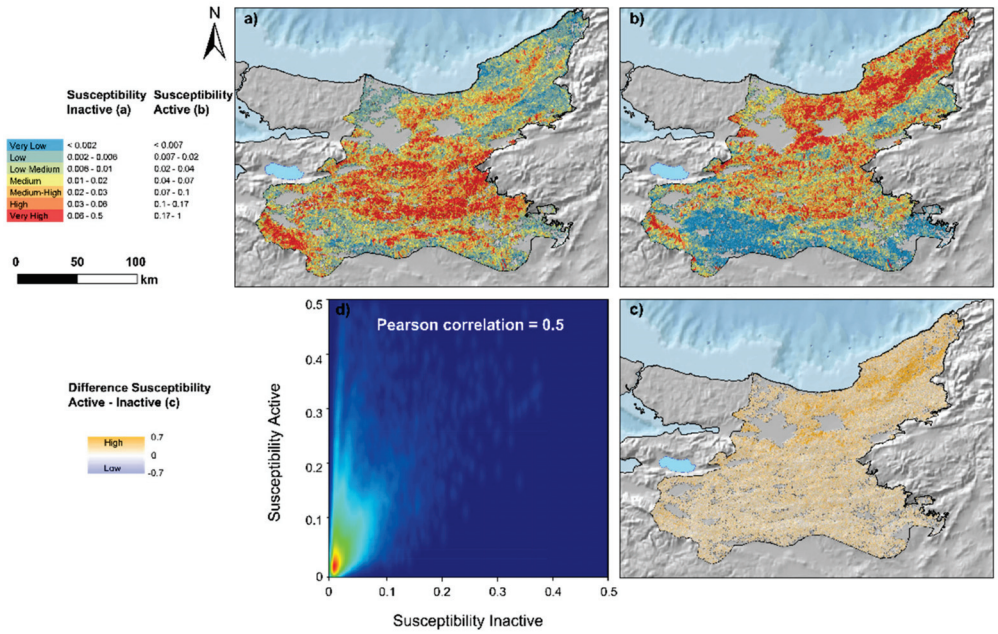

Figure 6. Susceptibility maps for inactive (**a**) and active (**b**) landslides. The maps are obtained by merging ten cross-validated subsets and thus entirely come from predicted estimates. The resulting probability values have been binned into seven susceptibility classes using a quantile criterion. The difference in susceptibility between (**a**) and (**b**) is shown in (**c**), while the graph in (**d**) displays their Pearson correlation.

5. Discussion

5.1. Controls and Fate of Active Landslides

From our analysis, it emerged that, consistently with the definition of relict landslides (used to classify the inactive landslides), the conditions that caused their occurrence in the past are distinct from those that are responsible for the active movements in the present. Moreover, the locations of the inactive landslides point to areas with high seismicity, suggesting that they may be earthquake-induced phenomena, now stabilised and insensitive to hydrometeorological forcing. Conversely, the distribution of active landslides reflects the pattern of present-time annual precipitation, suggesting the rainfall-induced nature of these phenomena. If we interpret the active landslides as slow-moving mass movements (that is, processes that remain active for a comparatively long time, and thus more easily captured by inventories), the correlation between the rainfall pattern and the spatial distribution of landslides makes very much sense. There is a large literature showing that the mobilisation and acceleration of slow-moving landslides along slopes is mostly governed by rainfall events causing an increase in pore water pressure and thus a reduction in the available shear strength [67]. On the other hand, in the absence of significant shifts in hydro-meteorological patterns, the stabilisation of these landslides should mostly be related to their transition from steeper to gentler slopes and/or to plains or valleys without significant fluvial erosion at the toe). In other words, active landslides could be described as meta-stable hillslopes materials experiencing creep and consolidation processes while the ratio between driving and resisting forces fluctuates over time mostly under the control of hydro-meteorological factors.

Here, we should stress that slow-moving landslides could rapidly turn into catastrophic landslides (and thus rapidly stabilise) if at some point the driving forces dramatically exceed their resisting counterparts. Various factors including seismicity or precipitation itself could trigger catastrophic landslides. Yet, this may seem a more likely scenario for a region exposed to intense seismic external forces rather than precipitation because, overall, even relatively low-intensity ground shaking may be more destructive than intense precipitation at triggering landslides [68]. In this context, it is not surprising that the relict

landslides are mostly distributed closer to the North Anatolian Fault zone, whereas the active landslides concentrate far from it.

5.2. Accuracy of the Active/Inactive Landslide Classification

The binary classification into active and inactive landslides in the inventory was performed well. This is demonstrated by the fact that it resulted in the production of two distinct and uncorrelated susceptibility maps. In other words, in addition to suggesting differences between the conditions responsible for landslides in the past and in the present in the study area (supporting a non-uniformitarian view in this highly dynamic context), this result also suggests that we are dealing with a well-done classification. Logically, active and relict landslides should not be difficult to discern, but the point here is that, if a bias existed in this classifier, it would have resulted in less distinct (and thus more spatially correlated) susceptibility maps. Seeing this the other way round, if a classifier is expected to define distinct regions of space and this does not occur, the severity of the classification bias could be quantified from the degree of correlation between the maps generated, separately, for the distinct values of the classifier.

6. Conclusions

The analyses presented in this work aimed at investigating differences in the spatial patterns of relict and active landslides in a landslide-rich geomorphological context. These differences, expected in the light of qualitative observations on the possible landslide triggers and predisposing factors, were expressed quantitatively using a purely data-driven approach, confirming the validity of such methodology, suggested in the literature [69], and the accuracy of the classification operated in the inventory. The result that the susceptibility patterns of relict and active landslides in the study area are spatially distinct and correlate with distinct explanatory variables suggests that, while current rainfall patterns may explain the distribution of active landslides, seismicity may have had an impact on the relict landslides.

Overall, we believe our work can represent a summary of good practices in the definition of landslide susceptibility mapping and hopefully serve as a reference standardised assessments in both common and specific applications. It also brings novelty as it presents a general slope unit-based susceptibility model through a Bayesian approach in a study area, namely the Turkish Northwesternmost Sector, so far not investigated with this technique.

Supplementary Materials: The following supporting information can be downloaded at: https://www.mdpi.com/article/10.3390/rs14061321/s1. Figure S1: Collinearity between the variables used in the model; Figure S2: Fixed effects expressed as marginal distributions for each lithological unit for landslide type; Table S1: List of lithologies used in the model.

Author Contributions: Conceptualisation and methodology, M.L., G.S., H.T., T.G. and L.L.; formal analysis, M.L., G.S. and L.L.; investigation, M.L.; data curation and original draft preparation, M.L.; review and editing, M.L., G.S., H.T., T.G. and L.L.; visualisation, M.L.; supervision, G.S. and L.L.; project administration, G.S. and M.L.; funding acquisition, G.S., M.L. and L.L. All authors have read and agreed to the published version of the manuscript.

Funding: M.L. appreciates the financial support given by the Charles University Grant Agency (GAUK) with project number 337121. Data analysis, manuscript preparation and publication were funded by the Grant Agency of the Czech Republic (GAČR Grant No. 20-28853Y) and the Fund for international mobility of researchers at Charles University (MSCA-IF IV; Project No. CZ.02.2.69/0.0/0.0/20_079/0017987). The research was also partially supported by the King Abdullah University of Science and Technology (KAUST) in Thuwal, Saudi Arabia (Grant URF/1/4338-01-01).

Data Availability Statement: Elaborated data are presented in the manuscript. Raw experimental data can be provided by the authors upon reasonable request.

Conflicts of Interest: The authors declare no conflict of interest. The funders had no role in the design of the study; in the collection, analyses, or interpretation of data; in the writing of the manuscript, or in the decision to publish the results.

References

1. Hutton, J.X. Theory of the Earth; or an Investigation of the Laws observable in the Composition, Dissolution, and Restoration of Land upon the Globe. *Trans. R. Soc. Edinb.* **1788**, *1*, 209–304. [CrossRef]
2. Lyell, C.; Clowes, W.; Deshayes, G.P.; Murray, J. Principles of Geology. In *Being an Attempt to Explain the Former Changes of the Earth's Surface, by Reference to Causes Now in Operation*; John Murray: London, UK, 1830; Volume 1. [CrossRef]
3. Reichenbach, P.; Rossi, M.; Malamud, B.D.; Mihir, M.; Guzzetti, F. A Review of Statistically-Based Landslide Susceptibility Models. *Earth Sci. Rev.* **2018**, *180*, 60–91. [CrossRef]
4. Guzzetti, F.; Reichenbach, P.; Cardinali, M.; Galli, M.; Ardizzone, F. Probabilistic Landslide hazard Assessment at the Basin Scale. *Geomorphology* **2005**, *72*, 272–299. [CrossRef]
5. Fan, X.; Yunus, A.P.; Scaringi, G.; Catani, F.; Subramanian, S.S.; Xu, Q.; Huang, R. Rapidly Evolving Controls of Landslides after a Strong Earthquake and Implications for Hazard Assessments. *Geophys. Res. Lett.* **2021**, *48*. [CrossRef]
6. Tang, R.; Fan, X.; Scaringi, G.; Xu, Q.; Van Westen, C.J.; Ren, J.; Havenith, H.-B. Distinctive Controls on the Distribution of River-Damming and Non-Damming Landslides Induced by the 2008 Wenchuan Earthquake. *Bull. Eng. Geol. Environ.* **2018**, *78*, 4075–4093. [CrossRef]
7. Orme, A.R. Shifting Paradigms in Geomorphology: The Fate of Research Ideas in an Educational Context. *Geomorphology* **2002**, *47*, 325–342. [CrossRef]
8. Ercanoglu, M.; Gokceoglu, C.; Van Asch, T.W.J. Landslide Susceptibility Zoning of North of Yenice (NW Turkey) by Multivariate Statistical Techniques. *Nat. Hazards* **2004**, *32*, 1–23. [CrossRef]
9. Goudie, A.S. (Ed.) *International Association of Geomorphologists Encyclopedia of Geomorphology*; Routledge: New York, NY, USA, 2004; ISBN 978-1-134-48275-7.
10. Saponaro, A.; Pilz, M.; Wieland, M.; Bindi, D.; Moldobekov, B.; Parolai, S. Landslide Susceptibility Analysis in Data-Scarce Regions: The Case of Kyrgyzstan. *Bull. Eng. Geol. Environ.* **2014**, *74*, 1117–1136. [CrossRef]
11. Zêzere, J.; Pereira, S.; Melo, R.; Oliveira, S.; Garcia, R. Mapping Landslide Susceptibility Using Data-Driven Methods. *Sci. Total Environ.* **2017**, *589*, 250–267. [CrossRef]
12. Jones, J.N.; Boulton, S.J.; Bennett, G.L.; Stokes, M.; Whitworth, M.R.Z. Temporal Variations in Landslide Distributions Following Extreme Events: Implications for Landslide Susceptibility Modeling. *J. Geophys. Res. Earth Surf.* **2021**, *126*. [CrossRef]
13. Scaringi, G.; Loche, M. A Thermo-Hydro-Mechanical Approach to Soil Slope Stability under Climate Change. *Geomorphology* **2022**, *401*, 108108. [CrossRef]
14. Domènech, G.; Fan, X.; Scaringi, G.; van Asch, T.W.; Xu, Q.; Huang, R.; Hales, T.C. Modelling the Role of Material Depletion, Grain Coarsening and Revegetation in Debris Flow Occurrences after the 2008 Wenchuan Earthquake. *Eng. Geol.* **2019**, *250*, 34–44. [CrossRef]
15. Lombardo, L.; Mai, P.M. Presenting Logistic Regression-Based Landslide Susceptibility Results. *Eng. Geol.* **2018**, *244*, 14–24. [CrossRef]
16. Loche, M.; Scaringi, G.; Yunus, A.P.; Catani, F.; Tanyaş, H.; Frodella, W.; Fan, X.; Lombardo, L. Surface Temperature Controls the Pattern of Post-Earthquake Landslide Activity. *Sci. Rep.* **2022**, *12*, 1–11. [CrossRef]
17. Duman, T.Y.; Çan, T.; Emre, Ö. *1: 1,500,000 Scaled Turkish Landslide Inventory Map*; General Directorate of Mineral Research and Exploration Publication: Ankara, Turkey, 2011; Volume 27.
18. Glade, T. Establishing the Frequency and Magnitude of Landslide-Triggering Rainstorm Events in New Zealand. *Environ. Earth Sci.* **1998**, *35*, 160–174. [CrossRef]
19. Fan, X.; Scaringi, G.; Domènech, G.; Yang, F.; Guo, X.; Dai, L.; He, C.; Xu, Q.; Huang, R. Two Multi-Temporal Datasets That Track the Enhanced Landsliding after the 2008 Wenchuan Earthquake. *Earth Syst. Sci. Data* **2019**, *11*, 35–55. [CrossRef]
20. Ali, M.Z.; Chu, H.-J.; Chen, Y.-C.; Ullah, S. Machine Learning in Earthquake- and Typhoon-Triggered Landslide Susceptibility Mapping and Critical Factor Identification. *Environ. Earth Sci.* **2021**, *80*, 1–21. [CrossRef]
21. Steger, S.; Brenning, A.; Bell, R.; Glade, T. The Propagation of Inventory-Based Positional Errors into Statistical Landslide Susceptibility Models. *Nat. Hazards Earth Syst. Sci.* **2016**, *16*, 2729–2745. [CrossRef]
22. Lima, P.; Steger, S.; Glade, T.; Tilch, N.; Schwarz, L.; Kociu, A. Landslide Susceptibility Mapping at National Scale: A First Attempt for Austria. In *Advancing Culture of Living with Landslides*; Mikos, M., Tiwari, B., Yin, Y., Sassa, K., Eds.; Springer International Publishing: Cham, Switzerland, 2017; pp. 943–951. [CrossRef]
23. Steger, S.; Kofler, C. Statistical Modeling of Landslides. In *Spatial Modeling in GIS and R for Earth and Environmental Sciences*; Elsevier: Amsterdam, The Netherlands, 2019; pp. 519–546. ISBN 978-0-12-815226-3.
24. Eeckhaut, M.V.D.; Hervás, J.; Jaedicke, C.; Malet, J.-P.; Montanarella, L.; Nadim, F. Statistical Modelling of Europe-Wide LandSlide Susceptibility Using Limited Landslide Inventory Data. *Landslides* **2011**, *9*, 357–369. [CrossRef]
25. Kirschbaum, D.; Stanley, T.; Zhou, Y. Spatial and Temporal Analysis of a Global Landslide Catalog. *Geomorphology* **2015**, *249*, 4–15. [CrossRef]
26. Petschko, H.; Bell, R.; Brenning, A.; Glade, T. Landslide Susceptibility Modeling with Generalized Additive Models–Facing the Heterogeneity of Large Regions. *Landslides Eng. Slopes Prot. Soc. Improv. Underst.* **2012**, *1*, 769–777.
27. Das, I.; Stein, A.; Kerle, N.; Dadhwal, V.K. Landslide Susceptibility Mapping along Road Corridors in the Indian Himalayas Using Bayesian Logistic Regression Models. *Geomorphology* **2012**, *179*, 116–125. [CrossRef]

28. Alvioli, M.; Marchesini, I.; Reichenbach, P.; Rossi, M.; Ardizzone, F.; Fiorucci, F.; Guzzetti, F. Automatic Delineation of Geomorphological Slope Units with r.slopeunits v1.0 and Their Optimization for Landslide Susceptibility Modeling. *Geosci. Model Dev.* **2016**, *9*, 3975–3991. [CrossRef]
29. Alvioli, M.; Marchesini, I.; Guzzetti, F. Nation-Wide, General-Purpose Delineation of Geomorphological Slope Units in Italy. *PeerJ Prepr.* **2018**, *6*, e27066v1.
30. Alvioli, M.; Guzzetti, F.; Marchesini, I. Parameter-Free Delineation of Slope Units and Terrain Subdivision of Italy. *Geomorphology* **2020**, *358*, 107124. [CrossRef]
31. Tanyas, H.; Rossi, M.; Alvioli, M.; van Westen, C.J.; Marchesini, I. A Global Slope Unit-Based Method for the Near Real-Time Prediction of Earthquake-Induced Landslides. *Geomorphology* **2018**, *327*, 126–146. [CrossRef]
32. Sengör, A.M.C.; Yilmaz, Y. Tethyan Evolution of Turkey: A Plate Tectonic Approach. *Tectonophysics* **1981**, *75*, 181–241. [CrossRef]
33. Okay, A.I. Geology of Turkey: A Synopsis. *Anschnitt* **2008**, *21*, 19–42.
34. Gorum, T.; Gonencgil, B.; Gokceoglu, C.; Nefeslioglu, H.A. Implementation of Reconstructed Geomorphologic Units in LandSlide Susceptibility Mapping: The Melen Gorge (NW Turkey). *Nat. Hazards* **2008**, *46*, 323–351. [CrossRef]
35. Görüm, T. Tectonic, Topographic and Rock-Type Influences on Large Landslides at the Northern Margin of the Anatolian Plateau. *Landslides* **2018**, *16*, 333–346. [CrossRef]
36. Akbaş, B.; Akdeniz, N.; Aksay, A.; Altun, İ.E.; Balcı, V.; Bilginer, E.; Bilgiç, T.; Duru, M.; Ercan, T.; Gedik, İ.; et al. *1:1.250.000 Scaled Geological Map of Turkey*; General Directorate of Mineral Research and Exploration Publication: Ankara, Turkey, 2011.
37. Geology and Tectonic Evolution of the Pontides. In *Regional and Petroleum Geology of the Black Sea and Surrounding Region*; American Association of Petroleum Geologists: Tulsa, OK, USA, 1997; pp. 183–226, ISBN 978-0-89181-348-4.
38. Okay, A.; Şengör, A.C.; Görür, N. Kinematic History of the Opening of the Black Sea and Its Effect on the Surrounding Regions. *Geology* **1994**, *22*, 559–562. [CrossRef]
39. Duman, T.Y.; Çan, T.; Emre, Ö.; Keçer, M.; Doğan, A.; Ateş, Ş.; Durmaz, S. Landslide Inventory of Northwestern Anatolia, Turkey. *Eng. Geol.* **2005**, *77*, 99–114. [CrossRef]
40. Ulusay, R.; Aydan, Ö.; Kılıc, R. Geotechnical Assessment of the 2005 Kuzulu Landslide (Turkey). *Eng. Geol.* **2007**, *89*, 112–128. [CrossRef]
41. Hijmans, R.J.; Cameron, S.E.; Parra, J.L.; Jones, P.G.; Jarvis, A. Very High Resolution Interpolated Climate Surfaces for Global Land Areas. *Int. J. Climatol.* **2005**, *25*, 1965–1978. [CrossRef]
42. Carrara, A. Drainage and Divide Networks Derived from High-Fidelity Digital Terrain Models. In *Quantitative Analysis of Mineral and Energy Resources*; Chung, C.F., Fabbri, A.G., Sinding-Larsen, R., Eds.; Springer: Dordrecht, The Netherlands, 1988; pp. 581–597, ISBN 978-94-010-8288-4.
43. Guzzetti, F.; Carrara, A.; Cardinali, M.; Reichenbach, P. Landslide Hazard Evaluation: A Review of Current Techniques and Their Application in a Multi-Scale Study, Central Italy. *Geomorphology* **1999**, *31*, 181–216. [CrossRef]
44. Guzzetti, F.; Reichenbach, P.; Ardizzone, F.; Cardinali, M.; Galli, M. Estimating the Quality of Landslide Susceptibility Models. *Geomorphology* **2006**, *81*, 166–184. [CrossRef]
45. Pokharel, B.; Alvioli, M.; Lim, S. Assessment of Earthquake-Induced Landslide Inventories and Susceptibility Maps Using Slope Unit-Based Logistic Regression and Geospatial Statistics. *Sci. Rep.* **2021**, *11*, 1–15. [CrossRef]
46. Camilo, D.C.; Lombardo, L.; Mai, P.M.; Dou, J.; Huser, R. Handling High Predictor Dimensionality in Slope-Unit-Based Landslide Susceptibility Models through LASSO-Penalized Generalized Linear Model. *Environ. Model. Softw.* **2017**, *97*, 145–156. [CrossRef]
47. Schlögel, R.; Marchesini, I.; Alvioli, M.; Reichenbach, P.; Rossi, M.; Malet, J.-P. Optimizing Landslide Susceptibility Zonation: Effects of DEM Spatial Resolution and Slope Unit Delineation on Logistic Regression Models. *Geomorphology* **2017**, *301*, 10–20. [CrossRef]
48. UNESCO Working Party On World Landslide Inventory A Suggested Method for Describing the Activity of a Landslide. *Bull. Int. Assoc. Eng. Geol.* **1993**, *47*, 53–57. [CrossRef]
49. Lombardo, L.; Cama, M.; Conoscenti, C.; Märker, M.; Rotigliano, E. Binary Logistic Regression Versus Stochastic Gradient Boosted Decision Trees in Assessing Landslide Susceptibility for Multiple-Occurring Landslide Events: Application to the 2009 Storm Event in Messina (Sicily, Southern Italy). *Nat. Hazards* **2015**, *79*, 1621–1648. [CrossRef]
50. Lombardo, L.; Opitz, T.; Huser, R. Point Process-Based Modeling of Multiple Debris Flow Landslides Using INLA: An Application to the 2009 Messina Disaster. *Stoch. Hydrol. Hydraul.* **2018**, *32*, 2179–2198. [CrossRef]
51. Bakka, H.; Rue, H.; Fuglstad, G.; Riebler, A.; Bolin, D.; Illian, J.; Krainski, E.; Simpson, D.; Lindgren, F. Spatial Modeling with R-INLA: A Review. *WIREs Comput. Stat.* **2018**, *10*, e1443. [CrossRef]
52. Lombardo, L.; Tanyas, H.; Nicu, I.C. Spatial Modeling of Multi-Hazard Threat to Cultural Heritage Sites. *Eng. Geol.* **2020**, *277*, 105776. [CrossRef]
53. Lindgren, F.; Rue, H. Bayesian Spatial Modelling with R-INLA. *J. Stat. Softw.* **2015**, *63*, 1–25. [CrossRef]
54. Allen, M.P. The Problem of Multicollinearity. In *Understanding Regression Analysis*; Springer: Boston, MA, USA, 1997; pp. 176–180, ISBN 978-0-306-45648-0.
55. Mela, C.F.; Kopalle, P.K. The Impact of Collinearity on Regression Analysis: The Asymmetric Effect of Negative and Positive Correlations. *Appl. Econ.* **2002**, *34*, 667–677. [CrossRef]

56. Pourghasemi, H.R.; Rossi, M. Landslide Susceptibility Modeling in a Landslide Prone Area in Mazandarn Province, North of Iran: A Comparison between GLM, GAM, MARS, and M-AHP Methods. *Arch. Meteorol. Geophys. Bioclimatol. Ser. B* **2016**, *130*, 609–633. [CrossRef]
57. Petschko, H.; Brenning, A.; Bell, R.; Goetz, J.; Glade, T. Assessing the Quality of Landslide Susceptibility Maps–Case Study Lower Austria. *Nat. Hazards Earth Syst. Sci.* **2014**, *14*, 95–118. [CrossRef]
58. Brenning, A. Spatial Prediction Models for Landslide Hazards: Review, Comparison and Evaluation. *Nat. Hazards Earth Syst. Sci.* **2005**, *5*, 853–862. [CrossRef]
59. Ploton, P.; Mortier, F.; Réjou-Méchain, M.; Barbier, N.; Picard, N.; Rossi, V.; Dormann, C.; Cornu, G.; Viennois, G.; Bayol, N.; et al. Spatial Validation Reveals Poor Predictive Performance of Large-Scale Ecological Mapping Models. *Nat. Commun.* **2020**, *11*, 1–11. [CrossRef]
60. Valavi, R.; Elith, J.; Lahoz-Monfort, J.J.; Guillera-Arroita, G. Block CV: An r Package for Generating Spatially or Environmentally Separated Folds for k -Fold Cross-Validation of Species Distribution Models. *Methods Ecol. Evol.* **2018**, *10*, 225–232. [CrossRef]
61. Wadoux, A.M.-C.; Heuvelink, G.B.; de Bruin, S.; Brus, D.J. Spatial Cross-Validation Is Not the Right Way to Evaluate Map Accuracy. *Ecol. Model.* **2021**, *457*, 109692. [CrossRef]
62. Zevenbergen, L.W.; Thorne, C.R. Quantitative Analysis of Land Surface Topography. *Earth Surf. Process. Landforms* **1987**, *12*, 47–56. [CrossRef]
63. Heerdegen, R.G.; Beran, M.A. Quantifying Source Areas through Land Surface Curvature and Shape. *J. Hydrol.* **1982**, *57*, 359–373. [CrossRef]
64. Böhner, J.; Selige, T. Spatial Prediction of Soil Attributes Using Terrain Analysis and Climate Regionalisation. In *SAGA—Analyses and Modelling Applications*; Böhner, J., McCloy, K.R., Strobl, J., Eds.; Göttinger Geographische Abhandlungen: Göttingen, Germany, 2006; Volume 115, pp. 13–28.
65. Moore, I.D.; Grayson, R.B.; Ladson, A.R. Digital Terrain Modelling: A Review of Hydrological, Geomorphological, and Biological Applications. *Hydrol. Process.* **1991**, *5*, 3–30. [CrossRef]
66. Hosmer, D.W.; Lemeshow, S. *Applied Logistic Regression*, 2nd ed.; Wiley: New York, NY, USA, 2000.
67. Lacroix, P.; Handwerger, A.L.; Bièvre, G. Life and Death of Slow-Moving Landslides. *Nat. Rev. Earth Environ.* **2020**, *1*, 404–419. [CrossRef]
68. Tanyaş, H.; Kirschbaum, D.; Görüm, T.; van Westen, C.J.; Lombardo, L. New Insight into Post-seismic Landslide Evolution Processes in the Tropics. *Front. Earth Sci.* **2021**, *9*, 700546. [CrossRef]
69. Lombardo, L.; Bakka, H.; Tanyas, H.; Van Westen, C.; Mai, P.M.; Huser, R. Geostatistical Modeling to Capture Seismic-Shaking Patterns from Earthquake-Induced Landslides. *J. Geophys. Res. Earth Surf.* **2019**, *124*, 1958–1980. [CrossRef]

remote sensing

MDPI

Article

An Efficient User-Friendly Integration Tool for Landslide Susceptibility Mapping Based on Support Vector Machines: SVM-LSM Toolbox

Wubiao Huang [1,2], Mingtao Ding [1,2,3,*], Zhenhong Li [1,2,3], Jianqi Zhuang [1,3], Jing Yang [1,2], Xinlong Li [1,2], Ling'en Meng [1,2], Hongyu Zhang [1,2] and Yue Dong [1,2]

[1] College of Geological Engineering and Geomatics, Chang'an University, Xi'an 710054, China; huangwubiao@chd.edu.cn (W.H.); zhenhong.li@chd.edu.cn (Z.L.); jqzhuang@chd.edu.cn (J.Z.); 2020126052@chd.edu.cn (J.Y.); xinlong.li@chd.edu.cn (X.L.); 2020226049@chd.edu.cn (L.M.); 2021226062@chd.edu.cn (H.Z.); 2020126048@chd.edu.cn (Y.D.)
[2] Big Data Center for Geosciences and Satellites, Chang'an University, Xi'an 710054, China
[3] Key Laboratory of Western China's Mineral Resource and Geological Engineering, Ministry of Education, Xi'an 710054, China
* Correspondence: mingtaoding@chd.edu.cn

Abstract: Landslide susceptibility mapping (LSM) is an important element of landslide risk assessment, but the process often needs to span multiple platforms and the operation process is complex. This paper develops an efficient user-friendly toolbox including the whole process of LSM, known as the SVM-LSM toolbox. The toolbox realizes landslide susceptibility mapping based on a support vector machine (SVM), which can be integrated into the ArcGIS or ArcGIS Pro platform. The toolbox includes three sub-toolboxes, namely: (1) influence factor production, (2) factor selection and dataset production, and (3) model training and prediction. Influence factor production provides automatic calculation of DEM-related topographic factors, converts line vector data to continuous raster factors, and performs rainfall data processing. Factor selection uses the Pearson correlation coefficient (PCC) to calculate the correlations between factors, and the information gain ratio (IGR) to calculate the contributions of different factors to landslide occurrence. Dataset sample production includes the automatic generation of non-landslide data, data sample production and dataset split. The accuracy, precision, recall, F1 value, receiver operating characteristic (ROC) and area under curve (AUC) are used to evaluate the prediction ability of the model. In addition, two methods—single processing and multiprocessing—are used to generate LSM. The prediction efficiency of multiprocessing is much higher than that of the single process. In order to verify the performance and accuracy of the toolbox, Wuqi County, Yan'an City, Shaanxi Province was selected as the test area to generate LSM. The results show that the AUC value of the model is 0.8107. At the same time, the multiprocessing prediction tool improves the efficiency of the susceptibility prediction process by about 60%. The experimental results confirm the accuracy and practicability of the proposed toolbox in LSM.

Keywords: landslide susceptibility mapping; toolbox; SVM; automatic; multiprocessing; the whole process

Citation: Huang, W.; Ding, M.; Li, Z.; Zhuang, J.; Yang, J.; Li, X.; Meng, L.; Zhang, H.; Dong, Y. An Efficient User-Friendly Integration Tool for Landslide Susceptibility Mapping Based on Support Vector Machines: SVM-LSM Toolbox. *Remote Sens.* **2022**, *14*, 3408. https://doi.org/10.3390/rs14143408

Academic Editors: Mirko Francioni, Stefano Morelli and Veronica Pazzi

Received: 3 June 2022
Accepted: 14 July 2022
Published: 15 July 2022

Publisher's Note: MDPI stays neutral with regard to jurisdictional claims in published maps and institutional affiliations.

1. Introduction

The occurrence of landslide disasters causes great losses to the economy and human life all over the world every year [1,2]. Natural events such as rainfall [3,4], earthquakes [5,6] and floods [7] often lead to a series of landslides. Landslide susceptibility mapping (LSM) is used to determine the probability of future landslides in the study area by comprehensively analyzing various topographic, geological and hydrological factors, as well as human activity, alongside historical landslide activity in the study area [8,9]. LSM is of great significance to landslide risk management, human life safety and urban future planning.

In recent years, LSM has attracted the attention of many scholars, and various related articles have been published. The methods of generating landslide susceptibility

mapping mainly include empirical modeling based on expert experience [10,11], physically based models [12], data-driven statistical modeling [13–15] and machine learning models [16–19]. Compared with traditional methods, the machine learning models do not rely on expert experience, which reduce the subjectivity of evaluation and generally have high accuracy. With the development of geographic information system (GIS) software and open-source machine learning libraries, the machine learning methods are becoming increasingly popular.

Compared with other machine learning algorithms, the support vector machine (SVM) method has been widely used in calculating landslide susceptibility because of its advantages in solving small-sample, nonlinear and high-dimensional classification problems [5,8]. However, the process of landslide susceptibility assessment using SVM is complicated, consisting of multiple steps such as data preprocessing, influencing factor selection, dataset production, model training and prediction. Generally, when using SVM to generate LSM, researchers must work with a cross-platform. Terrain factors based on the Digital Elevation Model (DEM) (e.g., slope, aspect) rely on platforms such as ArcGIS or QGIS. Model training and parameter optimization usually adopt widely used programming languages such as Python, R or MATLAB. In addition, Excel, SPSS software or programming languages have been used for model accuracy evaluation and statistical analysis in most previous studies.

Tools related to landslide susceptibility mapping are usually available in the form of academic code, which requires users to have programming skills. Some studies have proposed and applied several tools to evaluate landslide susceptibility. Osna et al. [20] developed an independent application (*GeoFIS*) to generate landslide susceptibility maps using the Mamdani fuzzy inference system (FIS). Sezer et al. [11] developed an LSM module based on expert experience with *NetCAD* architecture software. Jebur et al. [21] created a landslide susceptibility mapping toolbox using bivariate statistical analysis (BSA) based on ArcGIS. Zhang et al. [15] provided a landslide susceptibility assessment tool based on the optimized frequency ratio method, which itself is based on the ArcGIS platform. Torizin et al. [22] provided an independent landslide susceptibility assessment application written in Python, Project Manager Suite (LSAT PM). Bragagnolo et al. [23] developed a free and open-source plug-in, namely *r.landslide*, based on the GRASS software of open-source GIS, to generate landslide susceptibility mapping based on an artificial neural network. Sahin et al. [24] integrated R and ArcGIS software and developed a landslide susceptibility mapping toolkit (LSM tool pack) based on logistic regression and random forest. Guo et al. [25] introduced a Python QGIS plugin [26] named FSLAM, which allows us to compute regional shallow landslide susceptibility based on the effective antecedent water recharge and the event rainfall.

Most of the above toolboxes are based on expert experience models or statistical models, such as the weight of evidence method, frequency ratio method and so on. These methods are simple in principle and easy to implement, but with limited accuracy. To date, only a limited number of previous studies have involved the development of landslide susceptibility mapping tools based on machine learning methods. At the same time, most tools only involve model training and prediction, instead of the whole process of LSM. In addition, most studies only use the single-factor pixel value corresponding to landslide point locations as samples for model training. However, landslides usually occur within a region and are affected by characteristics from the surrounding environment. Therefore, problems exist when constructing samples based on a single pixel [27,28]. The realization of regional-scale data construction is often complicated and time-consuming.

To solve the above-mentioned problems, this research develops an LSM toolbox based on the ArcGIS platform (SVM-LSM toolbox). The toolbox includes data preprocessing, factor selection, SVM model training and evaluation, and landslide susceptibility map prediction, involving the whole process of LSM. Moreover, this toolbox only uses the ArcGIS platform, which avoids cross-platform operation and reduces user input parameters as much as possible. The operation is simple, convenient and user-friendly. The susceptibility prediction process based on sliding windows is time-consuming. This tool

provides a multiprocessing rapid prediction tool to sufficiently improve the production efficiency of landslide susceptibility mapping. In addition, a tool for the rapid production of multi-channel block datasets is constructed to improve the efficiency of dataset making. It is worth noting that this toolbox is not limited to the mapping of landslide susceptibility based on SVM and can also be used for other binary classification problems based on SVM. Section 2 of this paper introduces the basic functions of the toolbox and a description of each module; Section 3 discusses the experimental research on the landslide susceptibility mapping of the toolbox in Wuqi County, Shaanxi Province, China, and provides an analysis of the relevant results; and Section 4 presents the conclusion.

2. LSM Toolbox

2.1. LSM Workflow

An overall flow chart of LSM based on SVM is shown in Figure 1. The process of generating LSM based on SVM consists of data collection, data preprocessing, dataset making, feature selection, model training and susceptibility map prediction. The data collection includes historical landslide data, the coverage of the study area and landslide influencing factors, such as roads, rivers, faults, Normalized Difference Vegetation Index (NDVI), DEM, lithology and rainfall. Among them, landslide points, the coverage of the study area, roads, rivers and faults are vector data, NDVI, DEM and lithology are grid data, and rainfall is the NetCDF-4 (*nc4)* format. Data preprocessing includes calculating topographic factors (such as slope, aspect, etc.) based on DEM, converting line vector data to continuous raster factors, and *nc4* data processing. For raster data, it is also necessary to clip them to the same study area range. Subsequently, based on landslide points and the range of the study area, the same number of non-landslide points are randomly selected to construct negative samples. Then, the dataset is randomly divided into training samples and test samples in the ratio of 7:3. In addition, the Pearson correlation coefficient (PCC) and information gain ratio (IGR) are calculated for all the samples. Influencing factors are selected based on the calculation results; factors with high correlations or with less importance to landslide occurrence are removed. Then, the training and test sets are reconstructed according to the results of the feature selection. Finally, the training set is used to train the model, and an optimal SVM model is obtained through the comprehensive analysis of parameters and evaluation indicators such as accuracy, precision, recall, F1 value, receiver operating characteristics (ROC) and area under the curve (AUC). The optimal model is finally used to predict the susceptibility index of the study area and generate a susceptibility map of the study area for subsequent analysis.

In this paper, a toolbox is presented to generate landslide susceptibility maps according to the above-mentioned workflow. The LSM toolbox includes three sub-toolboxes: "1 influence factor production", "2 factor selection and dataset production" and "3 model training and prediction", as shown in Figure 2. This toolbox is developed based on *ArcPy* and Python language and can be directly integrated into ArcGIS 10.1 (or higher) or ArcGIS Pro software. It is efficient and user-friendly.

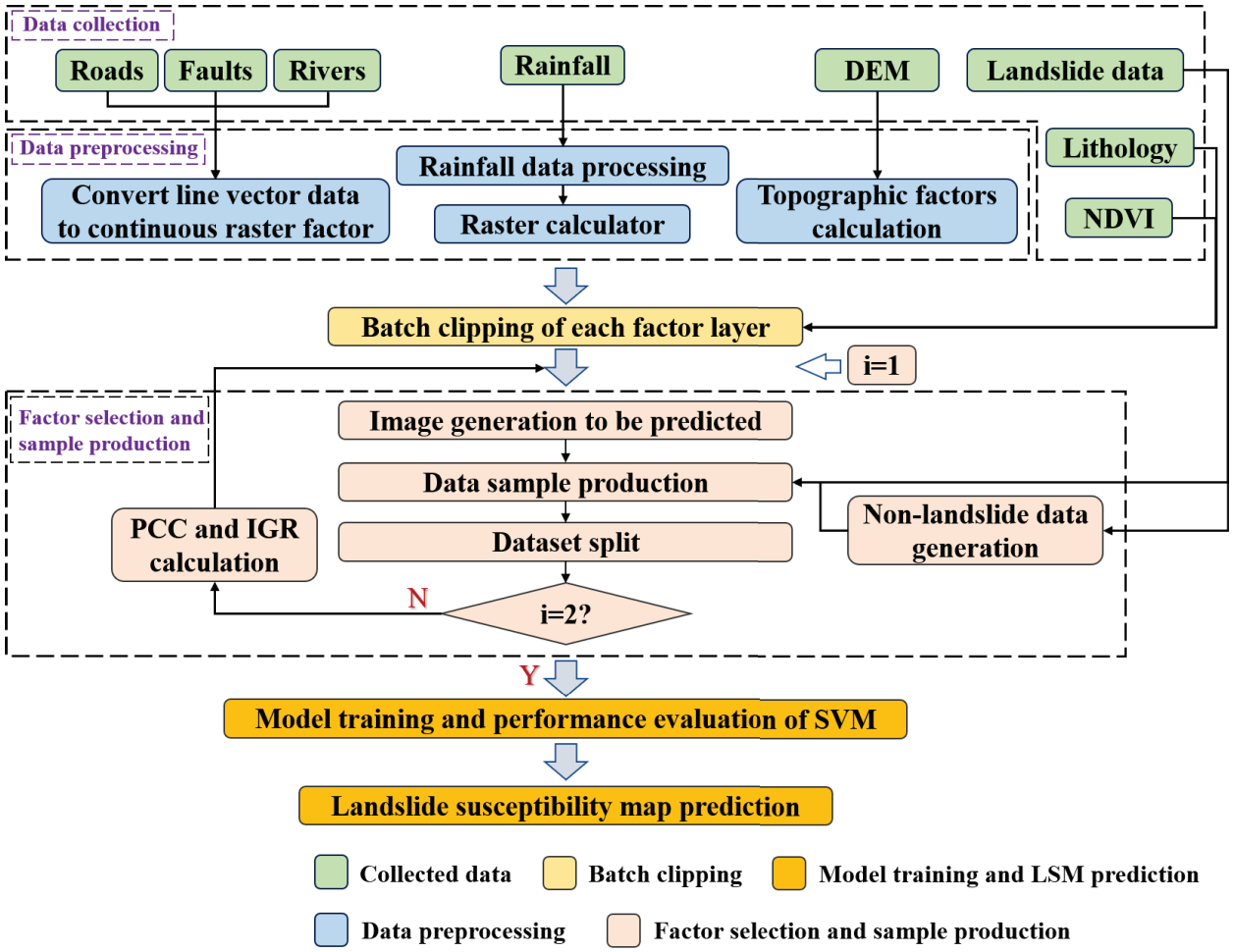

Figure 1. Flowchart of SVM-LSM toolbox.

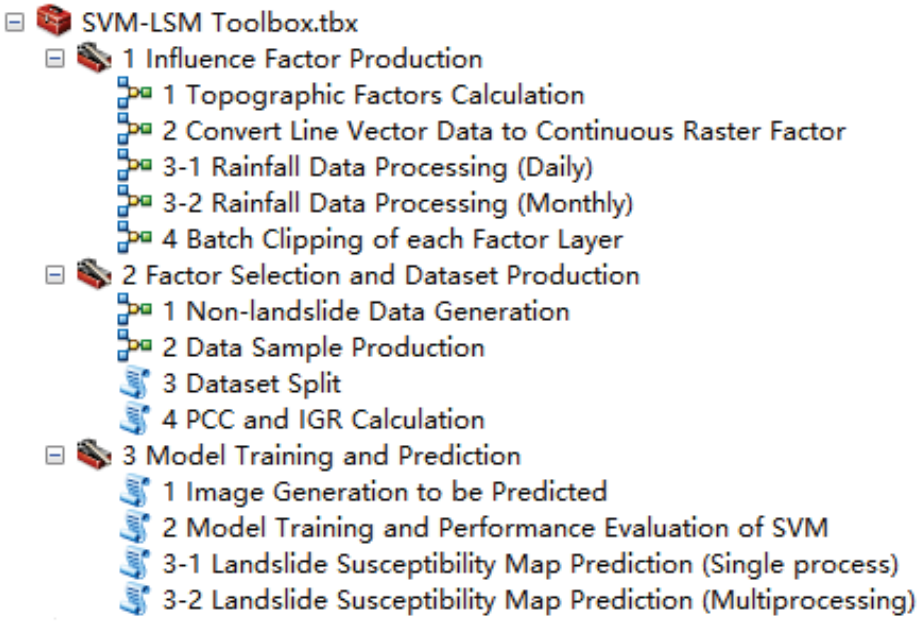

Figure 2. Overall module of SVM-LSM toolbox.

2.2. Influencing Factor Production

Landslide influencing factors are various factors that affect the occurrence of landslides through the study of the occurrence mechanism of landslides in the study area. The occurrence of landslides is affected by various influencing factors. At present, there is no unified standard for the selection of influencing factors. Pourghasemi et al. [29] conducted a statistical analysis on the influencing factors used in the study and found that topographic factors, geological factors and human activities are the most commonly used factors for landslide occurrence. This toolbox provides a tool for generating relevant topographic factors based on DEM, a tool for converting roads, faults and rivers into continuous raster data, and a rainfall processing tool.

2.2.1. Topographic Factor Calculation

This tool integrates other factors calculated by DEM, and automatically calculates other topographic factors such as slope, aspect, curvature, plane curvature, profile curvature, relief amplitude, surface roughness, topographic wetness index (TWI) and other topographic factors based on DEM data in the study area. As shown in Figure 3a, it is necessary to only input DEM data and select the factors that need to be calculated. These factors can be calculated optionally according to the needs of users by checking the box in front of the factors to be calculated, but aspect must be calculated when calculating plane curvature, and slope must be calculated when calculating profile curvature, surface roughness or TWI.

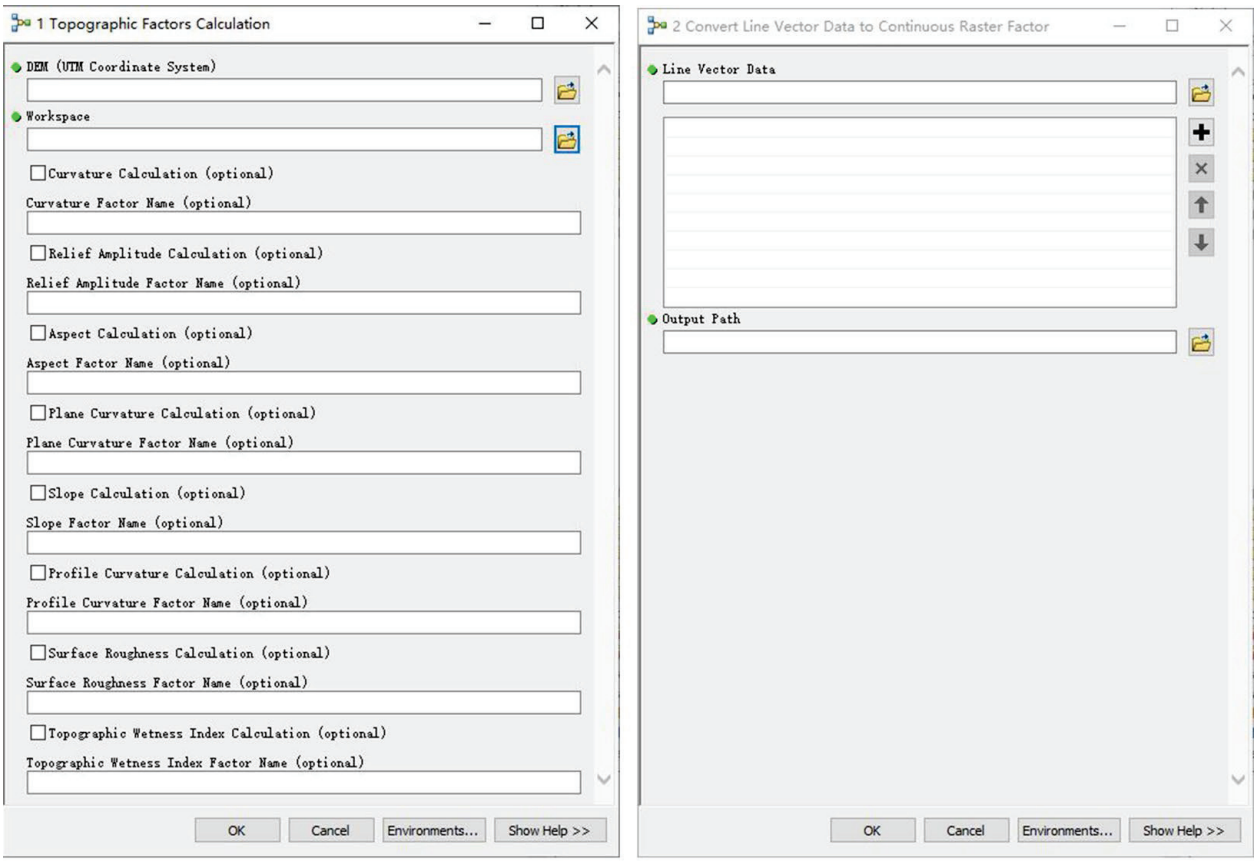

Figure 3. *Cont.*

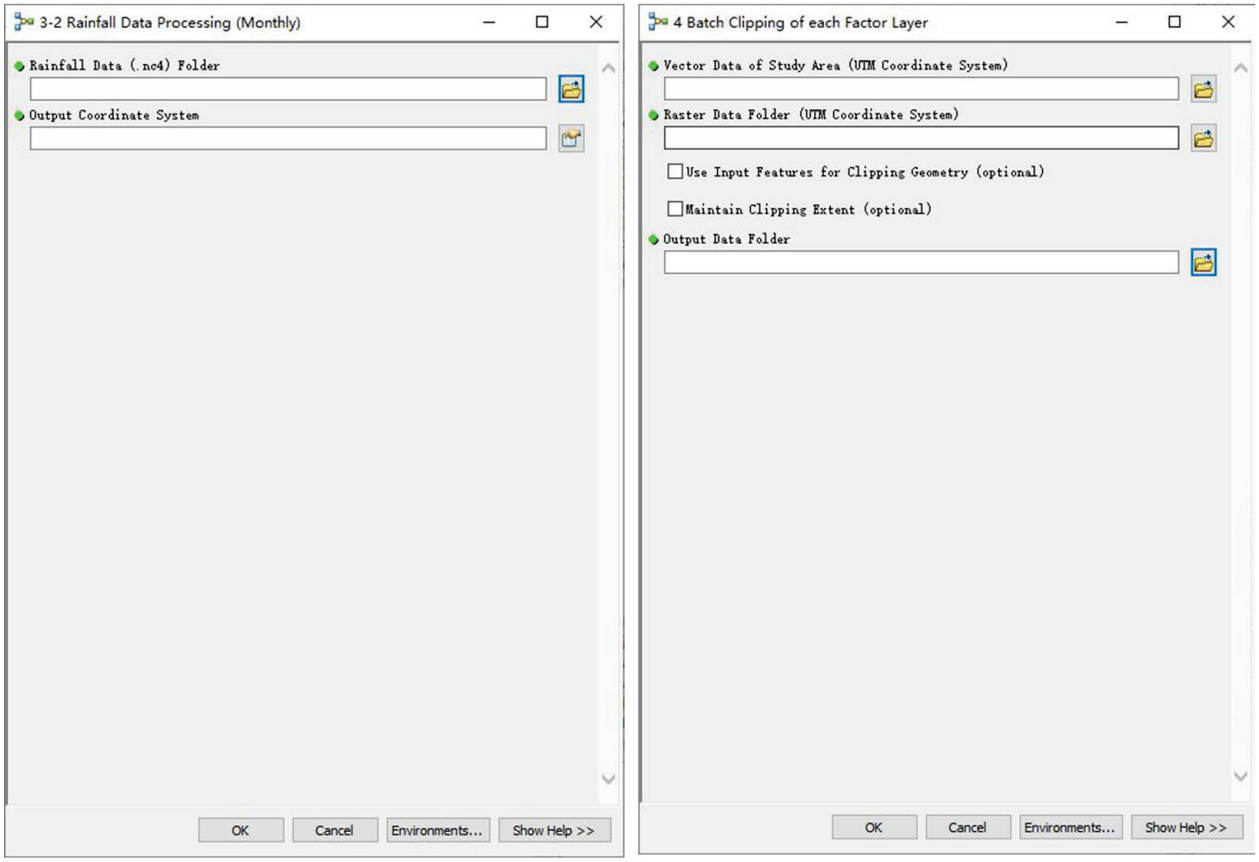

Figure 3. Influencing factor production toolbox interface: (**a**) topographic factors calculation; (**b**) convert line vector data to continuous raster factor; (**c**) rainfall data processing; and (**d**) batch clipping of each factor layer.

2.2.2. Convert Line Vector Data to Continuous Raster Factor

This tool automatically converts the line vector data of the study area into continuous raster data, such as distance to roads, distance to faults and distance to rivers. The conversion principle adopts Euclidean distance. As shown in Figure 3b, the user only needs to input the line vector data to be converted and the result save path.

2.2.3. Rainfall Data Processing

The National Aeronautics and Space Administration (NASA, https://gpm.nasa.gov/, accessed on 24 December 2020) provides a Global Precipitation Measurement Mission (GPM). These are high-precision precipitation data obtained using multi-sensors, multi-satellites and multi-algorithms combined with the satellite network and rainfall gauge inversion, with a spatial and temporal resolution up to 0.5 h, 0.1° × 0.1° [30]. The monthly or daily rainfall data downloaded from NASA are in the *.nc4* format, which is time-consuming and laborious to convert into raster data one by one. Therefore, this tool provides a rainfall batch conversion tool to convert the *.nc4* format data to the *.tif* format raster data. As shown in Figure 3c, the user only needs to input the rainfall data and specify the raster data output coordinate system.

2.2.4. Batch Clipping of Each Factor Layer

After the production of the factor layer data, the row and column numbers and coverage of each factor layer data are usually inconsistent. This tool is used to batch clip the raster data of each factor layer according to the vector data of the study area in order to obtain the factor layer data of the study area. As shown in Figure 3d, this tool only needs

the user to set the folder where the raster factors are located and the vector data of the study area; it can automatically iteratively select the *.tif* format files for clipping. All the raster data resolutions should be consistent.

2.3. Factor Selection and Dataset Production

2.3.1. Non-Landslide Data Generation

This tool is used to generate non-landslide point data within the study area vector data layer. As shown in Figure 4a, the user inputs landslide points and the study area vector file and specifies the number of non-landslide points to be selected outside of a buffer and how many meters from the landslide point. First, the tool generates a buffer zone at a specified distance from the landslide point and erases the buffer zone layer on the study area layer to obtain the selectable range of non-landslide sample points. It then uses random points to generate the same number of non-landslide points within the optional range. The non-landslide points should be selected as far from landslide points as possible.

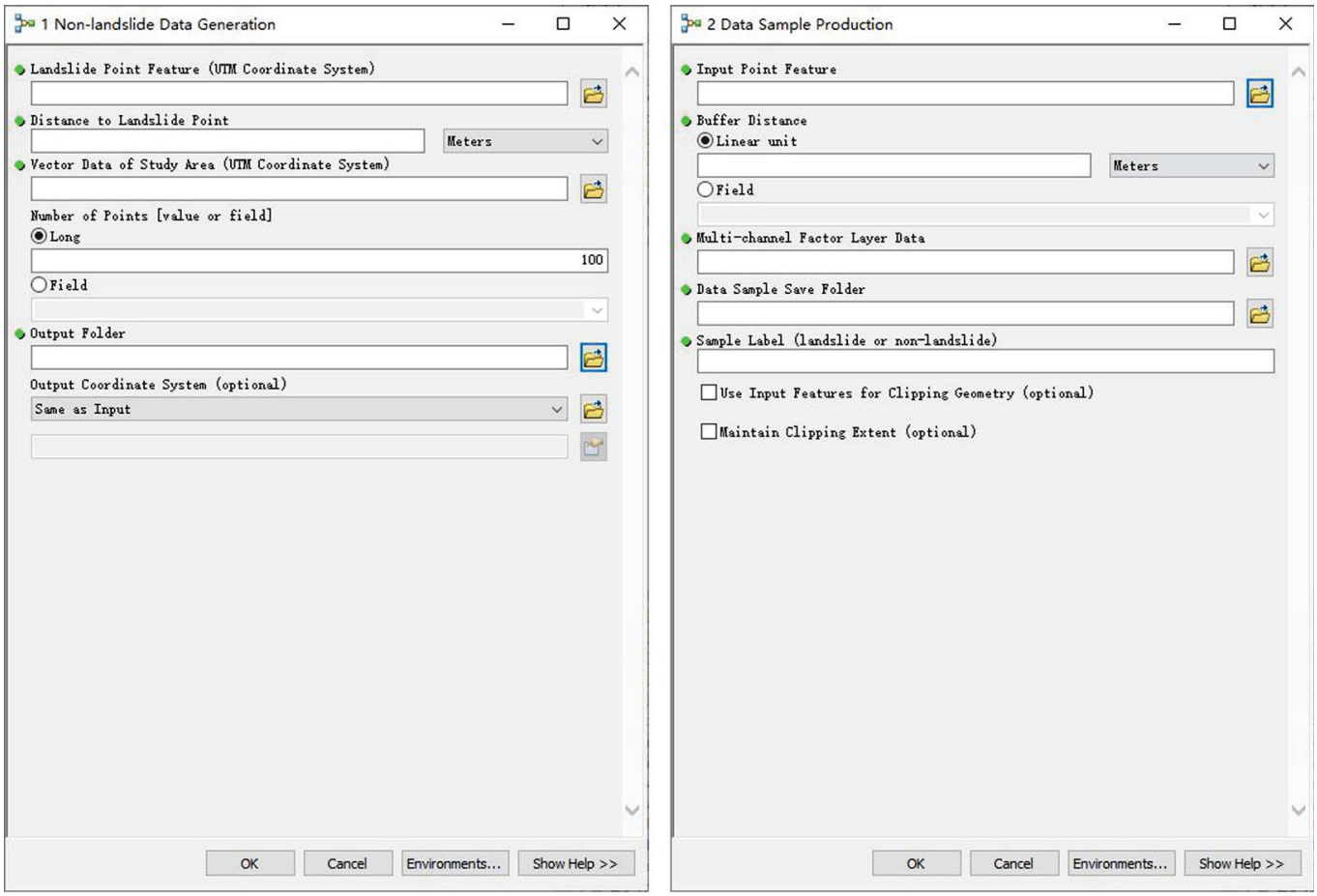

Figure 4. *Cont.*

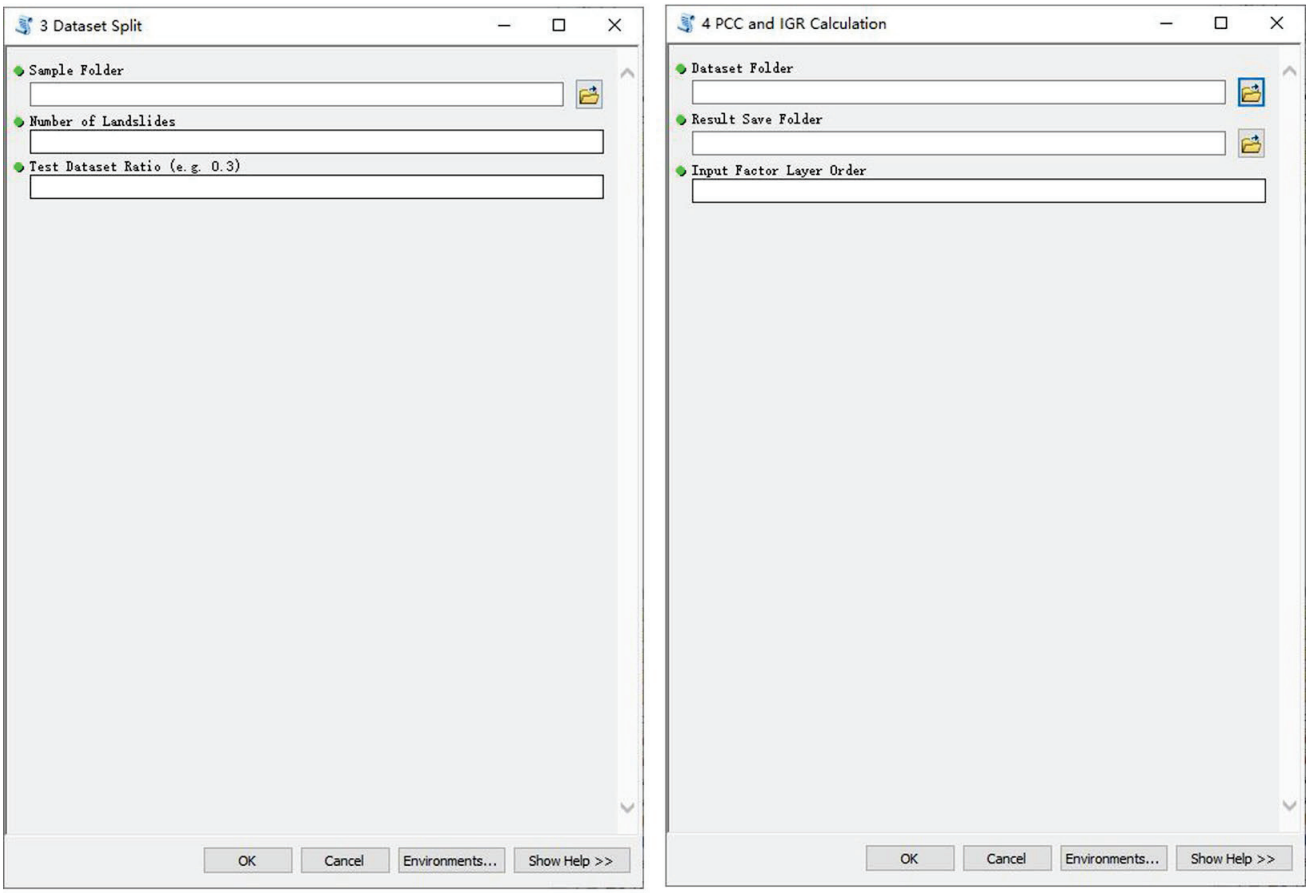

Figure 4. Dataset production and factor selected toolbox interface: (**a**) non-landslide data generation; (**b**) data sample production; (**c**) dataset split; and (**d**) PCC and IGR calculation.

2.3.2. Data Sample Production

This tool is used to generate multi-channel block sample raster data from vector point data. As shown in Figure 4b, the user inputs the vector point elements and the multi-channel factor layer data and specifies the buffer distance, which is half of the actual distance represented by the cropped raster size. The tool uses vector point data to create a buffer and iteratively selects the buffer range corresponding to each point vector in order to cut the multi-channel raster data one by one, resulting in a single multi-channel block dataset of each vector point named after the "*FID*" attribute value. When the buffer distance is less than the resolution of the raster data, the obtained sample has reached the point at which the landslide point is located.

2.3.3. Dataset Split

When using the machine learning methods for model training, it is common to split the samples into a training set and a test set in a certain ratio. The training set is used to train the model and the test set is used to test the generalization of the model and prevent overfitting. As shown in Figure 4c, users can specify the ratio of the training and test sets by themselves. Generally, the ratio of the training and test sets is 7:3. Finally, the sample paths and labels of the training and test sets will be given, respectively (0 for non-landslide and 1 for landslide), and the results are saved in a *txt* file.

2.3.4. PCC and IGR Calculation

Determining the most effective combination of the influencing factors for landslide susceptibility mapping is of great importance. If the influencing factors are not evaluated,

this will not only cause data redundancy but will also affect the execution efficiency and prediction accuracy of the model [31]. At present, there is no optimal solution for the selection of influencing factors, but they typically consist of two parts: correlation analysis and importance evaluation. This toolbox provides two of the most commonly used influencing factor selection methods: PCC and IGR. The PCC is an index used to measure the correlation between the influencing factors. The closer its absolute value is to 1, the stronger the correlation between the two factors. The information gain ratio is an index used to evaluate the importance of each factor layer on landslide occurrence. The higher the IGR value, the greater the impact of this factor on landslide occurrence. Any factor with zero IGR does not influence landslide occurrence. As shown in Figure 4d, this tool calculates PCC and IGR based on the generated data samples and saves them in a *txt* file. Upon comprehensively considering the calculation results, factors with strong correlation and little influence on landslide occurrence are eliminated based on the principle that the lower the correlation is, the greater the importance is.

2.4. Model Training and Prediction

2.4.1. Image Generation to Be Predicted

The different factor layers are stacked in a certain order to form multi-channel raster data, which is the image to be predicted. It is used for sample production and susceptibility map prediction. As shown in Figure 5a, this tool only requires the input of the path and stacking order of each factor layer. Here, the stacking order of the factor layers used for the image to be predicted should be consistent with the order of the factor layers in the model training samples.

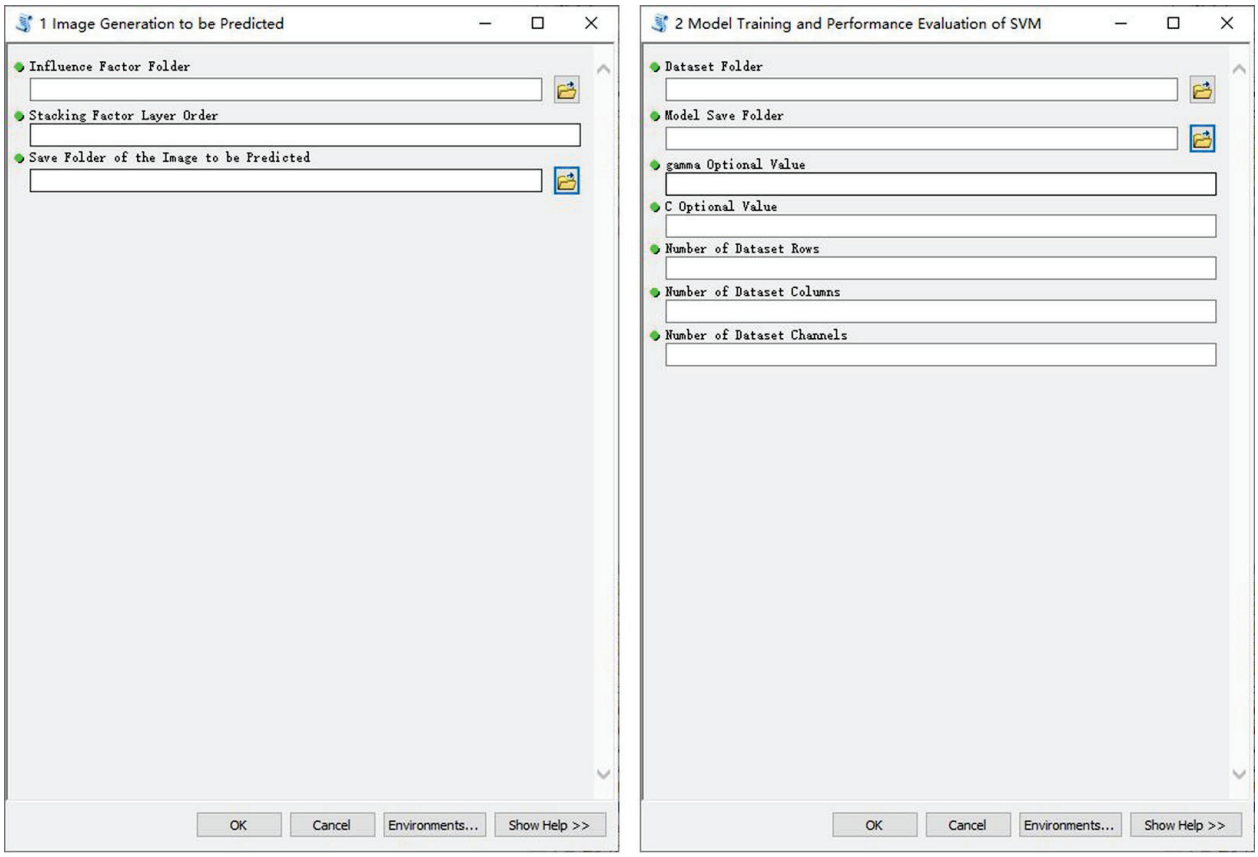

Figure 5. *Cont.*

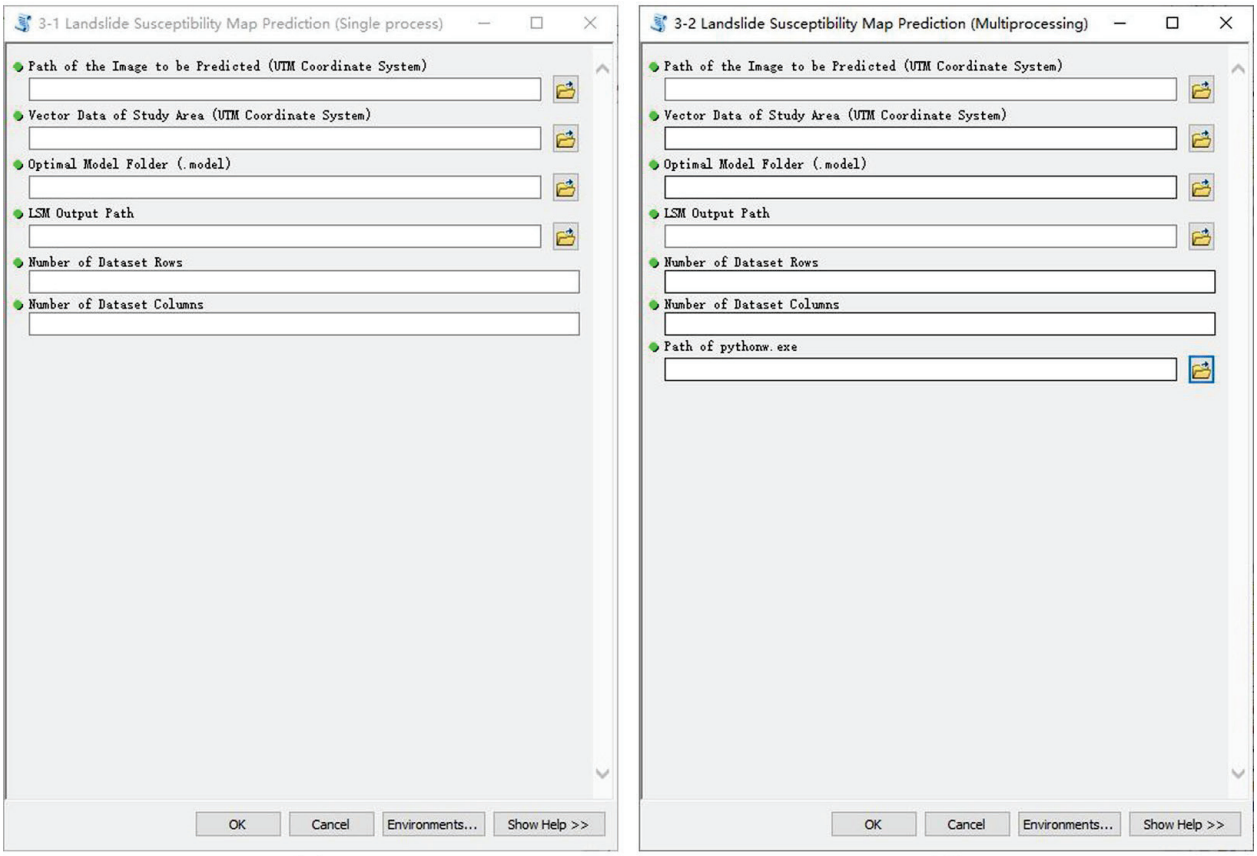

Figure 5. Model training and prediction toolbox interface: (**a**) image generation to be predicted; (**b**) model training and performance evaluation of SVM; (**c**) landslide susceptibility map prediction (single process); and (**d**) landslide susceptibility map prediction (multiprocessing).

2.4.2. Model Training and Performance Evaluation of SVM

This tool is used to generate SVM models with given parameters and provide evaluation results of the accuracy of each model. As shown in Figure 5b, the user enters the directory in which the dataset sample is located along with the number of rows, columns and channels of the dataset. At the same time, the optional values of parameter *gamma* and penalty factor *C* to be adjusted also should be given. The parameter adjustment method used in this tool is the grid search algorithm.

SVM has certain advantages in solving the problem of small-sample classification [32]. The kernel function and slack variable are used to deal with the linear indivisibility of the sample data. At the same time, because the classifier is only determined by the support vector, SVM can effectively avoid overfitting. SVM attempts to classify samples by introducing kernel functions that map landslide influencing factors to a high-dimensional feature space, from which it attempts to locate the optimal hyperplane with the maximum spacing between landslides and non-landslides from the feature space [33]. Xu et al. [5] discussed the influence of different kernel functions of SVM on landslide susceptibility mapping. The results show that the prediction effect of the radial basis function (RBF) in SVM is optimum. Therefore, the kernel function of this tool defaults to RBF.

The susceptibility map is equivalent to a binary classification problem. Landslides are marked as "1" and non-landslides marked as "0". Thus, the confusion matrix can be constructed according to different combinations of real value and predicted value, and the model accuracy evaluation index can be constructed based on the confusion matrix. In this tool, accuracy, precision, recall, *F*1 value, receiver operating characteristic (ROC) and

area under curve (AUC) were used to evaluate the prediction ability of the model. The calculation formula [6] is as follows.

$$\text{accuracy} = \frac{TN + TP}{TN + TP + FP + FN} \tag{1}$$

$$\text{precision} = \frac{TP}{TP + FP} \tag{2}$$

$$\text{recall} = \frac{TP}{TP + FN} \tag{3}$$

$$F1 \text{ value} = \frac{2 \times TP}{2 \times TP + FP + FN} \tag{4}$$

If the real result and predicted result are landslide, it is called true positive (*TP*); if the real result and predicted result are non-landslide, it is called true negative (*TN*); if the real result is landslide and the predicted result is non-landslide, it is called false negative (*FN*); if the real result is non-landslide and the predicted result is landslide, it is called false positive (*FP*).

In the ROC, false-positive rate (*FPR*) is the x-axis and true-positive rate (*TPR*) is the y-axis. At the same time, the area under the ROC (AUC) is used to quantitatively evaluate the prediction accuracy of methods. The AUC value range is [0, 1]. The larger the AUC value, the higher the accuracy of the model classification and the better the accuracy.

$$FPR = \frac{FP}{FP + TN} \tag{5}$$

$$TPR = \frac{TP}{FN + TP} \tag{6}$$

2.4.3. Landslide Susceptibility Map Prediction

This tool is used to predict landslide susceptibility in the study area, based on the optimal model, and obtain the landslide susceptibility map in the study area. In this tool, a sliding window with the same row and column numbers as the dataset is constructed to select the data to be predicted for input into the optimal model to obtain the susceptibility index until all rows and columns are sliding. The tool provides two options: single process (Figure 5c) and multiprocessing (Figure 5d). Single-process and multiprocessing tools can be used under ArcGIS and ArcGIS Pro, but the single-process tool speed is slow and the multiprocessing tool is fast. In a single process, the user must only give the image to be predicted, the optimal model and the number of rows and columns of the dataset. In multiprocessing, the user must also specify "*pythonw.exe*" location.

3. Results

Taking Wuqi County, Shaanxi Province, China as an example, the developed toolbox was applied to carry out a landslide susceptibility assessment.

3.1. Study Area

The study area is located in Wuqi County, Yan'an City, Shaanxi Province (107°38′57″E~108°32′49″E, 36°33′33″N~37°24′27″N). It covers a total area of 3791.5 km^2, encompasses a total population of 145,700 and has an altitude of 1233~1809 m. The study area has a warm, temperate, continental, semi-arid climate. It is dry and windy in spring, sees alternating drought and flood conditions in summer, is cool and wet in autumn and is cold and dry in winter, and the annual average temperature is 7.8 °C. The average annual rainfall is 483.4 mm, and the total coverage of forest and grass is 49.6%. The Wuding and Beiluo River systems lie within the study area. The landform belongs to the hilly and gully area of the Loess Plateau. The terrain fluctuates greatly, the gully is long and the slope is steep [34]. The landslide type in the study area mainly belongs to Loess landslides. During the flood

season, rainstorms or continuous rainfall will often induce landslides, collapses and debris flow of different scales, seriously threatening the lives and property safety of local people. Therefore, it is of great practical significance to carry out landslide susceptibility evaluation in Wuqi County. The location of the study area is shown in Figure 6.

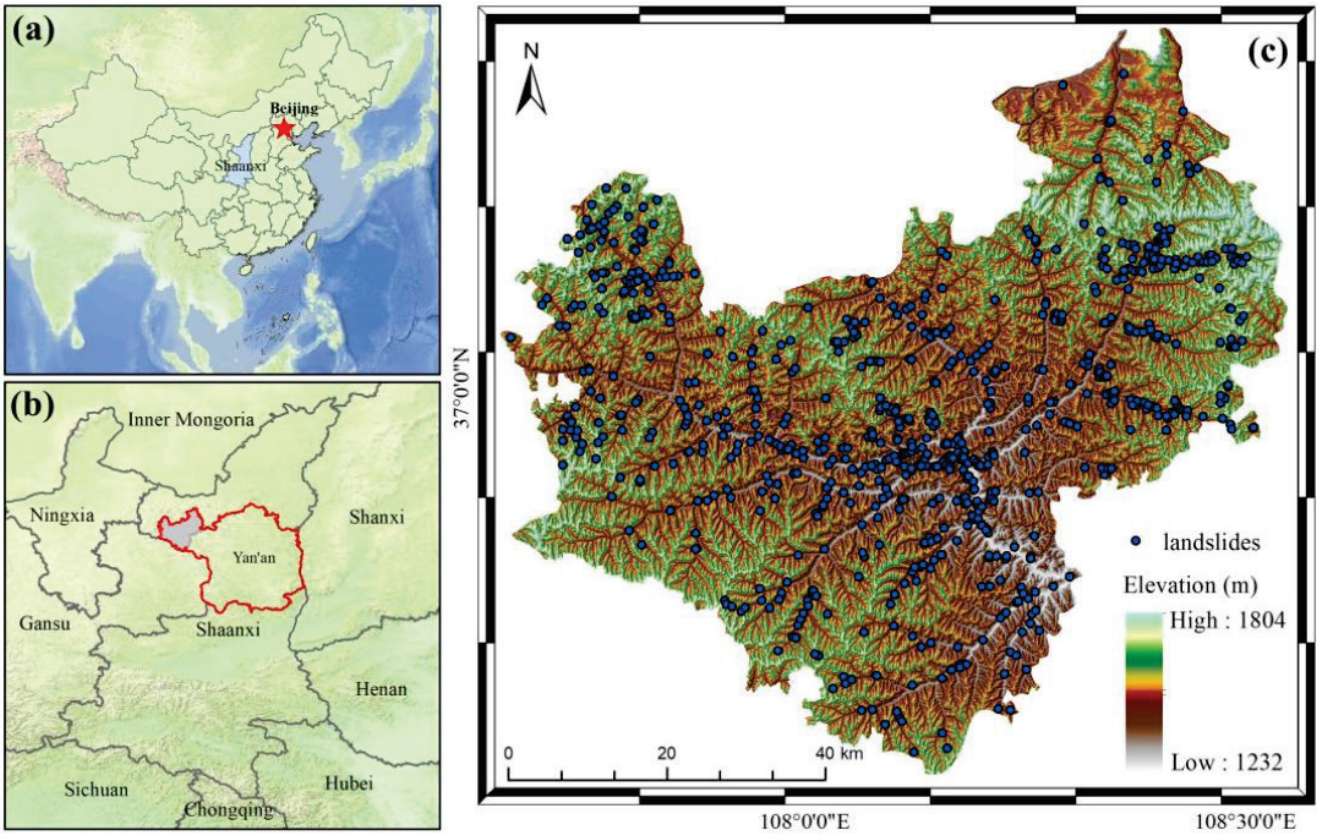

Figure 6. (**a**) Location of Shaanxi Province, (**b**) location of Wuqi County, Yan'an City, (**c**) landslide inventory mapping in Wuqi County.

3.2. Preprocessing of Influencing Factors

The influence factor data sources used in this example include DEM, roads, rivers, lithology, NDVI and rainfall. Lithology and NDVI were pre-processed into 30 m resolution raster data. For the acquired DEM data, the "topographic factor calculation" tool is used to generate slope, aspect, curvature, plane curvature, profile curvature, relief amplitude, surface roughness and a topographic wetness index (TWI). At the same time, the "convert line vector data to continuous raster factor" tool is used to produce the distance to rivers and distance to roads. Since there is no active fault in the study area and it is not affected by active faults, the distance to the fault is not considered. For the rainfall data (*.nc4*), the "rainfall data processing" tool is used to convert the monthly rainfall data obtained by NASA into the corresponding raster data in batches, and the raster calculator is used to accumulate monthly rainfall data in order to obtain annual rainfall data. Finally, the "batch clipping of each factor layer" tool is used to batch cut the generated influencing factor data according to the vector data of the study area. Finally, a total of 14 landslide influencing factors are generated (Figure 7), and the spatial resolutions of all the factor data are 30 m.

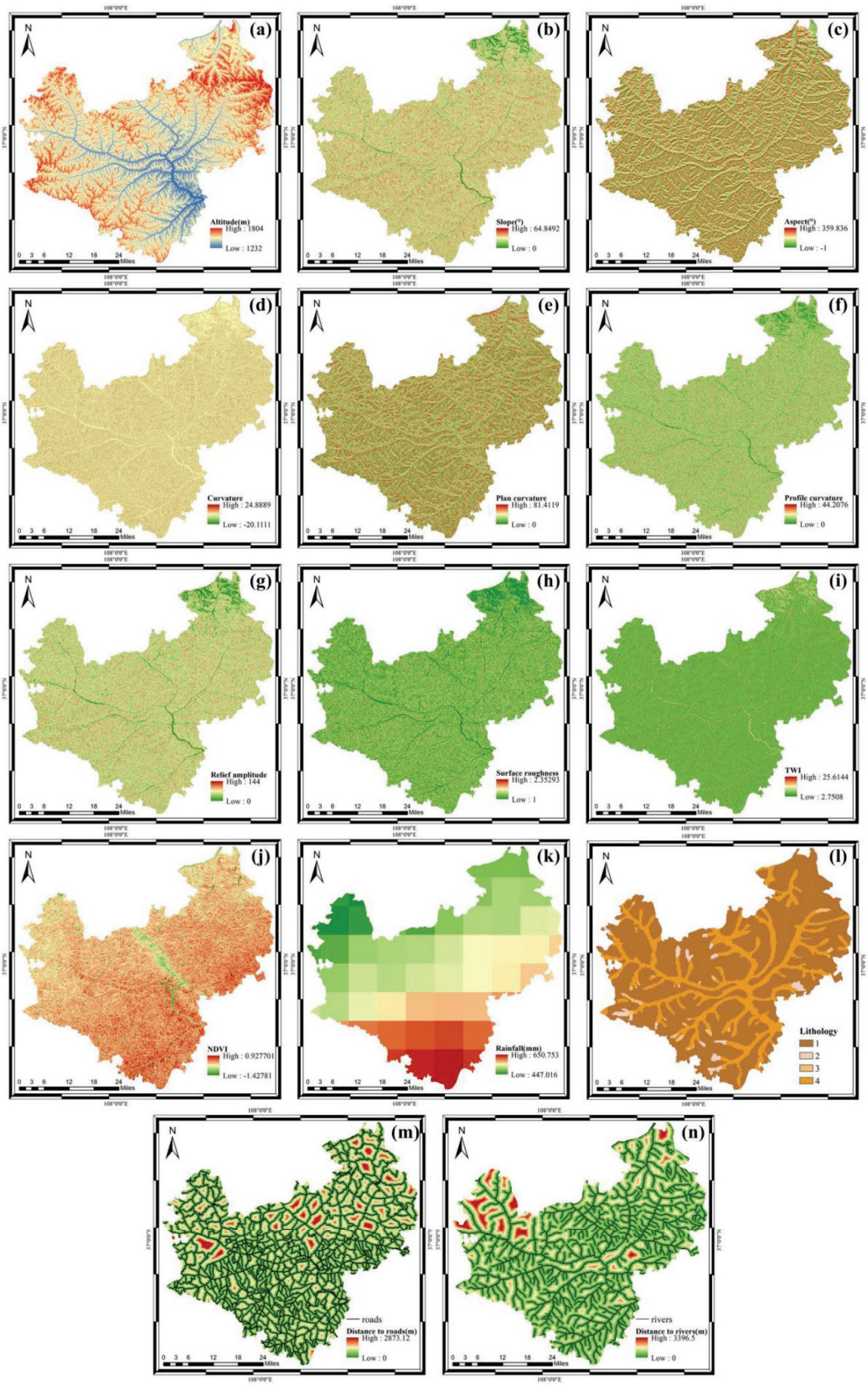

Figure 7. Landslide influencing factors in Wuqi County. (**a**) Altitude, (**b**) slope, (**c**) aspect, (**d**) curvature, (**e**) plane curvature, (**f**) profile curvature, (**g**) relief amplitude, (**h**) surface roughness, (**i**) topographic wetness index (TWI), (**j**) normalized difference vegetation index (NDVI), (**k**) rainfall, (**l**) lithology, (**m**) distance to roads, (**n**) distance to rivers.

3.3. Factor Selection and Sample Generation

There are 789 historical landslides in the study area, which can be divided into 175 large landslides, 417 medium landslides and 197 small landslides. In this study, all the landslide locations are used to construct the landslide dataset. Based on the landslide point data, the "non-landslide data generation" tool was used to randomly generate the same number of non-landslide points, each of which should be at least 1 km away from all of the landslide points in the study area.

Since the calculation of IGR and PCC must be based on all the sample data, the dataset needs to be created before the selection of influencing factors. Firstly, the "image generation to be predicted" tool is used to stack the generated data of 14 influencing factors in the study area in multiple channels. Then, the "data sample production" tool is used to make landslide and non-landslide block datasets based on the superimposed multi-channel images. In addition, the "dataset split" tool is used to divide the training samples and test samples in the ratio of 7:3, before saving the path and labels of the samples to the corresponding *txt* file, respectively. Finally, all the block datasets have fourteen channels, eight rows and eight columns. There are 1104 images in the training set and 474 images in the test set, in which the landslide dataset is marked as 1 and the non-landslide dataset is marked as 0.

After using the "PCC and IGR calculation" tool to calculate the PCC and information gain ratio of each factor layer based on the data samples, Figure 8 shows the results of the PCC calculation. It can be seen that the correlation coefficients between plane curvature and slope, TWI and slope, and relief amplitude and surface roughness are greater than 0.5. The study area is located in the hinterland of the Loess Plateau which is a typical hilly and gully landscape with high topographic fragmentation and loose soils. The reason for such strong correlations is that the study area often suffers from severe rainfall erosion and river erosion. On the one hand, the greater the slope, the more severe the soil erosion. Therefore, the more complex the surface morphology, the greater roughness and relief amplitude of the surface. On the other hand, the steep slopes with low water retention capacity lead to low soil water content (TWI), and vice versa. Figure 9 presents the calculation results of the information gain ratio. The IGR values of 14 landslide influencing factors are greater than 0, indicating that these factors have an impact on the occurrence of landslides in the corresponding areas. In this study area, lithology has the greatest impact on landslide occurrence, followed by NDVI, plane curvature, profile curvature and TWI, while curvature and relief amplitude have the least impact. Upon a comprehensive analysis of PCC and IGR, the two influencing factors of slope and relief amplitude were removed for Wuqi County, and the remaining 12 influencing factors were used for subsequent research.

According to the evaluation results, the steps of "image generation to be predicted", "data sample production" and "dataset split" should be repeated in decreasing order of information gain ratio (i.e., lithology, plane curvature, profile curvature, NDVI, TWI, aspect, surface roughness, distance to rivers, DEM, distance to roads, rainfall and curvature) to obtain the final image and sample data for further prediction. The number of channels of all the block datasets used is 12, and their row and column numbers are both eight in the subsequent analysis.

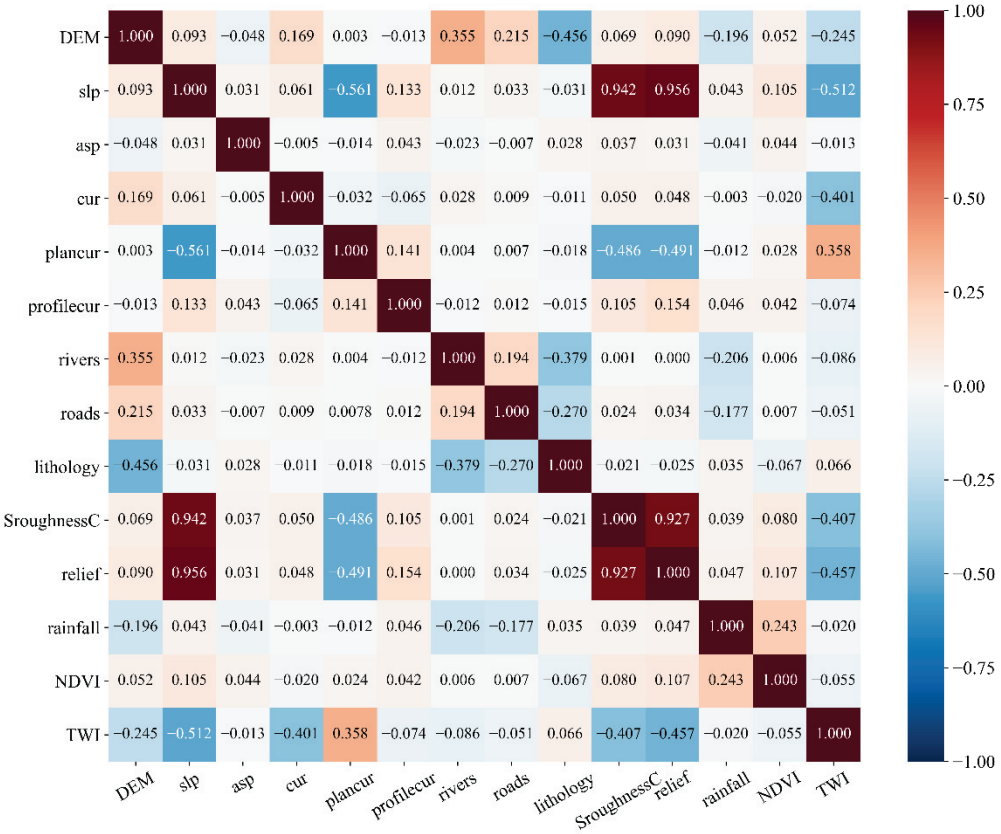

Figure 8. Pearson correlation coefficient matrix for the Wuqi County case study. Note that "slp" represents slope, "asp" represents aspect, "cur" represents curvature, "plancur" represents plane curvature, "profilecur" represents profile curvature, "rivers" represents distance to rivers, "roads" represents distance to roads, "lithology" represents lithology, "SroughnessC" represents surface roughness, "relief" represents relief amplitude, and "rainfall" represents rainfall.

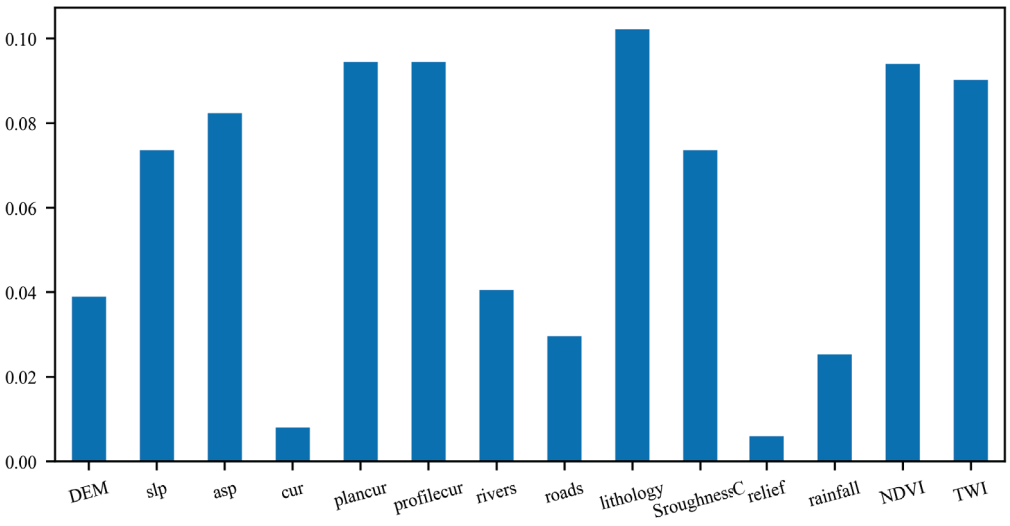

Figure 9. Information gain ratio for the Wuqi County case study. Note that "slp" represents slope, "asp" represents aspect, "cur" represents curvature, "plancur" represents plane curvature, "profilecur" represents profile curvature, "rivers" represents distance to rivers, "roads" represents distance to roads, "lithology" represents lithology, "SroughnessC" represents surface roughness, "relief" represents relief amplitude, and "rainfall" represents rainfall.

3.4. Model Training and Performance Evaluation

The "model training and performance evaluation of SVM" tool is used to train the model based on the generated training data, evaluate the performance with the test set and plot the ROC curve. Of these, the SVM model uses the RBF kernel function. The model has two parameters: *gamma* and penalty factor *C*. The grid search algorithm is used to optimize the parameters, find the optimal set of model parameters and generate the optimal model. The values of parameters *gamma* and *C* are selected from 0.01, 0.02, 0.05, 0.08, 0.1, 0.2, 0.5, 0.8, 1, 2 and 5. Figure 10 shows the AUC values and the difference in accuracy between the training and test sets for different *gamma* and *C* values, which used *gamma* values as horizontal coordinates and *C* values as vertical coordinates. In the figure, the size of the circle represents the AUC value. The larger the circle, the greater the AUC value and the better the model performance. The color of the circle represents the accuracy difference between the training and test sets. If it exceeds 0.5, it is represented by 0.5. The greater the accuracy difference, the higher the degree of overfitting of the model and the worse the generalization performance. Consequently, comprehensive analysis shows that when *gamma* is 0.02 and *C* is 2, the AUC value is high, the accuracy difference is small, and the model is optimal.

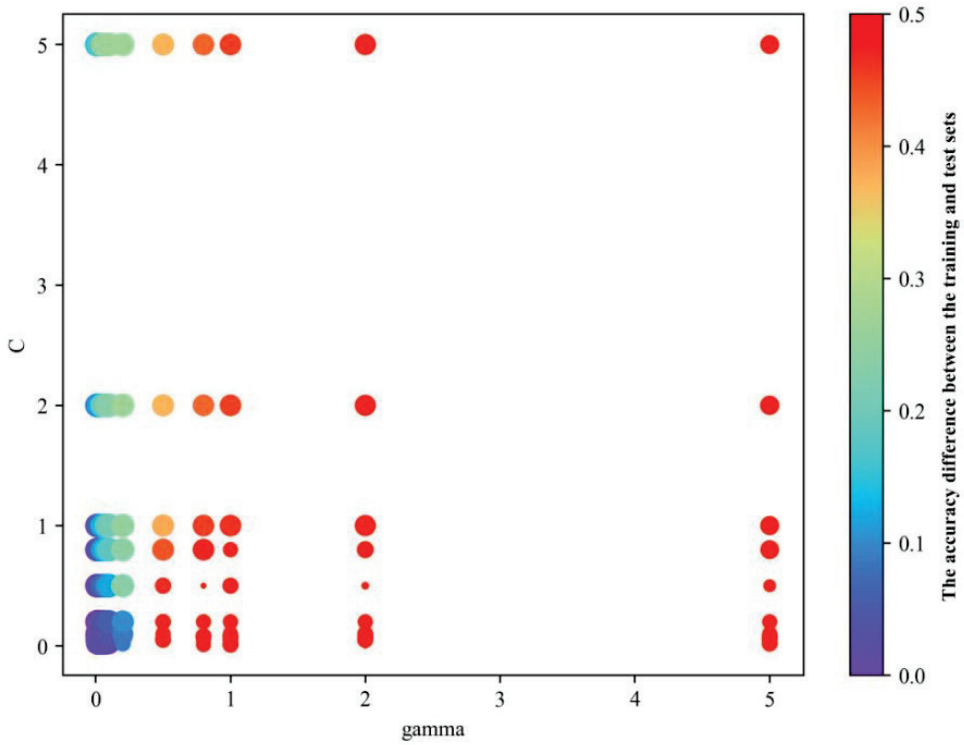

Figure 10. AUC values and accuracy differences under different parameter values.

Table 1 shows the performance of the optimal model with the testing dataset, and Figure 11 shows its corresponding ROC curve. Among the 474 testing datasets, 169 landslides and 171 non-landslides were correctly predicted, while 68 landslides and 66 non-landslides were incorrectly predicted. The correct samples predicted by the model accounted for 71.73% of the total samples, with a precision of 71.55% and a recall rate of 72.15%. At the same time, the AUC value of the model is 0.8029, indicating that the model has good prediction performance and the result of the landslide susceptibility map is reliable.

Table 1. Evaluation index of the model performance.

Evaluation Index		Results	
		Landslide	Non-landslide
Confusion matrix	Landslide	169	68
	Non-landslide	66	171
Accuracy		0.7173	
Precision		0.7155	
Recall		0.7215	
F1		0.7185	
AUC		0.8029	

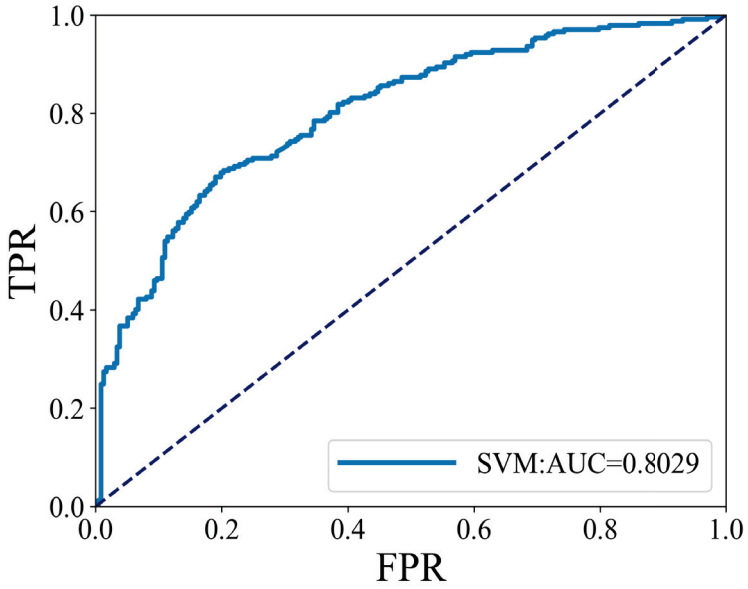

Figure 11. The ROC curve of the optimal model.

3.5. Landslide Susceptibility Map Generation and Analysis

With the trained optimal model, the "landslide susceptibility map prediction" tool is used to predict the generated image unit by unit according to the optimal model. The probability of each evaluation unit being predicted as a landslide is obtained to generate a landslide susceptibility map for the study area. The predicted susceptibility indexes lie between 0 and 1. The larger the susceptibility index is, the more susceptible the area is to landslides. The generated susceptibility map is divided into five levels—very low, low, moderate, high and very high—using the natural break method in ArcGIS. The landslide susceptibility map of Wuqi County after classification is obtained by SVM, as shown in Figure 12.

It is clear in Figure 12 that the areas in Wuqi County with high and very high susceptibility to landslides are mainly concentrated on both sides of rivers severely affected by soil erosion. Low- and very-low-susceptibility areas are mainly distributed in high-altitude areas with limited human activity. The locations of historical landslides are well fitted with the predicted results. The areas where landslides are relatively concentrated are predicted as high and very high susceptibility areas, which is in line with the actual situation. Table 2 shows the proportion of each graded area and the density of landslide points within each grade. It can be seen that the proportion of high- and very-high-susceptibility areas is 29.97%, and the proportion of low- and very-low-susceptibility areas is 49.18%. With increased susceptibility grade, the density of landslide points increases continuously, which is in line with the actual situation of the susceptibility grade. The density of landslide points in very-high-susceptibility areas is 0.77 and that in very-low-susceptibility areas is 0.04.

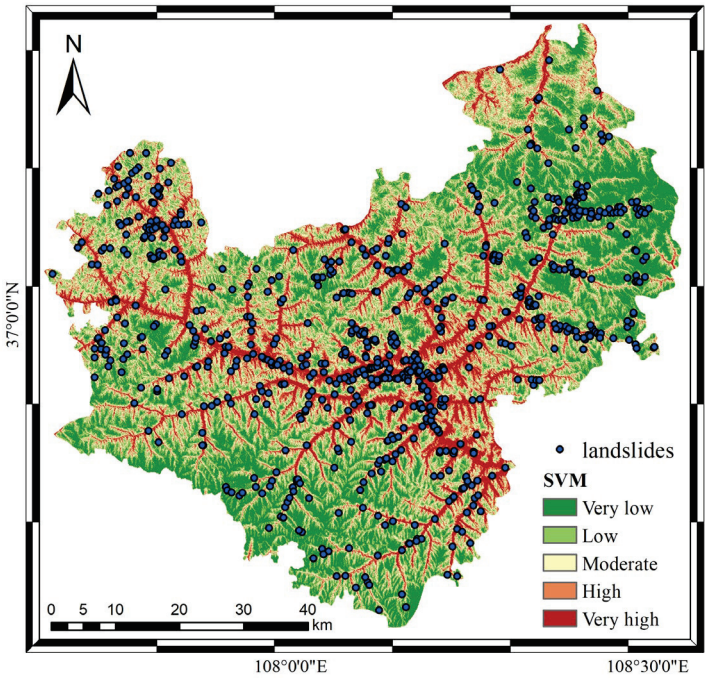

Figure 12. Classification map of landslide susceptibility in Wuqi County.

Table 2. Statistical analysis of each susceptibility class in Wuqi County.

Classes	Area (km^2)	Proportion (%)	Landslide Density (Number/km^2)
Very low	924.43	24.28	0.04
Low	948.24	24.90	0.08
Moderate	794.02	20.85	0.14
High	648.42	17.03	0.28
Very high	493.02	12.94	0.77

3.6. Toolbox Operation Efficiency Evaluation

Although the "landslide susceptibility map prediction (single process)" and "landslide susceptibility map prediction (multiprocessing)" tools can be used under ArcGIS and ArcGIS Pro, it is recommended that they be used with ArcGIS Pro. Since Python 2.7 installed in ArcGIS is generally 32-bit, it has extremely limited use of memory resources and can only use a maximum of 2G of memory when processing massive data. If it exceeds 2G, a "*Memory Error*" will appear. Meanwhile, the Python 3 environment used by ArcGIS Pro is 64-bit, which can use more memory than the 32-bit Python, and therefore the "*Memory Error*" rarely occurs.

Table 3 shows the computation statistics of various tools in ArcGIS and ArcGIS Pro software for Wuqi County, respectively. For evaluation, all the experiments are conducted on a Windows PC ×64 with a 2.30 GHz Gen Intel Core i7-11800H CPU, a 4 GB GeForce RTX 3050 Ti Laptop graphic card and 16 GB of RAM.

Table 3. Computation statistics of various tools with different software in Wuqi County.

Tool	ArcGIS	ArcGIS Pro
Topographic factor calculation	58 s	42 s
Convert line vector data to continuous raster factor	1 min 9 s	34 s
Rainfall data processing	57 s	50 s

Table 3. *Cont.*

Batch clipping of each factor layer		18 s	17 s
Non-landslide data generation		2 s	1 s
Data sample production *	landslide	5 min 22 s/4 min 46 s	4 min 34 s/4 min 29 s
	non-landslide	4 min 56 s/4 min 32 s	4 min 19 s/4 min 15 s
Dataset split *		0.5 s/0.5 s	0.5 s/0.5 s
PCC and IGR calculation		1 min 16 s	57 s
Image generation to be predicted *		3 min 38 s/2 min 45 s	1 min 32 s/1 min 13 s
Model training and performance evaluation of SVM		1 h 55 min 32 s	1 h 8 min 8 s
Landslide susceptibility map prediction (single process)		2 h 53 min 15 s	1 h 26 min 47 s
Landslide susceptibility map prediction (multiprocessing)		21 min 51 s	20 min 12 s
Total †		5 h 19 min 27 s/2 h 48 min 3 s	2 h 58 min 39 s/1 h 52 min 4 s

Notes: "Data sample production", "dataset split" and "image generation to be predicted" tools must be run twice. * indicates that the first run time and the second run time, and † shows the total single process running time and the total multiprocessing running time.

As shown in Table 3, the total time of the SVM-LSM toolbox for the ArcGIS single process is 5 h 19 min 27 s and that for the ArcGIS Pro single process is 2 h 58 min 39 s, which improves running efficiency by 44.08%. The main gap in running time is concentrated in the operation of the "susceptibility map prediction" tool. At the same time, the total time of the SVM-LSM toolbox in ArcGIS multiprocessing is 2 h 48 min 3 s and the total time in ArcGIS Pro multiprocessing is 1 h 52 min 4 s, which improves running efficiency by 33.31%. The main difference in the running time is concentrated in the step of the "model training and performance evaluation of SVM". The abovementioned two differences are mainly due to their difference in the number of bits. Therefore, it is recommended that the toolbox in ArcGIS Pro is run with 64-bit Python. In addition, under the ArcGIS platform, the running time of the "landslide susceptibility map prediction (multiprocessing)" tool is 2 h 48 min 3 s and the running time of the "landslide susceptibility map prediction (single process)" tool is 5 h 19 min 27 s, which shortens running time by nearly 2 h 31 min 24 s and improves running efficiency by 47.39%. Under the ArcGIS Pro platform, the running time of the "landslide susceptibility map prediction (multiprocessing)" tool is 20 min 12 s and the running time of the "landslide susceptibility map prediction (single process)" tool is 1 h 26 min 47 s, which shortens running time by nearly 1 h 6 min 35 s and improves running efficiency by 76.72%. This shows that the multiprocessing prediction tool for the sliding window in this tool can greatly improve the efficiency of susceptibility mapping.

3.7. Model Selection: SVM

As mentioned earlier, SVM is used in the toolbox. To assess whether it is optimal to employ SVM, comparisons with two other commonly used models, namely, decision tree (DT) and random forest (RF), are performed. Table 4 shows the operation efficiency and AUC values of different models. The DT model requires two parameters to be adjusted: *max_depth* and *min_samples_leaf*; the RF model requires five parameters to be adjusted: *max_depth*, *max_features*, *n_estimators*, *min_samples_leaf* and *min_samples_split*; and the SVM model requires two parameters to be adjusted: *gamma* and *C*. For the grid search method, the greater the number of model parameters, the higher the model training time complexity, and the more time-consuming the model tuning is. In terms of model accuracy, for the same training and testing datasets in Wuqi County, the AUC of the optimal RF model is 0.8372, the AUC of the optimal SVM model is 0.8029, and the AUC of the optimal DT model is 0.7774. The AUC values of SVM and RF model are both higher than 0.8, indicating that these two models can better reflect the landslide susceptibility in this area. Therefore, compared with the three models, the SVM model is friendlier to beginners, with fewer parameters to be adjusted, short running time and high accuracy. Therefore, we choose the SVM model to build the LSM toolbox.

Table 4. The operation efficiency and AUC values of different models.

Model	Number of Parameters	Training Time Complexity	LSM Prediction (Multiprocessing)	AUC
DT	2	$O(m*n)$	4 min 28 s	0.7774
RF	5	$O(m*n*l*k*j)$	1 h 21 min 25 s	0.8372
SVM (this study)	2	$O(m*n)$	20 min 12 s	0.8029

Notes: O represent the time complexity; m, n, l, k and j represent the number of optional values of different parameters, respectively.

4. Conclusions

This paper develops a tool known as the SVM-LSM toolbox, which integrates the whole process of landslide susceptibility mapping. The toolbox consists of three sub-toolboxes: (1) influence factor production, (2) factor selection and dataset production, and (3) model training and prediction. The tool can be integrated into ArcGIS 10.1 (or higher) as well as ArcGIS Pro. The interface is user-friendly, easy to implement and provides multiprocessing prediction, which greatly improves prediction efficiency. In order to assess the performance of the toolbox, Wuqi County (an area highly prone to Loess landslides) is selected as the study area. Six basic factors are selected and a total of fourteen landslide influencing factors are obtained based on the influencing factor production tool. In the selection of influencing factors, the slope and relief amplitude factors are eliminated according to the results of PCC and IGR. Finally, the model training tool is used to obtain the optimal model according to various evaluation indexes and generate a susceptibility map of the study area.

The results show that the model has good prediction performance and high prediction accuracy. The susceptibility areas of Wuqi County are mainly concentrated along rivers severely affected by soil erosion. In short, the SVM-LSM toolbox optimizes the complex susceptibility mapping process, avoids the cross-platform operation of traditional workflow and greatly shortens the prediction time of the susceptibility map. At present, the toolbox has only been tested with ArcGIS and ArcGIS Pro software on the Windows system. In the future, it will be integrated into other commonly used GIS processing software, such as QGIS, for expansion. Furthermore, more machine learning models can be incorporated, and automatic parameter tuning function can be developed to further improve the user-friendliness and universality of the toolbox.

Author Contributions: Conceptualization, W.H., M.D. and Z.L.; methodology, W.H. and M.D.; software, W.H.; validation, W.H., L.M. and H.Z.; formal analysis, M.D., J.Y. and W.H.; investigation, J.Z., Y.D. and X.L.; resources, W.H. and J.Y.; data curation, Y.D., L.M. and W.H.; writing—original draft preparation, W.H.; writing—review and editing, M.D., Z.L. and J.Y.; visualization, X.L. and H.Z.; supervision, Z.L.; project administration, M.D. and Z.L.; funding acquisition, Z.L. All authors have read and agreed to the published version of the manuscript.

Funding: This research was funded by the National Natural Science Foundation of China, grant numbers 41941019 and 42090053; the National Key Research and Development Program of China, grant number 2021YFC3000400; the Shaanxi Province Science and Technology Innovation team, grant number 2021TD-51; the Shaanxi Province Geoscience Big Data and Geohazard Prevention Innovation Team (2022); the Fundamental Research Funds for the Central Universities, CHD, grant numbers 300102260301, 300102261108, 300102262902, 300102269208 and 300102260404; the Fund Project of Shaanxi Key Laboratory of Land Consolidation, grant number 2019-ZD04.

Data Availability Statement: The code of the module is open-source and can be freely downloaded from https://github.com/HuangWBill/SVM-LSM-Toolbox (accessed on 2 June 2022). The case data can be applied by emailing huangwubiao@chd.edu.cn.

Conflicts of Interest: The authors declare no conflict of interest.

References

1. Koley, B.; Nath, A.; Saraswati, S.; Chatterjee, U.; Bandyopadhyay, K.; Bhatta, B.; Ray, B.C. Assessment of spatial distribution of rain-induced and earthquake-triggered landslides using geospatial techniques along North Sikkim Road Corridor in Sikkim Himalayas, India. *GeoJournal* **2022**, 1–39. [CrossRef]
2. Zêzere, J.L.; Pereira, S.; Melo, R.; Oliveira, S.C.; Garcia, R.A.C. Mapping landslide susceptibility using data-driven methods. *Sci. Total Environ.* **2017**, *589*, 250–267. [CrossRef] [PubMed]
3. Camera, C.A.S.; Bajni, G.; Corno, I.; Raffa, M.; Stevenazzi, S.; Apuani, T. Introducing intense rainfall and snowmelt variables to implement a process-related non-stationary shallow landslide susceptibility analysis. *Sci. Total Environ.* **2021**, *786*, 147360. [CrossRef] [PubMed]
4. Qi, T.; Zhao, Y.; Meng, X.; Chen, G.; Dijkstra, T. AI-Based Susceptibility Analysis of Shallow Landslides Induced by Heavy Rainfall in Tianshui, China. *Remote Sens.* **2021**, *13*, 1819. [CrossRef]
5. Xu, C.; Dai, F.; Xu, X.; Lee, Y.H. GIS-based support vector machine modeling of earthquake-triggered landslide susceptibility in the Jianjiang River watershed, China. *Geomorphology* **2012**, *145-146*, 70–80. [CrossRef]
6. Yang, X.; Liu, R.; Yang, M.; Chen, J.; Liu, T.; Yang, Y.; Chen, W.; Wang, Y. Incorporating Landslide Spatial Information and Correlated Features among Conditioning Factors for Landslide Susceptibility Mapping. *Remote Sens.* **2021**, *13*, 2166–2190. [CrossRef]
7. Costache, R.; Ali, S.A.; Parvin, F.; Pham, Q.B.; Arabameri, A.; Nguyen, H.; Crăciun, A.; Anh, D.T. Detection of areas prone to flood-induced landslides risk using certainty factor and its hybridization with FAHP, XGBoost and deep learning neural network. *Geocarto Int.* **2021**, 1–36. [CrossRef]
8. Ma, Z.; Mei, G.; Piccialli, F. Machine learning for landslides prevention: A survey. *Neural Comput. Appl.* **2020**, *33*, 10881–10907. [CrossRef]
9. Reichenbach, P.; Rossi, M.; Malamud, B.D.; Mihir, M.; Guzzetti, F. A review of statistically-based landslide susceptibility models. *Earth Sci. Rev.* **2018**, *180*, 60–91. [CrossRef]
10. Bathrellos, G.D.; Skilodimou, H.D.; Chousianitis, K.; Youssef, A.M.; Pradhan, B. Suitability estimation for urban development using multi-hazard assessment map. *Sci. Total Environ.* **2017**, *575*, 119–134. [CrossRef]
11. Sezer, E.A.; Nefeslioglu, H.A.; Osna, T. An expert-based landslide susceptibility mapping (LSM) module developed for Netcad Architect Software. *Comput. Geosci.* **2017**, *98*, 26–37. [CrossRef]
12. Medina, V.; Hürlimann, M.; Guo, Z.; Lloret, A.; Vaunat, J. Fast physically-based model for rainfall-induced landslide susceptibility assessment at regional scale. *Catena* **2021**, *201*, 105213. [CrossRef]
13. Chowdhuri, I.; Pal, S.C.; Arabameri, A.; Ngo, P.T.T.; Chakrabortty, R.; Malik, S.; Das, B.; Roy, P. Ensemble approach to develop landslide susceptibility map in landslide dominated Sikkim Himalayan region, India. *Environ. Earth Sci.* **2020**, *79*, 476. [CrossRef]
14. Li, L.; Lan, H.; Guo, C.; Zhang, Y.; Li, Q.; Wu, Y. A modified frequency ratio method for landslide susceptibility assessment. *Landslides* **2017**, *14*, 727–741. [CrossRef]
15. Zhang, Y.-x.; Lan, H.-x.; Li, L.-p.; Wu, Y.-m.; Chen, J.-h.; Tian, N.-m. Optimizing the frequency ratio method for landslide susceptibility assessment: A case study of the Caiyuan Basin in the southeast mountainous area of China. *J. Mt. Sci.* **2020**, *17*, 340–357. [CrossRef]
16. Goyes-Peñafiel, P.; Hernandez-Rojas, A. Landslide susceptibility index based on the integration of logistic regression and weights of evidence: A case study in Popayan, Colombia. *Eng. Geol.* **2021**, *280*, 105958. [CrossRef]
17. Sun, D.; Xu, J.; Wen, H.; Wang, D. Assessment of landslide susceptibility mapping based on Bayesian hyperparameter optimization: A comparison between logistic regression and random forest. *Eng. Geol.* **2021**, *281*, 105972. [CrossRef]
18. Wang, Y.; Feng, L.; Li, S.; Ren, F.; Du, Q. A hybrid model considering spatial heterogeneity for landslide susceptibility mapping in Zhejiang Province, China. *Catena* **2020**, *188*, 104425. [CrossRef]
19. Fang, Z.; Wang, Y.; Duan, G.; Peng, L. Landslide Susceptibility Mapping Using Rotation Forest Ensemble Technique with Different Decision Trees in the Three Gorges Reservoir Area, China. *Remote Sens.* **2021**, *13*, 238. [CrossRef]
20. Osna, T.; Sezer, E.A.; Akgun, A. GeoFIS: An integrated tool for the assessment of landslide susceptibility. *Comput. Geosci.* **2014**, *66*, 20–30. [CrossRef]
21. Jebur, M.N.; Pradhan, B.; Shafri, H.Z.M.; Yusoff, Z.M.; Tehrany, M.S. An integrated user-friendly ArcMAP tool for bivariate statistical modelling in geoscience applications. *Geosci. Model Dev.* **2015**, *8*, 881–891. [CrossRef]
22. Torizin, J.; Schüßler, N.; Fuchs, M. Landslide Susceptibility Assessment Tools v1.0.0b—Project Manager Suite: A new modular toolkit for landslide susceptibility assessment. *Geosci. Model Dev.* **2022**, *15*, 2791–2812. [CrossRef]
23. Bragagnolo, L.; da Silva, R.V.; Grzybowski, J.M.V. Landslide susceptibility mapping with r.landslide: A free open-source GIS-integrated tool based on Artificial Neural Networks. *Environ. Model. Softw.* **2020**, *123*, 104565. [CrossRef]
24. Sahin, E.K.; Colkesen, I.; Acmali, S.S.; Akgun, A.; Aydinoglu, A.C. Developing comprehensive geocomputation tools for landslide susceptibility mapping: LSM tool pack. *Comput. Geosci.* **2020**, *144*, 104592. [CrossRef]
25. Guo, Z.; Torra, O.; Hürlimann, M.; Abancó, C.; Medina, V. FSLAM: A QGIS plugin for fast regional susceptibility assessment of rainfall-induced landslides. *Environ. Model. Softw.* **2022**, *150*, 105354. [CrossRef]
26. Bartolini, S.; Cappello, A.; Marti, J.; Negro, C. QVAST: A new Quantum GIS plugin for estimating volcanic susceptibility. *Nat. Hazards Earth Syst. Sci. Discuss.* **2013**, *1*, 4223–4256. [CrossRef]

27. Gaidzik, K.; Ramírez-Herrera, M.T. The importance of input data on landslide susceptibility mapping. *Sci. Rep.* **2021**, *11*, 19334. [CrossRef]
28. Regmi, N.R.; Giardino, J.R.; McDonald, E.V.; Vitek, J.D. A comparison of logistic regression-based models of susceptibility to landslides in western Colorado, USA. *Landslides* **2013**, *11*, 247–262. [CrossRef]
29. Pourghasemi, H.R.; Yansari, Z.T.; Panagos, P.; Pradhan, B. Analysis and evaluation of landslide susceptibility: A review on articles published during 2005–2016 (periods of 2005–2012 and 2013–2016). *Arab. J. Geosci.* **2018**, *11*, 193. [CrossRef]
30. Stanley, T.A.; Kirschbaum, D.B.; Benz, G.; Emberson, R.A.; Amatya, P.M.; Medwedeff, W.; Clark, M.K. Data-Driven Landslide Nowcasting at the Global Scale. *Front. Earth Sci.* **2021**, *9*, 378. [CrossRef]
31. Tien Bui, D.; Ho, T.-C.; Pradhan, B.; Pham, B.-T.; Nhu, V.-H.; Revhaug, I. GIS-based modeling of rainfall-induced landslides using data mining-based functional trees classifier with AdaBoost, Bagging, and MultiBoost ensemble frameworks. *Environ. Earth Sci.* **2016**, *75*, 1101–1123. [CrossRef]
32. Awad, M.; Khanna, R. Support Vector Machines for Classification. In *Efficient Learning Machines: Theories, Concepts, and Applications for Engineers and System Designers*; Awad, M., Khanna, R., Eds.; Apress: Berkeley, CA, USA, 2015; pp. 39–66.
33. Pradhan, B. A comparative study on the predictive ability of the decision tree, support vector machine and neuro-fuzzy models in landslide susceptibility mapping using GIS. *Comput. Geosci.* **2013**, *51*, 350–365. [CrossRef]
34. Wang, S.; Zhuang, J.; Zheng, J.; Fan, H.; Kong, J.; Zhan, J. Application of Bayesian Hyperparameter Optimized Random Forest and XGBoost Model for Landslide Susceptibility Mapping. *Front. Earth Sci.* **2021**, *9*, 617. [CrossRef]

remote sensing

MDPI

Article

Enhanced Absence Sampling Technique for Data-Driven Landslide Susceptibility Mapping: A Case Study in Songyang County, China

Zijin Fu [1], Fawu Wang [1,2,*], Jie Dou [3], Kounghoon Nam [1] and Hao Ma [1]

[1] Department of Geotechnical Engineering, College of Civil Engineering, Tongji University, Shanghai 200092, China; fuzijin@tongji.edu.cn (Z.F.); soilnam@tongji.edu.cn (K.N.); mah@tongji.edu.cn (H.M.)
[2] Key Laboratory of Geotechnical and Underground Engineering of the Ministry of Education, Tongji University, Shanghai 200092, China
[3] Badong National Observation and Research Station of Geohazards, China University of Geosciences-Wuhan, Wuhan 430074, China; doujie@cug.edu.cn
* Correspondence: wangfw@tongji.edu.cn

Abstract: Accurate prediction of landslide susceptibility relies on effectively handling absence samples in data-driven models. This study investigates the influence of different absence sampling methods, including buffer control sampling (BCS), controlled target space exteriorization sampling (CTSES), information value (IV), and mini-batch k-medoids (MBKM), on landslide susceptibility mapping in Songyang County, China, using support vector machines and random forest algorithms. Various evaluation metrics are employed to compare the efficacy of these sampling methods for susceptibility zoning. The results demonstrate that CTSES, IV, and MBKM methods exhibit an expansion of the high susceptibility region (maximum susceptibility mean value reaching 0.87) and divergence in the susceptibility index when extreme absence samples are present, with MBKM showing a comparative advantage (lower susceptibility mean value) compared to the IV model. Building on the strengths of different sampling methods, a novel integrative sampling approach that incorporates multiple existing methods is proposed. The integrative sampling can mitigate negative effects caused by extreme absence samples (susceptibility mean value is approximately 0.5 in the same extreme samples and presence-absence ratio) and obtain significantly better prediction results (AUC = 0.92, KC = 0.73, POA = 2.46 in the best model). Additionally, the mean level of susceptibility is heavily influenced by the proportion of absent samples.

Keywords: presence-absence method; data-driven model; landslide susceptibility mapping; absence sampling method; integrative sampling; machine learning

Citation: Fu, Z.; Wang, F.; Dou, J.; Nam, K.; Ma, H. Enhanced Absence Sampling Technique for Data-Driven Landslide Susceptibility Mapping: A Case Study in Songyang County, China. *Remote Sens.* **2023**, *15*, 3345. https://doi.org/10.3390/rs15133345

Academic Editors: Stefano Morelli, Veronica Pazzi and Mirko Francioni

Received: 22 May 2023
Revised: 17 June 2023
Accepted: 27 June 2023
Published: 30 June 2023

1. Introduction

Landslides are devastating geological processes that frequently cause massive casualties and economic losses [1,2]. Due to their sudden occurrence, fast movement, and strong impact, landslides pose a serious threat to traffic, buildings, and residents, especially in well-developed mountainous areas. Therefore, accurate landslide forecasting is of paramount importance. In recent years, with the rapid development of 3S technology (remote sensing, geographic information system, and global positioning system), tremendous progress has been made in remote sensing for landslides, covering aspects of landslide detection, monitoring, and hazard assessment and prediction [3–5]. Landslide susceptibility mapping (LSM), which predicts the spatial probability of landslide occurrence under certain environmental conditions in an area, represents important regional landslide research work [6].

In an era of rapid development in computer science and GIS technology, various methods have been proposed for LSM. These methods can be categorized into three groups:

knowledge-based methods, physical methods, and data-driven methods [7]. While the subjectivity of expert knowledge is too strong and the wide-area parameters in physical models possess uncertainty, data-driven methods have more objective results and higher efficiency. Data-driven methods have been widely studied and applied in LSM. The kernel idea of data-based methods is to find a certain relationship by means of data science, relying on a landslide inventory and conditioning factors database. Researchers have developed and applied data-based models in LSM, including bivariate and machine-learning methods [8,9]. The classic and widely used bivariate methods include IV, certainty factor (CF), frequency ratio (FR), and fuzzy logic (FL). There are various types of machine learning models, such as logistic regression (LR), decision tree (DT), random forest (RF), support vector machine (SVM), Bayes, K-Nearest Neighbor (KNN), and artificial neural networks (ANN), as well as more complex models such as auto-encoder [10–15]. Data-driven methods in LSM can be further classified into two groups: presence-absence methods and presence-only methods [16]. The first group needs both landslide presence samples and landslide absence samples. The other group of methods needs only landslide samples, such as bivariate classification.

Sampling strategy, which involves using this acquired data to get a better prediction effect in LSM, is an important issue. The samples used for LSM prediction are usually divided into a training set and a testing set. For most machine learning methods in LSM, this includes presence and absence samples. Extracting and dividing these samples from a map are fundamental steps in LSM. The quality of the samples used for model training significantly impacts the performance of a data-driven model [17]. The presence samples (landslides) in LSM are usually generated from a landslide inventory map produced by field investigations and the interpretation of aerial photos or remote sensing images [18,19]. For the presence sampling locations, there are some commonly used sampling strategies, including the landslide scarp centroid, the centroid of the landslide body, the whole scarp polygon region, and the entire landslide body [20,21]. Different from the present samples, absence samples cannot be obtained directly. Therefore, studying the uncertainty of absence samples is particularly important for data-driven LSM.

Three strategies are commonly employed for absence sampling in current LSM research: geographic generation, feature-based generation, and generation from a prior model [22]. In geographic generation, common methods include random sampling (selection from randomly distributed circular zones) and buffer-controlled sampling (sampling from grid cells outside landslide buffer zones) [23], or selecting samples from areas where landslides are not likely to occur, such as a plain (based on expert judgment) [24,25]. Among these methods, buffer control sampling is the most frequently used [26]. However, this method does not guarantee that the selected area is free from potential landslides or has environmental parameters similar to landslides, either of which reduces the quality of the samples and has a negative influence on the accuracy of the LSM. Some studies aim to reduce the uncertainty associated with randomly selected samples in geographic space to improve the quality of absence samples [27]. In a feature-based generation, the theoretical foundation is the third law of geography, which states that landslides and non-landslides should be separated as much as possible in their feature space. Absence sampling from low-slope areas is an intuitive approach in a feature-based method, but the slope factor is overly magnified because of subjectivity. Some optimized absence sampling methods have been proposed, including target space exteriorization sampling (TSES) and similarity-based methods such as mahalanobis distance, bioclim, domain, and other improved similarity algorithms [22,28–30]. These methods select or create absence samples based on the feature space rather than the geographic space, enhancing the reliability of absence samples. TSES fabricates absence samples by modifying one or more features of a presence sample dataset into random values in the exteriorization feature space; these absence samples, produced in feature space, are not necessarily in geographic space and have some connection with the presence samples. Similarity-based methods select absence samples from the research area through quantitative indicators of similarity to landslide features. Another approach

to improving the quality of absence samples is through generation from a prior model, where absence samples are extracted from the low susceptibility zone of the prior model. In LSM, the scenario where labels are available only for landslide samples corresponds to a positive, unlabeled learning problem. The presence-only model is a suitable method for positive-unlabeled learning as a prior model. Presence-only models such as IV and CF are widely applied in hybrid models, such as CF-LR, CF-SVM, CF-RF, LV-LR, IV-SVM, and IV-RF, by combining with a presence-absence model [31–34], but most of these methods use only the output parameters of the presence-only model as the input parameters of the presence-absence model. In fact, the bridge between the two methods can also be built on samples. Research shows that a presence-only method may overestimate the susceptibility of landslides [16,29]. When regional susceptibility is overestimated, it is easier to expose low susceptibility zones from which absence samples can be selected with greater certainty. Some studies have used presence-only as an a priori model for the extraction of missing samples and obtained good prediction results [35,36]. Furthermore, the combination of presence-only methods with unsupervised learning has been explored to further enhance the absence sampling strategy [37]. The two-step approach is also an algorithm for solving the absence sample problem; it trains a prior model with presence samples and unlabeled samples to identify reliable absence samples [38]. Following similar concepts, a multiple-layer perceptron model and a two-step approach based on deep neural networks have been applied in some LSM studies [39–41].

In the field of landslide susceptibility prediction, absence sampling plays a crucial role. However, existing studies often overlook the quality of absence samples in absence sampling methods, leaving the impact of absence sample quality on landslide susceptibility prediction understudied. It is essential to conduct comparative studies using different methods and quality control measures to select appropriate absence sampling methods and ensure the quality of absence samples. Moreover, many LSM studies tend to focus solely on prediction performance scores, neglecting the importance of assessing the reasonableness of landslide susceptibility prediction results. This oversight can lead to disregarding the negative effects of selected absence samples. Therefore, it is necessary to establish a comprehensive and valid evaluation system for absence samples in order to consider their applicability. On this basis, an absence sampling method with strong applicability considering the quality of different methods needs to be proposed.

In this paper, four absence sampling methods are investigated, and an integrative sampling method is proposed based on the fusion of these methods for a data-driven LSM model. In order to control the quality of absence samples, a controlled target space exteriorization sampling (CTSES) method based on improved TSES is proposed. A less commonly used optimization clustering algorithm, mini-batch K-medoids (MBKM), is employed as a prior model. The sampling methods include BCS, CTSES, IV, and MBKM, as well as a novel integrative sampling. Sampling intervals were established for each method, and extensive training was conducted to investigate the effects of absence samples from different sources and of varying quality on LSM. SVM and RF models are applied as predictive models for LSM in Songyang County, Lishui City, Zhejiang Province, China, where five absence sampling methods were tested.

2. Materials

2.1. Study Area

The study area is Songyang County, which is located in the southwest of Zhejiang Province and northwest of Lishui City. The geographical coordinates are 119°10′0″E to 119°42′42″E, 28°14′23″N to 28°36′15″N. The largest diameter from north to south is 40.2 km, with a total area of about 1404 square kilometers. Figure 1 presents the location of the study area.

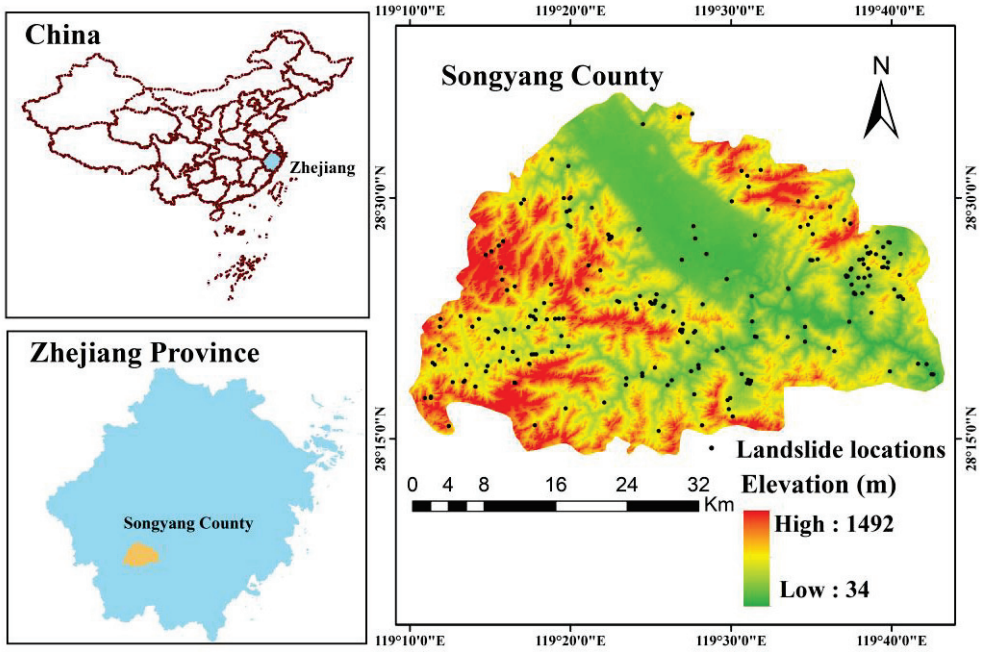

Figure 1. Geographical location of Songyang County.

Songyang County is located in the mountainous region of southern Zhejiang Province. The topography primarily consists of medium and low hills surrounded by mountains, with an open central basin known as "Songgu Basin". The terrain is higher in the northwest and lower in the southeast. The county has obvious layers of landforms, including accumulation landforms, erosion and denudation landforms, and structural erosion landforms. The lithology formation includes rhyolite, tuff, gneiss, granite, sandstone, quartz sandstone, and Quaternary sediments. Faults dominate the geological structure of the Songyang area, with over 30 large and small fault zones identified. Most of these faults align in the NNW and NNE directions, with the NNE fault belonging to the Yuyao-Lishui fault system, which is a deep fault traversing the lithosphere. This fault system formed in a tensioning process in the Cretaceous, with a strike of about 30° and 350 km in Zhejiang Province, and it runs through Songyang County [42,43]. The multistage tectonic activity that occurred in the ancient fault zone has resulted in the formation of a compressive fault zone, which spans 4–30 km in width. The fault zones in Songyang County exhibit intricate tectonic activities and fractured internal rock mass structures, significantly influencing the local geological and geomorphic environment and impacting the stability of the original slope [44]. The seismic peak acceleration in Songyang County is within the range of 0.05 g, indicating a stable crustal zone.

Songyang County is situated in a subtropical monsoon region characterized by a mild climate, abundant rainfall, and distinct seasonal variations, with notable variations in vertical climate. The annual precipitation is 1700 mm, with the period from March to June receiving the highest amount of rainfall, averaging 816.8 mm annually. November experiences the lowest rainfall, 40–50 mm. Additionally, the southeast coastal area is prone to frequent typhoon occurrences, with Songyang County being affected by an average of one to three typhoons each year. From 2015 to 2020, the county experienced the impact of several typhoons, including Sudillo, Moranti, Likima, and Hagupe. Each of these typhoons resulted in increased rainfall and triggered numerous landslides as they passed through the area. The rivers in Songyang County are part of the Oujiang River Basin. Songyin Creek and Xiaogang Creek meander from the northwest and southwest directions, respectively, toward the southeast. The area is characterized by a dense development of tributaries and numerous river valleys. During the rainy season, the water level of the rivers rises sharply.

2.2. Landslide Inventory

A landslide inventory is an important dependent variable in a calculation model and has a great influence on the accuracy of prediction results. In recent years, landslides have continued to occur in the study area. According to a relevant landslide survey report and remote sensing interpretation, 217 landslides were identified in the study area. These landslides occurred between 2000 and 2021, and the years with the most frequent occurrence were 2010, 2012, 2014, and 2016, which were also the years when Songyang County was severely affected by heavy rainfall/typhoons, and other catastrophic effects.

Landslides in Songyang County are divided into soil landslides and rock landslides, with soil landslides being the predominant type (Figure 2). The compositions of landslide masses are generally uniform, composed mainly of silty clay with gravel and a sandy, completely weathered layer in the metamorphic rock and granite distribution area. The thicknesses of landslide masses are generally small, ranging from 1 to 5 m. The volume sizes of landslides are generally below 10,000 m^3; about half of the landslides are less than 1000 m^3, while several reach 100,000 m^3. The smaller ones can measure tens of cubic meters. The soil within the sliding zone is often soft plastic powdery clay, and the sliding bed is often the underlying bedrock or a relatively denser rock-soil layer. From the perspective of a plane, landslides tend to exhibit generally semi-elliptical, tongue-shaped, or wide fan-shaped patterns, with the semi-elliptical shape being the most common. From the perspective of the longitudinal section, landslides primarily appear as linear or stepped features. The transition zone is where the terrain slope changes from steep to gentle, and the upper slope is mostly above 25°. According to an analysis of landslide triggering, fragile geological conditions are the primary causes. Additionally, extreme rainfall and human engineering activities (excavation, slope cutting, plowing, etc.) have created a landslide breeding environment.

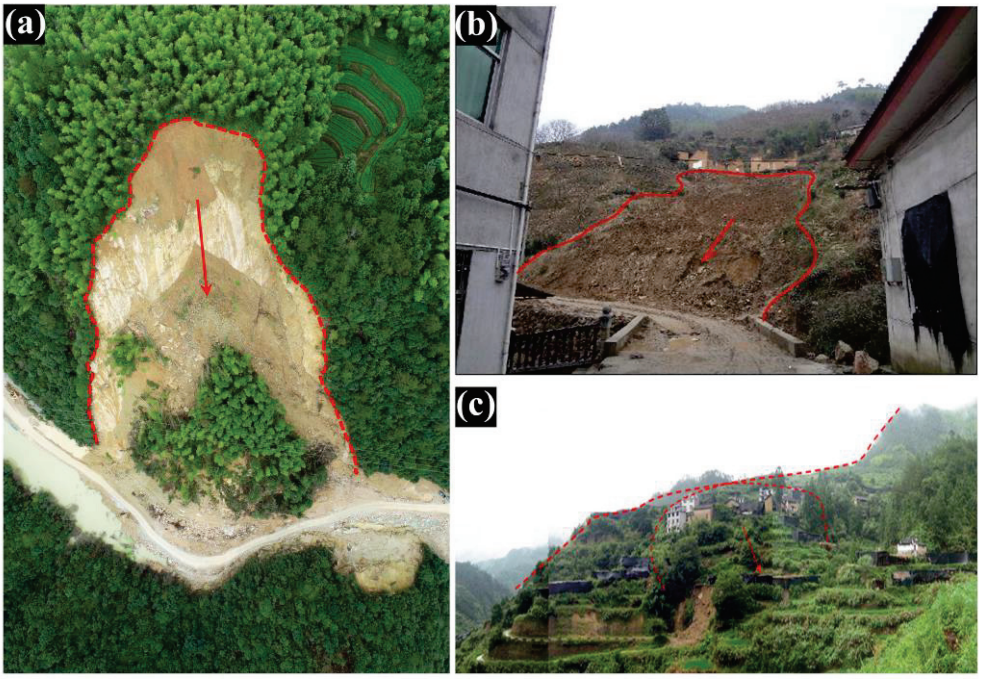

Figure 2. Typical landslides in Songyang County. (**a**) Chengtian landslide; (**b**) Xiangxi town landslide; (**c**) potential landslide in Fanshantui, Shaqiu Village. The red lines indicate the geometric boundary of the landslides and the arrow indicates the direction of the main slide.

2.3. Landslide Conditioning Factors

Factors affecting landslides can be divided into two categories: internal disaster-forming conditioning factors and external triggering factors. In this study, a total of 16 parameters were considered as potential conditioning factors for landslides, including elevation, slope, aspect, plan curvature, profile curvature, topographic roughness index (*TRI*), topographic wetness index (*TWI*), sediment transport index (*STI*), normalized difference vegetation index (*NDVI*), lithology, rainfall, distance to faults, distance to river network, distance to road, land use, and soil type (Figure 3). The grouping methods employed subjective division (for factors that are more subjective) and natural breaks (for factors that are more objective). The sources of all indicators are shown in Table 1. The formula for the relevant metrics is shown below:

$$TRI = \frac{A_{mean} - A_{min}}{A_{max} - A_{min}} \tag{1}$$

where the A_{mean}, A_{min}, and A_{max} indicate the mean, minimum, and maximum values of all cells in a 3 × 3 cell, respectively.

$$TWI = \ln \frac{A_s}{\tan \beta} \tag{2}$$

$$STI = \left(\frac{A_s}{22.13}\right)^{0.6} + \left(\frac{\sin \beta}{0.0896}\right)^{1.3} \tag{3}$$

where A_s and β indicate the specific catchment area (m^2/m) and slope gradient, respectively.

$$NDVI = \frac{NIR - Red}{NIR + Red} \tag{4}$$

where NIR is the reflection value in the near infrared band, and Red is the reflection value in the red band.

Table 1. Data sources of conditioning factors.

Conditioning Factor	Variable Type	Spatial Resolution (m)	Production Time (year)	Data Source
Altitude	Continuous	30	2009	ASTER GDEM 30M
Slope	Continuous	30	2009	Derived from DEM
Slope aspect	Continuous	30	2009	Derived from DEM
Plan curvature	Continuous	30	2009	Derived from DEM
Profile curvature	Continuous	30	2009	Derived from DEM
TRI	Continuous	30	2009	Derived from DEM
TWI	Continuous	30	2009	Derived from DEM
STI	Continuous	30	2009	Derived from DEM
Lithology	Discrete	30	2019	[41]
Distance to faults	Continuous	30	2019	[41]
Soil type	Discrete	30	2005	https://www.resdc.cn/ (accessed on 1 May 2022)
Annual rainfall	Continuous	30	2000–2021	http://data.cma.cn/ (accessed on 1 May 2022)
Distance to stream	Continuous	30	2021	https://lbs.amap.com/ (accessed on 1 May 2022)
Distance to road	Continuous	30	2021	https://lbs.amap.com/ (accessed on 1 May 2022)
Land use	Discrete	30	2020	https://www.resdc.cn/ (accessed on 1 May 2022)
NDVI	Continuous	30	2021	Landsat8

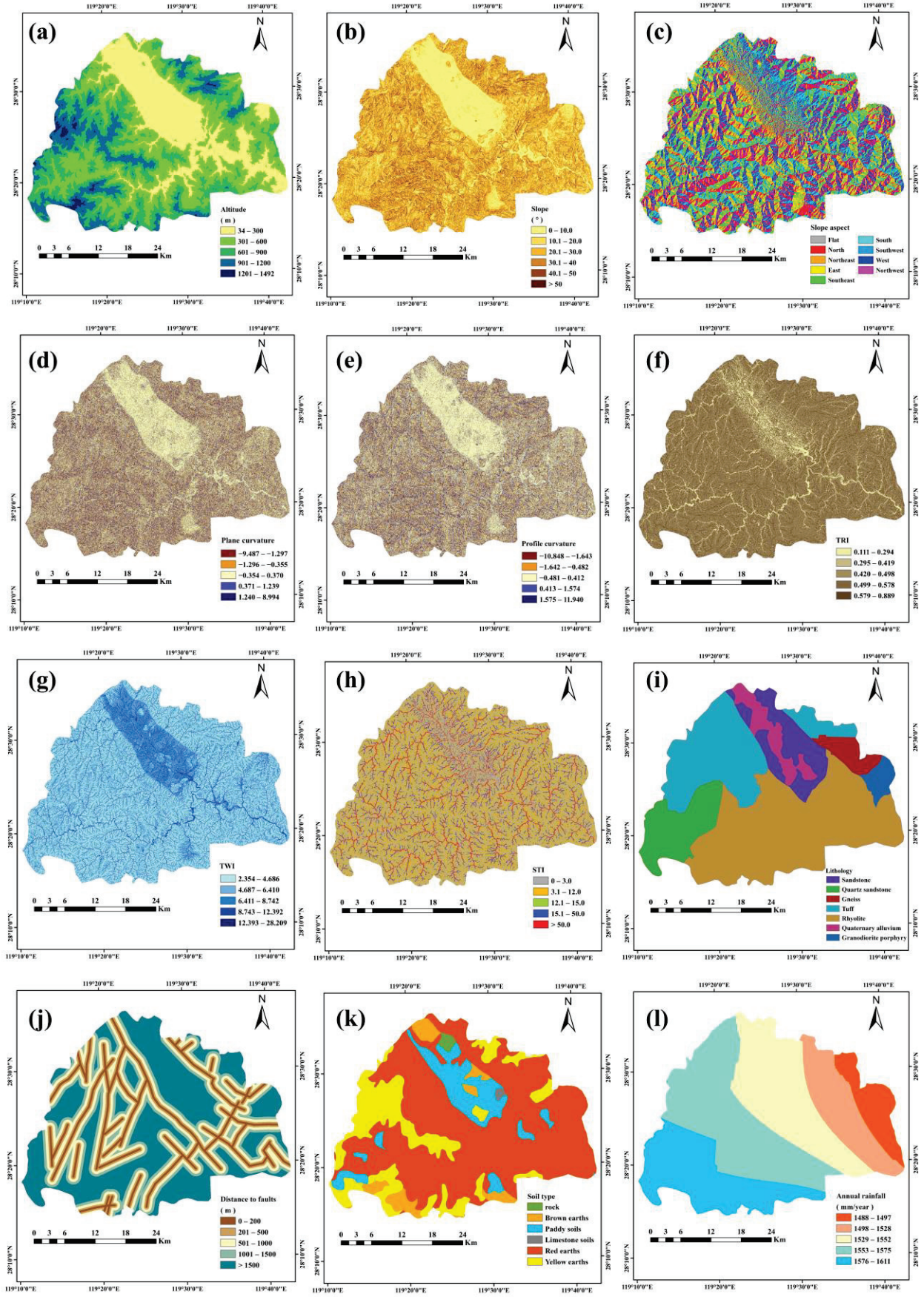

Figure 3. *Cont.*

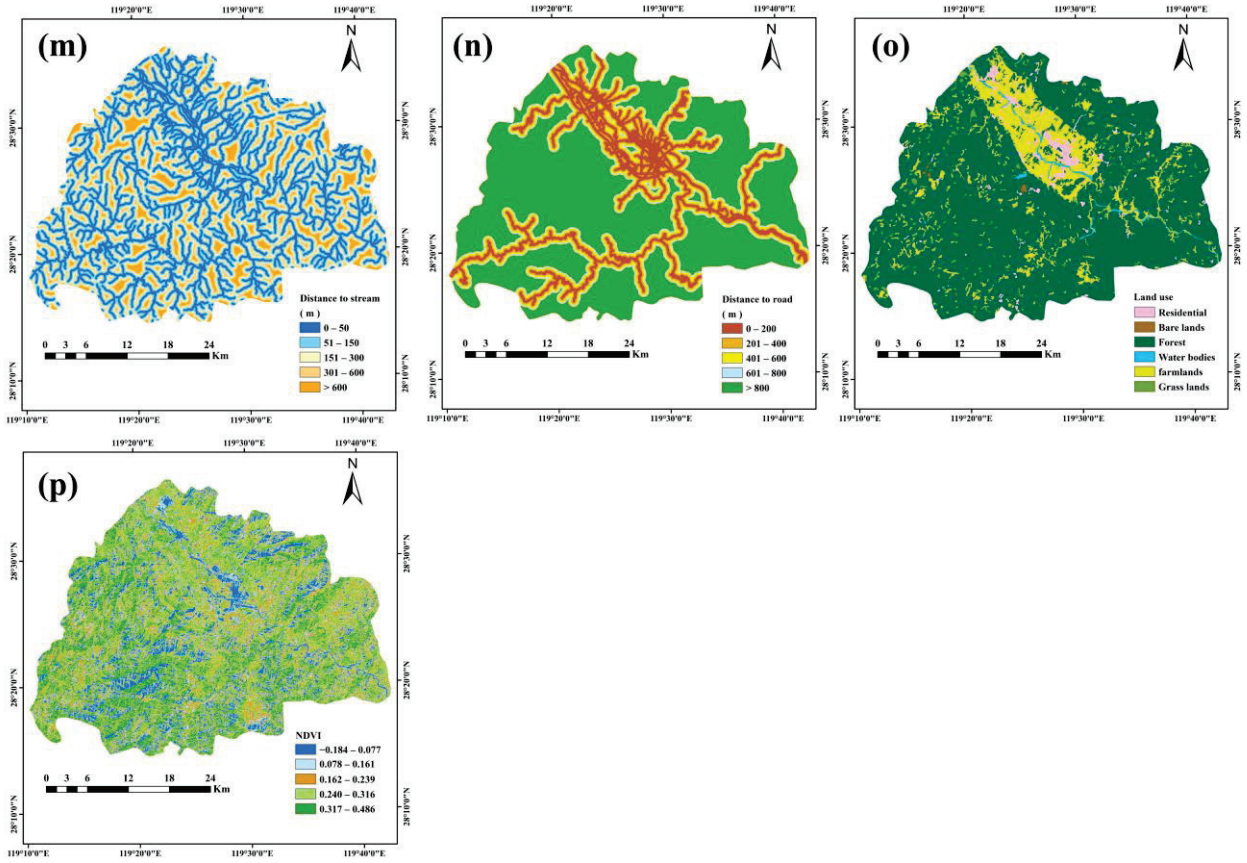

Figure 3. Conditioning factors of LSM. (**a**) Altitude; (**b**) slope; (**c**) slope aspect; (**d**) plan curvature; (**e**) profile curvature; (**f**) *TRI*; (**g**) *TWI*; (**h**) *STI*; (**i**) lithology; (**j**) distance to faults; (**k**) soil type; (**l**) annual rainfall; (**m**) distance to stream; (**n**) distance to the road; (**o**) land use; (**p**) *NDVI*.

As illustrated in Table 1, the production time of each conditioning factor is inconsistent. This is because this study is based on landslides that have occurred in the past 20 years, and numerous real-time data points are not necessary for the long timescale. The ideal data source would be produced at the same time as the landslide occurred. In the case of LSM studies based on abrupt events (earthquakes, extreme weather), the requirement for real-time data is higher. However, it is difficult to achieve consistency in timescales for landslides that have occurred consecutively over 20 years. For less variable data on a long time scale, such as DEM, lithology, faults, soil type, streams, and land use, momentary and reliable data need to be selected to represent the conditions of the region over two decades. For more variable data, such as rainfall, try to choose the average data over the research time as a representative. For the conditioning factors of roads and vegetation, the most recent data are considered representative of the average data of the last two decades by simplification. Based on the above considerations and the limitations of the data sources, more relatively reasonable layers of landslide conditioning factors were collected for this research. Due to the long timescale and the uncertainty of data quality, systematic errors introduced by the data sources are bound to exist but are not further discussed in this study.

Topographical factors have proved to be of great influence in LSM [45]. From the basic DEM, slope, aspect, plan curvature, profile curvature, *TRI*, *TWI*, and *STI* can be calculated using ArcGIS 10.8. Altitude and slope are intuitive factors in a landslide-hazard environment. The altitude values of the study area can be divided into five groups: 34–100 m, 301–600 m, 601–900 m, 901–1200 m, or 1201–1492 m. The slopes are divided into six categories at 10° intervals: 0°–10°, 10.1°–20°, 20.1°–30°, 30.1°–40°, 40.1°–50°, and >50°. The aspect of the study area is divided into the following nine categories: flat, north, northeast, east, southeast, south, southwest, west, and northwest. Profile curvature measures the

change in the slope of the surface and affects the acceleration or deceleration of water flow. It can be divided into the following groups by the natural breaks group method: −10.848–1.643, −1.642–−0.482, −0.481–0.412, 0.413–1.574, and 1.575–11.940. Plane curvature reflects the change in the lateral slope of the land surface, which affects the convergence or dispersion of surface water flow and, by the natural breaks, is divided into the following five groups: −9.487–−1.297, −1.298–−0.355, −0.354–0.370, 0.371–1.239, and 1.240–8.994. *TRI* expresses the degree of surface undulation and can be divided into five groups by natural breaks: 0.111–0.294, 0.295–0.419, 0.420–0.498, 0.499–0.578, and 0.579–0.889. *TWI* quantitatively describes the influence and cumulative effect of topography on watershed runoff and predicts the spatial spread of regional soil moisture. By natural breaks, it can be divided into the following five groups: 2.354–4.686, 4.687–6.410, 6.411–8.742, 8.743–12.392, and 12.393–28.209. *STI* can provide important information on the potential for sediment transport in a given river network; due to the uneven distribution of *STI* values in the study area, they are manually divided into the following categories: 0–3.0, 3.1–12.0, 12.1–15.0, 15.1–50.0, and >50.0.

Regional geological factors are important endogenous factors for landslides. The lithology map and fault map are based on a 1:200,000 geological map of China [44]. The lithology includes sandstone, quartz sandstone, gneiss, tuff, rhyolite, quaternary alluvium, and granodiorite porphyry. Areas in the fault map can be divided into five groups by the distance to a fault: 0–200 m, 201–500 m, 501–1000 m, 1001–1500 m, and >1500 m. Soil type was also included as an auxiliary conditioning factor and consists of rock, brown earths, paddy soils, limestone soils, red earths, and yellow earth. Meteorology and hydrology are the most important triggers for landslides. The average annual rainfall from 2000 to 2021 was divided into five groups according to the natural breaks: 1488–1497 mm/year, 1498–1528 mm/year, 1529–1552 mm/year, 1553–1575 mm/year, and 1576–1611 mm/year. The distance to the stream is divided into the following groups: 0–50 m, 51–150 m, 151–300 m, 301–600 m, and >600 m.

Other factors such as traffic, vegetation, and land use are also included. The traffic network can reflect the modification of slopes by human engineering activities. The distance to a road is divided into the following groups: 0–200 m, 201–400 m, 401–600 m, 601–800 m, and >800 m. Land use types involve human modification of the land surface; the classifications detected in the study area are residential, bare lands, forests, water bodies, and farmlands. The vegetation cover is represented by *NDVI* and is divided into the following groups by natural breaks: −0.184–0.077, 0.078–0.161, 0.162–0.239, 0.240–0.316, and 0.317–0.486.

3. Methodology

3.1. Study Route

This study was conducted in three stages (Figure 4). First, layers of the 16 conditioning factors for the study area were prepared, and correlation tests were performed. Then, the absence sample dataset with different qualities was constructed using different methods of absence sampling: BCS, CTSES, IV, MBKM, and integrative sampling. Finally, LSM work was produced by support vector machine and random forest algorithms, and evaluation and comparison of the models produced by each absence sampling method were completed.

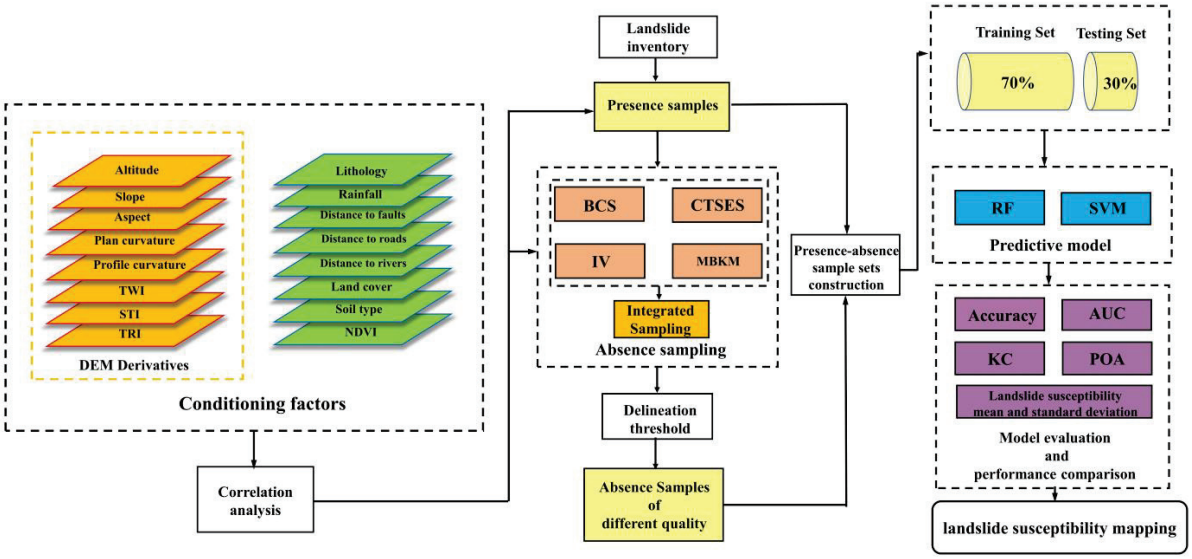

Figure 4. Flowchart of comparison and evaluation process of absence sample sampling methods.

3.2. Correlation Analysis of Conditioning Factors

Here, correlation analysis was performed to determine the statistical correlation among more than two variables. Multiple correlation analysis of conditioning factors in landslide susceptibility mapping is important and represents the screening process for selected indicators. If variables with strong correlations are input into the model, the complexity of the model will increase, and the training process of the model will also be affected. Thus, correlation analysis and screening of conditioning factors are indispensable steps in LSM [46]. In this study, commonly used correlation indicators, including the Pearson correlation coefficient (*PCC*), variance inflation factor (*VIF*), and tolerance (*TOL*), were selected to scan the correlation and multicollinearity between the conditioning factors.

Pearson correlation analysis is used to measure the strength and direction of the linear relationship between two variables. The value of the *PCC* is usually between −1 and 1, where −1 indicates a perfect negative correlation, +1 indicates a perfect positive correlation, and 0 indicates no linear correlation. The closer the absolute value of the PCC is to 1, the stronger the correlation, and the closer the absolute value of the PCC is to 0, the weaker the correlation. When the values are 0–0.2, 0.2–0.4, 0.4–0.6, 0.6–0.8, and 0.8–1, the correlation between the two conditioning factors is very weak, weak, moderate, strong, and very strong, respectively. The formula for calculating the PCC is as follows:

$$\rho_{x,y} = \frac{cov(x,y)}{\sigma_x \sigma_y} \tag{5}$$

where $cov(x,y)$ denotes the covariance of the conditioning factors x and y; σ_x and σ_y denote the standard deviation of x and y.

The *VIF* and *TOL* are indicators to test the multicollinearity of multiple conditioning factors. It is generally considered that when the value of *VIF* is less than 5 and the value of *TOL* > 0.2, the factor has no multicollinearity with other factors. Factors of *VIF* values in the range of 5–10 and *TOL* values in the range of 0.1–0.2 are considered to have weak multicollinearity. Factors with *VIF* values > 10 and *TOL* values < 0.1 are considered to have moderate or higher multicollinearity. The formulas for calculating *VIF* and *TOL* are as follows:

$$VIF_i = \frac{1}{1 - R_i^2} \tag{6}$$

$$TOL = 1 - R_i^2 \tag{7}$$

where R_i^2 is the sample decidability coefficient of the i-th conditioning factor.

3.3. Absence Sampling Methods

3.3.1. Buffer Control Sampling (BCS)

BCS is a quick, easy way to create non-landslide samples and is widely used in LSM [47]. The essential basis of BCS is similar to the first law of geography, which states that things close together in geographical space have a stronger connection. Accordingly, in the landslide inventory map, the area adjacent to a landslide is more susceptible to landslides. This is also consistent with the physical mechanics and disaster-forming environment of a landslide. Rock and soil in areas close enough to the landslide are more susceptible to further sliding due to the scraping or accumulation of previous landslides. Moreover, due to the continuity of engineering geological conditions, areas relatively close to landslides are more likely to develop the same geological environment and be exposed to strong external triggers. Therefore, the BCS method could set a buffer zone at a certain distance around the landslide location in the landslide inventory map and complete the sampling work in areas outside the buffer zone within the study area to reduce the strong effect of the spatial proximity of landslide events.

3.3.2. Controlled Target Space Exteriorization Sampling (CTSES)

TSES is proposed to create pseudo-absence data for LSM. The absence of data are produced from feature space instead of geographical space [28]. This method can make up for the defects of sampling in geospatial samples with geographical differences that may be similar in the feature space. The core principle of TSES is to extend landslide features beyond the feature space of all landslides (within the feature space of the study area) to obtain new non-landslide samples. It is reasonable for these absence samples to be created using landslide samples, as doing so preserves the regional character of the study area and enhances variability within landslide samples. Improved target space exteriorization sampling (ITSES) has been proposed to compensate for the non-existence absence samples in geographic space [29]. It maps the absence samples from feature exteriorizing space to geographic space, which gives the absence data more chances to be validated in remote sensing or field work.

Existing TSES methods exteriorize only one feature of the landslide sample during the process. In fact, landslide samples can be simultaneously exteriorized on multiple feature dimensions, and the number of such exteriorizing dimensions determines the degree of difference between absence and landslide samples. Whether this difference could affect the predictive performance of LSM is uncertain. In this study, controlled TSES (CTSES) is proposed to explore absence sampling methods from different exteriorizing dimensions by adding an artificially controlled number d of exteriorizing dimensions on the basis of the ITSES (Figures 5 and 6). The code is as follows:

Input: landslide samples S, number of exteriorizing feature dimension d
Output: non-landslide samples N_d with exteriorizing feature dimension d

(1) Initialization:

$$N = \varnothing$$

(2) For each landslide conditioning factor A:

Calculate the value range $V_{A\ max}$ of feature A of all units on the whole study area; calculate the value range V_A of feature A of all landslide samples;

determine the exteriorized feature space $V'_A = \bar{V}_A \cap V_{A\ max}$.

(3) Traverse every unit i in the study area:

(a) Set temporary variables a = 0;

(b) Traverse every landslide conditioning factor A:

if A of i is in V'_A, a = a + 1;

(c) If $a = d$, then run (d):

(d) $N_d = N_d \cup i$

(4) Return N_d

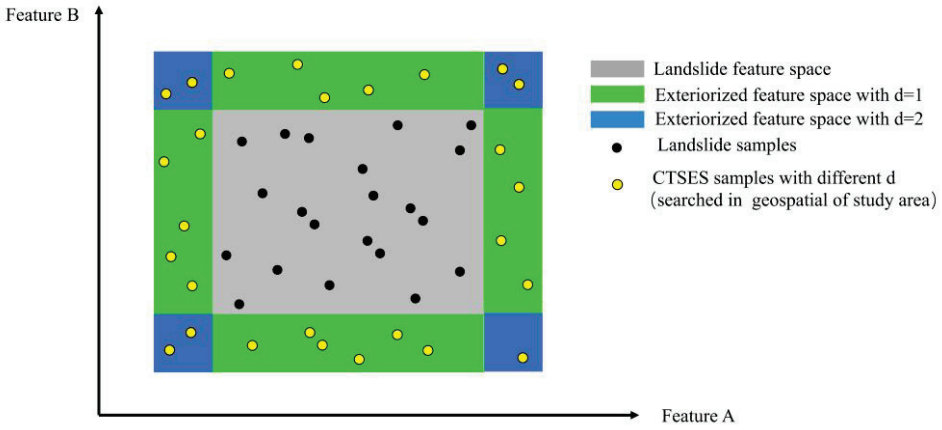

Figure 5. Schematic of the two-dimensional feature space of the CTSES method.

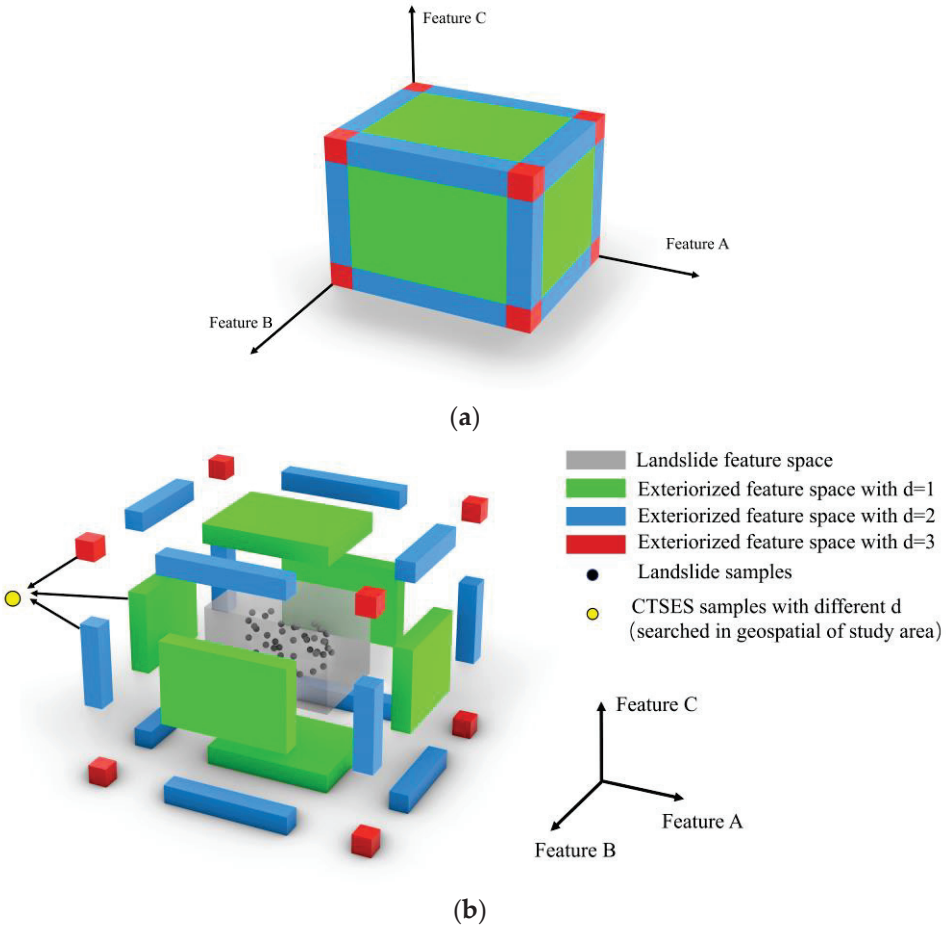

Figure 6. Schematic of the three-dimensional feature space of the CTSES method. (**a**) Three-dimensional feature space of the study area; (**b**) deconstruction map of the three-dimensional feature space in the CTSES method.

3.3.3. Information Value (IV)

As a bivariate analysis method, the IV method is often used in landslide susceptibility analysis. The method is consistent with the principles of several other bivariate analysis

methods, including certainty factor (CF) and frequency ratio (FR). Information theory is the basis of the IV method, in which the information gain measures the significance of features to the prediction results. The theory of the IV method assumes that the generation of geohazards depends on the quality and quantity of the information obtained. Probabilistic statistics and comparative mapping are used to derive the magnitude of the contribution of various conditioning factors to landslide generation from historical landslide data. The significance of each conditioning factor is expressed by the IV, and the larger the value, the more likely a geological hazard will occur under this factor.

The theoretical formula for the amount of information is:

$$I(x_i, \mathrm{A}) = \ln \frac{P(x_i \mid A)}{P(x_i)} \tag{8}$$

where $I(x_i, \mathrm{A})$ is the amount of information provided by the single-factor factor x_i to the occurrence of geohazard (A), $P(x_i \mid A)$ is the probability of x_i under geohazard conditions, and $P(x_i)$ is the probability of factor x_i in the study area.

In specific applications, the sampling frequency (area ratio) is often used as:

$$I_{ij} = ln \frac{\frac{N_{ij}}{S_{ij}}}{\frac{N}{S}} \tag{9}$$

where I_{ij} is the amount of information in the j-th classification of the i-th factor, S is the total study area; S_{ij} is the area under the j-th classification of the i-th factor in the study area. N is the total number of geological hazards in the study area, and N_{ij} is the number of the j-th classification of the i-th factor in the study area.

The sum of the I_{ij} of each unit is shown as the landslide sensitivity index, and the formula is:

$$LSI = \sum_{i=1}^{n} I_{ij} \tag{10}$$

3.3.4. Mini-Batch K-Medoids (MBKM)

K-medoids is an improved unsupervised algorithm for clustering based on K-means. Various clustering algorithms are often used for LSM, but the k-medoids method is minimally used in LSM [48,49]. The improvement of the K-medoids method is that it updates the centroid with the most centrally located object in the cluster instead of the center of mass formed by the average value in the K-means method. Therefore, K-medoids are far more adaptable to noise and outliers than K-means.

1. K initial centroids are randomly selected.
2. Assign the remaining points to the cluster represented by the closest medoids.
3. In each class, the sum of distances between each sample point and other points is calculated, and the point with the smallest sum of distances is selected as the new medoid.
4. Repeat the process in steps 2–3 until all medoid points no longer change or the upper limit of iterations is reached.

In this algorithm, the time complexity is much greater than that of K-means due to iterating through all data points, especially with large datasets. When the number of sample points reaches a million, huge computational resources will be required; however, the mini-batch algorithm will solve this problem well.

The MBKM method randomly samples several small sample sets from a large sample set and updates the initial centroids in each small sample set by substituting them into the K-medoids model. The combined training effect on a large number of small samples will be slightly lower than the training effect on the whole sample, but it will save computational resources and time.

3.3.5. Integrative Sampling

At its core, integrative sampling is similar to integrated learning but with added diversity. The specific operation is to mix the absence samples from each sampling method by a certain ratio to form a new absence sample set. The newly formed sample set has more diversity, which results in a more robust and generalized model and a reduced risk of overfitting (similar to the idea of bagging). Under the same sampling interval, the characteristic pattern of the generated absence samples may be singular or one-sided. Overly monotonic sample characteristics can make the model tend to overfit, and extreme samples can make the model perform poorly against new datasets. However, in integrative sampling, the learner receives samples from multiple sampling methods. Due to the different sampling methods for absence samples, the distribution of absence samples in the geographic space and feature space is diverse in order to give comprehensive information to the training model. Therefore, the training model that accepts the integrative sampling set can show good adaptability and generalization ability when faced with a diverse set of prediction data.

Integrated sampling combines four absence sampling methods, namely BCS, CTSES, IV, and MBKM, and the process is shown in Figure 7. The main processing steps are as follows: (1) defining sampling thresholds and sampling for absence samples of each method; (2) pre-training and evaluating combining with landslide samples; and (3) forming the new integrated absence samples by assembling the best-quality sample sets for each method. The best-quality sample sets are discriminated by the comprehensive predictive performance metrics in the pre-training results.

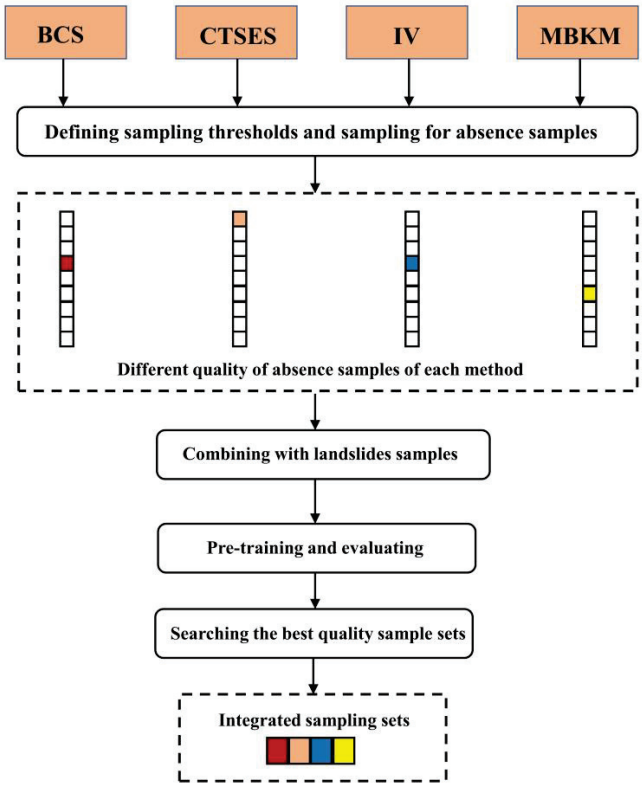

Figure 7. Schematic of the procession of integrated sampling. The different colors represent the best quality sample sets in each absence sampling method.

3.4. Machine Learning for Landslide Susceptibility Mapping

SVM and RF are among the most classical algorithms for prediction and classification and are widely used and known for their excellent performance in a wide range of industries. In recent years, SVM and RF have been prominent in LSM research due to their excellent performance. In fact, SVM and RF models are capable of not only classification but

also a probabilistic prediction that can be transformed into the assessment of susceptibility. Data-driven landslide prediction is a high-dimensional and nonlinear problem that is well suited to be solved with these two algorithms.

3.4.1. Random Forest

Random forest is a supervised machine learning integration algorithm based on bagging. Multiple sample sets and decision trees are constructed through bootstrap sampling (random sampling with put-back), and random features of the sample are selected for splitting on the basis of the decision tree. Due to its randomness, the random forest does not easily fall into overfitting and has good resistance to noise. After each decision tree split is completed (training completed), the set becomes a forest, and each decision tree is voted on to get the final result. Decision trees can achieve the tasks of classification and regression, and for LSM, landslide susceptibility indicators can be obtained by averaging the results of multiple decision trees [50]. Due to its excellent ability to handle high-dimensional and nonlinear data, the random forest method can achieve good prediction results in LSM [51].

3.4.2. Support Vector Machine

A support vector machine is a supervised machine learning algorithm commonly used in landslide susceptibility [52]. An SVM has the ability to solve problems with high-dimensional, small samples, and nonlinear features. The two main ideas of the SVM are the search for the best classification hyperplane and the use of kernel functions [53]. The hyperplane is a subspace of n-1 dimensions in an N-dimensional linear space; it can correctly classify the sample categories. The support vector is the closest training sample point to the hyperplane. The optimal hyperplane has the largest sum of the distances from it to different classes of support vectors. In the two-dimensional feature space, the hyperplane is a straight line that can divide the sample categories, and in the three-dimensional feature space, a hyperplane is a plane that can divide the sample categories. Once no hyperplane in the current feature space can linearly divide the sample categories, the original feature space can be mapped to a higher-dimensional feature space by a kernel function to make the samples linearly divisible in this space. The commonly used kernel functions are the linear kernel, polynomial kernel, radial basis function kernel (RBF-kernel), and sigmoid kernel; the polynomial kernel and the RBF-kernel are most frequently used and have a good predictive effect on landslide susceptibility [54,55].

3.5. Model Evaluation Methods

To assess and compare the predictive performance of models using different absence sample compositions, the models were evaluated from three perspectives. First, the accuracy of the model was examined, encompassing both the accuracy of the training sets and the testing sets. Accuracy is the most intuitive indicator of a model's predictive performance. The accuracy threshold is set to 0.5; it is considered a potential landslide when the prediction result is >0.5. Training accuracy reflects the model's ability to fit onto the training sets; the higher the testing accuracy, the better the model can learn the patterns and laws of the data. Testing accuracy reflects the model's ability to generalize, which represents the ability to perform on unseen data.

The second perspective involves evaluating the comprehensive performance of the model. Area under the curve (AUC), kappa coefficient (KC), and performance overall accuracy (POA) were used to evaluate the combined predictive performance of the model. The receiver operating characteristic curve (ROC) and AUC are commonly used methods to assess the performance of classification models. The AUC represents the area under the ROC curve and ranges from 0.5 to 1.0. A higher AUC value implies a better discrimination performance of the model. A confusion matrix is a table used to evaluate the performance of a classification model by comparing the predicted class labels with the actual class labels. The matrix contains four terms: true positives (TP), false positives (FP), true negatives (TN), and false negatives (FN). From the confusion matrix, several metrics can be calculated to

evaluate the performance of the classification model, such as precision, recall, accuracy, KC, Matthews correlation coefficient (MCC), and F1-score. KC measures the agreement between the predicted and actual class labels, correcting for the agreement expected by chance. KC values range from −1 to 1, where a value of 1 indicates perfect agreement, a value of 0 indicates agreement by chance, and a value of −1 indicates perfect disagreement. POA, which is the sum of accuracy, MCC, and F1-score, provides a more comprehensive assessment of the model's predictive performance than individual metrics [31,56].

The third is the mean and standard deviation of landslide susceptibility. The mean value reflects the overall overestimation or underestimation of the model's susceptibility, and the standard deviation represents the degree of dispersion of the susceptibility index. Therefore, the mean and standard deviation can be used as auxiliary parameters to assess the reasonableness of the model.

4. Results

4.1. Correlation Analysis

In ArcGIS 10.8, the band collection statistics function was used to calculate the *PCC* between two conditioning factors by inputting a total of 16 conditioning factor layers containing elevation, slope, aspect, profile curvature, plane curvature, *NDVI*, lithology, rainfall, distance to faults, distance to rivers, *TWI*, *TRI*, *STI*, distance to roads, land use, and soil type. The results are entered into Python for heat map visualization (Figure 8). In the heat map, the stronger the correlation, the darker the color, and the weaker the correlation, the lighter the color. The color tends to be brown for positive correlations and purple for negative correlations. Among the 16 conditioning factors, the maximum *PCC* value was −0.59, where the profile curvature and plane curvature were (relatively) most correlated, followed by the *PCC* value of 0.56, showing a relatively positive correlation between elevation and distance to the road. All *PCC* values are less than 0.6, which means that there is no strong correlation among the factors.

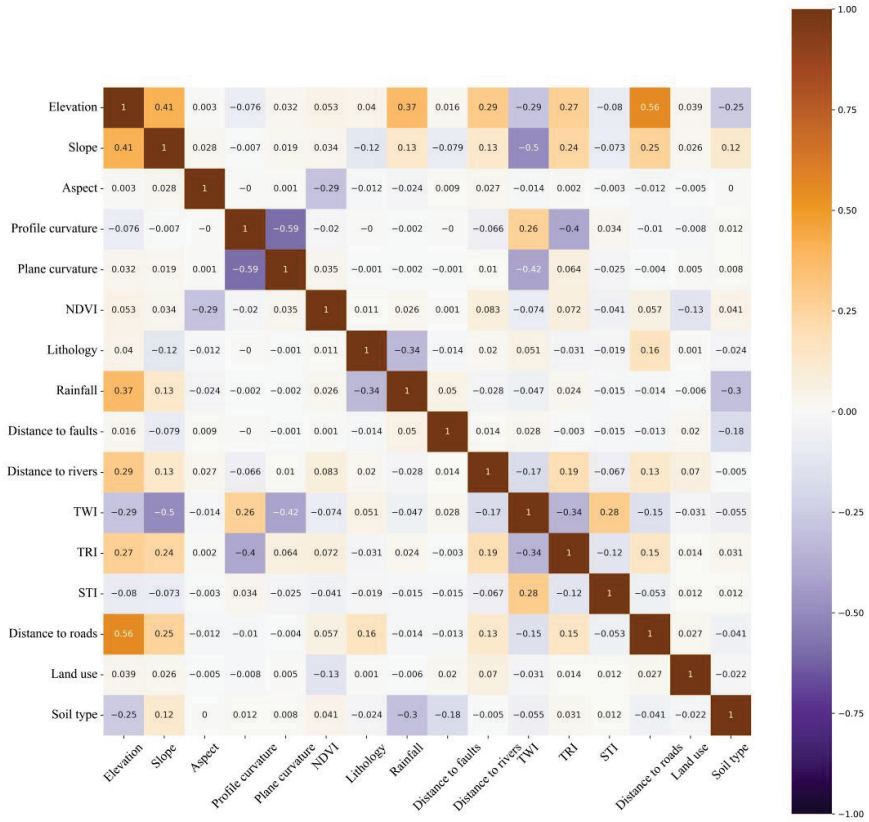

Figure 8. Pearson correlation coefficient heat map of 16 conditioning factors.

In all, 16 layers of conditioning factors were extracted from ArcGIS 10.8 for the whole study area, and the *VIF* and *TOL* values of the 16 conditioning factors were calculated using the statsmodels library in Python (Table 2). Elevation had the highest *VIF* value of 2.6 and the lowest *TOL* value of 0.383, with relatively strong multicollinearity with all other factors. In addition, *VIF* values for all conditioning factors were less than 10 and strictly less than 5, and all *TOL* values were greater than 0.1. Therefore, it can be assumed that there is no strong multicollinearity between these 16 conditioning factors.

Table 2. *VIF* and *TOL* results for 16 conditioning factors.

Factor	*VIF*	*TOL*
Elevation	2.613	0.383
Slope	1.685	0.594
Aspect	1.105	0.905
Profile curvature	2.010	0.498
Plane curvature	2.087	0.479
TRI	1.558	0.642
TWI	2.090	0.478
STI	1.118	0.894
NDVI	1.143	0.875
Lithology	1.223	0.818
Rainfall	1.570	0.637
Distance to faults	1.028	0.972
Distance to rivers	1.172	0.854
Distance to roads	1.613	0.620
Land use	1.032	0.969
Soil type	1.350	0.740

4.2. Results of Absence Sampling

The absence sample set for BCS is constructed by first constructing a buffer for 217 landslide sample points and then creating random points outside the buffer by taking the inverse of the function of the intersection set. By doing so, we can ensure that the random points do not fall inside the buffer or near the landslide. By constructing buffers of different scales, the sampling scales are divided into 300 m, 500 m, 800 m, 1000 m, and 1500 m, and 10 sets of random points are randomly selected under each scale as absence samples. In the BCS method, the relationship between the created absence sample location and the landslide location is shown in Figure 9. The number of absence samples per group was 217, which was used for the final training and testing after extracting 16 conditioning factors. The whole sampling process for BCS was conducted on ArcGIS 10.8.

The program for CTSES was done in Python, and subsequently, all pixels in the study area were entered and traversed in the program (the core code is shown in Section 3.3.2). The number of input pixels was 1,559,752. The search for absence samples of different quality was performed by changing the control parameters. In the sampling results of CTSES, the number of absence samples with $d = 1$, $d = 2$, $d = 3$, and $d = 4$ were 200,023, 22,765, 2888, and 323, accounting for 12.824%, 1.459%, 0.185%, and 0.021% of the overall pixels, respectively. When the controlled parameter d is increased to 5, the number of absence samples found is 21, and we cannot find any absence samples with d greater than 5. The location of these absence samples mapped to the study area is shown in Figure 10. Absence sample sets were created for training and testing from the CTSES data of $d = 1$, $d = 2$, $d = 3$, and $d = 4$. In all, 20 sets of 217 absence samples were randomly selected from each interval for final training and testing.

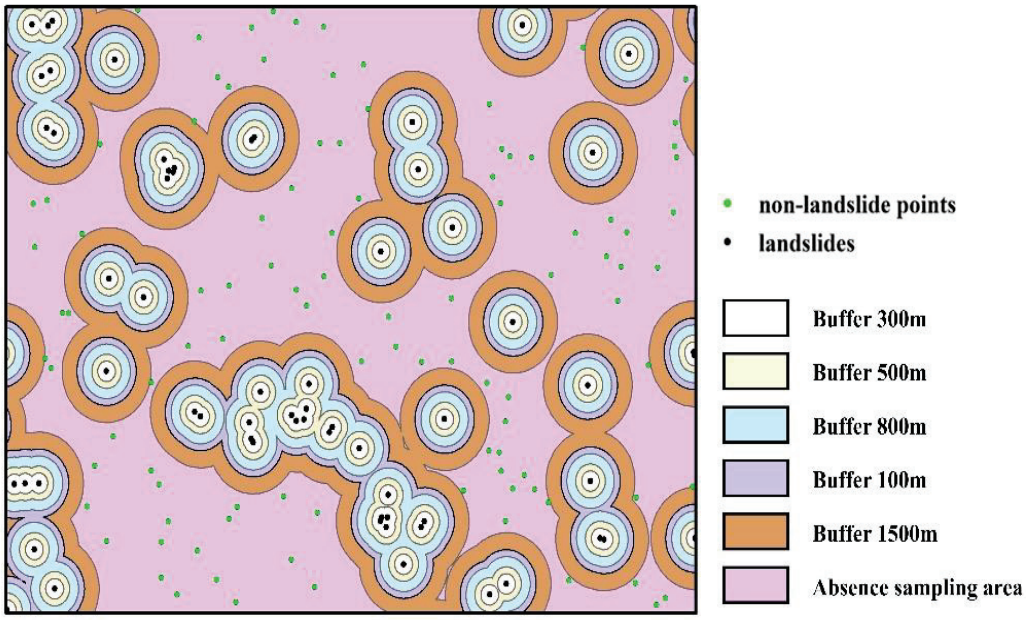

Figure 9. Absence sample location schematic of the BCS method.

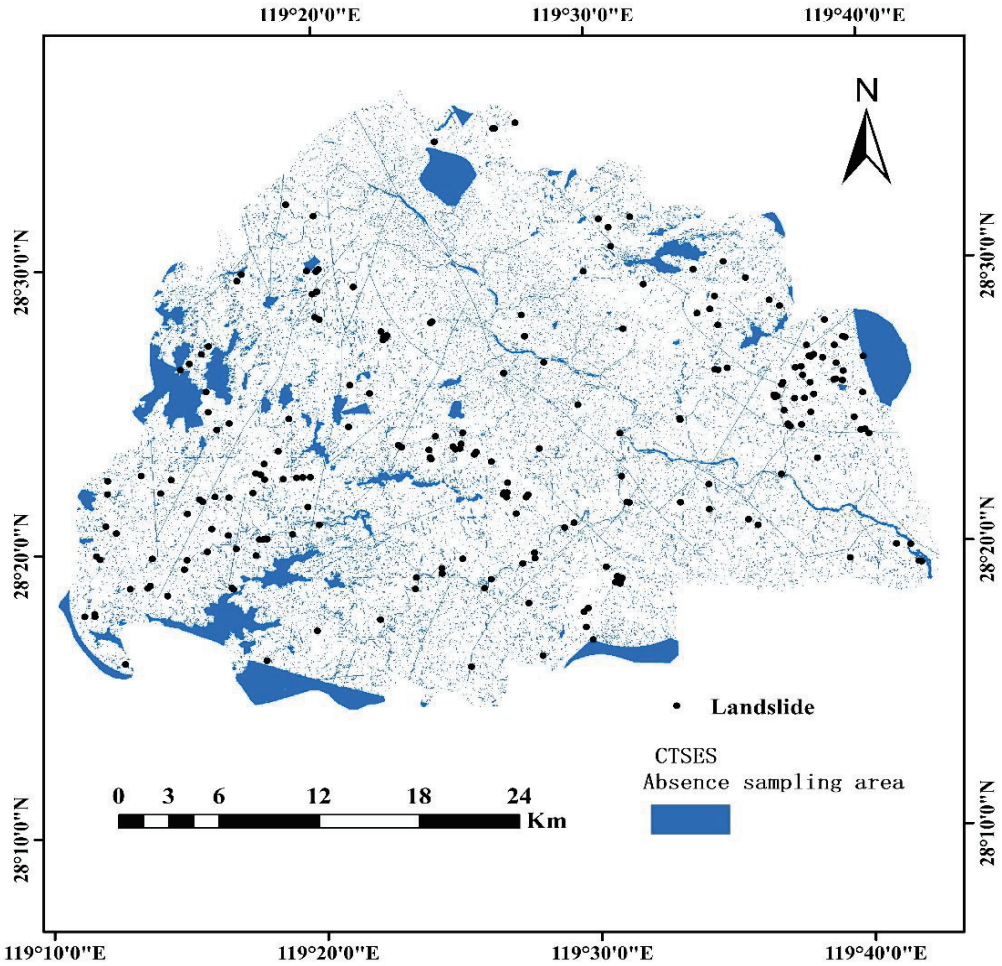

Figure 10. Absence sampling location of CTSES results.

The total number of landslides in the study area was 217, and the total number of pixels was 1,559,752, which was used to replace N and S in the IV model. The statistics of the number of landslides N_{ij} and the corresponding area S_{ij} within the interval of each conditioning factor are shown in Table 3. The IV values of the grading of each factor were calculated. After the initial susceptibility mapping of the IV model was conducted, the susceptibility was divided into 10 intervals based on the natural break method, as shown in Figure 11a. The absence sampling threshold was set according to the natural break, and a total of 10 sampling intervals were divided: <0.1, <0.2, <0.3, <0.4, <0.5, <0.6, <0.7, <0.8, <0.9, and <1.0.

Table 3. IV calculation table of IV model.

Factor	Class	No. of Landslides	No. of Pixels in Domain	IV
Altitude (m)	34–400	65	400,676	0.154
	301–600	105	529,308	0.355
	601–900	40	424,249	−0.389
	901–1200	7	191,726	−1.338
	1201–1492	0	13,793	0.000
Slope (°)	0–10	35	285,800	−0.128
	10.1–20	75	353,914	0.421
	20.1–30	60	484,962	−0.117
	30.1–40	37	339,129	−0.243
	40.1–50	10	84,504	−0.162
	>50	0	5759	0.000
Aspect (°)	0	0	5939	0.000
	0–22.5	11	89,012	−0.118
	22.6–67.5	34	202,755	0.187
	67.6–112.5	32	216,747	0.059
	112.6–157.5	35	202,523	0.217
	157.6–202.5	30	178,953	0.186
	202.6–247.5	24	182,953	−0.059
	247.6–292.5	26	194,308	−0.039
	292.6–337.5	16	192,853	−0.517
	337.6–360	9	88,025	−0.308
Plane curvature	(−9.487–−1.297)	7	90,832	−0.591
	(−1.296–−0.355)	57	358,239	0.134
	(−0.354–0.370)	89	646,319	−0.010
	(−0.371–1.239)	56	354,515	0.127
	(1.240–8.994)	8	109,847	−0.647
Profile curvature	(−10.848–−1.643)	4	78,385	−1.003
	(−1.642–−0.482)	36	318,609	−0.208
	(−0.481–0.412)	91	696,850	−0.063
	(0.413–1.574)	70	376,172	0.291
	(1.575–11.940)	16	89,736	0.248
TWI	(2.354–4.686)	85	656,862	−0.072
	(4.687–6.410)	69	524,863	−0.057
	(6.411–8.742)	40	250,590	0.137
	(8.743–12.392)	17	92,287	0.281
	(12.393–28.209)	6	29,466	0.381
TRI	(0.111–0.294)	23	85,999	0.654
	(0.295–0.419)	45	246,752	0.271
	(0.420–0.498)	80	535,396	0.071
	(0.499–0.578)	52	531,083	−0.351
	(0.579–0.889)	17	208,097	−0.532

Table 3. *Cont.*

Factor	Class	No. of Landslides	No. of Pixels in Domain	IV
STI	(0–3.0)	84	715,531	−0.170
	(3.1–12.0)	64	586,030	−0.242
	(12.1–15.0)	11	50,604	0.446
	(15.1 -50.0)	31	140,393	0.462
	(>50.0)	27	75,298	0.947
NDVI	(−0.184–0.077)	32	214,619	0.069
	(0.078–0.161)	54	270,357	0.362
	(0.162–0.239)	66	361,211	0.273
	(0.240–0.316)	49	403,597	−0.136
	(0.317–0.486)	16	309,958	−0.991
Rainfall (mm/year)	1488–1497	33	118,347	0.695
	1498–1528	33	211,130	0.116
	1529–1552	28	398,437	−0.683
	1553–1575	70	494,390	0.018
	1576–1611	53	337,453	0.121
Distance to rivers (m)	0–50	39	169,598	0.503
	51–150	79	327,307	0.551
	151–300	52	338,629	0.099
	301–600	39	498,642	−0.576
	>600	8	175,619	−1.116
Distance to roads (m)	0–200	66	222,151	0.759
	201–400	21	147,406	0.024
	401–600	8	119,129	−0.728
	601–800	13	102,609	−0.094
	>800	109	968,500	−0.212
Distance to faults (m)	0–200	17	146,962	−0.185
	201–500	21	213,815	−0.348
	501–1000	61	318,946	0.318
	1001–1500	37	256,177	0.037
	>1500	81	623,895	−0.069
Land use	Residential	3	42,047	−0.668
	Bare land	0	2209	0.000
	Forest	155	1,264,284	−0.126
	Water body	1	12,156	−0.525
	Farmland	56	216,100	0.622
	Grassland	2	21,548	−0.405
	Rock	0	9137	0.000
Soil type	Brown earth	3	78,111	−1.287
	Paddy soil	20	170,108	−0.168
	Limestone soil	1	4313	0.511
	Red earth	179	1,011,069	0.241
	Yellow earth	14	288,375	−1.053
Lithology	Sandstone	10	153,095	−0.756
	Quartz sandstone	47	179,684	0.631
	Gneiss	18	56,402	0.830
	Tuff	38	373,449	−0.313
	Rhyolite	86	679,184	−0.094
	Quaternary alluvium	3	78,859	−1.297
	Granodiorite Porphyry	15	38,986	1.017

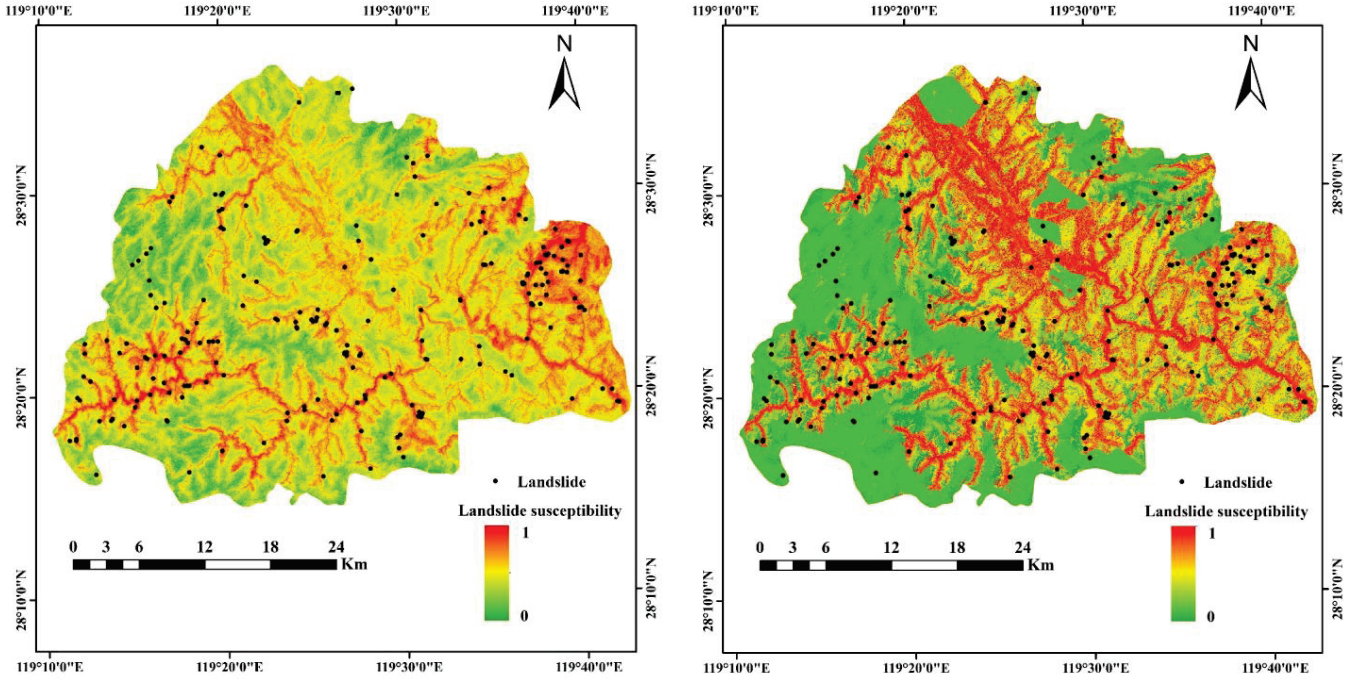

Figure 11. Results of the prior model. (**a**) IV model; (**b**) MBKM model. Absence samples were created by random sampling within 10 sampling intervals delineated by landslide susceptibility.

The 1,559,752 pixels with information values were normalized and processed into the MBKM algorithm for clustering calculations. The calculation process was based on Python's msmbuilder library [57]. The specific parameters were set as follows: n_clusters is 10, max_iter is 1000, batch_size is 20,000, and max_no_improvement is 50. After the clustering calculation, 10 clusters and 10 susceptibility rank intervals were obtained by sorting the size according to the information content value of each cluster center. The preliminary mapping of landslide susceptibility based on MBKM is shown in Figure 11b. The absence sample sampling threshold was set according to the natural break, and a total of 10 sampling intervals were divided as in the IV model: <0.1 through <1.0.

Absence samples extracted from low susceptibility intervals exhibited a lower probability of landslide occurrence in the IV and MBKM models. When the sampling threshold was close to 1.0, the absence samples were almost randomly selected over the entire area. Twenty sets of samples were created from each interval for training and prediction in the prior models of IV and MBKM.

The idea behind integrative sampling is to feed the model with as many samples with different characteristics as possible. Since the four sampling methods of BCS, CTSES, IV, and MBKM have different sampling intervals, the default interval with the best prediction performance metrics was the target interval for integrative sampling. According to the results (reported in Section 4.4), the 1000 m interval in BCS, the d = 4 intervals in CTSES, and the 0–0.1 interval in IV and MBKM had the best metrics (accuracy, AUC, KC, POA) such that the samples in them could input more correct absence sample information to the model. The selected absence sample sampling groups were BCS-1000m, CTSES-d = 4, IV-0.1, and MBKM-0.1 for integrative sampling. The final input from the integrative samples was obtained using random sampling from the intervals of different absence sampling methods. The ratio of mixing was 1:1:1:1 to evaluate the mixing effect simply. The number of absence samples in the input of prediction models was set to 217 and 506 to achieve presence-to-absence sample ratios of 1:1 and 3:7, respectively. The purpose was to test the effect of the training ratio on susceptibility prediction. This setting can explore whether

increasing the proportion of absence samples reduces the overestimation of susceptibility levels by comparing the results of different sample ratios of 1:1 and 3:7.

4.3. Landslide Susceptibility Mapping

4.3.1. LSM Results for Four Sampling Strategies with Different Sampling Intervals

The absence samples obtained in each of the above sampling methods were fed into the SVM and RF prediction models for training and prediction. The ratio of landslide samples to absence samples was set to 1:1. Optimal hyperparameters for SVM and RF prediction models were found by grid search based on 10-fold cross-validation. In the SVM training process, the RBF-kernel was used; the grid search range for hyperparameters C and gamma was set to 0–20 and 0–1.2. In the training process of RF, the grid search range for the hyperparameters n_estimators, max_depth, and min_samples_split were set to 10–100, 10–50, and 10–40, respectively. There were 10/20 sets of samples under each sampling threshold for each method, and the set with the highest AUC was selected for LSM visualization.

Figure 12 shows the results of the SVM-based models for different sampling intervals under four absence sampling strategies. In the BCS sampling method, the high landslide susceptibility areas were concentrated in the eastern part of Songyang County and near the east-west spreading gullies. Districts in the central flatlands exhibit a lower susceptibility to landslides. As the size of the landslide buffer increases, the distribution pattern of landslide susceptibility size little changes until it increases to 1000 m and 1500 m when the area of the high susceptibility zone in the east increases significantly. Under the CTSES sampling method, the high susceptibility areas at d = 1 are distributed in the eastern and central districts around the county seat and on the slopes on both sides of the gully. With the increase of parameter d, expansion of the high landslide susceptibility area and dispersion of the susceptibility index (deepening of LSM color) can be observed. When d = 4, most of the area is classified as having high susceptibility except for a small number of gullies, mountain fronts, and flatlands in the central county. The same expansion and dispersion of susceptibility are observed in the lower interval sampling of the IV prior model. When the sampling threshold of IV is 0.1 or 0.2, the high susceptibility area covers the majority of the study area. These two phenomena decrease as the IV sampling threshold increases and eventually stabilize above a sampling threshold of 0.5; they are close to the BCS predictions. The prediction model law based on the MBKM method of sampling is similar to that of the IV model, but the polarization and expansion phenomena are greatly reduced compared with the IV model, and most high landslide susceptibility areas in the low sampling interval are distributed on both sides of the gullies, which seems more reasonable. In addition, more areas of high landslide susceptibility occur in the central flatland county in the low sampling interval (threshold < 0.6) of the IV and MBKM sampling models and in the d = 3 and 4 intervals of the CTSES, which are mitigated in the other sampling intervals.

The RF-based model results for different sampling intervals under four absence sampling strategies are shown in Figure 13. The distribution pattern of susceptibility in the RF model is similar to that of the SVM, but there are significant differences. In the BCS method, when the buffer zone is 500 m, 800 m and 1000 m, the high susceptibility zone is more concentrated in the gully without excessive expansion or confusion. In the three sampling methods of CTSES, IV, and MBKM, expansion of high landslide susceptibility areas and dispersion of landslide susceptibility indices can be found with changes in sampling interval, which is consistent with the SVM prediction model. However, it is important to note that the expansion and polarization of the RF model are milder than those of the SVM model. Regardless, the expansion of high landslide susceptibility in the intermediate flatland counties can still be seen in the low sampling interval of the IV and MBKM sampling models and in the d = 4 sampling interval of CTSES.

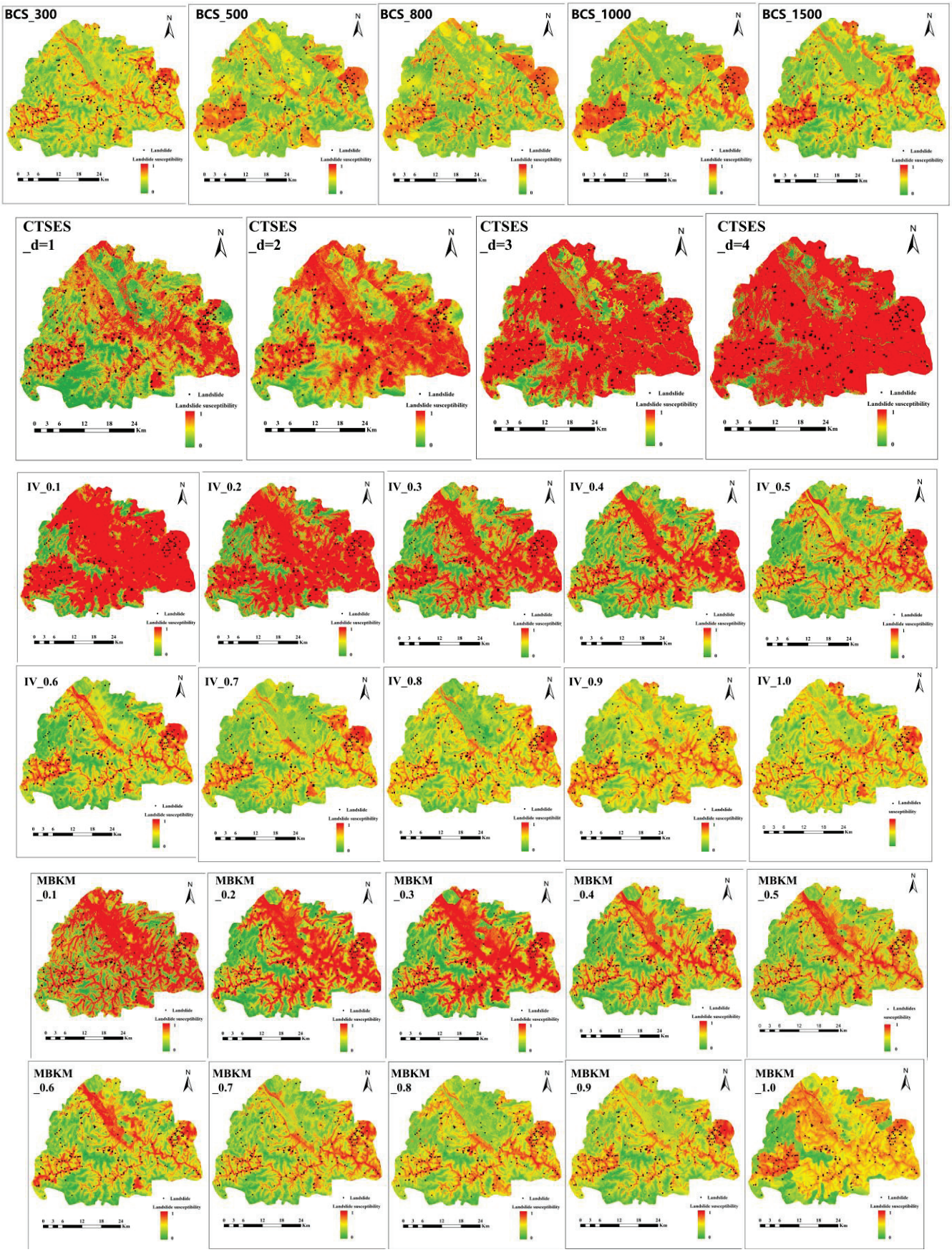

Figure 12. SVM-based LSM results of four absence sampling methods.

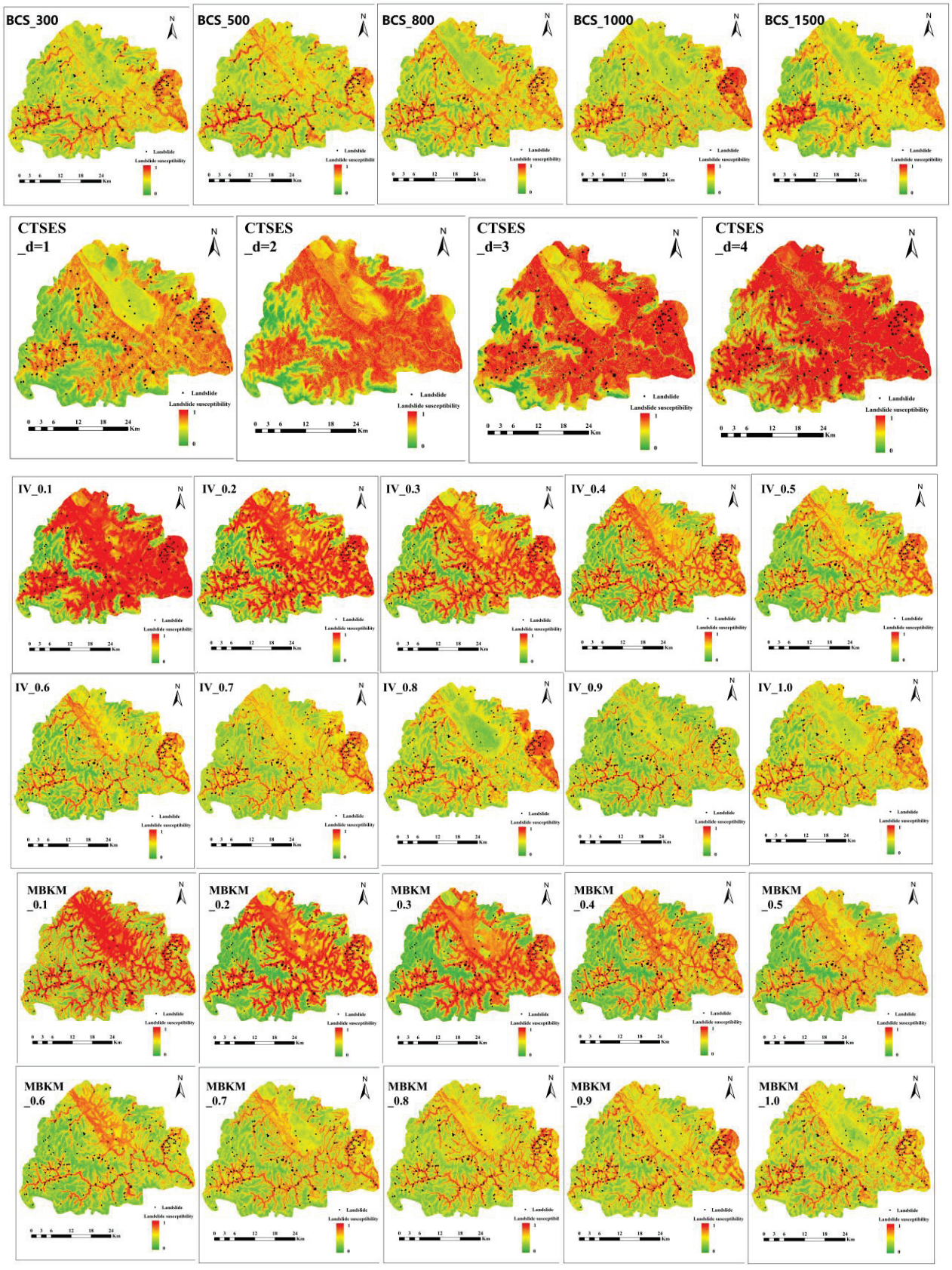

Figure 13. RF-based LSM results of four absence sampling methods.

4.3.2. LSM Results of the Integrative Sampling Method

The prediction plots of landslide susceptibility in SVM and RF prediction models with integrative sampling methods are shown in Figure 14; 1:1 and 3:7 presence-absence ratio sample sets are included respectively. In the training process of the SVM and RF, the hyperparameters are searched in the same range as in Section 4.3.1 for the grid search based on 10-fold cross-validation. The high landslide susceptibility areas are basically distributed on and on both sides of the gully, in the eastern part of Songyang County, and around the central prefecture. Widespread mountain peaks and flat areas in the central prefecture are designated as safety zones. The results of the integrative sampling did not reveal over-expansion or diversion of the high landslide susceptibility area, which is more reasonable than the results obtained from the previous CTSES, IV, and MBKM sampling. Comparing the results of presence-absence sample ratios of 1:1 and 3:7, the former has a larger area of high landslide susceptibility. The high susceptibility area predicted by SVM is slightly higher than in RF.

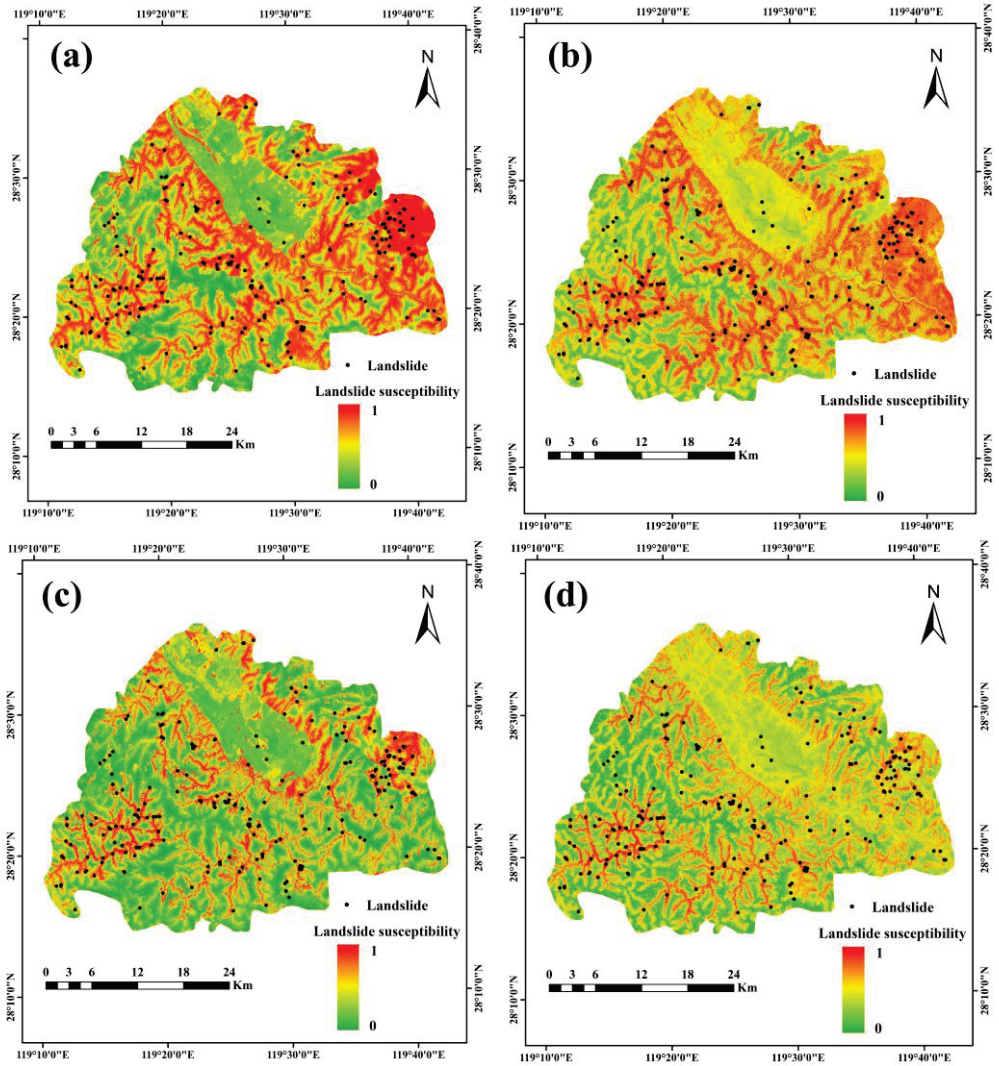

Figure 14. LSM of integrative sampling with different ratios. (**a**) SVM_IS_1:1; (**b**) RF_IS_1:1; (**c**) SVM_IS_3:7; (**d**) RF_IS_3:7.

4.4. Evaluation of Different Absence Sampling Methods

4.4.1. Model Accuracy of Four Absence Sampling Methods with Respective Sample Intervals

The training and testing accuracy of the models for different sampling intervals under each absence sampling method is presented in the form of box-line plots in Figures 15 and 16.

In the SVM and RF prediction models, a consistent pattern was found in the variation of accuracy with different sampling intervals. In the BCS method, the accuracy of the training and testing under SVM prediction increased slightly overall when the buffer rose from 300 to 1000 m and decreased slightly by 1500 m. In the RF model, training accuracy was relatively stable, mostly maintained above 0.9, and the amount and trend of testing accuracy were similar to those of the SVM prediction model. In CTSES, as d increased from 1 to 4, the accuracy of the training and testing sets under the SVM and RF prediction models tended to increase. The testing accuracy of SVM and RF reached 0.95 (nearly 1), as d = 4 and 3, respectively. In the IV and MBKM models, the accuracy of SVM decreased with increasing sampling threshold, and the testing accuracy of RF also decreased, but the training accuracy was maintained at a high level (>0.9). In addition, the testing accuracy of IV was higher than that of MBKM at the sampling thresholds of 0.1, 0.2, 0.3, 0.4, and 0.5; when the threshold was lowest, the testing accuracy was generally greater than 0.9 or close to 1.

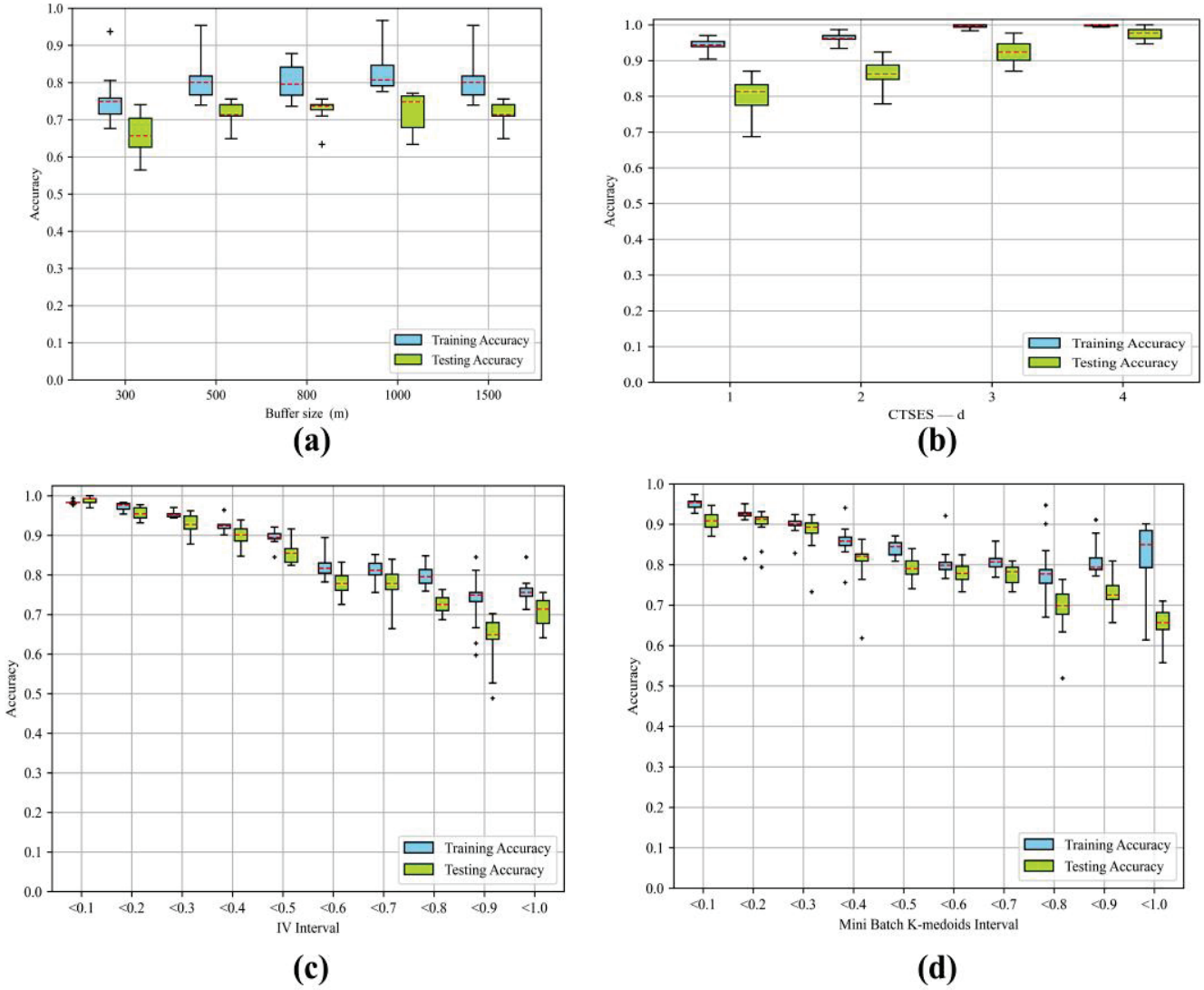

Figure 15. Accuracy results of SVM-based absence sampling. (**a**) BCS; (**b**) CTSES; (**c**) IV; (**d**) MBKM. The "+" represents a small number of abnormal values that are outside the normal range.

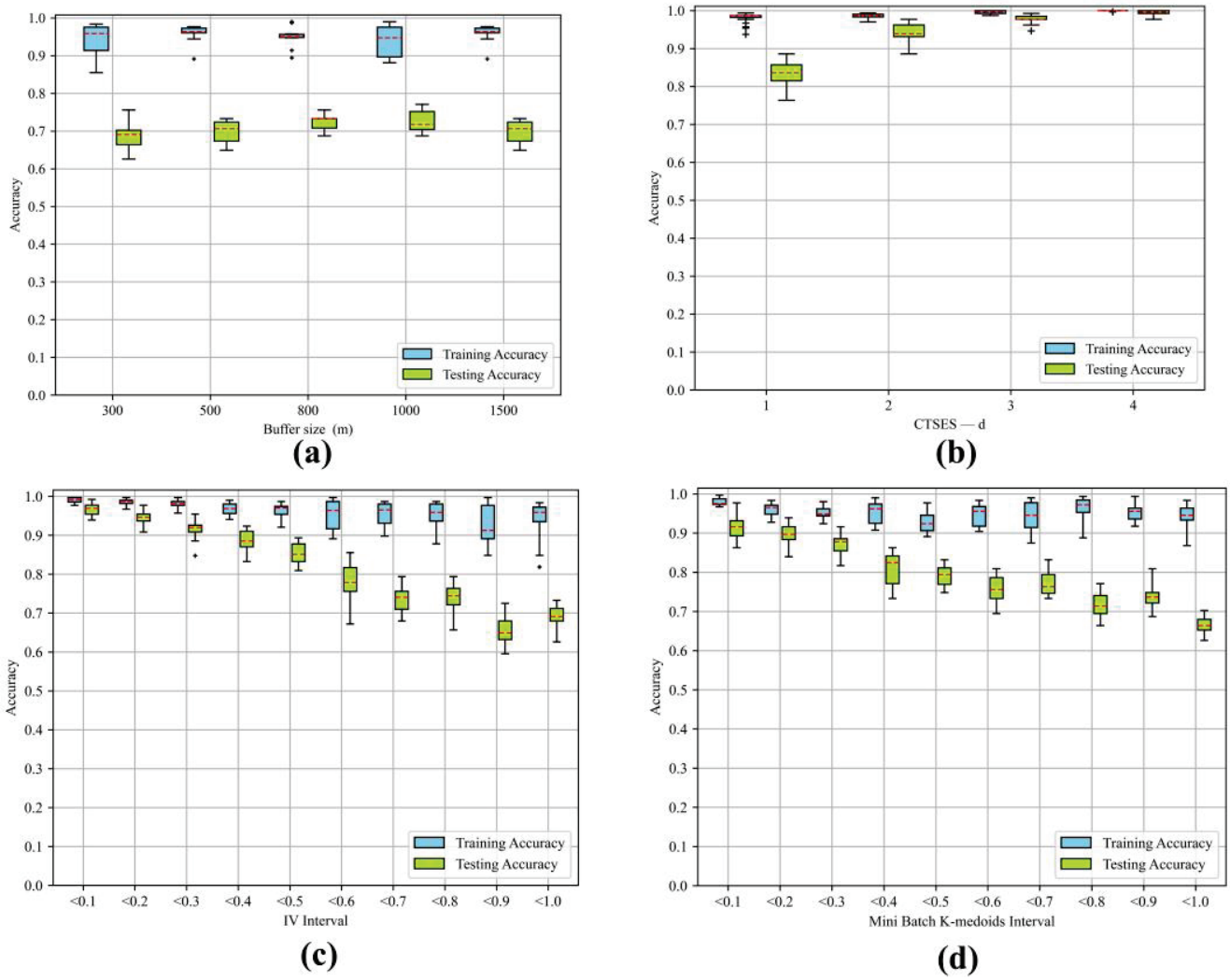

Figure 16. Accuracy results of RF-based absence sampling. (**a**) BCS; (**b**) CTSES; (**c**) IV; (**d**) MBKM. The "+" represents a small number of abnormal values that are outside the normal range.

4.4.2. Model Comprehensive Predictive Performance of Four Absence Sampling Methods with Respective Sample Intervals

Three metrics, namely AUC, KC, and POA, were used to weigh the comprehensive predictive performance of each model consisting of each group of samples. They are presented as box plots in Figures 17 and 18. The three metrics have a consistent pattern. In BCS, they increased slightly when the buffer size changed from 300 to 1000 m and decreased slightly to 1500 m. In BCS, the AUC was around 0.8, the KC did not exceed 0.6, and the POA reached a maximum of approximately 2.0. In CTSES, the three metrics gradually increased as d varied from 1 to 4. In IV and MBKM, the three metrics gradually decreased as the sampling threshold increased. In addition, the AUC approached 1 and even the POA approached 3 at low sampling intervals in IV and MBKM or a higher d in CTSES. In both the RF and SVM prediction models, the above-mentioned pattern was present.

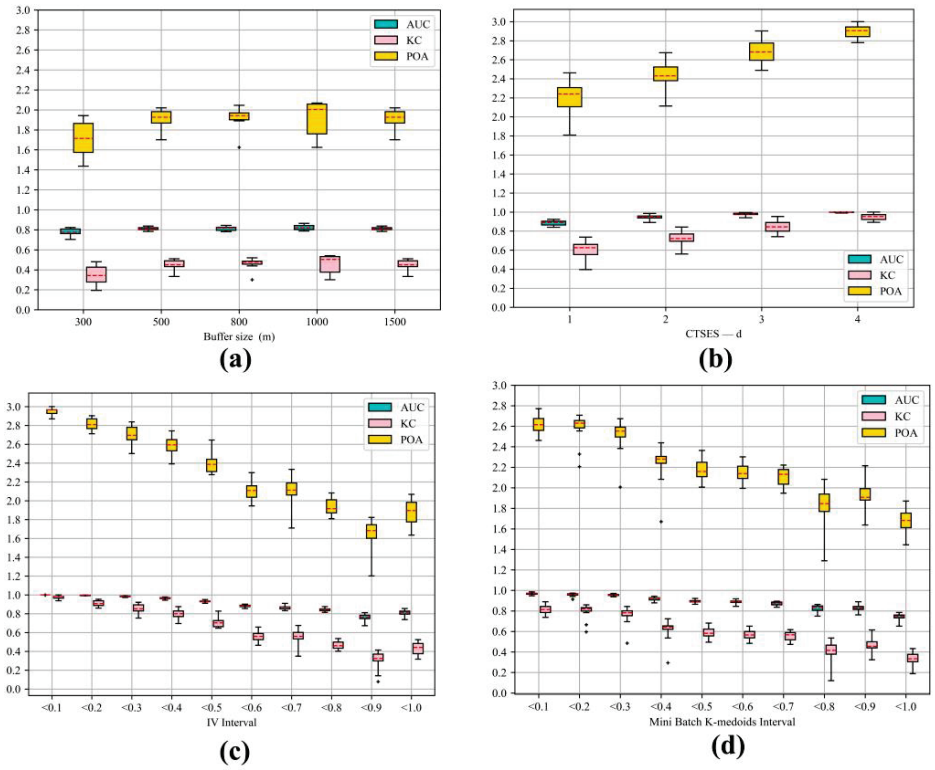

Figure 17. Prediction performance results of SVM-based absence sampling. (**a**) BCS; (**b**) CTSES; (**c**) IV; (**d**) MBKM.

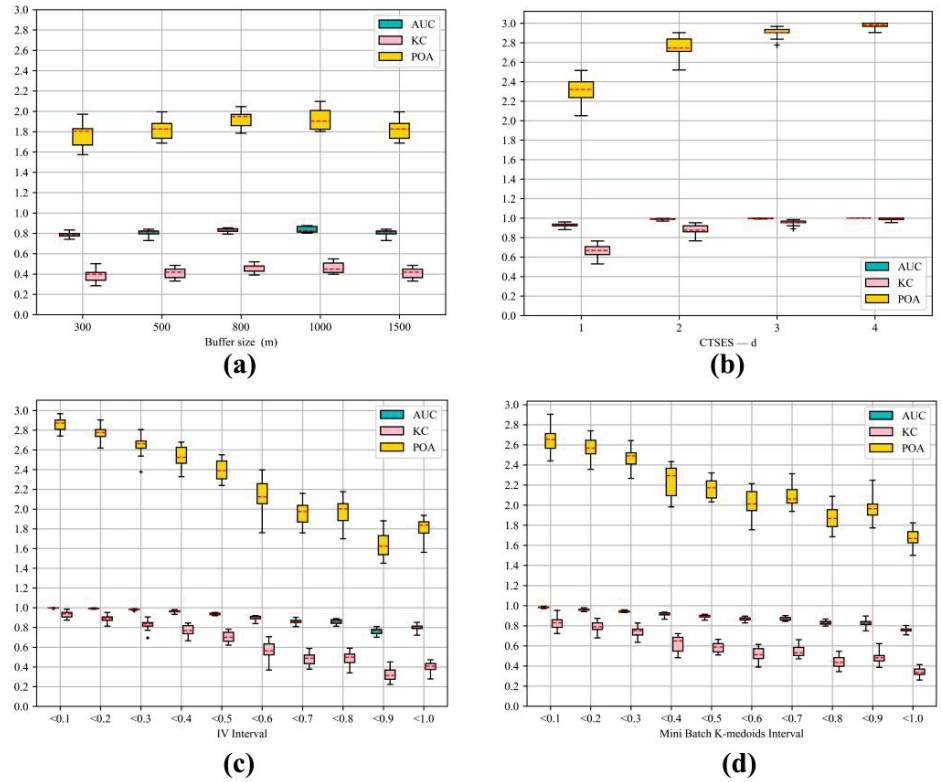

Figure 18. Prediction performance results of RF-based absence sampling. (**a**) BCS; (**b**) CTSES; (**c**) IV; (**d**) MBKM.

4.4.3. Model Susceptibility Distribution of Four Absence Sampling Methods with Respective Sample Intervals

Figure 19 shows the means and standard deviations of susceptibility for four absence sampling strategies with different intervals. In BCS, the change in mean and standard deviation was negligible. In the remaining three models, as *d* increased or the sampling threshold decreased, there was a significant increase in the mean and a weaker upward trend in the standard deviation. In CTSES, the change in the mean value was particularly pronounced, rising from 0.4 to 0.87. In IV and MBKM, the maximum mean values were approximately 0.65 and 0.8, respectively, when the threshold was 0.1. In terms of standard deviation, BCS had the lowest with a maximum value of about 0.2, while the other methods had a maximum value of 0.3 or above. In the comparison of the prediction models, the mean distributions of SVM and RF were about the same in BCS and IV, slightly higher for RF than SVM in CTSES, and higher for SVM than RF at low thresholds in MBKM. In addition, almost all standard deviations of the SVM model were larger than those of the RF model.

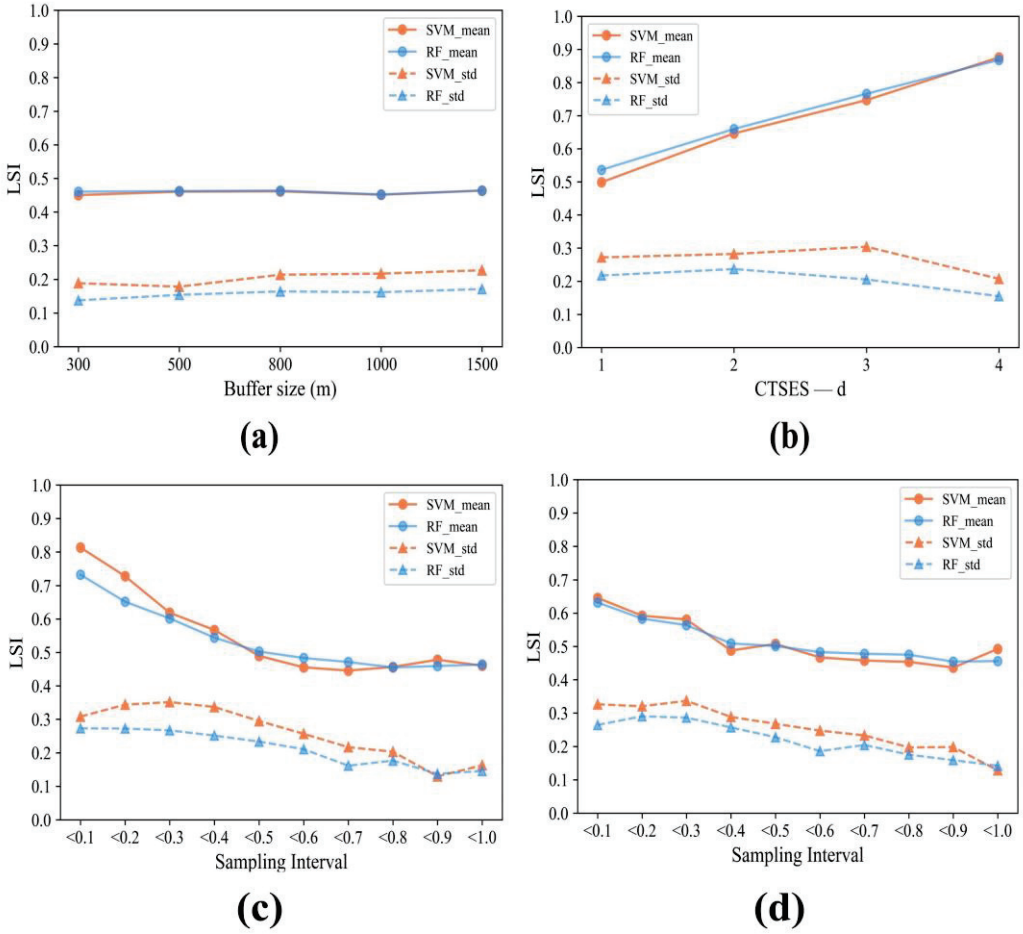

Figure 19. Means and standard deviations of four absence sampling methods with different intervals. (**a**) BCS; (**b**) CTSES; (**c**) IV; (**d**) MBKM.

4.4.4. Evaluation of the Integrative Sampling Model

The prediction model evaluation metrics for the integrative sampling approach are shown in Table 4. The training set accuracies were all greater than 0.9, while the training set accuracy of RF was maintained at a high level (>0.95). The testing accuracy and comprehensive predictive performance metrics, including the AUC, KC, and POA of SVM, were less than those of RF. When the ratio was 1:1, the various metrics fell within the region of the BCS and the other three models. The combined predictive performance of the integrative sampling model was stronger than that of BCS but weaker than the

performances of CTSES, IV, and MBKM under the same set of absence sample intervals. When the ratio changed from 1:1 to 3:7, each parameter decreased slightly, resulting in a slight decrease in prediction performance. In terms of susceptibility distribution, the mean value of integrative sampling was slightly higher than that of BCS but significantly lower than those of CTSES, IV, and MBKM. When the ratio changed from 1:1 to 3:7, further significant decreases in the mean value occurred (from 0.52 and 0.56 to 0.36 and 0.39).

Table 4. Metrics of the integrative sampling model.

Predictive Model	Presence: Absence	Training Accuracy	Testing Accuracy	AUC	KC	POA	Susceptibility Mean	Susceptibility SD
SVM	1:1	0.90	0.77	0.89	0.55	2.13	0.52	0.29
	3:7	0.93	0.81	0.87	0.56	2.06	0.36	0.28
RF	1:1	0.96	0.86	0.92	0.73	2.46	0.56	0.23
	3:7	0.97	0.83	0.91	0.60	2.15	0.39	0.21

5. Discussion

5.1. Effects of Absence Sampling Strategies and Sample Quality on LSM

Each of the four absence sample sampling models has its own control parameters. Figures 12 and 13 show the sensitivity of LSM to these parameters, and Figures 15–19 show the sensitivity of the model evaluation metrics to the parameters.

For BCS, various evaluation metrics show that buffer size has the best performance effect at 1000 m. The model's performance rises first when the buffer increases and then decreases when it increases to a certain level (1500 m). This scenario suggests that there may be a buffer size that is most suitable for generating negative samples. However, compared to the feature screening methods in CTSES, IV, and MBKM, the LSM prediction patterns and prediction performance metrics, as well as the susceptibility distribution of BCS, show little variation. This indicates that the improved geospatial-based absence sampling method has a certain upper limit and is less sensitive.

CTSES, IV, and MBKM were found to have significant sensitivity in LSM as well as various metrics to the control parameters, the main reason for which was absence sampling methods based on feature screening patterns. The control parameter d in CTSES and the sampling thresholds in IV and MBKM can be good representations of the negative sample quality. The larger the d or the lower the sampling threshold, the greater the difference between the features of the absence samples and the landslide samples, and the safer the region of the absence samples. These control parameters control the reliability or certainty of the absence of samples in the input model.

When the reliability and certainty of the absence samples are enhanced, an expansion of the high landslide susceptibility area and a divergence of the susceptibility index can be observed in the LSM results of these models and in the mean susceptibility level. Similar results can also be seen in other studies that have classified absence sample reliability [22]. These phenomena are particularly pronounced in IV and CTSES and slightly less pronounced in MBKM. At the same time, the model's predictive power indicators (accuracy, AUC, KC, and POA) are significantly improved or even close to full scores. These phenomena are due to the fact that when the non-landslide samples are too absent, the prediction model learns only the extreme features of the absent samples and the features of the landslides in the learning process. For those intermediate points between the extreme absence sample and the deterministic landslide sample, the model does not have enough information to assess them and overestimates them to a higher level of susceptibility. Since landslide samples and extreme absence samples are used for validation scores, the model's susceptibility overestimation will not lead to misjudgment of these samples; therefore, very high prediction scores can be obtained. The overestimation of the overall regional susceptibility by the model due to extreme samples is obviously unreasonable and difficult

to apply. This can be mitigated by reducing the *d* in CTSES or increasing the sampling threshold in IV and MBKM, but it will cause some degradation in prediction performance.

5.2. Advantages of Integrative Sampling

The integrative sampling absence sample set is combined with highly reliable absence samples, including CTSES-d = 4, IV-0.1, MBKM-0.1, and BCS-1000. Looking at the LSM prediction results for the integrative sampling method, it is surprising to see that the prediction pattern appears very reasonable. The flatland county in the central part of Songyang County is no longer misclassified as a high susceptibility area, and the excessive extension of the high susceptibility area in the gully to the banks has been significantly suppressed. The high landslide susceptibility areas are basically distributed in the gully and both sides of the gully, the eastern part of Songyang County, and around the central prefecture. The same samples (CTSES-d = 4, IV-0.1 and MBKM-0.1) would still be susceptible to overestimation and differentiation if returned to the original single absence sample sampling model, as Figures 12–14 show, but the integrated sampling method overcomes this. In addition, the normal mean level at a presence-absence ratio of 1:1 also indicates that the overall overestimation and divergence of regional susceptibility are greatly mitigated in integrative sampling (0.52 in SVM and 0.56 in RF compared with a max mean value of 0.87 in CTSES). Although the predictive assessment metrics (accuracy, AUC, KC, and POA) are lower than in the CTSES, IV, and MBKM methods, they are still much higher than in the BCS method. As shown in Table 4, the AUC of the integrative sampling method is around 0.9 for both SVM and RF models, with presence-absence ratios of 1:1 and 3:7, and the other metrics are within the excellent range (KC > 0.55, POA > 2.06).

Integrative sampling has the above advantages, mainly because the diversity of absence samples allows the prediction model to learn more non-landslide features. When predicting objects that are ambiguous, the model is able to synthesize the susceptibility value of the object based on the sample characteristics of each source. In the BCS individual model, the selection of absence samples is highly random and has the potential to give the model the wrong samples. In the CTSES, IV, and MBKM single models, the combination of features with high reliability absence samples may be highly similar, with insufficient information for the model to predict medium susceptibility objects. Integrative sampling combines various types of absence samples to obtain more information about the combination of absence sample features of CTSES, IV, and MBKM and also shares the error introduction rate of BCS. Thus, integrative sampling would give the predictive model a broader predictive capability rather than focusing on very low or very high susceptibility zones.

In addition, when the presence-absence ratio was changed from 1:1 to 3:7 in integrative sampling, a reduction in the high susceptibility zone and a decrease in the mean value of susceptibility were observed. Metrics of model predictive performance are reduced but within reasonable limits. Therefore, it is inferred that the overestimation level of regional susceptibility can be reduced by increasing the proportion of absence samples in the training process, as in another study [29]. Such an approach can be used in situations where the overall regional susceptibility is too high or where very high susceptibility areas need to be located quickly.

6. Conclusions

Four absence sampling methods were employed in LSM, namely BCS, CTSES, IV, and MBKM, and a new method of integrative sampling was proposed. In these methods, the TSES method was improved to obtain the CTSES method, and the less commonly used optimized clustering algorithm MBKM was introduced and showed a more reasonable prediction pattern than the IV model with the same set of samples. The absence of samples generated by these four methods were mixed for the test of the integrative sampling method. The above methods were applied to LSM in Songyang County, Lishui City, Zhejiang Province, China, and the effects of various absence sampling methods and the

quality of absence samples in LSM were discussed. Multiple sets of sampling intervals were set for each method, and extensive training computations were conducted in each interval. The results indicate that, as the certainty and reliability of the sample increase, expansion of the high susceptibility region and divergence of the susceptibility index occur in the CTSES, IV, and MBKM methods. This phenomenon can be significantly reduced, and very satisfactory prediction results can be achieved by employing the proposed integrative sampling method or a higher proportion of absence samples. Integrative sampling has a stronger prediction performance than the general independent absence sample sampling method and can combine the sample information of each sampling method for a more reasonable classification of high, low, and medium susceptibility areas. The integrative sampling method presents a valuable approach for constructing absence samples in LSM based on data-driven models.

Author Contributions: Z.F. drafted the manuscript and was responsible for the research design, experiment, and analysis; F.W. provided the supervision, funding acquisition, and overall recommendation for the study area. F.W., J.D., K.N. and H.M. contributed to reviewing and editing the manuscript. All authors have read and agreed to the published version of the manuscript.

Funding: This study was supported by the National Natural Science Foundation of China (grant nos. 42230715).

Data Availability Statement: The data that support the findings of this study are available from the first author upon reasonable request.

Acknowledgments: Thanks to the Geological hazard risk census report of Songyang County, Zhejiang Province for the basic landslide field information for this research.

Conflicts of Interest: The authors declare no conflict of interest.

References

1. Wang, F.; Sassa, K. Landslide Simulation by a Geotechnical Model Combined with a Model for Apparent Friction Change. *Phys. Chem. Earth Parts ABC* **2010**, *35*, 149–161. [CrossRef]
2. Adnan, M.S.G.; Rahman, M.S.; Ahmed, N.; Ahmed, B.; Rabbi, M.F.; Rahman, R.M. Improving Spatial Agreement in Machine Learning-Based Landslide Susceptibility Mapping. *Remote Sens.* **2020**, *12*, 3347. [CrossRef]
3. Scaioni, M.; Longoni, L.; Melillo, V.; Papini, M. Remote Sensing for Landslide Investigations: An Overview of Recent Achievements and Perspectives. *Remote Sens.* **2014**, *6*, 9600–9652. [CrossRef]
4. Zhao, C.; Lu, Z. Remote Sensing of Landslides—A Review. *Remote Sens.* **2018**, *10*, 279. [CrossRef]
5. Mohan, A.; Singh, A.K.; Kumar, B.; Dwivedi, R. Review on Remote Sensing Methods for Landslide Detection Using Machine and Deep Learning. *Trans. Emerg. Telecommun. Technol.* **2021**, *32*, e3998. [CrossRef]
6. Guzzetti, F.; Reichenbach, P.; Cardinali, M.; Galli, M.; Ardizzone, F. Probabilistic Landslide Hazard Assessment at the Basin Scale. *Geomorphology* **2005**, *72*, 272–299. [CrossRef]
7. Corominas, J.; van Westen, C.; Frattini, P.; Cascini, L.; Malet, J.-P.; Fotopoulou, S.; Catani, F.; Van Den Eeckhaut, M.; Mavrouli, O.; Agliardi, F.; et al. Recommendations for the Quantitative Analysis of Landslide Risk. *Bull. Eng. Geol. Environ.* **2014**, *73*, 209–263. [CrossRef]
8. Li, L.; Lan, H.; Guo, C.; Zhang, Y.; Li, Q.; Wu, Y. A Modified Frequency Ratio Method for Landslide Susceptibility Assessment. *Landslides* **2017**, *14*, 727–741. [CrossRef]
9. Dou, J.; Xiang, Z.; Qiang, X.; Zheng, P.; Wang, X.; Su, A.; Liu, J.; Luo, W. Application and Development Trend of Machine Learning in Landslide Intelligent Disaster Prevention and Mitigation. *Earth Sci.* **2022**.
10. Merghadi, A.; Yunus, A.P.; Dou, J.; Whiteley, J.; ThaiPham, B.; Bui, D.T.; Avtar, R.; Abderrahmane, B. Machine Learning Methods for Landslide Susceptibility Studies: A Comparative Overview of Algorithm Performance. *Earth-Sci. Rev.* **2020**, *207*, 103225. [CrossRef]
11. Nam, K.; Wang, F. An Extreme Rainfall-Induced Landslide Susceptibility Assessment Using Autoencoder Combined with Random Forest in Shimane Prefecture, Japan. *Geoenvironmental Disasters* **2020**, *7*, 6. [CrossRef]
12. Nam, K.; Wang, F. The Performance of Using an Autoencoder for Prediction and Susceptibility Assessment of Landslides: A Case Study on Landslides Triggered by the 2018 Hokkaido Eastern Iburi Earthquake in Japan. *Geoenvironmental Disasters* **2019**, *6*, 19. [CrossRef]
13. Huang, F.; Zhang, J.; Zhou, C.; Wang, Y.; Huang, J.; Zhu, L. A Deep Learning Algorithm Using a Fully Connected Sparse Autoencoder Neural Network for Landslide Susceptibility Prediction. *Landslides* **2020**, *17*, 217–229. [CrossRef]
14. Huang, F.; Cao, Z.; Guo, J.; Jiang, S.-H.; Li, S.; Guo, Z. Comparisons of Heuristic, General Statistical and Machine Learning Models for Landslide Susceptibility Prediction and Mapping. *Catena* **2020**, *191*, 104580. [CrossRef]

15. Huang, F.; Xiong, H.; Yao, C.; Catani, F.; Zhou, C.; Huang, J. Uncertainties of Landslide Susceptibility Prediction Considering Different Landslide Types. *J. Rock Mech. Geotech. Eng.* **2023**. [CrossRef]
16. Zhu, A.-X.; Miao, Y.; Yang, L.; Bai, S.; Liu, J.; Hong, H. Comparison of the Presence-Only Method and Presence-Absence Method in Landslide Susceptibility Mapping. *Catena* **2018**, *171*, 222–233. [CrossRef]
17. Atkinson, P.M.; Massari, R. Generalised linear modelling of susceptibility to landsliding in the central apennines, Italy. *Comput. Geosci.* **1998**, *24*, 373–385. [CrossRef]
18. Hearn, G.J.; Hart, A.B. Landslide Susceptibility Mapping: A Practitioner's View. *Bull. Eng. Geol. Environ.* **2019**, *78*, 5811–5826. [CrossRef]
19. Carrara, A.; Cardinali, M.; Guzzetti, F.; Reichenbach, P. Gis Technology in Mapping Landslide Hazard. In *Geographical Information Systems in Assessing Natural Hazards*; Carrara, A., Guzzetti, F., Eds.; Advances in Natural and Technological Hazards Research; Springer: Dordrecht, The Netherlands, 1995; pp. 135–175. ISBN 978-94-015-8404-3.
20. Dou, J.; Yunus, A.P.; Merghadi, A.; Shirzadi, A.; Nguyen, H.; Hussain, Y.; Avtar, R.; Chen, Y.; Pham, B.T.; Yamagishi, H. Different Sampling Strategies for Predicting Landslide Susceptibilities Are Deemed Less Consequential with Deep Learning. *Sci. Total Environ.* **2020**, *720*, 137320. [CrossRef]
21. Pourghasemi, H.R.; Kornejady, A.; Kerle, N.; Shabani, F. Investigating the Effects of Different Landslide Positioning Techniques, Landslide Partitioning Approaches, and Presence-Absence Balances on Landslide Susceptibility Mapping. *Catena* **2020**, *187*, 104364. [CrossRef]
22. Zhu, A.-X.; Miao, Y.; Liu, J.; Bai, S.; Zeng, C.; Ma, T.; Hong, H. A Similarity-Based Approach to Sampling Absence Data for Landslide Susceptibility Mapping Using Data-Driven Methods. *Catena* **2019**, *183*, 104188. [CrossRef]
23. Sameen, M.I.; Pradhan, B.; Bui, D.T.; Alamri, A.M. Systematic Sample Subdividing Strategy for Training Landslide Susceptibility Models. *Catena* **2020**, *187*, 104358. [CrossRef]
24. Lucchese, L.V.; de Oliveira, G.G.; Pedrollo, O.C. Investigation of the Influence of Nonoccurrence Sampling on Landslide Susceptibility Assessment Using Artificial Neural Networks. *Catena* **2021**, *198*, 105067. [CrossRef]
25. Pradhan, B.; Lee, S.; Buchroithner, M.F. A GIS-Based Back-Propagation Neural Network Model and Its Cross-Application and Validation for Landslide Susceptibility Analyses. *Comput. Environ. Urban Syst.* **2010**, *34*, 216–235. [CrossRef]
26. Wang, H.; Zhang, L.; Luo, H.; He, J.; Cheung, R.W.M. AI-Powered Landslide Susceptibility Assessment in Hong Kong. *Eng. Geol.* **2021**, *288*, 106103. [CrossRef]
27. Chang, Z.; Huang, J.; Huang, F.; Bhuyan, K.; Meena, S.R.; Catani, F. Uncertainty Analysis of Non-Landslide Sample Selection in Landslide Susceptibility Prediction Using Slope Unit-Based Machine Learning Models. *Gondwana Res.* **2023**, *117*, 307–320. [CrossRef]
28. Xiao, C.; Tian, Y.; Shi, W.; Guo, Q.; Wu, L. A New Method of Pseudo Absence Data Generation in Landslide Susceptibility Mapping with a Case Study of Shenzhen. *Sci. China Technol. Sci.* **2010**, *53*, 75–84. [CrossRef]
29. Hong, H.; Miao, Y.; Liu, J.; Zhu, A.-X. Exploring the Effects of the Design and Quantity of Absence Data on the Performance of Random Forest-Based Landslide Susceptibility Mapping. *Catena* **2019**, *176*, 45–64. [CrossRef]
30. Rabby, Y.W.; Li, Y.; Hilafu, H. An Objective Absence Data Sampling Method for Landslide Susceptibility Mapping. *Sci. Rep.* **2023**, *13*, 1740. [CrossRef]
31. Yuan, X.; Liu, C.; Nie, R.; Yang, Z.; Li, W.; Dai, X.; Cheng, J.; Zhang, J.; Ma, L.; Fu, X.; et al. A Comparative Analysis of Certainty Factor-Based Machine Learning Methods for Collapse and Landslide Susceptibility Mapping in Wenchuan County, China. *Remote Sens.* **2022**, *14*, 3259. [CrossRef]
32. Zhao, B.; Ge, Y.; Chen, H. Landslide Susceptibility Assessment for a Transmission Line in Gansu Province, China by Using a Hybrid Approach of Fractal Theory, Information Value, and Random Forest Models. *Environ. Earth Sci.* **2021**, *80*, 441. [CrossRef]
33. Xu, C.; Zhang, W.; Yi, Y.; Xu, Q. Landslide Susceptibility Mapping Using Logistic Regression Model Based on Information Value for the Region Along China-Thailand Railway from Saraburi to Sikhio, Thailand. In Proceedings of the IGARSS 2019—2019 IEEE International Geoscience and Remote Sensing Symposium, Yokohama, Japan, 31 July 2019; pp. 9650–9653.
34. Zhao, Z.; Liu, Z.Y.; Xu, C. Slope Unit-Based Landslide Susceptibility Mapping Using Certainty Factor, Support Vector Machine, Random Forest, CF-SVM and CF-RF Models. *Front. Earth Sci.* **2021**, *9*, 589630. [CrossRef]
35. Ji, J.; Zhou, Y.; Cheng, Q.; Jiang, S.; Liu, S. Landslide Susceptibility Mapping Based on Deep Learning Algorithms Using Information Value Analysis Optimization. *Land* **2023**, *12*, 1125. [CrossRef]
36. Li, Y.; Deng, X.; Ji, P.; Yang, Y.; Jiang, W.; Zhao, Z. Evaluation of Landslide Susceptibility Based on CF-SVM in Nujiang Prefecture. *Int. J. Environ. Res. Public. Health* **2022**, *19*, 14248. [CrossRef]
37. Huang, F.; Yin, K.; Huang, J.; Gui, L.; Wang, P. Landslide Susceptibility Mapping Based on Self-Organizing-Map Network and Extreme Learning Machine. *Eng. Geol.* **2017**, *223*, 11–22. [CrossRef]
38. Kaboutari, A.; Bagherzadeh, J.; Kheradmand, F. An Evaluation of Two-Step Techniques for Positive-Unlabeled Learning in Text Classification. *Int. J. Comput. Appl. Technol. Res.* **2014**, *3*, 592–594. [CrossRef]
39. Huang, F.; Cao, Z.; Jiang, S.-H.; Zhou, C.; Huang, J.; Guo, Z. Landslide Susceptibility Prediction Based on a Semi-Supervised Multiple-Layer Perceptron Model. *Landslides* **2020**, *17*, 2919–2930. [CrossRef]
40. Yao, J.; Qin, S.; Qiao, S.; Liu, X.; Zhang, L.; Chen, J. Application of a Two-Step Sampling Strategy Based on Deep Neural Network for Landslide Susceptibility Mapping. *Bull. Eng. Geol. Environ.* **2022**, *81*, 148. [CrossRef]

41. Chang, Z.; Du, Z.; Zhang, F.; Huang, F.; Chen, J.; Li, W.; Guo, Z. Landslide Susceptibility Prediction Based on Remote Sensing Images and GIS: Comparisons of Supervised and Unsupervised Machine Learning Models. *Remote Sens.* **2020**, *12*, 502. [CrossRef]
42. Zhu, L.P.; Chen, R.; Zeng, J.W.; Liao, S.B.; Yang, Z.L. Main structural characteristics of Yanshanian in Shengzhou area of Yuyao-Lishui fault zone (in Chinese). *Chin. Geol. Surv.* **2018**, *5*, 49–57.
43. Chen, L.F. Study on the Activity of NE Trending Faults along the Coast of Zhejiang Province (in Chinese). Master's Thesis, Zhejiang University, Hangzhou, China, 2010.
44. Wang, F.; Chen, Y.; Peng, X.; Zhu, G.; Yan, K.; Ye, Z. The Fault-Controlled Chengtian Landslide Triggered by Rainfall on 20 May 2021 in Songyang County, Zhejiang Province, China. *Landslides* **2022**, *19*, 1751–1765. [CrossRef]
45. Fabbri, A.G.; Chung, C.-J.F.; Cendrero, A.; Remondo, J. Is Prediction of Future Landslides Possible with a GIS? *Nat. Hazards* **2003**, *30*, 487–503. [CrossRef]
46. Yi, Y.; Zhang, Z.; Zhang, W.; Jia, H.; Zhang, J. Landslide Susceptibility Mapping Using Multiscale Sampling Strategy and Convolutional Neural Network: A Case Study in Jiuzhaigou Region. *Catena* **2020**, *195*, 104851. [CrossRef]
47. Xi, C.; Han, M.; Hu, X.; Liu, B.; He, K.; Luo, G.; Cao, X. Effectiveness of Newmark-Based Sampling Strategy for Coseismic Landslide Susceptibility Mapping Using Deep Learning, Support Vector Machine, and Logistic Regression. *Bull. Eng. Geol. Environ.* **2022**, *81*, 174. [CrossRef]
48. Hu, J.; Xu, K.; Wang, G.; Liu, Y.; Khan, M.A.; Mao, Y.; Zhang, M. A Novel Landslide Susceptibility Mapping Portrayed by OA-HD and K-Medoids Clustering Algorithms. *Bull. Eng. Geol. Environ.* **2021**, *80*, 765–779. [CrossRef]
49. Pokharel, B.; Althuwaynee, O.F.; Aydda, A.; Kim, S.-W.; Lim, S.; Park, H.-J. Spatial Clustering and Modelling for Landslide Susceptibility Mapping in the North of the Kathmandu Valley, Nepal. *Landslides* **2021**, *18*, 1403–1419. [CrossRef]
50. Kim, J.-C.; Lee, S.; Jung, H.-S.; Lee, S. Landslide Susceptibility Mapping Using Random Forest and Boosted Tree Models in Pyeong-Chang, Korea. *Geocarto Int.* **2018**, *33*, 1000–1015. [CrossRef]
51. Dou, J.; Yunus, A.P.; Tien Bui, D.; Merghadi, A.; Sahana, M.; Zhu, Z.; Chen, C.-W.; Khosravi, K.; Yang, Y.; Pham, B.T. Assessment of Advanced Random Forest and Decision Tree Algorithms for Modeling Rainfall-Induced Landslide Susceptibility in the Izu-Oshima Volcanic Island, Japan. *Sci. Total Environ.* **2019**, *662*, 332–346. [CrossRef]
52. Dou, J.; Yunus, A.P.; Bui, D.T.; Merghadi, A.; Sahana, M.; Zhu, Z.; Chen, C.-W.; Han, Z.; Pham, B.T. Improved Landslide Assessment Using Support Vector Machine with Bagging, Boosting, and Stacking Ensemble Machine Learning Framework in a Mountainous Watershed, Japan. *Landslides* **2020**, *17*, 641–658. [CrossRef]
53. Yao, X.; Tham, L.G.; Dai, F.C. Landslide Susceptibility Mapping Based on Support Vector Machine: A Case Study on Natural Slopes of Hong Kong, China. *Geomorphology* **2008**, *101*, 572–582. [CrossRef]
54. Hong, H.; Pradhan, B.; Jebur, M.N.; Bui, D.T.; Xu, C.; Akgun, A. Spatial Prediction of Landslide Hazard at the Luxi Area (China) Using Support Vector Machines. *Environ. Earth Sci.* **2015**, *75*, 40. [CrossRef]
55. Marjanović, M.; Kovačević, M.; Bajat, B.; Voženílek, V. Landslide Susceptibility Assessment Using SVM Machine Learning Algorithm. *Eng. Geol.* **2011**, *123*, 225–234. [CrossRef]
56. Wang, H.; Zhang, L.; Yin, K.; Luo, H.; Li, J. Landslide Identification Using Machine Learning. *Geosci. Front.* **2021**, *12*, 351–364. [CrossRef]
57. Beauchamp, K.A.; Bowman, G.R.; Lane, T.J.; Maibaum, L.; Haque, I.S.; Pande, V.S. MSMBuilder2: Modeling Conformational Dynamics on the Picosecond to Millisecond Scale. *J. Chem. Theory Comput.* **2011**, *7*, 3412–3419. [CrossRef]

land

MDPI

Article

Landslide Susceptibility Mapping Based on Deep Learning Algorithms Using Information Value Analysis Optimization

Junjie Ji [1,2,3], Yongzhang Zhou [1,2,3,*], Qiuming Cheng [1], Shoujun Jiang [4] and Shiting Liu [5]

[1] School of Earth Science and Engineering, Sun Yat-sen University, Zhuhai 519000, China
[2] Guangdong Provincial Key Laboratory of Geological Processes and Mineral Resource Survey, Guangzhou 510275, China
[3] School of Earth Sciences and Engineering, Center for Earth Environment & Resources, Sun Yat-sen University, Guangzhou 510275, China
[4] Guangdong Geological Survey Institute, Guangzhou 510275, China
[5] The Sixth Geological Team of Guangdong Geological Bureau, Jiangmen 529000, China
* Correspondence: zhouyz@mail.sysu.edu.cn

Abstract: Selecting samples with non-landslide attributes significantly impacts the deep-learning modeling of landslide susceptibility mapping. This study presents a method of information value analysis in order to optimize the selection of negative samples used for machine learning. Recurrent neural network (RNN) has a memory function, so when using an RNN for landslide susceptibility mapping purposes, the input order of the landslide-influencing factors affects the resulting quality of the model. The information value analysis calculates the landslide-influencing factors, determines the input order of data based on the importance of any specific factor in determining the landslide susceptibility, and improves the prediction potential of recurrent neural networks. The simple recurrent unit (SRU), a newly proposed variant of the recurrent neural network, is characterized by possessing a faster processing speed and currently has less application history in landslide susceptibility mapping. This study used recurrent neural networks optimized by information value analysis for landslide susceptibility mapping in Xinhui District, Jiangmen City, Guangdong Province, China. Four models were constructed: the RNN model with optimized negative sample selection, the SRU model with optimized negative sample selection, the RNN model, and the SRU model. The results show that the RNN model with optimized negative sample selection has the best performance in terms of AUC value (0.9280), followed by the SRU model with optimized negative sample selection (0.9057), the RNN model (0.7277), and the SRU model (0.6355). In addition, several objective measures of accuracy (0.8598), recall (0.8302), F1 score (0.8544), Matthews correlation coefficient (0.7206), and the receiver operating characteristic also show that the RNN model performs the best. Therefore, the information value analysis can be used to optimize negative sample selection in landslide sensitivity mapping in order to improve the model's performance; second, SRU is a weaker method than RNN in terms of model performance.

Keywords: landslide susceptibility mapping; information value analysis; recurrent neural network; simple recurrent unit

Citation: Ji, J.; Zhou, Y.; Cheng, Q.; Jiang, S.; Liu, S. Landslide Susceptibility Mapping Based on Deep Learning Algorithms Using Information Value Analysis Optimization. *Land* **2023**, *12*, 1125. https://doi.org/10.3390/land12061125

Academic Editors: Stefano Morelli, Veronica Pazzi and Mirko Francioni

Received: 24 April 2023
Revised: 18 May 2023
Accepted: 22 May 2023
Published: 25 May 2023

1. Introduction

Faced with current human societal challenges, it is more important than ever for geoscientists to use their understanding of the earth to benefit the society [1]. The most notable development in the field of mathematical geoscience in the last decade has been the introduction of big data and artificial intelligence algorithms. The ability of machine learning (ML) algorithms to handle nonlinear problems has tremendous advantages in dealing with complex geoscience problems [2–4]. As a result, ML is now being fully utilized in geoscience fields. For example, Wang et al. used unsupervised ML algorithms to identify multielement geochemical anomalies [5], and Yu et al. used hierarchical clustering,

singularity mapping, and the Kohonen neural network to identify Ag–Au–Pb–Zn polymetallic mineralization-associated geochemical anomalies [6]. In general, we are primarily focused on geological events that have a significant impact but occur infrequently, such as earthquakes, typhoons, vein formation, and landslides.

Landslides are natural disasters that pose a serious risk to human lives and property and represent one of the most destructive categories of natural disasters that occur globally [7]. Mountainous areas are especially affected by landslides, whose controlling mechanisms are the complex geological and geographical conditions present in that landscape. Seventy percent of China's area is mountainous, providing favorable conditions for landslide occurrences, resulting in casualties and considerable economic losses [8–11]. As a consequence, landslide susceptibility mapping (LSM), which can analyze possible spatial areas for landslide occurrence, is an effective technique for land managers to mitigate the effects of landslides [12,13].

Machine learning is a subdivision of artificial intelligence (AI) that uses computer technologies to analyze and predict information by learning from the training dataset. A variety of ML methods have been used for LSM, including Bayesian networks, decision trees, support vector machines, random forests, and artificial networks [14–18]. It is to be noted that in recent years, in the implementation and development of natural hazard modelling, researchers have begun to consider the use of hybrid models. Hybrid models combine individual models with metaheuristic algorithms, allowing the hybrid model to eliminate the weak points inherent to the individual models to obtain more accurate results. For example, adaptive neuro-fuzzy system-gradient-based optimization (ANFIS-GBO) is applied to the spatial modelling of flood hazards [19]; cuckoo optimization algorithm-multi-layer perceptron (COA-MLP) and SailFish optimizer- multi-layer perceptron (SFO-MLP) approaches are applied to the landslide susceptibility assessment [20]; and ANFIS integrated three optimization algorithms (ant colony optimization (ACO), genetic algorithm (GA), and particle swarm optimization (PSO)) applied to flood susceptibility maps [21]. A variety of machine learning and deep learning models have been used to improve the accuracy of LSM. In recent years, to obtain better deep learning and machine learning models, researchers have adopted a variety of improved methods, such as the deep-learning optimization algorithm [22], the hybrid ensemble-based deep-learning framework [23], and the class-weighted algorithm combined with ML models [24].

Deep learning models have been increasingly applied in the modeling of environmental variables, such as environmental remote sensing [25], PM2.5 prediction [26], and water temperature prediction [27]. Recurrent neural networks (RNNs) are a specific kind of neural network that not only considers the previous moment's input but also gives the network a "memory" function for the previous content. Based on this unique function of the RNN approach, the order of data input will affect the model's effectiveness. Exploring a sequential data representation method can take advantage of the memory function of RNNs, which allows for thorough exploration of the prediction potential of RNNs. RNNs have been applied to LSM. Thi Ngo et al. applied RNN and CNN techniques for an LSM of Iran at the national scale [28]. Liming Xiao et al. used long short-term memory (LSTM) to predict landslide susceptibility along the China–Nepal Highway [29]. The common variants of RNNs are LSTM [30] and gated recurrent units (GRUs) [31]. Recently, a simple recurrent unit (SRU) was proposed as a new RNN variant that has a faster processing speed than the LSTM and GRU approaches. The use of the new RNN variant, using an SRU, has less application in LSM, and its specific performance in LSM should be further studied.

Traditional binary classifiers for machine learning usually require two sets of samples with corresponding labels, including positive and negative samples [32]. There are often imperfect cases in the practical applications, however, most commonly manifesting when only positive and unlabeled samples are used in the training dataset. For non-landslide samples, there still needs to be a specific definition and a reasonable method to obtain them. In general, the study area is divided into landslide and non-landslide areas. Furthermore, samples from non-landslide areas can be drawn randomly from non-landslide

areas. These unlabeled samples cannot be directly considered negative samples, because the areas of these samples are likely to be the only areas where disasters have not yet occurred [33]. At present, the issue of non-landslide sample selection has received some attention. Yang et al. [34] used Bayesian optimization algorithms to optimize the proportion of landslide samples. Chang et al. [35] selected non-landslide samples multiple times and investigated the uncertainty of non-landslide sample selection. Huang et al. [36] selected the non-landslide samples from the non-landslide area with a low landslide susceptibility level based on a semi-supervised multiple-layer perceptron model. Overall, there is no universally accepted method for optimizing non-landslide sample selection due to the differences in study areas and the logic and mechanisms behind different algorithms, which need to be studied thoroughly.

Therefore, the main innovation of this study is to optimize the selection of negative samples using information value analysis. Information value analysis determines the input order of the data by calculating the influence factors and fully explores the prediction potential of RNNs with memory function. In addition, SRU has been less studied on LSM, and both RNN and SRU models are constructed to explore the prediction performance of SRU through a comparative study.

2. Study Area

2.1. Description

Xinhui District, located between latitudes 22°5′15″ and 22°35′01″ N and longitudes 112°46′55″ and 113°15′43″ E, is in the south-central part of Guangdong Province (Figure 1). The land area of the region contains 1354.71 square kilometers. Mountainous areas are distributed in the northwest and southwest of the district, accounting for 35.84% of the total area of the region. Plains are distributed in the southeastern, south-central and west-central parts of the district, accounting for 43.53% of the total area of the district. The region's waters account for 20.63% of the total area of the region. Xinhui has a southern subtropical maritime monsoon climate, abundant rainfall, sufficient sunshine, and mild and humid conditions year round. The average annual temperature is 22.4 °C, with the highest and lowest historical temperatures of 38.3 °C and 0.1 °C, respectively. The annual average precipitation is 1808.3 mm. The precipitation is concentrated from April through September. The average annual sunshine hours are 1734.1 h.

The list of landslides used in this paper, completed by the Guangdong Geological Survey Institute, consists of 178 landslides and locations of high-risk points (Figure 1), of which the landslide samples occurred from 2017 to 2020. Most of the landslides are classified as sliding landslides. All the landslides in this study can be classified as moderate (400–1000 m^2) and small (<400 m^2). In addition, there are rock landslides and earth landslides. According to the report, these landslides were triggered by rainfall events that occurred after anthropogenic activity.

2.2. Datasets

Heckmann et al. [37] stated that the increase in the samples accounted for has had a positive impact on the LSM and has increased the model's effectiveness. However, the training samples used for LSM are insufficient in many cases. To solve this problem, we collaborated with geologists to collect historical landslide points and locations with significant potential for landslides throughout the whole region, totaling 178 points. We used these points as samples to improve the effectiveness of the model.

In this study, 15 landslide influencing factors were considered, including elevation, slope, aspect, plan curvature, profile curvature, degree of relief, land use, rock type, topographic wetness index (TWI), terrain ruggedness index (TRI), topographic position index (TPI), normalized difference vegetation index (NDVI) on 15 April 2014, distance to faults, distance to rivers, and distance to roads. Detailed information on the landslide influencing factors is shown in Table 1. The following describes the preparation for each influencing factor.

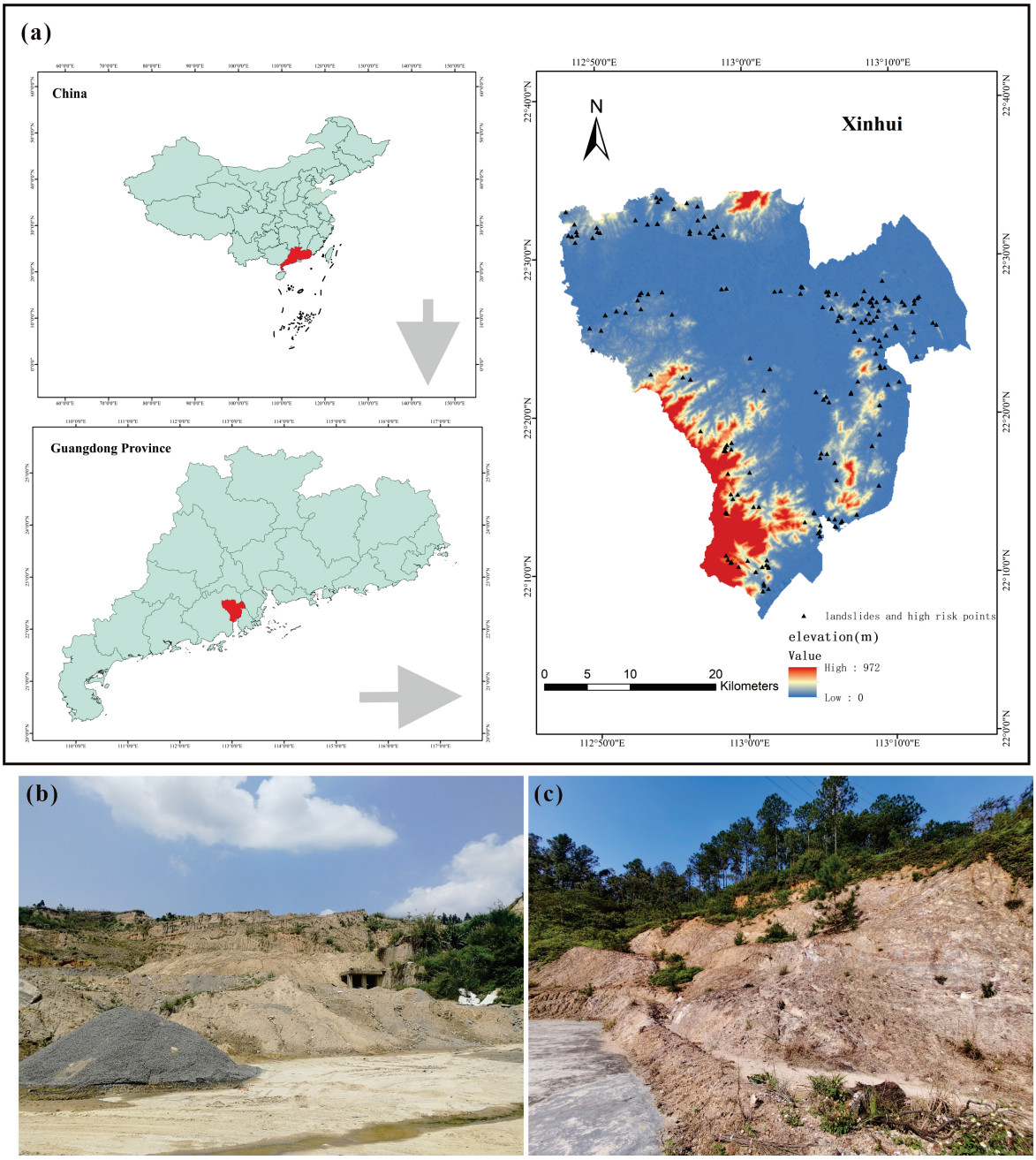

Figure 1. (**a**) Location of the study area; (**b**) and (**c**) are field photos.

The elevation, slope, aspect, plan curvature, profile curvature and degree of relief were extracted from a digital elevation model (DEM) obtained from the Advanced Spaceborne Thermal Emission and Reflection Radiometer Global Digital Elevation Model (ASTER GDEM V2) (http://www.gscloud.cn, accessed on 11 March 2021). Slope, aspect, plan curvature, profile curvature, and degree of relief were calculated in the MapGIS 10.2 software. The TWI and TPI were generated by the SAGA 6.1 software. The distance to roads and the distance to rivers were produced by ArcGIS based on topographic maps at a scale of 1:50,000. The distance to faults was produced by ArcGIS based on engineering geological maps at a scale of 1:50,000. We obtained NDVI data for the study area from the USGS (https://earthexplorer.usgs.gov, accessed on 20 March 2021). Land use data and rock type data were provided by the collaboration with geologists. All factors were converted into a raster form with a spatial resolution of 20 m. The descriptions of these factors are shown in Table 1. Figure 2 shows the spatial distribution of these factors.

Table 1. Description of landslide factors.

Factor Type	Factors	Range
Geologic Factors	Rock type	Granite, Sandstone, Slate, Quaternary sediments and rivers
	Distance to faults (m)	(0, 6046)
Topographic Factors	Elevation (m)	(0, 972)
	Slope	(0, 49.73)
	Aspect	Flat, North, Northeast, East, Southeast, South, Southwest, West, Northwest
	Plan curvature	(0, 65.46)
	Profile curvature	(0, 11.36)
	Degree of relief	(0, 40.73)
	TRI	(0, 83.00)
	TPI	(−6.49, 10.96)
Water-Related Factors	Distance to rivers (m)	(0, 3691)
	TWI	(0, 22.68)
Anthropogenic Factors	Land use	Farmland, Forest and grass, Residential, Bare, Water
	Distance to roads (m)	(0, 2704)
Vegetation Factors	NDVI	(−1, 1)

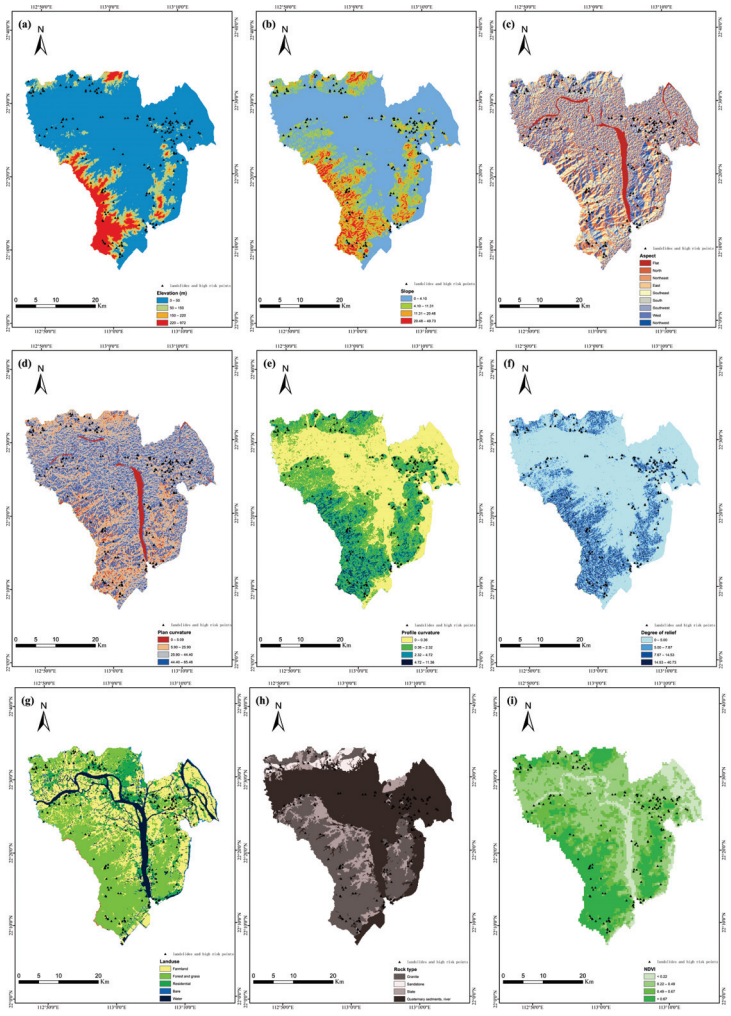

Figure 2. *Cont.*

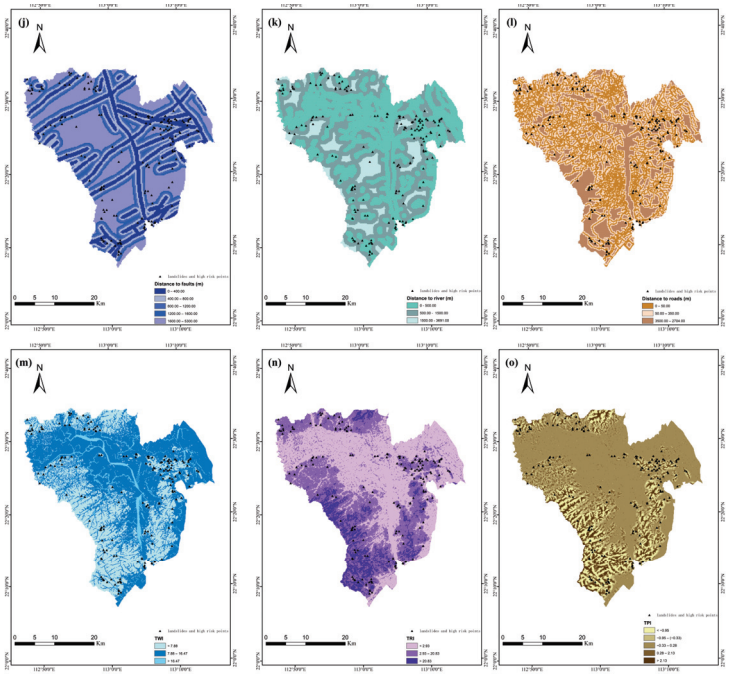

Figure 2. Spatial distribution of landslide influencing factors: (**a**) elevation, (**b**) slope, (**c**) aspect, (**d**) plan curvature, (**e**) profile curvature, (**f**) degree of relief, (**g**) land use, (**h**) rock type, (**i**) NDVI, (**j**) distance to faults, (**k**) distance to river, (**l**) distance to roads, (**m**) TWI, (**n**) TRI, and (**o**) TPI.

3. Materials and Methods

Figure 3 shows the process diagram used in this study. There are six steps in this process: (1) selecting the landslide influencing factors, (2) selecting typical negative samples and representing landslide data in series based on the information values (IVs), (3) preparing both the training and testing datasets by random partitioning, (4) constructing RNN and SRU models, (5) evaluating and comparing the landslide models, and (6) constructing a landslide susceptibility map.

3.1. Information Value Analysis

Information value analysis is a data exploration technique that helps determine which columns in a dataset have predictive power or influence on the value of a specified dependent variable. Information value is a very useful concept for variable selection during model building. The roots of the IVs are in the information theory that was proposed by Claude Shannon [38,39]. The IV analysis is a popular tool in the banking and bond ratings fields [40,41]. The effectiveness of landslide models can be enhanced by introducing IV into the processing of landslide factors for LSM. The correlation coefficient can be calculated as follows:

$$IV(x_i) = (n_{i1}/n_1 - n_{i0}/n_0)WOE(x_i) = (n_{i1}/n_1 - n_{i0}/n_0)\ln\frac{n_{i1}/n_1}{n_{i0}/n_0} \quad (1)$$

$$IV(x) = \sum_{i=1}^{N} IV(x_i) \quad (2)$$

where n_1 is the total number of landslide rasters, n_0 is the total number of non-landslide rasters, n_{i1} is the number of landslide rasters of class x_i for variable x, and n_{i0} is the number of non-landslide rasters of class x_i for variable x. In practice, the standard rule of using the IVs is shown in the Table 2.

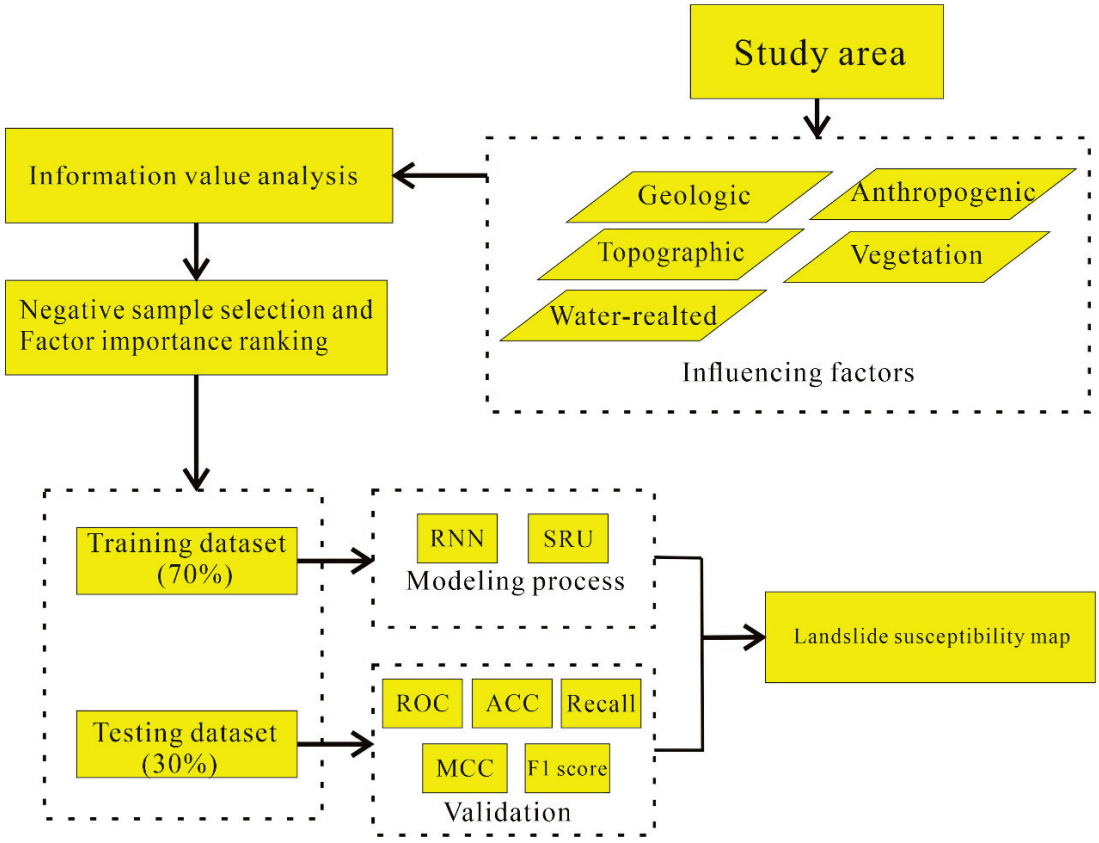

Figure 3. Methodology of the study.

Table 2. Standard rule for using the information value.

Information Value	Predictive Power
<0.02	Useless
0.02–0.1	Weak
0.1–0.3	Medium
0.3–0.5	Strong
>0.5	Suspiciously good

3.2. Recurrent Neural Network and Its Variants

3.2.1. Recurrent Neural Network

In traditional neural network models, the layers are fully connected from the input layer to the hidden layer to the output layer, and the nodes between each layer are unconnected [42,43]. Recurrent neural networks (RNNs) are a class of Artificial Neural Networks (ANNs), and RNNs are intended to be used to process sequential data (Figure 4). Specifically, the network remembers the previous information input and then applies it to the calculation of the current output. The nodes between the hidden layers are no longer connectionless but connected, and the input of the hidden layers includes not only the output of the input layer but also the output of the hidden layer at the previous moment.

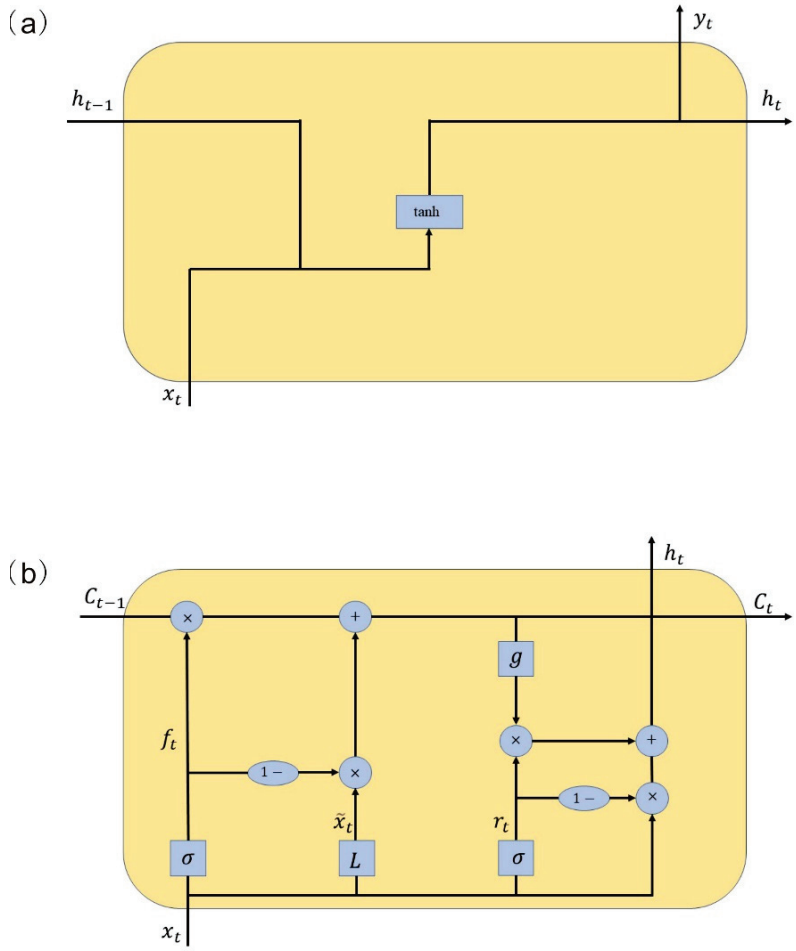

Figure 4. (**a**) RNN architecture and (**b**) SRU architecture.

Traditional recurrent neural networks are often implemented using Elman networks or Jordan networks, both of which are similar and are three-layer networks. The Elman network and the Jordan network are also known as "simple recurrent networks" (SRN) [44,45]. Let x_t, y_t, and h_t be the input vector, the output vector, and the hidden layer vector, then we can obtain

$$h_t = \sigma_h(W_h x_t + U_h h_{t-1} + b_h) \tag{3}$$

$$y_t = \sigma_y(W_y h_t + b_y) \tag{4}$$

where U and W are parameter matrices, b is the bias vector, and σ_h and σ_y are activation functions.

3.2.2. Simple Recurrent Unit

The SRU is a variant of the recently proposed RNN, and the SRU and the related work aim to propose and explore simple, fast, and more explanatory RNNs (Figure 4) [46]. Compared to other RNN variants, such as LSTM and GRU, SRU can achieve faster training speeds due to its designed structure. Figure 5 shows the basic structure of the SRU. The SRU is built on the same "gate" structure as the LSTM and GRU, but the difference is that SRU removes the limitation of parallelization of that LSTM and GRU adhere to, resulting in a much faster processing speed. The SRU has two components: "light recurrence" and "high network". Let x_t, f_t, C_t, r_t, and h_t be the input vector, the forget gate vector, the current state from light recurrence, the reset gate vector, and the hidden layer vector. The

light recurrence can be summarized as Equations (5)–(7), and the high network can be summarized as Equations (8) and (9).

$$\widetilde{x}_t = Wx_t \tag{5}$$

$$f_t = \sigma(W_f x_t + b_f) \tag{6}$$

$$C_t = f_t \odot c_{t-1} + (1 - f_t) \odot (Wx_t) \tag{7}$$

$$r_t = \sigma(W_r x_t + b_r) \tag{8}$$

$$h_t = r_t \odot g(C_t) + (1 - r_t) \odot x_t \tag{9}$$

where W and b are the parameter matrices. The value $\odot$ is the pointwise multiplication operation [47].

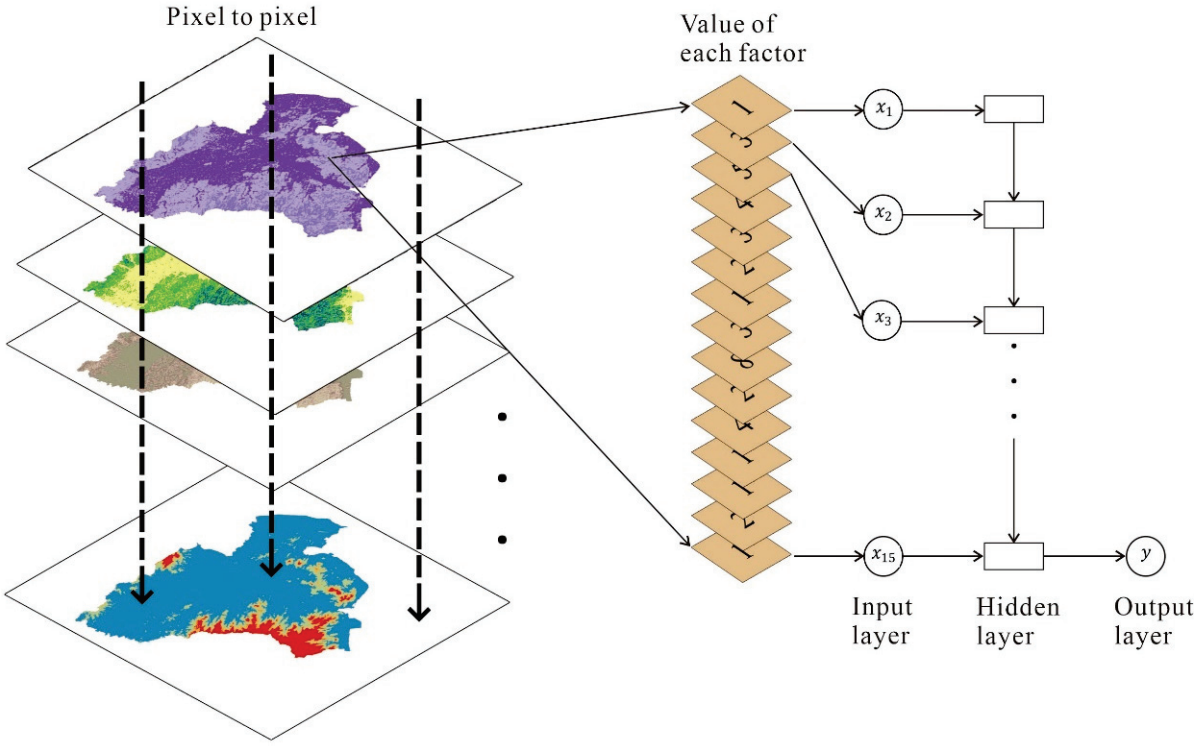

Figure 5. Data representation of models.

3.3. Selection of Landslide Influencing Factor

For LSM models, inputting more data does not necessarily result in a better model, as too much redundancy in the influencing factors considered will reduce the model's predictive capability [48]. Therefore, it is crucial to correctly select the landslide influencing factors [49]. The IV analysis method has been described above, and Table 3 shows the analysis of these influencing factors using Equations (1) and (2).

Table 3. Information value analysis of each landslide influencing factor.

Factor	Class	No. of Pixels	No. of Landslides	WOE	IV of Each Class	IV
Rock type	Granite	10,872	65	0.1029	0.0037	0.0996
	Sandstone	956	15	1.0678	0.0590	
	Slate	3832	11	−0.6308	0.0343	
	Quaternary sediments and rivers	17,340	87	−0.0724	0.0027	
Distance to faults (m)	0–400	7630	68	0.5021	0.0757	0.1031
	400–800	6770	37	0.0131	0.0000	
	800–1200	4824	16	−0.4863	0.0274	
	1200–1600	3634	22	0.1554	0.0016	
	1600–5300	10,142	35	−0.4466	0.0494	
Elevation (m)	0–50	25,588	138	−0.0001	0.0000	0.0492
	50–150	3469	27	0.3667	0.0171	
	150–220	1227	6	−0.0981	0.0003	
	220–972	2716	7	−0.7385	0.0317	
Slope	0–4.10	22,125	79	−0.4125	0.0935	0.3456
	4.10–11.31	5752	75	0.8827	0.2181	
	11.31–20.48	3531	21	0.0977	0.0011	
	20.48–49.73	1592	3	−1.0517	0.0330	
Aspect	Flat	1442	1	−2.0513	0.0781	0.1859
	North	3991	14	−0.4303	0.0182	
	Northeast	3899	17	−0.2128	0.0048	
	East	4313	18	−0.2565	0.0076	
	Southeast	4561	17	−0.3696	0.0158	
	South	3746	30	0.3952	0.0217	
	Southwest	3404	26	0.3479	0.0149	
	West	3670	29	0.3818	0.0197	
	Northwest	3974	26	0.1930	0.0050	
Plan curvature	0–5.09	2509	4	−1.2189	0.0653	0.1889
	5.09–25.90	10,913	92	0.4466	0.0831	
	25.90–44.40	11,148	42	−0.3589	0.0366	
	44.40–65.46	8430	40	−0.1282	0.0039	
Profile curvature	0–0.36	16,291	24	−1.2978	0.4657	0.6907
	0.36–2.32	12,123	125	0.6479	0.2170	
	2.32–4.72	3855	26	0.2234	0.0065	
	4.72–11.36	731	3	−0.2733	0.0014	
Degree of relief	0–5.00	25,944	115	−0.1963	0.0275	0.0994
	5.00–7.67	2721	25	0.5326	0.0309	
	7.67–14.53	3272	30	0.5305	0.0368	
	14.53–40.73	1063	8	0.3331	0.0042	

Table 3. *Cont.*

Factor	Class	No. of Pixels	No. of Landslides	WOE	IV of Each Class	IV
TRI	<2.93	16,246	19	−1.5287	0.5894	0.8827
	2.93–20.83	13,470	145	0.6910	0.2808	
	>20.83	3284	12	−0.3894	0.0125	
TPI	<−0.95	3392	21	0.1378	0.0021	0.4914
	(−0.95)–0.33	4460	58	0.8800	0.1678	
	0.33–0.28	18,924	46	−0.7971	0.2511	
	0.28–2.13	4648	45	0.5849	0.0655	
	>20.83	1576	6	−0.3484	0.0049	
Distance to rivers (m)	0–500	17,364	116	0.2139	0.0268	0.0985
	500–1500	12,263	55	−0.1845	0.0116	
	1,500–3691	3373	7	−0.9552	0.0601	
TWI	<7.88	11,184	108	0.5824	0.1560	0.3207
	7.88–16.47	20,184	68	−0.4707	0.1081	
	>16.47	1632	2	−1.4819	0.0566	
Land use	Farmland	11,517	35	−0.5738	0.0874	0.2750
	Forest and grass	13,492	95	0.2665	0.0333	
	Residential	3981	39	0.5968	0.0588	
	Bare	646	4	0.1380	0.0004	
	Water	3364	5	−1.2890	0.0952	
Distance to roads (m)	0–50	16,797	100	0.0987	0.0052	0.1372
	50–350	9534	64	0.2187	0.0155	
	350–2704	6669	14	−0.9437	0.1165	
NDVI	<0.22	3356	3	−1.7974	0.1525	0.2058
	0.22–0.49	12,749	61	−0.1199	0.0052	
	0.49–0.67	8974	66	0.3100	0.0306	
	>0.67	7921	32	−0.2891	0.0174	

Table 2 shows the standard rule of using the IV analysis. All IVs are higher than 0.02, indicating that all influencing factors have certain predictive power for the occurrence of landslides. Based on the above results, the TRI has the highest IV of 0.8827, indicating that it may be the dominant factor, and most of the other factors are between 0.1 and 0.4, proving that they also have a positive correlation with the landslide occurrence.

3.4. Factor Importance Ranking

From the above introduction of the architecture of RNNs and SRUs, it is clear that RNNs are effective in processing data that have sequential properties due to their special recurrent hidden states. Therefore, constructing models using RNNs should consider the problem of data redundancy and the input sequence of data. In this study, we propose a landslide data representation of RNNs, as shown in Figure 5. According to the results in Section 3.3, first, the IVs of all the influencing factors are arranged in a descending order, and then the influencing factors are ranked via their level of importance. Then, each pixel in the study area is converted into a continuous sample. Thus, the data are the input into the model in the previously ranked order of importance. Due to the special architecture inherent to RNNs, the previous input data are related to the latter input, and the key

information of each influencing factor that induces landslides is passed along the next hidden state.

3.5. Selection of Negative Sample

Landslides are geological events that occur infrequently but are hazardous to our society, and we can further define landslides as being rare events [50]. Identifying classes of rare events and representing them from a large quantity of data are challenging due to the insufficient number of positive samples and the absence of negative samples [51]. The lack of positive samples has been improved by adding the risk points above, and in this section, negative samples are selected by the weight of the evidence (WOE) method.

The WOE is calculated by Equation (1), from which it can be seen that the difference between the ratio of the number of landslides contained in the current class to the number of all landslide occurrences and the ratio of the number of non-landslide samples contained in the current class to the number of all non-landslide samples in this study is the logarithm of the two ratios. The larger the WOE is, the greater the probability of landslide events happening for the pixels belonging to this interval, and the opposite relation results in the probability of landslides being smaller.

To obtain the area for selecting the negative samples, the WOEs of the 15 influencing factors for all pixels were summed and averaged in order to obtain a WOE map of the study area, and then the region was divided into two areas: positive WOE and negative WOE (Figure 6). To verify the effectiveness of this method, two groups of negative samples were selected: one group was randomly selected in the area of negative WOE region, and the other group was randomly selected directly in the study area. The number of negative samples in both groups was the same as the number of positive samples.

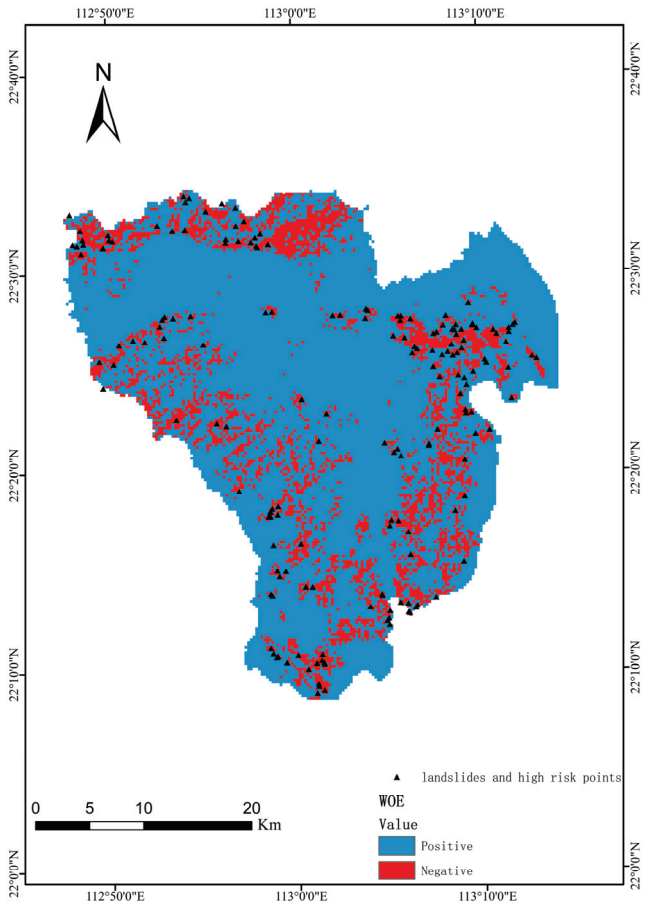

Figure 6. WOE and the selection of negative samples.

3.6. Evaluation and Comparison of Models

The validation of model strength or weakness is a key condition for assessing model performance. The fitting accuracy has been considered a significant feature and is obtained by comparing the model predictions with the true values in the training dataset. The analysis and evaluation of models using the receiver operating characteristic (ROC) curves are common in many related studies. The ROC curve is plotted by including the statistical index values of the false-positive and true-positive ratios. The area under the ROC curve (AUC) represents the model's predicted value. The AUC values range between 0.5 and 1.0, with larger areas indicating a better spatial prediction performance of the model [52]. Statistical indicators such as accuracy (ACC), Matthews correlation coefficient (MCC), F1 score, and recall are added to evaluate the predictive ability of the model, and these are calculated as follows [53–55]:

$$\mathrm{ACC} = \frac{\mathrm{TP} + \mathrm{TN}}{\mathrm{TP} + \mathrm{FP} + \mathrm{TN} + \mathrm{FN}} \tag{10}$$

$$\mathrm{MCC} = \frac{\mathrm{TP} \times \mathrm{TN} - \mathrm{FP} \times \mathrm{FN}}{\sqrt{(\mathrm{TP} + \mathrm{FP}) \times (\mathrm{TP} + \mathrm{FN}) \times (\mathrm{TN} + \mathrm{FP}) \times (\mathrm{TN} + \mathrm{FN})}} \tag{11}$$

$$\text{F1 score} = \frac{2 \times \mathrm{TP}}{2 \times \mathrm{TP} + \mathrm{FP} + \mathrm{FN}} \tag{12}$$

$$\text{recall} = \frac{\mathrm{TP}}{\mathrm{TP} + \mathrm{FN}} \tag{13}$$

where TP and TN represent true positives and true negatives, and FP and FN denote false positives and false negatives, respectively. The values of ACC, recall, and F1 score range between 0 and 1. MCC ranges between -1 and 1. The higher the ACC, F1, and MCC values, the better the predictive ability of the model.

4. Results

4.1. Performance of the Landslide Models

A dataset with negative samples selected by the IV analysis is input into the RNN and SRU models, named the RNN model and SRU model. A dataset randomly selected directly from the area of negative samples is input to the RNN and SRU models, named the RNN_random model and SRU_random model. The models are implemented in Python under scikit-learn (https://scikit-learn.org/stable/, accessed on 21 October 2022) and Keras (https://keras.io/, accessed on 21 October 2022). Parameters of the RNN model are as follows: hidden units = 40, learning rate =0.0001, batch size = 128, epoch = 500. Parameters of the RNN model are as follows: hidden units = 40, learning rate =0.0001, batch size = 128, epoch = 550, depth = 4, max features = 10,000.

The process of constructing the training and testing datasets is as follows: both of our datasets include 178 positive samples and 178 negative samples in order to construct the training and validation sets for the ML process; 70% of the positive samples (124) and negative samples (124) are used for training, and the remaining 30% (54 and 54) are used for testing. After training and testing the models, four machine learning models were evaluated using five criteria: AUC, ACC, MCC, F1 score, and recall. Table 4 shows the performance of the models. To verify that the method can work across data, we used the five-fold cross-validation, and Table 5 shows the averages of the statistical metrics of the five-fold cross-validation.

Table 4. Performance of the models.

Model Name	ACC	MCC	F1 Score	Recall
RNN	0.8598	0.7206	0.8544	0.8302
SRU	0.7850	0.5949	0.8099	0.9245
RNN_random	0.6887	0.3780	0.6796	0.6604
SRU_random	0.6132	0.2274	0.6306	0.6604

Table 5. The averages of the statistical metrics of 5-fold cross-validation.

Model Name	ACC	MCC	F1 Score	Recall
RNN	0.8220	0.6489	0.8278	0.8549
SRU	0.7591	0.5456	0.7639	0.8228
RNN_random	0.6570	0.3150	0.6601	0.6651
SRU_random	0.5834	0.1915	0.5869	0.5883

The results show that the performance of the RNN model and SRU model are higher than that of the RNN_random model and SRU_random model in all four statistical metrics, indicating that the dataset constructed with negative samples selected by information value analysis model fitting performance is significantly higher than that of the dataset with randomly selected negative samples. Regarding the ACC, the RNN model performs the best and achieves its highest ACC of 0.8598, which is over 0.0748 higher than that of the SRU (0.7850). The RNN model also achieves the highest MCC and F1 score (0.7206, 0.8544), which are 0.1257 and 0.0445 higher than those of the SRU model. In addition, it can be seen that the ML models trained with the IV analysis dataset outperform the ML model trained with the randomly selected negative samples dataset in terms of the RNN and SRU. This is evidenced by the fact that all statistical indicators for the ML models trained with the information value analysis dataset are greater than the ML model trained with the randomly selected negative samples dataset by more than 0.2.

Figure 7 plots the ROC curves of the four models. It can be seen that the AUC values of both the RNN model and the SRU model are above 0.90. In contrast, the AUC values of both the RNN_random model and the SRU_random model are low, indicating that the RNN and SRU techniques combined with the information value analysis show excellent predictive power for LSM. In addition, the RNN model achieves the highest AUC value (0.928), which is superior to the other models.

Figure 8 shows the accuracy and loss curves of four models, which are used to check the robustness of the results. When the model is optimized to the most stable level, the curves are presented as follows: as the epoch increases, the two accuracy curves gradually increase and level off; the two loss curves gradually decrease and level off (the loss curve of the training set decreases and the loss curve of the test set increases, indicating that the model may have an overfitting problem). All four models are optimized to the most robust level without overfitting problems.

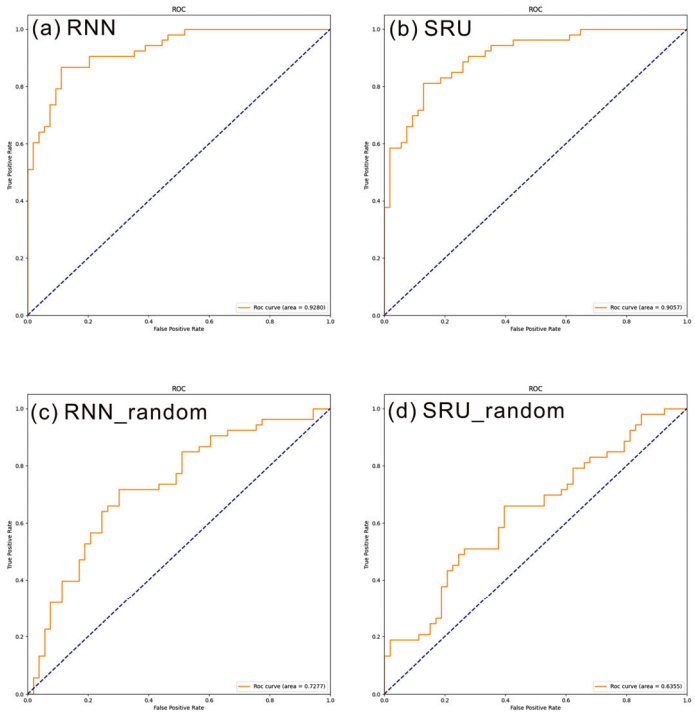

Figure 7. ROC curves of the four models.

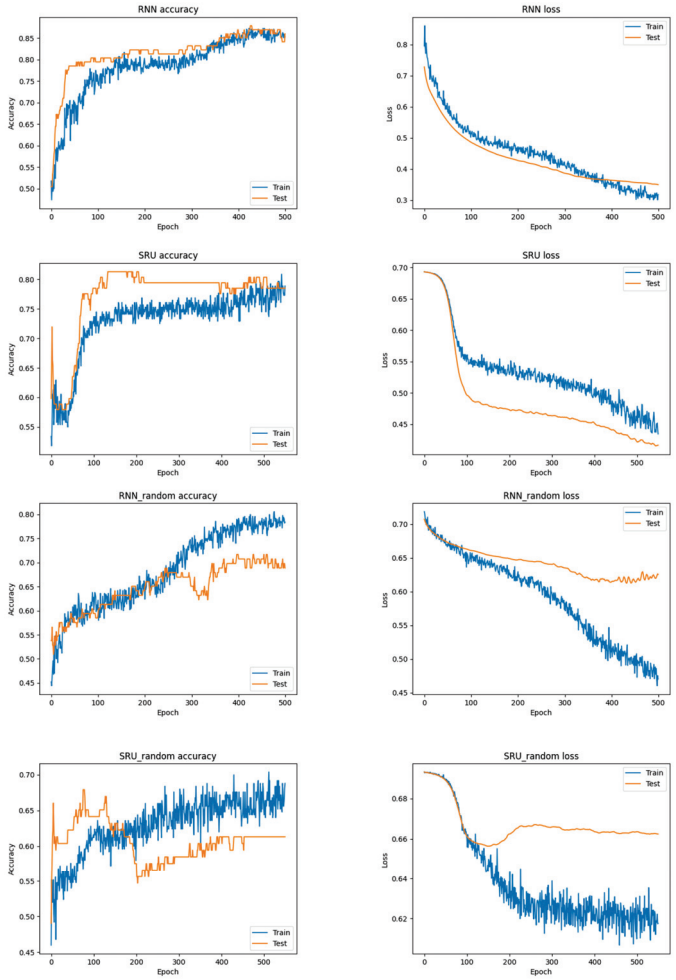

Figure 8. Accuracy and loss curves of the four models.

4.2. Landslide Susceptibility Maps

When LSM is used for comparison, the maps should be classified using quantitative methods [56]. The model output was analyzed and processed using ArcGIS. The maps were divided into five groups: very high, high, medium, low, and very low using the Jenks natural breaks classification method to finally obtain the landslide susceptibility maps (Figure 9). Among the four maps, most of the historical landslide and high-risk sites in Figure 9a–c are in the high landslide susceptibility areas, which are mainly located in the north, southwest, and southeast due to the mountainous terrain in the northwest and southwest of the study area and the strong human engineering activities in the northeast. According to the statistical indicators, the map shown in Figure 9a, which was constructed by the RNN model, is the best, compared to the map shown in Figure 9b, which was constructed by the SRU. Figure 9a does not have too many high susceptibility areas and does not predict low susceptibility areas such as rivers in the study area (Figure 2) as high susceptibility areas. Figure 9c, d also predict that some river areas are moderate and high susceptibility areas, which are not in accordance with the geomorphological conditions of the study area. Therefore, the map shown in Figure 9a is believed to be the best portrayal of the real-world conditions.

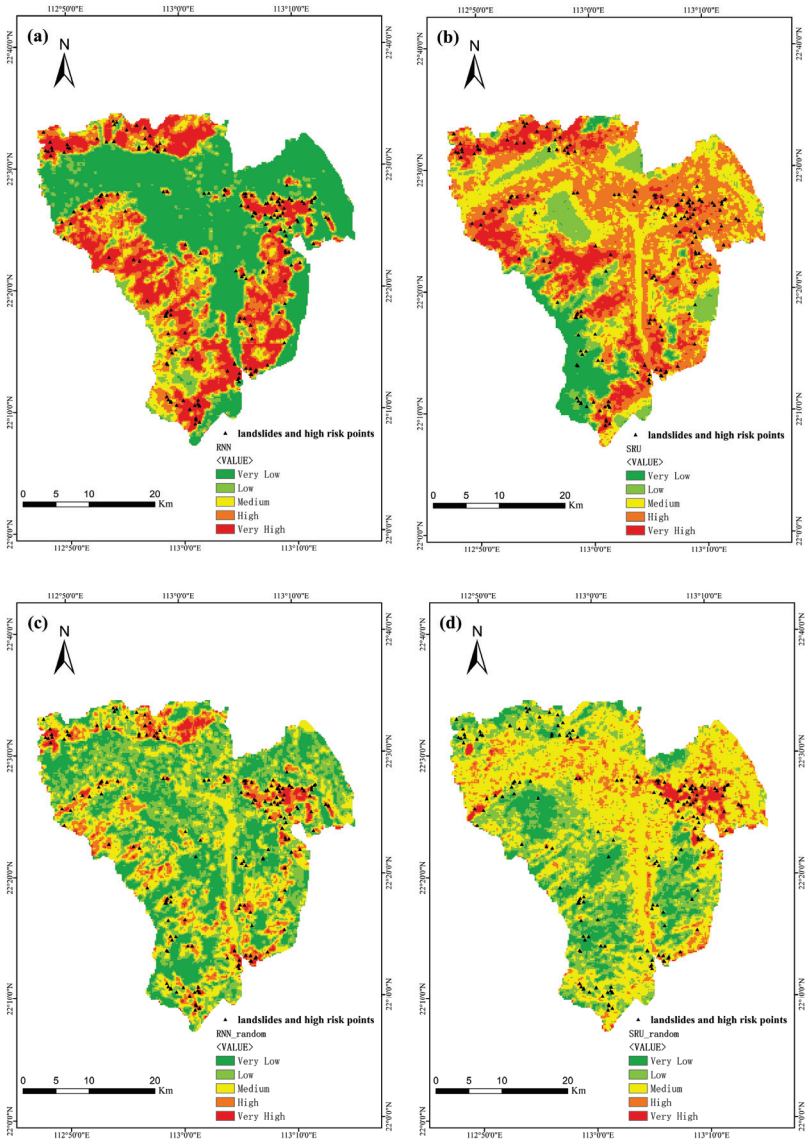

Figure 9. Landslide susceptibility maps by (**a**) RNN, (**b**) SRU, (**c**) RNN_random, and (**d**) SRU_random.

The visual data analysis initially shows the excellent results of the spatial predictive ability of the RNN model encompassing the LSM of the study area. The model evaluation results can still be described using mathematical-statistical methods (Table 6). LSM produces a model that focuses on high-susceptibility areas and models them simply and efficiently [57]. The evaluation of the practicability of models focuses on two groups, those with a rating of high and very high. First, we introduce the concept of landslide density (LD), which is the frequency ratio, referring to the ratio of the percentage of landslides (IV + V) to the percentage of groups (IV + V) in Table 6. It can be seen that the RNN model is more practical than the SRU model because although the RNN model covers fewer landslide and high-risk points than the SRU model (lower than 3.37%), the high susceptibility regions are much smaller than in the SRU model (lower than 16.31%). The low LD value of the high susceptibility regions of the SRU model also reflects the weak range of real-world applications when compared to that of the RNN model. The RNN_random model and SRU_random model cover too few landslide and high-risk points, indicating that the practical applications of these two models are poor.

Table 6. Practicability of the landslide susceptibility group.

Model	Group	No. of Pixels	Percentage of Group	Percentage of Group (IV + V)	No. of Landslide	Percentage of Landslide	Percentage of Landslide (IV + V)	LD
RNN	Very low (I)	13,854	40.34%	34.96%	3	1.69%	77.53%	0.042
	Low (II)	3846	11.20%		10	5.62%		0.502
	Medium (III)	4634	13.49%		27	15.17%		1.124
	High (IV)	5611	16.34%		48	26.97%		1.650
	Very high (V)	6396	18.62%		90	50.56%		2.715
SRU	Very low (I)	2537	7.39%	51.27%	4	2.25%	80.90%	0.304
	Low (II)	4054	11.81%		13	7.30%		0.619
	Medium (III)	10,144	29.54%		17	9.55%		0.323
	High (IV)	10,200	29.70%		59	33.15%		1.116
	Very high (V)	7406	21.57%		85	47.75%		2.214
RNN_random	Very low (I)	9165	26.69%	12.99%	3	1.69%	59.55%	0.063
	Low (II)	10,998	32.03%		10	5.62%		0.175
	Medium (III)	9717	28.30%		59	33.15%		1.171
	High (IV)	3374	9.82%		80	44.94%		4.574
	Very high (V)	1087	3.17%		26	14.61%		4.615
SRU_random	Very low (I)	4491	13.08%	12.54%	10	5.62%	32.86%	0.430
	Low (II)	8776	25.56%		41	23.03%		0.901
	Medium (III)	16,766	48.82%		69	38.76%		0.794
	High (IV)	3520	10.25%		45	25.28%		2.466
	Very high (V)	788	2.29%		13	7.30%		3.183

5. Discussion

5.1. Uniqueness of the Study Area

Although Xinhui District is neither an active seismicity area nor an extremely fragile geological environment area, and its climate is not special, its geographic location determines its unique economic location and its research value, as shown in Figure 1. As a new growth pole in the Guangdong Coastal Economic Belt and a destination for industrial transfer from the east to the west of the Guangdong–Hong Kong–Macao Greater Bay Area, the Xinhui District has become an important node district at the strategic intersection of the Guangdong Coastal Economic Belt and the Guangdong–Hong Kong–Macao Greater Bay Area in China, which is both an enormous opportunity and a great challenge. There will be more and more human activities in the Xinhui District, posing a very big challenge to future economic development and land use. Reasonable land planning cannot be separated from reliable geological hazard investigation and evaluation. Therefore, assessing the landslide susceptibility and the potential impacts of landslides on the economic environment can lay the foundation for optimizing the land use patterns and reducing the geological risk in the future.

5.2. Optimization of Non-Landslide Sample Selection

A variety of ML methods have been applied to LSM, with good results in recent years. However, previous studies have mostly focused on applying and comparing various ML methods to improve the performance of the models, but the selection of negative samples used to construct the models has affected the architecture construction of ML models. Randomly selecting non-occurring locations as negative samples will lead to considerable pollution, and conducting unsupervised cluster analysis to select negative samples still results in them being specified artificially, which also leads to a great deal of uncertainty in the resultant performance of the model. Therefore, we use the IV analysis to calculate the influencing factors based on historical landslide points to obtain negative samples that have less pollution to produce the landslide susceptibility maps.

The data in this study are different from the positive and negative sample problem that occurs in supervised learning; however, a positive and unlabeled (PU) problem occurs where there are only definite positive and unlabeled samples. It can only be assumed that the unlabeled samples may be negative samples without a level of certainty. Information value analysis was used to obtain the WOE for the entire study area as a basis for the selection of the negative samples. The final result comparison shows that this method works well, and that the negative data pollution is effectively limited. The groups of influencing factors within each pixel contain important data to consider both the positive and negative influences they have on landslides, and the negative value indicates that the importance is not in accordance with the daily logic. Therefore, we use the WOE with a proportional correction IV as an indicator for the most important factors for determining the order of the data for the input into the RNN model. The results indicate that the two slope-related factors, the TRI and profile curvature, were the most important factors in determining whether there was a chance of the occurrence of a landslide at that pixel location.

The problem of non-landslide sample selection has received attention, and many methods have been proposed recently, such as determining the proportion of non-landslide and landslide samples (because the value of negative samples is weaker than that of landslide samples, more non-landslide samples should be selected to improve the accuracy and avoid the imbalance of positive and negative samples caused by too many non-landslide samples), selecting non-landslide sample sets several times to find the best non-landslide sample set and using semi-supervised learning models. This study obtains negative samples with less pollution through the IV analysis. Overall, various studies on optimizing non-landslide sample selection have achieved satisfactory results. However, due to the differences in study areas and the logic and mechanisms behind different algorithms, there is no universally accepted method for optimizing non-landslide sample selection. A

comparative study using different methods for selecting non-landslide samples under the same conditions should be considered in the future.

5.3. Comprehensive Comparison of the Various Methods

Four datasets were input into the models, and Figure 9 shows that the dataset using less noisy negative data performs significantly better than the dataset with more noisy negative data in regard to their ROC, ACC, MCC, recall, and F1 values. After that, the traditional RNN model was compared to the newly proposed SRU model (which both use datasets that contain less noisy negative data) to produce two landslide susceptibility maps. Both models have excellent accuracy (AUC > 0.900), but from Tables 4 and 5, the RNN model generates a more reasonable area of high susceptibility for landslide events and identifies more historical points. Therefore, the map helps regional managers make effective decisions, and this study improves the prediction performance of deep learning techniques represented by RNNs in LSM.

6. Conclusions

This paper focuses on landslide susceptibility mapping (LSM) in the Xinhui District based on the RNN and SRU methods. Using the information value analysis, 15 landslide influencing factors were calculated, and their order of input in the recurrent neural network was determined. Then, the negative data were selected by the information value (IV) analysis. The 178 historical landslide and high-risk points were randomly divided into a training set and a test set for the model calculation, and the final landslide susceptibility maps were produced by the RNN and SRU for comparison purposes. The results led to the following conclusions: (1) the IV analysis method can improve the performance of machine learning methods in LSM by optimizing the selection of negative samples; (2) both the RNN and SRU models obtain excellent results in LSM (AUC > 0.900), but the LSM performance of the SRU, a newly proposed variant of RNNs, is weaker than the traditional RNN model in LSM; and (3) the RNN can produce accurate landslide susceptibility maps in areas that have the geography similar to that of the Xinhui District.

However, there are some limitations to be addressed in further studies, such as better consideration of the existing geomechanical properties, which are not well considered. Moreover, in addition to the characteristics of the non-landslide sample itself, whether the surrounding environment of the non-landslide area also influences the performance of the model needs to be better determined. In the future, more focus will be made on selecting more scientific non-landslide samples by increasing the influencing factors and analyzing the mutual influence of the surrounding environment, etc., to ensure the accuracy of the LSM results.

Author Contributions: Conceptualization, J.J. and Y.Z.; data curation, J.J., S.J. and S.L.; software, J.J.; supervision, Y.Z. and Q.C.; writing—original draft, J.J.; writing—review and editing, J.J., Y.Z. and Q.C. All authors have read and agreed to the published version of the manuscript.

Funding: This research was jointly supported by the National Natural Science Foundation of China (Grant No. U1911202), Guangdong Provincial Key R&D Project (Grant No.2020B1111370001) and China National Key R&D Project (Grant No. 2022YFF0800101).

Data Availability Statement: The data that support the findings of this study are available from the corresponding author, upon reasonable request.

Acknowledgments: The authors would like to thank Wei Cao, Hanyu Wang, the editors and anonymous reviewers who provided insightful comments to improve this article.

Conflicts of Interest: The authors declare no competing interest.

References

1. Press, F. Earth science and society. *Nature* **2008**, *451*, 301–303. [CrossRef] [PubMed]
2. Zhang, Q.; Zhang, Z.Y. Big data helps geology develop rapidly. *Acta Petrol. Sin.* **2018**, *34*, 3167–3172.
3. Zhou, Y.; Zhang, Q.; Shen, W.; Xiao, F.; Zhang, Y.; Zhou, S.; Huang, Y.; Ji, J.; Tang, L.; Ouyang, C. Construction and Applications of Knowledge Graph of Porphyry Copper Deposits. *Earth Sci. Subsoil Use* **2021**, *44*, 204–218. [CrossRef]
4. Li, X.; Ting, G.; Shen, W.; Zhang, J.; Zhou, Y. Quantifying the influencing factors and multi-factor interactions affecting cadmium accumulation in limestone-derived agricultural soil using random forest (RF) approach. *Ecotoxicol. Environ. Saf.* **2021**, *209*, 111773. [CrossRef] [PubMed]
5. Wang, J.; Zhou, Y.; Xiao, F. Identification of multi-element geochemical anomalies using unsupervised machine learning algorithms: A case study from Ag–Pb–Zn deposits in north-western Zhejiang, China. *Appl. Geochem.* **2020**, *120*, 104679. [CrossRef]
6. Yu, X.; Fan, X.; Zhou, Y.; Wang, Y.; Wang, K. Application of hierarchical clustering, singularity mapping, and Kohonen neural network to identify Ag-Au-Pb-Zn polymetallic mineralization associated geochemical anomaly in Pangxidong district. *J. Geochem. Explor.* **2019**, *203*, 87–95. [CrossRef]
7. Petley, D. Global patterns of loss of life from landslides. *Geology* **2012**, *40*, 927–930. [CrossRef]
8. Nohani, E.; Moharrami, M.; Sharafi, S.; Khosravi, K.; Pradhan, B.; Pham, B.T.; Lee, S.; Melesse, A.M. Landslide Susceptibility Mapping Using Different GIS-Based Bivariate Models. *Water* **2019**, *11*, 1402. [CrossRef]
9. Pham, B.T.; Prakash, I.; Bui, D.T. Spatial prediction of landslides using a hybrid machine learning approach based on Random Subspace and Classification and Regression Trees. *Geomorphology* **2018**, *303*, 256–270. [CrossRef]
10. Tsangaratos, P.; Ilia, I. Landslide susceptibility mapping using a modified decision tree classifier in the Xanthi Perfection, Greece. *Landslides* **2016**, *13*, 305–320. [CrossRef]
11. Wang, Y.; Wu, X.; Chen, Z.; Ren, F.; Feng, L.; Du, Q. Optimizing the Predictive Ability of Machine Learning Methods for Landslide Susceptibility Mapping Using SMOTE for Lishui City in Zhejiang Province, China. *Int. J. Environ. Res. Public Health* **2019**, *16*, 368. [CrossRef]
12. Akgun, A. A comparison of landslide susceptibility maps produced by logistic regression, multi-criteria decision, and likelihood ratio methods: A case study at İzmir, Turkey. *Landslides* **2012**, *9*, 93–106. [CrossRef]
13. Hong, H.; Pradhan, B.; Sameen, M.I.; Kalantar, B.; Zhu, A.; Chen, W. Improving the accuracy of landslide susceptibility model using a novel region-partitioning approach. *Landslides* **2018**, *15*, 753–772. [CrossRef]
14. Bui, D.T.; Tran, A.T.; Klempe, H.; Pradhan, B.; Revhaug, I. Spatial prediction models for shallow landslide hazards: A comparative assessment of the efficacy of support vector machines, artificial neural networks, kernel logistic regression, and logistic model tree. *Landslides* **2016**, *13*, 361–378.
15. Chen, W.; Wang, J.; Xie, X.; Hong, H.; Trung, N.V.; Bui, D.T.; Wang, G.; Li, X. Spatial prediction of landslide susceptibility using integrated frequency ratio with entropy and support vector machines by different kernel functions. *Environ. Earth Sci.* **2016**, *75*, 1344. [CrossRef]
16. Felicísimo, Á.M.; Cuartero, A.; Remondo, J.; Quiros, E. Mapping landslide susceptibility with logistic regression, multiple adaptive regression splines, classification and regression trees, and maximum entropy methods: A comparative study. *Landslides* **2013**, *10*, 175–189. [CrossRef]
17. Liang, W.-J.; Zhuang, D.-F.; Jiang, D.; Pan, J.-J.; Ren, H.-Y. Assessment of debris flow hazards using a Bayesian Network. *Geomorphology* **2012**, *171–172*, 94–100. [CrossRef]
18. Youssef, A.M.; Pourghasemi, H.R.; Pourtaghi, Z.S.; Al-Katheeri, M.M. Landslide susceptibility mapping using random forest, boosted regression tree, classification and regression tree, and general linear models and comparison of their performance at Wadi Tayyah Basin, Asir Region, Saudi Arabia. *Landslides* **2016**, *13*, 839–856. [CrossRef]
19. Nguyen, H.D. Spatial modeling of flood hazard using machine learning and GIS in Ha Tinh province, Vietnam. *J. Water Clim. Change* **2022**, *14*, 200–222. [CrossRef]
20. Ikram, R.M.A.; Dehrashid, A.A.; Zhang, B.; Chen, Z.; Le, B.N.; Moayedi, H. A novel swarm intelligence: Cuckoo optimization algorithm (COA) and SailFish optimizer (SFO) in landslide susceptibility assessment. *Stoch. Environ. Res. Risk Assess.* **2023**, *37*, 1717–1743. [CrossRef]
21. Termeh, S.V.R.; Kornejady, A.; Pourghasemi, H.R.; Keesstra, S. Flood susceptibility mapping using novel ensembles of adaptive neuro fuzzy inference system and metaheuristic algorithms. *Sci. Total Environ.* **2018**, *615*, 438–451. [CrossRef] [PubMed]
22. Hakim, W.L.; Rezaie, F.; Nur, A.S.; Panahi, M.; Khosravi, K.; Lee, C.-W.; Lee, S. Convolutional neural network (CNN) with metaheuristic optimization algorithms for landslide susceptibility mapping in Icheon, South Korea. *J. Environ. Manag.* **2022**, *305*, 114367. [CrossRef] [PubMed]
23. Lv, L.; Chen, T.; Dou, J.; Plaza, A. A hybrid ensemble-based deep-learning framework for landslide susceptibility mapping. *Int. J. Appl. Earth Obs. Geoinf.* **2022**, *108*, 102713. [CrossRef]
24. Zhang, H.; Song, Y.; Xu, S.; He, Y.; Li, Z.; Yu, X.; Liang, Y.; Wu, W.; Wang, Y. Combining a class-weighted algorithm and machine learning models in landslide susceptibility mapping: A case study of Wanzhou section of the Three Gorges Reservoir, China. *Comput. Geosci.* **2022**, *158*, 104966. [CrossRef]
25. Yuan, Q.; Shen, H.; Li, T.; Li, Z.; Li, S.; Jiang, Y.; Xu, H.; Tan, W.; Yang, Q.; Wang, J.; et al. Deep learning in environmental remote sensing: Achievements and challenges. *Remote Sens. Environ.* **2020**, *241*, 111716. [CrossRef]

26. Pak, U.; Ma, J.; Ryu, U.; Ryom, K.; Juhyok, U.; Pak, K.; Pak, C. Deep learning-based PM2.5 prediction considering the spatiotemporal correlations: A case study of Beijing, China. *Sci. Total Environ.* **2020**, *699*, 133561. [CrossRef]
27. Ikram, R.M.A.; Mostafa, R.R.; Chen, Z.; Parmar, K.S.; Kisi, O.; Zounemat-Kermani, M. Water temperature prediction using improved deep learning methods through reptile search algorithm and weighted mean of vectors optimizer. *J. Mar. Sci. Eng.* **2023**, *11*, 259. [CrossRef]
28. Ngo, P.T.T.; Panahi, M.; Khosravi, K.; Ghorbanzadeh, O.; Kariminejad, N.; Cerda, A.; Lee, S. Evaluation of deep learning algorithms for national scale landslide susceptibility mapping of Iran. *Geosci. Front.* **2021**, *12*, 505–519.
29. Xiao, L.; Zhang, Y.; Peng, G. Landslide Susceptibility Assessment Using Integrated Deep Learning Algorithm along the China-Nepal Highway. *Sensors* **2018**, *18*, 4436. [CrossRef]
30. Graves, A. *Long Short-Term Memory*; Springer: Berlin/Heidelberg, Germany, 2012.
31. Dey, R.; Salemt, F.M. Gate-variants of Gated Recurrent Unit (GRU) neural networks. In Proceedings of the 2017 IEEE 60th International Midwest Symposium on Circuits and Systems (MWSCAS), Boston, MA, USA, 6–9 August 2017; pp. 1597–1600.
32. Denis, F.; Gilleron, R.; Letouzey, F. Learning from positive and unlabeled examples. *Theor. Comput. Sci.* **2005**, *348*, 70–83. [CrossRef]
33. Wu, B.; Qiu, W.; Jia, J.; Liu, N. Landslide Susceptibility Modeling Using Bagging-Based Positive-Unlabeled Learning. *IEEE Geosci. Remote Sens. Lett.* **2021**, *18*, 766–770. [CrossRef]
34. Yang, C.; Liu, L.-L.; Huang, F.; Huang, L.; Wang, X.-M. Machine learning-based landslide susceptibility assessment with optimized ratio of landslide to non-landslide samples. *Gondwana Res.* 2022, *in press*. [CrossRef]
35. Chang, Z.; Huang, J.; Huang, F.; Bhuyan, K.; Meena, S.R.; Catani, F. Uncertainty analysis of non-landslide sample selection in landslide susceptibility prediction using slope unit-based machine learning models. *Gondwana Res.* **2023**, *117*, 307–320. [CrossRef]
36. Huang, F.; Cao, Z.; Jiang, S.-H.; Zhou, C.; Huang, J.; Guo, Z. Landslide susceptibility prediction based on a semi-supervised multiple-layer perceptron model. *Landslides* **2020**, *17*, 2919–2930. [CrossRef]
37. Heckmann, T.; Gegg, K.; Gegg, A.; Becht, M. Sample size matters: Investigating the effect of sample size on a logistic regression susceptibility model for debris flows. *Nat. Hazards Earth Syst. Sci.* **2014**, *14*, 259–278. [CrossRef]
38. Shannon, C. The lattice theory of information. *Trans. IRE Prof. Group Inf. Theory* **1953**, *1*, 105–107. [CrossRef]
39. Howard, R.A. Information Value Theory. *IEEE Trans. Syst. Sci. Cybern.* **1966**, *2*, 22–26. [CrossRef]
40. Freedman, S.; Jin, G.Z. The information value of online social networks: Lessons from peer-to-peer lending. *Int. J. Ind. Organ.* **2017**, *51*, 185–222. [CrossRef]
41. Kliger, D.; Sarig, O. The Information Value of Bond Ratings. *J. Financ.* **2000**, *55*, 2879–2902. [CrossRef]
42. Abiodun, O.I.; Jantan, A.; Omolara, A.E.; Dada, K.V.; Mohamed, N.A.; Arshad, H. State-of-the-art in artificial neural network applications: A survey. *Heliyon* **2018**, *4*, e00938. [CrossRef]
43. Tealab, A. Time series forecasting using artificial neural networks methodologies: A systematic review. *Future Comput. Inform. J.* **2018**, *3*, 334–340. [CrossRef]
44. Elman, J.L. Finding structure in time. *Cogn. Sci.* **1990**, *14*, 179–211. [CrossRef]
45. Jordan, M.I. Serial order: A parallel distributed processing approach. In *Advances in Psychology*; Elsevier: Amsterdam, The Netherlands, 1997.
46. Lei, T.; Zhang, Y.; Wang, S.I.; Dai, H.; Artzi, Y. Simple recurrent units for highly parallelizable recurrence. *arXiv* **2017**, arXiv:1709.02755.
47. Jiang, C.; Chen, S.; Chen, Y.; Bo, Y.; Han, L.; Guo, J.; Feng, Z.; Zhou, H. Performance Analysis of a Deep Simple Recurrent Unit Recurrent Neural Network (SRU-RNN) in MEMS Gyroscope De-Noising. *Sensors* **2018**, *18*, 4471. [CrossRef]
48. Chen, W.; Xie, X.; Wang, J.; Pradhan, B.; Hong, H.; Bui, D.T.; Duan, Z.; Ma, J. A comparative study of logistic model tree, random forest, and classification and regression tree models for spatial prediction of landslide susceptibility. *Catena* **2017**, *151*, 147–160. [CrossRef]
49. Zhao, X.; Chen, W. Optimization of Computational Intelligence Models for Landslide Susceptibility Evaluation. *Remote Sens.* **2020**, *12*, 2180. [CrossRef]
50. Karpatne, A.; Ebert-Uphoff, I.; Ravela, S.; Babaie, H.A.; Kumar, V. Machine learning for the geosciences: Challenges and opportunities. *IEEE Trans. Knowl. Data Eng.* **2018**, *31*, 1544–1554. [CrossRef]
51. Guo, Q.; Li, W.; Liu, Y.; Tong, D. Predicting potential distributions of geographic events using one-class data: Concepts and methods. *Int. J. Geogr. Inf. Sci.* **2011**, *25*, 1697–1715. [CrossRef]
52. Wang, Y.; Fang, Z.; Wang, M.; Peng, L.; Hong, H. Comparative study of landslide susceptibility mapping with different recurrent neural networks. *Comput. Geosci.* **2020**, *138*, 104445. [CrossRef]
53. Huang, J.; Ling, C. Using AUC and accuracy in evaluating learning algorithms. *IEEE Trans. Knowl. Data Eng.* **2005**, *17*, 299–310. [CrossRef]
54. Wang, Y.; Fang, Z.; Hong, H. Comparison of convolutional neural networks for landslide susceptibility mapping in Yanshan County, China. *Sci. Total Environ.* **2019**, *666*, 975–993. [CrossRef] [PubMed]
55. Powers, D.M.W. Evaluation: From precision, recall and F-measure to ROC, informedness, markedness and correlation. *arXiv* **2020**, arXiv:2010.16061.

56. Goetz, J.N.; Brenning, A.; Petschko, H.; Leopold, P. Evaluating machine learning and statistical prediction techniques for landslide susceptibility modeling. *Comput. Geosci.* **2015**, *81*, 1–11. [CrossRef]
57. Bui, D.T.; Tsangaratos, P.; Nguyen, V.-T.; Van Liem, N.; Trinh, P.T. Comparing the prediction performance of a Deep Learning Neural Network model with conventional machine learning models in landslide susceptibility assessment. *Catena* **2020**, *188*, 104426. [CrossRef]

sustainability

MDPI

Article

Buffer Capacity of Steel Shed with Two Layer Absorbing System against the Impact of Rockfall Based on Coupled SPH-FEM Method

Chun Liu [1,2,*] and Hongjun Liao [1]

[1] Guangdong Heli Civil Engineering Co., Ltd., Guangzhou 511400, China
[2] Guangdong Communication Planning and Design Institute Group Co., Ltd., Guangzhou 510507, China
* Correspondence: liuchun@ghdi.cn

Abstract: This study aimed to find the optimal thickness combination of the two-layered absorbing system combinated with an expanded polystyrene (EPS) cushion and a soil layer in a steel shed under dynamic loadings. The coupled Smooth Particle Hydrodynamic method (SPH) and Finite Element Method (FEM) were introduced to simulate the impact of the rockfall against the steel shed with a two-layer absorbing system. By comparing the numerical results with test data, the coupled numerical model was well validated. Through the verified numerical model, a series of numerical experiments were carried out to find the optimal combination for the two-layered absorbing system. The values of the EPS layer thickness as a percentage of the total thickness were set as 0% (P1), 20% (P2), 40% (P3), 60% (P4), 80% (P5), and 100% (P6). The results show that the coupled FEM–SPH method was an effective method to simulate rockfall impacting the steel rock shed; P4 (0.6 m thickness EPS cushion and 0.9 m thickness soil layer) was the most efficient combination, which can significantly reduce the structural displacement response by 43%. A two-layered absorbing system can effectively absorb about 90% of the total energy. The obtained results yield scientifically sound guidelines for further research on the design of steel sheds against rockfall.

Keywords: buffer capacity; rockfall; two-layered absorbing system; coupled SPH–FEM model; optimal combination

Citation: Liu, C.; Liao, H. Buffer Capacity of Steel Shed with Two Layer Absorbing System against the Impact of Rockfall Based on Coupled SPH-FEM Method. *Sustainability* **2022**, *14*, 13680. https://doi.org/10.3390/su142013680

Academic Editors: Stefano Morelli, Veronica Pazzi and Mirko Francioni

Received: 14 September 2022
Accepted: 20 October 2022
Published: 21 October 2022

1. Introduction

Rockfall hazards are natural disasters in mountainous areas. It poses a serious threat to engineering structures such as highways, railways, bridges, buildings, etc., and the huge impact force of falling rocks will destroy these structures [1,2]. There are mainly two protective structures used to reduce this hazard: passive ones and active ones. Because it is difficult to judge the potential source area of rocks, it is difficult to implement the active ones, and engineers usually choose the passive ones. Steel rock sheds are regarded as passive protective structures. Compared with reinforced concrete sheds, they have unique advantages such as low dead weight and fast construction speed and are widely used to prevent rocks from falling [3,4]. Most steel rock sheds are made of a steel column, steel beam, steel roof slab, and a buffer layer on top of the steel roof slab [5]. The buffer layer can effectively dissipate the rockfall impact energy, so as to reduce the maximum impact on the steel shed [6–8].

Conventionally, sand and soil, which are relatively cheap, are used as a cushion material; however, this kind of cushion has numerous disadvantages. The sand layer has to be very thick to form enough resistance capacity, which in turn makes the shed too much dead weight. Sheds also need massive foundations to support the heavy sands, which are impractical in narrow mountainous areas. In addition, the removal of fallen rocks and the replacement of cushion materials are difficult. In recent years, a two-layered absorbing system combinated with an expanded polystyrene (EPS) cushion and a soil layer

has been designed. It was found that the two-layered absorbing system provides better anti-impact effects and, at the same time, it makes the structure dead-weight small. However, the percentage of the thickness of the EPS layer to the total thickness of the two-layered absorbing system is rarely studied, which leads to a poor buffering effect of the system in practical engineering [6,9]. Therefore, in order to provide some helpful guidelines for designing a two-layered absorbing system in steel sheds for the risk mitigation of rockfall, it is urgently required to optimize the two-layered absorbing system.

In recent years, a series of experimental studies have been conducted in the field of rock shed protection. Schellenberg et al. introduced various types of protective cushions to search for better absorbing effects [10]. Calvetti et al. conducted a series of physical experiments to study the shock absorption effects of soil stratum, including the effect of various parameters such as falling height, block mass, and cushion thickness [11]. Bhatti et al. performed a real-scale experiment of rockfall impacting a reinforced concrete shed to study the dynamic responses [1]. Wu et al. developed a physical experiment of rockfall impacting a steel rock shed with a two-layered absorbing system [12]. The above studies are of positive significance in resisting rockfall impact. However, these studies are mainly focused on a single buffer layer, and there are few studies on the optimization thickness combination of a two-layered absorbing system. To date, in engineering practice, several empirical methods have been proposed to estimate the rockfall impact force, such as the Chinese, Swiss, and Japanese design codes [13–15]. He et al. proposed the calculation formula of impact forces based on the elastoplastic collision theory and the Hertz contact theory [16]. Yu et al. also established an impact force model [17]. The kinetic energy of the rock block, the impact angle of the block, and the modulus of elasticity of the rock were analyzed using the Buckingham theorem. Their results show that the buffer layer had a significant effect on the magnitude of the impact force. These methods are simple to use for a single buffer layer. However, these methods are not applicable to the combined absorbing system [12].

Because of its economy and maturity, the numerical method has gradually become the main research method for this kind of problem. In the present study, the numerical methods for analyzing the combined absorbing system are mainly as follows: (1) FEM (Finite Element Method); Wu et al. carried out numerical simulations to compare the impact forces obtained by the single soil layer and the two-layered absorbing system [12]. Ouyang analyzed the effects of various factors such as cushion strength and the thickness of the soil cushion on the impact force [6]. However, the FEM simulation of the soil layer is prone to grid distortion, which leads to a rough result. (2) DEM (Discrete Element Method); Zhang et al. employed a DEM model to study the energy propagation during rockfall impact on a granular material [18]. Shen investigated the various rock shape's effects on the response of block impacts against a buffer layer [19]. However, it is difficult to calibrate particle material parameters with DEM [20]. Moreover, the soil layer consists of an enormous number of fine particles, and the computer operation efficiency will be reduced. These numerical studies are useful for understanding the mechanical mechanism of steel sheds impacted by rockfall. However, these methods are not suitable for simulating steel sheds with buffer layers impacted by rockfall. Moreover, it is still difficult to quantitatively conclude the dynamic response of the combined absorbing system under rockfall impact.

Above all, the current research shows that the two-layered absorbing system has a significant influence on the response of the steel shed, but quantitative studies of the optimal thickness combination of the two-layered absorbing system combinated with EPS cushion and soil layer are lacking. So, it is urgently required to study the optimal thickness combination of the two-layered absorbing system based on a more robust numerical tool.

Smoothed particle hydrodynamics (SPH) is a convenient way to describe the particle physics features and capture the sup-large deformation of the soil layer [20,21]. For the finite element simulation of the steel column, steel beam, and steel slab, its algorithm is mature, which can ensure sufficient accuracy. The coupled FEM–SPH approach can

combine the advantages of SPH for simulating the sup-large deformation of soil and FEM for solving structural dynamics [20,22].

In this study, the coupled FEM–SPH method is used to find the optimal thickness combination between EPS and the soil layer under dynamic loadings. The content of this study is outlined as follows: In Section 2, a coupled SPH–FEM method in the LS-DYNA platform is introduced. In Section 3, a typical experiment of steel shed impacted by rockfall is described. The coupled FEM–SPH model can successfully reproduce the scale experiment. Section 4 conducts a series of numerical tests to find the optimal thickness combination for the two-layered absorbing system. Section 5 summarizes several conclusions.

2. Simulation Approaches

2.1. Brief SPH Description

The basic idea of the SPH method is to use a group of arbitrarily distributed particles to provide accurate and stable numerical solutions for the partial differential equations, which carry field variables such as density, mass, and stress tensor [23]. The SPH method can describe the mechanical state of the entire system by tracking the mechanical properties of each particle at any moment. The governing equations can be converted to the SPH form in two steps, including kernel approximation and particle approximation. In this way, the field variables can be recommended [23]:

$$\langle f(\mathbf{r}_i)\rangle = \int_{\Omega} f(\mathbf{r}')W(\mathbf{r}-\mathbf{r}',h)d\mathbf{r}' \tag{1}$$

where $f(\mathbf{r})$ is a function of the particle position vector $\mathbf{r}$, $\mathbf{r}'$ is a neighboring particle position vector in Ω, Ω is the support area of a particle with position vector $\mathbf{r}$, and W is the smoothing kernel function. In this study, the cubic B-spline function is selected as the smoothing kernel function [24]:

$$W(q,h) = \alpha_D \begin{cases} 1-\frac{3q^2}{2}+\frac{3q^3}{4}; 0 \le q < 1 \\ \frac{1}{4}(2-q)^3; 1 \le q < 2 \\ 0; q \ge 2 \end{cases} \tag{2}$$

where q is the normalized distance between particles $\mathbf{r}$ and $\mathbf{r}'$, $q = |\mathbf{r}-\mathbf{r}'|/h$, and h is the smoothing length defining the size of the influence area of W. α_D is the normalization factor; in three-dimensional space, $\alpha_D = 10/(7\pi h^2)$.

The particle approximation discretizes the continuous form of the SPH kernel approximation into the sum of adjacent particles by evaluating the field variables of the particles within the domain of influence as follows [24]:

$$\langle f(\mathbf{r}_i)\rangle = \frac{m_j}{\rho_j}\sum_{j=1}^{N} f(\mathbf{r}_j)W(\mathbf{r}_i-\mathbf{r}_j,h) \tag{3}$$

where N is the total number of particles within the influence domain of the particle at point $\mathbf{r}$, ρ_j is the density of neighboring particles, and m_j is the mass of the neighboring particles.

The governing equations for dynamic fluid flows can be written as a set of partial differential equations [24]:

$$\begin{cases} \frac{d\rho_i}{dt} = m_i \sum\limits_{j=1}^{N} \mathbf{v}_{ij}\cdot\nabla_i W_{ij} \\ \frac{d\mathbf{v}_i}{dt} = \sum\limits_{j=1}^{N} m_j\left(\frac{p_i}{{\rho_j}^2}+\frac{p_j}{{\rho_j}^2}\right)\nabla_i W_{ij} + F_i^{external}/m_i \end{cases} \tag{4}$$

where W_{ij} is the influence area of particle i with respect to particle j. $\mathbf{v}_{ij}$ is the velocity vector of particle i with respect to particle j. $F_i^{external}$ are external forces [25].

2.2. Coupled SPH-FEM Algorithm

The key problem of the coupled FEM–SPH method is dealing with the interface between FEM elements and SPH particles. The contact form is a node-surface contact, and the tangential impact force is obtained through the friction law. The normal impact force is obtained through the penalty contact algorithm [24]. The flowchart of the coupled SPH–FEM method is shown in Figure 1. At the beginning of every time step, it is determined whether any SPH particles have penetrated the FEM surfaces. If no penetration occurs, no processing is required, and these systems work as two separate processes. Otherwise, as shown in Figure 2, a contact force is generated between the SPH particles that meet the penetration conditions, and the parameters of the FEM elements and SPH particles will be updated [22].

The normal contact force $\mathbf{f}_n$ is calculated as follows [22]:

$$\mathbf{f}_n = (k_n\delta + c_n\dot{\delta})\mathbf{n} \tag{5}$$

where δ, c_n, $\dot{\delta}$, k_n, and $\mathbf{n}$ are the normal overlap, the normal damping coefficient, the relative normal velocity, the normal spring stiffness, and the unit normal displacement vector, respectively.

The tangential contact force $\mathbf{f}_t$ is calculated as follows [26,27]:

$$\mathbf{f}_t = \begin{cases} \left(k_t\boldsymbol{\delta}_t + c_t\dot{\boldsymbol{\delta}}_t\right); \text{if} \left|\mathbf{f}_n\right|\mu > \left|k_t\boldsymbol{\delta}_t + c_t\dot{\boldsymbol{\delta}}_t\right| \\ \frac{\left(k_t\boldsymbol{\delta}_t + c_t\dot{\boldsymbol{\delta}}_t\right)}{\left|k_t\boldsymbol{\delta}_t + c_t\dot{\boldsymbol{\delta}}_t\right|}\left|\mathbf{f}_n\right|\mu; \text{otherwise} \end{cases} \tag{6}$$

where k_t, $\boldsymbol{\delta}_t$, μ and c_t are the tangential spring stiffness, the incremental tangential displacement, the friction coefficient, and the tangential damping coefficient, respectively. In this paper, both c_n and c_t are set as 0 [26].

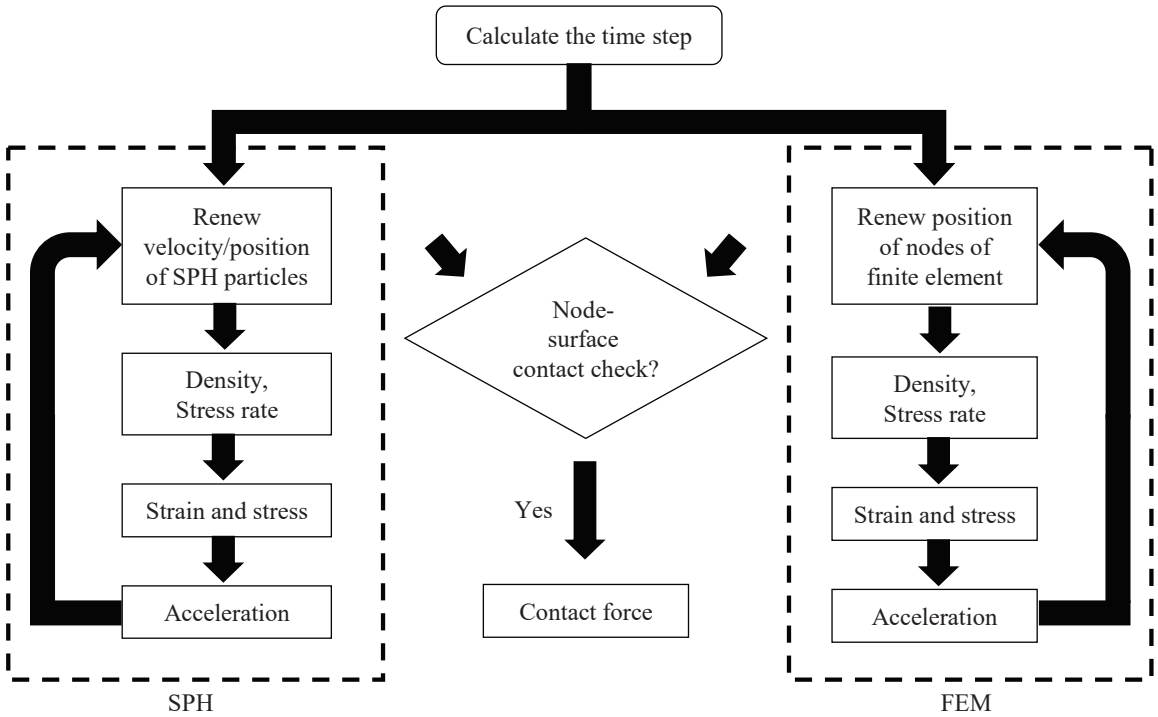

Figure 1. Flowchart of the coupled SPH–FEM method [27].

k_n and k_t are calculated as follows [27]:

$$k_n = k_t = k_1 \frac{Ks^2}{V} \tag{7}$$

where k_1 is a penalty scale factor and is set as 0.1 [26], s is the segment area, K is the bulk modulus, and V is the element volume.

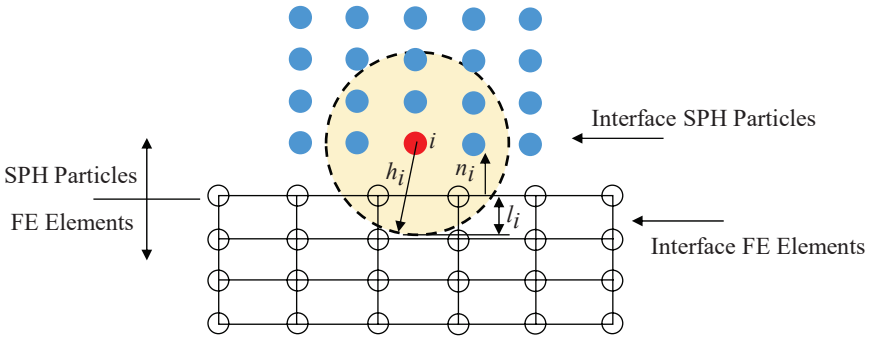

Figure 2. The finite elements in contact with the SPH particles.

3. Verification of Coupled SPH-FEM Model

3.1. Experimental Overview

The test shed structure is shown in Figure 3. The shed structure model consisted of a steel column, main girder, secondary beam, steel roof slab, and the two-layered absorbing system. The two-layered absorbing system consisted of EPS (30 cm thickness) and sand (40 cm thickness), in which EPS was laid under the sand. Specifications and material parameters of test shed components were shown in Table 1 [12]. The bottom of the steel column with a height of 0.7 m was fixed on the ground, and the top of the steel column was welded with a steel plate. The steel plate was connected with the lower flange of the main girder by bolts, the secondary beam was welded with the main girder, and the main girder was connected with the steel roof slab by welding. The absorbing material was replaced after each impact test. The impactor was a concrete polyhedral block [28]. The axial strain of the main girder and the secondary beam was measured to reflect the dynamic response of the shed under the impactor impact. As shown in Figure 4, the strain gauges 1 and 2 were attached to the lower flange of the main girder, 0.09 m and 0.17 m away from the center of the shed, respectively [12].

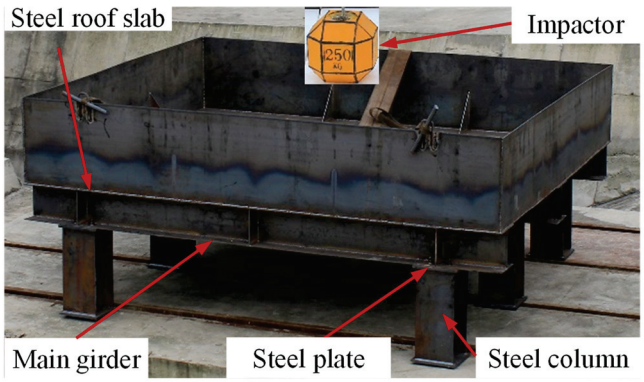

Figure 3. Test model of steel shed structure.

Table 1. Main component specifications.

Component Name	Specifications	Materials
Steel column	HW300 × 300 × 20 × 20	Q345
Main girder	HW300 × 300 × 6 × 6	Q345
Secondary beam	HW150 × 150 × 6 × 6	Q345
Steel roof slab	6 mm thickness	Q345
Two-layered absorbing system	30 cm thickness EPS + 40 cm thickness sand	EPS + Sand
Impactor	Standardized test block	Concrete + Cladding steel plates

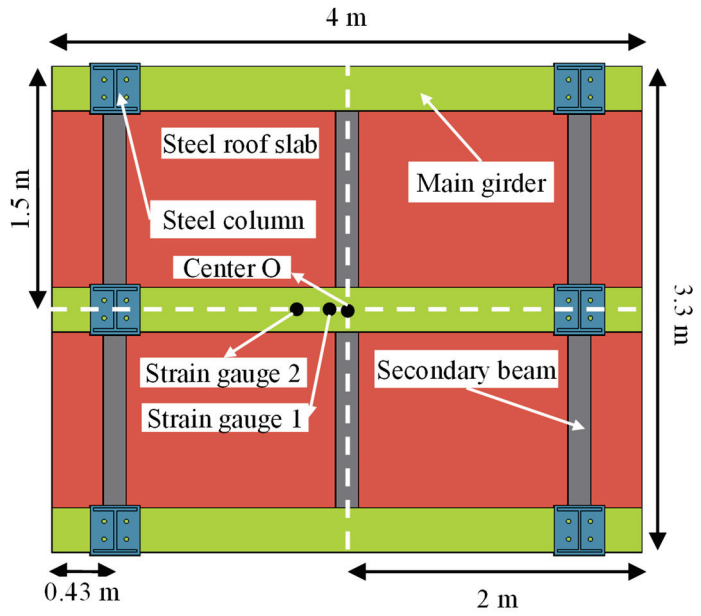

Figure 4. Bottom view of the steel shed and arrangement of the strain measuring points.

In the experiment, the impact test was conducted in accordance with the European code [28]. The impactor was a concrete polyhedral block with a mass of 0.25 t confined by steel plates, and the impact position of the impactor was the center position of the roof slab of the shed [12]. Through the gantry crane, the impactor was raised to the heights of 3 m (7.5 kJ impact energy), 6 m (15 kJ impact energy), and 8 m (20 kJ impact energy), respectively. A high-speed camera was placed right ahead of the test model to record the process of impacting with a frequency of 500 Hz. Through a dynamic acquisition system, the time-strain curves of beams were measured to obtain the dynamic response, with the acquisition frequency of 1000 Hz [12].

3.2. Numerical Model

3.2.1. Numerical Model Description

The calculation model is shown in Figure 5. The steel column, main girder, secondary beam, and steel roof slab adopted shell elements with the complete integration of three/four nodes, and the mesh size is 0.05 m. The EPS and impactor adopted solid elements with the complete integration of six nodes, and the mesh sizes are 0.06 m and 0.04 m, respectively. Due to the direct impact of the impactor, the sand cushion will experience a large deformation, which can easily cause mesh distortion and lead to the instability of the calculation [20,27]. Therefore, SPH simulation is adopted for sand, and the spacing between the adjacent SPH particles is about 0.05 m.

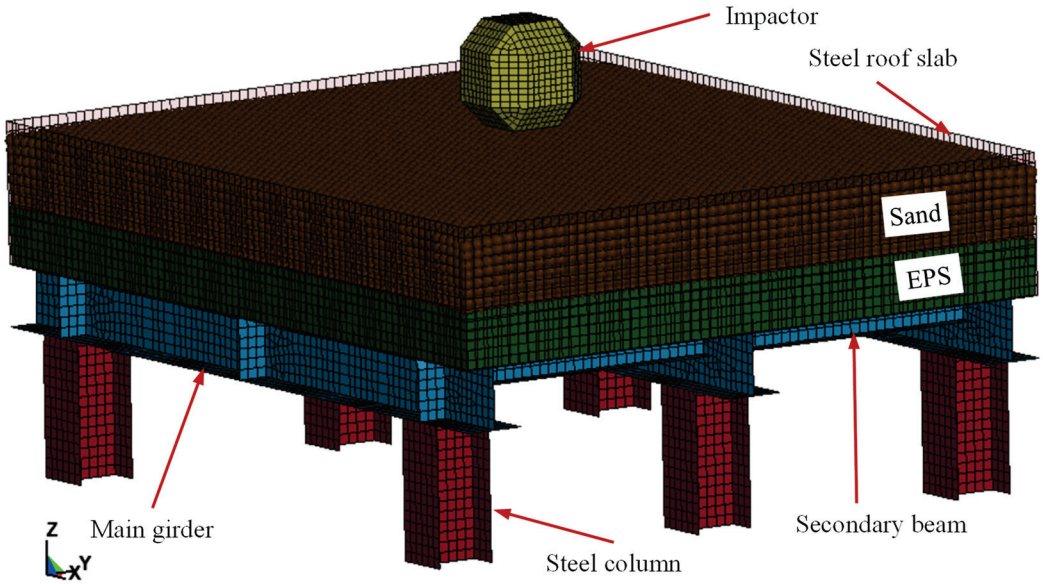

Figure 5. Numerical model of steel shed structure.

3.2.2. Constitutive Material Models

The properties of materials are shown in Table 2. Figure 6 shows the stress–strain relations for sand, EPS, and steel material. The constitutive models are briefly outlined below.

Table 2. Material parameters for simulation.

Material	Density (kg/m^3)	Elasticity Modulus (Pa)	Poisson Ratio	Reference
Sand	2000	10.0×10^9	0.060	[1]
EPS	22	0.0069×10^9	0.12	[29]
Steel	7850	200.0×10^9	0.300	[20]
Impactor	2515	30.0×10^9	0.300	[27]

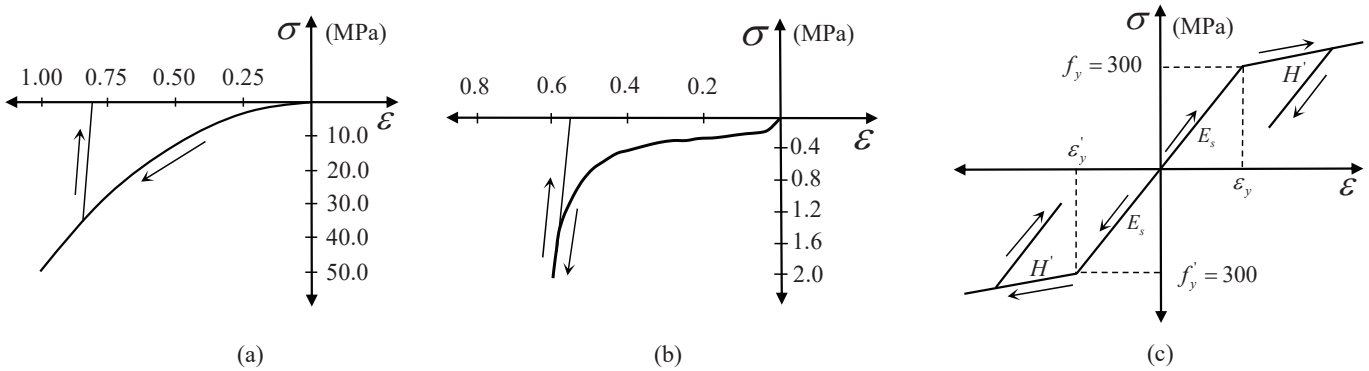

Figure 6. Constitutive model curve of material: (**a**) sand; (**b**) EPS; (**c**) steel.

Sand cushion. Figure 6a shows the constitutive model for the sand. The stress–strain relationship is described in the following expression [1]:

$$\sigma_{sand} = 50\varepsilon_{sand}^2 \tag{8}$$

where σ_{sand} is the stress and ε_{sand} is the volumetric strain. LS-DYNA material model MAT_CRUSHABLE_FOAM is used, which has a good simulation effect [1,20].

EPS. As shown in Figure 6b, under a uniaxial compression test, the EPS material will experience three stages: the linear elasticity stage, the yield stage characterized by platform stress, and the compaction stage where stress rapidly increases with strain [29]. MAT_CRUSHABLE_FOAM was also selected as the calculation model to simulate the mechanical properties of the EPS material during the impact process [29].

Steel. As shown in Figure 6c, for the steel column, main girder, secondary beam, and steel roof slab, an elastoplastic model is used, and the plastic hardening modulus *H*' is set to 1% of elastic modulus *E*s [1,20].

Impactor. A rigid material model (*MAT_RIGID in LS-DYNA) can be used to simulate some small deformation structures that do not require excessive attention, which can reduce computer time [27].

3.2.3. Boundary Conditions

The bottom of the steel column is constrained by three translational degrees of freedom [12]. The steel roof slab and main girder/secondary beam, steel column, and main girder are restricted by welding (Contact_Spotweld in LS-DYNA) [12]. Erosion contact is defined between the impactor and sand SPH particles (Contact_Eroding_Nodes_To_Surface in LS-DYNA), and the friction coefficient is set at 0.4 [30]. The interface between EPS and sand SPH particles is defined as the node-to-surface contact (Contact_Automatic_Nodes_To_Surface in LS-DYNA), and the friction coefficient is set as 0.4 [30]. The EPS finite element and the steel roof slab element adopt surface-to-surface contact (Contact_Automatic_Surface_To_Surface in LS-DYNA), and the friction coefficient is set at 0.3 [12].

Before the impact, gravity is applied to the entire shed structure [20]. The impact case with an impact height of 8 m is simulated. The impact time is defined as 200 ms when the impactor starts timing when it comes into contact with the sand [24]. During the impact process, the automatic time step is used. It means that the program automatically calculates the limit value of the time step. In addition, a viscous damping constant of 0.005 is considered, which is used for the lowest natural vibration mode [1].

The simulations are conducted on a 64-bit assembled Desktop with an Intel Core i7-10700K 2.9 GHz processor and 8 GB of Kingston DDR4 RAM (random access memory) bank. Run time refers to the real-world time, which is calculated from the onset of analysis to its end. In this numerical model, the run time is about 3 h.

3.3. Verification of Accuracy of Numerical Analysis

The numerical analysis results for time histories of strain at the main girder and secondary beam are compared with the steel shed test. From Figure 7, the waveforms of the test curve and simulation curve are very similar. The maximum strain of the lower flange of the main girder is only 520 $\mu\varepsilon$, indicating that the main girder is still in the elastic stage (the elastic limit strain is 1500 $\mu\varepsilon$), and it still has a large residual bearing capacity. Near the impact point of the impactor, the maximum strain of the main girder is much greater than that of the secondary beam.

A more detailed comparison is shown in Table 3. It can be seen from Table 3 that the maximum error of the maximum strain in the numerical simulation and test is only 9.0%, and the maximum error of the minimum strain is 12.2%. In this study, the time frame between the 1st strain being 0 and the 2nd strain being 0 is denoted as a wave crest propagation period. It can be seen from the table that the maximum error of the wave crest propagation period of the numerical simulation and test is only −8.3%. The six groups of key data are compared, of which the error of only one group is greater than 10%, but less than 13%.

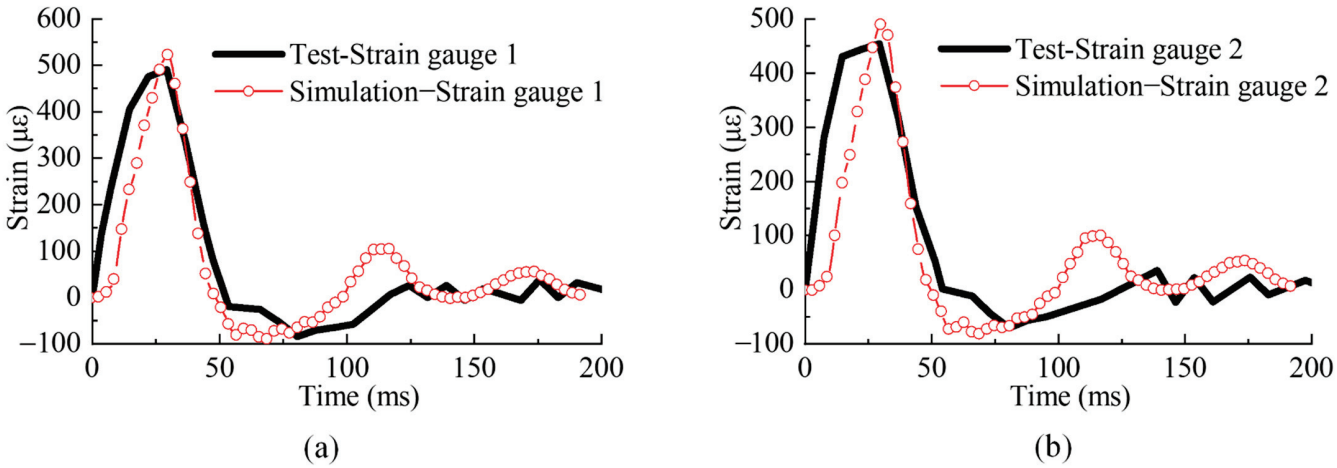

Figure 7. Comparison of the strain time history: (**a**) strain gauge 1; (**b**) strain gauge 2.

Table 3. Comparison of strain obtained from the experiment and simulation.

Strain Gauge	Maximum Strain (με)			Minimum Strain (με)			Wave crest Propagation Period (ms)		
	Test	Simulation	Error	Test	Simulation	Error	Test	Simulation	Error
1	490.6	522.9	6.6%	−81.1	−88.1	8.6%	54.2	49.7	−8.3%
2	456.5	497.8	9.0%	−70.3	−78.9	12.2%	52.5	48.5	−7.6%

The final penetration of the impactor into the sand cushion is shown in Figure 8. The penetration depth in the experiment is 0.16 m [12], while that in the simulation is 0.17 m. The error of the penetration depth between the experiment and the simulation is 6.25%.

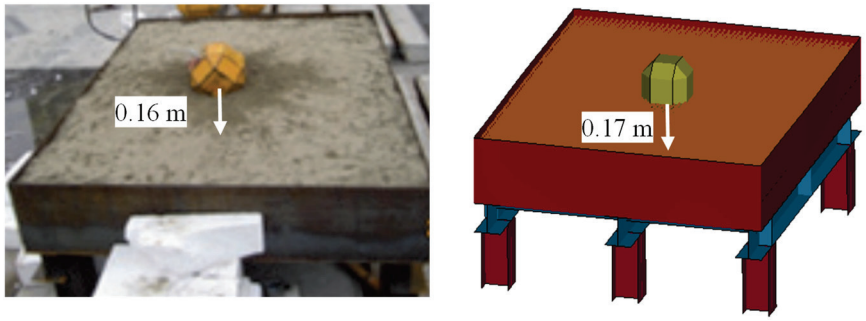

Figure 8. The final penetration of the impactor into the sand cushion.

Through the above comparison, the numerical model can be used for subsequent dynamic analysis.

4. Numerical Simulation of Steel Shed under Block Impact

Based on the above-validated simulation model, extensive numerical simulations are performed to investigate the dynamic response of steel sheds considering the effects of the different combined absorbing systems. The impact process, mid-span displacements of the steel shed, and the energy dissipation mechanism are summarized and discussed.

4.1. Computational Cases

Based on the statistical results [20], the average impact velocity of 90% of falling rockfalls is 25 m/s. Therefore, the impact velocity of the rockfall is set as 25 m/s. The mass of the rockfall is set to 0.75 t in the design energy level (elastic limit). It is stipulated that the thickness of the backfill soil laid on the roof plate of the shed should not be less than

1.5 m [30], so the thickness of the two-layered absorbing system in the model is set as 1.5 m. The thickness of EPS is set as 0% (P1), 20% (P2), 40% (P3), 60% (P4), 80% (P5), and 100% (P6) of the total thickness of the two-layered absorbing system, respectively.

4.2. Results and Discussion

4.2.1. Impact Process

Figure 9 illustrates the dynamic impact process of a 0.75 t impactor (EPS thickness = 40% of the total thickness of the buffer layer). As shown in Figure 9a, when t = 0.0 s, the impactor begins to invade the sand cushion. As shown in Figure 9b, when t = 0.013 s, it can be observed that the stress wave propagates radially downward from the impact point in the sand cushion. As shown in Figure 9c, when t = 0.057 s, the vertical displacement of the impactor reaches a maximum value of 0.508 m. During the transmission of the stress wave, the elastic modulus of the material changes from large to small in the propagation medium, and the maximum stress is located in the contact zone between the EPS and the sand cushion, with a value of 5.07 MPa. As shown in Figure 9d, when t = 0.2 s, the impact process of the block tends to be static, and the vertical block displacement is 0.499 m. Finally, a bowl-shaped pit forms in the sand layer. Due to the distributed stress acting on the EPS cushion, a small sag deformation appears in the EPS cushion.

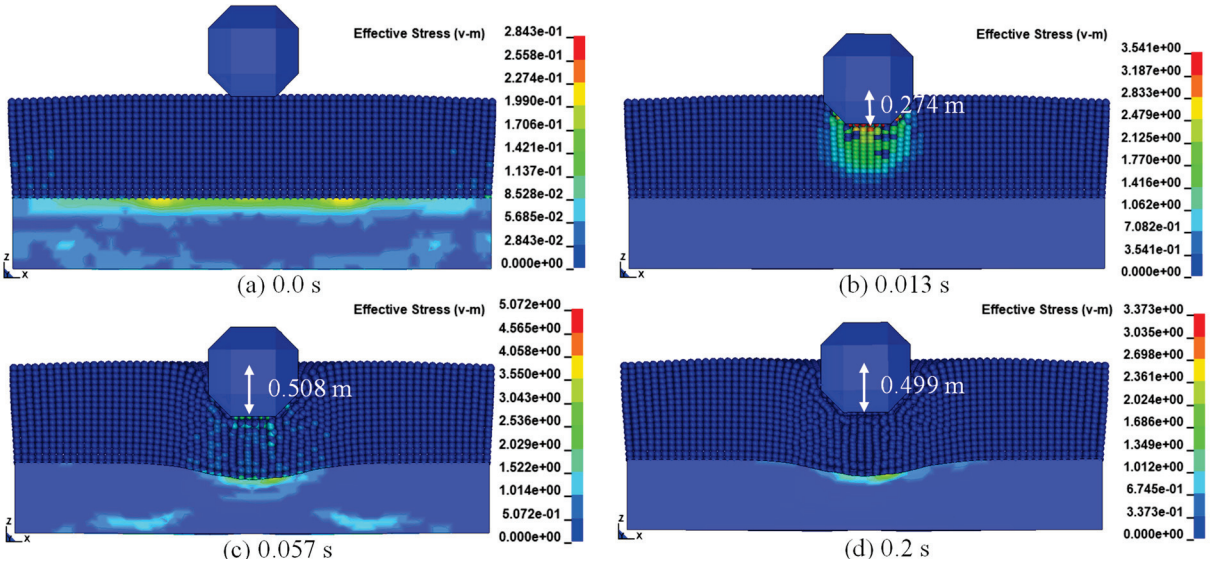

Figure 9. Dynamic impact process of a 0.75 t impactor (EPS thickness = 40% of the total thickness of the buffer layer) (stress unit: MPa): (**a**) t = 0.0 s; (**b**) t = 0.013 s; (**c**) t = 0.057 s; (**d**) t = 0.2 s.

4.2.2. Center Displacement of Main Girder

Figure 10 shows the center displacement of the main girder of the steel shed. The center displacement of the main girder is mainly generated by two parts, one is the deadweight of the buffer layer, and the other is the impact force. As shown in Figure 10a, when t = 0, the center displacement of the main girder is not 0, which is mainly caused by the dead weight of the buffer layer. With the increase of time, the center displacement of the main girder in each case increases first and then decreases.

As shown in Figure 10b, with the increase in EPS thickness, the center displacement of the main girder first decreases and then increases, and when EPS thickness is 40% of the buffer layer thickness, the center displacement of main girder reaches the minimum (6.9 mm). Compared with the single sand cushion, the combined cushion with an EPS thickness of 0.6 m reduces the structural displacement response by 43%. The larger the thickness of the sand cushion is, the smaller the impact force will be, but the corresponding dead weight of the cushion will also increase. When the thickness of the sand cushion is 60% of the buffer layer, the adverse impact reaction to the structure will be minimized.

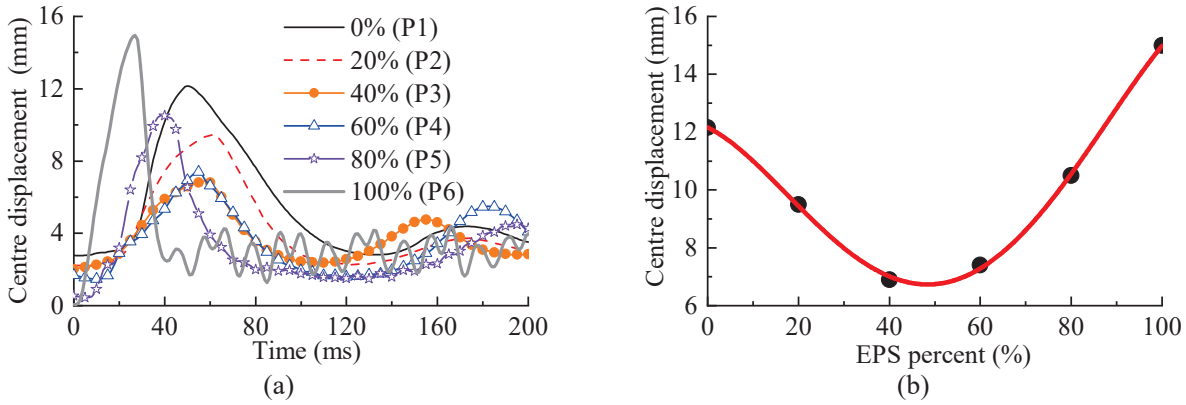

Figure 10. Center displacement of main girder of steel shed: (**a**) center displacement time history; (**b**) maximum center displacement under each case.

4.2.3. Steel Shed Energy Dissipation

Upon impact, the total energy (E_T) of the block is mainly converted into residual block kinetic energy (E_K), the internal energy of the EPS layer (E_E), the internal energy of the sand layer (E_S), the internal energy of the steel components (E_B), and the friction energy (E_F). The total energy (E_T) is defined as:

$$E_T = E_0 + M_0 g h_0 \quad (9)$$

where M_0 is the mass of the block, h_0 is the final vertical displacement of the block, and E_0 is the initial kinetic energy of the block.

Take a P3 case as an example (EPS thickness = 40% of the total thickness of the buffer layer). The evolution of all of the energy components is shown in Figure 11a. Upon impact, E_K decreases rapidly, and the sand cushion dissipates a large part of the E_K, accounting for about 76.3% of the E_K. The EPS layer also dissipates about 13.7% of the E_K. There is almost no dissipative impact energy in the steel components. The two-layered buffer layer consumes 90% of the total energy. In addition, according to statistics, the percentage of two-layered buffer layer energy consumption in total energy under six cases is 91.4% (P1), 90.1% (P2), 90% (P3), 88.8% (P4), 88.5% (P5), and 88.2% (P6) respectively, which indicates that the two-layered buffer layer is very effective in protecting the steel shed structure.

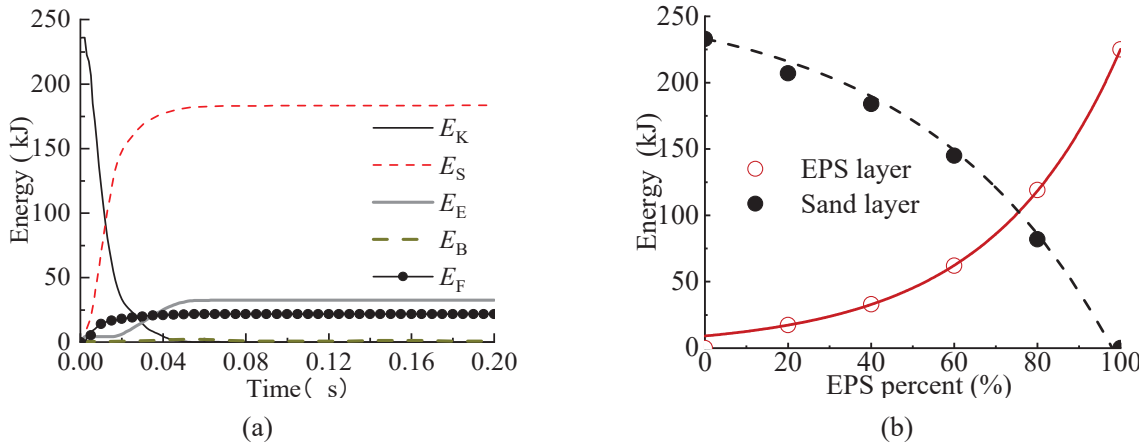

Figure 11. Evolution of the energy of steel shed: (**a**) evolution of the energy of P3 case (EPS thickness = 40% of the total thickness of the buffer layer); (**b**) energy consumption of the buffer layer.

Figure 11b also shows the effect of the EPS thickness on the energy consumption of the two-layered absorbing system. With the increase of EPS thickness, the energy consumption

of the EPS layer increases, and the rate of the increase of energy consumption increases as the EPS thickness increases. In addition, it can be seen that the energy dissipation effect of the sand buffer layer is better than that of the EPS buffer layer with the same thickness, and the key role of EPS is to reduce dead weight.

The coefficient of restitution (COR) is also an indicator of the material energy dissipation capacity [8]. The COR is calculated from the impact and rebound velocities using $COR = V_i / V_{re}$, where V_i is the impact velocity of the falling rock at the moment of contact with the cushion, and V_{re} is the rebound velocity [8]. Table 4 shows COR in some cases. As can be seen from Table 4, the simulation in this study is consistent with the test, and the maximum error between the simulation and the test is 5%. The energy dissipation capacity of the pure EPS foam layer is the worst, while the energy dissipation capacity of the pure soil layer is the strongest.

Table 4. COR in some cases.

Case	Thickness Ratio of EPS	COR		Error
		Test	Simulation	
P1	0	0 [8]	0	0
P6	1	0.42 [8]	0.4	5%

5. Conclusions

This paper aimed to quantitatively find the optimal thickness combination between EPS and soil layer under dynamic loadings. In order to solve the difficulty of the super large deformation of the two-layered absorbing system with the finite element method, the coupled Smooth Particle Hydrodynamic method (SPH) and the Finite Element Method (FEM) are introduced. SPH particles were used to simulate the soil layer which experienced a super large deformation. A numerical model for a steel shed impacted by a block was established and validated. The conclusions are drawn as follows:

The stress wave propagates radially downward into the cushion layer and then the steel structure during the block impact. With the increase of EPS thickness, the center displacement of the main girder first decreases and then increases, and when EPS thickness is 40% of the buffer layer thickness, the center displacement of the main girder reaches the minimum. Compared with the single sand cushion, the combined cushion with an EPS thickness of 0.6 m reduces the structural displacement response by 43%.

The two-layered buffer layer consumes about 90% of the total energy, which indicates that the two-layered buffer layer is very effective in protecting the steel shed. The energy dissipation effect of the sand buffer layer is better than that of the EPS buffer layer with the same thickness, and the key role of EPS is to reduce dead weight.

In engineering design, the optimal combination of more different buffer layers can be investigated and simulated.

Author Contributions: Conceptualization, C.L. and H.L.; methodology, C.L.; software, C.L.; validation, C.L., and H.L.; formal analysis, C.L.; investigation, C.L.; resources, C.L.; data curation, C.L.; writing—original draft preparation, H.L.; writing—review and editing, C.L.; visualization, C.L.; supervision, C.L.; project administration, C.L.; funding acquisition, C.L. All authors have read and agreed to the published version of the manuscript.

Funding: This research was supported by the China Postdoctoral Science Foundation under Grant No. 2021M690742.

Institutional Review Board Statement: Not applicable.

Informed Consent Statement: Not applicable.

Data Availability Statement: Publicly available datasets were analyzed in this study.

Conflicts of Interest: The authors declare there are no competing interests.

References

1. Bhatti, A.Q.; Khatoon, S.; Mehmood, A.; Dastgir, A.; Kishi, N. Numerical study for impact resistant design of full scale arch type reinforced concrete structures under falling weight impact test. *J. Vib. Control* **2011**, *18*, 1275–1283. [CrossRef]
2. Ferrari, F.; Giacomini, A.; Thoeni, K. Qualitative rockfall hazard assessment: A comprehensive review of current practices. *Rock Mech. Rock. Eng.* **2016**, *49*, 2865–2922. [CrossRef]
3. Kawahara, S.; Muro, T. Effects of dry density and thickness of sandy soil on impact response due to rockfall. *J. Terramech.* **2006**, *43*, 329–340. [CrossRef]
4. Mommessin, M.; Perrotin, P.; Ma, Y. Actions of snow avalanches on a protection gallery. *Cold Reg. Sci. Technol.* **2012**, *83*, 20–29. [CrossRef]
5. Kishi, N.; Konno, H. Numerical analysis model for three layer absorbing system under falling weight impact loading. *JSCE J. Struct. Eng.* **2003**, *49*, 1323–1332.
6. Ouyang, C.; Liu, Y.; Wang, D.; He, S. Dynamic Analysis of Rockfall Impacts on Geogrid Reinforced Soil and EPS Absorption Cushions. *KSCE J. Civ. Eng.* **2019**, *23*, 37–45. [CrossRef]
7. Zhong, H.; Lyu, L.; Yu, Z.; Liu, C. Study on mechanical behavior of rockfall impacts on a shed slab based on experiment and SPH–FEM coupled method. *Structures* **2021**, *33*, 1283–1298. [CrossRef]
8. Yan, S.; Wang, Y.; Wang, D.; He, S. Application of EPS geofoam in rockfall galleries: Insights from large-scale experiments and FDEM simulations. *Geotext. Geomembr.* **2022**, *50*, 677–693. [CrossRef]
9. Wu, Y.; He, S.M.; Li, X.P.; Wang, D.P. Dynamic response and optimization of an inclined steel rock shed by the graded energy dissipating method. *J. Mt. Sci.* **2019**, *16*, 141–155. [CrossRef]
10. Schellenberg, K.; Volkwein, A.; Roth, A.; Vogel, T. Rockfall-falling weight tests on galleries with special cushion layers. In Proceedings of the 3rd International Conference on Protection of Structures Against Hazards, Venice, Italy, 28–29 September 2006.
11. Calvetti, F. Rockfall shelters covered by granular layers: Experiments and design approach. *Eur. J. Environ. Civ. Eng.* **2011**, *15*, 73–100. [CrossRef]
12. Wu, J.N. *Seismic Vulnerability Analysis for Bridge Network and Algorithm Improvement*; Southwest Jiaotong University: Chengdu, China, 2018. (In Chinese)
13. Ministry of Transport of the People's Republic of China. *Specifications for Design of Highway Subgrades, (JTJ013-95)*; Ministry of Transport of the People's Republic of China: Beijing, China, 2015. (In Chinese)
14. Labiouse, V.; Descoeudres, F.; Montani, S. Experimental study of rock sheds impacted by rock blocks. *Struct. Eng. Int.* **1996**, *6*, 171–176. [CrossRef]
15. Japan Road Association. *Manual for Anti-Impact Structures Against Falling Rocks*; Japan Road Association: Tokyo, Japan, 2000.
16. He, S.; Liu, W.; Li, X. Prediction of impact force of debris flows based on distribution and size of particles. *Environ. Earth Sci.* **2016**, *75*, 298. [CrossRef]
17. Yu, B.; Yi, W.; Zhao, H. Experimental study on the maximum impact force by rock fall. *Landslides* **2018**, *15*, 233–242. [CrossRef]
18. Zhang, L.; Lambert, S.; Nicot, F. Discrete dynamic modelling of the mechanical behaviour of a granular soil. *Int. J. Impact Eng.* **2017**, *103*, 76–89. [CrossRef]
19. Shen, W.; Zhao, T.; Dai, F.; Jiang, M.; Zhou, G.G. DEM analyses of rock block shape effect on the response of rockfall impact against a soil buffering layer. *Eng. Geol.* **2019**, *249*, 60–70. [CrossRef]
20. Liu, C.; Phuong, N.; Zhao, S.C. Dynamic response of RC sheds against the impact of rock block with different shapes and angles. *Can. J. Civ. Eng.* **2022**, *49*. [CrossRef]
21. Bui, H.H.; Fukagawa, R.; Sako, K.; Ohno, S. Lagrangian meshfree particles method (SPH) for large deformation and failure flows of geomaterial using elastic–plastic soil constitutive model. *Int. J. Numer. Anal. Methods Geomech.* **2008**, *32*, 1537–1570. [CrossRef]
22. Liang, S.; Chen, Z. SPH-FEM coupled simulation of SSI for conducting seismic analysis on a rectangular underground structure. *Bull. Earthq. Eng.* **2019**, *17*, 159–180. [CrossRef]
23. Lucy, L.B. A numerical approach to the testing of fusion processes. *Astron. J.* **1977**, *82*, 1013–1024. [CrossRef]
24. Hallquist, J.O. *LS-DYNA Theory Manual*; Livermore Software Technology Corporation (LSTC): Livermore, CA, USA, 2017.
25. Xu, J.X.; Wang, J. Interaction methods for the SPH parts (multiphase flows, solid bodies) in LS-DYNA®. In Proceedings of the 13th International LS-DYNA Users Conference, Detroit, MI, USA, 8–10 June 2014; pp. 1–12.
26. Feng, S.J.; Gao, H.Y.; Gao, L.; Zhang, L.M.; Chen, H.X. Numerical modeling of interactions between a flow slide and buildings considering the destruction process. *Landslides* **2019**, *16*, 1903–1919. [CrossRef]
27. Liu, C.; Yu, Z.X.; Zhao, S.C. A coupled SPH-DEM-FEM model for fluid-particle-structure interaction and a case study of Wenjia gully debris flow impact estimation. *Landslides* **2021**, *18*, 2403–2425. [CrossRef]
28. EOTA. *ETAG 027–Guideline for the European Technical Approval of Falling Rock Protection Kits*; Tech. Rep.; European Organization for Technical Approvals: Brussels, Belgium, 2008.
29. Wang, Z.L.; Zhu, B. Experimental Study on impact compression and energy absorbing property of expanded polystyrene foam. *J. Build. Mater.* **2013**, *16*, 630–636. (In Chinese)
30. Li, L.P. *Research on Energy Dissipative Mechanism of Cushion Material on Shed under Rockfall Impact*; Sichuan University: Chengdu, China, 2015. (In Chinese)

sustainability

MDPI

Article

Post Evaluation of Slope Cutting on Loess Slopes under Long-Term Rainfall Based on a Model Test

Guodong Liu [1,2,*], Zhijun Zhou [2], Shiqiang Xu [2] and Yuanmeng Cheng [1]

[1] College of Urban, Rural Planning and Architectural Engineering, Shangluo University, Shangluo 726000, China
[2] School of Highway, Chang'an University, Xi'an 710046, China
* Correspondence: 234036@slxy.edu.cn; Tel.: +86-09-142-329-413

Abstract: The failure of treated slopes around the world, especially in China, is occurring at a noteworthy rate, resulting in an urgent requirement for post evaluation of the treated slopes; however, there is no mature technique established for post evaluation. By using a real loess slope treated by slope cutting in Shaanxi Province as the prototype, indoor geotechnical tests and model tests were performed to reveal the rainwater infiltration characteristics and pressure-varying characteristics inside the slope, the results of which were used to conduct a post evaluation of the slope in situ. The results mainly showed that the effect of rainwater scouring on the slope surface weakened gradually into a steady state at the end of the first year. The rainwater upon the slope surface preferentially infiltrated the platforms with gradually reducing rates; however, the observed wetting front cannot be regarded as the border between the unsaturated and saturated loesses. The soil pressures inside the slope did not increase, but decreased during the early period of rainfall. The displacements of key points mainly occurred during the first two years and then steady periods were entered. The above results were utilized to conduct a post evaluation of the slope prototype, by which a post evaluation framework was constructed.

Keywords: post evaluation; loess slope; rainfall; model test; soil pressure

Citation: Liu, G.; Zhou, Z.; Xu, S.; Cheng, Y. Post Evaluation of Slope Cutting on Loess Slopes under Long-Term Rainfall Based on a Model Test. *Sustainability* **2022**, *14*, 15838. https://doi.org/10.3390/su142315838

Academic Editors: Stefano Morelli, Veronica Pazzi and Mirko Francioni

Received: 2 November 2022
Accepted: 25 November 2022
Published: 28 November 2022

1. Introduction

In the 20th century, China started to develop the western area, which promoted the construction of houses, highways, railways, etc., which inevitably brought a large number of slopes under treatment. More than 70% of western China is covered by loess, characterized by collapsibility under rainfall, which is more evident in northern Shaanxi. Thus, long-term rainfall is the most active factor influencing slope stability in western China [1]. Comparably, the failures of loess slopes after treatment has occurred widely in other areas around the world, such as that of the Zemun Loess Plateau on the northern outskirts of Belgrade in Serbia [2] and that in the loess-mantled regions of the American Midwest and Hungary [3]. Evidently, the treated loess slopes that are widespread around the world require further treatments to defend their safety. This falls under the area of slope post evaluation, which is different from the safety investigation undertaken in the design stage [4].

Addressed by scholars, slope post evaluation concerns the whole situation of the subject, including its adaptations to the environment, displacements and cracks [5,6]. To make the post evaluation of slopes more reasonable, Fang [7] adopted a rectified concept of the post evaluation and made use of an evaluation method based on stress. However, the main post evaluation theory still falls under the scope of field investigations and judgment based on experience [5,7]. The developed post evaluation theories all fall under the scope of qualitative and semiquantitative methods, which do not consider rainfall. This is a limitation of the current post evaluation techniques.

Recently, an increasing number of scholars have made efforts in the field of slope stability evaluation when the slope is under rainfall and the associated failure mechanism,

including modeling tests [8–11], numerical simulations [12,13] and field monitoring [14,15]. Raj and Sengupta [16] studied the railway embankment slope failure in Malda, India, during rainfall and found that the rainfall intensity and duration were the two critical factors influencing soil slope safety. The draining of rockfill was an effective measure for strengthening the railway embankment slope stability. Zhang et al. [17] conducted a series of model tests on slopes under rainfall to reveal the hydrological mechanism for slope failures and concisely concluded that the volumetric water content response and the matrix suction response of the slopes occurred earlier than the pore water pressure response. The loess slopes failed when the volumetric water content and the matrix suction reached their maximum and minimum values, respectively; thus, a warning threshold model for the slope instability induced by rainfall was proposed. Huang et al. [18] developed a piezometer system to monitor the hydrological conditions of a highway earth slope in Taiwan under rainfall, from which it was found that the pore water pressures inside the slope were apparently pertinent to the rainfall pattern and the ground water flow. For a deep-seated slope failure, it was suggested to combine the imperatively monitored pore water pressures with the monitored stresses to establish a slope failure warning system. Perceivably, rainfall is the most critical factor influencing slope safety, causing surface erosion of slopes [19–23], reducing the strength of slope soils by infiltration [24–26] and degrading the stress situation in the slope soil as it becomes saturated [27–31]. Regarding a loess slope, rainwater flows can scour the slope surface easily, generating gullies and fall holes [32]. Thus, some researchers have employed a geobarrier system to defend soil slopes from rainwater-scouring and to ascertain the slope safety under rainfall [33]. It has been widely accepted that matrix suction plays an important role in the strength of the slope soil and is thus very critical to slope stability [34]. Under rainfall, rainwater infiltration leads to an increase in the water content of the slope soils, thus reducing the suction inside, which in turn causes instability of the slopes. For loess slopes incorporating more fines, this is more significant [35]. Moreover, during the rainfall process, the effective stress of the slope soil declines, which also causes a decrease in the soil strength, being adverse to the stability of the slope [36]. In summary, rainfall is a critical factor inducing slope instability. Thus, in the slope design consideration, drainage engineering is an compulsory measures.

Model tests have been used by a huge number of scholars to study slope stability and the slope failure mechanism to assess its reliability. Schenato et al. [37] employed optical fiber sensors in a model test to investigate the mechanical evolution in the slope. The results indicated the four stages of slope evolution under rainfall, from which the effectiveness of the fiber system in model tests was validated. Lan et al. [38] conducted model tests to investigate the expansion and contraction of loess slopes with moisture fluctuations, and established the relationship between the deformation of the loess slope and weather variation. Chen et al. [39] investigated the influence of the vegetation on rainwater scouring on the soil slope by model tests, and announced that the vegetation cover can adjust the rainfall patterns and alleviate rainwater splash erosion. Hung et al. [40] employed model tests to investigate the effects of earthquakes and rainfall on soil slopes. It was found that an earthquake is the factor influencing the slope stability most evidently. Sun et al. [41] used a model test to explore the influencing mechanism of rainfall on loess slopes and found that the infiltrated rainwater reduces the suction of the slope soils, causing a reduction in the shear strength of the slope loess, which eventually causes slope failure. In summary, it can be inferred that the ensuing studies of loess slopes mainly concern the pre-evaluation phase (regarding the design work), and only a very limited number of post evaluation studies have considered rainfall.

In order to facilitate the remediation of loess slopes treated in northern Shaanxi, a physical model of loess corresponding to a real slope was used to study the effects of slope-cutting treatment. The rainwater percolation and the variations in the pressures and displacements of representing positions were obtained, and they were utilized to conduct the post evaluation of the corresponding real slope. This technology of post evaluation presents an innovation for the assessment of the effects of the treatment of other types of slopes; meanwhile, the rainwater infiltration characteristics and the varying principles in

the displacements and pressures of the slope may facilitate further research and design work in this regard.

2. Prototype Failure

The current prototype slope is located in Luochuan County, Yan'an city, Shaanxi Province, with a latitude of 35°45′19.46″ north and a longitude of 109°25′34.63″ east, as shown in Figure 1. The elevation of Luochuan County fluctuates by approximately 1100 m. With a temperate continental monsoon climate, this area has an annual maximum temperature of 37.4 °C and an average temperature of 5~17 °C. The average precipitation of Luochuan County is approximately 606 mm per year, mainly occurring in July, August and September.

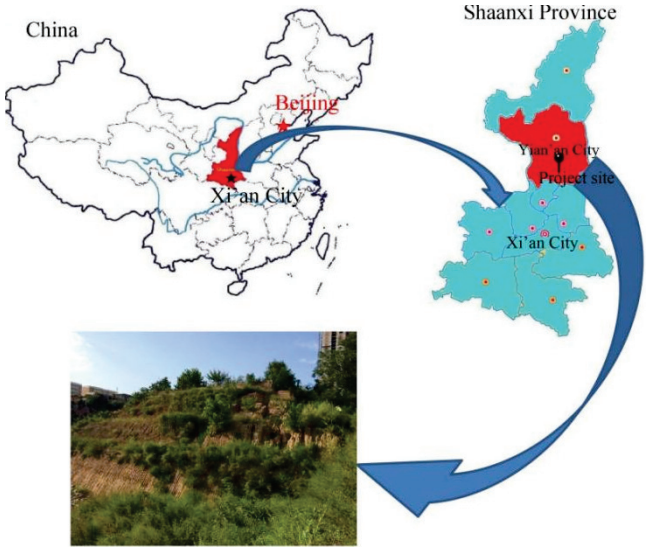

Figure 1. Slope prototype location in China (The red star denotes the capital of China while the black star denotes the provincial capital Xi'an).

Located on the Loess Plateau, the loess slope included in this study was treated by slope cutting, and has a group of houses on the crest. From the field investigation, the slope wholly consists of loess formed in the late Pleistocene epoch. As Figure 2 illustrates, the slope prototype was 7.6 m high, and was cut into three grades of the same gradients 56°. The first grade was 5 m high, while the second and the third grades were 4 m and 5.6 m high, respectively. The widths of the second and third grade platforms were both 3.8 m, while the length of the slope was approximately 38.7 m. With the gully close to the right of the slope, the slope was excavated inward by the rainwater vented by the gully, eventually forming the collapse area (see Figure 2).

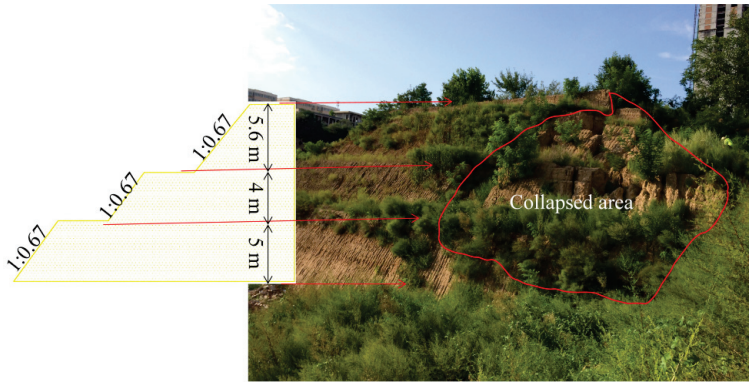

Figure 2. Slope prototype section with collapse.

According to the field investigation performed on 20 August 2017, this project was built in approximately 2012 and ran for approximately 5 years. After a long run, affected by rainfall, the slope had main damage on its right side (see Figure 2). From the above, it can be considered that this slope prototype was composed of homogeneous loess and was in operation for a relatively short period; however, a major collapse was caused by rainwater scouring. Thus, it was reasonably chosen as a typical loess slope treated by slope cutting, which was destroyed by rainwater, as this study concentrated on the effect of rainfall on the treatment effect of loess slopes under slope cutting regardless of other factors, such as geological conditions. To conduct the post evaluation of the current loess slope through a model test, it was determined that the total simulated duration should be 5 years to be consistent with the actual running period. According to the similarity theory, the simulated time can be shrunk by 100 times, allowing the model test to be finished in a reasonable duration.

3. Methodology and Test Model

3.1. Test Device

The model test was performed in the Soil Mechanics Laboratory of Shangluo University, China. From the report of Liu et al. [42], a model box with a width of 1 m, length of 2.5 m and height of 1.8 m was used in the test (see Figure 3a). The box walls of the left and right sides were made from organic glass, allowing the displacements inside the slope model to be captured by the camera. The base, front and back walls of the box were all made from planks, while the upper 1.5-m-high part of the front plank was removable, allowing the model slope surface to be free.

(**a**) (**b**)

Figure 3. Model test box and rainfall simulator: (**a**) Model test box, (**b**) Rainfall simulator.

The rainfall simulator was a steel frame with drilled holes of 1 mm in diameter on one side. A valve connected the rainfall simulator to the water source (see Figure 3b) and adjusted the rainfall intensity. Before the start of the experiment, the simulating rainfall intensity was calibrated to a certain value according to the real rainfall, in which a beaker and measuring cylinder was adopted as the calibrator. The rainfall intensity calibration steps were as follows: (1) three beakers were placed under the rainfall simulator at different positions after the valve connecting the water pipe and the rainfall simulator was opened; (2) the three beakers were moved out five minutes later, and the water volumes contained within them were measured by the cylinder; (3) the rainfall intensities of the three positions were calculated as the corresponding water volume divided by the cross-sectional area of the beaker; (4) the average rainfall intensity was calculated from the rainfall intensities of the three positions; and (5) if the average rainfall intensity did not equal the required value, the valve opening was adjusted, and the steps above were repeated until the required rainfall intensity was achieved. Additionally, from the collected water volumes in the three

beakers during the five minutes under the required rainfall intensity (31.94 mm/h), we derived that the uniformity coefficient of the rainfall simulator under a rainfall intensity of 31.94 mm/h was 0.93. This met the uniformity requirement of the model test. As the duration of each rainfall event was exactly two hours, the total rainfall amount from each rainfall event was derived as 31.94 mm/h multiplied by 2 h, resulting in a value of 63.88 mm.

3.2. Test Model

The current slope model was built to fully correspond to the prototype slope in Luochuan County, Yan'an City, Shaanxi Province, as depicted in Figure 1. With a scale of 1:10, the height of the model slope was 1.76 m, while the length of the model was 2.5 m. The three platforms of the slope model were approximately 0.38 m, while the gradients of the three grades of the slope were exactly 56°, identical to the slope prototype. In full correspondence with the slope prototype, the first, second and third grades of the slope heights were 0.5 m, 0.4 m and 0.56 m, respectively (Figure 4).

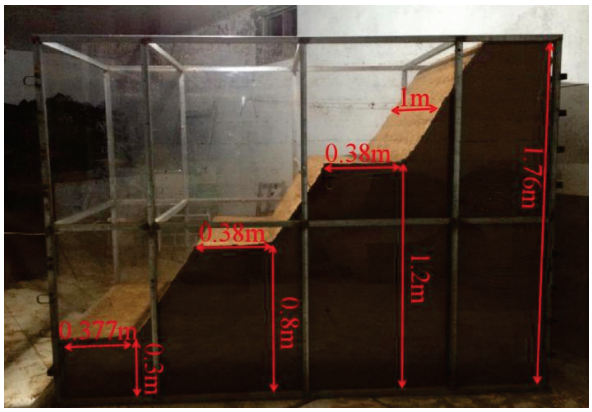

Figure 4. Slope model.

Similar to the research of Liu et al. [42], the slope in situ was first sampled by ring knife to obtain undisturbed samples, which was performed on 20 August 2017. The water content, density, permeability, grain size distribution and shear strength of the slope loess were obtained via laboratory tests. Reasonably, the loess of the model slope was collected from the site of the prototype slope. The slope model was built using the method of stratified compaction. That is, the soil was first prepared with a certain water content, and then, the loess mass of each layer of 10 cm was weighed before being used to fill the model box. As the box was filled to the certain height, the front upper plank of the model box was removed, and the filled model was cut to the dimensions corresponding to the slope prototype. Then, the constructed slope model was left standing for one year prior to the start of the rainfall experiment to simulate the formation process and the geological conditions of the slope prototype, to increase the reliability of the experimental results.

As Figure 5 shows, building the slope model was a complex process and it can be expressed by the following:

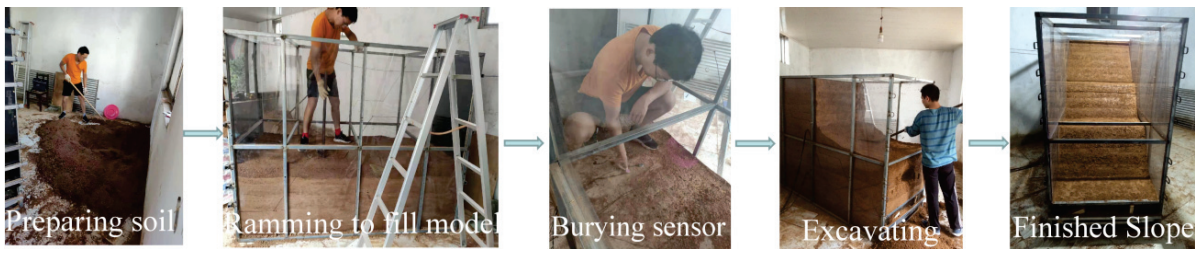

Figure 5. Slope model construction process.

The loess obtained from the slope site was prepared such that it had an identical water content to the prototype slope (ω = 17.4%), and then, a certain mass of the prepared loess was added to the model box as a layer, which was compacted to the thickness of 10 cm.

Within the model slope building process, the soil pressure sensors and pore-water pressure sensors were buried at the prescribed positions in the model.

Synchronously, inner displacement marks were set with colored sand particles next to the two side walls of the model box, to show the displacements inside the slope model.

As the model was compacted to the required height, it was cut to the same dimensions as the prototype.

Lastly, one displacement mark was fixed at each of the three slope shoulders.

3.3. Model Materials and Similarity Relations

The model slope was wholly constructed from the loess of the prototype slope. Thus, all the hydraulic and mechanical properties of the model slope loess were identical to the properties of the prototype. The critical soil property values are listed in Table 1.

Table 1. Key properties of the model soil material.

Parameters	Value	Parameters	Value
Water content (%)	1.42	Compression modulus (MPa)	5.58
Permeability coefficient (cm/s)	5.4×10^{-4}	Internal friction angle (°)	27.0
Density (g/cm^3)	17.4	Cohesion (kPa)	15.0

It is noteworthy that the parameters in Table 1 were obtained from geotechnical tests conducted according to Liu et al. [42]. The water content of the soil was taken from the water content experiment using the oven drying method. The permeability coefficient of the soil was obtained from the standard permeability test of varying head. The soil density was obtained from standard ring knife tests. The compression modulus of the soil was measured by the compression test. The cohesion and internal friction angle of the soil were obtained from the direct shear test of quick shear, as the quick and sudden failures of loess slopes usually happen under rainfall. For the sake of clarity, the geotechnical test process is depicted in Figure 6.

Figure 6. Photos of indoor geotechnical tests: (**a**) Density test, (**b**) Direct shear test, (**c**) Compression test, (**d**) Water content test.

According to the π theorem [43,44], the similarity criterion of variables in model tests can be derived from the dimension analysis. As the model slope is considerably complex, it is impossible to meet the similarities of all the parameters. Thus, only the parameters of geometric dimension, gravity acceleration and density were chosen as the fundamental dimensions considering the purpose of the model test. Relevant similar constants in the test are tabulated in Table 2.

Table 2. Similarity ratios of the test model.

Parameters	Similarity Relation	Similarity Constant
Geometric dimension (L)	C_L	10
Density (ρ)	C_ρ	1
Gravity acceleration (g)	C_g	1
Stress (σ)	$C_\sigma = C_\rho C_g C_L$	10
Strain (ε)	$C_\varepsilon = 1$	1
Displacement (s)	$C_s = C_L$	10
Cohesion (C)	$C_C = C_\rho C_g C_L$	10
Internal friction angle (φ)	$C_\varphi = 1$	1
Rainfall intensity (C_q)	$C_q = C\rho^0 Cg^{0.5} C_L{}^{0.5}$	$\sqrt{10}$

It is noteworthy that the similarity constant of the rainfall time was derived from a calculation according to Terzaghi's consolidation theorem [45] but not from the π theorem. This method was validated by Butterfield [46] and Garnier et al. [47] and was employed by Tang [48] in studies of the slope stability with rainfall. Though the size of the slope model was different from that of the slope in situ, the consolidation degrees of the slope model and the slope in situ should be identical in the testing process. According to Terzaghi's consolidation principle, the consolidation degree of the slope soils can be expressed as

$$U = 1 - \beta . e^{-\lambda . T_V} \tag{1}$$

Here, β and λ are the invariable constants and T_v is the time, which only varies with the time elapsed. Therefore, the consolidation degree U varies only with time t.

Reasonably, the parameters β and λ of the slope model and the slope prototype have the same value. Therefore, under the identical consolidation degree, the slope model has the same time factors with the slope prototype, i.e.,

$$T_{Vp} = T_{Vm} \tag{2}$$

Here, T_{Vm} and T_{Vp} are the time factors of the slope model and the slope prototype, respectively. Equations (3) and (4) depict the relationships between the time factors and the consolidation time.

$$t_p = \left({H_p}^2 / C_V \right) T_{Vp} \tag{3}$$

$$t_m = \left({H_m}^2 / C_V \right) T_{Vm} \tag{4}$$

Here, t_m is the consolidation time of the model slope and t_p is that of the the prototype slope; H_m and H_p denote the sizes of the model slope and the prototype slope, respectively; and C_v denotes the same consolidation constant of the model slope and the prototype slope. Therefore, we can derive the similarity constant of the rainfall time as

$$C_t = \frac{t_p}{t_m} = \frac{H_p^2}{H_m^2} = C_L^2 \tag{5}$$

Accordingly, C_L was 10 here; thus, C_t was derived as 100. As a result, the experimental time was shrunk by 100 times, allowing the experiment to be completed in a shorter period. According to the field investigation, the slope prototype had been in operation for approximately five years. Thus the experimental time was 0.05 years in this study.

3.4. Measuring System and Rainfall Scheme

In total, the model test employed seven pore pressure sensors and seven soil pressure sensors. The pore pressure sensor U4 was seated at a position 10 cm under the shoulder of the second grade of the model slope, and the seated depth of U3, U2, and U1 increased by 20 cm sequentially in a perpendicular line from U4. The pore pressure sensors U5, U6 and U7

were seated 10 cm under the slope toes of the first, second and third grades, respectively. To facilitate meaningful results, the soil pressure sensors P1, P2, P3, P4, P5, P6 and P7 were buried at identical positions with those of U1, U2, U3, U4, U5, U6 and U7, respectively. A strainometer was connected to the pressure sensors, and converted the pressures into digital signals for the computer to store. Although the model test analyzed a planar problem, the pressure sensors were seated close the axial plane of the model to deliver more reliable data [42].

Three displacement marks were set at the three slope shoulders, which are shown in Figure 7 as S5, S4, and S6 at the first, second and third grades of slope shoulder, respectively. Three points were marked by colored sand particles close to the right wall of the model box to measure the inner displacements of the model slope, which were S1, S2, and S3. Similarly, three displacement marks, S1′, S2′ and S3′, were set by colored sand particles close to the left wall of the model box, corresponding to the positions of S1, S2 and S3. To obtain meaningful data, the depths of S1 (S1′), S2 (S2′) and S3 (S3′) were the same as those of P1, P2 and P3, respectively, as shown in Figure 7. The displacements of the marked positions were defined as the distance differences before and during rainfall, which were measured by a laser rangefinder fixed in front of the model slope. A computer connected to the laser rangefinder was used to display the distance data. It is noteworthy that the accurate displacement of S1 was the average displacements of S1 and S1′, and the same applies for S2 and S3.

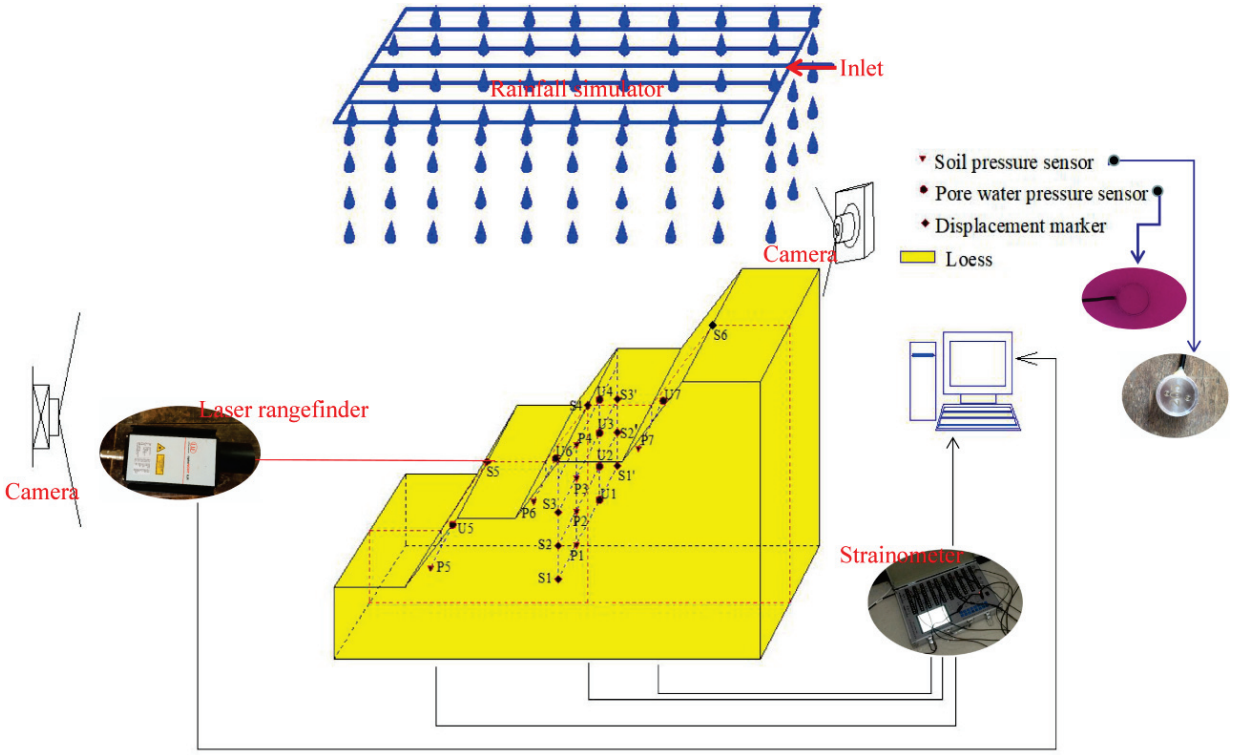

Figure 7. Full dimensions of the model slope and layout of the measurement points.

At constant time intervals, photos were taken from the front and two sides of the model; thus, we obtained the rainwater infiltration process and the deformation process of the model slope during rainfall.

As addressed above, the precipitation in Luochuan County mainly happens in July, August and September, with a total amount of approximately 606 mm per year. For this study, we assumed that the annual precipitation was spread over three months, with each month only having one rainfall event of 2 h. In the remaining period of the month after the rainfall, the model slope stayed undisturbed. Thus, the rainfall intensity in situ was calculated as being 101 mm/h constantly. The simulated rainfall intensity was derived

as 101 mm/h divided by the similarity constant $\sqrt{10}$, resulting in a value of 31.94 mm/h. In the same way, the total experimental time was derived as five years divided by the similarity constant 100 (see Equation (5)), producing a value of 0.05 years, i.e., 18 days. The time intervals between each of the 3 simulated rainfall events were derived as 30 days divided by the similarity constant 100, and then 2 h were subtracted, producing a period of 5.2 h. The testing scheme of one year is detailed in Table 3, and this was repeated 5 times to accomplish the rainfall of 5 years.

Table 3. Model test scheme (the scheme in this table was repeated 5 times to simulate 5 years of rainfall).

Simulated Time	Actual Time	Rainfall Start	Rainfall End	Read Data
0 h	0 h	Yes		Yes
2 h	2 h		Yes	Yes
7.2 h	30 d	Yes		Yes
7.2 h + 2 h	30 d + 2 h		Yes	Yes
14.4 h	60 d	Yes		Yes
14.4 h + 2 h	60 d + 2 h		Yes	Yes
21.6 h	90 d			Yes
28.8 h	120 d			Yes
36 h	150 d			Yes
43.2 h	180 d			Yes
50.4 h	210 d			Yes
57.6 h	240 d			Yes
64.8 h	270 d			Yes
72 h	300 d			Yes
79.2 h	330 d			Yes
86.4 h	360 d			Yes

In general, the experimental steps can be depicted as follows:

Before burying the pressure sensors in the model construction process, their original values were measured.

As the construction of the slope model was completed, the pressure sensor cables were attached to the strainometer, which was used to send the pressure data to the computer. Additionally, a laser rangefinder seated in front of the slope model was connected to the computer to obtain the distances between the fixed position and the displacement marks (S1, S1′, S2, S2′, S3, S3′, S4, S5, S6), thus deriving the horizontal displacements of the key points.

The rainfall intensity of the rainfall simulator was adjusted to 31.94 mm/h, and acted the rainfall simulator on the model slope while the computer program used for data-capture started.

The scheme in Table 3 was repeated 5 times to accomplish five years of rainfall simulation, as the computer recorded the data of the pore water pressures, soil pressures and horizontal displacements of the key points.

3.5. Compound Safety Factor Calculation

In the field of geotechnical engineering, safety factors have been widely accepted as indicators of the safety situations of slopes. As Equation (6) shows, the slope safety factor can be expressed as the ratio of the total anti-slide moment to the total sliding moment.

$$K = \frac{\sum M_{resisting}}{\sum M_{sliding}} \tag{6}$$

Here, $M_{resisting}$ is the anti-slide moment at a slice base within the sliding body, and $M_{sliding}$ is the sliding moment at the slice base. Within the limited equilibrium method, the sliding surface is occasionally assumed as an arc. In this situation, the arm of a moment is

identical to the arc radius, and the interslice forces are totally excluded from the calculation. Adopting this consideration, the slope safety factor was simplified as

$$K = \frac{\sum F_{resisting}}{\sum F_{sliding}} \tag{7}$$

Here, $F_{resisting}$ is the anti-slide force at the slice base, while $F_{sliding}$ is the sliding force at the slice base. Taking the suction in the slope soils into consideration, Wang and Zhang [49] reconstructed the anti-slide force and the sliding force equations of the slice as

$$F_{resisting} = W_i \cos\alpha_i \tan\varphi + \frac{\left(u_s \tan\varphi^b + c\right)B}{\cos\alpha_i} \tag{8}$$

$$F_{sliding} = W_i \sin\alpha_i \tag{9}$$

Accordingly, W_i and α_i are the weight and bottom inclination angle of sliding slice i, respectively; c and φ are the cohesion and internal friction angle at the bottom of sliding slice i, respectively; u_s and φ^b are the matrix suction and suction friction angle at the bottom of sliding slice i, respectively; φ^b usually has a value around $\varphi/2$, according to Fredlund and Rahardjo [50]; and B denotes the sliding slice width. If the vertical soil pressure σ_y at the bottom of the sliding slice can be obtained from the model test, W_i can be calculated by

$$W_i = \sigma_y \cdot B \tag{10}$$

Substituting Equation (10) into Equations (8) and (9), the results of which were then substituted into Equation (7), a new equation of the safety factor was constructed as

$$K = \frac{\sum\left[\sigma_y B \cos\alpha_i \tan\varphi + \frac{\left(u_s \tan\varphi^b + c\right)B}{\cos\alpha_i}\right]}{\sum\left[\sigma_y B \sin\alpha_i\right]} \tag{11}$$

Using Equation (11) to calculate the slope safety factors, the sliding body should first be divided into vertical slices. Then, assuming that the positions with the same burial depth had identical soil pressures and matrix suction, the soil pressures and suction at the bottoms of the slices can be obtained from the model test data. In most cases, the interpolation method could be an useful tool in the determination of the pressures and suction of the slice bottoms from adjacent points.

4. Results and Discussion

4.1. Slope Scour Failure Process

The camera seated in front of the model box was used to capture the scouring process of the model slope at certain time intervals. In accordance with the field investigation, the simulation period was five years, corresponding to five rounds of rainfall. Nevertheless, this section does not present the rainfall scouring process on the model slope due to its negligibility.

Figure 8 presents the scouring process of the slope model during rainfall. Evidently, the scouring effect in the first round was very significant. Within 25 min from the beginning of the first rainfall, the scour was reasonably categorized as splash erosion, as the raindrops impacted the slope surface and made shallow pits. Later on, from 25 min to 60 min, the scour form transformed into surface erosion. While the first rainfall progressed for 25 min, the formed shallow pits gradually connected, inducing shallow gullies. At 45 min from the start of the rainfall, a shallow sliding of a small size occurred on the left portion of the top grade of the model slope. Meanwhile, gullies on the model slope were completely formed. Lastly, in the period from 60 to 120 min, the scour pattern was found to constitute gully erosion and sliding. At 60 min from the start of the first rainfall, the left portion of the first slope grade developed a deep gully with a depth of 7~8 cm and a width of

5 cm, while the second slope grade showed a gully with a depth of 4~5 cm and a width of 3~4 cm. Meanwhile, larger slides happened on the middle portion of the third grade of the model slope, and ruined displacement mark S6. Understandably, the rainwater pooled on the left portion of the platform of second grade, softened the soil beneath it and promoted gully development there, which was inevitable for a loess slope under rainfall. Additionally, it was observed that the larger scale of slides on the third grade of the slope model was induced by rainwater pooled on the slope crest, which softened the loess there while percolating. In the later phase of the first rainfall, the developed gullies were widened and deepened by the downflow of the rainwater. When the first round of the first rainfall event ended, the main gully in the left part of the first slope grade was approximately 30 cm deep and 10 cm wide, as shown in Figure 9a.

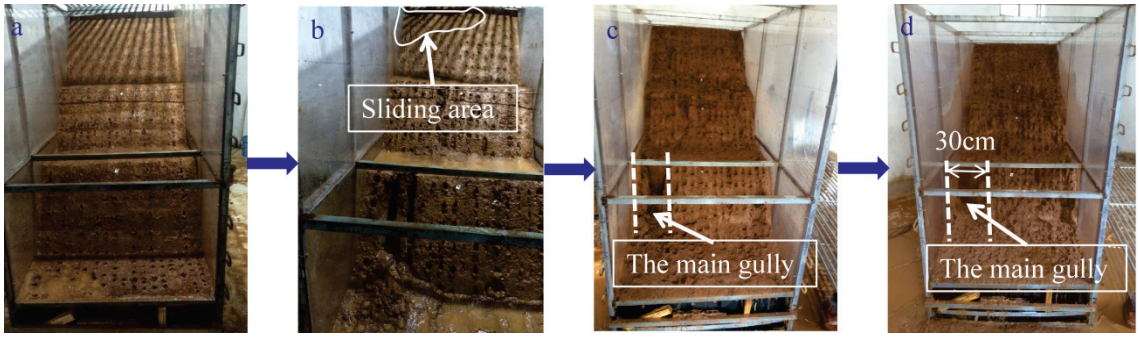

Figure 8. Scour failure process during three rounds of rainfall: (**a**) First round of the first rainfall event lasted for 5 min, (**b**) First round of the first rainfall event lasted for 70 min, (**c**) First round of the second rainfall event lasted for 120 min, (**d**) Third round of the third rainfall event lasted for 120 min.

As Figure 8 shows, different to the first rainfall event, the scour process of the second rainfall event consisted of only two phases, namely the undisturbed phase and the gully erosion with sliding phase. The period from the start of the rainfall to 20 min of rainfall comprised the undisturbed phase, which resulted in no perceivable surface erosion to the model slope, as the rainwater downflow was weak. Understandably, the loess within the shallow layer of the model slope consolidated in the interval between the two rainfall events, making further erosion difficult, which induced an undisturbed phase later in the process. As the rainfall continued, the shallow layer of loess softened again, inciting gully erosion with a sliding phase. The gully erosion with a sliding phase occurred in the period after 20 min of rainfall, where gullies developed and slides happened occasionally. Small scales of shallow slides occurred on the second grade of the model slope at 30 min, 40 min, 56 min and 78 min from the start of the second rainfall event, which fully ruined displacement mark S4. In the meantime, larger scales of slides occurred on the third grade of the model slope at 80 min and 100 min from the start of the second rainfall event, inducing the declination of the gradient of the third grade of the model slope. Evidently, different from first rainfall event, the slope slides in the second rainfall event had initiation stages compromising the duration of approximately the first 20 min of rainfall. As the rainfall progressed, the deeper layers of loess was wetted by the infiltrating rainwater, which caused declines in the matrix suctions, the cohesion and the frictional angles of the deeper loess. It is proven that the matrix suctions, the cohesion and the frictional angles have positive contributions to the soil shearing strength, which is the critical factor in slope safety. Thus, the decline in matrix suctions caused larger slope failures during the second rainfall event. Additionally, the dimensions and number of gullies also increased in this phase. When this rainfall event was over, the main gully at the left of the first grade of the model slope was approximately 13 cm wide, which can be seen in Figure 9a.

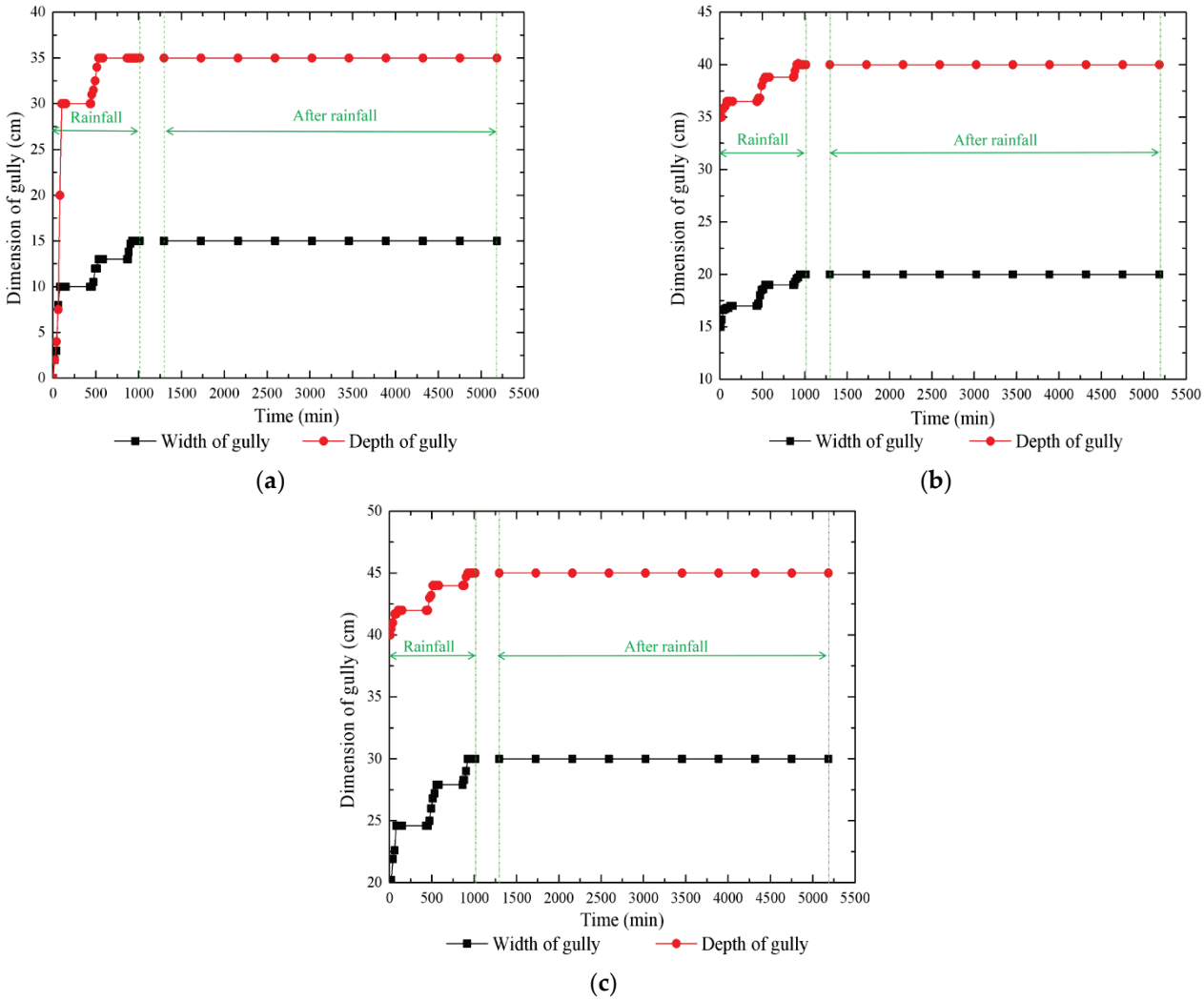

Figure 9. Development of the dimensions of the main gully on the left of the first slope grade: (**a**) During the first round, (**b**) During the second round, (**c**) During the third round.

Compared with the previous rainfall event, the scour effect in the first round of the third rainfall event was weaker, with a small scale of shallow slides occurring on the third grade of the slope at 85 min from the start of this rainfall, and the gullies evolved gradually. It was found that, the width of the main gully in the left portion of the first grade of the slope was approximately 15 cm when this rainfall event was over.

It was found that, during the second and third rounds of rainfall, the model slope was in a relatively steady state, with no slides resulting from the weak rainwater downflow. Nevertheless, the main gully to the first slope grade persistently evolved. At the end of the third round of rainfall, the width was approximately 30 cm, and the depth was approximately 45 cm. On the one hand, the first round of rainfall formed the outlet on the slope model surface, and alleviated the scour effect of the rainfall upon the model slope. On the other hand, the consolidation of the shallow layer of the model slope within the interval between the first and the second round of rainfall impeded further scour from the rainfall. It could be reasonably concluded that the loess model slope entered a relatively steady scour stage at the beginning of the second round of rainfall, while the gully persistently evolved.

It is noteworthy that there was no sinkhole formation caused by the rainwater during the five rounds of rainfall, which should be due to the absence of a perforated crack. As engineering practice revealed, sinkholes in loess slopes are developed from perforated cracks, which form the preferential paths for venting rainwater. While the rainwater flowed through the

perforated cracks, the walls of the cracks were scoured, which gradually formed sinkholes in the loess slope. Referring to the slope prototype, we can infer that a sinkhole could not form in the absence of a perforated crack in this model slope.

Figure 9 presents the dimension development of the main gully on the first grade of the slope within the first, second and third rounds of rainfall. As the dimension of this main gully showed no visible change after the third round, its development thereafter is not presented here. Obviously, the development of the dimensions of this main gully was most significant during the first round, particularly in the first round of the first rainfall event. The depth of this gully increased from 0 cm to 30 cm during the first round of the first rainfall and developed to 35 cm by the end of the first round of rainfall. The width of this gully increased from 0 cm to 10 cm during the first round of the first rainfall and developed to 15 cm by the end of the first round. In the following two rounds of rainfall, the dimensions of this main gully developed more slowly, particularly in regard to its depth. The depth of this gully only increased by 5 cm in both the second and third rounds. Comparably, the width of this gully increased by 5 cm and 10 cm in the second and third rounds, respectively. In summary, the development of the dimensions of the main gully on the first slope grade was the most significant, particularly in the first round of the first rainfall event, and gradually slowed over time. In the rounds after the third round, the gully dimensions showed no visible development and thus are not presented here. This could be mainly attributed to the consolidation effect of the slope soils in the intervals between rainfall events.

4.2. Rainwater Infiltration Characteristics

Rainwater percolates slope soils, inducing a higher pore water pressures in the slope, thus greatly influencing the slope stability. On the one hand, the percolated rainwater can lower the shear strength of the slope soils, which is not beneficial for treatment projects. On the other hand, the percolated rainwater can lead to large water pressures in the slope soils, which is also adverse for the safety of the slope. Scholars have investigated the effects of rainfall on slope safety and concluded that rainfall is the critical factor influencing the stability of slopes and that rainwater percolation controls the deformation processes of slopes [51,52]. In the current study, the model box sidewalls were made from transparent glass. Therefore, the camera could capture the wetting front advancing process from the sides.

Figure 10 shows the advancing process of the wetting front in the rainfall rounds. Evidently, the rainwater percolated into the platforms preferentially, which may have been caused by rainwater pooled on the platforms. The water pooled on the platforms generated water heads there, which actuated the water into the platforms with large rates. After 10 min of the first rainfall, the percolation depths beneath the three platforms were identical at 8 cm. After 20 min of the first rainfall, the percolation depths under the first, second and third grade of the platform were 9 cm, 11 cm and 10 cm, respectively. After 40 min of the first rainfall, the percolation depths beneath the first, second and third grade of the platform were 11.3 cm, 11.5 cm and 12 cm, respectively. Therefore, it can be derived that the percolation rate of the rainwater declined with the progression of rainfall. The average percolation rate was approximately 0.8 cm/min within the first 10 min of rainfall, decreased to approximately 0.2 cm/min after 20 min of the first rainfall, and then decreased to approximately 0.075 cm/min after 40 min of the first rainfall. The pores of the unsaturated soils are partly filled with air and water. Under rainfall conditions, the rainwater must discharge the pore air to percolate into the slope soils. In the shallow layers of slope soils, the pore air was easier to be discharged, and thus showed a higher permeability; therefore, it showed a larger percolation rate at the beginning of the rainfall event, which decreased gradually with the progress of the rainfall event. Eventually, by the end of the first rainfall event, after 120 min, the average vertical percolation rate declined to approximately 0.090 cm/min. In summary, the advancement rate of the wetting front declined gradually within the first round of the first rainfall event, and eventually stabilized at 0.090 cm/min.

Figure 10. Rainwater infiltration process within the slope model: (**a**) After 30 min of the first round of the first rainfall event, (**b**) After 120 min of the first round of the first rainfall event, (**c**) 5.2 h after the first round of the second rainfall event, (**d**) After 120 min of the second round of the third rainfall event, (**e**) After 120 min of the third round of the first rainfall event.

Additionally, the wetting front advancement rates after rainfall could be derived in the same way. Thirty minutes after the first rainfall event, the average advancement rate of the wetting fronts under the platforms was approximately 0.07 cm/min. Three hundred and twelve minutes after the first rainfall event, the percolation depths under the first, second and third grades of the platform were 25 cm, 36 cm and 38 cm, respectively, resulting in an average wetting front advancement rate of approximately 0.026 cm/min. Therefore, the wetting front advancement rates after rainfall were less than those during rainfall, with a declining trend over time. Furthermore, it can be seen from Figure 10b that the percolation depths beneath the slope shoulders were greater than those under the platforms and slope surfaces. This may have resulted from the combined influences of the percolation from the platforms and the slope surfaces, reasonably viewed as the superposition of the two influences.

Within the first round of the next two rainfall events, the wetting front persistently migrated downward at a rate lower than that during the first rainfall event, which decreased gently with time. When the third rainfall event was over, the mean advancement rate of the wetting front was approximately 0.05 cm/min. Moreover, when the rainfall events ceased, the wetting front was clear, but this became vague 5.2 h later (see Figure 11c). Five hours and twelve minutes after the second rainfall of this round, the wetting front was circular, which corresponded to the Swedish arc method for evaluating slope stability. Ultimately, 70 h after the first round of rainfall, most of the slope soils were soaked, while the lower-right triangular corner remained dry; the horizontal side of the dry area was approximately 1.3 m long.

The entire slope body was wetted 5.2 h after the second rainfall event in the third round; thus, the subsequent rainwater movement in the slope soils was not detectable. However, the shrink rate of the triangular dry area was very minor, and was even imperceptible, during the rainfall progress, at approximately 0.003 cm/min, 5.2 h after the third round of the second rain event, which is nearly 10 times lower than the shrink rate at the end of the first round.

Figure 11 presents the vertical infiltration distances under the three slope shoulders and the horizontal infiltration distance at the slope base over time. It is evident that the vertical infiltration distances under the slope shoulders increased sharply in the first round, particularly during rainfall. However, the increasing rates of the vertical infiltration distances gradually decreased over time. Forty-one hours after the second round of the third rainfall event, rainwater infiltrated the slope base beneath the third grade slope shoulder, while the vertical infiltration rate decreased to approximately 0.0056 cm/min. Thus, the vertical infiltration under the slope shoulders after that time was not presented. Similarly, the horizontal infiltration caused by the migration of the rainwater accumulated near the first grade slope toe with a gradually decreasing rate. The difference being that the horizontal infiltration at the base of the slope had an initiation stage, which occurred during the 500 min after the start of the first round of rainfall. It is most noteworthy that the horizontal infiltration rate was obviously higher than the vertical infiltration rates

under the slope shoulders. From Figure 11a, the average vertical infiltration rate under the slope shoulders was approximately 0.021 cm/min, while the average horizontal infiltration rate at the base of the slope was approximately 0.036 cm/min. This could be due to the structure of the horizontal layer of the slope model formed in the construction process, which provided a larger horizontal permeability compared with the vertical permeability.

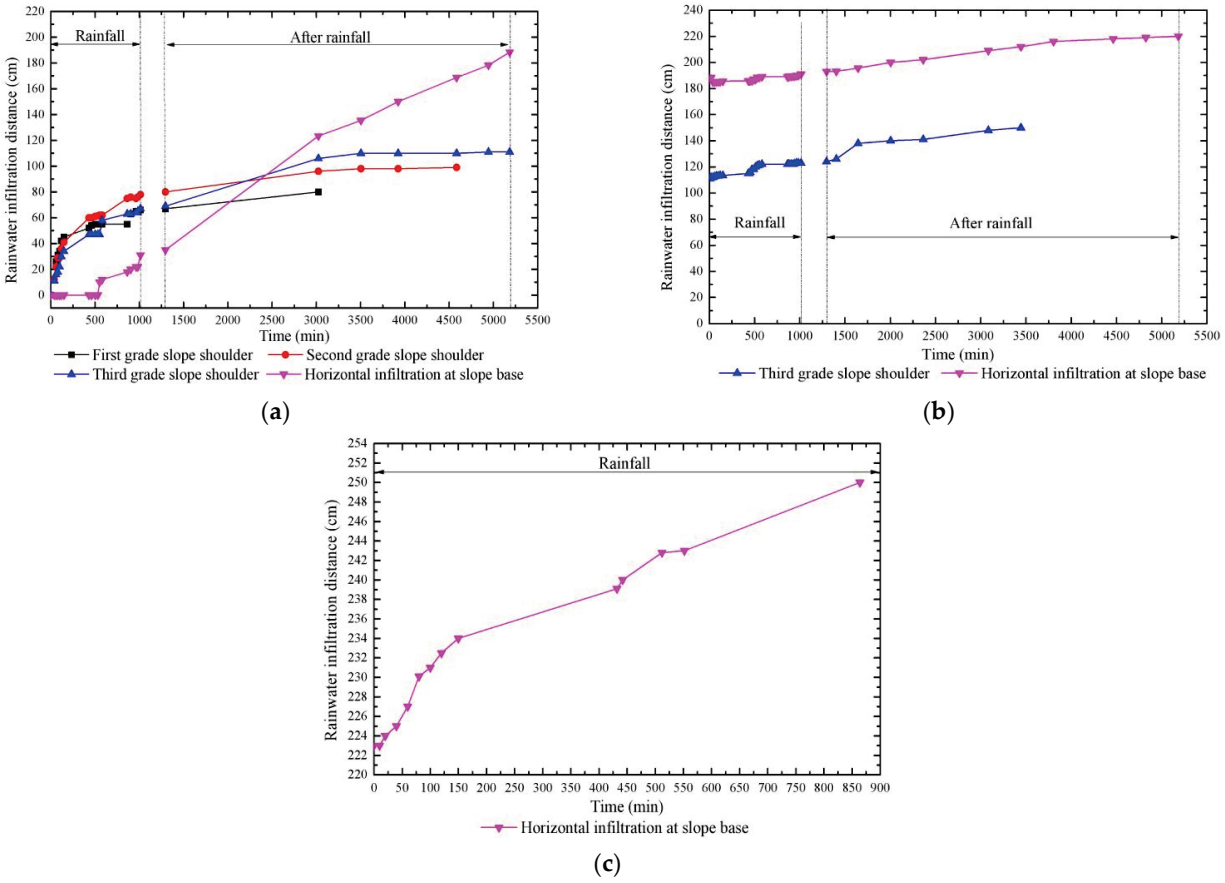

Figure 11. Rainwater infiltration distance with time: (**a**) Within the first round, (**b**) Within the second round, (**c**) Within the third round.

4.3. Pressure Variations of the Model Slope

The slope safety mainly depends on the internal pressures, including the soil pressures and the pore water pressures. Generally, during the rainfall event, only the top layer of the slope soils was evidently penetrated by the rainwater, causing an increase in the unit weight of the top layer. As the rise of the pore water pressure in the deep layer was very limited, the increase in the soil pressure there inevitably outweighed the pore water pressure, which in turn caused an increase in the shear stress. Moreover, the limit increase in the pore water pressures could have caused the significant drop in the shear strength. In a case where the shear stress increased to the limit value, the slope would begin to fail [53]. In the current research, prior to the rainfall test, a pressure coefficient was set for each of the pressure sensors in the computer program. The program automatically converted the signals delivered by the sensors into pressures. Lastly, they were subtracted by the initial pressures to obtain the actual pressure values.

4.3.1. Pore Water Pressure Variations

The pore water pressure variations of the seven points (U1, U2, U3, U4, U5, U6 and U7) over time are presented in Figure 12. As mentioned above, the precipitation was assumed to be concentrated within three months each year, with no precipitation in the other months. The precipitation of each month continually lasted two hours with a invariable intensity.

Generally, within the five rounds of rainfall, the pore water pressures of the seven points fluctuated sharply, with a total trend of declining, except for point U5. This result appeared inconsistent with the classical theoretics of soil mechanics [50]. Only point U5 showed positive pore water pressure values during the rainfall rounds, indicating nearby saturated conditions. It increased from almost 0 kPa to approximately 1.5 kPa in the first round of rainfall and then fluctuated up to approximately 2 kPa by the end of the fifth round, indicating that the infiltrated rainwater concentrated around the toe of the first slope grade. This is consistent with the findings of Chueasamat et al. [52]. Regarding the other key points, it is most evident that the pore water pressure of U1 declined persistently from −10.35 kPa to approximately −12 kPa, and the pore water pressure of U4 decreased persistently from −6.05 kPa to approximately −12 kPa, with a higher declining rate during the early rounds. For U1, at the deepest position, it was hard for the rainwater to recharge, while the underlying soils absorbed the water around it, and thus caused the declination of the saturation degree near U1. Adopting Fredlund's unsaturated soil theoretics [50], the negative pore water pressures in the soils bring on suction, with less saturation corresponding to higher suction. As a result, the pore water pressure on U1 declined within the rainfall rounds. Given that U4 was at the shoulder of the second slope grade, it was washed out by the rainwater in the first round of the first rainfall event. That is why the pore water pressure decreased abnormally, producing meaningless data. While U2 and U3 were situated at intermediate depths in the slope model, the water compensation effect from the soil above and the absorption effect from the soil below remained in balance, which led to no perceptive variation in the pore water pressures nearby.

However, carefully checking the pore water pressure data of U4, U5, U6 and U7 within the first round of rainfall, we found that there was an increasing trend in the pore water pressures for these four points during the first rainfall event, which implicates the saturation effects of the rainfall on the shallow layer of loess slopes. As the shallow layer of the loess was saturated, the matrix suction thereby vanished and the cohesion and internal friction angle attenuated, which caused the degradation of the shear strength of the loess overall. With a decline in the shear strength, the shear stress thereby exceeded it, thus causing the shallow slides stated above.

In addition, it was found from Figure 10e that almost the whole model slope was wetted in the test, with all pore water pressures in the model slope except U5 showing negative values from Figure 12, indicating unsaturated conditions. Therefore, we could infer that the wetting front cannot be considered as the boundary between the saturated and unsaturated regions during rain. According to the Green-Ampt infiltration model [54], the infiltrating rainwater persistently migrates forward after rainfall, resulting in an unsaturated region in front of the wetting front. Clearly, this finding of the Green-Ampt model is in agreement with the current study.

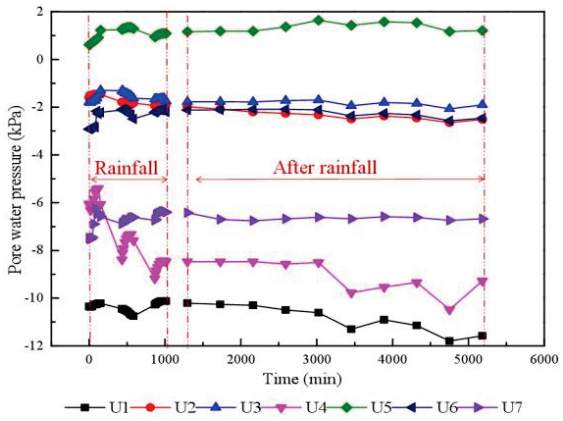

(**a**)

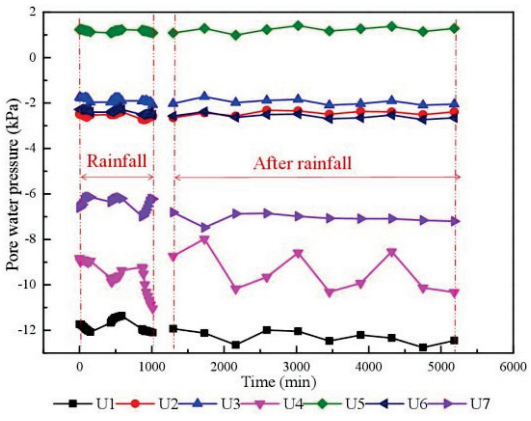

(**b**)

Figure 12. *Cont.*

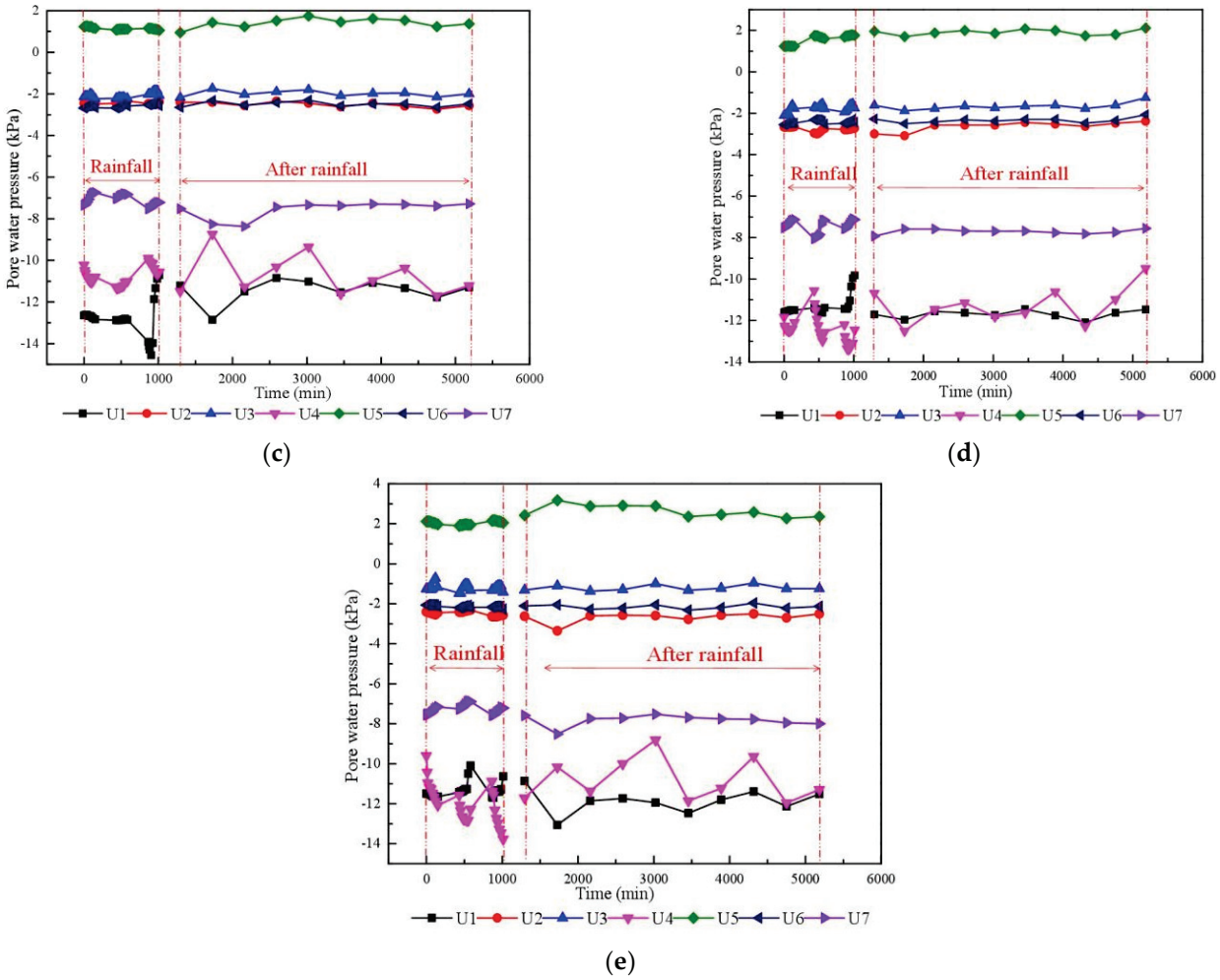

Figure 12. Pore water pressure variations within the test: (**a**) First round, (**b**) Second round, (**c**) Third round, (**d**) Fourth round, (**e**) Fifth round.

4.3.2. Soil Pressure Variations

The soil pressure variations of the seven representative points (P1, P2, P3, P4, P5, P6 and P7) over time are shown in Figure 13. During the first round of rainfall, it was in opposition to the developed soil mechanics as the soil pressures of all the representative points except P1 decreased sharply, which was caused by the in situ stress release as the rainwater infiltrated. This was most evident for P6, incorporating a decline from 14.3 kPa to 1.0 kPa in the first round of the rainfall event. After the first round of rainfall, all seven representative points presented no regular variation in the soil pressure with some small fluctuations, representing a relatively steady state of the slope model. Nevertheless, the soil pressure of P1 started to decline in the second round of rainfall, which was later than that of the other points. These results were caused by P1 being in the deepest location, which needed a longer duration for the rainwater influence to occur. Thus, the second deepest point, P2, represented a persistent decrease in soil pressure in the second round, implying that the release of the in situ stress was still in progress in the deeper positions at this duration. In the subsequent rounds, the soil pressure of P2 persistently declined at a smaller rate, as the soil pressure of P1 fluctuated. When the fifth round of rainfall was over, the soil pressures of P1 and P2 were approximately 3.5 kPa and 2.0 kPa, respectively. On the contrary, the soil pressures of the other points were steady over the entire second round, indicating the steady state of the shallower part of the slope model. In summary, induced by the release of in situ stress, the soil pressures in the slope model declined but did not increase, indicating that the influence of the in situ stress release was greater than that

of the self-weight increase through rainwater percolation, which is seemingly different from the classical soil mechanics [55]. Classical soil mechanics deems that the saturation of soils increases during rainfall, thus inducing a self-weight increase in the soil. As it does not consider the in situ stress increase inside the soils, theoretically, the soil pressures inevitably increase during the rainfall process. However, in the current study, the slope model construction process exactly simulated the loess-forming process, thus leading to high in situ stress in the slope soils, which was higher than the gravity stress. When the rainwater penetrated, the soils of the slope model were softened and dilated, causing the in situ stress to be released abruptly. As the greatest portion of the in situ stress is released, the measured soil stress must decrease rather than increase.

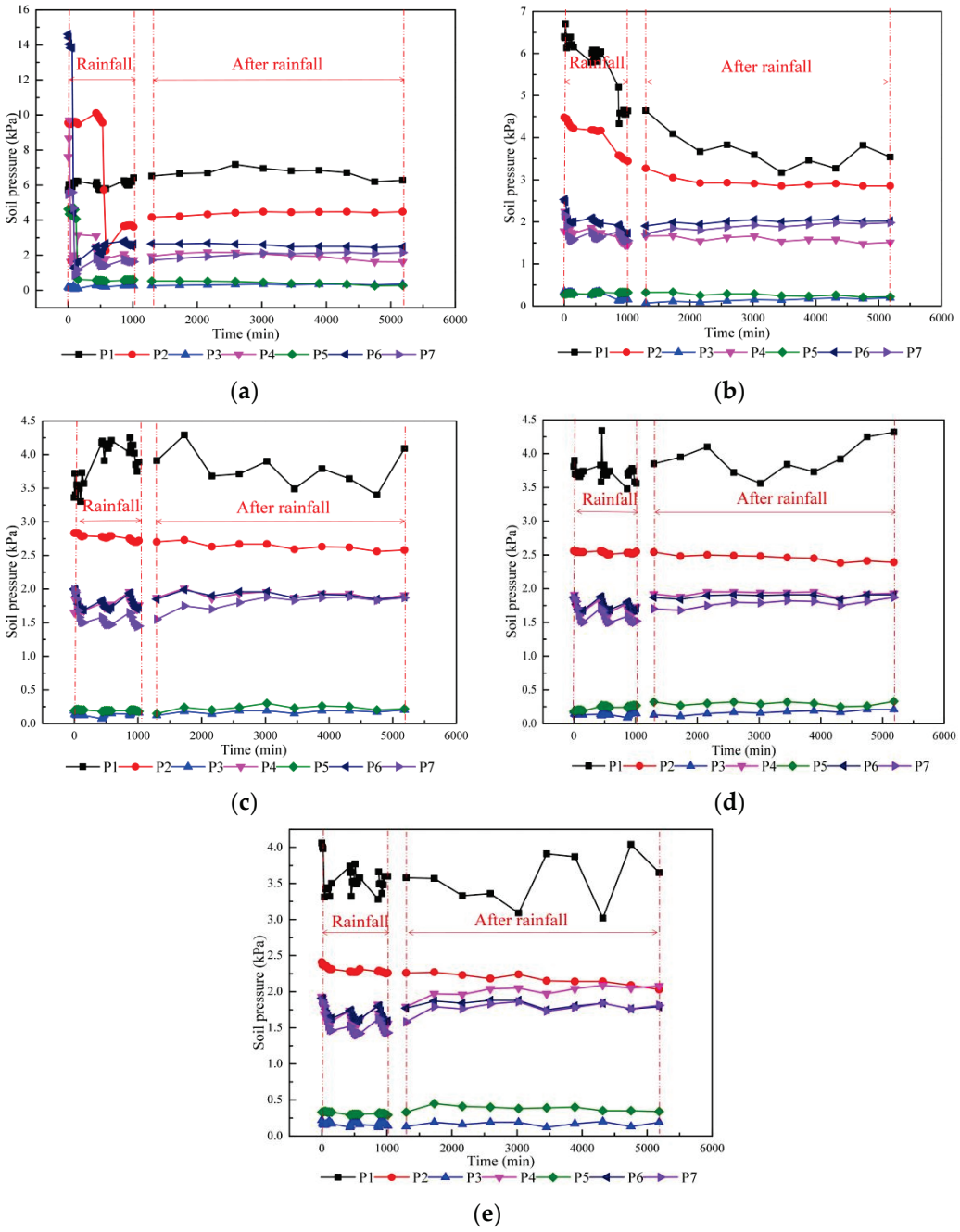

Figure 13. Variations in soil pressure inside the model slope: (**a**) First round, (**b**) Second round, (**c**) Third round, (**d**) Fourth round, (**e**) Fifth round.

4.4. Displacements of the Key Points

A laser rangefinder was used to measure the distances between the six key points (S1, S2, S3, S4, S5 and S6) and a fixed point, the changes in which before and during the rainfall events were the horizontal displacements of the corresponding positions. Figure 14 presents the variations of the horizontal displacements of the six points over time. In the first round, all six points except S1 had displacements rising from 0 mm, especially within the rainfall events. As the rainfall process advanced, the slope soils were humidified, and the internal frictional angle and the cohesion were lessened, causing the yielding of parts of the model slope, which in turn induced the displacements of the model slope. When the first round of rainfall was over, the horizontal displacements of S2, S3 and S5 rose up to 15.1 mm, 9.2 mm and 12.9 mm, respectively, while that of S1 fluctuated at approximately 0 mm. Understandably, the fluctuations in the displacements were brought about by the errors of the instruments. Additionally, the displacement of S6 rose to approximately 35 mm within the first round of the first rainfall event, and the displacement of S4 rose to approximately 20 mm within the same round of the second rainfall event. According to the rainwater scour data presented earlier, the displacement markers S4 and S6 were destroyed in the first round of the second and first rainfall events, respectively, hence bringing about oddly high increments of displacements. As a result, the figures of displacements do not include those of S4 and S6 after the second round of rainfall.

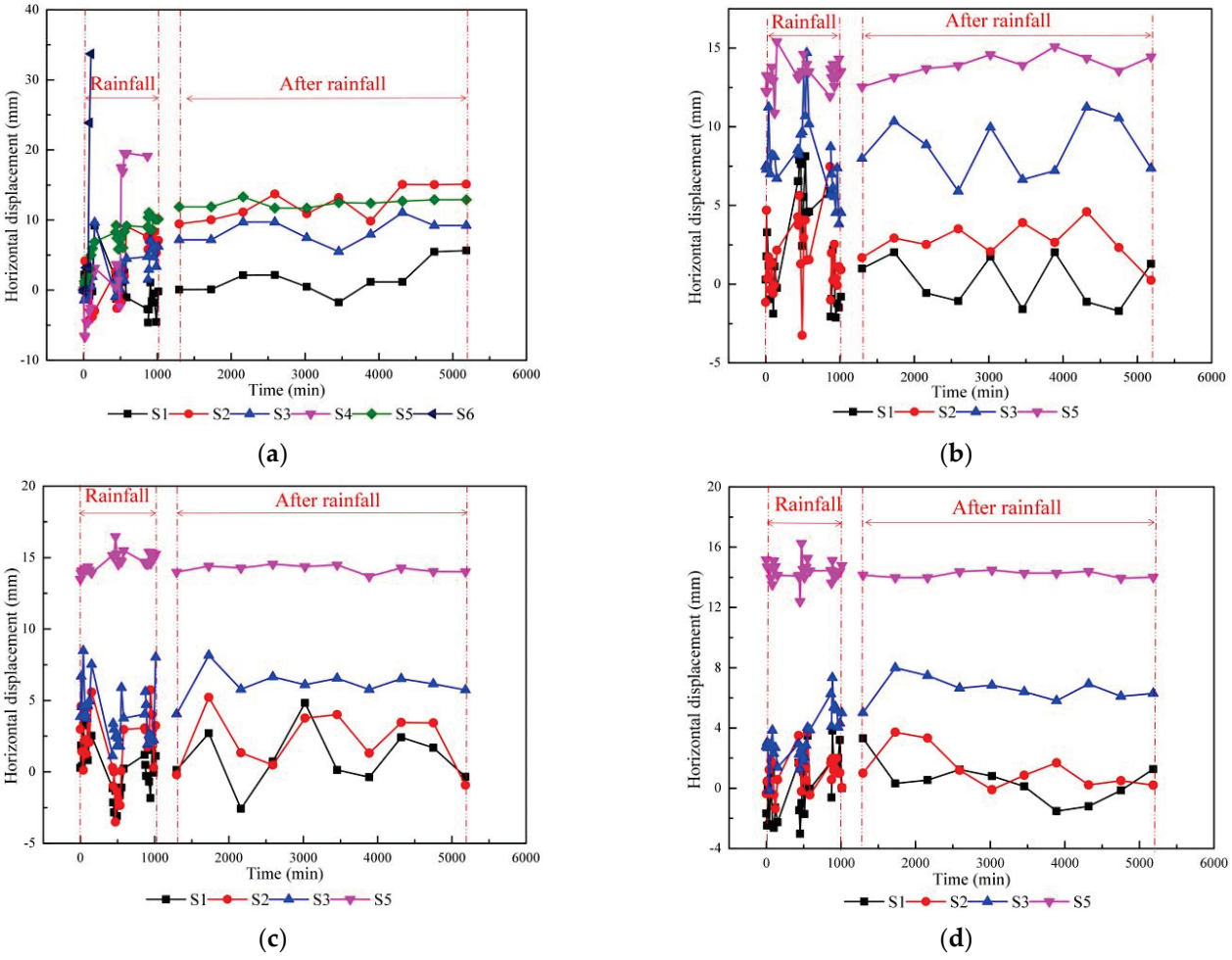

Figure 14. *Cont.*

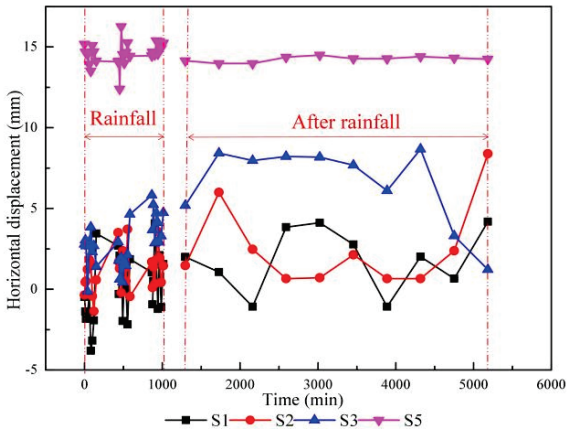

(**e**)

Figure 14. Variations in the horizontal displacements of the six key points over time: (**a**) First round, (**b**) Second round, (**c**) Third round, (**d**) Fourth round, (**e**) Fifth round.

Within the second round, the displacement for S5 fluctuated up to approximately 14 mm and was still fluctuating around this value in the subsequent rounds. The displacements for S2 and S3 fluctuated at approximately 2.5 mm and 9.2 mm, respectively, as the displacement for S1 kept fluctuating at approximately 0 mm. Reasonably, it could be concluded that point S1 remained stationary during all five rainfall rounds. Considering the points in a vertical line with S1, the longer the upward distance from S1, the larger the displacement. This result indicated that a potential slip surface was situated between S1 and S2. This finding is consistent with the research presented by Cui et al. [56], expressing the landslide progress in five stages: steady deformation, slow deformation, intense deformation, steady deformation and intense deformation. However, it was also found that the displacements of the four remaining points (S1, S2, S3 and S5) fluctuated with no increase after the second round, implying the status of the slope was ultimately stable.

5. Post Evaluation of the Treatment Project

Post evaluation was used in a slope treatment project in China by Zheng [4], who proposed the definition of the post evaluation of slope treatment. During slope design, engineers were concerned about the stability of the slope after the completion of construction. However, in post evaluation, engineers usually focused on the slope stability in the long-term. Zheng proposed a displacement rate threshold of 0.1 mm/day that could be used to judge slope stability. Additionally, a compound safety factor referring to the safety factor of slopes was employed to assess the treatment effect of slopes, presented in Table 4. Considering the deformation and failure extent, some quantitative standards [4] were also adopted into the post evaluation of the slope treatment effect, as shown in Table 4. In accordance with the employed standards, this section continues the post evaluation of the slope prototype using the field investigation and model test data.

Table 4. Post evaluation criteria of the treatment effect.

Compound Safety Factor (K)	Deformation and Failure Degree (D) %	Displacement Rate (R) mm/d	Treatment Effect
$K > 1.20$	$0.1 < D \leq 0.5$	$0.01 < R \leq 0.05$	Very good
$1.10 < K \leq 1.20$	$0.5 < D \leq 1.0$	$0.05 < R \leq 0.1$	Good
$1.0 < K \leq 1.10$	$1.0 < D \leq 10$	$0.1 < R \leq 0.5$	Not bad
$K \leq 1.0$	$R \leq 0.1$ or $D > 10$	$R \leq 0.01$ or $R > 0.5$	Conservative or failed

5.1. Post Evaluation Based on the Deformation and Failure Degree

As can be seen in Figure 14, when the fifth round was over, the maximum horizontal displacement of the slope model was approximately 14 mm, delivering the maximum horizontal displacement of the slope prototype of 140 mm. Additionally, the main gully in the first grade of the slope model was approximately 30 cm wide when the fifth round was over, and the entire range of the third grade of the slope model had slid. Accordingly, the ratio of the maximum displacement to the height of the slope was approximately 0.08, and the ratio of the collapsed area to the slope surface area was approximately 0.3. As a result, the collapse ratio could be 30.0%, with an overall collapse having a big influences on the project operation. Additionally, this matched the discoveries from the field investigation (see Figure 2). Hence, the treatment effect of the slope was preliminarily assessed as failed, referring to Zheng's qualitative criteria.

5.2. Post Evaluation Based on the Displacement Rate

Referring to Figure 14, the maximum displacement was approximately 14 mm of S5 when the fifth round was over, rendering the maximum displacement of the prototype as 140 mm at the end of the five years. Therefore, the average deformation rate of the slope project during the 5 years was approximately 0.08 mm/day, implying the security of the treatment project. Thus, the treatment project of the current slope was preliminarily evaluated as good, referring to the qualitative criteria of Zheng.

5.3. Post Evaluation Based on the Compound Safety Factor

The Morgenstern–Price method is a widely accepted way of calculating the safety factors of earth slopes, with a function to generate the slide surface considering every interslice force and satisfying every equilibria of the forces [57,58]. This section utilized the Morgenstern–Price method within the Geo Studio software to delineate the potential slide surface, with well-matched discoveries, as shown in Figure 14. The soil pressures from the model test were utilized to calculate the sliding force and resistance to sliding, thus delivering the factor of safety for the slope prototype. Incorporating Table 4, the treatment effect of the current slope was assessed.

Figure 15 illustrates the potential sliding surface by the end of the fifth year from the Morgenstern–Price method. Evidently, the generated sliding surface was situated between S1 and S2, which strictly matched the model test results.

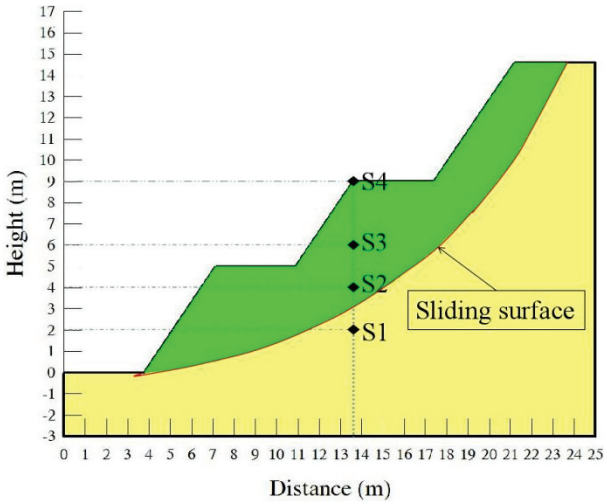

Figure 15. Critical sliding surface from the Morgenstern–Price method (S1, S2, S3 and S4 are displacement markers identical to those in Figure 7).

Firstly, the sliding body was divided into six vertical slices, as shown in Figure 16. The measured data of the key points were utilized to derive the soil pressures and suction of

the adjacent slices. In this way, the soil pressure and suction values on the bottoms of the slices were obtained, as shown in Table 5.

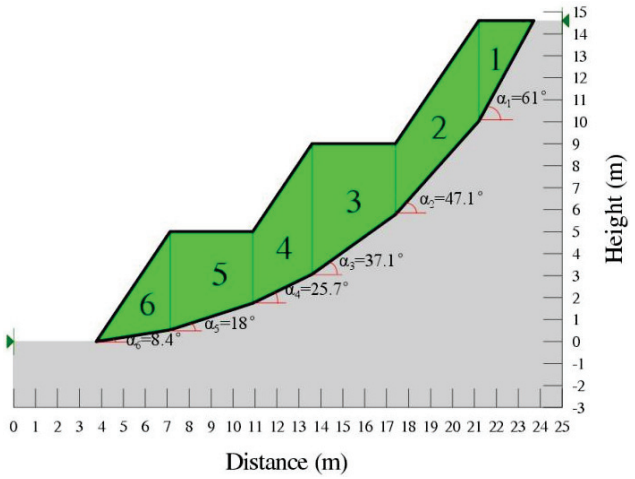

Figure 16. Slice division profile of the sliding mass.

Table 5. Sliding slice information.

Slice Number	1	2	3	4	5	6
σ_y (kPa)	19.45	9.46	6.63	5.68	12.30	19.90
u_s (kPa)	96.45	52.66	37.60	32.58	67.72	85.42
B (m)	2.6	3.8	3.7	2.8	3.7	3.5
α_i (°)	61	47.1	37.1	25.7	18	8.4
$F_{resisting}$ (kN)	219.01	166.92	121.12	78.29	143.77	160.67
$F_{sliding}$ (kN)	43.9959	26.24204	14.7186	6.83872	14.1081	10.4475

Referring to Equation (7), the safety factor of the slope was:

$$\begin{aligned} K &= \frac{\sum F_{resisting}}{\sum F_{sliding}} \\ &= \frac{889.79\ (kN)}{116.35\ (kN)} \\ &= 7.65 \end{aligned} \tag{12}$$

Clearly, the safety factor from the developed method combined with the model test data was substantially larger than the critical value of 1.2, implying the conservative design theory of the slope treatment research. This result was likely caused by the underestimation of the shear strength of loess in the slope treatment design theory of China, which did not incorporate the matrix suction under unsaturated conditions. Nevertheless, the obtained safety factor here delivers a result identical to those of the displacements from the model test. Combined with Table 4, it can be seen that the preliminary treatment effect of the slope prototype was very good.

5.4. Post Evaluation of Results

Combining the above post evaluation results, it can be considered that the slope prototype was generally stable, with no further sliding tendency, but considerably large amounts of destruction resulting from rainwater scouring. Accordingly, the destruction of the slope was categorized as a local collapse. Therefore, the treatment effect of the current slope was determined to be not bad.

Last, it is worth noting that the post evaluation framework formed here is useful to other slope treatment projects referring to slope cutting. Therefore, the post evaluation framework is presented in Figure 17.

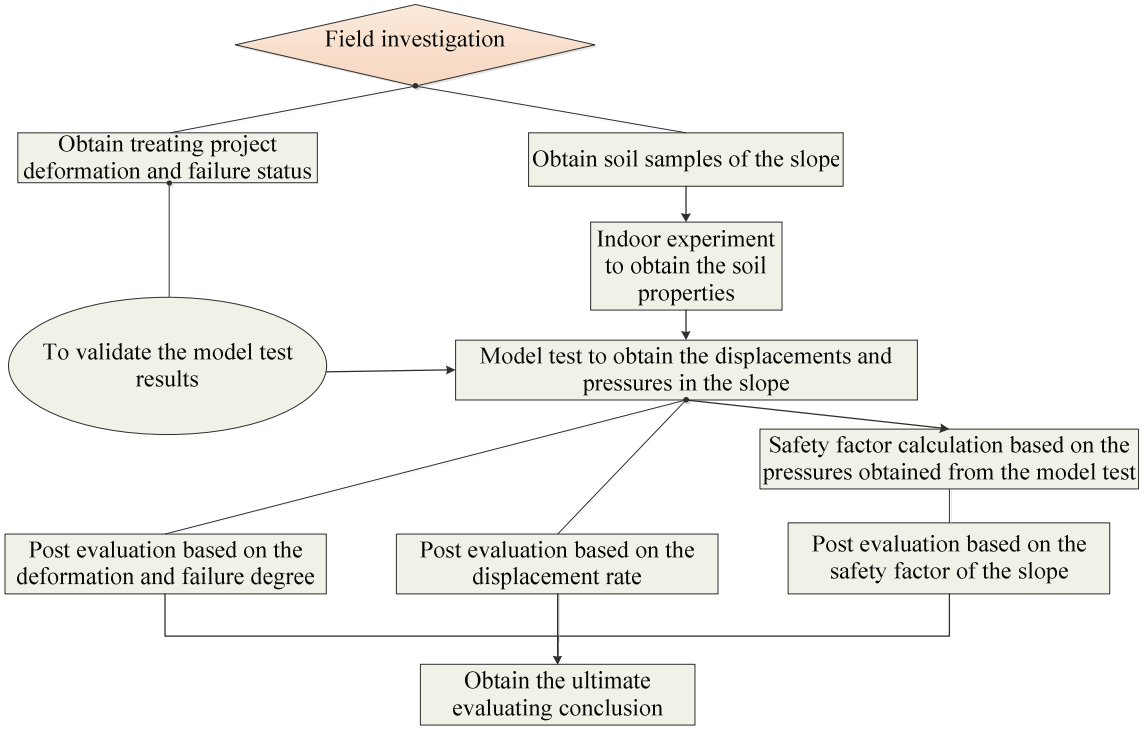

Figure 17. Post evaluation framework for slopes treated by slope cutting.

6. Conclusions

To clarify the influencing mechanism of long-term rainfall on loess slopes treated by slope cutting in Yan'an city of Shaanxi Province, a field investigation and an indoor model test were performed, based on the post evaluation of the loess slope with slope cutting. The main conclusions are as follows:

(1) The runoff of rainwater has serious scouring effects on slope surfaces, causing gullies and shallow slides. Mainly caused by the consolidation of the shallow soils within intervals of rainfall, the scouring effect becomes increasingly weaker over time, inducing a relatively steady state of the slope after the first round of rainfall.

(2) Rainwater percolates the platforms preferentially with large rates being observed where rainwater pools. Over the simulation duration, the wetting front advancement rate declined gradually.

(3) Caused by the release of in situ stress, the test soil pressures within the model slope declined drastically during the first rainfall round, especially for the deep positions inside the slope model.

(4) The horizontal displacements of the critical positions within the slope model increased evidently during the first round, with declining rates. After the second rainfall round, the horizontal displacements showed no regular rise, indicating the ultimately stable status of the slope.

(5) The model test results were utilized to perform the post evaluation of the slope-cutting treatment to the loess slope, forming a framework for the post evaluations of loess slopes under long-term rainfall. This evaluation framework can be of benefit to other slope treatment projects.

Author Contributions: All authors significantly contributed to the research. G.L. designed this research and drafted the paper. Y.C. performed the tests and collected the data. Z.Z. supervised the research. S.X. revised the manuscript. All authors have read and agreed to the published version of the manuscript.

Funding: This work was funded by the Science and Technology Bureau of Shangluo City under grant number 2020-Z-0111; and the Science and Technology Department of Shaanxi Province under grant number 2021JQ-844.

Institutional Review Board Statement: Ethical review and approval were waived for this study due to the exclusion of human and animal as studying subjects in this paper. The identifiable person in Figures 5 and 10 is the first author of this paper G.L.

Informed Consent Statement: Patient consent was waived due to the exclusion of human and animal as studying subjects in this paper. The identifiable person in Figures 5 and 10 is the first author of this paper G.L.

Data Availability Statement: Data is contained within the article.

Conflicts of Interest: The authors declare no conflict of interest.

References

1. Hu, S.; Qiu, H.; Wang, N.; Cui, Y.; Wang, J.; Wang, X.; Ma, S.; Yang, D.; Cao, M. The influence of loess cave development upon landslides and geomorphologic evolution: A case study from the northwest Loess-Plateau, China. *Geomorphology* **2020**, *359*, 107167. [CrossRef]
2. Lukić, T.; Bjelajac, D.; Fitzsimmons, K.E.; Marković, S.B.; Basarin, B.; Mlađan, D.; Micić, T. Factors triggering landslide occurrence on the Zemun loess plateau, Belgrade area, Serbia. *Environ. Earth Sci.* **2018**, *77*, 519. [CrossRef]
3. Bariss, M. Effects of lithology, time and exposure on the stabilization of loess matled slopes. A comparative study. *GeoJournal* **1987**, *15*, 167–172. [CrossRef]
4. Zheng, M.X. Study on the Post Evaluation of the Effectiveness of Landslide Control. PhD Thesis, Hohai University, Nanjing, China, 2005. (In Chinese)
5. Umrao, R.K.; Singh, R.; Sharma, L.K.; Singh, T.N. Soil slope instability along a strategic road corridor in Meghalaya, north-eastern India. *Arab. J. Geosci.* **2017**, *10*, 260. [CrossRef]
6. Das, R.; Phukon, P.; Singh, T.N. Understanding the cause and effect relationship of debris slides in Papum Pare district, Arunachal Himalaya, India. *Nat. Hazards* **2022**, *110*, 1735–1760. [CrossRef]
7. Fang, R. Study on Evaluation System for Project Efficiency of Highway Slope Treatment Project. PhD Thesis, China Academy of Railway Sciences, Beijing, China, 2009. (In Chinese).
8. Wu, L.Z.; Huang, R.Q.; Li, H.L.; Li, X.; Sun, P. The model tests of rainfall infiltration in two-layer unsaturated soil slopes. *Eur. J. Environ. Civ. En.* **2019**, *25*, 1555–1569. [CrossRef]
9. Lee, K.; Suk, J.; Kim, H.; Jeong, S. Modeling of rainfall-induced landslides using a full-scale flume test. *Landslides* **2021**, *18*, 1153–1162. [CrossRef]
10. Sharma, L.K.; Sirdesai, N.N.; Sharma, K.M.; Singh, T.N. Experimental study to examine the independent roles of lime and cement on the stabilization of a mountain soil: A comparative study. *Appl. Clay Sci.* **2018**, *152*, 183–195. [CrossRef]
11. Sun, Y.; Gu, X.; Xu, X. Experimental study on hydraulic erosion characteristics of ecological slope of tailings reservoir under rainfall. *KSCE J. Civ. Eng.* **2021**, *25*, 2426–2436. [CrossRef]
12. Qiu, X.; Li, J.; Jiang, H.; Ou, J.; Ma, J. Evolution of the transient saturated zone and stability analysis of slopes under rainfall conditions. *KSCE J. Civ. Eng.* **2022**, *26*, 1618–1631. [CrossRef]
13. Sharma, L.K.; Singh, T.N. Regression-based models for the prediction of unconfined compressive strength of artificially structured soil. *Eng. Comput.* **2018**, *34*, 175–186. [CrossRef]
14. Yuan, M.; Zhang, Y.; Zhao, Y.; Deng, J. Effect of rainfall gradient and vegetation restoration on gully initiation under a large-scale extreme rainfall event on the hilly Loess Plateau: A case study from the Wuding River basin, China. *Sci. Total Environ.* **2020**, *739*, 140066. [CrossRef]
15. Bordoni, M.; Meisina, C.; Valentino, R.; Lu, N.; Bittelli, M.; Chersich, S. Hydrological factors affecting rainfall-induced shallow landslides: From the field monitoring to a simplified slope stability analysis. *Eng. Geol.* **2015**, *193*, 19–37. [CrossRef]
16. Raj, M.; Sengupta, A. Rain-triggered slope failure of the railway embankment at Malda, India. *Acta Geotech.* **2014**, *9*, 789–798. [CrossRef]
17. Zhang, S.; Zhang, X.; Pei, X.; Wang, S.; Huang, R.; Xu, Q.; Wang, Z. Model test study on the hydrological mechanisms and early warning thresholds for loess fill slope failure induced by rainfall. *Eng. Geol.* **2019**, *258*, 105135. [CrossRef]
18. Huang, A.B.; Lee, J.T.; Ho, Y.T.; Chiu, Y.F.; Cheng, S.Y. Stability monitoring of rainfall-induced deep landslides through pore pressure profile measurements. *Soils Found.* **2012**, *52*, 737–747. [CrossRef]
19. Zhao, B.; Zhang, L.; Xia, Z.; Xu, W.; Xia, L.; Liang, Y.; Xia, D. Effects of rainfall intensity and vegetation cover on erosion characteristics of a soil containing rock fragments slope. *Adv. Civ. Eng.* **2019**, *2019*, 7043428. [CrossRef]
20. Pan, C.; Shangguan, Z. Runoff hydraulic characteristics and sediment generation in sloped grassplots under simulated rainfall conditions. *J. Hydrol.* **2006**, *331*, 178–185. [CrossRef]
21. Fang, H.; Sun, L.; Tang, Z. Effects of rainfall and slope on runoff, soil erosion and rill development: An experimental study using two loess soil. *Hydrol. Process.* **2015**, *29*, 2649–2658. [CrossRef]

22. Chen, H.; Zhang, X.; Abla, M.; Lu, D.; Yan, R.; Ren, Q.; Ren, Z.; Yang, Y.; Zhao, W.; Lin, P.; et al. Effects of vegetation and rainfall types on surface runoff and soil erosion on steep slopes on the Loess Plateau, China. *Catena* **2018**, *170*, 141–149. [CrossRef]
23. Arnaez, J.; Lasanta, T.; Ruiz-Flaño, P.; Ortigosa, L. Factors affecting runoff and erosion under simulated rainfall in the Mediterranean vineyards. *Soil Till. Res.* **2007**, *93*, 324–334. [CrossRef]
24. Sun, D.M.; Li, X.M.; Feng, P.; Zang, Y.G. Stability analysis of unsaturated soil slope during rainfall infiltration using coupled liquid-gas-solid three-phase model. *Water Sci. Eng.* **2016**, *9*, 183–194. [CrossRef]
25. Yang, K.H.; Huynh, V.D.A.; Nguyen, T.S.; Portelinha, F.H.M. Numerical evaluation of reinforced slopes with various backfill-reinforcement-drainage systems subject to rainfall infiltration. *Comput. Geotech.* **2018**, *96*, 25–39. [CrossRef]
26. Cai, F.; Ugai, K. Numerical analysis of rainfall effects on slope stability. *Int. J. Geomech.* **2004**, *4*, 69–78. [CrossRef]
27. Oh, S.; Lu, N. Slope stability analysis under unsaturated conditions: Case studies of rainfall-induced failure of cut slopes. *Eng. Geol.* **2015**, *184*, 96–103. [CrossRef]
28. Lu, N.; Şener-Kaya, B.; Wayllace, A.; Godt, J.W. Analysis of rainfall-induced slope instability using a field of local factor of safety. *Water Resour. Res.* **2012**, *48*, W09524. [CrossRef]
29. Borja, R.I.; White, J.A. Continuum deformation and stability analyses of a steep hillside slope under rainfall infiltration. *Acta Geotech.* **2010**, *5*, 1–14. [CrossRef]
30. Liu, J.X.; Liu, Y.T.; Hu, Q.J. Stability of embankment slope subject to rainfall infiltration considering both runoff-underground seepage and fluid-solid coupling. *Rock Soil Mech.* **2010**, *31*, 903–910.
31. Cho, S.E. Infiltration analysis to assess the surficial stability of two-layered slopes considering rainfall characteristics. *Eng. Geol.* **2009**, *105*, 32–43. [CrossRef]
32. Wang, G.; Ye, W.; Lv, Y. Loess geoheritage and geohazard protective measures at luochuan loess national geopark in NW China. *Geoheritage* **2019**, *11*, 1089–1100. [CrossRef]
33. Rahardjo, H.; Kim, Y.; Gofar, N.; Satyanaga, A. Analysis and design of steep slopes with GeoBarrier System (GBS) under heavy rainfall. Geotext. *Geomembranes* **2020**, *48*, 157–169. [CrossRef]
34. Fredlund, D.G. Slope stability analysis incorporating the effect of soil suction. In *Slope Stability*; Wiley: New York, NY, USA, 1987; pp. 113–144.
35. Shen, J.H.; Hu, M.J.; Wang, X.; Zhang, C.Y.; Xu, D.S. SWCC of calcareous silty sand under different fines contents and dry densities. *Front. Env. Sci.* **2021**, *9*, 1–13. [CrossRef]
36. Lu, X.B.; Ye, T.L.; Zhang, X.H.; Cui, P.; Hu, K.H. Experimental and numerical analysis on the responses of slope under rainfall. *Nat. Hazards* **2012**, *64*, 887–902. [CrossRef]
37. Schenato, L.; Palmieri, L.; Camporese, M.; Bersan, S.; Cola, S.; Pasuto, A.; Galtarossa, A.; Salandin, P.; Simonini, P. Distributed optical fibre sensing for early detection of shallow landslides triggering. *Sci. Rep.* **2017**, *7*, 14686. [CrossRef]
38. Lan, H.; Zhao, X.; Macciotta, R.; Peng, J.; Li, L.; Wu, Y.; Zhu, Y.; Liu, X.; Zhang, N.; Liu, S.; et al. The cyclic expansion and contraction characteristics of a loess slope and implications for slope stability. *Sci. Rep.* **2021**, *11*, 2250. [CrossRef]
39. Chen, J.; Lei, X.W.; Zhang, H.L.; Lin, Z.; Wang, H.; Hu, W. Laboratory model test study of the hydrological effect on granite residual soil slopes considering different vegetation types. *Sci. Rep.* **2021**, *11*, 14668. [CrossRef] [PubMed]
40. Hung, W.Y.; Tran, M.C.; Yeh, F.H.; Lu, C.W.; Ge, L. Centrifuge modeling of failure behaviors of sandy slope caused by gravity, rainfall, and base shaking. *Eng. Geol.* **2020**, *271*, 105609. [CrossRef]
41. Sun, P.; Wang, G.; Wu, L.Z.; Igwe, O.; Zhu, E. Physical model experiments for shallow failure in rainfall-triggered loess slope, Northwest China. *B. Eng. Geol. Environ.* **2019**, *78*, 4363–4382. [CrossRef]
42. Liu, G.; Zhou, Z.; Xu, S.; Mi, W. Experimental assessments of treating effect on retaining walls for loess slopes under long-term rainfall. *Adv. Civ. Eng.* **2021**, *2021*, 5542727. [CrossRef]
43. Brand, L. The Pi theorem of dimensional analysis. *Arch. Ration. Mech. An.* **1957**, *1*, 35–45. [CrossRef]
44. Curtis, W.D.; Logan, J.D.; Parker, W.A. Dimensional analysis and the pi theorem. *Linear Algebra Appl.* **1982**, *47*, 117–126. [CrossRef]
45. Terzaghi, K.; Peck, R.B.; Mesri, G. *Soil Mechanics in Engineering Practice*; John Wiley & Sons, Inc.: Hoboken, NJ, USA, 1996; pp. 23–33.
46. Butterfield, R. Scale-modelling of fluid flow in geotechnical centrifuges. *Soils Found.* **2000**, *40*, 39–45. [CrossRef]
47. Garnier, J.; Gaudin, C.; Springman, S.M.; Culligan, P.J.; Goodings, D.; Konig, D.; Kutterr, B.; Phillips, R.; Randolph, M.F.; Thorel, L. Catalogue of scaling laws and similitude questions in geotechnical centrifuge modelling. *Int. J. Phys. Model. Geo.* **2007**, *7*, 1–23. [CrossRef]
48. Tang, J. In High Fill Slope Stability Analysis under the Condition of Heavy Rainfall by Panzhihua Airport as an Example. PhD Thesis, Chengdu University of Technology, Chengdu, China, 2014. (In Chinese).
49. Wang, K.; Zhang, S. Rainfall-induced landslides assessment in the Fengjie County, Three-Gorge reservoir area, China. *Nat. Hazards* **2021**, *108*, 451–478. [CrossRef]
50. Fredlund, D.G.; Rahardjo, H. *Soil Mechanics for Unsaturated Soils*; Wiley: Hoboken, NJ, USA, 1993; pp. 87–91.
51. Song, X.; Tan, Y. Experimental study on failure of temporary earthen slope triggered by intense rainfall. *Eng. Fail. Anal.* **2020**, *116*, 104718. [CrossRef]
52. Chueasamat, A.; Hori, T.; Saito, H.; Sato, T.; Kohgo, Y. Experimental tests of slope failure due to rainfalls using 1g physical slope models. *Soils Found.* **2018**, *58*, 290–305. [CrossRef]

53. KC, D.; Dangi, H.; Hu, L. Assessing landslide susceptibility in the northern stretch of Arun Tectonic Window, Nepal. *Civil Eng.* **2022**, *3*, 525–540. [CrossRef]
54. Herber Green, W.; Ampt, G.A. Studies of soil physics I. The flow of air and water through soils. *Int. J. Nonlin. Sci. Num.* **2015**, *4*, 1–24.
55. Whitlow, R. *Basic Soil Mechanics*, 3rd ed.; Longman Group Limited: London, UK, 1995; pp. 114–120.
56. Cui, Y.; Bao, P.; Xu, C.; Fu, G.; Jiao, Q.; Luo, Y.; Shen, L.; Xu, X.; Liu, F.; Lyu, Y.; et al. A big landslide on the Jinsha River, Tibet, China: Geometric characteristics, causes, and future stability. *Nat. Hazards* **2020**, *104*, 2051–2070. [CrossRef]
57. Zhu, D.Y.; Lee, C.F.; Qian, Q.H.; Chen, G.R. A concise algorithm for computing the factor of safety using the Morgenstern Price method. *Can. Geotech. J.* **2005**, *42*, 272–278. [CrossRef]
58. Bai, T.; Qiu, T.; Huang, X.; Li, C. Locating global critical slip surface using the Morgenstern-Price method and optimization technique. *Int. J. Geomech.* **2014**, *14*, 319–325. [CrossRef]

sustainability

MDPI

Review

Understanding the Mechanisms of Earth Fissuring for Hazard Mitigation in Najran, Saudi Arabia

Mabkhoot Alsaiari [1], Basil Onyekayahweh Nwafor [2], Maman Hermana [2,*], Al Marzouki Hassan H. M. [3] and Mohammed Irfan [4]

[1] Empty Quarter Unit, Chemistry Department at Sharurah, Najran University, Najran P.O. Box 1988, Saudi Arabia
[2] Department of Geoscience, Universiti Teknologi PETRONAS, Seri Iskandar 32610, Malaysia; basil_20001931@utp.edu.my
[3] Saudi Geological Survey, Jeddah 21514, Saudi Arabia
[4] Electrical Engineering Department, College of Engineering, Najran University, Najran P.O. Box 1988, Saudi Arabia
* Correspondence: maman.hermana@utp.edu.my

Abstract: Being a fast-growing city with a high rate of urbanization and agricultural development, the city of Najran, situated in the southwest of the Kingdom of Saudi Arabia, has witnessed a series of earth fissuring events and some other geo-environmental hazards in recent times. These fissures have posed a significant threat to inhabitants and infrastructure in the area. A few studies suggest that excessive groundwater withdrawal is responsible for fissuring activities. Because of the intensity of this geo-hazard, this article presupposes that groundwater extraction alone cannot be responsible for the magnitude of fissuring activity in the area and discusses other severe factors that could be responsible for the earth fissures. The study proposes that the cause of the problem is multifaceted and synergistic, and outlines threatening factors that can inherently trigger more fissures in the region, based on the geologic history of the area and a critical review of investigative studies conducted in the area and beyond. Predicated on the region's structural history, some undiscovered elements that can potentially cause fissuring in the region were identified and discussed. Some of these include the pre-existence of a fault system, a crack from the bedrock ridge, the existence of paleochannels, the collapsibility of loess, the tectonic (earthquake) history of the area, and differential compaction due to heterogeneity. The use of a metaheuristic and a combined application integrating other optimization algorithms can be utilized to determine optimum hyperparameters and present their statistical importance, thereby improving accuracy and dependability in fissure prediction in Najran. Reliable models would primarily be used to monitor active fissures and identify key factors utilizing spatial information, subsidence, groundwater-related data sets, etc.

Keywords: earth fissures; groundwater; subsidence; geo-hazard; environmental; Najran

Citation: Alsaiari, M.; Nwafor, B.O.; Hermana, M.; Hassan H. M., A.M.; Irfan, M. Understanding the Mechanisms of Earth Fissuring for Hazard Mitigation in Najran, Saudi Arabia. *Sustainability* **2023**, *15*, 6006. https://doi.org/10.3390/su15076006

Academic Editors: Stefano Morelli, Veronica Pazzi and Mirko Francioni

Received: 18 December 2022
Revised: 30 January 2023
Accepted: 15 March 2023
Published: 30 March 2023

1. Introduction

Recently, earth fissures, which are deformations or cracks at the Earth's surface that occur in regions with little or no rain, mainly caused by the immoderate withdrawal or pumping of groundwater [1,2], have become one of the disturbing environmental problems across different cities in the world. It causes damage to homes and businesses, highways, bridges, waterways, drains, powerlines, farmland, pipeline infrastructure, animals, ecosystems, biodiversity, and individual lives, as well as providing a pathway for toxins to enter groundwater. According to [2–8], several researchers have confirmed that groundwater is vulnerable to impurity through earth fissures, and cleaning these contaminants can be an arduous and time-consuming task. As a result, this geological risk has had a huge impact on business activities, social security, and environmental conservation, garnering more attention in recent decades [9]. The occurrence of and damage caused by earth fissures have been recorded in different places around the world, including the southeast corner of the North China Plain, the southwest of the American Basin, the North Indian River Plain,

the west Asian valley, the Somaliland coast in East Africa, the Iceland region, the valley of Najran in Saudi Arabia, and so on [4,10–14].

Focusing on the city of Najran, the increased consumption of groundwater for crop watering in the city of Najran has induced earth rifts of varying degrees in the zones susceptible to tensile stress [2]. This unexpected occurrence of earth fissures has created fear among the farmers and private owners of the area as it might render the land useless for agricultural and other purposes. Because of its inherent geomorphologic and geologic disposition, the territory is vulnerable to a variety of geo-hazards. As a rapidly expanding city, with a high rate of urbanization and agricultural development, the earth's fissuring and some other geo-environmental hazards have posed a significant threat to inhabitants and infrastructure in Najran [15]. Due to the obvious rapid rise of the populace and the increased use of the existing infrastructure, the Saudi government is now building facilities such as motorways and urban and agricultural fields in areas near hazard zones [15]. Increased ground fissures in Najran can obstruct the building of both surface and subsurface infrastructure, according to prior events. When buildings are built in an area where there are ground fissures, issues such as structural failure or cracking, groundwater leaks, damage to already-existing buildings, and long-term structural instability may arise, because of the activity of the ground fissure [16]. Sub-layer subsidence, post-construction ground settlement following the dissipation of porewater pressure brought on by structural loads, disturbance introduced by nearby building projects, shifts in the hydrological system and aquifer infiltration, and cyclic loading of trains are a few factors that could contribute to the destabilization of structures in fissure-prone regions. These elements might lead to the expansion of ground fissures, and in the most extreme scenarios, brand-new dangers such as rail track deformation might appear [16]. Therefore, in Najran and other fissure-prone cities, remedies must be used to guarantee the long-term stability of the ground as well as the overlying structures.

Groundwater depletion or over-pumping has been identified by scientists as the main cause of earth fissuring [1,2,17–22] because it creates significant tensions in the aquifer. To maintain an equilibrium in the aquifer volume, it adjusts itself, thereby causing compression, and pressure that could result in enormous ground subsidence, and consequent fissures. According to [17], it is believed that due to various lateral motions inside the aquifer caused by groundwater harvesting from the unlithified aquifer, ground fractures begin at deep levels underneath the surface [18]. Some researchers think that these fissures are caused by the differential deformation of confined layers in the horizontal axis, and others maintain that it is a result of the forceful gradient effects of groundwater harvesting [19–21]. However, further studies have proven that the impact of groundwater on fissure formation can be horizontal, vertical, and oblique [18,22]. Other factors such as soil friability, non-consolidation, and the presence of pre-existing fractures can also cause earth fissures. Several investigative studies have been conducted across the world to ascertain the causes of fissure formation. Although these studies adopted different evaluation techniques at unique geologic locations, the conclusions drawn from them are somewhat similar. Some of these studies are listed in Table 1 below, which highlights the study locations, techniques adopted, and the causes of the fissure formations in the study area.

Table 1. Showing fissure investigation locations, evaluation techniques, and their causes.

S/N	Location	Technique	Causes	References
1	Najran, Saudi Arabia	Remote sensing, hydrological, investigation studies, and electrical resistivity techniques	The major drivers in the development of earth fissures are excessive groundwater withdrawal owing to irrigation activity and the area's underlying topography.	[2,15]

Table 1. *Cont.*

S/N	Location	Technique	Causes	References
2	Qinglong Graben in Yuncheng Basin, China	A variety of geological investigations including site inspection, drilling, and trench excavation were employed to define the characteristics and examine how earth fissures are formed.	The formation of earth fissures in Qinglong Graben is divided into three steps, namely (1) regional extension creating normal faults under the surface, (2) inadequate groundwater extraction causing normal faults to rupture the surface, and (3) erosion widening the cracks	[23]
3	Haram-to-Haram Highway, Iran	Extensive field mapping, on-site experiments, sampling, and evaluation of soil in the laboratory.	Fissure development and expansion in the studied area were aided by a combination of shallow and deep mechanisms as well as other environmental agents, with soil features playing a key role.	[24]
4	Central and northern Arabia	Integration of field, interferometric synthetic-aperture radar (InSAR), groundwater geology, geodetic studies, and geospatial analysis were conducted to decipher the cause of fissuring.	The fissures were mostly constrained by a graben fault system which played a role in the development of the fissures. Fissuring activity was triggered by aquifer depletion.	[25]
5	Weihe Basin, China	Field mapping, trench excavation, geophysics, and geotechnical testing methods were applied	The ground fissures mirrored the deeply buried faults on the surface. Loess collapsibility and seepage were involved in the mechanism of the fissures. Differential settlement occurred in the collapsible and non-collapsible portions of the loess, with ground fissures serving as the borderline.	[26]
6	Su-Xi-Chang, southeast corner of northern China	The geologic history and piezometric features of the area were studied. Based on this, a physics model was used to evaluate the mechanism of ground fissure creation.	The creation of fissures in the location is caused by repeated groundwater impoundment and pumping, as well as peculiar geological conditions.	[18]
7	Yingxian area, Datong Basin, China	Trench excavation analysis, spudding, seismic exploration techniques, and the geologic history of the area were employed.	The findings and interpretations show that (1) the fissures are connected to two large active faults that provide the background for the fissure formation; (2) intensified groundwater harvesting has revived the underlying faults and exacerbated fissure growth; and (3) assuagement is best achieved by ceasing excess groundwater exploitation, suitable engineering design, and avoiding major structure location.	[27]

Table 1. *Cont.*

S/N	Location	Technique	Causes	References
8	Northeastern Beijing Plain, China	To determine the origins of fissure formation, an integrated ground survey with trenches and geophysical prospecting profiles was conducted.	The pre-existence of buried channels and faults offered a favorable condition for the origination of fissures, and groundwater pumping further accelerated the expansion and the fissures.	[28]
9	Shuanghuaishu, Shaanxi Province, China	An on-site water immersion test was performed to study the cause of fissures	The creation of collapsible earth fissures resulted from tensile tension and strain caused by the unequal collapse of loess. The loess encountered tensile failure and developed an earth fissure when the force was greater than the eventual deformation	[29]
10	Wuxi, China	Stress displacement assessment using an interface infinite model that was developed from an impermeable and non-compressible rock cliff.	The shape of the underlying ridge is the most important determinant.	[30]
11	Taiyuan Basin, northwestern China	Integrated the analytic hierarchy process (AHP), the area under the curve (AUC), and the certainty factor model (CFM).	Active faults are the principal cause of earth fissure creation. Fissures are liable to emerge in alluvial–diluvial clinoplain as well as the intermediate zone at the geomorphologic borderline.	[31]
12	Al-Yutamah Valley, Western Arabia	Used InSAR products generated by the JPL-Caltech ARIA project to locate regions with short-wavelength abnormalities, and then manually reprocessed InSAR products at a higher resolution to optimize spatial and temporal coverage. MintPy processes were used to build the InSAR time series from post-processed InSAR products.	Aquifer depletion and the existence of pre-existing sedimentary deposits such as lake deposits promote friable soil compaction.	[32]

From the reviews and ongoing discussion among scientists about fissure formation processes, it can be summarized that (a) deep dynamic tectonism controls ground fissure location, (b) the internal tectonic force of the earth's crust leads to a collection of ground fissures, (c) stresses at the fault planes induces the formation of ground fissures, (d) groundwater overmining results in the reactivation and expansion of subsurface faults, leading to fissure formation, and (e) buried paleo geomorphology aids the collapsibility of soils and formation of fissures. The assemblage and appearance of ground fissures are thus majorly influenced by the geological environment. More crucially, the combined impacts of interior geological forces (such as crustal instability, tectonic forces within a craton, and motions

at fault zones) and human-instigated stresses, such as excessive groundwater extraction, heavy engineering structures, etc., cause ground fissure propagation.

A more detailed understanding of the mechanism and causative factors of fissures would assist in designing suitable ways to mitigate the fissure hazards. This paper (1) identifies and discusses five major factors that cause ground fissures by reviewing scientific studies conducted by different researchers, (2) relates these factors to suggested causes of fissures in the city of Najran for a better understanding of its development mechanism, (3) shares insightful conclusions about other potential factors that could contribute to the development of fissures in in the city of Najran, (4) presents honest opinions about fissure occurrences in Najran, and (5) makes recommendations on potential approaches that could be taken to study, monitor, and mitigate fissuring in the city.

2. Geological Background

Najran is the administrative center of the Najran region in the southwest of Saudi Arabia, close to the Yemeni border (Figure 1a,b). Najran is one of the kingdom's extremely fast-developing municipalities, with a populace that has increased nearly tenfold across an area of around 360,000 km^2. In the last four decades, both the government and the private sector have invested significantly in Najran. The area is primarily an agricultural zone in Wadi Najran's floodplain. The elevation rises to 1447 m, with elevations ranging from 883 m east to 2330 m west [2]. Three distinct geomorphic groups exist, namely (a) elevated zones in the western part, (b) lowland regions with sediments deposited across the Wadi, and (c) up the east dominated by sandy dunes. Najran is composed of volcanic Precambrian rocks, as well as Wajeed sandstone deposited during Cambrian–Ordovician age, and the later deposited tertiary bedrock [33,34]. Wadi Najran is covered in alluvial quaternary sediments, especially dunes prevailing eastward near the Empty Quarter fields atop alluvial soils.

In the study area, Wajid sandstone is found in a sequence of hill and rock formations at scattered outcrops. It lays unconformably atop the roughly flat basement rocks of the Shield of Arabia. The topmost exposure of the Wajid sandstone formations does not quite extend into the research region, but it does unconformably underlie the Permian Khuff Formation to the northeast. The Wadi Najran region is made up of Arabian–Nubian basement massif rocks such as granites, metamorphosed andesite, basalt, gneisses, granitoid formed during orogeny, and gabbro and diorite volcanic rocks. The Arabian plate's N–S trending structures were created by extensional tectonic movements of the Arabian–Nubian Shield [35,36]. The NW–SE trending dextral fault system of Najid was created in the very last phase of its rifting tectonic system, after which the Arabian Shield was made almost plain, and the Wajid Group was accumulated during the Paleozoic in the southern region of Saudi Arabia [37]. Numerous tectonic events, mostly in the Phanerozoic, reactivated the Precambrian underlying structures [38–41]. The Wajid Group's regional-scale fissures are most likely the result of the reactivation of those structures [42]. Sedimentary rocks cover the eastern section of the Najran region as well (Figure 1b).

The Wajid Group is a siliciclastic sequence that was deposited during the Cambrian and Permian ages and underlies the southwestern zone of Saudi Arabia [43,44]. Its exposures extend from Wadi Al-Dawasir in the south of Najran, with just a small exceptional case in some areas [44] (Figure 1b). The Wajid Group in Najran is divided into five stratigraphic units, from the earliest to the most recent formation, and they include Dibsiyah, Sanamah, Qalibah, Khusayyayn, and Juwayl [43,45], as shown in Figure 2. Based on the previous lithologic description, the lower Dibsiyah Formation is a reddish cross-stratified sandstone with some conglomerate layers deposited in some kind of fluvial channels. The topmost of Dibsiyah Formation's intercalated massive and bioturbated sandstones were accumulated in transitional shallow marine settings. The Sanamah Formation is composed of coarse-grained conglomeratic sandstones, considered a mix of glacial and fluvial sediments. The Khusayyayn Formation is composed of river- and wind-deposited sandstone with grain sizes ranging from medium to coarse. The Juwayl Formation is massive and/or layered, consisting of grains that range from fine to coarse, deposited in a glaciofluvial

setting [42,46–48]. The Group's sandstones range in texture from fine to coarse, are slightly sorted, and are partly rounded to sub-angular in form. Quartz arenites that are composed of limited percentages of feldspars form the basal units; however, Khusayyayn Formation sandstone is a subarkose sandstone having a highly disproportionate amount of feldspar grains [42], as illustrated in Figure 2.

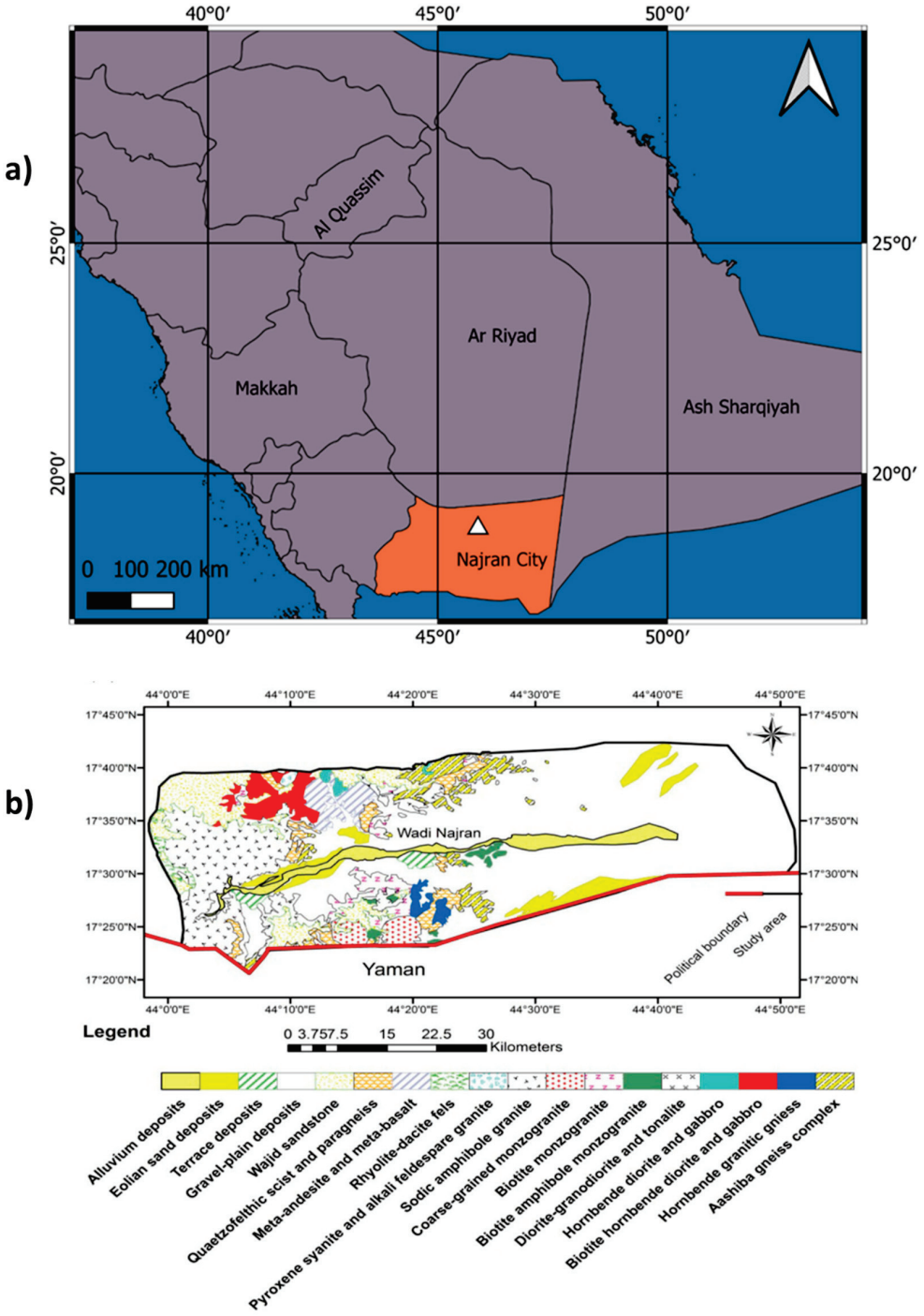

Figure 1. (**a**) Location map of the city of Najran, the Kingdom of Saudi Arabia; (**b**) digitized geologic map of Najran from [15].

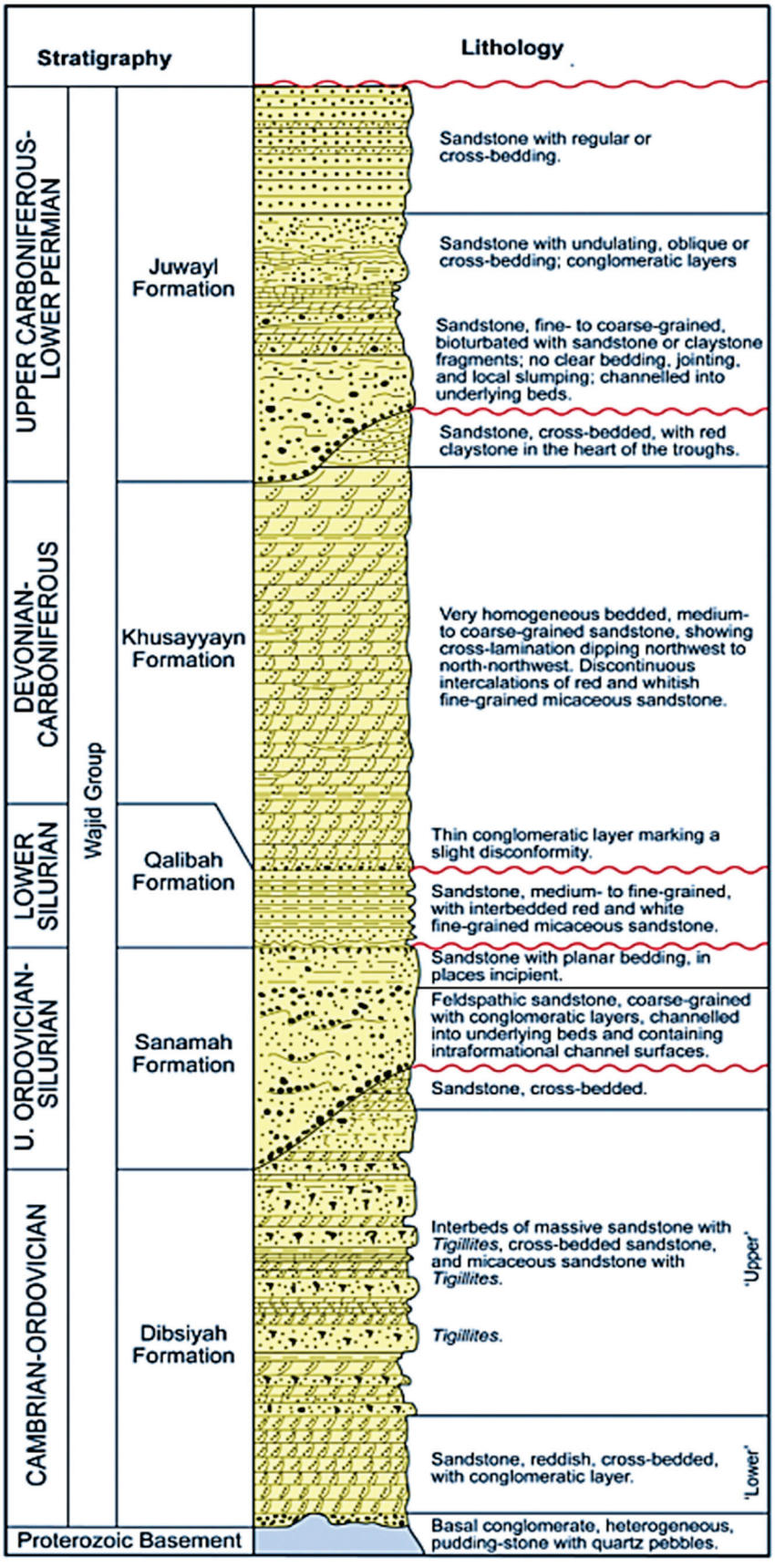

Figure 2. Shows the stratigraphic sequence of the Wajid Group sandstones together with their litho characteristics in the right column (after [49,50]).

3. The Causes and Mechanisms of Fissures Formation

To better comprehend the fissuring process and establish a plan to mitigate earth fissuring and, consequently, reduce hazards, it is essential to identify the elements that influence earth fissuring. However, it is unclear how these factors affect the development and evolution of earth cracks. In the intervening decades, several theories have been put forth to elucidate how groundwater loss causes surface faulting as well as earth fissuring. Some include localized vertical differential compaction, regional variable compaction, and capillary stress related to a lowering water table [51]. It has also been proposed by [52] and [53] that aquifer displacement, particularly lateral movement, is the cause of earth fissures associated with groundwater depletion. The complicated processes of earth fissuring resulting from inordinate groundwater drawdown, as perhaps the major influential anthropogenic factor, are quite well discussed in the literature [54–62]. By pressurizing susceptible aquifer systems, groundwater exploitation significantly contributes to soil slope failure and fissure emergence. The subsidence associated with the extraction of liquids such as water from subterranean strata is likely the most well-studied of all anthropogenic and natural sources of subsidence [63]. In aquifer systems, lateral deformation is caused by removal and occasional recharge/discharge pressures [17,64–67]. Earth fissure is most often provincial and widespread in aquifer systems undergoing compaction, with provincial lateral stresses rarely exceeding 2 ppm and regional misalignments rarely surpassing 240 arcseconds. Linear strains can be substantial locally, especially near pumping boreholes with higher pressure gradients, along with inflections in the bedrock landforms of underground water systems, and near the borders of hydrogeologic units with differing hydraulic and (or) mechanical characteristics [63]. Enough scientific work is necessary to clarify the role of lateral strains in the formation of geological fissures in basins predisposed to aquifer system compression. Research has shown that not only horizontal deformation but shear on vertical planes and rotating stresses also play a part in the development of certain earth cracks [20]. However, scientists have argued that lateral displacement of the earth's surface was only detected in a few spots in areas of subsidence related to groundwater depletion. They maintain that lithologic differences, such as the amount of consolidation or cementation in alluvial deposits [68], and subsurface structures such as faults, both influence the formation and placement of fissures [58], whereas the inordinate exploitation of groundwater only activates them. Based on previous studies, this paper categorizes the mechanisms of fissure formation into three, namely tectonic, non-tectonic, and anthropogenic (Table 2). Figure 3 illustrates how these mechanisms are interrelated and dependent on each other, with groundwater pumping as the central factor that triggers other processes.

Table 2. Categories of earth fissure formation mechanisms and processes.

S/N	Non-Tectonic	Tectonic	Anthropogenic
1	Collapsibility of Loess	Bedrock topography	Groundwater pumping
2	Differential compaction	Pre-existence of faults	Structural loading
3	Existence of paleochannels	Earthquake/subsidence	Underground tunneling

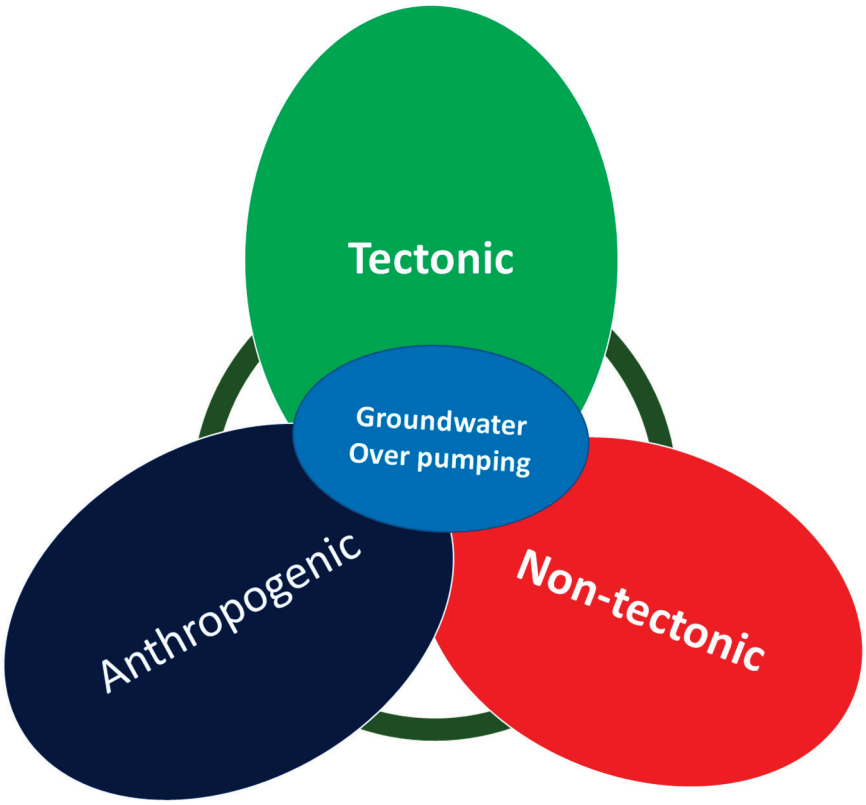

Figure 3. Illustrates the interdependence of earth fissure formation processes.

The following subsections discuss these processes and how they are triggered by disequilibrium caused by groundwater over-pumping and other natural hydrological conditions.

3.1. Tectonic Mechanism

3.1.1. Crack from the Bedrock Ridge

The strata structure of the aquifer system is influenced by the bedrock ridge. The large differential settlement arises because of sediment consolidation under higher effective pressures from groundwater drawdown when groundwater is removed disproportionately for a long time. Bending can cause tensile deformation in sediments above the bedrock ridge, as shown in Figure 4. A fissure occurs when tension surpasses the tensile strain limit of soils. The elastic deformation of sediments under plane strain circumstances can be calculated using Equations (1)–(3), as the fissure develops longitudinally along the bedrock ridge.

$$Ex = dv/dy;\ Ey = du/dx;$$

$$Ex = \frac{dv}{dy} \tag{1}$$

$$Ey = \frac{du}{dx} \tag{2}$$

$$\mathrm{p}_{xy} = \frac{dv}{dx} + \frac{dv}{dx} \tag{3}$$

where u = lateral displacement (m), v = vertical displacement (m), Ex = perpendicular strain in the horizontal direction, Ey = perpendicular strain in the vertical direction, and p_{xy} = shear deformation (strain)

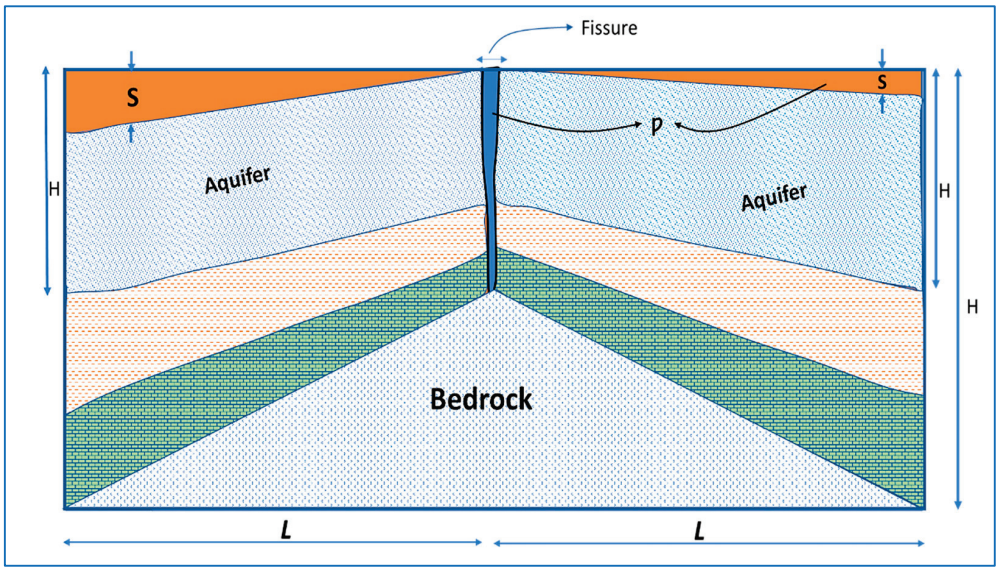

Figure 4. Illustrating the deformation mechanism of bedrock-induced fissures, where S is the vertical displacement due to differential stress, P is horizontal displacement which is a function of S, and H and L are vertical and horizontal thickness, respectively.

For illustration, [30] studied land subsidence and the accompanying ground fissures in the Suzhou, Wuxi, and Changzhou (Su-Xi-Chang) areas of southern Jiangsu Province in China in 2010. Excessive groundwater drawdown, in combination with the underlying bedrock ridge, was identified as the causal element in previous site investigations and geophysical surveys. As per new findings, earth fissures may have ruptured from the underlying bedrock cliffs or ridges to the surface of the ground. Ref. [68] asserted that previously postulated mechanisms to produce fissures from groundwater were predicated on assumptions and abstract justifications which might or might not be coherent with the physics of fissure formation from water table decrease. In the research, the authors aimed to better understand the mechanical mechanism which culminates in the creation of earth fissures in an unconfined aquifer due to fluctuating groundwater level fall, as well as the important elements that regulate the commencement of earth fissures. Ref. [68] found that earth cracks in aquifers emerging from groundwater over-pumping are created by the effect of shearing on vertical planes and spinning, rather than tension, as is usually assumed. It demonstrates how the gradient of the subduction bowl, which is composed of simple shear deformation and spin can be used to anticipate the onset of earth fissures. This finding supported the idea that applied stress could cause earth fissures to fracture from the bedrock cliff face to the outer surface of the earth. Ref. [56] shed more light by outlining two distinct mechanisms that are involved in the formation of fissures influenced by bedrock ridge: first, bending or draping of horizontal bedding planes over the ridge by differential vertical compaction and, second, tensile failure at depth along the top of the ridge caused by horizontal movement of the aquifer in at least one direction away from the ridge. According to the study by [69], the upper layers on either one or both sides of the ridge drape or spin in a reverse orientation as a result of the vertical compression at a range from the ridge. Aquifer fabric may be stretched horizontally over a rigid bedrock ridge as a consequence of uneven vertical compression close to the ridge, creating a tension region in which the aquifer material is thinnest. The latter process is predicated on a groundwater aquifer that is moving horizontally and is partially or completely terminated by the bedrock. This denotes a fresh impetus for the beginning and propagation of an earth fissure. Additionally, this horizontal displacement may result in a deep tensile failure. If there are two pumping centers on each side, this failure might happen in the material next to the ridge in the axis of pumpage, but it may also happen right over the ridge's highest point where the aquifer material is moving away from the ridge on both flanks. As the

horizontal aquifer migration intensifies, so any collapse might ultimately migrate upward and start a fracture in the layers above.

3.1.2. Pre-Existence of Faults

Existing faults in constant shear states may become more active and stretch to the ground surface, causing cracks in the hanging fault block. Besides that, sustained aquifer depletion in such an area can cause the faults' hanging wall to consolidate and settle, increasing the unequal settlement on both blocks of the faults and hastening the mobility and formation of the ground fissure [70]. Fault zones and buried fault scarps can have an impact on the accumulation of stresses over time. The faulted zones have a considerable influence on extensional and compressional patterns, whereas the buried fault scarp has a greater impact on shear stress patterns. Ref. [58] discovered that a fissure caused by tension is near the faulted block at the sliding wall, affirming that fissures begin near the surface and make their way downward, terminating near the boundary between the saturated and unsaturated column. The presence of a fault zone has been established as a determinant in a fissure's propagation course. This was further confirmed by the authors of [28], who used site evaluation, drilling, and trench unearthing to define and assess the basis for fissure formation in Qinglong Gaben, China. Syn-sedimentary faults, as well as an excessive drawdown of groundwater and erosion processes, were shown to be major drivers in the creation and multiplication of fissures in the region, according to the research. Recent research has revealed that earth fissure cluster formation is polygenetic and the result of the earth's internal forces and anthropogenic actions. The origination of fault-induced earth cracks can be subdivided into three developmental phases: first, initial extension resulting from fault planes underground, followed by the excessive pumping of groundwater, and then, washouts aided by the development of the fissure. Deep crustal movements underneath the basin influence earth fissuring, which is driven by the local geodynamic stress of the nearby fault zones [71]. The fault displacement increases as the depth of the fault grows, which is typical of synthetic and other syn-depositional faults. Vertical displacement characterizes these fissures, which can have a yearly growth rate that ranges from 1 to 3 cm. The tectonic structure of a basin's hidden faults is thought to have an influence on the formation of large-scale fissures, which may also be influenced by the basin's regional extensional stress. Over-exploitation of groundwater further increases the level of activities leading to fissure formation [72]. As a result, groundwater exploitation is an important contributor to fault-induced earth fissure development. Intensive groundwater extraction results in the establishment of an inner multi-directional (radial) compression zone near pumping wells and an external radial tensional zone outside them. Lateral tensile stress (σ) minimizes the resisting force on the fissure surface and increases its activation in fissures in the external radial tensional zone. If a well is bored in one of the fault compartments, for example, the rate of the water table decrease in the sliding (or hanging) wall will be faster than it is in the footwall, resulting in more shear stress (τ) in the vertical plane of the fissure. Unequal surface settling ($\Delta H > \Delta F$) causes tensional stress around the ground fissure, which encourages fissure migration and expansion as shown in Figure 5. The sediment thickness in the hanging wall is generally greater than thickness of the accumulated sediment in the footwall due to the build-up of pre-existing faults. Fissuring can form aberrant layer placements and subsequently stretch to pre-existing faults as groundwater pumping intensifies.

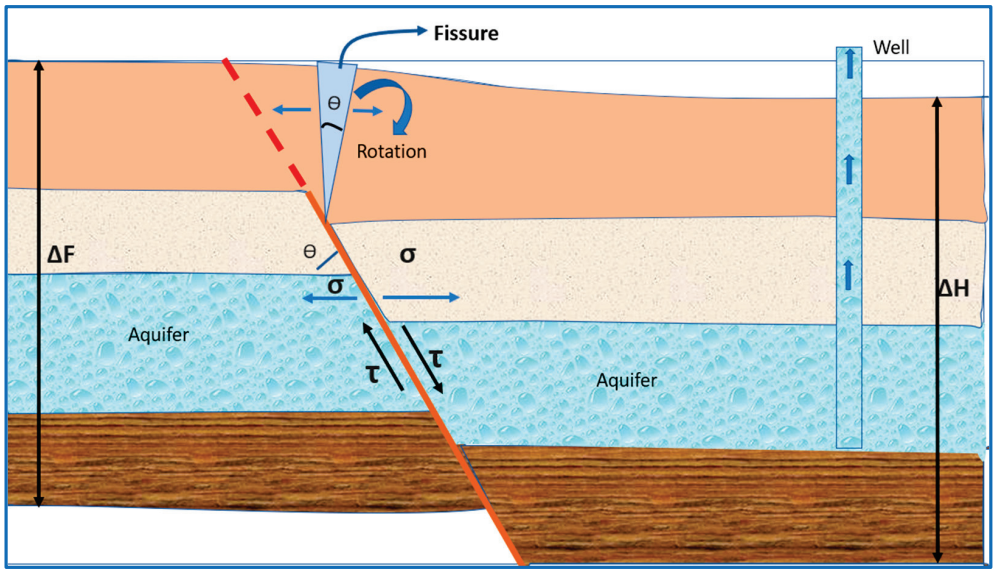

Figure 5. The aquifer-driven dynamics of ground fissuring. τ = shear stress; σ = tensile stress; θ = inclination of earth fissure; ΔH and ΔF = the settling rate of the ground surface.

3.2. Non-Tectonic Mechanisms

3.2.1. Existence of Paleochannels

Paleochannels affect the creation of rock fissures, which are commonly caused by intense rains, squeezing, or earthquakes, and inadequate groundwater pumping [73,74]. It creates an ideal environment for fissure formation [71]. Because of the inhomogeneity, anisotropy, and friability of shallowly buried ancient channel deposits, instabilities and uneven settling are common, resulting in fissure development, piping, and surface erosion, among other things, and human activities hasten this process. Earth fissures linked with paleochannels have short lengths and superficial depths overall, as well as the forming trend of earth fissures on the edges of paleochannels, which reflects the channel's meandering model [73,75]. Due to gravitational force and extra pressures, the top has strata curves and breaks above the empty spaces when unequal vertical strain occurs in the compressible layer. According to a theoretical examination of their characteristics, channel controlled fissures are generated by gravity, initial joint stresses, and groundwater withdrawal operations, and are driven by paleo-fluvial factors [74]. The base of paleochannel-induced fissures usually coincides with curving or meandering surfaces or gradational zones between valley slopes and terraces, implying that they are generated by the self-weight of overlying strata [75].

3.2.2. Collapsibility of Loess

In recent years, experts have become increasingly interested in nontectonic ground cracks. Nontectonic ground fissures were explored, and their causes were investigated in [6,29]. They used field study, trenching, and geotechnical testing to conclude that nontectonic ground cracks are mostly caused by loess collapsibility [6], determined that earth cracks are produced by loess collapsibility and erosion is caused by infiltration, and that loess cracks create a favorable environment for the creation of earth fissures. The studies reached these conclusions by studying groundwater variability, topology, soil physico-mechanical indexes, as well as the lithological backdrop. Ref. [26] looked at the relationship connecting four soft soil properties and earth fissuring: density of dry loess, its porosity, water saturation, and self-gravity collapsibility coefficient. They described how earth fissures are generated by employing the spinning mechanism of a loess cantilever beam, as well as the computation equation of tensile force. Although the following research on fissures caused by factors other than tectonic forces has distinct foci and creation mechanisms, they all agree that nontectonic fissure formation is linked to

the ability of loess to collapse and allow fluids to infiltrate. According to [24], all fissures formed by soil collapsibility go through a phase from emergence to maturity, starting with microcracks and ending with eroded fissures as broad as gullies. It is said that as surface water accumulates and infiltrates into the ground, the wetness of the soil increases while its tensile strength falls, causing fissures to form. The saturation of collapsible soil occurs because of water infiltration, which is followed by hydro-compaction and the creation of new nascent hairline fissures. Additional water infiltrates inside the subsurface through tiny cracks, eroding telescopic soils and forming underground passageways that are not obvious on the earth's surface in the initial state of growth and can only be observed through some cave-ins along the fissures. More water erosion broadens and increases the subway, causing the roofs to collapse and forming pits along the fissures. Finally, owing to piping erosion, these potholes connect, producing more collapse. Continuous erosion enlarges the collapsed structures and transforms them into eroded gullies, which are the mature stage of the fissures.

3.2.3. Differential Compaction Due to Heterogeneity

Aquifer heterogeneity results in a sudden shift in an aquifer's thickness or in its bed composition. According to [53], such thickness fluctuations could lead to rotation, vertical shear, or even lateral expansion at depth. For instance, the author in [56] illustrated that the vertical compaction strength varies on either side of a geometric heterogeneity. He explained that localized differential vertical movement in the underlying, non-compacting interval is caused by a geometric anomaly that migrates upward, causing tilting and shearing at the surface of the terrain. On the other hand, localized differential horizontal distortions may cause fissures at the ground surface as well as a deep extensional zone and induce an opposite direction of rotation (see Figure 6).

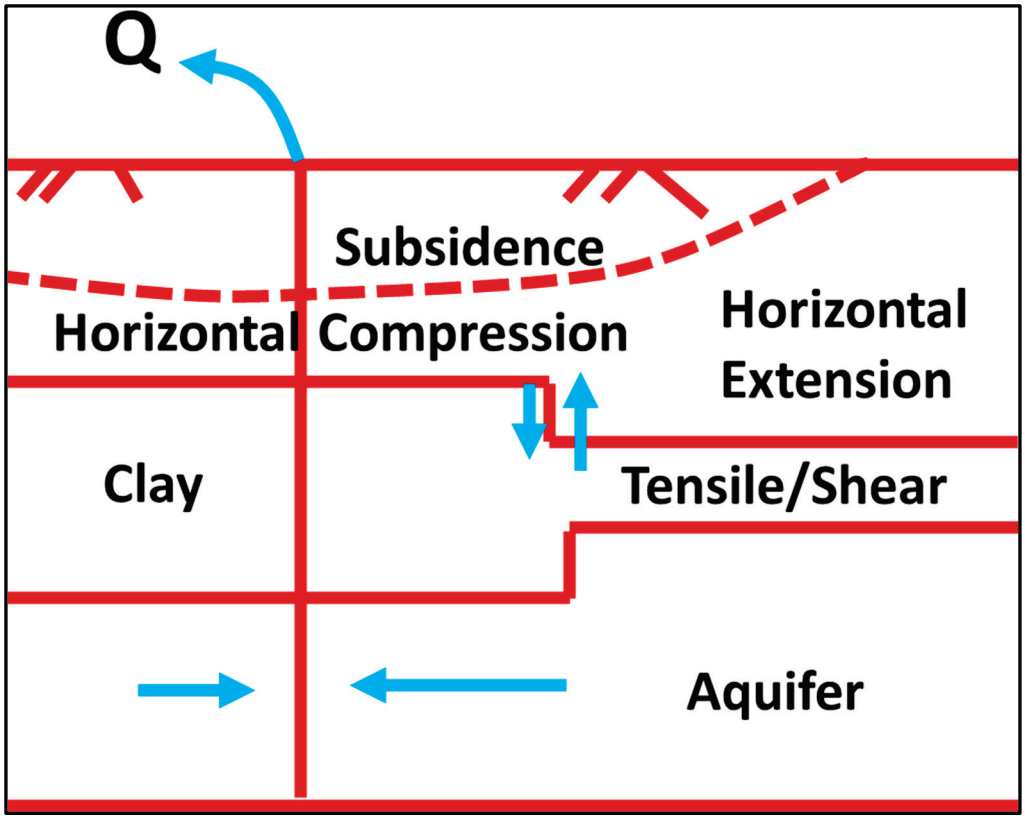

Figure 6. Heterogeneous layer of a highly compressible clay causes differential compaction, leading to vertical shear, rotation, and horizontal extension [56].

The ongoing discussion is summarized in Table 3, which highlights the major factors and processes of fissure formation as discussed above. Other anthropogenic factors and processes such as groundwater over-pumping is an integral part of the processes discussed above since they facilitate them.

Table 3. Summary table of the formation mechanisms of earth fissures.

S/N	Mechanism	Factors	Process of Formation
(1)	Bedrock ridge crack	• Subsurface topography • Compressibility of rock units • Rupture due to brittleness	• Bending and/or rupturing due to differential compaction • Horizontal displacement due to groundwater harvesting
	Pre-existence of faults	• Buried fault scarps • Unequal settling of foot and hanging walls • Fault/fracture zones • Deep crustal movement	• Fault activation due to over-pumping • Initial extension of fault heave • Washout due to erosion
	Pre-existence of Paleochannels	• Intense rain • Instability of recent channel deposits • Uneven settling of sediments • Overburdened weight of soil	• Initial joint stress • Piping and surface erosion • Soil collapse due to differential pumping • Stratal curves due to gravity and pressure
	Differential compaction	• Heterogeneity of rock units	• Thickness fluctuation • Vertical shearing and lateral expansion • Rotation due to differential loading
	Collapsibility of loess	• Physico-mechanical properties of rocks	• Tensile strength failure due to water infiltration and soil wetness • Hydro compaction exerted by water pressure • Piping erosion, underground tunnelling, and cave-ins

4. Earth Fissures in Najran

From the previous discussion, we can see that it is a popular opinion among researchers that groundwater depletion makes a significant contribution to the formation of fissures. Researchers have attributed inadequate groundwater removal as the primary cause of land subsidence and earth fissures in several locations throughout the Kingdom of Saudi Arabia [2,32,34,76]. Ref. [34] highlighted the diverse kinds of ground fissures (Figure 7) found in the country based on their various causative factors, some of which include (a) earth fissures induced by the excessive withdrawal of groundwater; (b) earth fissures due to the swelling and shrinkage of clay deposits such as in Hail, Al Qasim; (c) earth fissures caused by dewatering impacts on Khabra deposits, such as in the Al Qasim geopolitical zone; (d) ground fissuring connected to subsurface structures and groundwater over-pumping; and (e,f) earth fissures emanating from the effects of an earthquake.

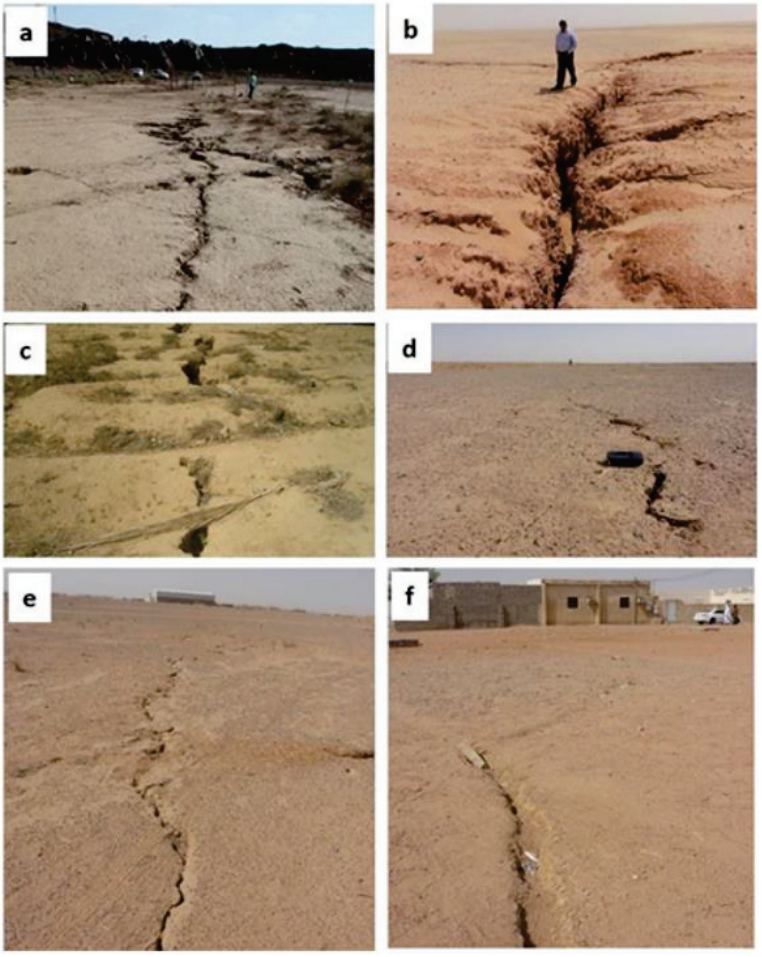

Figure 7. Images of ground fissures found in different parts of Saudi Arabia [34].

A study conducted in [2] estimated that the city of Najran witnesses only about 31.3×106 m^3 rainfall per year. This is the reason for the constant reduction in water table levels, which caused the drying of more than a thousand wells in the city. Rapid groundwater depletion remains one of the most profound sustainability challenges facing many cities. In Najran, the authors in [2] indicated that the Najran fissures have varying lengths and widths; one of the fissures elongated to about 600 m in a northeast direction and has a varying breadth of thirty or fifty centimeters (see Figure 8). Although these reported initial widths of the fissures might seem small, the authors in [77] asserted from their investigation of fissures in south–central Arizona that similar fissures being initially narrow and having a width of about 2 cm wide and 1–2 km long, widen and elongate as time passes. As discussed above, in Section 2, the length of the fissures or the extent of deformations resulting from fissuring activity typically depends on the underlying geology of the area, with causes such as pre-existing faults, the degree of groundwater depletion, and the resultant pressure imbalance. As reported from a survey carried out in Su-Xi-Chang Plain, in the southeastern part of the North China Plain, earth fissures can be up to two thousand meters long [20]. It is therefore acceptable to presume that earth fissures in Najran might become worse than they are presently.

Figure 8. Fissures linked to subsidence because of groundwater over-withdrawal in Najran are shown in subfigures (**a**,**b**) in non-residence locations [2].

In Najran, most exposed ground fissures caused by groundwater depletion appear on the surface as linear ruptures with some vertical displacements, and the resulting surface scarps result in myriad destruction on roadways, farms, and residences with a range of influence of 30 to 400 m. Due to tensile forces caused by excessive groundwater extraction, earth cracks in the city of Najran can stretch for tens of meters to kilometers [51]. Studies have shown that Najran's earth fissures are linked to groundwater depletion ((Interdisciplinary Earthquake Hazard Research in Gulf of Aqaba and Strait of Tiran (GAST)-NASA/ADS, n.d.) [34,78]. The rapid drop in the water table level caused subsidence as well as ground failure, which was evidenced by earth rifts, owing to the aquifer's composition of poorly consolidated sands with high porosity and aquitards with low pore connectivity and high compressibility [2,34]. If increased water exploitation in the city of Najran persists, fissuring and some other environmental threats including sinkholes, seismic events, and structural failure to engineering constructions will also persevere, causing the size of existing subsidence and fissures throughout the location to grow even larger [15].

Research has proven that factors causing the formation of fissures are synergistic, implying that, although groundwater depletion triggers or enhances the process, other pre-existing geologic tectonic and nontectonic factors play major roles in enabling their formation [23]. Apart from the excessive drawdown of the groundwater table in Najran, the subsurface topography of the study area has been also suggested as a major factor contributing to the formation of the fissures in that area. As discussed earlier, subsurface slopes such as bedrock ridges can influence the formation of fissures [21,58]. This secondary cause of the Najran fissure was proposed by the authors in [2], who used advanced electrical resistivity tomography (ERT) to evaluate the subsurface extent, topological information, and the spread of fissures in the Najran metropolis.

Several regional and local active seismic zones have been reported in the western region of Saudi Arabia, including the Red Sea, the Gulf of Aqaba, and the Najid Fault system in addition to many others that can potentially accommodate different magnitudes of earthquakes such as the destructive 1993 (Mw 6.1) and 1995 (Mw 7.3) earthquakes that occurred in the Gulf of Aqaba [79,80]. These seismic zones activate tectonic deformation of the earth and consequent faulting across the region, and the city of Najran, being in the western region, is not entirely free from their impacts. The Wajid Group which underlies the city of Najran is reported to be fractured on a regional scale as a result of the paleo

reactivation of the Arabian Shield structures [42]. These structures can be easily reactivated due to the stress imbalance accruing from excessive groundwater pumping. Although it has been suggested that subsurface topography is a key factor in the fissure's formation, it is not exhaustive and can be an insignificant contributor to the fissuring process. It is, therefore, required to conduct fault or fracture mapping studies across the fissuring zones. An in-depth understanding of the structural architecture and fault history of the Najran Basin would be an immense guide toward understanding other unknown factors responsible for fissuring in the area. There is a need to conduct further research into the other potential causes of this hazard. A robust understanding of this would enable the government to develop holistic mitigation and control measures to protect life and properties in the area.

4.1. Najran Fissure Monitoring Recommendation

So many arithmetical, theoretic, geomechanical, and physics models have earlier been established to explore the configurations, tensile forces, and resumption of fissuring predicated on underground water lateral motion, drainage, agrarian operations, subsidence, continuous soil cracking, bedrock characteristics, and aquifer/aquitard layer thickness, as evidenced by the ongoing discussions in the literature [29,81–85]. We have shown that the factors responsible for fissuring in Najran are multifaceted and may be more serious than previously thought. If all the probable sources of hazard are identified, they can be combined to create more robust conceptual and/or predictive models of the fissure development mechanism in the area. It is especially important to have a holistic model of the earth fissure hazards in the area to recognize susceptible groundwater areas for the proper enactment of water management policies and efficacious implementation of groundwater recharge strategies to achieve environmentally friendly preservation plans and protect existing groundwater resources [86]. Predicting and comprehending hazardous locations can assist policymakers in managing susceptible areas and reducing the likelihood of damage. The findings would also be useful for water resource managers in formulating judgments on how to properly regulate groundwater extraction. To investigate the creation mechanism of fissuring in Najran, statistically based models such as time series models or artificial intelligence (AI) can be applied. These models would primarily be used to monitor active fissures and identify key factors, utilizing spatial information, subsidence, groundwater-related data sets, etc. [85–89]. As discussed by the authors of [90] for landslide prediction, metaheuristic algorithms such as artificial bee colony (ABC), genetic algorithms (GAs), [90–93], gray wolf optimization (GWO) algorithms [94,95], particle swarm optimization (PSO) algorithms [96,97], and water cycle algorithms (WCAs) [97] can also be implemented for fissure predictions. Ref. [90] further demonstrates that a combined application integrating k-fold cross-validation, metaheuristic support vector regression, and nonparametric Friedman tests can be utilized to determine optimum hyperparameters and present their statistical significance, thereby improving the accuracy and dependability of AI-based forecasts, and with the help of these methods, different machine-learning-based geo-hazard models might be analyzed and contrasted to ensure high prediction precision [98].

4.2. Future Fissure Studies in Najran

It is suggested that fissure-related studies in Najran and the surrounding cities focus on identifying all the major potential contributors to their formation processes, as well as assessing the contribution of an ephemeral variability of predictors such as rainfall, groundwater drawdown, groundwater variability, and so on, in order to develop a reliable model that can be utilized to forecast and monitor fissure formation in the area. This would be a great opportunity to learn more about the earth fissures. The primary determinants in fissure formation can be revealed through a sensitivity analysis of the predictors. Future findings could serve as a foundation for fissure research in other sections of Saudi Arabia and beyond. The increased demand for the prediction of possible hazards and susceptibility

mapping can be met by constructing a credible fissuring model [7,99–102]. Irregular bedrock topography, low groundwater recharge, excessive aquifer depletion, water table decline, a high density of groundwater wells, a high density of constructed roads, collapsible sediment distribution, fault zones, and other factors could make these areas more vulnerable to fissure hazards, and an accurate predictive model could help the government monitor these areas.

5. Conclusions

The factors that cause fissures are complex and synergistic. The investigation of this danger in many areas has revealed that multiple elements contribute to its creation. Because of the stress imbalance caused by groundwater extraction, pre-existing geologic features such as faults, fractures, joints, or sloppy terrain are mostly activated. The likelihood of pre-existing underground faults being activated by excessive groundwater extraction is quite likely, given the fracture history of the underlying geology of the city of Najran. Because prior studies of the fissures in this area failed to account for pre-existing faults or channels, future research should concentrate on this and other potential variables. Moreover, additional research might focus on finding all probable fissure predictors in this area and constructing holistic, realistic, and efficient predictive models that could be used to monitor areas with significant fissuring potentials. Such models would aid the government in making critical choices on facility development, city planning, agricultural expansion, and groundwater extraction regulation for both irrigation and domestic use.

Author Contributions: Conceptualization, B.O.N. and M.H.; methodology, B.O.N.; validation, A.M.H.H.M. and M.H.; writing—original draft preparation, B.O.N.; writing—review and editing, M.A. and M.I.; supervision, M.H. and A.M.H.H.M.; project administration, M.H.; funding acquisition, A.M.H.H.M. All authors have read and agreed to the published version of the manuscript.

Funding: This research received no external funding.

Institutional Review Board Statement: Not applicable.

Informed Consent Statement: Not applicable.

Data Availability Statement: Not applicable.

Acknowledgments: The authors are thankful to the Deanship of Scientific Research at Najran University for funding this work under the National Research Priorities Funding program grant code (NU/NRP/SERC/11/1). We also acknowledge the In-ternational Grant (015ME0-310) for supporting and funding this project. We also appreciate everyone who took the time to comment on this piece during the discussion and critical review stages.

Conflicts of Interest: The authors declare no conflict of interest. The funders had no role in the design of the study; in the collection, analyses, or interpretation of data; in the writing of the manuscript; or in the decision to publish the results.

References

1. Conway, B.D. Land subsidence and earth fissures in south-central and southern Arizona, USA. *Hydrogeol. J.* **2015**, *24*, 649–655. [CrossRef]
2. Youssef, A.M.; Sabtan, A.A.; Maerz, N.H.; Zabramawi, Y.A. Earth fissures in Wadi Najran, kingdom of Saudi Arabia. *Nat. Hazards* **2013**, *71*, 2013–2027. [CrossRef]
3. Huang, G.; Liu, C.; Sun, J.; Zhang, M.; Jing, J.; Li, L. A regional scale investigation on factors controlling the groundwater chemistry of various aquifers in a rapidly urbanized area: A case study of the Pearl River Delta. *Sci. Total Environ.* **2018**, *625*, 510–518. [CrossRef]
4. Zhu, H.-H.; Shi, B.; Zhang, C.-C. FBG-based monitoring of geohazards: Current status and trends. *Sensors* **2017**, *17*, 452. [CrossRef] [PubMed]
5. Liao, F.; Wang, G.; Shi, Z.; Huang, X.; Xu, F.; Xu, Q.; Guo, L. Distributions, sources, and species of heavy metals/trace elements in shallow groundwater around the Poyang lake, East China. *Expo. Health* **2017**, *10*, 211–227. [CrossRef]
6. Zhang, F.; Huang, G.; Hou, Q.; Liu, C.; Zhang, Y.; Zhang, Q. Groundwater quality in the Pearl River Delta after the rapid expansion of industrialization and urbanization: Distributions, main impact indicators, and driving forces. *J. Hydrol.* **2019**, *577*, 124004. [CrossRef]
7. Howard, K.W.F.; Zhou, W. Overview of ground fissure research in China. *Environ. Earth Sci.* **2019**, *78*, 97. [CrossRef]

8. Feng, Y.; Xiang-Yang, L. Improving emergency response to cascading disasters: Applying case-based reasoning towards urban critical infrastructure. *Int. J. Disaster Risk Reduct.* **2018**, *30*, 244–256. [CrossRef]
9. Li, Z.; Lai, J.; Li, Y.; Qiu, J.; Shi, Y.; Li, B.; Fan, F. Ground fissure disasters and mitigation measures for hazards during metro system construction in Xi'an, China. *Arab. J. Geosci.* **2021**, *15*, 5. [CrossRef]
10. Al-Harthi, A.A.; Bankher, K.A. Collapsing loess-like soil in western Saudi Arabia. *J. Arid. Environ.* **1999**, *41*, 383–399. [CrossRef]
11. Singh, A.; Mishra, O. Seismological evidence for monsoon induced micro to moderate earthquake sequence beneath the 2011 Talala, Saurashtra earthquake, Gujarat, India. *Tectonophysics* **2015**, *661*, 38–48. [CrossRef]
12. Bankher, K.A.; Al-Harthi, A.A. Earth fissuring and land subsidence in Western Saudi Arabia. *Nat. Hazards* **1999**, *20*, 21–42. [CrossRef]
13. El Baruni, S.S. Earth fissures caused by groundwater withdrawal In Sarir south agricultural project area, Libya. *Hydrogeol. J.* **1994**, *2*, 45–52. [CrossRef]
14. Hauksson, E. Episodic rifting and volcanism at Krafla in north Iceland: Growth of large ground fissures along the plate boundary. *J. Geophys. Res. Atmos.* **1983**, *88*, 625–636. [CrossRef]
15. El Aal, A.A.; Kamel, M.; Al-Homidy, A. Using remote sensing and GIS techniques in monitoring and mitigation of geohazards in Najran Region, Saudi Arabia. *Geotech. Geol. Eng.* **2019**, *37*, 3673–3700. [CrossRef]
16. Wang, Z.-F.; Shen, S.-L.; Cheng, W.-C.; Xu, Y.-S. Ground fissures in Xi'an and measures to prevent damage to the Metro tunnel system due to geohazards. *Environ. Earth Sci.* **2016**, *75*, 511. [CrossRef]
17. Helm, D.C. Hydraulic forces that play a role in generating fissures at depth. *Environ. Eng. Geosci.* **1994**, *xxxi*, 293–304. [CrossRef]
18. Xu, J.; Peng, J.; An, H. Experimental study on Su-Xi-Chang earth fissures induced by repeated groundwater pumping and impounding. *Geomat. Nat. Hazards Risk* **2019**, *10*, 2051–2068. [CrossRef]
19. Burbey, T. The influence of faults in basin-fill deposits on land subsidence, Las Vegas Valley, Nevada, USA. *Hydrogeol. J.* **2002**, *10*, 525–538. [CrossRef]
20. Budhu, M. Earth fissure formation from the mechanics of groundwater pumping. *Int. J. Geéomeéch.* **2011**, *11*, 1–11. [CrossRef]
21. Hernandez-Marin, M.; Burbey, T.J. The role of faulting on surface deformation patterns from pumping-induced groundwater flow (Las Vegas Valley, USA). *Hydrogeol. J.* **2009**, *17*, 1859–1875. [CrossRef]
22. Xu, J.; Meng, L.; An, H.; Wang, L. The bending mechanism of Anping ground fissure in the Hebei Plain, North China. *Environ. Earth Sci.* **2015**, *74*, 6859–6870. [CrossRef]
23. Qiao, J.; Peng, J.; Deng, Y.; Leng, Y.; Meng, Z. Earth fissures in Qinglong Graben in Yuncheng Basin, China. *J. Earth Syst. Sci.* **2018**, *127*, 10. [CrossRef]
24. Nikbakhti, O.; Hashemi, M.; Banikheir, M.; Basmenj, A.K. Geoenvironmental assessment of the formation and expansion of earth fissures as geological hazards along the route of the Haram-to-Haram Highway, Iran. *Bull. Eng. Geol. Environ.* **2017**, *77*, 1421–1438. [CrossRef]
25. Othman, A.; Sultan, M.; Becker, R.; Sefry, S.; Alharbi, T.; Alharbi, H.; Gebremichael, E. Groundwater-related land deformation over the mega aquifer system in Saudi Arabia: Inferences from InSAR, GRACE, earthquake records, field, and spatial data analysis. In Proceedings of the American Geophysical Union, Fall Meeting, New Orleans, LA, USA, 11–15 December 2017. Abstract #NH31B-0217.
26. Lu, Q.; Qiao, J.; Peng, J.; Liu, Z.; Liu, C.; Tian, L.; Zhao, J. A typical Earth fissure resulting from loess collapse on the loess plateau in the Weihe Basin, China. *Eng. Geol.* **2019**, *259*, 105189. [CrossRef]
27. Wang, F.; Peng, J.; Meng, Z.; Qiao, J.; Wen, H.; Ma, P.; Liu, Y.; Jia, Z.; Zhao, J. The origin and impact of the Shizhuang ground fissure, Yingxian area, Datong Basin, China. *Eng. Geol.* **2019**, *261*, 105283. [CrossRef]
28. Wan, J.; Li, B.; Tan, C.; Feng, C.; Zhang, P.; Qi, B. Characteristics and main causes of earth fissures in northeastern Beijing Plain, China. *Bull. Eng. Geol. Environ.* **2020**, *79*, 2919–2935. [CrossRef]
29. Lu, Q.; Liu, Y.; Peng, J.; Li, L.; Fan, W.; Liu, N.; Sun, K.; Liu, R. Immersion test of loess in ground fissures in Shuanghuaishu, Shaanxi Province, China. *Bull. Eng. Geol. Environ.* **2020**, *79*, 2299–2312. [CrossRef]
30. Wang, G.Y.; You, G.; Shi, B.; Qiu, Z.L.; Li, H.Y.; Tuck, M. Earth fissures in Jiangsu Province, China and geological investigation of Hetang earth fissure. *Environ. Earth Sci.* **2010**, *60*, 35–43. [CrossRef]
31. Zang, M.; Peng, J.; Xu, N.; Jia, Z. A probabilistic method for mapping earth fissure hazards. *Sci. Rep.* **2021**, *11*, 8841. [CrossRef]
32. Shehata, W.; Amin, A. Geotechnical hazards associated with desert environment. *Nat. Hazards* **1997**, *16*, 81–95. [CrossRef]
33. Al-Shanti, A.; El-Mahdy, O.; Hassan, M.; Hussein, A. A comparative study of five volcanic-hosted sulfide mineralizations in the Arabian shield. *J. King Abdulaziz Univ. Sci.* **1993**, *6*, 1–33. [CrossRef]
34. Youssef, A.M.; Al-Harbi, H.M.; Zabramwi, Y.A.; El-Haddad, B.A. Human-Induced Geo-Hazards in the Kingdom of Saudi Arabia: Distribution, Investigation, Causes and Impacts. In *Geohazards Caused by Human Activity*; InTech: London, UK, 2016. [CrossRef]
35. Edgell, H.S. Basement tectonics of Saudi Arabia as related to oil field structures. In *Basement Tectonics 9. Proceedings of the International Conferences on Basement Tectonics, Canberra, Australia, July 1990*; Rickard, M.J., Harrington, H.J., Williams, P.R., Eds.; Springer: Berlin/Heidelberg, Germany, 1992; Volume 3, p. 3. [CrossRef]
36. Al-Husseini, M.I. Origin of the Arabian Plate structures: Amar collision and Najd Rift. *Geoarabia* **2000**, *5*, 527–542. [CrossRef]
37. Sharland, P.R.; Casey, D.M.; Davies, R.B.; Simmons, M.D.; Sutcliffe, O.E. Arabian plate sequence stratigraphy—Revisions to SP2. *Geoarabia* **2004**, *9*, 199–214. [CrossRef]

38. Beydoun, Z.R. *Arabian Plate Hydrocarbon Geology and Potential—A Plate Tectonic Approach*; American Association of Petroleum Geologists: Tulsa, OK, USA, 1991; Volume 33, p. 77.
39. Bosworth, W.; Huchon, P.; McClay, K. The Red Sea and gulf of Aden basins. *J. Afr. Earth Sci.* **2005**, *43*, 334–378. [CrossRef]
40. Davies, F.B. Strain analysis of wrench faults and collision tectonics of the Arabian-Nubian Shield. *J. Geol.* **1984**, *92*, 37–53. [CrossRef]
41. Faqira, M.; Rademakers, M.; Afifi, A.M. New insights into the Hercynian Orogeny, and their implications for the Paleozoic Hydrocarbon system in the Arabian Plate. *Geoarabia* **2009**, *14*, 199–228. [CrossRef]
42. Benaafi, M.; Hariri, M.; Abdullatif, O.; Makkawi, M.; Al-Shaibani, A. Analysis of lineaments within the Wajid Group, SW Saudi Arabia, and their tectonic significance. *Arab. J. Geosci.* **2017**, *10*, 106. [CrossRef]
43. Kellogg, K.S.; Smith, C.W. Geology and tin-greisen mineralization of the Akash granite, northern Arabian Shield. *J. Afr. Earth Sci. 1983* **1986**, *4*, 205–210. [CrossRef]
44. Powers, R.; Ramirez, L.F.; Redmond, C.; Elberg, E. *Geology of the Arabian Peninsula: Sedimentary geology of Saudi Arabia*; U.S. Geological Survey: Asheville, NC, USA, 1966. [CrossRef]
45. Stump, T.; Van der Eem, J. The stratigraphy, depositional environments and periods of deformation of the Wajid outcrop belt, southwestern Saudi Arabia. *J. Afr. Earth Sci.* **1995**, *21*, 421–441. [CrossRef]
46. Al-Ajmi, H.F.; Keller, M.; Hinderer, M.; Filomena, C.M. Lithofacies, depositional environments and stratigraphic architecture of the Wajid Group outcrops in southern Saudi Arabia. *Geoarabia* **2015**, *20*, 49–94. [CrossRef]
47. Abdulkadir, I.T.; Abdullatif, O.M. Facies, depositional environments, reservoir potential and palaeogeography of the cambro-ordovician dibsiyah formation, Wajid outcrop belt, Saudi Arabia. *Arab. J. Sci. Eng.* **2012**, *38*, 1785–1806. [CrossRef]
48. Laboun, A.A. Paleozoic tectono-stratigraphic framework of the Arabian Peninsula. *J. King Saud Univ. Sci.* **2010**, *22*, 41–50. [CrossRef]
49. Knox, R.W.; Franks, S.G.; Cocker, J.D. Stratigraphic evolution of heavy-mineral provenance signatures in the sandstones of the Wajid Group (Cambrian to Permian), southwestern Saudi Arabia. *Geoarabia* **2007**, *12*, 65–96. [CrossRef]
50. Al-Husseini, M.I. Pre-Unayzah unconformity, Saudi Arabia. In *Carboniferous, Permian and Early Triassic Arabian Stratigraphy*; Gulf PetroLink: Manama, Bahrain, 2014.
51. Holzer, T.L. Ground failure induced by ground-water withdrawal from unconsolidated sediment. In *Man-Induced Land Subsidence*; Geological Society of America: Boulder, CO, USA, 1984; Volume 6.
52. Lofgren, B.E. Hydraulic stresses cause ground movement and fissures, Picacho, Arizona. In *Geological Society of America Abstracts with Programs*; Geological Society America: Boulder, CO, USA, 1978; Volume 10, p. 113.
53. Helm, D.C. Horizontal aquifer movement in a Theis-Thiem confined system. *Water Resour. Res.* **1994**, *30*, 953–964. [CrossRef]
54. Zhang, Y.; Xue, Y.-Q.; Wu, J.-C.; Yu, J.; Wei, Z.-X.; Li, Q.-F. Land subsidence and earth fissures due to groundwater withdrawal in the Southern Yangtse Delta, China. *Environ. Geol.* **2007**, *55*, 751–762. [CrossRef]
55. Xu, J.; Peng, J.; Deng, Y.; Wang, F. Development characteristics and formation analysis of Baixiang earth fissure on North China plain. *Bull. Eng. Geol. Environ.* **2018**, *78*, 3085–3094. [CrossRef]
56. Sheng, Z.; Helm, D.C.; Li, J. Mechanisms of earth fissuring caused by groundwater withdrawal. *Environ. Eng. Geosci.* **2003**, *9*, 351–362. [CrossRef]
57. Higgins, C.G.; Coates, D.R. *Groundwater Geomorphology: The Role of Subsurface Water in Earth-Surface Processes and Landforms*; Geological Society of America: Boulder, CO, USA, 1990.
58. Hernandez-Marin, M.; Burbey, T.J. Controls on initiation and propagation of pumping-induced earth fissures: Insights from numerical simulations. *Hydrogeol. J.* **2010**, *18*, 1773–1785. [CrossRef]
59. Gregory, J.; Mueller, J.E. Earth fissures of the Mimbres Basin, southwestern New Mexico. *New Mex. Geol.* **1991**, *13*, 69–74.
60. Budhu, M.; Adiyaman, I. Earth fissure formation from groundwater pumping and the influence of a stiff upper cemented layer. *Q. J. Eng. Geol. Hydrogeol.* **2012**, *45*, 197–205. [CrossRef]
61. Budhu, M.; Adiyaman, I. The influence of clay zones on land subsidence from groundwater pumping. *Groundwater* **2013**, *51*, 51–57. [CrossRef]
62. Aisong, D.; Jianhua, J. Land subsidence, sinkhole collapse and earth fissure occurrence and control in China. *Hydrol. Sci. J.* **1994**, *39*, 245–256. [CrossRef]
63. Burbey, T.J. Storage coefficient revisited: Is purely vertical strain a good assumption? *Groundwater* **2001**, *39*, 458–464. [CrossRef] [PubMed]
64. Burbey, T.J. Stress-strain analyses for aquifer-system characterization. *Groundwater* **2001**, *39*, 128–136. [CrossRef]
65. Bawden, G.W.; Thatcher, W.; Stein, R.S.; Hudnut, K.W.; Peltzer, G. Tectonic contraction across Los Angeles after removal of groundwater pumping effects. *Nature* **2001**, *412*, 812–815. [CrossRef]
66. Hsieh, P.A. Deformation-induced changes in hydraulic head during ground-water withdrawal. *Groundwater* **1996**, *34*, 1082–1089. [CrossRef]
67. Wolff, R.G. Relationship between horizontal strain near a well and reverse water level fluctuation. *Water Resour. Res.* **1970**, *6*, 1721–1728. [CrossRef]
68. Budhu, M.; Adiyaman, I.B. Mechanics of land subsidence due to groundwater pumping. *Int. J. Numer. Anal. Methods Geéomeéch.* **2009**, *34*, 1459–1478. [CrossRef]

69. Jachens, R.C.; Holzer, T.L. Differential compaction mechanism for earth fissures near Casa Grande, Arizona. *GSA Bull.* **1982**, *93*, 998–1012. [CrossRef]
70. Zhao, J.; Liu, C.; Peng, J.; Qiao, J.; Meng, Z.; Wen, H.; Wang, F.; Ma, P.; Wang, Z.; Jia, Z.; et al. Characteristics and formation mechanism of the Yangjiazhuang-Maguduo ground fissure, western Linfen Basin, Northern China. *J. Asian Earth Sci.* **2022**, *226*, 105043. [CrossRef]
71. Peng, J.; Qiao, J.; Sun, X.; Lu, Q.; Zheng, J.; Meng, Z.; Xu, J.; Wang, F.; Zhao, J. Distribution and generative mechanisms of ground fissures in China. *J. Asian Earth Sci.* **2020**, *191*, 104218. [CrossRef]
72. Gaur, V.P.; Kar, S.K.; Srivastava, M. Development of ground fissures: A case study from southern parts of Uttar Pradesh, India. *J. Geol. Soc. India* **2015**, *86*, 671–678. [CrossRef]
73. Pacheco-Martínez, J.; Hernandez-Marín, M.; Burbey, T.J.; González-Cervantes, N.; Ortíz-Lozano, J.Á.; Zermeño-De-Leon, M.E.; Solís-Pinto, A. Land subsidence and ground failure associated to groundwater exploitation in the Aguascalientes Valley, México. *Eng. Geol.* **2013**, *164*, 172–186. [CrossRef]
74. Xu, Z.; Liu, C.; Zhou, X.; Gao, G.; Feng, X. Full-scale physical modelling of fissure grouting in deep underground rocks. *Tunn. Undergr. Space Technol.* **2019**, *89*, 249–261. [CrossRef]
75. Xu, J.; Peng, J.; An, H.; Wang, F.; Sun, H.; Hu, H.; Yang, B. Paleochannel-controlled earth fissures in Daming, North China Plain and their implication for underground paleogeomorphology. *Geomorphology* **2019**, *327*, 523–532. [CrossRef]
76. Amin, A.; Bankher, K. Geotechnical aspects of loess in kingdom of Saudi Arabia. *J. King Abdulaziz Univ. Sci.* **2004**, *15*, 163–179. [CrossRef]
77. Schumann, H.H.; Poland, J.F. Land subsidence, earth fissures and groundwater withdrawal in south-central Arizona, USA. In Proceedings of the International Conference on Land Subsidence, Tokyo, Japan, 1969; Volume 1, pp. 295–302.
78. Mousavi, S.M.; Shamsai, A.; el Naggar, M.H.; Khamehchian, M. A GPS-based monitoring program of land subsidence due to groundwater withdrawal in Iran. *Can. J. Civ. Eng.* **2001**, *28*, 452–464. [CrossRef]
79. El-Hussain, I.; Al-Shijbi, Y.; Deif, A.; Mohamed, A.M.E.; Ezzelarab, M. Developing a seismic source model for the Arabian Plate. *Arab. J. Geosci.* **2018**, *11*, 435. [CrossRef]
80. Purkis, S.J.; Shernisky, H.; Swart, P.K.; Sharifi, A.; Oehlert, A.; Marchese, F.; Benzoni, F.; Chimienti, G.; Duchâtellier, G.; Klaus, J.; et al. Discovery of the deep-sea NEOM brine pools in the Gulf of Aqaba, Red Sea. *Commun. Earth Environ.* **2022**, *3*, 146. [CrossRef]
81. Peng, J.-B.; Chen, L.-W.; Huang, Q.-B.; Men, Y.-M.; Fan, W.; Yan, J.-K. Physical simulation of ground fissures triggered by underground fault activity. *Eng. Geol.* **2013**, *155*, 19–30. [CrossRef]
82. Gao, M.; Gong, H.; Li, X.; Chen, B.; Zhou, C.; Shi, M.; Guo, L.; Chen, Z.; Ni, Z.; Duan, G. Land subsidence and ground fissures in Beijing Capital International Airport (BCIA): Evidence from Quasi-PS InSAR analysis. *Remote. Sens.* **2019**, *11*, 1466. [CrossRef]
83. Yang, C.-S.; Zhang, Q.; Zhao, C.-Y.; Wang, Q.-L.; Ji, L.-Y. Monitoring land subsidence and fault deformation using the small baseline subset InSAR technique: A case study in the Datong Basin, China. *J. Geodyn.* **2014**, *75*, 34–40. [CrossRef]
84. Xulong, G.; Gu, C.; Lu, Y.; Lü, F. Model test for evolution of ground fissures due to extraction of groundwater. *J. Eng. Geol.* **2018**, *26*, 951–958. [CrossRef]
85. Robineau, T.; Tognelli, A.; Goblet, P.; Renard, F.; Schaper, L. A double medium approach to simulate groundwater level variations in a fissured karst aquifer. *J. Hydrol.* **2018**, *565*, 861–875. [CrossRef]
86. Choubin, B.; Mosavi, A.; Alamdarloo, E.H.; Hosseini, F.S.; Shamshirband, S.; Dashtekian, K.; Ghamisi, P. Earth fissure hazard prediction using machine learning models. *Environ. Res.* **2019**, *179*, 108770. [CrossRef] [PubMed]
87. Hamamin, D.F.; Nadiri, A.A. Supervised committee fuzzy logic model to assess groundwater intrinsic vulnerability in multiple aquifer systems. *Arab. J. Geosci.* **2018**, *11*, 176. [CrossRef]
88. Ngien, S.K.; Rahman, N.A.; Lewis, R.W.; Ahmad, K. Numerical modelling of multiphase immiscible flow in double-porosity featured groundwater systems. *Int. J. Numer. Anal. Methods Geéomeéch.* **2011**, *36*, 1330–1349. [CrossRef]
89. Davoodijam, M.; Motagh, M.; Momeni, M. Land Subsidence in Mahyar Plain, Central Iran, investigated using envisat SAR data. *Int. Assoc. Geod. Symp.* **2014**, *140*, 127–130. [CrossRef]
90. Ma, J.; Xia, D.; Guo, H.; Wang, Y.; Niu, X.; Liu, Z.; Jiang, S. Metaheuristic-based support vector regression for landslide displacement prediction: A comparative study. *Landslides* **2022**, *19*, 2489–2511. [CrossRef]
91. Li, X.Z.; Kong, J.M. Application of GA–SVM method with parameter optimization for landslide development prediction. *Nat. Hazards Earth Syst. Sci.* **2014**, *14*, 525–533. [CrossRef]
92. Cai, Z.; Xu, W.; Meng, Y.; Shi, C.; Wang, R. Prediction of landslide displacement based on GA-LSSVM with multiple factors. *Bull. Eng. Geol. Environ.* **2016**, *75*, 637–646. [CrossRef]
93. Miao, F.; Wu, Y.; Xie, Y.; Li, Y. Prediction of landslide displacement with step-like behavior based on multialgorithm optimization and a support vector regression model. *Landslides* **2017**, *15*, 475–488. [CrossRef]
94. Guo, Z.; Chen, L.; Gui, L.; Du, J.; Yin, K.; Do, H.M. Landslide displacement prediction based on variational mode decomposition and WA-GWO-BP model. *Landslides* **2020**, *17*, 567–583. [CrossRef]
95. Liao, K.; Wu, Y.; Miao, F.; Li, L.; Xue, Y. Using a kernel extreme learning machine with grey wolf optimization to predict the displacement of step-like landslide. *Bull. Eng. Geol. Environ.* **2020**, *79*, 673–685. [CrossRef]
96. Zhou, C.; Yin, K.; Cao, Y.; Ahmed, B. Application of time series analysis and PSO–SVM model in predicting the Bazimen landslide in the Three Gorges Reservoir, China. *Eng. Geol.* **2016**, *204*, 108–120. [CrossRef]

97. Zhang, L.; Shi, B.; Zhu, H.; Yu, X.B.; Han, H.; Fan, X. PSO-SVM-based deep displacement prediction of Majiagou landslide considering the deformation hysteresis effect. *Landslides* **2020**, *18*, 179–193. [CrossRef]
98. Ma, J.; Xia, D.; Wang, Y.; Niu, X.; Jiang, S.; Liu, Z.; Guo, H. A comprehensive comparison among metaheuristics (MHs) for geohazard modeling using machine learning: Insights from a case study of landslide displacement prediction. *Eng. Appl. Artif. Intell.* **2022**, *114*, 105150. [CrossRef]
99. Li, M.; Ge, D.; Liu, B.; Zhang, L.; Wang, Y.; Guo, X.; Wang, Y.; Zhang, D. Research on development characteristics and failure mechanism of land subsidence and ground fissure in Xi'an, monitored by using time-series SAR interferometry. *Geomat. Nat. Hazards Risk* **2019**, *10*, 699–718. [CrossRef]
100. Peng, J.; Qiao, J.; Leng, Y.; Wang, F.; Xue, S. Distribution and mechanism of the ground fissures in Wei River Basin, the origin of the Silk Road. *Environ. Earth Sci.* **2016**, *75*, 718. [CrossRef]
101. Peng, J.; Xu, J.; Ma, R.; Wang, F. Characteristics and mechanism of the Longyao ground fissure on North China Plain, China. *Eng. Geol.* **2016**, *214*, 136–146. [CrossRef]
102. Peng, J.B.; Sun, X.H.; Wang, W.; Sun, G.C. Characteristics of land subsidence, earth fissures and related disaster chain effects with respect to urban hazards in Xi'an, China. *Environ. Earth Sci.* **2016**, *75*, 1190. [CrossRef]

sustainability

MDPI

Article

A Scenario-Based Case Study: Using AI to Analyze Casualties from Landslides in Chittagong Metropolitan Area, Bangladesh

Edris Alam [1,2,*], Fahim Sufi [3,*] and Abu Reza Md. Towfiqul Islam [4]

[1] Faculty of Resilience, Rabdan Academy, Abu Dhabi P.O. Box 114646, United Arab Emirates
[2] Department of Geography and Environmental Studies, University of Chittagong, and Disaster Action and Development Organisation (DADO), Chittagong 4331, Bangladesh
[3] School of Public Health and Preventive Medicine, Monash University, Melbourne, VIC 3000, Australia
[4] Department of Disaster Management, Begum Rokeya University, Rangpur 5400, Bangladesh
* Correspondence: ealam@ra.ac.ae (E.A.); research@fahimsufi.com (F.S.)

Abstract: Understanding the complex dynamics of landslides is crucial for disaster planners to make timely and effective decisions that save lives and reduce the economic impact on society. Using the landslide inventory of the Chittagong Metropolitan Area (CMA), we have created a new artificial intelligence (AI)-based insight system for the town planners and senior disaster recovery strategists of Chittagong, Bangladesh. Our system generates dynamic AI-based insights for a range of complex scenarios created from 7 different landslide feature attributes. The users of our system can select a particular kind of scenario out of the exhaustive list of 1.054×10^{41} possible scenario sets, and our AI-based system will immediately predict how many casualties are likely to occur based on the selected kind of scenario. Moreover, an AI-based system shows how landslide attributes (e.g., rainfall, area of mass, elevation, etc.) correlate with landslide casualty by drawing detailed trend lines by performing both linear and logistic regressions. According to the literature and the best of our knowledge, our CMA scenario-based AI insight system is the first of its kind, providing the most comprehensive understanding of landslide scenarios and associated deaths and damages in the CMA. The system was deployed on a wide range of platforms including Android, iOS, and Windows systems so that it could be easily adapted for strategic disaster planners. The deployed solutions were handed down to 12 landslide strategists and disaster planners for evaluations, whereby 91.67% of users found the solution easy to use, effective, and self-explanatory while using it via mobile.

Keywords: AI; landslides; causalities; hazards

Citation: Alam, E.; Sufi, F.; Islam, A.R.M.T. A Scenario-Based Case Study: Using AI to Analyze Casualties from Landslides in Chittagong Metropolitan Area, Bangladesh. *Sustainability* **2023**, *15*, 4647. https://doi.org/10.3390/su15054647

Academic Editors: Stefano Morelli, Veronica Pazzi and Mirko Francioni

Received: 6 January 2023
Revised: 22 February 2023
Accepted: 23 February 2023
Published: 6 March 2023

1. Introduction

Landslides are natural phenomena that have an adverse effect on human life, as well as the economy [1]. For the purpose of reducing the negative impact of landslides and to have an increased level of disaster preparedness [2], it is crucial to have a multi-dimensional understanding the attributes of landslides. The complex nature of landslide dynamics makes it extremely difficult to understand the impact of a particular type of landslide. Bangladesh is susceptible to a variety of natural and human-induced hazards including tropical cyclones, floods, droughts, earthquakes, tsunamis, and landslides [2]. In particular, landslides have become recurrent phenomena in the Southeast Bangladesh in recent decades. Therefore, the Government of Bangladesh (GoB) and its coastal residents have been engaged in reducing resultant deaths from tropical cyclones, but landslides have still caused over 500 deaths in Southeast Bangladesh with the majority occurring in informal settlements in Chittagong and Rangamati districts since 2000. The root causes contributing to the vulnerability of three different communities in the southeast part of Bangladesh. These communities are Bengali, Tribal, and Rohingya refugees, [3] and effective local risk governance was also promulgated [4]. Studies were also conducted to identify the root causes and impacts of landslides using qualitative methods (e.g.,

interviews and surveys) in Chittagong city and Rangamati district [5]. However, there is further scope for applying artificial intelligence (AI)-driven techniques to identify physical parameters that significantly influence deaths associated with landslides. As such, in this paper, we deployed a new scenario-based AI insight system, that facilitates an in-depth understanding of landslide hazards, enhances "risk perception", and raises the level of "disaster preparedness" in relation to landslides.

Geo-structural and causative factor-based analyses were applied for exploring landslide susceptibility zoning. Landslide susceptibility and risk assessment have been studied at global levels [6,7]. Geo-spatial technologies such as the application of geographical information systems (GIS), global positioning systems (GPS), and remote sensing (RS) have recently taken prominence in hazard assessment and risk identification to assist in decision making related to landslide disaster risk management [8,9]. GPS is a space-based navigation satellite system that acquires information relating to exact location and time in all weather conditions, anywhere in the world and it assists with the collection and storage of landslide information. GIS is used in collecting, storing, and analyzing geographic information and their non-spatial attributes. A plethora of studies have been conducted using GIS for landslide hazard and risk assessment [10]. Remote sensing is a system where information about the earth's surface is obtained without direct contact with it. In recent decades, RS has been widely applied for the identification of landslide areas, vulnerability, and risk mapping [11]. Apart from the aforementioned techniques, machine learning algorithms are gaining prominence in enhancing disaster preparedness and response.

There are varieties of methods available to study landslide susceptibility. These include but are not limited to landslide inventory-based probabilistic, deterministic, heuristic, and statistical techniques [12]. The most used landslide inventory-based probabilistic techniques involve the development of the inventory of landslides, geo-morphological analysis, and generating susceptibility maps based on provided parameters [13]. Deterministic approaches are also familiar as quantitative methods that involve quantifying factors such as physical factors, e.g., soil, rainfall, vegetation, and slope variables to generate maps that display the spatial distribution of input data [14,15]. A qualitative approach (heuristic analysis) involves analyzing aerial photographs or conducting field surveys to identify the intrinsic properties of a landform [16]. Statistical analysis uses sample data to identify the relationship between the dependent variable (the presence or absence of landslides), and the independent variables (landslides triggering/causative factors [17].

Artificial intelligence (AI) methods use some of the statistical concepts. These methods are based on assumptions, predetermined algorithms, and output. AI methods or machine learning methods that are used for landslide studies include artificial neural networks (ANN), fuzzy-based, hybrid, kernel-based, and tree-based methods [18]. These methods are suitable for generating results regardless of data types (i.e., both discrete and continuous data) and data limitation (i.e., the types and number of conditioning factors). For example, the research in [19] uses machine learning algorithms to understand the complex dynamics of global landslides which may help strategic decision makers.

Although these studies provide valuable insight into landslide susceptibility as well as the causes and impacts of landslides on the poor in Chittagong, there is a dearth of research that focuses on using AI systems to analyze casualties from landslides on a small scale. Reducing disaster deaths through AI at both the national and local levels is aligned with the United Nations' Sendai Framework (2015–2030) for Disaster Risk Global Target A: 'Substantially reduce global disaster mortality by 2030′ and Global Target G: 'Substantially increase the availability of and access to multi-hazard early warning systems and disaster risk information and assessments to people by 2030 [20]. Since Bangladesh is a signatory to the Sendai Framework; it is important that multi-hazard early warning systems and disaster risk information for all hazards are available at the community level by the year 2030.

In this paper, first, we designed and developed a new scenario-based AI insight system that can connect to a landslide database, so as to find out unknown insights from

landslide data. Second, we connected our scenario-based AI insight system to a dataset containing landslide information and finally, we demonstrated the dynamic generation of AI-based insights based on specific scenarios. It should be noted that the methodology described within this paper allows for the automatic generation of AI insights, without the need to manually execute statistical methods. As opposed to the traditional statistical methods, where a data scientist is required to manually prepare, execute, and analyze, the methodology presented in this paper automates the entire process and provides AI-driven insights in a fast and efficient manner. The results in Section 3 (results) show the positive correlation of area of mass as well as rainfall towards the number of casualties.

Equipped with these AI insights, a disaster recovery planner and strategist can make informed, timely, and evidence-based decisions that can save lives and reduce the economic impact of likely disasters on a society. Moreover, the AI insights would support policy planners in understanding the characteristics of landslides in a particular area and provide useful guidance for policy implementation.

2. Materials and Methods

First, the data was obtained from previous landslide catalogues, local histories, archive of institutional and administrative records, newspapers, reports, digital archives, and published peer-reviewed journal papers dedicated to landslides in the Chittagong Metropolitan Area (CMA), and subsequently cleaned and transformed before modelling. Data collected from secondary sources were validated through field visits and investigations to identify accurate locations of landslide occurrences. Following this, data modelling using the best practice was performed and then the data was visualized and analyzed using AI systems and algorithms. The details of these AI-based analyses are portrayed within this section. Finally, data-driven insights were generated. Figure 1 demonstrates the step-by-step process for generating AI insights on the CMA landslide data. The following subsections describe the study area selection, the sources of the data, preparation of the data, modelling of the data, visualization of the data, and analysis with AI-based algorithms (like linear regression, logistic regression, and decomposition tree analysis).

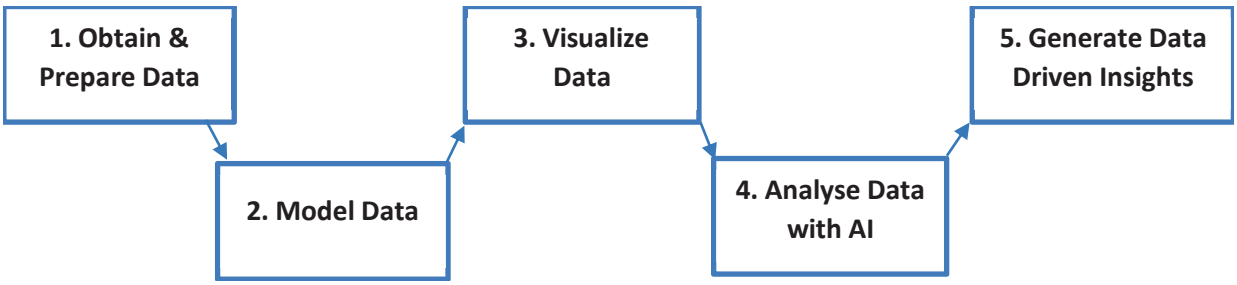

Figure 1. High level methodology of AI insight system for analyzing landslides in the CMA of SE Bangladesh, particularly the landslide susceptible areas in the Chittagong, Rangamati, and Cox's Bazar districts.

2.1. Study Area Selection

Chittagong was selected as the area of study, as the residents of the city have experienced a record of deaths associated with landslides since the year 2000. For example, on the 11 June 2007, landslide events alone caused the death of 128 casualties and 100 injuries in places adjacent to hilly areas, because landslides were triggered by heavy rainfall (610 mm) for eight consecutive days. Five years later, on the 26 June 2012, another eight days of continuous rainfall (889 mm) triggered landslides that led to 90 casualties [2]. These landslide events occurred in hill cutting areas that are characterized by high angles/slopes. Slope failure in these fragile hilly areas occurs during the rainy season between the months of June and September. It is important to note that the population in Chittagong

has increased six times in number since 1974, creating a significant number of people that live in highly vulnerable areas (Figure 2).

Figure 2. Landslide vulnerability in different areas of Chittagong (map and photo) (Source: Field visit, October 2018).

Chittagong lies along the western margin of the tectonically active Chittagong-Tripura Fold Belt. The district is located between 20′35°N and 22′59° N latitude, and 91′27° E and 92′22° E longitude (Figure 3). Hills in the district are mainly composed of weathered and loose sedimentary rocks of tertiary (65–1.8 Ma) age, which are prone to landslides. The mean monthly maximum and minimum temperatures range between 78.76–90.44° F and 55.88–77.38° F, and the monthly average minimum rainfall is 0.66 mm in the month of January and maximum rainfall 74.70 mm in the month of July. The average rainfall per year is about 2794 mm [21]. The northwestern and monsoon clouds are primarily responsible for the rainfall in the area and almost 90% of the total yearly precipitation takes place between the months of June and October [21]. The total area of Chittagong City Corporation is about 170.41 km^2. The urban population of the Chittagong district was only 0.90 million in 1974 which increased to 5.13 million in 2021, representing an approximate increase of six times of the urban population in the last 47 years [21].

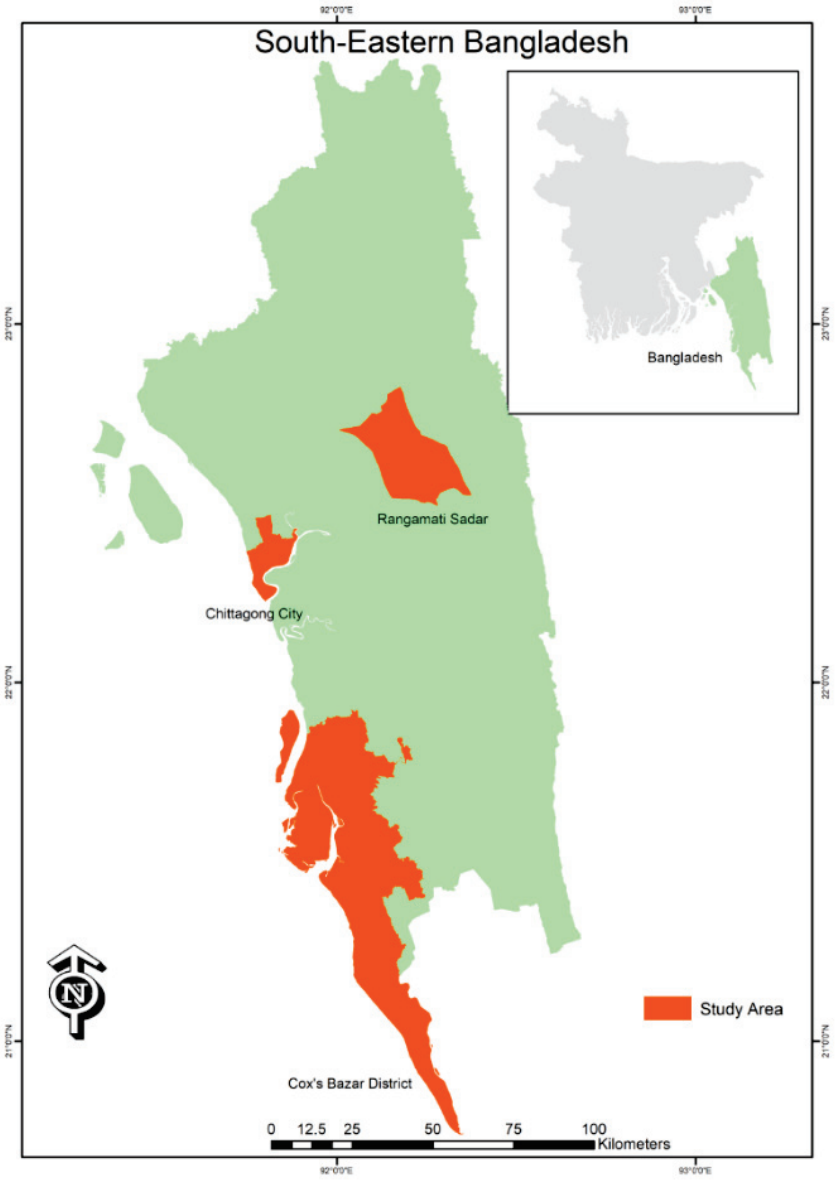

Figure 3. Location of SE Bangladesh, particularly the landslide susceptible areas in the Chittagong, Rangamati, and Cox's Bazar districts.

2.2. Obtaining and Preparing the Data

Data can be sourced from one or more sources and these sources can be multiple, ranging from online databases, websites, excel files, flat files, web-based application programming interfaces (APIs), or even PDF files. After identifying the data sources, the data was obtained with integration tools like SQL Server Integration Services (SSIS), Power BI Query Editor, Oracle Data Integrator, Tibco Pervasive Integration, etc. These data integration tools facilitate the export, transform, load (ETL) process, which obtains data from many different sources and forms them into a data warehouse, whereas specialized programming languages like the Mashup (M) language is used for data transformations and data cleansing.

Data transformation and data cleansing can be referred to as "data preparation", since data needs to first be transformed into the right format before the data is modelled or analyzed. For our research, we obtained publicly available data directly from PDF files [22] and then we transformed the data into a suitable format that allowed for faster analysis. Following data transformation, the feature attributes of the CMA landslide data can be better understood after completing data preparation. Table 1 shows the detailed statistics

of the CMA landslide data. Understanding the statistics for the CMA landslide feature attribute details is crucial before proceeding to the next steps of the methodology, namely modelling the data, visualizing the data, and analyzing the data with AI.

Table 1. Landslide attribute, data type, and data distribution.

Type of Attribute	Data Type	Attribute Distribution	Other Attribute Details
ID	Integer	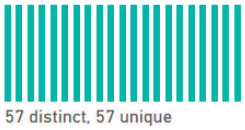	57 Distinct, 57 Unique Value Example: Ranges from 1 to 57
Latitude	Decimal	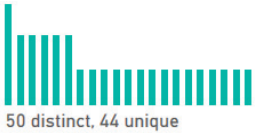	50 Distinct, 44 Unique
Longitude	Decimal		54 Distinct, 51 Unique
Elevation	Decimal	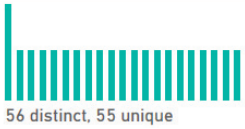	56 Distinct, 55 Unique
Date	Date (dd-mm-yyyy)		6 Distinct, 0 Unique, 34 Empty 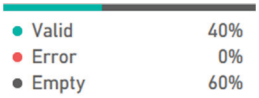
Hill Name	Text	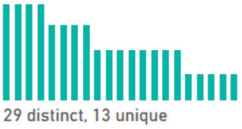	29 Distinct, 13 Unique Value Example: Lebu Bagan, Ctg. University, Foy'z Lake Zoo Hill, Medical Hill, Tankir Pahar, Sekandar Para, etc.
Area of Mass	Decimal		56 Distinct, 55 Unique
Types	Text		3 Distinct, 0 Unique Value Example: Slide, Fall, Topple
State	Text		4 Distinct, 0 Unique Value Example: Active, Stabilized, Dormant, Reactivated
Style	Text		2 Distinct, 0 Unique Value Example: Single, Successive

Table 1. *Cont.*

Type of Attribute	Data Type	Attribute Distribution	Other Attribute Details
Rainfall	Integer	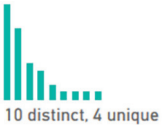	10 Distinct, 4 Unique, 18 Empty 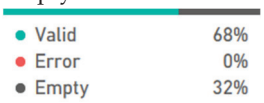
Casualty	Integer		12 Distinct, 8 Unique

2.3. Modelling the Data

Data modelling is the most important stage in the process of generating data-driven insights and when it is done correctly, an AI-driven solution can produce powerful insights with minimum delay. During this stage, relationships among different sets of data are drawn with the right cardinality.

As seen in Figure 4, the data obtained for this paper were arranged in a star schema [23], where the main factual data resides in the center (referred to as landslide DB). Surrounding the fact tables, there are dimension tables that include: types, state, date, hill name, and style. This arrangement of star schema allows for the control of the fact table (i.e., Landslide DB) with one-way filtering of information by type, state, date, and hill name as well as style. The main benefit of the star schema technique over other data modelling techniques (e.g., flattened table, snowflake, etc.) is the speed, since it provides more accurate results during data analysis [24].

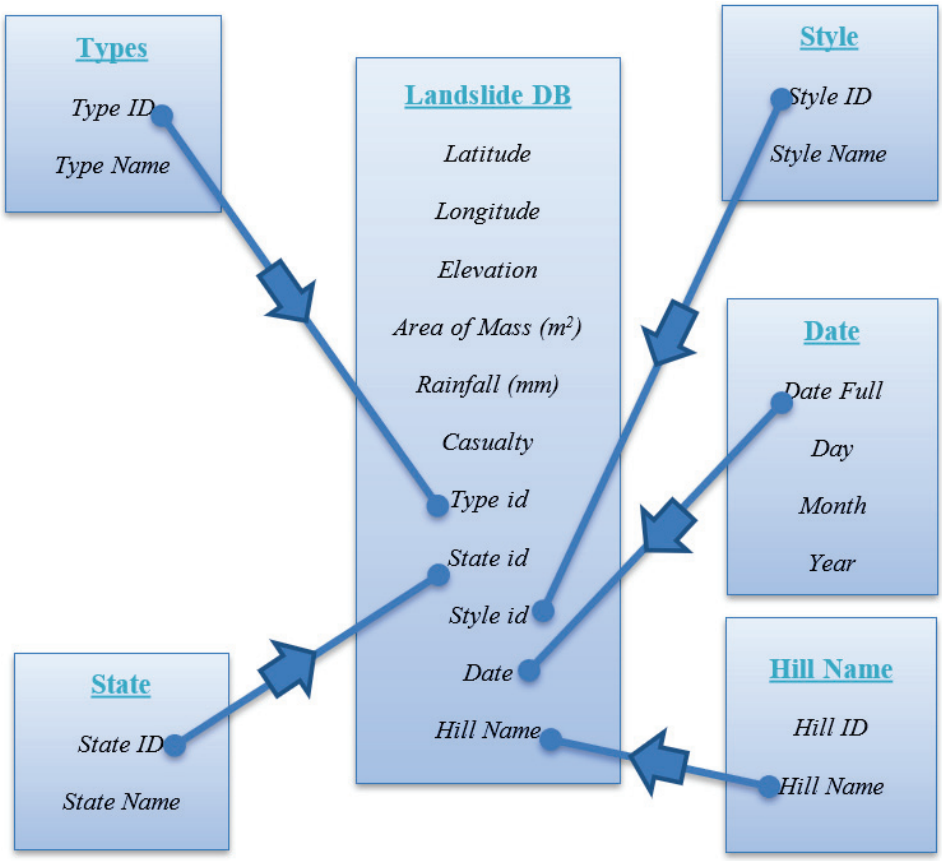

Figure 4. Data modelling of the CMA landslide database.

2.4. Visualizing the Data

Once the data modelling was completed, we used state, rainfall (mm), elevation (m), and type information to filter the factual data that drives the AI-based insights. A wide range of visualizations like slicer, Bing Maps, and key influencers were used. Changing the values for each of the filters (e.g., state to dormant or stabilized), filters the fact table landslide DB, which in turn changes the key influences (Figure 5).

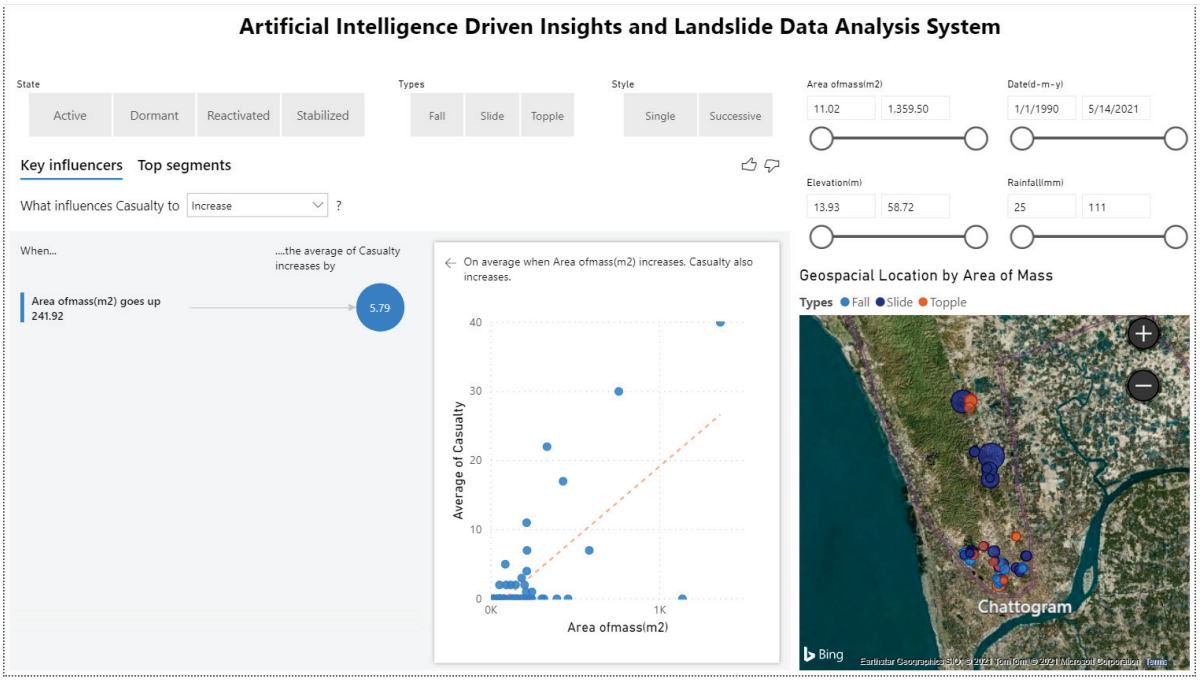

Figure 5. AI-based insights and landslide analysis system.

2.5. Analyzing Data with AI

This paper focused on automatically identifying the relationships that may exist between an outcome variable (i.e., landslide related casualty) with a range of other variables (e.g., rainfall, area of mass, elevation, etc.). Therefore, we used a particular AI-based regression tool called the key influencers visualization (i.e., https://learn.microsoft.com/en-us/power-bi/visuals/power-bi-visualization-influencers?tabs=powerbi-desktop, accessed on 20 December 2022). There are many other AI-based as well as non-AI-based statistical techniques that may suit other research objectives. For example, to find the similarities and dissimilarities between past landslides, AI-based automated clustering techniques could be used. Within this research, Microsoft Power BI's Key Influencer visualization was used to analyze casualties (from landslide) and they were explained by the following list of feature attributes as named below:

- Area of Mass (m^2)
- Elevation (m)
- Hill Name
- Rain fall (mm)
- State
- Style
- Types
- Date

This analysis used machine learning algorithms provided by ML.NET [25] to figure out what matters the most in driving landslide feature attributes. As seen in Figure 6, the analysis process uses the CMA landslide data, ranks the factors that matter, contrasts

the relative importance of these factors, and displays them as key influencers for both categorical and numeric metrics.

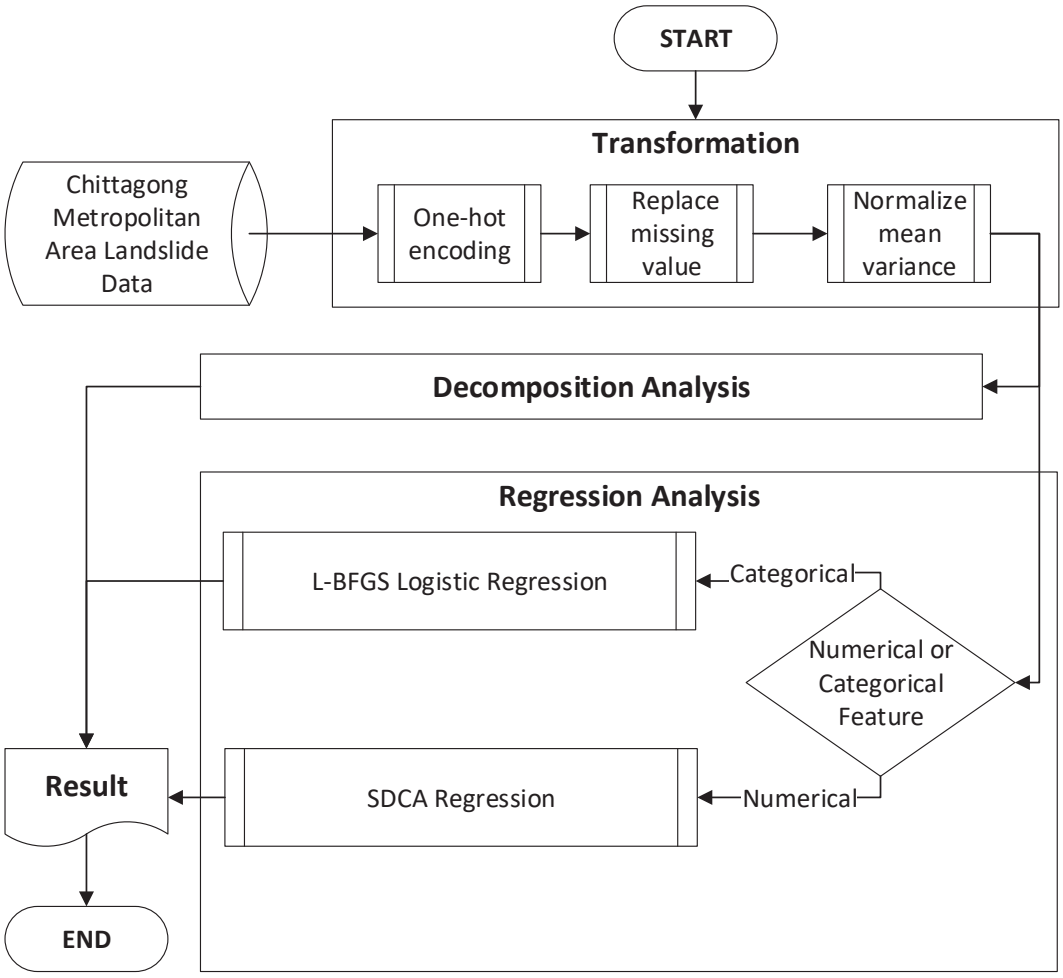

Figure 6. The process of obtaining AI insights from CMA landslide data using machine learning algorithms.

As seen in Figure 6, two main categories of AI-based statistical analysis are executed on the CMA Landslide data, namely transformation [25], decompression analysis [25], and regression analysis. Transformation analysis is executed for preparing the CMA landslide data before running the regression analysis. Within the transformation, three algorithms are executed and they include:

One-hot encoding: Calling on the OneHotEncoding() method within Microsoft.ML.Transforms class results in a conversion of categorical information into numeric values for efficient and effective processing of machine learning algorithms [25].

Replacing missing value: Calling on the ReplaceMissingValues() method within Microsoft.ML.Transforms class results in a replacement of the missing value with either default, minimum, maximum, mean, or the most frequent value [25].

Normalize mean variance: Calling on the NormalizeMeanVariance() method within Microsoft.ML.Transforms class results in an adjustment of values measured on different scales to a notionally common scale with computed mean and variance of the data [25].

Once the CMA landslide data are prepared for regression analysis, two different types of regressions are performed. For numerical features, linear regression is performed using Microsoft's ML.Net's SDCA regression implementation [19,25]. Linear regression is one of the simplest machine learning algorithms that falls under supervised learning techniques, and it is used for solving regression problems. Moreover, it is used for predicting the

continuous dependent variable with the help of independent variables. The goal of the linear regression is to find the best fit line that can accurately predict the output for the continuous dependent variable by finding the best fit line, so that the algorithm establishes the linear relationship between dependent variable and independent variable in the form of $y = b_0 + b_1 x_1 + \varepsilon$. On the other hand, for the categorical feature, logistic regression is performed using ML.Net's L-BFGS logistic regression [26]. Logistic regression is one of the most popular machine learning algorithms that falls under supervised learning techniques since it can be used for classification as well as for regression problems. Logistic regression is used to predict the categorical dependent variable with the help of independent variables using $\log\left[\frac{y}{1-y}\right] = b_0 + b_1 x_1 + b_2 x_2 + \ldots b_n x_n$. As seen in Figure 6, depending on the variable type (i.e., categorical or numerical), either logistic or linear regression is selected.

Other than using linear regression and logistic regression, this study also used decomposition analysis with a decomposition tree. Decomposition tree visualization is a valuable tool for ad hoc exploration and for conducting root cause analysis, whilst allowing the user to visualize the data across multiple filter attributes or dimensions.

Our implementation of decomposition analysis allows for the visualization of landslide casualty data over a range of landslide feature attributes, namely: area of mass, elevation, rainfall, state, and types. As shown in Figure 7, interactive root cause analysis and data exploration were supported by the aggregation of data and drill-down, where a user can click and find out what feature attribute causes the highest or lowest number of casualties.

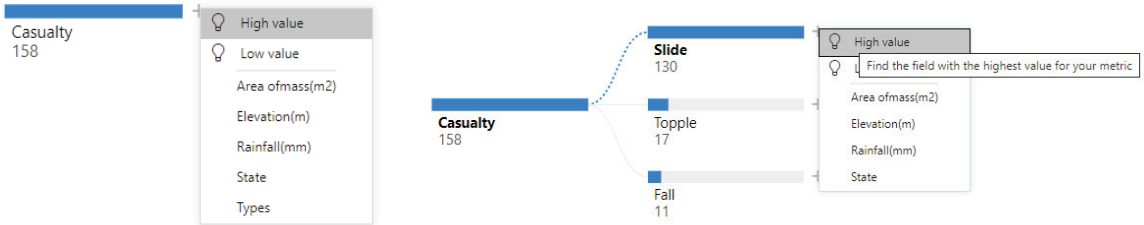

Figure 7. Decomposition tree visualization allows the user to perform interactive analysis by area of mass, elevation, rainfall, state, and types.

For feature attributes (i.e., area of mass, elevation, rainfall, state, type, date, etc.), $T = \{T^1, T^2, T^3, \ldots, T^N\}$, where N is the number of total filter attributes within a dataset (i.e., the cardinality of T, $|T| = N$), each feature attribute can form one or many filtered conditions, as follows:

$$T^1 = \left\{T_1^1, T_2^1, T_3^1, \ldots, T_P^1\right), \; such\ that \left|T^1\right| = P \tag{1}$$

$$T^2 = \left\{T_1^2, T_2^2, T_3^2, \ldots, T_Q^2\right), \; such\ that \left|T^2\right| = Q \tag{2}$$

$$T^3 = \left\{T_1^3, T_2^3, T_3^3, \ldots, T_U^3\right), \; such\ that \left|T^3\right| = U \tag{3}$$

$$T^N = \left\{T_1^N, T_2^N, T_3^N, \ldots, T_N^3\right), \; such\ that \left|T^3\right| = V \tag{4}$$

Each of these filter conditions can filter r number of rows, $r \in \{1, 2, 3, \ldots R\}$ from the dataset. Proceeding with this context, we defined casualty count from landslides as Equation (5).

$$C_i^n = \sum_{i=0}^{r} (casulty\_count), \; Where, \; r \; is \; the \; rows \; effected \; by \; filter \; attribute \; condition \; T_i^n \tag{5}$$

Our decomposition tree visualization (supported by AI) allows the user to find the next filter attribute condition to drill down into, based on either high or low values.

High Value: This mode considers all available filter attribute conditions and determines which one to drill into to obtain the highest value of the measure being analyzed. Therefore, the high-value AI split mode finds the most influential filter attribute condition T_i^n, for which the highest level of casualties occur, which is represented by

$$\exists T_i^n \subseteq T | \; C_i^n > C_j^m, \; \forall n, m \subseteq \{1, 2, 3, \ldots, N\} \wedge \forall i, j \subseteq \{1, 2, 3, \ldots\} \tag{6}$$

Low Value: This mode considers all available filter attribute conditions and determines which one to drill into to obtain the lowest value of the measure being analyzed. Therefore, the low-value AI split mode finds the most influential filter attribute condition T_i^n, for which the lowest level of casualties occur, which is represented by

$$\exists T_i^n \subseteq T \Big| \; C_i^n < C_j^m, \; \forall n, m \subseteq \{1, 2, 3, \ldots, N\} \wedge \forall i, j \subseteq \{1, 2, 3, \ldots\} \tag{7}$$

In this way, the AI split allows the user to understand the details of the root cause. This AI split-based decomposition analysis was used in our most recent study on knowledge discovery for landslides globally.

2.6. Generating Data-Driven Insights

In this phase, valuable insights are produced. The success of this phase depends on the success of previous activities such as preparation (i.e., transformation and cleaning) of the data, selection of the right AI visualization, and most importantly data modelling. Following the employment of the AI-based key influencers visualization, the key factor that influences the number of casualties was area of mass (m^2). The other factor that influences the number of casualties under specific conditions was elevation (m). Data-driven insights are generated by configuring one or more scenarios. A scenario can easily be created using our system either by clicking the desired buttons shown in Figure 8 or by changing the sliders as shown in Figure 8. In our system, we have created scenarios (S) from 7 different attributes namely, types (T^1), state (T^2), style (T^3), elevation (T^4), area of mass (T^5), rainfall (T^6), and date (T^7) as parameters. Therefore,

$$S = [x, y, z, m, n, p, q \mid x \subseteq T^1, y \subseteq T^2, z \subseteq T^3, m \subseteq T^4, n \subseteq T^5, p \subseteq T^6, q \subseteq T^7] \tag{8}$$

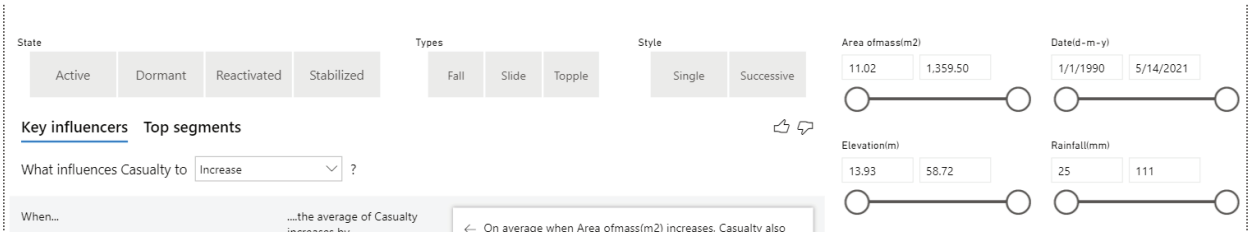

Figure 8. Filter area for the selection of landslide attributes.

Equation (9) to Equation (15) provide the unique values obtained from our dataset for each of the landslide parameters. For example, as seen from Equation (9), possible values for types (T^1) were "slide", "fall", or "topple". Similarly, the possible values for state (T^2) were "active", "stabilized", "dormant", or "reactivated" as seen from Equation (10). On the other hand, style (T^3) had only two unique values (i.e., single and successive) as it appears from Equation (11).

$$T^1 = \{Slide, Fall, Topple\} \tag{9}$$

$$T^2 = \{Active, Stabilized, Dormant, Reactivated\} \tag{10}$$

$$T^3 = \{Single, Successive\} \tag{11}$$

$$T^4 = \{\ 13.93, 15.11, 15.93, 18.1, 18.1, 19.33, 19.84, 21.31, 21.59, 22.64, 23.12, 23.5, 24.71, 26.57, 26.98, 27, 28.41, 29.28, 30.82, 31.66, 32.39, 32.44, 32.56, 34.21, 34.63, 35, 35.18, 36.68, 37.54, 37.64, 37.92, 38.51, 38.64, 39.81, 40.19, 40.68, 41.18, 41.22, 44.26, 44.46, 45.12, 45.36, 45.42, 45.69, 46.07, 46.4, 46.51, 47.04, 48.36, 48.51, 48.67, 50.12, 51.79, 55.03, 55.95, 56.36, 58.72\} \quad (12)$$

$$T^5 = \{\ 11.02, 15.03, 16.5, 31.67, 33, 45.86, 47.04, 50.17, 50.26, 52.3, 56.05, 59.1, 71.93, 71.93, 75.88, 76.43, 77.81, 84.56, 89.91, 105.38, 116.32, 118.34, 126.7, 130.32, 136, 145.06, 145.5, 152.79, 153.55, 157.07, 175.81, 181.7, 184.13, 188.59, 191.64, 198.89, 208.57, 209.12, 211.06, 211.61, 212.7, 213.26, 226.23, 232.52, 233.06, 241.79, 242.53, 301.06, 313.42, 331.84, 390.34, 427.04, 456.7, 582.27, 757.61, 1134.77, 1359.5\} \quad (13)$$

$$T^6 = \{\emptyset, 25, 26, 46, 50, 54, 55, 77, 88, 111\} \quad (14)$$

$$T^7 = \{\emptyset, 11/6/2007, 1/1/1990, 1/7/2011, 3/8/2005, 5/14/2021\} \quad (15)$$

Equations (14) and (15) contains null values represented by ∅.

To calculate the number of possible scenarios, we first need to calculate the possible filter options for each of the feature attributes. For example, as it appears from Equation (8), the type attribute could have the following filter options:

{}
{*Fall*}
{*Topple*}
{*Slide*, *Fall*}
{*Fall*, *Topple*}
{*Slide*, *Topple*}
{*Slide*, *Fall*, *Topple*}

Therefore, for the type attribute, there could be 7 possible filter settings as represented by $(2^{|T^1|} - 1)$, and the formula to calculate a power set of type attribute minus 1 (i.e., $P(T^1) - 1$). The number 1 is deducted since the power set also includes empty set and the selection of empty set is not a supported option by the system presented.

Hence, the total number of possible scenarios can be calculated as,

$$|S| = (2^{|T^1|} - 1) \times (2^{|T^2|} - 1) \times (2^{|T^3|} - 1) \times (2^{|T^4|} - 1) \times (2^{|T^5|} - 1) \times (2^{|T^6|} - 1) \times (2^{|T^7|} - 1) = 1.054 \times 10^{41} \quad (16)$$

The purpose of this section is not only to produce an exhaustive list of insights from the landslide data, but also to demonstrate the ability of the designed AI solution for producing insights on any scenario out of the 1.054×10^{41} possible scenarios (as shown in Equation (16)). In the next section we will explore results (i.e., AI insights obtained from a few of these scenarios).

3. Results

This study was reported based on two different AI-based techniques namely: automated regression analysis and decomposition analysis. Therefore, within the results section we will briefly describe AI insights derived from both methodologies. Table 2 demonstrates the outcome of conducting regression analysis on various scenarios. Seven rows of Table 2 represent five different scenarios since row 3 and row 4 represent the same scenario and row 5 and row 6 represent another single scenario. Table 2 has three columns representing the AI-based insight, the results obtained through the system interface, and the scenario condition. Row 5 and row 7 of Table 2 has the following scenario condition (i.e., both belong to the same scenario):

1. State = *"Stabilized"*,
2. Type = *All*,
3. Style = *All*,

4. Area of Mass = *All*,
5. Date = *All*,
6. Elevation = $\{p \mid 29.05 \leq p \leq 58.72\}$,
7. Rainfall = $\{n \mid 43 \leq n \leq 111\}$

Table 2. Ai insights generated on specific scenarios.

AI Insight	AI-Based System Settings	Scenario
1. When area of mass goes up 241.92, the average of causalities increases by 5.79	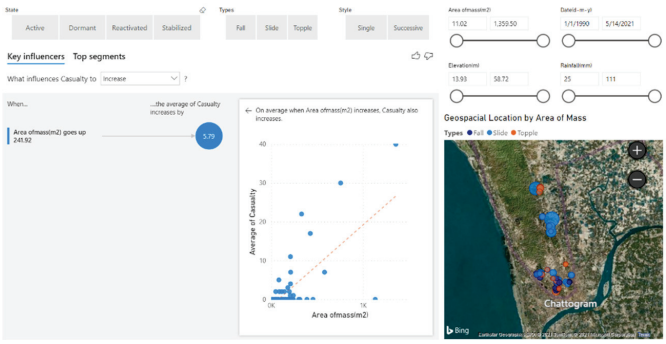	State = *All*, Type = *All*, Style = *All*, Area of Mass = *All*, Date = *All*, Elevation = *All*, Rainfall = *All*
2. When area of mass (m^2) goes up 539.49, the average of causalities increases by 15.97	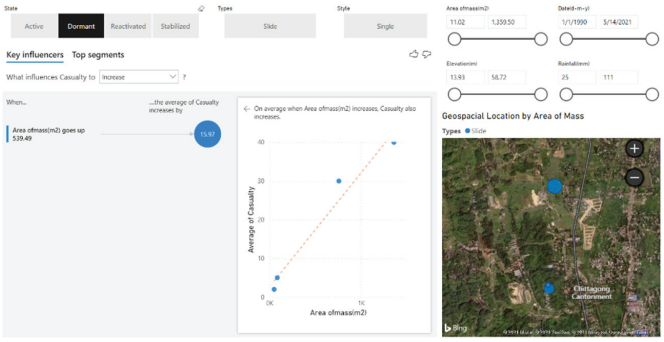	State = *"Dormant"*, Type = *All*, Style = *All*, Area of Mass = *All*, Date = *All*, Elevation = *All*, Rainfall = *All*
3. When area of mass (m^2) goes up 137.08, the average of causalities increases by 1.53	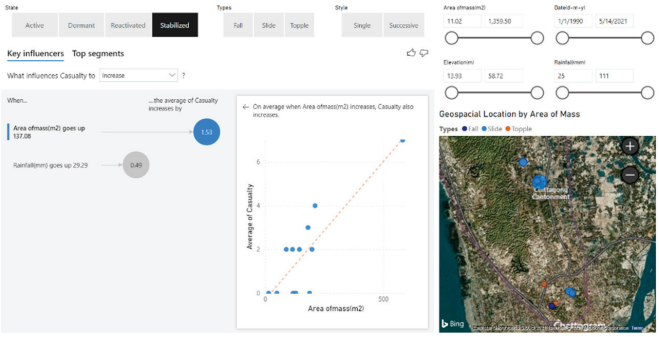	State = *"Stabilized"*, Type = *All*, Style = *All*, Area of Mass = *All*, Date = *All*, Elevation = *All*, Rainfall = *All*
4. When rainfall (mm) goes up 29.29, the average of causalities increases by 0.49	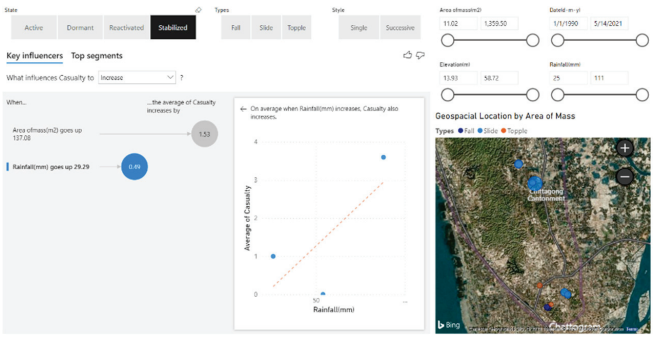	State = *"Stabilized"*, Type = *All*, Style = *All*, Area of Mass = *All*, Date = *All*, Elevation = *All*, Rainfall = *All*

Table 2. *Cont.*

AI Insight	AI-Based System Settings	Scenario
5. When area of mass (m^2) goes up 71.31, the average of casualties increases by 0.69	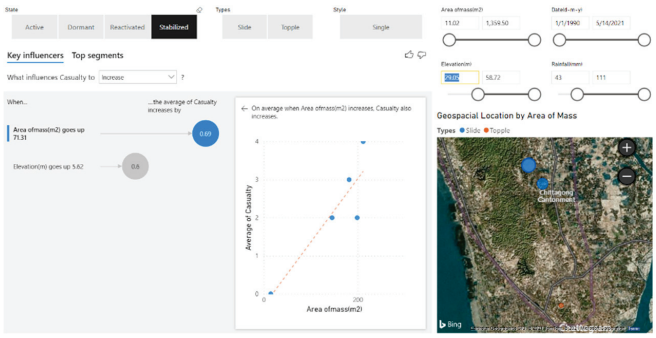	State = *"Stabilized"*, Type = *All*, Style = *All*, Area of Mass = *All*, Date = *All*, Elevation = $\{p \mid 29.05 \leq p \leq 58.72\}$, Rainfall = $\{n \mid 43 \leq n \leq 111\}$
6. When elevation (m) goes up 5.62, the average of casualties increases by 0.6	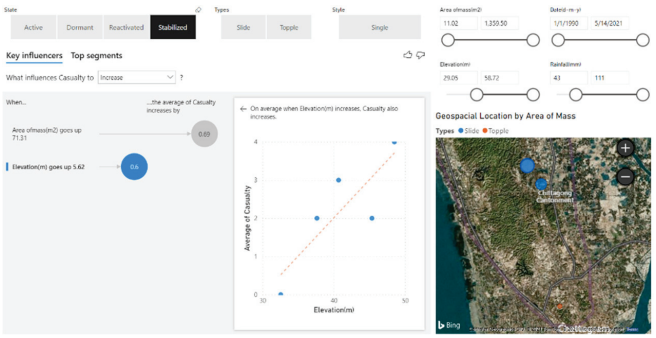	State = *"Stabilized"*, Type = *All*, Style = *All*, Area of Mass = *All*, Date = *All*, Elevation = $\{p \mid 29.05 \leq p \leq 58.72\}$, Rainfall = $\{n \mid 43 \leq n \leq 111\}$
7. When, area of mass goes up 149.35, the average of casualties increases by 1.76	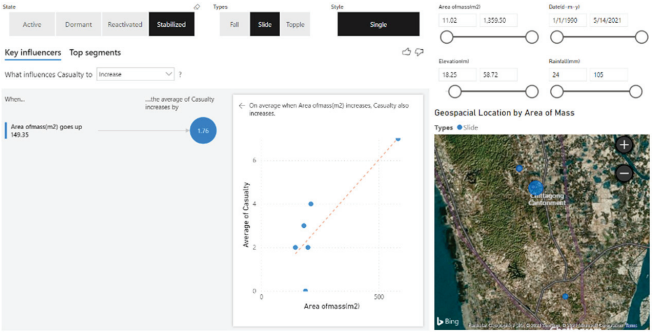	State = *"Stabilized"*, Type = *"Slide"*, Style = *"Single"*, Area of Mass = *All*, Date = *All*, Elevation = $\{p \mid 18.25 \leq p \leq 58.72\}$, Rainfall = $\{n \mid 24 \leq n \leq 105\}$

The above scenario conditions can be located in the scenario column of Table 2.

Once the above scenario was configured using the software interface (as shown previously in Figure 8), the AI insight dynamically executed the regression analysis and described the following insights into plain English:

When Area of Mass (m^2) goes up 71.31, the average of Casualty increases by 0.69

When Elevation (m) goes up 5.62, the average of Casualty increases by 0.6

In other words, for the selected scenario, casualties are positively correlated with both elevation and area of mass. The system dynamically calculated the coefficients of the positive correlation as soon as the user configured the scenario. Hence, the user of the system does not need to know the complexity of ML algorithms, and the user does not need to understand when to use linear regression and when to use logistic regression. The proposed interactive system executes the right regression depending on the configured scenario of the user. A strategic decision maker can obtain the AI insight in plain English and make appropriate decisions based on the AI insight.

The purpose of this section is not just to generate an exhaustive list of AI insights for all 1.054×10^{41} possible scenarios. The rest of the Table 2 demonstrates some other AI insights generated by 4 other scenarios to demonstrate the applicability of the system.

Both Figures 9 and 10 show insights generated through decomposition analysis. Firstly, in Figure 9, a user selected the entire range of data using the option box and sliders at the top of the figure. Then, the user selected "High Value" (as shown previously in Figure 7) to find out what caused the highest number of casualties. Immediately after selection, the system showed the user that when type is "slide" casualty is highest. The system also provides visual cues to the user showing type = slide caused 130 casualties out of total 158 casualties. Hence, the user can confidently perform root cause analysis without any knowledge of underlying statistical methods. Furthermore, the user can select "High Value" again (as shown previously in Figure 7), and find out that when rainfall is 88, the number of casualties is at its peak (i.e., Figure 9 shows when rainfall is 88, there were 98 casualties). Similarly, the user can continue drilling down into further root causes to find out all of the features and the corresponding feature values that caused the highest number of recorded casualties. Following from a condition like "type is slide" and "rainfall is 88", Figure 9 shows the other feature conditions that caused the highest number of casualties, namely: "state is dormant", "area of mass is 1269.5", and "elevation is 46.07". Therefore, Figure 9 shows an interactive tool for discovering hidden insights into what caused the highest number of casualties.

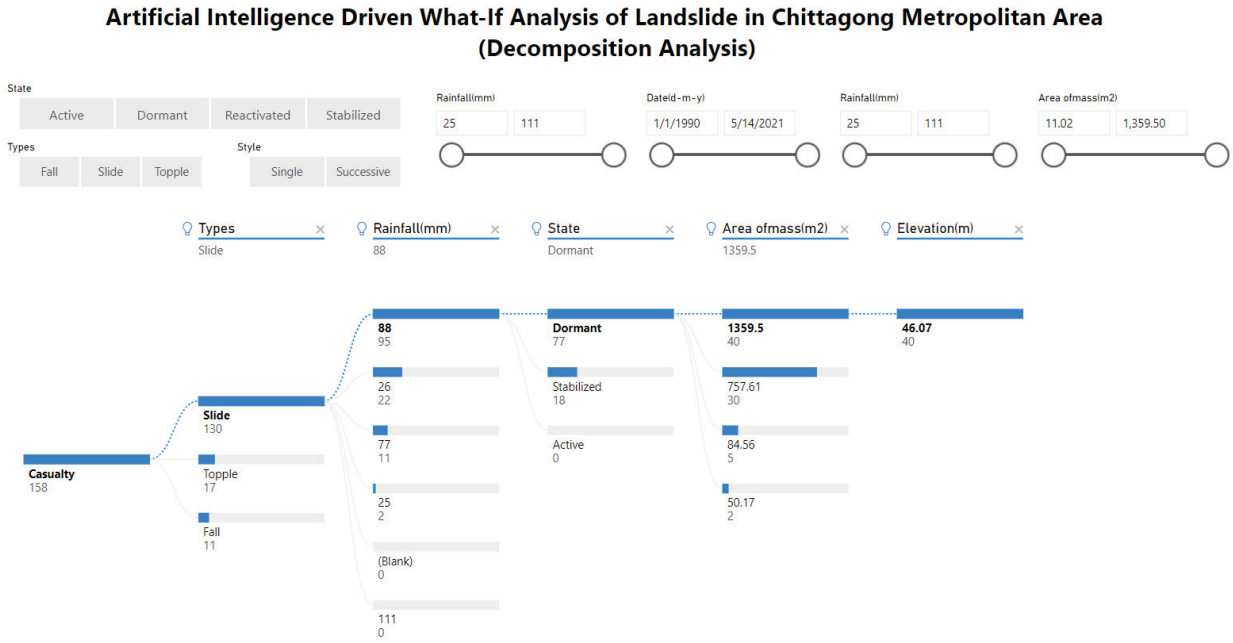

Figure 9. Decomposition analysis showing what causes the most casualties.

Using the decomposition tree visualization, the user can also find out what causes the lowest number of casualties and to find out how a particular feature effects the number of casualties. For example, Figure 10 shows what caused the highest casualties when types= "Topple". As depicted in Figure 9, the highest number of casualties (for types= "Topple") was found to be state = active (i.e., most important factor) and area of mass= 427.04 (m^2) (i.e., second most important factor), elevation = 31.66 (m) (i.e., third most important factor), and Rainfall = 55 (mm) (i.e., least important factor).

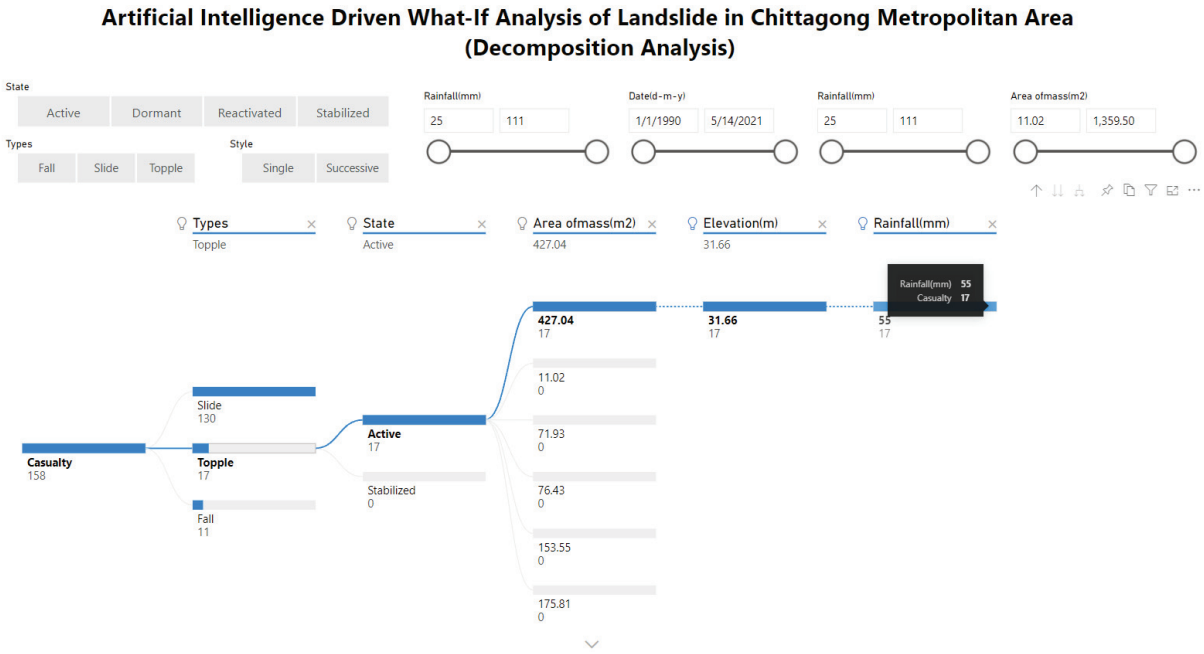

Figure 10. Decompression analysis showing what caused the highest casualties when types= "Topple".

It is crucial to highlight the fact that the proposed system is robust enough to provide critical insights from the underlying data on any number of scenarios as shown in Table 2, Figure 9, and Figure 10 using regression analysis and decompression analysis.

4. Discussion

Since all of the existing studies in landslide research do not support mobile app-based AI insight [1–28], it is not possible for a strategic decision maker to obtain instant insights if he or she is only equipped with mobile phone. In this study, we have deployed the proposed solution in desktop, tablet, and even mobile environments since the strategic decision maker can be eager to find out AI-based insights when they are remotely located at a possible landslide incident. As shown in Figure 11a, the AI-based auto-regression was executed on a Samsung Note 10 mobile phone. Figure 11b shows the decomposition analysis on the user's selected scenario was executed in a mobile environment as well. Figure 11c demonstrates the solution deployed through an iOS App on an Apple iPad 9th generation, running iOS version 15.1. Figure 11d showcases the deployed Android app running on a Samsung Galaxy Tab A7, running Android 11.

To test, assess, and evaluate the proposed AI-based landslide analysis system, the fully deployed solutions were given to 12 landslide researchers, disaster strategists, and town planners. The users were primarily located in the following area using their GPS-enabled devices for obtaining location-based insights using the proposed solution:

- Colony para, the University of Chittagong
- Motijharna, Chittagong City
- Matiranga, Rangamati

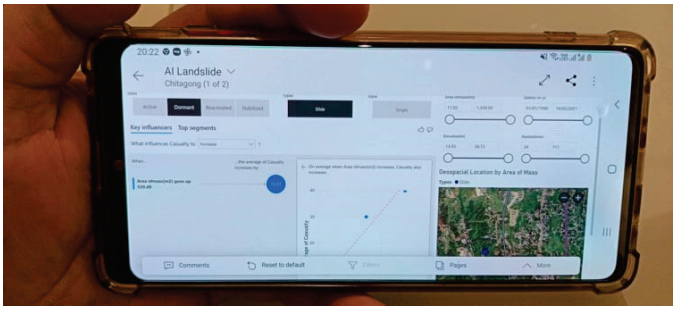

(**a**) Regression analysis on a Samsung Note 10 mobile device

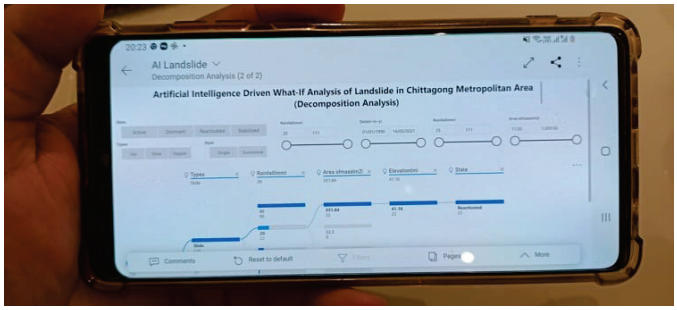

(**b**) Decompression tree analysis on a Samsung Note 10 mobile device

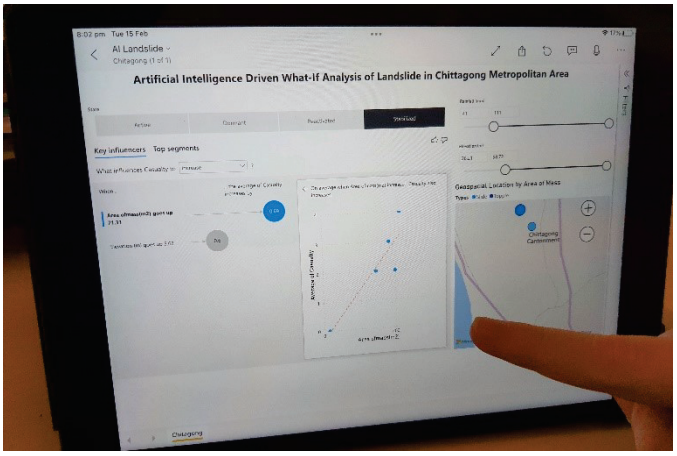

(**c**) Linear regression on an Apple iPad 9th Generation (iOS 15.1)

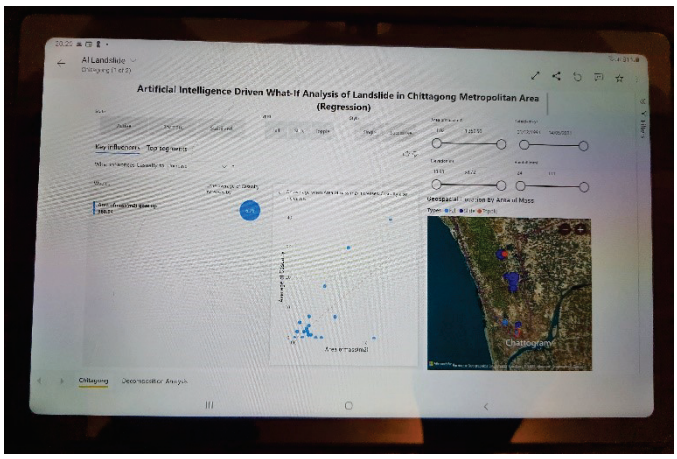

(**d**) Linear regression on a Samsung Galaxy Tab A7 (Android 11)

Figure 11. The proposed system running on mobile devices and providing AI-based insights on CMA landslides.

Table 3 shows the platform and user details for these tests and evaluations. As seen from Table 3, the proposed solution was tested on a wide range of devices, including both mobile devices and tablets. Since strategic decision makers often make their decisions on the site of the landslide or away from offices, they need mobile solutions deployed on tablets and mobile devices through iOS or Android apps. After the completion of the test and evaluation, detailed feedback regarding usability and appropriateness of the deployed solutions were obtained via Microsoft Form-based questionnaires (i.e., office 365 cloud-hosted). A total of 11 out of the 12 users (i.e., 91.67%) found the solution easy to use, effective, and self-explanatory. However, one user preferred using the solution in his desktop computer through the cloud-based interface.

Table 3. Details for deployment platforms and users.

Number of Users	Device Name	OS Version
2	Samsung Note 10 Lite (Mobile)	Android 11
1	Samsung Note 10 Lite (Mobile)	Android 12
2	Samsung Galaxy Tab A7 (Tablet)	Android 11
2	iPhone 13 (Mobile)	iOS 15
1	iPhone 12 (Mobile)	iOS 14
2	iPad 9th Generation (Tablet)	iOS 15.2
2	iPad Mini 6 (Tablet)	iOS 15

Hence, this mobile-based AI insight system provides a robust and innovative solution for the strategic decision maker who does not need to depend on a data scientist to conduct data modelling to obtain valuable insight. By interacting with the proposed system, a strategic decision maker can harness powerful ML algorithms automatically and obtain useful insights.

The process described within this paper is applicable for all different types of data on different types of scenarios to answer several different types of research questions. For example, this methodology was applied to obtain AI-driven insights on tornado-related casualties in Bangladesh [29]. Similarly, the study in [30] utilized this methodology in critically analyzing Australian cyclones. Moreover, this method could also be used to monitor disasters from any global location as demonstrated in [31,32] by analyzing live social media data. As shown in [31], AI-driven disaster intelligence solutions could be up to 97% accurate.

As it becomes apparent from these recent publications [29–33], it is first required that the dataset be cleansed and transformed. Pre-processing the available dataset with appropriate data cleansing and transformation is the key to obtaining better AI-driven insights on the casualties. Then, the Microsoft Power BI's key influencers visualization is used to analyze the outcome variable (e.g., casualties) with respect to a list of available "explain by" variables (e.g., elevation, rainfall, area of mass, longitude, latitude, number of injuries, style, types, etc.). The detailed process of using Microsoft Power BI's key influencers visualization is explained at https://learn.microsoft.com/en-us/power-bi/visuals/power-bi-visualization-influencers?tabs=powerbi-desktop, accessed on 20 December 2023. The machine learning (ML)-based feature analysis (e.g., linear regression or logistic regression) depends on the availability of many feature attributes for understanding their correlations to the outcome variable. In this study, casualty was deemed as an outcome variable, since strategic decision makers are always keen on saving precious lives resulting from landslides. Within our dataset, we only had few available features to analyze (e.g., latitude, longitude, elevation, area of mass, rainfall, etc.). After applying our innovative method, our solution found a positive correlation of casualty with area of mass (as shown in Figure 5, Row 1 of Table 2, Row 2 of Table 2, Row 3 of Table 2, Row 4 of Table 2, Row 5 of Table 2, Row 6 of Table 2, Row 7 of Table 2), rainfall (as shown in Row 3 of Table 2, Row 4 of Table 2), and elevation (as shown in Row 5 of Table 2, Row 6 of Table 2). Even though we utilized all of the available features present within our dataset to obtain relationships with the observed variable (i.e., casualty), we considered appropriate data cleansing prior to the automated ML process. As a result of the cleansing process, elevation and area of mass turned out to be a decimal data type and rainfall turned out to be integer data types.

5. User Notes

The ML-based knowledge discovery solution presented in this study was implemented using Microsoft Power BI, which is freely available for download from https://app.powerbi.com/, accessed on 20 December 2023. The user can download the complete source files (.pbix), along with the CMA landslide data (.csv) files from the author's GitHub site (i.e., https://github.com/DrSufi/landslide, accessed on 20 December 2023). After downloading and opening the entire solution using MS Power BI Desktop, the user can host the solution on either the Microsoft Cloud or within a local network to make it available to other researchers or strategic planners.

The typical users of this system are strategic disaster planners, disaster risk assessors, policymakers, and disaster strategists who are concerned with landslides or landfalls and their subtle impact on society, groups, and locations. This system would allow users to understand the characteristics of global events in a particular area since it provides useful guidance for policy implementation.

6. Conclusions

This paper provides a detailed methodological framework for generating AI-based insights on landslides in the CMA. This experimentation was performed on a limited dataset containing only 57 records. Sadly, there were several limitations due to the relatively small dataset in terms of empty values within date and rainfall attributes. As is evident from Table 1, the date attribute has 34 empty values (i.e., 40% valid and 60% empty values) and rainfall has 18 empty values (i.e., 68% valid and 32% empty).

AI-based automated insight generation processes as depicted in this research are often referred to as data-driven insights. For data-driven insights, having a robust and complete set of data is often a mandate. In case the data suffers from irregular/missing values (or any other data quality issues hampering the overall quality of the dataset) then several pre-processing techniques (e.g., StandardScaler, MinMaxScaler, StandardScaler, OneHotEncoder, etc.) could enhance the performance of data-driven insight solutions. Despite these limitations on available information, the AI-based techniques like automated regressions (both linear and logistic) as well as a decomposition algorithm successfully derived useful insights for the strategic decision maker.

In the future, we will endeavor to work with more records of landslides outside of the CMA region. Using these large-scale records, we hope to deploy more sophisticated AI-based techniques like convolution neural network (CNN)-based deep learning to generate useful insights (since our recent study in [30–32] has demonstrated that applying CNN on disaster monitoring harnesses better results). Other than CNN, we also want to use sophisticated AI-based techniques as demonstrated in our recent and past studies [29–34].

Author Contributions: Conceptualization, E.A. and F.S.; methodology, F.S. and E.A.; A.R.M.T.I.; validation, F.S., E.A. and A.R.M.T.I.; resources, E.A.; data curation, F.S.; writing—original draft preparation, E.A. and F.S.; writing—review and editing, E.A., A.R.M.T.I. and F.S.; visualization, F.S.; supervision, E.A. All authors have read and agreed to the published version of the manuscript.

Funding: This research received no external funding.

Institutional Review Board Statement: Not applicable.

Informed Consent Statement: Not applicable.

Data Availability Statement: Data are available upon request.

Acknowledgments: Support received for data collection from the Bangladesh from Disaster Action and Development Organisation (DADO) is highly appreciated. Funding support for article processing charges (APCs) from the Rabdan Academy is greatly appreciated.

Conflicts of Interest: The authors declare no conflict of interest.

References

1. Rabby, Y.W.; Li, Y. Landslide Inventory (2001–2017) of Chittagong Hilly Areas, Bangladesh. *Data* **2020**, *5*, 4. [CrossRef]
2. Alam, E. Landslide Hazard Knowledge, Risk Perception and Preparedness in Southeast Bangladesh. *Sustainability* **2020**, *12*, 6305. [CrossRef]
3. Ahmed, B. The root causes of landslide vulnerability in Bangladesh. *Landslides* **2021**, *18*, 1707–1720. [CrossRef]
4. Alam, E.; Ray-Bennett, N.S. Disaster risk governance for district-level landslide risk management in Bangladesh. *Int. J. Disaster Risk Reduct.* **2021**, *59*, 102220. [CrossRef]
5. Sultana, N. Analysis of landslide-induced fatalities and injuries in Bangladesh: 2000–2018. *Cogent Soc. Sci.* **2020**, *6*, 1737402. [CrossRef]
6. Lin, L.; Lin, Q.; Wang, Y. Landslide susceptibility mapping on a global scale using the method of logistic regression. *Nat. Hazards Earth Syst. Sci.* **2017**, *17*, 1411–1424. [CrossRef]
7. Stanley, T.; Kirschbaum, D.B. A heuristic approach to global landslide susceptibility mapping. *Nat. Hazards* **2017**, *87*, 145–164. [CrossRef]
8. Lissak, C.; Bartsch, A.; De Michele, M.; Gomez, C.; Maquaire, O.; Raucoules, D.; Roulland, T. Remote Sensing for Assessing Landslides and Associated Hazards. *Surv. Geophys.* **2020**, *41*, 1391–1435. [CrossRef]
9. Tan, Q.; Bai, M.; Zhou, P.; Hu, J.; Qin, X. Geological hazard risk assessment of line landslide based on remotely sensed data and GIS. *Measurement* **2021**, *169*, 108370. [CrossRef]

10. Senouci, R.; Taibi, N.-E.; Teodoro, A.; Duarte, L.; Mansour, H.; Meddah, R. GIS-Based Expert Knowledge for Landslide Susceptibility Mapping (LSM): Case of Mostaganem Coast District, West of Algeria. *Sustainability* **2021**, *13*, 630. [CrossRef]
11. Mohan, A.; Singh, A.K.; Kumar, B.; Dwivedi, R. Review on remote sensing methods for landslide detection using machine and deep learning. *Trans. Emerg. Telecommun. Technol.* **2021**, *32*, e3998. [CrossRef]
12. Guzzetti, F.; Carrara, A.; Cardinali, M.; Reichenbach, P. Landslide hazard evaluation: A review of current techniques and their application in a multi-scale study, Central Italy. *Geomorphology* **1999**, *31*, 181–216. [CrossRef]
13. Duman, T.Y.; Çan, T.; Emre, Ö.; Keçer, M.; Doğan, A.; Ateş, Ş.; Durmaz, S. Landslide inventory of northwestern Anatolia, Turkey. *Eng. Geol.* **2005**, *77*, 99–114. [CrossRef]
14. Godt, J.; Baum, R.; Savage, W.; Salciarini, D.; Schulz, W.; Harp, E. Transient deterministic shallow landslide modeling: Requirements for susceptibility and hazard assessments in a GIS framework. *Eng. Geol.* **2008**, *102*, 214–226. [CrossRef]
15. Yilmaz, I. Landslide susceptibility mapping using frequency ratio, logistic regression, artificial neural networks and their comparison: A case study from Kat landslides (Tokat—Turkey). *Comput. Geosci.* **2009**, *35*, 1125–1138. [CrossRef]
16. Sendir, H.; Yilmaz, I. Structural, geomorphological and geomechanical aspects of the Koyulhisar landslides in the North Anatolian Fault Zone (Sivas, Turkey). *Environ. Geol.* **2002**, *42*, 52–60.
17. Ahmed, B. Landslide susceptibility mapping using multi-criteria evaluation techniques in Chittagong Metropolitan Area, Bangladesh. *Landslides* **2015**, *12*, 1077–1095. [CrossRef]
18. Qi, T.; Zhao, Y.; Meng, X.; Chen, G.; Dijkstra, T. AI-Based Susceptibility Analysis of Shallow Landslides Induced by Heavy Rainfall in Tianshui, China. *Remote Sens.* **2021**, *13*, 1819. [CrossRef]
19. Sufi, F.K.; Alsulami, M. Knowledge Discovery of Global Landslides Using Automated Machine Learning Algorithms. *IEEE Access* **2021**, *9*, 131400–131419. [CrossRef]
20. UN. Sendai Framework for Disaster Risk Reduction 2015–2030. *United Nations Office for Disaster Risk Reduction (UNISDR): Geneva, Switzerland*. 2015. Available online: http://www.unisdr.org/we/inform/publications/43291 (accessed on 20 November 2021).
21. BBS. *Bangladesh Population Census-2021*; Bangladesh Bureau of Statistics (BBS), Government of Bangladesh: Dhaka, Bangladesh, 2021.
22. Rahman, M.S.; Ahmed, B.; Huq, F.F.; Rahman, S.; Al-Hussaini, T.M. Landslide inventory in an urban setting in the context of Chittagong Metropolitan area, Bangladesh. In Proceedings of the 3rd International Conference on Advances in Civil Engineering, CUET, Chittagong, Bangladesh, 21–23 December 2016; pp. 170–178.
23. Microsoft Documentation. Understand Star Schema and the Importance for Power BI. Available online: https://docs.microsoft.com/en-us/power-bi/guidance/star-schema#:~:text=Star%20schema%20is%20a%20mature,and%20concepts%20including%20time%20itself (accessed on 20 November 2021).
24. Ferrai, A. The Importance of Star Schemas in Power BI. 2021. Available online: https://www.sqlbi.com/articles/the-importance-of-star-schemas-in-power-bi/ (accessed on 20 November 2021).
25. Sufi, F.K. AI-Landslide: Software for acquiring hidden insights from global landslide data using Artificial Intelligence. *Softw. Impacts* **2021**, *10*, 100177. [CrossRef]
26. Nocedal, J. Updating Quasi-Newton Matrices with Limited Storage. *Math. Comput.* **1980**, *35*, 773–782. [CrossRef]
27. Varnes, D.J. *Landslide Hazard Zonation: A Review of Principles and Practice*; Unesco: Paris, France, 1984.
28. Kavzoglu, T.; Teke, A. Predictive Performances of Ensemble Machine Learning Algorithms in Landslide Susceptibility Mapping Using Random Forest, Extreme Gradient Boosting (XGBoost) and Natural Gradient Boosting (NGBoost). *Arab. J. Sci. Eng.* **2022**, *47*, 7367–7385. [CrossRef]
29. Sufi, F.; Alam, E.; Alsulami, M. A new interactive system for analyzing historical records of tornedoes in Bangladesh. *Sustainability* **2022**, *14*, 6303. [CrossRef]
30. Sufi, F.; Alam, E.; Alsulami, M. Automated Analysis of Australian Tropical Cyclones with Regression, Clustering and Convolutional Neural Network. *Sustainability* **2022**, *14*, 9830. [CrossRef]
31. Sufi, F.; Khalil, I. Automated Disaster Monitoring from Social Media Posts using AI based Location Intelligence and Sentiment Analysis. *IEEE Trans. Comput. Soc. Syst.* **2022**, 1–11. [CrossRef]
32. Sufi, F. A decision support system for extracting artificial intelligence-driven insights from live twitter feeds on natural disasters. *Decis. Anal.* **2022**, *5*, 100130. [CrossRef]
33. Sufi, F.K.; Alsulami, M. Automated Multidimensional Analysis of Global Events with Entity Detection, Sentiment Analysis and Anomaly Detection. *IEEE Access* **2021**, *9*, 152449–152460. [CrossRef]
34. Sufi, F.K. AI-GlobalEvents: A Software for analyzing, identifying and explaining global events with Artificial Intelligence. *Softw. Impacts* **2022**, *11*, 100218. [CrossRef]

sustainability

MDPI

Article

A Spatial Model of Landslides with a Micro-Topography and Vegetation Approach for Sustainable Land Management in the Volcanic Area

Heni Masruroh [1,2,*], Soemarno Soemarno [3], Syahrul Kurniawan [3] and Amin Setyo Leksono [4]

[1] Postgraduate Program, Universitas Brawijaya, Malang 65145, Indonesia
[2] Geography Department, University of Malang, Lowokwaru 65141, Indonesia
[3] Soil Science Department, Faculty of Agriculture, Universitas Brawijaya, Malang 65145, Indonesia
[4] Biology Department, Faculty of Mathematics and Natural Science, Universitas Brawijaya, Malang 65145, Indonesia
* Correspondence: heni.masruroh.fis@um.ac.id

Abstract: This study aims to produce a spatial model for sustainable land management in landslide-prone areas, based on exploring non-stationary relationships between landslide events, geomorphological and anthropogenic variables on tropical hillsides, especially in Taji Village, Jabung District, East Java Province, Indonesia. A series of approaches combine in this research, and methods are used to construct independent and dependent variables so that GWR can analyze them to obtain the best model. Transformation of categorical data on microtopography, landform, and land cover variables was carried out. When modelled, landscape metrics can explain landslide events in the study area better than distance metrics with adj. R^2 = 0.75 and AICc = 2526.38. Generally, local coefficient maps for each variable are mapped individually to reveal their relationship with landslide events, but in this study they are integrated to make it more intuitive and less confusing. From this map, it was found that most of the variables that showed the most positive relationship to the occurrence of landslides in the study area were the divergent footslopes. At the same time, the negative one was plantation land. It was concluded that the methodological approach offered and implemented in this study provides significant output results for the spatial analysis of the interaction of landslide events with geomorphological and anthropogenic variables locally, which cannot be explained in a global regression. This study produces a detailed scale landslide-prone conservation model in tropical hill areas and can be reproduced under the same geo-environmental conditions.

Keywords: landslide; geographical regression analysis; land management

Citation: Masruroh, H.; Soemarno, S.; Kurniawan, S.; Leksono, A.S. A Spatial Model of Landslides with a Micro-Topography and Vegetation Approach for Sustainable Land Management in the Volcanic Area. *Sustainability* **2023**, *15*, 3043. https://doi.org/10.3390/su15043043

Academic Editors: Stefano Morelli, Veronica Pazzi and Mirko Francioni

Received: 9 January 2023
Revised: 1 February 2023
Accepted: 2 February 2023
Published: 7 February 2023

1. Introduction

Land degradation for several countries is one of the problems that can lead to disasters [1,2] by causing a reduction or loss of land productivity, resulting in economic losses. Based on [3] 25% of land area worldwide is degraded, and as much as 24 billion tons of fertile soil are lost every year due to degradation. Land degradation not only causes disasters, but disasters also cause land degradation, one of which is landslides.

Landslides are natural disasters that usually occur in mountainous or hilly areas. These disasters often cause extensive economic losses and yearly fatalities [4]. Indonesia is located above the confluence of three major plates, namely the Eurasian plate, the Pacific plate and the Indo-Australian plate, reflecting high tectonic activity with a tropical climate and intensive anthropogenic activity, which often causes natural disasters. According to the Indonesian Disaster Information Data, landslides are ranked 3rd (9047 incidents) after tornadoes (11,016 incidents) and floods (13,723 incidents) recorded since 1822 until now [5]. Landslide disasters in Java Island, Indonesia tend to be caused by high rainfall, which often occurs in remote hilly areas that are prone to these events [6,7]. In the vicinity of Mount Bromo, landslides occur due to precipitated volcanic material, steep slopes, and

high rainfall which often damage road accessibility [8]. Landslides caused by high rainfall are a global problem yearly [9]. Landslides in Taji Village—one of the villages in the Mount Bromo area—are caused by high-intensity rains and extreme weather (La nina), and often damage the connecting roads between villages which causes residents to be isolated, thus hindering farmer and gardening activities in the fields. In addition, the houses of affected residents have also occurred, but there were no fatalities.

In addition to high rainfall as a trigger, the phenomenon of slope instability that causes landslides can also be affected by landform conditions in terms of morphology, morphoprocess, morphochronology, and morphoarrangement [10]. In addition, geomorphological mapping in mountainous and hilly areas is the most complex type of information and the most subjective for landslide hazard assessment [11]. However, geomorphological mapping is selective because it only focuses on certain features in an area of interest with a certain scale for a particular study. The latest remote sensing techniques, namely by utilizing Unmanned Aerial Vehicles (UAV) data and Digital Terrain Models (DTM) can expand their application in geomorphological and topographical mapping for the identification and mapping of landslide hazards [12–14] in more detailed area coverage at a precise scale. In addition, recently, low-cost UAVs (more commonly called drones) have become a trend among academics, practitioners and commercial circles because they are effective in collecting large amounts of elevation data in a relatively short time, which can change the perspective and analysis by geomorphologists to study geomorphometrics and topography in certain landscapes [15,16].

One of the geomorphological features on a detailed scale is the microtopography built from the DTM. Micro-topography is defined as topographic changes on a small scale that is divided into seven units, including crest slope, upper side slope, head hollow, lower side slope, flood terrace and riverbed [17,18]. Chimner dan Hart (1996) defines microtopography into three units: hummock, pool and intermediate area. In terms of the scope of soil development, microtopography is divided into two types: pit and mound on soil morphology caused by fallen trees forming drumlin landforms [19,20]. Another definition of microtopography is the difference in size and shape in the local terrain caused by soil erosion, thus affecting the heterogeneity of habitat conditions such as moisture and soil nutrients on a scale of 1 m^2 or more [21,22] with Microtopographic types include platform, gully, sink hole, scarp and ephemeral gully [23]. Thus, the definition and type of microtopography is "variable", which adjusts to the study in a particular field. In this study, microtopography is defined as changes in local topography in terms of size and shape, as seen from differences in morphology [24,25]. Morphological mapping is based on line shape mapping, which focuses on identifying the types of slope bends using a symbology system that is unambiguous, clear, and reproducible [26]. In other words, microtopography is a reflection of its morphology.

In general, geomorphological features have a major influence on landslide events. Anthropogenic activity also plays an important role in slope instability, part of which is land cover [27,28], and even contributes positively to landslide events [29]. However, land cover and geomorphological features are closely related, allowing different spatial relationships to landslide events [30]. In addition, vegetation density can also explain the pattern of landslide occurrence, but often has an inverse relationship, namely the higher the vegetation density, the lower the landslide vulnerability [13,31].

Spatial modeling of landslide susceptibility is crucial for further understanding the assessment of disaster mitigation and preventive measures to conserve land in landslide-prone areas. Approaches for landslide hazard mapping are developing rapidly, starting from combined methods to produce the best models to emerging innovations for model updates. In general, they include the evaluation of landslide models using qualitative approaches [32], quantitatively based on the relationship of controlling factors and landslides [33], and even a combination of both [34,35]. However, the spatial interaction between landslide points and their controlling factors in the quantitative approach is not explained [35], it only relies on stationary parameter estimation to examine the relationship

between the two. One of the quantitative approaches, local regression analysis, can explain these spatial interactions in a non-stationary manner [36]. Feuillet et al.'s (2014) study examined the strength of the spatial relationship between paraglacial factors and landslide events. In addition, the authors of [29] investigated the local spatial relationship between land use change resulting from human intervention and landslide events. Research [24] also explains that different vegetation classes on different microtopography give different responses to the process of soil loss in the form of erosion. These studies prove that the occurrence of landslides has a non-stationary relationship to the predictor variable, which is at the same time better than global regression in general. However, the coverage area of the two studies is on a regional scale.

In this context, there are rarely studies that discuss the spatial relationship between landslide events and landslide control factors at a detailed scale, especially in the tropical hills of Indonesia. In fact, the spatial relationship of landslides with their controlling factors can provide information on the biggest factors causing landslides spatially. Consequently, it will be known that the arrangement of the microtography and vegetation parts that have a positive and negative effect on landslides. This information can be essential information in the management of sustainable land management.

As previously explained, drones are currently becoming a trend and are applied for specific purposes, as well as an alternative to optical satellite imagery data with very high spatial resolution that are quite expensive, and user demands are also high. Thus, this study aims to produce a detailed scale conservation model in landslide-prone areas based on exploring the local spatial relationship between landslide events and micro-topographical variables, land cover, and vegetation density at a detailed scale in a small hilly area in Taji Village, Jabung District, Province East Java, Indonesia uses the Geographically Weighted Regression (GWR) method.

2. Materials and Methods

2.1. Study Area

The study area is in the Bromo Tengger Semeru Area (Figure 1). Astronomically, it is located at 7°56′34.98′–7°57′6.1″ South Latitude and 112°48′49″–112°49′30.58″ East Longitude. The study area covers 61.2 ha with an average elevation of 1110 ± 59 masl. The topographical characteristics in the study area are hillsides that are quite steep to steep and cut by rivers to form a fairly deep valley. The use of agricultural land and plantations tends to dominate in the study area. On land that is not vegetated erosion is found to be more intensive. The geological conditions in the study area consist of lower quarter volcanic rocks (i.e., Mount Gendis) during the middle Pleistocene. The rock materials include volcanic breccias, tuff-breccias, lava, and agglomerates. In addition, areas with andesitic rock deposits, namely lava and breccia-tuff, tend to be prone to landslides [37]. The complex topography configuration, high erosion rate, and rock materials in the study area have great potential for future landslides.

2.2. Methodology

Exploration of spatial relationships locally using the GWR model between landslides and microtopographical variables, landform, land cover, and vegetation density through several stages, involved: (1) building a Digital Terrain Model (DTM) from overlapping drone photos in the study area; (2) creating imagery orthomosaic based on dense point cloud, mesh, and texture data; (3) preparing raw data in the form of orthomosaic imagery acquired from UAV drones and landslide inventory via orthomosaic; (4) orthomosaic imagery used for land cover analysis using the Geographically Object-based Image Analysis (GEOBIA) method) based on spectral features, haralick texture, and shape index, which then attribute selection is carried out for all features through WEKA software to produce optimal land cover classification; (5) individual stand identification from orthomosaic image interpretation for vegetation density analysis; (6) curvature-based landform classification by classification system Pennock uses DTM; (7) micro-topography constructed through

on-screen digitization based on elevation contour lines and the landscape appearance of the study area, which is then zoning micro-topography using the Voronoi diagram or Thiessen polygon method; (8) integrating landslide data, landform, land cover, and vegetation densityinto microtopography zoning as a spatial unit based on the value of the results of transforming categorical data into numeric (specifically for microtopography, landform, and land cover); (9) using three types of model for each variable, namely Type I model (proximity factor), Type II (Principal Component (PC) with the highest percentage of eigenvalues on the landscape metric comprehensive index), and Type III (PC on the landscape metric comprehensive index with the largest contribution using the Relief-F attribute selection method from WEKA software) prepared for GWR model fitting; and 10) local spatial relationship analysis based on the best fit GWR model with the four variables bell is modeled simultaneously. This series of stages can be simplified through the research flowchart in (Figure 2).

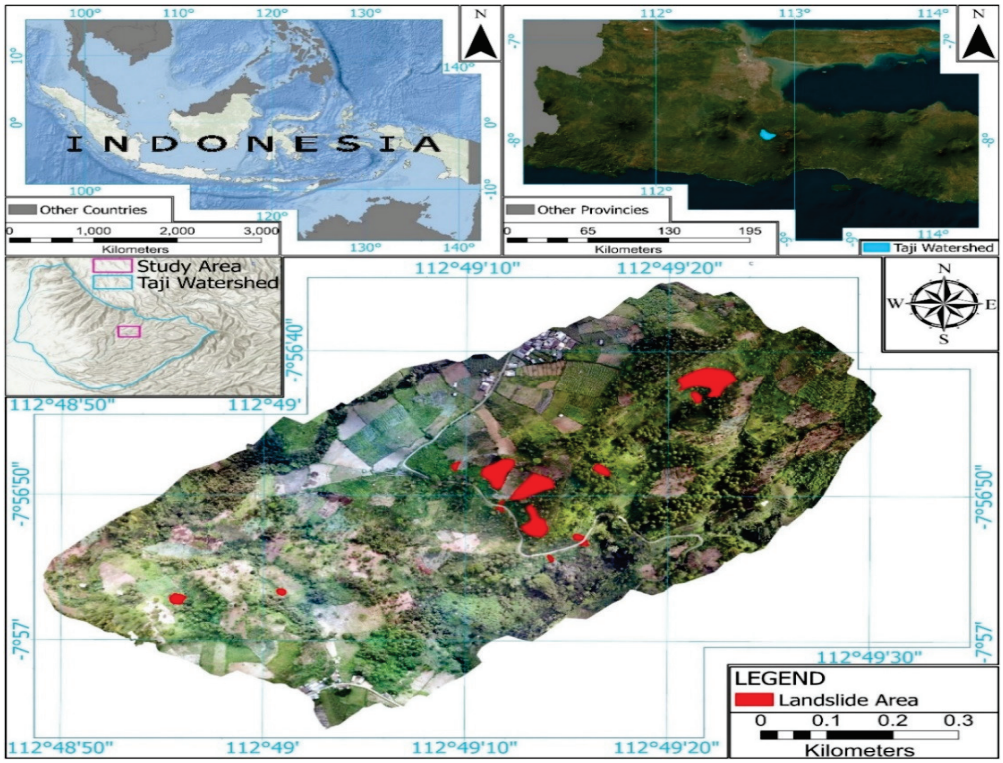

Figure 1. Location of the study area in a small part of the Taji watershed.

2.3. Data Collection and Processing

2.3.1. Orthomosaic Image and Digital Terrain Model (DTM) from Unmanned Aerial Vehicle (UAV)

Very high-resolution aerial photos were acquired through photogrammetric processing using a UAV (a multirotor-type drone, the DJI Phantom 4). The Pix4Dcapture software [38] is used for automatic flight control and aerial photo acquisition to retrieve information on surface objects in the study area. In addition, geometric correction of orthorectified images is also automatically performed in Pix4D. The mapping was carried out at an altitude of about 70 m, producing an image with a spatial resolution of 2.4 cm per pixel. For the flight path, forward and side overlap when shooting is set optimally at around 80% and 70%, respectively. This is due to reducing the canopy height error in vegetation, which is a larger proportion than non-vegetation in the study area [39]. The aerial photos that have been acquired are then processed using third-party software Agisoft PhotoScan [40] to build orthomosaic images and Digital Terrain Models (DTM), which are often used in previous research for experimental and other scientific fields, especially land cover mapping [39,41–45].

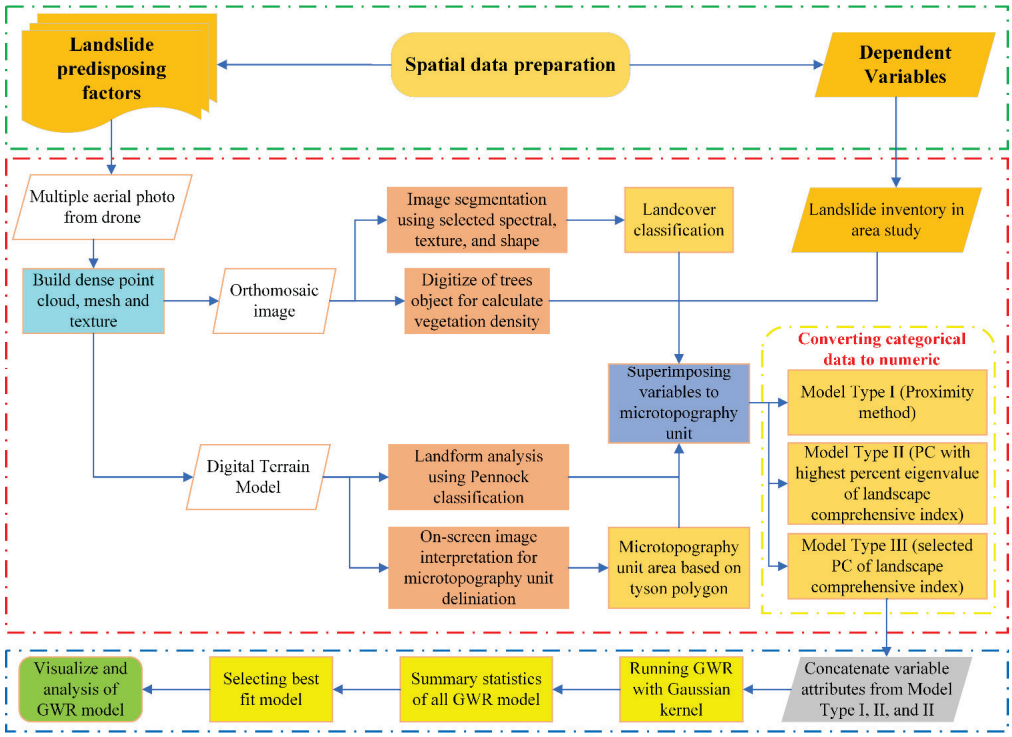

Figure 2. Flowchart of research on landslide local spatial relationships using the GWR model.

2.3.2. Landslide Inventory

The landslide inventory map was compiled from orthomosaic imagery, because historical data on past landslide events were not recorded. High-resolution imagery from Google Earth with a timestamp also cannot help to identify landslide events because the scope and scale in the study area is very detailed. A total of 14 landslide points were detected in the study area (Figure 1). Then these landslide data are aggregated into micro-topographic units as the dependent variable for the GWR model. Generally, landslides are denoted as a binary class, namely, 0 (not landslide) and 1 (landslide). However, this does not represent the actual landslide events when overlaid onto microtopographic units. In other words, overlapping landslide areas do not always completely intersect with microtopographic units because these spatial units certainly form non-uniform areas such as grids with a fixed area shape. In addition, a statistical model for slope instability can use the percentage of landslide area in each unit of analysis [33].

2.3.3. Microtopographic Zoning

The morphology to be mapped refers to the basic classification of Cooke dan Doornkamp (1974), including cliff, an angular convex break of slope, an angular concave break of slope, smoothly convex change in slope, smoothly concave change in slope, and convex and concave too close together (breaks of slope and smooth change in slope, respectively). However, the use of this classification is slightly subjective as there are no definitive rules as to what an angular or smooth break of slope actually looks like, the extent to which small undulations (<1 m) can or should be mapped, and where a break of slope no longer occurs [26]. Apart from that, this research may change or add morphological classes based on the landscape characteristics in the study area. The morphological mapping process utilizes elevation contour lines from the DTM data that have been made. The on-screen image interpretation technique [10,46] is used for morphological delineation through observing contour line patterns and orthomosaic imagery to see the characteristics of the landscape. Additionally, the output from the results of morphological mapping is used for micro-topographical zoning.

However, the spatial form of morphology is in the form of vector lines. Microtopographic zoning should be in the form of areas or polygons so that an approach is needed to convert the form of spatial data. The buffer zone approach defines the area's boundaries within the morphological unit to the adjacent morphology. In fact, each unit's buffer zones can overlap because the buffer distance is fixed [47]. The expected output is a flexible buffer zone that does not coincide, meaning that microtopographic zoning will be formed when the buffer zone boundary in the morphological unit touches the buffer zone boundary of the adjacent unit. Therefore, the Tyson polygon technique, also called the Thiessen polygon, is used to overcome the problem of overlapping buffer zones. The morphological output results are converted into points because vector lines consist of more than one vertex point, so the Thiessen polygon technique can be executed. Then, each point vertex whose area has been formed is aggregated based on the same ID, namely the morphological unit. For more details, see the schematic diagram for microtopographic zoning in (Figure 3).

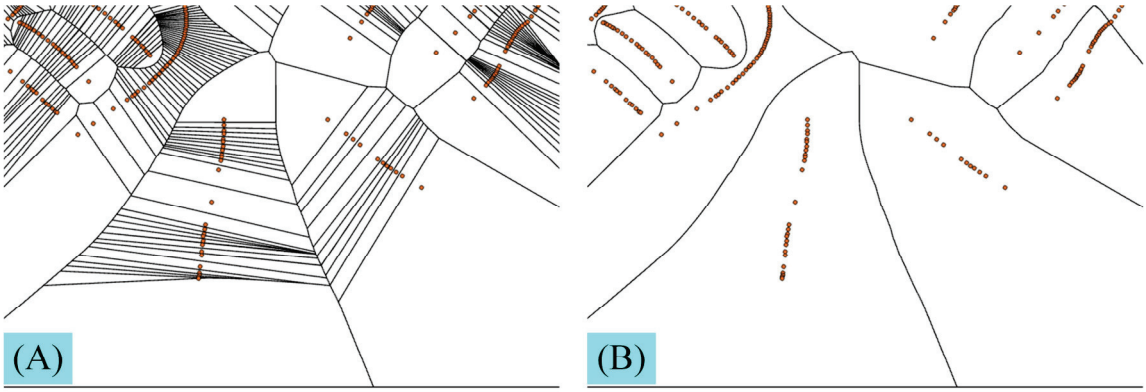

Figure 3. Schematic diagram of microtopographic zoning using (**A**) vertex point line morphology; and (**B**) Aggregation polygon based on the ID of each morphological unit.

2.3.4. Landforms of the Pennock Classification System

The landform analyzed in this study includes the landform elements based on the surface shape on the slopes of the hills, which are explained by topographical derivatives, namely slope, plan curvature and profile curvature proposed by [48]. DTM data are used for the classification of landforms that include: Convergent Shoulder (LF1); Convergent Backslope (LF2); Convergent Footslope (LF3); Divergent Shoulder (LF4); Divergent Backslope (LF5) and Divergent Footslope (LF6). Each of these landform classes is identified based on the threshold value of the combination of degrees of slope and curvature described in Table 1. In this study, the ArcGIS geomorphometric toolbox developed by Evans et al. (2016) was used to classify the Pennock landform [49].

Table 1. Pennock landform classification criteria based on slope, plan curvature and profile curvature by Pennock et al. (1987).

Profile Curvature (°/m)	Kemiringan Lereng (°)	Plan Curvature (°/m)	Elemen Bentuklahan
Concave (<−0.10) Linear (>−0.10, <0.10) Convex (>0.10)	>3.0	Concave (<0.0)	Convergent Shoulder
	>3.0	Concave (<0.0)	Convergent Backslope
	>3.0	Concave (<0.0)	Convergent Footslope
	>3.0	Convex (>0.0)	Divergent Shoulder
	>3.0	Convex (>0.0)	Divergent Backslope
	>3.0	Convex (>0.0)	Divergent Footslope

This landform is closely related to the pattern of movement and distribution of water flow, which can explain the morphological properties of the soil of each class of landform

elements. In addition, it can also identify the morphoprocess of each landform feature, being erosional on the surface and so can develop and trigger landslides [50].

2.3.5. Land Cover Classification

Geographical Object-Based Image Analysis (GEOBIA) is implemented as the first stage for land cover classification from orthomosaic imagery [51]. GEOBIA is an image segmentation method that groups a set of segments in an image based on a group of pixels that display homogeneous features, namely spectral, radiometric, geometric, and others [51–53]. This method is more suitable for very high-resolution imagery, namely orthomosaic from drones, because it can show the presence of massive shadows, low spectral information, and a low signal-to-noise ratio [54,55].

One of the algorithms in the GEOBIA approach is multi-resolution segmentation (Baatz, 2000) that is implemented in the eCognition software to create a set of objects in the image. For segmentation settings, the weights of all three bands (RGB) in the orthomosaic image are equated to be segmented in the scale parameter 150, and the shape/compactness homogeneity criterion is set to 0.3/0.5. In this study, several additional features such as spectral, texture and shape were analyzed through eCognition in each object, followed by feature selection using the Correlation-based Feature Selection (CFS) method in WEKA software [56], as was done in previous research by Ma [56]. Later, the Random Forest (RF) classifier was implemented for land cover classification [57,58] because it is less sensitive to data dimensionality; however, the training sample size was small [57]. In addition, RF is often used as a guided classification for GEOBIA because it can produce land cover and land use maps with good accuracy, both images at medium and very high scales [59–61]. Finally, the randomized training and validation samples were used for the RF classifier. This study used sample proportions of about 70% and 30% for training and validation samples, respectively. Classification validation uses a confusion matrix followed by accuracy metrics, namely overall accuracy and kappa coefficient [62,63].

2.3.6. Vegetation Density

The drone only carries a digital camera sensor, which can only photograph objects in the visible spectrum, so it cannot calculate the vegetation density index that requires the near-infrared band. Therefore, vegetation density was analyzed based on the number of vegetation stands per microtopographic unit in km^2. This is because the vegetation pattern is related to geomorphic processes—including the morphology of the scars—in topographical units [24,25].

2.4. Transformation of Categorical Data into Numeric on Microtopography, Landform and Land Cover

Microtopographic zoning, landform, land cover and vegetation density have been constructed to be used as independent variables in the GWR model. However, microtopography, landform and land cover variables are categorical data, which is a problem for the regression model due to data redundancy. To fulfill the requirements in the GWR analysis it is necessary to transform categorical data into numeric. Two data transformation analyses were implemented in this study, namely the proximity factor to feature boundaries based on Euclidean Distance and landscape metrics using FRAGSTATS developed by Dr. Kevin McGarigal with Eduard Ene and Chris Holme as programmers [64]. Thus, this study offers three types of data transformations to find the most suitable GWR model.

2.4.1. Type I Data Transformation

Type I data transformation is based on the distance to feature boundary metrics (using Euclidean Distance) for each class of microtopographic, landform and land cover variables. Previous studies in other fields also used data transformation based on distance metrics, namely land cover variables for spatial modeling [65–67]. Technically, each class is analyzed by distance metrics, where the closer to the class feature boundaries, the smaller the distance value (in meters). In addition, the area within the class feature boundary is set

to a minus value so that the closer to the midpoint within the class feature area, the greater the distance value with a minus value. This setting is used to distinguish between classes and non-classes and is also considered to represent conventional transformations, namely class 0 (non-class) and 1 (class) dummy variables.

After that, the distance metrics for micro-topography, landform and land cover variables were calculated. Then, a zonal statistical analysis was carried out to calculate the average distance metric for each class that was then aggregated into micro-topographic units.

2.4.2. Type II Data Transformation

Landscape metric analysis is used to transform Type II data, especially the landform and land cover variables as independent variables. This is because the unit of analysis used for the GWR model is the microtopographical unit. In other words, microtopographic units can only be transformed into Type I data. Landscape metrics reflect spatial pattern characteristics. Generally, landscape metrics are often used as predictor variables for ecological analyses, especially for evaluating changes in land cover and land use [68]. However, in this study, landscape metrics—like the distance metric method—were used to transform data into land cover and landform variable categories that could reduce redundancy [69]. In this study, 11 class-level based landscape metrics were taken from several previous studies [69–72] and implemented to each of the landform and land cover classes, respectively, as shown in Table 2. Landscape metrics analysis utilizes the 'landscape metrics' package (reimplementation of FRAGSTATS) rather than FRAGSTATS software via R language [73]. This is because it can calculate landscape metrics locally and simultaneously (Nowosad, 2022), i.e., per microtopographic unit.

Table 2. Summary of 11 landscape metrics (Hesselbarth et al., 2019a).

Metrik	Rumus	Range
Aggregation index (AI)	$AI = \left[\frac{g_{ii}}{max - g_{ii}}\right](100)$	$0 \leq AI \leq 100$
Class area (CA)	$CA = sum\left(AREA\left[patch_{ij}\right]\right)$	$CA > 0$
Clumpiness index (CLUMPY)	$Given\ G_i = \left(\frac{g_{ii}}{(\sum_{k=1}^{m} g_{ik}) - min\ e_i}\right)$ $CLUMPY = \left[\frac{G_i - P_i}{P_i}\ for\ G_i < P_i \& P_i < 0.5;\ else\ \frac{G_i - P_i}{1 - P_i}\right]$	$-1 \leq CLUMPY \leq 1$
Patch cohesion index (COHESION)	$COHESION = 1 - \left(\frac{\sum_{j=1}^{n} p_{ij}}{\sum_{j=1}^{n} p_{ij}\sqrt{a_{ij}}}\right) \times \left(1 - \frac{1}{\sqrt{Z}}\right)^{-1} \times 100$	$0 \leq COHESION \leq 100$
Landscape division index (DIVISION)	$DIVISION = \left(1 - \sum_{j=1}^{n}\left(\frac{a_{ij}}{A}\right)^2\right)$	$0 \leq DIVISION \leq 100$
Edge density (ED)	$ED = \frac{\sum_{k=1}^{m} e_{ik}}{A} \times 10,000$	$ED \geq 0$
Largest patch index (LPI)	$LPI = \frac{max_{j=1}^{n}(a_{ij})}{A} \times 100$	$0 < LPI \leq 100$
Landscape shape index (LSI)	$LSI = \frac{e_i}{min\ e_i}$	$LSI \geq 0$
Number of patches (NP)	$NP = n_i$	$NP \geq 0$
Patch density (PD)	$PD = \frac{n_i}{A} \times 10,000 \times 100$	$0 < PD \leq 1 \times 10^6$
Percentage of class (PLAND)	$PLAND = \frac{\sum_{j=1}^{n} a_{ij}}{A} \times 100$	$0 < PLAND \leq 100$

The 11 landscape metrics calculated for each land cover and landform class can produce many features, causing multicollinearity and redundancy between metrics [74,75]. Therefore, the Principal Component Analysis (PCA) approach was implemented to reduce dimensionality by compressing landscape metric features in each class, which was also studied [75–80] From the results of PCA calculations, the highest percentage of eigenvalues in the Principal Component (PC) is chosen to represent all landscape metrics for each land cover and landform class, which is named the comprehensive index of landscape metrics.

2.4.3. Type III Data Transformation

The comprehensive index of landscape metrics is also used in transforming Type III data but does not use (PC) with the highest percentage of eigenvalues. Instead, the

PC shows the greatest contribution when it is linked to the landslide data. Odhiambo Omuya et al. (2021) developed a combination of PCA and Information Gain methods to reduce dimensionality while selecting the best features of a PC. The result is that it can significantly improve the performance of machine learning classifiers compared to other feature selection methods, including Correlation-based feature selection (CFS), Gain Ratio, and Relief-F. Thus, this study uses the conceptual approach [76] but the aim is to investigate the best PC for each landform and land cover class. In addition, the Relief-F algorithm [77,78] is implemented because it can analyze target data (i.e., landslide data) in numerical form. Relief-F calculates the average merits (AM) in each land cover class and landform which show the ranking of PC attributes. The initial hypothesis for the transformation of Type III data is that it is not always that the Principal Component with the largest percentage of eigenvalues shows a strong contribution to the landslides in the study area.

2.5. Geographically Weighted Regression Model Analysis

The GWR model was run to explore the local spatial relationships of landslides with microtopographical variables, landform, land cover, and vegetation density. GWR is a local regression developed by Brunsdon et al. (1998), an update of the Ordinary Least Squares (OLS) method. The GWR model was built based on the percentage of landslide area as the dependent variable and microtopography, landform, land cover, and vegetation density—with all kinds of data transformations carried out—as independent variables that are integrated with microtopographic units. GWR analysis was performed through the GWR4 software originally developed by [79]. The GWR model formula is described as follows [36]:

$$Y_i = \beta_0(\mu_i, v_i) + \sum_{k=1}^{p} \beta_k(\mu_i, v_i) x_{ik} + \varepsilon_i, i = 1, 2, \ldots, n \quad (1)$$

where (μ_i, v_i) represents the coordinates of the observed data; $\beta_0(\mu_i, v_i)$ is the intercept parameter at location i; p is the number of independent variables; $\beta_k(\mu_i, v_i)$ is the local regression coefficient for the independent variable kth at location i; x_{ik} is kth independent variable in ith unit; and ε_i is a random error. The regression coefficient is calculated using the local weighted least squares function with the following formula:

$$\hat{\beta}_k(\mu_i, v_i) = \left[X^T W(\mu_i, v_i) X\right]^{-1} X^T W(\mu_i, v_i) Y \quad (2)$$

where $W(\mu_i, v_i)$ is the spatial weighting matrix of the observation data at the sample point i which represents the effect of sample point i around the regression point on other regression points. In other words, the closer to the sample point i, the greater the influence of the local regression parameter with a larger weight value, and vice versa. Then, the selection of the kernel function is important to determine the scope of the degree of spatial autocorrelation [80]. In this study, the adaptive bi-square kernel was used because the distribution of observational data was not uniform [79]. Here is the bi-square kernel formula:

$$w_{ij} = \left(1 - \left(\frac{d_{ij}}{\theta_{i(k)}}\right)^2\right)^2 \text{ if } d_{ij} < \theta_{i(k)} \text{ and } w_{ij} = 0 \text{ otherwise} \quad (3)$$

where d_{ij} is the Euclidean distance between sample point j and point i; and $\theta_{i(k)}$ is a measure of adaptive bandwidth that shows the spatial variation in the GWR model. Bandwidth selection is also crucial because it measures how well the GWR model generalizes data similar to the data that have been trained. The golden search function determines the optimum bandwidth for the adaptive bi-square kernel function. The optimum bandwidth is determined by the corrected Akaike Information Criterion (AICc) method [79]. The AICc method is known to overcome the problem of over-fitting the model rather than the cross-validation method [80]. When AIC is minimum, bandwidth size is the best.

3. Results

3.1. Results of Mapping Microtopographic Zoning, Landforms, Land Cover, and Vegetation Density

Morphological mapping has been carried out systematically through a remote sensing approach in the study area with a slight modification from the morphological mapping system by Cooke and Doornkamp, namely the Ridge and Valley classes divided into major and minor. Thus, this study's original morphological class numbered 8 was updated to 15 classes (Figure 4). Then, thiessen polygons were applied to construct the microtopographic zoning of each morphological class shown in (Figure 5). A total of 300 microtopographic units were formed in the study area. The symbolization system on micro-topographic maps is based on a combination of colors and textures. Red, purple, blue, brown, and green represent head scarp/cliff, ridge, valley, break of slope, and smooth slope change, respectively.

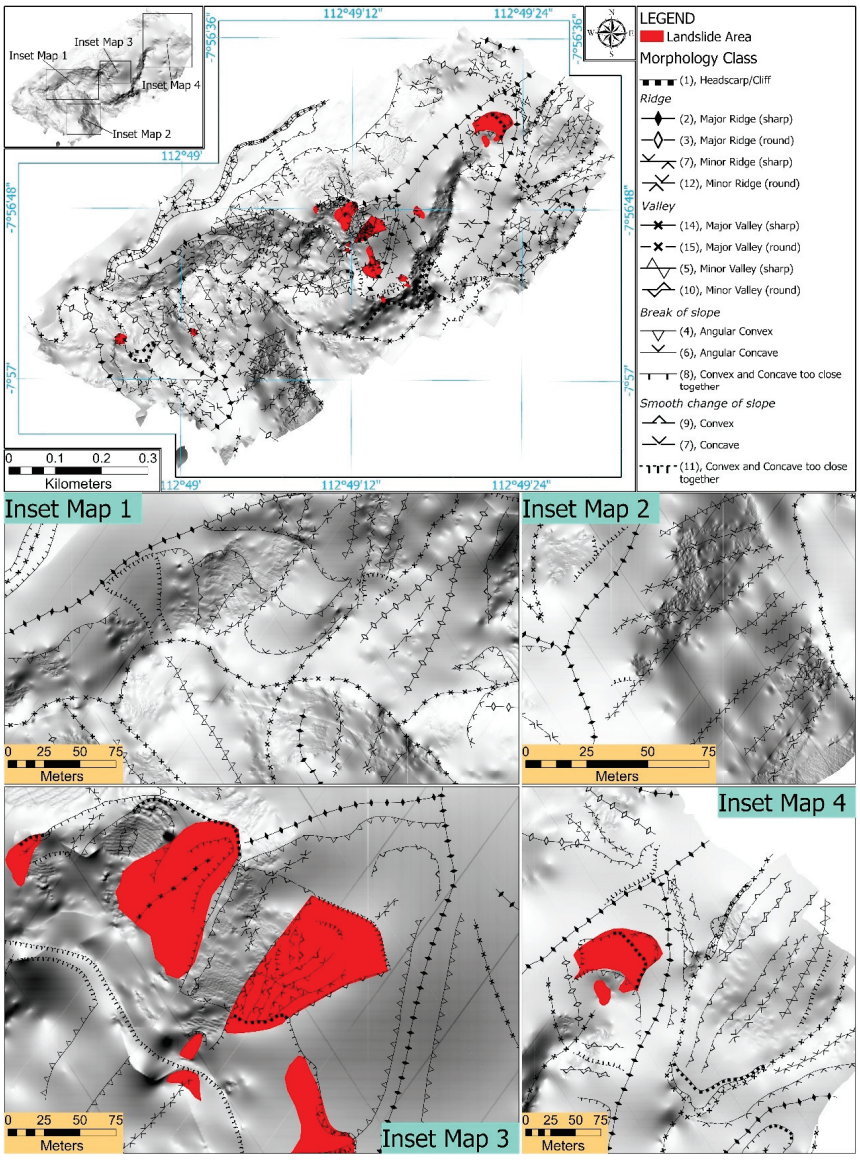

Figure 4. Morphological mapping with a modified geomorphological symbolization system.

Microtopography is part of the geomorphological study that has an essential role in landslides. Microtopography is defined as changes in topography that can be identified and mapped on a detailed scale. Based on Figure 4, the microtopography in the study area is divided into four essential parts: (i) ridge, which is divided into the major ridge

and minor ridge in the form of sharp and round; (ii) valley, which is divided into major valley and minor valet in sharp and round form; (iii) break of slope which is divided into angular convex, angular concave, and convex and concave too close; and (iv) smooth change in slope, which is divided into convex, concave and convex and concave too close together. Each form of microtopography has a different effect on landslides. The movement of soil material will increase on sharp slope morphology. In addition, differences in microtopography will also affect the value of the shape of the land surface in the form of plan curvature and curvature profile. Both influence the acceleration and deceleration of the water flow. In ridge microtopography, the water flow will be accelerated so that the potential for material movement increases.

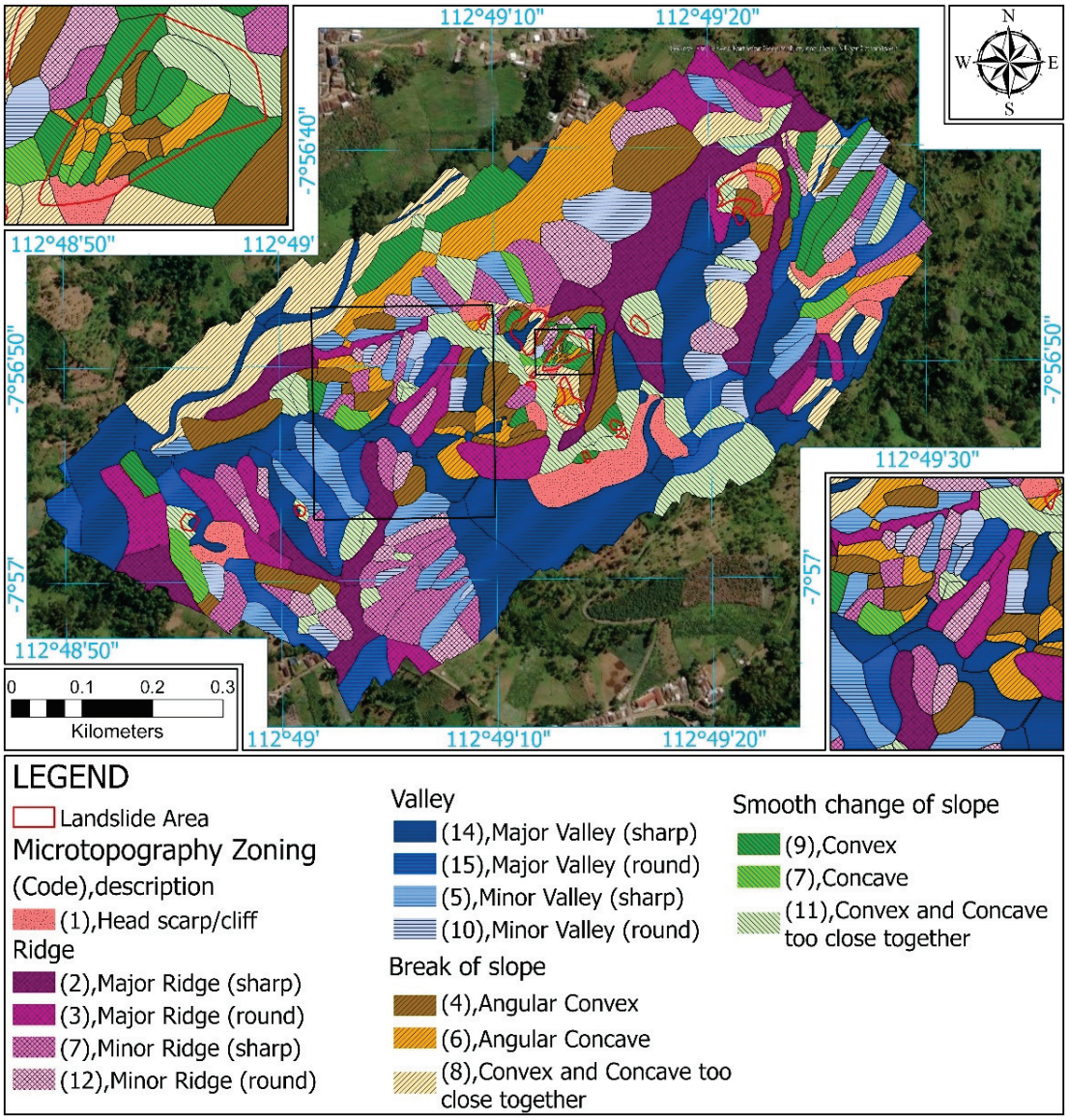

Figure 5. Microtopographic Zoning Map from Morphology in the Study Area.

The pattern of microtopographic distribution in the study area can be said to be heterogeneous. The southwestern part is dominated by ridge and valley morphology with various class variations. The shape of the zoning in this area tends to be elongated, reflecting the presence of hills. The major valley (sharp) with a large proportion of the area is a perennial river channel stretching east to west. Then, the central part is formed by a fragmented microtopography, namely the form of zoning with a relatively small proportion

of areas and various morphological classes. This implies complex slope configurations and slight fluctuations. The northeastern part is almost the same as the southwest, namely the form of an elongated zonation, but the morphology is relatively fragmented. Meanwhile, the northern part shows a more compact, elongated form of microtopographic zoning and a large proportion of areas indicating a less volatile slope configuration.

Then, the shape-based landform variables by the Pennock system have been estimated and classified. In contrast to microtopographic zoning, the Pennock landform in the study area is defined by curvature and slope indices, namely profiles and plans with a neighborhood radius of 40 m each. As shown in Figure 4a, the predetermined neighborhood radius scale reflects the detailed landform pattern. Generally, in the Pennock method of landform the slope is divided into three arrangements, covering the upper (shoulder), middle (backslope), and lower (footslope), with almost the same proportions. However, the Pennock method classifies a convergent/divergent backslope of around 3% of all existing landforms in the study area. Meanwhile, the proportion of convergent/divergent shoulders and footslopes is almost equal, but the spatial pattern still varies. In addition, the landform in the study area tends to have a convex-concave pattern that repeats over short distances.

Class 1 hierarchical land cover classification on orthomosaic imagery based on GEOBIA shows very good accuracy, with an overall accuracy of 98.26% and a kappa coefficient of 0.97. Table 3 presents the results of the confusion matrix calculation using the Random Forest guided classification. The selection of attributes on spectral features, texture, and shape index also influences satisfactory accuracy. Of the 27 features used as predictor variables for classification, 13 features were selected based on the results of attribute filtering using CFS (Correlation-based Feature) from WEKA software. In Figure 4b, most of theland cover in the study area is dominated by herbaceous (45.77%) and forest (36.56%), followed by bare soil (12.71%), shrub (3.58%), and built-up (1.36%). In addition, the density of moderate to very high vegetation classes has spread from the north to northeast and slightly in the center and southwest (Figure 6c).

Table 3. Results of land cover classification accuracy test from orthomosaic imagery based on the confusion matrix.

Landcover	Forest	Shrub	Herbaceous	Bare Soil	Built-up	Total	User Accuracy (%)
Forest	816	0	2	1	0	819	99.63
Shrub	4	177	5	1	0	187	94.65
Herbaceous	7	0	1050	2	0	1059	99.15
Bare soil	7	0	7	371	0	385	96.36
Built-up	3	0	3	3	125	134	93.28
Total	837	177	1067	378	125	Overall = 98.26%	
Producer Accuracy (%)	97.49	100	98.4	98.15	100	Kappa = 0.97	

3.2. Comprehensive Index Analysis of Landscape Metrics on Landform and Land Cover

A comprehensive index of landscape metrics for each land cover and landform class is analyzed using the PCA algorithm to compress metric landscape features. As shown in Tables 4 and 5, the highest percentage of eigenvalues is PC1, which is overall above 30% and the eigenvalues are above 1. This indicates that the PC1 component has most of the feature information from all landscape metrics, so it is used for data GWR Type II model independent variable input. In addition, while each PC is associated with landslide data and the results are not always PC1, it has a large contribution to explaining landslides in the study area, though best represents all landscape metrics. Interestingly, the LF1 and LF6 classes show that PC6 contributes the most, although the eigenvalue is below 1. In fact, negative AM values appear in PC1, namely classes LC2 and LC5, which means that it has the lowest contribution among other classes to landslides, even though the negative AM value is still used for the GWR model input.

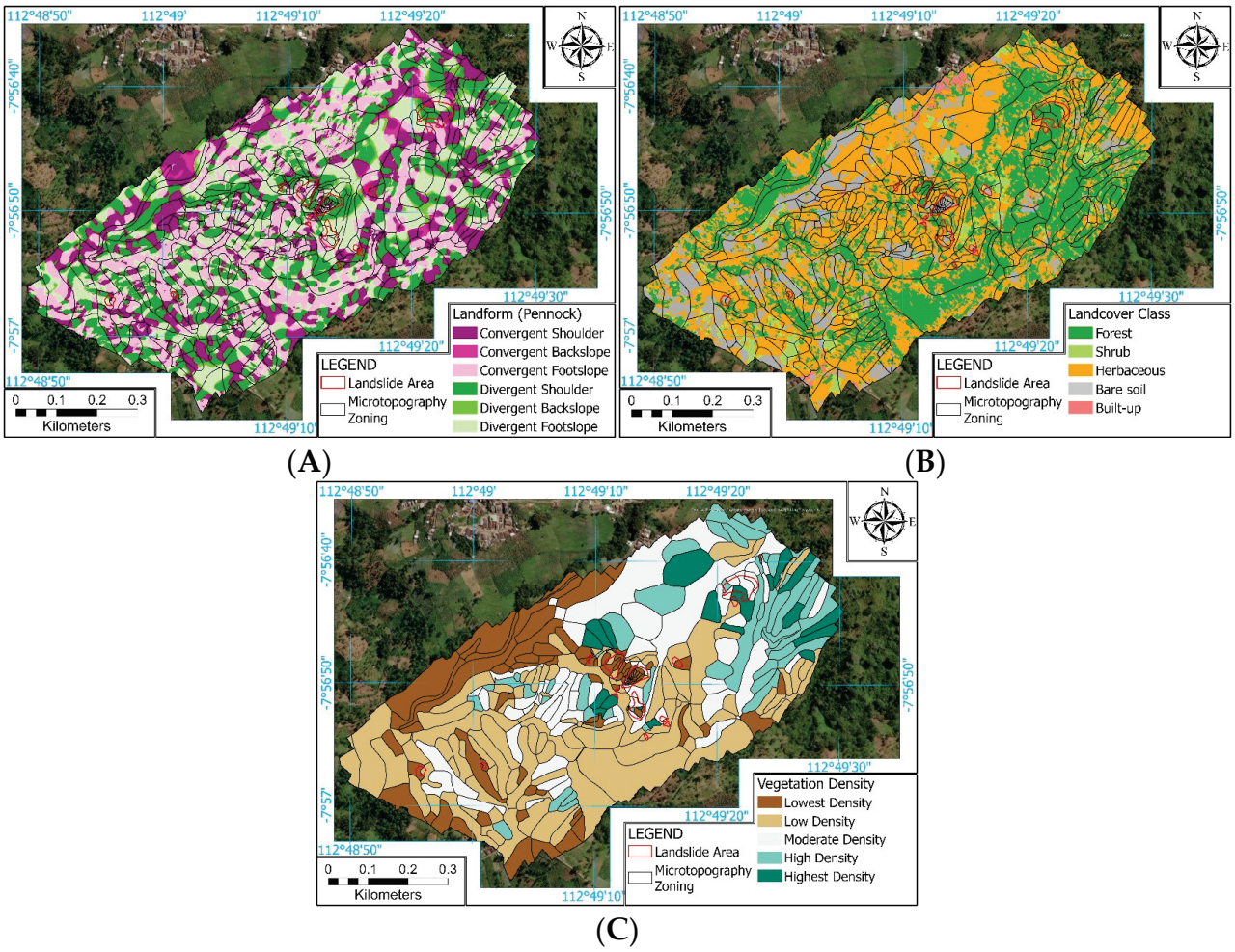

Figure 6. The independent variables include (**A**) curvature-based landform; (**B**) land cover; and (**C**) vegetation density.

Table 4. Eigenvalues, merit values and ranking percentages of the main component's contribution to the landslide.

		LF1	LF2	LF3	LF4	LF5	LF6
PC1	Eigen	4.18	4.52	3.89	3.81	4.99	4.51
	% Eigen	37.98%	41.12%	35.42%	34.64%	45.44%	40.96%
	AM	0.0147	−0.0005	−0.0003	0.009	−0.0002	0.0094
PC2	Eigen	2.36	2.19	2.28	2.58	1.9	2.23
	% Eigen	21.44%	19.86%	20.74%	23.48%	17.30%	20.29%
	AM	0.0059	0.01218	−0.0041	0.0016	0.00944	0.002
PC3	Eigen	1.92	1.81	1.65	1.77	1.78	1.63
	% Eigen	17.42%	16.43%	15.02%	16.09%	16.19%	14.86%
	AM	0.0108	−0.0042	0.01716	0.0264	−0.0001	0.0025
PC4	Eigen	1.55	1.36	1.41	1.45	1.28	1.56
	% Eigen	14.08%	12.36%	12.81%	13.21%	11.67%	14.23%
	AM	−0.003	−0.0054	−0.007	0.0049	−0.0011	0.0037
PC5	Eigen	0.44	0.56	0.88	0.53	0.44	0.42
	% Eigen	4.00%	5.16%	8.04%	4.82%	4.05%	3.83%
	AM	−0.003	−0.0067	−0.0012	0.0187	0.00039	7×10^{-5}
PC6	Eigen	0.21	0.29	0.46	0.44	0.29	0.28
	% Eigen	1.91%	2.68%	4.32%	4.07%	2.71%	2.58%
	AM	0.0269	0.00359	−0.008	0.0154	0.00863	0.0241

Table 5. The eigenvalues and eigen percentages of the principal component.

		LC1	LC2	LC3	LC4	LC5
PC1	Eigen	4.87	7.39	3.45	4.47	6.63
	% Eigen	44.27%	67.22%	31.33%	40.67%	60.29%
	Merit	−0.004	−0.0123	−0.003	0.0033	−0.0117
PC2	Eigen	2.24	1.69	3.1	2.72	1.84
	% Eigen	20.38%	15.45%	28.22%	24.70%	16.69%
	Merit	−0.005	−0.013	0.01053	0.0405	−0.0119
PC3	Eigen	1.91	0.98	1.75	1.39	1.52
	% Eigen	17.38%	8.95%	15.89%	12.67%	13.82%
	Merit	−0.01	−0.0147	−0.0012	0.0006	−0.0129
PC4	Eigen	1.15	0.56	0.98	0.95	0.64
	% Eigen	10.42%	5.11%	8.98%	8.59%	5.81%
	Merit	0.0038	−0.0145	0.00085	0.0334	−0.0141
PC5	Eigen	0.42	-	0.88	0.64	-
	% Eigen	3.89%	-	7.97%	5.78%	-
	Merit	0.0033	-	0.00503	0.0232	-
PC6	Eigen	-	-	0.5	0.46	-
	% Eigen	-	-	4.57%	4.19%	-
	Merit	-	-	0.00644	0.0219	-

3.3. Model the Local Spatial Relationship between the Landslide and the Selected Independent Variable Model Type for Priority Land Management Sustainability

In this study, the GWR model was implemented to investigate the spatial pattern of local landslide relationships with independent variables collected in spatial units of microtopographic areas. Table 6 shows the GWR fit model on the data group of predictor variables influencing landslide events (microtopography, landform, land cover, and vegetation stand density), adjusted for R^2 and AICc. All models use the Gaussian kernel, whose bandwidth size is checked and calculated based on the Golden Search method. AICc is used as a selection criterion to find the optimal bandwidth of 300 observational data.

Overall, in the univariate local sub-model the LC model Type I variable group indicates the covariate most related to the landslide event, namely the value of adj. The highest R^2 (0.789) and the lowest AICc (2478.33) are even more important than all the univariate and multivariate sub-models analyzed. A multivariate model of two groups and three groups of variables, the Type I model shows better performance (adj. R^2 above 0.7) compared to the Type II and Type II models. The univariate and multivariate sub-models, based on the type of model, suggest that Type I shows the best fit model compared to Type II and Type III. In addition, the Type III model is better than the Type II but performs lower than Type I. On the other hand, the sub-model with all variable groups included shows a different pattern of Type model results, namely Type III is the highest (adj R^2 = 0.755) with the third lowest AICc value (2526.38), after the LC group Type III (2515.51) and Type I (2478.33) sub-models. Thus, the Type III group sub-model with four variables was chosen to provide additional insight, namely the local spatial relationship experiment of the landslide. However, in terms of calibration the fit model is not the best compared to other sub-models.

Table 6 is a summary of the results of univariate and multivariate comparisons of the GWR model with four groups of predictor variables: microtopography (MT); landform (LF); land cover (LC); and standing vegetation density (VD). Each predictor variable has sub-variables for each class whose data form is divided into three types: proximity factor (Type I); PC with the highest percentage of eigenvalues from the landscape metric comprehensive index (Type II); and PC on the comprehensive metric index.

In the summary output of the GWR model (Table 6), the F-statistics in the ANOVA comparison test shows that the entire GWR model significantly increases global model performance (OLS). Thus, the null hypothesis of the GWR model being unable to improve the performance of the global model is rejected. Figure 5 shows the local R^2 generated from the GWR, that the GWR model is fit to map local landslides, which are explained through

the MT, LF, LC, and VD predictor variable groups that are modeled simultaneously. The distribution of R^2 in the study area tends to be homogeneous and clustered. About 80% of the local model area has an R^2 above 0.73, and at least 10% of the area in the southwestern region shows that the local model is less fit (fit) with an R^2 below 0.43. This implies that additional covariates are needed to explain the slides in the study area, particularly the southwest region. Then, the positive value of the standardized residual indicates over-estimation. Likewise, negative values that appear indicate an underestimation. Overall, the GWR model shows an over-/under-estimated distribution pattern that tends to be random in the study area (Figure 7).

Table 6. Summary of univariate and multivariate GWR model comparison results.

Model	Model Types	Global Regression vs. GWR						
		AICc			Significance Test (with 99% Confident Interval)		R^2, Adjusted R	
		OLS	GWR	Diff.	F-Statistic	*p*-Value	OLS	GWR
MT	Type I	2759.16	2625.24	133.92	5.52	<0.001	R^2 = 0.36, adj R^2 = 0.32	R^2 = 0.80, adj R^2 = 0.71
LF	Type I	2854.12	2738.12	116	4.08	<0.001	R^2 = 0.07, adj R^2 = 0.05	R^2 = 0.67, adj R^2 = 0.51
	Type II	2796.78	2681.95	114.83	4.15	<0.001	R^2 = 0.23, adj R^2 = 0.21	R^2 = 0.69, adj R^2 = 0.57
	Type III	2701.27	2667.08	34.19	2.66	<0.001	R^2 = 0.44, adj R = 0.43	R^2 = 0.59, adj R^2 = 0.52
LC	Type I	2788.88	2478.33	310.55	10.12	<0.001	R^2 = 0.24, adj R^2 = 0.23	R^2 = 0.85, adj R^2 = 0.79
	Type II	2764.29	2630.03	134.26	4.6	<0.001	R^2 = 0.30, adj R^2 = 0.29	R^2 = 0.73, adj R^2 = 0.64
	Type III	2619.84	2515.51	104.33	3.94	<0.001	R^2 = 0.57, adj R^2 = 0.56	R^2 = 0.81, adj R^2 = 0.75
VD	-	2850.2	2659.06	191.14	8.21	<0.001	R^2 = 0.05, adj R^2 = 0.04	R^2 = 0.61, adj R^2 = 0.54
LF + LC	Type I	2775.45	2588.26	187.19	6.08	<0.001	R^2 = 0.31, adj R^2 = 0.28	R^2 = 0.87, adj R^2 = 0.77
	Type II	2748.56	2674.62	73.94	3.36	<0.001	R^2 = 0.37, adj R^2 = 0.34	R^2 = 0.66, adj R^2 = 0.56
	Type III	2598.19	2565.58	32.61	2.44	<0.001	R^2 = 0.62, adj R^2 = 0.60	R^2 = 0.75, adj R^2 = 0.68
LF + LC + VD	Type I	2776.41	2612.5	163.91	5.6	<0.001	R^2 = 0.31, adj R^2 = 0.28	R^2 = 0.87, adj R^2 = 0.76
	Type II	2748.15	2679.12	69.03	3.21	<0.001	R^2 = 0.37, adj R^2 = 0.34	R^2 = 0.66, adj R^2 = 0.55
	Type III	2600.37	2573.24	27.13	2.3	<0.001	R^2 = 0.62, adj R^2 = 0.60	R^2 = 0.75, adj R^2 = 0.68
MT + LF + LC + VD	Type I	2662.22	2608.1	54.12	3.08	<0.001	R^2 = 0.58, adj R^2 = 0.54	R^2 = 0.77, adj R^2 = 0.68
	Type II	2667.68	2651.18	16.5	2.17	<0.001	R^2 = 0.57, adj R^2 = 0.53	R^2 = 0.68, adj R^2 = 0.59
	Type III	2566	2526.38	39.62	2.72	<0.001	R^2 = 0.69, adj R^2 = 0.66	R^2 = 0.83, adj R^2 = 0.75

The local coefficients shown in Table 7 indicate that the relationship between the landslide and the independent variables is non-stationary. The relationship varies spatially with a range of magnitudes and directions. The independent variables in the MT, LF, LC, and VD groups showed that the magnitude of the relationship varied in both negative and positive directions in terms of min and max values. This can be interpreted as the presence of an increasing variable that will also increase the occurrence of landslides, but the presence

of variables can also reduce the occurrence of landslides. However, several independent variables only show an inverse correlation to landslides, including Micro2, Micro6, LF3, and LC3. This suggests that these four variables do not contribute to landslides within this feature area. In addition, the variables LF4 and LF6 positively contribute to the occurrence of landslides in all study areas in this feature. However, the VD variable has the smallest relationship magnitude compared to the other variables, with a two-way relationship.

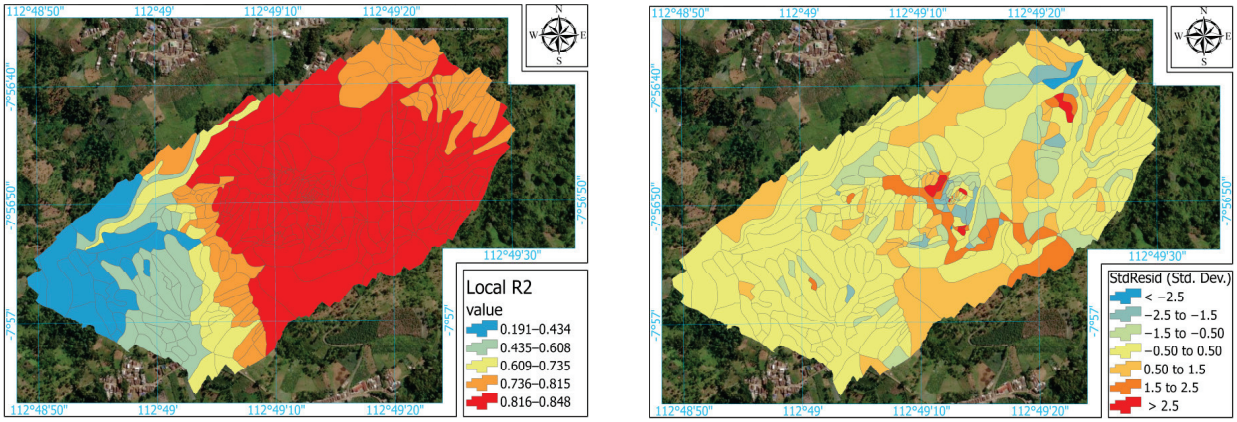

Figure 7. Map of the local coefficient of determination (R^2) between the observed values and the fit of the GWR model (**left**) and the standardized residual (**right**).

Table 7. Statistical summary of the local regression coefficients of GWR for each independent variable in the MT, LF, LC, and VD groups.

Variables		Coefficients			
Code	**Description**	**Min**	**Mean**	**Max**	**StdDev**
	Intercept	−0.54209	23.27006	41.68737	8.60305
	Microtopography				
Micro1	Head scarp/cliff	−2.03661	0.29145	1.11392	0.64287
Ridge					
Micro2	Major Ridge (sharp)	−0.24350	−0.11556	−0.01758	0.06421
Micro3	Major Ridge (round)	−0.07844	0.00832	0.07987	0.03425
Micro7	Minor Ridge (sharp)	−0.00361	0.11336	0.25198	0.07270
Micro12	Minor Ridge (round)	−0.18980	−0.01034	0.18657	0.10481
Valley					
Micro14	Major Valley (sharp)	−0.13701	0.03425	0.23303	0.09773
Micro15	Major Valley (round)	−0.09968	0.08097	0.24498	0.08325
Micro5	Minor Valley (sharp)	−0.07213	-3.2×10^{-5}	0.11751	0.04632
Micro10	Minor Valley (round)	−0.16003	−0.02185	0.17120	0.08092
Break of Slope					
Micro4	Angular Convex	−0.01100	0.08009	0.20867	0.05505
Micro6	Angular Concave	−0.46316	−0.21412	−0.01252	0.13734
Micro8	Convex and concave too close together	−0.30881	−0.08370	−0.01487	0.05277
	Smooth Change in Slope				
Micro9	Convex	−0.02343	0.14797	0.40619	0.11046
Micro11	Concave	−1.19064	−0.36578	2.03376	0.63251
Micro13	Convex and concave too close together	−0.52585	−0.22090	0.02616	0.15946
Landform					
LF1	Convergent Shoulder	−4.28159	−1.66346	2.41592	1.45241
LF2	Convergent Backslope	−1.86977	0.27553	4.02760	1.89846
LF3	Convergent Footslope	−4.01443	−2.83184	−1.87514	0.49353
LF4	Divergent Shoulder	0.48987	1.22543	1.99219	0.31014
LF5	Divergent Backslope	−0.39145	0.35599	1.88111	0.46366
LF6	Divergent Footslope	1.65203	4.29289	6.70036	1.07773

Table 7. *Cont.*

Variables		Coefficients			
Code	**Description**	**Min**	**Mean**	**Max**	**StdDev**
Landcover					
LC1	Forest	−2.62464	−1.12012	1.43396	1.26063
LC2	Shrub	−1.25680	0.69419	2.43403	1.19657
LC3	Herbaceous	−7.27211	−4.94960	−0.54137	1.69933
LC4	Bare soil	−6.25056	−3.49079	0.20763	2.19209
LC5	Built-up	−0.89751	0.30802	1.46729	0.65149
VD	Vegetation Density	-2.41×10^{-4}	7.00×10^{-6}	2.34×10^{-4}	1.04×10^{-4}

Generally, in local relationship analysis research the local coefficients of each independent variable in the GWR model are imported and visualized as a map using the GIS environment. The coefficient values are mapped taking into account the two-tailed t value, i.e., t values above 1.96 and −1.96 are considered significant (equal to $p < 0.05$). However, in this study the local coefficient maps are summarized in one map by integrating the four groups of variables based on the largest local coefficient values (negative or positive values). This is because the spatial units used are microtopographic units, so the other three variables are superimposed and the value of the feature slices included in each unit is calculated. In this case, the value of the principal component comprehensive index of the selected landscape metrics is calculated. The estimated values of parameters or local coefficients on the microtopography are searched for and adjusted to each class of unit so that misinterpretation does not occur, e.g., extracting the Micro1 coefficient values based on the attributes of the Micro1 class microtopographic units so that outside the area has been selected. Likewise, with the landform and land cover, only the unit containing information from the two variables is taken for the coefficient value.

As shown in Figure 8, there are 14 classes combined with the local coefficients of the independent variables of each group. Signs "+" and "−" are interpreted as the relationship's direction. Map visualization uses a combination of colors and textures to make it easier to read map symbols and their information. Each unit of the analysis found several variables positively or negatively related to landslides. In other words, the characteristics and patterns of landslides in the study area can be explored through several variables related to the unit of analysis.

In the map in Figure 8, MT classes that show a positive relationship to landslides are green, and tend to be spread over the central area, being most prominent in the northeast. Class LF2, LF6, and LC2 also show a positive relationship. However, units with no significant positive or negative relationship are clustered in the southwestern region with white symbols. This can also be attributed to the low R^2 value in the region, as shown in Figure 7. Interestingly, the units that only show a negative relationship, namely the MT, LC3, and LC4 classes, appear in the northern region with a grayish color symbol. Vice versa, which only shows a positive relationship appears in the south with a dark purple color, but only one unit, namely the LF6 class.

As shown in Table 8, the number of units that have a positive and negative relationship are 190 and 248, respectively. LF6 showed the most positive relationship (131 units), followed by MT (38 units), LC2 (16 units), and LF2 (5 units). Meanwhile, LC3 showed the most dominant negative relationship (224 units), compared to MT (17 units) and LC4 (7 units). Then, the positively related microtopographic classes include micro9 (14 units), micro14 (7 units), micro15 (7 units), micro7 (6 units), micro12 (3 units), and micro5 (1 unit). Meanwhile, only micro2 (1 unit) and micro6 (3 units) have a negative relationship. Thus, LF6 and LC3 have an important role in understanding the landslide mechanism in the study area. Figure 9 shows a map inset focused on landslide and non-slip areas overlapping the most significant micro-topographical units and classes. The current landslides were associated with LF6, rather than MT and LC2. Regardless of the significance of the

local relationship, the current landslides predominately occur at micro6, micro8, micro9, and micro13.

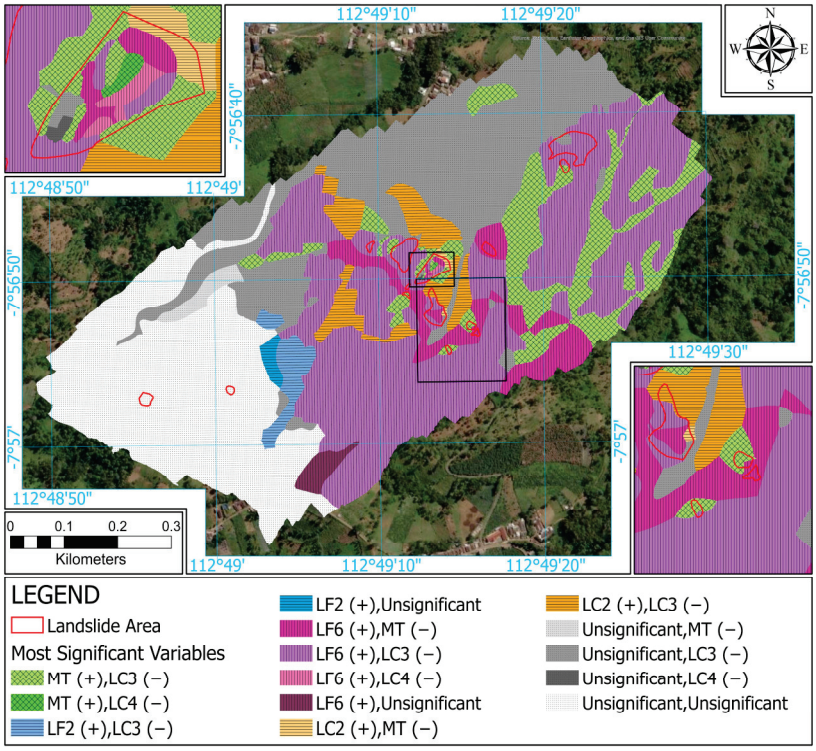

Figure 8. Map of integration of multivariate local coefficients that have the largest (positive) and smallest (negative) significant impacts on landslides.

Table 8. The number of microtopographic units showing the most statistically significant variables in each microtopographic class.

Microtopography Class		Significant Count of Units								
		Positive Sign					Negative Sign			
Code	Description	MT	LF2	LC2	LF6	Sum	MT	LC3	LC4	Sum
Micro1	Head scarp/cliff	-	-	-	9	9	-	12	-	12
Ridge										
Micro2	Major Ridge (sharp)	-	1	1	3	5	1	7	-	8
Micro3	Major Ridge (round)	-	-	1	5	6	-	10	-	10
Micro7	Minor Ridge (sharp)	6	1	2	8	17	-	19	-	19
Micro12	Minor Ridge (round)	3	1	-	7	11	-	16		16
Valley										
Micro14	Major Valley (sharp)	7	-	-	10	17	-	24	-	24
Micro15	Major Valley (round)	7	1	-	1	9	-	8	-	8
Micro5	Minor Valley (sharp)	1	-	-	10	11	-	15	-	15
Micro10	Minor Valley (round)	-	-	1	10	11	-	13	-	13
	Break of Slope									
Micro4	Angular Convex	-	-	6	14	20	-	23	3	26
Micro6	Angular Concave	-	-	-	12	12	3	15	-	18
Micro8	Convex and concave too close together	-	-	1	14	15	-	24	-	24
	Smooth Change in Slope									
Micro9	Convex	14	-	-	6	20	-	21	1	22
Micro11	Concave	-	1	1	3	5	-	4	3	7
Micro13	Convex and concave too close together	-	-	3	19	22	13	13	-	26
	Total	38	5	16	131	190	17	224	7	248

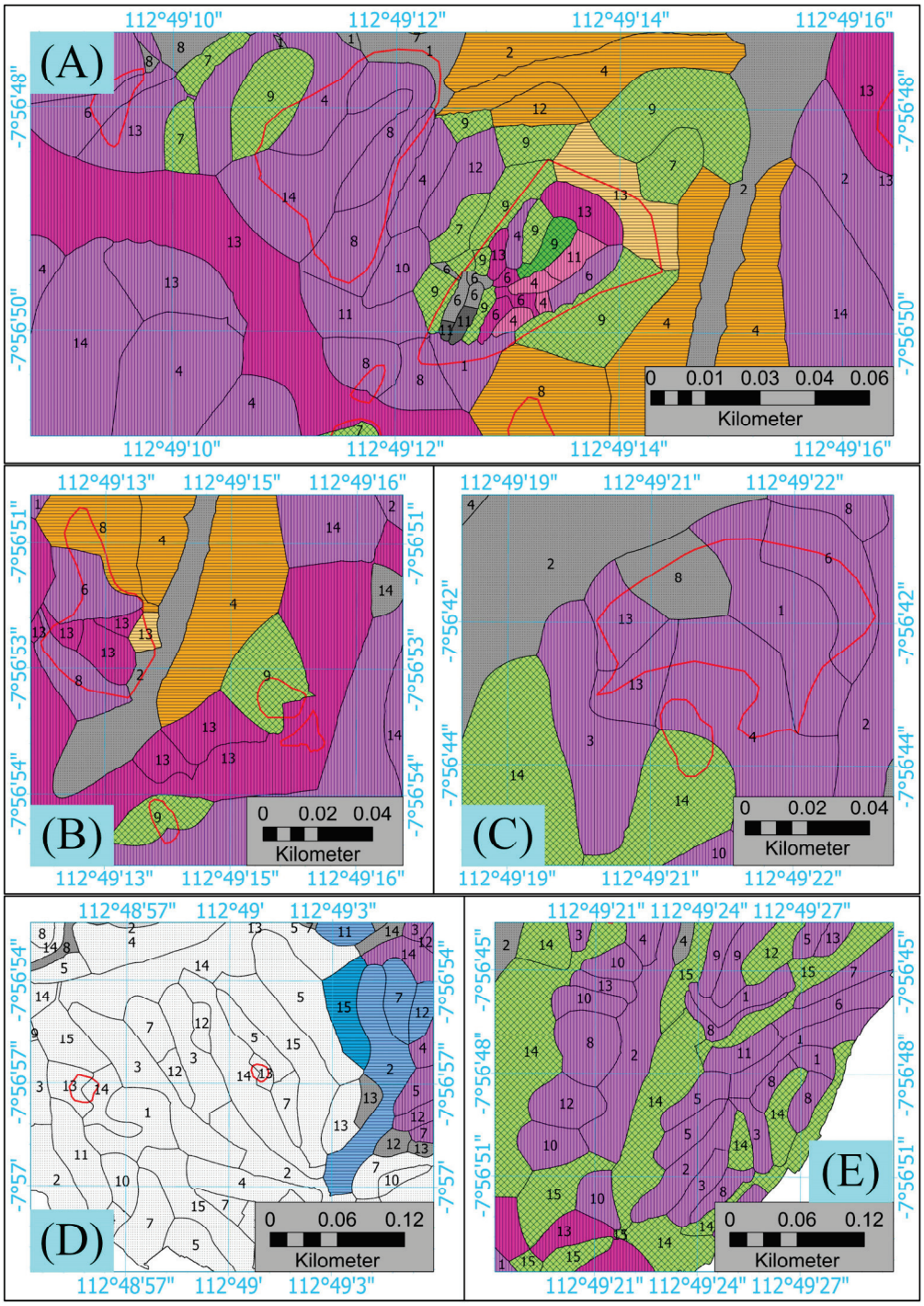

Figure 9. Inset map of the integration map of multivariate local coefficients focused on landslide areas (**A**–**C**); and non-slip areas (**D**,**E**).

4. Discussion

4.1. Mapping Microtopography, Landforms, Land Cover, and Vegetation Density

Microtopographic zoning mapping can be said to be rarely discussed in the field of geomorphology. In addition, Yang et al. used the Thiessen polygon approach to construct karst landform zoning precisely based on the spatial proximity of peak and nadir points, namely positive and negative landscapes [81]. In this study, microtopographic zoning was also derived from the results of thiessen polygon-based buffering on the morphology of the Cooke and Doornkamp system. Each mapped morphological boundary is used as a

Thiessen polygon control point to build micro-topographic zoning. The results show that the shape and size of the microtopographic units vary (Figure 5). The large and rounded unit shapes indicate that the distance between morphological boundaries is farther apart than the small and elongated unit shapes. It can also reflect the degree of geomorphic processes to form different microtopography. In other words, different morphologies allow different morpho processes to form different surface material characteristics [10].

Elemental landforms based on the Pennock system have been classified using high-resolution DTM data. The radius scale for the plan and profile curvature, which is 40 m each, is set based on more detailed spatial variability, but this is visual, so there may be uncertainty in the classification. In addition, the Pennock method identified the slope arrangement of the shoulder and footslope sections on both convergent and divergent slope shapes. Unfortunately, the Pennock method seems less sensitive for identifying the backslope. This problem is contrary to the study of Evans et al. that the Pennock method failed to identify the arrangement of shoulder and footslope slopes on agricultural land with low relief configurations [49]; it is also reported that the study area could not map divergent footslope landforms but was dominated by divergent back slopes with more complex relief configurations [82]. Thus, the differences in the problems in this study with other studies may be caused by differences in spatial resolution, unique relief configurations, and setting the radius parameter scale for which there is no definitive rule.

GEOBIA works well in class 1 hierarchical land cover classification with orthomosaic imagery: forest, shrubs, herbaceous plants, open land, and built-up land. Overall, producer accuracy and user accuracy for all classes reach above 90%. For the user, accuracy metric value of built land is the lowest among the other classes. This may be due to several built-up land objects having similarities in spectra, shape, and texture with forest areas, herbaceous plants and open land. However, this problem is not significant because it basically meets the land cover mapping requirements, which are above 85% [83].

There are several reasons why the accuracy of this land cover map is satisfactory. First, the method offered by [60], namely the combination of GEOBIA and selection of spectral features, shapes and textures, can classify land cover from orthomosaic imagery very well. Furthermore, segmentation parameters such as scale, shape, and compactness are obtained through trial and error, especially for scales set with a range of 50 to 500 in multiples of 50. As explained in the method Section 2.3.4., the optimum scale parameter is found, namely 150. Third, the CFS method works well in selecting all features into 13 optimal features for land cover classification in the study area. In addition, the RF classifier also performs very well, which is even slightly superior to the study by De Luca et al. with orthomosaic imagery equipped with near-infrared bands [61].

4.2. GWR Model Implementation with Different Independent Variable Data Transformation

Categorical data transformation for each class of independent variable has been carried out for the needs of the GWR model. The Type I model represents numerical data based on distance metrics microtopographic, landform and land cover variables. Then, the Type II and Type III models represent a comprehensive index of landscape metrics for each class of land cover and landform variables using PCA. These three types of models are crucial for the GWR model to work well because of the conventional-based data transformation problems, namely binary classes. However, there is a uniqueness in the Type III model, which breaks the standardization of PCA analysis that PC1 retains most of the information by maximizing the variance of the data from the comprehensive index of landscape metrics compiled in the Type II model. In other words, the PC with the highest AM value has the greatest correlation with landslides, although the eigenvalue is less than 1. Class variables with low variation are not unimportant [84] when associated with landslide data. This case is like the climate study by Jolliffe, in which the low variation component relates to the response variable rather than the high variation component [85]. In addition, discarding PCs with small eigenvalues can lead to bias [86]. Hadi and Ling also reported that PCs selected based on the breakdown of principal components that depend only on the variation

in variable X (i.e., the independent variable) might fail to account for regression fit because they do not contribute anything to the response variable (or the dependent variable) [87]. It was proven in the results of this study that when the Type II and Type III models were analyzed byboth univariate and multivariate GWR, the overall values of AICc and adj. R^2 in Type III is higher than Type II (Table 6). In addition, when the Type III model on landform and land cover is combined with the microtopography and vegetation density variables that are modeled simultaneously, it shows a higher regression fit than the variables in the Type I and Type II models. Meanwhile, the univariate model in Type I showed a higher regression fit than Type II and Type III. This indicates that setting compression and selecting landscape metric features on landform and land cover can increase the predictive power of the GWR model for exploring local spatial relationships of landslides in the study area.

4.3. Modeling Local Spatial Relationships of Landslides

The GWR model has been analyzed to identify the local spatial relationship between the landslide and the micro-topography, landform, land cover, and vegetation density in the study area. The Type III model with the best regression fit among the others was chosen as the independent variable input and the percentage of landslide area as the response variable. The result is that most of the independent variables can explain the landslides in the study area but not for the southwestern region. The statistical summary of parameter estimation (Table 7) shows that almost all variables spatially have positive and negative estimates which indicate a non-stationary relationship to landslides. The local coefficient integration map is the result of a synthesis of all variables that have been selected based on their significance and adjustment of feature information for each variable (namely, local coefficients that intersect with their features). This map is more intuitive and less confusing in examining the most significant variables, both the positive and negative relationship direction to landslides in each unit (Figure 6).

Variables positively related to landslides include microtopography, convergent backslope, divergent footslope and shrubs. In contrast, those negatively related include a small portion of microtopography, herbaceous plants, and open land. Meanwhile, the variables that showed the most positive and negative relationships were divergent footslopes and herbaceous plants, respectively. Sato et al. reported that landslides in the mountains of the northwestern Himalayas occurred relatively on convex slopes rather than concave slopes [88]. The study by [89] reported that landslides in Changshou Valley, Baoji City in Shaanxi Province often occur in surface relief with convex slope shapes. Pourghasemi et al. also reported that the shape of the convex slope had a major effect on landslides in the Jumunjin Area, South Korea [28]. Havenith et al., revealed that the reasons why landslides occur on convex slopes include: (1) convex slopes are relatively less stable under similar hydrogeological conditions (lower factor of safety) because a larger slope body (larger driving force) acts on the same sliding surface (more the same resistance); and (2) they allow for the presence of a accumulated material (colluvium), which reflects lower shear strength [90].

This statement supports the results of this study, namely that convex slopes are closely related to landslides in the study area. In addition, this convex slope is specifically located at the foot of the slope with surface material that holds a higher water content than the backslope and upper slope arrangement [48]. Then, when the water content in the surface material increases, the pore water pressure increases, which can result in a low Factor of Safety (increased shear stress and decreased shear strength) resulting in landslides [91]. In addition, the dynamics of surface material moisture content can be affected by rainfall intensity. As additional information, the divergent footslope in the study area is under an average slope of $28.8^\circ \pm 15.2^\circ$, thereby increasing the potential for landslides to occur. Specifically, herbaceous plant land cover is plantation land that is negatively related to landslides in the study area. This finding can be explained as land that was not initially maintained, such as shrubs and grasslands; open land converted to cultivation implies better water and land management practices that can allow for reduced slope instability [27].

However, several other significant variables also need not be ignored; although, only a few units.

Based on the findings of the spatial relationship of landslides with micro-topographical and vegetation variables, it can be used as a basis for the conservation of research areas to reduce the potential for landslides. Based on the results of the GWR, it shows that landslides occur on convergent backslopes with surface cover in the form of shrubs. In addition, landslides also have the potential to occur on convex slopes that are on the toe slopes. These findings can become a model for micro-topography and vegetation-based conservation arrangements, so that to reduce landslides the community in the study area is not advised to plant species in the form of shrubs on steep slopes, or to carry out intensive processing on footslopes with convex slope shapes. Herbaceous plants show a negative relationship to landslides, so as part of the landslide conservation effort planting of herbaceous plant species such as *Rumput gajah (Pennisettrum Purpureum), Pakis (Diplazium esculentum), Mindih (Melia azedarach L),* and *Waru (Hibiscus tiliaceus)* can be applied. Several herbaceous plants in the study area are conservative if planted using multi strata techniques, thereby reducing the potential for movement of soil material.

4.4. Research Implications and Limitations

This study reveals local relationships between landslides and microtopography, landforms, land cover, and vegetation density. However, the novelty offered is to build a natural unit of analysis compared to a grid basis, which is based on micro-topography derived from morphological thiessen polygons. Pennock system-based landform element independent variables are also taken into account. To our knowledge, they are rarely analyzed for detailed scale landslide studies because they are indirectly related to geomorphic processes. Land cover classification uses a reliable method that produces the best accuracy—using the method from the study of Ma et al. applied to drone-based orthomosaic imagery, which can be replicated for other studies. Then, three types of transformation of categorical data on independent variables become new insights with an analytical approach for the study of regression-based spatial modeling that can be reapplied, especially in research on geo-environmental disasters. In addition, the last and most important thing is to offer the output of the GWR model with a local coefficient integration map for the most significant classification of variables related to landslides (positive or negative). This map information can be used as a reference for landslide disaster management in the study area, namely convergent backslope, divergent footslope, some microtopographical classes, and shrubs that need to be watched out for in their land use and require special treatment to reduce slope instability.

However, there are several limitations in this study, including: (1) the mapped study area contains canopied vegetation, which is a weakness in building DTMs, so that it can cause land surface elevation estimation errors; (2) microtopographic zoning does not have field validation, so objectivity is still questionable because this study relies on interpretation remote sensing; and (3) the results of the GWR model with the transformation of landscape metric-based category data are not discussed further as to how the spatial configuration of landforms and land cover can specifically explain landslides in the study area. For further research, additional issues such as climate and anthropogenic factors can be added to the GWR model to obtain more complete results and to explain landslides in the entire study area.

5. Conclusions

Exploration of local spatial relationships between landslide occurrences in tropical hills, especially in Taji Village, Jabung District, East Java Province, can explain the factors that most influence landslides. A series of approaches and methods were introduced and implemented to construct independent variables to be analyzed by GWR and produce reliable model outputs. Microtopographical zoning is used as a unit of analysis to synthesize all information on the independent variables—which incidentally have different

spatial forms—as well as the dependent variable, namely the percentage of avalanche area. Categorical data transformation brought independent variables to be modeled, even better than global regression. However, the best results for the independent variables modeled simultaneously fell to the change in landscape metric data on landform and land cover features that had been compressed through PCA analysis, and selected component features associated with landslide occurrence data. GWR can reveal a non-stationary relationship between landslide events and independent variables in the study area. Information on the local coefficients of each independent variable is integrated into a single entity based on the significance of the t values (i.e., ≤ -1.96 and ≥ 1.96) and the selection of features of each variable that intersect with the microtopographic unit. The majority of the variables that show the most positive relationship to the occurrence of landslides are divergent footslopes where colluvial (colluvial) material accumulates from the upper slopes (i.e., the shoulders and backslope), which have a low Factor of Safety so that the slopes are less stable. In addition, the slopes of the footslope accommodate more water content, and when heavy rain occurs it can increase the pore water pressure so that the Factor of Safety is lower and there is a potential for landslides to happen, especially since the angle of the slopes in the study area is sufficient to support this. On the other hand, it was herbaceous plants or plantation land in the study area that surprisingly reduced the occurrence of landslides, due to good water and land management being able to maintain slope stability longer. The methodological approach developed and introduced in this study is reproducible and further analyzed in other tropical hills at a detailed and regional scale prone to landslides.

Author Contributions: Conceptualization, H.M. and S.S. methodology, H.M., S.K. and A.S.L.; validation, H.M., S.S. and S.K.; writing; review and editing H.M., S.S., S.K. and A.S.L. All authors have read and agreed to the published version of the manuscript.

Funding: This research received no external funding.

Institutional Review Board Statement: Not applicable.

Informed Consent Statement: Not applicable.

Data Availability Statement: Not applicable.

Conflicts of Interest: The authors declare no conflict of interest.

References

1. Chalise, D.; Kumar, L.; Kristiansen, P. Land degradation by soil erosion in Nepal: A review. *Soil Syst.* **2019**, *3*, 12. [CrossRef]
2. Kirui, O.K.; Mirzabaev, A.; von Braun, J. Assessment of land degradation 'on the ground' and from 'above'. *SN Appl. Sci.* **2021**, *3*, 318. [CrossRef]
3. Chasek, P. From land degradation to land restoration. *Policy Briefs* **2022**, *29*, 2.
4. AGU. The Human Cost of Landslides in 2016. The Landslide Blog—AGU Blogosphere. 2017. Available online: https://blogs.agu.org/landslideblog/2017/01/30/human-cost-of-landslides-2016/ (accessed on 7 January 2023).
5. BNPB. Data Informasi Bencana Indonesia (DIBI). 2008. Available online: https://gis.bnpb.go.id/ (accessed on 7 January 2023).
6. Setiawan, H.; Wilopo, W.; Wiyoso, T.; Fathani, T.F.; Karnawati, D. Investigation and numerical simulation of the 22 February 2018 landslide-triggered long-traveling debris flow at Pasir Panjang Village, Brebes Regency of Central Java, Indonesia. *Landslides* **2019**, *16*, 2219–2232. [CrossRef]
7. Karnawati, D.; Fathani, T.F.; Ignatius, S.; Andayani, B.; Legono, D.; Burton, P.W. Landslide hazard and community-based risk reduction effort in Karanganyar and the surrounding area, central Java, Indonesia. *J. Mt. Sci.* **2011**, *8*, 149–153. [CrossRef]
8. Bachr, I.S.; Stötter, J.; Monreal, M.; Sartohadi, J. The calamity of eruptions, or an eruption of benefits? Mt. Bromo human–volcano system a case study of an open-risk perception. *Nat. Hazards Earth Syst. Sci.* **2015**, *15*, 277–290. [CrossRef]
9. Marc, O.; Stumpf, A.; Malet, J.-P.; Gosset, M.; Uchida, T.; Chiang, S.-H. Initial insights from a global database of rainfall-induced landslide inventories: The weak influence of slope and strong influence of total storm rainfall. *Earth Surf. Dyn.* **2018**, *6*, 903–922. [CrossRef]
10. Bachri, S.; Shrestha, R.P.; Yulianto, F.; Sumarmi, S.; Utomo, K.S.B.; Aldianto, Y.E. Mapping Landform and Landslide Susceptibility Using Remote Sensing, GIS and Field Observation in the Southern Cross Road, Malang Regency, East Java, Indonesia. *Geosciences* **2020**, *11*, 4. [CrossRef]
11. Van Westen, C.J.; Soeters, R.; Sijmons, K. Digital geomorphological landslide hazard mapping of the Alpago area, Italy. *Int. J. Appl. Earth Obs. Geoinf.* **2000**, *2*, 51–60. [CrossRef]

12. Mallet, C.; David, N. Digital Terrain Models Derived from Airborne LiDAR Data. In *Optical Remote Sensing of Land Surface*; Elsevier: Amsterdam, The Netherlands, 2016; pp. 299–319.
13. Tempa, K.; Peljor, K.; Wangdi, S.; Ghalley, R.; Jamtsho, K.; Ghalley, S.; Pradhan, P. UAV technique to localize landslide susceptibility and mitigation proposal: A case of Rinchending Goenpa landslide in Bhutan. *Nat. Hazards Res.* **2021**, *1*, 171–186. [CrossRef]
14. Pellicani, R.; Argentiero, I.; Manzari, P.; Spilotro, G.; Marzo, C.; Ermini, R.; Apollonio, C. UAV and Airborne LiDAR Data for Interpreting Kinematic Evolution of Landslide Movements: The Case Study of the Montescaglioso Landslide (Southern Italy). *Geosciences* **2019**, *9*, 248. [CrossRef]
15. Granados-Bolaños, S.; Quesada-Román, A.; Alvarado, G.E. Low-cost UAV applications in dynamic tropical volcanic landforms. *J. Volcanol. Geotherm. Res.* **2021**, *410*, 107143. [CrossRef]
16. Sofia, G. Combining geomorphometry, feature extraction techniques and Earth-surface processes research: The way forward. *Geomorphology* **2020**, *355*, 107055. [CrossRef]
17. Nagamatsu, D.; Miura, O. Soil disturbance regime in relation to micro-scale landforms and its effects on vegetation structure in a hilly area in Japan. *Plant Ecol.* **1997**, *133*, 191–200. [CrossRef]
18. Chimner, R.A.; Hart, J.B. Hydrology and microtopography effects on northern white-cedar regeneration in Michigan's Upper Peninsula. *Can. J. For. Res.* **1996**, *26*, 389–393. [CrossRef]
19. Schaetzl, R.J.; Follmer, L.R. Longevity of treethrow microtopography: Implications for mass wasting. *Geomorphology* **1990**, *3*, 113–123. [CrossRef]
20. Kabrick, J.M.; Meyers, N.L.; McSweeney, K. Comparison of Sampling Methods for Estimating Pit and Mound Microtopography. *Soil Sci. Soc. Am. J.* **1997**, *61*, 1423–1427. [CrossRef]
21. Wang, J.; Zhu, Q.K.; Qin, W.; Zhang, H.Z.; Yun, L.; Xie, J.; Kuang, G.M. Differentiation of vegetation characteristics on slope micro-topography of fenced watershed in loess area of north Shaanxi province, Northwest China. *J. Appl. Ecol.* **2012**, *23*, 694–700.
22. Zhu, Q.K.; Zhang, Y.; Zhao, L.L. *Vegetation Restoration and Simulated Natural Forestation in the Loess Plateau, Northern Shaanxi, China*; Beijing Science Press: Beijing, China, 2012.
23. Zhao, W.; Zhang, Y.; Zhu, Q.; Qin, W.; Peng, S.; Li, P.; Zhao, Y.; Ma, H.; Wang, Y. Effects of microtopography on spatial point pattern of forest stands on the semi-arid Loess Plateau, China. *J. Arid Land* **2015**, *7*, 370–380. [CrossRef]
24. Sakai, A.; Ohsawa, M. Topographical pattern of the forest vegetation on a river basin in a warm-temperate hilly region, central Japan. *Ecol. Res.* **1994**, *9*, 269–280. [CrossRef]
25. Sakai, A.; Ohsawa, M. Vegetation pattern and microtopography on a landslide scar of Mt Kiyosumi, central Japan. *Ecol. Res.* **1993**, *8*, 47–56. [CrossRef]
26. Knight, J.; Mitchell, W.A.; Rose, J. Geomorphological Field Mapping. In *Geomorphological Mapping Methods and Application*, 1st ed.; Smith, M.J., Paron, P., Griffiths, J.S., Eds.; Elsevier: Amsterdam, Netherlands, 2011; pp. 151–187.
27. Pisano, L.; Zumpano, V.; Malek, Ž.; Rosskopf, C.M.; Parise, M. Variations in the susceptibility to landslides, as a consequence of land cover changes: A look to the past, and another towards the future. *Sci. Total Environ.* **2017**, *601*, 1147–1159. [CrossRef] [PubMed]
28. Pourghasemi, H.; Gayen, A.; Park, S.; Lee, C.-W.; Lee, S. Assessment of Landslide-Prone Areas and Their Zonation Using Logistic Regression, LogitBoost, and NaïveBayes Machine-Learning Algorithms. *Sustainability.* **2018**, *10*, 3697. [CrossRef]
29. Jones, S.; Kasthurba, A.K.; Bhagyanathan, A.; Binoy, B.V. Impact of anthropogenic activities on landslide occurrences in southwest India: An investigation using spatial models. *J. Earth Syst. Sci.* **2021**, *130*, 70. [CrossRef]
30. Shu, H.; Hürlimann, M.; Molowny-Horas, R.; González, M.; Pinyol, J.; Abancó, C.; Ma, J. Relation between land cover and landslide susceptibility in Val d'Aran, Pyrenees (Spain): Historical aspects, present situation and forward prediction. *Sci. Total Environ.* **2019**, *693*, 133557. [CrossRef]
31. Akgun, A.; Türk, N. Landslide susceptibility mapping for Ayvalik (Western Turkey) and its vicinity by multicriteria decision analysis. *Environ. Earth Sci.* **2010**, *61*, 595–611. [CrossRef]
32. Castellanos Abella, E.A.; van Westen, C.J. Qualitative landslide susceptibility assessment by multicriteria analysis: A case study from San Antonio del Sur, Guantánamo, Cuba. *Geomorphology* **2008**, *94*, 453–466. [CrossRef]
33. Guzzetti, F.; Carrara, A.; Cardinali, M.; Reichenbach, P. Landslide hazard evaluation: A review of current techniques and their application in a multi-scale study, Central Italy. *Geomorphology* **1999**, *31*, 181–216. [CrossRef]
34. Zhang, W.; Liu, S.; Wang, L.; Samui, P.; Chwała, M.; He, Y. Landslide Susceptibility Research Combining Qualitative Analysis and Quantitative Evaluation: A Case Study of Yunyang County in Chongqing, China. *Forests* **2022**, *13*, 1055. [CrossRef]
35. Pourghasemi, H.R.; Kariminejad, N.; Gayen, A.; Komac, M. Statistical functions used for spatial modelling due to assessment of landslide distribution and landscape-interaction factors in Iran. *Geosci. Front.* **2020**, *11*, 1257–1269. [CrossRef]
36. Brunsdon, C.; Fotheringham, S.; Charlton, M. Geographically Weighted Regression. *J. R. Stat. Soc. Ser. D Stat.* **1998**, *47*, 431–443. [CrossRef]
37. Wang, H.B.; Sassa, K. Comparative evaluation of landslide susceptibility in Minamata area, Japan. *Environ. Geol.* **2005**, *47*, 956–966. [CrossRef]
38. Pix4D. *Pix4Dcapture*; Pix4D: Renens, Switzerland, 2022; Available online: https://www.pix4d.com/ (accessed on 1 August 2022).
39. Dandois, J.; Olano, M.; Ellis, E. Optimal Altitude, Overlap, and Weather Conditions for Computer Vision UAV Estimates of Forest Structure. *Remote Sens.* **2015**, *7*, 13895–13920. [CrossRef]

40. Agisoft LLC. *Agisoft PhotoScan*; Agisoft LLC: Saint Petersburg, Russia, 2022; Available online: https://www.agisoft.com/ (accessed on 1 August 2022).
41. Kaimaris, D.; Patias, P.; Sifnaiou, M. UAV and the comparison of image processing software. *Int. J. Intell. Unmanned Syst.* **2017**, *5*, 18–27. [CrossRef]
42. Nebiker, S.; Lack, N.; Deuber, M. Building Change Detection from Historical Aerial Photographs Using Dense Image Matching and Object-Based Image Analysis. *Remote Sens.* **2014**, *6*, 8310–8336. [CrossRef]
43. Goodbody, T.; Coops, N.; Hermosilla, T.; Tompalski, P.; Pelletier, G. Vegetation Phenology Driving Error Variation in Digital Aerial Photogrammetrically Derived Terrain Models. *Remote Sens.* **2018**, *10*, 1554. [CrossRef]
44. Yilmaz, V.; Konakoglu, B.; Serifoglu, C.; Gungor, O.; Gökalp, E. Image classification-based ground filtering of point clouds extracted from UAV-based aerial photos. *Geocarto Int.* **2018**, *33*, 310–320. [CrossRef]
45. Cooke, R.U.; Doornkamp, J.C. *Geomorphology in Environmental Management*; Clarendon Press: Oxford, UK, 1974.
46. Rashid, I.; Romshoo, S.A.; Hajam, J.A.; Abdullah, T. A semi-automated approach for mapping geomorphology in mountainous terrain, Ferozpora watershed (Kashmir Himalaya). *J. Geol. Soc. India* **2016**, *88*, 206–212. [CrossRef]
47. Yang, H.; Zhao, Z.; Jiang, C.; Wen, Y.; Muneeb Abid, M. Spatially Varying Relation between Built Environment and Station-Level Subway Passenger-Distance. *J. Adv. Transp.* **2022**, *2022*, 1–18. [CrossRef]
48. Pennock, D.J.; Zebarth, B.J.; de Jong, E. Landform classification and soil distribution in hummocky terrain, Saskatchewan, Canada. *Geoderma* **1987**, *40*, 297–315. [CrossRef]
49. Evans, D.A.; Williard, K.W.J.; Schoonover, J.E. Comparison of Terrain Indices and Landform Classification Procedures in Low-Relief Agricultural Fields. *J. Geospat. Appl. Nat. Resour.* **2016**, *1*, 1.
50. Pradhan, B.; Chaudhari, A.; Adinarayana, J.; Buchroithner, M.F. Soil erosion assessment and its correlation with landslide events using remote sensing data and GIS: A case study at Penang Island, Malaysia. *Environ. Monit. Assess.* **2012**, *184*, 715–727. [CrossRef] [PubMed]
51. Blaschke, T. Object based image analysis for remote sensing. *ISPRS J. Photogramm. Remote Sens.* **2010**, *65*, 2–16. [CrossRef]
52. Modica, G.; de Luca, G.; Messina, G.; Praticò, S. Comparison and assessment of different object-based classifications using machine learning algorithms and UAVs multispectral imagery: A case study in a citrus orchard and an onion crop. *Eur. J. Remote Sens.* **2021**, *54*, 431–460. [CrossRef]
53. BBlaschke, T.; Hay, G.J.; Kelly, M.; Lang, S.; Hofmann, P.; Addink, E.; Feitosa, R.Q.; van der Meer, F.; van der Werff, H.; van Coillie, F.; et al. Geographic Object-Based Image Analysis—Towards a new paradigm. *ISPRS J. Photogramm. Remote Sens.* **2014**, *87*, 180–191. [CrossRef]
54. Torres-Sánchez, J.; López-Granados, F.; Peña, J.M. An automatic object-based method for optimal thresholding in UAV images: Application for vegetation detection in herbaceous crops. *Comput. Electron. Agric.* **2015**, *114*, 43–52. [CrossRef]
55. De Castro, A.; Torres-Sánchez, J.; Peña, J.; Jiménez-Brenes, F.; Csillik, O.; López-Granados, F. An Automatic Random Forest-OBIA Algorithm for Early Weed Mapping between and within Crop Rows Using UAV Imagery. *Remote Sens.* **2018**, *10*, 285. [CrossRef]
56. Hall, M.A.; Holmes, G. Benchmarking attribute selection techniques for discrete class data mining. *IEEE Trans. Knowl. Data Eng.* **2003**, *15*, 1437–1447. [CrossRef]
57. Ma, L.; Fu, T.; Blaschke, T.; Li, M.; Tiede, D.; Zhou, Z.; Ma, X.; Chen, D. Evaluation of Feature Selection Methods for Object-Based Land Cover Mapping of Unmanned Aerial Vehicle Imagery Using Random Forest and Support Vector Machine Classifiers. *ISPRS Int. J. Geo-Inf.* **2017**, *6*, 51. [CrossRef]
58. Breiman, L. Random Forests. *Mach. Learn.* **2001**, *45*, 5–32. [CrossRef]
59. Li, M.; Ma, L.; Blaschke, T.; Cheng, L.; Tiede, D. A systematic comparison of different object-based classification techniques using high spatial resolution imagery in agricultural environments. *Int. J. Appl. Earth Obs. Geoinf.* **2016**, *49*, 87–98. [CrossRef]
60. Ma, L.; Li, M.; Ma, X.; Cheng, L.; Du, P.; Liu, Y. A review of supervised object-based land-cover image classification. *ISPRS J. Photogramm. Remote Sens.* **2017**, *130*, 277–293. [CrossRef]
61. De Luca, G.N.; Silva, J.M.; Cerasoli, S.; Araújo, J.; Campos, J.; di Fazio, S.; Modica, G. Object-Based Land Cover Classification of Cork Oak Woodlands using UAV Imagery and Orfeo ToolBox. *Remote Sens.* **2019**, *11*, 1238. [CrossRef]
62. Stehman, S.V. Estimating the kappa coefficient and its variance under stratified random sampling. *Photogramm. Eng. Remote Sens.* **1996**, *62*, 401–407.
63. Congalton, R.G.; Green, K. *Assessing the Accuracy of Remotely Sensed Data*; CRC Press: Boca Raton, FL, USA, 2019.
64. McGarigal, K.; Cushman, S.A.; Neel, M.C.; Ene, E. FRAGSTATS: Spatial Pattern Analysis Program for Categorical Maps. Computer Software Program Produced by the Authors at the University of Massachusetts, Amherst. 2002. Available online: https://fragstats.software.informer.com/4.2/ (accessed on 23 July 2022).
65. Schultz, C.; Alegría, A.C.; Cornelis, J.; Sahli, H. Comparison of spatial and aspatial logistic regression models for landmine risk mapping. *Appl. Geogr.* **2016**, *66*, 52–63. [CrossRef]
66. Alzaga, V.; Tizzani, P.; Acevedo, P.; Ruiz-Fons, F.; Vicente, J.; Gortázar, C. Deviance partitioning of host factors affecting parasitization in the European brown hare (*Lepus europaeus*). *Naturwissenschaften* **2009**, *96*, 1157–1168. [CrossRef] [PubMed]
67. Romero, D.; Olivero, J.; Real, R. Comparative assessment of different methods for using land-cover variables for distribution modelling of Salamandra salamandra longirotris. *Environ. Conserv.* **2013**, *40*, 48–59. [CrossRef]
68. Uuemaa, E.; Mander, Ü.; Marja, R. Trends in the use of landscape spatial metrics as landscape indicators: A review. *Ecol Indic.* **2013**, *28*, 100–106. [CrossRef]

69. Wang, X.; Zhang, F. Multi-scale analysis of the relationship between landscape patterns and a water quality index (WQI) based on a stepwise linear regression (SLR) and geographically weighted regression (GWR) in the Ebinur Lake oasis. *Environ. Sci. Pollut. Res.* **2018**, *25*, 7033–7048. [CrossRef]
70. Dinesh, S. Analysis of Landform Metrics of Mountains Extracted from Multiscale Digital Elevation Models. *Aust. J. Basic Appl. Sci.* **2009**, *3*, 3997–4010.
71. Galicia, L.; Zarco-Arista, A.E.; Mendoza-Robles, K.I.; Palacio-Prieto, J.L.; García-Romero, A. Land use/cover, landforms and fragmentation patterns in a tropical dry forest in the southern Pacific region of Mexico. *Singap. J. Trop. Geogr.* **2008**, *29*, 137–154. [CrossRef]
72. Ramachandra, T.V.; Bharath, A.H.; Sowmyashree, M.V. Monitoring urbanization and its implications in a mega city from space: Spatiotemporal patterns and its indicators. *J. Environ. Manag.* **2015**, *148*, 67–81. [CrossRef] [PubMed]
73. Hesselbarth, M.H.K.; Sciaini, M.; With, K.A.; Wiegand, K.; Nowosad, J. Landscapemetrics: An open-source R tool to calculate landscape metrics. *Ecography* **2019**, *42*, 1648–1657. [CrossRef]
74. Frazier, A.E.; Kedron, P. Landscape Metrics: Past Progress and Future Directions. *Curr. Landsc. Ecol. Rep.* **2017**, *2*, 63–72. [CrossRef]
75. Liu, S.; Li, X.; Chen, L.; Zhao, Q.; Zhao, C.; Hu, X.; Li, J. A New Approach to Investigate the Spatially Heterogeneous in the Cooling Effects of Landscape Pattern. *Land* **2022**, *11*, 239. [CrossRef]
76. Odhiambo Omuya, E.; Onyango Okeyo, G.; Waema Kimwele, M. Feature Selection for Classification using Principal Component Analysis and Information Gain. *Expert Syst. Appl.* **2021**, *174*, 114765. [CrossRef]
77. Kononenko, I. Estimating attributes: Analysis and extensions of RELIEF. In *ECML-94*; Bergadano, F., de Raedt, L., Eds.; Machine Learning; Springer: Berlin/Heidelberg, Germany, 1994; pp. 171–182.
78. Kira, K.; Rendell, L.A. A Practical Approach to Feature Selection. In *Machine Learning Proceedings 1992*; Sleeman, D., Edwards, P., Eds.; Elsevier: Amsterdam, The Netherlands, 1992; pp. 249–256.
79. Fotheringham, A.S.; Brunsdon, C.; Charlton, M. *Geographically Weighted Regression: The Analysis of Spatially Varying Relationships*; John Wiley & Sons: Hoboken, NJ, USA, 2002.
80. Li, Y.; Liu, X.; Han, Z.; Dou, J. Spatial Proximity-Based Geographically Weighted Regression Model for Landslide Susceptibility Assessment: A Case Study of Qingchuan Area, China. *Appl. Sci.* **2020**, *10*, 1107. [CrossRef]
81. Yang, X.; Tang, G.; Meng, X.; Xiong, L. Classification of Karst Fenglin and Fengcong Landform Units Based on Spatial Relations of Terrain Feature Points from DEMs. *Remote Sens.* **2019**, *11*, 1950. [CrossRef]
82. Prasannakumar, V.; Vijith, H.; Geetha, N. Terrain evaluation through the assessment of geomorphometric parameters using DEM and GIS: Case study of two major sub-watersheds in Attapady, South India. *Arab. J. Geosci.* **2013**, *6*, 1141–1151. [CrossRef]
83. Lillesand, T.M.; Kiefer, R.W. *Remote Sensing and Image Interpretation*, 4th ed.; John Wiley & Sons: New York, NY, USA, 2000; p. 469.
84. Hu, X.; Xu, C.; Chen, J.; Lin, Y.; Lin, S.; Wu, Z.; Qiu, R. A Synthetic Landscape Metric to Evaluate Urban Vegetation Quality: A Case of Fuzhou City in China. *Forests* **2022**, *13*, 1002. [CrossRef]
85. Jolliffe, I.T. A Note on the Use of Principal Components in Regression. *Appl. Stat.* **1982**, *31*, 300. [CrossRef]
86. Mason, R.L.; Gunst, R.F. Selecting principal components in regression. *Stat. Probab. Lett.* **1985**, *3*, 299–301. [CrossRef]
87. Hadi, A.S.; Ling, R.F. Some Cautionary Notes on the Use of Principal Components Regression. *Am. Stat.* **1998**, *52*, 15–19.
88. Sato, H.P.; Hasegawa, H.; Fujiwara, S.; Tobita, M.; Koarai, M.; Une, H.; Iwahashi, J. Interpretation of landslide distribution triggered by the 2005 Northern Pakistan earthquake using SPOT 5 imagery. *Landslides* **2007**, *4*, 113–122. [CrossRef]
89. Wang, H.B.; Li, J.M.; Zhou, B.; Zhou, Y.; Yuan, Z.Q.; Chen, Y.P. Application of a hybrid model of neural networks and genetic algorithms to evaluate landslide susceptibility. *Geoenvironmental Disasters* **2017**, *4*, 15. [CrossRef]
90. Havenith, H.-B.; Strom, A.; Caceres, F.; Pirard, E. Analysis of landslide susceptibility in the Suusamyr region, Tien Shan: Statistical and geotechnical approach. *Landslides* **2006**, *3*, 39–50. [CrossRef]
91. Ray, R.L.; Jacobs, J.M. Relationships among remotely sensed soil moisture, precipitation and landslide events. *Nat. Hazards* **2007**, *43*, 211–222. [CrossRef]

sustainability

MDPI

Article

Numerical Analysis of an Explicit Smoothed Particle Finite Element Method on Shallow Vegetated Slope Stability with Different Root Architectures

Xichun Jia [1], Wei Zhang [1], Xinghan Wang [2], Yuhao Jin [1,*] and Peitong Cong [1,*]

[1] College of Water Conservancy and Civil Engineering, South China Agricultural University, Guangzhou 510642, China
[2] Water Resources Remote Sensing Department, Pearl River Water Resources Research Institute, Guangzhou 510610, China
* Correspondence: yuhao.jin@scau.edu.cn (Y.J.); slxyky@scau.edu.cn (P.C.)

Abstract: Planting vegetation is an environmentally friendly method for reducing landslides. Current vegetated slope analysis fails to consider the influence of different root architectures, and the accuracy and effectiveness of the numerical simulations need to be improved. In this study, an explicit smoothed particle finite element method (eSPFEM) was used to evaluate slope stability under the influence of vegetation roots. The Mohr–Coulomb constitutive model was extended by incorporating apparent root cohesion into the shear strength of the soil. The slope factors of safety (FOS) of four root architectures (uniform, triangular, parabolic, and exponential) for various planting distances, root depths, slope angles, and planting locations were calculated using the shear strength reduction technique with a kinetic energy-based criterion. The results indicated that the higher the planting density, the stronger the reinforcement effect of the roots on the slope. With increasing root depth, the FOS value first decreased and then increased. The FOS value decreased with an increase in slope angle. Planting on the entire ground surface had the best improvement effect on the slope stability, followed by planting vegetation with a uniform root architecture in the upper slope region or planting vegetation with triangular or exponential root architecture on the slope's toe. Our findings are expected to deepen our understanding of the contributions of different root architectures to vegetated slope protection and guide the selection of vegetation species and planting locations.

Keywords: explicit smooth particle finite element method; vegetated slope; root architectures; shear strength reduction technique; factor of safety

Citation: Jia, X.; Zhang, W.; Wang, X.; Jin, Y.; Cong, P. Numerical Analysis of an Explicit Smoothed Particle Finite Element Method on Shallow Vegetated Slope Stability with Different Root Architectures. *Sustainability* **2022**, *14*, 11272. https://doi.org/10.3390/su141811272

Academic Editors: Stefano Morelli, Veronica Pazzi and Mirko Francioni

Received: 29 July 2022
Accepted: 6 September 2022
Published: 8 September 2022

1. Introduction

Landslides and debris flows are common natural disasters that cause environmental damage, human casualties, and economic losses [1,2]. To tackle this problem, measures, such as nailing, vegetation, ground improvement, geosynthetic reinforcement, and improved drainage have been taken. Among these, vegetation is an economically, sustainable, and environmentally friendly bio-remediation technique [3,4]. Further studies on the effects of vegetation on slope stability are essential.

It is now understood that vegetation contributes to the stability of civil infrastructure, including shallow slopes (i.e., slopes with vertical depths less than 2 m), road and railway slopes, dams, embankments, and dykes [5–9]. Vegetation roots (e.g., from grasses, shrubs, and trees) are believed to stabilise slopes and slow the large-scale movement of landslides by strengthening soils with increased cohesion [10–13]. Planting trees on slopes can reduce the occurrence of shallow landslides by up to 95% compared with similar areas without trees [14,15].

To date, a large body of literature has documented studies that have focused on quantifying the contribution of roots to soil shear strength. These studies included in situ

direct shear tests [16,17] and laboratory direct shear tests [18,19] on soil blocks containing plant roots, as well as laboratory direct shear tests of soils reinforced by fibres that simulate roots [20–22]. The finite element method (FEM) can also be applied in this vein of research [23,24]. These studies have shown that roots can increase the shear strength of the soil. Therefore, it is necessary to incorporate the effects of root reinforcement into landslide prediction models and slope-stability analyses.

The limit equilibrium method (LEM) [25,26] and FEM [27,28] have been widely used in slope-stability analyses. The advantages of FEM compared to LEM are that it does not need to presuppose the shape and position of the critical slip surface, and the stress–strain relationship and soil deformation behaviour can be considered using the FEM. Slope-stability analysis based on the FEM has been recognised as an effective tool in geotechnical engineering [29]. The FEM has also been applied to the analysis of vegetated slopes [30]. The traditional FEM can correctly describe the initial failure surface, but for the large deformation problem of the slope after the initial failure, the numerical simulation may be inaccurate or even impossible owing to mesh distortion; therefore, FEM has limitations to such problems [29,31].

An alternative solution for overcoming the FEM mesh distortion problem is the meshless technique, which uses a set of particles to replace the mesh in FEM-based approaches [32]. Many meshless numerical frameworks have been presented to solve large-deformation problems in geomechanics so far [33], such as discrete element method (DEM) [34,35], smoothed particle hydrodynamics (SPH) [36,37], and the material point method (MPM) [38,39]. However, meshless methods require neighbours' searching, which needs high computation costs. Moreover, meshless methods usually necessitate special treatment techniques to deal with boundary conditions [32]. The particle finite element method (PFEM) [40,41] uses particles to represent materials that are similar to those in the mesh-free method, and it has been proven as a powerful numerical means to analyse the post-failure mechanisms in geo-engineering [32]. In recent years, many novel methods have been improved on the basis of PFEM, such as the smoothed particle finite element method (SPFEM) [30,32,42,43], edge-based smoothed PFEM (ES-PFEM) [44], node-based smoothed PFEM (NS-PFEM) [45], and stable node-based smoothed PFEM (SNS-PFEM) [46,47].

In previous studies, the numerical analysis of the influence of roots on slope stability usually involved the change of material parameters at a certain depth of the soil layer, and the effect of specific root architecture has seldom been considered. Plant roots penetrate the soil matrix to form a root-soil composite [29,31]. Nevertheless, existing analytical models generally concentrate on the ultimate limit state, and they neglect the complicated interactions between root systems and soil [48]. Therefore, quantifying the root contribution and determining the critical slip surface remains a challenge.

Based on the shortcomings of previous investigations, this study proposes a novel method for evaluating the stability of shallow vegetated slopes. An eSPFEM with a kinetic-energy-based criterion was used for the numerical simulation. The apparent root cohesion is incorporated into the Mohr–Coulomb constitutive model. The FOS of the four root architectures for various planting distances, root depths, slope angles, and planting locations were calculated using the shear strength reduction technique. To the best of our knowledge, this is the first study to use eSPFEM to calculate the effects of different root architectures on slope stability. This study is expected to provide a reference for improving the slope stability and optimising the management of mountain shelter forests. Nonetheless, the limitation of this study lies in the need for a large amount of calculation and accurate parameterisation, so it is currently only applicable to small and shallow slopes.

2. Materials and Methods

2.1. The eSPFEM Approaches

The PFEM solves the governing equations using a standard finite element approach [30]. Therefore, it not only has the flexibility of mesh-free particle methods for arbitrary changes in geometry but also inherits the solid mathematical foundation of the traditional FEM [49].

The PFEM is based on an updated Lagrangian (UL) fashion for modelling the motion of a continuum medium. The continuum medium is discretised into a set of Lagrangian nodes (particles) that contain and transmit all of the information present. The computational mesh was built using the Delaunay triangulation technique, and the boundary of the computational mesh was identified using the alpha-shape approach. A mesh was then used to solve the governing equations. However, in the PFEM, excessive mesh distortion is avoided by frequent remeshing, and the state variables (i.e., stress and strain) are mapped from old Gauss points to new ones. This mapping procedure inevitably introduces errors, which increase the complexity of the calculation process [30,32,42].

The SPFEM [50,51] uses a strain smoothing technique for nodal integration based on the PFEM to achieve the balance of governing equations at nodes or particles. In the SPFEM, all of the field variables are calculated at particles instead of Gauss points in the PFEM, which can avoid information transfer between Gauss points and particles, thus reducing the calculation error. In addition, the SPFEM possesses the upper-bound property and provides a conservative estimate for problems in geomechanics. Finally, low-order triangle elements can be used directly without volumetric locking [30,32,42]. The SPFEM can consider the entire dynamic failure process of a slope in slope-stability analysis and therefore simulate the large deformation and post-failure of soil to obtain a more reliable FOS value [32].

In SPFEM, the computation domain is discretized into strain smoothing cells associated with nodes. The physical volume, Ω, is correspondingly discretized into particles. As shown in Figure 1, The smoothing cell associated with the particle k is created by connecting sequentially the mid edge point to the central points of the surrounding triangular elements of particle k. A strain smoothing operation is then performed based on the set of smoothing cells that are created based on the triangulation mesh [32].

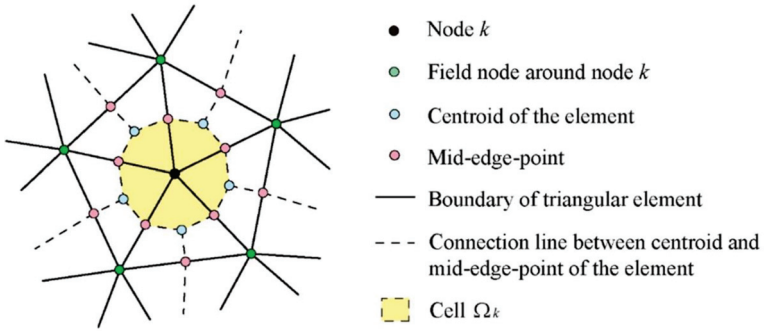

Figure 1. Construction of smoothing cell associated with particle k.

In the smoothed strain technique, the area, A_k, of the smoothing cell, Ω_k, associated with node k is calculated by:

$$A_k = \int_{\Omega_k} d\Omega = \frac{1}{3}\sum_{j=1}^{N_k} A_j \tag{1}$$

where N_k is the number of elements related to particle k and A_j is the area of the jth element. The smoothed strain matrix is calculated by:

$$\widetilde{\boldsymbol{B}}_k = \frac{1}{A_k}\sum_{j=1}^{N_k} \frac{1}{3} A_j \boldsymbol{B}_j \tag{2}$$

where B_j represents the strain gradient matrix used in the standard FEM for the jth element. More details regarding the strain smoothing technique are available in Liu et al. [51] and Chen et al. [52].

The discretization of the computational formulations of eSPFEM is now briefly presented. The motion of a continuum can be described as:

$$\rho \boldsymbol{a} = \nabla \cdot \boldsymbol{\sigma} + \rho \boldsymbol{b} \tag{3}$$

where, ρ is the material density, $\boldsymbol{a}$ is the acceleration, $\boldsymbol{\sigma}$ is the Cauchy stress tensor, and $\boldsymbol{b}$ is the specific body force density. Considering the principle of virtual displacement and the divergence theorem, the weak form is expressed as:

$$\int_{\Omega} \delta \boldsymbol{u} \cdot \rho \boldsymbol{a} d\Omega = \int_{S} \delta \boldsymbol{u} \cdot \boldsymbol{\tau}_S dS + \int_{\Omega} \delta \boldsymbol{u} \cdot \rho \boldsymbol{b} d\Omega - \int_{\Omega} \delta \boldsymbol{u} : \boldsymbol{\sigma} d\Omega \tag{4}$$

where $\boldsymbol{u}$ is the displacement vector, Ω represents the configuration domain, S represents the boundary, and $\boldsymbol{\tau}_S$ is the prescribed traction. After the node-based discretization, the above equation reads:

$$\sum_{k=1}^{T} \rho \boldsymbol{a}_k A_k = \sum_{k=1}^{T} \int_{S} \boldsymbol{N}_k \boldsymbol{\tau}_S dS + \sum_{k=1}^{T} \rho \boldsymbol{b}_k A_k - \sum_{k=1}^{T} \widetilde{\boldsymbol{B}}_k^T \boldsymbol{\sigma}_k A_k \tag{5}$$

where T is the total number of nodes in the computation domain. The above discrete form can then be written in the vector or matrix form as:

$$\boldsymbol{M}\boldsymbol{a} = \boldsymbol{F}^{ext} - \boldsymbol{F}^{int} \tag{6}$$

in which:

$$\boldsymbol{F}^{ext} = \sum_{k=1}^{T} \int_{S} \boldsymbol{N}_k \boldsymbol{\tau}_S dS + \sum_{k=1}^{T} \rho \boldsymbol{b}_k A_k \tag{7}$$

$$\boldsymbol{F}^{int} = \sum_{k=1}^{T} \widetilde{\boldsymbol{B}}_k^T \boldsymbol{\sigma}_k A_k \tag{8}$$

$$\boldsymbol{M} = \sum_{k=1}^{T} \rho A_k \tag{9}$$

where $\boldsymbol{F}^{ext}$ and $\boldsymbol{F}^{int}$ are termed as the external and internal forces, respectively, and $\boldsymbol{M}$ is the diagonal mass matrix.

A typical computational cycle of eSPFEM is shown as follows [43]:

(1) Generate mesh using Delaunay triangulation and alpha shape technique;
(2) Acquire basic data of elements and nodes;
(3) Calculate smoothed strains of nodes;
(4) Update stresses of nodes through constitutive integration;
(5) Calculate internal forces of nodes;
(6) Update velocities and position.

Compared with the implicit SPFEM [30], the eSPFEM adopts an explicit time-integration scheme, which has a more concise formulation, lower computational cost, and wider applications. We used a self-developed code that aims to develop a GPU-accelerated SPFEM for large deformation analysis in geomechanics based on CUDA [43], which is released by NVIDIA to perform high-performance computing and has gained popularity rapidly in geomechanics recently [53,54]. Details of the eSPFEM theory can be found in Yuan et al. [32,42] and Zhang et al. [43,55,56].

2.2. Modelling the Mechanical Effect of Roots

Plant roots extend into the soil matrix and form a soil-root composite material with a mechanical effect that enhances the shear strength of the soil [57]. This effect is often considered as additional soil cohesion (known as apparent root cohesion) [23,58,59].

Different theoretical models have been created to estimate the mechanical effect of roots on slope stability, such as the Wu model [17,60] and the fibre bundle model (FBM) [61]. The Wu model assumes that all roots are moved and broken simultaneously, which is not true in reality. However, it is the most commonly used model owing to its simplicity. The Wu model is a perpendicular root-strengthening model established using two variables: root area ratio (*RAR*) and root tensile strength [48].

The Wu model is used to describe the increase in soil shear strength caused by the mechanical effect of the roots, as follows:

$$c_r = \zeta \times T_r \times R_f \times RAR \tag{10}$$

where c_r is the additional soil cohesion and ζ represents the correction factor, which takes into account the influence of roots breaking progressively in reality on soil shear strength; in the present study, ζ equals 0.4 [62].

T_r is the root tensile strength. For simplicity, the effects of the root diameter distributions were ignored, and a constant root tensile strength was considered [63]. Available current data on tree roots indicate that T_r ranges from 5 to 60 MPa [11,64]; in the present study, T_r equals 20 MPa.

R_f stands for the root orientation factor, which is defined as follows:

$$R_f = \sin\theta + \cos\theta \tan\varphi' \tag{11}$$

where θ represents the angle between the root and failure surface when the root breaks, and φ' is the effective angle of internal friction. It should be noted that roots do not always grow perpendicular to the slope's surface, as their growth is influenced by ambient conditions (e.g., gravity and nutrition) [57]. In many cases, θ is between 48° and 72° at failure, so the range of $\sin\theta + \cos\theta \tan\varphi'$ is narrow, i.e., approaching 1.2 [11]. In the present study, R_f equals 1.2.

The *RAR* (in Equation (1)), which is defined as the proportion of the cross-sectional area of the soil occupied by roots, is determined as follows:

$$RAR = \frac{A_r}{A} \tag{12}$$

where A_r and A represent the cross-sectional area of root and soil, respectively. In the present study, *RAR* equals 0.45% [64].

Many researchers have estimated the value of c_r for various vegetation species growing in different environments, and its typical values vary from 1.0 to 94.3 kPa [29]. According to Equation (1), the original c_r score in this study is 43.2 kPa.

2.3. Mechanical Effect of Root-Soil on Shallow Slope Stability

Most of the results from the direct-shear tests showed that roots increased the cohesion [60], whereas the friction angle remained mostly unchanged [64]. For undrained loading, the shear strength of saturated vegetated soils, s, can commonly be determined by incorporating the additional soil cohesion, c_r, into the Mohr–Coulomb failure criterion [64,65], which can be modified as follows:

$$s = c_r + c' + \sigma_n \tan\varphi' \tag{13}$$

where, c' is effective cohesion and σ_n is total normal stress.

The shear strength reduction technique was adopted to analyse the slope stability, which is defined as follows:

$$\begin{gathered} s_f = \frac{s}{\mathrm{SRF}} \\ \varphi' f = \arctan\left(\frac{\tan\varphi'}{\mathrm{SRF}}\right) \end{gathered} \tag{14}$$

where s_f and φ'_f are the reduced shear strength and the reduced effective angle of internal friction, respectively. SRF is the shear strength reduction factor. First, the initial value of the SRF was set to an adequately low value to keep the slope stable under gravitational loading. Then, the value of the SRF increases gradually until the slope becomes unstable and failure occurs. The critical value of the SRF leading to slope instability is considered to be the FOS of the slope [30].

2.4. The Four Patterns of Root Geometry

2.4.1. Idealisation of Typical Patterns of Root Architecture

The spatial location of thick roots determines the arrangement of related thin roots; thus, root distribution presents a high degree of complexity [8]. Existing methods for quantifying root architecture include the extraction of roots, the complete washing of soil, and image analysis of roots [66]. The spatial distribution of roots is an important factor in determining the reinforcement behaviour and mechanical properties of roots, and the generalisation of root morphology is essential for evaluating the influence of vegetation on slope stability [9,67].

Based on experimental observations, researchers have summarised four typical patterns of root geometry: uniform distribution [10,68], triangular distribution [68], parabolic distribution [69], and exponential distribution [10]. Table 1 lists the characteristics of different root architectures, typical species, and their growing regions. Figure 2 shows the root architecture of four different real roots.

Table 1. Introduction to different root architectures.

Root Architectures	Characteristics	Typical Species	Growing Regions
Uniform distribution	A root system with a large taproot and large horizontal lateral roots	Aleppo pine [10]	Mediterranean, Southern Europe, Asia, and North Africa [70]
		Pulsatilla pratensis [68]	Sub-polar areas of Europe, Asia, North America Central, and Eastern Europe [71]
Triangular distribution	A root taproot system with small lateral roots	Trigonella balansae [68]	Europe, and Asia [72]
Parabolic distribution	A concentrated root system	Cynodon dactylon [69]	North Africa, Asia, Australia, and Southern Europe [73]
Exponential distribution	A plate-shaped root system	Beech and Mature oaks [10]	Europe, and North America [74,75]

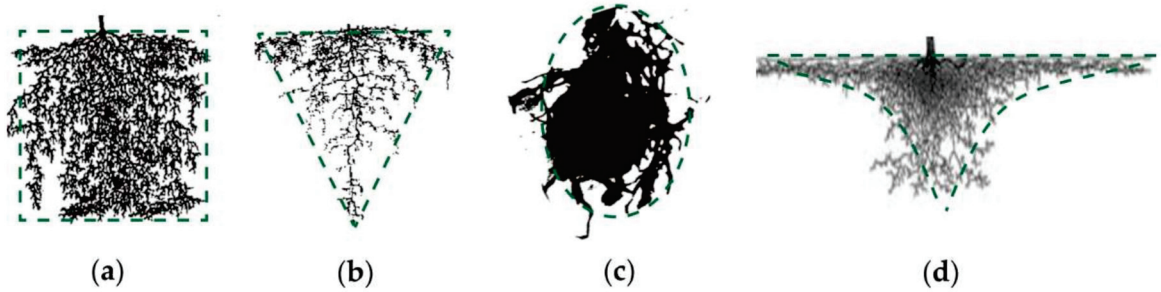

Figure 2. Different real root architectures: (**a**) Uniform distribution [68]; (**b**) Triangular distribution [68]; (**c**) Parabolic distribution [69]; (**d**) Exponential distribution [10].

Root biomass can be expressed by root volume, mass, area, or length, and the most commonly adopted measure is the soil area occupied by the roots [76]. In order to achieve a fair comparison, the symmetric parts of the four root architecture profiles are normalised to the same unit area. Figure 3 describes their normalised function curves. It is assumed

that these root architectures have the same root depth and are homogeneously distribute in the root zone.

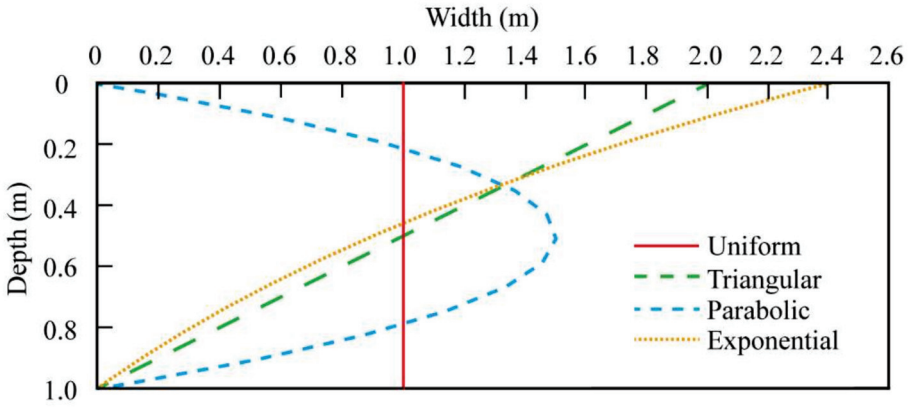

Figure 3. Normalised function curves of the four different root architectures.

2.4.2. Root Architecture Functions on Slope

The coordinate system on the slope can be defined as $x'o'y'$, and the extent between the bottom of the root zone and the slope's surface is defined by the root depth, z_r. Figure 4 describes the boundaries of the four different root zones, and the green areas indicate the root zones. The mathematical functions derived from the root zone boundaries are as follows:

1. Uniform distribution

$$\begin{cases} y' = \frac{1}{z_r} \\ y' = -\frac{1}{z_r} \\ x' = 0 \\ x' = -z_r \end{cases} \quad (15)$$

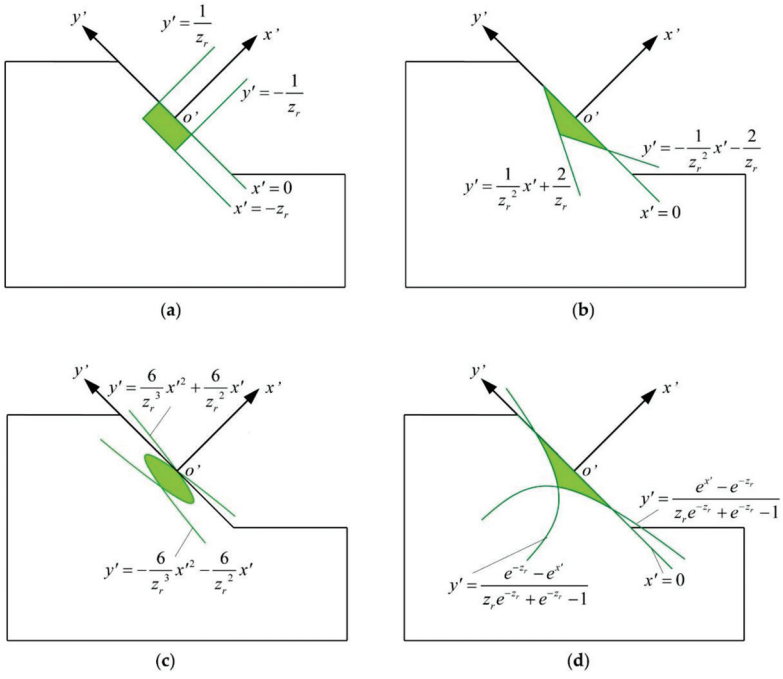

Figure 4. Boundaries of the four different root zones: (**a**) Uniform distribution; (**b**) Triangular distribution; (**c**) Parabolic distribution; (**d**) Exponential distribution.

2. Triangular distribution

$$\begin{cases} y' = -\frac{1}{{z_r}^2}x' - \frac{2}{z_r} \\ y' = \frac{1}{{z_r}^2}x' + \frac{2}{z_r} \\ x' = 0 \end{cases} \tag{16}$$

3. Parabolic distribution

$$\begin{cases} y' = \frac{6}{{z_r}^3}{x'}^2 + \frac{6}{{z_r}^2}x' \\ y' = -\frac{6}{{z_r}^3}{x'}^2 - \frac{6}{{z_r}^2}x' \end{cases} \tag{17}$$

4. Exponential distribution

$$\begin{cases} y' = \frac{e^{x'} - e^{-z_r}}{z_r e^{-z_r} + e^{-z_r} - 1} \\ y' = \frac{e^{-z_r} - e^{x'}}{z_r e^{-z_r} + e^{-z_r} - 1} \\ x' = 0 \end{cases} \tag{18}$$

2.4.3. Root Architecture Functions after Coordinate Transformation

The coordinate transformation formula from the coordinate system $x'o'y'$ to the rectangular coordinate system xoy is assembled as:

$$\begin{bmatrix} x \\ y \end{bmatrix} = \begin{bmatrix} \cos\alpha & -\sin\alpha \\ \sin\alpha & \cos\alpha \end{bmatrix} \begin{bmatrix} x' \\ y' \end{bmatrix} + \begin{bmatrix} C_1 \\ C_2 \end{bmatrix} \tag{19}$$

where α is the complementary angle of the slope angle and β, C_1, and C_2 are parameters related to the planting position. Equation (10) can be expressed as:

$$\begin{cases} x' = x\cos\alpha + y\sin\alpha - C_1\cos\alpha - C_2\sin\alpha \\ y' = y\cos\alpha - x\sin\alpha + C_1\sin\alpha - C_2\cos\alpha \end{cases} \tag{20}$$

According to Equations (15) and (20), the scope boundaries of the uniform distribution were obtained.

$$\begin{cases} y\cos\alpha - x\sin\alpha + C_1\sin\alpha - C_2\cos\alpha \le 1/z_r \\ y\cos\alpha - x\sin\alpha + C_1\sin\alpha - C_2\cos\alpha \ge -1/z_r \\ x\cos\alpha + y\sin\alpha - C_1\cos\alpha - C_2\sin\alpha \le 0 \\ x\cos\alpha + y\sin\alpha - C_1\cos\alpha - C_2\sin\alpha \ge -z_r \end{cases} \tag{21}$$

According to Equations (16) and (20), the scope boundaries of the triangular distribution were obtained.
when ${z_r}^2 - 2\tan\alpha > 0$,

$$\begin{cases} y\cos\alpha - x\sin\alpha + C_1\sin\alpha - C_2\cos\alpha \ge -\frac{2}{{z_r}^2}(x\cos\alpha + y\sin\alpha - C_1\cos\alpha - C_2\sin\alpha) - \frac{2}{z_r} \\ y\cos\alpha - x\sin\alpha + C_1\sin\alpha - C_2\cos\alpha \le \frac{2}{{z_r}^2}(x\cos\alpha + y\sin\alpha - C_1\cos\alpha - C_2\sin\alpha) + \frac{2}{z_r} \\ x\cos\alpha + y\sin\alpha - C_1\cos\alpha - C_2\sin\alpha \le 0 \end{cases} \tag{22}$$

when ${z_r}^2 - 2\tan\alpha \le 0$,

$$\begin{cases} y\cos\alpha - x\sin\alpha + C_1\sin\alpha - C_2\cos\alpha \ge -\frac{2}{{z_r}^2}(x\cos\alpha + y\sin\alpha - C_1\cos\alpha - C_2\sin\alpha) - \frac{2}{z_r} \\ y\cos\alpha - x\sin\alpha + C_1\sin\alpha - C_2\cos\alpha \ge \frac{2}{{z_r}^2}(x\cos\alpha + y\sin\alpha - C_1\cos\alpha - C_2\sin\alpha) + \frac{2}{z_r} \\ x\cos\alpha + y\sin\alpha - C_1\cos\alpha - C_2\sin\alpha \le 0 \end{cases} \tag{23}$$

According to Equations (17) and (20), the scope boundaries of the parabolic distribution were obtained.

$$\begin{cases} y\cos\alpha - x\sin\alpha + C_1\sin\alpha - C_2\cos\alpha \geq \frac{6}{z_r{}^3}(x\cos\alpha + y\sin\alpha - C_1\cos\alpha - C_2\sin\alpha)^2 \\ \qquad\qquad + \frac{6}{z_r{}^2}(x\cos\alpha + y\sin\alpha - C_1\cos\alpha - C_2\sin\alpha) \\ y\cos\alpha - x\sin\alpha + C_1\sin\alpha - C_2\cos\alpha \leq -\frac{6}{z_r{}^3}(x\cos\alpha + y\sin\alpha - C_1\cos\alpha - C_2\sin\alpha)^2 \\ \qquad\qquad - \frac{6}{z_r{}^2}(x\cos\alpha + y\sin\alpha - C_1\cos\alpha - C_2\sin\alpha) \end{cases} \tag{24}$$

According to Equations (18) and (20), the scope boundaries of the exponential distribution were obtained.

$$\begin{cases} y\cos\alpha - x\sin\alpha + C_1\sin\alpha - C_2\cos\alpha \geq \frac{e^{x\cos\alpha + y\sin\alpha - C_1\cos\alpha - C_2\sin\alpha} - e^{-z_r}}{z_r e^{-z_r} + e^{-z_r} - 1} \\ y\cos\alpha - x\sin\alpha + C_1\sin\alpha - C_2\cos\alpha \leq \frac{e^{-z_r} - e^{x\cos\alpha + y\sin\alpha - C_1\cos\alpha - C_2\sin\alpha}}{z_r e^{-z_r} + e^{-z_r} - 1} \\ x\cos\alpha + y\sin\alpha - C_1\cos\alpha - C_2\sin\alpha \leq 0 \end{cases} \tag{25}$$

C_1, C_2, and α in Equations (21)–(25) are discussed under three different conditions: vegetation growth on the slope's surface, upper slope region, and lower slope region. Figure 5 shows the geometric parameters of the vegetated slope (taking a uniform distribution as an example), green areas indicate the root zones.

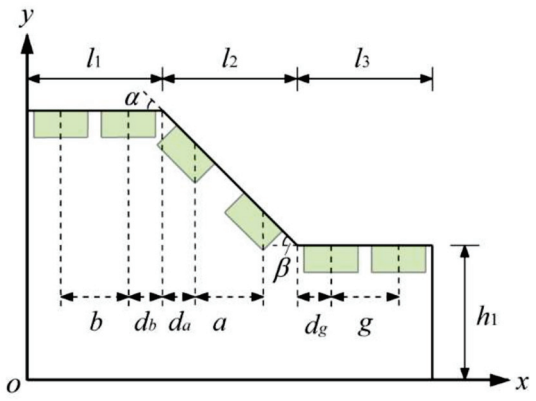

Figure 5. Geometric parameters of the vegetated slope.

When vegetation is planted on the slope's surface:

$$\begin{cases} \alpha = 90^{\circ} - \beta \\ C_{1,surface} = l_1 + d_a - a(i_{\text{tree}} - 1) \\ C_{2,surface} = h_1 + \{l_2 - [d_a + a(i_{\text{tree}} - 1)]\}\tan\beta \end{cases} \tag{26}$$

where a is the horizontal interval between root centres on the slope's surface, d_a is the horizontal distance between the root centre of the highest vegetation and the near edge of the upper slope region, $d_a = a/2$, i_{tree} is the amount of vegetation on the slope's surface, $1 \leq i_{\text{tree}} \leq l_2/a$, and l_2/a is an integer.

When vegetation grows on the upper slope region:

$$\begin{cases} \alpha = 90^{\circ} \\ C_{1,upper} = d_b + b(j_{\text{tree}} - 1) \\ C_{2,upper} = h_1 + l_2\tan\beta \end{cases} \tag{27}$$

where b is the horizontal interval between root centres on the upper slope region, d_b is the horizontal distance between the root centre of the vegetation closest to the slope's surface and the top edge of the slope's surface, $d_b = b/2$, j_{tree} is the number of vegetation on the upper slope region, $1 \leq j_{\text{tree}} \leq l_1/b$, and l_1/b is an integer.

When vegetation is planted on the lower slope region:

$$\begin{cases} \alpha = 90^{o} \\ C_{1,lower} = l_1 + l_2 + d_g + g(k_{\text{tree}} - 1) \\ C_{2,lower} = h_1 \end{cases} \quad (28)$$

where g is the horizontal interval between the root centres in the lower slope region, d_g is the horizontal distance between the root centre of the vegetation closest to the slope's surface and the bottom edge of the slope's surface, $d_g = g/2$, k_{tree} is the amount of vegetation in the lower slope region, $1 \leq k_{\text{tree}} \leq l_3/g$, and l_3/g is an integer.

2.5. Numerical Implementation

The geometry and boundary conditions of the slope-stability problem are shown in Figure 6. The boundary conditions were set as rollers along the left and right vertical boundaries and were fully fixed at the base.

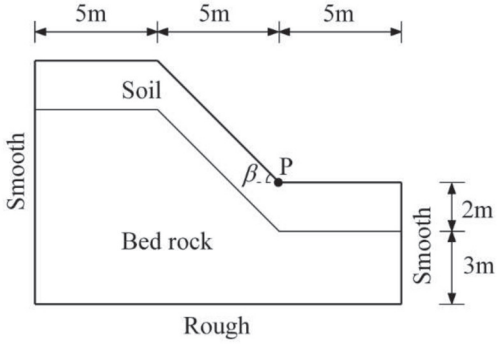

Figure 6. Geometry and boundary conditions of the slope-stability problem.

The soil behaviour was modelled by an elastic-perfectly plastic Mohr–Coulomb material, and the material properties are listed in Table 2. The material parameters were obtained by referring to [30,77]. The slope was divided into lower bedrock and upper soil. The root zone is the soil elements influenced by vegetation [29]. It is assumed that two adjacent root zones may overlap without affecting root distribution. Figure 7 shows root zones and overlapping root zones of different root architectures in vegetated slopes (slope angle of 45°, root depth of 1 m, root zone area of 2 m^2, planting distances of 2.5 m, and planting location on the slope's surface).

Table 2. Material properties.

Material	Unit Weight γ (kN/m^3)	Young's Modulus E/MPa	Poisson's Ratio v	Cohesion c'/kPa	Friction Angle φ'(°)
Bedrock	21	100	0.3	30	35
Soil	20	60	0.3	10	20
Root zone	20	60	0.3	53.2	20
Overlapping root zone	20	60	0.3	96.4	20

To guarantee both the numerical accuracy and the computational efficiency, a non-uniform initial particle distribution is assumed. A very fine mesh discretisation is used for the soil and root zones near the slope's surface, and a coarser mesh discretisation is used for the bedrock, which is situated away from the slope's surface. The meshes adopt six-node triangular elements. Table 3 shows the mesh parameters of slopes angle of 40°, 45°, and 50°.

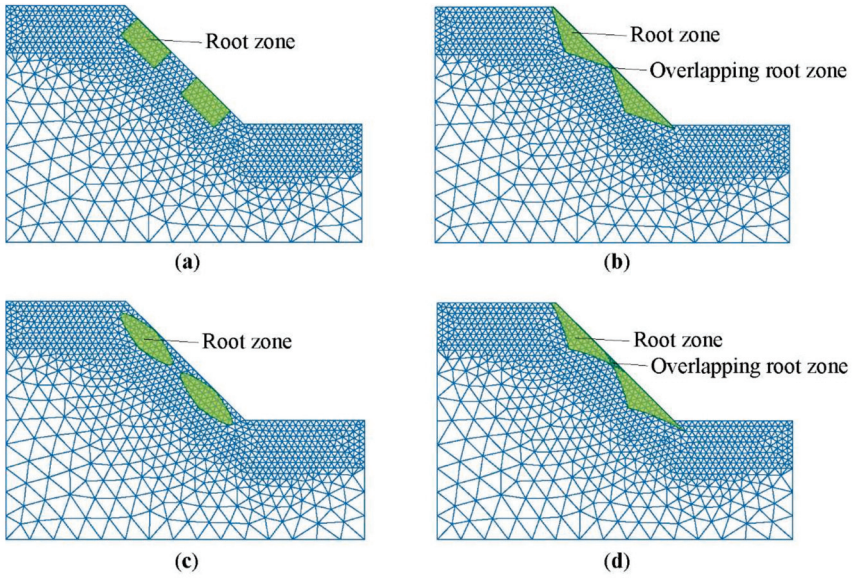

Figure 7. Root zones and overlapping root zones of different root architectures in vegetated slopes: (**a**) Uniform distribution; (**b**) Triangular distribution; (**c**) Parabolic distribution; (**d**) Exponential distribution.

Table 3. Mesh parameters.

Slope Angle β	**40°**	**45°**	**50°**
Number of elements	1695	1744	1863
Number of nodes (particles)	3498	3599	3842

In this study, the eSPFEM is utilised to simulate the failure process of the entire vegetated slope and predict the large deformation behaviour and final deposit of the slope failure. A kinetic energy-based criterion [32] is adopted to analyse the stability of vegetated slopes. This approach is based on the relation of the kinetic energy of the slope with the simulation time [32]. The peak value of kinetic energy curve can be considered as an indicator of the critical state, because the failure of the slope is related to large deformation, and the kinetic energy increases significantly after failure occurs. The value of SRF at the peak of the kinetic energy curve is interpreted as the FOS of the slope, and kinetic energy reaches a steady state in a short period after the peak.

The simulation is divided into two stages: first, the displacements of all of the particles are fixed, and gravity is applied to all of the particles to achieve the initial stress field; then, the particles are allowed to move, and after the initial shear failure, the unstable soil moves and reaches an equilibrium state at a new slope configuration. The horizontal displacement of point P, which is located at the slope's toe, is monitored (see Figure 5).

Slope failure was calculated using the shear strength reduction technique by gradually increasing the SRF. For different SRFs, the simulation was implemented with eSPFEM, and a physical time of 6 s [32] was considered for each SRF to obtain a new steady state for the slope after failure. To evaluate the effect of roots on slope stability, five variables (root architecture, planting distance, root depth, slope angle, and planting location) were systematically varied to calculate FOS values under different conditions.

3. Results

3.1. Comparison of the Instability of the Vegetated Slope and Bare Slope

Case 1 compares the failure mechanisms of the bare and vegetated slopes. The eSPFEM was used to analyse the stability of bare and vegetated slopes with a slope angle of 45° (planting location is the slope's surface, root depth of 1 m, root zone area of 2 m^2, planting

distance of 2.5 m, and a uniform root distribution) for various SRFs. Figure 8 shows the evolution of the kinetic energy with time. Figure 9 shows the variation in the maximum horizontal displacement at the slope's toe with time. Figure 10 shows the equivalent plastic strain and final configurations for various SRFs, and the grey zones indicate the initial root areas.

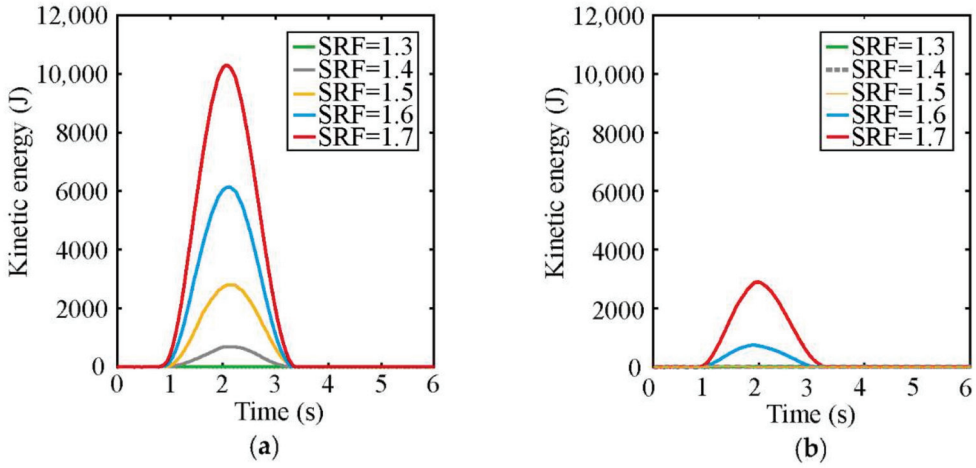

Figure 8. Evolution of kinetic energy with time for various SRFs: (**a**) Bare slope; (**b**) Vegetated slope.

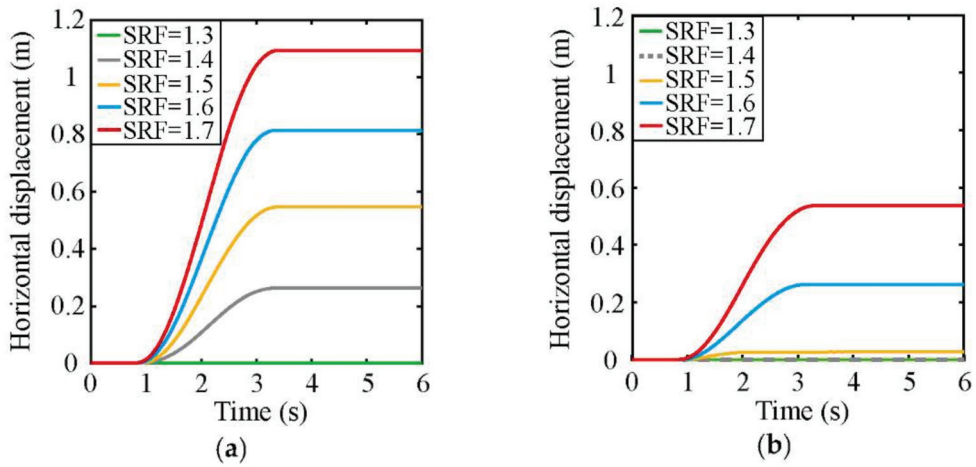

Figure 9. Variation of maximum horizontal displacement at the slope's toe with time for various SRFs: (**a**) Bare slope; (**b**) Vegetated slope.

For the bare slope (Figure 8a), when SRF $\leq$ 1.3, the slope is stable, and no obvious kinetic energy occurs. When SRF $\geq$ 1.4, the kinetic energy-time curve exhibits a peak value, and then the kinetic energy reaches a steady state within a short time. Therefore, the critical SRF value was 1.3, which was regarded as the FOS of the slope. Displacement at the slope's toe (Figure 9a) also occurred when SRF $\geq$ 1.4. In addition, from the results of the equivalent plastic strain (Figure 10a), it can be seen that when SRF = 1.2, a plastic strain develops at the weak band between bedrock and soil as well as at the slope's toe. When SRF = 1.3, a narrow local band of plastic strain was detected, and the plastic zone subsequently extended from the slope's toe to the slope top. The plastic strain band was dark near the top of the slope, indicating that the slope was not completely damaged. When SRF = 1.4, a continuous band of plastic strain localisation was observed, and slope failure occurred, accompanied by a large increment in displacement. The deformation of the slope was mainly concentrated on the slope's surface, and the maximum deformation occurred at the centre of the slope's surface.

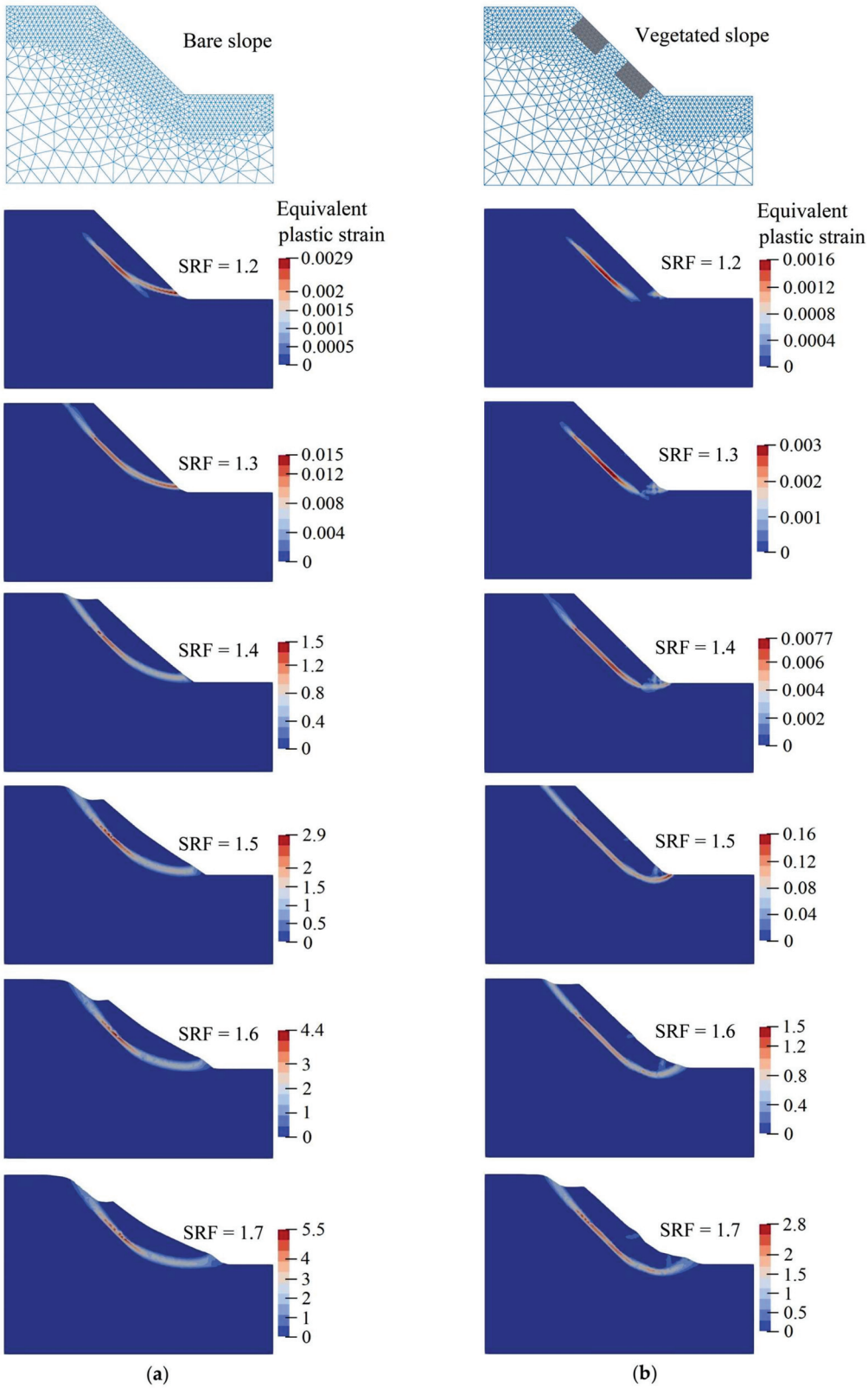

Figure 10. Equivalent plastic strain and final configurations for various SRFs: (**a**) Bare slope; (**b**) Vegetated slope.

For the vegetated slope (Figure 8b), no obvious kinetic energy appears when SRF $\leq$ 1.5, whereas the kinetic energy-time curve shows a peak value when SRF $\geq$ 1.6. The FOS of the slope was 1.5. A large deformation displacement at the slope's toe (Figure 9b) also

occurs during FOS $\geq$ 1.6. Moreover, according to the equivalent plastic strain diagram (Figure 10b), when SRF = 1.6, the slope produces a continuous band of plastic strain, and the upper soil mass creates a displacement. The depth of the shear band corresponded to the root zone depth.

3.2. Effects of the Planting Distance on the Stability of the Vegetated Slopes

The research object of case 2 was a vegetated slopes with a slope angle of 45°, root depth of 1 m, root zone area of 2 m^2, and planting location on the slope's surface. The effects of the root architecture on slope stability are discussed when the planting distances, *a*, are set to 5 m, 2.5 m, and 1.25 m, respectively. Figures 11 and 12 show the maximum horizontal displacement at the slope's toe after the failure of the vegetated slopes with the increase in SRF for different planting distances.

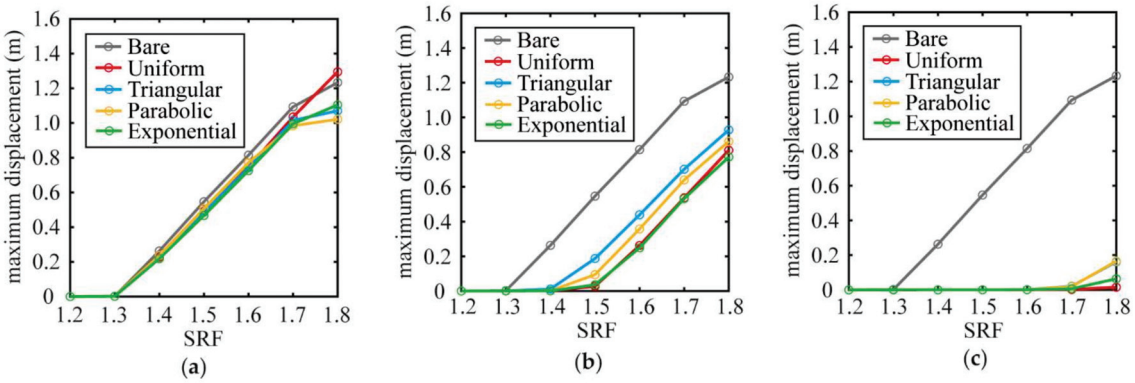

Figure 11. With the increase in SRF, the maximum horizontal displacement at the slope's toe for different root architectures after slope failure: (**a**) $a = 5\ m$; (**b**) $a = 2.5\ m$; (**c**) $a = 1.25\ m$.

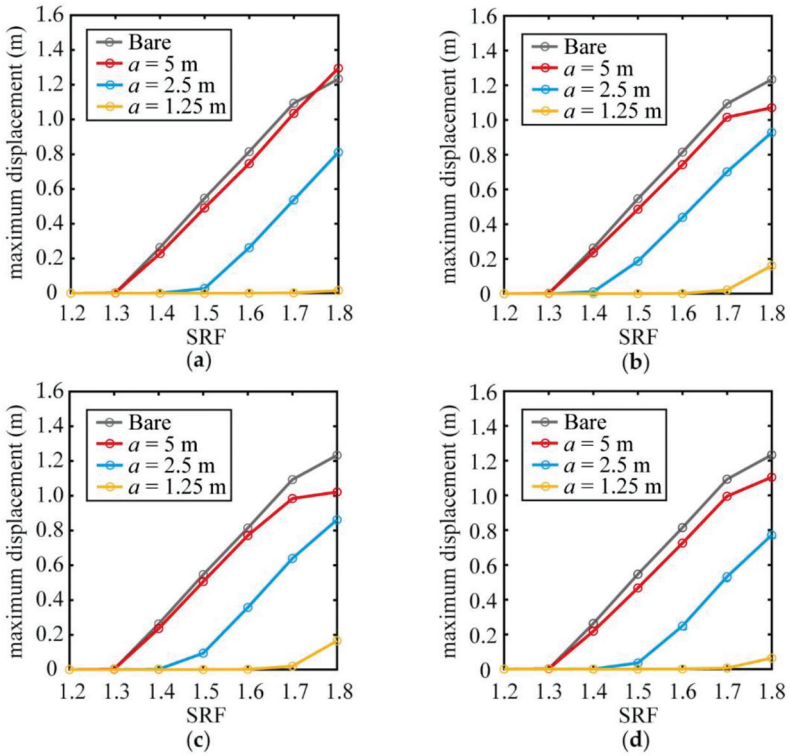

Figure 12. With the increase in SRF, the maximum horizontal displacement at the slope's toe for various planting distances after slope failure: (**a**) Uniform distribution; (**b**) Triangular distribution; (**c**) Parabolic distribution; (**d**) Exponential distribution.

As shown in Figures 11 and 12, when the planting distance on the slope's surface was 2.5 m or 1.5 m, the slope stability was significantly improved compared with the bare slope (Figure 11b,c). However, the effect was not evident when the distance was 5 m (Figure 11a). When the planting distance is 5 m, the slope FOS is 1.3 for the four root architectures, which is equal to that of the bare slope. When the distance is 2.5 m, the FOS of the uniform and exponential root architectures is 1.5, and that of the triangular and parabolic root architectures is 1.4. The FOS of the four root architectures was 1.7 when the distance was 1.25 m.

3.3. Role of the Root Depth in the Stability of the Vegetated Slopes

The study object of case 3 is a vegetated slope with a slope angle of 45°, planting distances of 2.5 m, root zone area of 2 m^2, and planting location on the slope's surface. The effects of root architecture on the slope stability are discussed when the root depths, z_r, are set to 0.5 m, 0.75 m, 1.0 m, 1.25 m, and 1.5 m, respectively. Figures 13 and 14 show the maximum horizontal displacement at the slope's toe after the failure of the vegetated slopes with an increase in SRF for various root depths.

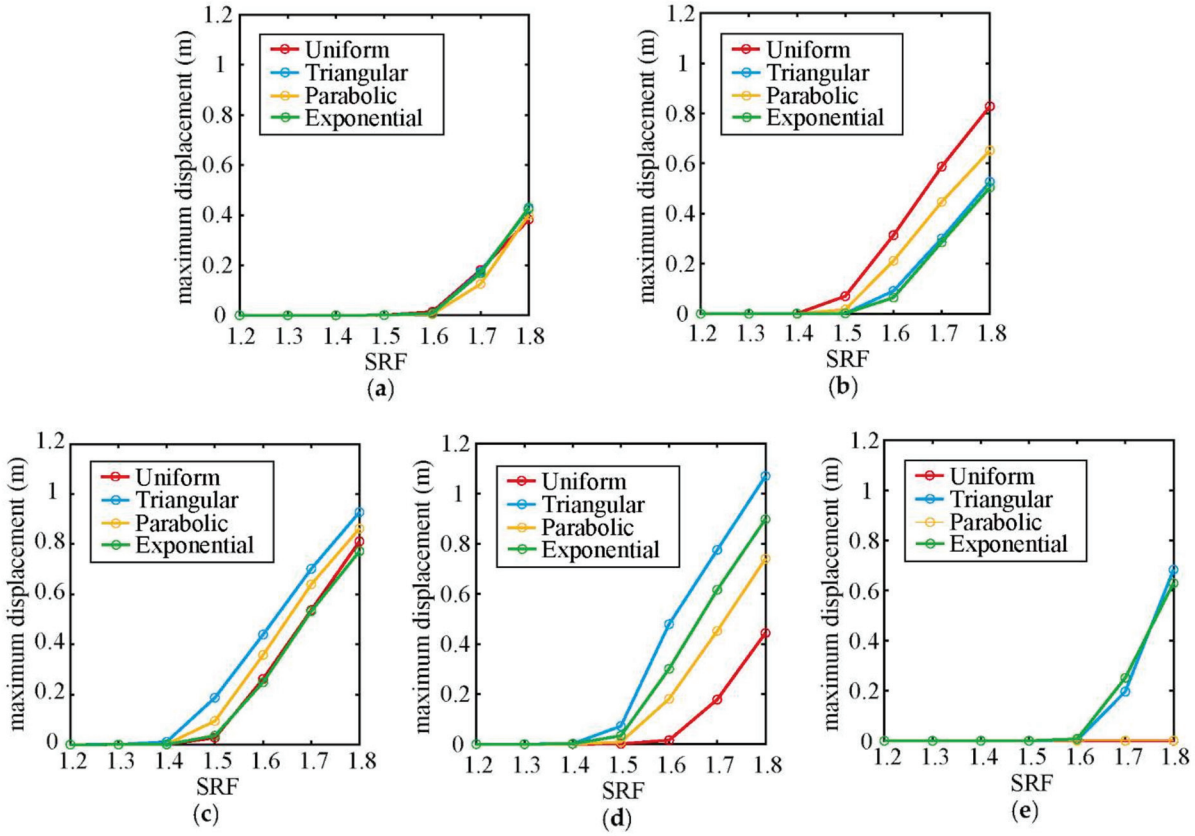

Figure 13. With the increase in SRF, the maximum horizontal displacement at the slope's toe for different root architectures after slope failure: (**a**) $z^r = 0.5\ m$; (**b**) $z^r = 0.75\ m$; (**c**) $z^r = 1\ m$; (**d**) $z^r = 1.25\ m$; (**e**) $z^r = 1.5\ m$.

As shown in Figure 13, after slope failure, the horizontal displacement at the slope's toe with root depths of 0.5 m and 1.5 m is smaller than that with root depths of 0.75 m, 1.0 m, and 1.25 m. When the root depth is 1.5 m, the FOS of the triangular and exponential root architectures is 1.6, whereas that of the uniform and parabolic root architectures is greater than 1.8. The FOS of the four root architectures was 1.6 when the root depth was 0.5 m.

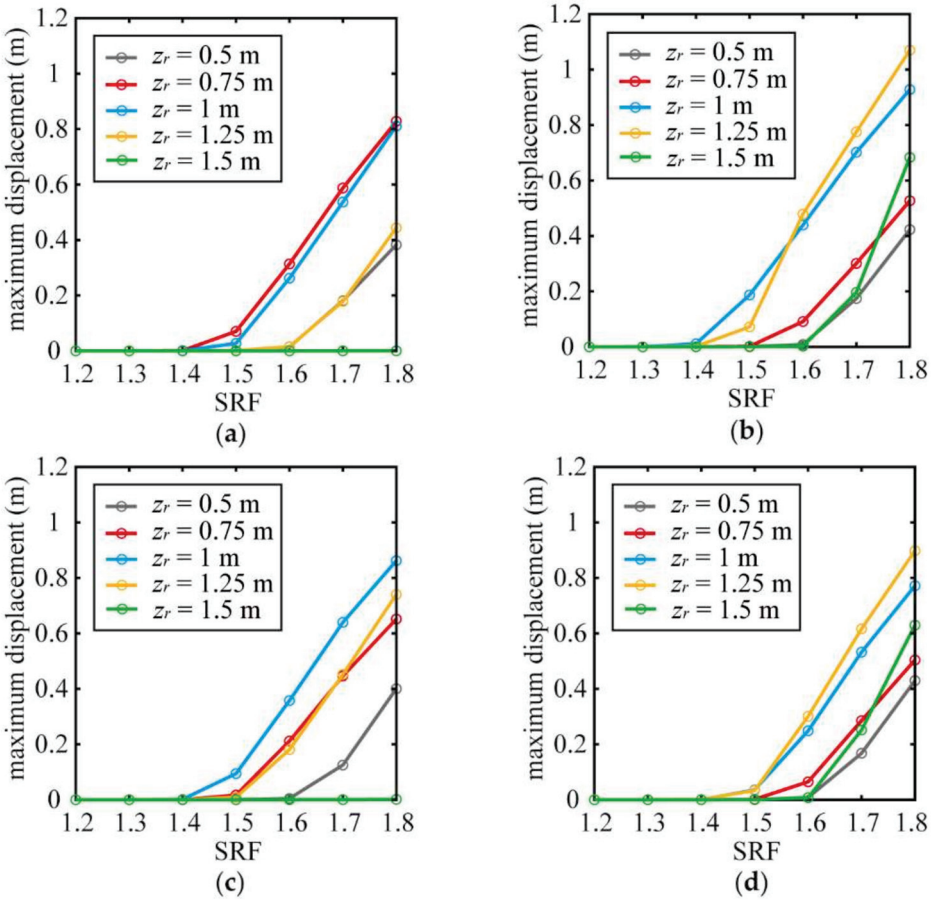

Figure 14. With the increase in SRF, the maximum horizontal displacement at the slope's toe for various root depths after slope failure: (**a**) Uniform distribution; (**b**) Triangular distribution; (**c**) Parabolic distribution; (**d**) Exponential distribution.

Figure 14 illustrates that, for uniform (Figure 14a) and parabolic root architectures (Figure 14c), the slope stability is the best when the root depth is 1.5 m (FOS > 1.8). When the root depth of the uniform root architecture was 0.75 m and that of the parabolic root architecture was 1.0 m, the slope stability was the worst (FOS = 1.4). For triangular (Figure 14b) and exponential (Figure 14d) root architectures, the FOS reaches the maximum when root depths are 0.5 m and 1.5 m (FOS = 1.6); and the FOS is the lowest when the root depths are 1.0 m and 1.25 m (FOS = 1.4).

3.4. Effects of the Slope Angle on the Stability of the Vegetated Slopes

The research object of case 4 is a vegetated slope with a planting distance of 2.5 m, root depth of 1 m, root zone area of 2 m^2, and planting location is the slope's surface. The influence of root architecture on slope stability is discussed when the slope angles, β, are set to 40°, 45°, and 50°, respectively. Figures 15 and 16 show the maximum horizontal displacement at the slope's toe after the failure of vegetated slopes with an increase in the SRF for different slope angles.

As shown in Figures 15 and 16, when the slope angles are 40°, 45°, and 50°, the FOS are 1.3, 1.5, and 1.7, respectively, for the uniform and exponential root architectures; for triangular root architecture, the FOS are 1.2, 1.4, and 1.6, and for parabolic root architecture, the FOS are 1.3, 1.4, and 1.6, respectively.

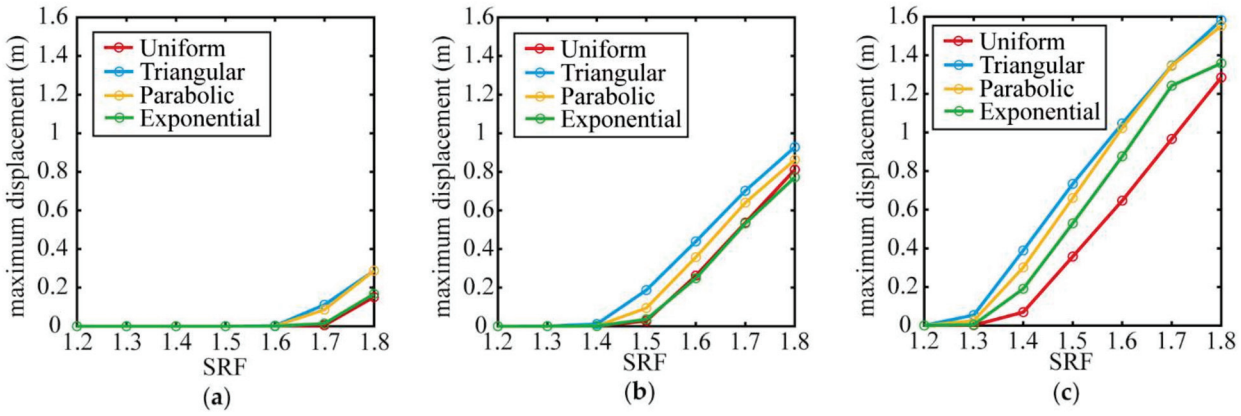

Figure 15. With the increase in SRF, the maximum horizontal displacement at the slope's toe for different root architectures after slope failure: (**a**) $\beta = 40°$; (**b**) $\beta = 45°$ (**c**) $\beta = 50°$.

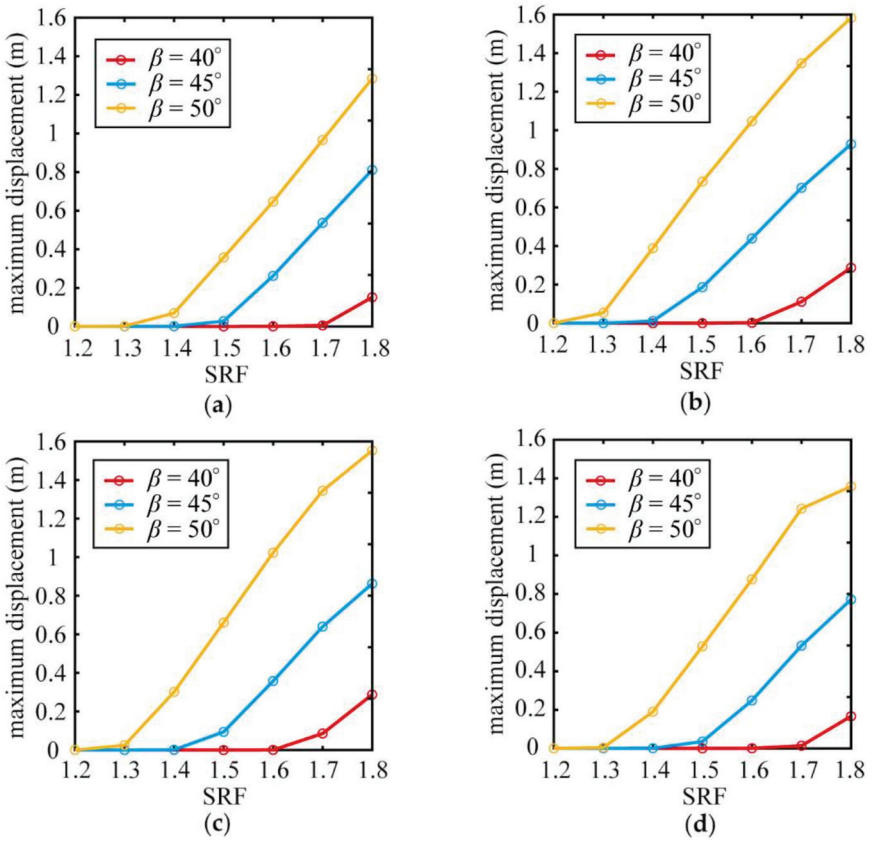

Figure 16. With the increase in SRF, the maximum horizontal displacement at the slope's toe for various slope angles after slope failure: (**a**) Uniform distribution; (**b**) Triangular distribution; (**c**) Parabolic distribution; (**d**) Exponential distribution.

3.5. Influence of the Planting Location on the Stability of the Vegetated Slopes

The study object of case 5 is a vegetated slope with a slope angle of 45°, planting distance of 2.5 m, root depth of 1 m, and root zone area of 2 m^2. The effects of the root architecture on slope stability when the location of the root zone changes are discussed. We referred to Chok et al. [29] for the planting locations. Figure 17 shows the slopes with the planting positions of the slope's surface, slope's toe, the slope's surface and toe, upper slope region, lower slope region, upper and lower slope regions, and entire ground surface, as well as their final equivalent plastic strains during FOS = 1.6. The grey area represents

the root zone (taking uniform root architecture as an example). Figures 18 and 19 show the maximum horizontal displacement at the slope's toe after slope instability with an increase in SRF for different planting locations.

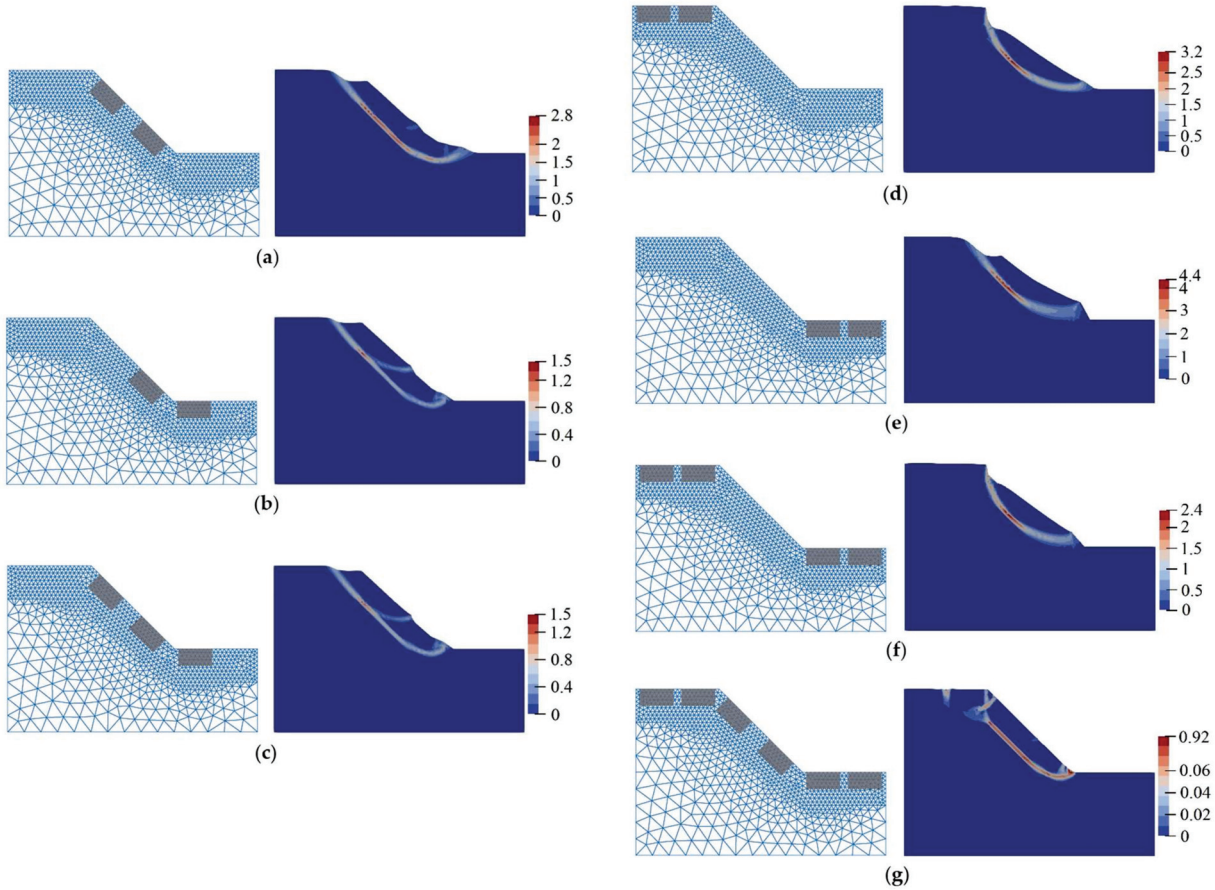

Figure 17. Vegetated slopes for different planting locations and the final equivalent plastic strain for FOS = 1.6: (**a**) slope's surface; (**b**) slope's toe; (**c**) slope's surface and toe; (**d**) upper slope region; (**e**) lower slope region; (**f**) upper and lower slope regions; (**g**) entire ground surface.

Figure 17 shows that different planting positions have different influences on the shear band of the slope failure. The improvement in slope stability was the most obvious in the entire ground surface planting. Planting at the slope's toe can effectively reduce the sliding displacement of the slope soil.

As shown in Figure 16, vegetation on the entire ground surface (Figure 18g) had the best effect on the slope stability (FOS > 1.8). Planting on the lower slope region (Figure 18e) has little impact on the FOS, which is equal to that of the bare slope (FOS = 1.3). Planting on the slope's surface (Figure 18a) was better than that on the lower slope region, and the influence of uniform and exponential root architectures (FOS = 1.5) was better than that of triangular and parabolic root architectures (FOS = 1.4). The effects of planting on the slope's toe (Figure 18b) and the slope's surface and toe (Figure 18c) were both similar. Both were better than the slope's surface, and the impacts of the triangular and exponential root architectures (FOS = 1.7) were better than those of uniform and parabolic root architectures (FOS = 1.5). The effects of planting on the upper slope region (Figure 18d) and upper and lower slope regions (Figure 18f) were similar, and the influence of uniform architecture (FOS > 1.8) was better than that of the other three root architectures (FOS = 1.5).

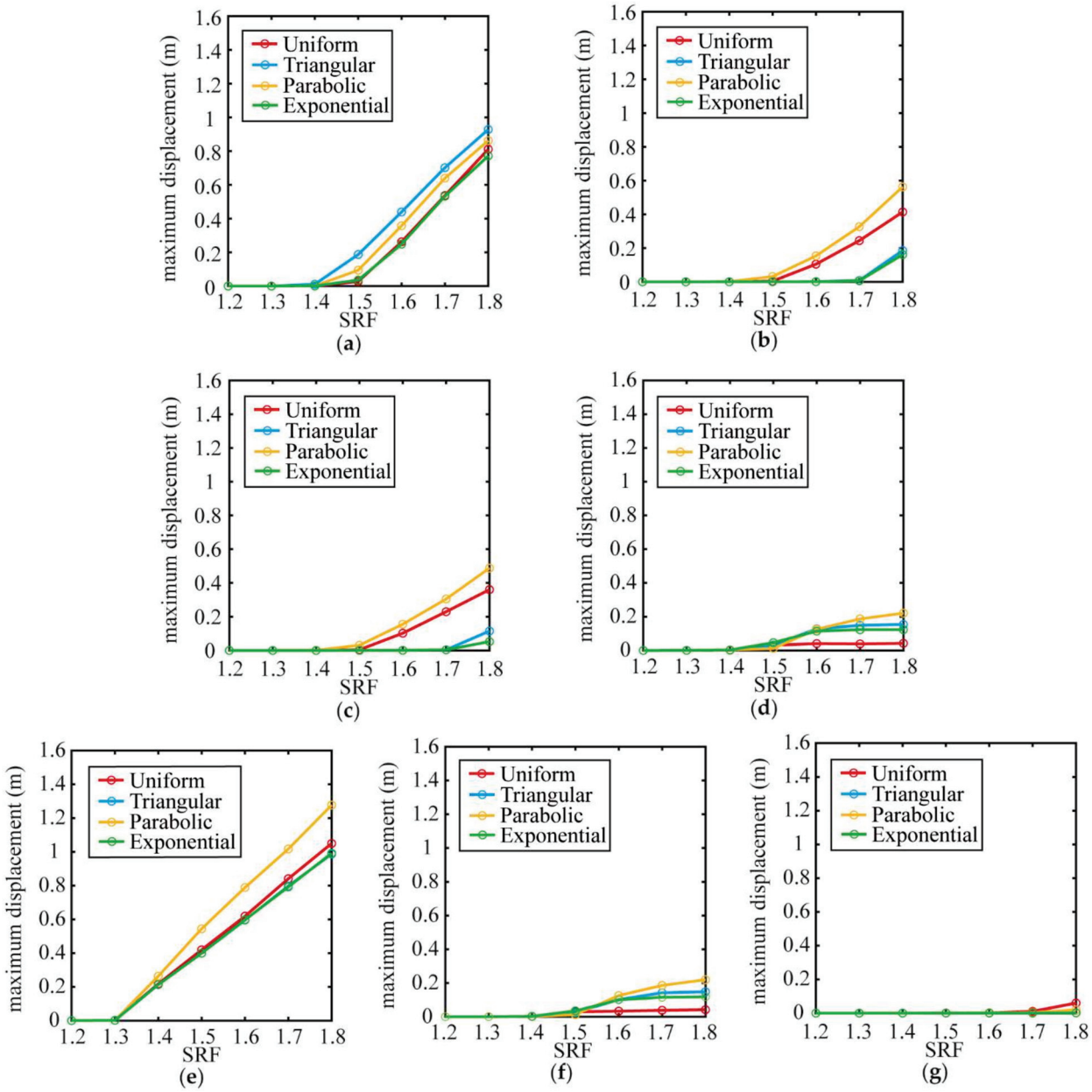

Figure 18. With the increase in SRF, the maximum horizontal displacement at the slope's toe for different root architectures after slope failure: (**a**) slope's surface; (**b**) slope's toe; (**c**) slope's surface and toe; (**d**) upper slope region; (**e**) lower slope region; (**f**) upper and lower slope regions; (**g**) entire ground surface.

In Figure 19, the planting of uniform root architecture (Figure 19a) on the upper and lower slope regions, upper slope region, and entire ground surface (FOS > 1.8) are better than those on the slope's surface and toe, as well as on the slope's surface (FOS = 1.5). The planting effects of parabolic root architecture (Figure 19c) on the upper and lower slope regions, slope's surface, and upper slope region were weaker than those of the uniform root architecture. The effects of triangular (Figure 19b) and exponential root architectures (Figure 19d) are similar, and they have a greater advantage when they are present at the slope's toe, as well as the slope's surface and toe (FOS = 1.7).

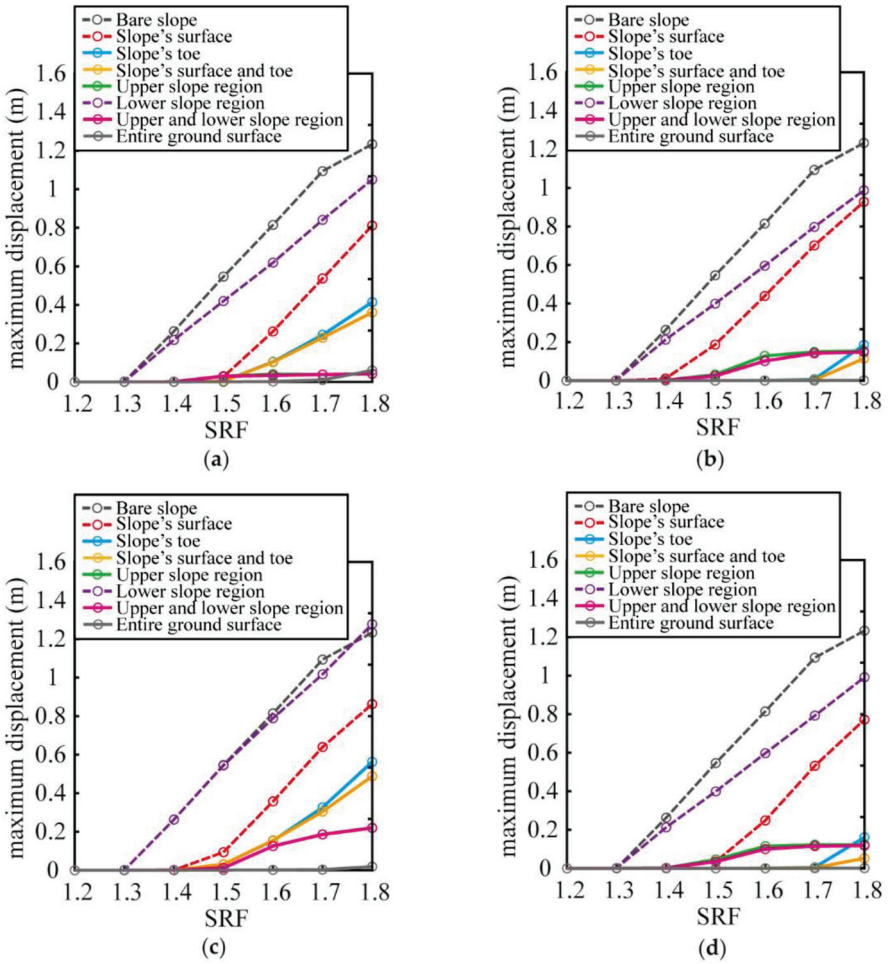

Figure 19. With the increase in SRF, the maximum horizontal displacement at the slope's toe of the slopes with different planting locations after slope failure: (**a**) Uniform distribution; (**b**) Triangular distribution; (**c**) Parabolic distribution; (**d**) Exponential distribution.

4. Discussion

In this study, the slip surface of the bare slope was mainly distributed in the weak layer at the interface of the rock and soil, whereas the slip surface of the vegetated slope was distributed at the bottom of the root zone, and the upper layer of soil entrains the root system to slip. The tensile strength and adhesion properties of the roots reinforced the soil. Plant roots with high tensile strength increase the confining stress of the soil through their compact root matrix system [29]. The results of the finite element analysis showed that reinforcement of the root can improve the stability of the slope, reduce the displacement of the landslide, and increase the FOS value.

The FOS value of the vegetated slope increased with decreasing planting distance. The higher the planting density, the stronger the root-strengthening effect. It should be noted that if the planting distance exceeds a certain range, then the slope stability may not improve. In this study, when the planting distance on the slope was 5 m, the effect was similar to that on the bare slope. The stability of a slope with a uniform root architecture is most sensitive to the planting distance.

For many slopes, the root depth is usually limited by bedrock, which is usually shallow and less than 2 m [58]. The failure depth of most slopes is between 0.5 m and 1 m, and the root zone plays a role in mechanical stability only when the root depth reaches the deeper soil layer [78]. With an increase in root depth, the FOS first decreased and then increased. When the root depth is 0.5 m, the slope's surface is covered with overlapping roots, which is similar to the geosynthetic reinforcement on the slope's surface. When the root depth

was 1.5 m, it was similar to installing anti-slide piles or anchors. In addition, for uniform and parabolic root architectures, a greater root depth is more beneficial for slope stability. For triangular and exponential root architectures, shallow roots were more conducive. In addition, the stability of a slope with a uniform and parabolic root architecture is more sensitive to its root depth.

The slope FOS of the four root architectures decreased with an increase in slope angle. Regardless of whether the slope is steep or has a slight incline, uniform and exponential root architectures are more effective in improving the slope stability.

The position of the plants on the slope also affects their contribution to stability. Except for planting in the lower slope region, the stability of the vegetated slope in the other planting positions was better than that of the bare slope. If there is no restriction on planting location and vegetation quantity, planting on the entire ground surface of a slope has the best effect on improving slope stability, which is similar to the conclusion of [29]. Moreover, it is better to plant vegetation with a uniform root architecture in the upper slope region or plant vegetation with a triangular or exponential root architecture on the slope's toe. When the vegetated slope is unstable, the depth of the plastic strain at the top and toe of the slope is shallower; therefore, it is more conducive for roots to play a role. Tensile cracks may occur at the top of a slope, and the roots provide traction and support soil to prevent landslides [79]. The roots bear pressure at the toe of the slope, which can act as a support and inhibit soil sliding [80].

5. Conclusions

In this study, the eSPFEM was utilised to simulate the instability of vegetated slopes with large deformations. This method can reasonably predict the deformation process of the slope structure and the final deposition, avoiding the difficulty of numerical calculations and loss of calculation accuracy.

The Mohr–Coulomb constitutive model was extended by introducing the additional soil cohesion, c_r, generated by roots and therefore increasing the shear strength of the soil. The boundary functions of the four root architectures (uniform, triangular, parabolic, and exponential) on the slope were derived. The FOS values of the four root architectures for various planting distances, root depths, slope angles, and planting locations were calculated using the shear strength reduction technique with a kinetic energy-based criterion, and the effects of root architecture on slope stability were evaluated.

Their results showed that roots can effectively improve slope stability and reduce landslide displacement. The higher the planting density, the stronger the root-strengthening effect. With an increase in root depth, the FOS first decreased and then increased. For uniform and parabolic root architectures, deeper roots are more beneficial to slope stability, whereas for triangular and exponential root architectures, shallower roots are more conducive. The FOS decreases with the increase in slope angle; uniform and exponential root architectures are more effective in improving slope stability, no matter whether the slope is steep or has a slight incline. Vegetation at the slope's toe can effectively reduce the sliding displacement of the slope soil. Planting on the entire ground surface had the best effect on slope stability improvement, followed by planting vegetation with uniform root architecture in the upper slope region or planting vegetation with triangular or exponential root architectures on the slope's toe.

This study provides valuable information on the contribution of different root architectures to slope stability and can guide the selection of vegetation species and planting locations, which can contribute to improving slope stability and optimising the management of mountain shelter forests. Nonetheless, the limitation of this model lies in the need for accurate parameterisation and a large amount of calculation, so it is currently only applicable to small slopes.

Author Contributions: Conceptualization, X.J., W.Z. and P.C.; methodology, X.J. and W.Z.; software, Y.J. and W.Z.; validation, X.J. and X.W.; data curation, X.J. and Y.J.; writing—original draft preparation, X.J.; writing—review and editing, X.J., Y.J. and P.C.; visualization, X.J. and X.W.; funding acquisition, Y.J. and P.C. All authors have read and agreed to the published version of the manuscript.

Funding: This research was funded by the Science and Technology Program of Guangzhou, grant numbers 201605030009 and 201803020036, the National Natural Science Foundation of China, grant number 42101422, Effect of changes of underlying surface on precipitation based on radar and optical remote sensing: A case study of Guangzhou City, grant number 202102021287, Research Project on Key Technologies of Watershed Water Governance, grant number 2021-09, the characteristic innovation project of Guangdong Provincial Department of Education, grant number 2022KTSCX013, Guangdong Engineering and Research Center for Unmanned Aerial Vehicle Remote Sensing of Agricultural Water and Soil Information, and Shenzhen Smart Water Project Phase I—Soil and water conservation Information construction project.

Institutional Review Board Statement: Not applicable.

Informed Consent Statement: Not applicable.

Data Availability Statement: The data presented in this study are available upon request from the corresponding author.

Conflicts of Interest: The authors declare no conflict of interest.

References

1. Heaphy, M.J.; Lowe, D.J.; Palmer, D.J.; Jones, H.S.; Gielen, G.J.H.P.; Oliver, G.R.; Pearce, S.H. Assessing drivers of plantation forest productivity on eroded and non-eroded soils in hilly land, eastern North Island, New Zealand. *N. Z. J. For. Sci.* **2014**, *44*, 24. [CrossRef]
2. Schwarz, M.; Phillips, C.; Marden, M.; McIvor, I.R.; Douglas, G.B.; Watson, A. Modelling of root reinforcement and erosion control by 'Veronese'poplar on pastoral hill country in New Zealand. *N. Z. J. For. Sci.* **2016**, *46*, 4. [CrossRef]
3. Rees, S.W.; Ali, N. Tree induced soil suction and slope stability. *Geomech. Geoengin.* **2012**, *7*, 103–113. [CrossRef]
4. Liu, H.W.; Feng, S.; Ng, C.W.W. Analytical analysis of hydraulic effect of vegetation on shallow slope stability with different root architectures. *Comput. Geotech.* **2016**, *80*, 115–120. [CrossRef]
5. Montgomery, D.R.; Schmidt, K.M.; Greenberg, H.M.; Dietrich, W.E. Forest clearing and regional landsliding. *Geology* **2000**, *28*, 311–314. [CrossRef]
6. Osman, N.; Barakbah, S.S. Parameters to predict slope stability—soil water and root profiles. *Ecol. Eng.* **2006**, *28*, 90–95. [CrossRef]
7. Ni, J.; Leung, A.K.; Ng, C.W.W. Unsaturated hydraulic properties of vegetated soil under single and mixed planting conditions. *Géotechnique* **2019**, *69*, 554–559. [CrossRef]
8. Stokes, A.; Atger, C.; Bengough, A.G.; Fourcaud, T.; Sidle, R.C. Desirable plant root traits for protecting natural and engineered slopes against landslides. *Plant Soil* **2009**, *324*, 1–30. [CrossRef]
9. Schwarz, M.; Preti, F.; Giadrossich, F.; Lehmann, P.; Or, D. Quantifying the role of vegetation in slope stability: A case study in Tuscany (Italy). *Ecol. Eng.* **2010**, *36*, 285–291. [CrossRef]
10. Ghestem, M.; Sidle, R.C.; Stokes, A. The influence of plant root systems on subsurface flow: Implications for slope stability. *Bioscience* **2011**, *61*, 869–879. [CrossRef]
11. Wu, T.H. Root reinforcement of soil: Review of analytical models, test results, and applications to design. *Can. Geotech. J.* **2013**, *50*, 259–274. [CrossRef]
12. Hawley, J.G.; Dymond, J.R. How much do trees reduce landsliding? *J. Soil Water Conserv.* **1988**, *43*, 495–498.
13. Dymond, J.R.; Ausseil, A.-G.; Shepherd, J.D.; Buettner, L. Validation of a region-wide model of landslide susceptibility in the Manawatu–Wanganui region of New Zealand. *Geomorphology* **2006**, *74*, 70–79. [CrossRef]
14. Abe, K.; Iwamoto, M. Preliminary experiment on shear in soil layers with a large-direct-shear apparatus. *J. Jpn. For. Soc.* **1986**, *68*, 61–65. [CrossRef]
15. Docker, B.B.; Hubble, T.C.T. Quantifying the enhanced soil shear strength beneath four riparian tree species. *Geomorphology* **2008**, *100*, 400–418.
16. Waldron, L.J. The shear resistance of root-permeated homogeneous and stratified soil. *Soil Sci. Soc. Am. J.* **1977**, *41*, 843–849. [CrossRef]
17. Waldron, L.J.; Dakessian, S. Effect of grass, legume, and tree roots on soil shearing resistance. *Soil Sci. Soc. Am. J.* **1982**, *46*, 894–899. [CrossRef]
18. Gray, D.H.; Ohashi, H. Mechanics of fiber reinforcement in sand. *J. Geotech. Eng.* **1983**, *109*, 335–353. [CrossRef]
19. Jewell, R.A.; Wroth, C.P. Direct shear tests on reinforced sand. *Geotechnique* **1987**, *37*, 53–68. [CrossRef]
20. Wu, T.H.; McOmber, R.M.; Erb, R.T.; Beal, P.E. Study of soil-root interaction. *J. Geotech. Eng.* **1988**, *114*, 1351–1375. [CrossRef]

21. Frydman, S.; Operstein, V. Numerical simulation of direct shear of rootreinforced soil. *Proc. Inst. Civ. Eng. Ground Improv.* **2001**, *5*, 41–48. [CrossRef]
22. Fourcaud, T.; Blaise, F.; Lac, P.; Castéra, P.; De Reffye, P. Numerical modelling of shape regulation and growth stresses in trees. *Trees* **2003**, *17*, 31–39. [CrossRef]
23. Sidle, R.C. A theoretical model of the effects of timber harvesting on slope stability. *Water Resour. Res.* **1992**, *28*, 1897–1910. [CrossRef]
24. Watson, A.; Phillips, C.; Marden, M. Root strength, growth, and rates of decay: Root reinforcement changes of two tree species and their contribution to slope stability. *Plant Soil* **1999**, *217*, 39–47. [CrossRef]
25. Bishop, A.W. The use of the slip circle in the stability analysis of slopes. *Geotechnique* **1955**, *5*, 7–17. [CrossRef]
26. Morgenstern, N.R.; Price, V.E. The analysis of the stability of general slip surfaces. *Geotechnique* **1965**, *15*, 79–93. [CrossRef]
27. Zienkiewicz, O.C.; Humpheson, C.; Lewis, R.W. Associated and non-associated visco-plasticity and plasticity in soil mechanics. *Geotechnique* **1975**, *25*, 671–689. [CrossRef]
28. Griffiths, D.V.; Lane, P.A. Slope stability analysis by finite elements. *Geotechnique* **1999**, *49*, 387–403. [CrossRef]
29. Chok, Y.H.; Jaksa, M.B.; Kaggwa, W.S.; Griffiths, D.V. Assessing the influence of root reinforcement on slope stability by finite elements. *Int. J. Geo-Eng.* **2015**, *6*, 12. [CrossRef]
30. Zhang, W.; Yuan, W.; Dai, B. Smoothed particle finite-element method for large-deformation problems in geomechanics. *Int. J. Geomech.* **2018**, *18*, 04018010. [CrossRef]
31. Gray, D.H.; Barker, D. Root-soil mechanics and interactions. *Riparian Veg. Fluv. Geomorphol.* **2004**, *8*, 113–123. [CrossRef]
32. Yuan, W.-H.; Liu, K.; Zhang, W.; Dai, B.; Wang, Y. Dynamic modeling of large deformation slope failure using smoothed particle finite element method. *Landslides* **2020**, *17*, 1591–1603. [CrossRef]
33. Yin, Z.-Y.; Jin, Y.-F.; Zhang, X. Large deformation analysis in geohazards and geotechnics. *J. Zhejiang Univ. A* **2021**, *22*, 851–855. [CrossRef]
34. Peng, C.; Zhan, L.; Wu, W.; Zhang, B. A fully resolved SPH-DEM method for heterogeneous suspensions with arbitrary particle shape. *Powder Technol.* **2021**, *387*, 509–526. [CrossRef]
35. Zhan, L.; Peng, C.; Zhang, B.; Wu, W. A surface mesh represented discrete element method (SMR-DEM) for particles of arbitrary shape. *Powder Technol.* **2021**, *377*, 760–779. [CrossRef]
36. Bui, H.H.; Fukagawa, R.; Sako, K.; Ohno, S. Lagrangian meshfree particles method (SPH) for large deformation and failure flows of geomaterial using elastic–plastic soil constitutive model. *Int. J. Numer. Anal. Methods Geomech.* **2008**, *32*, 1537–1570. [CrossRef]
37. Lin, J.; Naceur, H.; Coutellier, D.; Laksimi, A. Geometrically nonlinear analysis of two-dimensional structures using an improved smoothed particle hydrodynamics method. *Eng. Comput.* **2015**, *32*, 779–805. [CrossRef]
38. Abe, K.; Soga, K.; Bandara, S. Material point method for coupled hydromechanical problems. *J. Geotech. Geoenviron. Eng.* **2014**, *140*, 04013033. [CrossRef]
39. Soga, K.; Alonso, E.; Yerro, A.; Kumar, K.; Bandara, S. Trends in large-deformation analysis of landslide mass movements with particular emphasis on the material point method. *Géotechnique* **2016**, *66*, 248–273. [CrossRef]
40. Oñate, E.; Idelsohn, S.R.; Del Pin, F.; Aubry, R. The particle finite element method—an overview. *Int. J. Comput. Methods* **2004**, *1*, 267–307. [CrossRef]
41. Monforte, L.; Arroyo, M.; Carbonell, J.M.; Gens, A. Numerical simulation of undrained insertion problems in geotechnical engineering with the Particle Finite Element Method (PFEM). *Comput. Geotech.* **2017**, *82*, 144–156. [CrossRef]
42. Yuan, W.-H.; Wang, B.; Zhang, W.; Jiang, Q.; Feng, X.-T. Development of an explicit smoothed particle finite element method for geotechnical applications. *Comput. Geotech.* **2019**, *106*, 42–51. [CrossRef]
43. Zhang, W.; Zhong, Z.-H.; Peng, C.; Yuan, W.-H.; Wu, W. GPU-accelerated smoothed particle finite element method for large deformation analysis in geomechanics. *Comput. Geotech.* **2021**, *129*, 103856. [CrossRef]
44. Jin, Y.F.; Yuan, W.H.; Yin, Z.Y.; Cheng, Y.M. An edge-based strain smoothing particle finite element method for large deformation problems in geotechnical engineering. *Int. J. Numer. Anal. Methods Geomech.* **2020**, *44*, 923–941. [CrossRef]
45. Wang, Z.Y.; Jin, Y.F.; Yin, Z.Y.; Wang, Y.Z. A novel coupled NS-PFEM with stable nodal integration and polynomial pressure projection for geotechnical problems. *Int. J. Numer. Anal. Methods Geomech.* **2022**, *46*, 2535–2560. [CrossRef]
46. Jin, Y.-F.; Yin, Z.-Y.; Zhou, X.-W.; Liu, F.-T. A stable node-based smoothed PFEM for solving geotechnical large deformation 2D problems. *Comput. Methods Appl. Mech. Eng.* **2021**, *387*, 114179. [CrossRef]
47. Jin, Y.-F.; Yin, Z.-Y. Two-phase PFEM with stable nodal integration for large deformation hydromechanical coupled geotechnical problems. *Comput. Methods Appl. Mech. Eng.* **2022**, *392*, 114660. [CrossRef]
48. Meijer, G.J.; Muir Wood, D.; Knappett, J.A.; Bengough, G.A.; Liang, T. Analysis of coupled axial and lateral deformation of roots in soil. *Int. J. Numer. Anal. Methods Geomech.* **2019**, *43*, 684–707. [CrossRef]
49. Zhang, X.; Krabbenhoft, K.; Sheng, D.; Li, W. Numerical simulation of a flow-like landslide using the particle finite element method. *Comput. Mech.* **2015**, *55*, 167–177. [CrossRef]
50. Liu, G.R.; Nguyen-Thoi, T.; Nguyen-Xuan, H.B.; Lam, K.Y. A node-based smoothed finite element method (NS-FEM) for upper bound solutions to solid mechanics problems. *Comput. Struct.* **2009**, *87*, 14–26. [CrossRef]
51. Liu, G.R.; Dai, K.Y.; Nguyen, T.T. A smoothed finite element method for mechanics problems. *Comput. Mech.* **2007**, *39*, 859–877. [CrossRef]

52. Chen, J.S.; Wu, C.T.; Yoon, S.; You, Y. A stabilized conforming nodal integration for Galerkin mesh-free methods. *Int. J. Numer. Methods Eng.* **2001**, *50*, 435–466. [CrossRef]
53. Dong, Y.; Cui, L.; Zhang, X. Multiple-GPU parallelization of three-dimensional material point method based on single-root complex. *Int. J. Numer. Meth. Engng.* **2022**, *123*, 1481–1504. [CrossRef]
54. Fan, N.; Jiang, J.; Dong, Y.; Guo, L.; Song, L. Approach for evaluating instantaneous impact forces during submarine slide-pipeline interaction considering the inertial action. *Ocean Eng.* **2022**, *245*, 110466. [CrossRef]
55. Yuan, W.-H.; Liu, M.; Zhang, X.-W.; Wang, H.-L.; Zhang, W.; Wu, W. Stabilized smoothed particle finite element method for coupled large deformation problems in geotechnics. *Acta Geotech.* **2022**, *18*, 04018010. [CrossRef]
56. Yuan, W.-H.; Zhu, J.-X.; Liu, K.; Zhang, W.; Dai, B.-B.; Wang, Y. Dynamic analysis of large deformation problems in saturated porous media by smoothed particle finite element method. *Comput. Methods Appl. Mech. Engrg.* **2022**, *392*, 114724. [CrossRef]
57. Feng, S.; Liu, H.W.; Ng, C.W.W. Analytical analysis of the mechanical and hydrological effects of vegetation on shallow slope stability. *Comput. Geotech.* **2020**, *118*, 103335. [CrossRef]
58. Schmidt, K.M.; Roering, J.J.; Stock, J.D.; Dietrich, W.E.; Montgomery, D.R.; Schaub, T. The variability of root cohesion as an influence on shallow landslide susceptibility in the Oregon Coast Range. *Can. Geotech. J.* **2001**, *38*, 995–1024. [CrossRef]
59. Kokutse, N.K.; Temgoua, A.G.T.; Kavazović, Z. Slope stability and vegetation: Conceptual and numerical investigation of mechanical effects. *Ecol. Eng.* **2016**, *86*, 146–153. [CrossRef]
60. Wu, T.H.; McKinnell, W.P., III; Swanston, D.N. Strength of tree roots and landslides on Prince of Wales Island, Alaska. *Can. Geotech. J.* **1979**, *16*, 19–33. [CrossRef]
61. Pollen-Bankhead, N.; Simon, A. Enhanced application of root-reinforcement algorithms for bank-stability modeling. *Earth Surf. Processes Landf.* **2009**, *34*, 471–480. [CrossRef]
62. Preti, F.; Schwarz, M. On root reinforcement modelling. *Geophys. Res. Abstr.* **2006**, *8*, 04555.
63. Ni, J.J.; Leung, A.K.; Ng, C.W.W.; So, P.S. Investigation of plant growth and transpiration-induced matric suction under mixed grass–tree conditions. *Can. Geotech. J.* **2017**, *54*, 561–573. [CrossRef]
64. Karimzadeh, A.A.; Leung, A.K.; Hosseinpour, S.; Wu, Z.; Fardad Amini, P. Monotonic and cyclic behaviour of root-reinforced sand. *Can. Geotech. J.* **2021**, *99*, 1915–1927. [CrossRef]
65. Fredlund, D.G.; Rahardjo, H. *Soil Mechanics for Unsaturated Soils*; John Wiley & Sons: Hoboken, NJ, USA, 1993.
66. Garg, A.; Leung, A.K.; Ng, C.W.W. Comparisons of soil suction induced by evapotranspiration and transpiration of S. heptaphylla. *Can. Geotech. J.* **2015**, *52*, 2149–2155. [CrossRef]
67. Cohen, D.; Schwarz, M.; Or, D. An analytical fiber bundle model for pullout mechanics of root bundles. *J. Geophys. Res. Earth Surf.* **2011**, *116*, F03010. [CrossRef]
68. Lynch, J. Root architecture and plant productivity. *Plant Physiol.* **1995**, *109*, 7. [CrossRef]
69. Leung, A.K.; Garg, A.; Coo, J.L.; Ng, C.W.W.; Hau, B.C.H. Effects of the roots of Cynodon dactylon and Schefflera heptaphylla on water infiltration rate and soil hydraulic conductivity. *Hydrol. Processes* **2015**, *29*, 3342–3354. [CrossRef]
70. Pernek, M.; Lacković, N.; Lukić, I.; Zorić, N.; Matošević, D. Outbreak of Orthotomicus erosus (Coleoptera, Curculionidae) on Aleppo pine in the Mediterranean region in Croatia. *South-East Eur. For. SEEFOR* **2019**, *10*, 19–27. [CrossRef]
71. Ciosek, M.T.; Piórek, K.; Sikorski, R.; Trebicka, A. Population dynamics of Pulsatilla patens (L.) Mill. in a new locality in Poland. *Biodivers. Res. Conserv.* **2016**, *41*, 61. [CrossRef]
72. Dundas, I.S.; Nair, R.M.; Verlin, D.C. First report of meiotic chromosome number and karyotype analysis of an accession of Trigonella balansae (Leguminosae). *N. Z. J. Agric. Res.* **2006**, *49*, 55–58. [CrossRef]
73. Shabi, M.M.; Raj, C.D.; Sasikala, C.; Gayathri, K.; Joseph, J. Negative inotropic and chronotropic effects of phenolic fraction from Cynodon dactylon (Linn) on isolated perfused frog heart. *J. Sci. Res.* **2012**, *4*, 657–663. [CrossRef]
74. Huntley, B.; Bartlein, P.J.; Prentice, I.C. Climatic control of the distribution and abundance of beech (Fagus L.) in Europe and North America. *J. Biogeogr.* **1989**, *16*, 551–560. [CrossRef]
75. Haavik, L.J.; Billings, S.A.; Guldin, J.M.; Stephen, F.M. Emergent insects, pathogens and drought shape changing patterns in oak decline in North America and Europe. *For. Ecol. Manag.* **2015**, *354*, 190–205. [CrossRef]
76. Zhu, H.; Zhang, L.M.; Garg, A. Investigating plant transpiration-induced soil suction affected by root morphology and root depth. *Comput. Geotech.* **2018**, *103*, 26–31. [CrossRef]
77. Liang, Y.; Chandra, B.; Soga, K. Shear band evolution and post-failure simulation by the extended material point method (XMPM) with localization detection and frictional self-contact. *Comput. Methods Appl. Mech. Eng.* **2022**, *390*, 114530. [CrossRef]
78. Arnone, E.; Caracciolo, D.; Noto, L.V.; Preti, F.; Bras, R.L. Modeling the hydrological and mechanical effect of roots on shallow landslides. *Water Resour. Res.* **2016**, *52*, 8590–8612. [CrossRef]
79. Schwarz, M.; Cohen, D.; Or, D. Spatial characterization of root reinforcement at stand scale: Theory and case study. *Geomorphology* **2012**, *171*, 190–200. [CrossRef]
80. Schwarz, M.; Rist, A.; Cohen, D.; Giadrossich, F.; Egorov, P.; Büttner, D.; Stolz, M.; Thormann, J.J. Root reinforcement of soils under compression. *J. Geophys. Res. Earth Surf.* **2015**, *120*, 2103–2120. [CrossRef]

sustainability

MDPI

Article

Numerical Investigation of the Dynamic Response of a Sand Cushion with Multiple Rockfall Impacts

Yu Zhang [1], Jierui Feng [2], Longhuan Du [1,*], Peng Zhao [3], Jiao Peng [3], Chen Yang [4], Hua Fan [5] and Liangpu Li [6]

[1] College of Architecture and Environment, Sichuan University, Chengdu 610065, China
[2] The Fifth Oil Production Plant of Petrochina Changqing Oil Field Company, Xi'an 710020, China
[3] State Key Laboratory of Geohazard Prevention and Geoenvironment Protection, Chengdu University of Technology, Chengdu 610059, China
[4] Chengdu Eighth Construction Engineering Co., Ltd. of CDCEG, Chengdu 610084, China
[5] Lingchuang Green House Construction Technology Co., Ltd., Chengdu 610095, China
[6] Sichuan Communication Surveying & Design Institute Co., Ltd., Chengdu 610017, China
* Correspondence: longhuandu@scu.edu.cn

Abstract: A shed cave structure with a sand cushion is often used as a protective structure for rockfall disasters. Because of the randomness and unpredictability of rockfall disasters, the cushions of shed caves often suffer multiple impacts from rockfalls. Aiming at the problem of multiple impacts of rockfall, this paper uses the three-dimensional discrete element method to study the dynamic response of multiple rockfall impacts on sand cushions from different heights. Before conducting large-scale simulation studies, the input parameters in the numerical model are verified with data from laboratory experiments. Analyzing the simulation results shows that when the same point is impacted multiple times, the maximum impact force and the maximum penetration depth will increase with the number of impacts. According to the numerical results, a calculation formula of the maximum impact force that considers the number of impacts is fitted. At the same time, considering the impact response when the rockfall impacts different positions multiple times, the distance range that the subsequent impact is not affected by the previous impact is given. The significance of studying the multiple impacts of rockfalls is shown by a numerical study of rockfalls impacting a sand cushion multiple times from different heights, and it provides a reference for the design of rockfall disaster-protection structures in practical engineering.

Keywords: rockfall disaster; sand cushion; multiple impacts; discrete element method; impact positions

Citation: Zhang, Y.; Feng, J.; Du, L.; Zhao, P.; Peng, J.; Yang, C.; Fan, H.; Li, L. Numerical Investigation of the Dynamic Response of a Sand Cushion with Multiple Rockfall Impacts. *Sustainability* **2023**, *15*, 3554. https://doi.org/10.3390/su15043554

Academic Editors: Stefano Morelli, Veronica Pazzi and Mirko Francioni

Received: 14 January 2023
Revised: 10 February 2023
Accepted: 13 February 2023
Published: 15 February 2023

1. Introduction

Rockfall disasters are one of the most common geological disasters near mountain roads. The occurrence of rockfall disasters has had a great impact on the economic development of mountainous areas. In China, with the advancement of the western development strategy, it is even more necessary to reasonably and effectively protect against rockfall disasters. In addition, casualties and damage to roads and railways due to rockfall disasters should be avoided. The shed cave structure with a buffer layer is a typical structure for rockfall-protection in mountainous areas and it is widely used in rockfall disaster-protection in mountainous areas [1–3].

Sand is a cushion material commonly used in rockfall-protection engineering [4]. It is a conveniently obtained material that has good durability, high economic benefit, and good buffering performance. Many scholars have studied the buffer performance of sand buffer layers. A series of laboratory experiments were conducted to investigate the effect of the dry density and thickness of the sand pad on the impact pressure applied to the soil surface, the earth pressure at the bottom of the mold, and the transferability of the impact pressure [5]. In recent years, the discrete element method (DEM) has emerged as a suitable numerical tool for analyzing the impact of rockfalls from micro- to macroscales [6]. The calibration

of validated DEM models with corresponding experimental data provides researchers with data that are nearly impossible to obtain experimentally. Using the commercial DEM software PFC3D 5.0, the initial kinetic energy of a rockfall can be set to 5000 kJ, which is difficult to achieve experimentally, to study the impact of the rockfall on bunkers covered by a soil buffer layer [7]. It is also possible to study the energy propagation and block bouncing in the process of a rock block impacting a granular medium, as well as the evolution of the shock-induced force chain and its relationship with the global mechanical response of the granular buffer layer through the 3D discrete element model [8,9]. At the same time, the effect of the particle size on the buffering efficiency of the soil buffer layer can be studied by combining the experiments [10]. The influence of the sand buffer layer thickness and porosity on the buffer performance can also be analyzed by the discrete element numerical method [11]. In these studies, the DEM was found to be an effective method for studying the impact response of sand buffers.

Because of the high frequency and randomness of rockfall disasters, it is difficult to conduct monitoring and provide feedback in time. Often, the shed-hole cushion cannot be repaired and replaced in time, and it will be impacted again. In addition, rockfall impact is often accompanied by multiple rocks. Therefore, the shed cavity cushion is often repeatedly impacted. Such an occurrence will compact the sand buffer layer and reduce the ability to disperse the impact force of falling rocks, which will lead to the destruction of the shed cave structure in the long run. At present, few reports are available on the multiple impacts of rockfall on shed cave cushions. A new type of energy dissipator is designed for the place where the rockfall occurs so that the structural energy-dissipating rock shed can withstand the multiple impacts of the rockfall [12]. Tests of spherical rockfall impacting a sand buffer layer and foam composite cushion layer were performed. In these multiple impact laboratory tests, after the first impact, with an increasing number of impacts of the buffer layer, the acceleration of the falling weight is greater [13,14]. The impact force is a key parameter in the structural design of shed tunnels. In the case of multiple impacts, few studies have reported on the impact force calculation after each impact. Simultaneously, under multiple impacts, the impact position is not fixed. If the distance between two adjacent impact positions is close, the effect of the second impact will be affected by the first impact. However, at present, research is lacking on the influence of the distance between different impact locations on the impact effect for multiple impacts.

This paper studies and analyzes the phenomenon of multiple shocks in rockfall disasters. A small-scale laboratory multiple shock test was carried out to verify the discrete element model. The dynamic process of a large-scale rockfall impacting a sand buffer layer multiple times is simulated using a calibrated numerical model. The difference between the dynamic response of multiple rockfall impacts and a single impact is explored, and a calculation method for the impact force during multiple impacts is given in combination with the existing rockfall impact force calculation formula. Furthermore, considering the influence of the distance between impact points on the impact effect during two adjacent impacts, the distance effect on the impact effect at different impact positions is given. The experimental and numerical study on the multiple impacts of rockfall on the sand buffer layer provides a basis for considering multiple impact problems in practical engineering.

2. Reduced-Scale Impact Test

Firstly, the dynamic response of the sand cushion under multiple impacts of rockfall is studied by a laboratory impact test.

2.1. Overview of the Test

In this paper, the impact test of rockfall on a sand buffer layer is performed in a self-designed drop weight impact test device. In this laboratory test, spherical rockfalls made four consecutive impacts on the center point of the sand buffer layer from a height of 1 m. The rockfall has a radius of 0.057 m, a mass of 1.7 kg, and a density of 2187 kg/m^3. The

size of the sand buffer layer is 1 m × 1 m × 0.3 m. The falling height is 1 m. The laboratory test device and schematic diagram are shown in Figure 1.

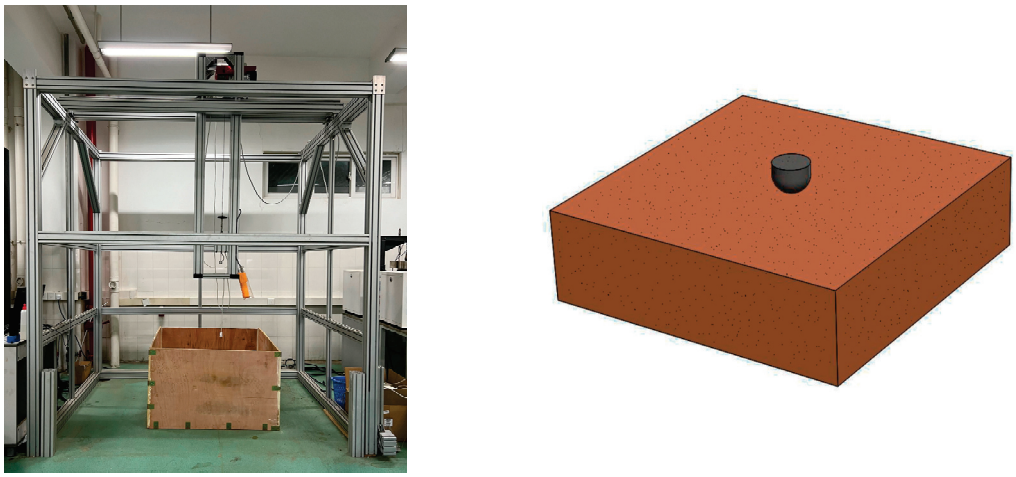

(**a**) (**b**)

Figure 1. Laboratory test device and schematic diagram: (**a**) test device; (**b**) schematic diagram.

2.2. Test Method

In the laboratory test, the acceleration time–history curve of the falling weight is collected by the acceleration sensor installed on the upper surface of the drop hammer, and the impact force time–history curve is obtained according to Newton's second law. In order to avoid errors in the test as much as possible, three groups of tests with multiple impacts under the same conditions were carried out. Judging from the signals collected by the accelerometer, the acceleration trends in the three groups of tests are the same, and the peak accelerations are slightly different, but the difference is small. The impact force results are shown in Section 3.2.

3. Numerical Model Establishment and Validation

As a common and reliable scientific research method, numerical simulations are often used in civil engineering research [15–17]. As discrete element software, PFC3D is mainly used to study the micromechanical behavior between particles [18,19]. The ball and the wall are the basic components of the software, and different numerical models are established by assigning them different parameters. The choice of the particle radius in the model is crucial and determines the speed of the numerical simulations. After the model is built, mesoscopic parameters must be assigned to the particles to achieve the macroscopic properties of the material, that is, to match the macroscopic parameters by selecting the appropriate mesoscopic parameters. No clear conversion relationship holds between macro parameters and meso parameters. In this paper, the model parameters in the numerical model are corrected by performing laboratory experiments to determine the particle size, stiffness, damping coefficient, and other simulation parameters.

Simulating the rockfall impact buffer layer mainly involves three types of rockfall, buffer layers, and protective structures. Considering that the rockfall is less likely to break after impacting the sand, the rockfall is simulated by a single rigid sphere (ball) [20], which is colored in red. The sand buffer layer is generated by a Gaussian distribution of spheres with different radii, and the thickness of the buffer layer is set by controlling the number and position of the spheres [21]. The size of the spherical particles is a key parameter. The actual size of the sand particles is approximately 0.1 mm. However, simulating a sand pad with a particle size of 0.1 mm is impractical, especially on a practical engineering scale. Considered comprehensively, the particle size range of the sand buffer layer in this model will be larger than the actual particle size range [4,22]. The main analysis in the simulation is the impact of rockfall on the buffer layer. The protective structure is directly treated as a

wall element. That is, the surroundings of the sand buffer layer are constrained by rigid wall elements. In this study, a linear model was used to simulate the sand buffer layer, the contact between the sand buffer layer and the rockfall, and the contact between the sand buffer layer and the protective structure. When applying PFC3D software to simulate the dynamic impact process of rockfall under vertical falling conditions, factors such as gravity, viscous resistance, and viscous damping need to be considered [23]. The acceleration of gravity in the model is 9.8 m/s^2, the damping is set to 0.01, and the friction coefficient is set to 0.5. The normal contact force of the rigid sphere in the simulation is the rockfall impact force. Since this paper considers multiple impacts of falling rocks, the rigid sphere is deleted after each impact, and a new rigid sphere is established to continue the impact.

3.1. Numerical Model Establishment

Before conducting the analysis and research of a rockfall impacting a sand buffer layer multiple times, a numerical model of the same size as the laboratory test was established to verify the feasibility of using PFD3D software to calculate the sand buffer layer of the rockfall impact.

According to the description of the test, rockfalls and cushions of the same size were established in PFC3D software, and the dynamic impact process was simulated for a height of 1 m. The numerical model is shown in Figure 2. The density of rockfall shall refer to the value in the test. The size of the falling rock shall be replaced by a sphere with the same volume as the falling hammer in the test. Only one particle is used to represent the falling stone, which is because the falling rock is regarded as a rigid body. The size of the sand buffer layer is 1 m $\times$ 1 m $\times$ 0.3 m. The material parameters of the falling rock and the sand cushion are the same as those in the laboratory experiment, and the other input parameters in the model are shown in Table 1. The bottom and four sides of the cushion is a fixed constraint.

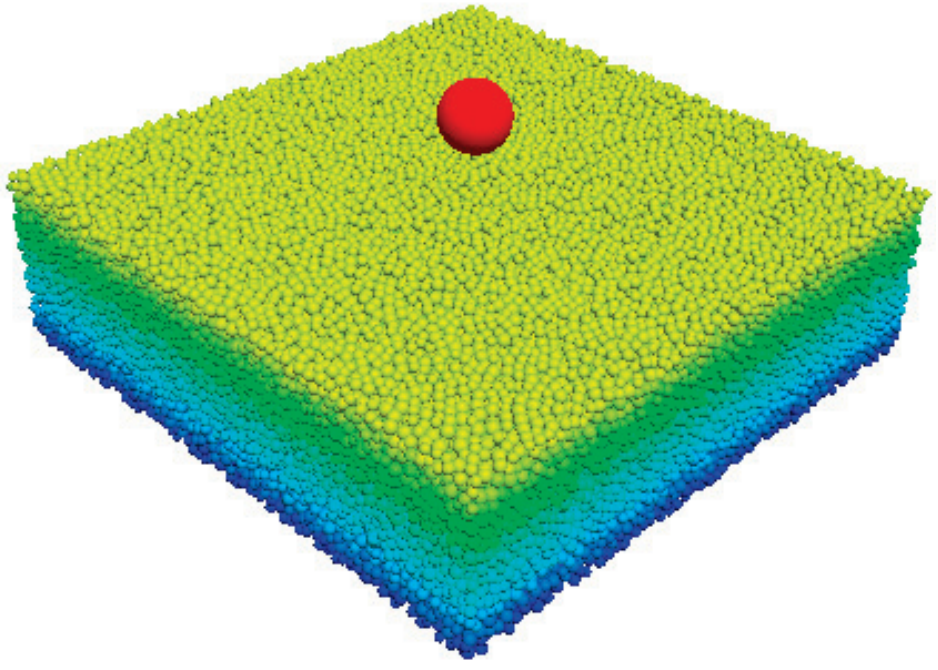

Figure 2. Small-scale numerical model diagram.

Table 1. Input parameters.

Sand Porosity	Normal-to-Shear Stiffness Ratio	Sand Effective Modulus	Sand Density	Sand Radius
0.35	10	30 MPa	2600 kg/m^3	0.007–0.01 m

3.2. Numerical Model Validation

The sphere rockfall with a mass of 1.7 kg impacts the sand cushion multiple times at the falling height of 1 m. Figure 3 compares the time–history curve of the impact force obtained by the laboratory test under multiple impacts with the curve that was extracted by the numerical model.

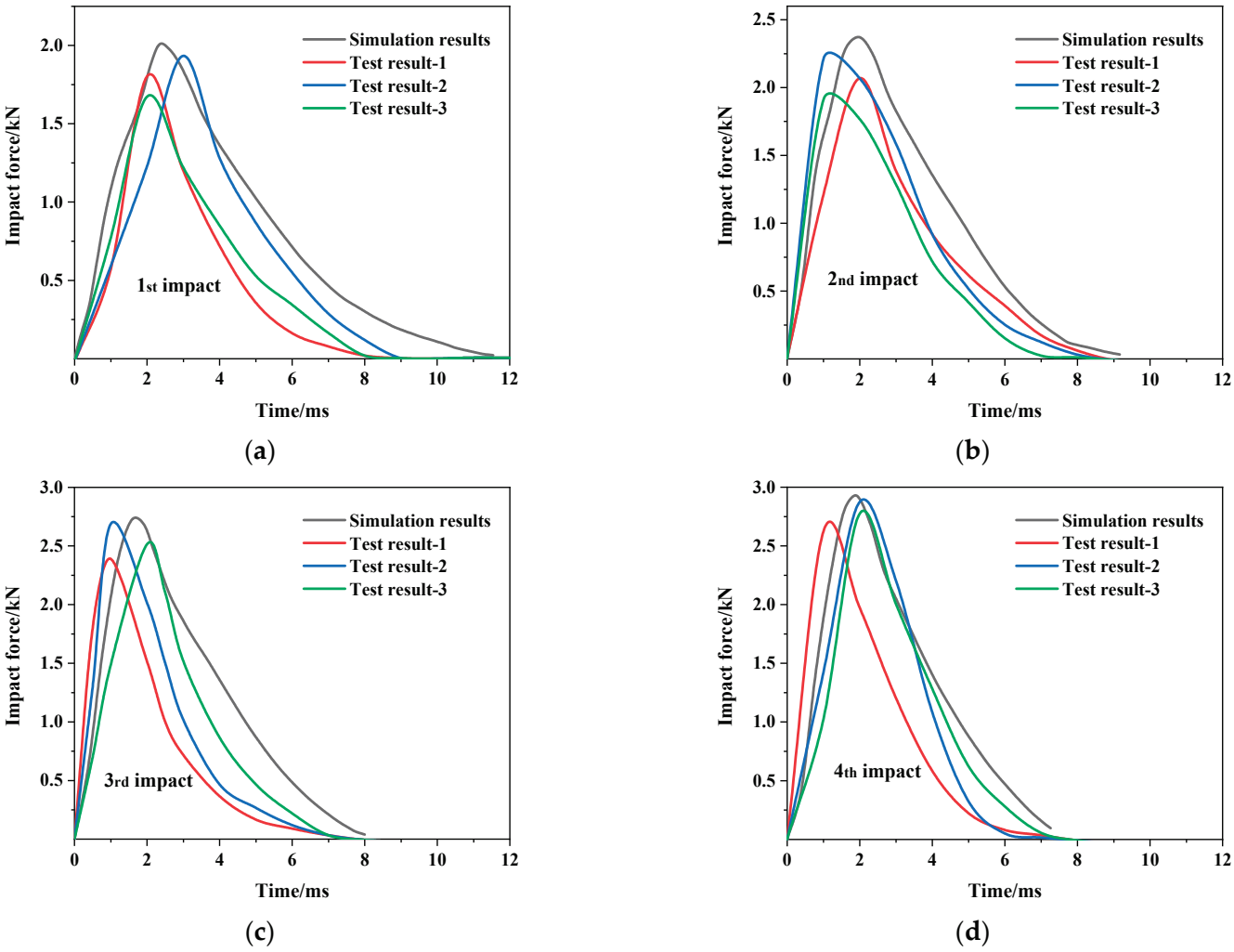

Figure 3. Comparison of the impact force time–history curve between the laboratory tests and numerical model under multiple impacts: (**a**) first impact; (**b**) second impact; (**c**) third impact; and (**d**) fourth impact.

The instant when the rockfall starts to contact the cushion is set to zero. The impact force increases rapidly when the rockfall contacts the sand buffer layer and quickly decreases to zero after reaching the maximum impact force. The entire shock process is very brief. Under the four impacts, the numerical simulation results obtained by using discrete element software are close to the experimental results, and the error is small. In general, the average value of the maximum impact force results of the three groups of laboratory tests was compared with the numerical results. The two results differ in maximum impact force by 10.76%, 7.04%, 2.79%, and 5.59%, respectively. In terms of the duration of the impact process and the change trend of the impact force, the simulation results agree well with the test results.

Therefore, the analytical model and method proposed above can more reliably reflect the dynamic response of rockfalls impacting a sand buffer layer. This is applied to the study in the next section considering the multiple impacts of rockfall on a sand buffer layer at the engineering scale.

4. Results and Discussion

Now, consider the dynamic process of rockfall impacting a sand buffer layer multiple times at the engineering scale. The impact energy of rockfall disasters along Japanese railways was calculated. Rockfall energies are approximately normally distributed. The proportion of rockfall events with an impact energy of less than 100 kJ was 68%, and the proportion of rockfall events with an impact energy of less than 1000 kJ reached 90% [24]. A study conducted off the east coast of New Wales, Australia, found that the average diameter of rockfalls in the sandstone and granite areas of the basin was 0.45 m, and 95% of the rockfalls had an impact energy of less than 1340 kJ [25]. Therefore, in the research of this paper, the diameter of the rockfall is 0.5 m, the density is consistent with that in the laboratory experiment, and the mass of the rockfall is 1.144 t. The drop heights are 10 m, 20 m, 30 m, 40 m, and 50 m, respectively. The impact energy corresponds to 112 kJ, 224 kJ, 336 kJ, 448 kJ, and 560 kJ, respectively.

4.1. Large-Scale Impact Numerical Model

In the research for this paper, the influence of the constraints around the sand buffer layer on the impact effect is ignored, and the size of the buffer layer is guaranteed to be large enough. When the ratio of the size of the buffer layer to the diameter of the rockfall exceeds five, the effect of the lateral boundary constraints of the buffer layer can be ignored [26]. Therefore, the size of the cushion is selected as 5 m × 5 m × 2 m. Since the size of the buffer layer is much larger than that of the laboratory test in Section 2, the soil radius has also been adjusted accordingly, ranging from 0.03 m to 0.06 m. Except for the adjustment of the soil radius in the cushion layer, the parameters of the cushion layer do not change. The number of spherical particles in the buffer layer in the numerical model is 76801. The model diagram is shown in Figure 4.

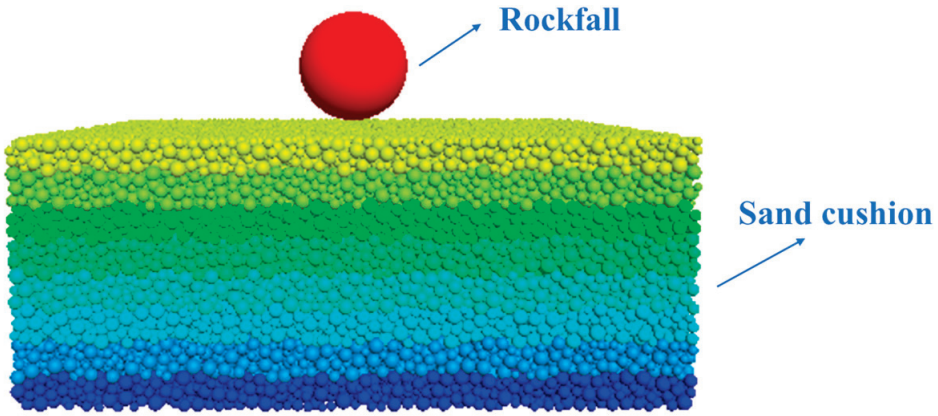

Figure 4. Large-scale numerical model diagram.

Next, we discuss the dynamic response of rockfall on the sand cushion for multiple impacts. The analysis focuses on the impact force and penetration depth on the sand cushion. The purpose is to reveal the importance of considering the multiple impacts of rockfalls.

4.2. Multiple Impact Cushion Center Positions

4.2.1. Analysis of the Rockfall and Cushion after Multiple Impacts

Figure 5 shows the cloud map of the change in the position of the rockfall and the cushion after each impact when the rockfall falls from the same height and impacts the sand cushion several times, for a total of four impacts. To observe the changes more intuitively in the position of the rockfall and the impact point on the top surface of the cushion after the impact of the rockfall, the model was cut along the *xOz* plane to observe the cross-section. The upper black line is the starting surface of the sand cushion, and the lower black line is the plane of the maximum penetration depth after impact. The vertical distance between the two black lines is the maximum penetration depth. The area enclosed by the white line and the upper black line is the range of particles affected by the impact. The impact of the rockfall caused a certain penetration into the top surface of the cushion, and some particles near the impact point were lifted. With the increase in the number of impacts, the height of the rockfall relative to the top surface of the cushion gradually decreased, and the affected particles in the lower part of the impact point in the cushion and near the impact point on the top surface of the cushion tended to increase.

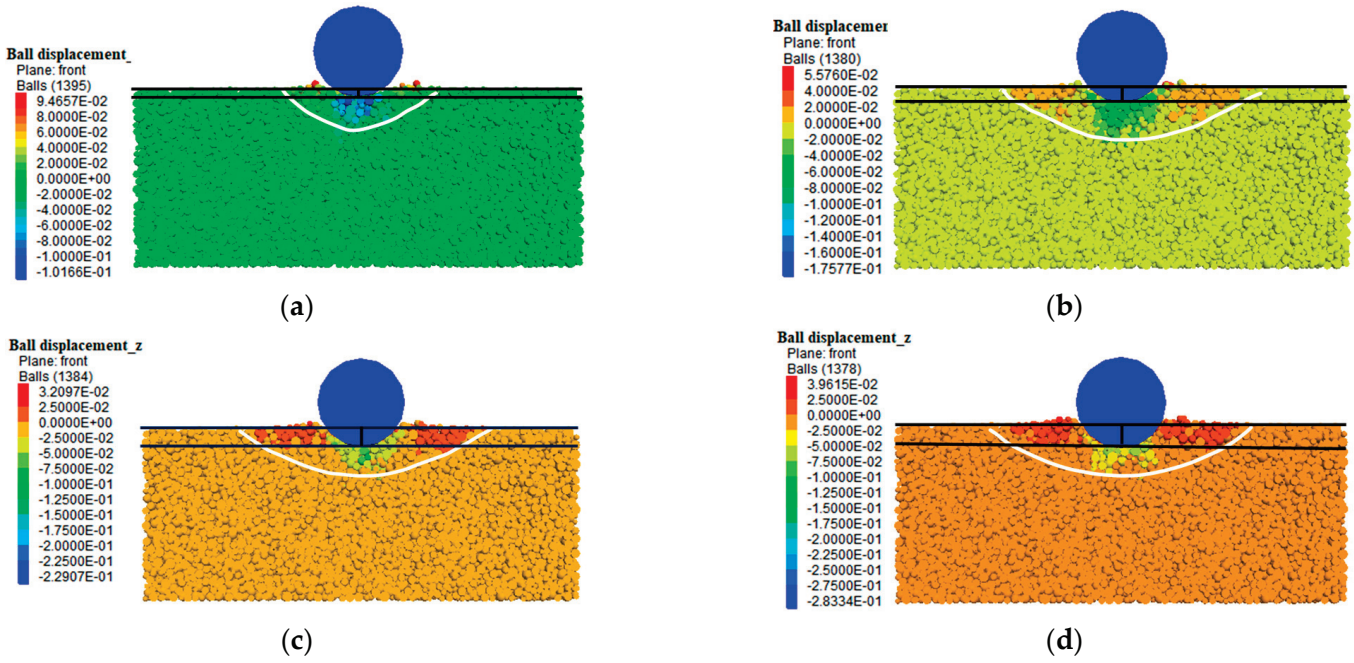

Figure 5. Nephogram of rockfall and cushion position changes (t = 0.05 s): (**a**) first impact; (**b**) second impact; (**c**) third impact; and (**d**) fourth impact.

4.2.2. Impact Force at the Center of Multiple Impacts

Figure 6 shows the time–history curve of the impact force of the spherical rockfall impacting the sand cushion multiple times from different heights. The instant when the falling rock and the cushion first contacted was taken as time zero. The change rule of the rockfall impact force is that at the moment of contact with the cushion, the impact force rapidly increases to the peak impact force and then decreases relatively slowly to zero. Since each impact will cause a certain penetration into the cushion, the time of contact with the cushion will be delayed for the next impact compared with the previous impact. With the increase in the number of impacts, the time lag of the peak impact force and the magnitude of the impact force increase, but the duration of the entire impact process is gradually shortened. The maximum impact force and impact duration are important factors to be considered in actual rockfall-protection projects. It can be seen that the impact number will affect the impact response of rockfall. Therefore, it is obvious that when

discussing the dynamic response to rockfall impact, it is not comprehensive enough to consider the consequences of only one rockfall impact.

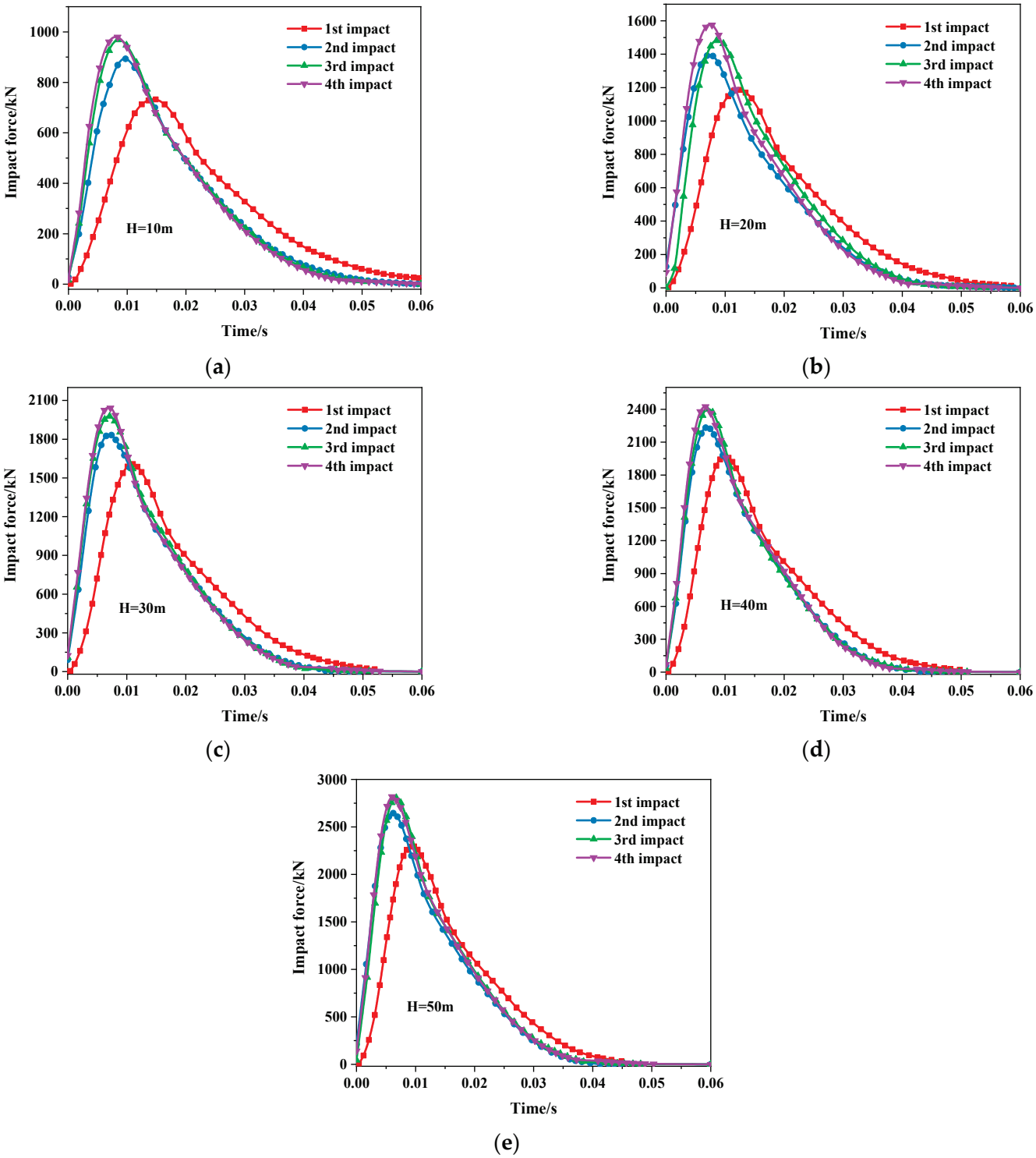

Figure 6. Time–history curve of the impact force of a spherical rockfall impacting a sand cushion multiple times from different heights. (**a**) H = 10 m; (**b**) H = 20 m; (**c**) H = 30 m; (**d**) H = 40 m; and (**e**) H = 50 m.

Figure 7 shows the results of the maximum impact force of the spherical rock falling on the sand cushion multiple times from five falling heights. The impact force increases with the drop height. Regardless of the drop height, the impact force results of the four impacts show a gradually increasing trend, but the increasing range gradually decreases. For example, the impact force results for the drop height of 50 m are 2299 kN, 2645 kN, 2807 kN, and 2819 kN for the four impacts. The results of the second, third, and fourth impacts were increased by 15%, 22.1%, and 22.6%, respectively, compared with the first impact. The fourth impact force is slightly larger than the third impact force. Therefore, only four shocks are considered in this paper to study multiple shocks. For different drop heights, the total increase in the impact force of the four impacts is different. For heights of 10 m, 20 m, 30 m, 40 m, and 50 m, the fourth impact force increased by 33.9%, 32.7%, 27.4%, 23.1%, and 22.6%, respectively, compared with the first impact force. Because of the different falling heights, the impact energy of the falling rock varies greatly. With the increase in the number of impacts, the main reason for the gradual increase in the impact force is the gradual increase in the compactness of the cushion. However, the increase in the compactness of the cushion has a limit. After the first impact, the compactness of the cushion increases more at higher drop heights. During the last few impacts, the change in cushion disorientation decreases with an increasing drop height. Therefore, a phenomenon is observed in which an increasing falling height results in an impact force that is smaller under multiple impacts than under a single impact. However, since the maximum impact force increases with the increasing impact height, a higher impact height must still be considered.

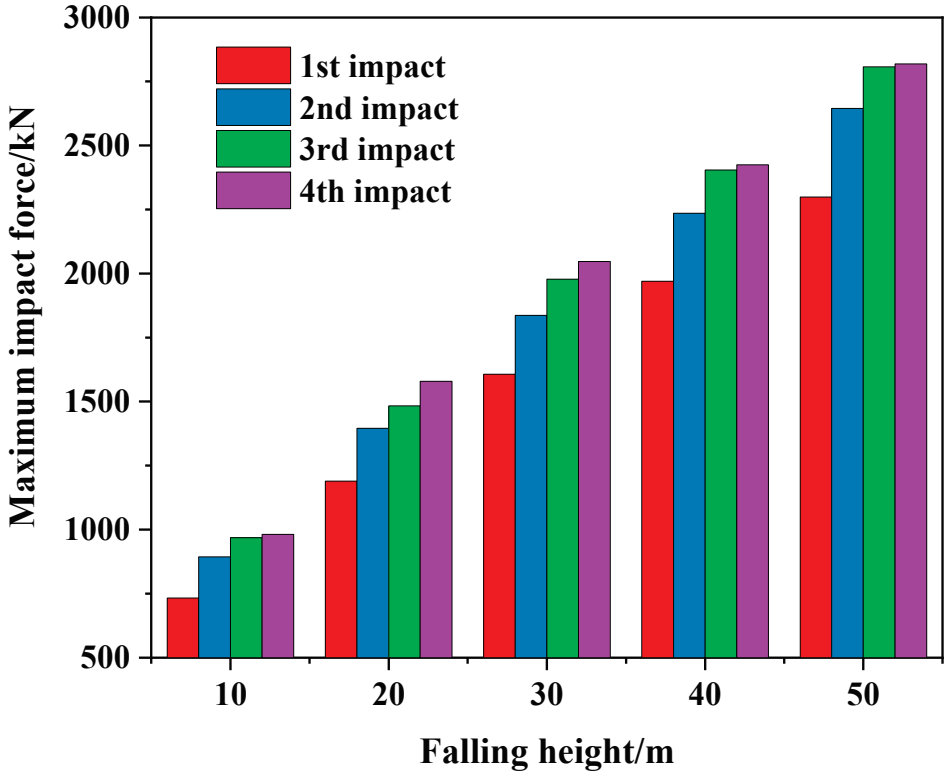

Figure 7. Maximum impact force of a spherical rock falling on a sand cushion multiple times from five falling heights.

The impact force of rockfall on the shed cavity cushion is a crucial inspection index in the design of shed cavity structures. No existing impact force algorithm considers the calculation of the impact force during multiple impacts. The maximum impact force algorithm of rockfalls proposed by Labiouse et al. [27] based on Hertzian contact theory is modified by introducing a coefficient, α, related to the number of impacts, t, through the numerical results of the maximum impact force under multiple impacts.

The maximum impact force equation can be expressed as the following:

$$P_{\max} = \alpha \cdot 1.765 \cdot (M_E)^{\frac{2}{5}} \cdot R^{\frac{1}{5}} \cdot (WH)^{\frac{3}{5}} \quad (1)$$

In the formula, $P_{\max}$ is the maximum impact force (kN); M_E is the modulus of the subgrade reaction obtained from a standardized plate bearing test on the soil cushion (kN/m^2); R is the radius of the falling block in contact with the cushion (m); W is the weight of the falling rock (kN); and H is the falling height (m).

Combined with the impact force results of the falling rock impacting the sand cushion for the first time from different heights, take M_E = 5200 kN/m^2, R = 0.5 m, W = 11.2 kN, and H = 10 m, 20 m, 30 m, 40 m, and 50 m. The selection of parameters comes from the conditions in the numerical model. At this time, α = 1. Figure 8 below compares the impact force calculated by the maximum impact force formula with the numerical results for different heights.

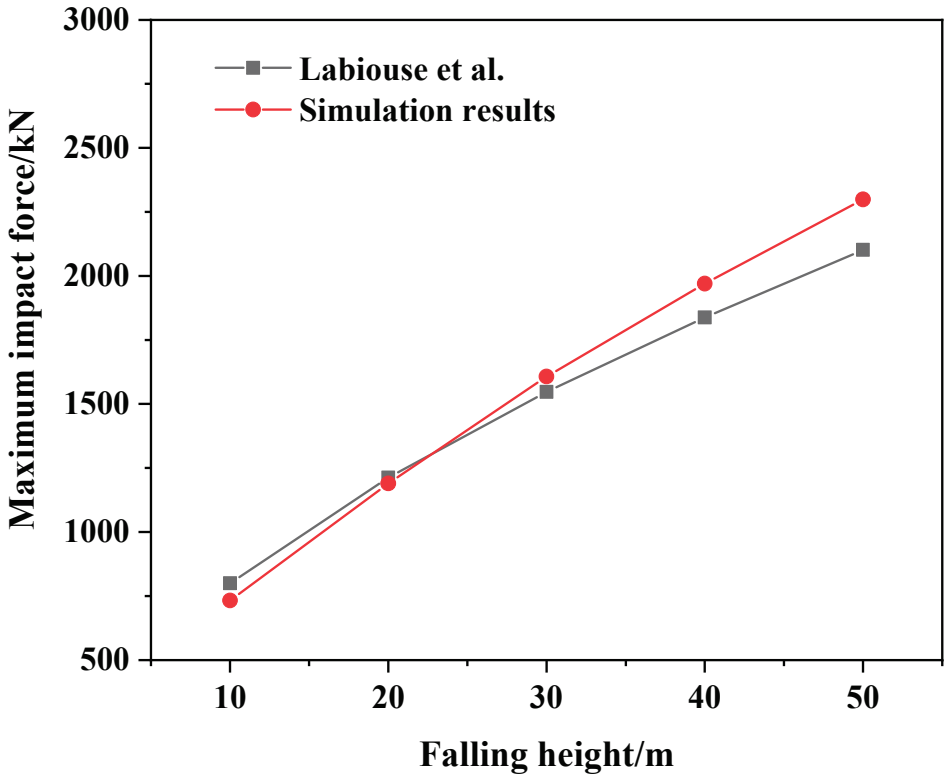

Figure 8. Comparison of the formula and simulated impact force results [27].

Comparing the two curves in Figure 8 shows that the maximum impact force calculated by the formula proposed by Labiouse et al. agrees well with the impact force result of the numerical model in this paper. The error of the calculated result can be controlled within 10%. Therefore, this formula can be combined with the numerical results to explore the calculation of the maximum impact force when the rockfall hits the buffer layer many times.

The numerical results for the impact force of the falling rock impacting the sand cushion multiple times from heights of 10 m, 20 m, 30 m, 40 m, and 50 m are analyzed and discussed. Consider the ratio of the impact force after the second, third, and fourth impacts to the impact force of the first impact for a given height. Considering the five drop heights comprehensively, the expression for α corresponding to the number of impacts t is obtained by performing a fit. Figure 9 compares the numerical results of the impact force with the results of the fitting formula for different drop heights.

$$\alpha = 1.314 - 0.67 \times 0.469^{t} \tag{2}$$

where t is the number of impacts and α is an expression that only relates to the number of impacts.

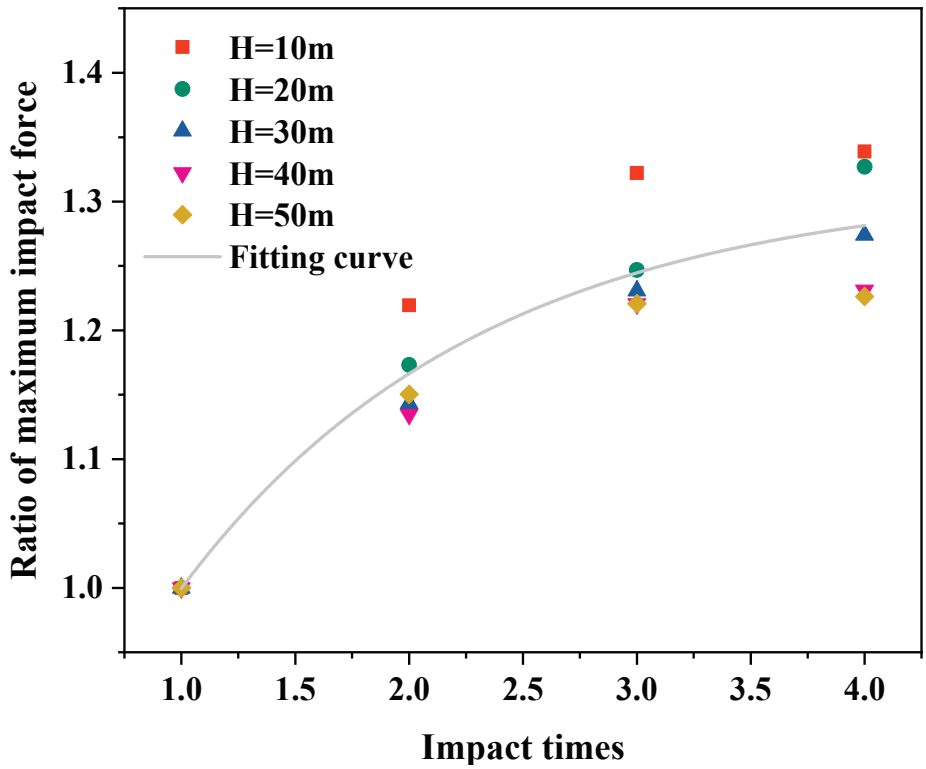

Figure 9. Comparison of impact force results between numerical and fitted formulas.

Impact force algorithm for multiple impacts:

$$P_{\max} = (1.314 - 0.67 \times 0.469^{t}) \cdot 1.765 \cdot (M_E)^{\frac{2}{5}} \cdot R^{\frac{1}{5}} \cdot (WH)^{\frac{3}{5}} \tag{3}$$

The numerical results for the impact force of the falling rock impacting the sand cushion multiple times from heights of 10 m, 20 m, 30 m, 40 m, and 50 m are analyzed and discussed. Consider the ratio of the impact force after the second, third, and fourth impacts to the impact force of the first impact for a given height. Considering the five drop heights comprehensively, the expression for α corresponding to the number of impacts t is obtained by performing a fit. Figure 9 compares the numerical results of the impact force with the results of the fitting formula for different drop heights.

Figure 10 compares the calculated results of the improved maximum impact force algorithm with the numerical simulation results.

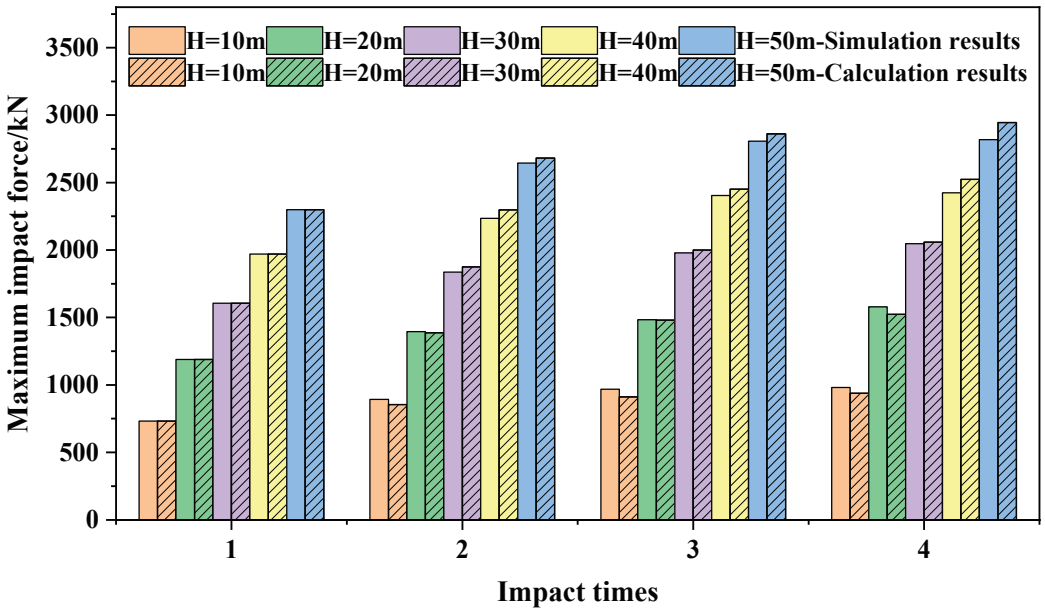

Figure 10. Impact force results from improved algorithms and numerical simulations.

The impact forces of the impacts in the figure correspond to drop heights of 10 m, 20 m, 30 m, 40 m, and 50 m, respectively, from left to right. Solid color, unpatterned fills represent the numerical results, and diagonal striped fills represent the calculation results of formulas. The results calculated by the improved impact force algorithm agree well with the numerical simulation results as a whole, and the maximum error of the calculated results is 5.87%. For the more dangerous, high-impact energy cases, the error is controlled within 5%. Therefore, the maximum impact force algorithm modified by fitting the numerical simulation results in this paper can be considered reasonable.

4.2.3. Penetration Depth at the Center of Multiple Impacts

In addition to the maximum impact force of the rockfall, the maximum penetration depth of the rockfall into the buffer layer is also an important parameter to be considered in engineering design [20,28]. During the experiment, because of the special backfilling phenomenon of the sand cushion, the depth of the cushion after the rockfall impact is difficult to obtain. However, the change in the penetration depth can be observed intuitively in the numerical simulation. Figure 11 shows the time–history curve of the penetration depth of the spherical rockfall impacting the sand cushion multiple times from different heights. After the rockfall is in contact with the cushion, the penetration depth gradually increases. After reaching the peak penetration depth, the penetration depth recovers to a certain extent because of the rebound phenomenon of the rockfall. Similarly, with an increasing number of impacts, the maximum penetration depth appears slightly later and gradually increases. This result confirms that the size of the maximum penetration depth can provide a basis for selecting the thickness of the buffer layer of the shed cavity structure. It also confirms the necessity of considering multiple impacts of rockfalls.

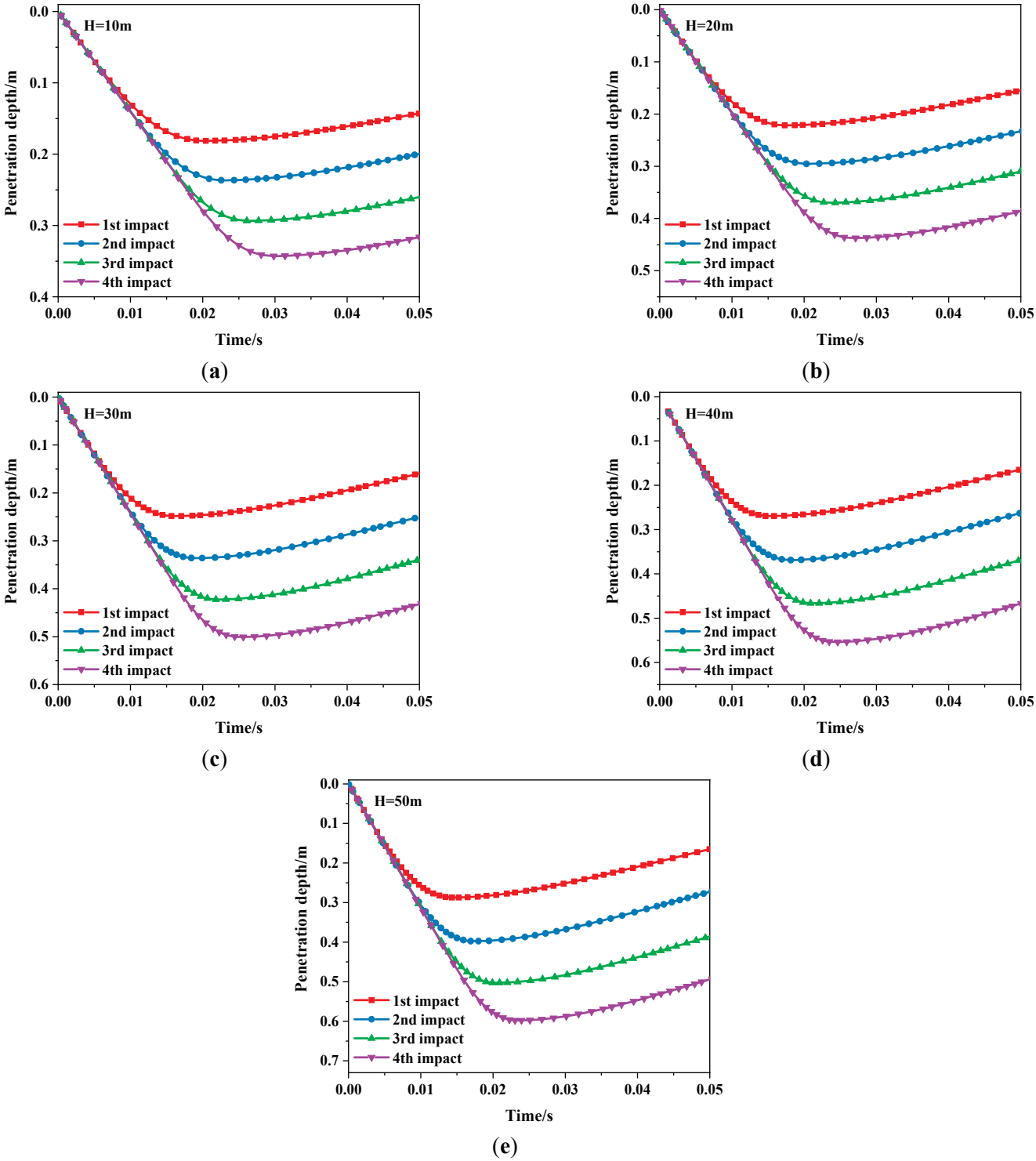

Figure 11. Time–history curve of the penetration depth of a spherical rockfall impacting a sand cushion multiple times from different heights. (**a**) H = 10 m; (**b**) H = 20 m; (**c**) H = 30 m; (**d**) H = 40 m; and (**e**) H = 50 m.

Figure 12 shows the results of the maximum penetration depth of the spherical rockfall with multiple impacts on the sand cushion for five drop heights. As with the maximum impact force results, the maximum penetration depth increases with the number of impacts regardless of the drop height. However, unlike the results for the maximum impact force, the maximum penetration depth increases with the same magnitude as the number of impacts increases. For example, when the drop height is 10 m, the maximum penetration depths are 0.181 m, 0.236 m, 0.293 m, and 0.343 m, respectively. Compared with the first impact, the maximum penetration depth of the latter three increased by 30.4%, 61.8%, and 89%, respectively. At different drop heights, the total increase in the penetration depth under the four impacts is roughly the same. However, the penetration depth increases slightly with an increasing drop height. At heights of 10 m, 20 m, 30 m, 40 m, and 50 m, the ratios of the fourth penetration depth to the first penetration depth were 1.89, 1.97, 2.02, 2.06, and 2.08, respectively.

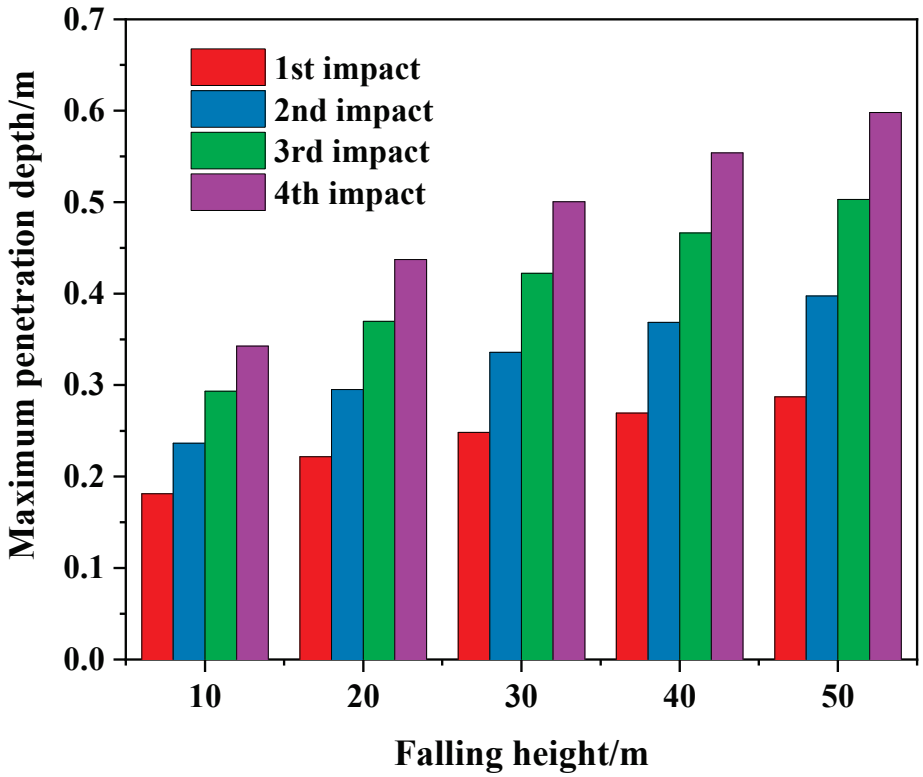

Figure 12. Maximum penetration depth of a spherical rock falling on a sand cushion multiple times at five falling heights.

4.3. Distance between Different Impact Positions

At present, the only research on multiple impacts of rockfalls is limited to consecutive multiple impacts of rockfalls on the same location. Notably, when a rockfall disaster occurs, the impact position of the multiple impacts of the rockfall on the cushion may change. After the impact position changes, it needs to be considered whether the dynamic response between two adjacent shocks is affected by the distance between the shock positions. To address this problem, this paper studies the effect of the distance between the impact points on the impact response when the rockfall impacts different impact locations. The approximate distance that the second impact is not affected by the first impact when two consecutive impacts are at different positions is given.

Considering the rockfall radius R and the size of the cushion, in addition to the first impact at the center of the cushion, six impact positions are also considered. They are 0.5R, 1R, 1.5R, 2R, 3R, and 4R from the center point O, corresponding to six points A, B, C, D, E, and F, respectively, as shown in Figure 13.

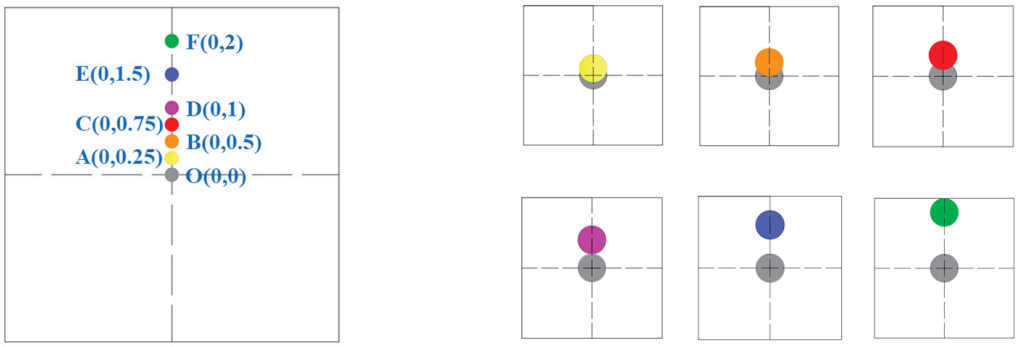

Figure 13. Schematic diagram of different impact positions.

To compare the effect of the distance between shock locations on the shock response, two shock simulations were performed. Taking point *A* as an example, the other five points are the same. For the convenience of comparison, the first one impacts point *A* only once. The second carries out the simulation of rockfall impacting the sand cushion twice: the first impact is at point *O*, the center point of the cushion, and the second impact is at point *A*. The numerical results of the two shocks were compared and analyzed, and the distance between the two shock locations that did not affect each other was explored.

4.3.1. Impact Force at Different Positions

Taking the falling height of 50 m as an example, Figure 14 shows the time–history curve of the impact force of the rockfall at different positions on the top surface of the sand cushion. The left picture is the curve of impacting the selected impact position only once, and the right picture is the time–history curve of impacting the center point of the cushion and then impacting the selected position. The time–history curve of the impact force at each point in the left figure shows the same change trend. The instantaneous impact force of the rockfall contacting the cushion rapidly increases to the maximum impact force and then gradually decreases to zero. The time–history curves of different shock points in the right figure are quite different, especially point *A*. The main reason for this is that after the first impact on point *O*, the particles of the cushion layer are partially arched, as shown in Figure 5, the sand particles here are relatively loose, and point *A* is located in the arched part of the particles. Therefore, the maximum impact force is delayed. The impact force time–history curves of other impact locations are consistently in trend with those with only one impact, and the magnitude of the peak impact force is slightly different.

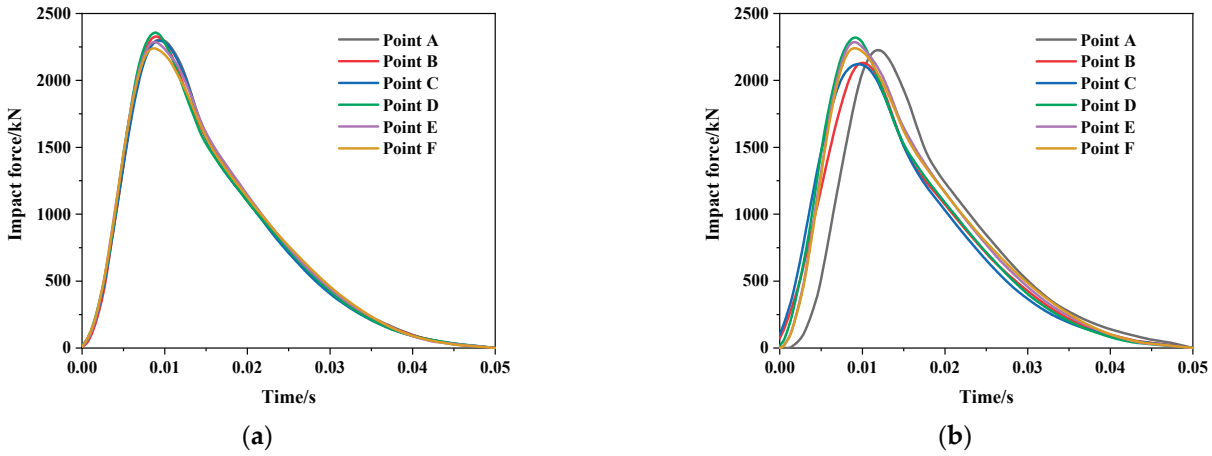

Figure 14. Time–history curve of the impact force of the falling rock at different positions on the top surface of the sand cushion when falling from 50 m. (**a**) Impact only once; (**b**) second impact.

Figure 15 shows the impact force results of rockfall impacting different positions of the top surface of the sand cushion from different heights. The results corresponding to each impact position in the figure correspond to drop heights of 10 m, 20 m, 30 m, 40 m, and 50 m from left to right. A solid, unpatterned fill represents the first impact simulation, and a horizontal stripe fill represents the second impact simulation. Since the particles in the mat are spheres, this results in slightly different levels of compaction at each location in the mat. At the same time, as the impact position approaches the cushion boundary, boundary constraints will also have a certain impact. Therefore, in the first impact simulation, the impact force slightly differs between impact locations. Taking the drop height of 50 m as an example, the impact force at point *A* to point *F* is 2306 kN, 2327 kN, 2297 kN, 2356 kN, 2287 kN, and 2238 kN, respectively. The maximum error is 5%. This error can be cancelled out when comparing two shock results. This method can still be considered reasonably reliable for investigating the effect of the distance between different impact locations.

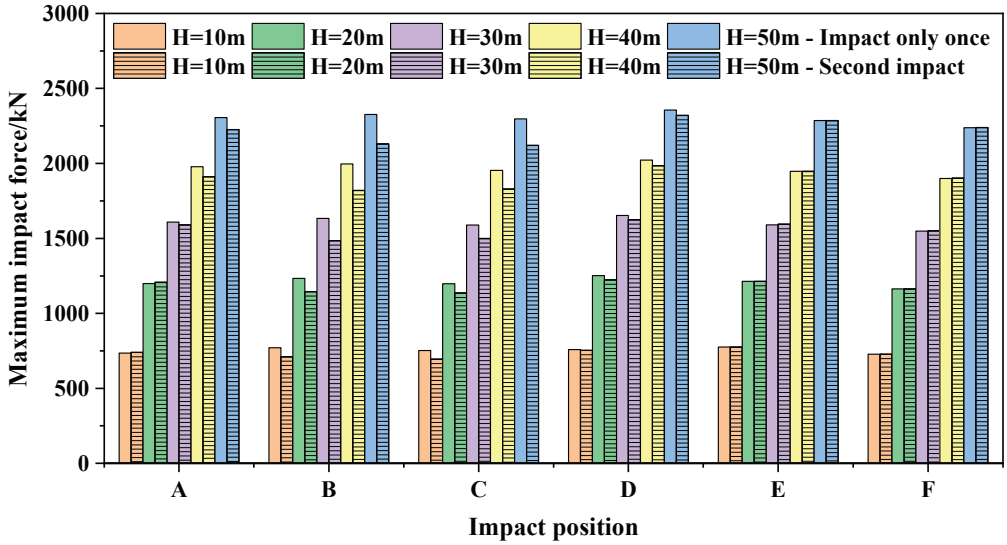

Figure 15. Impact force results of rockfall impacting different positions on the top surface of the sand cushion from different heights.

The abscissa in Figure 15 is from point *A* to point *F* from left to right, and the distance from point *O* increases gradually. That is, the distance between the impact positions increases gradually during multiple impacts. First, it can be observed that at different drop heights and different impact positions, an impact is smaller if the center point of the cushion is impacted first. This is mainly because after the first impact on the center point, the particles near the impact point are smashed, while the particles at other positions become sparser than the initial state. Therefore, the impact force is slightly larger when the impact occurs only once. Taking the drop height of 50 m as an example, the difference between the impact forces without and with a prior impact on the center point is 3.45%, 8.46%, 7.65%, 1.53%, 0.04%, and 0.08%. Judging from the difference in the impact force, point *B*, which is a radius from point *O*, is the most affected point, followed by point *C*, point *A*, and point *D*. Starting from point *E* at 1.5 m from point *O*, that is, when the distance from the impact position is 3*R*, the impact force results in consistency between the two impact modes. This finding means that when the distance between the impact positions of two adjacent impacts is greater than 3*R*, the maximum impact force during the second impact is not affected by the first impact. The same conclusion is obtained for drop heights of 10 m, 20 m, 30 m, and 40 m.

4.3.2. Penetration Depth at Different Positions

Taking the falling height of 50 m as an example, Figure 16 shows the time–history curve of the penetration depth of the rockfall at different positions on the top surface of the sand cushion. This curve is the same as the time–history curve of the impact force. The left picture shows the curve of only one impact on the selected impact position, and the right picture shows the time–history curve of the impact on the center point of the cushion and then the selected position. The time–history curve of the penetration depth of each point in the left figure shows the same trend of change. After the rockfall contacts the cushion, the penetration depth gradually increases to the maximum penetration depth and then recovers to a certain extent. The time–history curves of different shock points in the right figure are quite different, particularly point *A*. The penetration depth is substantially different from other impact locations at point *A*. The maximum penetration depth is quite different from the result when only point *A* is impacted, as shown in the left picture, and is much larger than the penetration depth of other impact points, as shown in the right picture. At other impact locations, the time–history curves of the penetration depth are consistently in trend with those with only one impact, and the magnitude of the peak penetration depth is slightly different. In order to achieve more intuitive understanding, the vertical displacement nephogram of particles at different impact positions is shown in Figure 17.

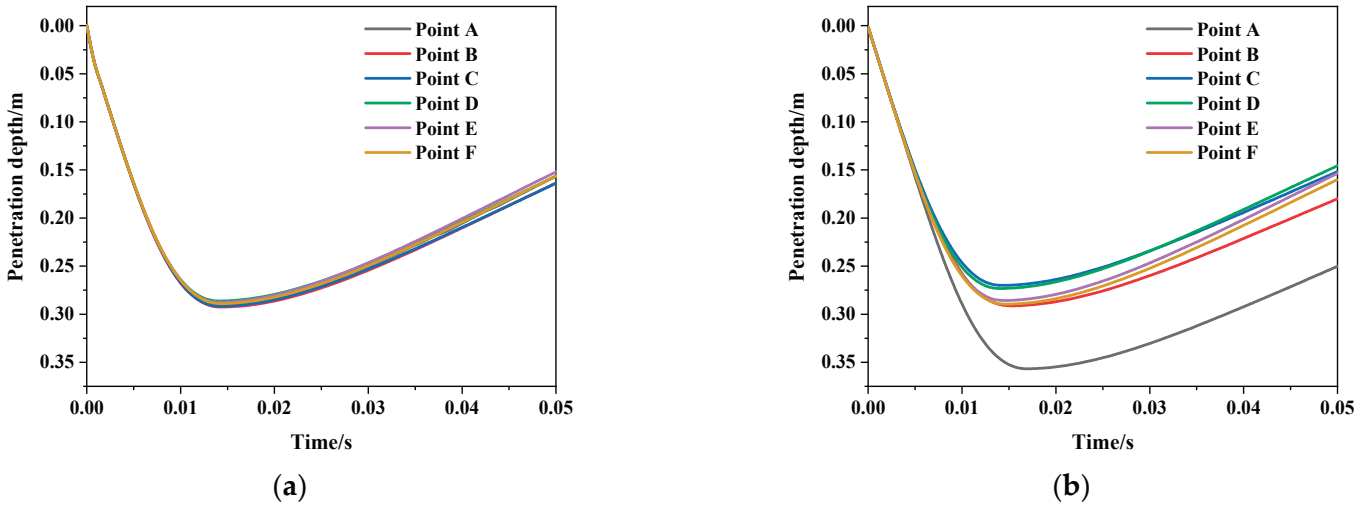

Figure 16. Time–history curve of the penetration depth of the falling rock at different positions on the top surface of the sand cushion when falling from 50 m. (**a**) Impact only once; (**b**) second impact.

Figure 18 shows the results for the penetration depth of the rockfall from different heights impacting different positions on the top surface of the sand cushion. The results for each impact position in the figure correspond to drop heights of 10 m, 20 m, 30 m, 40 m, and 50 m from left to right. A solid, unpatterned fill represents the first impact simulation, and a horizontal stripe fill represents the second impact simulation. Consistent with the reason for the different impact force results at different positions when only one impact is performed, the penetration depths at different locations are also not the same when only one impact is performed, but the difference is very small. Taking the penetration depth results when the drop height is 50 m as an example, the penetration depths from point *A* to point *F* are 0.2903 m, 0.2925 m, 0.2918 m, 0.2863 m, 0.2875 m, and 0.2891 m, respectively. The maximum error is 1.9%. The distance between the impact locations where the impact effect is affected between two consecutive impacts can still be explored by comparing the maximum penetration depths of the two impact modes.

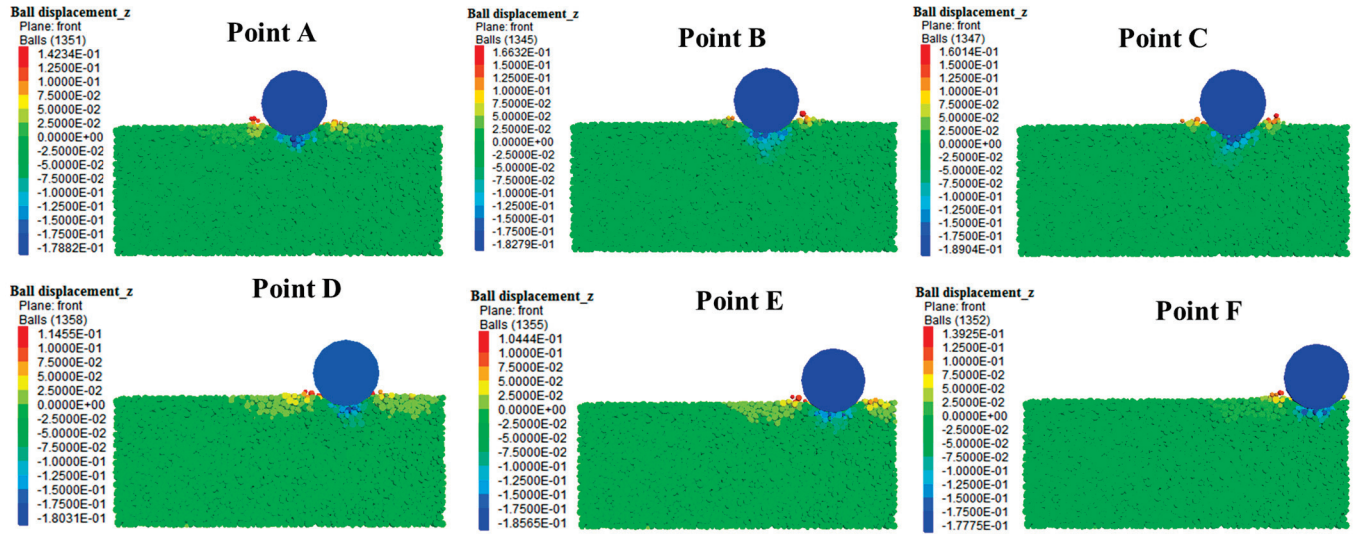

(**a**)

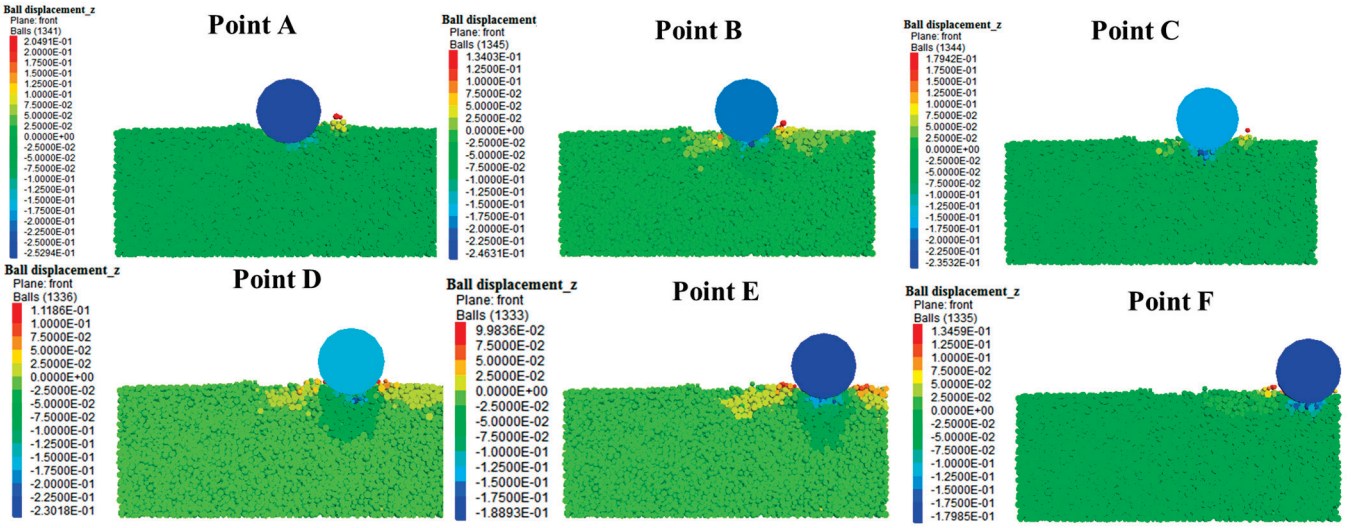

(**b**)

Figure 17. The vertical displacement nephogram of particles at different positions when falling from 50 m (t = 0.05 s). (**a**) Impact only once; (**b**) second impact.

The abscissa in Figure 18 is from point *A* to point *F* from left to right, and the distance from point *O* increases gradually; that is, the distance between the impact positions increases gradually during multiple impacts. Taking the drop height of 50 m as an example, the difference between the penetration depth results without and with a prior impact at the center point is 22.86%, 0.40%, 7.44%, 4.53%, 0.60%, and 0.15%, respectively. From the difference in the penetration depths, point *A* at the shortest distance from point *O* is the most affected point, followed by point *C*. After the first impact on point *O*, the sand particles near the impact point are relatively loose. Point *A* is located in the loose part of the particles, so the phenomenon of the maximum depression depth at point *A* changes greatly. Likewise, starting from point *E* at 1.5 m from point *O*, that is, at a distance of 3*R* from the impact location, the difference between the penetration depth results for the two impact modes is very small. This observation shows that when the distance between the impact positions of two adjacent impacts is greater than 3*R*, the maximum penetration depth of the second impact is slightly affected by the first impact. The same conclusion is obtained for drop heights of 10 m, 20 m, 30 m, and 40 m.

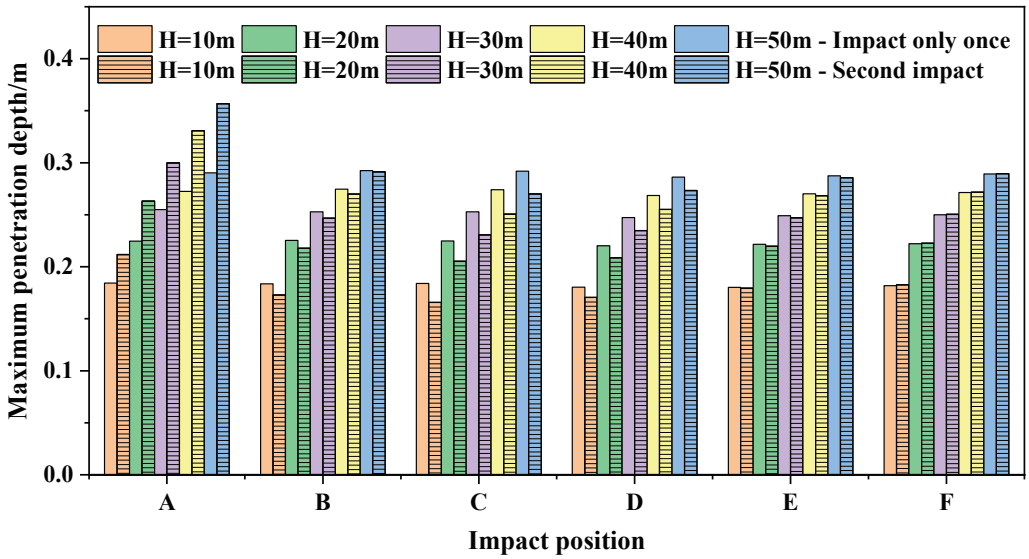

Figure 18. Penetration depth results of rockfall impacting different positions on the top surface of the sand cushion from different heights.

5. Conclusions

This paper focuses on the dynamic response of spherical rockfalls' multiple impacts on a sand cushion from different falling heights. First of all, carry out the reduced-scale impact test. Secondly, a numerical model is established and compared with the test results to verify the reliability of the model. On this basis, an engineering scale numerical model is established to discuss the effect of multiple impacts on the impact response, including multiple impacts at the same location and multiple impacts at different locations. In addition, based on the numerical simulation results of the maximum impact force, the existing impact force algorithm is modified to provide a reference basis for the design of rockfall prevention engineering. The specific conclusions are as follows:

(1) When rockfall disasters occur, there are often multiple impacts. Therefore, it is necessary to consider the multiple impacts of rockfall. Both the test and numerical simulation show that the maximum impact force and the maximum penetration depth increase to varying degrees with the increase in the number of impacts. For a given drop height, the increase in the maximum impact force decreases gradually, and the increase in the maximum penetration depth is almost constant. With the increase in the impact height, the increase in the impact force decreases and the increase in the penetration depth slightly increases.

(2) Based on the numerical simulation results, the maximum impact force equation proposed by Labiouse et al. was revised, and a coefficient related to the number of impacts was introduced to obtain the impact force after each impact under multiple impacts. It can provide a more direct reference for the design of shed tunnel structures.

(3) In the rockfall disaster, there is the possibility that the two adjacent impact positions are different during multiple impacts. Therefore, with the help of numerical simulation, this paper explores the impact of the distance between impact positions on the response to the impact. The numerical results of the maximum impact force and the maximum penetration depth show that the impact response of the second impact is not affected by the first impact when the distance between the impact positions of two adjacent impacts is three times the radius of the falling rock. Under this condition, the impact response of rockfall can be ignored for the first impact and only the second impact is considered.

Author Contributions: Conceptualization, Y.Z. and L.D.; Methodology, Y.Z., J.F. and L.D.; Software, Y.Z. and P.Z.; Validation, J.F. and P.Z.; Formal analysis, Y.Z.; Investigation, J.F. and J.P.; Resources, Y.Z., L.D. and C.Y.; Data curation, Y.Z., J.P. and H.F.; Writing—original draft, Y.Z.; Writing—review & editing, J.F., L.D., P.Z., C.Y. and H.F.; Visualization, J.P.; Supervision, L.D., P.Z. and L.L.; Funding acquisition, L.D. and L.L. All authors have read and agreed to the published version of the manuscript.

Funding: This research was funded by the Department of Transportation of Sichuan Province, grant number 2020-MS3-101/2020-B-01.

Institutional Review Board Statement: Not applicable.

Informed Consent Statement: Not applicable.

Data Availability Statement: This study did not report any data.

Acknowledgments: We are grateful for the constructive comments from the reviewers and our editor.

Conflicts of Interest: The authors declare no conflict of interest.

References

1. Bhatti, A.Q. Falling-weight impact response for prototype RC type rock-shed with sand cushion. *Mater. Struct.* **2014**, *48*, 3367–3375. [CrossRef]
2. Zhao, P.; Xie, L.; He, B.; Zhang, Y. Experimental study of rock-sheds constructed with PE fibres and composite cushion against rockfall impacts. *Eng. Struct.* **2018**, *177*, 175–189. [CrossRef]
3. Zhao, P.; Xie, L.; Li, L.; Liu, Q.; Yuan, S. Large-scale rockfall impact experiments on a RC rock-shed with a newly proposed cushion layer composed of sand and EPE. *Eng. Struct.* **2018**, *175*, 386–398. [CrossRef]
4. Naito, N.; Maeda, K.; Konno, H.; Ushiwatari, Y.; Suzuki, K.; Kawase, R. Rockfall impacts on sand cushions with different soil mechanical characteristics using discrete element method. *Soils Found* **2020**, *60*, 384–397. [CrossRef]
5. Kawahara, S.; Muro, T. Effects of dry density and thickness of sandy soil on impact response due to rockfall. *J. Terramechanics* **2006**, *43*, 329–340. [CrossRef]
6. Cundall, P.A.; Strack, O.D.L. A Discrete Numerical Model for Granular Assemblies. *Géotechnique* **1979**, *29*, 47–65. [CrossRef]
7. Calvetti, F.; Prisco, C.D.; Vecchiotti, M. Experimental and numerical study of rock-fall impacts on granular soils. *Riv. Ital. Geotec.* **2005**, *4*, 95–109.
8. Zhang, L.; Nguyen, N.G.H.; Lambert, S.; Nicot, F.; Prunier, F.; Djeran-Maigre, I. The role of force chains in granular materials: From statics to dynamics. *Eur. J. Environ. Civ. Eng.* **2016**, *21*, 874–895. [CrossRef]
9. Zhang, L.; Lambert, S.; Nicot, F. Discrete dynamic modelling of the mechanical behaviour of a granular soil. *Int. J. Impact. Eng.* **2017**, *103*, 76–89. [CrossRef]
10. Shen, W.; Zhao, T.; Dai, F. Influence of particle size on the buffering efficiency of soil cushion layer against rockfall impact. *Nat. Hazards* **2021**, *108*, 1469–1488. [CrossRef]
11. Yuan, S.; Zhao, P.; Li, L.; Wang, X.; Liu, J.; Zhang, B. A Discrete Numerical Study of the Effect of the Thickness and the Porosity of the Sand Cushion on the Impact Response Due to the Rockfall. *Comput. Model. Eng. Sci.* **2022**, *130*, 1683–1698. [CrossRef]
12. Xie, Q.; Su, L.; Bai, H.; Tang, H.; Zhang, C.; Yu, F. An novel energy dissipator with self-recovery capability after deformation for structurally energy-dissipating rock-shed. *J. Mt. Sci.-Engl.* **2021**, *18*, 3058–3068. [CrossRef]
13. Zhao, P.; Yuan, S.; Li, L.; Ge, Q.; Liu, J.; Du, L. Experimental study on the multi-impact resistance of a composite cushion composed of sand and geofoam. *Geotext. Geomembr.* **2021**, *49*, 45–56. [CrossRef]
14. Ge, Q.; Zuo, W.; Liu, R.; Zhu, B.; Zhao, P.; Wan, L.; Wang, Y.; Zhao, R. Experimental Studies for Shear and Multi-Impact Resistance Performance of Sand–Geofoam Material. *Buildings* **2022**, *12*, 633. [CrossRef]
15. Watanabe, T.; Masuya, H.; Satoh, A.; Nakamura, S. Analysis of Impact Response of Sand Cushion for Rockfall by Distinct Element Method. *Appl. Mech. Mater.* **2011**, *82*, 92–99. [CrossRef]
16. Roethlin, C.; Calvetti, F.; Yamaguchi, S.; Vogel, T. *Numerical Simulation of Rockfall Impact on a Rigid Reinforced Concrete Slab with a Cushion Layer*; Eidgenössische Technische Hochschule ETH: Zürich, Switzerland, 2013; Volume 8.
17. Zhang, Y.; Shao, J.; Liu, Z.; Shi, C. Numerical study on the dynamic behavior of rock avalanche: Influence of cluster shape, size and gradation. *Acta Geotech.* **2022**, *18*, 299–318. [CrossRef]
18. Bourrier, F.; Nicot, F.; Darve, F. Physical processes within a 2D granular layer during an impact. *Granul. Matter.* **2008**, *10*, 415–437. [CrossRef]
19. Albaba, A.; Lambert, S.; Nicot, F.; Chareyre, B. Relation between microstructure and loading applied by a granular flow to a rigid wall using DEM modeling. *Granul. Matter.* **2015**, *17*, 603–616. [CrossRef]
20. Pichler, B.L.A.; Hellmich, C.; Mang, H.A. Impact of rocks onto gravel Design and evaluation of experiments. *Int. J. Impact Eng.* **2005**, *31*, 559–578. [CrossRef]
21. Calvetti, F. Discrete modelling of granular materials and geotechnical problems. *Eur. J. Environ. Civ. Eng.* **2008**, *12*, 951–965. [CrossRef]

22. Gabrieli, F.; Cola, S.; Calvetti, F. Use of an up-scaled DEM model for analysing the behaviour of a shallow foundation on a model slope. *Geomech. Geoengin.* **2009**, *4*, 109–122. [CrossRef]
23. Itasca Consulting Group Inc. *Particle Flow Code in 3 Dimensions User's Guide in PFC3D 4.00*; Itasca Consulting Group: Minneapolis, MN, USA, 2008.
24. Muraishi, H.; Samizo, M.; Sugiyama, T. Development of a Flexible Low-Energy Rockfall Protection Fence. *Q. Rep. RTRI* **2005**, *46*, 161–166. [CrossRef]
25. Spadari, M.; Kardani, M.; De Carteret, R.; Giacomini, A.; Buzzi, O.; Fityus, S.; Sloan, S.W. Statistical evaluation of rockfall energy ranges for different geological settings of New South Wales, Australia. *Eng. Geol.* **2013**, *158*, 57–65. [CrossRef]
26. Seguin, A.; Bertho, Y.; Martinez, F.; Crassous, J.; Gondret, P. Experimental velocity fields and forces for a cylinder penetrating into a granular medium. *Phys. Rev. E. Stat. Nonlin. Soft Matter Phys.* **2013**, *87*, 012201. [CrossRef] [PubMed]
27. Labiouse, V.; Descoeudres, F.; Montani, S. Experimental Study of Rock Sheds Impacted by Rock Blocks. *Struct. Eng. Int.* **1996**, *6*, 171–176. [CrossRef]
28. di Prisco, C.; Vecchiotti, M. Design Charts for Evaluating Impact Forces on Dissipative Granular Soil Cushions. *J. Geotech. Geoenviron. Eng.* **2010**, *136*, 1529–1541. [CrossRef]

water

MDPI

Article

Some Considerations for Using Numerical Methods to Simulate Possible Debris Flows: The Case of the 2013 and 2020 Wayao Debris Flows (Sichuan, China)

Xianzheng Zhang [1], Chenxiao Tang [2,*], Yajie Yu [3], Chuan Tang [1], Ning Li [4], Jiang Xiong [1] and Ming Chen [1]

[1] State Key Laboratory of Geohazard Prevention and Geoenvironment Protection, Chengdu University of Technology, Chengdu 610059, China; zhangxianzheng@stu.cdut.edu.cn (X.Z.); tangc@cdut.edu.cn (C.T.); xiongjiang@stu.cdut.edu.cn (J.X.); chenminggeo@163.com (M.C.)
[2] Key Laboratory of Mountain Surface Process and Hazards, Institute of Mountain Hazards and Environment, Chinese Academy of Sciences, Chengdu 610041, China
[3] The Second Institute of Surveying and Mapping, Department of Natural Resources of Hebei Province, Shijiazhuang 050000, China; sjyykfc@126.com
[4] School of Emergency Science, Xihua University, Chengdu 610039, China; cdutln617@gmail.com
* Correspondence: c.tang@imde.ac.cn

Abstract: Using a numerical simulation method based on physical equations to obtain the debris flow risk range is important for local-scale debris flow risk assessment. While many debris flow models have been used to reproduce processes after debris flow occurrence, their predictability in potentially catastrophic debris flow scenarios has mostly not been evaluated in detail. Two single-phase flow models and two two-phase models were used to reproduce the Wayao debris flow event in 2013. Then the Wayao debris flow event in 2020 was predicted by the four models with the same parameters in 2013. The depth distributions of the debris source and deposition fan were mapped by visual interpretation, electric resistivity surveys, field measurements, and unmanned aerial vehicle (UAV) surveys. The digital elevation model (DEM), rainfall data, and other simulation parameters were collected. These models can reproduce the geometry and thickness distribution of the debris flow fan in 2013. However, the predictions of the runout range and the deposition depth are quite different from the actuality in 2020. The performance and usability of these models are compared and discussed. This could provide a reference for selecting physical models to assess debris-flow risk.

Keywords: debris flow; numerical modeling; risk assessment; single-phase models; two-phase models

Citation: Zhang, X.; Tang, C.; Yu, Y.; Tang, C.; Li, N.; Xiong, J.; Chen, M. Some Considerations for Using Numerical Methods to Simulate Possible Debris Flows: The Case of the 2013 and 2020 Wayao Debris Flows (Sichuan, China). *Water* **2022**, *14*, 1050. https://doi.org/10.3390/w14071050

Academic Editors: Stefano Morelli, Veronica Pazzi and Mirko Francioni

Received: 10 February 2022
Accepted: 25 March 2022
Published: 27 March 2022

1. Introduction

Hazard maps of a debris flow can be obtained through two major kinds of methods: Empirical methods based on analysis of historical events and numerical methods using physically based equations [1,2]. An empirical method often uses correlations between the debris flow runout and topographic parameters, sediment supply, or dynamic parameters to make a prediction [3,4]. There are three major factors influencing the debris flow runout distance: The volume of removable sediment, catchment area, and internal relief [5]. Zhou et al. [6] established a multivariate relationship between runout distance and the debris volume or the internal catchment relief.

While empirical methods are useful to make hazard assessments at a regional scale, the positive prediction accuracy of the runout area covered by debris-flow deposits may be less than 40% [7,8]. Furthermore, empirical methods cannot provide comprehensive information on the processes of debris flows and the final deposit topography [9]. An accurate prediction of the potentially exposed areas can be fundamental for the safety of human lives. The numerical methods can overcome some of these limitations, as they can reproduce the debris flow process through physical equations.

Two kinds of rheological closure models are commonly used in numerical simulation: Single-phase flow models and two-phase flow models. Single-phase flow models are commonly based on the Bingham rheology [10], the Voellmy rheology [11,12], and the Bagnold rheology [13,14]. O'Brien et al. [15] designed a two-dimensional (2D) mudflow program FLO-2D based on the Bingham rheology, and Beguería et al. [16] designed a GIS-based debris flow program Massmove2D based on the Voellmy rheology. Ouyang et al. [17] designed the two-dimensional debris flow program Massflow based on Coulomb and Voellmy frictional laws. Takahashi [18] proposed a 2D granular flow model based on the Bagnold rheology and coupled with Coulomb flow resistance. Then, several modified granular models were developed by researchers [19–23]. Based on Bagnold rheology, a new particle shear stress equation is derived for a wide range of particle flows [24]. The equation was used to establish the continuum granular model Flow-3D [25], which yielded promising results for the simulation of debris flow behavior [26,27].

Two-phase flow models mainly include the flow model composed of solid–fluid mixtures [28–30], two-fluid debris flow model [31,32], general two-phase debris flow model [33], Euler–Euler model [34], a depth-averaged two-phase model [35], and the depth-integrated model [36]. The general two-phase debris flow model allows smooth transitions between non-viscous flow, hyper-concentrated sediment-laden flow, and debris flows. Moreover, Bout et al. [37] developed OpenLISEM for the debris flow simulation. OpenLISEM couples the two-phase debris flow equations and a full hydrological catchment model. It can recreate the impact of both floods and debris flow runout. Furthermore, it involves simulating runoff, entrainment of sediment, and the formation of debris flow from intense erosion. In this paper, we call OpenLISEM without a full hydrological catchment model OpenLISEM_A, and we call OpenLISEM with a full hydrological catchment model OpenLISEM_B.

In this work, the single-phase flow models Massflow and Flow-3D and the two-phase flow models OpenLISEM_A and OpenLISEM_B were used to reproduce the process and depositional topography of debris flow. Two debris flow events occurred in the Wayao catchment in 2013 and 2020, and both debris flows were initiated from runoff. The topography of debris fan, erosion depth of channel deposition, and debris flow density were collected to calibrate simulation parameters and verify prediction ability. First, the four models were applied to reproduce the debris flow event in 2013. Second, the four models were used to predict the debris flow event in 2020, and the same set of parameters as the debris flow in 2013 is adopted, which is considered satisfactory. The prediction abilities of the four models are validated from the transport process and accumulation characteristics of the 2020 debris flow. The purposes are to discuss the advantages and limitations of the different models for debris flow prediction and provide suggestions for the physically based hazard assessments in mountainous areas.

2. Study Sample

The Wayao catchment is located in Gaodian, Sichuan, China (Figure 1). It is located in the Longmen Shan range, a region between the Qinghai-Tibet Plateau and the Sichuan Basin [38,39]. The catchment area is 11.7 km^2, and the main channel length is 2.2 km. The terrain elevation varies between 1191 m and 2973 m, and the slope range is 35–50°. The geological setting consists mostly of Proterozoic magmatic rocks. The Wayao catchment is located southeast of the Wenchuan-Maoxian fault, a thrust fault with a strike of 25° N–45° E [40] that ruptured in the Wenchuan earthquake [41]. Several landslides were triggered by the 2008 Wenchuan earthquake in the Wayao catchment, and most of them were deposited on the slope or along the channel. They provided the main debris source for the debris flow in 2013. The Wayao catchment is in a typically humid subtropical monsoon climate zone, with rainfall mainly concentrated between June and September. Heavy rainfall triggered two debris flow events in the Wayao catchment in 2013 and 2019.

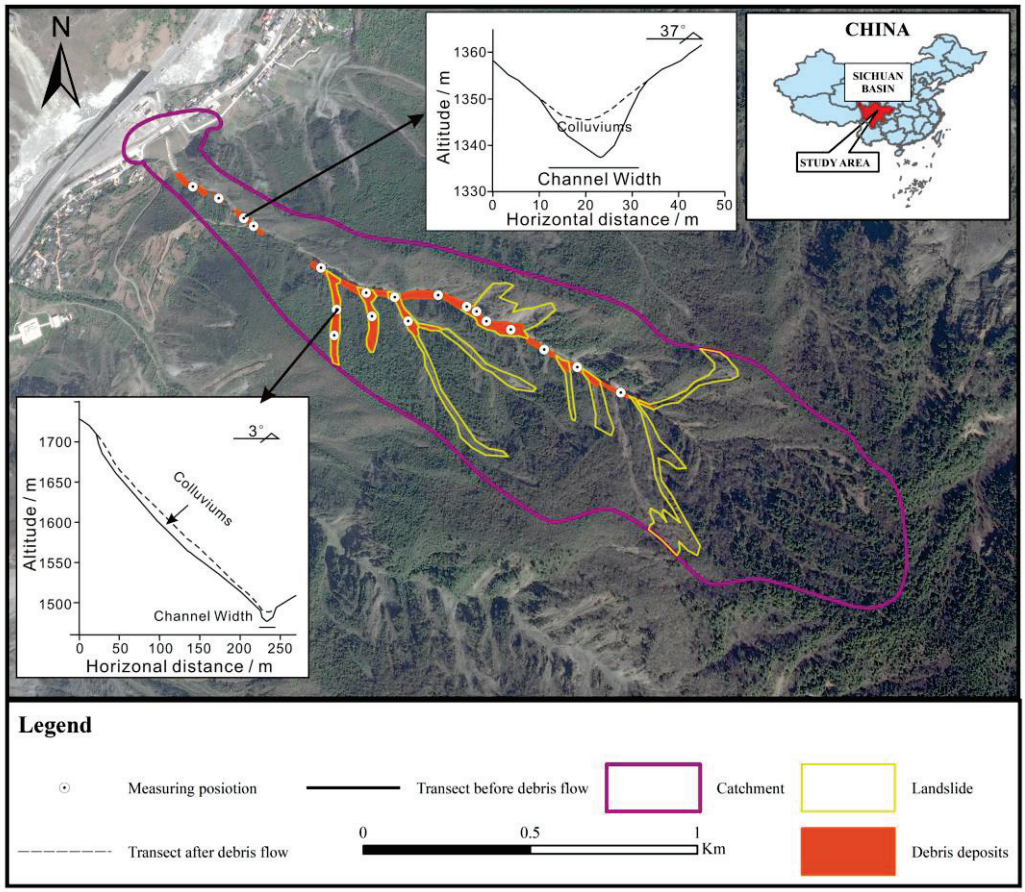

Figure 1. Overview of the study area. The landslides and deposits along the channel were identified on a satellite image from 15 April 2015.

On 10 July 2013, a catastrophic debris flow triggered by heavy rainfall destroyed the village located in the Wayao catchment outlet (Figure 2). The triggering rainfall of the debris flow was 18.6 mm/h at 9 a.m. on 10 July 2013. The rainfall data are from a rain gauge approximately 9 km from the study area [42]. The debris flow was triggered by the channel runoff, and several landslides were triggered by heavy rainfall [43]. The deposition in the channel and several landslides along the channel provided source material for the debris flow. The debris flow eroded the deposited debris along the channel and stopped at the mouth of the catchment. Approximately 1.41×10^5 m^3 of debris was transported out, and the average depth of the debris fan was 5 m. The debris flow buried 27 houses and cut national road G213. Then, the local government built a check dam and drainage channel in 2014 to avoid possible debris flows.

On 17 August 2020, during a rainstorm, the Wayao catchment suffered from a debris flow. The triggering rainfall of the debris flow was 18.8 mm/h at 4 p.m. The rainfall data are from a rain gauge about 18 km from the catchment and provided by the Sichuan Provincial Meteorological Service. The debris flow was triggered by the channel runoff, and three landslides were triggered by heavy rainfall. The three landslides provided the main source material for the debris flow, and some of the deposition along the channel was eroded by the debris flow. When the debris flow was transported to the check dam, the check dam was filled by the debris flow deposition. Then the debris flow was transported along the drainage channel, and most of the debris flow was transported into the Min River (Figure 3).

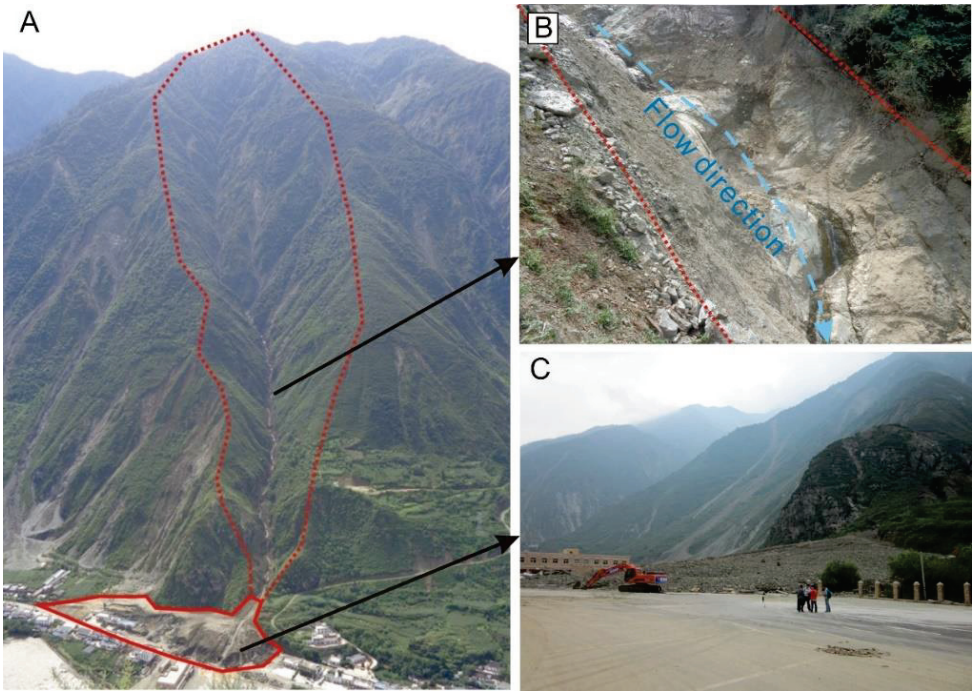

Figure 2. (**A**) Panoramic view of Wayao debris flow taken on 7 August 2013. The dashed red line indicates the catchment boundary, and the solid red line indicates the extent of the debris fan. (**B**) The debris deposition along the channel was eroded by the debris flow in 2013. The blue line indicates the debris flow direction, and the red lines indicate the trace of the debris flow. (**C**) The debris fan of the Wayao debris flow in 2013.

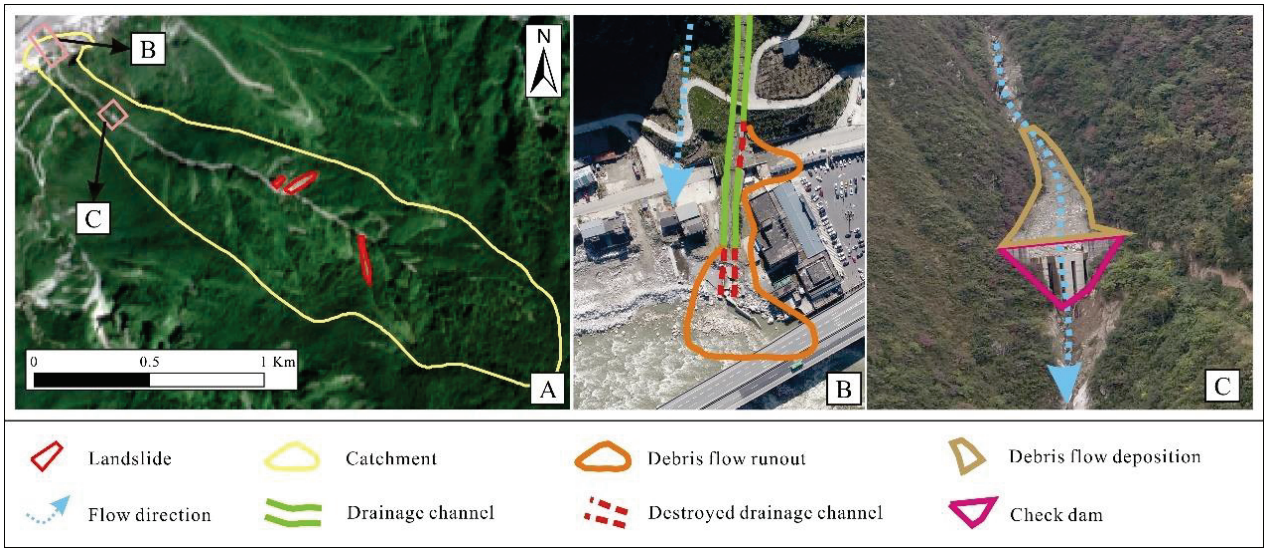

Figure 3. (**A**) The landslides are identified on a satellite image from 27 August 2020. It shows the locations of (**B**,**C**). (**B**) Destroyed drainage channel and debris flow runout on UAV image from 25 October 2020. (**C**) A drone photo shows that the check dam was filled with debris-flow deposits after the debris flow, and it was taken on 25 October 2020.

3. Measuring Debris Flow Volume

The depth distribution of landslides, deposition along the channel, and the debris fan were measured by multiple methods. The volumes of landslides and deposits along the channel are important input parameters of the debris flow simulation. Moreover, the depth distribution of the debris fan is an important factor to evaluate the simulation results.

For the debris flow event in 2013, the locations of landslides were mapped by visual interpretation [44] using the image from Google Earth taken on 15 April 2015, and the depths of landslides were measured by field measurement. The depth distribution of debris fan, landslides, and eroded debris along the channel is shown in Figure 4A, and the volumes are shown in Table 1. Eight sections along the channel and ten sections on the slope were measured. The depth distributions of landslides and deposits along the channel in 2013 are shown in Figure 3A. The depth distribution of the debris fan was measured by electrical resistivity tomography (ERT). ERT is widely used to delineate the contact surface between the debris fan and the underlying rock layer [45,46]. ERT measurements were carried out on the deposition fan, and the instrument was a WDJD-3 system from Chongqing Benteng Digital Control Technical Institute. L1 and L2 were two measuring lines on the deposition fan (Figure 4A). Sixty electrodes were placed on measuring line L1, and the distance between the electrodes was 2 m.

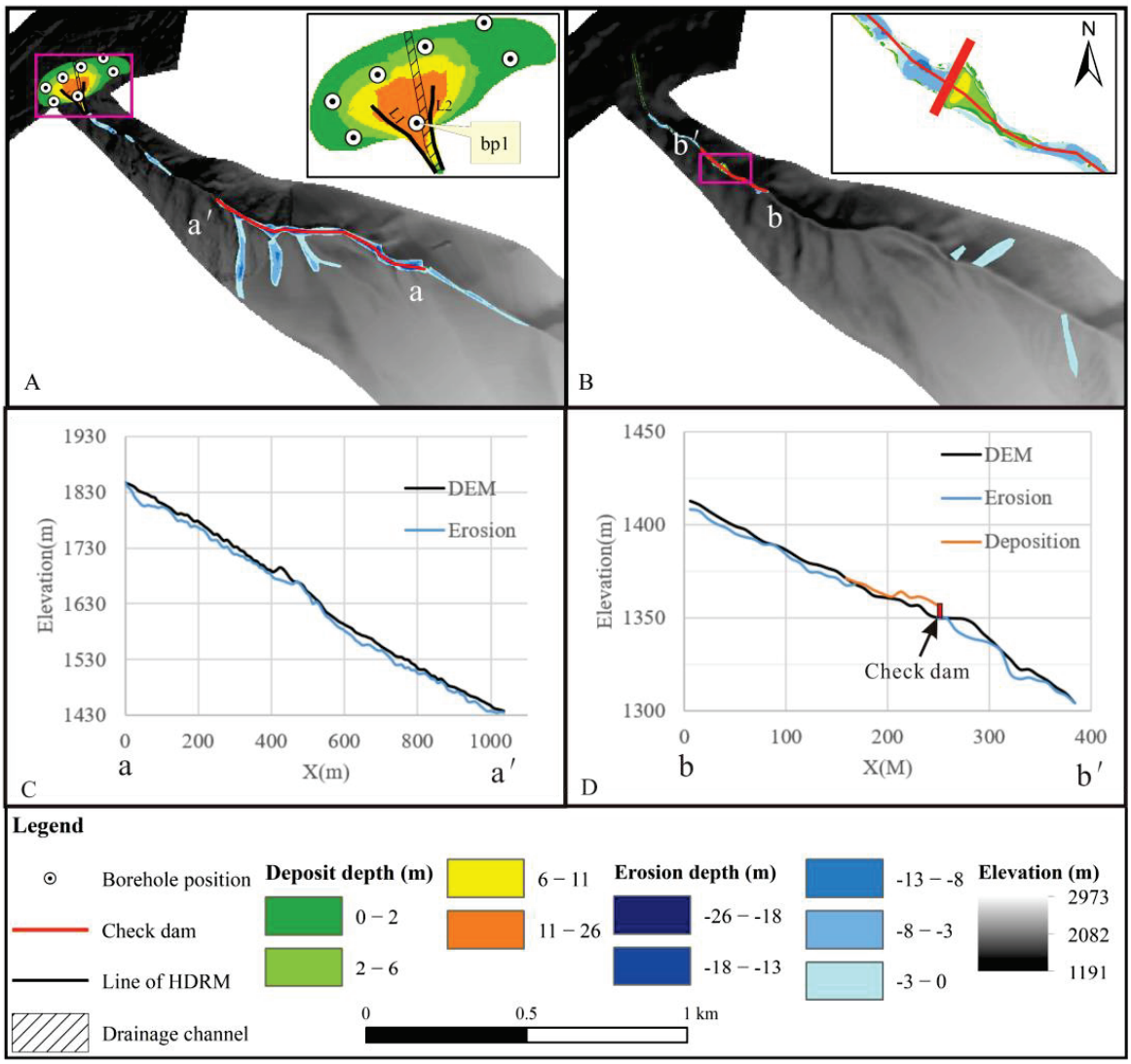

Figure 4. (**A**,**B**) The depth distributions of eroded debris and deposited debris in the 2013 debris flow event and the 2020 debris flow event, respectively. (**C**,**D**) The longitudinal profiles along the channel, and their positions are shown in A and B, respectively. The location of profiles a-a′ is shown in (**A**) and the location of profile b-b′ is shown in (**B**).

Table 1. The volumes of landslides, eroded debris along the channel, debris fan, and the deposition after the barrier.

Year	2013	2020
Volume of the landslides (m^3)	2.6×10^6	1.9×10^4
Volume of the eroded debris along the channel (m^3)	5.3×10^6	1.1×10^4
Volume of the debris fan (m^3)	7.9×10^6	/ [1]
Volume of the deposition after the barrier (m^3)	/ [2]	0.3×10^4

[1] The debris flow did not form a debris fan in 2020, as it transported into Min River. [2] There was no debris deposition after the barrier in 2013, as the barrier was built in 2014.

The total length of the L1 was 118 m. Fifty-four electrodes were placed on measuring line L2, and the distance between the electrodes was 2 m. The total length of L2 was 106 m. Res2DInv software was used for mesh refinement and robust inversion, and Figure 5 shows the resistivity inversion results. At depths of 2 to 14 m, the electrical resistivity ranges from 40 to 200 Ω·m. At depths of 14 to 16 m, the values suddenly increase to 700–1000 Ω·m. The depth value of the debris fan is consistent with the value obtained by drilling (bp1). The location of bp1 was between the two measuring lines. Kriging [47] was used to interpolate the depth values obtained by ERT and drilling. A 1:2000 topographic map, provided by the Sichuan Metallurgical and Geological Exploration Bureau of the Chengdu Geological Survey Institute, was used to build the terrain model for simulation of the debris flow in 2013.

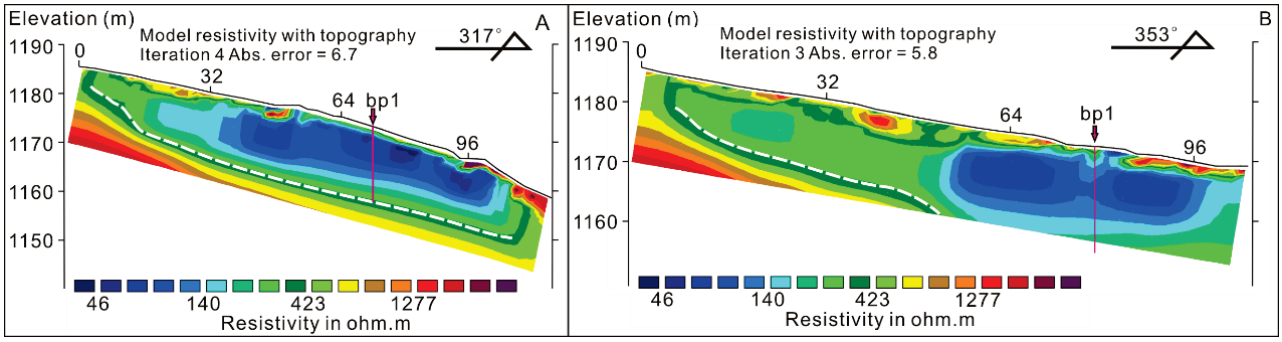

Figure 5. Resistivity results and interpretations. (**A**) Resistivity profile along L1. (**B**) Resistivity profile along with L2. The white dotted line is the dividing line between the debris fan and the underlying rock layer. L1, L2, and bp1 are shown in Figure 3.

For the debris flow event in 2020, the image from Sentinel-2 taken on 25 October 2020 was used to interpret the locations of rainfall-triggered landslides. Field measurements and UAV surveys measured the depths of landslides, eroded debris along the channel, and the deposition after the barrier. Their depth distributions are shown in Figure 4B. Their volumes are shown in Table 1. Two UAV stereo photo-derived digital elevation models (DEMs) were measured on 19 April 2019, and 25 October 2020. They are used to analyze the depth distribution of deposits along the channel by comparing. The DEM, measured on 19 April 2019, was used to build the terrain model for simulation of the debris flow in 2020.

4. Model Description

Four different models, Massflow, Flow-3D, OpenLISEM_A, and OpenLISEM_B, were used to simulate. They all require an input file of the debris volume in the release area. For Massflow and Flow-3D, the debris flow was assumed as a single-phase fluid, and the initial density of debris flow was measured by field survey. For OpenLISEM_A and OpenLISEM_B, the debris flow was assumed as a two-phase fluid mixed with fluid and solid. For OpenLISEM_A, the initial volume ratios of solid and liquid can be inversely calculated by debris flow density. For OpenLISEM_B, the input data was the debris

source triggered by the rainfall. The debris source's initial porosity and moisture content were measured by the field survey provided by the Sichuan Metallurgical and Geological Exploration Bureau of the Chengdu Geological Survey Institute.

They have different boundary conditions. For Massflow, OpenLISEM_A, and OpenLISEM_B, a hydrograph can be specified as boundary conditions. For Flow-3D, an outflow boundary condition was set to allow debris flow to continue through the boundary with minimal reflection [25]. A man-made structure can be input into the four models, and the effort can be included in the simulation.

4.1. Massflow

Massflow is a program that adopts a depth-integrated continuum method to analyze the debris flow progress. It obtained good Hongchun debris flow simulation results in Wenchuan County [17,48]. For debris flow simulation, Massflow uses the Voellmy rheology. The Voellmy rheology assumes no shear deformation, and the mean velocity (u) over the height of the flow (h) of the flow is the same. The basal friction stress τ is given by:

$$\tau = \mu \cos\varphi + \frac{u^2}{\xi h} \quad (1)$$

where φ is the terrain's downslope angle (positive), μ is the dry Coulomb-type friction. ξ is the viscous resistance. Massflow uses the MacCormack-TVD scheme to solve the shallow water equations [17,49].

The input parameters of Massflow are the depth distribution of debris flow, the resistance parameters μ, and ξ. For the simulation, the resolution of 5 m grid post-event topography data was adopted, and the data of the debris fan was replaced with the topographic map taken before the event. The dry friction factor was calculated as the surface slope of the debris fan, and its value was in a range between 0.4 and 0.45. According to past research, the viscous resistance was chosen in a range between 100 and 300 m/s^2 [50,51]. Then the inversion method was used to determine the specific parameter values. A series of numerical simulations were performed to refine the parameter values by comparing the depth distribution of the debris fan. Parameter values for Massflow are summarized in Table 2. The running time was 300 s, with a time step $\Delta t \leq 1$ s.

Table 2. Best-fit model parameters used in Massflow, Flow-3D, OpenLISEM_A, and OpenLISEM_B simulations of the Wayao debris flow in 2013. A range of some debris parameters was measured by field measurement and laboratory tests.

Parameter	Massflow	Flow-3D	OpenLISEM_A	OpenLISEM_B
Rheological model	Coulomb frictional	Granular flow	general two-phase debris flow model	
Topographic mesh resolution	5 m	5 m	5 m	5 m
Debris flow density (kg/m^3), ρ	1986	1986	1986	-
Cohesion (pa), c	-	-	1250	1250
Friction angle (degrees), θ	—	32	24	20
Coulomb-type friction, μ	0.439	-	-	-
viscous resistance, ξ	200	-	-	-
Average grain diameter, D	-	0.05	0.05	0.05
Grain density (kg/m^3), ρ_s	-	2700	2700	2700
Fluid density (kg/m^3), ρ_f	-	1000	-	-
Fluid viscosity (kg/m/s)	-	0.01	-	-

Table 2. *Cont.*

Parameter	Massflow	Flow-3D	OpenLISEM_A	OpenLISEM_B
Minimum volume fraction of granular phase	-	0.001	-	-
XY mesh cell size	5 m	5 m	5 m	5 m
Z mess cell size	-	2 m	-	-
Manning	-	-	0.1	0.1
Porosity	-	-	0.38	0.38
Initial moisture content	-	-	-	0.114
Rainfall (mm/h)	-	-	-	18.6

4.2. Flow-3D

Flow-3D is a general-purpose computational fluid dynamic (CFD) program. For debris flow simulation, Flow-3D uses the high concentration granular model. The designation of high concentration granular flow here means the volume fraction of the granular material is 50% or greater. A strong coupling exists between the solid particles and surrounding fluid at high concentrations, so their mixture can be approximated as a single composite fluid [25]. The shear stress in non-cohesive granular flow consists of three parts: Impact among solid particles τ_i, additional viscous shear stress due to the presence of solid particles τ_v, and Shear stress in the fluid τ_f.

$$\tau = \tau_i + \tau_v + \tau_f = 7.8\mu_f \frac{\lambda^2}{1+\lambda}\frac{du}{dy} + \rho_s \frac{0.015}{1+\frac{0.5\rho_f}{\rho_s}} \frac{1+e}{(1-e)^{0.5}} \left(\lambda D \frac{du}{dy}\right)^2 + 0.00062\rho_f \left(\Delta R \frac{du}{dy}\right)^2 / (1+\lambda) \quad (2)$$

where μ_f is the fluid's dynamic viscosity. λ is the diameter to the minimum gap ratio. du/dy is the velocity gradient of the mixture. ρ_s is the density of the solid sphere. ρ_f is the density of the fluid sphere. e is the coefficient of restitution of the solid particle, and a typical coefficient of restitution for debris of 0.7 is assumed as a good general value. D is the diameter of spherical particles. ΔR is the gap of a Couette flow. λ is a function of the maximum solid volume fraction f_s^{mx} divided by the solid volume fraction f_s.

$$\lambda = \frac{1}{\left(\frac{1.032 f_s^{mx}}{f_s}\right)^{1/3} - 1} \quad (3)$$

when the volume fraction of solid material reaches or exceeds a value of about 0.99 f_s^{mx}, the flow velocity is set to zero, and the material is considered to be fully packed. A typical close packing volume fraction f_s^{cp} for debris of 0.68 and the typical value of loose packing volume fraction for debris f_s^{lp} of 0.11 are assumed as good general values. As granular material packs to a density where individual grains begin to touch one another, it becomes more difficult for the mixture to flow. This state is sometimes referred to as mechanical jamming and has a typical volume fraction of f_s^{jam} = 0.62.

The simulation area at the Wayao catchment includes the debris source and the deposition fan areas. The terrain model was resampled with a 5-m triangular mesh, and it contains more than 996,000 facets. The landslide and deposit along the channel models were resampled with a 2-m triangular mesh containing more than 63,000 facets. According to the field survey, the density and viscosity of the fluid were set to 1000 kg/m^3 and 0.01 kg/m/s, respectively. The density of the solid was set to 2700 kg/m^3. The average grain diameter was set to 0.05 m, which was calculated by the measured value of the final deposit [18]. The friction angle (degrees) was between 20 and ~35, as provided by the Sichuan Metallurgical and Geological Exploration Bureau of the Chengdu Geological Survey Institute. The debris

flow density was in a range between 1850 and 2030 kg/m^3. The best simulation parameters were obtained through repeated analysis, and the simulation results were satisfactory. Table 2 shows the full set of parameters used in the simulation. The running time was 300 s, with a time step $\Delta t \leq 0.5$ s.

4.3. OpenLISEM_A and OpenLISEM_B

OpenLISEM is a physically based numerical program for simulating flood, erosion, and debris flow [37]. It is based on the two-phase debris flow equations [33] and a full hydrological catchment model that includes pressure, gravitational forces, viscous forces, non-Newtonian viscosity, two-phase drag, and a Mohr–Coulomb type friction force. It can simulate the flow dynamics and interactions of the flood and the nonuniform debris flow [37,52]. The following is a constitutive equation:

$$S_{x,s} = \alpha_s\left(g\left(\frac{\partial b}{\partial x}\right) - \frac{u_s}{\left|\vec{u}_s\right|}\tan\delta P_{b_s} - \varepsilon P_{b_s}\left(\frac{\partial b}{\partial x}\right) - \varepsilon\alpha_s\gamma P_{b_f}\left(\frac{\partial h}{\partial x} + \frac{\partial b}{\partial x}\right) + C_{DG}(u_f - u_s)\left|\vec{u}_f - \vec{u}_s\right|^{j-1}\right. \tag{4}$$

$$S_{y,s} = \alpha_s\left(g\left(\frac{\partial b}{\partial y}\right) - \frac{u_s}{\left|\vec{u}_s\right|}\tan\delta P_{b_s} - \varepsilon P_{b_s}\left(\frac{\partial b}{\partial y}\right) - \varepsilon\alpha_s\gamma P_{b_f}\left(\frac{\partial h}{\partial y} + \frac{\partial b}{\partial y}\right) + C_{DG}(v_f - v_s)\left|\vec{u}_f - \vec{u}_s\right|^{j-1}\right. \tag{5}$$

$$\begin{aligned} S_{x,f} = \alpha_f\Big\{ & g\left(\tfrac{\partial b}{\partial x}\right) \\ & -\varepsilon\Big\{\Big[\tfrac{1}{h}\tfrac{\partial}{\partial x}\left(\tfrac{h^2}{2}P_{b_f}\right) + P_{b_f}\tfrac{\partial b}{\partial x} - \tfrac{1}{\alpha_f N_R}\left(2\tfrac{\partial^2 u_f}{\partial x^2} + \tfrac{\partial^2 v_f}{\partial y \partial x} + \tfrac{\partial^2 u_f}{\partial x^2} - \tfrac{\aleph u_f}{\varepsilon^2 h^2}\right) \\ & + \tfrac{1}{\alpha_f N_R}\left(2\tfrac{\partial}{\partial x}\left(\tfrac{\partial \alpha_s}{\partial x}(u_f - u_s)\right) + \tfrac{\partial}{\partial y}\left(\tfrac{\partial \alpha_s}{\partial x}(v_f - v_s)\right) + \left(\tfrac{\partial \alpha_s}{\partial y}(u_f - u_s)\right)\right) - \tfrac{\epsilon\alpha_s(v_f - v_s)}{\varepsilon^2\alpha_f N_{R_A} h^2}\Big]\Big\} \\ & -\tfrac{1}{\gamma}C_{DG}(u_f - u_s)\left|\vec{u}_f - \vec{u}_s\right|^{j-1} \end{aligned} \tag{6}$$

$$\begin{aligned} S_{y,f} = \alpha_f\Big\{ & g\left(\tfrac{\partial b}{\partial y}\right) \\ & -\varepsilon\Big[\tfrac{1}{h}\tfrac{\partial}{\partial y}\left(\tfrac{h^2}{2}P_{b_f}\right) + P_{b_f}\tfrac{\partial b}{\partial y} - \tfrac{1}{\alpha_f N_R}\left(2\tfrac{\partial^2 v_f}{\partial y^2} + \tfrac{\partial^2 v_f}{\partial y \partial x} + \tfrac{\partial^2 v_f}{\partial y^2} - \tfrac{\aleph v_f}{\varepsilon^2 h^2}\right) \\ & + \tfrac{1}{\alpha_f N_R}\left(2\tfrac{\partial}{\partial y}\left(\tfrac{\partial \alpha_s}{\partial y}(v_f - v_s)\right) + \tfrac{\partial}{\partial y}\left(\tfrac{\partial \alpha_s}{\partial y}(u_f - u_s)\right) + \left(\tfrac{\partial \alpha_s}{\partial x}(v_f - v_s)\right)\right) - \tfrac{\epsilon\alpha_s(u_f - u_s)}{\varepsilon^2\alpha_f N_{R_A} h^2}\Big]\Big\} \\ & -\tfrac{1}{\gamma}C_{DG}(u_f - u_s)\left|\vec{u}_f - \vec{u}_s\right|^{j-1} \end{aligned} \tag{7}$$

where α_s is the volume fraction of solid phases (-), α_f is the volume fraction of fluid phases (-). δ is the internal friction angle. P_b is the pressure at the surface (Kg/ms^2). b is the basal surface of the flow (m). N_R is the Reynolds number (-). N_{RA} is the quasi-Reynolds number (-). C_{DG} is the drag coefficient (-). ρ_f is the density of the fluid (kg/m^3), ρ_s is the density of the solids (kg/m^3), γ is the density ratio between the fluid and solid phase (-). χ is the vertical shearing of fluid velocity (m/s). ε is the aspect ratio of the model (-). ξ is the vertical distribution of α_s (m^{-1}).

We performed two kinds of simulations using the OpenLISEM model. First, we applied a model that does not include the interception model (OpenLISEM_A), and it is the same as Massflow and Flow-3D, which ignore the initiation process of debris flow. According to the field survey, the solid's density was set to 2700 kg/m^3. The friction angle (degrees) was in a range between 20 and ~35. The debris flow density was in a range between 1850 and 2030 kg/m^3. The value of manning was between 0.02 and 0.1. The porosity was set to 0.38. According to the research results [17], the cohesion was in a range between 0 and 2500 pa.

Second, we ran a model that includes the interception and slope failure models (OpenLISEM_B). It is used to analyze the influence of rainfall conditions on debris flow prediction. In OpenLISEM_B, the slope failure and debris flow runout would be triggered by rainfall. According to the field survey, the value of the initial moisture content of the

debris source is set to 0.114, and the rainfall was set to 18.6 mm/h. The debris flow density would change dynamically with rainfall.

A series of numerical simulations were performed to refine the parameter values by comparing the depth distribution of the debris fan. Parameters values for OpenLISEM_A and OpenLISEM_B are summarized in Table 2. Both models were run for 15 min of real-event duration, with a time step constrained to $\Delta t \leq 1$ s.

5. Results

5.1. Application to the Debris Flow Event in 2013

The debris fan's depth distribution was used to test the numerical parameters in four models. Table 3 shows the analysis of the dependence of the final deposition volume in the debris fan area on the various parameters. Figure 6 shows the four models' simulation results with different numerical parameters.

Table 3. Analysis of the final deposition volume dependence in the debris fan area on the various parameters. When a variable is analyzed, the other parameters are the same as those in Table 1. Vr means the simulated debris fan volume to measured debris fan volume.

		Massflow			**Flow-3D**	
ID	ξ	μ	Vr	ρ	θ	Vr
1	200	0.4	76%	1986	20	49%
2	200	0.439	85%	1986	32	67%
3	200	0.45	66%	1986	35	39%
4	100	0.439	57%	1850	32	32%
5	300	0.439	71%	2030	32	1%
	Common parameters			OpenLISEM_A		OpenLISEM_B
ID	D	c	θ	ρ	Vr	Vr
1	0.04	1250	24	1986	0.43	-
2	0.05	0	24	1986	0.68	-
3	0.05	1250	20	1986	0.7	0.59
4	0.05	1250	24	1850	0.52	-
5	0.05	1250	24	1986	0.73	0.53
6	0.05	1250	24	2030	0.65	-
7	0.05	1250	27	1986	0.65	-
8	0.05	1250	35	1986	0.52	0.49
9	0.05	2500	24	1986	0.59	-
10	0.06	1250	24	1986	0.5	-
11	0.04	1250	20	-	-	0.36
12	0.05	0	20	-	-	0.58
13	0.05	1250	17	-	-	0.56
14	0.05	2500	20	-	-	0.54

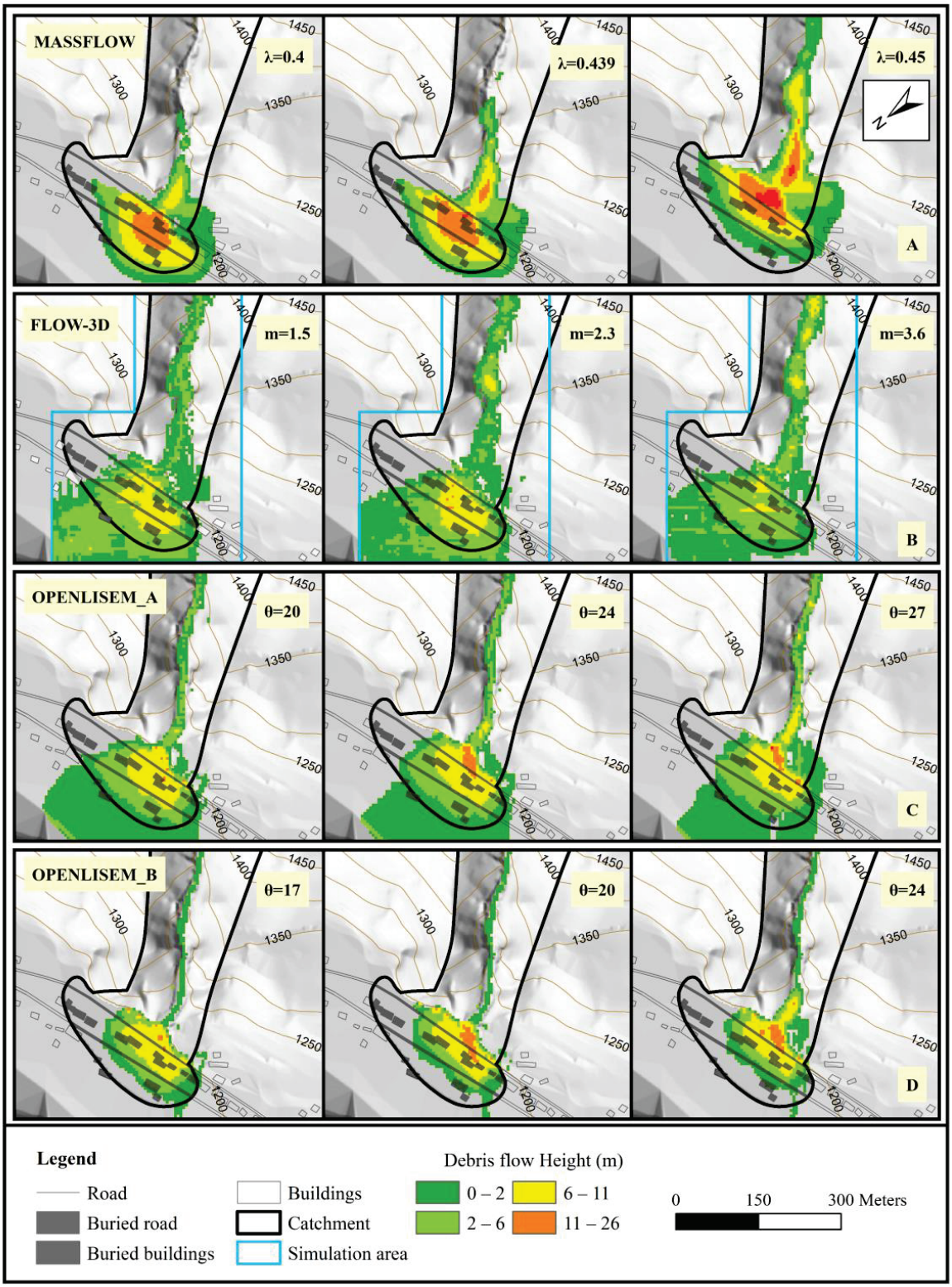

Figure 6. Wayao debris flow fan reproduced by four models. (**A**) Massflow simulations-sensitivity to the Coulomb-type friction μ = 0.4, μ = 0.439, and μ = 0.45. (**B**) Flow-3D simulations-sensitivity to multiplier in internal friction angle θ = 20, θ = 32, and θ = 35. (**C**) OpenLISEM_A simulations-sensitivity to internal friction angle θ = 20, θ = 24, and θ = 27. (**D**) OpenLISEM_B simulations-sensitivity to internal friction angle coefficient θ = 17, θ = 20, and θ = 24.

For the Massflow simulations, we found that the final debris fan volume is sensitive to the Coulomb-type friction (μ) and viscous resistance (ξ). Figure 6A shows the geometry of the debris fan with several different choices for the Coulomb-type friction (μ = 0.4, 0.439, and 0.45). The simulation results show that the extent of the debris fan tends to be smaller than that of the real debris fan. However, Massflow reproduces the thickness distribution of debris deposition. Only the western part of the actual debris fan is slightly overestimated, and the eastern part is slightly underestimated. The simulation result with μ = 0.439 is considered to best reproduce the debris flow deposition, and the volume of the simulated debris fan is 85% of the actual debris fan volume. However, this would lead to the selection of a very low friction angle, and this situation is the same as that found in Scaringi et al. [53].

For the Flow-3D model, we found that the debris fan volume is more sensitive to the debris density and the friction angle. When the value of debris flow density is 2030 kg/m^3, most of the debris flow deposits in the channel. When the value of debris flow density is 1850 kg/ m^3, most of the debris flow runs out of the catchment at an abnormal velocity. The friction angle (θ) is another key parameter to the deposition and entrainment of the debris flow. A larger friction angle will cause the debris flow to deposit quickly, while a smaller friction angle will cause the solid particles to be more easily transported. Different simulations were performed to understand the friction angle (θ) influence on the debris flow process. We found that the multiplier in the friction angle significantly impacts the deposition rate of debris flow. The simulation result with θ = 32 is considered to best reproduce the debris flow deposition, and the volume of the simulated debris fan is 67% of the actual debris fan volume. However, the deposition thicknesses in the middle and east of the debris fan are underestimated.

For OpenLISEM_A, we found that debris fan volume is more sensitive to debris flow density, manning, and friction angle (θ), while less sensitive to cohesion. When the value of the friction angle was 20 degrees, most of the debris flow ran out of the catchment at an abnormal velocity. When the value of the friction angle is larger than 30 degrees, the velocity of debris flow will decrease significantly as the internal friction angle increase. The simulation results show that the extent of the debris fan tends to be larger than that of the real debris fan, and the deposit thickness in the east of the debris fan is underestimated (Figure 6C). The simulation with θ = 24 is considered to best reproduce the debris flow deposition, and the volume of the simulated debris fan is 73% of the actual debris fan volume.

For OpenLISEM_B, we found that debris fan volume is more sensitive to manning and the friction angle (θ) while less sensitive to cohesion. The influence on the debris flow behavior of the friction angle was similar to that in OpenLISEM_A. However, the simulation result with θ = 20 is considered to reproduce the debris flow deposition best, and the value is smaller than that of OpenLISEM_A. The failure volume of the slope is determined based on the infinite slope method. The failure part may slide into the channel and participate in the debris flow. Figure 6D shows that the extent of the debris fan tends to be smaller than the real extent, and the thickness distribution of debris deposition is also underestimated. The simulation with θ = 20 is considered to best reproduce the debris flow deposition, and the volume of the simulated debris fan is 59% of the actual debris fan volume. The extent and volume of the debris fan in OpenLISEM_B is smaller than that in OpenLISEM_A. It is speculated that part of the debris source was transported out of the debris fan extent by the channel flood under the rainfall condition.

The four models can reproduce the geometry and thickness distribution of the debris flow fan (Figure 7). The schematic diagram of verification results is shown in Figure 8, and the accuracy [9] of the four models is shown in Table 4. The Massflow and OpenLISEM_A models seem to reproduce the actual deposit area and volume more accurately than other models. The positive accuracy area of Massflow and OpenLISEM_A was higher than 70%, and the positive accuracy volume of Massflow (86%) was the best of all. The positive accuracy area and volume of Flow-3D were lower than 70%. Flow-3D shows a runout spread of debris flow larger than that in the actual event, and the negative accuracy area of

Flow-3D was 73%. OpenLISEM_B shows a runout spread of debris flows smaller than that in the actual event. The positive accuracy area and volume of OpenLISEM_B were lower than 60%, but the negative accuracy area was the smallest. All models underestimate the eastern part of the debris fan, which was discussed in Section 6.

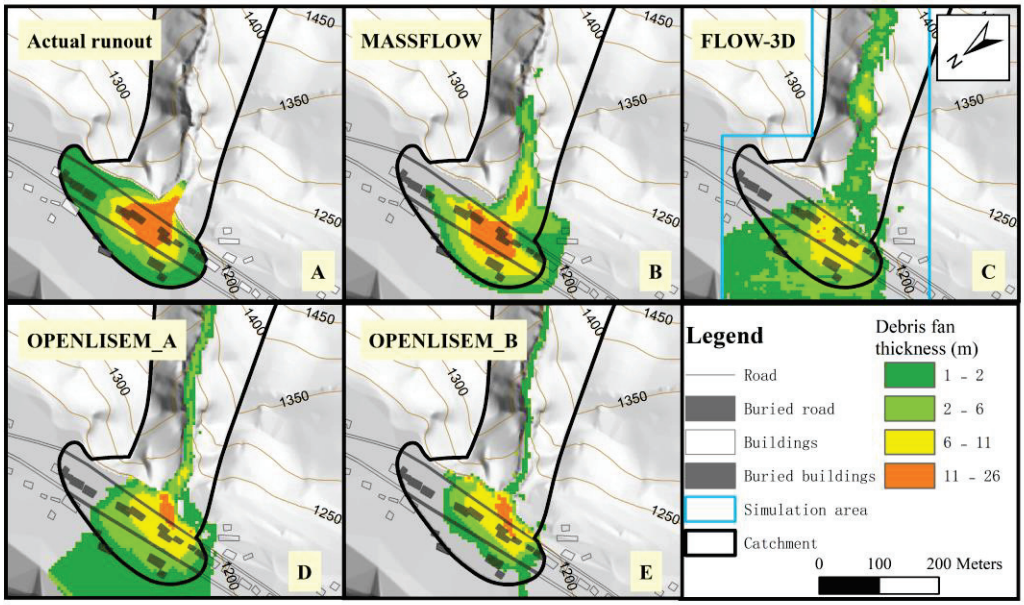

Figure 7. Debris flow fan in 2013: Actual runout (**A**) and best simulations by Massflow (**B**), Flow-3D (**C**), OpenLISEM_A (**D**), OpenLISEM_B (**E**). The full sets of model parameters are given in Table 1.

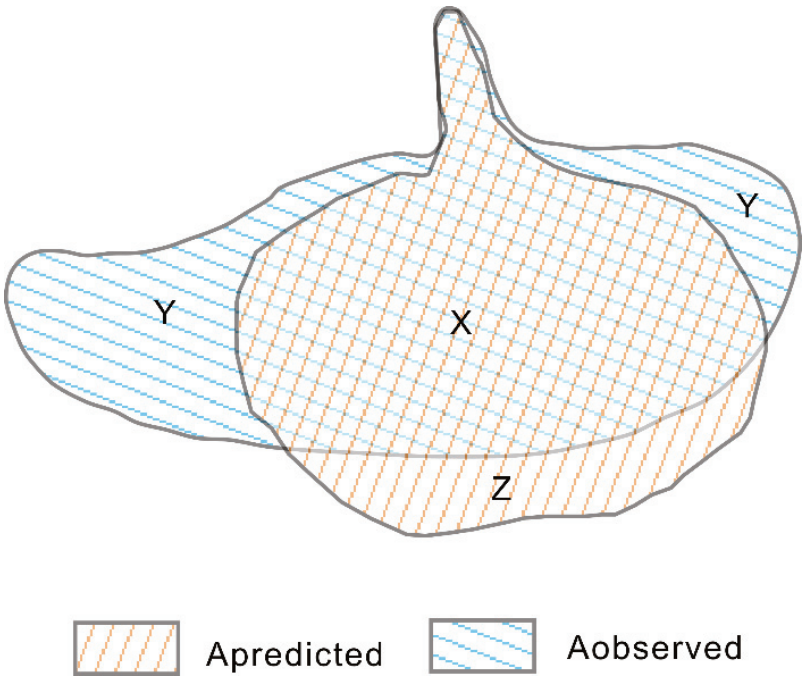

Figure 8. Schematic diagram of verification results of debris flow events. A predicted area was measured, and the observed area was from the simulation result. X is the positive accuracy area, Y represents the missing accuracy area, Z is negative.

Table 4. Comparison of the simulation accuracy of four models. Ap means the positive accuracy area. An means the negative accuracy area. Am means the missing accuracy area. Vp means the positive accuracy volume. Mean depth means the mean depth of the debris fan.

Models	Area ($\times 10^4$ m^2)						Volume ($\times 10^5$ m^3)		Mean Depth (m)	
	Ap	%	An	%	Am	%	Vp	%	H	%
Actual	2.9	100%	0	0%	0	0%	1.4	100%	4.8	100%
Massflow	2.1	71%	1.0	33%	0.9	29%	1.2	86%	7.3	152%
Flow-3D	2.0	69%	2.1	73%	0.9	31%	0.9	67%	4.7	97%
OpenLISEM_A	2.2	75%	2.7	94%	0.7	25%	1.0	73%	4.7	97%
OpenLISEM_B	1.6	55%	0.04	1%	1.3	45%	0.8	58%	5.1	106%

The thickness of the debris fan in the best-fit simulations of various models was compared (Figure 9). Massflow and Flow-3D present the same thickness distribution in section a-a′. The thickness values of Massflow are closer to the actual values than Flow-3D. Those values are approximately 5 m larger than that of Flow-3D. OpenLISEM_A and OpenLISEM_B present almost the same thickness distribution in two sections as they use the same debris flow equations. The depth distribution of Massflow in section b-b′ is closer to the actual depth distribution than the other three models. Massflow presents the same thickness distribution shape as reality, and only the peak value is shifted. Flow-3D, OpenLISEM_A, and OpenLISEM_B have similar thickness distributions of debris fan, and they all underestimate the thickness distribution at 100–250 m (Figure 9C).

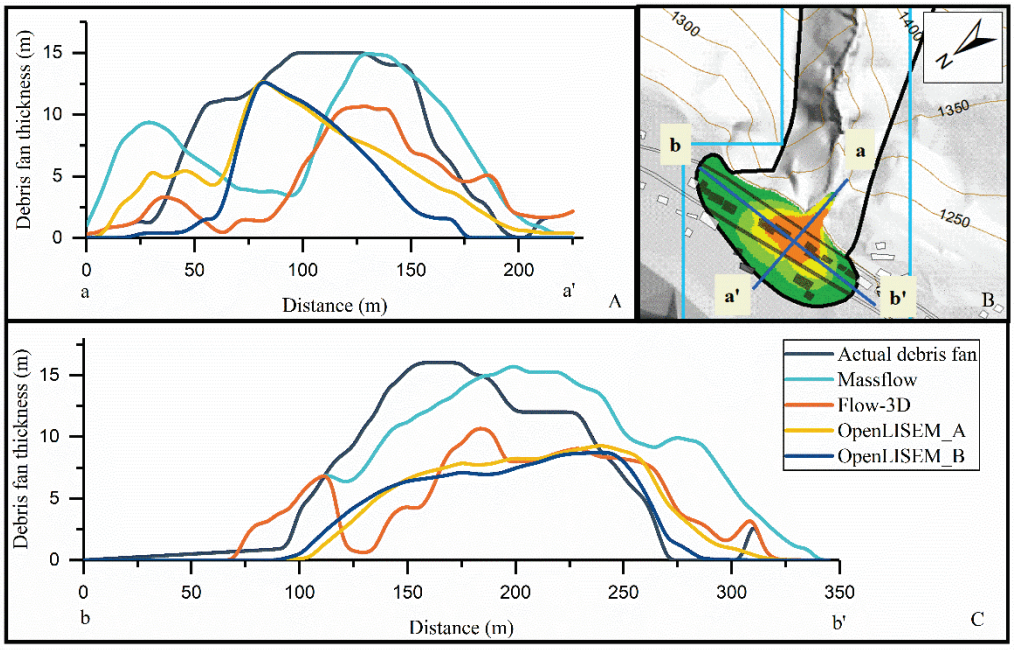

Figure 9. Comparison of debris fan thickness in 2013 (along two representative cross-sections). Including the actual debris fan and the debris fan of best-fit simulations by Massflow, Flow-3D, OpenLISEM_A, and OpenLISEM_B. (**A**) shows the debris fan thickness along the cross-section a-a′, and (**C**) shows the debris fan thickness along the cross-section b-b′. The locations of a-a′ and b-b′ are shown in (**B**).

The depth distribution of the debris flow at four representative moments after the initiation of the debris flow was compared (Figure 10). Despite the different modeling methods, the depth distributions resulting from the Massflow and Flow-3D simulations are very similar in terms of runouts versus time and the spatial distribution of depth at

each moment. Due to the different resistance terms of debris flows in the models, the flow velocities of debris flow in Massflow and Flow-3D simulations are significantly higher than OpenLISEM_A and OpenLISEM_B. Compared with OpenLISEM_B, OpenLISEM_A does not include the hydrological model, so the processes of rainfall infiltration and slope failure were omitted. Therefore, the time for the debris flow to reach the catchment mouth in OpenLISEM_A is less than that in OpenLISEM_B (Figure 10C,D).

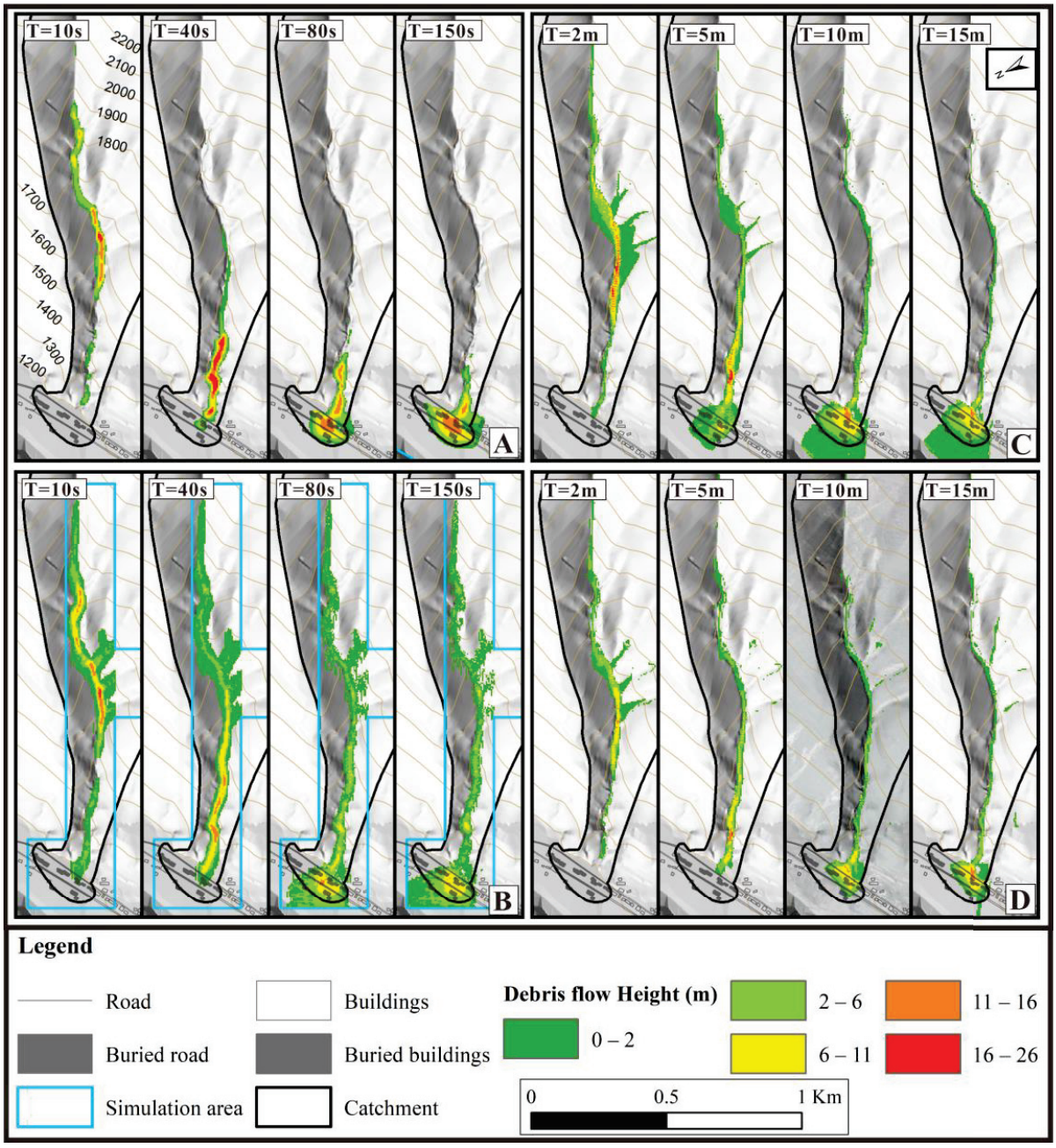

Figure 10. Snapshots of the debris flow height of Wayao debris flow in 2013 simulated by Massflow (**A**), Flow-3D (**B**), OpenLISEM_A (**C**), and OpenLISEM_B (**D**). Abbreviations: s means seconds, and m means minutes.

5.2. Prediction to the Debris Flow Event in 2020

To evaluate the prediction ability of the four models for possible debris flows, we use the simulation results of the Wayao debris flow event in 2020. The sets of parameters for prediction were the same as those for the Wayao debris flow in 2013 simulations. The

depth distribution of the debris flow in 2020 was created as the input file. The rainfall value was 18.8 mm/h in 2020. The depth distribution verified the prediction ability of different models.

The simulation results of the four models are shown in Figure 11 to compare the runout areas of different models. According to the UAV survey, the debris flow filled the check dam in 2020, and the max depth value of the deposition was 7.6 m. Most of the debris flow ran into the Min River, and only a few were deposited along the channel.

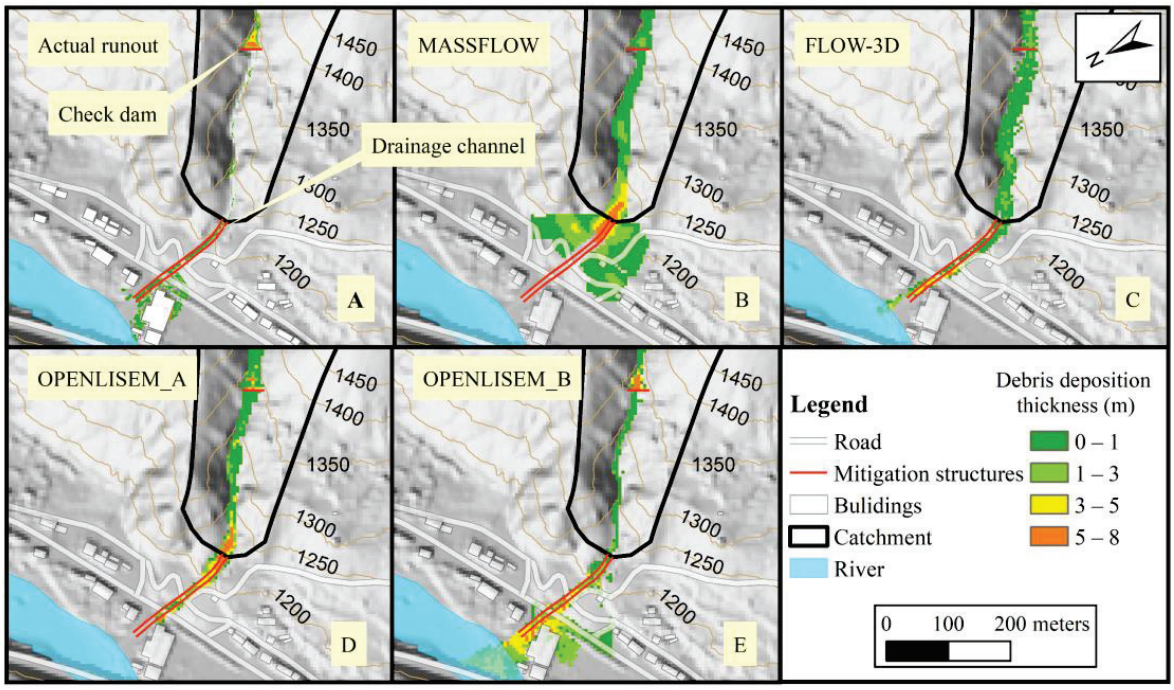

Figure 11. Debris flow runout in 2020: actual runout (**A**) and simulations by Massflow (**B**), Flow-3D (**C**), OpenLISEM_A (**D**), OpenLISEM_B (**E**).

For Massflow, the simulation result shows that the runout extent of the debris flow was more significant than the real in 2020. Some of the debris flow was deposited after the check dam, and the max depth of the deposition was 1.9 m. Most of the debris flow deposits at the junction of the catchment channel and the drainage channel, and the max deposition depth was 8.3 m.

For Flow-3D, the simulation result shows that most of the debris flow ran into the Min River which is consistent with reality. The deposition depth in the drainage channel was slightly overestimated, and the value range was between 0.2 and 4.3 m. The deposition depth after the check dam was underestimated, and the max value of depth was 2.2 m.

For OpenLISEM_A, the simulation result shows debris flow transported along the drainage channel. However, most of the debris flow was deposited at the junction of the catchment channel and the drainage channel, and the max depth of deposition was 5.6 m. The deposition depth after the check dam was underestimated, and the max value of depth was 3.6 m.

Among all the models, OpenLISEM_B yields the result most consistent with the actual situation. The simulation and the actual error are approximately 25% at the deposition depth and volume behind the dam. Most debris flows ran into the Min River along the drainage channel. A small part of the debris flow was deposited in the drainage channel, and the depth was approximately 0.5–1.1 m.

Figure 12 shows the comparison of the depth distribution of the debris flow at four representative moments after the initiation of the debris flow. The simulation results of Massflow and Flow-3D show that the time when debris flow reaches the mouth of the

catchment is approximately 3 min. The time for OpenLISEM_A and OpenLISEM_B is approximately 20~30 min. For Massflow and OpenLISEM_A, the debris flow deposited along the channel in the simulation results. For Flow-3D and OpenLISEM_B, most of the debris flow ran into the Min River in the simulation result. The comparison between OpenLISEM_A and OpenLISEM_B indicates that when the debris flow arrives at the channel with a gentle slope, the channel flow formed by rainfall could provide momentum for the debris flow. If the debris flow model does not include the hydrological model, the debris flow would rapidly deposit along the channel with a gentle slope.

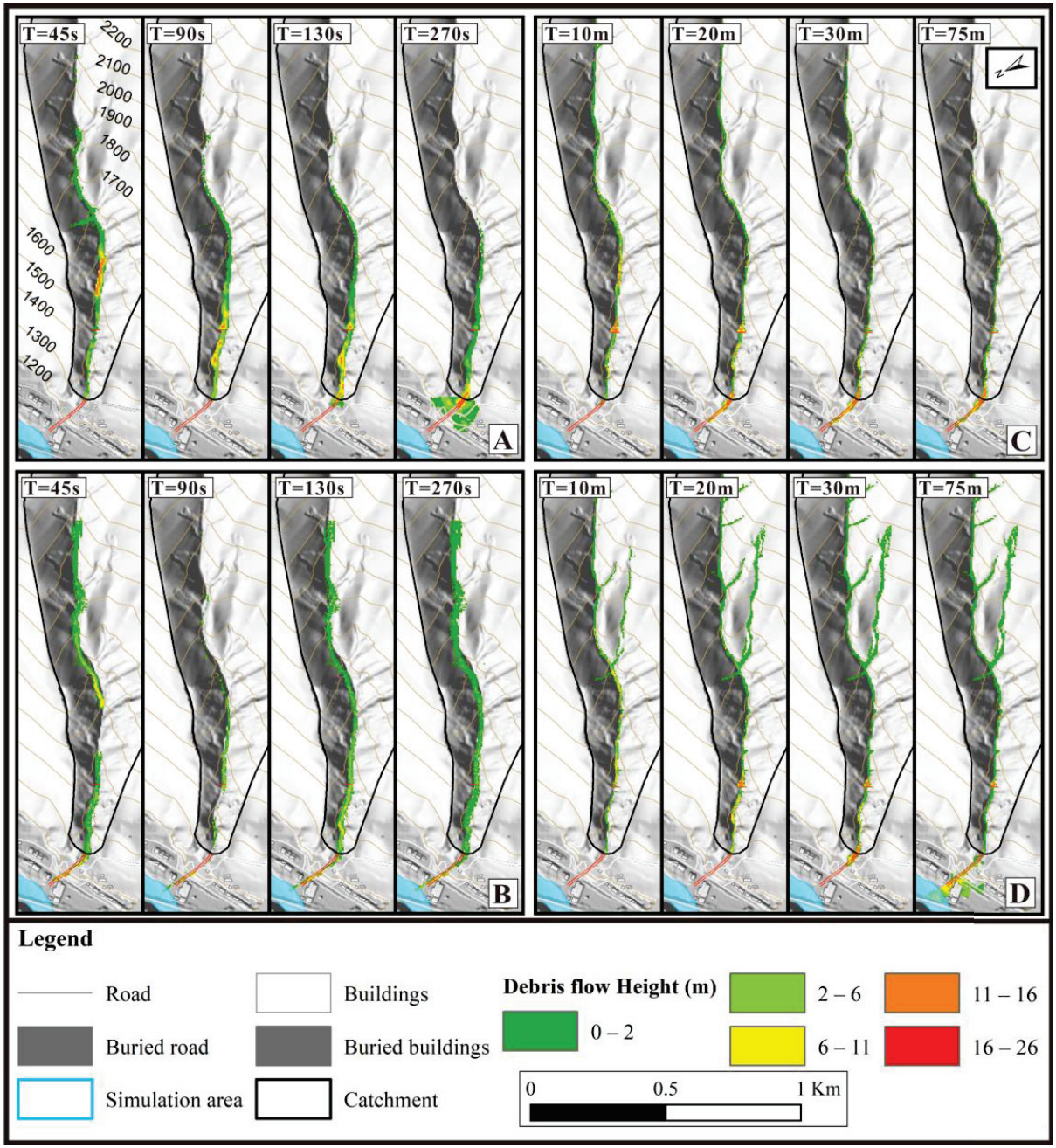

Figure 12. Snapshots of the debris flow height of Wayao debris flow in 2020 simulated by Massflow (**A**), Flow-3D (**B**), OpenLISEM_A (**C**), and OpenLISEM_B (**D**). Abbreviations: s means seconds, and m means minutes.

5.3. Scenario without Mitigation Structures

We evaluated the impacts of mitigation structures on the uncertainty of predication with the depth distribution of debris flow deposition. The four models were used to predict without mitigation structures. The simulation parameters were the same as those in Section 5.2, and the mitigation structures were taken out from the models. Figure 13 shows the prediction results of the four models. The simulation results show that the debris flow ran out of the catchment. However, the depth distributions of the debris flow deposition were different.

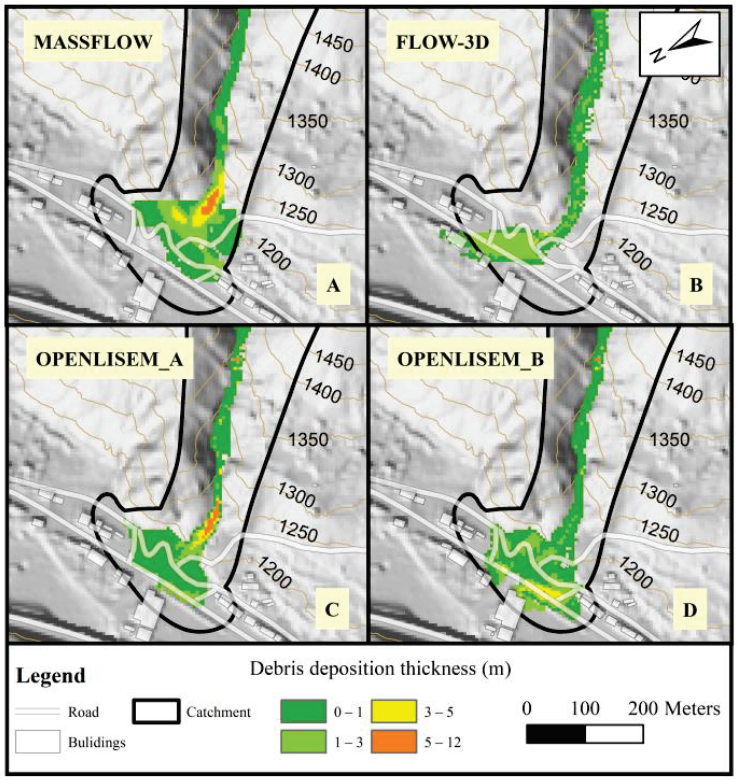

Figure 13. The prediction results without mitigation structures. Simulations for Massflow (**A**), Flow-3D (**B**), OpenLISEM_A (**C**), and OpenLISEM_B (**D**).

For Massflow and OpenLISEM_A, most of the debris flow was deposited at the mouth of the catchment, and the main deposit area was along the channel. This result indicates that the structures had limited effort on the deposition progress of debris flow in Figure 12.

For Flow-3D, OpenLISEM_A, and OpenLISEM_B, the simulation results show that the extent of runout areas was more significant than that in Figure 12. The debris flow buried part of the road and several houses. The simulation result for Flow-3D shows that the main threat area was located east of the catchment mouth. The debris flow buried five houses and part of the roads. However, the west area of the catchment mouth was safe. This result indicates that the mitigation structures played an essential role in reducing the danger of the debris flow event in 2020.

The results of debris-flow risk assessment have important guiding significance for land planning and the construction of prevention and control projects in mountainous areas. When selecting debris-flow risk assessment models, each model's advantages and disadvantages should be thoroughly evaluated. A simulation model suitable for the study area should be selected. Alternatively, a multi-model combination method should be adopted.

6. Discussion

Table 2 shows that the value of friction angle in the different models is significantly different. The models assume that the parameters of debris flow are constant. However, they are not evenly distributed in all catchments, such as particle size and internal friction Angle. The parameters values obtained by the field survey are in a range. The parameter values in Table 2 are optimal simulation values, and they were obtained by parameter correction.

Figure 8 shows that all models underestimated the eastern part of the debris fan in 2013. According to reports from villagers who witnessed the debris flow, the Wayao debris flow ran out several times on 10 July 2013. Moreover, we infer that numerous debris flows formed the deposits in the eastern part of the debris fan. The phenomenon is related to rainfall scenarios, random rainfall-triggered landslides [54], natural debris dams in the channel, and natural dam failure [55].

The hydrological condition is one of the critical parameters in debris-flow simulation. There is interaction or feedback between the hydrology and a debris flow. When this interaction is not considered in the model, the model's predictive power is limited [37]. As we can see in Section 5.2, the debris flows in the simulation results for OpenLISEM_A stopped at the drainage channel. However, most of the debris flow in the simulation result for OpenLISEM_B ran into the Min River. According to Equations (4)–(7), for OpenLISEM_A, the initial volume fraction for solid and fluid phases is constant. However, for OpenLISEM_B, the two values change dynamically with rainfall, and this is an important reason why the prediction result of OpenLISEM_B is better than that of OpenLISEM_A.

In the Massflow prediction results, the runout distance of debris flow was underestimated. According to the dependence analysis, the value of the Coulomb-type friction is proportional to the runout distance of debris flow. In Equation (1), the value of the Coulomb-type friction is proportional to the basal friction stress. Therefore, we believe that the value of the Coulomb-type friction was underestimated in the debris flow simulation in 2020.

The quantity and accuracy of rainfall data affect the simulation results, as OpenLISEM_B is sensitive to rainfall. In mountainous areas, precipitation may vary significantly in space [56,57]. The uncertainty error between the measured and actual rainfall values is a limitation of this manuscript, although we have obtained acceptable measured results by parameter calibration.

In some cases, parameter calibration can obtain satisfactory results, such as the simulation results in Section 5.1. However, the simulation accuracy may be significantly reduced when these parameters are applied to debris flow prediction. None of the models used in this work can be considered superior to the others. Discrimination among models should also evaluate the actual usability of the model and its results. For example, a model should be assessed in terms of the ease of use, the quantitative and physical significance of the parameter assessment or calibration, the possibility of incorporating the model into early warning systems [58,59], and finally, the calculation time. In the case of incorporating the model into a real-time risk assessment system, the last factor may be decisive since the inputs to the model may change over time, and the new solutions must be recalculated in time to alert. On the other hand, in the situations that the imminent failure is not expected or detailed risk assessment in land use is required, priority should be given to the accuracy of debris flow prediction. It needs to combine more field surveys and experiments to obtain physical parameters, and reproduce the complex debris flow process.

If the computation time is considered unique (Table 5), not including the modeling time, Massflow can simulate the entire debris flow process in less than 5 min. A desktop computer (CPU, AMD 2700X, 16 cores, 3.7 GHz; RAM, 16 G) was used, and the resolution terrain grid was 5-m. When the same simulation is performed on a 10-m resolution grid, Flow-3D takes 14 min. At the same time, the calculation on a 5-m grid takes approximately 2 h. Of course, the performance of Flow-3D models can be significantly improved by using multicore/parallel solvers to run the code on a powerful workstation [25]. OpenLISEM_A takes approximately half an hour on the same machine, but with a less precise (10 m)

grid, the time is cut in half. However, the simulation time of OpenLISEM_B with the hydrological model is much longer. The time for 10 m resolution exceeds one hour, while the 5 m resolution requires more than two hours.

Table 5. With different mesh resolutions, the computational times required to simulate the debris flow event in 2013.

Model	Topographic Mesh Resolution	Time for Computation
Massflow	5 m	~4 min
	10 m	~2 min
Flow-3D	5 m	~2 h
	10 m	~14 min
OpenLISEM_A	5 m	~28 min
	10 m	~16 min
OpenLISEM_B	5 m	~2.5 h
	10 m	~1.3 h

The topographic mesh resolution affects the time for computation and the simulation result. So, the appropriate resolution requires consideration of both computational efficiency and debris flow progresses [60]. For Massflow and Flow-3D, the simulation results on the 5-m grid and the 10-m grid were similar. However, for OpenLISEM_A and OpenLISEM_B, the grid size significantly influenced the debris flow height and velocity and this is the consistent result of Bout and Jetten [52]'s sensitivity test on terrain resolution.

The advantages of Massflow are its simple parameter requirements and high computational efficiency, and the data can be directly exported through a geographical information system (GIS). When the accuracy of the debris flow deposition range is not high, preliminary hazard prediction can be made by Massflow. OpenLISEM requires more parameters than the other two models, but GIS can also integrate input parameters. Flow-3D has the most parameters, and its terrain model needs to utilize professional modeling software, so there may be some difficulties in operation. However, a three-dimensional description of the structure of prevention measures can be realized, which is a significant advantage in evaluating debris flow prevention projects for the future.

A common shortcoming of the simple-phase models used is that the initial spatial distribution of the simplified variables (e.g., porosity, saturation, and cohesion in the soil) cannot be easily considered. For example, the particle size distribution and the angle of internal friction in the debris source are single values for the entire catchment (Table 1). Similarly, in two-phase models, the input of a material parameter is its spatial distribution. This input has important implications for hazard assessment using numerical methods and developing early warning systems to mitigate risks.

Finally, it is worth re-emphasizing predictions of future events.

1. Different models have different predictive capabilities, and this may be due to the different sensitivity to debris flow densities or considering the interactions between the hydrology and the debris flow. Therefore, it should be considered when evaluating model predictive reliability.
2. Adopting multiple methods in hazard assessment and early warning systems may achieve ideal results. For example, a model with higher computational efficiency is used for preliminary prediction. Moreover, a model with higher accuracy is used for detailed prediction.
3. It is unclear whether a model is always the best performance model for prediction. Therefore, combining various models to form a multi-model real-time risk assessment and early warning system requires further research.

7. Conclusions

In this work, two single-phase models (Massflow and Flow-3D) and two-phase flow models (OpenLISEM_A and OpenLISEM_B) were applied to reproduce the main movement and deposition characteristics of the Wayao debris flow event in 2013. Moreover, the four models were applied to predict the Wayao debris flow event in 2020, and the parameters are the same as those in 2013. The depth distribution of debris flow was used to analyze prediction accuracy. Some conclusions can be drawn:

1. All four models provided satisfactory results for the geometry and depth distribution of the debris fan in 2013.
2. Combining the simulation results in the scenario without mitigation structures indicates that the mitigation structures played an essential role in reducing the danger of the debris flow event in 2020.
3. Considering the prediction of the debris flow event in 2020, including the deposition depth of debris behind the check dam and the runout extent of the debris flow, OpenLISEM_B has the best performance among the four models. However, they are different for both the adopted theoretical rheological model and the numerical scheme. So, it is not easy to understand the different behavior.
4. OpenLISEM_B (the model with an entire hydrological catchment) has the advantage of higher prediction accuracy of debris flow deposition depth than OpenLISEM_A (the model without considering). Since the cases in this paper were triggered by runoff, the comparison can only stand for debris flows triggered by runoff.

While each model has its limitations, the simulation of possible future debris flows using back analysis of debris flow parameters based on existing debris flow events and field investigation of potential debris sources can be a helpful tool for local risk assessment. The ability to recalculate new solutions in a short time is necessary for a real-time early-warning system. The accuracy of model prediction under different rainfall scenarios is critical in hazard assessments of significant projects. Therefore, in different application scenarios, such as debris flow risk assessment or early warning systems, comprehensively consider the accuracy of the model prediction, the difficulty of parameter acquisition, and the computational time.

Author Contributions: Conceptualization, X.Z. and C.T. (Chenxiao Tang); Validation, C.T. (Chenxiao Tang); Formal Analysis, X.Z.; Investigation, X.Z., Y.Y., J.X. and M.C.; Resources, C.T. (Chenxiao Tang) and C.T. (Chuan Tang); Data Curation, X.Z. and N.L.; Writing—Original Draft Preparation, X.Z.; Writing—Review & Editing, C.T. (Chenxiao Tang) and C.T. (Chuan Tang). All authors have read and agreed to the published version of the manuscript.

Funding: This research was funded by the National Key Research and Development Program of China, grant number 2017YFC1501004 and the Special Research Assistant Foundation of the Chinese Academy of Sciences, grant number 292020000076.

Institutional Review Board Statement: Not applicable.

Informed Consent Statement: Not applicable.

Data Availability Statement: Not applicable.

Acknowledgments: This work was supported by the National Key Research and Development Program of China (grant number 2017YFC1501004) and the Special Research Assistant Foundation of Chinese Academy of Sciences (292020000076). The authors thank the anonymous reviewers for their helpful suggestions for improving the paper.

Conflicts of Interest: The authors declare no conflict of interest. The funders had no role in the design of the study; in the collection, analyses, or interpretation of data; in the writing of the manuscript, or in the decision to publish the results.

References

1. Hungr, O.; Morgan, G.C.; Kellerhals, R. Quantitative analysis of debris torrent hazards for design of remedial measures. *Int. J. Rock Mech. Min. Sci. Geomech. Abstr.* **1985**, *22*, 129. [CrossRef]
2. Glade, T.; Crozier, M.J. A Review of Scale Dependency in Landslide Hazard and Risk Analysis. In *Landslide Hazard and Risk*; John Wiley & Sons: Hoboken, NJ, USA, 2012.
3. Hürlimann, M.; Copons, R.; Altimir, J. Detailed debris flow hazard assessment in Andorra: A multidisciplinary approach. *Geomorphology* **2006**, *78*, 359–372. [CrossRef]
4. Prochaska, A.B.; Santi, P.M.; Higgins, J.D.; Cannon, S.H. Debris-flow runout predictions based on the average channel slope (ACS). *Eng. Geol.* **2008**, *98*, 29–40. [CrossRef]
5. Tang, C.; Zhu, J.; Chang, M.; Ding, J.; Qi, X. An empirical–statistical model for predicting debris-flow runout zones in the Wenchuan earthquake area. *Quat. Int.* **2012**, *250*, 63–73. [CrossRef]
6. Zhou, W.; Fang, J.; Tang, C.; Yang, G. Empirical relationships for the estimation of debris flow runout distances on depositional fans in the Wenchuan earthquake zone. *J. Hydrol.* **2019**, *577*, 123932. [CrossRef]
7. Simoni, A.; Mammoliti, M.; Berti, M. Uncertainty of debris flow mobility relationships and its influence on the prediction of inundated areas. *Geomorphology* **2011**, *132*, 249–259. [CrossRef]
8. Scheidl, C.; Rickenmann, D. Empirical prediction of debris-flow mobility and deposition on fans. *Earth Surf. Process. Landf.* **2010**, *35*, 157–173. [CrossRef]
9. Chang, M.; Tang, C.; Van Asch, T.W.J.; Cai, F. Hazard assessment of debris flows in the Wenchuan earthquake-stricken area, South West China. *Landslides* **2017**, *14*, 1783–1792. [CrossRef]
10. Johnson, A.M.; Rahn, P.H. Mobilization of debris flows. *Z. Geomorphol.* **1970**, *9*, 168–186.
11. Hungr, O. A model for the runout analysis of rapid flow slides, debris flows, and avalanches. *Can. Geotech. J.* **1995**, *32*, 610–623. [CrossRef]
12. Voellmy, A. Uber die Zerstorungskraft von Lawinen. *Schweiz. Bauztg. Jahrg.* **1955**, *73*, 212–285.
13. Bagnold, R.A. *The Physics of Blown Sand and Desert Dunes*; Dover Earth Science Series; Dover Publications: Mineola, NY, USA, 1941.
14. Bagnold, R.A. Experiments on a gravity-free dispersion of large solid spheres in a Newtonian fluid under shear. *Proc. R. Soc. Lond. Ser. A Math. Phys. Sci.* **1954**, *225*, 49–63. [CrossRef]
15. O'Brien, J.S.; Julien, P.Y.; Fullerton, W.T. Two-Dimensional Water Flood and Mudflow Simulation. *J. Hydraul. Eng.* **1993**, *119*, 244–261. [CrossRef]
16. Beguería, S.; Asch, T.W.J.V.; Malet, J.-P.; Gröndahl, S. A GIS-based numerical model for simulating the kinematics of mud and debris flows over complex terrain. *Nat. Hazards Earth Syst. Sci.* **2009**, *9*, 1897–1909. [CrossRef]
17. Ouyang, C.; He, S.; Tang, C. Numerical analysis of dynamics of debris flow over erodible beds in Wenchuan earthquake-induced area. *Eng. Geol.* **2015**, *194*, 62–72. [CrossRef]
18. Takahashi, T. Mechanical Characteristics of Debris Flow. *J. Hydraul. Div.* **1978**, *104*, 1153–1169. [CrossRef]
19. Savage, S.B.; Hutter, K. The motion of a finite mass of granular material down a rough incline. *J. Fluid Mech.* **1989**, *199*, 177–215. [CrossRef]
20. Johnson, P.C.; Jackson, R. Frictional-colhsional constitutive relations for granular materials with application to plane shearing. *J. Fluid Mech.* **1987**, *176*, 67–93. [CrossRef]
21. Lun, C.K.K.; Savage, S.B.; Jeffrey, D.J.; Chepurniy, N. Kinetic theories for granular flow: Inelastic particles in Couette flow and slightly inelastic particles in a general flow field. *J. Fluid Mech.* **1984**, *140*, 223–256. [CrossRef]
22. Savage, S.B.; Jeffrey, D.J. The stress tensor in a granular flow at high shear rates. *Fluid Mech.* **1981**, *110*, 255–272. [CrossRef]
23. Armanini, A.; Fraccarollo, L.; Rosatti, G. Two-dimensional simulation of debris flows in erodible channels. *Comput. Geosci.* **2009**, *35*, 993–1006. [CrossRef]
24. Mih, W.C. High concentration granular shear flow. *J. Hydraul. Res.* **2010**, *37*, 229–248. [CrossRef]
25. FLOW-3D. *FLOW-3D® Version 12.0 Users Manual*; Flow Science Inc.: Santa Fe, NM, USA, 2016.
26. Wang, J. Research on the Debris Flow Buried Risk Based on Dynamic Processes. Ph.D. Thesis, Chinese Academy of Sciences, Beijing, China, 2015.
27. Xu, P.; Yuan, Z.; Li, G.; Li, G.; Du, W.; Wang, Y. Prediction on the Hazardous Extent of the Secondary Debris Flow Induced by Volcanic Disaster of Changbai Moutains. *Jilin Univ. Earth Sci. Ed.* **2015**, *45*, 1155–1163. [CrossRef]
28. Iverson, R.M.; Logan, M.; LaHusen, R.G.; Berti, M. The perfect debris flow? Aggregated results from 28 large-scale experiments. *J. Geophys. Res.* **2010**, *115*, F03005. [CrossRef]
29. Iverson, R.M. The physics of debris flows. *Rev. Geophys.* **1997**, *35*, 245–296. [CrossRef]
30. Iverson, R.M.; Denlinger, R.P. Flow of variably fluidized granular masses across three-dimensional terrain: 1. Coulomb mixture theory. *J. Geophys. Res. Solid Earth* **2001**, *106*, 537–552. [CrossRef]
31. Pitman, E.B.; Le, L. A two-fluid model for avalanche and debris flows. *Philos. Trans. R. Soc. A Math. Phys. Eng. Sci.* **2005**, *363*, 1573–1601. [CrossRef]
32. Ni Jinren, W.G. Conceptual two-phase flowmodel of debris flow: I. Theory. *Acta Geogr. Sin.* **1998**, *53*, 67–77.
33. Pudasaini, S.P. A general two-phase debris flow model. *J. Geophys. Res. Earth Surf.* **2012**, *117*, F03010. [CrossRef]
34. Greco, M.; Di Cristo, C.; Iervolino, M.; Vacca, A. Numerical simulation of mud-flows impacting structures. *J. Mt. Sci.* **2019**, *16*, 364–382. [CrossRef]

35. Li, J.; Cao, Z.; Hu, K.; Pender, G.; Liu, Q. A depth-averaged two-phase model for debris flows over fixed beds. *Int. J. Sediment Res.* **2018**, *33*, 462–477. [CrossRef]
36. Chen, H.X.; Zhang, L.M. EDDA 1.0: Integrated simulation of debris flow erosion, deposition and property changes. *Geosci. Model Dev.* **2015**, *8*, 829–844. [CrossRef]
37. Bout, B.; Lombardo, L.; van Westen, C.J.; Jetten, V.G. Integration of two-phase solid fluid equations in a catchment model for flashfloods, debris flows and shallow slope failures. *Environ. Model. Softw.* **2018**, *105*, 1–16. [CrossRef]
38. Zhou, R.; Li, Y.; Alexander, L.D.; Michael, A.E.; Yulin, H.; Wwang, F.; Li, X. Active tectonics of the eastern margin of the tibet plateau. *J. Mineral. Petrol.* **2006**, *26*, 40–51.
39. Xiao, X.; Wang, J. A Brief Review of Tectonic Evolution and Uplift of the Qinghai-Tibet Plateau. *Geol. Rev.* **1998**, *44*, 372–381.
40. Li, Z.; Liu, S.; Chen, H.; Liu, S.; Guo, B.; Tian, X. Late quaternary slip rate in the central part of the longmenshan fault zone from terrace deformation along the Minjiang river. *J. Chengdu Univ. Technol. Sci. Technol. Ed.* **2008**, *35*, 440–454.
41. Jiang, W.; Xie, X. The Surface Rupture Zone and the Back Range Faults at the Longmen Mountain Fault Zone. *Recent Dev. World Seismol.* **2009**, *4*, 4. [CrossRef]
42. Yan, Y.; Yonggang, G.; Jianqiang, Z.; Chao, Z. Research on the Debris Flow Hazards in Cutou Gully, Wenchuan County on July 10, 2013. *J. Catastrophol.* **2013**, *29*, 229–234.
43. Chen, M.; Tang, C.; Gan, W.; Cai, Y.H. Characteristics and dynamical process of debris flow at urgent steep gully in the earthquake areas——illustrated with case of Wayao gully in Wenchuan. *J. Yunnan Univ. Nat. Sci. Ed.* **2018**, *40*, 272–278.
44. Harp, E.L.; Keefer, D.K.; Sato, H.P.; Yagi, H. Landslide inventories: The essential part of seismic landslide hazard analyses. *Eng. Geol.* **2011**, *122*, 9–21. [CrossRef]
45. Dietrich, A.; Krautblatter, M. Evidence for enhanced debris-flow activity in the Northern Calcareous Alps since the 1980s (Plansee, Austria). *Geomorphology* **2017**, *287*, 144–158. [CrossRef]
46. Perrone, A.; Lapenna, V.; Piscitelli, S. Electrical resistivity tomography technique for landslide investigation: A review. *Earth-Sci. Rev.* **2014**, *135*, 65–82. [CrossRef]
47. Oliver, M.A.; Webster, R. Kriging: A method of interpolation for geographical information systems. *Int. J. Geogr. Inf. Syst.* **1990**, *4*, 313–332. [CrossRef]
48. Horton, A.J.; Hales, T.C.; Ouyang, C.; Fan, X. Identifying post-earthquake debris flow hazard using Massflow. *Eng. Geol.* **2019**, *258*, 105134. [CrossRef]
49. Ouyang, C.; He, S.; Xu, Q. MacCormack-TVD Finite Difference Solution for Dam Break Hydraulics over Erodible Sediment Beds. *J. Hydraul. Eng.* **2015**, *141*, 06014026. [CrossRef]
50. Ouyang, C.; Wang, Z.; An, H.; Liu, X.; Wang, D. An example of a hazard and risk assessment for debris flows—A case study of Niwan Gully, Wudu, China. *Eng. Geol.* **2019**, *263*, 105351. [CrossRef]
51. Cesca, M.; D'Agostino, V. Comparison between FLO-2D and RAMMS in debris-flow modelling: A case study in the Dolomites. In *Monitoring, Simulation, Prevention and Remediation of Dense Debris Flows II*; WIT Press: Southampton, UK, 2008; pp. 197–206.
52. Bout, B.; Jetten, V.G. The validity of flow approximations when simulating catchment-integrated flash floods. *J. Hydrol.* **2018**, *556*, 674–688. [CrossRef]
53. Scaringi, G.; Fan, X.; Xu, Q.; Liu, C.; Ouyang, C.; Domènech, G.; Yang, F.; Dai, L. Some considerations on the use of numerical methods to simulate past landslides and possible new failures: The case of the recent Xinmo landslide (Sichuan, China). *Landslides* **2018**, *15*, 1359–1375. [CrossRef]
54. Varnes, D.J. Slope movement types and processes. In *Landslides: Analysis and Control*; Special Report 176; Schuster, R.L., Krizek, R.J., Eds.; Transportation Research Board: Washington, DC, USA, 1978.
55. Jing, Z.; Chuan, T.; Ming, C.; Maohua, L.; Xun, H. Field Observations of the Disastrous 11 July 2013 Debris Flows in Qipan Gully, Wenchuan Area, Southwestern China. In *Engineering Geology for Society and Territory—Volume 2*; Springer: Berlin/Heidelberg, Germany, 2015; pp. 531–535.
56. Guo, X.; Cui, P.; Marchi, L.; Ge, Y. Characteristics of rainfall responsible for debris flows in Wenchuan Earthquake area. *Environ. Earth Sci.* **2017**, *76*, 596. [CrossRef]
57. Nikolopoulos, E.I.; Crema, S.; Marchi, L.; Marra, F.; Guzzetti, F.; Borga, M. Impact of uncertainty in rainfall estimation on the identification of rainfall thresholds for debris flow occurrence. *Geomorphology* **2014**, *221*, 286–297. [CrossRef]
58. Massimo, A.; Lorenzo, M.J.S. Systems and Sensors for Debris-flow Monitoring and Warning. *Sensors* **2008**, *8*, 2436–2452.
59. Antolini, F.; Aiassa, S.; Barla, M. An Early Warning System for Debris Flows and Snow Avalanches. In *Geotechnical Research for Land Protection and Development*; Lecture Notes in Civil Engineering; Springer: Berlin/Heidelberg, Germany, 2020; pp. 338–347.
60. Horton, P.; Jaboyedoff, M.; Rudaz, B.; Zimmermann, M. Flow-R, a model for susceptibility mapping of debris flows and other gravitational hazards at a regional scale. *Nat. Hazards Earth Syst. Sci.* **2013**, *13*, 869–885. [CrossRef]

water

MDPI

Article

Dynamic Response Law and Failure Mechanism of Slope with Weak Interlayer under Combined Action of Reservoir Water and Seismic Force

Wenpeng Ning [1,2] and Hua Tang [2,*]

[1] School of Civil Engineering, Architecture and Environment, Hubei University of Technology, Wuhan 430068, China; ningwenpeng1998@163.com
[2] State Key Laboratory of Geomechanics and Geotechnical Engineering, Institute of Rock and Soil Mechanics, Chinese Academy of Sciences, Wuhan 430071, China
* Correspondence: hua005066@163.com

Abstract: The southwestern region of China is close to the Eurasian earthquake zone. Many engineering areas in southwestern China are affected by earthquakes and are close to the epicenter of earthquakes that occur in this region. During earthquakes, slopes with weak interlayers are more likely to cause large-scale landslides. In response to the low stability of slopes with weak interlayers in reservoir dam areas, the dynamic response law and failure mechanism of weak interlayered slopes under the combined action of reservoir water and seismic forces were studied through shaking table model tests and finite element numerical simulation software. The height of the water level and the size of the seismic waves were changed during these tests. The research results indicate that seismic waves are influenced by weak interlayers and are repeatedly superimposed between the weak interlayers and the slope surface, resulting in an acceleration amplification effect that increases by approximately 1.8 times compared to homogeneous slopes. Vertical earthquakes have a significant impact on the dynamic response of slopes, and their peak acceleration amplification coefficient can reach 0.83 times the horizontal peak acceleration. The stability of weak interlayers during earthquakes is the worst within the range of the direct action of reservoir water. The failure mode of a slope is as follows: earthquake action causes cracking in the upper part of the slope, and as the earthquake increases in intensity, and the infiltration of reservoir water intensifies, the cracks expand. The soft and muddy interlayer in the front section of the slope forms a sliding surface, and ultimately, the sliding failure forms an accumulation body at the foot of the slope. In reservoir dam areas, the stability of a slope is closely related to the engineering safety of the reservoir dam. Therefore, when a strong earthquake and the water level in a reservoir jointly affect a weak-interlayer slope, the slope is in the stage of plastic deformation and instability. The stability of the slope may be overestimated, and the slope is likely vulnerable to sliding instability, which needs to be monitored and treated.

Keywords: weak intercalation; vibration table test; dynamic response; permanent displacement; reservoir water slope; argillization

Citation: Ning, W.; Tang, H. Dynamic Response Law and Failure Mechanism of Slope with Weak Interlayer under Combined Action of Reservoir Water and Seismic Force. *Water* **2023**, *15*, 1956. https://doi.org/10.3390/w15101956

Academic Editors: Stefano Morelli, Veronica Pazzi and Mirko Francioni

Received: 7 April 2023
Revised: 18 May 2023
Accepted: 19 May 2023
Published: 21 May 2023

1. Introduction

In southwest China, the Earth's crust moves vigorously, with strong earthquakes frequently occurring. Large crustal uplift in this area has formed hills, deeply embedded rivers, and high and steep slopes. In the vast mountainous area in this region, a large amount of side (sliding) slopes are distributed. Vast engineering construction projects are taking place in the southwest to cut paths in mountains and meet water to build bridges, resulting in a large number of artificial slopes. Reservoir areas contain weak mezzanine slopes, which occupy a considerable proportion of these areas. As a kind of weak structural layer, the elastic modulus and strength of soft interlayers are lower than that of surrounding rock. Under the combined action of reservoir water and a strong earthquake, rocks are more

likely to slip along the soft interlayer, resulting in major geological disasters and serious economic and livelihood losses [1,2]. For example, the 7.3-magnitude earthquake in Taiwan in 1999 caused a large number of bedding landslides (partial weak interlayer landslides), resulting in multiple traffic interruptions, and the maximum area affected by the landslides reached 5 square kilometers [3]. In 2008, the Tangjiashan landslide in Beichuan swept into a river valley, blocked the Jianjiang River channel, formed the dammed Tangjiashan lake, killed 84 people, and threatened the lives of 1.3 million who lived downstream of the river [4]. The landslide of Zhengjiashan in Pingwu buried houses, schools, and roads at the foot of the slope, causing a large number of casualties, including students and villagers, and direct economic losses of about CNY 3.5 million [5]. Therefore, it is very important to study the stability of slopes under the combined effect of water and an earthquake in an earthquake-stricken area; it is especially important to determine the damage process and sliding instability mechanism of weak sandwiches under the influence of water and an earthquake.

Physical model tests [6–9] and numerical simulation tests [10–12] are important methods of studying the stability of different factors. Domestic and foreign scholars have carried out much research on the stability of a slope under the effect of water, mainly focusing on changes in a slope's stability and the forms of its destruction alongside changes in the water level. Wang, R., Jiang, Z.H., and others used physical models to imitate the fluctuation of the water level in a river, which proved that changes in the water level would seriously endanger the stability of a slide. Among these changes, the distortion and destruction of the slide mostly occurred in the weak sandwiched area, and the model construction showed similar results [13,14]. Upomo, T.C. et al. analyzed a landslip caused by a change in the water level due to heavy rain through a numerical simulation. Then, a model was established to predict the damage caused by the landslip [15]. Many research results have been obtained on the dynamic response of slopes under the effect of an earthquake [16]. K. L. Wan and M. L. Lin carried out research based on the limit balance analysis, PIV analysis, and accelerated time history records. They used the vibration table model to study the starting and destruction process of a slope [17]. Hailong Yang and others studied the dynamic response of a saturated weak sandwiched slope under the effect of multiple earthquakes. They demonstrated that the response increased with the increase in the input wave, but they did not carry out a qualitative analysis [18]. Wang Liwei used the Newmark sliding block analysis method to study whether the dynamic safety factor and permanent displacement of a slope under vertical seismic action were considered [19]. Yan Zhixin et al. used the finite difference method to compare the similarities and differences in a slope's dynamic response with or without a vertical earthquake [20].

Many studies have been carried out on the stability of rock slopes under the combined effect of water and earthquakes, but few of them have focused on the two major factors: water and an earthquake. Most of them have focused on the dynamic response of a dam under the combined effect of water and an earthquake, and the mechanism of weak sandwiches in a slope has scarcely been studied. Under the combined effect of water and the force of an earthquake, the dynamic response of a slope with weak sandwiches was studied. The indoor vibration platform model test and the limited element simulation software were used to study the dynamic response mechanism of a slope with weak sandwiches under the combined effect of water and the force of an earthquake and to analyze the impact of soft sandwiches on the transmission of earthquake waves. It was clear that weak sandwiches were destroyed under the influence of water and the force of an earthquake and the sliding and losing mechanism.

Section 2 illustrates and briefly explains the preparation work for the preliminary model test: determining the parameters, similarity ratio, material ratio, monitoring point layout, and loading seismic plan. Section 3 discusses the dynamic response and displacement law for each monitoring point on the slope surface based on an analysis of the simulation results of the vibration table. Section 4 describes work in which numerical simulation software was used to calculate and analyze the dynamic response and perma-

nent displacement law of the slope, which was compared and verified with the model test results. Section 5 summarizes the triggering factors and failure mechanisms in the sliding of weak intercalated slopes under the action of reservoir water and seismic forces, based on observations of the failure morphology of the slope. The conclusions are presented in Section 6.

2. Shaking Table Model Test Scheme

2.1. General Situation of Engineering Geological Environment

The water depth in front of the dam in the reservoir area of the hydropower station is about 130 m. This section of the valley is a V-shaped, longitudinal monoclinic valley with symmetrical topography on both sides. The mountain is abundant and the terrain is rugged, and the slope topography is largely uniform, as shown in Figure 1. Due to the influence of the tropospheric occurrence and the steep slope along the river, the two sides of the bank slope form a stepped topography. The left bank is a downhill slope with an overall slope of 20°–30°. A series of 30 m–60 m high and continuous steep ridges develop diagonally along the bank slope, and the slopes of steep ridges can reach more than 45°.

Figure 1. Topography of engineering area.

The outcrop beds in the engineering area are mainly the upper part of the upper Permian basalt formation, including basalt, almond basalt, volcanic breccia lava, and tuff, as shown in Figure 2. According to 13 boreholes and 3 adits at the dam site, the tuff is produced in layers with a thickness of 1 m–2 m, and there is obvious extrusion, dislocation, and argillation between the tuff and the tuff layer. Due to changes in the water level, the front section of the tuff interlayer is immersed for a long time in reservoir water, which leads to the gradual formation of slime in the soft interlayer with good permeability, and the corresponding strength parameters are greatly reduced, which seriously affects the stability of the reservoir slope.

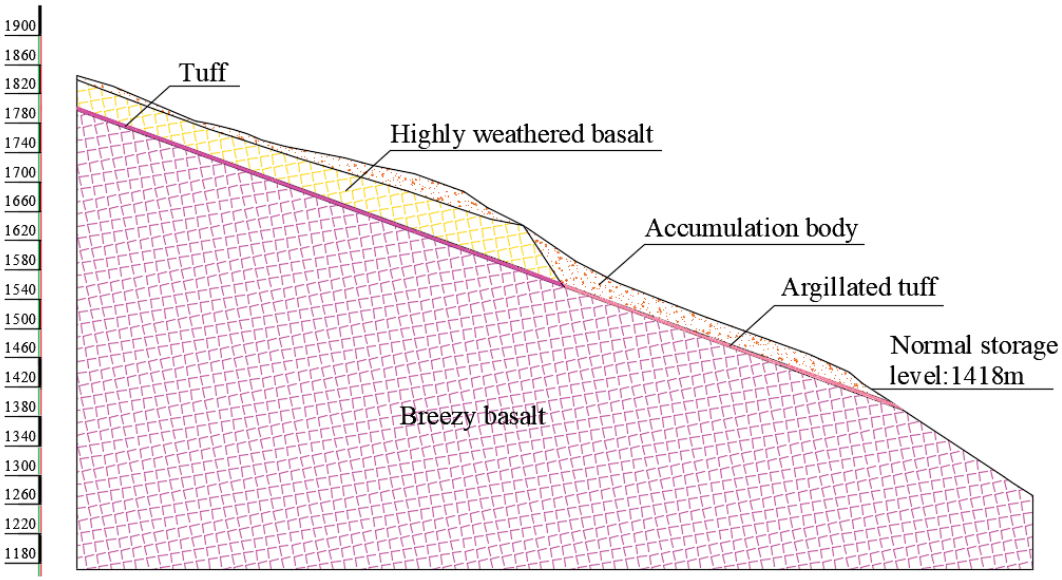

Figure 2. Geological section of the left bank of the reservoir area.

2.2. Determining the Physical Parameters of Each Rock Layer

According to the borehole and adit sampling test near the engineering area, the shear strength, tensile strength, and compressive strength of basalt were measured using a triaxial test. See Figure 3 for the instrument used in the test and the test curve. The specifications of the main machine of the MTS815−03 triaxial testing machine were as follows: static, 2667 kN; tensile load, 1335 kN; and loading rigidity of cross member, 10.5×10^9 N/m. The maximum lateral pressure of the triaxial pressure chamber of the test machine was 500 MPa. Specimen size was $\Phi 50 \sim 100$ mm $\times$ $(100 \sim 150)$ mm; measuring range of displacement was ± 50 mm; range of strain measurement was ± 0.03 mm. Four pieces of equipment are commonly used for in situ shear tests: pressure plate (size 500×500 mm); loading system−hydraulic jack; reaction system−transmission column with sufficient stiffness and 360×360 mm bracket; measuring system−a pressure gauge, dial gauge, and magnetic gauge holder.

(**a**) (**b**)

Figure 3. Laboratory and in situ tests. (**a**) Model MTS815−03 Triaxle Tester. (**b**) Original rock shear test.

For the calculation and analysis, we determined the physical and mechanical parameters of the rock mass with weak interlayers in the reservoir area, as shown in Table 1, by comprehensively considering indoor tests and field tests such as the deformation of rock mass and the shear resistance of rock mass and weak surfaces and consulting recommended values from various codes and empirical values from hydraulic manuals. It can be seen from the table that the mechanical parameters of the argillized layer of tuff are lower than those of tuff.

Table 1. Physical and mechanical parameters of rock mass.

Material Name	Volume Weight γ/kN/m^3	Elasticity Modulus E/MPa	Poisson's Ratio μ	Cohesion c/Mpa	Frictional Angle $\varphi/^\circ$
Accumulation body	24	25	0.38	0.03	31
Highly weathered basalt	30	1000	0.26	0.8	35
Tuff	29	80	0.30	0.09	28
Argillated tuff	30	40	0.33	0.05	24
Breezy basalt	30	20,000	0.23	1.5	43

Based on their theoretical and practical experience in rock behavior, H ° ek and Br ° wm established the principal stress relationship for rock mass failure, namely the H ° ek−Br ° wm criterion. By linking this criterion with *RMR*, the strength parameters of the rock mass can be estimated. The H ° ek−Br ° wm criterion has the following relationship:

$$\sigma_1 = \sigma_3 + \sqrt{m\sigma_c\sigma_3 + s\sigma_3} \quad (1)$$

In the formula, σ_1 is the maximum stress at failure; σ_3 is the minimum principal stress acting on the rock mass; m and s are the rock material constant.

The key to applying the above equation is how to determine the material parameters, the m and s values, of rocks. H ° ek and Br ° wm introduced the *RMR* classification system into the criteria and proposed using the following equation to estimate the material constants m and s:

For disturbed rock masses:

$$\frac{m}{mi} = \exp\left(\frac{RMR - 100}{14}\right) \quad (2)$$

$$s = \exp\left(\frac{RMR - 100}{6}\right) \quad (3)$$

For undisturbed rock mass:

$$\frac{m}{mi} = \exp\left(\frac{RMR - 100}{28}\right) \quad (4)$$

$$s = \exp\left(\frac{RMR - 100}{9}\right) \quad (5)$$

In the formula, m and s are the material parameters of the rock mass; mi is the m value of a complete rock.

Once the m and s values have been calculated, the normal stress on the sliding surface of the slope can be estimated, and C is determined according to the tangent line of the

envelope of the main stress circle in the definition of the H ° ek−Br ° wm criterion, φ. The specific process is as follows:

$$\begin{cases} h = 1 + 16(m\sigma_n + s\sigma_c)/3m^2\sigma_c \\ \theta = [90^\circ + \arctan(1/\sqrt{h^3 - 1})]/3 \\ \phi = \arctan(1/\sqrt{4h\cos^2\theta - 1}) \\ \tau = (\cot\phi - \cos\sigma)m\sigma_c/8 \\ C = \tau - \sigma_n \tan\phi \end{cases} \tag{6}$$

2.3. Similar Relationships and Material Ratios

Being affected by the site, quantity, and economy, an indoor model test usually reduces the model size according to similar criteria. In order to achieve change characteristics that are as close as possible to the actual engineering and create a similar relationship between the slope model and bridge site slope prototype, the compatibility equation, physical equation, geometric equation, balance equation, and boundary condition of the slope model and bridge site slope prototype should be guaranteed. The similar relationship is shown in the following formula, where m represents the physical quantity of the slope model, and p represents the physical quantity of the slope prototype at the site:

$$C_\sigma = C_1 = C_x, \qquad C_\sigma = C_\varepsilon C_E, \qquad C_\mu = 1, \qquad C_\varepsilon = 1, \qquad C_x = C_\sigma \tag{7}$$

C_σ is the stress ratio:

$$C_\sigma = \frac{(\sigma_x)_p}{(\sigma_x)_m} = \frac{(\sigma_y)_p}{(\sigma_y)_m} = \frac{(\tau_{xy})_p}{(\tau_{xy})_m} = \frac{\sigma_p}{\sigma_m} \tag{8}$$

C_l is the geometric proportion:

$$C_l = \frac{x_p}{x_m} = \frac{y_p}{y_m} = \frac{u_p}{u_m} = \frac{v_p}{v_m} = \frac{l_p}{l_m} \tag{9}$$

C_ε is the strain ratio:

$$C_\varepsilon = \frac{(\varepsilon_x)_p}{(\varepsilon_x)_m} = \frac{(\varepsilon_y)_p}{(\varepsilon_y)_m} = \frac{(\varepsilon_{xy})_p}{(\varepsilon_{xy})_m} = \frac{\varepsilon_p}{\varepsilon_m} \tag{10}$$

C_E is the modulus of elasticity ratio:

$$C_E = \frac{E_p}{E_m} \tag{11}$$

C_μ is Poisson's ratio:

$$C_\mu = \frac{\mu_p}{\mu_m} \tag{12}$$

The above equation is satisfied, and the similar relationship between the slope model and the prototype of the bridge site slope is consistent. According to the similarity theory [21,22], the similarity constant of the basic dimension of this test is determined from the actual size of the slope with weak interlayers and the inside diameter of the model box: the dimension similarity constant $C_l = 400$; the density similarity constant $C_\rho = 1$; the vibration acceleration similarity constant $C_a = 1$. We determined the size of the experimental model to be 2.6 m × 1.4 m × 1.5 m (length × height × width). As shown in Table 2, according to the dimension analysis method [23,24] and the Buckingham quantitative method [25], the similar constants of other physical quantities were calculated. Based on

the main similarity ratios of the model tests and repeated matching tests, the material ratios corresponding to the physical and mechanical parameters of each rock layer in the model were determined (see Table 3).

Table 2. Main similarities between model tests.

Physical Quantity	Similar Relationships	Similarity Ratio
Geometric dimension L	C_L	400
Accelerated speed a	$C_a = 1$	1
Material density ρ	C_ρ	1
Cohesion c	$C_c = C_\rho \times C_L$	400
Friction angle φ	$C_\varphi = 1$	1
Unit weight γ	$C_\gamma = C_\rho$	1
Elastic modulus E	$C_E = C_\rho \times C_L$	400
Poisson's ratio μ	$C_\mu = 1$	1

Table 3. Material ratio and parameters for model test.

Material Name	Material Ratio	Cohesion *c*/kPa	Friction Angle *φ*/°
Accumulator	Talc powder: Sand 2.4:1.6	1.55	31.8
Strongly weathered basalt	Steel slag: Sand: Gypsum: Water 5:4:1.3:2.2	9.3	34.4
Microweathered basalt	Iron powder: Barite powder: Water: Cement 30.0:10.0:3.5:1.4	14.3	43.4
Tuff	Hardboard	0.9	26.6

2.4. Layout of Monitoring Points

According to the layout principle of monitoring points and considering the influence of a tuff interlayer on the dynamic response of a slope with a weak interlayer, 15 monitoring points were set on the slope surface, interlayer, overburden, and bedrock (see Figure 4) to monitor the acceleration time history change process of a slope during an earthquake.

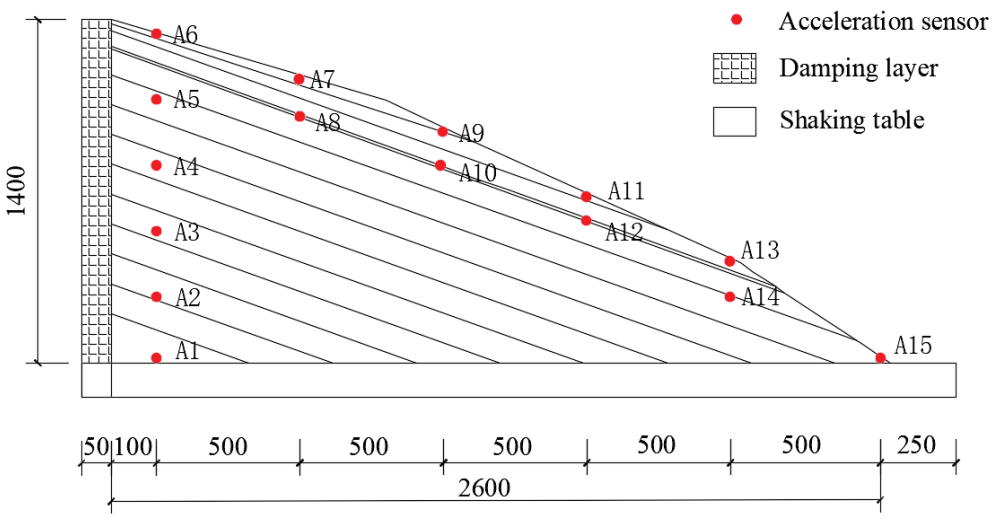

Figure 4. Layout position diagram of monitoring point A1–A15 (unit: mm).

2.5. Seismic Input and Loading Scheme

Structurally, the project area is located in the active tectonic area in northwest Yunnan. Neotectonic movement, deep tectonic deformation, fault activity, modern crustal deformation, etc. are relatively strong and are affected by seismic tectonic activities in the peripheral areas of the east and west sides. The basic seismic intensity in the project area is measured in degrees, and the peak horizontal acceleration is 0.30 g. As shown in Figure 5, the maximum acceleration of the input seismic wave was mainly concentrated within 6 s–10 s, and the peak acceleration occurred at 6.93 s. When considering inputting seismic waves with different peak accelerations, the seismic waves are proportionally scaled to preserve the consistent waveform of the seismic waves. The peak accelerations of horizontal and vertical seismic waves are scaled to 0.1 g, 0.2 g, 0.3 g, and 0.4 g.

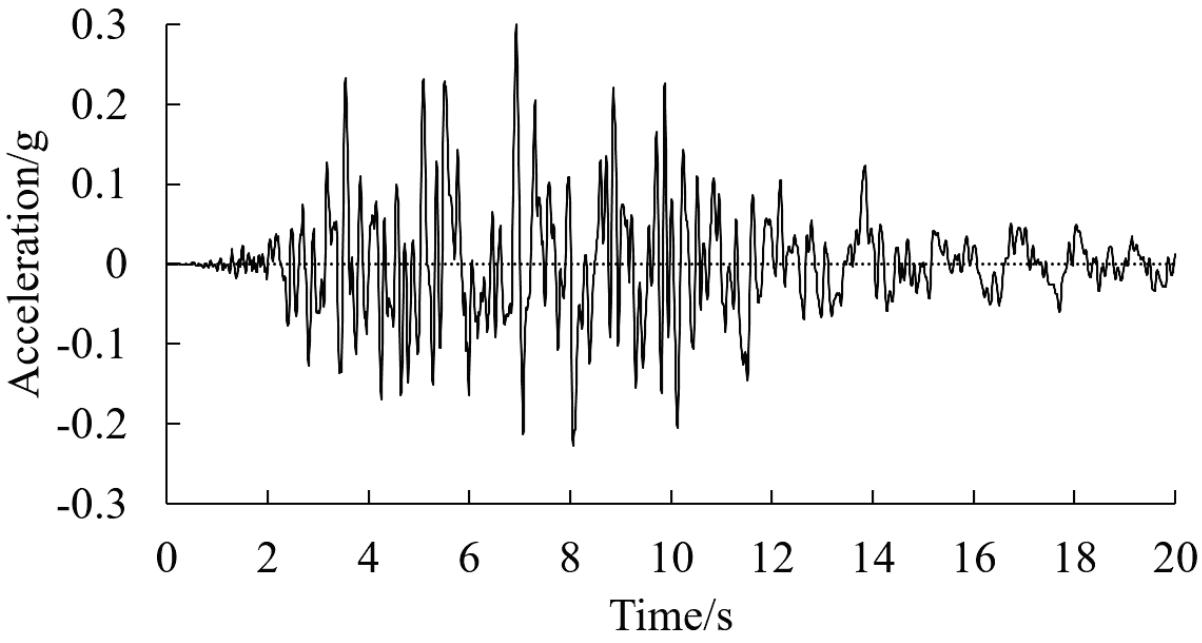

Figure 5. Input horizontal seismic wave curve.

The experimental simulation was divided into two conditions: no water and normal water level. First, the input of the seismic wave changed from a vertical seismic wave to a horizontal seismic wave, and the seismic acceleration gradually increased from 0 g to 0.4 g. Different seismic conditions were simulated.

In order to study the dynamic responses of slope models under different directions of seismic wave input conditions, the seismic load excitation direction was designed to be loaded first in the vertical direction and then in the horizontal direction, and the seismic acceleration was loaded in increments of 0.1 g, 0.2 g, 0.3 g, and 0.4 g. In order to study the influence of the mud deposition of reservoir water on the dynamic response of the model, a low water level test was conducted first, followed by a high water level test. The test plan is shown in Table 4, and the low water level condition is shown in Figure 6.

Table 4. Test loading conditions.

Loading Conditions	Earthquake Direction	Seismic Peak Acceleration/g	Reservoir Water Status
1	Vertical earthquake	0.1 g	Normal water level
2			No water level
3		0.2 g	Normal water level
4			No water level
5		0.3 g	Normal water level
6			No water level
7		0.4 g	Normal water level
8			No water level
9	Horizontal earthquake	0.1 g	Normal water level
10			No water level
11		0.2 g	Normal water level
12			No water level
13		0.3 g	Normal water level
14			No water level
15		0.4 g	Normal water level
16			No water level

Figure 6. Initial model.

3. Shaking Table Test Results and Analysis

3.1. Dynamic Response Analysis during Earthquake

By analyzing the data collected using the acceleration sensor in the slope model, we plotted the PGA change curve of each monitoring point in the model slope. Figure 7 shows the variation curve of the PGA amplification factor under the input vertical and horizontal earthquakes. H and N represent conditions with normal storage and no water, respectively. The analysis of Figure 7 shows the following:

1. It can be seen that when the input seismic acceleration was the same, the PGA at the normal water level was greater than that with no water, indicating that the mudding effect of reservoir water had a significant amplification effect on the PGA of the slope. The sedimentation of reservoir water also had a certain influence on the PGA distribution of the slope, and the enlarged area of PGA in the slope obviously increased after sedimentation. This is because after the front section of the weak interlayer was cemented, the cohesive force of the weak interlayer decreased, and the slope surface was damaged under the action of seismic waves, so the acceleration amplification effect at the slope angle was more obvious.
2. When both horizontal and vertical seismic waves were input, the acceleration response of the slope increased from the bottom to the top along the slope surface, reaching the maximum value at the top of the slope, with the maximum amplification factor of 2.5 with the input of vertical seismic waves, 3.25 with the input of horizontal seismic waves, and 0.83 times at the peak dynamic response of vertical seismic waves. By observing the slope of the folding line of the amplification coefficient change in PGA, it can be seen that, when increasing the slope height of the same height, the change in PGA at the slope angle of 250–500 mm is not significant. PGA rapidly increases in the middle part of the slope at 500–1000 mm, and the increase rate slows down again at 1000–1250 mm. Analyzing this phenomenon indicates that the impact of earthquakes on the slope is mainly evident in the middle part of the slope, and it can be considered that the middle part of the slope should be reinforced. It can reduce the PGA growth rate.
3. Upon comparing normal water storage conditions with no water level conditions, it can be observed that an increase in water level significantly increases the PGA amplification coefficient of the slope surface. When inputting vertical seismic waves, the peak value of PGA without water level is 1.82, and under normal water storage conditions, the peak value of PGA is 2.43, an increase of 33%. When inputting horizontal seismic waves, the PGA peak without water level is 2.76, and under normal water storage conditions, the PGA peak is 3.07, an increase of 11%. By analyzing the above data, it can be found that changes in water level have a significant impact on the dynamic response of the slope; especially, when inputting vertical seismic waves, the change in PGA is more severe. This indicates that, when analyzing the dynamic response of the slope, reservoir water and vertical earthquakes are two important factors affecting the stability of the slope.

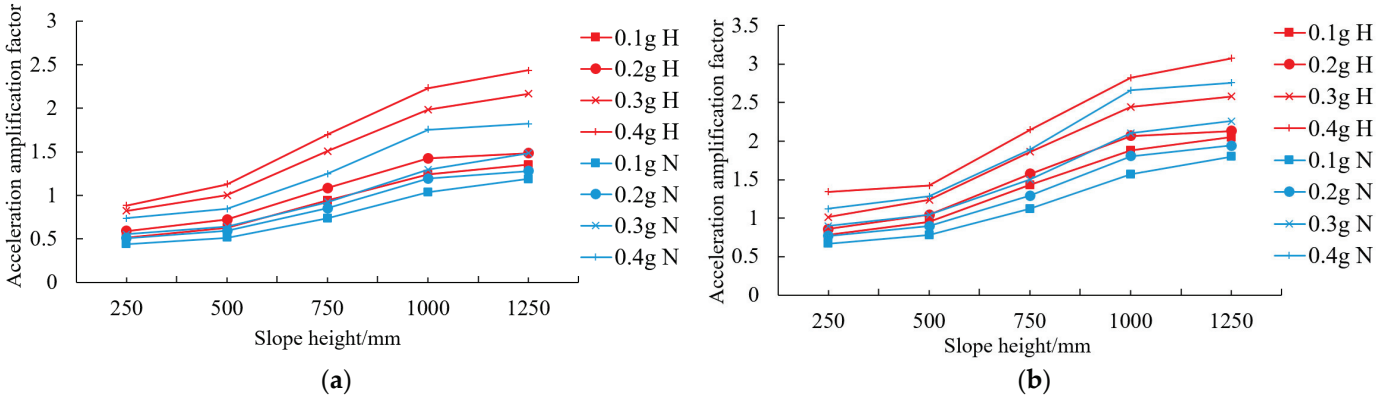

Figure 7. Variation curve of PGA amplification coefficient under different earthquakes. (**a**) Vertical seismic waves. (**b**) Horizontal seismic waves.

3.2. Analysis of Permanent Displacement during Earthquake

The maximum surface deformation of each measuring point under different seismic loads was plotted as a curve, from high to low, in different slope surface heights, and the relationship between the surface deformation of the slope and the input seismic acceleration was analyzed. Figure 8 shows the relationship between the maximum surface deformation and the input seismic acceleration. It can be seen from the diagram that the displacement of the slope surface increased with the increase in the input seismic wave acceleration.

For vertical input loads, when the input seismic acceleration was 0–0.3 g, the displacement increased uniformly. The surface displacement increased sharply when the input seismic acceleration reached 0.3 g. When the input seismic acceleration was 0.4 g, the maximum slope displacement appeared at up to 16.8 mm. When the input seismic acceleration reached 0.45 g, a steep drop in surface displacement occurred, which indicated that the dynamic response of a slope surface changes from the linear area to the plastic area.

For horizontal input loads, the displacement curve could be divided into three stages. In the first stage, when the input seismic acceleration was 0–0.3 g, the displacement increased uniformly, which was elastic deformation. In the second stage, when the input seismic acceleration was 0.3–0.45 g, the displacement first decreased and then increased, which was plastic deformation. The maximum slope displacement also appeared at up to 31.2 mm. In the third stage, when the input seismic acceleration reached 0.45 g, the surface displacement decreased abruptly, which was sliding destabilization, indicating that the landslide began at this time, and the slope was already unstable. When the input seismic acceleration reached 0.4 g, it coincided with the failure process of the slope in the test. The surface displacement increased sharply at first and then decreased sharply, indicating that the slope was unstable and slid completely, entering the post-failure stage. Upon comparing the data obtained from displacement measurement points arranged at different heights along the slope, it can be found that there is a sudden change in displacement at a distance of 400 mm from the top of the slope. The measurement points are located on the steeply inclined structural surface of the trailing edge, and obvious through cracks appear during the failure process.

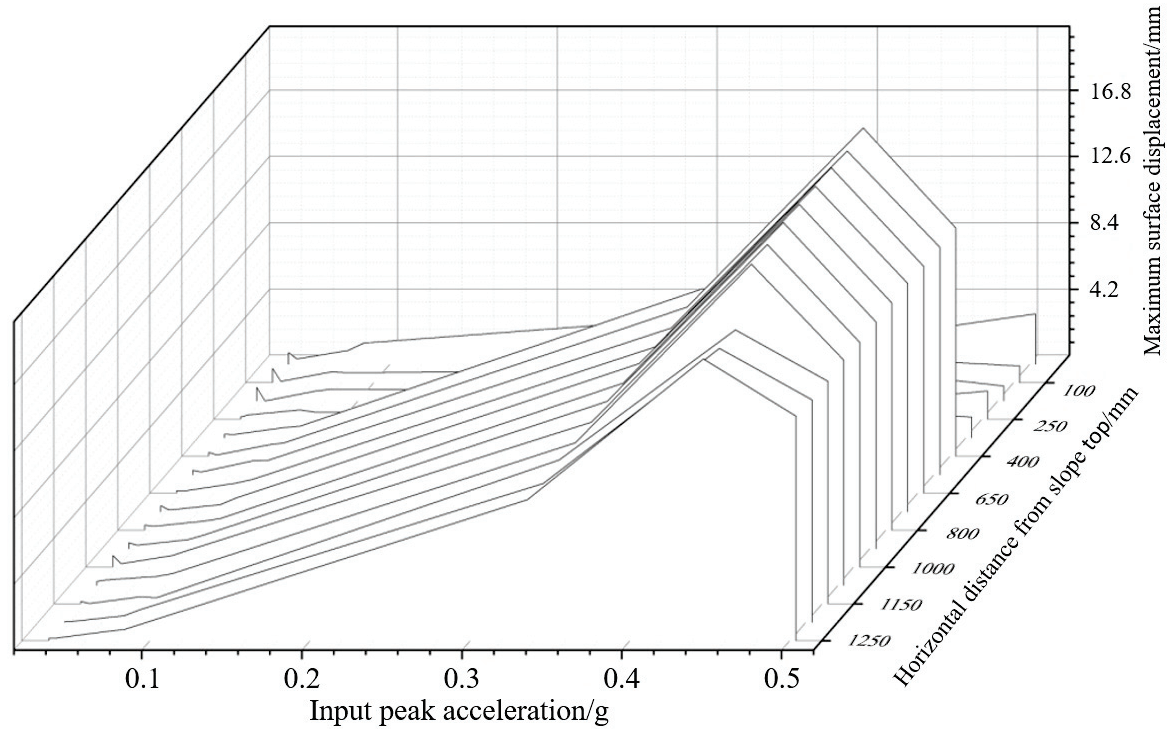

(**a**)

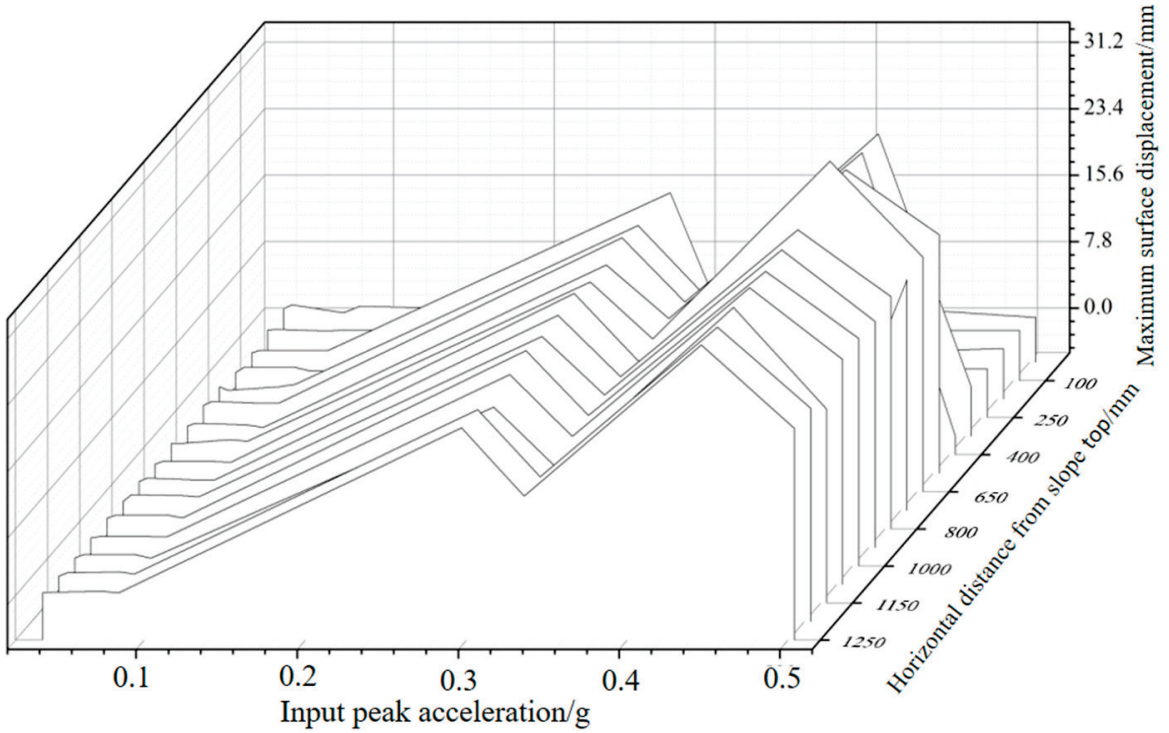

(**b**)

Figure 8. Evolution curve of surface displacement. (**a**) Vertical square load. (**b**) Horizontal load.

4. Numerical Simulation Analysis

4.1. Analysis Software and Constitutive Model Selection

Geostudio is a finite element software widely used in the field of geological engineering, in which the QUAKE/W modules and SLOPE/W modules are used to analyze dynamic responses and permanent displacements under the action of earthquakes. Therefore, in this paper, Geostudio software was used to calculate and analyze the dynamic response and permanent displacement of the slope under different seismic actions, in which the material constitutive model was the Linear Elastic Model. The Linear Elastic Model is immensely useful for education, testing, and verification purposes [26,27]. As there are no convergence problems with this model, many other issues can be resolved without convergence complications. For example, performing linear elastic analyses can be useful to determine the effects of various boundary conditions and confirm that they are being applied and used correctly or to confirm the effects of varying in situ conditions. The Linear Elastic Model in QUAKE/W is useful for verifying that the software provides the same solution.

4.2. The Establishment and Calculation of Numerical Model

The numerical model was established according to the optimal boundary requirements of the model proposed by Zhang Jiangwei et al. [28]. In the analysis of the model, the finite element mesh was divided into quadrilateral and triangular mesh, and the mesh size was determined according to the principle of 1/8–1/10 of the wavelength corresponding to the highest frequency of the input seismic wave, meaning the mesh needed to meet the accuracy requirements. The static boundary conditions of the finite element model were set as the left and right boundary normal constraint, the bottom fixed constraint, and the free slope. It should be noted that the above left and right boundary conditions should be changed to free states in the follow-up dynamic analysis. The model grouping and grid division are shown in Figure 9, and the finite element calculation model with an extended boundary at both ends considering the boundary effect is shown in Figure 10. Considering the influence of the tuff interlayer on the dynamic response of the slope, four columns of monitoring points were arranged on the slope surface, interlayer, overlying layer, and bedrock (as shown in Figure 11) to monitor the time-history variation process of acceleration, velocity, and displacement during an earthquake.

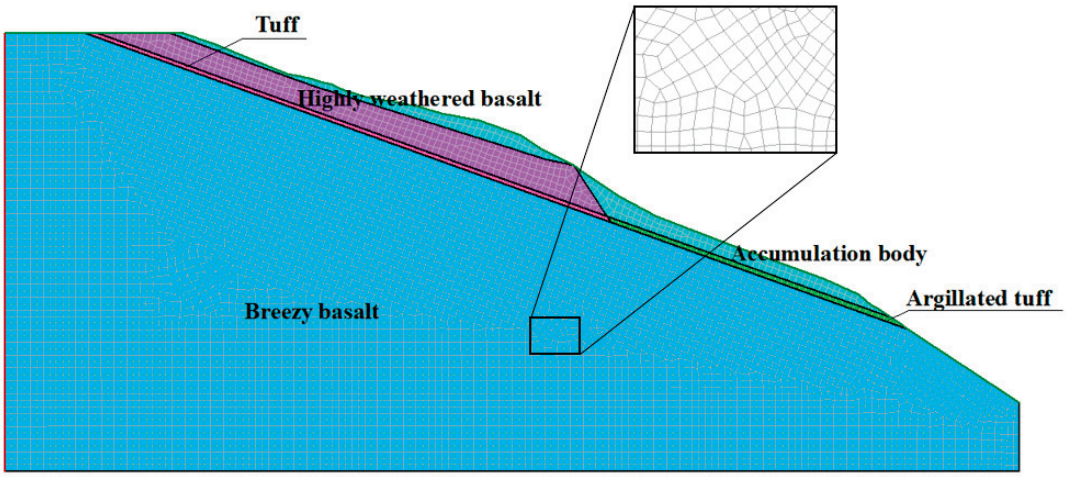

Figure 9. Model grouping and mesh division.

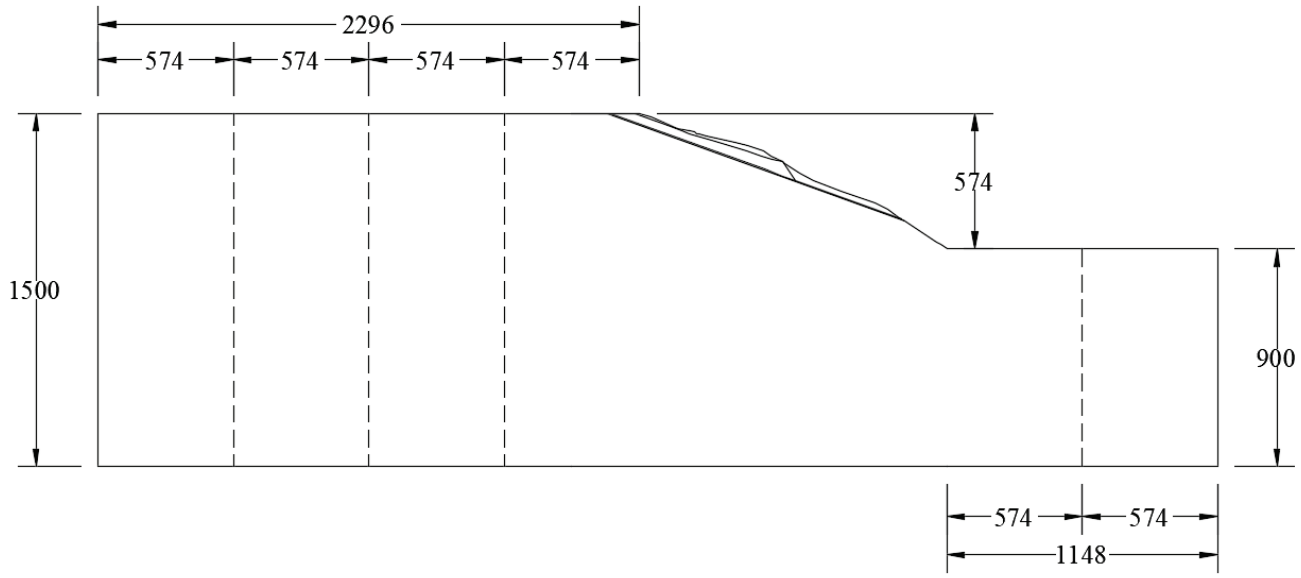

Figure 10. Finite element model of the slope (unit: m).

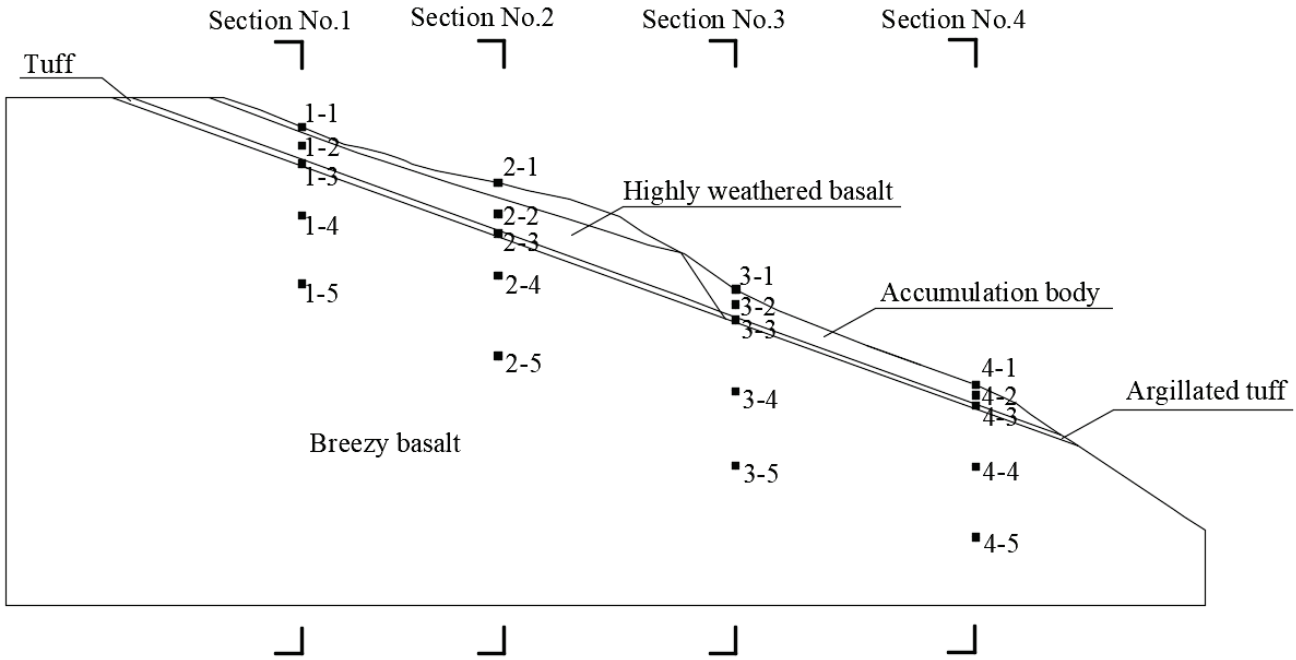

Figure 11. Layout of monitoring points.

4.3. Effect of Reservoir Water and Earthquake on Weak Sandwich Slope

4.3.1. Acceleration Response Analysis

In order to analyze the dynamic response of a slope to a vertical earthquake, the peak acceleration of the monitoring points on the slope surface was compared by inputting different vertical seismic accelerations. We defined the ratio of peak response acceleration at the monitoring point to peak input seismic wave acceleration as the acceleration amplification factor (PGA) at the monitoring point. Figure 12 shows the change in the peak acceleration of the slope, which is visually displayed by X-direction and Y-direction acceleration clouds during different earthquakes. It can be seen from the graph that with the increase in input seismic acceleration, the maximum area of peak acceleration was mainly distributed in the upper part of the slope, and the acceleration of rock mass near the slope surface was significantly different. The peak acceleration increased compared

with the peak input seismic wave. As the input vertical earthquake increased, the peak acceleration of the entire slope in the X direction gradually moved towards the foot of the slope. The peak acceleration of the whole slope in the Y direction increased significantly at the top and foot of the slope. The acceleration in the Y direction of the lower rock mass of the weak interlayer tended to increase in the slope, which indicated that the lower part of a slope is liable to be damaged when a vertical earthquake is involved.

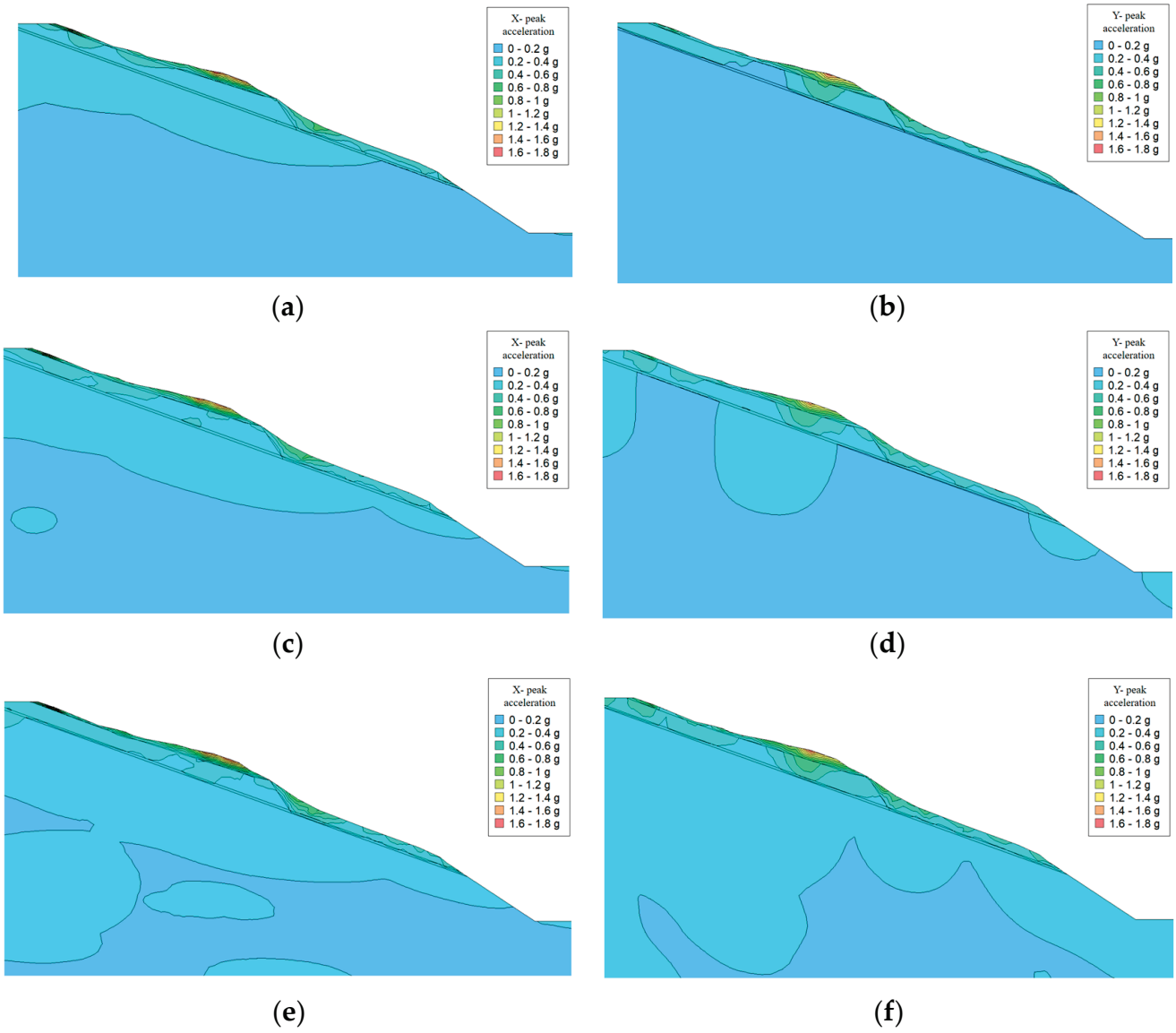

Figure 12. Acceleration cloud map in X and Y directions under different earthquakes. (**a**) X−direction acceleration cloud image at 0.1 g. (**b**) Y−direction acceleration cloud image at 0.1 g. (**c**) X−direction acceleration cloud image at 0.2 g. (**d**) Y−direction acceleration cloud image at 0.2 g. (**e**) X−direction acceleration cloud image at 0.3 g. (**f**) Y−direction acceleration cloud image at 0.3 g.

Compared with the acceleration cloud in the X and Y directions under the same seismic acceleration, with an increase in the input seismic wave, the acceleration response of the upper and lower rock mass of the weak interlayer gradually increases, but there is no obvious change in the dynamic response of the weak interlayer, which indicates that the weak interlayer has a certain energy absorption effect on the slope. However, when the input seismic wave acceleration is 0.3 g, the dynamic response of the upper and lower rock mass of the weak interlayer increases sharply. This indicates that the ability of the weak interlayer to absorb a seismic wave is saturated, and the

wave begins to affect the surrounding rock mass. Let us observe the acceleration cloud in the Y direction. With an increase in the input seismic wave, the dynamic response in the Y direction at the foot of slope is significantly larger than that in the X direction. This shows that the participation of vertical earthquakes has a strong influence on the dynamic response of the slope, which makes it easier for the slope to be destroyed at its foot.

In order to analyze the influence of mud in the front section of the tuff interlayer on the slope response, different vertical seismic accelerations were input to carry out slope dynamic response calculations. The analysis of Figure 13a,b is an intuitive means of determining whether the different heights of the slope surface are affected by the mudding of the weak interlayer. Upon comparing the PGA curve in the X and Y directions, the following conclusions were obtained:

1. By analyzing the PGA variation curves of different vertical seismic actions in the X direction, it can be seen from Figure 13a that the influence of reservoir water mud was mainly 300 m away from the bottom of the slope. With the increase in the input vertical seismic acceleration, the PGA within 300 m of the bottom of the slope changed most obviously among the four monitoring points on the slope surface. Compared with the normal water level and no water, only the PGA gap within 300 m of the bottom of the slope was large, and the PGA in other areas was very similar. This shows that when the weak interlayer in the front of a slope is muddled, the dynamic response of the slope will increase, i.e., the muddied, weak interlayer in the X direction can amplify the seismic wave.
2. By analyzing the PGA variation curves of different vertical seismic actions in the Y direction, it can be seen from Figure 13b that the influence of reservoir water mud was mainly 400 m from the bottom of the slope, and the PGA in other areas were very similar with the normal water level and with no water, which indicates that vertical seismic waves mainly affect the middle of a slope. When the weak interlayer in front of the slope was muddy, the dynamic response in the Y direction was mainly reflected in the middle and upper part of the slope. The maximum PGA value in the Y direction was 3.0, which could reach 0.85 times the maximum PGA value in the X direction, which was 3.5. These were very similar to the results of the model test, which showed that the numerical simulation had a high level of reliability.

By summarizing and analyzing the results in Figures 12 and 13, it is demonstrated that the presence of weak interlayers can cause seismic waves to overlap between the weak interlayers and the slope surface. The weak interlayers have the function of absorbing and isolating seismic waves, but their ability to absorb seismic waves is limited. When the seismic waves are large, the weak interlayers will stop absorbing seismic waves, thus exhibiting the phenomenon of amplifying seismic waves. When the weak interlayer undergoes mudification, the ability of the weak interlayer to absorb seismic waves decreases again, manifested as a significant increase in the transmission of seismic waves to the upper soil layer when they pass through the muddied weak interlayer; However, the muddy weak interlayer had little effect on other areas, which meant that the muddy weak interlayer was more likely to be destroyed in the project.

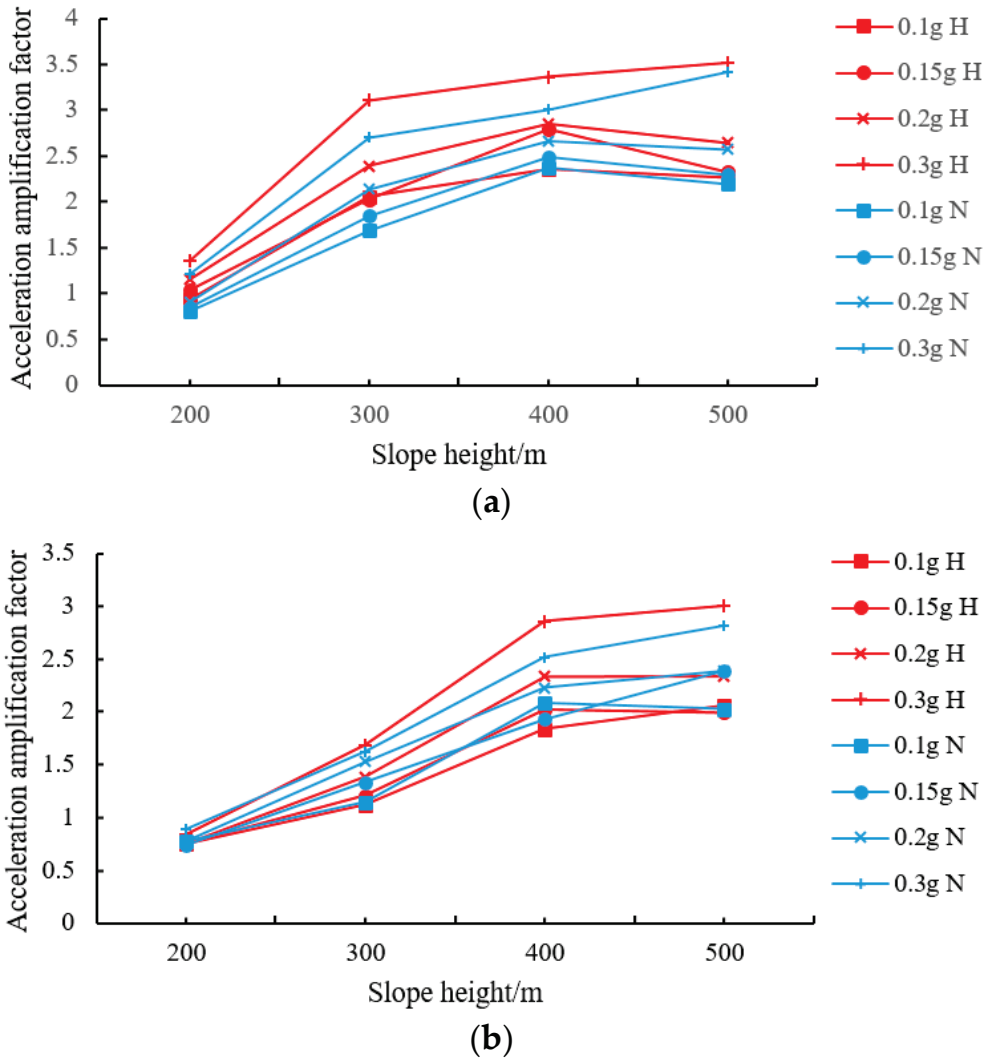

Figure 13. Variation curve of PGA amplification coefficient during different earthquakes. (**a**) Variation regularity of PGA during different vertical earthquakes in X direction. (**b**) Variation regularity of PGA during different vertical earthquakes in Y direction.

4.3.2. Permanent Displacement Analysis

In order to illustrate the influence of mud in the front section of tuff on permanent displacement, here, we considered the mud state in the front section of the interlayer. The calculation results are shown in Figure 14. It can be seen that the permanent displacement of the slope increased with the increase in the vertical seismic acceleration. Taking the slope displacement of the muddy interlayer as an example, the permanent displacement of the slope was 32 cm when the vertical earthquake reached 0.3 g. In the shaking table model test, when the input seismic wave reached 0.3 g, the measured displacement value was 0.86 mm, and the model similarity ratio was 400. The calculated true displacement value of the slope was 31.2 cm. The test results agreed with the numerical simulation results, which showed that the numerical simulation analysis method was feasible and had greater reliability.

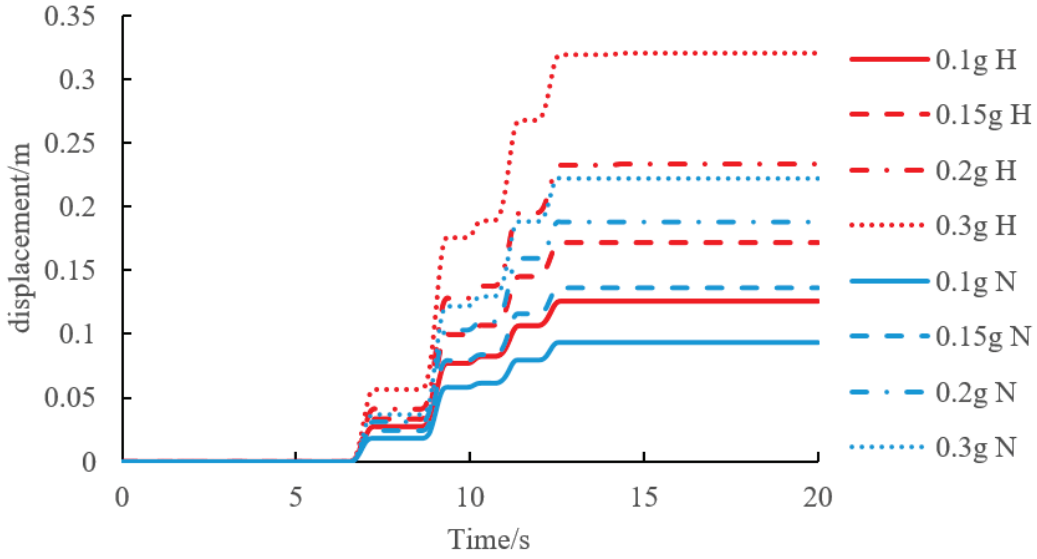

Figure 14. Permanent displacement of slope due to different seismic accelerations.

According to Jibson et al., when the permanent displacement of the slope exceeds 15 cm, the degree of failure of the slope is superelevation. It can be seen from the above figure that, if the argillization of reservoir water on the tuff interlayer and vertical seismic action are not considered, from the permanent displacement of the slope, the damage degree of the slope is only high, but there is argillization of reservoir water on the tuff interlayer in the project, so the actual damage caused to the slope is ultra-high.

5. Failure Pattern and Instability Mechanism Analysis

5.1. Slope Failure Pattern

After each input of different seismic waves, the crack positions and shedding parts of the slope surface after different seismic waves were determined by measuring the crack data on the model surface (see Figure 15). With the increase in the input seismic wave, the deformation and failure of model slope was a process of progressive evolution.

It can be seen from Figure 15a,b that when the input seismic acceleration was 0–0.1 g, no cracks occurred on the surface of the model slope after applying small seismic loads, i.e., the model slope vibration, which basically indicated that the model had not been damaged. When the input seismic acceleration was 0.2 g, a small number of cracks formed on the surface of the model slope, and a low level of shedding occurred in the middle and at the foot of the slope. It can be seen from Figure 15c,d that with the increase in the applied seismic load, i.e., when the input seismic acceleration was 0.3 g, the cracks on the surface of the model slope extended in the left and right directions, and there were penetrating cracks in the middle of the slope. The shedding phenomenon of the surface rock mass was mainly concentrated in the middle and lower part of the slope. It can be seen from Figure 15e,f that with the increase in the applied seismic load, when the input seismic acceleration was 0.4 g, several penetrating cracks appeared on the model slope. On the whole model surface, the slope surface was divided into several blocks, and the front section of the model with a weak interlayer (about 35 cm from the foot elevation) was completely destroyed.

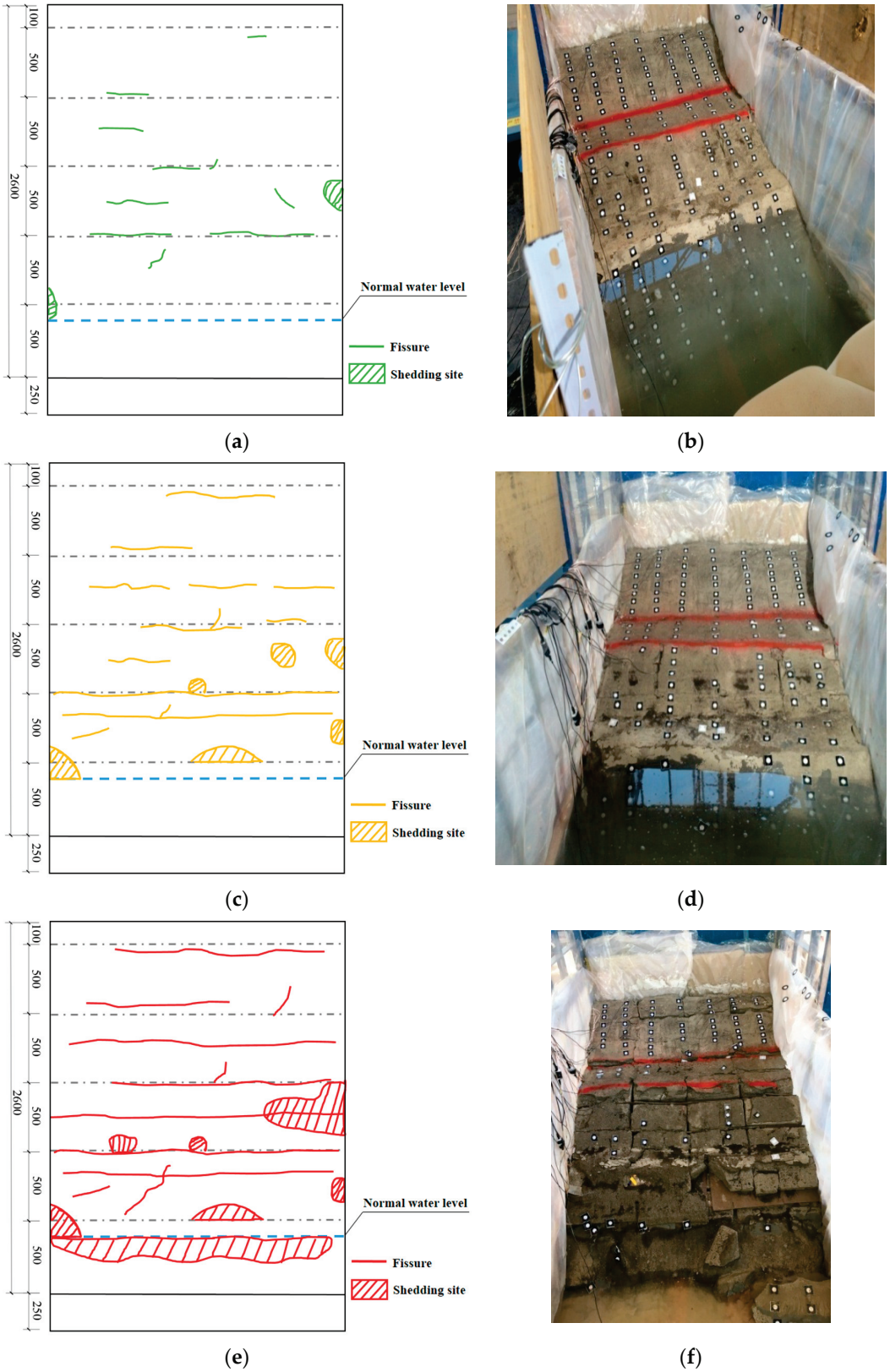

Figure 15. Failure of model slope during earthquake. (**a**) Description of 0–0.2 g crack. (**b**) A 0–0.2 g normal water level crack. (**c**) Description of 0.3 g crack. (**d**) Photograph of 0.3 g normal water level crack. (**e**) Depiction of 0.4 g cracks and damage. (**f**) Pictures depicting 0.4 cracks and damage.

When the model was unstable as a whole, there were a lot of cracks on the surface of the model. The damage was obvious with the change in model gradient, and the damage occurred completely at the foot of the slope. At a level of elevation of about 35 cm from the slope, the surface slope body overturned and slid out in block form. The reservoir water was pumped out, and the slope model was removed in layers, as shown in Figure 16.

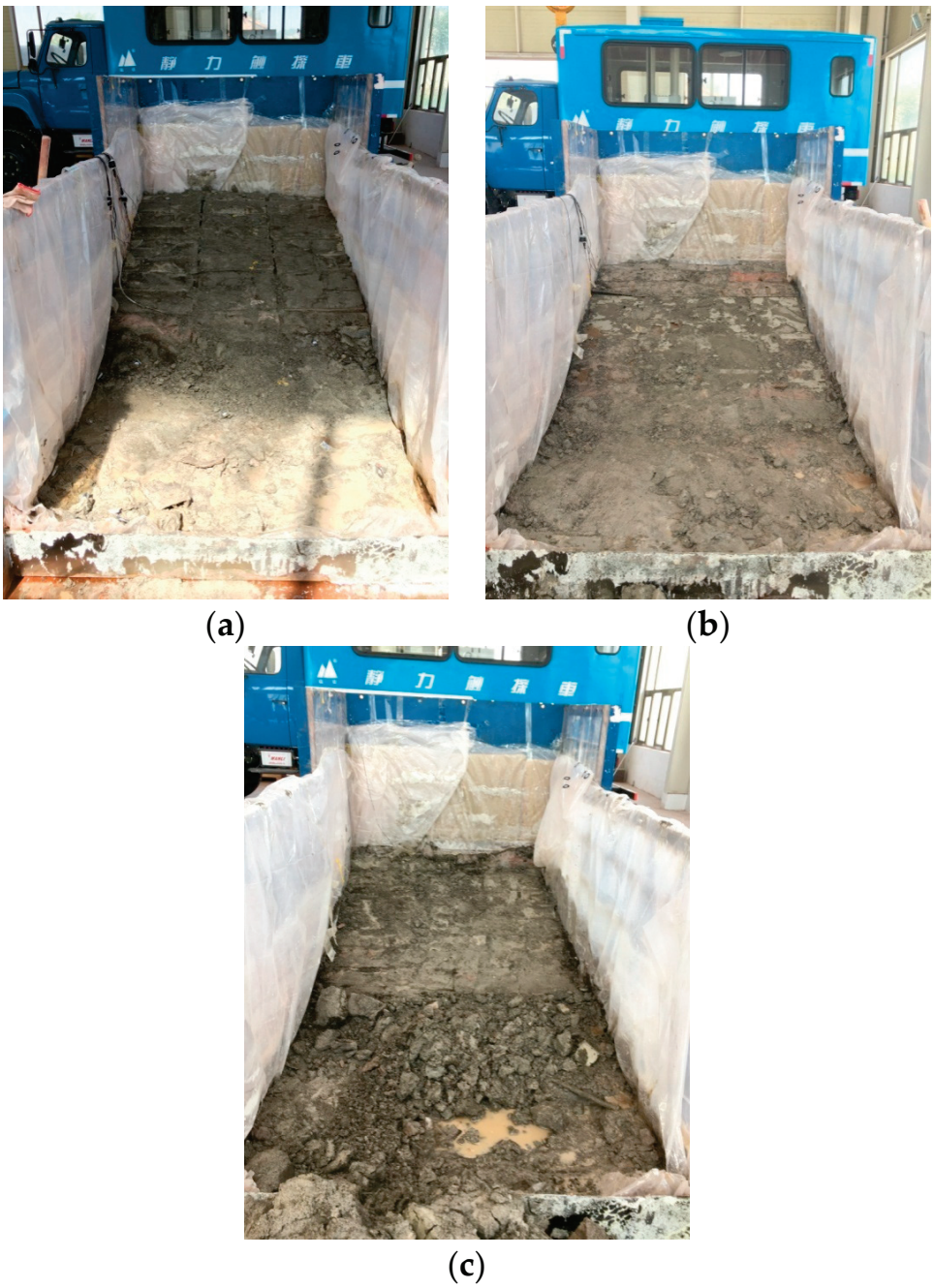

Figure 16. Photos of model layer removal. (**a**) Photo after removal of the first layer. (**b**) Photo after removal of the second layer. (**c**) Photo after removal of the third layer.

After the first layer was removed, the foot of the model slope was completely destroyed, the remaining slope body was relatively complete as a whole, and the surface water content of the remaining slope was high, which indicated that the surface slope body was destroyed and the reservoir water penetrated into the slope body. After removing the

second layer, the foot of the model slope was destroyed, the remaining slope was more complete as a whole, and the remaining slope surface was drier, showing that the reservoir water did not seep through the second layer of the slope surface. This showed that this layer of the slope surface did not undergo high levels of deformation and was relatively complete. It can be inferred that cracks appeared on the surface of the rear edge structure of the model, and the first layer was fully penetrated but did not extend to the second and third layers. After three layers were removed, the slope body was still dry, and the lowest layer of the model was seriously damaged near the foot of the slope, which was caused by damage to the foot due to reservoir water penetration. In conclusion, in the topmost slope of the model slope, overturning and sliding failure occurred to a great extent along the upper structural plane.

5.2. Induced Factors and Failure Mechanism of Slope Slip

Under the action of seismic load, due to the difference in the acceleration vector directions between the upper blocks of the slope and the phenomenon of the acceleration in the front block being greater than that in the rear block, cracks along joints occurred between blocks, which provided favorable conditions for block formation. The reservoir water seeped into the cracks and the upper structural plane, which quickly reached the saturation state, weakened its strength, further enlarged the cracks, and promoted the formation of massive and sliding zones. The sudden drop in the level of reservoir water caused a large increase in PGA on the uphill slope as well as a large increase in the downhill sliding force on the uphill slope. The acceleration in the rear block of the upper slope was greater than that in the front block, while the rear block pushed the front block to overturn and slide at a distance of 35 cm from the front edge to the bottom of the model, and they collided with each other during the sliding process to form debris flow based on the foot of the slope. Therefore, it can be concluded that the main process of a landslide is as follows: the upper part of the slope cracks due to an earthquake; with the increase in the intensity of the earthquake, the muddied weak interlayer in the front section of the slope forms a sliding surface; during an earthquake, sliding damage gradually occurs in the front section of the slope, and finally, accumulation occurs at the foot of the slope.

Through detailed analyses of acceleration, dynamic soil pressure, dynamic strain and displacement response during an earthquake, sliding induction factors, and failure mechanisms of model slopes, the slope failure phenomena we observed were analyzed. Cracks caused by seismic loads provide favorable conditions for the formation of induced landslides and the slide deformation of a slope body. Under the action of seismic load, different acceleration response directions exist among rock layers, which result in different rock layers in the direction of motion. Under the action of vertical seismic waves, upward vibrations between rock layers will occur, and speed and direction differences will occur during the deformation process of a slope during an earthquake, resulting in dislocation and tension between rock layers and the formation of cracks. Due to the difference in the acceleration response direction, under the action of horizontal seismic waves, the acceleration of the foot of a slope is higher than that of the top of a slope; thus, a tension crack is formed at the rock layer boundary.

6. Conclusions

In this study, using a shaking table test and finite element numerical simulation, the dynamic response law of slopes with weak interlayers under the combined action of reservoir water and seismic force was defined, and the ring breaking mechanism of weak interlayers was revealed. The main conclusions are as follows:

1. Seismic waves are affected by weak interlayers, which overlap repeatedly between a weak interlayer and a slope surface. The acceleration amplification effect is about 1.8 times larger than that of a homogeneous slope. The acceleration response of the input vertical and horizontal seismic waves in a slope is magnified from the bottom to the top along the slope surface and reaches the maximum value at the top of the slope. A vertical earthquake has a significant influence on the dynamic response of a slope. The magnification factor of peak acceleration can reach 0.83 times the horizontal peak acceleration. An increase in the intensity of a vertical earthquake is more likely to induce damage on the top and in the middle of a slope.
2. When considering the mud action of reservoir water on weak interlayers, with the increase in the input seismic acceleration, sliding failure first occurs in the mud area located in the weak interlayer. The shear entrance and shear exit of slope sliding are located in the middle and at the foot of the slope, respectively, which indicates that the stability of the weak interlayer directly affected by reservoir water is the worst.
3. The displacement of a slope can be generalized into three stages with the increase in a seismic wave. The first stage is elastic deformation, when the displacement increases uniformly from 0 to 0.3 g. In the second stage, when the displacement is 0.3–0.45 g, the displacement first decreases and then increases, which is the plastic deformation stage. The maximum displacement of the slope surface also appears, up to 31.2 mm. The third stage is when the surface displacement decreases sharply after reaching 0.45 g, which is the sliding destabilization stage, indicating that the slope begins to slide and destabilize at this time.
4. The failure mode of the slope is as follows: cracking occurs in the upper part of the slope due to an earthquake. With the increase in the intensity of the earthquake and reservoir water infiltration, the crack propagation is aggravated, and sliding damage occurs gradually in the front section of the slope. Finally, accumulation occurs at the foot of the slope. The failure mode of the slope model reveals that the sliding surface is controlled by a weak interlayer. When a strong earthquake and the water level in the reservoir area jointly affect the weak-interlayer slope, the slope is in the plastic deformation and instability stage. The stability of the slope may be overestimated, and sliding instability easily occurs. Therefore, monitoring and treatment must be carried out.

In the numerical simulation part of this study, we only considered the effect of the static water load of reservoir water, which is not in line with reality and requires the dynamic calculation of fluid structure coupling.

Author Contributions: Conceptualization, H.T. and W.N.; methodology, H.T. and W.N.; software, H.T. and W.N.; validation, H.T. and W.N.; formal analysis, H.T. and W.N.; investigation, H.T. and W.N.; resources, H.T. and W.N.; data curation, H.T. and W.N.; writing—original draft preparation, H.T. and W.N.; writing—review and editing, H.T. and W.N. All authors have read and agreed to the published version of the manuscript.

Funding: This research received no external funding.

Institutional Review Board Statement: Not applicable.

Informed Consent Statement: Not applicable.

Data Availability Statement: Data used to support the findings of this study are available from the corresponding author upon request.

Conflicts of Interest: The authors declare that the research was conducted in the absence of any commercial or financial relationships that could be construed as potential conflicts of interest.

References

1. Zhang, J.M. Research status and development trend of rock slope stability with weak interlayer. *Chin. J. Eng. Geol.* **2020**, *28*, 626–638. [CrossRef]
2. Niu, Y.; Yang, X.Z.; Zhao, J.L.; Ji, W.K. Seismic stability analysis of slope with sandwich based on upper limit analysis. *J. Highw. Transp. Sci. Technol.* **2019**, *36*, 38–45.
3. Lin, M.L.; Lin, C.H.; Li, C.H.; Liu, C.Y.; Hung, C.H. 3D modeling of the ground deformation along the fault rupture and its impact on engineering structures: Insights from the 1999 Chi-Chi earthquake, Shigang District, Taiwan. *Eng. Geol.* **2021**, *281*, 105993. [CrossRef]
4. Li, S.D.; Li, X.; Zhang, J.; He, J.M.; Li, S.H.; Wang, Y.C. Research on formation mechanism of Tangjiashan landslide and overall stability of barrier dam. *Chin. J. Rock Mech. Eng.* **2010**, *29* (Suppl. S1), 2908–2915.
5. Xu, L.; Pei, X.J.; Wu, J.H. Stability evaluation and treatment of Zhengjiashan Landslide in Sichuan Earthquake stricken area. *J. Chang. Inst. Technol. (Nat. Sci. Ed.)* **2010**, *11*, 68–70+81.
6. Haeri, S.M.; Kavand, A.; Rahmani, I.; Torabi, H. Response of a group of piles to liquefaction-induced lateral spreading by large scale shake table testing. *Soil Dyn. Earthq. Eng.* **2012**, *38*, 25–45. [CrossRef]
7. Panah, A.K.; Eftekhari, Z. Shaking table tests on polymeric-strip reinforced-soil walls adjacent to a rock slope. *Geotext. Geomembr.* **2021**, *49*, 737–756. [CrossRef]
8. Wang, H.L.; Jiang, Z.H.; Xu, W.Y.; Wang, R.B.; Xie, W.C. Physical model test on deformation and failure mechanism of deposit landslide under gradient rainfall. *Bull. Eng. Geol. Env.* **2022**, *81*, 66. [CrossRef]
9. Xiao, J.F.; Li, Y.A.; Hu, Y.; Zhang, S.; Cai, J.M. Model tests on deformation characteristics of ancient bank landslide under water level fluctuation and rainfall. *Rock Soil Mech.* **2021**, *42*, 471–480. [CrossRef]
10. Mburu, J.W.; Li, A.-J.; Lin, H.-D.; Lu, C.-W. Investigations of Unsaturated Slopes Subjected to Rainfall Infiltration Using Numerical Approaches—A Parametric Study and Comparative Review. *Sustainability* **2022**, *14*, 14465. [CrossRef]
11. Zhang, M.S.; Dong, Y.; Sun, P.P. Impact of reservoir impoundment-caused groundwater level changes on regional slope stability: A case study in the Loess Plateau of Western China. Environ. *Earth Sci.* **2012**, *66*, 1715–1725. [CrossRef]
12. Manenti, S.; Amicarelli, A.; Palazzolo, N.; Bordoni, M.; Creaco, E.; Meisina, C. Post-Failure Dynamics of Rainfall-Induced Landslide in Oltrepò Pavese. *Water* **2020**, *12*, 2555. [CrossRef]
13. Wang, R.; Wan, J.; Cheng, R.; Wang, Y.; Wang, Z. Physical and Numerical Simulation of the Mechanism Underpinning Accumulation Layer Deformation, Instability, and Movement Caused by Changing Reservoir Water Levels. *Water* **2023**, *15*, 1289. [CrossRef]
14. Jiang, Z.H.; Wang, H.L.; Xie, W.C. Deformation mechanism of deposit landslide induced by fluctuations of reservoir water level based on physical model tests. Environ. *Earth Sci.* **2021**, *80*, 410. [CrossRef]
15. Upomo, T.C.; Chang, M.; Kusumawardani, R.; Prayitno, G.A.; Kuo, C.-P.; Nugroho, U. Assessment of Petobo Flowslide Induced by Soil Liquefaction during 2018 Palu–Donggala Indonesian Earthquake. *Sustainability* **2023**, *15*, 5371. [CrossRef]
16. Kim, H.; Kim, D.; Lee, Y.; Kim, H. Effect of Soil Box Boundary Conditions on Dynamic Behavior of Model Soil in 1 g Shaking Table Test. *Appl. Sci.* **2020**, *10*, 4642. [CrossRef]
17. WANG, K.L.; LIN, M.L. Initiation and displacement of landslide induced by earthquake—A study of shaking table model slope test. *Eng. Geol.* **2011**, *122*, 106–114. [CrossRef]
18. Yang, H.; Cui, S.; Pei, X.; Fan, X.; Lei, J. Multiple earthquake-induced progressive failure of bedding slopes with a saturated weak layer: Shaking table model tests. *Soil Dyn. Earthq. Eng.* **2023**, *170*, 107906. [CrossRef]
19. Wang, L.W.; Wen, H.; Zhang, Z.P.; Du, Y.X.; Fu, X.D. Seismic dynamic response analysis and stability evaluation of Ganjiazhai Landslide based on QUAKE/W and SLOPE/W. *Sci. Technol. Eng.* **2018**, *18*, 274–280.
20. Yan, Z.X.; Gao, L.; Peng, N.B.; Ren, Z.H.; Guo, B. Study on seismic dynamic response of bedding rock slope. *Rock Soil Mech.* **2012**, *33* (Suppl. S2), 85–90. [CrossRef]
21. Jin, Y.; Kim, D.; Jeong, S.; Kim, H. Analysis of Multilayered Ground Amplification Characteristics by Scaled-Down Model Tests. *Appl. Sci.* **2022**, *12*, 3432. [CrossRef]
22. Huang, D.; Xie, Z.Z.; Song, Y.X.; Meng, Q.J.; Luo, S.L. Centrifuge model test study on the toppling deformation of the anti-dip soft-hard interbedded rock slopes. *Chin. J. Rock Mech. Eng.* **2021**, *40*, 1357–1368. [CrossRef]
23. Málaga-Chuquitaype, C. Estimation of peak displacements in steel structures through dimensional analysis and the efficiency of alternative ground-motion time and length scales. *Eng. Struct.* **2015**, *101*, 264–278. [CrossRef]
24. Guo, M.-Z.; Gu, K.-S.; Wang, C. Dynamic Response and Failure Process of a Counter-Bedding Rock Slope under Strong Earthquake Conditions. *Symmetry* **2022**, *14*, 103. [CrossRef]
25. Buckingham, E. On physically similar systems, illustrations of the use of dimensional equations. *Phys. Rev.* **1914**, *4*, 345–376. [CrossRef]
26. Cai, G.-Q.; Su, Y.-L.; Zhou, A.-N.; Yin, F.-J.; Shi, Y.-H. An elastic-viscoplastic model for time-dependent behavior of unsaturated soils. *Comput. Geotech. Vol.* **2023**, *159*, 105415. [CrossRef]

27. Rizzitano, S.; Cascone, E.; Biondi, G. Oupling of topographic and stratigraphic effects on seismic response of slopes through 2D linear and equivalent linear analyses. *Soil Dyn. Earthq. Eng.* **2014**, *67*, 66–84. [CrossRef]
28. Zhang, J.W.; Zhou, A.H.; Chi, M.J.; Wang, Y.S.; Chen, S. Study on optimal boundary range in numerical simulation of slope seismic response. *J. Disaster Prev. Mitig. Eng.* **2022**, *42*, 34–41. [CrossRef]

remote sensing

MDPI

Article

A Monitoring Method Based on Vegetation Abnormal Information Applied to the Case of Jizong Shed-Tunnel Landslide

Qing Guo [1,*], Lianzi Tong [1,2] and Hua Wang [1,2]

[1] Aerospace Information Research Institute, Chinese Academy of Sciences, Beijing 100094, China
[2] School of Electronic, Electrical and Communication Engineering, University of Chinese Academy of Sciences, Beijing 100049, China
* Correspondence: guoqing@aircas.ac.cn; Tel.: +86-010-82178961

Abstract: Landslides are one of the most dangerous natural disasters, which have affected national economic development and social stability. This paper proposes a method to indirectly monitor the deformation characteristics of landslides by extracting the abnormal vegetation information, especially for the inaccessible high-mountain landslides in southwestern China. This paper extracts the vegetation anomaly information in the Jizong Shed-Tunnel landslide which is located on the main traffic road to Tibet by the optical remote sensing Gaofen-1 (GF-1) data, and analyzes the temporal and spatial characteristics of the vegetation anomaly information through a time series. Then, we use the small baseline subsets interferometry synthetic aperture radar (SBAS-InSAR) technology to process Sentinel-1 data to obtain the time-series surface deformation information. Finally, we analyze and verify the results of the two methods. The results show that there is obvious vegetation coverage (VC) decline, with a maximum increasing percentage of 8.77% for the low and medium VC, and obvious surface deformation around the landslide, with the highest settlement rate of between 0 mm/year and 30 mm/year. Through the time-series analysis, we find that the change trends of the two methods are basically the same. This paper shows that the method of using abnormal vegetation information to monitor the Jizong Shed-Tunnel landslide has a certain degree of reliability and practicability. It can provide a new idea and effective supplement for landslide monitoring.

Keywords: landslide monitoring; Jizong Shed-Tunnel landslide; optical remote sensing; vegetation coverage; SBAS-InSAR; surface deformation

Citation: Guo, Q.; Tong, L.; Wang, H. A Monitoring Method Based on Vegetation Abnormal Information Applied to the Case of Jizong Shed-Tunnel Landslide. *Remote Sens.* **2022**, *14*, 5640. https://doi.org/10.3390/rs14225640

Academic Editors: Stefano Morelli, Veronica Pazzi and Mirko Francioni

Received: 20 September 2022
Accepted: 4 November 2022
Published: 8 November 2022

1. Introduction

Landslides are defined as the instability and destruction of rock, soil, or other artificial materials under the action of gravity. They have become one of the most dangerous natural disasters due to their suddenness and destructive power and being prone to secondary disasters, causing huge casualties and economic losses all over the world [1–4]. China is also one of the countries prone to landslide disasters. Especially in the southwest of China, due to the large undulation terrain, the loose soil structure, and heavy rainfall, landslide disasters are extremely prone to occurring [5–10]. The Jizong Shed-Tunnel landslide is located in the southwestern Yunnan Province. The area is rich in mountains and is located next to the G214 National Highway known as the "lifeline" of Sichuan and Tibet. Once a landslide occurs, it will block the normal passage of the G214 National Highway and cause serious casualties and economic losses. Therefore, the identification and continuous monitoring of landslides is an effective way to prevent and control landslide hazards.

Many scholars have done a lot of work on landslide monitoring. Common landslide monitoring methods include the global navigation satellite system (GNSS) methods and the interferometry synthetic aperture radar (InSAR) methods. The global positioning system (GPS), as one part of the GNSS system, is widely used. GPS monitoring has the advantages of high automation degree, high precision, no need to meet the visibility between monitoring

sites, and all-weather real-time monitoring [11]. In the era of single GPS, GPS methods already have many precise applications for monitoring landslides [12–14]. In recent years, with the development of GNSS technology, GNSS technology has more combined applications and is developing towards low costs. Peng et al. [15] have used the BeiDou Navigation Satellite System (BDS)/GPS single-point positioning method to effectively monitor sliding landslides. Notti et al. [16] have used the low-cost GPS to continuously monitor unstable slopes in northwestern Italy, which verifies the accuracy of the method. At the same time, Šegina et al. [17] developed a low-cost GNSS monitoring system for a deep-seated landslide in north-western Sloveni, further demonstrating the effectiveness of low-cost GNSS. However, GPS satellite signals are easily blocked in complex terrain and dense vegetation coverage areas, such as high-mountain areas, which affects the accuracy. Moreover, GPS collects data at points, so it is difficult to monitor landslides comprehensively [18,19].

InSAR technology has the characteristics of all-weather and all-day operation and can obtain large-area, long-term series of surface deformation information [20]. InSAR also can generate the regional digital elevation model (DEM) from paired radar images, which has particular significance for areas without terrain data and can provide basic data for landslide hazard assessments [21]. In 2016, He et al. [22] used the optical and InSAR technology to monitor loess landslides and accurately analyzed the change of landslide surface elevation. In 2019, Huang et al. [23] used the small baseline subsets (SBAS)-InSAR technology to monitor the deformation trend of Baige landslides, which proves the feasibility of SBAS-InSAR technology for landslide monitoring. In 2020, Jiang et al. [24] used the coherent scanner (CS)-InSAR Technology for monitoring potential landslides in western China. However, InSAR is susceptible to the phase delay of water vapor in mountainous areas. Simultaneously, the characteristics of InSAR technology slant-range imaging can easily cause registration errors and spatial baseline decoherence in areas with large terrain undulations [14,19]. In Yunnan Province, as the southwest region of China, the terrain is undulating. The high-mountain landslides in this area are mostly lush vegetation, and the high vegetation coverage can also affect the InSAR results.

Landslide creeping is a stage in the development process of landslide deformation which is slow for a long time and difficult to be detected at the beginning [25]. During the creep stage of the landslide, there will be sudden changes to the water level, the uplift of the soil slope, and the collapse or relaxation of the surrounding rock mass. This is reflected in the growth status of vegetation on the landslide. Of course, not all the landslides at the creeping stage show obvious characteristics of changes to surface vegetation, but some do exist (such as Baige landslide [26] and Su village landslide [27]). At present, many scholars use remote sensing images to study the vegetation in landslide areas. In 2012, Lu et al. [28] calculated the normalized difference vegetation index (NDVI) on Landsat5 TM data before and after the earthquake, and have studied the vegetation recovery status of the Maoxian landslide in Sichuan after the earthquake. In 2015, He and Zhang [29] used the NDVI value to set a threshold to identify landslides, extract landslide feature information, and perform area statistics. In 2020, Piroton et al. [30] used the NDVI difference values of the pre-landslide image from the post-landslide image as a complementary qualitative analysis for landslide monitoring. In 2022, Xun et al. [31] selected the NDVI as a feature describing the vegetation information for the extraction of potential landslides. However, most studies are aimed at monitoring the restoration of vegetation after landslides or as one of the characteristics of identifying landslides. The studies on the analysis and monitoring of landslide creep using vegetation cover changes are few currently.

Both GPS and InSAR methods have certain limitations in the high-mountain areas of southwest China. In 2020, Guo et al. [32] used Gaofen (GF) satellite data to explore the relationship between vegetation anomalies and landslides, taking the Xinmocun landslide as an example. Subsequently, by studying the Baige landslide, Guo et al. [33] believe that potential landslides in high-mountain areas can be preliminarily investigated economically and effectively through vegetation change. Therefore, in order to further verify the possibility of using vegetation changes to monitor landslides, this paper uses the method of

calculating the vegetation coverage to extract the abnormal vegetation information of the Yunnan Jizong Shed-Tunnel landslide from optical remote sensing Gaofen-1 (GF-1) data. Meanwhile, the SBAS-InSAR method, which more easily obtains more comprehensive monitoring the GPS method, is used to obtain the time-series surface deformation of the landslide area, to further support the indirect optical monitoring method. The two aspects are combined to analyze the temporal and spatial characteristics of landslide creep and verify the feasibility and effectiveness of the method in this paper. This study uses the abnormal vegetation information to indirectly monitor the Jizong Shed-Tunnel landslides in an effective and sequential manner and provides a new idea and monitoring technology for high-mountain landslides in the southwest region, which can effectively supplement the landslide monitoring methods.

2. Study Area and Data

2.1. Study Area

The Jizong Shed-Tunnel landslide is located in Ladong Mountain on the east bank of the Jinsha River, in Diqing Tibetan Autonomous Prefecture, Yunnan Province (Figure 1). The geographic coordinates of the center of the landslide source area are 99°23′43″E, 28°7′53″N. This is the active landslide that can be seen on the G214 National Highway. As one of the main highways of the Chinese transportation network, the G214 National Highway is the only main transportation road from Yushu area to Xining and Sichuan-Tibet. It is the economic line and lifeline of the surrounding areas. Therefore, maintaining the safety of G214 National Highway is an important task to guarantee the economic stability and social stability of the surrounding areas [34].

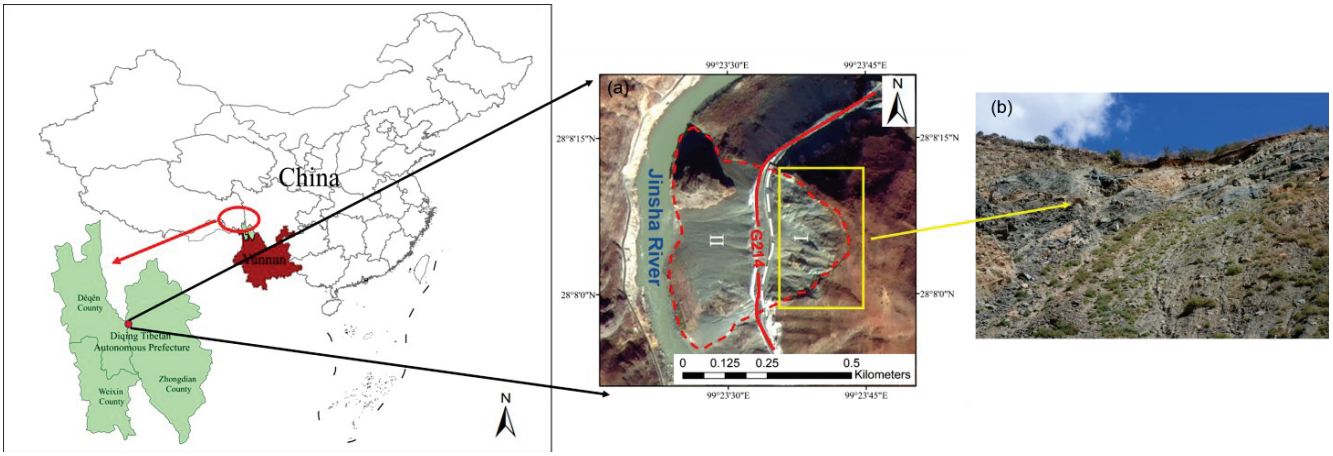

Figure 1. The location and Google Earth image of Jizong Shed-Tunnel landslide. (**a**) Optical GF-1 fused true color image; (**b**) Site investigation image.

The Jizong Shed-Tunnel landslide is near the normal fault, which is mainly composed of volcanic rock, slate, and limestone. The overall slope is between 30° and 45°. Moreover, there is abundant precipitation in the study area. Due to road construction and precipitation, the Jizong Shed-Tunnel landslide experienced a large slide in 2015, then the landslide was in a slow creep stage. The landslide moves along the slope layer from the top of the hillside and slides to the Jinsha River for accumulation, which can be divided into the source area (Figure 1a(I)) and the accumulation area (Figure 1a(II)) of the landslide. The creep of the landslide is mainly caused by the slight deformation and cracks at the rear edge of the upper landslide area. Therefore, the main analysis area is located in the upper landslide area.

2.2. Data

This paper selects GF-1 optical images for vegetation anomaly information extraction, Sentinel-1 A satellite radar images for deformation monitoring, and shuttle radar topogra-

phy mission digital elevation model (SRTM DEM) data as the auxiliary external DEM to eliminate the influence of terrain factors on the deformation monitoring.

2.2.1. GF-1 Optical Image

The GF-1 satellite is equipped with a panchromatic/multispectral PMS camera. The PMS camera can acquire panchromatic (PAN) images with a resolution of 2 m and multispectral (MS) images with a resolution of 8 m (blue, green, red, and near-infrared 4 bands), while the imaging width is 60 km. Thus, the GF-1 satellite provides reliable data formations for Earth observation.

Because the high cloud cover in the Jizong Shed-Tunnel landslide in the summer and the growth of vegetation in spring is easily affected, this paper selects eight GF-1 datapoints around November from 2013 to 2020 to analyze the abnormal vegetation information in order to avoid the influence of the season on the growth of plants. The image data are shown in Table 1.

Table 1. GF-1 image data.

Number	Image Time	Number	Image Time	Number	Image Time
1	5 November 2013	4	22 December 2016	7	24 November 2019
2	8 November 2014	5	11 November 2017	8	30 November 2020
3	16 November 2015	6	19 November 2018		

2.2.2. Sentinel-1 A Radar Image

The Sentinel-1 satellite which carries a C-band synthetic aperture radar is composed of Sentinel-1 A and Sentinel-1 B. It provides reliable and repeated wide-area monitoring all-day and through all weather, so it can be used to obtain surface deformation and monitor large-scale resources. It has four working modes: stripmap (SM), interferometric wide swath mode (IW), extra wide swath mode (EW), and wave mode (WM). The Sentinel-1 satellite has an ultra-high radiation resolution and excellent coverage performance and revisit performance, which meets the research requirements of this paper.

Since the time interval of the Sentinel-1 satellite data in the study area from 2014 to 2016 was too large, and this paper mainly studies the subsequent landslide creep stage after 2015, in order to ensure the correlation between the InSAR data, this paper selects 57 scenes of the Sentinel-1 A satellite's single look complex (SLC) data with the IW working mode from 2017 to 2020 with the largest time interval of 24 days. All images are from the ascending orbit data with the same orbit path number 99 and frame number 1270. The image data are shown in Table 2.

Table 2. Sentinel-1 A image data.

Number	Image Time	Polarization	Number	Image Time	Polarization
1	18 March 2017	VV	30	12 February 2019	VV
2	30 March 2017	VV	31	8 March 2019	VV
3	23 April 2017	VV	32	1 April 2019	VV
4	17 May 2017	VV	33	25 April 2019	VV
5	10 June 2017	VV	34	19 May 2019	VV
6	4 July 2017	VV	35	12 June 2019	VV
7	9 August 2017	VV	36	6 July 2019	VV
8	2 September 2017	VV	37	30 July 2019	VV
9	26 September 2017	VV	38	23 August 2019	VV
10	20 October 2017	VV	39	16 September 2019	VV
11	13 November 2017	VV	40	10 October 2019	VV

Table 2. *Cont.*

Number	Image Time	Polarization	Number	Image Time	Polarization
12	7 December 2017	VV	41	3 November 2019	VV
13	31 December 2017	VV	42	27 November 2019	VV
14	24 January 2018	VV	43	21 December 2019	VV
15	17 February 2018	VV	44	14 January2020	VV
16	13 March 2018	VV	45	7 February2020	VV
17	6 April 2018	VV	46	2 March 2020	VV
18	30 April 2018	VV	47	26 March 2020	VV
19	24 May 2018	VV	48	19 April 2020	VV
20	17 June 2018	VV	49	13 May2020	VV
21	11 July 2018	VV	50	6 June 2020	VV
22	4 August 2018	VV	51	30 June 2020	VV
23	28 August 2018	VV	52	24 July 2020	VV
24	21 September 2018	VV	53	17 August 2020	VV
25	15 October 2018	VV	54	10 September 2020	VV
26	8 November 2018	VV	55	4 October 2020	VV
27	2 December 2018	VV	56	28 October 2020	VV
28	26 December 2018	VV	57	21 Nevember 2020	VV
29	19 January 2019	VV			

2.2.3. SRTM DEM Data

SRTM DEM data are synthesized in the United States using the SRTM system to obtain the radar image data from 60 degrees north latitude to 60 degrees south latitude.

SRTM DEM data can be divided into SRTM 1 (resolution of 30 m) and SRTM 3 (resolution of 90 m) data. This article uses SRTM 1 data with a latitude and longitude span of $1^\circ \times 1^\circ$. In order to cover the study area, we selected the SRTM N28E099 and N27E099 data.

3. Methods

3.1. Image Pre-Processing Method

Image fusion can complement the feature attributes of different data and make up for the incompleteness and uncertainty caused by single pieces of information, which is beneficial to the target recognition, analysis, and application of remote sensing [35].This paper adopts and compares the five fusion methods which are generally accepted by the public: nearest neighbor diffusion (NND) [36], principal component analysis (PCA) [37], Gram-Schmidt (GS) [38], high pass filter (HPF) [39], and Pansharpening fusion [40], and analyzes the fusion method suitable for the Jizong Shed-Tunnel landslide area. This enables MS images to improve the spatial resolution while ensuring the spectral information is unchanged as much as possible, so as to enhance the visual interpretation effect of the Jizong Shed-Tunnel landslide and improve the ability to detect vegetation growth and change information.

3.2. Vegetation Abnormal Information Extraction Method

In ideal theory, since this paper obtains optical images at nearly the same time every year for the same study area, the vegetation information is basically unchanged. Therefore, when there is obvious vegetation change information, it means that the vegetation in this area is abnormal. We use the vegetation coverage (VC) to obtain the information about vegetation abnormalities caused by the landslide creep. The VC is an important parameter to describe the ground vegetation cover. The commonly used remote sensing calculation method for VC is to estimate it based on the vegetation index. This paper adopts the pixel dichotomy model proposed by Li [41] and uses the vegetation index to estimate the VC. Since the vegetation in the study area is susceptible to the influence of the bare soil background, NDVI which is commonly used is difficult to apply to this area, while other vegetation indexes such as the green normalized difference index (GNDVI) can avoid this phenomenon. Therefore, this paper chooses the GNDVI to conduct the experiment and

finds that GNDVI can indeed be well applied in the study area. So, we finally chose GNDVI as the vegetation index of the study area. GNDVI, as the vegetation index that extracts the vegetation information and accurately reflects the vegetation coverage through the ratio processing, can eliminate the errors of the altitude of the Sun, the atmospheric attenuation, and the terrain changes. The formula is shown in Formula (1):

$$\mathrm{GNDVI} = \frac{\rho_{\mathrm{NIR}} - \rho_{\mathrm{G}}}{\rho_{\mathrm{NIR}} + \rho_{\mathrm{G}}} \tag{1}$$

Herein, ρ_{NIR} is the reflectivity in the near-infrared band, and ρ_{G} is the reflectivity in the green band.

The specific formula of the pixel dichotomy model to calculate VC is shown in (2):

$$\mathrm{VC} = \begin{cases} 0 & , \ \mathrm{GNDVI} \le \mathrm{GNDVI_{soil}} \\ \frac{\mathrm{GNDVI} - \mathrm{GNDVI_{soil}}}{\mathrm{GNDVI_{veg}} - \mathrm{GNDVI_{soil}}}, & \mathrm{GNDVI_{soil}} \le \mathrm{GNDVI} \le \mathrm{GNDVI_{veg}} \\ 1 & , \ \mathrm{GNDVI} \le \mathrm{GNDVI_{soil}} \end{cases} \tag{2}$$

Herein, VC is the value of vegetation coverage. $\mathrm{GNDVI_{soil}}$ is the value of GNDVI in the bare soil or areas without vegetation cover, and $\mathrm{GNDVI_{veg}}$ is the value of GNDVI in areas completely covered by plants, which are pure vegetation pixels. Low VC values near 0 represent completely barren surfaces (rock or soil) or no vegetation-covered areas, while high VC values near 1 represent luxuriant vegetation.

When using the pixel dichotomy model to calculate the VC, the most important thing is to obtain the values of $\mathrm{GNDVI_{soil}}$ and $\mathrm{GNDVI_{veg}}$. In the actual situation, according to the definition of the parameters, these two values will change with time and space [42]. At present, we mainly count the value of GNDVI from the remote sensing images and set the confidence interval according to the cumulative percentage to define the value of $\mathrm{GNDVI_{soil}}$ and $\mathrm{GNDVI_{veg}}$. Because there are many remote sensing images in this article, in order to avoid the result analysis error caused by different confidence interval selections, this article makes multiple adjustments and calculations to obtain a unified confidence interval. The VC calculation flow chart is in Figure 2, and the specific operation steps are as follows:

(1) Calculate the initial $\mathrm{GNDVI_{soil}}$ and $\mathrm{GNDVI_{veg}}$ values of each time phase. We count the cumulative percentage of each GNDVI value in the image at first and select the initial confidence interval based on empirical values. We first use the 5–95% confidence interval [43] as the initial value to try. Then, we calculate the initial $\mathrm{GNDVI_{soil}}$ and $\mathrm{GNDVI_{veg}}$ based on the left and right boundaries of the confidence interval;

(2) Adjust the confidence interval for each time phase. We calculate the VC by using the values of $\mathrm{GNDVI_{soil}}$ and $\mathrm{GNDVI_{veg}}$GNDVIveg determined in step (1) and enhance results through the pseudo color density segmentation to visually judge the agreement degree of the bare land and vegetation area between in the VC map and in the original image. If not, repeat the above steps to redefine the confidence interval and perform the calculation again until the obtained result is the optimal fit;

(3) Determine the final uniform confidence interval. In order to unify the thresholds of each time phase and obtain the consistent and best-fitting VC as much as possible, we comprehensively consider the confidence intervals of each phase and unify them to obtain the final confidence interval consistent with each time phase.

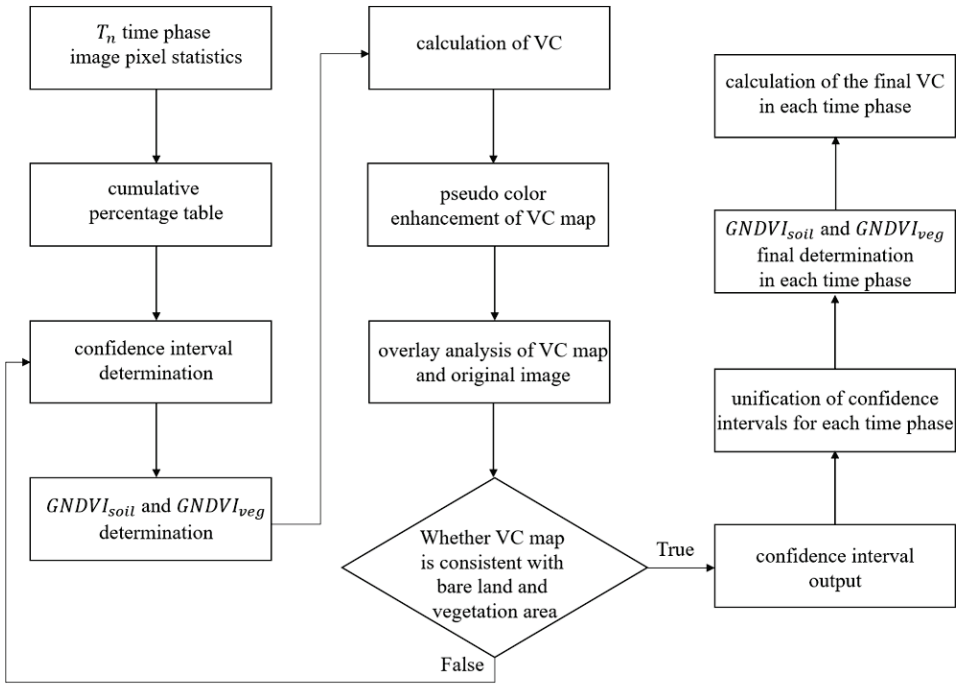

Figure 2. The VC calculation flow chart.

3.3. SBAS-InSAR Method

The traditional differential (D)-InSAR method is affected by factors such as the baseline length, atmospheric propagation delay, and spatial resolution, so it cannot be monitored well in most areas [44,45]. In recent years, researchers have successively proposed time-series InSAR methods such as the permanent scatterer (PS)-InSAR technology [46,47] and SBAS-InSAR technology [48] with the development of InSAR technology. The coherence requirements of PS points are higher than those obtained by SBAS, so PS-InSAR technology is often used for deformation monitoring in urban areas, and the SBAS-InSAR method is more effective than the PS-InSAR method in monitoring landslides in mountainous areas. Meanwhile, SBAS-InSAR is based on multi-master images, which overcomes the poor coherence shortcoming of some interferograms caused by using only one master image. Moreover, in SBAS-InSAR where only interferograms with small baselines are selected for the time-series analysis, the deformation results are denser and more reliable. At the same time, SBAS-InSAR method can still monitor the deformation rate in the vegetation coverage area [49]. The study area of this paper is with the vegetation coverage and in the mountainous area, so this paper chooses the SBAS-InSAR method to study the surface deformation of the Jizong Shed-Tunnel landslide.

The SBAS-InSAR method is a time-series InSAR method proposed by Berardino et al. [48]. This method mainly uses multiple synthetic aperture radar (SAR) images as the main image and forms different short baseline subsets according to the principle of short baseline interference to generate differential interference images. Then, based on the least square rule, the average surface deformation rate of the study area and the time series of the surface deformation are obtained by using the singular value decomposition (SVD) [48,50].

The basic principles of the SBAS-InSAR method are as follows:

(a) When there are *N* scenes of SAR images in the study area, each SAR image will be differentially interfered with by at least another *N-1* scenes image to form an interference image pair. Finally, *M* interference image pairs will be obtained. Meanwhile, the

image with most interference pairs is chosen as the main image, and the rest of the images are the slave images. The value range of M is shown in Formula (3) [51]:

$$N/2 \leq M \leq (N(N-1))/2 \tag{3}$$

(b) Differential interferogram is collected from M interferometric pairs by using the InSAR phase deformation extraction method. The final interferogram is obtained through the phase filtering and unwrapping. The interference phase of the j-th interferogram φ_j can be expressed as Formula (4):

$$\Delta\varphi_j\,(x,y) = \varphi_B\,(x,y) - \varphi_A\,(x,y) \approx 4\pi/\lambda\,[d(t_B,x,y) - d(t_A,x,y)] \tag{4}$$

Herein, t_A is the acquisition time of the main image, t_B is the acquisition time of the slave image, λ is the central wavelength, and x, y are the azimuth and distance coordinates of the image, respectively, φ_A, φ_B are the interference phase of the main image and the slave image, respectively.

The interferograms after the phase filtering and unwrapping are arranged in the time order of the image, and then, the vector phase of the interferogram can be directly expressed in the form of matrix. In the matrix, each row corresponds to a differential phase interferogram and each column corresponds to the SAR images at different times. The column of the main image and the slave image in the matrix is ± 1, and the remaining columns are all 0, as shown in Formula (5):

$$G\varphi = \Delta\varphi \tag{5}$$

Herein, G is an $M \times N$ matrix, expressed as: $G = \begin{bmatrix} 0 & -1 & 0 & 1 & \cdots & 0 & 0 & 0 \\ -1 & 0 & 1 & 0 & \cdots & 0 & 0 & 0 \\ \vdots & \vdots & \vdots & \vdots & \vdots & \vdots & \vdots & \vdots \\ 0 & 0 & 0 & 0 & \cdots & -1 & 0 & 1 \end{bmatrix}$,

φ is the interference phase.

(c) The G matrix is solved by using the SVD method through the least square rule, as shown in Formula (6):

$$G = USV^T \tag{6}$$

Herein, U is the orthogonal matrix, S is the diagonal matrix, V^T is the average phase rate. The solving equation of V^T is as shown in Formula (7):

$$V^T = \left[V_1 = \frac{\varphi_1}{t_1 - t_0}, \cdots V_N = \frac{\varphi_N - \varphi_{N-1}}{t_N - t_{N-1}}\right] \tag{7}$$

(d) Through the above steps, the optimal solution of the velocity vector can be obtained, and thus, the surface deformation information can be obtained. The surface deformation information still has the atmospheric delay and other errors, so they need to be filtered to obtain the final accurate surface deformation information [8].

4. Results

4.1. Evaluation of Image Preprocessing Results

In this paper, we first performed radiometric correction to convert the DN value into the surface reflectance in PAN and MS images and performed geometric correction to eliminate geometric distortion. Then, we performed five fusion methods for PAN image and MS image: NND, GS, PCA, HPF, and Pansharpening fusion. This paper uses the ENVI tool to perform NND, GS, and PCA fusion, uses the ERDAS IMAGINE 9.2 tool to perform HPF fusion, and uses the PIE tool to perform Pansharpening fusion. The five fusion methods have achieved good visual effects. At the same time, the fidelity of the spectral performance is an important index for evaluating image fusion applications. Therefore,

we focus on the comparison and analysis of these five fusion methods from the aspect of spectral performance. After the comprehensive evaluation of these indicators, the fusion method with the best overall performance will be adopted.

4.1.1. The Spectral Curve of Image Fusion Features

Since we need to mainly extract the abnormal vegetation information in optical images for our landslide research, it is important to distinguish the vegetation from the bare land. In this paper, we compare and analyze the five fusion methods by viewing the shape and range of the spectral reflectance curves of vegetation and bare land, as shown in Figures 3 and 4.

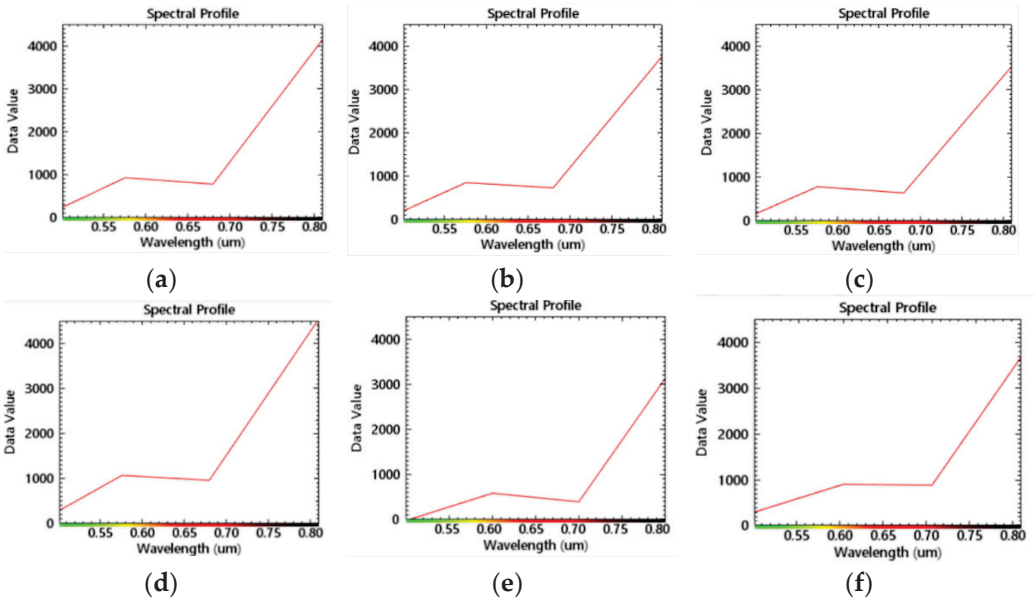

Figure 3. The vegetation spectrum curves of different fusion images. (**a**) MS image; (**b**) GS fusion image; (**c**) PCA fusion image; (**d**) NND fusion image; (**e**) Pansharpening fusion image; (**f**) HPF fusion image.

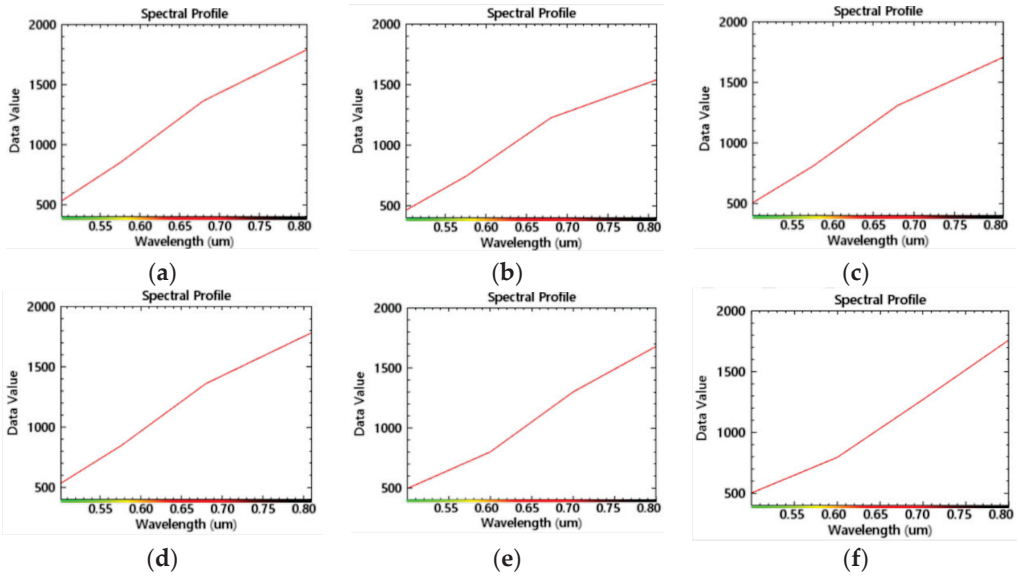

Figure 4. The bare ground spectrum curves of different fusion images. (**a**) MS image; (**b**) GS fusion image; (**c**) PCA fusion image; (**d**) NND fusion image; (**e**) Pansharpening fusion image; (**f**) HPF fusion image.

It can be seen from Figure 3 that in the vegetation reflectance spectrum curve, the vegetation spectrum curves of the five fusion images are consistent with the curve trend

of the MS image. In terms of the reflectance spectrum curve range, GS, PCA, HPF, and Pansharpening fusion images are all lower in the near-infrared, and only the NND fusion images tend to have the same range as a whole, which preserves the good spectrum information of NND.

For Figure 4, about the reflectance spectrum curve on the bare ground, the curve trend of the HPF fusion image is obviously inconsistent with that of MS image, and the trends of the other fusion images are relatively consistent. In terms of the reflectance spectral curve range, the NND, PCA, and Pansharpening fusion image and MS image tend to be the same, but the overall reflectance of the GS fusion image was relatively lower.

According to the spectral reflectance curves of bare land and vegetation, the overall quality of the five fusion methods is NND fusion method > PCA fusion method > Pansharpening > GS fusion method > HPF fusion method.

4.1.2. GNDVI Results

This paper needs to calculate the VC in the subsequent extraction of abormal vegetation information. The basis of calculating the VC is to calculate the GNDVI. Therefore, this paper chooses the GNDVI as the index of image fusion quality evaluation. The GNDVI results calculated from the above five fusion images are shown in Table 3.

Table 3. Comparison of GNDVI statistical results of different fusion images.

GNDVI	MS	NND	GS	PCA	HPF	Pansharpening
Mean	0.27	0.27	0.26	0.28	0.28	0.28
Max	0.68	0.69	0.75	0.72	0.74	0.74
Min	0.03	0.03	−0.39	−0.17	−0.22	−0.27

According to the GNDVI data in Table 3, it can be seen that the overall GNDVI value of the fused image is not much different from the MS image. Among them, the GNDVI value of the NND fusion image is the closest to the MS image, and the fidelity of the NND spectral information is the best.

After comprehensive evaluation of the above three different indicators, the NND fusion image has better performance in the details of the visual effect and the fidelity of the spectral curve. At the same time, the obtained GNDVI value of the NND fusion is also the closest to the MS image, which proves that it is reasonable and effective to use NND fusion images for subsequent vegetation monitoring.

4.2. Vegetation Abnormal Information Extraction Results Based on GF-1 Images

This paper determines 6% and 94% as the confidence interval of GNDVI according to the above method of determining the confidence interval. Finally, the VC is calculated and displayed in pseudo color. The VC results between 2013 and 2020 are shown in Figure 5.

During the creeping stage of the landslide, the slight deformation of the slope and the shear failure will cause cracks in the trailing edge. Based on this phenomenon, this paper mainly analyzes the vegetation cover change at the trailing edge of the landslide. Therefore, this paper mainly analyzes the change in VC at the trailing edge of the landslide. However, there are the landslide body and landslide trailing edge in the pseudo-color map of VC in Figure 5. In order to make an accurate analysis, this paper uses a black line to distinguish. On the left side of the black line, it is the landslide body. On the right side of the black line, it is the vegetation on the trailing edge of the landslide and the hillside.

According to the pseudo-color VC map of the landslide trailing edge shown in Figure 5, the overall VC shows a downward trend from 2013 to 2014 due to the large landslide in 2015. Compared with 2015, the VC at the trailing edge of the landslide has a certain recovery in 2016. The overall VCs change a little from 2017 to 2020, but from the perspective of subdivision areas, the changes in VC can be observed between the red box area and the green box area in Figure 5.

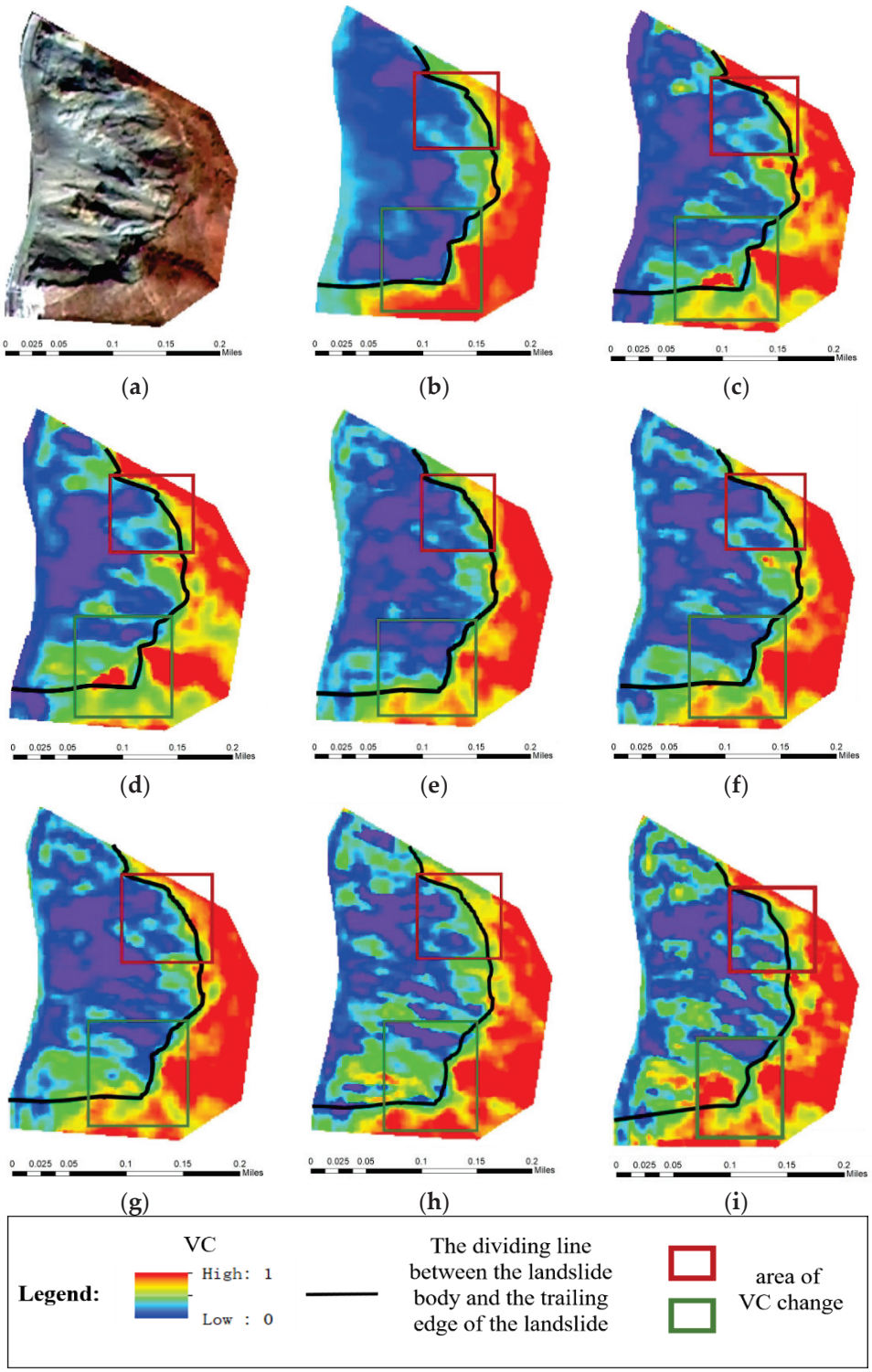

Figure 5. Pseudo-color VC maps in the upper of the Jizong Shed-Tunnel landslide. (**a**) Optical GF-1 fused true color image; (**b**) VC Map in 2013; (**c**) VC Map in 2014; (**d**) VC Map in 2015; (**e**) VC Map in 2016; (**f**) VC Map in 2017; (**g**) VC Map in 2018; (**h**) VC Map in 2019; (**i**) VC Map in 2020.

In the red box at the upper right corner, the bare land at the back edge of the landslide has a trend of gradual upward development and the VC is decreasing from 2013 to 2015, which corresponds to the known landslide in 2015. It provides a certain basis for the method of monitoring the Jizong Shed-Tunnel landslide creep with abnormal vegetation information. After 2016, the red area with high VC on the trailing edge of the landslide in

the red box gradually moves backward, and the original red area changes into yellow and green, which shows that the VC decreased.

In the green box at the lower right corner, from 2013 to 2015, the area next to the high vegetation red area protruding from the trailing edge of the landslide changes from red to yellow and green, which is consistent with the trend of the landslide in 2015. In 2016, the areas on both sides are slightly eased. After 2016, the protruded part on the trailing edge of the landslide in the green box gradually shrinks, and the bare land part gradually moves upward. The area under the green box also changes from red to yellow and green from 2016 to 2020, which expresses the decreased VC.

The above research and analysis are mainly based on the visual interpretation of the vegetation cover classification map of time series for qualitative analysis. In order to more accurately analyze the VC change and monitor the vegetation growth in the area of Jizong Shed-Tunnel landslide, the quantitative analysis and discussion are needed. For the whole area in Figure 5, we use the classification grade [52] to divide the VC and calculate the number and percentage of corresponding pixels for quantitative analysis. In order to correspond to the actual situation of the study area and reduce the influence of the shadow part of the landslide body on the result analysis, the low and medium VC is set VC $\leq$ 0.85 (VC above 0.85 is the red area in the subplots of Figure 5). The statistics of the number of pixels and the cumulative percentage of low and medium VC are shown in Table 4. At the same time, the curve is made as shown in Figure 6.

Table 4. Number and percentage of pixels with low and medium VC.

Image Time	$F_v \leq$ 0.85 Pixels Number	$F_v \leq$ 0.85 Pixels Percentage
5 November 2013	21,103	76.39%
8 November 2014	22,317	80.78%
16 November 2015	23,525	85.16%
22 December 2016	22,506	81.47%
11 November 2017	22,138	80.14%
19 November 2018	22,280	80.65%
24 November 2019	22,522	81.53%
30 November 2020	22,547	81.62%

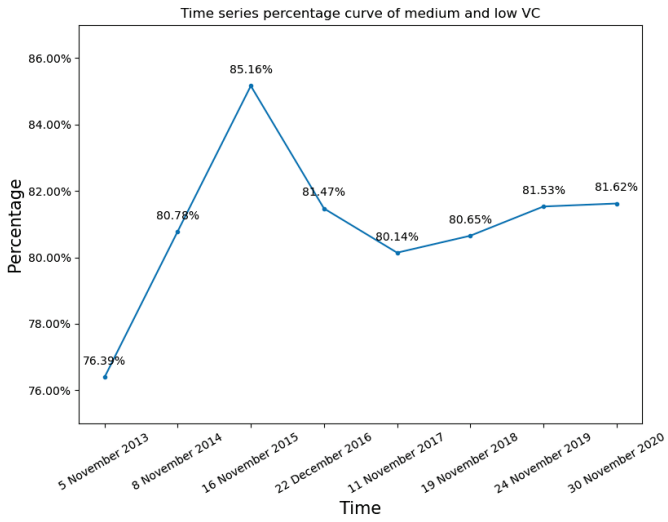

Figure 6. Time series change curve of the pixel number percentage with medium and low VC values.

According to the statistical results in Table 4 and Figure 6, the number and percentage of low and medium pixels gradually increased between 2013 and 2015, indicating that the vegetation growth situation gradually deteriorated, which is consistent with the above analysis results based on the VC classification map. With the time approaching the landslide in 2015, the vegetation growth became worse, with the maximum increasing percentage,

8.77%, of the low and medium VC, and the range of abnormal vegetation information expands. From 2015 to 2017, the number of the abnormal vegetation pixels decreased, which indicates that the vegetation had a certain recovery. After 2017, the pixels with low and medium coverage increased slowly, which is consistent with the conclusion that the overall VC change a little, but change in small areas.

According to the statistical results in Table 4 and Figure 6, the number and percentage of low and medium pixels gradually increased between 2013 and 2015, indicating that the vegetation growth situation gradually deteriorated, which is consistent with the above analysis results based on the VC classification map. With the time approaching the landslide in 2015, the vegetation growth becomes worse, and the range of abnormal vegetation information expands. From 2015 to 2017, the number of the abnormal vegetation pixels decreases, which indicates that the vegetation has a certain recovery. After 2017, the pixels with low and medium coverage increase slowly, which is consistent with the conclusion that the overall VC change a little, but change in small areas.

4.3. Surface Deformation Extraction Results Based on SBAS-InSAR

This paper uses the ENVI SARscape tool to process Sentinel-1 A data to obtain the average deformation rate of the ground highcoherence points and the cumulative surface deformation along the line of sight (LOS) of the satellite in the study area. However, because these points are scattered and only have latitudes and longitudes, it is inconvenient for visual interpretation and impossible to clearly observe and verify the specific surface deformation of the study area. Therefore, the average deformation rate map obtained by the SBAS-InSAR technology is superimposed with the GF-1 image. In order to better analyze the surface subsidence, only the coherent points (with the threshold 0.2 of the coherent points) of subsidence along the LOS direction are displayed, as shown in Figure 7.

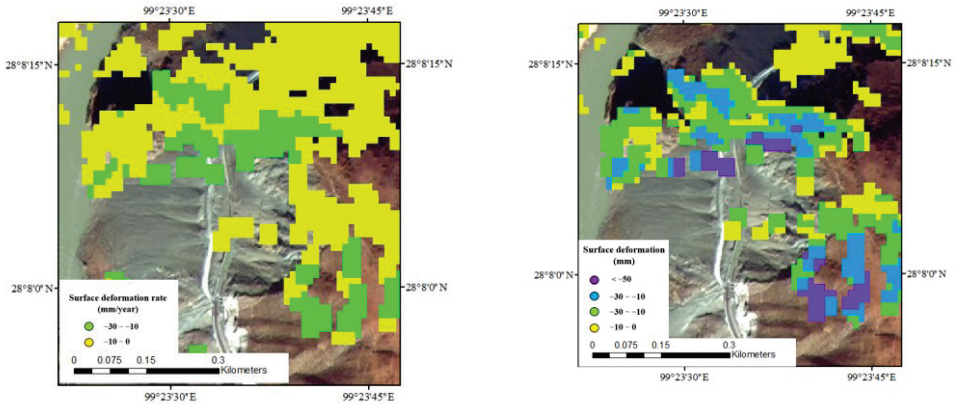

(**a**) (**b**)

Figure 7. The surface deformation extraction result map of the study area (LOS direction). (**a**) The surface subsidence rate map; (**b**) The surface cumulative deformation map.

We can find that the settlement rate of the Jizong Shed-Tunnel landslide along LOS direction is mostly between 0 mm/year and 30 mm/year from Figure 7a. According to the sliding speed threshold in Table 5, that is also the annual average surface deformation rate, this landslide is identified as the very slow type or the slightly slow type [53], so we find that the Jizong Shed-Tunnel landslide is in the landslide creep stage after a large slide in 2015. From Figure 7b, it can also be found that the Jizong Shed-Tunnel landslide has obvious settlements as a whole, reaching more than 50 mm in some places, which also proves that the landslide is sliding.

Table 5. Classification of landslide type according to the sliding speed [53].

Speed Grade	Landslide Type	Sliding Speed Threshold	Destructive Force Description
1	Very slow	<0.016 m/year	No damage will occur to buildings that have been protected in advance.
2	Slightly slow	0.016 m/year~1.6 m/year	Some permanent buildings are not damaged;even if the building cracks due to sliding, it is repairable.
3	Slow speed	1.6 m/year~13 m/month	If the slip time is short and the movement of the edge of the landslide is distributed over a wide area, the road and fixed structures can be preserved after several major repairs.
4	Medium speed	13 m/month~1.8 m/h	Fixed buildings at a certain distance from the foot of the landslide can't be damaged; the buildings located on the upper part of the sliding body are extremely damaged.
5	Fast speed	1.8 m/h~3 m/min	It has time for escape and evacuation; houses, property and equipment are damaged by landslide.
6	High fast	3 m/min~5 m/s	The destructive power of the disaster is large, and due to its high speed, it is impossible to transfer all personnel, resulting in some casualties.
7	Super fast	>5 m/s	The destructive force is huge, the surface buildings are completely destroyed, and the impact or disintegration of the sliding body causes huge casualties.

From the perspective of the spatial subdivision of landslides, the trailing edge of the landslide is the main deformation area. Not only are most of the coherent points located at the trailing edge of the landslide, but also the settlement rate and cumulative deformation of the trailing edge of the landslide are relatively large. In addition, the upper part of the landslide body has partial deformation, while the lower part of the landslide has no obvious deformation information, which is in line with the movement pattern of the landslide creep stage.

5. Discussion

Refarding the spatio-temporal analysis of surface deformation in abnormal vegetation areas, this paper superimposes the vegetation anomaly area information on the optical GF-1 image and compares it with the average land subsidence rate obtained by using the SBAS-InSAR technology in Section 4.3, as shown in Figure 8.

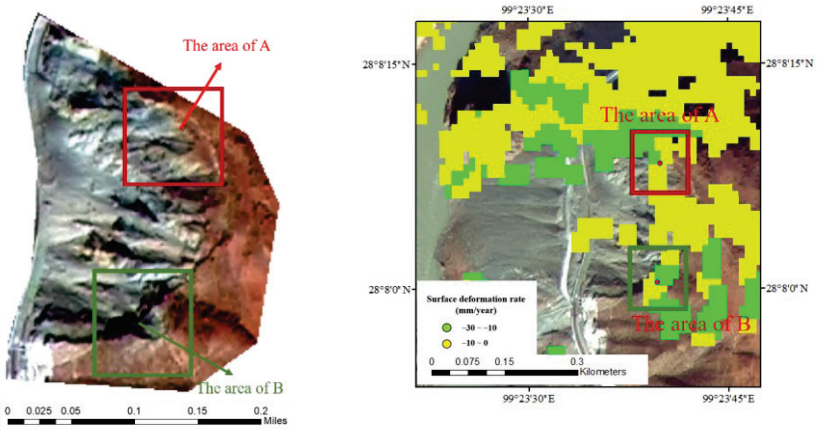

(**a**) (**b**)

Figure 8. Location maps of the abnormal vegetation area. (**a**) The location on optical GF-1 fused true color image; (**b**) The location on the surface subsidence rate map.

According to Figure 8, this paper superimposes the abnormal vegetation A and B areas extracted from the GF-1 image to the surface subsidence rate map and finds that these two areas are located in the subsidence area of the coherent point in the surface subsidence rate map. At the same time, the subsidence range of these areas is 10 mm/year to 30 mm/year, which belongs to the landslide creep stage, reflecting the consistency between the monitoring of landslides through the abnormal vegetation information in optical images and the monitoring of landslides using the InSAR method.

Similar to the time series analysis of the abnormal vegetation information area, we also analyze the time series deformation of the A and B areas. Since the cumulative surface deformation obtained in SBAS-InSAR is displayed by points, this paper selects the center point of the vegetation anomaly area to approximate the cumulative surface deformation of the two areas. Moreover, we extract the low and medium VC in A and B areas for the quantitative analysis and make a specific comparison analysis, as shown in Figure 9.

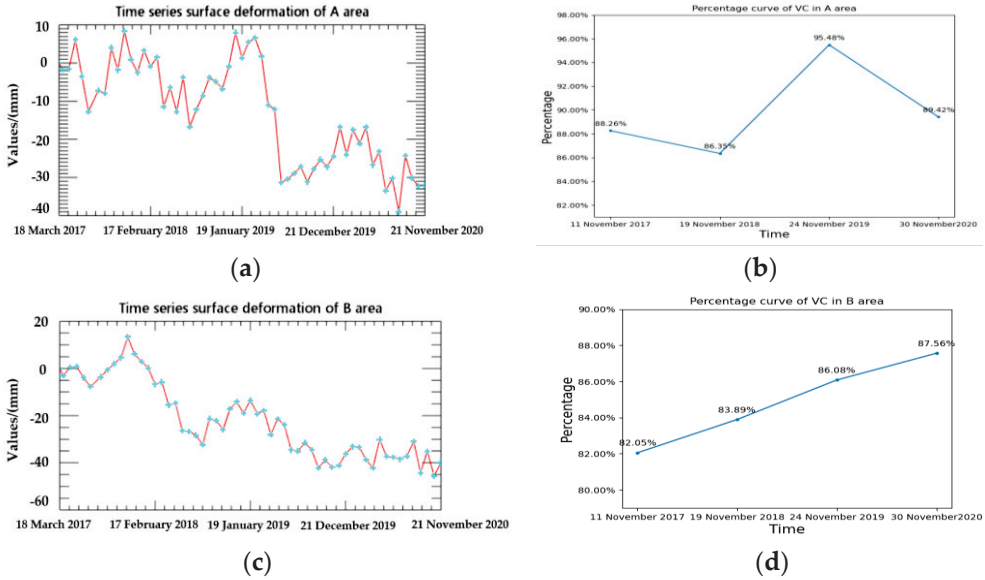

Figure 9. Time series diagrams of the abnormal vegetation information and the surface deformation. (**a**) Time series surface deformation of A area; (**b**) Time series of VC changes in A area; (**c**) Time series surface deformation of B area; (**d**) Time series of VC changes in B area.

According to Figure 9a, the overall deformation of the center point of A area is decreasing, and the maximum accumulated settlement is 40 mm. The time series deformation in this area rises slightly from June 2017 to March 2019, and the maximum amount of uplift is 9 mm, which may be caused by the surface movement of the surrounding area of the center point squeezing each other. Although the area has undergone certain deformation during this time period, it is still in a relatively stable state. In the percentage change curve of VC in Figure 9b, it is also found that the decrease in the percentage of low and medium VC from 2017 to 2018 indicates that the vegetation has recovered to a certain extent. This indicates that the surface deformation trend is consistent with the change trend of the VC. From January 2019 to November 2019, the overall time series surface deformation has a sudden downward trend. It seems that this area is unstable. After 2020, the time series deformation is not large, and the cumulative deformation is 7 mm, indicating that the area is still creeping. Similarly, in the percentage change curve of VC in Figure 9b, it is also found that the percentage of low and medium VC in 2019 has a rapid upward trend. It is basically consistent with the time series deformation trend of the ground surface. In 2020, the VC is slightly restored compared to 2019 but the overall trend is still declining.

According to Figure 9c, the maximum cumulative settlement at the center of B area is 45 mm. Except for a certain uplift from March to November 2017, the cumulative deformation of this area shows a downward trend, indicating that the area has been

creeping and deforming. From the percentage change curve of VC in Figure 9d, it can also be seen that the percentage of low and medium VC increased from 2017 to 2020, indicating a decline in VC. The overall trend is the same as the change in the surface deformation.

In order to more accurately analyze the correlation between vegetation anomaly information and surface deformation, this paper evaluates the accuracy of the two methods through the correlation and linear regression. In the previous comparison and analysis of the curves of the two methods, we find that the forms of surface activities in A area are relatively changeable, and B area is always in a creeping state and the form of the surface activity in B area is relatively stable. Moreover, since our study area is often covered by clouds, the optical images that we obtain most suitable for our conditions are all in autumn, which may cause the vegetation change to be less obvious. Therefore, we select B area as the typical analysis. Simultaneously, since the time of the used optical and SAR image is very difficult to be completely matched, and the time of the last SAR image in 2020 is earlier than that of the optical image, in order to maintain the time consistency, we select the SAR image time (20 October 2017, 8 November 2018, 3 November 2019, 21 November 2020) earlier than but closest to the optical image time (11 November 2017, 19 November 2018, 24 November 2019, 30 November 2020) for accuracy analysis, as shown in Figure 10. The x coordinate is the statistical average of the surface deformation. The y coordinate is the abnormal vegetation information, that is the percentage of the medium and low VC.

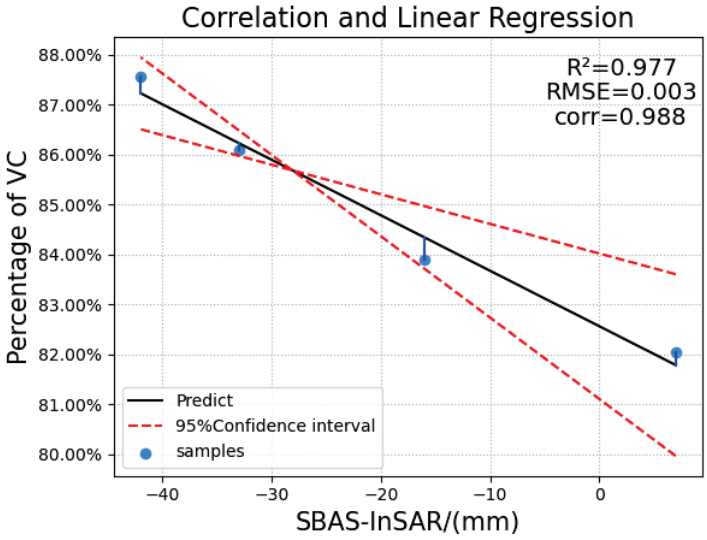

Figure 10. The correlation and regression analysis of the abnormal vegetation information and the surface deformation.

According to Figure 10, the correlation coefficient between the cumulative surface deformation and VC is 0.988, and the R^2 of the linear regression model is 0.977, indicating that the two methods have a significant linear correlation. When the deformation of the land surface subsidence increases, the pixels with medium and low VC also gradually increase, which provides reliable support for monitoring the Jizong Shed-Tunnel landslide using abnormal vegetation information. Simultaneously, the root mean squared error (RMSE) values of the error analysis and the upper and lower limits of the 95% confidence intervals are both small. This further proves the reliability of the accuracy analysis in B area.

Based on the comparative analysis and accuracy assessment of the cumulative time series variables and the changes in vegetation anomalies in these two areas, it was found that the vegetation anomalies are similar to the surface deformation variables, which proves that the use of abnormal vegetation information to monitor the Jizong Shed-Tunnel landslide has a certain degree of correctness and reliability.

6. Conclusions

In order to make up for the deficiencies of traditional GPS and InSAR technologies in monitoring landslides with large ups and downs, inaccessible by manpower, and lush with vegetation, based on the correlation between landslide creep and vegetation abnormality, this paper proposes a method to indirectly monitor the deformation characteristics of landslides by extracting the abnormal vegetation information from optical remote sensing images. We use the GF-1 optical data from 2013 to 2020 to monitor the vegetation anomaly information of the Jizong Shed-Tunnel landslide and use the SBAS-InSAR technology to extract the surface deformation information of the study area from 2017 to 2020. Then, we compare and analyze them. The results are as follows:

(1) This paper calculates the GNDVI index based on GF-1 time series data, and finally, obtains the vegetation coverage information of each scene. Through the multi-temporal qualitative and quantitative analysis of the extracted vegetation anomaly information, the VC decreased from 2013 to 2015. In reality, the landslide did occur in the study area in 2015, indicating that the early creep stage of landslides brings about a decrease in the VC. This verifies that the method of using vegetation anomaly information to monitor the Jizong Shed-Tunnel landslide is feasible. At the same time, it was discovered that there were two areas on the trailing edge of the landslide showing a downward trend in VC after 2017.

(2) Through the SBAS-InSAR technology based on the Sentinel-1 data, the main deformation area is located at the rear edge of the landslide, and the surface subsidence rate ranges from 0 mm/year to 30 mm/year, indicating that the Jizong Shed-Tunnel landslide is in a slow creep stage.

(3) After superimposing the abnormal vegetation area in the optical data with the surface deformation information in the radar data and performing time series analysis and accuracy assessment, it is found that the vegetation abnormality and the change trend of the surface deformation are basically consistent. When the surface deformation of the landslide decreases, the VC also shows a downward trend. When the deformation accelerates, the change in VC also intensifies. Even when the decline in the deformation is not large, the vegetation growth status can reflect these changes, which indicates the effectiveness and reliability of using vegetation abnormalities to monitor the Jizong Shed-Tunnel landslide, and the results of the two methods are similar. This method can provide new ways and ideas for the high-mountain landslide monitoring in southwestern China and can make up for some of the shortcomings of existing landslide monitoring methods.

Nevertheless, not all landslides at the creeping stage show obvious characteristic changes on surface vegetation, but some do exist. So, the landslide monitoring method in this paper is suitable for landslides with vegetation or vegetation change. Since the vegetation information needs to select the appropriate optical image with similar imaging time in each year, and the optical image is easily occluded by clouds, this method has some limitations in areas with cloud coverage. In addition, the impact of landslides on vegetation is a complex process, and this method has high monitoring accuracy for landslides that are in the creeping stage for a long time. In the future, we will also explore accurate pixel distinction models to improve the accuracy of vegetation information extraction.

Author Contributions: Q.G. proposed the research concept, designed the framework of this research, participated in data collection, reviewed and revised the manuscript. L.T. processed the GF-1 and Sentinel-1 data, analyzed data and wrote the manuscript. H.W. reviewed the manuscript and revised the figure. All authors have read and agreed to the published version of the manuscript.

Funding: This research was funded by the Leading Foundation on Frontier Sciences and Disruptive Technology Research of the Aerospace Information Research Institute, Chinese Academy of Sciences, grant number E0Z218010F.

Data Availability Statement: Thanks to the global availability of free and open Sentinel-1 SAR data with Europe Space Agency (ESA), the SAR data be accessible in https://sentinel.esa.int/web/sentinel/missions/sentinel-1 accessed on 20 March 2020; meanwhile, we are very grateful for the GF-1 data provided by China Centre for Resources Satellite Data and Application. Finally, we are also very grateful for SRTM DEM of 30 m resolution provided by United States Geological Survey (USGS); the DEM data be accessible in http://earthexplorer.usgs.gov/.

Acknowledgments: We are very grateful to the reviewers who significantly contributed to the improvement of this paper.

Conflicts of Interest: The authors declare no conflict of interest.

References

1. Li, W.; Xu, Q.; Lu, H.; Dong, X.; Zhu, Y. Tracking the Deformation History of Large-Scale Rocky Landslides and Its Enlightenment. *Geomat. Inf. Sci. Wuhan Univ.* **2019**, *44*, 1043–1053. [CrossRef]
2. Murakmi, S.; Nishigaya, T.; Tien, T.; Sakai, N.; Lateh, H.; Azizat, N. Development of historical landslide database in Peninsular Malaysia. In Proceedings of the 2014 IEEE 2nd International Symposium on Telecommunication Technologies (ISTT), Langkawi, Malaysia, 24–26 November 2014; pp. 149–153. [CrossRef]
3. Balbi, E.; Terrone, M.; Faccini, F.; Scafidi, D.; Barani, S.; Tosi, S.; Crispini, L.; Cianfarra, P.; Poggi, F.; Ferretti, G. Persistent Scatterer Interferometry and Statistical Analysis of Time-Series for Landslide Monitoring: Application to Santo Stefano d'Aveto (Liguria, NW Italy). *Remote Sens.* **2021**, *13*, 3348. [CrossRef]
4. Mourin, M.; Ferdaus, A.; Hossain, M. Landslide Susceptibility Mapping in Chittagong District of Bangladesh using Support Vector Machine integrated with GIS. In Proceedings of the 2018 International Conference on Innovation in Engineering and Technology (ICIET), Dhaka, Bangladesh, 27–28 December 2018; pp. 1–5. [CrossRef]
5. Zhao, J. Spatial-Temporal Distribution and Disaster Analysis of Landslide Disasters in Typical Karst Areas in My Country. Master's Thesis, Shandong Normal University, Shandong, China, 2014.
6. Zhang, L.; Dai, K.; Deng, J.; Ge, D.; Liang, R.; Li, W.; Xu, Q. Identifying Potential Landslides by Stacking-InSAR in Southwestern China and Its Performance Comparison with SBAS-InSAR. *Remote Sens.* **2021**, *13*, 3662. [CrossRef]
7. Lv, G.; Zhu, Y. Analysis of the surge process of the Fuquan landslide hitting the pond in Guizhou. *Chin. J. Geol. Hazard Contr.* **2017**, *28*, 1–5. [CrossRef]
8. Yang, J. Research on Slope Deformation Monitoring Based on InSAR Technology. Master's Thesis, University of Electronic Science and Technology of China, Sichuan, China, 2019.
9. Tang, Y.; Wang, L.; Ma, G.; Jia, H.; Jin, X. Using domestic remote sensing satellites for emergency monitoring of Jinsha River landslide disaster. *J. Remote Sens.* **2019**, *23*, 72–81. [CrossRef]
10. Wu, M.; Pi, X.; Wu, X.; Liu, H.; Ma, L. Analysis of Meteorological Causes and Meteorological Service of Landslides in Songtao County. *Mod. Agr. Technol.* **2020**, *24*, 172–173+177.
11. Gili, J.A.; Corominas, J.; Rius, J. Using Global Positioning System Techniques in Landslide Monitoring. *Eng. Geol.* **2000**, *55*, 167–192. [CrossRef]
12. Zhu, Y.; Zhou, S.; Lu, T. Research on the Application of GPS in the Slope Safety Monitoring Technique Using in Opencast Uuranium Mine Based on VBA. In Proceedings of the 2009 International Forum on Information Technology and Applications, Chengdu, China, 15–17 May 2009; pp. 760–763. [CrossRef]
13. Lytvyn, M.; Pöllabauer, C.; Troger, M.; Landfahrer, K.; Hörmann, L.; Steger, C. Real-Time landslide monitoring using single-frequency PPP: Proof of concept. In Proceedings of the 2012 6th ESA Workshop on Satellite Navigation Technologies (Navitec 2012) & European Workshop on GNSS Signals and Signal Processing, Noordwijk, The Netherlands, 5–7 December 2012; pp. 1–6. [CrossRef]
14. Jiang, S.; Wen, B.; Zhao, C.; Li, R.; Li, Z. Kinematics of a giant slow-moving landslide in Northwest China: Constraints from high resolution remote sensing imagery and GPS monitoring. *J. Asian Earth Sci.* **2016**, *123*, 34–46. [CrossRef]
15. Peng, F.; Nie, G.; Xue, C.; Wu, S.; Li, H.; Wang, J.; Liu, W. Application research of GPS/BDS precision single point positioning technology in landslide deformation monitoring. *Nav. Position. Tim.* **2019**, *6*, 103–112. [CrossRef]
16. Notti, D.; Cina, A.; Manzino, A.; Colombo, A.; Bendea, I.H.; Mollo, P.; Giordan, D. Low-Cost GNSS Solution for Continuous Monitoring of Slope Instabilities Applied to Madonna Del Sasso Sanctuary (NW Italy). *Sensors* **2020**, *20*, 289. [CrossRef]
17. Šegina, E.; Peternel, T.; Urbančič, T.; Realini, E.; Zupan, M.; Jež, J.; Caldera, S.; Gatti, A.; Tagliaferro, G.; Consoli, A.; et al. Monitoring Surface Displacement of a Deep-Seated Landslide by a Low-Cost and near Real-Time GNSS System. *Remote Sens.* **2020**, *12*, 3375. [CrossRef]
18. Akbarimehr, M.; Motagh, M.; Haghshenas-Haghighi, M. Slope Stability Assessment of the Sarcheshmeh Landslide, Northeast Iran, Investigated Using InSAR and GPS Observations. *Remote Sens.* **2013**, *5*, 3681–3700. [CrossRef]
19. Zhang, H.; Liu, S.; Wang, R. Landslide displacement field monitoring method based on high-resolution images and ASIFT algorithm. *J. Northeast. Univ. Nat. Sci.* **2017**, *38*, 1468–1472+1476. [CrossRef]
20. Bamler, R.; Hartl, P. Synthetic aperture radar interferometry. *Inverse Probl.* **1998**, *14*, R1. [CrossRef]

21. Huang, Y.; Yu, M.; Xu, Q.; Sawada, K.; Moriguchi, S.; Yashima, A.; Liu, C.; Xue, L. InSAR-derived digital elevation models for terrain change analysis of earthquake-triggered flow-like landslides based on ALOS/PALSAR imagery. *Environ. Earth Sci.* **2015**, *73*, 7661–7668. [CrossRef]
22. He, Y. Application of High-Resolution Remote Sensing and InSAR Technology in the Identification and Monitoring of Loess Landslides. Master's Thesis, Chang'an University, Shanxi, China, 2016. [CrossRef]
23. Huang, J.; Xie, M.; Wang, L. Study on deformation monitoring of Baige landslide based on SBAS-InSAR technology. *Yangtze Riv.* **2019**, *50*, 101–105. [CrossRef]
24. Jiang, Y.; Xu, Q.; Lu, Z. Landslide Displacement Monitoring by Time Series InSAR Combining PS and DS Targets. In Proceedings of the IEEE International Geoscience and Remote Sensing Symposium, Waikoloa, HI, USA, 26 September–2 October 2020; pp. 1011–1014. [CrossRef]
25. Qiu, Z.; Shen, P. *Encyclopedia of China Water Conservancy*, 2nd ed.; China Water Conservancy and Hydropower Press: Beijing, China, 2006; p. 576.
26. Ouyang, C.; An, H.; Zhou, S.; Wang, Z.; Su, P.; Wang, D.; Cheng, D.; She, J. Insights from the failure and dynamic characteristics of two sequential landslides at Baige village along the Jinsha River, China. *Landslides* **2019**, *16*, 1397–1414. [CrossRef]
27. Ouyang, C.; Zhao, W.; An, H.; Zhou, S.; Wang, D.; Xu, Q.; Li, W.; Peng, D. Early identification and dynamic processes of ridge-top rockslides: Implications from the Su Village landslide in Suichang County, Zhejiang Province, China. *Landslides* **2019**, *16*, 799–813. [CrossRef]
28. Lu, T.; Zeng, H.; Luo, Y.; Wang, Q.; Shi, F.; Sun, G.; Wu, Y.; Wu, N. Monitoring vegetation recovery after China's May 200 Wenchuan earthquake using Landsat TM time-series data: A case study in Mao County. *Ecol. Res.* **2012**, *27*, 955–966. [CrossRef]
29. He, B.; Zhang, X. Remote sensing survey and development trend analysis of landslide on Sichuan-Tibet Highway 102. *Chin. J. Geol. Hazard Contr.* **2015**, *26*, 103–109. [CrossRef]
30. Piroton, V.; Schlöge, R.; Barbier, C.; Havenith, H. Monitoring the recent activity of landslides in the Mailuu-Suu Valley (Kyrgyzstan) using radar and optical remote sensing techniques. *Geosciences* **2020**, *10*, 164. [CrossRef]
31. Xun, Z.; Zhao, C.; Kang, Y.; Liu, X.; Liu, Y.; Du, C. Automatic extraction of potential landslides by integrating an optical remote sensing image with an InSAR-derived deformation map. *Remote Sens.* **2022**, *14*, 2669. [CrossRef]
32. Guo, X.; Guo, Q.; Feng, Z. The relationship between landslide creep and vegetation anomalies on remote sensing images. *J. Remote Sens.* **2020**, *24*, 776–786. [CrossRef]
33. Guo, X.; Guo, Q.; Feng, Z. Detecting the Vegetation Change Related to the Creep of 2018 Baige Landslide in Jinsha River, SE Tibet Using SPOT Data. *Front. Earth Sci.* **2021**, *9*, 706998. [CrossRef]
34. Ge, C.; He, B. The application of geological route selection principles in the survey and design of the section from Jiegu to Batang Airport in Yushuzhou, National Highway 214. *Highw. Trans. Sci. Tech.* **2014**, *10*, 122–126.
35. Ghassemian, H. A review of remote sensing image fusion methods. *Inf. Fusion* **2016**, *32*, 75–89. [CrossRef]
36. Sun, W.; Chen, B.; Messinger, D. Nearest-neighbor diffusion-based pan-sharpening algorithm for spectral images. *Opt. Eng.* **2014**, *53*, 013107. [CrossRef]
37. Shah, V.; Younan, N.; King, R. An efficient pansharpening method via a combined adaptive PCA approach and contourlets. *IEEE Trans. Geosci. Remote Sens.* **2008**, *46*, 1323–1335. [CrossRef]
38. Aiazzi, B.; Baronti, S.; Selva, M. Improving component substitution Pansharpening through multivariate regression ofMS+ Pan data. *IEEE Trans. Geosci. Remote Sens.* **2007**, *45*, 3230–3239. [CrossRef]
39. Guo, L.; Yang, J.; Shi, L.; Zhan, Y.; Zhao, D.; Zhang, C.; Sun, J.; Ji, J. Comparison of SPOT6 remote sensing image fusion methods. *Remote Sens. Land Res.* **2014**, *26*, 71–77. [CrossRef]
40. Jiang, H.; Xing, X.; Liang, L.; Wang, M. Study on Pansharpening auto-fusion arithmetic and application. *Geo. Spat. Inform. Tech.* **2008**, *31*, 72–78. [CrossRef]
41. Li, M. Research on Remote Sensing Estimation Method of Vegetation Coverage. Master's Thesis, Graduate University of Chinese Academy of Sciences (Institute of Remote Sensing Applications), Beijing, China, 2003.
42. Kaufman, Y.; Tanre, D. Atmospherically resistant vegetation index (ARVI) for EOS-MODIS. *IEEE Trans. Geosci. Remote Sens.* **1992**, *30*, 261–270. [CrossRef]
43. Li, M.; Wu, B.; Yan, C.; Zhou, W. Estimation of Vegetation Fraction in the Upper Basin of Miyun Reservoir by Remote Sensing. *Res. Sci.* **2004**, *26*, 153–159. [CrossRef]
44. Gheorghe, M.; Armaş, I. Comparison of multi-temporal differential interferometry techniques applied to the measurement of Bucharest City Subsidence. *Procedia Environ. Sci.* **2016**, *32*, 221–229. [CrossRef]
45. Zhou, S.; Ouyang, C.; Huang, Y. An InSAR and depth-integrated coupled model for potential landslide hazard assessment. *Acta Geotech.* **2022**, *17*, 3613–3632. [CrossRef]
46. Ferretti, A.; Prati, C.; Rocca, F. Nonlinear subsidence rate estimation using permanent scatterers in differential SAR interferometry. *IEEE Trans. Geosci. Remote Sens.* **2000**, *38*, 2202–2212. [CrossRef]
47. Intrieri, E.; Raspini, F.; Fumagalli, A.; Lu, P.; Conte, S.; Farina, P.; Allievi, J.; Ferretti, A.; Casagli, N. The Maoxian landslide as seen from space: Detecting precursors of failure with Sentinel-1 data. *Landslides* **2018**, *15*, 123–133. [CrossRef]
48. Berardino, P.; Fornaro, G.; Lanari, R.; Sansosti, E. A new algorithm for surface deformation monitoring based on small baseline differential SAR interferograms. *IEEE Trans. Geosci. Remote Sens.* **2002**, *40*, 2375–2383. [CrossRef]

49. Ma, S.; Xu, C.; Shao, X.; Xu, X.; Liu, A. A Large Old Landslide in Sichuan Province, China: Surface Displacement Monitoring and Potential Instability Assessment. *Remote Sens.* **2021**, *13*, 2552. [CrossRef]
50. Liu, X.; Zhao, C.; Zhang, Q.; Lu, Z.; Li, Z.; Yang, C.; Zhu, W.; Liu, J.; Chen, L.; Liu, C. Integration of Sentinel-1 and ALOS/PALSAR-2 SAR datasets for mapping active landslides along the Jinsha River corridor, China. *Eng. Geol.* **2021**, *284*, 106033. [CrossRef]
51. Zhao, R.; Li, Z.; Feng, G.; Wang, Q.; Hu, J. Monitoring surface deformation over permafrost with an improved SBAS-InSAR algorithm: With emphasis on climatic factors modeling. *Remote Sens. Environ.* **2016**, *184*, 276–287. [CrossRef]
52. Peng, J.; Zhang, C. Remote sensing monitoring of vegetation cover based on Gaofen-1 remote sensing image—Taking Xiamen as an example. *Remote Sens. Land Res.* **2019**, *31*, 137–142. [CrossRef]
53. Standard of Classification for Geological Hazard. Available online: https://www.cgs.gov.cn/ddztt/jqthd/fzjz/xmjz/bzgf/202006/P020200602403973808311.pdf (accessed on 21 June 2022).

remote sensing

MDPI

Technical Note

Study on the Source of Debris Flow in the Northern Scenic Spot of Changbai Mountain Based on Multi-Source Data

Jiahao Yan [1], Yichen Zhang [1,*], Jiquan Zhang [2], Yanan Chen [1] and Zhen Zhang [1]

[1] School of Jilin Emergency Management, Changchun Institute of Technology, Changchun 130021, China
[2] School of Environment, Northeast Normal University, Changchun 130024, China
* Correspondence: zhangyc@ccit.edu.cn; Tel.: +86-1384-402-8326

Abstract: The northern scenic area of Changbai Mountain is a high-incidence area of debris flow disasters, which seriously threaten the safety of tourist's lives and property. Monitoring debris flow and providing early warning is critical for timely avoidance. Monitoring the change of debris flow source is an effective way to predict debris flow, and the change of source can be reflected in the settlement deformation of the study area. The offset tracking technique (OT) is insensitive to the coherence of SAR images and can resist the decoherence of D-InSAR and SBSA-InSAR to a certain extent. It is a technical means for monitoring large gradient deformation. It has been widely used in the field of seismic activity, glaciers and landslides in recent years, but few scholars have applied this technique in the field of debris flow. In this paper, we use OT techniques in combination with field surveys, Google imagery and Sentinel-1 data to monitor surface deformation in the northern scenic area of Changbai Mountain in 2017 and use D-InSAR techniques to compare and complement the OT monitoring results. The results of this study show that for monitoring surface deformation in the study area after a mudslide, it is better to use both methods to determine the surface deformation in the study area rather than one, and that both methods have their own advantages and disadvantages and yet can complement each other. Finally, we have predicted the development trend of mudflows in the study area by combining the calculated single mudflow solids washout, which will help to improve the long-term monitoring and warning capability of mudflows in the study area. The study also enriches the application of offset-tracking technology and D-InSAR in the field of geohazard monitoring and provides new ideas and methods for the study of mudflow material source changes.

Keywords: Changbai Mountain North Scenic Area; debris flow source; D-InSAR; offset-tracking; surface deformation

Citation: Yan, J.; Zhang, Y.; Zhang, J.; Chen, Y.; Zhang, Z. Study on the Source of Debris Flow in the Northern Scenic Spot of Changbai Mountain Based on Multi-Source Data. *Remote Sens.* **2023**, *15*, 2473. https://doi.org/10.3390/rs15092473

Academic Editors: Stefano Morelli, Veronica Pazzi and Mirko Francioni

Received: 14 March 2023
Revised: 20 April 2023
Accepted: 4 May 2023
Published: 8 May 2023

1. Introduction

Debris flow is a sudden geological disaster that occurs in mountainous or ditch areas [1–4], widely distributed in some areas of the world with special topography or geomorphology [5–9]. Debris flows are very destructive [10–14]; they can rush out a large amount of material sources in a short time, which even include huge rocks, which will pose a great threat and damage to the ecological environment, life, property and construction facilities in the basin [15–19]. Therefore, how to monitor and warn debris flow is the focus of current research, and it is also a key problem that needs to be solved urgently.

The formation of debris flows needs to meet three conditions: steep terrain, sufficient rainfall and rich debris flow source. The total quantity of material sources determines the occurrence of debris flow and its degree of risk. The greater the reserves of material sources, the greater the risk of debris flow. It is necessary to know the quantity of material sources in the source area of debris flow to accurately evaluate the hazards of debris flow in the basin [20,21].

Changbai Mountain is an area which is highly prone to geological disasters. It has a main debris flow ditch and eight branch ditches. Almost every year, disasters of different

scales occur, which seriously threaten the safety of tourists' lives and property. In order to better carry out geological disaster warnings in time, it is urgent to carry out the professional monitoring of important hidden danger points of geological disaster in order to minimize the possible losses caused by such disasters. In recent years, with the rapid development of observation technology, scholars have used different technologies to obtain the provenance of the study area. For example, aerial photos taken from aircraft or drones [22], satellite images [23] and aerial laser scanning [24]. However, if we also adopt the same method to evaluate the source of debris flow in the northern scenic spot of Changbai Mountain, it is not enough for us to dynamically monitor the debris flow in the dangerous area; because we do not know the source of the change in the source area after a debris flow occurs, using the same method to assess the source will be very cumbersome and time-consuming [25–29]. Therefore, the deformation monitoring of debris-flow-dangerous areas is of great significance to the early warning of debris flow. The main observation method of traditional settlement observation technology is to use a total station, a level and other equipment to lay a certain number of monitoring points on the ground for continuous observation, and then to invert the surface deformation of the whole study area according to the deformation of the monitoring points, which belongs to the single-point measurement method. This method cannot reflect the deformation state of the whole study area and has great limitations [30,31].

Previous studies have mostly applied offset-tracking technology to the fields of earthquakes, glaciers and landslides, but few people have applied this technology to the surface deformation monitoring of debris flows [32–36]. Chen used SBAS-InSAR technology to monitor the deformation of the debris flow source area of Xulong Ditch and obtain the annual deformation of the area [20]. However, the premise of their application of this method is that there is no debris flow or landslide in the study area, and the annual settlement is very small. Once a large area of deformation occurs due to natural disasters in this area, the method will fail. In addition, in areas with complex terrain, some noise information will be added in the image processing process, and some accuracy will be lost in small-scale monitoring; hence, it is easy to form unreliable monitoring results. Therefore, the accuracy of offset tracking (OT) is not high enough, but it is a powerful tool when other methods fail.

In this study, first, we conducted a field survey of the study area and calculated the storage of loose solid matter sources in the study area; the second step calculated the quantity of solid matter sources flushed out of each debris flow ditch in the study area in 2017; in the third step, we used offset tracking to monitor the deformation of the research area, and we obtained the deformation of the research area in each season; in the fourth step, D-InSAR was used to monitor the deformation of the research area, although decoherence will occur in severely deformed areas, but it can be used as a supplement to the offset-tracking technology in the slow-deformation area to obtain higher-precision deformation values. Combining remote sensing images and field surveys, the debris flow danger zone was delineated, and the development of debris flows was predicted based on the surface deformation of each debris flow ditch combined with the calculated amount of debris flow solids. These research results will help to improve the long-term monitoring and of mudslides in the study area and, with improved early-warning capabilities, further protect people's lives and properties. The research also enriches the application of offset-tracking technology and D-InSAR in the field of geohazard monitoring and provides new ideas and methods for the study of mudflow material source changes.

2. Study Area

Changbai Mountain North Scenic Area is located in the southeast mountainous area of Jilin Province, China, with the geographic coordinates of 127°28′–128°16′E and 41°42′–42°25′N. It belongs to the humid area of the mid-latitude continental monsoon climate. The climate is characterized by long and cold winters and warm and short summers. Affected by the terrain and the continental and Pacific air flow, the vertical zoning is obvious, and the temperature and rainfall are controlled by altitude. According to the

relevant data, the terrain increased by 100 m, the temperature decreased by 0.5~0.6 °C and precipitation increased by 30 mm. The average annual precipitation is 1407.6 mm, and the precipitation is concentrated in June and August. The precipitation in three months accounts for more than 60% of the total annual precipitation, and most of it results from rainstorms. The highest peak in the study area is Tianwen Peak, which is located in the northeast of Tianchi and has an altitude of 2670 m. The peak is composed of gray and pale white pumice and is opposite Longmen Peak, forming a "U"-type valley between them. From south to north, Changbai Mountain's waterfall forms the source of the two white rivers. The main types of geomorphological genesis in the study area are eroded volcanic terrain and tectonic erosion terrain. The two sides of the "U"-shaped valley are formed by volcanic cones and their extended mountains, and the canyon area is a ditch formed by the Erdaobai River fault. Figure 1 is distribution of disaster sites in study area.

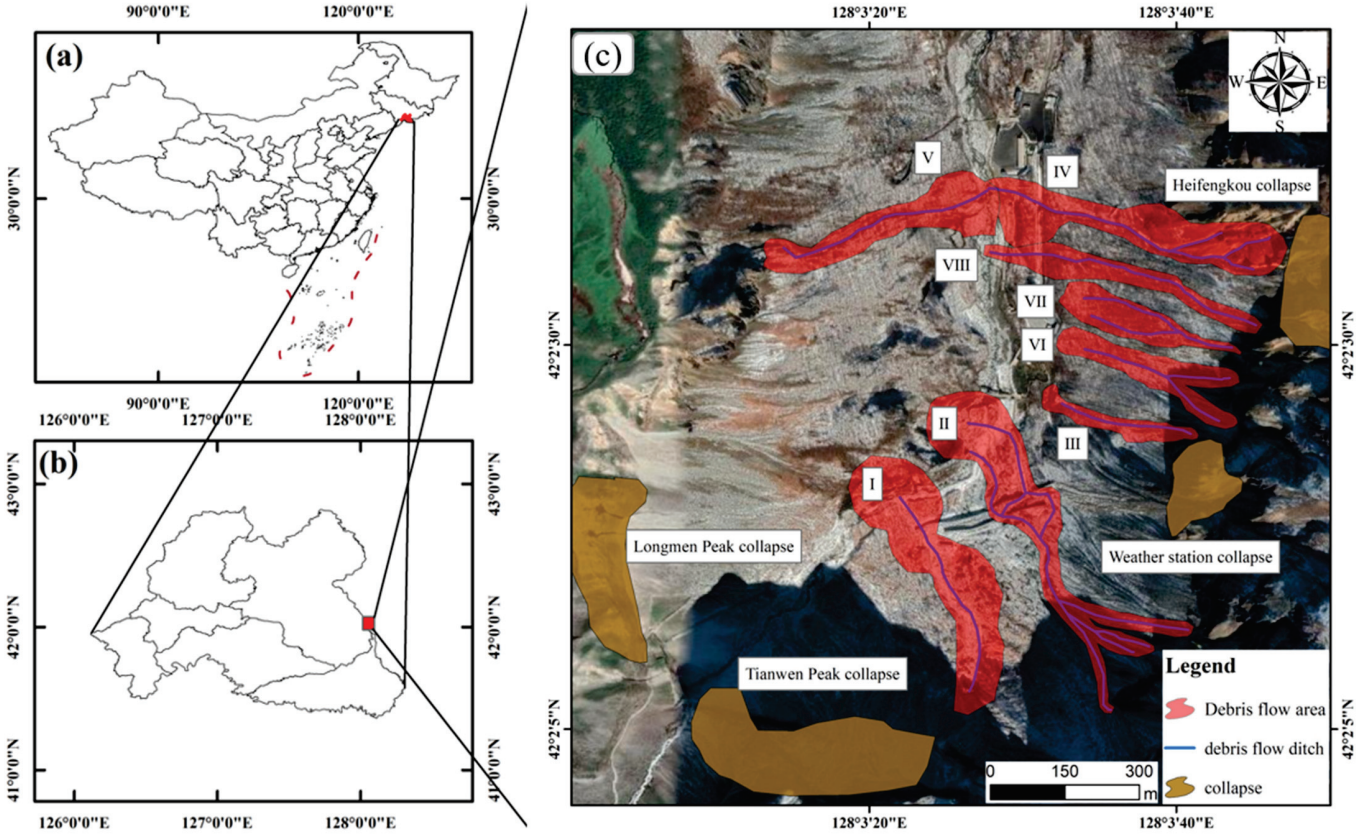

Figure 1. Distribution of disaster sites in study area. (**a**) Location of the study area in China; (**b**) location of the study area in Baishan City; (**c**) extent of debris flow and location of the collapse in the study area.

There are eight debris flows along the Erdaobai River in the northern scenic area of Changbai Mountain (Table 1). The Erdaobai River is generally a deep-cutting "U"-type valley, which has the characteristics of a steep slope and a large cutting depth. The longitudinal length of the main ditch is 9.1 km, and the average longitudinal slope of the main ditch is 48‰. Among them, the longitudinal slope of the upper reaches from the Tianchi waterfall to the intersection of the No. 6 branch ditch is steep, with an average longitudinal slope of 237‰, and the middle part of the Guanyatai section is slightly slow, with an average longitudinal slope of 105‰. In the lower reaches of the main ditch, the longitudinal slope is slightly slow, with a longitudinal slope of 51‰, and it shows obvious spatial variation characteristics of steep up and slow down.

Table 1. Statistical table of basic characteristics of each debris flow tributary ditches of Erdaobai River.

The Serial Number	Ditch Length (km)	Ditch Area (km^2)	Relative Elevation Difference (m)	Mean Longitudinal Slope (‰)
1	1.53	0.48	618	403
2	1.45	0.46	664	458
3	0.76	0.10	434	569
4	0.80	0.10	356	446
5	0.79	0.08	390	466
6	0.82	0.09	429	522
7	0.80	0.07	392	487
8	0.84	0.08	393	468

The eight tributaries in the study area are not composed of typical formation areas, formation circulation areas and accumulation areas. Therefore, according to the formation conditions and movement mechanism of debris flow and the distribution of loose solid sources of debris flow, the ditch area is divided into three areas: the catchment area in the upper reaches of the ditch, the formation circulation section in the middle reaches and the circulation accumulation area at the intersection of the ditch mouth to the Erdaobai River. The No. 1 ditch has the largest ditch area. Taking the No. 1 ditch as an example, Figure 2 is the GIS interpretation map of three sections of the No. 1 ditch, and Figure 3 is the cross section of the No. 1 ditch.

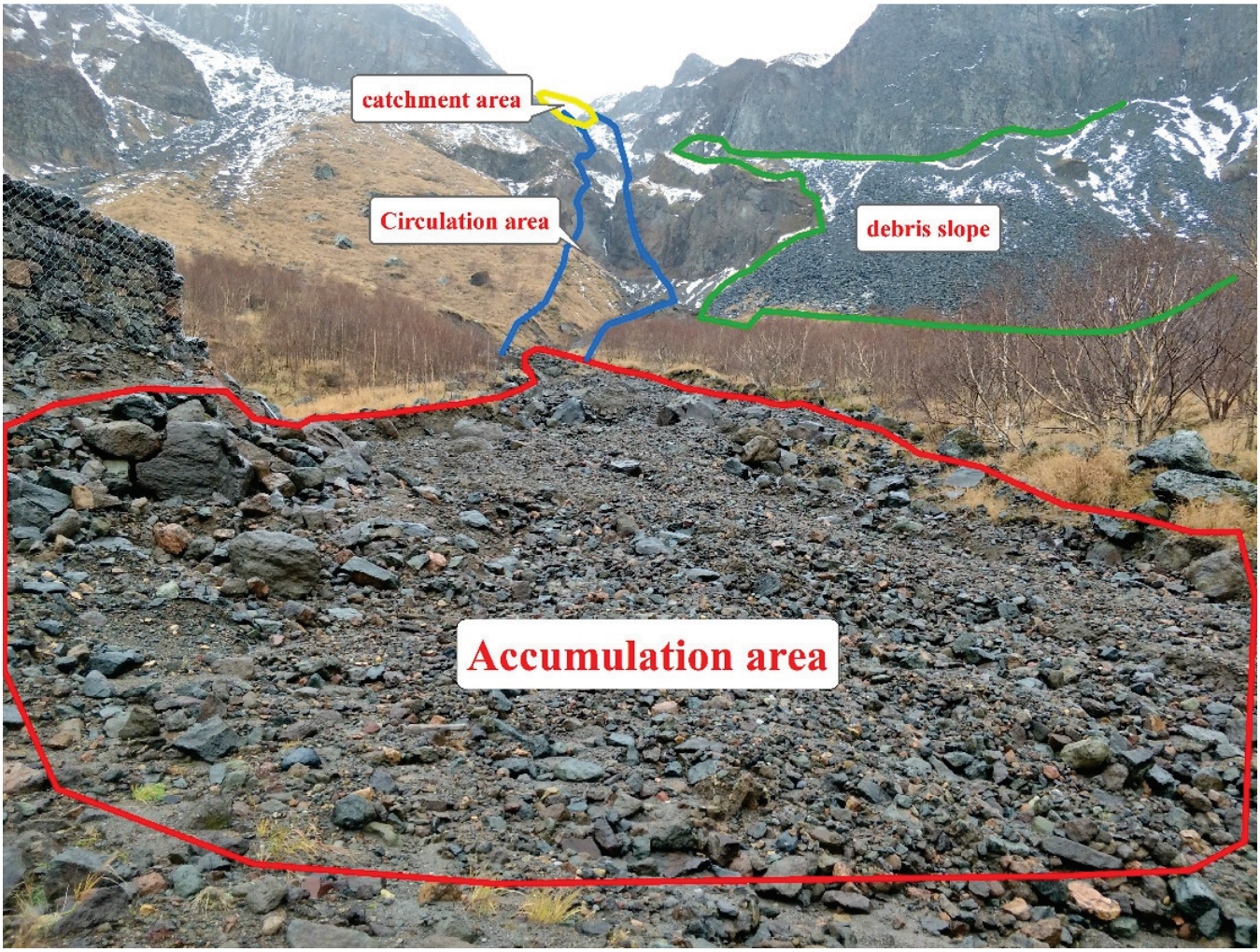

Figure 2. No. 1 debris flow ditch, three sections.

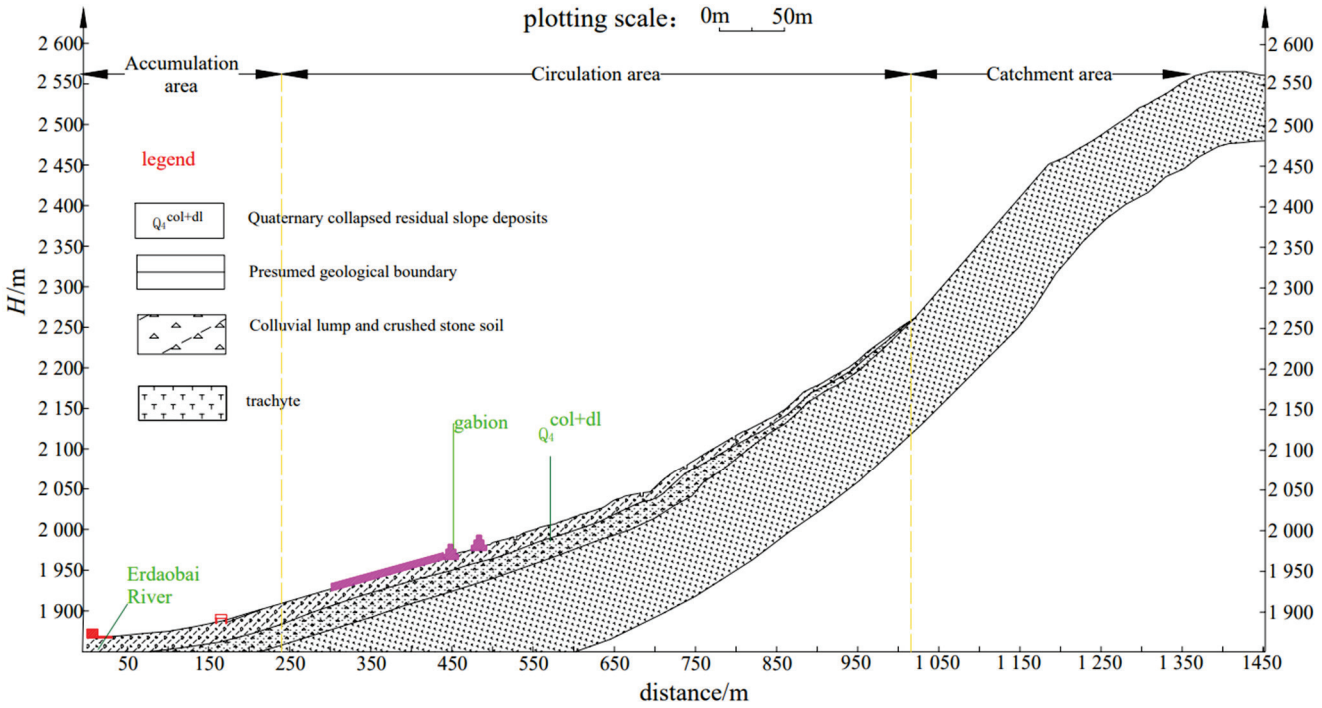

Figure 3. No. 1 debris flow ditch sectional drawing.

3. Data and Methods

3.1. Field Investigation

From 6 September 2018 to 15 October 2018, project team members conducted a 40-day on-site geological survey of the North Changbai Mountain Scenic Area. The topography and geomorphology of the working area, the environmental geological problems in the area, the development history, the genetic mechanism and stability of the deformation and the failure of the hidden danger points of geological disasters were investigated. In addition, geophysical exploration work is carried out by the high density resistivity method in the debris flow formation and accumulation area. The geophysical prospecting in the accumulation area mainly elucidates the thickness, erosion and deposition amplitude, distribution range and lithology composition of the debris flow accumulation fan, which lays the foundation for finding out the formation conditions and characteristics of the debris flow. The geophysical exploration of the formation area needs to elucidate the source reserves. The source types mainly include the following: landslide accumulation source, slope erosion source and ditch accumulation source.

3.2. Calculation of Solid Discharge of Debris Flow

On 2 July 2017, a heavy rainfall with an hourly rainfall intensity of 22.4 mm·h^{-1} in the northern scenic spot of Changbai Mountain triggered debris flows in 8 branch ditches. The relationship between the loose source, basin shape and debris flow discharge can be analyzed by calculating the single debris flow solid discharge. At the same time, the maximum amount of debris flow is an important parameter in the design of a debris flow disaster prevention and mitigation project, which can provide a scientific basis for debris flow disaster prevention and control. The single debris flow solid ejecta is calculated according to the calculation formula provided of the "Debris Flow Disaster Prevention Engineering Exploration Specification" (DT/T0220-2006),

$$Q_H = Q(\gamma_c - \gamma_w)/(\gamma_H - \gamma_w) \quad (1)$$

where Q_H—total amount of solids washed out by debris flow (m^3); Q—total amount of debris flow (m^3); γ_c—debris flow severity (t/m^3); γ_w—water severity (t/m^3); and γ_H—solid material weight of debris flow (t/m^3).

The total amount of debris flow in one time, Q, is calculated according to the formula provided of the Code for Exploration of Debris Flow Disaster Prevention Engineering (DT/T0220-2006):

$$Q = KTQ_c. \quad (2)$$

In the formula, T—debris flow duration (s); and Q_c—debris flow maximum flow (m/s).

Through inquiry with the supervision staff of the scenic spot, it became known that the debris flow lasted for 900 s except for ditches No. 3 and No. 8, for which is lasted about 15 min, and the debris flow in the remaining trenches lasted 10 min (600 s). The values of K are shown in Table 2:

Table 2. K value reference table.

Catchment Area *F*	Value of *K*
$F < 5$ km^2	$K = 0.202$
$F = 5$~10 km^2	$K = 0.113$
$F = 10$~100 km^2	$K = 0.0378$
$F > 10$~100 km^2	$K < 0.0252$

The peak flow of debris flow, Q_c, is calculated according to the calculation formula provided of 'Debris Flow Disaster Prevention Engineering Exploration Specification' (DT/T0220-2006):

$$Q_c = (1 + \phi)Q_p D_c, \quad (3)$$

where Q_c—debris flow section peak flow (m^3/s); ϕ—sediment correction factor, determined by look-up table method as $\phi = 0.88$; Q_p—rainstorm peak discharge; and D_c—blockage coefficient, determined as $D_c = 1.8$ according to survey specification Table 1.

Q_p calculated the surface water catchment flow according to the empirical formula proposed by China Institute of Highway Science:

When the catchment area $F \geq 3$ km^2, the formula is

$$Q_p = \psi F^{\frac{2}{3}} S. \quad (4)$$

When the catchment area $F < 3$ km^2, the formula is

$$Q_p = \psi F S, \quad (5)$$

where Q_p—storm flood peak discharge (m^3/s); ψ—rainstorm runoff coefficient; F—catchment area (km^2); and S—hourly rain intensity (mm/h).

3.3. Offset-Tracking Technology

The principle of offset-tracking technology is to calculate the cross-correlation of the two time phases with a certain window size so as to obtain the sum of the offset caused by satellite orbit and surface deformation [37,38]. Then, according to the orbit data of the satellite, the offset caused by the satellite orbit is subtracted to obtain the deformation caused by the surface deformation. According to the information used in the cross-correlation calculation, offset-tracking technology can be divided into two implementations: intensity tracking and coherence tracking [39,40]. Because the intensity tracking method can overcome the phenomenon of decoherence, this algorithm is generally used for offset tracking. OT is mostly used in studies of large gradient deformation, and the study area experienced heavy rainfall in 2017 with a once-in-20-year event, with many areas deforming significantly; thus, using this method gives relatively reliable results.

The data processing flow is shown as follows (Figure 4).

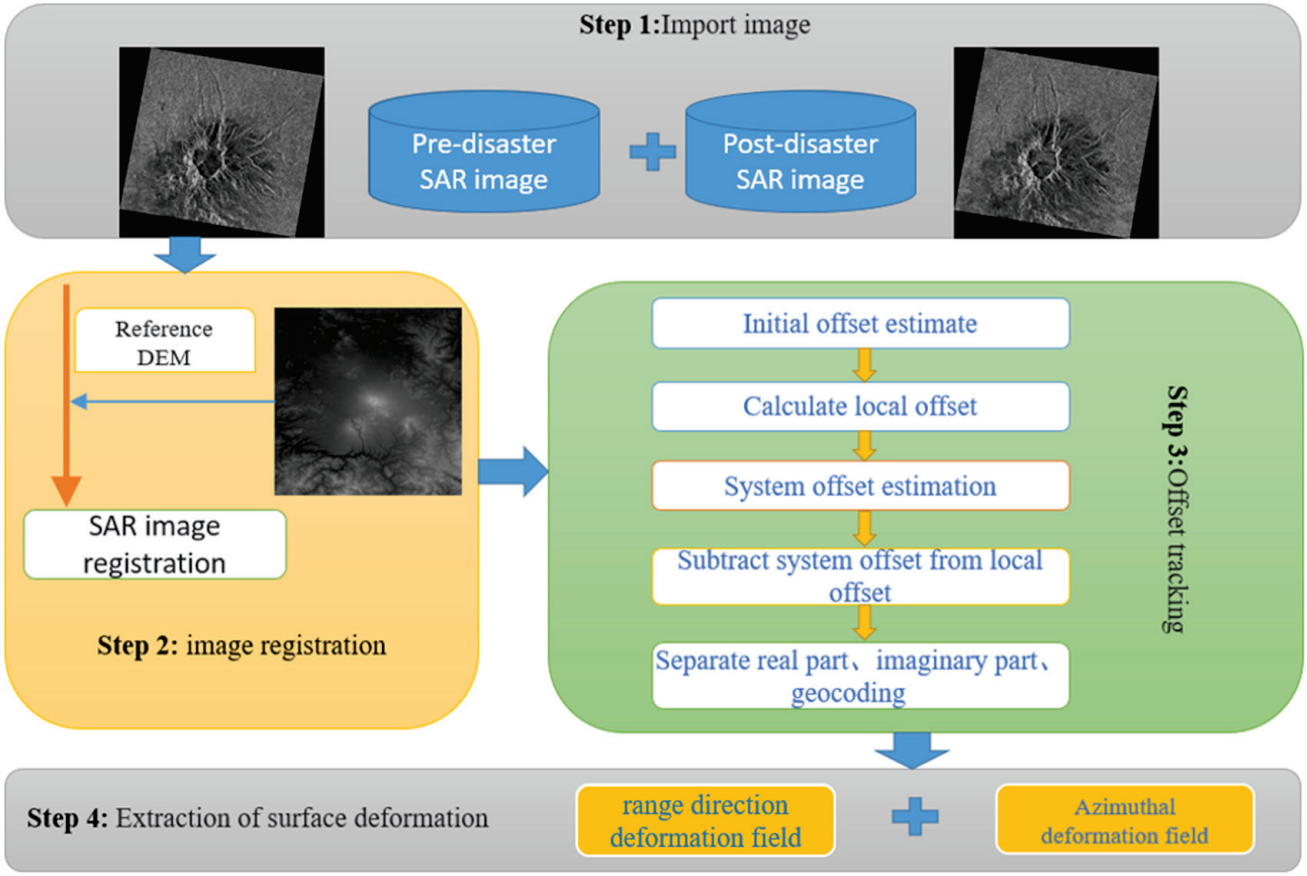

Figure 4. Flowchart of offset tracking data processing.

1. The SAR images of two time phases before and after the change are selected. According to the orbit parameter file during the satellite imaging, the offset of the SAR image caused by orbit error is calculated, and the image is roughly registered;
2. Accurate registration of two SAR images using the local window method to obtain a certain number of corresponding points from the two images, and then using the least squares polynomial fitting method to fit the mapping relationship between the two images. The registration of this step is crucial for the subsequent steps;
3. Using the intensity tracking method [41], we track the offset of the image to obtain the local offset;
4. The offset caused by the orbit is removed from the local offset obtained in the previous step, and the joint interferometry and offset tracking of the surface are obtained to extract the large gradient surface deformation offset. The range and azimuth deformation fields are separated from the offset, and the range and azimuth offset maps are geocoded and converted to the geographic coordinate system.

3.4. Differential Interferometry Synthetic Aperture Radar (D-InSAR) Technique

According to the interferometric mode, the D-InSAR technique can be divided into two-track, three-track and four-track differential interferometry, among which the two-track D-InSAR technique is the most widely used. The basic idea is to conjugate and multiply the SAR images before and after deformation, and then differential interferometric stripe maps are generated with DEM data to achieve the purpose of removing topography, i.e., weakening interference information, so as to obtain the topographic changes of ground targets in the study area [42–47].

In this paper, we use SARscape for differential interferometric radar (D-InSAR) processing, which consists of seven steps: data focusing, baseline estimation, interferogram generation, adaptive filtering and coherence generation, phase de-entanglement, track re-

finement and re-deplatforming and deformation conversion. In addition, there are several modules containing different operation steps. For example, in the interferogram generation, the interferometric data pair alignment and multi-view processing are included, and then the interferogram is generated after the processing, and the generated interferogram is based on the reference DEM image after the de-leveling of the interferometric image.

D-InSAR is prone to producing low frequency images when large-scale deformation occurs, so we simply use the method as a complement to OT, i.e., to verify OT where slow deformation can yield reliably deformed regions.

3.5. Remote Sensing Data

The SAR images used are collected by Sentinel-1, an earth observation satellite launched by the European Space Agency, which is equipped with a C-band SAR sensor. Sentinel-1 data can be registered and downloaded on the Sentinel Scientific Data Hub website at http://scihub.copernicus.eu/dhus (accessed on 3 May 2017). Details are shown in (Table 3). The acquisition mode of the image is IW, and the data format is SLC. The selection of 2017 Sentinel-1 data is due to the occurrence of debris flow in 8 gullies this year, of which No. 1 and No. 2 gullies occurred twice, and a large area of collapse and landslide occurred at Longmen Peak. Taking this as the source data can help us to obtain better offset-tracking demonstration results, and, using Google Maps as the base map to distinguish the deformation location, the resolution is 2.5 m. Considering the large topographic relief in this area, a 30 m resolution digital elevation model (SRTM1 Arc-Second Global, shuttle radar topography mission) (https://earthexplorer.usgs.gov/ (accessed on 3 May 2017)) is introduced to assist image registration and final terrain correction.

Table 3. Sentinel-1 data and imaging parameters.

Serial Number	Image Acquisition Time	Absolute Orbits	Relative Orbit	Azimuth Angle (°)	Incidence Angle (°)	Satellite Geometry
01	2017/01/01	3660	134	193	41	descending
8910310002	2017/03/07	4608	32	193	34	descending
03	2017/05/30	5833	32	193	34	descending
04	2017/09/03	3354	32	193	34	descending
05	2017/11/26	4058	32	193	34	descending
06	2017/12/20	3660	32	193	34	descending
07	2017/12/27	8910	134	193	41	descending
08	2018/03/03	9858	32	193	34	descending

4. Result

4.1. Debris Flow Solid out Volume

In order to explore the physical sources and the extent of each debris flow trench in the study area, we conducted a one-month geological survey of the study area in September 2018. According to the field investigation results, we have ascertained the provenance and reserves of the formation area, and, according to the type of provenance, they can be divided into three types: collapse-slip accumulation source, slope erosion source and channel accumulation source (Table 4).

On 2 July 2017, debris flow occurred in eight debris flow gullies in the northern scenic spot. According to the formula given in 3.2, the solid outflow of each debris flow ditch was calculated. The calculation results for each parameter are shown in Table 5. Among the debris flows caused by the rainfall, the No. 2 ditch has the most solid outflow, reaching 0.34×10^4 m^3, and the No. 7 ditch has the least solid outflow, reaching 0.01×10^4 m^3. Through regression analysis, we found that there is a strong power function correlation between the loose material reserves (V_m) of the debris flow ditch and the single debris flow solid source discharge (Q_H) (Figure 5): $V_m = 0.0089 Q_H^{1.3156}$, $R^2 = 0.9935$. The amount of debris flow solid material increased with the increase of loose material reserves; that is, when the study area has more material source reserves, the greater the risk of debris flow.

Table 4. Statistical table of sources of debris flow ditches in the Changbai Mountain North Scenic Area.

Ditch Number	Landslide Accumulation Source (10^4 m^3)	Slope Erosion Source (10^4 m^3)	Ditch Accumulation Source (10^4 m^3)	Total (10^4 m^3)
No. 1 ditch	6.13	2.91	1.96	11
No. 2 ditch	7.65	3.4	4.55	15.6
No. 3 ditch	1.7	1.8	0.19	3.69
No. 4 ditch	2.95	0.74	1.38	5.07
No. 5 ditch	0.59	1.71	0	2.3
No. 6 ditch	0.6	1.6	0	2.2
No. 7 ditch	0.62	1.28	0	1.9
No. 8 ditch	1.8	0.34	0.22	2.36
total	21.45	12.07	8.3	44.12

Table 5. Solid discharge of each debris flow ditch.

Ditch Number	Total Amount of Debris Flow (10^4 m^3)	Debris Flow Severity (t/m^3)	Water Severity (t/m^3)	Solid Material Weight of Debris Flow (t/m^3)	Solid Material Discharge of Debris Flow (10^4 m^3)
No. 1 ditch	0.49	1.70	1	2.50	0.23
No. 2 ditch	0.70	1.72	1	2.50	0.34
No. 3 ditch	0.06	1.48	1	2.50	0.02
No. 4 ditch	0.09	1.77	1	2.50	0.04
No. 5 ditch	0.07	1.48	1	2.50	0.03
No. 6 ditch	0.05	1.53	1	2.50	0.02
No. 7 ditch	0.04	1.49	1	2.50	0.01
No. 8 ditch	0.09	1.57	1	2.50	0.03

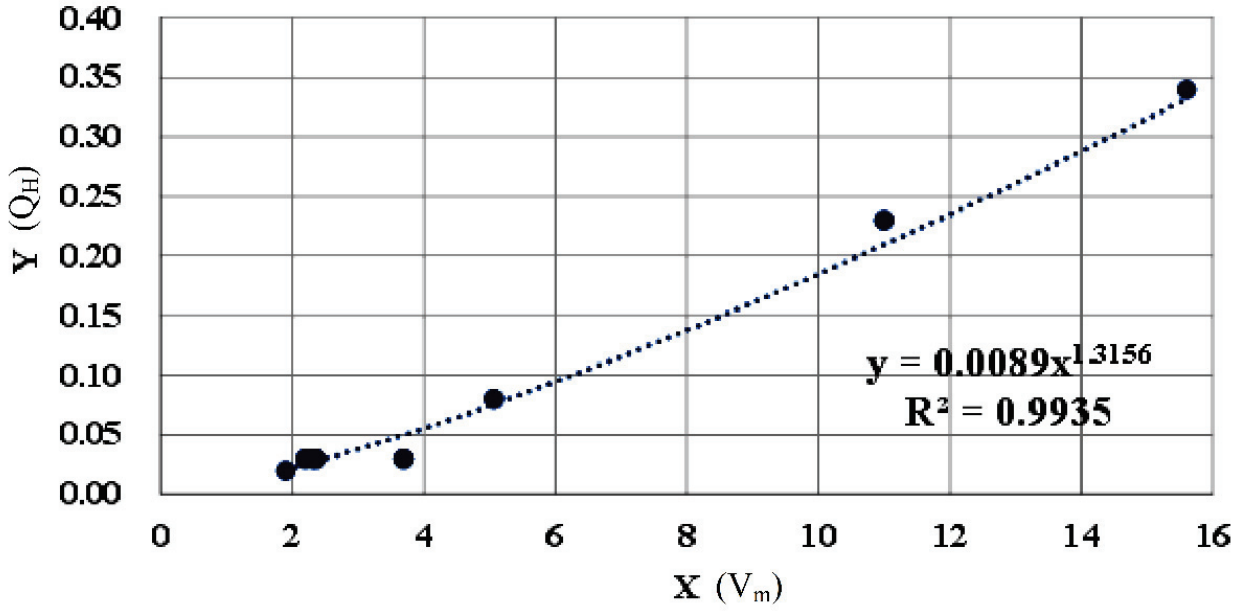

Figure 5. Relationship between source reserves and solid discharge of debris flow in the study area.

4.2. Offset Tracking Processing Results

The cross-correlation window size was adjusted and set to 16 × 16; the window size coherence was 8 × 8, and the coherence coefficient was 0.3. The Sentinel-1 data of the study area on 1 January 2017 and 27 December 2017 were processed by offset tracking to obtain the range direction (along the satellite line of sight) and azimuth direction (satellite orbit direction) of the study area during this time period. The results of displacement deformation in the direction of travel are shown in Figure 6. It can be seen from the figure that the range deformation in the study area in 2017 was very small, mainly in the azimuth direction. In order to ascertain the variation of provenance in the study area in each season, we use the six-scene Sentinel-1 data (since the end of each season is close to the beginning

of another season, the same scene data are used) to study the surface deformation of the area in each season which has been monitored. By using the formula $\Delta x = \sqrt{\Delta l^2 + \Delta p^2}$, the deformation of azimuth and distance is transformed into total displacement (Δl, Δp are the range offset and azimuth offset) (Figure 7). From the graph, it can be observed that the deformation in the study area is at its maximum during summer, with a maximum positive deformation of 130 mm/qr and a maximum negative deformation of 138 mm/qr. It should be noted that varying amounts of deformation are observed near each debris flow channel, which is due to the presence of large areas of slope debris near these channels. However, based on field surveys, it was found that these solid debris do not participate in the debris flow process; hence, they were not considered (Figure 8). Moreover, due to the growth of vegetation during summer, densely vegetated areas may cause signal obstruction or reflection, leading to increased precision error in offset tracking. The growth and change in vegetation can also cause changes in surface height, affecting the accuracy of offset tracking. Another point to consider is that the deposition areas of each debris flow channel are close to Erdaobai river; as the peak flow of Erdaobai river during the rainy season reaches 140 m^3/s, the debris flow materials are more likely to be carried away by the main river flow. Therefore, some deposition areas of debris flow may not exhibit positive deformation during summer, and channels numbered 4, 6 and 7 may even be affected by floods, resulting in negative deformation. In the circulation area of debris flow gully, due to the entrainment of debris flow, the deformation is basically negative in the figure, while the deformation amount in the formation area of the debris flow channel also varies depending on the size of the landslide supply from upstream. Therefore, the OT result alone is insufficient to determine the physical characteristics of the debris flow area and must be combined with field surveys or interpretations of remote sensing images to obtain more accurate results. However, analyzing the deformation amount in different areas based on OT results can help to determine the trend of debris flow development.

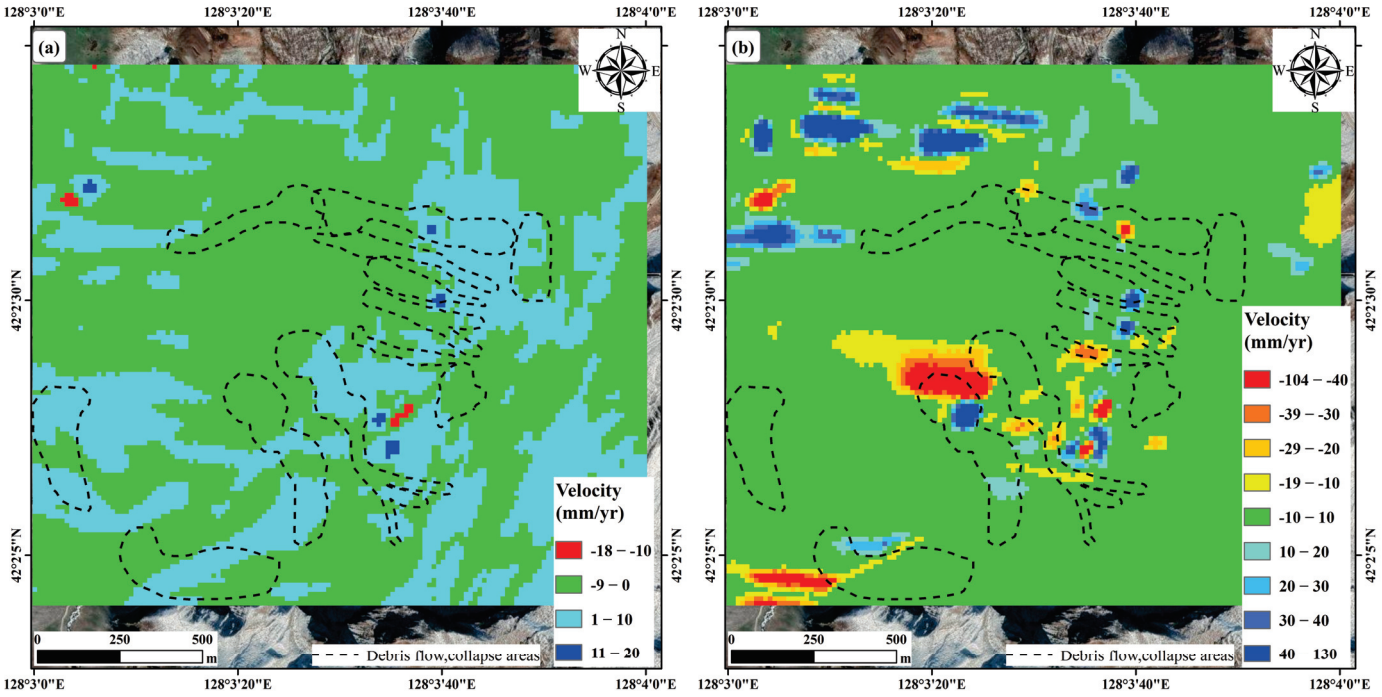

Figure 6. Results of surface deformation offset tracking in the study area (2017/01/01–2017/12/27). (**a**) Range direction; (**b**) azimuth direction.

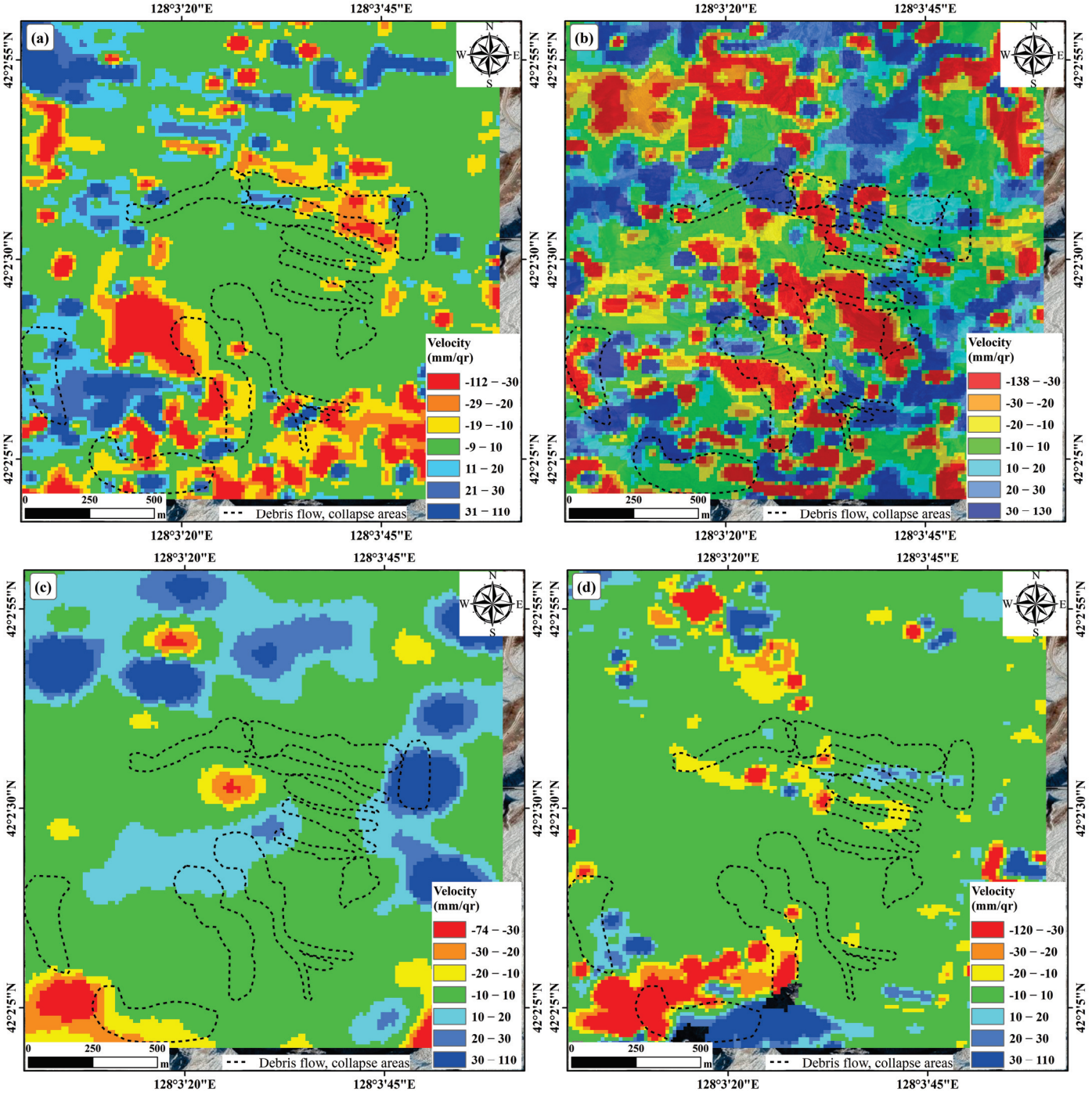

Figure 7. OT processing results of surface deformation in the study area in 2017. (**a**) Spring deformation (2017/03/07–2017/05/30); (**b**) summer deformation (2017/05/30–2017/09/03); (**c**) autumn deformation (2017/09/03–2017/11/26); (**d**) winter deformation (2017/11/26–2018/03/03).

Figure 8. The slope debris near the debris flow channel and the vegetation that begins to grow in summer.

4.3. D-InSAR Processing Results

Following the surface deformation analysis of the study area using the offset-tracking technique, we monitored the deformation of the study area by seasonal variation sing D-InSAR. The coherence threshold is 0.3, and the results are shown in the Figure 9. It can be seen from the figure that for each season, there is a certain range of blocky coherence loss areas (blank areas in the figure), where the maximum positive deformation that can be represented in the figure for each season is 78 mm, and the maximum negative deformation is 80 mm. Although D-InSAR does not provide a complete picture of deformation at every location in the study area, the ability to detect deformation in areas of slow deformation (e.g., autumn and winter) is unmatched by offset tracking. For example, the OT results for the study area in autumn and winter only reveal a trace of deformation but not the location, whereas D-InSAR demonstrates complete performance. However, D-InSAR results are not completely reliable and need to be used in conjunction with OT to obtain better analysis; for example, in Figure 9a, the low-frequency image, possibly due to Unwrap error, shows a south-to-north transition in the image, which is clearly not reliable.

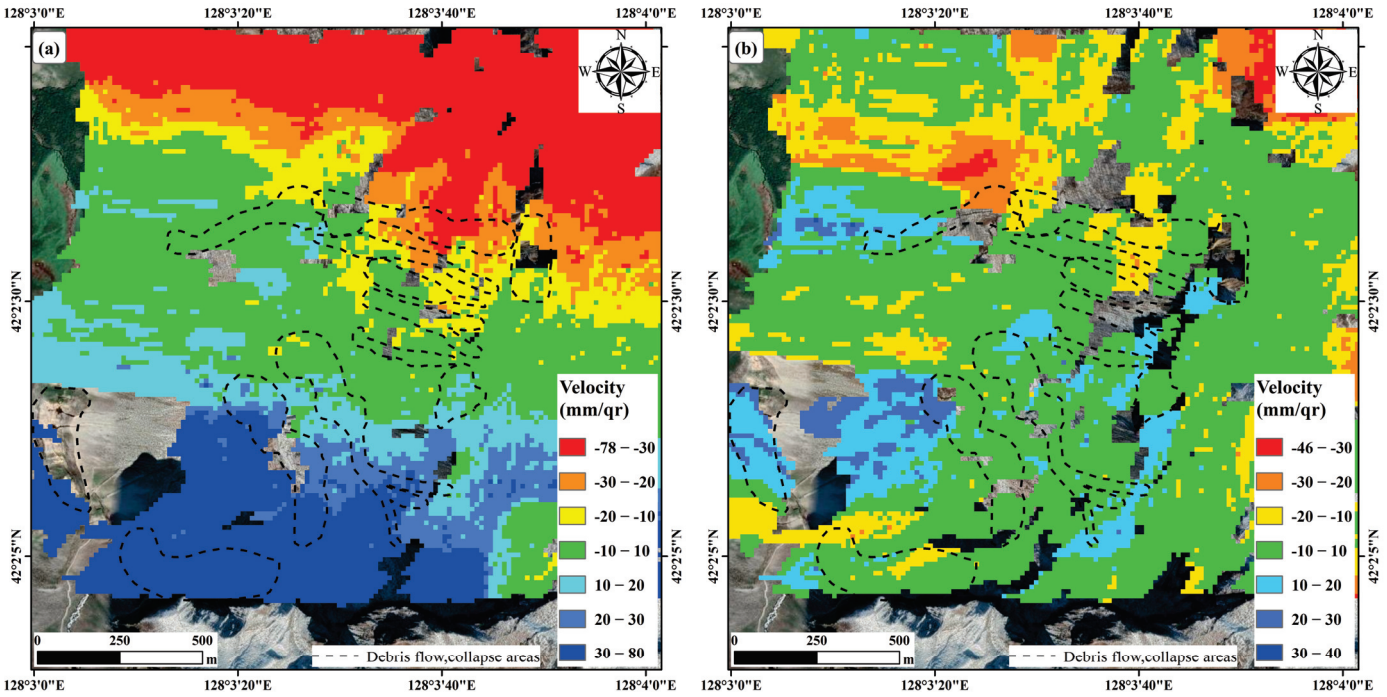

Figure 9. *Cont.*

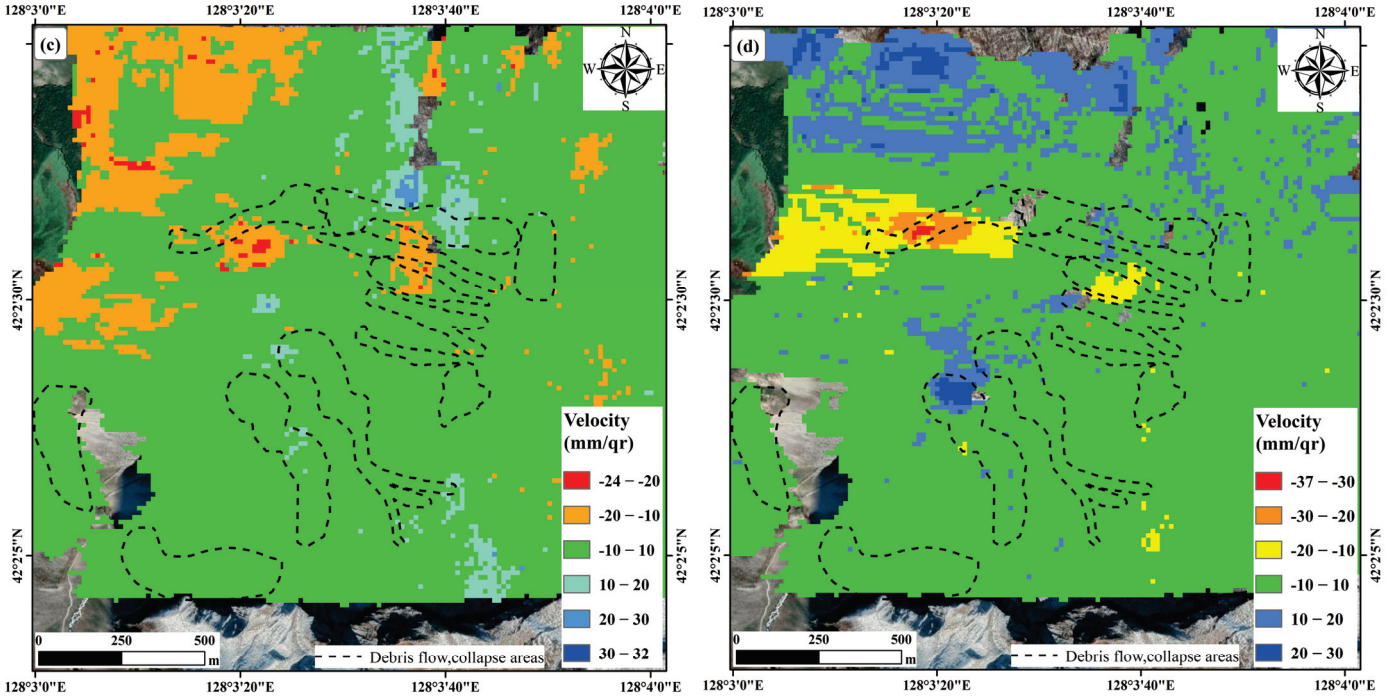

Figure 9. D-InSAR processing results of surface deformation in the study area in 2017. (**a**) Spring deformation (2017/03/07–2017/05/30); (**b**) summer deformation (2017/05/30–2017/09/03); (**c**) autumn deformation (2017/09/03–2017/11/26); (**d**) winter deformation (2017/11/26–2018/03/03).

4.4. Debris Flow Danger Zone in Scenic Area

According to the surface deformation monitoring results in the study area, combined with remote sensing images and field surveys, six debris flow risk areas in the scenic area of the study area were delineated, as shown in (Figure 10). Red is the monitored dangerous area determined according to the debris flow accumulation area, and yellow is the debris flow dangerous area determined by the field investigation. We can see that the monitoring results are very close to the field investigation results, which proves that OT has applicability in debris flow disaster prevention and mitigation. Among them, (a) is the No. 1 debris flow ditch danger zone, which includes the waterfall viewing platform, and the preliminary statistics threat number is 30,000 people; (b) is the No. 2 ditch debris flow dangerous area, which includes the scenic area's downstream trestle waterfall viewing platform, and the preliminary statistics threat number is 40,000 people; (c) and (h–f) are, respectively, No. 3 and No. 6–8 debris flow ditch dangerous areas, including the Julong hot spring scenic area and ditch mouth scenic area infrastructure, and the preliminary statistics threat number is 20,000 people; (d) is the No. 4 ditch debris flow danger zone, which includes the scenic parking lot and highway, and the preliminary statistics threat number is 40,000 people; (e) is the No. 5 ditch debris flow danger zone, for which there is no direct threat; (i) is the Longmen peak collapse landslide danger zone. It can be seen from the scope of the danger zone delineated in the figure that the danger range of No. 1 and No. 2 ditches is much larger than those of other debris flow ditches, which is positively correlated with the amount of solid outflow calculated by us. In the No. 2 ditch, solids flowed out of the accumulation area near the Erdaobai River, but because the debris flow outbreak season is the rainy season, the Erdaobai River peak flow of 140 m^3/s debris flow material will flow away with the main river water, so it will not cause a blocking the Erdaobai River's main channel.

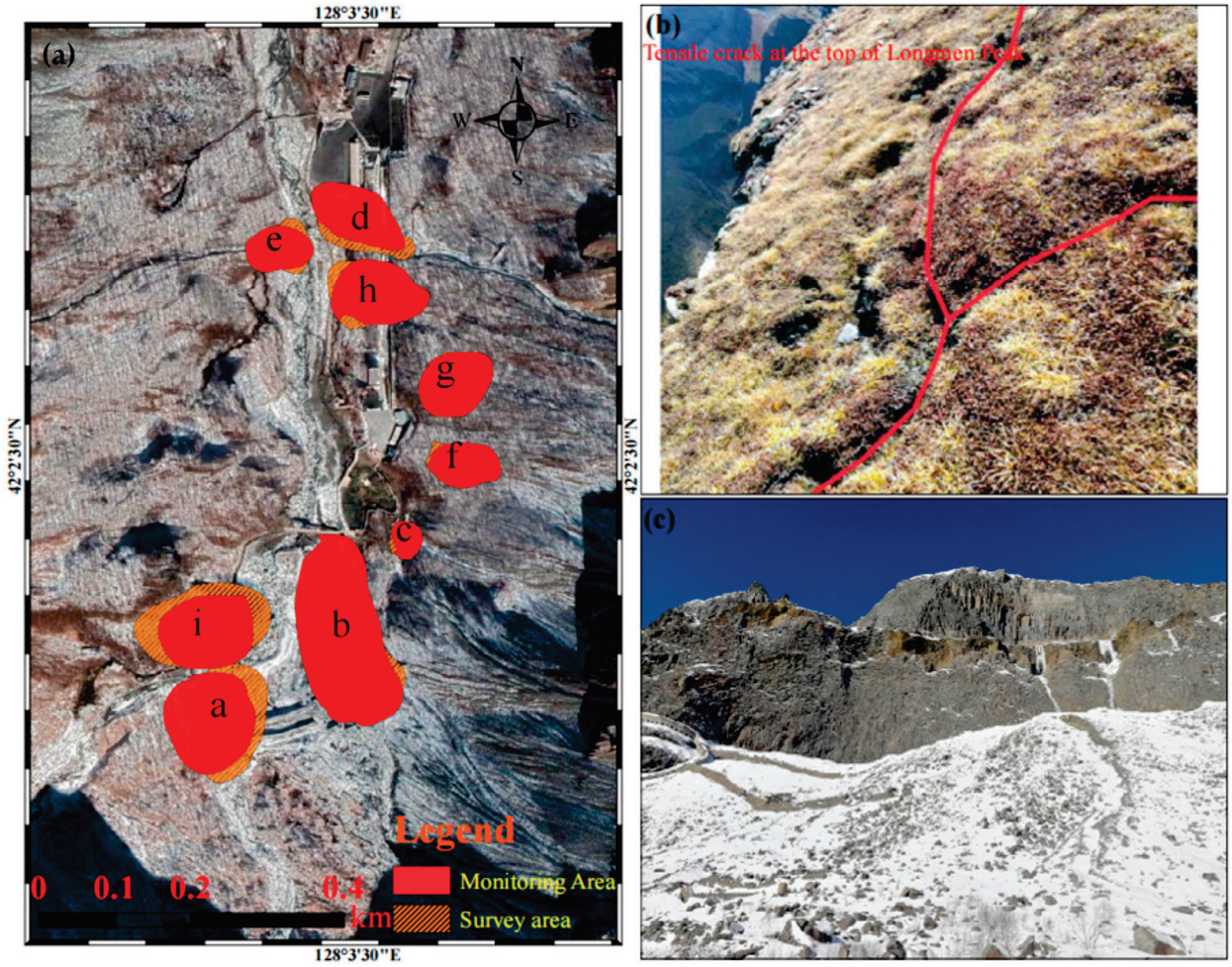

Figure 10. (**a**) North scenic dangerous area; (**b**) Longmen peak dangerous rock belt top; (**c**) Longmen peak dangerous rock belt side.

5. Discussion

5.1. Error Analysis

The root mean square error (RMSE) of D-InSAR and OT is an error metric used to evaluate the results of surface deformation measurements, and it is usually used to evaluate the accuracy and reliability of D-InSAR and OT algorithms. The minimum accuracy requirement is satisfied when the result is less than 100, and the smaller it is, the higher the reliability of the result. The RMSE values can be accessed in the report of the result file after the processing is completed. The RMSE values of offset tracking are 12.9, 95.8, 5.7 and 13.6, and the RMSE values of D-InSAR are 135, 217, 35.8 and 45.5, respectively. The RMSE values of D-InSAR are higher in both spring and summer, while OT meets the minimum value of reliability. Therefore, the combination of these two methods has some reliability when used to determine the changes of the source within the mudflow range that we have investigated in the field and interpreted by remote sensing. However, both methods are subject to certain limitations, leading to errors in accuracy. These include the height change due to the growth of vegetation in summer, which we mentioned in the previous section, and which will affect the monitoring accuracy, and the obscuring effect of terrain and vegetation may also lead to the unfolding error of D-InSAR. The radar reflection signal is affected by terrain and vegetation, and these effects will lead to different propagation times and paths of the signal between different areas, thus causing phase differences in unfolding [48]. Thus, phase differences occur and cause unfolding errors. Therefore, it is difficult and unreliable for researchers to rely on this method to determine the extent of the mudslide area, which

requires a combination of field survey and high-precision remote sensing images. There is also the fact that the time baseline we used in the paper is too long for to be used to obtain the variation of the source under different seasons, which will increase the ranging error in the data and thus reduce the positioning accuracy. In addition, a long time baseline also means that the signal is reflected or interfered with several times, which will further increase the accuracy error, and improving accuracy and reliability requires the selection of appropriate techniques and algorithms for data processing and correction [49].

For OT, although it can show a good performance in large gradient deformation, large gradient deformation also increases the difficulty of image alignment during processing, and incomplete alignment can have a large impact on accuracy, and the lower root mean square error in the summer period may be related to incomplete alignment. Preprocessing is needed to improve the stability and accuracy of the whole matching process. Jia H. proposed an improved uniform sample-based adaptive noncoherent scattering offset-tracking algorithm, which improves the speed and accuracy of co-alignment.

In addition to showing poor results in large gradient deformation monitoring, D-InSAR is not and will not be completely reliable for deformation monitoring in slowly deforming areas. For example, in this study on the amount of spring variation of mudflow sources using D-InSAR, the resultant images show a low frequency image transitioning from south to north during the unfolding process. In D-InSAR processing, low-frequency images caused by unfolding errors are generated due to the limitation of interferometric stripes, and the unfolding errors are usually caused by two factors: the large-scale deformation of the Earth's surface and the inhomogeneity of the propagation medium. The study area is covered with ice and snow in winter, and the shape of the medium changes when the ice melts in spring, resulting in possible changes in the path of the light, which affects the accuracy and reliability of phase untwisting. In addition, the melting of snow and ice will produce a large amount of water vapor, which will interfere with the propagation of light, and which will also cause some difficulties for phase decoupling. Therefore, for the ice-covered areas, the introduction of information from other data sources as constraints can be considered in the calculation process, or the D-InSAR method with multiple time phases can be used so as to reduce the influence of the unfolding error and improve the accuracy and reliability of deformation monitoring.

5.2. Offset Tracking Processing Results

In this study, we analyzed the relationship between the amount of debris flow solid discharge and the source reserves, but in fact, the amount of debris flow solid discharge is affected by many characteristic parameters [50]. By studying the relationship between the amount of loose source in the basin, the relative height difference of the basin and the amount of debris flow discharge, the prediction research is carried out by Bovis [51]. By analyzing the characteristics of the debris flow in the Wenchuan earthquake area, the mathematical relationship between the debris flow discharge and the loose material source is obtained by Ma [52]. An American scholar, Gartner, combined the three factors of debris flow basin area [53], landslide source area and cumulative rainfall to count the debris flow ditch in Corolla, analyzed the relationship between debris flow discharge and the three factors, and established the prediction model of debris flow discharge. The type and influence degree of these parameters can provide some data support for the prevention and control project of debris flow in the study area, suggesting that the prevention and control project can maximize the effect of disaster prevention and mitigation [54–56].

We analyzed the correlation and significance between debris flow solid outflow (Q_H) and ditch length (GL), ditch area (AOC), relative elevation difference (RED), mean longitudinal slope (MLS), source reserve (V_m), collapse accumulation source (LAS), slope erosion source (SES) and ditch accumulation source (GAS). Here, we also divide the provenance into slump deposit source, slope erosion source and ditch deposit source. Because of different debris flow gullies due to the different ditch forms, rainfall conditions and the distribution of material sources in the ditch, the main types of material sources involved

in debris flow will be different. The correlation and significance analysis results pertaining to these characteristic parameters and the number of solid debris flows are shown in Figures 11 and 12.

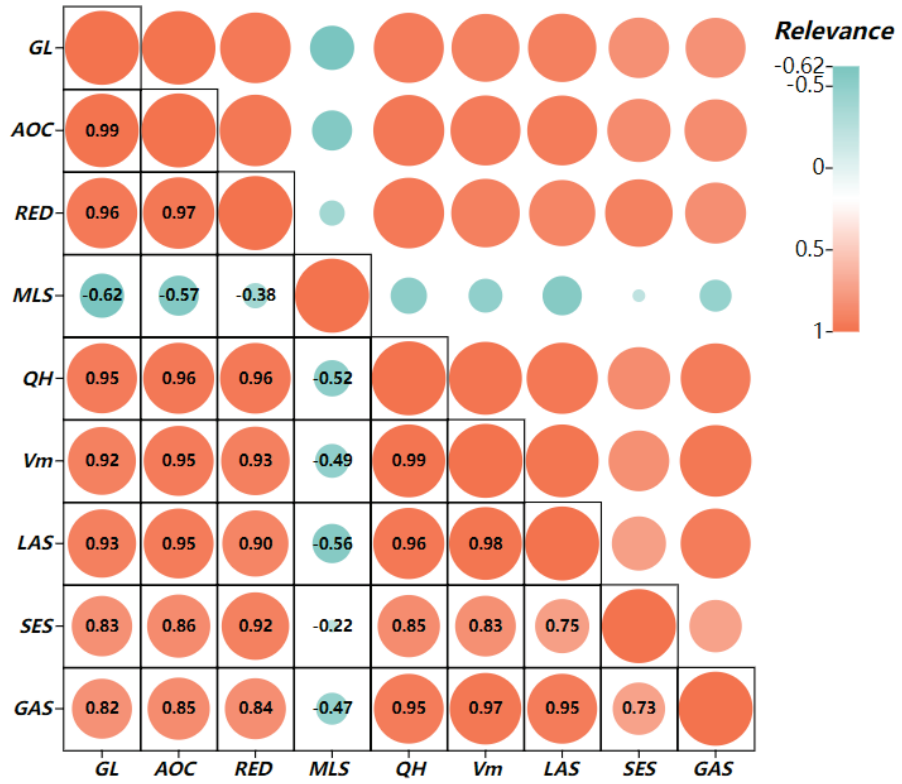

Figure 11. Correlation analysis results.

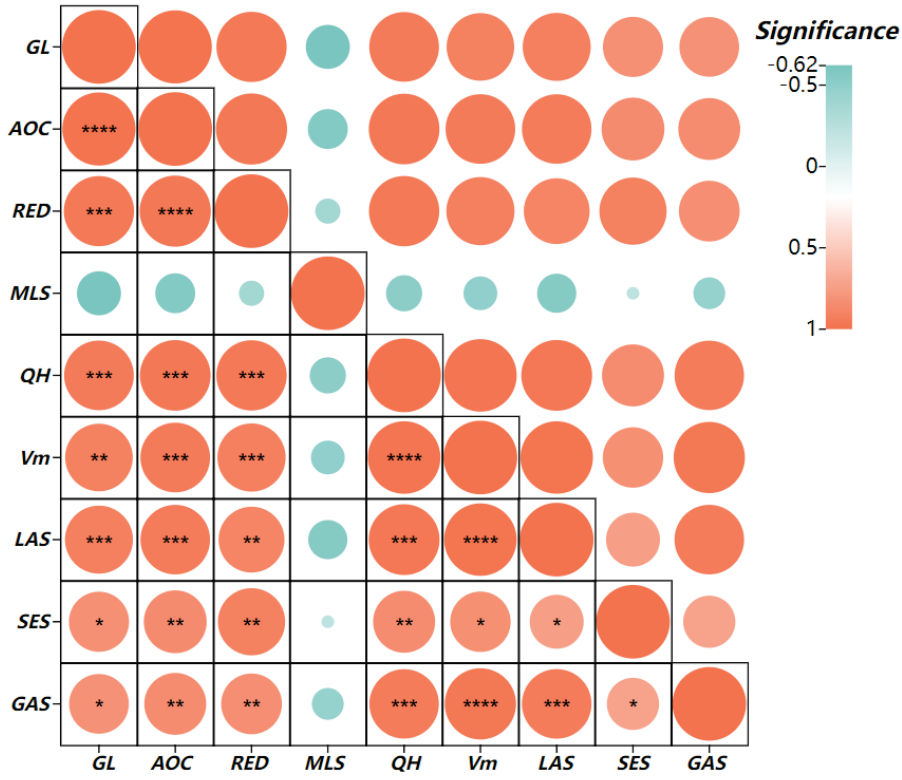

Figure 12. Significance analysis results. * expressed $p < 0.05$, ** expressed $p < 0.01$, *** expressed $p < 0.001$, **** expressed $p < 0.0001$.

According to the analysis results, except that the *p* value of the average longitudinal slope is negative, there is a strong positive correlation between the amount of debris flow and other parameters. It shows that these characteristic parameters have a strong influence on the amount of solid debris flow in this study area. There is a strong correlation between the three types of material sources of landslide accumulation, slope erosion, ditch accumulation and the amount of solid debris flow. Among them, the sources of landslide accumulation and ditch accumulation are up to 0.98 and 0.97, respectively, indicating that these two types of sources participate in debris flow activities. In the future monitoring of disaster prevention and mitigation, we should pay special attention to the changes of these two parameters.

6. Conclusions

Monitoring the change of provenance in the study area is an effective means of debris flow early warning and prevention. In this paper, we combine field investigation, remote sensing imaging and offset-tracking technology to monitor the deformation of solids in the study area. The conclusions are as follows:

1. According to the comparison between the solid washout from the mudflow we calculated, and the loose material source reserves obtained from the survey, the solid washout from a single mudflow is much smaller than the material source reserves. Combined with the analysis of the OT results, even after the occurrence of mudflow, the formation area of multiple mudflows will be recharged by material sources due to the collapse landslide above, and the recharge will be even greater than the consumption. Therefore, the frequency of mudflow outbreaks in the study area may be more frequent in the summer when heavy rainfall is encountered for a long time in the future;
2. Although OT is widely used for large gradient deformation, and although we can use it to determine the physical source variability of mudflows in the study area, for different study purposes, the OT results are not completely reliable. For example, as we mentioned in 4.2, we cannot use the OT results alone to delineate the extent of mudflows, and its results are affected by various factors such as vegetation, rainfall and weather. Therefore, in the study of mudslides, it is necessary to combine field surveys or remote sensing images to delineate the extent of mudslides;
3. Combined with remote sensing images, field survey and offset tracking results delineated the mudslide danger zone in the scenic area of the study area. Due to the huge number of visitors in the scenic area—according to our preliminary statistics, the total number of people threatened reached 130,000—it is necessary to do a good job of disaster prevention and mitigation and protection work in the danger zone, especially at the danger zone of the collapse of Longmen Peak, where there have been many incidents of falling rocks injuring people;
4. We have used D-InSAR for deformation monitoring after deformation monitoring using offset tracking, a method which, although subject to many factors when deforming large gradients, can be used as a complement to offset-tracking techniques. D-InSAR can operate effectively in areas with slow deformation, and it can be used in combination with offset tracking to obtain more highly accurate surface shape information. We see an opportunity here to develop a hybrid velocity product combining D-InSAR and offset tracking results in the areas where one method or the other- or both-perform best, as suggested by Joughin [54] and Liu [55], in order to obtain more reliable deformation monitoring results;
5. In snow and ice covered areas, the effect of snow and ice melting may increase the error of phase untwisting, which, in turn, leads to low-frequency images. Therefore, the monitoring accuracy and results of D-InSAR will be greatly affected during the ice and snow melting in spring, and even if the deformation is small, the monitoring results cannot be fully trusted and need to be used in combination with other methods;

6. We learned from analyzing the relationship between various parameters in the watershed, as well as the quantity of washed out debris flow solids, that the source of avalanche-slip accumulation and the source of channel accumulation have a high correlation with the amount of debris flow solids washed out, and we should consider increasing the weight of these two factors when predicting the development trend of debris flow.

Author Contributions: Conceptualization, J.Y.; Data curation, J.Y. and Y.Z.; Formal analysis, J.Y. and Y.C.; Methodology, J.Y. and Y.C.; Writing—Original draft, J.Y.; Funding acquisition, J.Z. and Z.Z.; Writing—Review and Editing, Z.Z. All authors have read and agreed to the published version of the manuscript.

Funding: This study was funded by the major scientific and technological research project of Jilin 404 Province (20220203185SF) and the soft science research project of Jilin Provincial Department of 405 Natural Resources (120200073).

Institutional Review Board Statement: Not applicable.

Informed Consent Statement: Not applicable.

Data Availability Statement: The codes and data for this article are freely available at http://scihub.copernicus.eu/dhus (accessed on 3 May 2017), https://earthexplorer.usgs.gov/ (accessed on 3 May 2017).

Conflicts of Interest: The authors declare no conflict of interest.

References

1. Rickenmann, D.; Zimmermann, M. The 1987 debris flows in Switzerland: Documentation and analysis. *Geomorphology* **1993**, *8*, 175–189. [CrossRef]
2. Costa, J. Physical geomorphology of debris flows. In *Developments and Applications of Geomorphology*; Springer: Berlin/Heidelberg, Germany, 1984; pp. 268–317.
3. Hungr, O.; Evans, S.G.; Bovis, M.J.; Hutchinson, J.N. A review of the classi fication of landslides of the flow type. *Phys. Geomorphol. Debrisflows* **2001**, *7*, 221–238.
4. Hungr, O.; Leroueil, S.; Picarelli, L. The Varnes classification of landslide types. *Landslides* **2014**, *11*, 167–194. [CrossRef]
5. Iverson, R.M. The physics of debris flows. *Rev. Geophys.* **1997**, *35*, 245–296. [CrossRef]
6. Innes, J.L. Debris flows. *Prog. Phys. Geogr. Earth Environ.* **1983**, *7*, 469–501. [CrossRef]
7. Cesca, M.; D'Agostino, V. Comparison between FLO-2D and RAMMS in debrisflow modelling: A case study in the Dolomites. *WIT Trans. Eng.* **2008**, *60*, 197–206.
8. De Haas, T.; Braat, L.; Leuven, J.R.F.W.; Lokhorst, I.R. Kleinhans MGEffects of debrisflow composition on runout, depositional mechanisms, and deposit morphology in laboratory experiments. *Geophys. Res. Earth Surf.* **2015**, *120*, 1949–1972. [CrossRef]
9. Ji, F.; Dai, Z.; Li, R. A multivariate statistical method for susceptibility analysis of debris flow in southwestern China. *Hazard. Earth Syst.* **2020**, *20*, 1321–1334. [CrossRef]
10. Viesca, R. Debris flow: Mechanics, prediction and countermeasures by Tamotsu Takahashi. *Pure Appl. Geophys.* **2008**, *165*, 995. [CrossRef]
11. Chen, H.X.; Zhang, L.M.; Chang, D.S.; Zhang, S. Mechanisms and runout characteristics of the rainfall-triggered debris fow in Xiaojiagou in Sichuan Province, China. *Nat. Hazard.* **2012**, *62*, 1037–1057. [CrossRef]
12. Simoni, A.; Mammoliti, M.; Graf, C. Performance of 2D debris fow simulation model RAMMS. Back-analysis of feld events in Italian Alps. *Annu. Int. Conf. Geol. Earth Sci.* **2012**, *20*, 1521–1534.
13. Breien, H.; De Blasio, F.V.; Elverhøi, A.; Høeg, K. Erosion and morphology of a debris flow caused by a glacial lake outburst flood, Western Norway. *J. Landslides* **2008**, *5*, 271–280. [CrossRef]
14. Bel, C.; Li'ebault, F.; Navratil, O.; Eckert, N.; Bellot, H.; Fontaine, F.; Laigle, D. Rainfall control of debris-flow triggering in the Real Torrent, Southern French Prealps. *Geomorphology* **2017**, *291*, 17–32. [CrossRef]
15. Dowling, C.A.; Santi, P.M. Debris flows and their toll on human life: A global analysis of debris-flow fatalities from 1950 to 2011. *Nat. Hazard.* **2014**, *71*, 203–227. [CrossRef]
16. Lee, S.G.; Winter, M.G. The effects of debris flow in the Republic of Korea and some issues for successful risk reduction. *Eng. Geol.* **2019**, *251*, 172–189. [CrossRef]
17. Pastorello, R.; D'Agostino, V.; Hürlimann, M. Debris flow triggering characterization through a comparative analysis among different mountain catchments. *Catena* **2020**, *186*, 104–348. [CrossRef]
18. Bernard, M.; Gregoretti, C. The use of rain gauge measurements and radar data for the model-based prediction of runoff-generated debris-flow occurrence in early warning systems. *Water Resour.* **2021**, *57*, e2020WR027893. [CrossRef]
19. Berti, M.; Bernard, M.; Gregoretti, C.; Simoni, A. Physical interpretation of rainfall thresholds for runoff-generated debris flows. *Geophys. Res. Earth Surf.* **2017**, *125*, e2019JF005513. [CrossRef]

20. Cao, C.; Zhang, W.; Chen, J.; Shan, B.; Song, S.; Zhan, J. Quantitative estimation of debris flow source materials by integrating multisource data: A case study. *Eng. Geol.* **2019**, *291*, 106–222.
21. Caine, N. The rainfall intensity-duration control of shallow landslides and debris flows. *Geogr. Ann. Ser.* **1980**, *62*, 23–27.
22. Dewitte, O.; Jasselette, J.C.; Cornet, Y.; Van Den Eeckhaut, M.; Collignon, A.; Poesen, J.; Demoulin, A. Tracking landslide displacements by multi-temporal DTMs: A combined aerial stereophotogrammetric and LIDAR approach in western Belgium. *Eng. Geol.* **2008**, *99*, 11–22. [CrossRef]
23. Stumpf, A.; Malet, J.-P.; Allemand, P.; Ulrich, P. Surface reconstruction and landslide displacement measurements with Pl'eiades satellite images. *Photogramm. Remote Sens.* **2004**, *95*, 1–12. [CrossRef]
24. Tseng, C.M.; Lin, C.W.; Stark, C.P.; Liu, J.K.; Fei, L.Y.; Hsieh, Y.C. Application of a multi-temporal, LiDAR-derived, digital terrain model in a landslide-volume estimation. *Earth Surf. Process. Landf.* **2013**, *38*, 1587–1601. [CrossRef]
25. Feng, G.; Hetland, E.A.; Ding, X.; Li, Z.; Zhang, L. Coseismic fault slip of the 2008 Mw 7.9 Wenchuan earthquake estimated from InSAR and GPS measurements. *Geophys. Res. Lett.* **2010**, *37*, 73–78. [CrossRef]
26. Strozzi, T.; Luckman, A.; Murray, T.; Wegmuller, U.; Werner, C.L. Glacier motion estimation using SAR offset-tracking proce dures. *J. IEEE Trans. Geosci. Remote Sens.* **2002**, *40*, 2384–2391. [CrossRef]
27. Elliott, J.L.; Freymueller, J.T.; Rabus, B. Coseismic deformation of the 2002 Denali fault earthquake: Contributions from synthetic aperture radar range offsets. *Geophys. Res. Solid Earth* **2007**, *112*, B6. [CrossRef]
28. Wang, T.; Jónsson, S. Improved SAR amplitude image offset measurements for deriving three-dimen sional coseismic displacements. *J. Sel. Top. Appl. Earth Obs. Remote Sens.* **2015**, *8*, 3271–3278. [CrossRef]
29. Schellenberger, T.; Dunse, T.; Kääb, A.; Kohler, J.; Reijmer, C. Surface speed and frontal ablation of kronebreen and kongsbreen, NW Svalbard, from SAR offset tracking. *Cryosphere* **2015**, *9*, 2339–2355. [CrossRef]
30. Wang, C.; Mao, X.; Wang, Q. Landslide displacement monitoring by a fully polarimetric SAR offset tracking method. *Remote Sens.* **2010**, *8*, 624. [CrossRef]
31. Fielding, E.J.; Lundgren, P.R.; Taymaz, T.; Yolsal-Çevikbilen, S.; Owen, S.E. Fault-slip source models for the 2011 M 7.1 van earthquake in Turkeyfrom SARinterferometry, pixel offset tracking, GPS, and seismic waveform analysis. *Seismol. Res.* **2013**, *84*, 579–593. [CrossRef]
32. Bai, C.; Wang, F.; Wang, L.; Xu, C.; Yue, X.; Yang, S.; Wang, P.; Bi, Y.; Wei, H. Dynamic Monitoring of Debris-Covered Glacier Surface Velocity and Ice Thickness of Mt.Tomur, Tian Shan, China. *Remote Sens.* **2023**, *15*, 150. [CrossRef]
33. Yang, H.; Tang, L.; Zhu, H.; Xu, A.; Li, B. A Concise Method for Calibrating the Offset of GPS Precise Satellite Orbit. *Remote Sens.* **2023**, *15*, 8. [CrossRef]
34. Yang, C.; Wei, C.; Ding, H.; Wei, Y.; Zhu, S.; Li, Z. Inversion of Glacier 3D Displacement from Sentinel-1 and Landsat 8 Images Based on Variance Component Estimation: A Case Study in Shishapangma Peak, Tibet, China. *Remote Sens.* **2023**, *15*, 4. [CrossRef]
35. Feng, J.; Qiu, Y.; Dong, C.; Ni, X.; Lin, W.; Teng, H.; Pan, A. Interannual Variabilities of the Southern Bay of Bengal Cold Pool Associated with the El Niño–Southern Oscillation. *Remote Sens.* **2023**, *14*, 6169. [CrossRef]
36. Zhu, Y.; Qiu, H.; Liu, Z.; Wang, J.; Yang, D.; Pei, Y.; Ma, S.; Du, C.; Sun, H.; Wang, L. Detecting Long-Term Deformation of a Loess Landslide from the Phase and Amplitude of Satellite SAR Images: A Retrospective Analysis for the Closure of a Tunnel Event. *Remote Sens.* **2021**, *13*, 4841. [CrossRef]
37. Gray, A.L.; Mattar, K.E.; Vachon, P.W.; Bindschadler, R.; Jezek, K.C.; Forster, R.; Crawford, J.P. InSAR results from the RADARSAT Antarctic Mapping Mission data: Estimation of glacier motion using a simple registration procedure. IGARSS'98. Sensing and Managing the Environment. 1998 IEEE International Geoscience and Remote Sensing. *Symp. Proc.* **1998**, *3*, 1638–1640. [CrossRef]
38. Yoo, J.C.; Han, T.H. Fast normalized cross-correlation. *Circuits Syst. Signal Process.* **2009**, *28*, 819–843. [CrossRef]
39. Jia, H.; Wang, Y.; Ge, D.; Deng, Y.; Wang, R. Improved offset tracking for predisaster deformation monitoring of the 2018 Jinsha River landslide (Tibet, China). *Remote Sens. Environ.* **2020**, *247*, 111899. [CrossRef]
40. Du, S.; Mallorqui, J.J.; Zhao, F. Patch-Like Reduction (PLR): A SAR Offset Tracking amplitude filter for defor mation monitoring. *Int. J. Appl. Earth Obs. Geoinf.* **2022**, *113*, 102976. [CrossRef]
41. Rott, H.; Stuefer, M.; Siegel, A.; Skvarca, P.; Eckstaller, A. Mass fluxes and dynamics of Moreno Glacier, Southern Patagonia Icefield. *Geophys. Res. Lett.* **1998**, *25*, 1407–1410. [CrossRef]
42. Chen, B.; Deng, K.; Fan, H.; Hao, M. Large-scale deformation monitoring in mining area by D-InSAR and 3D laser scanning technology integration. *Int. J. Min. Sci. Technol.* **2013**, *23*, 555–561. [CrossRef]
43. Mura, J.C.; Paradella, W.R.; Gama, F.F.; Silva, G.G.; Galo, M.; Camargo, P.O.; Silva, A.Q.; Silva, A. Monitoring of Non-Linear Ground Movement in an Open Pit Iron Mine Based on an Integration of Advanced DInSAR Techniques Using TerraSAR-X Data. *Remote Sens.* **2016**, *8*, 409. [CrossRef]
44. Debella-Gilo, M.; Kääb, A. Sub-pixel precision image matching for measuring surface displacements on mass movements using normalized cross-correlation. *Remote Sens. Environ.* **2011**, *115*, 130–142. [CrossRef]
45. Cheng, X.Q.; Ma, C.; Kang, J.R.; Zou, Y. Simulation and time series analysis of mining subsidence by integrating DInSAR and PIM technology. *J. China Univ. Min. Technol.* **2018**, *47*, 1141–1148.
46. Pawluszek-Filipiak, K.; Borkowski, A. Integration of DInSAR and SBAS Techniques to Determine Mining-Related Deformations Using Sentinel-1 Data: The Case Study of Rydułtowy Mine in Poland. *Remote Sens.* **2020**, *12*, 242. [CrossRef]
47. Xu, B.; Li, Z.; Zhu, Y.; Shi, J.; Feng, G. SAR Interferometric Baseline Refinement Based on Flat-Earth Phase without a Ground Control Point. *Remote Sens.* **2020**, *12*, 233. [CrossRef]

48. Zhao, X.; Zhou, D.; Fang, J. Satellite-based Studies on Large-Scale Vegetation Changes in China. *J. Integr. Plant Biol.* **2012**, *54*, 713–728. [CrossRef]
49. Mirmohammadian, F.; Asgari, J.; Verhagen, S.; Amiri-Simkooei, A. Multi-GNSS-Weighted Interpolated Tropospheric Delay to Improve Long-Baseline RTK Positioning. *Sensors* **2022**, *22*, 5570. [CrossRef]
50. D'Agostino, V.; Marchi, L. Debris flow magnitude in the eastern italian alps: Data collection and analysis. *J. Phys. Chem. Earth* **2001**, *26*, 657–663. [CrossRef]
51. Bovis, M.J.; Jakob, M. The role of debris supply conditions in predicting debris flow activity. *J. Earth Surf. Process. Landf.* **1999**, *24*, 1039–1054. [CrossRef]
52. Ma, C.; Hu, K.; Tian, M. Comparison of debris-flow volume and activity under different formation conditions. *Nat. Hazard.* **2013**, *67*, 261–273. [CrossRef]
53. Gartner, J.E.; Cannon, S.H.; Santi, P.M.; Dewolfe, V.G. Empirical models to predict the volumes of debris flows generated by recently burned basins in the western U.S. *Geomorphology* **2008**, *96*, 339–354. [CrossRef]
54. Chang, M.; Tang, C.; Van Asch, T.W.; Cai, F. Hazard assessment of debris flows in the Wenchuan earthquake-stricken area, South West China. *J. Landslides* **2017**, *14*, 1783–1792. [CrossRef]
55. Joughin, I. Ice-sheet velocity mapping: A combined interferometric and speckle-tracking approach. *Ann. Glaciol.* **2002**, *34*, 195–201. [CrossRef]
56. Liu, H.X.; Zhao, Z.Y.; Jezek, K.C. Synergistic fusion of interferometric and speckle-tracking methods for deriving surface velocity from interferometric SAR data. *IEEE Geosci. Remote Sens. Lett.* **2007**, *4*, 102–106. [CrossRef]

water

MDPI

Article

In Situ Experimental Study of Natural Diatomaceous Earth Slopes under Alternating Dry and Wet Conditions

Zhixing Deng [1], Wubin Wang [1,2,*], Tengfei Yan [1], Kang Xie [3], Yandong Li [1], Yangyang Liu [1] and Qian Su [1]

[1] School of Civil Engineering, Southwest Jiaotong University, Chengdu 610031, China; 2020210063@my.swjtu.edu.cn (Z.D.); yantfxnjd@163.com (T.Y.); yandongli@my.swjtu.edu.cn (Y.L.); liuyy@my.swjtu.edu.cn (Y.L.); su1896swjtu@163.com (Q.S.)
[2] National Engineering Research Center of Geological Disaster Prevention Technology in Land Transportation, Southwest Jiaotong University, Chengdu 611731, China
[3] Department of Civil Engineering, Central South University, Changsha 410075, China; xiekang1995@csu.edu.cn
* Correspondence: wangwubin.sju@outlook.com

Abstract: Very few studies have focused on diatomaceous earth slopes along high-speed railways, and the special properties of diatomaceous earth under alternating dry and wet conditions are unknown. This paper studies diatomaceous earth in the Shengzhou area, through which the newly built Hangzhou–Taizhou high-speed railway passes, and the basic physical and hydraulic properties of diatomaceous earth are analyzed by indoor test methods. A convenient, efficient, and controllable high-speed railway slope artificial rainfall simulation system is designed, and in situ comprehensive monitoring and fissure observation are performed on site to analyze the changes in various diatomaceous soil slope parameters under rainfall infiltration, and to explore the cracking mechanisms of diatomaceous earth under alternating dry and wet conditions. The results indicate extremely poor hydrophysical properties of diatomaceous earth in the Shengzhou area; the disintegration resistance index values of natural diatomaceous earth samples subjected to dry and wet cycles are 1.8–5.6%, and the disintegration is strong. Comprehensive indoor tests and water content monitoring show that natural diatomaceous earth has no obvious influence when it contacts water, but it disintegrates and cracks under alternating dry and wet conditions. The horizontal displacement of both slope types mainly occurs within 0.75–2.75 m of the surface layer, indicating shallow surface sliding; after testing, natural slope crack widths of diatomaceous earth reach 10–25 mm, and their depths reach 40–60 cm. To guarantee safety during high-speed railway engineering construction, implementing proper protection for diatomaceous earth slopes is recommended.

Keywords: high-speed railway; diatomaceous earth; dry and wet cycle; artificial rainfall simulation systems; in situ monitoring

Citation: Deng, Z.; Wang, W.; Yan, T.; Xie, K.; Li, Y.; Liu, Y.; Su, Q. In Situ Experimental Study of Natural Diatomaceous Earth Slopes under Alternating Dry and Wet Conditions. *Water* **2022**, *14*, 831. https://doi.org/10.3390/w14050831

Academic Editor: Stefano Morelli

Received: 31 January 2022
Accepted: 3 March 2022
Published: 7 March 2022

1. Introduction

As of the end of 2020, China's operating railway mileage had reached 146,000 km, of which 37,900 km were high-speed railways. As the density of high-speed railway networks increases, high-speed railway construction will inevitably pass through special land areas. The newly built Hangzhou–Taizhou high-speed railway passes through Shengzhou city. A large amount of diatomaceous earth is present in the tertiary basalts and lacustrine deposits in the basalt platform area. Diatomaceous earth has well-developed joints, and is highly compressible; it easily softens when exposed to water, and its mechanical properties decrease substantially. Diatomaceous earth is in a hard-plastic-to-plastic state, and its engineering properties are extremely poor [1–6]. During on-site construction, diatomaceous earth slopes are exposed to the natural environment after excavation. The permeability coefficients of undisturbed diatomaceous earth are less than 10^{-6} cm/s, signaling an impervious layer in a given project. However, under alternating wet and dry conditions, depths of 40 to 60 cm are affected by the environment, resulting in cracks that greatly affect

the safe development of railway construction. Therefore, under the action of alternating wet and dry conditions, the destruction mechanism of diatomaceous earth and the dynamic evolution of diatomaceous earth slope parameters have become issues that urgently need to be studied.

At present, diatomaceous earth is widely used for environmental protection, and in chemical, electrical, and other fields, because of its high porosity and light weight [7–11]. However, the existing literature contains very few studies on diatomaceous earth slopes, and the special properties of diatomaceous earth under the action of dry and wet cycles are not well understood. On loess and expansive soil slopes, a lot of work has been done by scholars in the past; there is deeper research on the special properties of loess and swelling soil under the action of alternating wet and dry conditions, and a lot of practice has been done in combination with actual slope engineering; the main research results are shown in Table 1.

Table 1. Literature review table.

N°	Reference	Research Methods and Content	Research Findings
1	[12]	Artificial rainfall simulation experiments were conducted on loess slopes to study the damage mechanism of landslides under rainfall conditions.	Rainfall and landslides on loess slopes have a time lag.
2	[13]	The changes in shear strength, cohesion, and internal friction angle of loess samples under different dry and wet cycles were determined by indoor direct shear tests.	Under the same dry–wet cycle conditions, the larger the variation range of the water content, the lower the shear strength of the loess sample appears to be.
3	[14]	The influence of pore water pressure on the stability of loess slopes was analyzed by combining field monitoring and laboratory tests.	Rainfall can reduce the stability of loess slopes.
4	[15]	Indoor tests on loess soils were conducted.	The permeability coefficient of loess increases after dry–wet cycling, and the dry–wet cycling action causes damage to the microstructure of loess.
5	[16]	Indoor dry and wet cycle tests were conducted on expansive soils.	The shear strength of expansive soil decreased with the increase in the number of cycles, and finally reached a constant state
6	[17]	Indoor tests on natural expansive soils were conducted in Nanning.	The effective cohesion, which is an important factor affecting the occurrence of surface damage on expansive soil slopes, was reduced.
7	[18]	Centrifugal model tests were conducted on swelling soil slopes to analyze the changes in slope settlement, horizontal displacement, damage mechanism, and accumulated cracks under alternating wet and dry conditions.	The accumulation of cracks caused by dry–wet cycles is key to the progressive failure of slopes.
8	[19]	The variation patterns of shear strength parameters of expansive soils under different dry and wet cycles were analyzed by indoor tests.	The shallow damage of the expansive slope was mainly caused by the dry and wet effects of the natural environment.

A few studies have found that diatomaceous earth has high structural strength and is susceptible to disintegration and deterioration when exposed to water [20–24]. These properties derived from previous studies are slightly similar to those of loess and expansive soils, but are for reference only, and are not fully applicable to the field of high-speed railroad diatomaceous earth slopes. Meanwhile, compared with loess and expansive soil slopes, there are very few studies on diatomite slopes at home and abroad, and they are mainly concentrated in the fields of highway and marine engineering. For example, Zhang [22] conducted an in-depth study on the swelling properties of diatomite distributed in Tengchong, Yunnan, and showed the existence of light-swelling diatomite with strong swelling and disintegration in the area. Guo [25] studied the distribution characteristics and formation mechanisms of diatomite (soil) landslides by taking the new Tenglu highway slope landslide as an example, and pointed out that diatomite slopes are susceptible to cracking, delamination, and reduction in mechanical properties of diatomite on the slope

surface under the influence of artificial disturbance and external rainfall, etc. Wiemer [26] et al. studied the effect of diatoms on the shear strength of diatom sediments and the stability of submarine slopes, and pointed out that the shear strength of the diatom soil layer would be reduced under the condition of disturbance. Currently, no corresponding research results have been found in the field of high-speed railways, and there is no better solution for the damage problem of diatomaceous earth slopes under the alternating action of wet and dry conditions.

To gain a more thorough understanding of the diatomaceous earth slope damage caused by alternating dry and wet cycles, a research project was carried out for the diatomaceous earth in the Shengzhou area along the new Hangzhou–Taizhou high-speed railway. The study was performed through indoor testing, analysis of physical and hydraulic properties, and evaluation of the mechanisms of disintegration and degradation. Because previous rainfall simulation equipment cannot undertake the problem of rapid rainfall on high-speed railway slopes, a convenient, efficient, and controllable high-speed railway slope artificial rainfall system was designed, and alternating dry–wet cycle simulations were carried out on the test site. At the same time, in situ comprehensive monitoring and fissure observation were carried out before and after the alternating dry–wet simulations of natural diatomaceous earth slopes, in order to analyze the changing patterns of various diatomaceous earth slope parameters under rainfall infiltration conditions and explore the disintegration and cracking mechanisms of diatomaceous earth under the action of dry–wet cycles.

2. Project Overview

The diatomaceous earth natural slope test site was located between Dongdawan village and Xibanban village, on Lushan Street, in Shengzhou city, and next to Shangdawan Reservoir. To study the engineering characteristics of diatomaceous earth and the damage mechanism of diatomaceous earth under the action of dry–wet cycles, a diatomaceous earth cutting slope with mileage of DK85 + 824 − DK85 + 840 was selected as the test section (Figure 1a). The test section was covered with silty clay with a thickness of less than 3 m, and the underlying white diatomaceous earth was 9–12 m thick. The strata below the white diatomaceous earth were blue diatomaceous earth, black diatomaceous earth, basalt, stomatal basalt, and diatomaceous earth sandstone. After the excavation of the slope, the exposed surface and the depth interval of 10–27 m were mainly white diatomaceous earth (Figure 1b,c). Therefore, the properties of diatomaceous earth listed in this article and related tests are all white diatomaceous earth.

(**a**)

Figure 1. *Cont.*

(**b**) (**c**)

Figure 1. Test site and white diatomaceous earth: (**a**) Shengzhou diatomaceous earth slope test section; (**b**) white diatomaceous earth; (**c**) white diatomaceous earth drilling and construction.

3. Diatomaceous Earth Characteristics

Studies have found that diatomaceous earth has the undesirable property of degradation when in contact with water. To understand the mechanisms of diatomaceous earth's disintegration and degradation, an outdoor observation test of natural diatomaceous earth slopes was first carried out. Part of the cutting slope of the test section was graded with a slope ratio of 1:1.5. However, after a period of alternating dry and wet action, penetrating cracks were generated, and the depths of the cracks were between 0.5 and 0.8 m, as shown in Figure 2.

To solve the problem of damage to diatomaceous earth slopes under the action of dry and wet cycles, diatomaceous earth in the slope test section was used as the research object. First, basic geotechnical tests were carried out so as to become familiar with the basic physical properties of the diatomaceous earth in the area. Then, through water immersion observation and disintegration tests, the changes in diatomaceous earth after exposure to water were assessed, and the mechanisms of its disintegration and deterioration were initially evaluated.

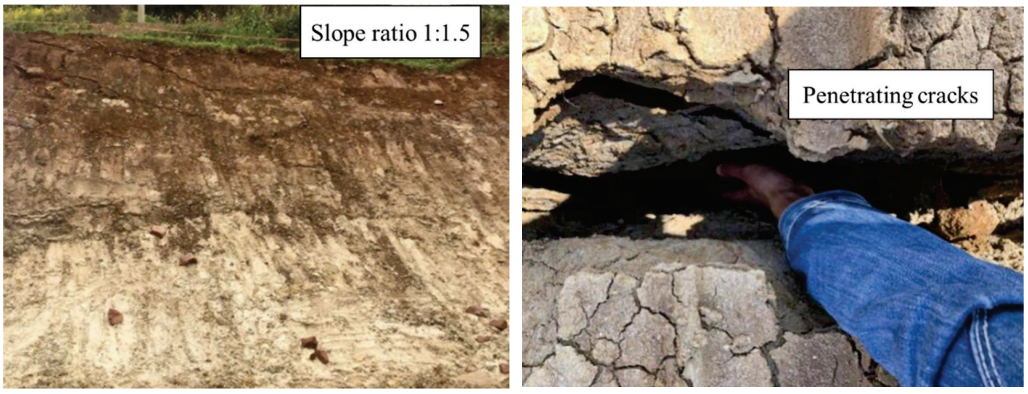

(**a**) (**b**)

Figure 2. Slope failure problem: (**a**) natural slope with a slope ratio of 1:1.5; (**b**) penetrating cracks that appear under the alternating action of dry and wet conditions.

3.1. Basic Physical Properties of Diatomaceous Earth

By taking samples at different depths at the foot of the natural slope on the right side of the line, ~155 m from the test slope, the original site was wax-sealed in time, and anti-vibration and sun protection measures were taken during transportation to ensure that the

original sample was not disturbed and did not lose water. Corresponding physical property tests were performed on the samples in time, in accordance with the "Geotechnical Test Procedure for Railway Engineering" [27]. In this study, white diatomaceous earth was used as the main research object, and representative samples were selected for corresponding tests. The properties of diatomaceous earth in this test section are shown in Table 2. Due to the large number of test results, it is inconvenient to list the specific data in each group. Through sampling at different depths, the results show that the natural density values of the diatomaceous earth were 1.55–1.73 g/cm^3, which are extremely low, and are similar to those of pumice. The void ratio and water content of the diatomaceous earth samples were very high. The void ratios of the seven samples were all greater than 1.0; the maximum water content was 72.11%, and the average value was 55.78%. The diatomaceous earth was dominated by the particle size ranges of 0.075–0.005 mm and < 0.002 mm, with a combined fraction of 80%, and the proportion of particles in the particle size range of 0.25–0.075 mm was the lowest. The mean plasticity index value of diatomaceous earth specimens was 36.30, which was much larger than 10, so it was classified as clay.

Table 2. Basic physical properties and particle analysis of diatomaceous earth.

N°	—	Basic Physical Properties							Particle Size Range (mm)				
		Density (g/cm^3)	Dry Density (g/cm^3)	Water Content (%)	Void Ratio	W_P(%)	W_L(%)	I_P	0.50–0.25 (%)	0.25–0.075 (%)	0.075–0.005 (%)	0.005–0.002 (%)	<0.002 (%)
1	Maximum value	1.73	1.58	72.11	1.70	46.45	92.88	49.30	17.1	9.7	54.3	40.9	65.1
2	Minimum value	1.55	0.64	46.66	1.13	40.60	73.80	32.65	0.1	0.3	21.4	8.9	18.7
3	Average value	1.63	1.11	55.78	1.36	42.98	79.28	36.30	2.9	2.1	35.6	16.3	44.0
4	Number of groups	7	7	6	8	7	7	7	8	8	8	8	8

3.2. Hydrological Properties of Diatomaceous Earth

Ten samples of white diatomaceous earth collected in the field test section were divided into two groups with variable water contents. Each group consisted of five samples. The average mass of the samples was consistent with the disintegration test (151.22 g). The first group was left untreated, keeping each sample in its natural state. The second group was placed in a cool place in the laboratory to undergo the drying process. The test phenomena are shown in Figure 3. The natural diatomaceous earth had no obvious change after being immersed in water, and only a small amount of soil fell off on the surface. After the natural diatomaceous earth dried in the shade, cracks appeared, and then it was soaked in water. Because of its small specific gravity, the sample floated on the water for a few seconds, sank under the water, and quickly disintegrated into a fine scaly and powdery form.

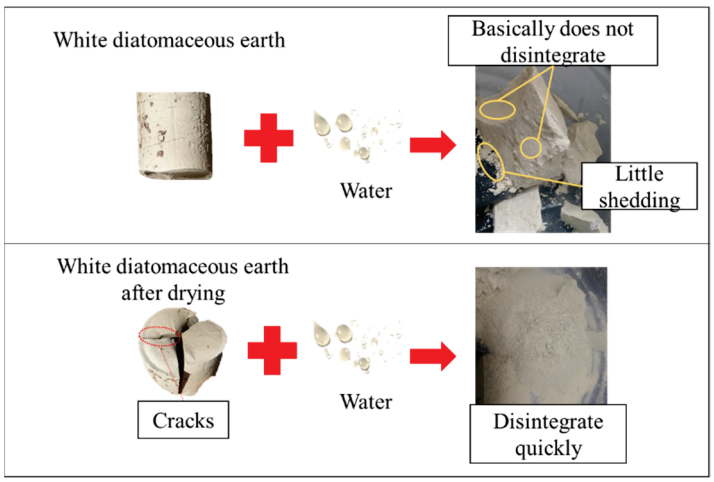

Figure 3. Natural diatomaceous earth and natural diatomaceous earth after shade-drying to observe the phenomenon of water immersion.

According to the above test phenomena of diatomaceous earth after encountering water, natural diatomaceous earth experiencing no obvious impact after encountering water. When natural diatomaceous earth dries, cracks appear and fragmentation occurs; then, the diatomaceous earth disintegrates quickly when exposed to water. The main reasons for this damage are as follows:

1. Natural diatomaceous earth has a high water content. In a natural environment or under high temperatures, due to the existence of a large number of clay minerals in the sample that are prone to strong shrinkage, the sample dries and shrinks [22,28]. At the same time, the shallow free water continues to evaporate, and air begins to enter the pores of the shallow soil particles, causing matrix suction between the particles on the soil surface. As water continues to evaporate, the suction of the matrix gradually increases, and the force on the soil particles becomes increasingly strong. When there are impurities or stress concentrations on the surface of the diatomaceous earth, the tensile strength of the diatomaceous earth is insufficient, and initial cracks are formed on the surface [29,30];
2. Since natural diatomaceous earth has a high void ratio and high water content, the dry density is significantly lower than the natural density, so the sample floats on the water surface for several seconds after the dry diatomaceous earth is immersed in water;
3. The natural diatomaceous earth that was dried in the shade forms cracks due to the above reasons. After being immersed in water, the water can dissolve and soften certain minerals in diatomaceous earth, resulting in further enlargement of the cracks and weakening of the connections between the soil particles. Then, because clay minerals such as montmorillonite and kaolinite swell because of water, the tensile strength of diatomaceous earth at the joints or microcracks is not enough to overcome the swelling force, leading to its rapid disintegration [31,32].

Through the abovementioned water immersion observation test, the state of diatomaceous earth after immersion in water is initially assessed. To further analyze the properties of diatomaceous earth after encountering water, two sets of white diatomaceous earth disintegration tests were designed. There were five samples in each group, and the average mass of the two groups of samples was 151.22 g. The effect of time and the total amount of disintegration and disintegration resistance of the two groups of samples under alternating natural dry and wet conditions when exposed to water were tested.

The diatomaceous earth sample was placed into a water-permeable sample box and immersed in a water tank to disintegrate. The mass of the residual sample was weighed with an electronic balance, and the ratio of the residual mass of the sample after disintegration to the total mass of the sample—that is, the disintegration resistance index (%)—was used to evaluate the disintegration characteristics of each sample.

$$I = \frac{M_r}{M_t} \times 100\% \quad (1)$$

where I is the resistance to disintegration index (%), M_r is the mass of the residual sample (g), and M_t is the total mass of the sample (g).

The test results are shown in Figure 4, and are summarized as follows:

1. The disintegration resistance index values of diatomaceous earth samples under natural conditions range from 89.6% to 92.8%, with an average value of 91.2%. The disintegration resistance index values of the sample after drying and wetting are 1.8–5.6%, and the average value is 3.7%. The comparison shows that the disintegration resistance index values of the natural diatomaceous earth samples are much higher than those of the diatomaceous earth samples after drying and wetting, and the drying and wetting effect has a great influence on the disintegration resistance of diatomaceous earth;

2. The water physical properties of the diatomaceous earth are extremely poor. The maximum disintegration resistance index value of the diatomaceous earth sample after alternating wet and dry action is 5.6%, which indicates extremely strong disintegration. The disintegration resistance of the sample is lower than that of soils with common parent rocks, such as basalt residual soil, mudstone, and granite [33–37];
3. The disintegration rate of the diatomaceous earth sample after alternating wet and dry conditions is lower in the first 30 s of being placed into the water. This phenomenon occurs because water gradually enters the pores of the sample during this period, and some of the air is surrounded by water in the pores. The high-speed disintegration of the sample occurs within 1–2 min after the start of the test, after which the disintegration rate decreases and tends to stabilize until the end of the test.

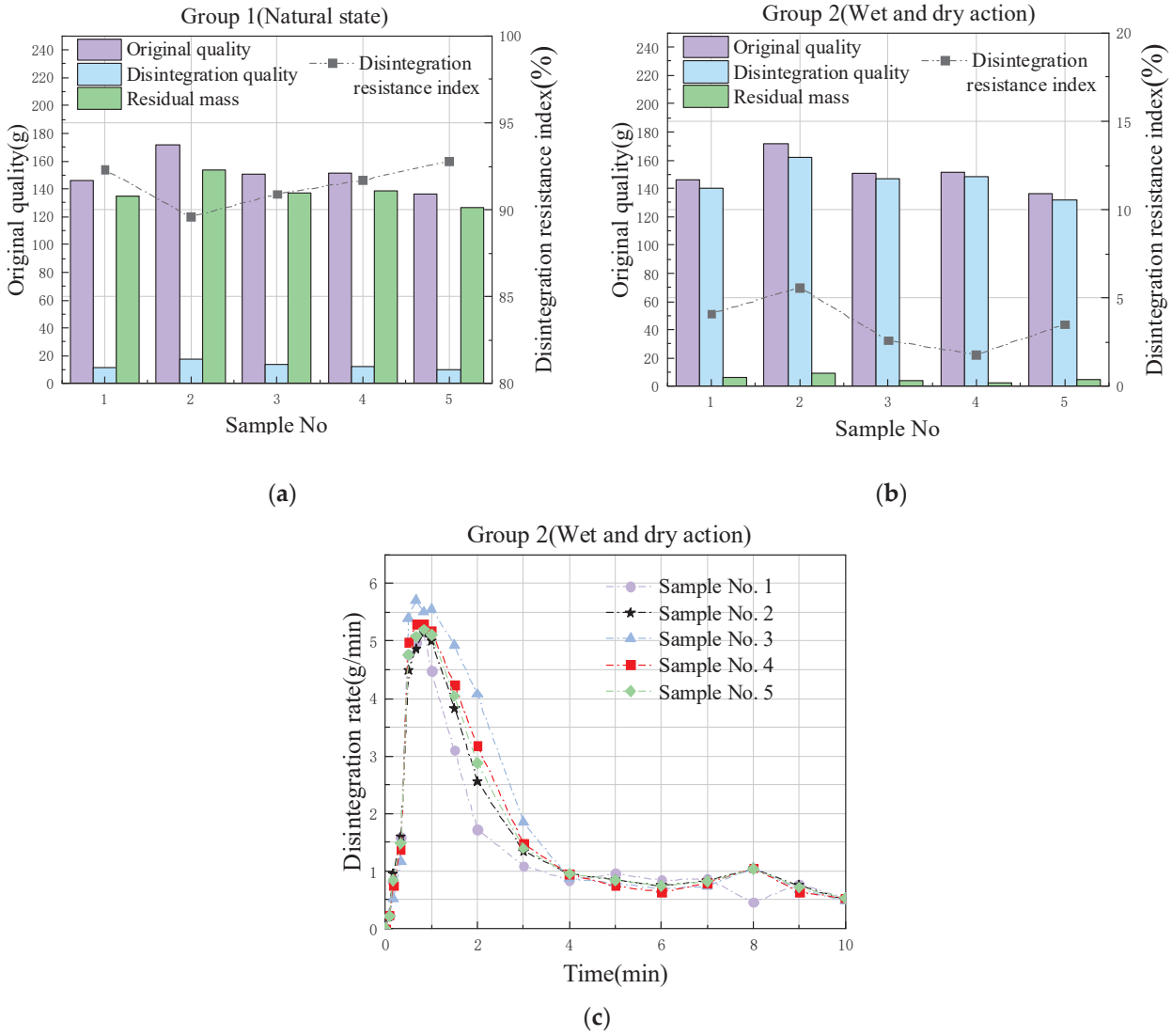

Figure 4. Disintegration test results of the two sets of samples: (**a**) comparison chart showing the disintegration resistance index values of the first group of samples; (**b**) comparison chart showing the disintegration resistance index values of the second group of samples; (**c**) comparison chart showing the disintegration rates of the first group of samples (average mass of 151.22 g).

4. Diatomaceous Earth Slope Tests

By combining the preliminary field investigation and indoor tests, it can be concluded that undisturbed diatomaceous earth has a high water content, high void ratio, and low permeability coefficient, and is often recognized as an impervious layer in the engineering

community. On the other hand, when the undisturbed diatomaceous earth loses water in the sun, cracks develop, and the diatomaceous earth disintegrates into lumps. The dried diatomaceous earth in the sun disintegrates quickly after being placed into water. This implies that the change in the water content is the most direct cause of the destruction of diatomaceous earth. Because this observation has not been analyzed and verified in conjunction with in situ tests, the resulting changes in soil deformation, soil pressure, and groundwater level in the slope soil are still unclear. Therefore, in order to obtain a more thorough understanding of the diatomaceous earth slope damage caused by alternating wet and dry conditions, two diatomaceous soil slopes with different slope ratios (1:1.5 and 1:2) in the test section were selected to conduct cycle simulations in the field, and comprehensive in situ monitoring and fissure observation of the slopes were carried out.

4.1. Simulation of Alternating Dry and Wet Cycles

4.1.1. Artificial Rainfall Simulation System for High-Speed Railway Slopes

To build an alternating dry and wet test environment for diatomaceous earth slopes, a convenient, efficient, and controllable high-speed railway slope artificial rainfall system was designed. The system mainly includes three parts, namely, the water supply module, control module, and rainfall module, as shown in Figure 5. The water supply module is used to provide a water source for the rainfall module, and the water supply module is connected to a control module. The control module is used to control the water supply intensity and flow rate of the water supply module, thereby controlling the rainfall process of the rainfall module. The rainfall module adopts a prefabricated rainfall bracket. Each rainfall bracket is composed of a ground anchor and a rainfall column with a pin bolt, which arbitrarily adjusts the height of the rainfall bracket and efficient installation, disassembly, and transportation. The rain sprinkler uses a detachable downward spray atomization sprinkler, which has two types of large diameters and small diameters that adjust the rainfall intensity and enrich the rainfall diversity. The control module controls the whole process of water supply and rainfall through a closed-loop control system composed of PU water pipes, valves, water meters, and pressure gauges, and its operation is simple and convenient. The water supply module stores and supplies water through water storage buckets, generators, water pumps, and water supply pipes.

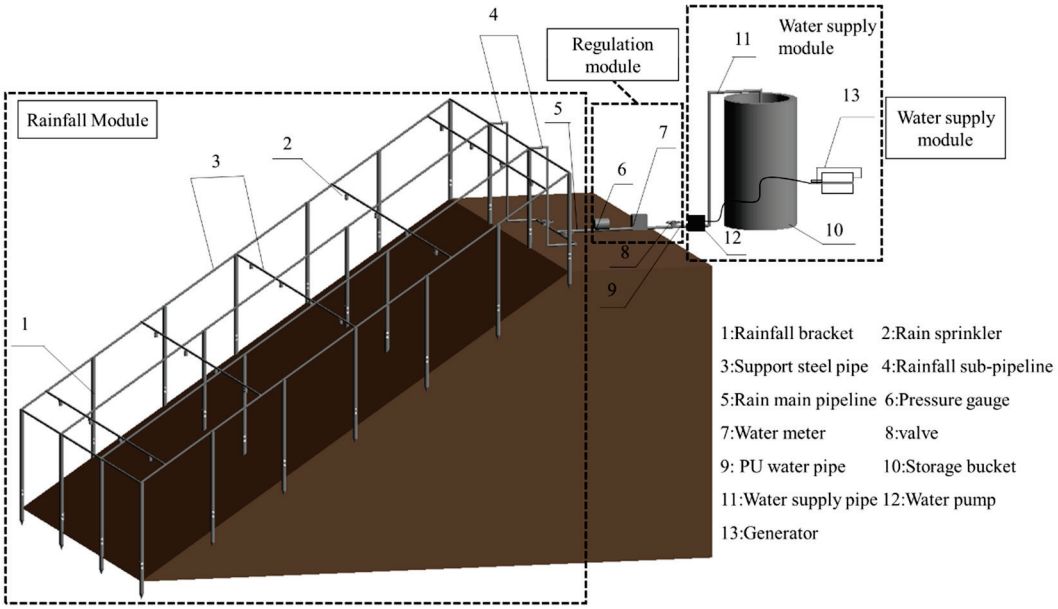

Figure 5. Schematic diagram of a convenient, efficient, and controllable high-speed railway slope artificial rainfall simulation system.

During use, the system can satisfactorily meet the needs of diatomaceous earth slopes to simulate artificial rainfall, match the intensity of natural rainfall, and achieve rainfall on slopes with different slope rates. The system has simple daily operations, easy disassembly and assembly, and easy transportation; it can be repeatedly tested at multiple test sites, which provides a strong guarantee for the development of high-speed rail projects. The actual installation and layout of the test site are shown in Figure 6.

Figure 6. Site installation of the rainfall system.

4.1.2. Test Plan of the Dry and Wet Cycle Simulation

The alternating dry and wet test process is shown in Table 3. In the field test, to simulate the effects of the dry and wet cycles in the natural environment, the rainfall was set to occur at night, and outside sunlight was used to evaporate water during the day, as shown in Figure 7a,b. On rainy days, to reduce the influence of rainwater on the rainfall test, a layer of colored striped cloth and a layer of plastic film were used to cover the supporting steel frame, as shown in Figure 7c.

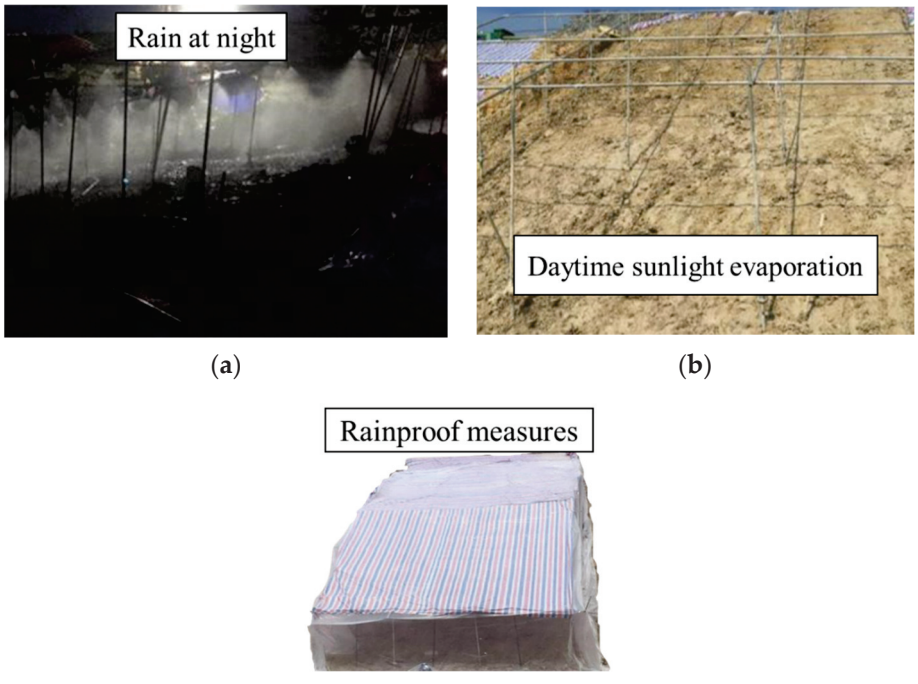

Figure 7. Dry and wet cycle simulation test: (**a**) rain at night; (**b**) dry during the day; (**c**) rainproof measures.

Table 3. Experimental history.

N°	Date	Test Slope	Rainfall Intensity	Daily Rainfall Time
1	27 June–2 July	1:2	8 mm/h	15 h
2	3 July–4 July	1:2	0 (Natural placement)	0
3	5 July–7 July	1:2	15 mm/h	15 h
4	13 July–18 July	1:1.5	8 mm/h	15 h
5	19 July–20 July	1:1.5	0	0
6	21 July–23 July	1:1.5	15 mm/h	15 h

4.2. In Situ Comprehensive Monitoring

Before and after the simulated rainfall test on the natural diatomaceous earth slope, comprehensive in situ monitoring was carried out. In the field test, the sensor layout of the two types of natural diatomaceous earth slope was the same, and monitoring profiles R1, R2, and R3 were positioned at the top, middle, and toe of the natural diatomaceous earth slope, respectively. Sensors were embedded at different depths to monitor the changes in the water content, horizontal displacement, earth pressure, and groundwater level of each profile, as shown in Figure 8.

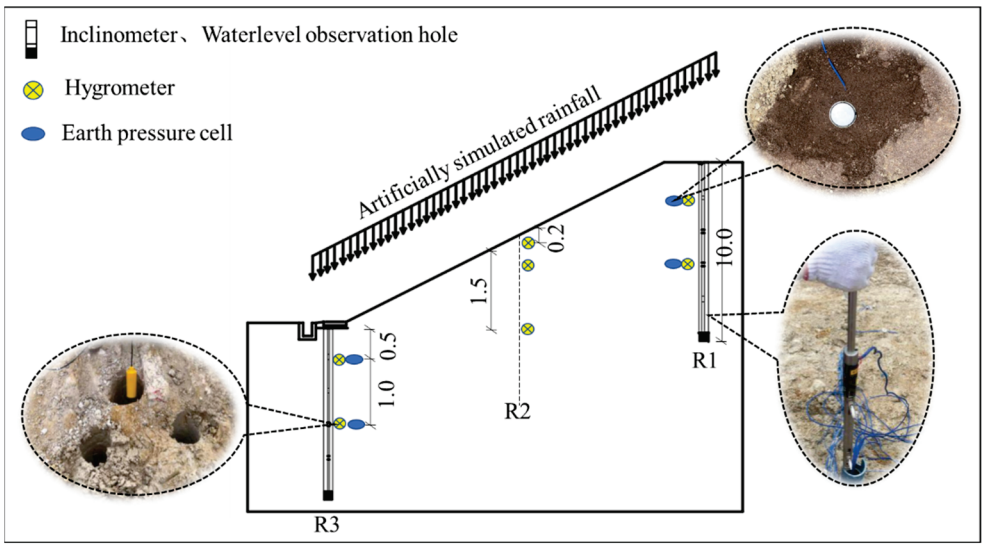

Figure 8. Sensor layout (side view).

5. Results

5.1. Water Content Analysis

By reading the monitoring data of the automatic acquisition instrument, the monitored distribution pattern of the water contents in each section on the 1:2 slope and 1:1.5 slope are shown in Figure 9a,b, respectively. The results are summarized as follows:

1. Heavy rain and artificial simulated rainfall both led to an abrupt increase in the water content at each measuring point. For example, after the natural rainstorm on 18 June, the change in water content at the depth of 0.2 m on the slope of section R2 with a slope rate of 1:2 was the largest, changing from 48.1% to 59.4%—an increase of 11.3%—and the average value of the change in water content of each section was 4.4%. This indicates that rainfall has a significant impact on the water content at the measuring point. Before and after artificial simulated rainfall, on the slope with a slope ratio of 1:2, the water content at a depth of 1.5 m in the R1 section of the top of the slope increased the most—from 57.2% to 76.1%. On the slope with a slope ratio of 1:1.5, the water content at a depth of 1.5 m in the R2 section in the middle of the slope increased the most—from 58.8% to 78.9%. The reason for the sudden change in the water content was that the original

structure of the diatomaceous earth was destroyed by the borehole construction at the measurement point [38], and the backfill was not dense, resulting in rapid infiltration after the rainfall began; thus, the water content increased abruptly;

2. The diatomaceous earth slope was excavated during artificial rainfall simulation, and rainfall infiltration was assessed. The diatomaceous earth flowed only within the range of 0.02–0.1 m from the surface of the slope, and the following diatomaceous earth structure was complete. Rainwater could not penetrate into the lower diatomite layer, and the measured water content was the same as that before rainfall, as shown in Figure 9c. This phenomenon is consistent with the results of the indoor hydraulic property observation test, again showing that natural diatomaceous earth experiences no obvious impact after encountering water;
3. In the week before the end of the alternating dry–wet simulation, the water contents at 0.2 m on the two types of slopes remained stable, and subsequently fluctuated greatly. Approximately two and a half months after the end of the alternating dry and wet simulation, the water content at 0.5 m was greatly affected by the climate. The analysis shows that this occurred due to the initial fissures in the diatomaceous earth produced by the alternating dry and wet external environment. Over time, the fissures gradually developed from the surface of the slope to these two locations [39].
4. After the alternating dry–wet simulation, the water contents at the top of the two types of slopes and at depth greater than 0.5 m remained stable, and the range of change was small, indicating that the soil at the measuring point reached a saturated state; this phenomenon is consistent with the analysis obtained by Zhao [40], and occurs due to the hindering of the evaporation of water vapor by the surface soil. Consequently, the lower soil is less affected by the natural environment, and the water content remains stable.

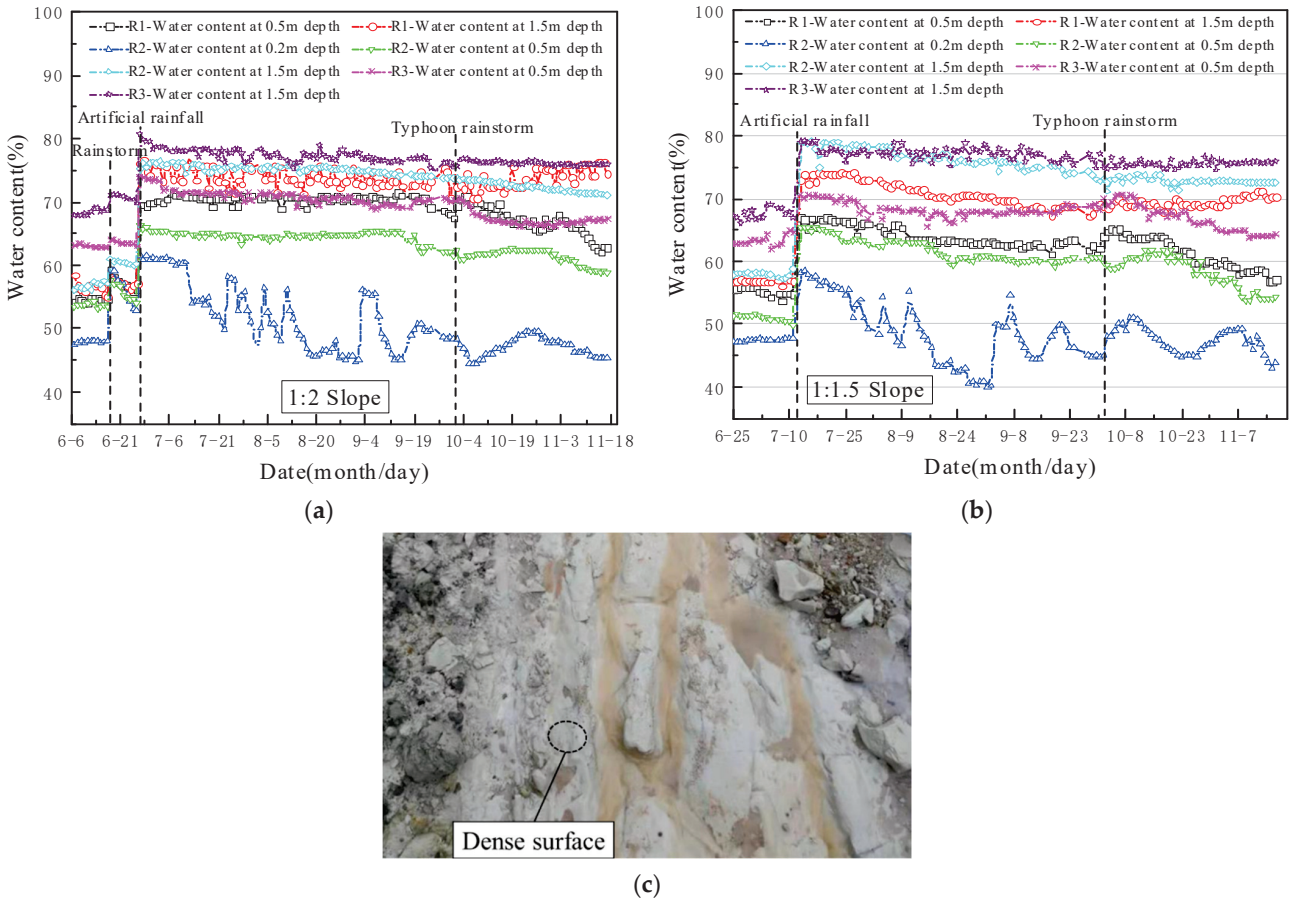

Figure 9. Water content analysis: (**a**) 1:2 natural slope water content variation trend; (**b**) 1:1.5 natural slope water content variation trend; (**c**) excavation of the diatomaceous earth slope.

5.2. Horizontal Displacement Analysis

By reading the monitoring data of the automatic acquisition instrument, the monitored horizontal displacement distribution of each section on the two types of slopes is shown in Figure 10a,b, and the following are indicated:

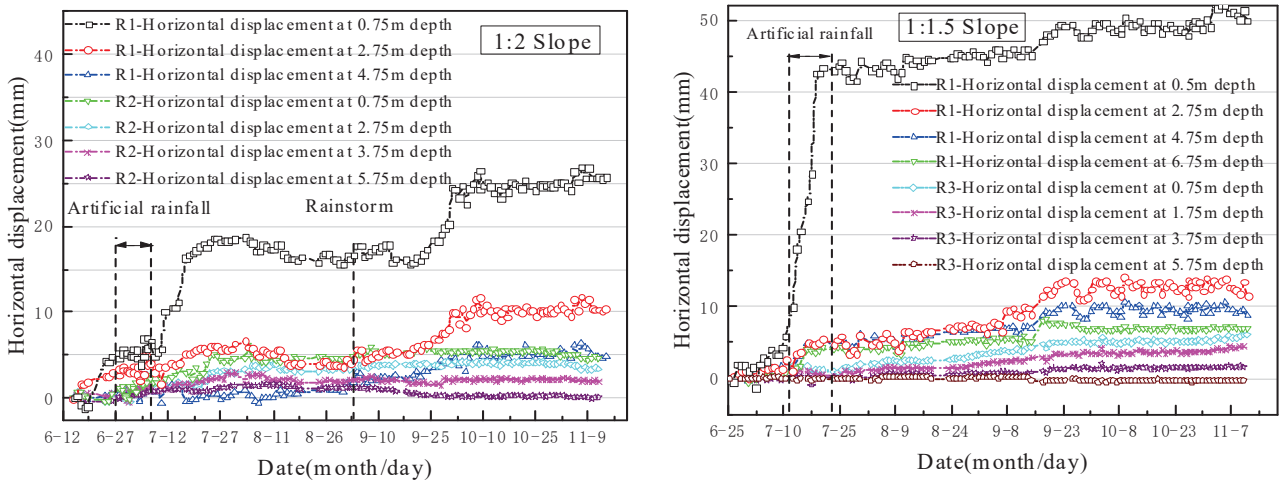

Figure 10. Horizontal displacement analysis: (**a**) 1:2 natural slope horizontal displacement variation trend; (**b**) 1:1.5 natural slope horizontal displacement variation trend.

On a slope with a ratio of 1:2, the monitored horizontal displacements at the depths of 0.75 m, 2.75 m, and 4.75 m at the top of the slope exhibited an overall increasing trend with depth, and were 25.7 mm, 10.8 mm, and 6.4 mm, respectively, after stabilization. However, during the dry–wet cycle simulation, the monitored horizontal displacement of the top of the 1:2 slope increased slightly, and a larger increase occurred after the rainfall ended, indicating that the monitored horizontal displacement of the 1:2 slope had a hysteresis effect relative to the rainfall; this phenomenon is similar to the landslide hysteresis effect of loess slopes obtained by Zhang [41]. After the dry–wet cycle simulation, the monitored horizontal displacements at the depths of 0.75 m and 2.75 m on the top of the slope increased to 20 mm and 6 mm, respectively, and temporarily stabilized. A heavy rainstorm occurred in the test area on 4 September, which resulted in a relatively large increase in the displacement of these two places on the slope. The displacement increased from 16.6 mm to 24.5 mm at 0.75 m depth and from 4.5 mm to 9.9 mm at 2.75 m depth, and stabilized at a later stage. However, the horizontal displacement at a depth of 4.75 m on the top of the slope was less affected by the environment, and was always in a relatively stable state, showing that the slope displacement mainly occurred between 0.75 m and 2.75 m from the surface, indicating shallow surface slip.

On a slope with a ratio of 1:1.5, the monitored horizontal displacements at the top of the slope at 0.75 m, 2.75 m, 4.75 m, and 6.75 m were 51.3 mm, 13.9 mm, 10.5 mm, and 7.4 mm, respectively. The horizontal displacement of the slope top mainly occurred on the shallow surface within 0.75–2.75 m, and the displacement increased abruptly at a depth of 0.75 m during the dry–wet cycle simulation. The main reason for this increase was that the slope with a ratio of 1:1.5 was relatively steep. After rainfall, the slope formed a relatively rapid current, which caused the shallow surface soil on the slope to produce larger displacements; this is consistent with the analysis obtained by Zhang [42]. The displacements of the slope top and the slope toe were not synchronized. The slope top displacement occurred only during the dry–wet cycle simulation, while the slope toe displacement continued to occur and gradually stabilized after 1 October. This phenomenon occurred because the top of the slope was mainly affected by the shallow surface displacement caused by rainfall, and the

foot of the slope was mainly affected by the overall displacement of the top of the slope, so it gradually stabilized in the later stage.

Comparing the 1:2 and 1:1.5 slopes, the horizontal displacement of the top surface of the 1:2 slope was much smaller than the horizontal displacement of the top surface of the 1:1.5 slope. The displacement difference between the surface layer and the bottom layer of the 1:2 slope was smaller than that of the 1:1.5 slope, indicating that the overall working performance of the 1:2 slope was stronger [43].

5.3. Lateral Earth Pressure Analysis

By reading the monitoring data of the automatic acquisition instrument, the monitored distribution pattern of the lateral earth pressure on each section of the 1:2 slope and 1:1.5 slope is shown in Figure 11a,b.

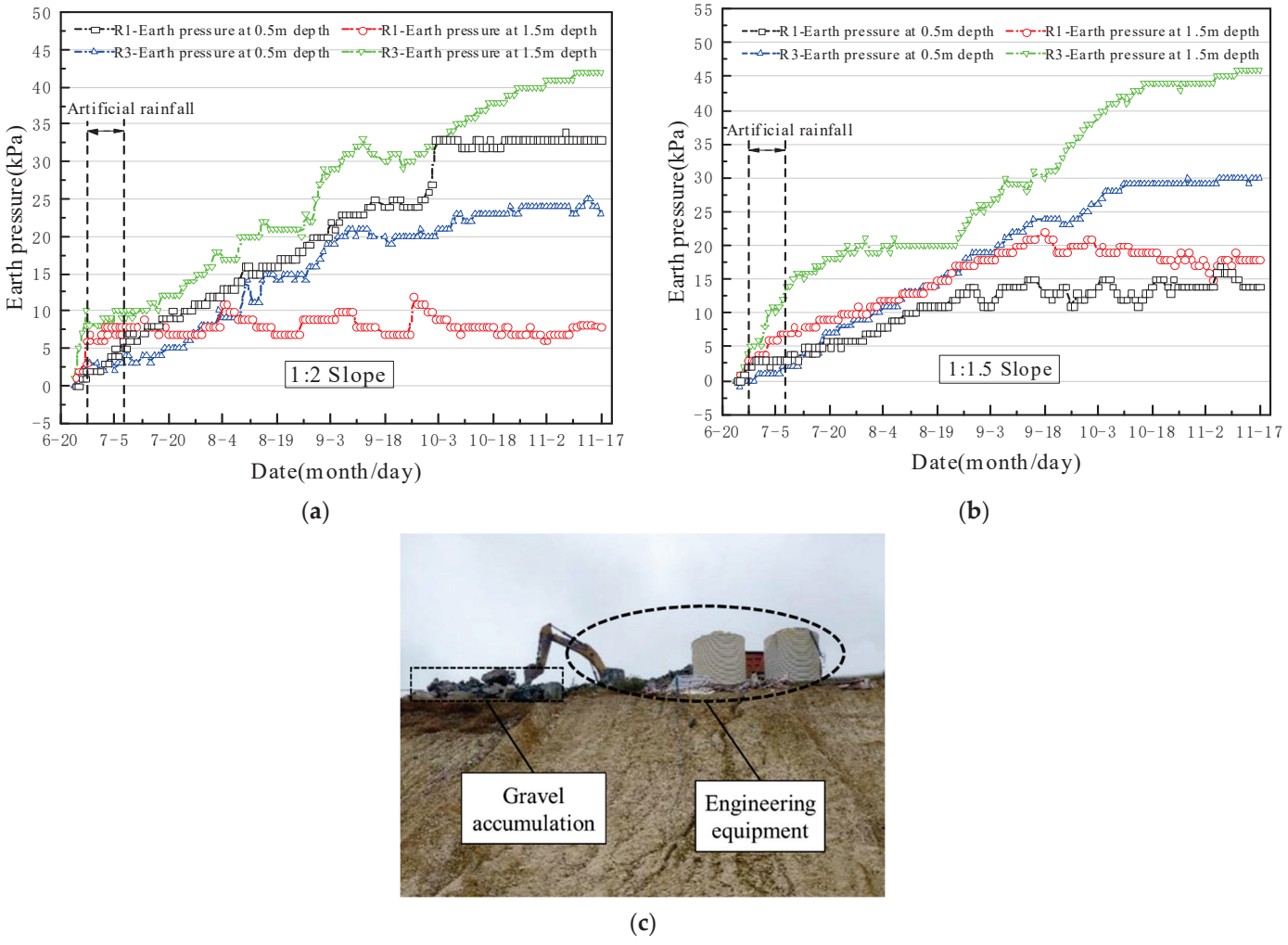

Figure 11. Lateral earth pressure analysis: (**a**) 1:2 natural slope lateral earth pressure variation trend; (**b**) 1:1.5 natural slope lateral earth pressure variation trend; (**c**) stacking on the top of the slope.

On a slope with a slope ratio of 1:2, the earth pressure at 0.5 m from the top of the slope continued to increase until it stabilized on 4 October, and the earth pressure at 1.5 m from the top of the slope gradually increased in the initial stage. Then, the earth pressure remained stable and experienced small fluctuations. The observations indicate that no significant change in earth pressure occurred after the artificial rainfall. An analysis of the reasons shows that artificial rainfall did not penetrate the slope, and had no effect on the internal earth pressure of the slope [44]. The earth pressure at the top of the slope at 0.5 m was greater than the earth pressure at the top of the slope at 1.5 m, mainly because of the

continuous accumulation of gravel on the top of the slope, which caused the earth pressure at the top of the slope to increase continuously [45]. The burial depth at 1.5 m was larger, and the impact of the piled load on it was small, as shown in Figure 11c.

On a slope with a ratio of 1:1.5, the lateral earth pressure at the top and toe of the slope both increased in the early stage, and gradually stabilized in the later stage. However, the R1 section at the top of the slope still fluctuated slightly after being stabilized. It may be the case that the piled load on the top of the slope tended to be stable in the later stage; however, every day, there were new abandoned slags, and some of the abandoned slags were used for filling; thus, a small fluctuation in the stacking load occurred, as shown in Figure 11c. An analysis of the earth pressure during artificial rainfall simulation showed that the artificial rainfall had no obvious impact on the 1:1.5 slope, indicating that the artificial rainfall did not penetrate into the interior of the 1:1.5 slope.

5.4. Groundwater Level Analysis

The groundwater level observation point of the test site was buried 6.5 m below the toe of the slope. As shown in Figure 12, no significant change in the groundwater level occurred before or after rainfall. The figure shows that the rainfall did not penetrate into the diatomaceous soil slope, and the groundwater level did not rise overall [46,47].

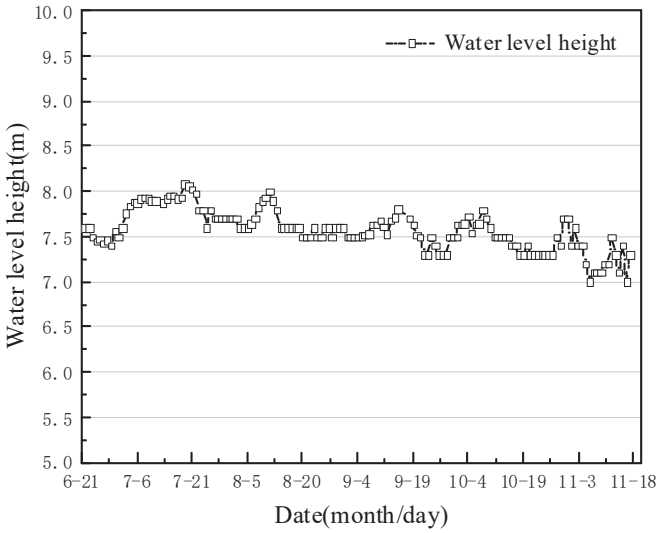

Figure 12. Groundwater level change.

5.5. Crack Analysis

To study the process of crack development in diatomaceous earth under the action of an external environment, it is necessary to constantly observe the changes in cracks during the test. Field observations and measurements after the end of the test showed that the crack widths of the 1:2 slope were 10–25 mm, and the crack depths were 50–60 cm, while for the 1:1.5 slope, the widths of the cracks in the slope were 10–20 mm, and the depths of the cracks were 40–55 cm, as shown in Figure 13. The development process of the above cracks was as follows:

Diatomaceous earth has a high water content and low permeability [48,49]. Natural diatomaceous earth with a high water content after slope excavation is exposed to the natural environment, and water evaporates quickly under sunlight. Due to the high surface temperature, the water evaporates quickly, the internal diatomaceous earth is affected by the surface layer, and the water of that layer has difficultly evaporating, resulting in a large difference in the upper and lower water contents, and leading to initial cracks [50,51]. Under the action of rainfall, the surface diatomaceous earth forms a hard shell layer because of rainwater, and the rainwater enters the cracks, which intensifies the development of the cracks. Because of evaporation, the fissures develop rapidly, and the integral diatomaceous

earth slope is cut into several small pieces. This process is consistent with the above water physical property test results of diatomaceous earth. Because diatomaceous earth has a certain bedding structure, diatomaceous earth disintegrates from a monolithic soil layer into large rocks because of evaporation. Then, it breaks down into small rocks, which intensifies the infiltration of rainwater. If this process continues, under long-term alternating dry and wet conditions, the shallow diatomaceous soil is completely disintegrated, and residual soil is formed at the foot of the slope because of rainfall. The failure mode of the slope is shallow instability failure, as shown in Figure 14.

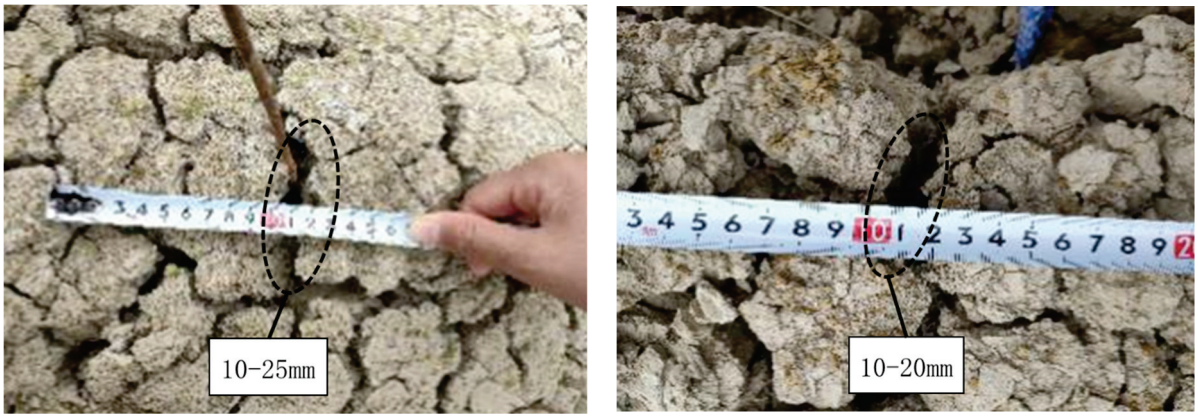

(**a**) (**b**)

Figure 13. Slope fissure diagram: (**a**) test section on the 1:2 side slope; (**b**) test section on the 1:1.5 side slope.

Figure 14. Natural side slope observation map.

6. Conclusions

In this paper, based on the newly built Hangzhou–Taizhou high-speed railway diatomaceous earth natural slope test section, indoor tests, in situ comprehensive monitoring, and fissure observation, as well as other methods, the following conclusions were obtained:

1. The hydrological properties of diatomaceous earth in the Shengzhou area are extremely poor, and natural diatomaceous earth samples do not change significantly when exposed to water. The disintegration resistance index values are 89.6–92.8%, and the disintegration resistance is strong. After the natural diatomaceous earth samples were dried in the shade, cracks appeared and fragmentation occurred due to dry–wet cycle effects. Then, the samples disintegrated rapidly when exposed to water, with disintegration resistance index values of 1.8–5.6% and an average value of 3.7%. The disintegration resistance was very weak, and the disintegration was strong;
2. A convenient, efficient, and controllable high-speed railway slope artificial rainfall simulation system was designed to provide strong support for the development of

alternating dry and wet simulations. During the artificial rainfall simulation period, the diatomaceous earth was in a flowing state within the range of 0.02–0.1 m from the surface of the slope, and rainwater could not seep into the soil. After the alternating dry–wet simulation, cracks developed within the range of 0–0.5 m on the slope, and the water content was greatly affected by the environment. Comprehensive indoor water physical property observations and water content monitoring results show that natural diatomaceous earth has no obvious impact when exposed to water, but it disintegrates and cracks under the action of alternating dry and wet cycles;

3. For the 1:2 diatomaceous earth slope, the monitored horizontal displacements at depths of 0.75 m, 2.75 m, and 4.75 m at the top of the slope were 25.7 mm, 10.8 mm, and 6.4 mm, respectively; for the 1:1.5 diatomaceous earth slope, the monitored horizontal displacements at the depths of 0.75 m, 2.75 m, and 4.75 m at the top of the slope were 51.3 mm, 13.9 mm, and 10.5 mm, respectively; The horizontal displacement of the two types of slopes mainly occurred on the surface within 0.75–2.75 m, indicating shallow slip;
4. After the test, the crack widths of the natural diatomaceous earth slope reached 10–25 mm, and the depth reached 40–60 cm. The natural slope of diatomaceous earth is prone to complete disintegration of shallow soil under the effect of long-term alternating wet and dry conditions, and residual soil is formed at the foot of the slope under the effect of rainfall, resulting in shallow destabilization damage, which greatly affects the safe development of railroad construction;
5. The key to preventing the damage to diatomaceous earth slopes is to protect the original diatomaceous earth, isolate the alternating dry and wet effects of the outside atmosphere on the surface layer of the diatomaceous earth slope, prevent the original diatomaceous earth from producing a water content gradient, and avoid the fissure of the surface layer of the diatomaceous earth slope. In the actual high-speed railroad construction, it is recommended to provide proper protection for diatomite slopes.

Because of the limited number of research years of the authors, the issues that can be further studied in the future are as follows:

1. Since the monitoring time of the field test is too short and the alternating wet and dry action fails to fully develop the slope fissures, it is suggested to monitor the diatomite slope for ~3 years in order to further quantify the influence range of diatomite fissures, and to monitor the displacement, water content, pore water pressure, earth pressure, and groundwater level changes for a long time;
2. On-site fissure diatomite strength tests should be conducted to provide strong support for analyzing the influence of fissures on the stability of diatomite slopes, and the influence of rainfall scouring on the stability of diatomite slopes should be considered;
3. Further numerical simulation and theoretical analysis of diatomite slope stability under the action of alternating wet and dry conditions should be carried out.

Author Contributions: Conceptualization, W.W. and Z.D.; methodology, Z.D.; software, Z.D.; validation, Z.D., W.W. and T.Y.; formal analysis, Z.D.; investigation, Q.S.; resources, Y.L. (Yandong Li); data curation, W.W. and Y.L. (Yangyang Liu); writing—original draft preparation, W.W. and Z.D.; writing—review and editing, Z.D. and K.X.; visualization, Q.S.; supervision, T.Y.; project administration, T.Y.; funding acquisition, Q.S. All authors have read and agreed to the published version of the manuscript.

Funding: This research was funded by China Railway Construction Co., Ltd., under grant no. 2018-A01, and the National Natural Science Foundation of China, grant number 51978588.

Institutional Review Board Statement: Not applicable.

Informed Consent Statement: Not applicable.

Data Availability Statement: Not applicable.

Conflicts of Interest: The authors declare no conflict of interest.

References

1. Day, R.B. Engineering properties of diatomaceous fill. *J. Geotech. Eng.* **1995**, *121*, 908–910. [CrossRef]
2. Tateishi, Y. Geotechnical Properties of Diatom Earth and Stability of Surface Layer for the Cut Slope. Ph.D. Thesis, Saga University, Saga City, Japan, 1997.
3. Shigematsu, H.; Yashima, A.; Nishio, M.; Saka, Y.; Hatanaka, S. Geotechnical properties of diatomaceous earth in northern gifu prefecture and cut slope stability. *Doboku Gakkai Ronbunshu* **2001**, *2001*, 139–154. [CrossRef]
4. Díaz-Rodríguez, J.; González-Rodríguez, R. Influence of diatom microfossils on soil compressibility. In Proceedings of the 18th International Conference on Soil Mechanics and Geotechnical Engineering, Paris, France, 2–5 September 2013.
5. Caicedo, B.; Mendoza, C.; López, F.; Lizcano, A. Behavior of diatomaceous soil in lacustrine deposits of Bogotá, Colombia. *Rock Mech. Geotech. Eng.* **2018**, *10*, 367–379. [CrossRef]
6. Ovalle, C.; Arenaldi-Perisic, G. Mechanical behaviour of undistursubgrade bed diatomaceous soil. *Mar. Georesources Geotechnol.* **2021**, *39*, 623–630. [CrossRef]
7. Chu, H.; Cao, D.; Dong, B.; Qiang, Z. Bio-diatomite dynamic membrane reactor for micro-polluted surface water treatment. *Water Res.* **2010**, *44*, 1573–1579. [CrossRef]
8. Jeffryes, C.; Campbell, J.; Li, H.; Jiao, J.; Rorrer, G. The potential of diatom nanobiotechnology for applications in solar cells, batteries, and electroluminescent devices. *Energy Environ. Sci.* **2011**, *4*, 3930–3941. [CrossRef]
9. Liu, D.; Gu, J.; Liu, Q.; Tan, Y.; Li, Z.; Zhang, W.; Su, Y.; Li, W.; Cui, A.; Gu, C.; et al. Metal-Organic Frameworks Reactivate Deceased Diatoms to be Efficient CO2Absorbents. *Adv. Mater.* **2013**, *26*, 1229–1234. [CrossRef]
10. Li, J.; Xu, J.; Xie, Z.; Gao, X.; Zhou, J.; Xiong, Y.; Chen, C.; Zhang, J.; Liu, Z. Diatomite-Templated Synthesis of Freestanding 3D Graphdiyne for Energy Storage and Catalysis Application. *Adv. Mater.* **2018**, *30*, e1800548. [CrossRef] [PubMed]
11. Zhou, F.; Li, Z.; Lu, Y.-Y.; Shen, B.; Guan, Y.; Wang, X.-X.; Yin, Y.-C.; Zhu, B.-S.; Lu, L.-L.; Ni, Y.; et al. Diatomaceous Earth derived hierarchical hybrid anode for high performance all-solid-state lithium metal batteries. *Nat. Commun.* **2019**, *10*, 1–11.
12. Tu, X.B.; Kwong, A.F.L.; Dai, F.C.; Tham, L.G.; Min, H. Field monitoring of rainfall infiltration in a loess slope and analysis of failure mechanism of rainfall-induced landslides. *Eng. Geol.* **2009**, *105*, 134–150. [CrossRef]
13. Ye, W.; Zhang, Y. Effect of Dry-wet Cycle on the Formation of Loess Slope Spalling Hazards. *Civ. Eng. J.* **2018**, *4*, 785. [CrossRef]
14. Yates, K.; Russell, A.; Fentonl, C. Field and laboratory investigation of rainfall-triggered slope failure in unsaturated loess soils, New Zealand. *E3S Web Conf.* **2020**, *195*, 01017. [CrossRef]
15. Xu, J.; Ren, C.; Wang, S.; Gao, J.; Zhou, X. Permeability and Microstructure of a Saline Intact Loess after Dry-Wet Cycles. *Adv. Civ. Eng.* **2021**, *2021*, 6653697. [CrossRef]
16. Zeng, Z.T.; Lu, H.B.; Zhao, Y.L. Wetting-Drying Effect of Expansive Soils and its Influence on Slope Stability. *Appl. Mech. Mater.* **2012**, *170–173*, 889–893. [CrossRef]
17. Xiao, J.; Yang, H.; Zhang, J.; Tang, X. Surficial failure of expansive soil cutting slope and its flexible support treatment technology. *Adv. Civ. Eng.* **2018**, *2018*, 1609608. [CrossRef]
18. Chen, T.-L.; Zhou, C.; Wang, G.-L.; Liu, E.-L.; Dai, F. Centrifuge Model Test on Unsaturated Expansive Soil Slopes with Cyclic Wetting–Drying and Inundation at the Slope Toe. *Int. J. Civ. Eng.* **2017**, *16*, 1341–1360. [CrossRef]
19. Zhai, J.-Y.; Cai, X.-Y. Strength Characteristics and Slope Stability of Expansive Soil from Pingdingshan, China. *Adv. Mater. Sci. Eng.* **2018**, *2018*, 3293619. [CrossRef]
20. Perisic, G.A.; Ovalle, C.; Barrios, A. Antonio Barrios. Compressibility and creep of a diatomaceous soil. *Eng. Geol.* **2019**, *258*, 105145. [CrossRef]
21. Hong, Z.; Tateishi, Y.; Han, J. Experimental study of macro-and microbehavior of natural Diatomaceous Earth. *J. Geotech. Geoenviron. Eng.* **2006**, *132*, 603–610. [CrossRef]
22. Zhang, Y.; Guo, C.; Yao, X.; Qu, Y.; Zhou, N. Engineering geological characterization of clayey diatomaceous earth deposits encountered in highway projects in the Tengchong region, Yunnan, China. *Eng. Geol.* **2013**, *167*, 95–104. [CrossRef]
23. Shiwakoti, D.R.; Tanaka, H.; Tanaka, M.; Locat, J. Influences of Diatom Microfossils on Engineering Properties of Soils. *Soils Found.* **2002**, *42*, 1–17. [CrossRef]
24. Wiemer, G.; Dziadek, R.; Kopf, A. The enigmatic consolidation of diatomaceous sediment. *Mar. Geol.* **2017**, *385*, 173–184. [CrossRef]
25. Guo, C.; Zhou, N.; Fu, X.; Zhang, Y.; Zhang, R. The optimization design of the research on the formation mechanism, preven-tion and control of landslide along clayey diatomite highway in Tengchong, Yunnan Pzovince. *Geol. Bul. China* **2013**, *32*, 2021–2030. (In Chinese)
26. Wiemer, G.; Moernaut, J.; Stark, N.; Kempf, P.; De Batist, M.; Pino, M.; Urrutia, R.; De Guevara, B.L.; Strasser, M.; Kopf, A. The role of sediment composition and behavior under dynamic loading conditions on slope failure initiation: A study of a subaqueous landslide in earthquake-prone South-Central Chile. *Geol. Rundsch.* **2015**, *104*, 1439–1457. [CrossRef]
27. Ministry of Railways of the People's Republic of China. *Geotechnical Test Procedures for Railroad Engineering (TB10102-2004)*; China Railway Press: Beijing, China, 2004. (In Chinese)
28. Zhang, Y.; Qu, Y.; Liu, G.; Wu, S. Engineering geological properties of Miocene hard clays along the middle line of the North–South Diversion Water Project in China. *Bull. Eng. Geol. Environ.* **2003**, *62*, 213–219. [CrossRef]
29. Leng, T.; Tang, C.; Li, D.; Li, Y.; Zhang, Y.; Wang, K.; Shi, B. Advance on the engineering geological characteristics of expansive soil. *J. Eng. Geol.* **2018**, *26*, 112–128. (In Chinese)

30. Tang, C.; Shi, B.; Liu, C. Study on desiccation cracking behaviour of expansive soil. *J. Eng. Geol.* **2012**, *20*, 663–673. (In Chinese)
31. Zhang, Y.; Guo, C.; Qu, Y.; Yao, X. Research on mechanical properties of swelling diatomite and their geohazard effects. *Rock Soil Mech.* **2013**, *34*, 23–30. (In Chinese)
32. Guo, C.; Zhang, Y.; Meng, Q.; Zheng, G.; Li, H. Research on shear strength of remolding diatomite by ring shear tests. *Rock Soil Mech.* **2013**, *34*, 92–100. (In Chinese)
33. Zhang, Y.; Guo, C.; Qu, Y.; Zhang, M. Discovery of swelling diatomite at tengchong, yunnan province and its implication in engineering geology. *J. Eng. Geol.* **2012**, *20*, 266–275. (In Chinese)
34. Tang, J.; Yu, P.; Wei, H.Z.; Meng, Q.S. Slaking behaviour of weathered basalt residual soil in guizhou. *J. Eng. Geol.* **2011**, *19*, 778–783. (In Chinese)
35. Zhang, Z.; Liu, W.; Cui, Q.; Han, L.; Yao, H. Disintegration characteristics of moderately weathered mudstone in drawdown area of Three Gorges Reservoir, China. *Arab. J. Geosci.* **2018**, *11*, 405. [CrossRef]
36. Li, C.; Kong, L.; Shu, R.; An, R.; Zhang, X. Disintegration characteristics in granite residual soil and their relationship with the collapsing gully in South China. *Open Geosci.* **2020**, *12*, 1116–1126. [CrossRef]
37. Luo, X.; Gao, H.; He, P.; Liu, W. Experimental investigation of dry density, initial moisture content, and temperature for gran-ite residual soil disintegration. *Arab. J. Geosci.* **2021**, *14*, 1–9. [CrossRef]
38. Zhou, S.; Tian, Z.; Di, H.; Guo, P.; Fu, L. Investigation of a loess-mudstone landslide and the induced structural damage in a high-speed railway tunnel. *Bull. Eng. Geol. Environ.* **2020**, *79*, 2201–2212. [CrossRef]
39. Zhang, J.-M.; Luo, Y.; Zhou, Z.; Chong, L.; Victor, C.; Zhang, Y.-F. Effects of preferential flow induced by desiccation cracks on slope stability. *Eng. Geol.* **2021**, *288*, 106164. [CrossRef]
40. Zhao, Y.; Feng, J.; Liu, K.; Xu, H.; Wang, L.; Liu, H. Study of the Stability of a Soil-Rock Road Cutting Slope in a Permafrost Region of Hulunbuir. *Adv. Civ. Eng.* **2020**, *2020*, 6701958. [CrossRef]
41. Zhang, S.; Zhang, X.; Pei, X.; Wang, S.; Huang, R.; Xu, Q.; Wang, Z. Model test study on the hydrological mechanisms and early warning thresholds for loess fill slope failure induced by rainfall. *Eng. Geol.* **2019**, *258*, 105135. [CrossRef]
42. Zhang, G.; Wang, R.; Qian, J.; Zhang, J.-M.; Qian, J. Effect study of cracks on behavior of soil slope under rainfall conditions. *Soils Found.* **2012**, *52*, 634–643. [CrossRef]
43. Yang, Z.; Lv, J.; Shi, W.; Zhang, Q.; Lu, Z.; Zhang, Y.; Ling, X. Model Test Study on Stability Factors of Expansive Soil Slopes with Different Initial Slope Ratios under Freeze-Thaw Conditions. *Appl. Sci.* **2021**, *11*, 8480. [CrossRef]
44. Chang, Z.; Huang, F.; Huang, J.; Jiang, S.-H.; Zhou, C.; Zhu, L. Experimental study of the failure mode and mechanism of loess fill slopes induced by rainfall. *Eng. Geol.* **2020**, *280*, 105941. [CrossRef]
45. Hou, H.-J.; Wang, B.; Deng, Q.-X.; Zhu, Z.-W.; Xiao, F. Model Experimental Study on Stress Transfer and Redistribution in a Clay Landslide under Surcharge Load. *Adv. Mater. Sci. Eng.* **2020**, *2020*, 4269043. [CrossRef]
46. Krisnanto, S.; Rahardjo, H.; Kartiko, R.D.; Satyanaga, A.; Nugroho, J.; Mulyanto, N.; Rachma, S.N. Characteristics of Rain-fall-Induced Slope Instability in Cisokan Region, Indonesia. *J. Eng. Technol. Sci.* **2021**, *53*, 1–21. [CrossRef]
47. Hamdhan, I.; Schweiger, H. Finite element method–based analysis of an unsaturated soil slope subjected to rainfall infiltration. *Int. J. Geomech.* **2013**, *13*, 653–658. [CrossRef]
48. Chaika, C.; Dvorkin, J. Porosity Reduction During Diagenesis of Diatomaceous Rocks. *AAPG Bull.* **2000**, *84*, 1173–1184. [CrossRef]
49. Burger, C.A.; Shackelford, C.D. Soil-Water Characteristic Curves and Dual Porosity of Sand–Diatomaceous Earth Mixtures. *J. Geotech. Geoenviron. Eng.* **2001**, *127*, 790–800. [CrossRef]
50. Wu, L.Z.; Zhang, L.M.; Zhou, Y.; Xu, Q.; Yu, B.; Liu, G.G.; Bai, L.Y. Theoretical analysis and model test for rainfall-induced shallow landslides in the red-bed area of Sichuan. *Bull. Eng. Geol. Environ.* **2017**, *77*, 1343–1353. [CrossRef]
51. Li, Q.; Wang, Y.M.; Zhang, K.B.; Yu, H.; Tao, Z.Y. Field investigation and numerical study of a siltstone slope instability induced by excavation and rainfall. *Landslides* **2020**, *17*, 1485–1499. [CrossRef]

remote sensing

MDPI

Article

Landslide Deformation Extraction from Terrestrial Laser Scanning Data with Weighted Least Squares Regularization Iteration Solution

Lidu Zhao [1,*], Xiaping Ma [2], Zhongfu Xiang [1], Shuangcheng Zhang [3], Chuan Hu [1], Yin Zhou [1] and Guicheng Chen [1]

[1] School of Civil Engineering, Chongqing Jiaotong University, Chongqing 400074, China; xzf6058@163.com (Z.X.); hucch@cqjtu.edu.cn (C.H.); yin_zhou935215@163.com (Y.Z.); chenguicheng968@163.com (G.C.)
[2] College of Geomatics, Xi'an University of Science and Technology, Xi'an 710054, China; xpmaxkd16@xust.edu.cn
[3] College of Geological Engineering and Geomatics, Chang'an University, Xi'an 710054, China; shuangcheng369@chd.edu.cn
* Correspondence: zhaolidu@cqjtu.edu.cn

Abstract: The extraction of landslide deformation using terrestrial laser scanning (TLS) has many important applications. The landslide deformation can be extracted based on a digital terrain model (DTM). However, such methods usually suffer from the ill-posed problem of a multiplicative error model as illustrated in previous studies. Moreover, the edge drift of commonly used spherical targets for point cloud registration (PCR) is ignored in the existing method, which will result in the unstable precision of the PCR. In response to these problems, we propose a method for extracting landslide deformations from TLS data. To archive the PCR of different period point clouds, a new triangular pyramid target is designed to eliminate the edge drift. If a fixed target is inconvenient, we also propose a PCR method based on total station orientation. Then, the use of the Tikhonov regularization method to derive the weighted least squares regularization solution is presented. Finally, the landslide deformation is extracted by DTM deference. The experiments are conducted on two datasets with more than 1.5 billion points. The first dataset takes Lashagou NO. 3 landslide in Gansu Province, China, as the research object; the point cloud data were collected on 26 February 2021 and 3 May 2021. The registration accuracy was 0.003 m based on the permanent triangular pyramid target and 0.005 m based on the total station orientation. The landslide deforms within 3 cm due to the ablation of the frozen soil. The second dataset is TLS data from the Lihua landslide in Chongqing, China, collected on 20 April 2021 and 1 May 2021. The overall deformation of the Lihua landslide is small, with a maximum value of 0.011 m. The result shows that the proposed method achieves a better performance than previous sphere-based registration and that the weighted least square regularization iterative solution can effectively reduce the ill-condition of the model.

Keywords: point cloud; point cloud registration (PCR); ill-posed multiplicative error model; landslide deformation extraction; terrestrial laser scanning (TLS)

Citation: Zhao, L.; Ma, X.; Xiang, Z.; Zhang, S.; Hu, C.; Zhou, Y.; Chen, G. Landslide Deformation Extraction from Terrestrial Laser Scanning Data with Weighted Least Squares Regularization Iteration Solution. *Remote Sens.* **2022**, *14*, 2897. https://doi.org/10.3390/rs14122897

Academic Editors: Stefano Morelli, Veronica Pazzi and Mirko Francioni

Received: 9 May 2022
Accepted: 15 June 2022
Published: 17 June 2022

1. Introduction

The extraction of landslide deformation is important for many applications [1–4], such as disaster management and deformation detection. Laser scanning can be used to acquire accurate and dense 3D points from a target surface and has unique advantages when it comes to landslide monitoring, deformation extraction, and disaster management.

As the most direct manifestation of landslide stability, landslide surface deformation has received special attention from scholars [5–7]. Conventional landslide monitoring methods, such as using the GNSS (Global Navigation Satellite System) [8–10], leveling [11,12],

crack gauges [13,14], etc., can only obtain sparse measurements at a few locations or within the affected slopes. Therefore, it is difficult to interpret the overall deformation characteristics of a landslide [15,16]. Terrestrial laser scanning (TLS) is a ground-based active imaging method that rapidly acquires precise and dense 3D point clouds on the surface of objects through laser ranging. Guo et al. [17] used point cloud data and the digital elevation model visualization method capable of a sky view to carry out geological disaster identification research and verified the reliability of airborne LiDAR identification results through field investigation. Abellan et al. [18] used TLS technology to monitor a dangerous rock mass in Spain, and discussed the feasibility of millimeter-level high-precision monitoring. Kayen et al. [19] used TLS to monitor nearly 400 large landslides induced by the Chuetsu earthquake in Niigata Prefecture, Japan, and greatly improved the efficiency of post-earthquake disaster assessment. Liu et al. [20] proposed a landslide displacement monitoring method based on point cloud density characteristics; the method identified the slope variation area and directly reflected the landslide surface deformation.

PCR can merge these individually scanned period point clouds. The basic idea of PCR is to seek the best transformation parameters to transform a point cloud with a local coordinate system to the same reference system [21]. PCR is divided into real-time registration and accurate registration of point clouds in different periods. Real-time registration refers to the detection of the surrounding environment while scanning and registering the real-time scanning point cloud using mobile laser scanning with the acquired point cloud. It is widely used for fast modeling, indoor navigation, and simultaneous localization and mapping (SLAM). It is a low-precision PCR method. The point cloud data of different periods is typically obtained using fixed scanners (such as TLS). The main PCR methods for different period data are marker-based registration and data-based registration.

However, there are still many problems with the application of landslide monitoring using TLS technology [22,23]. When using TLS to monitor landslide deformation, it is necessary to collect a multi-period landslide point cloud and calculate the landslide deformation by comparing the spatial position of the point cloud. Unfortunately, each period point cloud is based on an independent coordinate system, and the reference data are not unified, resulting in the low accuracy and unreliable results of landslide deformation detection [24].

The widely used marker in TLS is the standard spherical target [25,26]. Spherical targets have high precision and are easy to carry, but they are expensive, require high precision in manufacturing and maintenance, and cause edge drift because of their excessive laser reflection angle. The spherical target is shown in Figure 1, and the spherical target cloud is shown in Figure 2. Since the edge drift is concentrated away from the scanning side, it does not receive uniformly distributed random noise, which will cause non-negligible calculation errors in the spherical center coordinates. An ICP algorithm is the most used data-based PCR method due to its simple iteration and fast convergence [27]. The principle of ICP is to find the nearest correspondence in the source and the target point cloud and use the distance matrix of the nearest correspondence to estimate the rotation and translation parameters [28].

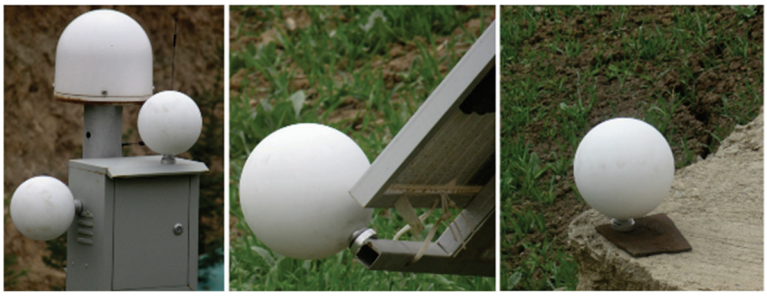

Figure 1. Spherical target.

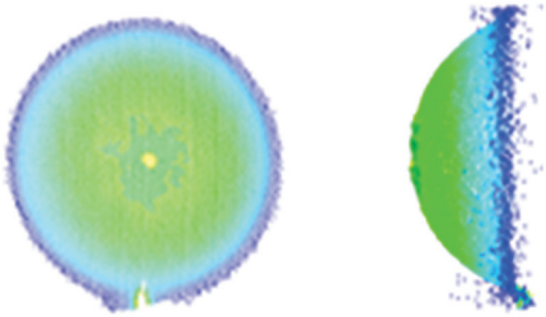

Figure 2. Point cloud of spherical target.

The landslide deformation can be extracted based on DTM [29,30]. Unfortunately, the DTM adjustment model is a typical ill-posed multiplicative random error model [31]. The ill-posed error model widely exists in the processing of remote sensing causing the instability of the parameter solution and even serious deviations from the true value. Xu et al. [32] first proposed the least square solution for the multiplicative error model. Shi et al. [33] summarized the least square, weighted the least square, and bias-corrected the weighted least square method of the multiplicative error model, and deduced the accuracy formula for the parameter estimation. If these three methods are used to deal with the ill-posed multiplicative error model without considering the ill-posed feature of the coefficient matrix, the parameter estimation will be biased and unstable. To avoid the ill-posed coefficient matrix, Wang et al. [34] built a DTM using the points at the peaks in the simulated data. This model can only be used to process simulation data and cannot be applied to practical observational data. Due to the ill-posed coefficient matrix, the complex collinearity between the column vectors of the coefficient matrix causes the condition number of the normal equation to be too large and thus the solution is unstable. Therefore, research on ill-posed multiplicative random error model adjustment theory needs to be further studied. At present, the methods for dealing with ill-posed multiplicative error models mainly include truncated singular-value decomposition (TSVD) [35], the Tikhonov regularization method [36], the ridge estimation method [37], and the virtual observation value solution [38]. The Tikhonov regularization method is a general adjustment method that strictly adheres to the theory. It is commonly used to solve the ill-posed multiplicative random error model.

The works mentioned above have carried out detailed studies on the landslide deformation extraction from TLS. The PCR of different period point cloud and the DTM construction are the vital procedures for deformation extraction. However, the number of point clouds on a marker sphere is sparse in the scanning process of a landslide. Edge drift caused by an excessively large laser reflection angle inevitably occurs due to the characteristics of the sphere. Thus, the calculation error of the spherical center coordinates cannot be disregarded. In this research, a new triangular pyramid target was developed which can unify the data of the multi-period point cloud by three non-parallel surfaces. In addition, aiming to address the problems of poor site access conditions and inconvenient traffic, we also propose a new scheme of data acquisition and registration based on total station orientation. The DTM adjustment model is an ill-posed multiplicative error model. If an ill-posed coefficient matrix is not considered, the parameter estimation will be biased and unstable. Hence, we utilize the Tikhonov regularization method to derive the weighted least squares regularization solution.

2. Methodology

The method proposed in this paper mainly consists of three steps. First, the PCR of the multi-period point cloud data is performed. Then, considering the ill-multiplicative error model, a weighted least square regularization iterative solution is proposed for DTM construction. Finally, the landslide deformation is obtained by differential DTMs.

2.1. PCR of Multi-Period Point Cloud Data

2.1.1. PCR Based on Triangular Pyramid Target

Multi-phase point cloud is characterized by three fixed triangular pyramid vertices of concrete in the field. The source point set $X \triangleq \left\{\vec{x}_i\right\}_{i=1}^{N_x} (N_x \in \mathbb{N})$ and the target point set $Y \triangleq \left\{\vec{y}_i\right\}_{i=1}^{N_y} (N_y \in \mathbb{N})$ are assumed in the n-dimensional space $\mathbb{R}^n$. The objective of the rigid-body registration algorithm is to find a rotation matrix and translational matrix so that the source point set and target point set can optimally correspond in space. The optimization criterion based on Euclidean distance can be written as follows [39],

$$\min_{R,\vec{t},c(i)\in\{1,2,\cdots,N_y\}} \sum_{i=1}^{N_x} \left\| (R\vec{x}_i + \vec{t}) - \vec{y}_{c(i)} \right\|_2^2 \text{ s.t. } R^T R = I_3, \det(R) = 1 \tag{1}$$

ICP algorithm is widely used in rigid body registration due to its simple iteration and fast convergence. The ICP algorithm iteratively computes the rigid transformation parameters R and $\vec{t}$ until the objective function converges to a local minimum. In the kth iteration, the algorithm is implemented through the following two steps,

(1) Setting up the matching point correspondence of two point sets,

$$c_{k(i)} = \text{argmin} \left\| (R_{k-1}\vec{x}_i + \vec{t}_{k-1}) - \vec{y}_{c(i)} \right\|_2^2 \tag{2}$$

where i $= 1, \cdots, N_x$, R_{k-1}, $\vec{t}_{k-1}$ is the argument of iteration k $-$ 1.

(2) The new rotation matrices and shift vectors are computed by minimizing the square distance [40],

$$\left(R_k, \vec{t}_k\right) = \underset{R^T R = I_n, \det(R)=1, \vec{t}}{\text{argmin}} \sum_{i=1}^{N_x} \left\| R\vec{x}_i + \vec{t} - \vec{y}_{c_k(i)} \right\|_2^2 \tag{3}$$

The condition for the end of iteration for the ICP algorithm is that the registration error is small enough or the number of iterations reaches its maximum number, then the algorithm terminates, otherwise the iteration continues [41]. We use root mean square (RMS) ε to evaluate the registration accuracy,

$$\varepsilon = \frac{1}{N} \sum_{i=1}^{N_s} \left\| R_k \vec{x}_i + \vec{t}_k - \vec{y}_{c_k(i)} \right\|_2^2 \tag{4}$$

where R_k, $\vec{t}_k$ is the argument of iteration k.

2.1.2. PCR Based on Total Station Orientation

The point cloud coordinates are converted to the independent coordinate system using the Bursa–Wolf transformation model. The Bursa–Wolf transformations are conformal 3D Cartesian coordinate transformations commonly used in surveying, photogrammetry, and geodesy [42].

2.2. Landslide DTM Using the Weighted Least Squares Regularization Solution

Unlike common Gauss–Markov models with additive random error [43–45], we suppose a set of observations with multiplicative random error $y_i (i = 1, 2, \cdots n)$, and the multiplicative error model can be defined as follows [46],

$$y_i = f_i(\beta)(1 + \varepsilon_i), i = 1, 2, \cdots, n \tag{5}$$

where ε_i is the zero mean random error, $f(\beta)$ and ε are the random variables, β is the t-dimensional unknown parameter vector to be estimated, $\odot$ is the Hadamard product of matrices or vectors, and 1 is the n dimensional column vectors with all values set to 1.

Assuming that the variances of the elements in vector ε are equal and independent, if every $f_i(\cdot)$ is a linear function of variable β, that is, $f_i(\beta) = x_i^T\beta$, x_i^T is a t-dimensional row vector, the multiplicative error model can be written as follows,

$$y = (X\beta) \odot (1 + \varepsilon) \tag{6}$$

The Formula (6) can be rewritten in the following form,

$$\bar{e} = y - X\beta = (X\beta) \odot \varepsilon_m \tag{7}$$

where $X = (x_1, x_2, \cdots, x_n)^T$.

It is evident that the accuracy of the observation value in the multiplicative error model is proportional to the signal intensity. The stronger the signal $X\beta$, the greater the error. The covariance matrix Q_y is a function of the unknown parameter β. The commonly used methods for solving the multiplicative error model include the least squares method and the deviation correction weight least squares method. The weighted least square regularization algorithm is applied to the ill-posed multiplicative error model in this paper.

We utilize the least square (LS) method to calculate the parameter; the parameter estimation can be expressed as follows [47],

$$\hat{\beta}_{LS} = \left(\boldsymbol{X}^T\boldsymbol{X}\right)^{-1}\boldsymbol{X}^T\boldsymbol{y} \tag{8}$$

where $\hat{\beta}_{LS}$ is the least square estimation of the multiplicative error model.

According to the law of cofactor propagation, the cofactor matrix of $\bar{e}$ and y is,

$$Q_{\bar{e}} = Q_y = \begin{bmatrix} x_1^T\beta & 0 & 0 & 0 \\ 0 & x_2^T\beta & 0 & 0 \\ 0 & 0 & \ddots & 0 \\ 0 & 0 & 0 & x_n^T\beta \end{bmatrix} \tag{9}$$

We also utilize an unbiased estimation of weighted least-square (bcWLS) method; the parameter estimation can be expressed as follows [48],

$$\hat{\beta}_{bc} = (\mathrm{X}^T\mathrm{Q}_y^{-1}\mathrm{X})^{-1}\mathrm{X}^T\mathrm{Q}_y^{-1}y \tag{10}$$

where $\hat{\beta}_{bc}$ is the parameter estimation using bcWLS method.

If the normal equation $N = (X^TX)^{-1}$ is ill-posed, the LS solution is unreliable. Hence, to overcome the ill-posed state of the normal equation, we use the weighted least squares regularization iterative solution (RWLS). First, a regularization factor α is introduced to construct the regularization criterion of the ill-posed multiplicative error model,

$$\phi = \bar{e}^TQ_{\bar{e}}^{-1}\bar{e} + \alpha\beta^T\beta = \min \tag{11}$$

According to the definition of RWLS, the parameter estimation can be expressed as follows [49],

$$\hat{\beta}_{RWLS} = (A^TQ_{\bar{e}}^{-1}A + \alpha I_n)^{-1}A^TQ_{\bar{e}}^{-1}y \tag{12}$$

where $\hat{\beta}_{RWLS}$ is the *RWLS* solution of ill-posed multiplicative error model, and I_n is identity matrix. The term αI_n is added to the inversion of the normal equation, which effectively weakens the ill-posed state of the normal equation. Therefore, we can obtain a reliable and stable solution.

As evident from Equation (11), $\left\|y - A\hat{\beta}\right\|$ and $\left\|\hat{\beta}\right\|$ are the function of the regularization parameter α, and the L curve method is used to calculate the regularization parameters α. The main procedures are as follows [50,51],

(1) Taking $\left\|y - A\hat{\beta}\right\|$ as the x-axis coordinate and $\left\|\hat{\beta}\right\|$ as the y-axis coordinate, we get multiple sets of coordinate points ($\left\|y - A\hat{\beta}\right\|$, $\left\|\hat{\beta}\right\|$),
(2) These coordinate points are fitted to a curve similar to L shape, and the α value corresponding to the point with the largest curvature is used as the estimation of the regularization parameter.

As evident from Equation (12), $Q_{\bar{e}}$ is the nonlinear function of $\hat{\beta}_{RWLS}$ on the left side of the Equation (12), and $\hat{\beta}_{RWLS}$ is the nonlinear function of $Q_{\bar{e}}$ on the right side of Equation (12). Hence, there is no analytical solution, only a numerical solution [52]. We can only use approximation methods to iteratively calculate the numerical solution.

The detailed procedure of RWLS solution is as follows,

(1) The LS solution is used as the RWLS initial value of iteration;
(2) Compute the cofactor matrix $Q_{\bar{e}_i}$;

$$Q_{\bar{e}_i} = \begin{bmatrix} x_1^T \hat{\beta}_{RWLS}^i & 0 & 0 & 0 \\ 0 & x_2^T \hat{\beta}_{RWLS}^i & 0 & 0 \\ 0 & 0 & \ddots & 0 \\ 0 & 0 & 0 & x_n^T \hat{\beta}_{RWLS}^i \end{bmatrix} \tag{13}$$

(3) The regularization parameter α_i is obtained by L curve method;
(4) The iterative formula is as follows:

$$\hat{\beta}_{RWLS}^{i+1} = \left(A^T Q_{\bar{e}_i}^{-1} A + \alpha_i I_n\right)^{-1} A^T Q_{\bar{e}_i}^{-1} y, i = 0, 1, \cdots \tag{14}$$

(5) Repeat steps (2)–(4) until the value of the parameter subtraction is smaller than the threshold,

$$\left\|\hat{\beta}_{RWLS}^{i+1} - \hat{\beta}_{RWLS}^{i}\right\| < \varepsilon_{th} \tag{15}$$

where ε_{th} is defined as 10^{-10} in this paper.

The unit weight variance is always an important quality index for evaluating observation results and data processing results. It is defined as follows by using the LS method,

$$\hat{\sigma}_{LS}^2 = \frac{V_{LS}^T V_{LS}}{tr\left\{\hat{Q}_y - \left(X^T X\right)^{-1} X^T \hat{Q}_y X\right\}} \tag{16}$$

where $\hat{\sigma}_{LS}^2$ = unit weight variance.

The unit weight variance using bcWLS can be expressed as follows [53],

$$\hat{\sigma}_{bc}^2 = \frac{V_{bc}^T \hat{Q}_y^{-1} V_{bc}}{r} \tag{17}$$

where $\hat{\sigma}_{bc}^2$ = unit weight variance, r = freedom degree, and its value correlates with the number of observation value and parameter estimation.

The unit weight variance of the ill-posed multiplicative random error model can be expressed as follows [54],

$$\hat{\sigma}_0^2 = \frac{\hat{\bar{e}}^T Q_{\bar{e}}^{-1} \hat{\bar{e}}}{r} \tag{18}$$

where $\hat{\bar{e}} = A\hat{\beta}_{RWLS} - y = \left[A\left(A^T Q_{\bar{e}}^{-1} A + \alpha I_n\right)^{-1} A^T Q_{\bar{e}}^{-1} - I\right] y$.

The unit weight variance using RWLS can be expressed as follows [52],

$$\hat{\sigma}^2_{RWLS} = \hat{\sigma}^2_0 tr(Q_{\hat{\beta}_{RWLS} \times \hat{\beta}_{RWLS}}) + tr(b_{\hat{\beta}_{RWLS}} b^T_{\hat{\beta}_{RWLS}}) \tag{19}$$

where $\hat{\sigma}_{RWLS}$ is the unit weight variance. In Equation (19), $b_{\hat{\beta}_{RWLS}}$ is defined as follows,

$$b_{\hat{\beta}_{RWLS}} = -\alpha (A^T Q^{-1}_{\bar{e}} A + \alpha I_n)^{-1} \hat{\beta}_{RWLS} \tag{20}$$

In this paper, we use LS, bcWLS, and the RWLS method to estimate the parameters and calculate the accuracy of parameters.

In addition, the noise of point cloud data has been shown with a nature of multiplicative random error [55–57]. Therefore, the multiplicative error model of DTM with 6 unknown parameters is as follows [33],

$$H(\mathrm{X_i}, y_i) = F(\mathrm{X_i}, y_i) \odot (1 + \varepsilon_m) \tag{21}$$

where $(\mathrm{X_i}, y_i)$ represents the x and y coordinates of the ground point, $H(\mathrm{X_i}, y_i)$ represents the corresponding elevation of the point, and ε_m represents the multiplicative error vector,

$$F(\mathrm{X_i}, y_i) = \beta_1 + \beta_2 x_i + \beta_3 y_i + \beta_4 x_i y_i + \beta_5 x_i^2 + \beta_6 y_i^2 \tag{22}$$

Then, we apply LS, bcWLS, and RWLS method to calculate the parameter estimation and unit weight variance. Finally, we extract the landslide deformation by the difference of DTM.

3. Experiments Data

3.1. Simulation Experiment

3.1.1. Simulation Experiment I: GNSS Elevation Point Disturbed by Multiplicative Error

GNSS is used to measure the elevation of the ground point of a road center line in a certain area. It is assumed that the ground point elevation and distance conform to the following functional model,

$$y = 10 + 4x + 2x^2 + x^3 + 0.5x^4 + 2x^5 \tag{23}$$

In this example, the value range of x is 0–300 m, and 31 points are equally spaced within the value range of x. The truth values of the parameters are 10, 4, 2, 1, 0.5, and 2.

Assuming that y is disturbed by the multiplicative random error, where the multiplicative random errors are independent of each other and follow a normal distribution with a mean value of 0 and a standard deviation of 0.1, and the corresponding observation equation of the multiplicative error model is,

$$Y(x) = y(x) \odot (1 + \varepsilon_m) \tag{24}$$

where Y is the vector disturbed by multiplicative error, 1 is the 31-dimensional column vector with all elements being 1, and ε_m is the 31-dimensional multiplicative random error vector. The simulation values of the ground elevation points obtained from Equation (23) are shown in Table 1.

Table 1. Simulation Data.

Point Number	y	Point Number	y
1	8.8529	17	52.9943
2	9.3072	18	66.6330
3	10.0079	19	80.6002
4	8.0547	20	80.1413
5	13.7458	21	106.8200
6	13.1323	22	112.3601
7	12.5329	23	136.7752
8	16.5769	24	184.5394
9	13.1390	25	254.6235
10	17.2795	26	242.7289
11	19.0292	27	323.5583
12	22.8096	28	360.2978
13	26.2168	29	482.2399
14	27.0681	30	453.0284
15	34.8363	31	595.4323
16	40.9079		

To show that the elevation points are affected by multiplicative error, the data of the ground elevation points before and after interference from multiplicative error are plotted in Figure 3.

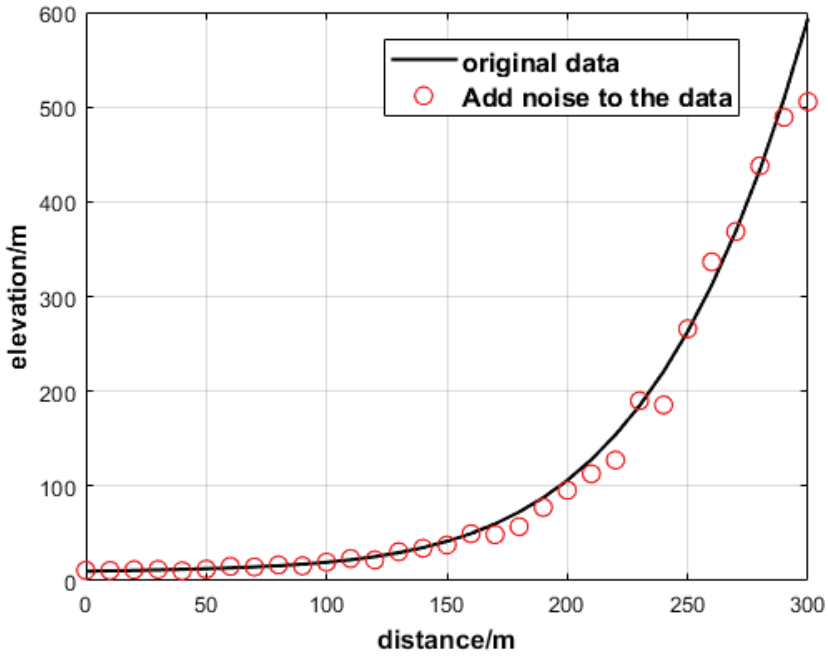

Figure 3. GNSS elevation point before and after being disturbed by multiplicative error.

3.1.2. Simulation Experiment II

This simulation uses DTM data. This paper mainly considers that the model is ill-posed, so it simulates the ill-conditioned DTM model and generates the DTM using the interpolation function method [53]

$$\overline{f}_{xy} = \sum_{i=1}^{4} \beta_i f_i(x, y) \tag{25}$$

where $\overline{f}_{xy}$ represents the elevation obtained by the interpolation function, x and y range from 0 m to 80 m, the interval is 2 m, and the truth values of the four parameters are -1.5, 20, 5, and -4, respectively.

The function $f_i(x, y)$ is as follows,

$$f_1(x, y) = \exp\left\{-((x-22)^2 + (y-22)^2)/500\right\} \tag{26}$$

$$f_2(x, y) = \exp\left\{-((x-28)^2 + (y-28)^2)/500\right\} \tag{27}$$

$$f_3(x, y) = \exp\left\{-((x-25)^2 + (y-25)^2)/500\right\} \tag{28}$$

$$f_4(x, y) = \exp\left\{-((x-20)^2 + (y-20)^2)/500\right\} \tag{29}$$

The multiplicative error model is as follows,

$$h(x, y) = \overline{f}(x, y) \odot (1 + \varepsilon_m) \tag{30}$$

where $h(x, y)$ is the vector of the observation values disturbed by multiplicative errors, 1 is the 1681-dimensional column vector whose elements are all 1, and ε_m is the 1681-dimensional multiplicative error vector values which are independent of each other. To illustrate that the DTM model is affected by multiplicative error, the DTM without the errors are plotted in Figure 4 and the DTM influenced by multiplicative random error is plotted in Figure 5. As can be seen from Figures 4 and 5, although the DTM with the standard deviation has a 0.1 multiplicative error, it has a great influence on the elevation, and the condition number of the normal equation $N = A^T Q_{\tilde{e}}^{-1} A$ is 4.456×10^4; therefore, the equation is seriously ill.

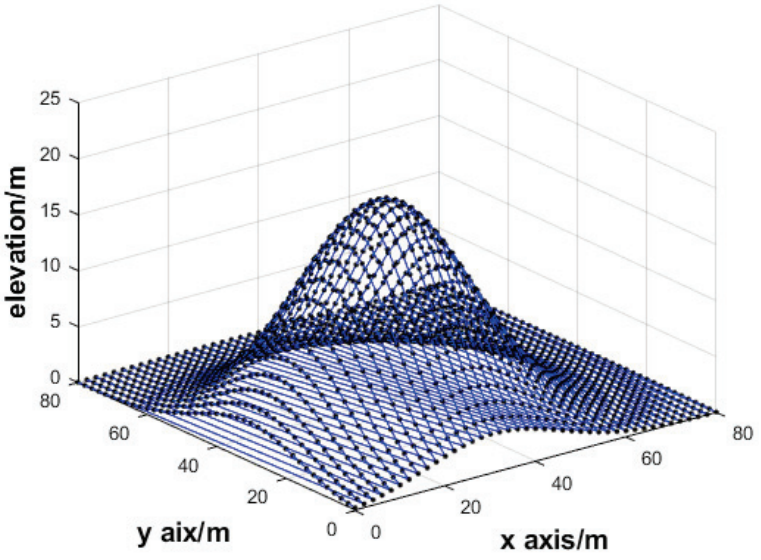

Figure 4. DTM.

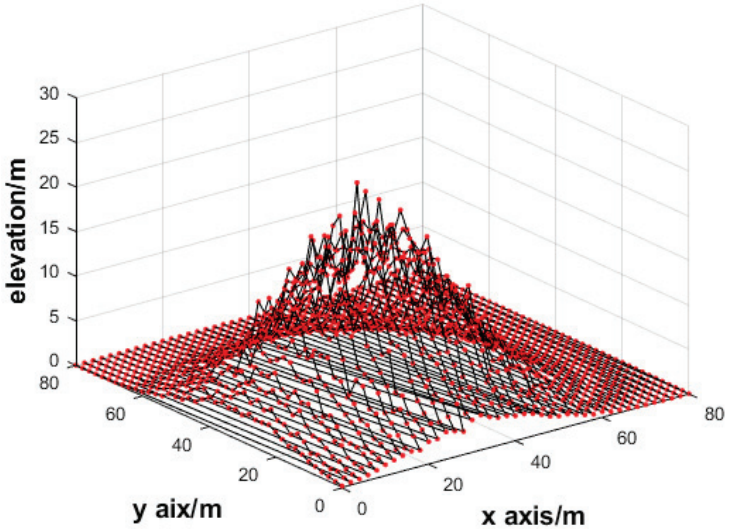

Figure 5. DTM with multiplicative error.

3.2. Actual Experiment

3.2.1. Actual Experiment I

(I) Experiment 1

The Lashagou NO. 3 landslide was a loess landslide located at Lashagou village, Jishishan county, Gansu province, China. Its geographical coordinates are 35° 35′ 23″E, 102° 57′ 12″N. It is in the transition zone between the Tibetan Plateau and the Loess Plateau, which is typical of an excavation-related shallow loess engineering landslide [58,59]. The main stratum of the landslide is Holocene residual slope silty clay and the main stratum of the slide bed is middle and lower Pleistocene fluvial and lacustrine maroon silty clay. The central width of the slide body is 60–100 m, the axial length is 80–130 m, the area is about 25,000 m^2, the thickness is 3–8 m, and the volume is about 150,000 cubic meters, belonging to the middle-shallow medium and small-sized landslide groups. The rear wall of the landslide was 0.2–0.4 m high, the natural slope was 15°, and the main slide direction was 85°. The front slope of this landslide group is mainly damaged by slime in the surface 1–3 m, but the lower soil is relatively stable, and the back edge of the landslide group is in the shape of an armchair and a gentle arc, which belongs to the traction cohesive soil landslide group. The optical remote sensing imagery of the landslide is shown in Figure 6a. As shown in Figure 6b, the toe of the Lashagou NO. 3 landslide is close to the G310 highway, which is activated or generated by the slope excavation during the construction of the G310 mountain highway. The main effects of the Lashagou NO. 3 landslide are shown in Figure 7. Figure 7b shows a local diagram of a crack 10 cm wide. Figure 7c shows the local displacement diagram of a 0.6 m staggered platform in the vertical direction of road surface formed by landslide. Figure 7d shows the local map of the road cracks formed by the landslide.

In this study, a Leica P50 laser scanner was used for data acquisition. The scanner is a ground-based 3D laser scanner with medium and long range, which has the advantages of obtaining high-quality point cloud data in harsh environments and a wide scanning range with minimal noise. The parameters of the Leica P50 laser scanner are shown in Table 2. In addition, A Leica Nova TS30 total station and some prism spheres are also required to collect data. The parameters of the Leica TS30 total station are shown in Table 3.

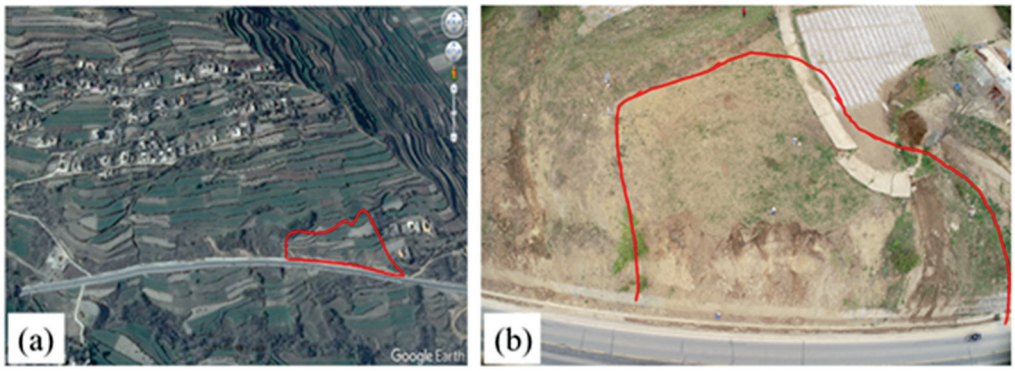

Figure 6. (**a**) Optical remote sensing imagery of Lashagou NO. 3 landslide acquired from Google Earth; (**b**) UAV image of Lashagou NO. 3 landslide.

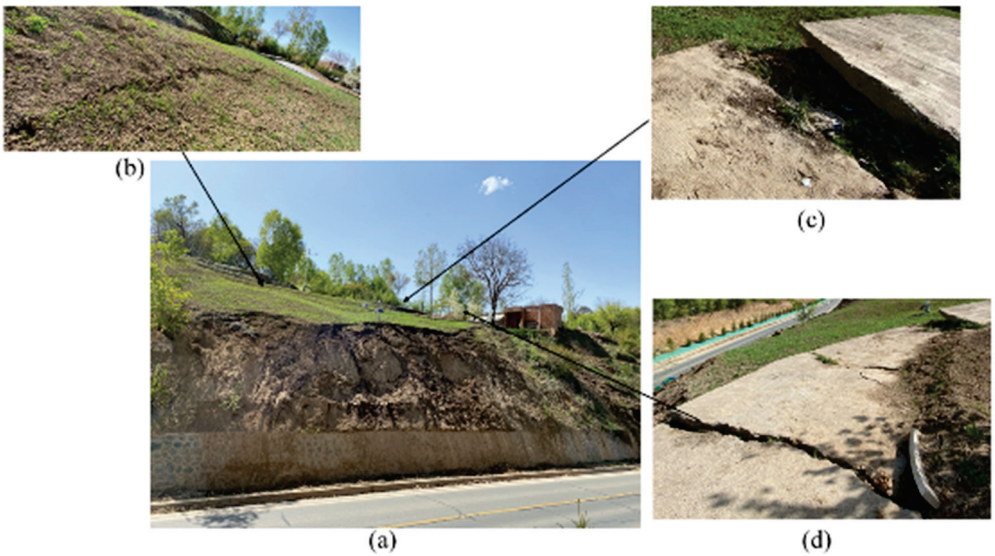

Figure 7. (**a**) Study area and photos showing Lashagou NO. 3 landslide disease. (**b**) ground fracture (**c**) staggered platform (**d**) tensile crack caused by the landslide.

Table 2. Parameters of Leica P50 3D laser scanner [60].

Parameter	Value
Scan range mode	from 0.4 to120 m from 0.4 to 270 m from 0.4 to 570 m, >1 km
Scan Rate	up to 1,000,000 points per second
Vertical/horizontal field-of-view	360°/290°
Range noise *	0.4 mm rms at 10 m 0.5 mm rms at 50 m
Operating temperature	−4° F to + 122° F
Dual-axis compensator	accuracy 1.5″

* at 78% albedo.

Table 3. Parameters of Leica TS30 total station [61].

Parameter		Value
Accuracy of angle	Horizontal and Vertical	0.5″
Distance Measurement Range	Round Prism (GPR1)	3500 m
Accuracy of distance	Standard (prism)	1 mm + 1 ppm

(I) Triangular pyramid target point cloud acquisition

In this paper, a triangular pyramid target was developed, and three concrete triangular pyramids were poured in the study area, among which any triangular pyramid target is shown in Figure 8. The size of the triangular pyramid template is an equilateral triangle with a side length of 50 cm and a height of 15 cm. The point cloud of the triangular pyramid is shown in Figure 9.

Figure 8. Triangular pyramid target.

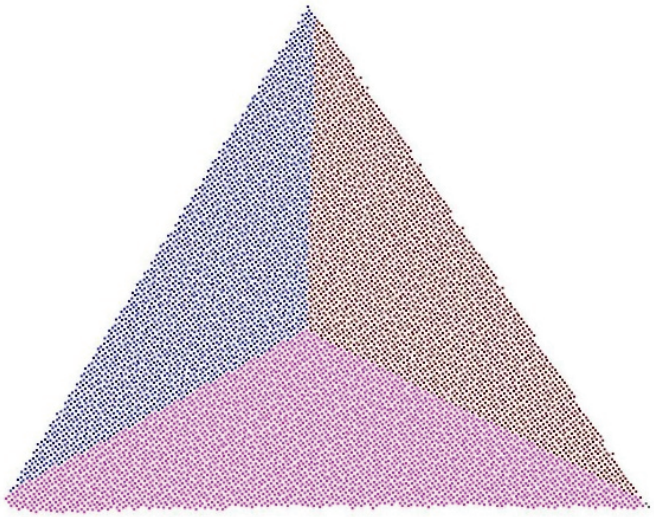

Figure 9. The point cloud of triangular pyramid.

(II) Data collection based on total station orientation

In the monitoring of the landslide and other deformation forms, points in the stable zone should be taken as the monitoring benchmark. The coordinates of the four control points in the stable zone in this paper are shown in Table 4.

Table 4. The coordinates of control points.

Control Point	x/m	y/m	z/m
SCP1	531.375	533.190	761.551
SCP2	535.557	522.346	762.020
SCP3	479.548	473.771	766.402
SCP4	412.943	401.501	772.336

The point cloud of the prism sphere was collected using a Leica P50 scanner. We used the Leica Nova TS30 total station to collect the 3-D coordinates of the prism sphere simultaneously. The experiment was divided into three steps,

(1) Leica TS30 total station was used to collect the coordinates of the prism balls near the landslide area.

The total station was set up at any position, and the coordinates of any two control points in the stability area were intersected to obtain the coordinates of the current measuring station. Then the central coordinates of the prism balls near the landslide area were measured. The photos of the prism balls are shown in Figure 10.

Figure 10. Prism ball target.

(2) The coordinates of the prism balls near the landslide area were obtained by fitting point cloud data collected by TLS simultaneously.

The Leica P50 scanner was set up at any position, and the point cloud data of the prism balls were obtained. Then the center coordinates of the prism balls were calculated by fitting the point cloud data of the prism balls. The transformation parameters from the point cloud coordinate system to the total station coordinate system can be obtained by using the Bursa–Wolf model.

(3) The unification of the data.

The point cloud coordinates of each period were converted to the control point coordinate system of the stable area by using the transformation parameters to realize the unification of the data.

The creep deformation of a landslide is a slow dynamic process. In this paper, a one-station measurement method was adopted to avoid the error caused by multi-station data PCR, which improved the accuracy of the landslide deformation monitoring. The Leica P50 scanner was set on the highest point of the slope opposite the landslide, and the scanning accuracy was set to 3 mm@ 10 m. Considering the influence of permafrost ablation and other factors on the landslide, two period point cloud data were collected on 26 February 2021 (temperature 3 degrees Celsius, before permafrost ablation) and 3 May 2021 (temperature 28 degrees Celsius, after permafrost ablation) to analyze the landslide

deformation. The data collection photo from period I (May 3, 2021) is shown in Figure 11, and the point cloud of Lashagou NO.3 landslide is shown in Figure 12.

Figure 11. Prism ball target.

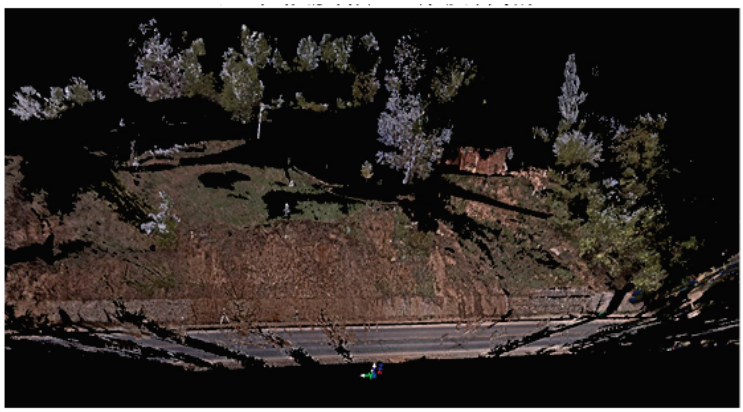

Figure 12. Point cloud of phase 1.

3.2.2. Actual Experiment II

The Lihua landslide was on the left side of the Lihua road at Nan'an District, Chongqing, China. The relative height difference was about 10 m. It was a typical excavation-induced shallow loess engineering landslide. Once a large-scale instability occurs, it may block the Lihua road and threaten the lives and property of the nearby residents and pedestrians. We collected a two-phase point cloud of the landslide with a Leica P50 3D laser scanner on 20 April 2021 (phase 1) and 1 May 2021 (phase 2). The Lihua landslide point cloud of phase 1 is shown in Figure 13. The UAV image of the Lihua landslide acquired on 4 June 2022 is shown in Figure 14.

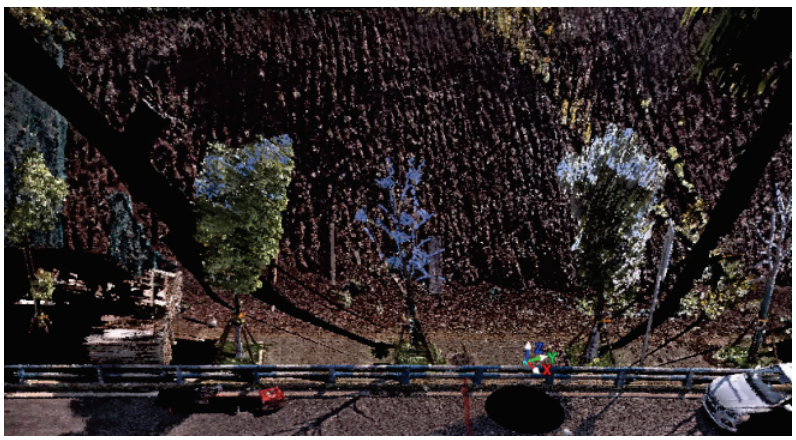

Figure 13. Lihua landslide point cloud of phase 1.

Figure 14. UAV image of Lihua landslide.

4. Analysis of Result and Discussion

4.1. The Results of Simulation Experiments

4.1.1. The Result of Simulation Experiment I

In simulation experiment 1, the square root of unit weight variance is 0.3. The parameter values obtained using the three methods are shown in Table 5.

Table 5. Parameter estimation and accuracy.

Method	$\hat{\beta}_1$	$\hat{\beta}_2$	$\hat{\beta}_3$	$\hat{\beta}_4$	$\hat{\beta}_5$	$\hat{\beta}_6$	$\hat{\sigma}_0$	$\left\|\Delta\hat{\beta}\right\|_2$
True value	10	4	2	1	0.5	2	0.3	—
LS	19.64	−147.21	442.38	−453.75	189.92	−25.37	12.0984	678.47
bcLS	11.45	−2.19	6.27	7.96	−8.11	3.99	20.98	13.61
RWLS	10.77	2.12	1.46	2.52	−1.46	2.46	1.26	3.28

The comparison between the RWLS method and the classical LS method is shown in Figure 15.

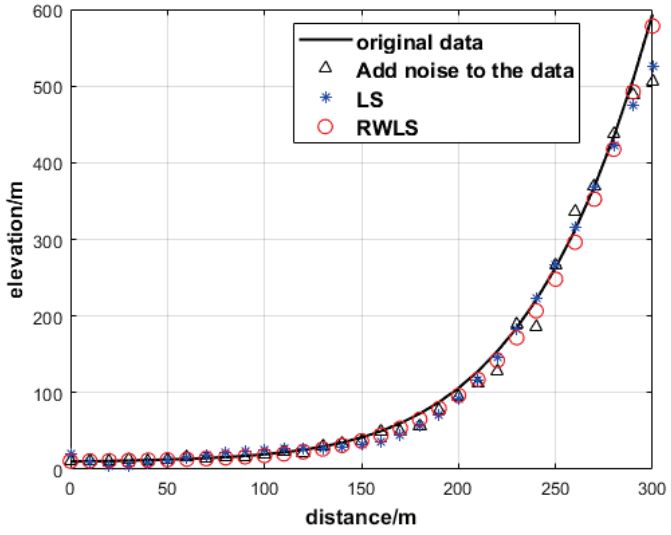

Figure 15. GNSS elevation obtained by the RWLS method and LS.

The condition number of the normal equation $N = A^T Q_{\bar{e}}^{-1} A$ is 8.3098×10^5, the equation is ill-posed. The regularization parameter values in this algorithm change dynamically, and the change of the regularization parameters with the number of iterations is shown in Figure 16.

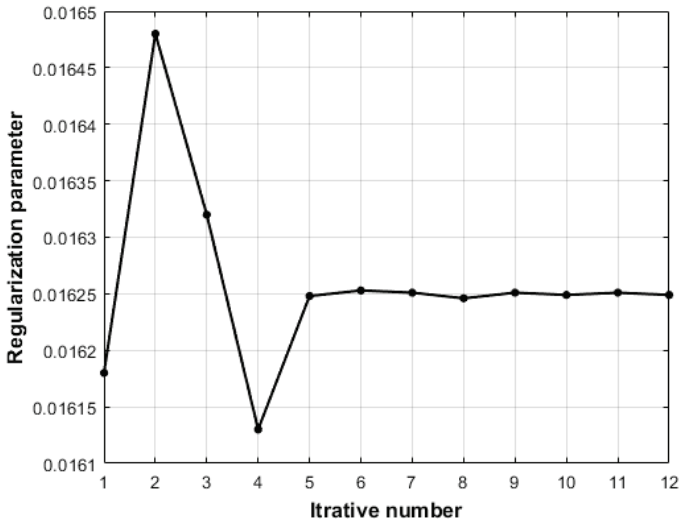

Figure 16. The regularization parameters with the number of iterations.

It is evident from Figure 15 that ground elevation points are influenced by multiplicative error, resulting in serious deviation. It is evident from Table 5 that the $\|\Delta\beta\|_2$ obtained by LS method is the largest. The $\|\Delta\beta\|_2$ calculated by the bcWLS method is 13.61, which still deviates greatly from the truth value because the ill-posed state of the model is not considered. The $\|\Delta\beta\|_2$ calculated by the RWLS algorithm in this paper is 3.28, and the parameter estimation is closer to the true value, indicating that the RWLS algorithm has a certain effect on reducing ill-condition. It is evident from Table 5 that the bcWLS method does not consider the ill-posed nature of the model, which led to $\hat{\sigma}_0$ deviating from the true value. However, the RWLS algorithm takes these factors into account and the $\hat{\sigma}_0$ is closer to the true value, further verifying the advantages of the algorithm in this paper.

4.1.2. The Result of Simulation Experiment II

Following Xu et al. (2013), it is here assumed that $\hat{\sigma}_0$ is 0.3, and that the multiplicative random error vectors are independent from each other. The parameter estimation, $\|\Delta\beta\|_2$ and $\hat{\sigma}_0$, calculated by LS, bcWLS, and RWLS, are listed in Table 6. The DTM made using the RWLS method is shown in Figure 17. The regularization parameters with the number of iterations are shown in Figure 18.

Table 6. Parameter estimation and accuracy.

Method	$\hat{\beta}_1$	$\hat{\beta}_2$	$\hat{\beta}_3$	$\hat{\beta}_4$	$\hat{\sigma}_0$	$\left\|\Delta\hat{\beta}\right\|_2$
true value	−3.5	15	8	−3	0.3	—
LS	21.68	21.00	−11.25	−14.87	4.52	34.38
bcWLS	−6.44	18.99	8.59	−1.69	4.36	3.18
RWLS	−1.94	14.91	7.46	−3.91	0.42	1.88

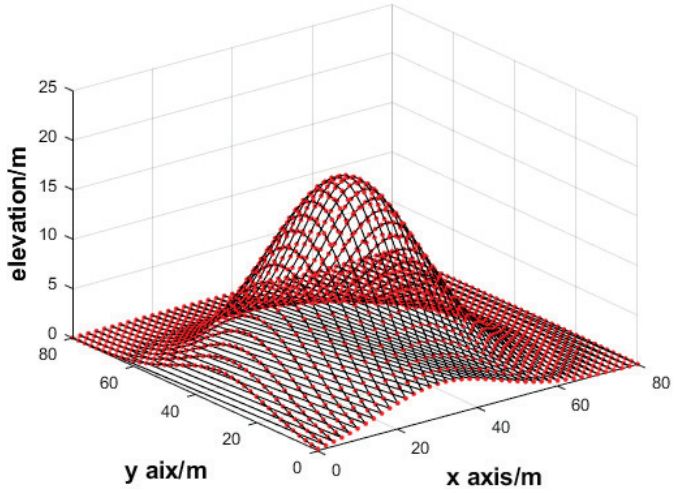

Figure 17. DTM by the RWLS method.

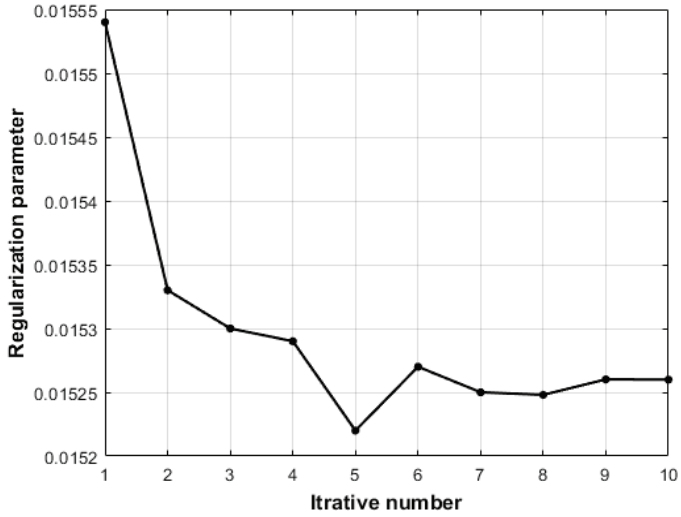

Figure 18. The regularization parameters with the number of iterations.

As can be seen from Table 6, the parameter estimation obtained by bcWLS deviates seriously from the true value because the ill-posed state of the model is not considered, while the result obtained by the RWLS algorithm is closer to the true value. The parameter $\|\Delta\beta\|_2$ calculated by RWLS is 1.88. It is less than that of the LS method and bcWLS method, which further indicates that the algorithm in this paper has a certain effect on reducing the ill-posed state. It is evident from Table 6 that the $\hat{\sigma}_0$ obtained by the LS method is 4.52, and that $\hat{\sigma}_0$ seriously deviates from the true value. The $\hat{\sigma}_0$ calculated by the bcWLS method is 4.36, which is closer to the truth value, because it considers the weight of the observation value. The RWLS method considered the influence of ill-condition on the $\hat{\sigma}_0$, hence the $\hat{\sigma}_0$ is the closest to the true value.

4.2. The Result of the Actual Experiment

(I) The result of experiment I

4.2.1. The result of PCR Based on Triangular Pyramid Target

Three planes can be fitted using the point cloud of a triangular pyramid, and then triangular pyramid vertices can be intersected through the three planes. The coordinates of three triangular pyramid vertices in phase 1 and phase 2 are shown in Tables 7 and 8, respectively.

Table 7. Coordinates of three triangular pyramid vertices in phase 1.

Point Number	x/m	y/m	z/m
CP1	5.989	22.562	−4.090
CP2	12.648	15.101	−4.803
CP3	32.494	−6.676	−6.480

Table 8. Coordinates of three triangular pyramid vertices in phase 2.

Point Number	x/m	y/m	z/m
CP1	−12.412	19.621	−4.134
CP2	−2.413	19.380	−4.847
CP3	27.049	18.977	−6.523

The initial landslide point cloud of phase 1 and phase 2 is shown in Figure 19. The translation vector obtained by the fine algorithm is (0.134, 0.080, −0.038). In this paper, the rotation matrix is transformed into the rotation angle around the coordinate axis, in which the rotation angle around the X axis is 0.164°, the rotation angle around the Y axis is −0.180°, and the rotation angle around the Z axis is −46.886°.

Figure 19. Initial point cloud of landslide in two phases.

The point cloud after unifying the data through the obtained rotation and translation parameters is shown in Figure 20. The image of the Lashagou NO.3 landslide is shown in Figure 21. It is evident that the two-phase point cloud has been accurately registered based on the triangular pyramid target. The point cloud data of the two periods are unified, which lays a foundation for landslide deformation detection.

Figure 20. Landslide point cloud after the PCR of two period data.

Figure 21. Photos of Lashagou NO.3 landslide.

The standard sphere target has often been used in previous studies [50–53]. Figure 1 shows that edge drift caused by an excessively large laser reflection angle will inevitably occur. Thus, the calculation error of the spherical center coordinates cannot be disregarded. Compared with previous studies [52,53], our methods handle this problem by designing a new triangular pyramid marker. As shown in Figure 9, three planes can be fitted through the triangular pyramid point cloud, and then the triangular pyramid vertices can be intersected through the three planes. The registration accuracy of the point cloud based on the triangular pyramid target is 0.003 m.

4.2.2. The result of PCR Based on Total Station Orientation

Figure 22 shows the point cloud after fine registration using the total station orientation theory. The two-phase point cloud has been accurately transformed into the control point coordinate system in the stable area, realizing the unification of the multi-phase point cloud data. The method is rigorous in theory, easy to operate in practice, free from the restriction of landslide terrain conditions, and has a wide applicability. The registration accuracy based on the total station orientation was 0.005 m.

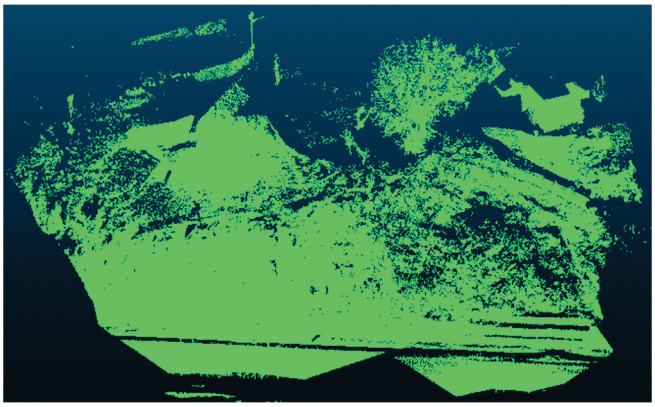

Figure 22. Point cloud after accurate registration.

By comparing the two PCR method with other PCR methods, it is evident that:

(1) In terms of data acquisition, to ensure the accuracy of registration, the data acquisition mode which is based on a fixed triangular pyramid target is simple and is capable of fast operation. It is suitable for good visibility and convenient transportation and is easy to cast in a concrete environment. In addition, based on the total station orientation data acquisition mode, it is not limited by field conditions and has a

wide applicability. Especially, in a situation where there are some control points in the stable area, the point cloud can be directly and effectively transformed into the existing coordinate system, which is of great significance to the continuous dynamic monitoring of landslide disasters based on point cloud data.

(2) In terms of PCR, the PCR theory based on a fixed triangular pyramid target and total station orientation is strict. The PCR based on a fixed triangular pyramid target can overcome the problem of low precision in the sphere-based PCR method. The advantage of PCR based on total station orientation is that the point cloud coordinates can be converted to the existing control point coordinate system, which is favorable for the utilization of survey area engineering.

The proposed approach strives at addressing the unstable precision of different period TLS data. Figure 23 shows the TLS data of the 1 m wide detailed image shown in Figure 20.

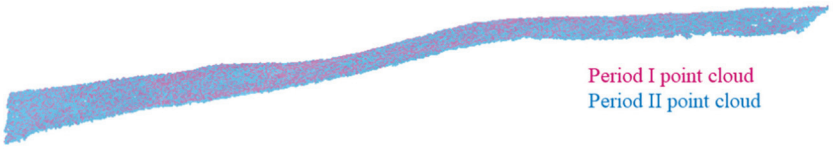

Figure 23. PCR based on triangular target (1 m wide detail in Figure 20).

As shown in Figure 23, the result after applying the target-based (triangular pyramid) PCR method suggests that the precision is stable. This may also indicate that in TLS data such methods tend to retain point cloud detail features. Compared with the spherical target [25,26], the triangular target can overcome the edge drift. After applying the PCR method based on total station backward orientation, the precision of PCR is high. Compared with a target-based PCR method [27], the station setup is flexible. In addition, it is suitable for the situations that are not easily accessible.

Our PCR method is easy to use. The center of sphere has often been used for PCR in previous studies [25]. Our conclusion about PCR based on spherical target is similar to [27], which is that it is difficult to calculate the spherical center precisely because of edge drift. Thus, a new PCR target is necessary. Compared with previous studies, our method handles this problem by designing a triangular target. The vertices can be precisely intersected by three triangular planes.

4.2.3. Landslide Based on DTM Difference

Parameter estimation values and their accuracy values are shown in Table 9. The coefficient matrix of the LS method and bcWLS method is singular and the parameter estimation does not converge due to the influence of the ill-condition. The algorithm in this paper takes ill-condition into account and has advantages for processing real data.

Table 9. Parameters of DTM estimation and accuracy.

Method	$\hat{\beta}_1$	$\hat{\beta}_2$	$\hat{\beta}_3$	$\hat{\beta}_4$	$\hat{\beta}_5$	$\hat{\beta}_6$	$\hat{\sigma}_0$
LS	−0.368	0.340	0.128	−0.007	−0.015	0.0003	13.12
bcWLS	−0.265	0.135	0.313	−0.023	−0.062	0.0005	6.93
RWLS	−0.165	0.102	0.033	0.016	−0.002	0.0267	2.34

The DTM of the Lashagou NO.3 landslide is shown in Figure 24. The deformation of the Lashagou NO.3 landslide is shown in Figure 25. It is evident from Figure 25 that from 26 February 2021 to 3 May 2021, the overall deformation of the landslide was small, and its maximum value was 0.031 m. The landslide will continue to maintain a stable state without special factors, such as earthquakes, heavy rainfall, and artificial excavation.

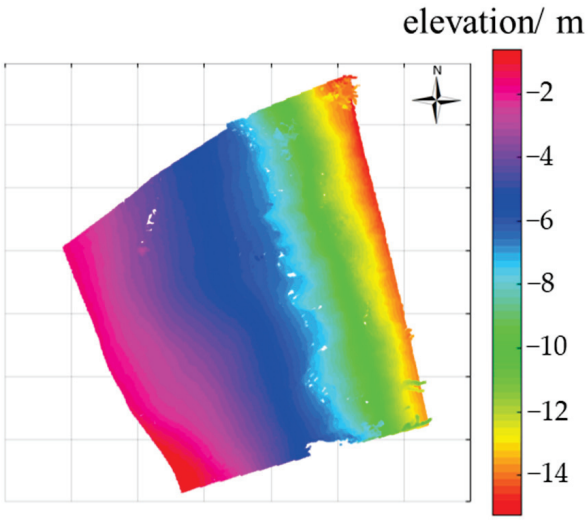

Figure 24. Lashagou NO.3 landslide DTM.

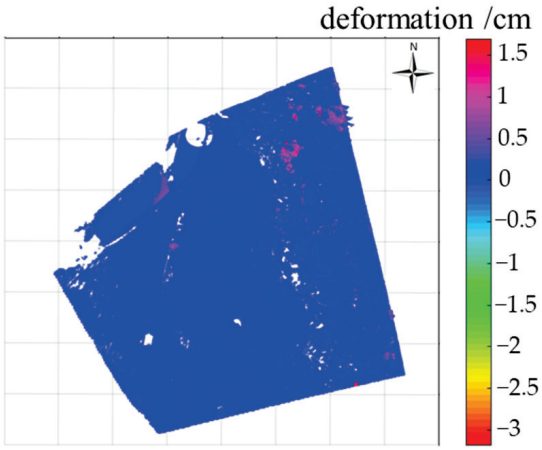

Figure 25. Deformation of Lashagou NO.3 landslide.

(II) The result of experiment II

The point cloud of the Lihua landslide (phase I) is shown in Figure 26. The DTM disturbed by multiplicative error obtained in this paper is shown in Figure 27.

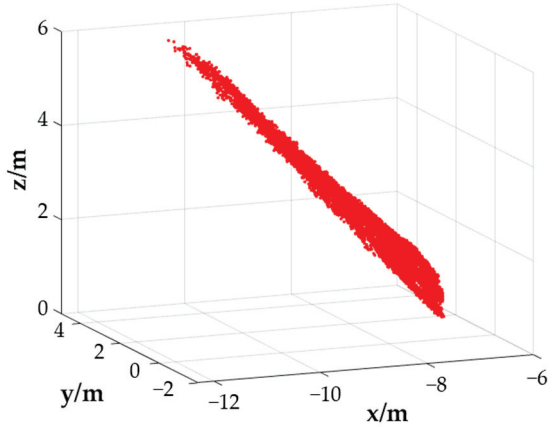

Figure 26. Point cloud of Lihua landslide.

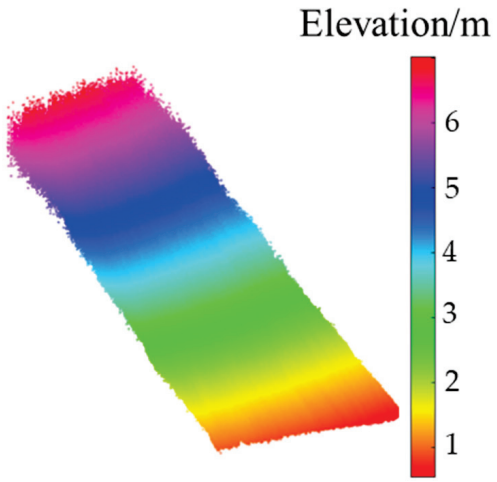

Figure 27. DTM disturbed by multiplicative error.

The estimation and accuracy of the parameters are shown in Table 10.

Table 10. The estimation and accuracy of DTM parameters.

Method	$\hat{\beta}_1$	$\hat{\beta}_2$	$\hat{\beta}_3$	$\hat{\beta}_4$	$\hat{\beta}_5$	$\hat{\beta}_6$	$\hat{\sigma}_0$
LS	−0.532	1.234	0.568	−0.146	−0.051	0.021	26.16
bcWLS	−0.389	0.657	0.425	−0.072	−0.081	0.0063	8.24
RWLS	−0.132	0.231	0.046	0.024	−0.006	0.001	2.34

The $\hat{\sigma}_0$ obtained by the LS method is too large, which does not conform to reality, further indicating that the LS method cannot process actual data. It can also be seen from Table 10 that the error of the parameter estimation obtained by the LS method is the largest, and that the error obtained by the RWLS method is much smaller than LS and bcWLS method.

The deformation of the Lihua landslide is shown in Figure 28. It is evident from Figure 28 that from 20 April 2021 to 1 May 2021, the overall deformation of the Lihua landslide was small, with a maximum value of 0.011 m.

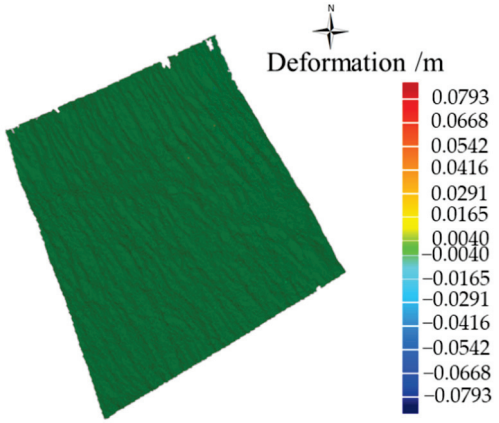

Figure 28. Deformation of Lihua landslide.

As shown in Figure 26, the DTM has a huge deviation because of the multiplicative random errors. As indicated in Tables 9 and 10, the $\hat{\sigma}_0$ obtained by LS and bcWLS deviates from the true value, but RWLS can obtain a relatively reasonable result. The results show that the RWLS method is applicable to solve the ill-posed state of DTM in practical applications.

The ill-posed problem of the coefficient matrix has been ignored in previous studies, which results in an unstable or non-convergent solution [62]. We used the Tikhonov regularization method to derive the RWLS solution for an ill-posed multiplicative error model. The results of simulation I and simulation II suggest that RWLS's solution has a better performance than other methods, such as LS [47] and bcWLS [48]. In the test on two actual landslide data sets, the LS and bcWLS methods dealt poorly with DTM construction [29,30,54], because the DTM has a huge deviation due to the random errors. Our method takes ill-condition into account. Hence, the results of actual experiment I and actual experiment II are consistent with the results of the simulation data. Thus, the RWLS method provides a new solution for the ill-posed multiplicative error model.

5. Conclusions

In this paper, TLS technology was used to extract the deformation of a landslide. We discussed the major factors affecting the landslide deformation, and attempted to reveal the relevant deformation mechanism. A new measurement and data processing strategy is proposed in this paper, aiming at extracting the deformation of a landslide. Finally, the landslide deformation was extracted by using two datasets. The first dataset is the point cloud data of the Lashagou NO.3 landslide collected on 26 February 2021 and 3 May 2021. The second dataset is the point cloud data of the Lihua landslide collected on 20 April 2021 and 1 May 2021. The main conclusions drawn from this study are as follows.

In this study, we designed a new triangular pyramid PCR marker, and a PCR experiment for different period TLS datasets based on the new marker was carried out. Compared with the commonly used spherical target, the edge drift of the sphere is overcome by the new marker-based PCR proposed in this paper. The registration accuracy based on the permanent triangular pyramid is 0.003 m. If it is not convenient to make a fixed target, we also propose a new PCR method based on total station orientation. The registration accuracy based on the unified theory of backward orientation using the total station method is 0.005 m. The results show that the new method precisely aligns the point cloud system with the engineering independent coordinate system.

The weighted least square regularization iterative method can effectively solve the ill-posed multiplicative error problem. In the tests of two simulation data set, the accuracy and reliability of the RWLS algorithm outperformed previous methods. Then, two actual landslide experiment were conducted. The results show that the RWLS solution can effectively reduce the ill-posed state of the model. The deformation of the Lashagou NO.3 landslide was small, with a maximum value of 0.031 m. The maximum deformation of the Lihua landslide was 0.011 m.

In general, the monitoring results of the DTM subtraction based on TLS data technology show that the Lashagou NO.3 landslide and Lihua landslide will continue to maintain a stable state without special factors, such as earthquakes, heavy rainfall, or artificial excavations. In cases where the point cloud system and engineering independent coordinate system are different and the DTM is disturbed by the multiplicative random error, our method is a more practical choice with stabler precision compared with previous methods.

Author Contributions: Methodology, L.Z., X.M., Z.X., S.Z., C.H. and G.C.; software, L.Z., Z.X. and G.C.; validation, Y.Z.; writing—original draft preparation, L.Z.; writing—review and editing, C.H.; visualization, C.H.; funding acquisition, S.Z. All authors have read and agreed to the published version of the manuscript.

Funding: This work was supported in part by the National Natural Science Foundation of China under grant no. 42074041 and no. 41904171.

Data Availability Statement: Not applicable.

Conflicts of Interest: The authors declare no conflict of interest.

References

1. Yao, L.; Sun, H.; Zhu, L.; Zhou, Y. Development and application of deformation monitoring system for lanslide at Funchunjiang Dam. *Surv. Rev.* **2014**, *46*, 444–452. [CrossRef]
2. Gikas, V. 3D Terrestrial laser scanning for geometry documentation and construction management of highway tunnels during excavation. *Sensors* **2012**, *12*, 11249–11270. [CrossRef]
3. Vezocnik, R.; Ambrozic, T.; Sterle, O.; Bilban, G.; Pfeifer, N.; Stopar, B. Use of terrestrial laser scanning technology for long term high precision deformation monitoring. *Sensors* **2009**, *9*, 9873–9895. [CrossRef] [PubMed]
4. He, M.; Zhu, Q.; Du, Z.; Hu, H.; Ding, Y.; Chen, M. A 3D shape descriptor based on contour clusters for damaged roof detection using airborne LiDAR point clouds. *Remote Sens.* **2016**, *8*, 189. [CrossRef]
5. Kasperski, J.; Delacourt, C.; Allemand, P.; Potherat, P.; Jaud, M.; Varrel, E. Application of a terrestrial laser scanner (TLS) to the study of the Séchilienne Landslide (Isère, France). *Remote Sens.* **2010**, *2*, 2785–2802. [CrossRef]
6. Crepaldi, S.; Zhao, Y.; Lavy, M.; Amanzio, G.; Suozzi, E.; De Maio, M. Landslide analysis by multi-temporal terrestrial laser scanning (TLS) data: The Mont de la Saxe landslide. *Rend. Online Della Soc. Geol. Ital.* **2015**, *35*, 92–95. [CrossRef]
7. Wang, D.; Hollaus, M.; Schmaltz, E.; Wieser, M.; Reifeltshammer, D.; Pfeifer, N. Tree stem shapes derived from TLS data as an indicator for shallow landslides. *Procedia Earth Planet. Sci.* **2016**, *16*, 185–194. [CrossRef]
8. Wang, G.; Philips, D.; Joyce, J.; Rivera, F. The integration of TLS and continuous GPS to study landslide deformation: A case study in Puerto Rico. *J. Geod. Sci.* **2011**, *1*, 25–34. [CrossRef]
9. Cina, A.; Piras, M. Performance of low-cost GNSS receiver for landslides monitoring: Test and results. *Geomat. Nat. Hazards Risk* **2015**, *6*, 497–514. [CrossRef]
10. Senkaya, M.; Babacan, A.E.; Karslı, H.; San, B.T. Origins of diverse present displacements in a paleo-landslide area (Isiklar, Trabzon, northeast Turkey). *Environ. Earth Sci.* **2022**, *81*, 1–24. [CrossRef]
11. Stiros, S.C.; Vichas, C.; Skourtis, C. Landslide monitoring based on geodetically derived distance changes. *J. Surv. Eng.* **2004**, *130*, 156–162. [CrossRef]
12. Tzenkov, T.; Gospodinov, S. Geometric analysis of geodetic data for investigation of 3D landslide deformations. *Nat. Hazards Rev.* **2003**, *4*, 78–81. [CrossRef]
13. Klimeš, J.; Rowberry, M.D.; Blahůt, J.; Briestenský, M.; Hartvich, F.; Košťák, B.; Rybář, J.; Stemberk, J.; Štěpančíkováet, P. The monitoring of slow-moving landslides and assessment of stabilisation measures using an optical–mechanical crack gauge. *Landslides* **2012**, *9*, 407–415. [CrossRef]
14. Baroň, I.; Supper, R. Application and reliability of techniques for landslide site investigation, monitoring and early warning–outcomes from a questionnaire study. *Nat. Hazards Earth Syst. Sci.* **2013**, *13*, 3157–3168. [CrossRef]
15. Shi, X.; Hu, X.; Sitar, N.; Kayen, R.; Qi, S.; Jiang, H.; Wang, X.; Zhang, L. Hydrological control shift from river level to rainfall in the reactivated Guobu slope besides the Laxiwa hydropower station in China. *Remote Sens. Environ.* **2021**, *265*, 112664. [CrossRef]
16. Guo, F.; Meng, X.; Qi, T.; Dijkstra, T.; Thorkildsen, J.K.; Yue, D.; Chen, G.; Zhang, Y.; Dou, X.; Shi, P. Rapid onset hazards, fault-controlled landslides and multi-method emergency decision-making. *J. Mt. Sci.* **2022**, *19*, 1357–1369. [CrossRef]
17. Guo, C.; Xu, Q.; Dong, X.; Liu, X.; Yu, J. Geohazard Recognition by Airborne LiDAR Technology in Complex Mountain Areas. *Geomat. Inf. Sci. Wuhan Univ.* **2021**, *46*, 1538–1547.
18. Abellán, A.; Vilaplana, J.; Calvet, J.; García-Sellés, D.; Asensio, E. Rockfall monitoring by terrestrial laser scanning-case study of the basaltic rock face at Castellfollit de la Roca (Catalonia, Spain). *Nat. Hazards Earth Syst. Sci.* **2011**, *11*, 829–841. [CrossRef]
19. Kayen, R.; Pack, R.; Bay, J.; Collins, B. Ground-Lidar visualization of surface and structural deformatios of the Niigata Ken Chuetsu. *Earthq. Spectra* **2006**, *S1*, 147–162. [CrossRef]
20. Liu, W.; Xie, M. Landslide monitoring based on point cloud density characteristics. *Rock Soil Mech.* **2020**, *41*, 3748–3756.
21. Zhao, J.; Du, S.; Liu, Y.; Saif, B.S.; Hou, Y.; Guo, Y.C. Evaluation of the stability of the palatal rugae using the three-dimensional superimposition technique following orthodontic treatment. *J. Dent.* **2022**, *119*, 104055. [CrossRef] [PubMed]
22. Yang, M.; Gan, S.; Yuan, X.; Gao, S.; Zhu, Z.; Yu, H. Study on data acquisition and registration experiment of terretrial laser scanning point clouds under complicated banded terrain condition. *Bull. Surv. Mapp.* **2018**, *5*, 35–40.
23. Zeybek, M.; Şanlıoğlu, İ. Accurate determination of the Taşkent (Konya, Turkey) landslide using a long-range terrestrial laser scanner. *Bull. Eng. Geol. Environ.* **2015**, *74*, 61–76. [CrossRef]
24. Hsieh, Y.C.; Chan, Y.C.; Hu, J.C.; Chen, Y.Z.; Chen, R.F.; Chen, M.M. Direct measurements of bedrock incision rates on the surface of a large dip-slope landslide by multi-period airborne laser scanning DEMs. *Remote Sens.* **2016**, *8*, 900. [CrossRef]
25. Xian, Y.; Xiao, J.; Wang, Y. A fast registration algorithm of rock point cloud based on spherical projection and feature extraction. *Front. Comput. Sci.* **2019**, *13*, 170–182. [CrossRef]
26. Kümmerle, J.; Kühner, T.; Lauer, M. Automatic calibration of multiple cameras and depth sensors with a spherical target. In Proceedings of the 2018 IEEE/RSJ International Conference on Intelligent Robots and Systems (IROS), Madrid, Spain, 1–5 October 2018; pp. 1–8.
27. Zhou, Y.; Han, D.; Hu, K.; Qin, G.; Xiang, Z.; Ying, C.; Zhao, L.; Hu, X. Accurate virtual trial assembly method of prefabricated steel components using terrestrial laser scanning. *Adv. Civ. Eng.* **2021**, *2021*, 9916859. [CrossRef]

28. Li, J.; Hu, Q.; Ai, M. Point cloud registration based on one-point ransac and scale-annealing biweight estimation. *IEEE Trans. Geosci. Remote Sens.* **2021**, *59*, 9716–9729. [CrossRef]
29. Chen, Z.; Zhang, B.; Han, Y.; Zuo, Z.; Zhang, X. Modeling accumulated volume of landslides using remote sensing and DTM data. *Remote Sens.* **2014**, *6*, 1514–1537. [CrossRef]
30. Artese, S.; Perrelli, M. Monitoring a landslide with high accuracy by total station: A DTM-based model to correct for the atmospheric effects. *Geosciences* **2018**, *8*, 46. [CrossRef]
31. Pawluszek, K.; Borkowski, A.; Tarolli, P. Sensitivity analysis of automatic landslide mapping: Numerical experiments towards the best solution. *Landslides* **2018**, *15*, 1851–1865. [CrossRef]
32. Xu, P.; Shimada, S. Least squares parameter estimation in multiplicative noise models. *Commun. Stat. Simul. Comput.* **2000**, *29*, 83–96. [CrossRef]
33. Shi, Y.; Xu, P.; Peng, J.; Shi, C.; Liu, J. Adjustment of measurements with multiplicative errors: Error analysis, estimates of the variance of unit weight, and effect on volume estimation from LiDAR-type digital elevation models. *Sensors* **2014**, *14*, 1249–1266. [CrossRef] [PubMed]
34. Wang, L.; Yu, D. Virtual observation method to ill-posed total least squares problem. *Acta Geod. Cartogr. Sin.* **2014**, *43*, 575–581.
35. Xu, P. Truncated SVD methods for discrete linear ill-posed problems. *Geophys. J. Int.* **1998**, *135*, 505–514. [CrossRef]
36. Koch, K.R.; Kusche, J. Regularization of geopotential determination from satellite data by variance components. *J. Geod.* **2002**, *76*, 259–268. [CrossRef]
37. Hoerl, A.E.; Kennard, R.W. Ridge regression: Biased estimation for nonorthogonal problems. *Technometrics* **1970**, *12*, 55–67. [CrossRef]
38. Wang, L.; Chen, T. Virtual Observation Iteration Solution and A-Optimal Design Method for Ill-Posed Mixed Additive and Multiplicative Random Error Model in Geodetic Measurement. *J. Surv. Eng.* **2021**, *147*, 04021016. [CrossRef]
39. Du, S.; Zheng, N.; Ying, S.; Liu, J. Affine iterative closest point algorithm for point set registration. *Pattern Recognit. Lett.* **2010**, *31*, 791–799. [CrossRef]
40. Li, P.; Wang, R.; Wang, Y.; Tao, W. Evaluation of the ICP algorithm in 3D point cloud registration. *IEEE Access* **2020**, *8*, 68030–68048. [CrossRef]
41. Pomerleau, F.; Colas, F.; Siegwart, R.; Magnenat, S. Comparing ICP variants on real-world data sets. *Auton. Robot.* **2013**, *34*, 133–148. [CrossRef]
42. Deakin, R.E. *A note on the Bursa-Wolf and Molodensky-Badekas Transformations*; School of Mathematical and Geospatial Sciences, RMIT University: Melbourne, VIC, Australia, 2006; pp. 1–21.
43. Golub, G.H.; Van Loan, C.F. An analysis of the total least squares problem. *SIAM J. Numer. Anal.* **1980**, *17*, 883–893. [CrossRef]
44. Oktaba, W. Tests of Hypotheses for the General Gauss-Markov Model. *Biom. J.* **1984**, *26*, 415–424. [CrossRef]
45. Jeng, F.C.; Woods, J.W. Compound Gauss-Markov random fields for image estimation. *IEEE Trans. Signal Processing* **1991**, *39*, 683–697. [CrossRef]
46. Shi, Y.; Xu, P. Adjustment of measurements with multiplicative random errors and trends. *IEEE Geosci. Remote Sens. Lett.* **2020**, *18*, 1916–1920. [CrossRef]
47. Davidon, W.C. New least-square algorithms. *J. Optim. Theory Appl.* **1976**, *18*, 187–197. [CrossRef]
48. Heyde, C.C. *Quasi-Likelihood and Its Application: A General Approach to Optimal Parameter Estimation*; Springer: New York, NY, USA, 1997; pp. 32–69.
49. Gregor, J.; Fessler, J.A. Comparison of SIRT and SQS for regularized weighted least squares image reconstruction. *IEEE Trans. Comput. Imaging* **2015**, *1*, 44–55. [CrossRef]
50. Hansen, P.C. Analysis of discrete ill-posed problems by means of the L-curve. *SIAM Rev.* **1992**, *34*, 561–580. [CrossRef]
51. Vogel, C.R. Non-convergence of the L-curve regularization parameter selection method. *Inverse Probl.* **1996**, *12*, 535. [CrossRef]
52. Wang, L.; Chen, T.; Zou, C. Weighted least squares regularization iteration solution and precision estimation for ill-posed multiplicative error mode. *Acta Geod. Cartogr. Sin.* **2021**, *50*, 589–599.
53. Xu, P.; Shi, Y.; Peng, J.; Liu, J.; Shi, C. Adjustment of geodetic measurements with mixed multiplicative and additive random errors. *J. Geod.* **2013**, *87*, 629–643. [CrossRef]
54. Shi, Y.; Xu, P. Comparing the estimates of the variance of unit weight in multiplicative error models. *Acta Geod. Geophys.* **2015**, *50*, 353–363. [CrossRef]
55. Hill, C.A.; Harris, M.; Ridley, K.D.; Jakeman, E.; Lutzmann, P. Lidar frequency modulation vibrometry in the presence of speckle. *Appl. Opt.* **2003**, *42*, 1091–1100. [CrossRef] [PubMed]
56. Leigh, C.L.; Kidner, D.B.; Thomas, M.C. The use of LiDAR in digital surface modelling: Issues and errors. *Trans. GIS.* **2009**, *13*, 345–361. [CrossRef]
57. Hladik, C.; Alber, M. Accuracy assessment and correction of a LIDAR-derived salt marsh digital elevation model. *Remote Sens. Env.* **2012**, *121*, 224–235. [CrossRef]
58. Jia, C.; Jin, Z.; Yang, P.; Tang, Z. Stability analysis on landslide in section K181 + 840 ~ K182 + 040 of Lin − Da Highway. *J. Lanzhou Petrochem. Polytech.* **2018**, *18*, 26–28.
59. Jia, X.; Yin, X.; Ren, Y.; Fu, Z. Climate change of Linxia of Gansu Province in recent 43 years. *J. Arid Meteorol.* **2012**, *30*, 249–254.

60. Leica ScanStation P50—Long Range 3D Terrestrial Laser Scanner. Available online: https://leica-geosystems.com/products/laser-scanners/scanners/leica-scanstation-p50 (accessed on 3 June 2022).
61. Leica TS30 Champion's League. Available online: https://www.bandwork.my/product/pdf/731201461738PMTS30_Brochure_en.pdf (accessed on 3 June 2022).
62. Kobler, A.; Pfeifer, N.; Ogrinc, P.; Todorovski, L.; Oštir, K.; Džeroski, S. Repetitive interpolation: A robust algorithm for DTM generation from Aerial Laser Scanner Data in forested terrain. *Remote Sens. Environ.* **2007**, *108*, 9–23. [CrossRef]

sustainability

MDPI

Article

Combined ERT and GPR Data for Subsurface Characterization of Weathered Hilly Slope: A Case Study in Zhejiang Province, Southeast China

Yajing Yan [1], Yongshuai Yan [2], Guizhang Zhao [3], Yanfang Zhou [4] and Zhoufeng Wang [5,*]

1 Collaborative Innovation Center for Efficient Utilization of Water Resources, North China University of Water Resources and Electric Power, Zhengzhou 450046, China; yajinghappy123@163.com
2 School of Resources and Environmental Engineering, Hefei University of Technology, Hefei 230002, China; 2020010056@mail.hfut.edu.cn
3 School of Geosciences and Engineering, North China University of Water Resources and Electric Power, Zhengzhou 450046, China; zhaoguizhang@ncwu.edu.cn
4 School of Foreigh Studies, North China University of Water Resources and Electric Power, Zhengzhou 450046, China; zhouyanfang@ncwu.edu.cn
5 Key Laboratory of Subsurface Hydrology and Ecological Effect in Arid Region, Chang'an University, Xi'an 710054, China
* Correspondence: wangzf@chd.edu.cn

Abstract: Rain-triggered landslides frequently threaten public safety, infrastructure, and the economy during typhoon seasons in Zhejiang Province. Landslides are complex structural systems, and the subsurface features play a significant role in their stability. Their early identification and the evaluation of potential danger in terms of the rupture surface and unstable body are essential for geohazard prevention and protection. However, the information about the subsurface acquired by conventional exploration approaches is generally limited to sparse data. This paper describes a joint application of ground-penetrating radar (GPR) with a 100 MHz antenna and the electrical resistivity tomography (ERT) method with the Wenner configuration to identify the stratum structure and delineate the potentially unstable body of a clay-rich slope, the results of which were further verified using borehole data and field observation. The acquired results from the GPR and ERT surveys, consistent with each other, indicate two stratigraphic layers comprising silty clay and silty mudstone. Moreover, the potential rupture zone very likely exists in the highly weathered mudstone in the depth range of 3–7 m, and the average depth is 5 m. In addition, the thickness of the unstable mass is greater on the east and crest parts of the slope. Conclusively, the optimum combination of ERT and GPR is reliable for conducting rapid and effective delineation of subsurface characteristics of clayey slopes for risk assessment and mitigation during the typhoon season.

Keywords: hilly slope; electrical resistivity tomography (ERT); ground-penetrating radar (GPR); subsurface structure; potential sliding surface; Zhejiang; typhoon

Citation: Yan, Y.; Yan, Y.; Zhao, G.; Zhou, Y.; Wang, Z. Combined ERT and GPR Data for Subsurface Characterization of Weathered Hilly Slope: A Case Study in Zhejiang Province, Southeast China. *Sustainability* **2022**, *14*, 7616. https://doi.org/10.3390/su14137616

Academic Editors: Stefano Morelli, Veronica Pazzi and Mirko Francioni

Received: 7 May 2022
Accepted: 21 June 2022
Published: 22 June 2022

1. Introduction

Zhejiang Province, an economically developed and densely populated region in the subtropical zone of China, is exposed to a high risk of rainfall-triggered landslides caused by an incremental occurrence of extreme weather events [1–5]. Moreover, the province's landscape is dominated by mountains and hills, accounting for about 75% of its total area, which can easily lead to landslides. Additionally, increasing demand for modern infrastructure has caused more engineering disturbance, thus multiplying human risks. At present, the occurrence of landslides is still one of the greatest threats to local inhabitants and infrastructure, as exemplified by the Xiashan village landslide in 2001 [4], the Lidong village rockslide in 2015 [6], the Sucun village rockslide in 2016 [7–9], and the Shanzao landslide in 2019 [10]. Currently, many slopes are still slide-prone, the majority of which

are typically small in volume. It is a time- and resource-consuming task to thoroughly investigate them. According to Mccann and Foster [11], estimation of landslide stability has to consider the definition of the 3D shape of the unstable body with particular reference to the failure surface. Hence, there is a pressing need for developing and implementing actions for the accurate and rapid identification of subsurface features of natural slopes in Zhejiang.

As regards the practical techniques of identifying subsurface objects, conventional geotechnical (e.g., drilling, tunneling, and trenching) and geophysical approaches (e.g., electrical, electromagnetic, and seismic methods) are the most known ones, which have been broadly applied around the world. The former geotechnical approaches allow a detailed subsurface description at sparse locations, but they fail to delineate continuous spatial information. Moreover, they are very costly and relatively time-consuming. Indeed, underground materials often show high lithological and tectonic variability within short distances. However, the geophysical techniques, which are flexible, relatively quick, and deployable on slopes, can provide bulk spatial data directly or indirectly linked with the lithological, hydrological, and geotechnical characteristics of unstable slopes [11,12], therefore providing continuous geophysical mapping of subsurface features, and overcoming the drawbacks of geotechnical measurements.

Among all geophysical methods, the electrical resistivity tomography (ERT) and ground-penetrating radar (GPR) methods have proven to be highly efficient approaches in landslide research [13]. By analyzing the reflected signal of transmitted waves from the interface where there is a difference in materials, the GPR technique can image shallow subsurface structures (even small cavities) and determine the distance at which they are located. Since the 1980s, GPR has been increasingly accepted for the localization of fractures or cracks [14–18], the identification of stratigraphy or shear deformation [19–23], and the characterization of soil water variations [24–27] in the geological, environmental, and engineering areas. However, the transmitted waves of GPR are strongly attenuated in conductive zones (e.g., water-rich, clay-rich) and cannot penetrate at greater depths to identify unknown objects of interest. For a slope with high vegetation coverage, this phenomenon might be further exacerbated. With a lower resolution and greater penetration depths than GPR in conductive environments, the ERT technique has been used widely for various landslides, from rockslides to debris slides, in different geological environments from rock to soil materials, to identify the slip surface and hydrological conditions, depict the internal structures, monitor the movement, and disclose the underground faults and cracks [28–34]. Falae et al. [31] discussed the recent trend in applying ERT in landslide studies. This method relies on measuring the electrical properties between two electrodes when transmitting a pulsed current between two other electrodes, which allows for characterizing the unsteady body compared with the material having different electrical potentials.

Given the non-uniqueness of dataset interpretation, and the drawbacks of individual techniques in resolution and penetration depth, GPR and ERT have been jointly used for the investigation of subsurface features thanks to their complementarity [35–43]. Jongmans and Garambois [28] concluded that almost all the advantages of the geophysical method corresponded well to the disadvantages of the conventional geotechnical techniques. Perrone et al. [13] stated that the joint application of GPR and ERT could solve and overcome the resolution problems of every single method. Specifically speaking, GPR provides more helpful information on the shallow layers, while ERT is preferable for the intermediate–thick layers. The combination of the above-mentioned methods is therefore believed to have the potential to become a valuable tool for the pre-evaluation of high-risk sliding areas. However, more attempts seem to be necessary regarding its accuracy and applicability when probing clayey slopes.

For these reasons, this work aimed to test the ability of the joint use of ERT and GPR to distinguish the subsurface characteristics of a clayey slope, and to discuss the optimum combination. Two geophysical measurements were performed along with three profiles, at three sites where three boreholes are also available. Validated and calibrated with borehole data and field observation, the unstable body and potential slip surface could be sufficiently inferred. The effectiveness and limitations of ERT–GPR surveys for fast characterization of the subsurface are also highlighted. The novel aspects of this study are as follows: (1) it was conducted on a clay-rich slope which is usually not friendly for GPR surveys to distinguish different stratum layers (clay and mudstone); (2) variations in amplitude and energy with depth for three single-channel GPR waves are also analyzed, unlike in previous similar studies focusing on the GPR profile; (3) it optimizes the typical GPR profile superimposed with the elevation level; (4) a 3D model of the potentially unstable body is drawn for direct visualization. These findings provide a reliable alternative for a more comprehensive and faster investigation of active slopes in regions where typhoons are frequent and unstable terrain is abundant.

2. Materials and Methods

2.1. Site Description

The studied slope (27°34′59″ N, 119°54′10″ E) is located in Yuxi village in Taishun County, Wenzhou (Figure 1). It is about 300 km away from the capital city of Hangzhou, in the southeast of Zhejiang Province, which belongs to a subtropical marine monsoonal region with average annual precipitation of about 2000 mm. Moreover, the distribution of rainfall over a whole year is not uniform. About 71.2 percent of the rainfall events concentrate from May to September due to the influence of monsoons or typhoons, during which geological disasters are highly likely to occur. For example, the super typhoon Lekima in 2019 induced more than 400 landslides, debris flows, and numerous unstable points, including the famous Shanzao rockslide causing 32 casualties in Wenzhou city, according to the government report of Zhejiang Province [10]. In the future, climate change will continue to exacerbate the frequency and intensity of disasters in China [44] (p. 14).

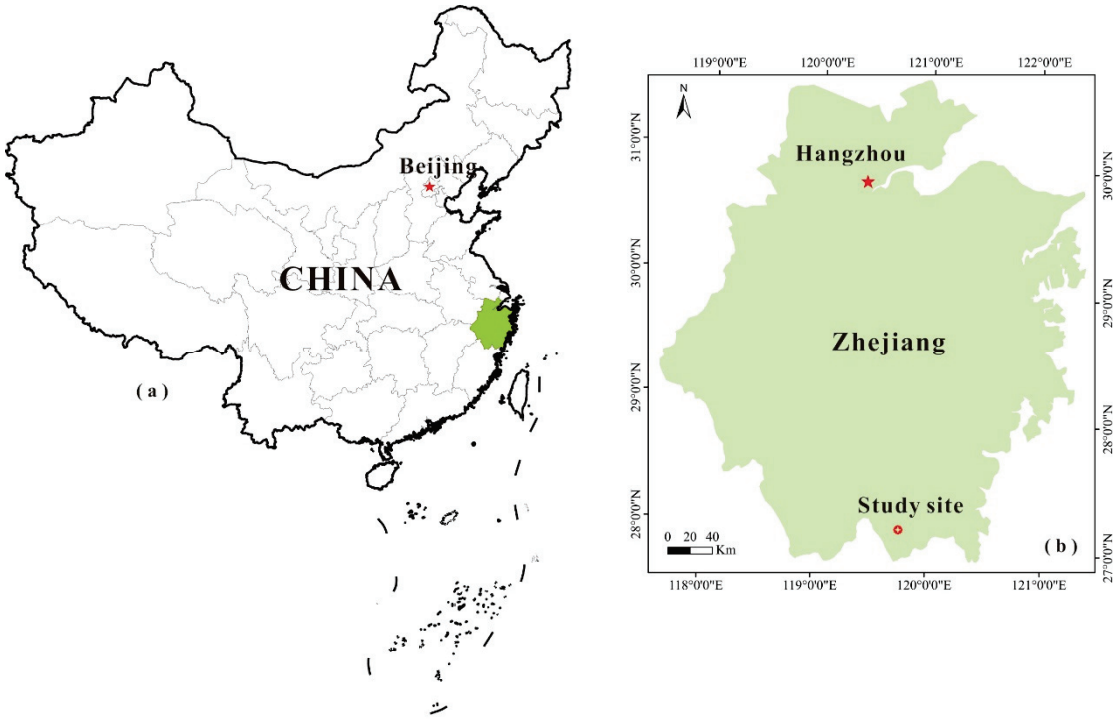

Figure 1. Location of the study site (red circle) in Zhejiang Province. (**a**) Map of China and its capital city Beijing, and of (**b**) Zhejiang Province and its capital city Hangzhou.

In Taishun County, more than 200 landslides have occurred since 2001 [45], in which small and shallow movements were common, putting a great strain on the county's people, resources, and environment. Although no fatal landslide disasters have been recorded, all villages in this county are still, to varying extents, facing negative impacts from geological disasters as a result of climate change, rapid economic growth, and urbanization.

Geomorphologically, the entire terrain of the slope is inclined from the south toward the north and drops in a step form due to artificial agricultural activities for the bayberry plant, having an average slope gradient of 30° and an original dip of 5° in the NE direction (Figure 2a). The area of the study site is a hilly terrain, the elevation of which varies between 370 and 402 m a.s.l. Geologically, its stratum units were precisely disclosed using rock and soil samples collected from boreholes, whose locations and details are shown in Figure 3, and further verified by stratum outcropping (Figure 2c). The lithological properties of different layers were disclosed by drilling core samples, as shown in Figure 4. There are two primary stratum layers in the sedimentary succession according to the borehole information. At the base of the stratigraphic column, silty mudstone of the lower Cretaceous Guantou Group (K_1g) is overlain by a 1–5 m-thin Quaternary (Q) soil, containing strongly weathered and fresh rock. More precisely, the near-surface layer is mainly composed of silty clay with granular gravels, the majority of which are loose colluvial sediments with large pores and high porosity. Over 80% of the landslides in Zhejiang Province occur along the colluvium–bedrock contact resulting from the varying soil moisture and pore water pressure of the colluvial deposits [46]. The upper grayish K_1g mudstone is strongly weathered and fractured, while the bottom is rarely weathered or fresh. The slope's potential failure will probably develop between these two stratum layers.

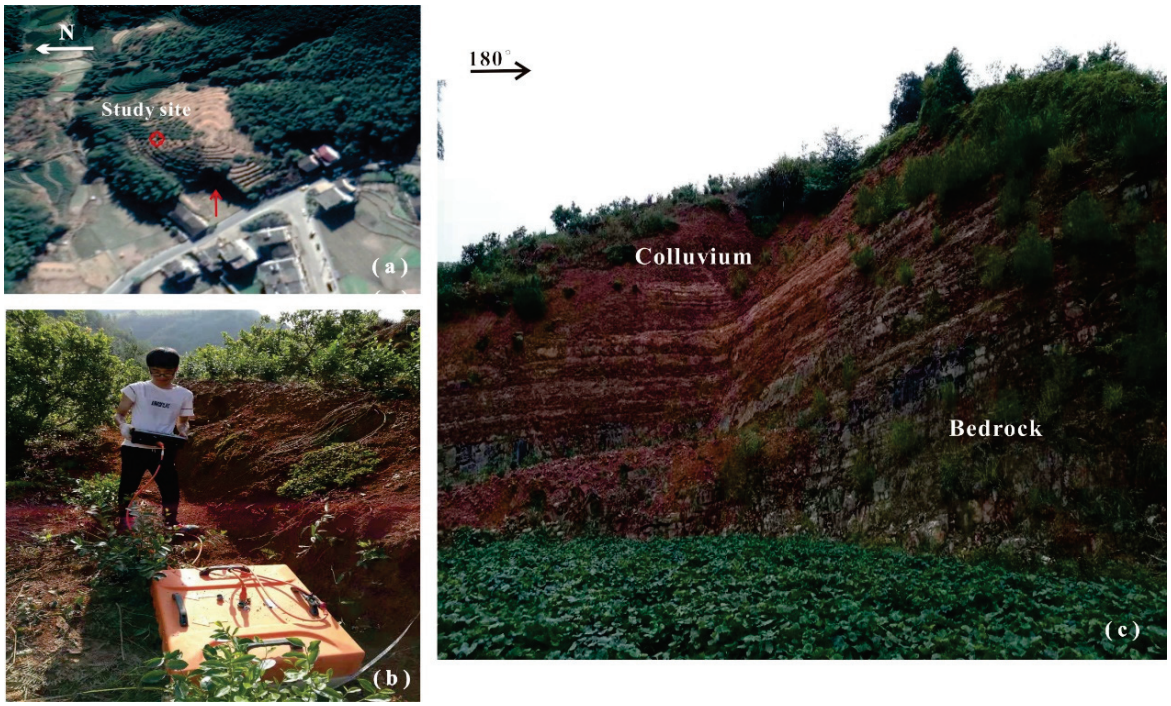

Figure 2. (**a**) Photo of the study site from the air. The red circle marks the study site, and the red arrow represents the direction of the camera that obtained the photo shown in (**c**). (**b**) Photo of the acquisition work showing the GPR system, step-shape landform, and vegetation coverage. (**c**) Field observation of the stratum.

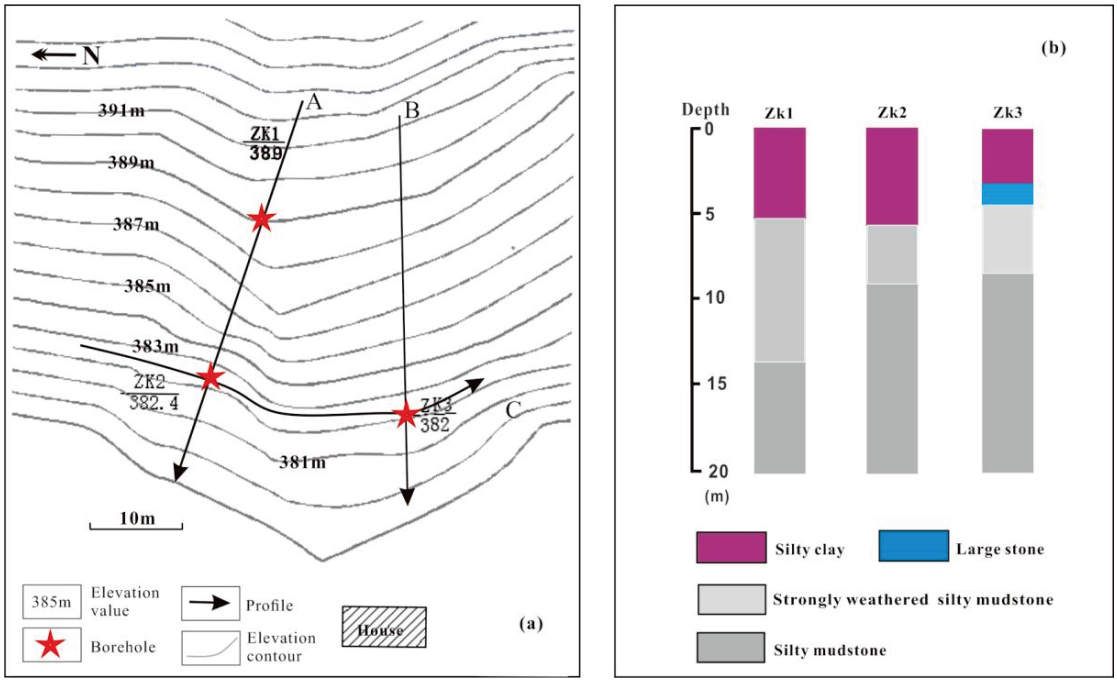

Figure 3. (**a**) Locations of geophysical survey lines (A, B, C) and boreholes (ZK1, ZK2, ZK3). (**b**) Drilling core logs of the three boreholes (ZK1, ZK2, ZK3).

Figure 4. *Cont.*

Figure 4. Drilling core samples from three boreholes (ZK1, ZK2, ZK3).

During drilling campaigns, soil and rock samples from three boreholes were carefully collected and transported to the laboratory for basic physical properties, mineralogical compositions, and direct resistivity measurements. The Atterberg limits and particle size distribution of the soil samples were determined following the Chinese National Standards (CNS) GB/T50123-2019 [47] (pp. 29–43). The bulk mineralogy and clay mineralogy of the rock samples were measured using an X-ray diffractometer following the methods described by Moore and Reynolds [48] (p. 378). More specifically, clays in the soil samples ranged from 41 to 47%, silts from 27 to 30%, sands from 20 to 25%, and gravels from 4 to 7%. Their liquid limits and plastic limits were in the range of 39.7 to 42.4 and 20.8 to 23.2, respectively (Table 1). The results of the semi-quantitative XRD analysis show that clay minerals (50–52%) and quartz (34–36%) were the primary minerals, followed by mica and feldspar, in all rock samples. In terms of the clay mineralogy, these samples were primarily

composed of illite, with some chlorite and kaolinite (Table 2). Apparently, the slope under probing is a clay-rich body.

Table 1. Basic physical properties of the soil samples.

Soil Sample	Atterberg Limits (%)		Particle Size Distribution (mm, %)			
	Liquid Limit (%)	Plastic Limit (%)	Clay (<0.005)	Silt (0.005–0.075)	Sand (0.075–2)	Gravel (>2)
ZK1	42.4	23.2	47	28	20	5
ZK2	39.7	20.8	41	30	22	7
ZK3	40.9	21.5	44	27	25	4

Table 2. Mineralogical compositions and resistivity of the rock samples.

Rock Sample	Whole Rock (%)				Clay (%)			Resistivity (Ωm)	
	Quartz	Feldspar	Mica	Clay	I	K	C	Weathered	Fresh
ZK1	34	8	6	52	56	23	21	785	1432
ZK2	36	8	5	51	55	26	19	801	1365
ZK3	34	7	9	50	53	22	25	812	1309

Note: I—illite; K—kaolinite; C—chlorite.

The studied slope threatens the safety of county road No. 601 and the safety of 15 residents in 5 households, with a potential economic loss exceeding CNY 1 million. Furthermore, it was chosen because of its clayey conditions and typical geological structure (two stratum layers: unconsolidated topsoil and bedrock), representing the most common type of landslide that has not received sufficient attention in Zhejiang Province. There are the upper loose topsoil layer allowing infiltration of rainwater, and the relatively dense bedrock layer serving as an aquiclude. Usually, the contact zone between these two layers has a high likelihood of developing into the rupture surface or area in intensive rainstorms.

2.2. Methodology

In collaboration with drilling core samples, we combined ERT and GPR to identify the subsurface features of the studied slope, in particular with delineation of the shape of the potential unstable body and potential slip surface, which were tentatively assumed to be fault and/or joint planes, and interfaces between topsoils and/or highly fractured rocks with intact bedrock [49]. All geophysical tests were conducted following the Standard of Ministry of Water Resources of the People's Republic of China: SL/T 291.1-2021 [50] (pp. 6–10, 15–56, 143). Information about ERT profiles A, B, and C is shown in Figure 2. In what follows, the details of the ERT and GPR measurements are described.

2.2.1. Data Acquisitions

Based on Ohm's law, ERT measurements are accomplished by measuring electrical potentials (ΔV) between an electrode pair while introducing a direct current (I) between another pair of electrodes [51] (p. 806). Then, the resistive properties of the underground medium can be acquired, commonly expressed in the form of apparent resistivity. In this study, acquisition was carried out using the DUK-2B high-density resistivity imaging system with 64 electrodes spaced by 1 m from Chongqing geological instruments. Two-dimensional (2D) resistivity profiles along three survey lines (labeled A, B, and C) were obtained using the Wenner configuration. The length of the survey lines varied from 51 m to 60 m, while the expected investigation depth was between 11 m and 20 m, correlating with the elevation and topography conditions of the studied slope. Profiles A and B (longitudinal profiles), striking SE and SW, were obtained down-slope, while profile C (cross-profile) was obtained perpendicular to the dip direction of the slope.

Three drill holes (ZK1, ZK2, and ZK3) were created using a mobile drilling rig installed on a truck for stratum identification, which could provide information about the lithology up to the depth of 25 m based on the extracted core samples. The exact locations of these boreholes are shown in Figure 3.

Founded on Maxwell's equations, GPR measurement can be conducted by transmitting pulses of high-frequency electromagnetic (EM) waves that travel through the subsurface, and receiving EM signals by receiver antennas. When EM energy emits into the ground, these EM waves can encounter different interfaces, resulting in part of the GPR signals being reflected to the receiver [52]. These interfaces commonly represent changes in the physical properties of the subsurface system that are expressed by contrasts in relative dielectric permittivity. Subsequently, waveform depth, time–frequency, and amplitude characteristics of the reflected signals generated at the interfaces are collected and then analyzed. In the pioneer studies (summarized in [28]), it was concluded that an antenna with a higher frequency corresponded to a higher resolution and smaller penetrating depth. A 100 MHz antenna commonly has a higher resolution to image small features up to the depth of 4–5 m and a lower resolution up to a depth of 20 m. In order to ensure a sufficient detecting depth and resolution at the same time, the ground-penetrating radar SIR-3000 from Geophysical Survey Systems, Inc. (GSSI) Co., Ltd. a was employed at three measured points close to the three boreholes, along with three profiles similar to the ERT lines, coupled to a 100 MHz antenna with an average penetrating depth of 15 m. Based on GPR datasets, the depth of unknown targets transformed from the travel time was calculated using a GPR wave velocity of 0.12 m/ns, estimated using the borehole data. The calculation process was demonstrated by [36]; no more details are presented herein.

2.2.2. Data Processing

The collected resistivity datasets along all profiles were inverted using the programming code and algorithms of the software RES2DINV, developed by [53]. The 2D resistivity images were obtained by performing elimination of bad data points, topographic correction, an RMS convergence restraint, least squares inversion, and a robust smoothness constraint [53]. All of the resistivity profiles were created after a maximum of 8 iterations, and the RMS error in percentage of the last iteration was controlled to lower than 3%, indicating the good and reliable results of the ERT surveys.

Radar data processing was accomplished using RADAN (version 6.0, Geophysical Survey Systems Inc., Nashua, NH, USA), including static corrections, background removal, distance norm, range gain, finite impulse response (FIR) filtering, deconvolution, and time–depth conversion.

3. Results and Discussion

In what follows, information about the subsurface in terms of the amplitude/energy of a single-channel radar wave, inverted resistivity section, and GPR reflection profile is presented in Figures 5–9 and further verified using borehole data and field observation.

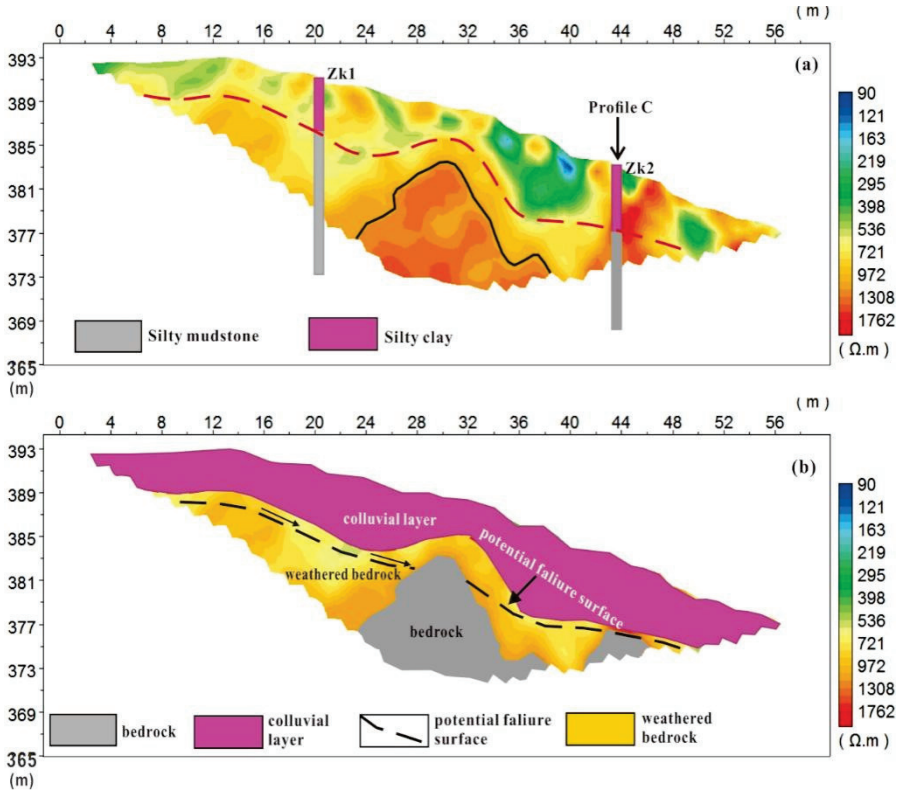

Figure 5. ERT profile A and its geological interpretations. (**a**) ERT image of profile A, (**b**) geological interpretations from ERT profile A.

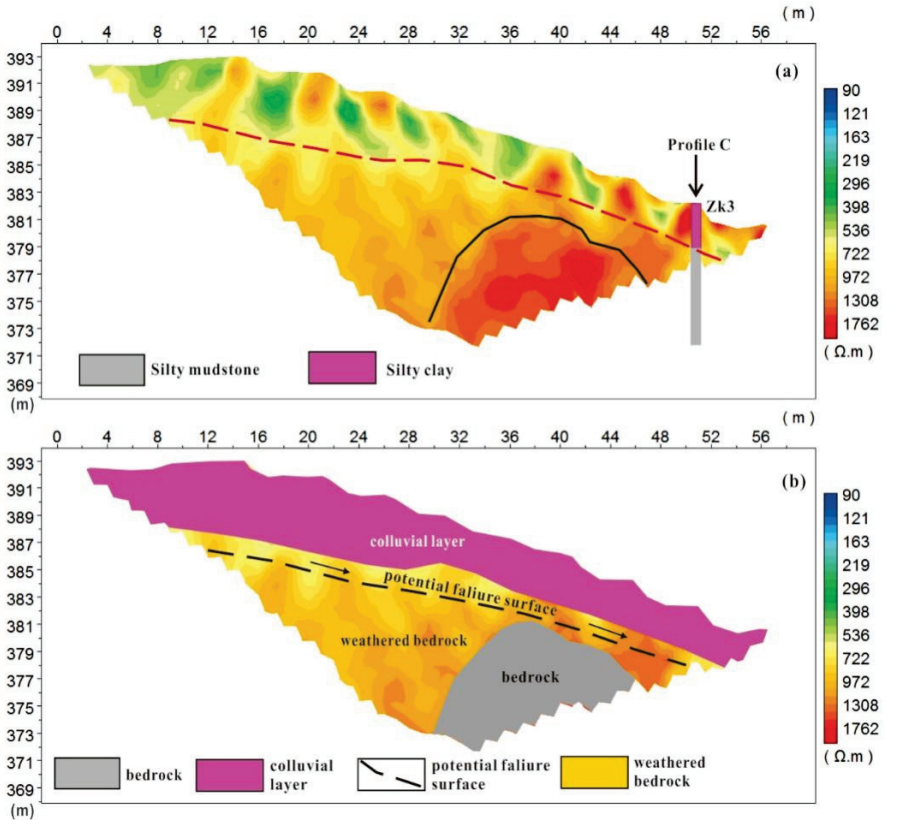

Figure 6. ERT profile B and its geological interpretations. (**a**) ERT image of profile B, (**b**) geological interpretations from ERT profile B.

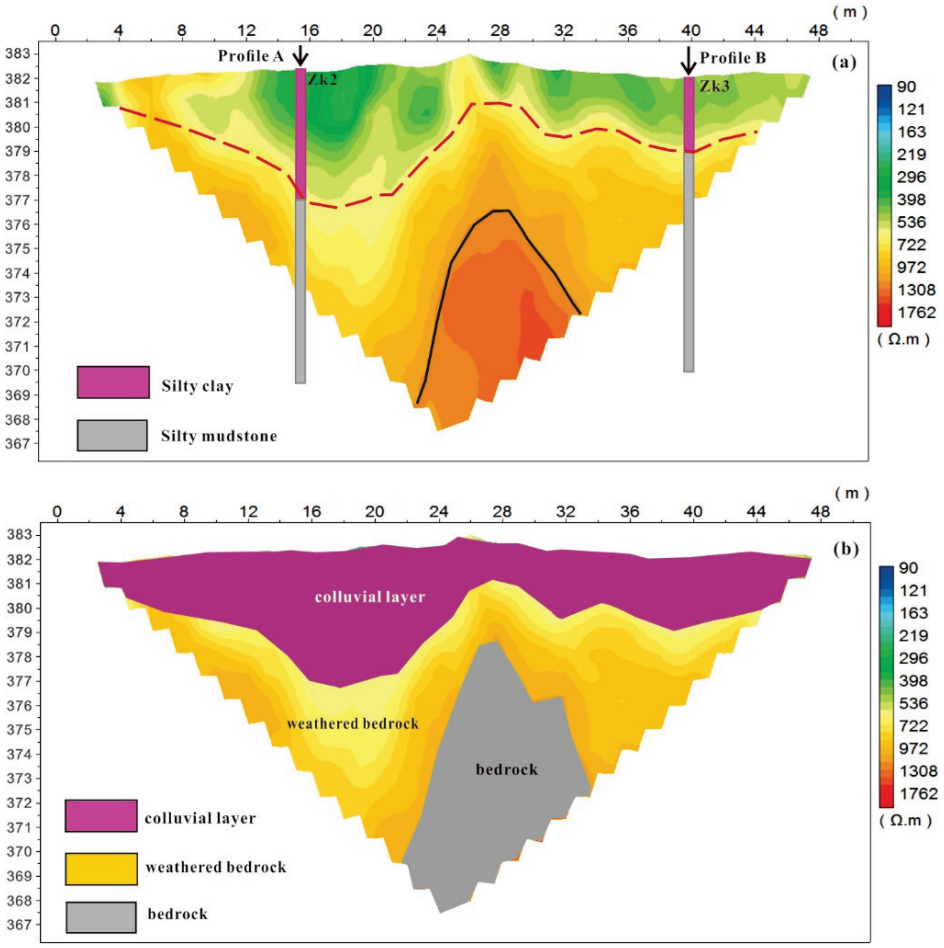

Figure 7. ERT profile C and its geological interpretations. (**a**) ERT image of profile C, (**b**) geological interpretations from ERT profile C.

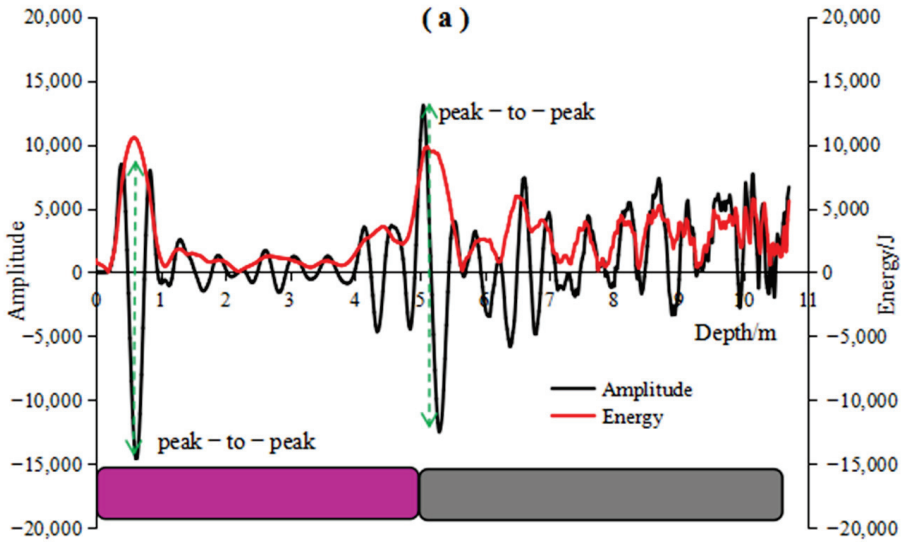

Figure 8. *Cont.*

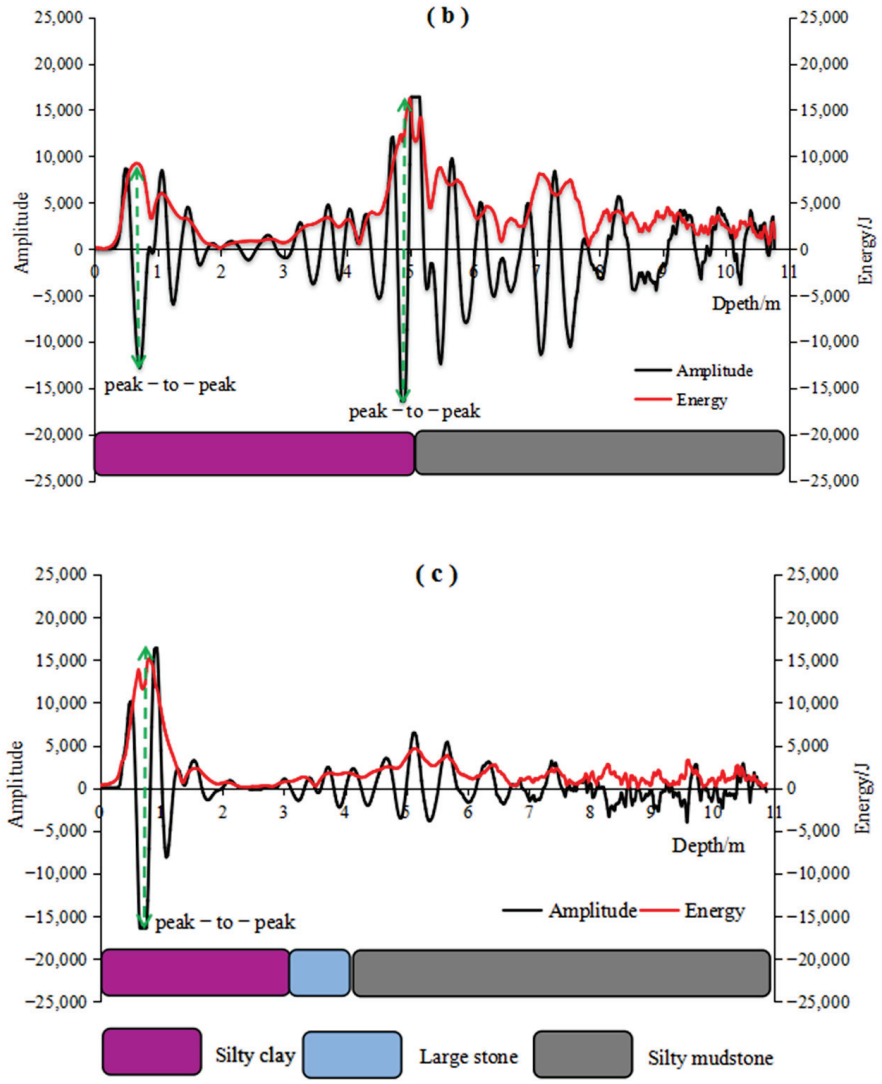

Figure 8. Waveforms of a single-channel GPR wave at three sites near the three boreholes, showing variations in amplitude and energy with depth. The black solid lines represent the amplitude, while the red solid lines denote the energy. The green dashed line with two arrows corresponds to the peak-to-peak phenomenon. (**a**) Waveform of ZK1, of (**b**) ZK2, and of (**c**) ZK3.

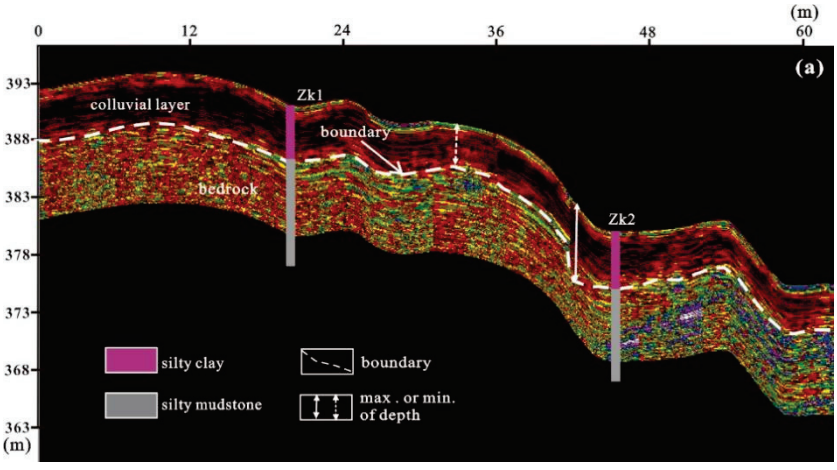

Figure 9. *Cont.*

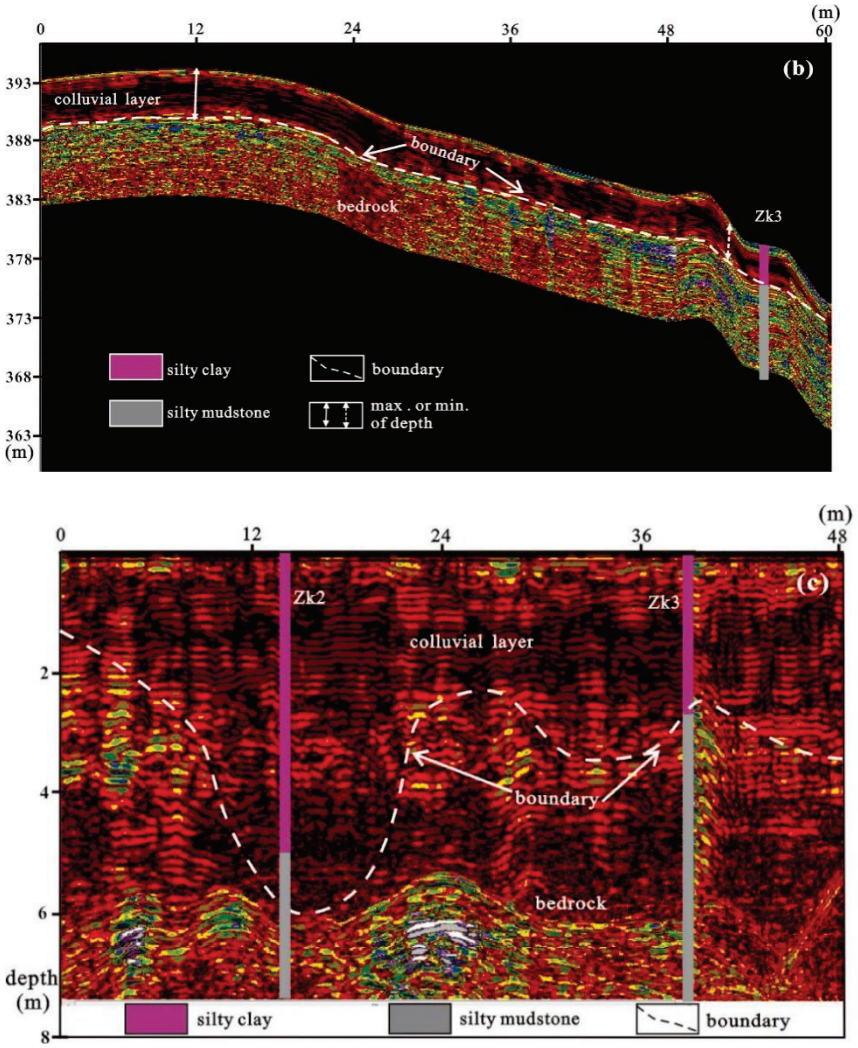

Figure 9. GPR image profiles. (**a**) Profile A superimposed elevation values (*Y* axis), (**b**) profile B superimposed elevation values (*Y* axis), and (**c**) profile C at the elevation of approximately 384 m. The white dashed line indicates the boundary between different geological layers, while the white solid and dashed line with two-way arrows in (**a**,**b**) represents the maximum and minimum thicknesses of the overlying layer.

3.1. ERT Profiles and Interpretations

To obtain electrical properties of the subsurface, ERT surveys along three profiles (A, B, and C) were carried out to image inverted resistivity variations with depth in autumn at the end of the wet season. The inverted resistivity sections and their corresponding geological interpretations are described in Figures 5–7, respectively. Of particular note is that profiles A and B superimpose the elevation values, while profile C is a raw image. Boreholes ZK2 and ZK3 were located at the bottom of the slope, while ZK1 was laid near its crest. The effective probing depth of ERT was in the range between 12 m and 20 m, which was greatly dependent upon the electrode spacing, resistivity contrast, broken properties of the medium, and landform of the slope [54]. Due to its step-shape landform, the variations in resistivity might also be impacted by the installed location of the electrodes, besides the mineral components, underground water, and its chemical composition and temperature.

The resistivity range measured in this study was between 90 and 1762 Ohm.m, and its distribution pattern can provide information about the stratigraphic distribution. The ERT images from Figures 5–7 with the constraints of geological field observations (Figure 2c) and drilling core samples (Figure 4) highlight two main resistive zones and their corresponding stratigraphic layers in all probing profiles. In profile A (Figure 5), the near-surface layer,

with a variable thickness between 1 and 7 m, has a relatively low resistivity distribution (<722 Ohm.m), which can be associated with the overlying colluvium composed of silty clay with granular gravels. The underlying layer at a depth ranging between 8 and 20 m is primarily characterized by relatively high resistivity values (>722 Ohm.m) and can be related to the bedrock consisting of silty mudstone. Meanwhile, the average thickness of the colluvial layer is about 4 m. The colluvium thickness approaches its maximum at the location of 38 m, but it goes down to its minimum on the middle and crest parts of the slope, indicating the fluctuation in the bedrock surface. Additionally, a higher-resistivity body (>1308 Ohm.m) exists in the range between 22 and 38 m at an elevation level of about 383 m, which most likely represents the rarely weathered bedrock by comparing with ZK3 that is the closest exposure site of the subsurface medium. Differently, the thickness of the colluvial layer in profile B decreases gradually from the crest to the toe of the slope, with an average value of 3 m, ranging from 2 m to 6 m. According to Figure 6, the depth to the bedrock is the smallest at the position between 48 and 58 m. Similarly, there is also a higher-resistivity zone delimited by the black thick line existing in the right part of profile B at an elevation below 382 m. These findings indicate that a rugged bedrock surface does not exist in profile B in the range of the horizontal distance.

Since profile C has approximately an EW routing direction at an average elevation level of about 384 m, it is roughly perpendicular to the slope's other two ERT profiles. Its inverted section evidences a fluctuating cover of colluvial materials, which further supports the interpretations of the other ERT profiles. It is clearly seen in Figure 7 that the colluvium thickness of profile C is about 5 m near the position 15.3 m, decreases to <1 m at the point of 28 m, and then increases to 2.5 m at its right edge, in good agreement with those variations in profiles A and B. Apparently, the colluvial material cover is non-uniform on this slope, implying the limitations of drilling or trench technology at several points.

In short, the bedrock surface is rugged with obvious undulation on the east part of the slope, while it follows the topography without any noticeable fluctuation on its west part. The transition zone or interface between the silty clay and weathered mudstone layer could be interpreted as the potential failure zone or surface. Similar interpretations were also made by many researchers based on ERT results [32,36,41]. In the literature, ERT has been used in geology, where [36] summarized the resistivity values of common materials, with the resistivity value being about 10–2000 Ohm.m for silts, 1–100 Ohm.m for clay, 100–1400 Ohm.m for gravel, and >1000 Ohm.m for rocks. Similar to the values reported by [54,55], herein, the resistivity of <722 Ohm.m for the overlying layer composed of gravelly silty clay acquired from ERT matches well with a mixture of silt, gravel, and clay materials. Consistent with the direct value from the laboratory tests (Table 2), the average resistivity of bedrock from ERT was about 1000–1100 Ohm.m, and it reduced to the range of 722–1000 Ohm.m in the upper weathered zone, probably due to the increased content of finer and clayey particles resulting from the weathering of the mudstone. The same variations in resistivity between weathered and fresh rocks are observable in previous studies [32,54].

To further validate the accuracy and effectiveness of the ERT results, GPR measurements involving three lines that are the same as the ERT arrangements and three other points near these three boreholes were carried out. Therefore, in what follows, the GPR results are systematically provided and discussed.

3.2. GPR Results and Interpretations

The GPR results of three surveying lines (A, B, and C) and three probing sites close to the boreholes as well as their main interpreted features are presented in Figures 8a–c and 9a–c, respectively.

3.2.1. Waveforms in Depth Domain and Interpretations

To directly depict the propagation process of EM waves, GPR signals containing amplitude and energy information are exhibited firstly in the depth domain based on an

estimated velocity of 0.12 m/ns, which was determined by measuring the travel time in a known borehole. In Figure 8, the variations in the amplitude and enemy of the EM waves with depth are revealed by analyzing three single-channel EM waves acquired from three probing sites close to Zk1, Zk2, and Zk3. It should be pointed out that errors in the depths obtained using GPR and boreholes are inevitable due to changes in the water content in subsurface materials.

In all profiles, the waveform in the depth domain highly assists in delineating the lithological boundaries up to a maximum depth of 12 m in Figure 8. When the peak amplitude of the radar wave represents an interface between layers or mediums with different dielectric properties during propagation [55], as can be seen in Figure 8a,b, the amplitude variations (black line) of the EM wave exhibit two significant peak-to-peak phenomena around the depths of 0.5 m and 5.1 m for ZK1, and 0.5 m and 4.9 m for ZK2. Let us compare the waveform with the geological stratigraphy (colorful legends). The first peak-to-peak amplitude is highly related to the air–ground interface at a depth of about 0.5 m, and the second peak-to-peak position can be interpreted to represent the topsoil–bedrock interface at a depth of 4.9 m for ZK1 and 5.05 m for ZK2. As the energy of the EM wave is proportional to the square of the amplitude, it exhibits consistent undulating trends similar to the amplitude with depth, having two principal peak values at similar positions (red line). It is thus believed that the amplitude and energy of radar waves could be in a relatively stable state when propagating in the same medium, whereas they fluctuate dramatically around these interfaces.

However, for the GPR signal of ZK3 in Figure 8c, the amplitude displays only one peak-to-peak phenomenon at a depth of about 0.5 m, and it thereafter shows a decreasing trend with slight fluctuation. Correspondingly, the energy reaches a peak value around the 0.5 m depth, and afterward, it shows little change with the increase in depth. For this surveying site, the interpretation of the amplitude and energy dataset does not coincide well with the borehole data. This contradiction may be mainly because of the fact that broken anomalous rock bodies exist in the depth range between 3 and 4 m. Generally, the fragments of rock existing in the underground medium are more likely to produce interference signals, during which the GPR signals are most attenuated. The observations made in drilling hole ZK3 delimited by the yellow dashed line in Figure 4 further confirm the presence of an altered rock (fractured) zone.

Apparently, the amplitude/energy–depth curves obtained from sites near ZK1 and ZK2 distinctly show two similar relatively stable stages separated by a transition zone, implying two layers with different dielectric constants of mediums at the probing points. However, the anomalous bodies (large stones or boulders) in geological units possibly contribute to the strong attenuation of electromagnetic waves [41], leading to the reduction in the energy and amplitude of the radar signals. This explains why the amplitude and energy of the point close to ZK3 gradually decreased with a slight change. In other words, the broken properties of the subsurface medium except for the dielectric capability also contribute to the stronger reflection, refraction, and diffraction behaviors of the radar waves. This indicates that the variation in the amplitude or energy of the radar waves with depth is also suitable for identifying the internal structure of slopes, whereas its applicability may be worse in more broken masses.

3.2.2. GPR Reflection Profiles and Interpretations

Generally, GPR signals of geological formations vary mainly depending on the nature of the components and their textures, and banded sediments often present superimposition of layered reflections [36,41]. Overall, the radargram in Figure 9 allows the characterization of heterogeneous deposits in the slope, and it contains abundant GPR signals marked with different colors representing various amplitude values. In this study, the richer the color, the richer the reflection, and vice versa. Accordingly, all GPR images indicate a similar reflected pattern over the topsoil versus the bedrock.

Figure 9a explores subsurface information up to 13 m depth, and two distinctive reflected zones are observed in profile A. The area along the upper part above the white dashed line showing darker and continuous to moderately continuous reflectivity corresponds to the colluvial layer composed of gravelly silty clay, as disclosed by ZK1 and ZK2. However, it is essential to note that the top area of the colluvium ranging from the surface to about 1 m depth presents brighter and discontinuous reflectors. The effect of the complex root systems of plants could explain this colorful phenomenon. Below this layer, the abundant (colorful) and discontinuous reflectors most likely illustrate the strongly reflective behaviors of the GPR waves, which are interpreted as highly fractured or strongly weathered silty mudstone bedrock. The maximum and minimum depth values to the bedrock surface occur at 33 m and 42 m, respectively, agreeing with the occurrences in ERT profile A (Figure 5a). Additionally, the lithological samples collected from the drilling holes provide further support for the interpretations of GPR profile A.

The GPR investigation of profile B (Figure 9b) reached a maximum depth of 11.5 m, presenting two primary radar reflected zones. The overlying area is expressed by moderately continuous darker reflectors with some occurrences of brighter discontinuous reflectors in the depth range of 0–1 m, having a thickness range between 1 and 5 m. This is highly likely related to the gravelly silty clay layer. A number of brighter discontinuous reflectors are detected within the underlying layer, which corresponds to the bedrock of the strongly weathered silty mudstone layer. Moreover, the contact boundary illustrated by the white dashed line between these two lithological units is delineated, being subparallel to the slope's surface without noticeable fluctuations.

As previously mentioned, GPR profile C ran from southeast to southwest along the stepwise flat arc trace and had an effective penetration depth of 7.5 m during the GPR surveys. Comparing the radar reflector signatures and their corresponding geological interpretations described in Figure 9a,b, we can see two central lithological units and a rugged bedrock structure in GPR profile C (Figure 9c). Similarly, the overlying material expressed by moderately continuous and darker reflectors relates to the colluvial layer composed of gravelly silty clay. In comparison, the underlying medium with brighter and discontinuous reflectors correlates with the bedrock of silty mudstone. From 0 m to 48 m in the horizontal distance, it seems that the boundary between the colluvium and bedrock fluctuates with notable troughs and crests, in agreement with the interpretation of ERT profile C (Figure 7a). The maximum and minimum depths to the bedrock occur at 16 m and 27 m, close to the 18 m and 28 m exhibited in ERT profile C in Figure 7a.

Conclusively, the GPR images better indicate the thickness of the topsoil and boundary from the underlying bedrock and show detailed information on the subsurface material, especially in the near-surface zone. However, they fail to detect the interfaces separating strongly weathered and rarely weathered rock, due to the strong attenuation of the radar waves penetrating fractured rocks.

3.3. Comparison between ERT and GPR Results

To further compare the ERT and GPR measurement results and hereby discuss the effectiveness and accuracy of these two combined geophysical methods in the delineation of subsurface characteristics, the inverted resistivity image and processed radargram of profile B were plotted and are shown in Figure 10. First, we have to point out that the errors in the topographical and lithological interpretations between the ERT and GPR images are unavoidable due to the differences in the manipulation and manifestation of databases using two geophysical technologies. The contrast both in the resistivity and the reflected pattern make it easier to see two stratigraphic layers with diverse features as described earlier in previous parts, showing an upper layer with a decreased trend in thickness from the crest to the toe of the slope, which is separated by a boundary being subparallel to the ground from the underlying bedrock. Obviously, in clay-rich conditions, GPR is able to distinguish the clay layer from mudstone layer by reflected profile when superimpos-

ing elevation values. This may be mainly because of the difference in internal structure (e.g., extent of consolidation) and compositions between clay and mudstone.

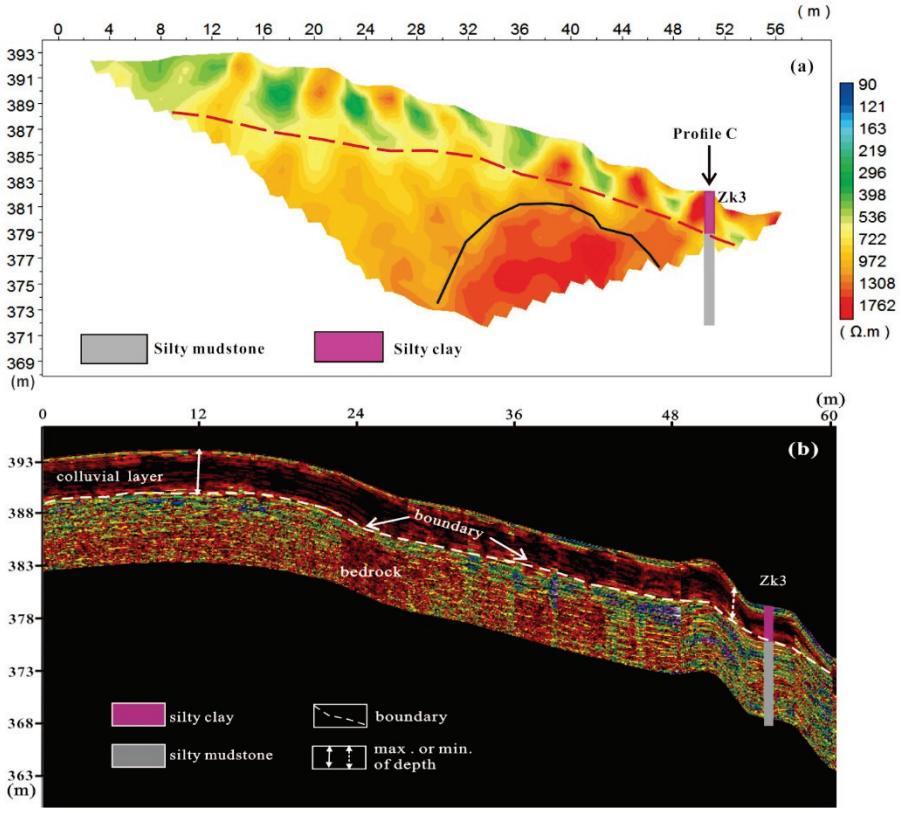

Figure 10. Comparison between ERT and GPR images of profile B. (**a**) ERT image of profile B, (**b**) GPR image of profile B.

Moreover, ERT is more likely to detect the area of rarely weathered bedrock between a distance of 30 and 48 m below the elevation of 381 m, whereas GPR fails to exhibit this phenomenon owing to its particular propagating ability. Commonly, the deeper the penetration depth, the poorer the resolution. In short, GPR is more accurate in reflecting shallow unknown objects (such as the planting soil layer in Figure 9a,b) and faster in gathering information, but it has a smaller probing depth than ERT.

3.4. Model of Potentially Unstable Body

Figure 11 shows the 3D interpreted model of a potentially unstable body built from the above analysis of the subsurface features through the combined ERT and GPR surveys as well as the borehole datasets. Obviously, 3D visualization of it enables us to extract essential information concerning the geometric shape, boundary, initial thickness, and lithological variation of the unstable body, which is important for its volume estimation. Indeed, the volume of the slide mass is one of the most important parameters for understanding its kinetic behavior and the potential effect on objects at risk. Suppose the surface area and average thickness are known. In that case, the volume of the potential landslide and its potential influence area can be rapidly calculated, the results of which are the fundamental basis for risk assessment and mitigation, and disaster protection and prevention.

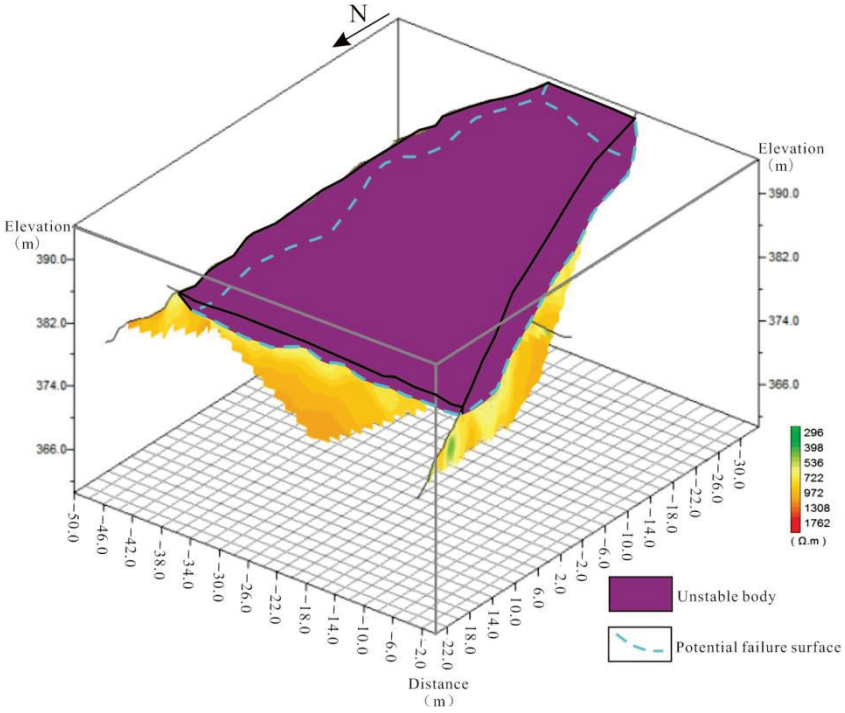

Figure 11. Three-dimensionally (3D) interpreted model of a potentially unstable body based on ERT and GPR images. The light blue dashed lines represent the boundary of the potential failure surface.

Further, the unstable mass's thickness is inhomogeneous and significantly undulates on the east part of the slope, as shown in Figure 11. Under this context, the commonly used drilling techniques are less likely to distinguish all these irregular distributions due to the insufficient survey points at the slope scale. The integrated preliminary and non-invasive geophysical surveys are particularly critical, as they can provide helpful references for the location selection of boreholes during geological investigations. It can also be inferred that the potential rupture surface might be located at the transition zone between the silty clay and the mudstone bedrock, probably in the heavily weathered rock (rich in clay, underground water, and cracks). Based on the identification of the potentially unstable body, more attention should be paid to the surface drainage to reduce the influence of rainfall infiltration in the typhoon season.

Although numerous studies have highlighted the inherent ambiguity of any individual geophysical method when interpreting unknown underground objects, they have also emphasized reducing uncertainty by incorporating multiple pieces of information acquired from diverse data sources, e.g., geophysical, geotechnical, and geological data. In the successful work published by [41], information on a colluvial layer, bedrock interface, potential sliding surface, and underground seepage system was illustrated by employing multi-geophysical methods and drilling data. Similarly, ref. [36] investigated the undulating topography of the bedrock beneath clay by integrating GPR and ERT data as well as boreholes. In this case study, the joint application of ERT and GPR was further confirmed to be capable of decreasing such uncertainty and applicable when delineating the subsurface features in clayey environments. Consequently, for Zhejiang Province where landslides mainly occur along the contact zone between unconsolidated deposits and the bedrock and are commonly shallow, the combination of ERT and GPR could be a reliable tool to obtain information about potential sources of risk. However, it is difficult to extract a precise threshold representing the potential failure zone in terms of the resistivity, amplitude, or energy from the above results.

4. Conclusions

Amid a changing climate, China is facing the specter of even more significant disaster risks in the future, which may also bring global cascading impacts. In Zhejiang Province, a large number of small hilly slopes are in an unstable state and have not been effectively investigated due to the difficulties of human surveys, the drawbacks of conventional geotechnical tools, and the limits of financial resources. This paper demonstrated how a combined geophysical method consisting of ERT and GPR with borehole data could effectively identify the subsurface characteristics of a clayey slope in a relatively short time, and how this delineated the potential unsteady body.

The inverted resistivity sections, radargram images, and single-channel waveform in terms of the amplitude/energy versus the depth indicated two lithological layers, consistent with the field observation and borehole data. The potential failure surface will most likely develop in the strongly weathered mudstone in the depth range of 3–7 m, and the average depth is 5 m. In addition, the thickness of the unstable mass is non-uniform in this slope, being much greater on its east and crest parts.

The GPR survey was suitable for identifying the shallow subsurface features with high-resolution imaging capability. Its reflection profile and the waveform of a single-channel GPR signal provided a valuable contribution to the analysis of the stratum structure and unstable body, even in a clay-rich environment. However, GPR could not distinguish the strongly weathered layer from the intermediary or rarely weathered layer due to their similarity in dielectric properties. The GPR wave was strongly attenuated when encountering anomalous stones or boulders in the topsoil layer. ERT could simultaneously assure both the resolution and exploration depth up to a maximum of 20 m and could be applied to detect the degree of weathering of the bedrock. The fresh bedrock was illustrated to exist at deeper zones in the ERT profiles. However, it was not easy to propose precise resistivity thresholds for different lithological layers.

In conclusion, the combined method of ERT and GPR was beneficial for fast field investigation of the subsurface features in a clay-rich condition, which could support a reference for geohazard prediction and prevention when precise knowledge of the subsurface is absent. It could also offer guidance for selecting borehole and trench locations.

Author Contributions: Conceptualization, Y.Y. (Yajing Yan) and Y.Y. (Yongshuai Yan); methodology, G.Z.; software, Y.Y. (Yongshuai Yan); validation, Y.Y. (Yongshuai Yan) and G.Z.; formal analysis, Y.Y. (Yajing Yan); writing—original draft preparation, Y.Y. (Yajing Yan); writing—review and editing, Y.Z.; supervision, Z.W. All authors have read and agreed to the published version of the manuscript.

Funding: This research was funded by the Open Research Fund of Key Laboratory of Subsurface of Hydrology and Ecological Effect in Arid Region (Chang'an University), Ministry of Education (No. 300102290503), Ministry of Education, and the Belt and Road Special Foundation of the State Key Laboratory of Hydrology—Water Resources and Hydraulic Engineering (No. 2021490511).

Institutional Review Board Statement: Not applicable.

Informed Consent Statement: Not applicable.

Data Availability Statement: Not applicable.

Acknowledgments: The authors would like to express their heartfelt gratitude to the anonymous reviewers for their constructive comments that were valuable for improving this manuscript.

Conflicts of Interest: The authors declare no conflict of interest.

References

1. Wang, Z.P. Current situation of geological disasters and the prevention measures in Zhejiang Province. *J. Catastrophol.* **2001**, *16*, 63–66. (In Chinese)
2. Yue, L.X.; Wang, Y.; Yu, S.J. Debris fow types and their distribution in Zhejiang province. *Bull. Soil Water Conserv.* **2010**, *30*, 185–189. (In Chinese) [CrossRef]
3. Zhang, G.P.; Song, J.Y.; Shao, X.L. Case analysis of forecast and evacuation of recent large geological disasters in china. *J. Nat. Disasters* **2015**, *24*, 20–27. (In Chinese) [CrossRef]

4. Zhi, M.; Shang, Y.; Zhao, Y.; Lü, Q.; Sun, H. Investigation and monitoring on a rainfall-induced deep-seated landslide. *Arab. J. Geosci.* **2016**, *9*, 182. [CrossRef]
5. Ding, J.; Zhang, G.; Gao, J.; Wang, S.; Xue, B.; Wang, K.; Yang, J.; Jiang, R.; Lian, J. The rainfall thresholds and soil characteristics of large geological disasters in Zhejiang, China. *Arab. J. Geosci.* **2022**, *15*, 559. [CrossRef]
6. Chen, X.; Ma, T.; Li, C.; Liu, H.; Ding, B.; Peng, W. The catastrophic 13 November 2015 rock-debris slide in Lidong, south-western Zhejiang (China): A landslide triggered by a combination of antecedent rainfall and triggering rainfall. *Geomat. Nat. Hazards Risk* **2018**, *9*, 608–623. [CrossRef]
7. Ouyang, C.J.; Zhao, W.; Xu, Q.; Peng, D.L.; Li, W.L.; Wang, D.P.; Zhou, S.; Hou, S.W. Failure mechanisms and characteristics of the 2016 catastrophic rockslide at Su village, Lishui, China. *Landslides* **2018**, *15*, 1391–1400. [CrossRef]
8. Ouyang, C.J.; Zhao, W.; An, H.; Zhou, S.; Wang, D.; Xu, Q.; Li, W.; Peng, D. Early identification and dynamic processes of ridge-top rockslides: Implications from the Su Village landslide in Suichang County, Zhejiang Province, China. *Landslides* **2019**, *16*, 799–813. [CrossRef]
9. Tian, H.; Gan, J.; Jiang, H.; Tang, C.; Luo, C.; Wan, C.; Xu, B.; Gui, F.; Liu, C.; Liu, N. Failure Mechanism and Kinematics of the Deadly September 28th 2016 Sucun Landslide, Suichang, Zhejiang, China. *Adv. Civ. Eng.* **2020**, *2020*, 8828819. [CrossRef]
10. Wu, Y.; Zhang, M.; Yang, L.; Liu, T.; Zhang, T.; Sun, Q.; Wang, B.; Xie, X. Failure mechanisms and dynamics of the Shanzao rockslide in Yongjia County, China on 10 August 2019. *Landslides* **2021**, *18*, 2565–2574. [CrossRef]
11. McCann, D.M.; Forster, A. Reconnaissance geophysical methods in landslide investigations. *Eng. Geol.* **1990**, *29*, 59–78. [CrossRef]
12. Hack, R. Geophysics for slope stability. *Surv. Geophys.* **2000**, *21*, 423–448. [CrossRef]
13. Perrone, A.; Lapenna, V.; Piscitelli, S. Electrical resistivity tomography technique for landslide investigation: A review. *Earth-Sci. Rev.* **2014**, *135*, 65–82. [CrossRef]
14. Arosio, D.; Deparis, J.; Zanzi, L.; Garambois, S. Fracture characterization with GPR: A comparative study. In Proceedings of the 2016 16th International Conference on Ground Penetrating Radar (GPR), Hong Kong, China, 13–16 June 2016; pp. 1–6. [CrossRef]
15. Arosio, D.; Zanzi, L.; Longoni, L.; Papini, M. Fracture thickness from GPR measurements. In Proceedings of the 2015 8th International Workshop on Advanced Ground Penetrating Radar (IWAGPR), Florence, Italy, 7–10 July 2015; pp. 1–4. [CrossRef]
16. Van den bril, K.; Grégoire, C.; Swennen, R.; Lambot, S. Ground-penetrating radar as a tool to detect rock heterogeneities (channels, cemented layers and fractures) in the Luxembourg Sandstone Formation (Grand-Duchy of Luxembourg). *Sedimentology* **2007**, *54*, 949–967. [CrossRef]
17. Jeannin, M.; Garambois, S.; Grégoire, C.; Jongmans, D. Multiconfiguration GPR measurements for geometric fracture characterization in limestone cliffs (Alps). *Geophysics* **2006**, *71*, B85–B92. [CrossRef]
18. Abbasi Baghbadorani, A.; Hole, J.A.; Baggett, J.; Ripepi, N. Radar imaging of fractures and voids behind the walls of an underground mine. *Geophysics* **2021**, *86*, H27–H41. [CrossRef]
19. Davis, J.L.; Annan, A.P. Ground-penetrating radar for high-resolution mapping of soil and rock stratigraphy. *Geophys. Prospect.* **1989**, *37*, 531–551. [CrossRef]
20. Gerber, R.; Felix-Henningsen, P.; Behrens, T.; Scholten, T. Applicability of ground-penetrating radar as a tool for nondestructive soil-depth mapping on Pleistocene periglacial slope deposits. *J. Plant Nutr. Soil Sci.* **2010**, *173*, 173–184. [CrossRef]
21. Campbell, S.; Affleck, R.T.; Sinclair, S. Ground-penetrating radar studies of permafrost, periglacial, and near-surface geology at McMurdo Station. Antarctica. *Cold Reg. Sci. Technol.* **2018**, *148*, 38–49. [CrossRef]
22. Lang, J.; Sievers, J.; Loewer, M.; Igel, J.; Winsemann, J. 3D architecture of cyclicstep and antidune deposits in glacigenic subaqueous fan and delta settings: Integrating outcrop and ground-penetrating radar data. *Sediment. Geol.* **2017**, *362*, 83–100. [CrossRef]
23. Khan, M.Y.; Shafique, M.; Turab, S.A.; Ahmad, N. Characterization of an Unstable Slope Using Geophysical, UAV, and Geological Techniques: Karakoram Himalaya, Northern Pakistan. *Front. Earth Sci.* **2021**, *9*, 668011. [CrossRef]
24. Karim, N.I.; Kamaruddin, S.A.; Hasan, R.C. Performance of Soil Water Content Using Ground Penetrating Radar with Different Antenna Frequencies. *Int. J. Eng. Technol.* **2018**, *7*, 815–820. [CrossRef]
25. Cao, Q.; Song, X.; Wu, H.; Gao, L.; Liu, F.; Yang, S.; Zhang, G. Mapping the response of volumetric soil water content to an intense rainfall event at the field scale using GPR. *J. Hydrol.* **2020**, *583*, 124605. [CrossRef]
26. Pan, X.; Zhang, J.; Huang, P.; Roth, K. Estimating field-scale soil water dynamics at a heterogeneous site using multi-channel GPR. *Hydrol. Earth Syst. Sci.* **2011**, *16*, 4361–4372. [CrossRef]
27. Weihermüller, L.; Huisman, J.A.; Lambot, S.; Herbst, M.; Vereecken, H. Mapping the spatial variation of soil water content at the field scale with different ground penetrating radar techniques. *J. Hydrol.* **2007**, *340*, 205–216. [CrossRef]
28. Jongmans, D.; Garambois, S. Geophysical investigation of landslides: A review. *Bull. Soc. Geol. Fr.* **2007**, *178*, 101–112. [CrossRef]
29. Jongmans, D.; Bièvre, G.; Renalier, F.; Schwartz, S.; Beaurez, N.; Orengo, Y. Geophysical investigation of a large landslide in glaciolacustrine clays in the Trièves area (French Alps). *Eng. Geol.* **2009**, *109*, 45–56. [CrossRef]
30. Colangelo, G.; Lapenna, V.; Loperte, A.; Perrone, A.; Telesca, L. 2D electrical resistivity tomographies for investigating recent activation landslides in Basilicata Region (Southern Italy). *Ann. Geophys.* **2008**, *51*, 275–285. [CrossRef]
31. Falae, P.O.; Kanungo, D.P.; Chauhan, P.K.; Dash, R.K. Recent Trends in Application of Electrical Resistivity Tomography for Landslide Study. In *Renewable Energy and its Innovative Technologies*; Springer: Singapore, 2018; pp. 195–204. [CrossRef]
32. Falae, P.O.; Kanungo, D.P.; Chauhan, P.K.; Dash, R.K. Electrical resistivity tomography (ERT) based subsurface characterisation of Pakhi Landslide, Garhwal Himalayas, India. *Environ. Earth Sci.* **2019**, *78*, 430. [CrossRef]

33. Huntley, D.; Bobrowsky, P.T.; Hendry, M.T.; Macciotta, R.; Elwood, D.E.; Sattler, K.; Best, M.E.; Chambers, J.E.; Meldrum, P.I. Application of multi-dimensional electrical resistivity tomography datasets to investigate a very slow-moving landslide near Ashcroft, British Columbia, Canada. *Landslides* **2019**, *16*, 1033–1042. [CrossRef]
34. Tsai, W.; Chen, C.; Chiang, C.; Chen, P.; Kuo, C.; Wang, K.; Lin, M.; Chen, R. Electrical Resistivity Tomography (ERT) Monitoring for Landslides: Case Study in the Lantai Area, Yilan Taiping Mountain, Northeast Taiwan. *Front. Earth Sci.* **2021**, *9*, 737271. [CrossRef]
35. Bichler, A.; Bobrowsky, P.; Best, M.; Douma, M.; Hunter, J.; Calvert, T.; Burns, R. Three-dimensional mapping of a landslide using a multi-geophysical approach: The Quesnel Forks landslide. *Landslides* **2004**, *1*, 29–40. [CrossRef]
36. Diallo, M.C.; Cheng, L.; Rosa, E.M.; Gunther, C.; Chouteau, M. Integrated GPR and ERT data interpretation for bedrock identification at Cléricy, Québec, Canada. *Eng. Geol.* **2019**, *248*, 230–241. [CrossRef]
37. Imani, P.; Tian, G.; Hadiloo, S.; El-Raouf, A.A. Application of combined electrical resistivity tomography (ERT) and seismic refraction tomography (SRT) methods to investigate Xiaoshan District landslide site: Hangzhou, China. *J. Appl. Geophys.* **2021**, *184*, 104236. [CrossRef]
38. Huntley, D.; Bobrowsky, P.T.; Hendry, M.T.; Macciotta, R.; Best, M.E. Multi-technique Geophysical Investigation of a Very Slow-moving Landslide near Ashcroft, British Columbia, Canada. *J. Environ. Eng. Geophys.* **2019**, *24*, 87–110. [CrossRef]
39. Hu, Z.; Guo, Y.; Shan, W. Landslide Investigations in the Northwest Section of the Lesser Khingan Range in China Using Combined HDR and GPR Methods. *Bull. Eng. Geol. Environ.* **2017**, *75*, 591–603. [CrossRef]
40. Malehmir, A.; Bastani, M.; Krawczyk, C.M.; Gurk, M.; Ismail, N.; Polom, U.; Persson, L. Geophysical assessment and geotechnical investigation of quick-clay landslides—A Swedish case study. *Near Surf. Geophys.* **2013**, *11*, 341–350. [CrossRef]
41. Su, L.; Xu, X.; Geng, X.; Liang, S. An integrated geophysical approach for investigating hydro-geological characteristics of a debris landslide in the Wenchuan earthquake area. *Eng. Geol.* **2017**, *219*, 52–63. [CrossRef]
42. Tao, M.; Chen, X.; Cheng, Q.; Binley, A. Evaluating the joint use of GPR and ERT on mapping shallow subsurface features of karst critical zone in southwest China. *Vadose Zone J.* **2021**, *21*, 20172. [CrossRef]
43. Ebong, E.D.; George, A.M.; Ekwok, S.E.; Akpan, A.E.; Asfahani, J. 2D electrical resistivity inversion and ground penetrating radar investigation of near surface cave in New Netim area, southeastern Nigeria. *Acta Geod. Geophys.* **2021**, *56*, 765–780. [CrossRef]
44. GFDRR; World Bank. *Learning from Experience—Insights from China's Progress in Disaster Risk Management*; World Bank Press: Washington, DC, USA, 2020; p. 14.
45. Bureau of Land and Resources of Wenzhou. Geological Environment Bulletin of Wenzhou. 2001–2020. Available online: http://zrzyj.wenzhou.gov.cn/col/col1341265/index.html (accessed on 30 September 2021).
46. Zhang, C.Y.; Zhang, M.; Zhang, T.L.; Dai, Z.W.; Wang, L.Q. Influence of intrusive granite dyke on rainfall-induced soil slope failure. *Bull. Eng. Geol. Environ.* **2020**, *79*, 5259–5276. [CrossRef]
47. *GB/T50123-2019*; Standard for Soil Test Method. China Planning Press: Beijing, China, 2019; pp. 29–43. (In Chinese)
48. Moore, D.M.; Reynolds, R.C., Jr. *X-ray Diffraction and the Identification and Analysis of Clay Minerals*, 2nd ed.; Oxford University Press: Oxford, UK, 1997; p. 378.
49. Duc, D.M. Rainfall-triggered large landslides on 15 December 2005 in Van Canh District, Binh Dinh Province, Vietnam. *Landslides* **2012**, *10*, 219–230. [CrossRef]
50. *SL/T 291.1-2021*; Code for Exploration of Water Resources and Hydropower Projects Part 1: Geophysical Exploration. China Water&Power Press: Beijing, China, 2021; pp. 6–10, 15–56, 143. (In Chinese)
51. Reynolds, J.M. *An Introduction to Applied and Environmental Geophysics*; Wiley & Sons: Chichester, UK, 2011; p. 806.
52. Neal, A. Ground-penetrating radar and its use in sedimentology: Principles, problems and progress. *Earth Sci. Rev.* **2004**, *66*, 261–330. [CrossRef]
53. Loke, M.H. Least-squares inversion of large 3D resistivity data sets using auxiliary storage. In Proceedings of the 58th EAGE Conference and Exhibition, Amsterdam, The Netherlands, 3–7 June 1996. [CrossRef]
54. Pellicer, X.M.; Gibson, P. Electrical resistivity and ground penetrating radar for the characterisation of the internal architecture of quaternary sediments in the midlands of Ireland. *J. Appl. Geophys.* **2011**, *75*, 638–647. [CrossRef]
55. Kaplanvural, İ.; Özkap, K.; Pekşen, E. Influence of water content investigation on GPR wave attenuation for early age concrete in natural air-drying condition. *Constr. Build. Mater.* **2021**, *297*, 123783. [CrossRef]

GeoHazards

MDPI

Article

Comparing Root Cohesion Estimates from Three Models at a Shallow Landslide in the Oregon Coast Range

Collin Cronkite-Ratcliff [1,*], Kevin M. Schmidt [1] and Charlotte Wirion [2]

[1] U.S. Geological Survey, Moffett Field, CA 94035, USA
[2] ETH Zurich, 8092 Zürich, Switzerland
* Correspondence: ccronkite-ratcliff@usgs.gov

Abstract: Although accurate root cohesion model estimates are essential to quantify the effect of vegetation roots on shallow slope stability, few means exist to independently validate such model outputs. One validation approach for cohesion estimates is back-calculation of apparent root cohesion at a landslide site with well-documented failure conditions. The catchment named CB1, near Coos Bay, Oregon, USA, which experienced a shallow landslide in 1996, is a prime locality for cohesion model validation, as an abundance of data and observations from the site generated broad insights related to hillslope hydrology and slope stability. However, previously published root cohesion values at CB1 used the Wu and Waldron model (WWM), which assumes simultaneous root failure and therefore likely overestimates root cohesion. Reassessing published cohesion estimates from this site is warranted, as more recently developed models include the fiber bundle model (FBM), which simulates progressive failure with load redistribution, and the root bundle model-Weibull (RBMw), which accounts for differential strain loading. We applied the WWM, FBM, and RBMw at CB1 using post-failure root data from five vegetation species. At CB1, the FBM and RBMw predict values that are less than 30% of the WWM-estimated values. All three models show that root cohesion has substantial spatial heterogeneity. Most parts of the landslide scarp have little root cohesion, with areas of high cohesion concentrated near plant roots. These findings underscore the importance of using physically realistic models and considering lateral and vertical spatial heterogeneity of root cohesion in shallow landslide initiation and provide a necessary step towards independently assessing root cohesion model validity.

Keywords: root reinforcement; shallow landslides; slope stability

Citation: Cronkite-Ratcliff, C.; Schmidt, K.M.; Wirion, C. Comparing Root Cohesion Estimates from Three Models at a Shallow Landslide in the Oregon Coast Range. *GeoHazards* **2022**, *3*, 428–451. https://doi.org/10.3390/geohazards3030022

Academic Editors: Stefano Morelli, Veronica Pazzi and Mirko Francioni

Received: 30 March 2022
Accepted: 18 July 2022
Published: 1 September 2022

1. Introduction

Vegetation plays a critical role in protecting slopes against shallow landslides, primarily because of the mechanical reinforcement that plant roots provide to the soil on steep slopes [1–4]. In many upland areas, shallow landslide susceptibility increases in response to population and urbanization pressure, overgrazing, timber harvest [5], and climate-induced wildland fire size and frequency [6]. Over the last several decades, researchers have developed a variety of root breakage models to quantify the additional root cohesion provided to the soil [7,8]. These models vary significantly in their assumptions about the root reinforcement mechanics. For example, the earliest model developed by T.H. Wu, L.J. Waldron, and colleagues [9–11], known as the Wu and Waldron model (WWM), assumes that all roots break at once. This assumption was challenged by Pollen and Simon [12] in their fiber bundle model (FBM), a stress-controlled model that represents root breakage as a progressive process in which the weakest roots break and cause the load to be redistributed to the surviving roots. Instead of a stress-controlled model, Schwarz et al. [13] proposed a strain-controlled model called the root bundle model-Weibull (RBMw) that uses the Weibull distribution to represent the probability of breakage with increasing strain.

Since its publication, the WWM has been found to result in overestimation of root reinforcement in numerous studies due to its assumption of simultaneous failure [12,14]. By contrast, the FBM and the RBMw are generally considered to have more realistic assumptions [7]. However, despite the important role that root reinforcement plays in preventing shallow landslides, the authors are not aware of any studies that have compared results from these three models at a landslide site with the detailed measurements of root characteristics that are necessary for computing root cohesion with all three models. To the authors' knowledge, only the study of Zydron and Skorski [15] has compared results from all three models together, but this study was conducted at an agricultural plot rather than at a landslide site. Similarly, while some studies have computed root cohesion using root data collected from shallow landslide sites [16,17], none of these studies compared more than two models. In this study, we use a unique dataset with detailed measurements of root characteristics, collected from the scarp of a shallow landslide, to calculate root cohesion using these three root breakage models. The comparison we present in this paper demonstrates how the choice of root breakage model affects root reinforcement estimates across an entire landslide site.

The study we present in this paper is important because the differences between the results of the three models at a landslide site could have significant implications for making engineering and land management decisions, such as the type, quantity, and extent of vegetation required to reinforce a slope [2,18]. Comparing these models at the same site would allow practitioners to adjust values that were previously estimated with one model to obtain values equivalent to estimation with another model. This type of comparison could be particularly valuable if other models are thought to be more realistic at that site. A better understanding of the magnitude and spatial variation of root reinforcement provided by different plant assemblages is necessary to evaluate potential negative impacts from different land use scenarios.

The previously instrumented research catchment in the Oregon Coast Range, CB1, is a thoroughly studied landslide site, with tightly constrained site characteristics, that is well suited for this type of comparative study. This catchment was heavily instrumented with hydrologic monitoring for several years before experiencing a landslide in 1996 [19]. Following the landslide, data from the catchment became the subject of several research studies on hillslope hydrology and slope stability [19–24]. As part of this research, Schmidt et al. [25] measured the tensile strength of vegetation roots at the site and used these data to estimate root reinforcement in the slope using the WWM. Since then, the development of the newer root breakage models, including the FBM and the RBMw, present the opportunity to revisit estimates of root cohesion at CB1.

This paper has two main objectives:

1. To reexamine previously published root cohesion estimates for the CB1 landslide by Schmidt et al. [25], which was evaluated before the development of breakage models accounting for progressive root failure. Because root cohesion values for the CB1 slide have been cited and used in subsequent studies [19,21,22,26,27], reexamining these values has implications for these existing studies as well as future investigations.
2. To compare the results of these three models at an instrumented landslide site where interpretations have implications for other shallow landslides. Because roots in the landslide scarp were surveyed and measured post-failure, data from the CB1 site is uniquely suited to this purpose.

In this study, we apply three different root breakage models to data from the CB1 catchment: (1) the WWM; (2) the global load-sharing FBM; and (3) the strain-controlled RBMw. These three models are representative of the major developments in root breakage models since the original publication of the WWM, as outlined by Dias et al. [7]. First, we review how root tensile strength was calculated based on laboratory analysis of root specimens collected at several locations in the Oregon Coast Range. We use these data to estimate regression models for predicting root tensile strength for roots of a given diameter and species. We then review the root data that were collected from the CB1 site after

landsliding and use the regression models to calculate root tensile strengths. We then apply the three root breakage models to obtain estimates for apparent root cohesion. Finally, we investigate how root cohesion varies both laterally along the scarp perimeter and vertically with depth. We also investigate the contribution of each of five vegetation species to the overall root cohesion as a step towards independently validating cohesion estimates from different model frameworks.

2. Materials and Methods

2.1. Root Breakage Models

Plant roots reinforce a soil mass against shear failure because roots are strong in tension and weak in compression, whereas soil is weak in tension and strong in compression [28]. Root-reinforced soil is a composite material where roots of relatively high tensile strength reinforce a soil matrix of relatively low tensile strength [29]. The contribution of roots to the shear strength of soil can be described as an additional term in the widely adopted Mohr–Coulomb failure criterion:

$$s = c' + c_r + (\sigma - u) \tan \phi', \quad (1)$$

where s is shear strength, σ is normal stress, u is pore-water pressure, ϕ' is effective angle of soil internal friction, and c' is the effective soil cohesion. The apparent root cohesion c_r represents the additional shear strength provided by roots [29]. Roots produce an apparent cohesion via fiber reinforcement, hereafter referred to as root cohesion. Most research quantifying root cohesion focuses on the tensile resistance of the root "bundle". We focus on "breakage" models that calculate maximum tensile resistance of a root bundle where tensile strengths of the individual roots are known [7].

The WWM, the first quantitative model for estimating root bundle tensile strength, assumes that all roots fail simultaneously, mobilizing the sum of the full tensile strength of all roots. Several studies indicated that the WWM overestimates the strength because the assumption that all roots break simultaneously is not realistic; instead, roots break progressively, with the load from broken roots being redistributed onto surviving threads [12,14]. Pollen and Simon [12] therefore developed the fiber bundle model (FBM) to simulate progressive failure due to loading.

The greatest drawback of the FBM is that it does not account for root elasticity; the stress-step approach does not allow roots of different sizes to respond differently to the same applied load [15]. To address this shortcoming, Schwarz et al. [30] proposed a new model, the root bundle model (RBM), which uses a strain-step approach. Subsequently, Schwarz et al. [13] published an extension of the RBM, the root bundle model-Weibull (RBMw), which uses a Weibull probability distribution to account for variability in mechanical properties among roots of the same diameter.

Several studies have compared root cohesion estimates obtained between at least two of the published models. Preti and Schwarz [31] suggested multiplying the root cohesion by a correction factor to account for overestimation. Several studies have estimated this correction factor for the purpose of adjusting results obtained using the WWM [16,32,33]. One of the original authors of the WWM suggested reducing WWM estimates by a factor of 0.3–0.5 [34]. Arnone et al. [32] reports that the ratio of FBM-estimated cohesion to the WWM-estimated cohesion ranges from 0.34 to 1, with an average of 0.4 proposed by Preti and Schwarz [31]. Comparisons between the WWM and the RBMw suggest similar values for the ratio of WWM-estimated cohesion to RBMw-estimated cohesion, in the range of 0.4–0.6 [13,15], with Zydron and Skorski [15] proposing a correction factor of 0.5 for adjusting WWM-estimated cohesion.

2.2. CB1 Landslide Site

The 860 m^2 CB1 catchment was monitored for unsaturated and saturated hydrologic flow response magnitude and pathways in the context of shallow-soil slope stability. CB1 is located below Mettman Ridge in the Oregon Coast Range, approximately 15 km northeast

of Coos Bay, Oregon, USA [35]. The ridge crest elevation is approximately 300 m. A detailed physical description of the site and its soils is provided in Montgomery et al. [19] and Anderson et al. [20]. CB1 is one of two adjacent catchments used for experimental work on landslide failure [20,23,24]. The site was clearcut logged in 1987 and replanted with Douglas fir saplings in 1989; instrumentation was installed starting in 1989 and remained in place until November 1996, when it was destroyed by a landslide and the associated debris flow [19]. Figure 1 shows an aerial view of the CB1 catchment immediately after the landslide, and Figure 2 shows photos of the catchment both before and after the landslide taken from the same vantage point.

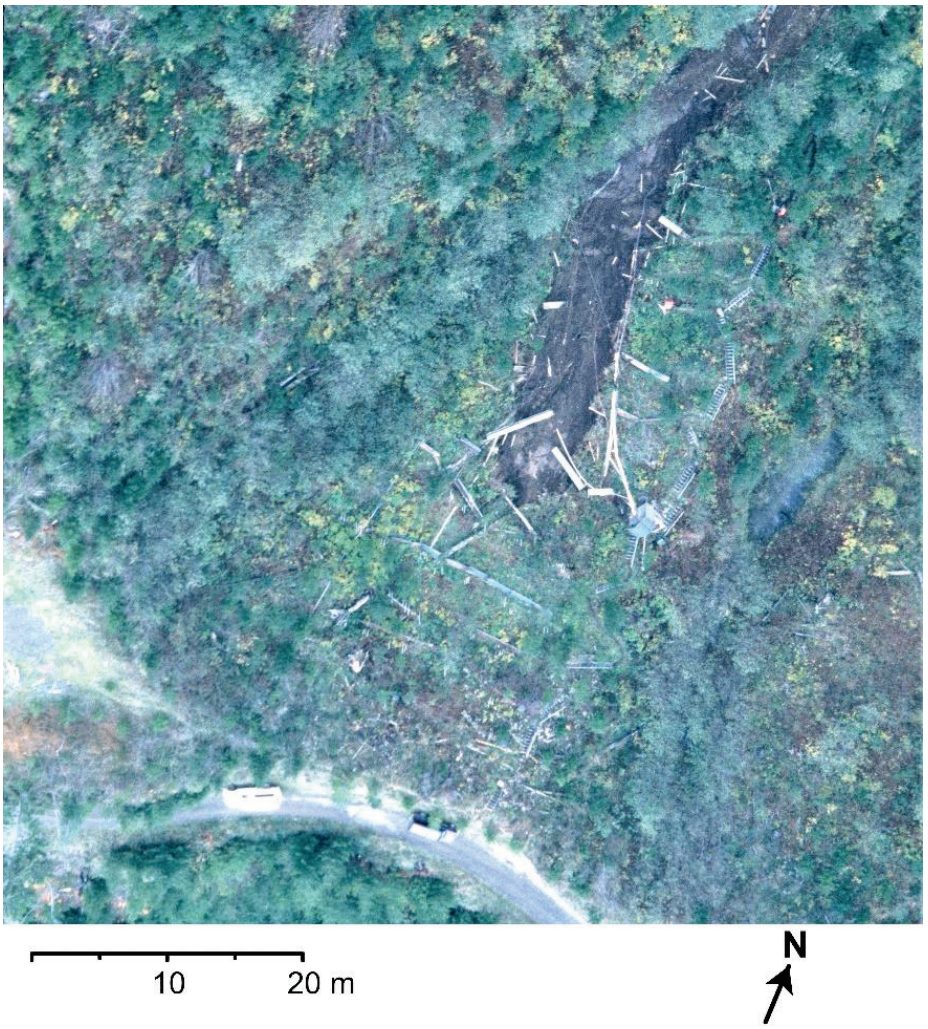

Figure 1. Post-landslide oblique aerial photo, taken roughly towards the NNW direction, reveals both upslope shallow landslide extent and downslope debris flow scour. Vehicles on the road near the bottom of the image indicate the relative size of the landslide area. Photograph by K.M. Schmidt, U.S. Geological Survey.

Figure 2. View of the CB1 catchment (**a**) before and (**b**) after the landslide. Both images are taken from the same location at the top of the scarp. The view is to the north, looking directly down the central axis of the hollow. Panel (**a**) shows some of the instrumentation which was installed at the site before the landslide. The instrumentation included tipping bucket rain gages, tensiometers, piezometers, catwalks to minimize ground surface disturbance, and a downslope weir. Photograph by K.M. Schmidt, U.S. Geological Survey.

The CB1 site used artificial sprinkling experiments to understand hydrologic response [20,23,24]. Montgomery et al. [19] provides several photographs of the site before and after failure, as well as analysis of hydrologic conditions at the time of landslide initia-

tion. The initial landslide source area was confined to the colluvium overlying sandstone bedrock with post-event observations constraining the failure mass upslope of the weir. The landslide and associated surface water flow stripped off most of the colluvium down to bedrock in the source area. After the landslide, the depth of the landslide scar from remnant ground surface to landslide failure surface was measured around the perimeter of the scar including lateral and head scarps components. The average depth of the landslide failure plane around the perimeter of the slide was 0.7 m but varied from 0.3 m to 1.2 m. The basal surface of the landslide scar was relatively planar, with an average slope of 43°, generally parallel to the ground surface. The basal area of the landslide scar was 157 m^2 and the total length of the upper scar was 58 m. However, roots from only 37 m of the scar perimeter could be collected and measured because of physical disturbance and obstruction by catwalk infrastructure [19].

After the 1996 failure, Schmidt et al. [25] meticulously measured and collected vegetation roots from the failure scarp. Vegetation in the vicinity of the failure scarp is dominated by Douglas fir (*Pseudotsuga menziesii*) saplings planted two years after the clear cut, blue elderberry (*Sambucus caerulea*), thimbleberry (*Rubus parviflorus*), foxglove (*Digitalis purpurea*), and Himalayan blackberry (*Rubus discolor*). All the plant species are native except for Himalayan blackberry, which is non-native and invasive [36]. Low confining stress triaxial tests on undisturbed material determined the colluvium was essentially cohesionless, with an internal friction angle of 40° [19]. Because very few roots intersected the basal landslide surface, and all the roots intersecting the lateral margin were observed to have broken, Schmidt et al. [25] concluded that plant roots mainly provided lateral reinforcement.

Previous root cohesion estimates at CB1, obtained using only the WWM [19,25], estimated a spatially averaged root cohesion of 4.6 kPa over the entire 37 m perimeter of the landslide scarp. These estimates were calculated in vertical and lateral profiles, revealing that root cohesion is spatially heterogeneous, with values ranging from near 0 to 13 kPa in the vertical profile dimension and near 0 to 14 kPa laterally along the scarp [19]. The basal component of root cohesion was estimated to be 0.1 kPa [19], a small fraction of the estimation for the roots exposed in the lateral scarp. The relatively low estimate for the basal component highlights the fact that most of the roots are constrained within the overlying colluvium, with few roots piercing the colluvium–bedrock interface.

2.3. Estimation of Root Thread Strength from Experimental Data

Schmidt et al. [25] carried out tensile strength tests for root threads of 12 species at multiple sites throughout the Oregon Coast Range, including the Mettman Ridge area near Coos Bay. Schmidt et al. [25] collected root specimens measuring up to 6.5 mm in diameter by identifying healthy plant species in the field, excavating their roots, trimming suitable lengths of similar diameter, and determining the tensile force at failure for given diameter classes. Thread strength tests were conducted by adhering the ends of 15–20 cm-long threads into clamps, pulling by hand with a consistent force until the thread failed, and measuring the maximum force required for failure with calibrated springs. Healthy roots were identified based on bark characteristics and relatively high elasticity. We use the same method of estimating thread tensile strength as Schmidt et al. [25], who used a second-order polynomial regression model to represent maximum tensile load. To obtain results in units of tensile strength, which is necessary to apply the FBM, we convert the results of the polynomial regression model to a power law representing tensile strength (see Appendix A). We estimate maximum tensile load at failure for all species except Douglas fir. Because the Douglas fir roots measured were relatively fine and not representative of larger Douglas fir roots, we instead used the equation from Burroughs and Thomas [37] for the tensile load of Coast Douglas fir, which is based on a sample with greater representation of large-diameter roots. The experimental data and equations for tensile load are shown in Figure 3.

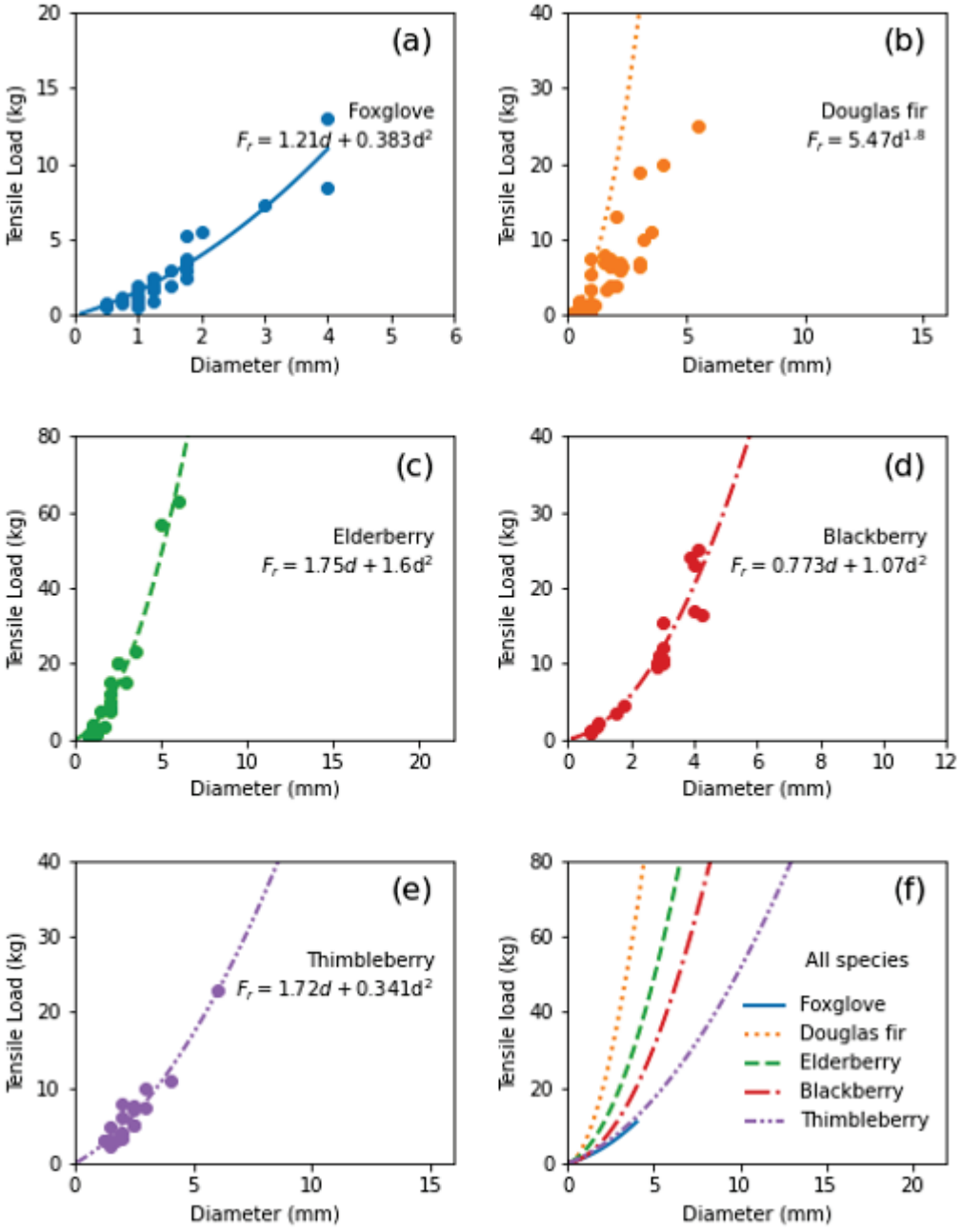

Figure 3. Field-measured relations of species type with tensile load at failure (solid circles) for a given thread diameter with best fit second-order polynomial model from Equation (A1) (see Appendix A) (except for Douglas fir, where the equation of Burroughs and Thomas [37] was used). Equations are shown for foxglove (**a**), Douglas fir (**b**), elderberry (**c**), blackberry (**d**), and thimbleberry (**e**). Panel (**f**) shows the estimated curves for all species color-coded by the individual species. In all plots, the diameter range of the curves represents the range over which the tensile load was estimated. All data are available in Schmidt and Cronkite-Ratcliff [35].

2.4. Root Data from the CB1 Landslide Site

Root data obtained from the CB1 landslide scarp are available in Schmidt and Cronkite-Ratcliff [35]. These data were collected by Schmidt et al. [25] and consist of 349 roots, 41 of which are located in the basal surface. All roots intersecting the slide scarp were broken during landsliding. These roots represent five different species: foxglove, Douglas fir, elderberry, blackberry, and thimbleberry. Of the remaining 308 roots that were not in the basal surface, 280 were live and generally oriented perpendicular to the failure surface

and failed during landsliding. A subset of roots aligned roughly parallel to the slide scarp were exposed but did not fail during landsliding. The majority (211 out of 280; 75%) belonged to thimbleberry plants. It should be noted that the roots identified in the landslide headscarp were not excavated to the plant of origin to determine species. Rather, species were identified based on proximity to remaining above-ground plant biomass, and also by characteristic species traits (e.g., color, texture, tortuosity, bark, etc.) of the roots observed during the measurements of thread strength vs. diameter for the different species examined. The scarp was divided into 16 segments ranging from 1 to 6.2 m in width and from 0.29 to 1.2 m in average depth. However, roots were measured in only 12 of these 16 segments, with 4 segments occluded by ground disturbance (Figure 4). Segments are inclined at angles of 39–87° from horizontal. The area of each segment ranged from 0.5 to 4 m^2.

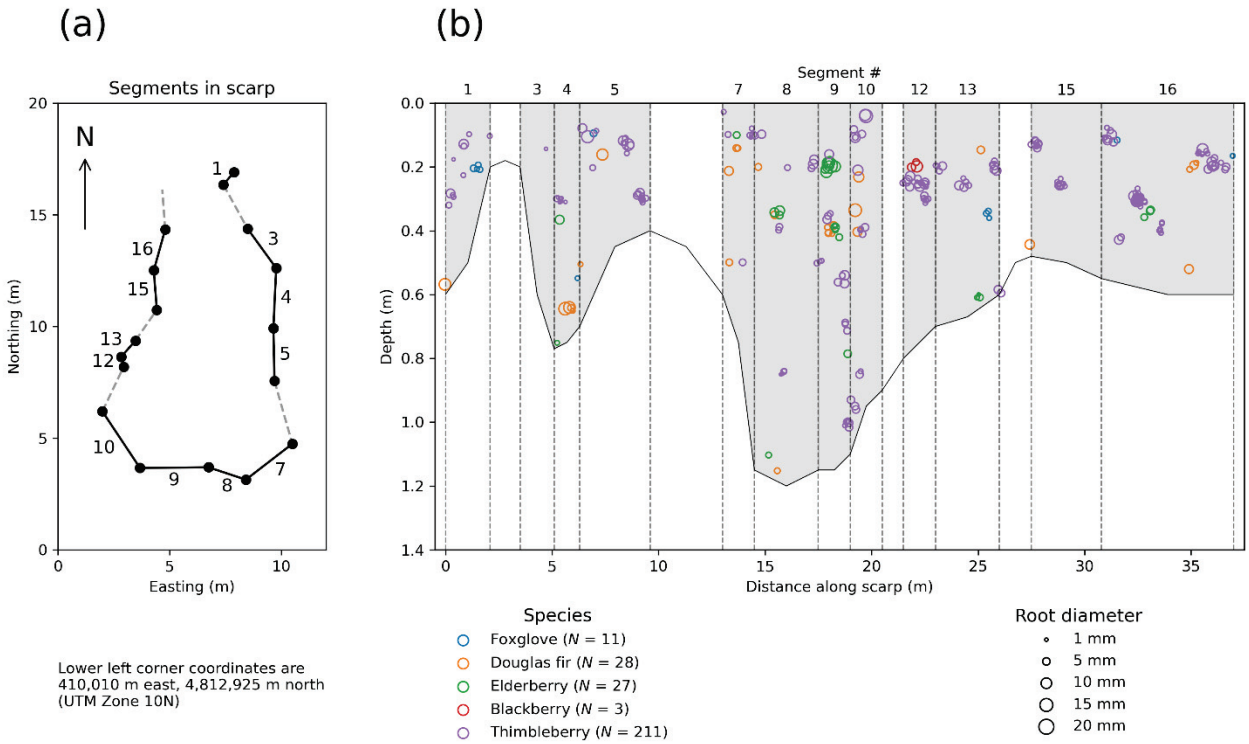

Figure 4. Panel (**a**) shows the plan view of the landslide scarp perimeter constructed with a tape and compass survey, showing the locations of numbered segments. Only segments where roots were measured are numbered. Segments where no roots were measured (because of obstructions including collapsed soil masses and broken site infrastructure) are shown as dashed lines. Segments of scarp perimeter are constrained to the boundary of the initial landslide and do not include the downslope debris-flow. Data on the location of the scarp segments are available in Schmidt and Cronkite-Ratcliff [35]. Panel (**b**) shows the location and diameter of live roots in the scarp, showing the depth below ground surface and the position along the landslide scarp perimeter for each root. The vertical dashed lines demarcate the lateral boundaries of each segment along the scarp perimeter, with shaded areas showing the approximate areal extent of each scarp segment. A small amount of "jitter" (Gaussian noise with variances of 0.1 m and 0.01 m in the horizontal and vertical dimensions, respectively) has been applied to the location and depth to visually differentiate roots located at the same perimeter and depth location. Data on the location and diameter of roots are available in Schmidt and Cronkite-Ratcliff [35].

Figure 4 shows the location and diameter of the roots broken in the landslide scarp, and Figures 5 and 6 show the diameter distribution and depth distribution for the roots broken in the landslide scarp. All the root species exhibit a roughly similar diameter distribution that is positive-skewed, with most values falling below 10 mm, and with

modal values between 2 and 6 mm. The thickest observed root was an elderberry root with a diameter of 20 mm. The depth distributions for all species appear to be relatively similar, showing that most roots are located at relatively shallow depths. Approximately 90% of all roots are located within 50 cm of the ground surface. This is consistent with earlier research showing that in general, at least 80% of the biomass is within 40–50 cm of the ground surface [2].

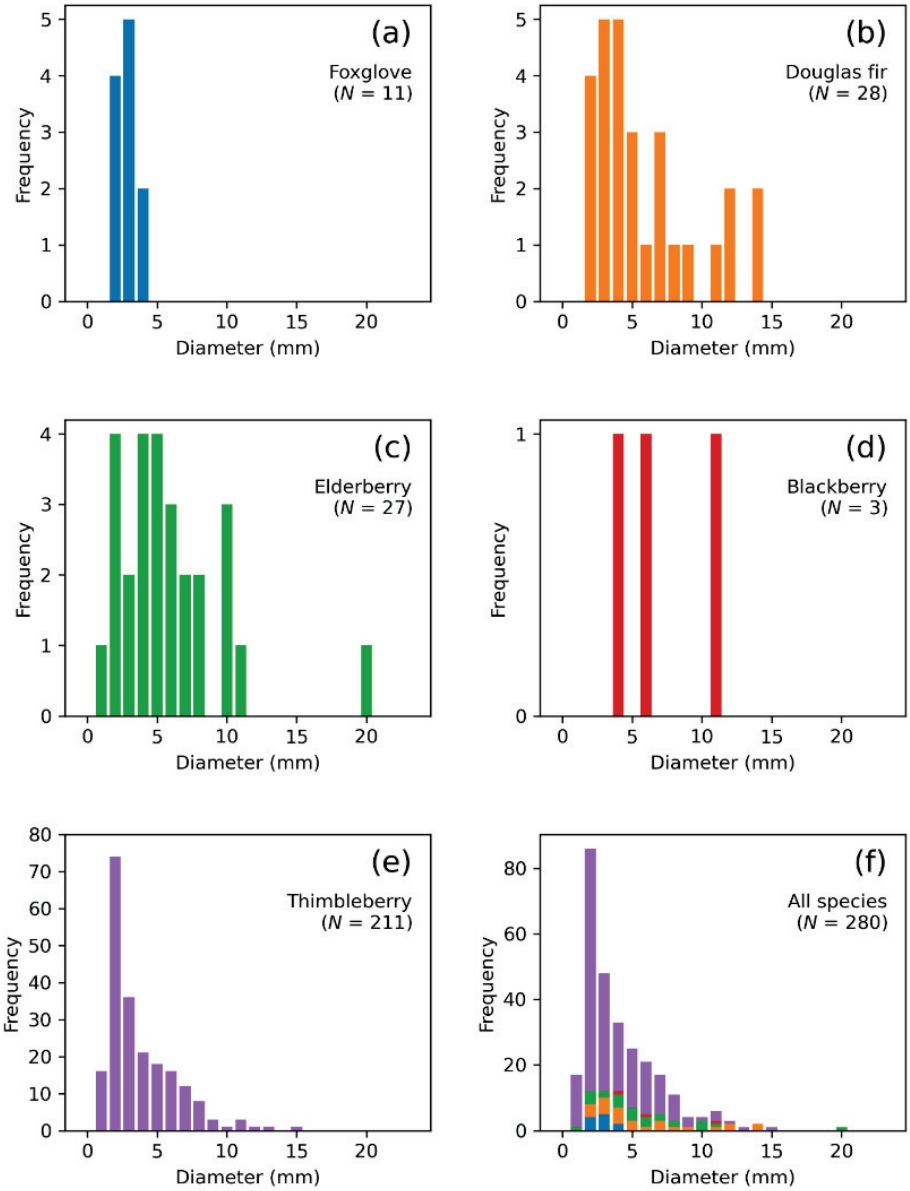

Figure 5. Histograms of broken live root diameter for each of the vegetation species identified along the landslide scarp. Histograms of broken live root diameter are shown for foxglove (**a**), Douglas fir (**b**), elderberry (**c**), blackberry (**d**), and thimbleberry (**e**). Panel (**f**) shows the histogram of broken live root diameter for roots of all species together.

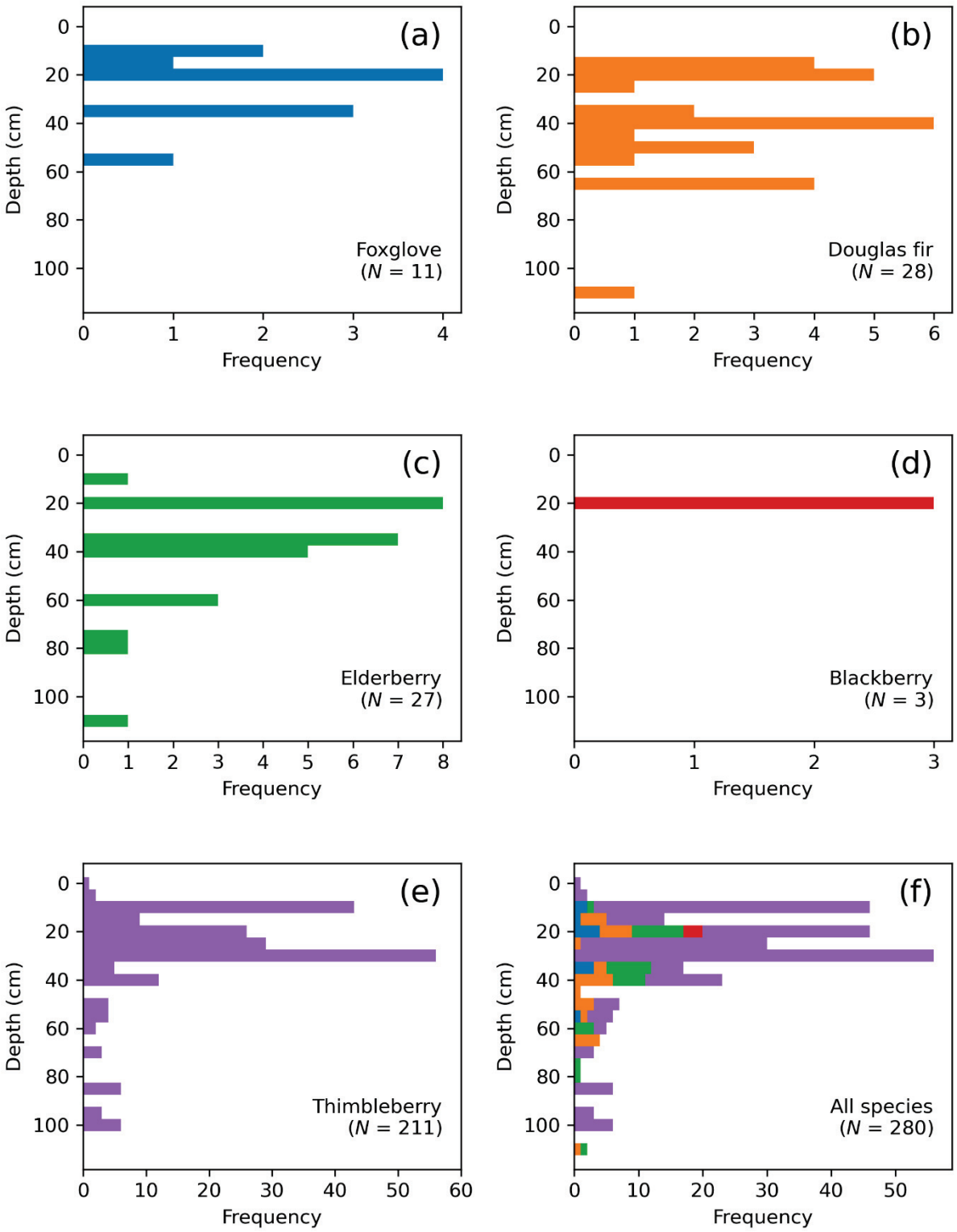

Figure 6. Histograms of depth below ground surface for the roots of each of the vegetation species identified along the landslide scarp. Histograms of depth below ground surface are shown for foxglove (**a**), Douglas fir (**b**), elderberry (**c**), blackberry (**d**), and thimbleberry (**e**). Panel (**f**) shows the histogram of depth below ground surface for roots of all species together.

2.5. Application of Root Breakage Models

2.5.1. Wu and Waldron Model (WWM)

The WWM uses a simple calculation where the total force that can be sustained by the root bundle is the sum of the tensile strengths of all the individual roots in the bundle, multiplied by their cross-sectional areas.

$$F_b = R_f \sum_{i=1}^{N} T_i A_i, \quad (2)$$

where T_i is the tensile strength of the i-th root (in units of stress), A_i is area of the i-th root, and R_f is a correction factor for the inclination angle of the root. We use a value of 1.0 for R_f, following the conclusion of Thomas and Pollen-Bankhead [28] that an R_f value of 1.0 was most appropriate for sites with friction angles between 5° and 45° and failure surface angles between 10° and 90°.

2.5.2. Fiber Bundle Model (FBM)

Pollen and Simon [12] developed the FBM to address the systematic overestimation of root cohesion by the WWM, which assumes simultaneous failure of all roots. A single force is applied to a bundle of parallel fibers according to a load apportionment rule which determines the applied stress on each individual fiber. If the applied stress on a fiber exceeds its tensile strength, the fiber breaks, and it is no longer available to support the applied load in subsequent iterations. Effectively, this process finds the maximum total force that can be sustained by the entire bundle without breaking all the roots. Flowcharts describing the FBM are shown in Pollen and Simon [12] and Dias et al. [7].

In this study, we applied the FBM assuming global load sharing, in which the load is distributed equally among all fibers, rather than local load sharing, in which the load from a broken fiber is distributed disproportionally to its closer neighbors. In this study, we implement the FBM such that the load is distributed equally to each individual root, following the recommendation of Mao et al. [38]. This method of load apportionment ensures that the largest roots break last, making the total bundle strength dependent on the larger roots. This assumption is supported by Cohen et al. [39], who showed that small diameter roots will always be the first to break, and Giadrossich et al. [40], who showed that small roots provide almost no contribution to root reinforcement at the stand scale.

Note that any subset of roots with the same tensile strength and diameter will fail simultaneously. Therefore, in this study, where tensile strength is a function of diameter only, roots of the same species and diameter will either survive or fail together in a single model iteration.

Root Bundle Model-Weibull (RBMw)

The root bundle model-Weibull (RBMw) was developed to account for the effects of elastic deformation on root failure. Schwarz et al. [30] proposed a strain-controlled model, the RBM, that imposes successive displacements to a root bundle and calculates the resisting tensile force that results from the given strain. It is thus possible to calculate the forces acting on the root bundle for any displacement [41]. Schwarz et al. [13] further extended the RBM to account for variability in strength for roots of the same diameter. This extension was named the RBMw (root bundle model-Weibull) because they used a Weibull survival function to represent the decreasing probability of survival as the root is stretched beyond its original length.

The Weibull survival function represents the probability that a root remains unbroken when it has been stretched to a specific displacement. To model the elastic response of the root in a way that is independent of the root diameter, the displacement is normalized based on the elastic properties of the root. For details on how we implemented the RBMw, see Appendix B. The shape parameter ω and the scale parameter λ^* of the Weibull survival function are estimated separately for each species. The resulting parameter values are shown in Figure 7.

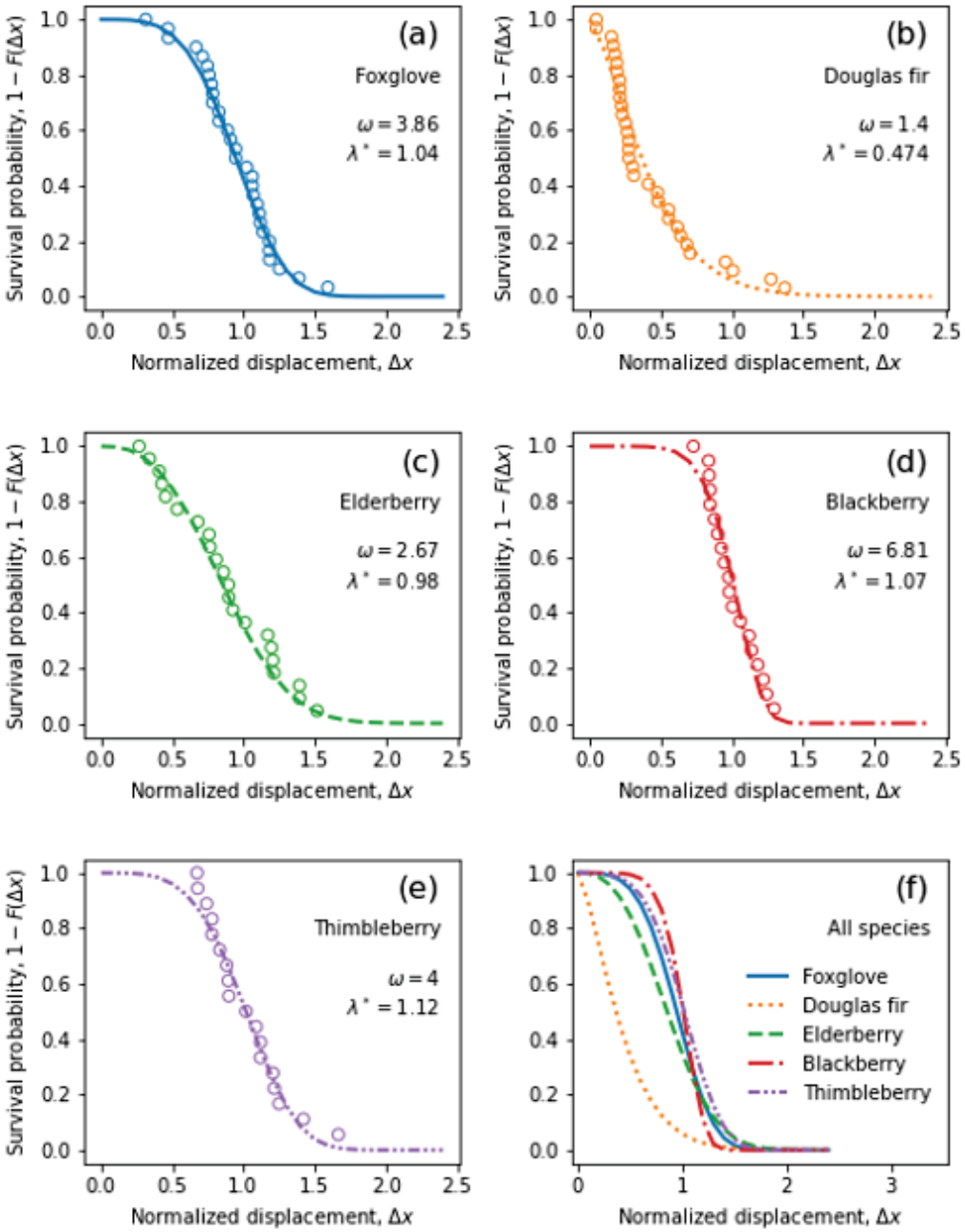

Figure 7. Estimated normalized displacement data (circles) and curve from the fitted Weibull survival function (see Appendix B). Estimated normalized displacement and fitted Weibull survival curves are shown for foxglove (**a**), Douglas fir (**b**), elderberry (**c**), blackberry (**d**), and thimbleberry (**e**). Panel (**f**) shows the estimated normalized displacement and the fitted Weibull survival curves for roots of all species plotted together.

2.6. Calculation of Root Cohesion

For each of the three models (WWM, FBM, and RBMw), the goal is to obtain the maximum force that can be sustained by the bundle. While the WWM directly gives an estimate of the maximum force, the FBM and RBMw produce a force value as a function of the nominal applied force or displacement, respectively. The FBM and RBMw therefore require application over a range of inputs to find the maximum force that can be sustained by the bundle. The root cohesion is calculated as the ratio of the maximum force F_b to the area of the failure surface (A):

$$c_r = F_b / A \tag{3}$$

The root cohesion can be calculated to give a scarp-averaged cohesion value for the entire bundle, without accounting for any spatial variability due to the spatial distribution of roots in the scarp. To obtain a spatially distributed estimate for root cohesion, the domain is discretized into sections (laterally and/or vertically), and the maximum force is calculated individually for each of these smaller sections ranging in cross-sectional area from 0.57 to 4.0 m^2 (when binned by segment) and from 0.42 to 3.3 m^2 (when binned by 10-cm depth intervals).

3. Results

First, we describe the results of the maximum force calculation across the entire landslide scarp without considering any spatial variability in the root cohesion. Figure 8 shows the number of surviving roots as a function of applied force from the FBM. Figure 9 shows the force-displacement curve from the RBMw. Whereas the WWM predicts a maximum force of 101.2 kN, the FBM predicts a much lower maximum force of 26.1 kN. The maximum force from the RBMw is lower still at 18.3 kN. These results are consistent with earlier research showing that the WWM overpredicts cohesion relative to the FBM and the RBMw [12,14]. Additionally, we draw the reader's attention to the strain at which each species reaches its maximum activated force. Whereas both elderberry and Douglas fir exhibit peak values at about 200–300 mm of displacement, the maximum thimbleberry contribution to strength occurs at a much lower displacement value of about 40 mm.

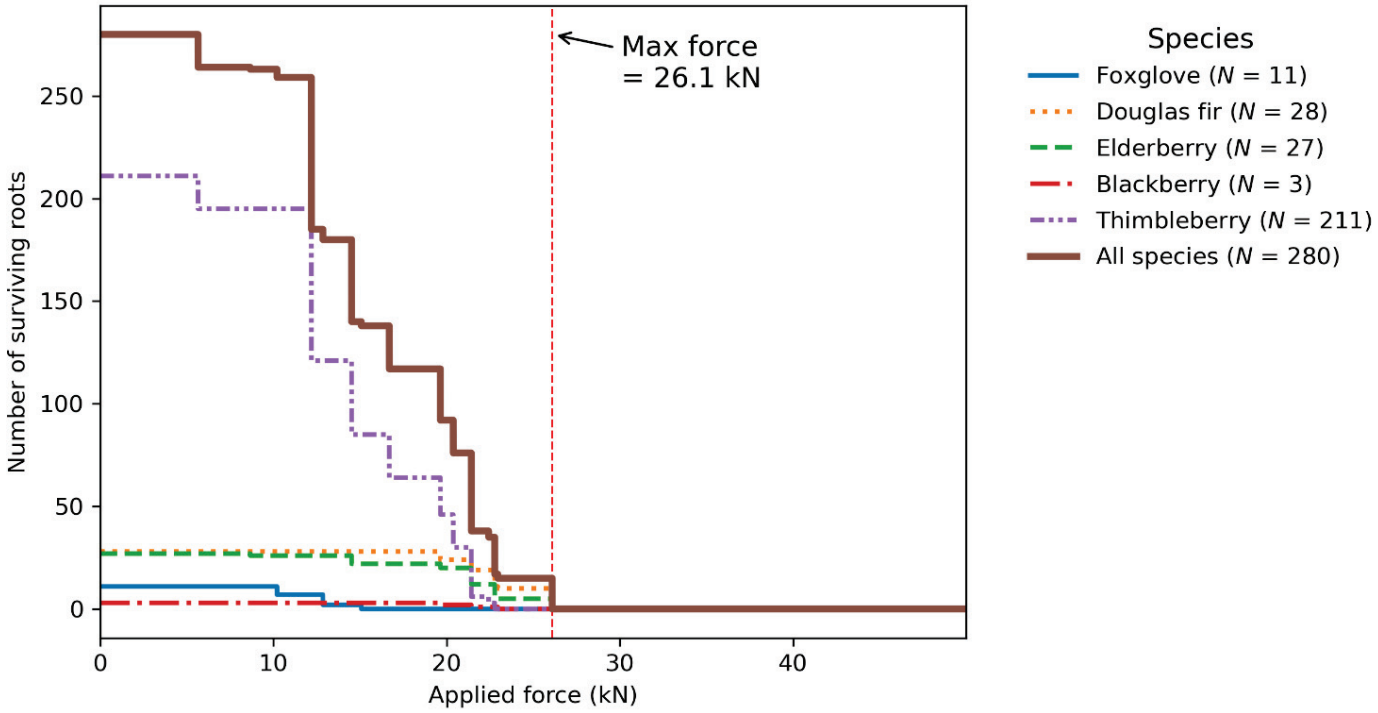

Figure 8. Results from the FBM, showing the number of surviving roots after application of different loads. Vertical dashed line indicates the maximum activated force.

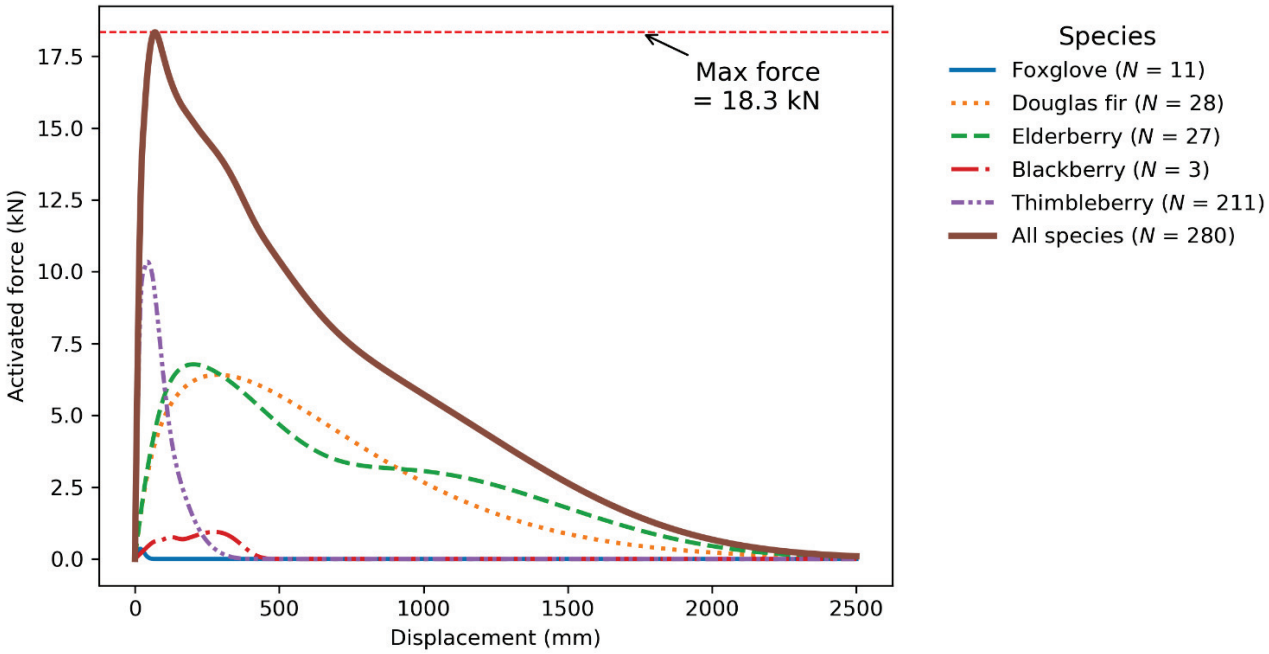

Figure 9. Force-displacement curve resulting from the RBMw model. Horizontal dashed line shows the maximum activated force.

In addition to the scarp-averaged values, we calculated the root cohesion distributed vertically and laterally within the scarp. Along with these distributed values, we describe the percent contribution to the overall bundle strength from vertical and lateral sections of the scarp. Because of the nonlinearity of the FBM and RBMw models, a general formula for the contribution of any one section k of the bundle is posed as a percent reduction in strength (PRS) for the bundle without group k:

$$PRS_k = 100\left[\frac{\left(F_b - F_{(b-k)}\right)}{F_b}\right] \quad (4)$$

where F_b is the maximum force for the entire bundle, and $F_{(b-k)}$ is the maximum force for the bundle with all the roots belonging to group k removed. Group k could represent a group of roots at a particular depth, a particular section along the perimeter of the scarp, and/or roots belonging to a specific species.

3.1. Scarp-Averaged Cohesion

When converted to root cohesion averaged over the entire 37 m long slide scarp, which has a total cross-sectional area of 21.8 m^2, the root cohesion is 4.6 kPa for the WWM, 1.2 kPa for the FBM, and 0.8 kPa for the RBMw. In their comparative study of the three models, Zydron and Skorski [15] obtained similar results for the relative cohesion estimates for two different tree species. However, the ratios of FBM-estimated cohesion and RBMw-estimated cohesion to the WWM-estimated cohesion, which are 0.18 and 0.26, respectively, are somewhat lower than estimates of comparable ratios from other researchers (see Section 2.1). Results for the scarp-averaged root cohesion are summarized in Table 1.

Table 1. Results for root cohesion averaged over the entire CB1 landslide scarp.

Model	Maximum Force (kN)	Root Cohesion (kPa)	WWM Reduction Factor
WWM	101.2	4.6	1
FBM	26.1	1.2	0.26
RBMw	18.3	0.8	0.18

3.2. Root Cohesion by Depth

Root cohesion was calculated along different depth bins to highlight variability with depth below the ground surface. All three models show that cohesion diminishes below a depth of about 80 cm, with no model predicting cohesion greater than 2 kPa below this depth. However, there are substantial discrepancies in the cohesion values as well as the relationship versus depth that depend on the breakage model. The maximum root cohesion calculated by the WWM, for example, is 11.4 kPa, which is approximately 40% greater than the root cohesion calculated from the FBM at 8.1 kPa, and five times greater than the root cohesion calculated by the RBMw method at 2.3 kPa. The maximum activated forces and the root cohesion for the 10-cm depth bins are shown in Figure 10.

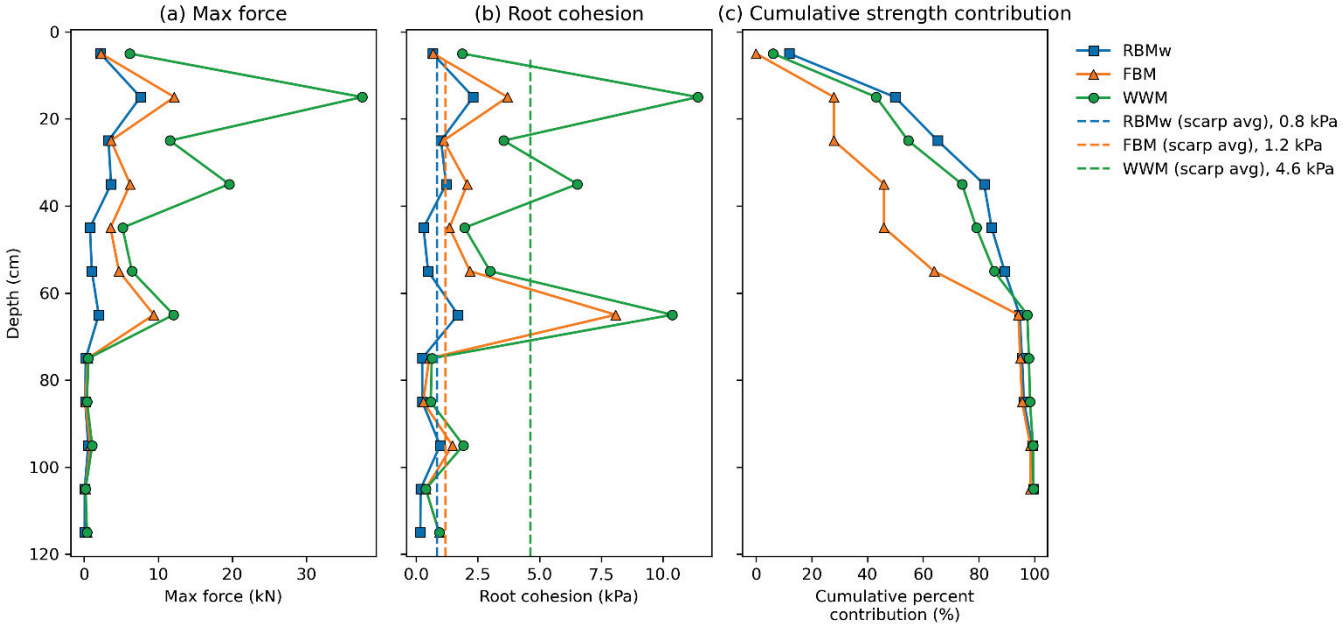

Figure 10. Root strength variation by depth calculated over the perimeter of the landslide scarp. Panel (**a**) shows maximum activated force, and (**b**) shows cohesion, superimposed over the scarp-averaged cohesion values for comparison depicted as vertical dashed lines. Panel (**c**) shows the cumulative strength contribution with increasing depth for each of the three models. All quantities are calculated over all roots within 10-cm depth increments along the scarp plane; negligible roots intersecting the basal surface are not included.

For the WWM and RBMw models, root cohesion reaches its maximum at a depth of 10–20 cm below the ground surface, and for these two models, roughly 80% of the root cohesion provided by these shallowly rooted plants species is in the top 40 cm of the regolith, with background negligible values at deeper soil depths. However, when using the FBM, the maximum cohesion occurs at a depth of approximately 60–70 cm below the ground surface. These results demonstrate the influence of the root strength model in calculating root cohesion and the implications for applying these values in the context of slope stability modeling in landscapes with plant species expressing different characteristic rooting depths. Similar results were reported by Zydron and Skorski [15], who reported that the WWM consistently produced the highest root cohesion values with depth, the RBMw produced the lowest, and the FBM produced values that fell between the results of the other two models.

3.3. Root Cohesion along the Scarp Perimeter

The results also show that root cohesion is not homogeneous in the planform dimension along the perimeter of the landslide scarp. The maximum force and the cohesion calculated along the segments of the scarp are shown in Figure 11. For segment 3, the

cohesion is <0.05 kPa for all three models, while in segment 9, the cohesion ranges from 3.1 kPa when calculated by the RBMw to 12.9 kPa when calculated by the WWM. The differences in the relative magnitudes of cohesion estimated by each of the three models are also evident in the depth-dependent and scarp-averaged cohesion values.

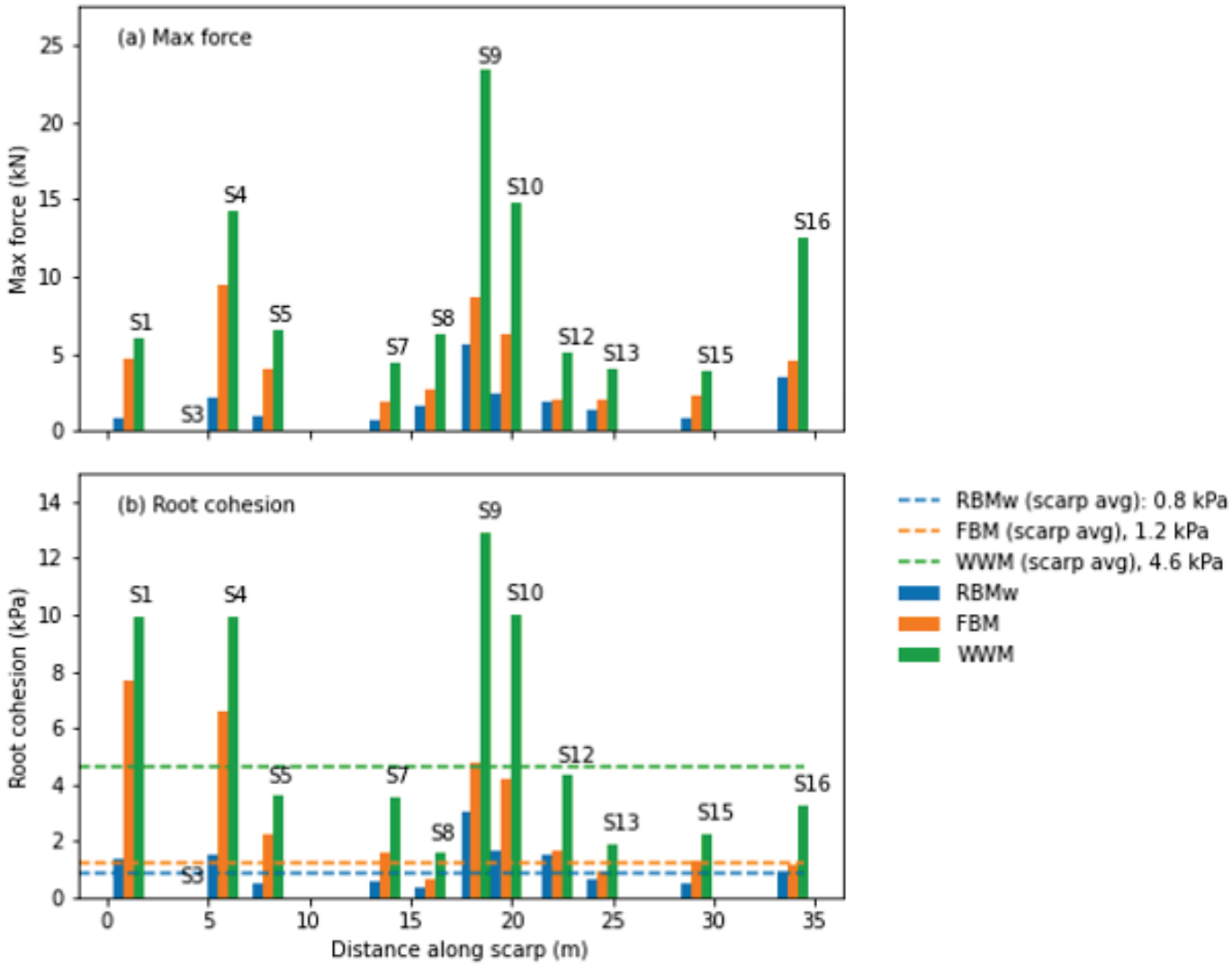

Figure 11. Maximum activated force (**a**) and root cohesion (**b**) calculated independently for each scarp segment, showing lateral variation along the perimeter of the landslide scarp. Panel (**a**) shows maximum activated force, and (**b**) shows root cohesion, with the scarp-averaged cohesion superimposed as horizontal dashed lines for comparison. Both quantities are calculated within each segment along the length of the scarp perimeter; negligible roots intersecting the basal surface are not included. S1 through S16 denote the scarp segments depicted in Figure 4a.

The planform distribution of root cohesion may be less informative than the depth distribution, since it mostly reflects the spatial location of roots belonging to specific plants, whereas the vertical distribution may be more indicative of a generalized relationship with depth. However, the lateral root distribution indicates areas of low root cohesion along the scarp perimeter, which could indicate gaps in vegetative root reinforcement and initiation areas for shallow landslides. For instance, Roering et al. [42] suggested that shallow landslides occur in areas of low root cohesion between trees; they presented a simple method for mapping of the distribution of trees and their canopies in hollows to quantify the landslide susceptibility.

Calculating the root cohesion by segment and by depth, as shown in Figure 12, provides more evidence that the cohesion has significant spatial heterogeneity. Although depth bins have a uniform size of 10 cm, the variation in the width of each segment results in the areas over which cohesion was calculated varying between 0.08 m^2 and 0.65 m^2. Figure 12 shows that cohesion is highly concentrated within areas that have a high density of elderberry and Douglas fir roots, which have the greatest tensile strengths. For all three models, the cohesion distribution among the different depth/segment sections has a skewness greater than 5, indicating the very high degree of spatial concentration. For the depth/segment sections with the greatest contribution, while most depth/segment sections contribute <1% to the overall root cohesion, the percent contribution for the strongest section is 16% for the WWM, 23% for the FBM, and 12% for the RBMw. Alternatively, the cohesion of the strongest individual section is 123 kPa for the WWM, 99 kPa for the FBM, and 34 kPa for the RBMw, values which are greater than the scarp-averaged cohesion calculated from the respective model by a factor greater than 25. This relation highlights the great spatial variability and localized maxima adjacent to denser, spatially concentrated, plant roots.

3.4. Contribution of Cohesion by Species

The amount of cohesion contributed by each of the species within the CB1 landslide scarp is an especially important question from a geotechnical engineering point of view because it addresses which species could be most effective for slope stabilization [2,18]. The contribution of root cohesion by a particular species represents the PRS that would occur if roots from that species were removed from the bundle, calculated using Equation (4). Figure 13 shows the contribution of root cohesion by species for each of the three models. The best way to interpret the results shown in Figure 13 is to compare the contributions from different species in the FBM and RBMw to those in the WWM. This figure reveals two interesting results. First, in the FBM model, the only two species that contribute to the cohesion are Douglas fir and elderberry, which have the greatest tensile strength for large diameter roots. This suggests that the results of the FBM are especially sensitive to the tensile strength of the largest diameter roots. Second, the greatest strength contribution in the RBMw model derives from thimbleberry and slightly exceeds that of either Douglas fir or elderberry. The force-displacement curve in Figure 9 shows that the maximum resisting force of each species is mobilized at different displacements. Furthermore, those resisting forces activate over different ranges of displacement. While thimbleberry roots impart a high strength, most of this strength is activated at displacements generally less than 250 mm, whereas the strength of Douglas fir and elderberry roots is activated over a much wider range of displacements. Although thimbleberry is relatively weak in tensile strength compared to Douglas fir and elderberry, its peak resisting force is concentrated at a different displacement than Douglas fir and elderberry, allowing it to complement the cohesion from the two stronger species.

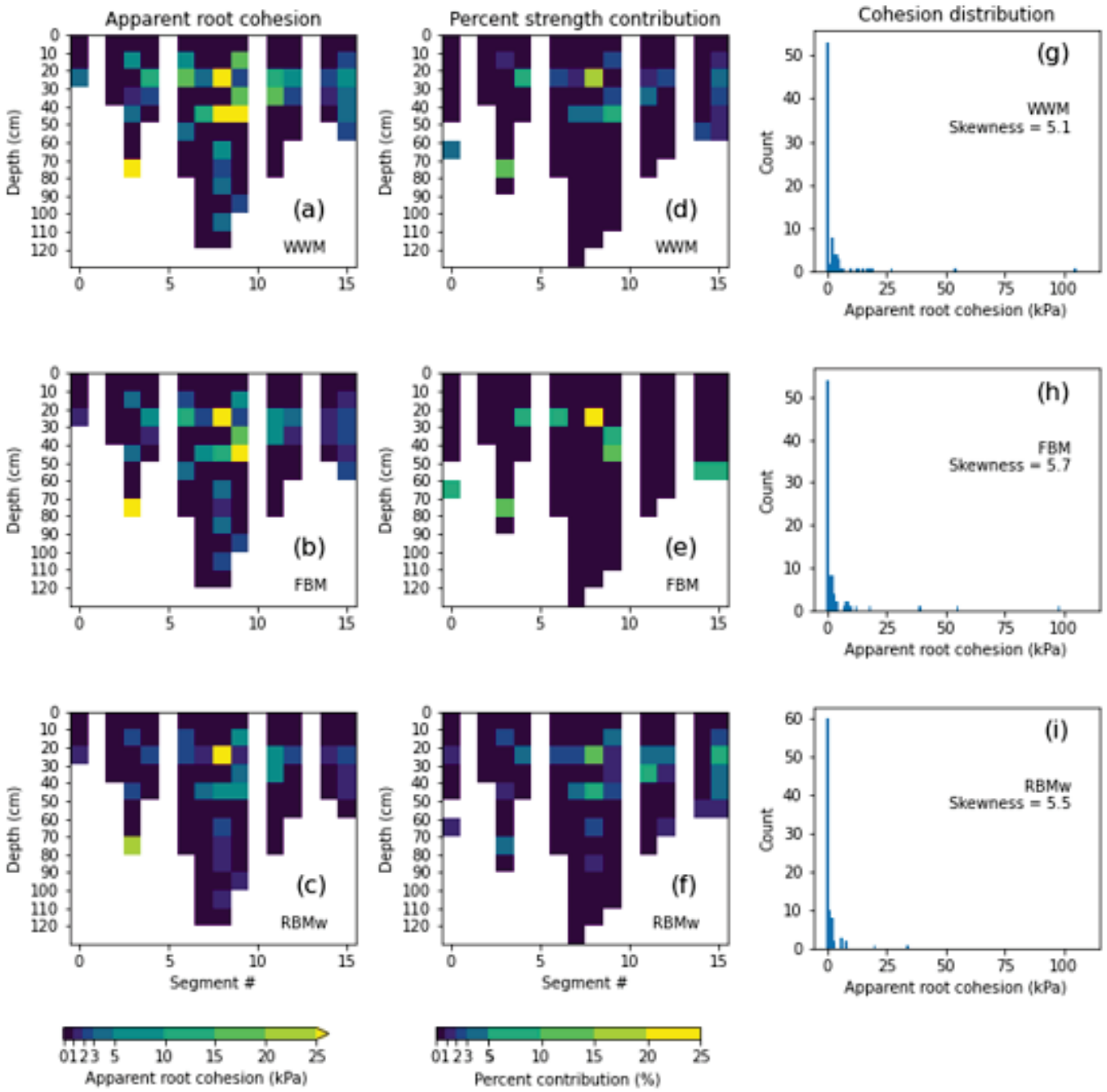

Figure 12. Root cohesion (**a**–**c**) and percent strength contribution (**d**–**f**) calculated by segment and 10-cm depth bin along the landslide scarp for each of the three models. The distribution of cohesion across different segment and depth bins (**g**–**i**) shows that cohesion has a high degree of spatial heterogeneity across the scarp.

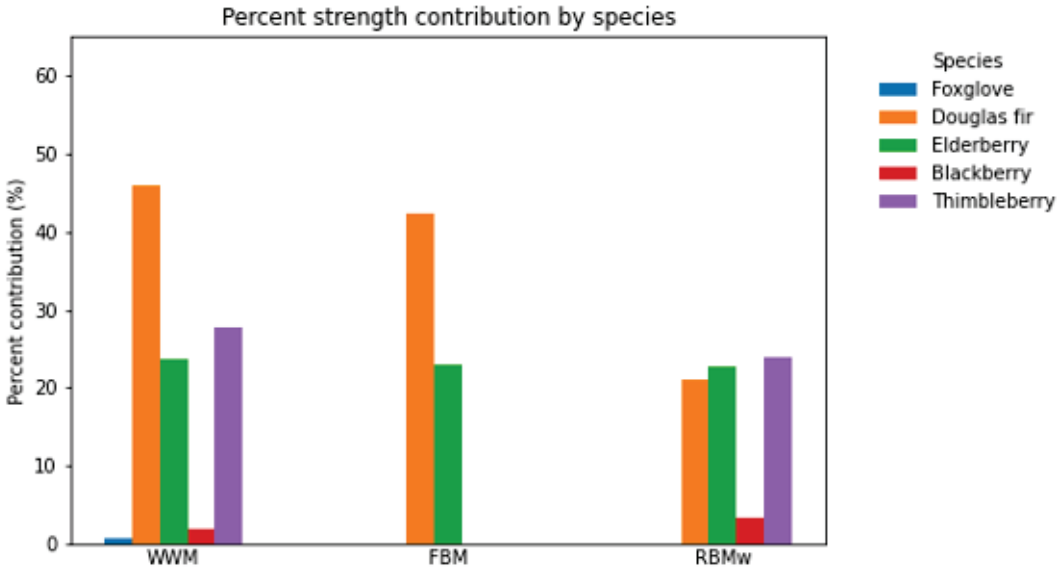

Figure 13. Contribution of root cohesion by species calculated for each of the three models. Because of the nonlinearity of the FBM and RBMw models, the contributions for FBM and RBMw will not necessarily sum to 100%.

4. Discussion

Although our results clearly show that cohesion estimates by both the FBM and the RBMw are substantially less than those estimated by the WWM, at present, we have no independent means to evaluate which model results are the most representative of actual site conditions. It is well known that the assumptions of simultaneous failure in the WWM are unrealistic and represent an upper bound on the strength of a root bundle. Both the RBMw and FBM were developed to represent progressive failure, which we believe is much more realistic generally. Although the results on the accuracy of root breakage models compared to experimental and field tests varies widely (see Table 1 in Ji et al. [43]), it is well established that the WWM overestimates the root strength [12,14]. Schwarz et al. [17] report that for lateral reinforcement along a landslide scarp, the WWM overpredicts root cohesion by approximately a factor of three, a finding supported by other studies [12,39,44]. Our results also indicate that progressive failure models produce scarp-averaged cohesion values that are 18% and 26% of the WWM-estimated value for RBMw and FBM, respectively, a result which is approximately consistent with these studies and others [15]. These results are strong evidence that the WWM-estimated values represent overestimation of the root strength at CB1 as well. However, the magnitude of overestimation is expected to vary depending on the local root diameter distribution and the thread strength of individual species.

The likely overestimation of root cohesion by the WWM has important implications beyond the CB1 site. Schmidt et al. [25] investigated CB1 as one of several landslide sites and compared the root cohesion values in terms of the land use and disturbance history, particularly in terms of the forest management. The results of that study indicated that the root cohesion at CB1 was broadly consistent with values (a range of 1.5–6.7 kPa) for other clearcuts with a disturbance less than 11 years old. By comparison, Schmidt et al. [25] estimated that median lateral root cohesion in industrial forests up to 123 years old fell in the range of 6.8–23.2 kPa and old growth forests fell in the range of 25.6–94.3 kPa. If these estimates, obtained using the WWM, overestimate the root strength by the degree suggested in this study and others, these results are likely to be overestimates as well, and caution should be exercised when quoting or applying these values in new investigations. As previously reported values from Schmidt et al. [25] have been cited in other publications [19,21,22,26,27], these values in the literature should be used with great discretion.

There are major discrepancies between the root strength values calculated using the various models. These results point to the importance of using models that are physically realistic and account for the important processes governing root behavior under tension, including differential displacement and load redistribution. The three models have differences in which species impart the greatest contribution to the overall bundle strength. For instance, the FBM-modeled cohesion is contributed entirely by two species, Douglas fir and elderberry (Figure 13). However, field observations revealed broken roots of all five species measured along the scarp. Observations of broken root threads are consistent with a mobilization of a finite contribution of strength by a broader array of roots than indicated by the FBM approach. Alternatively, the RBMw model results highlight the control of species on the resisting forces activated over a range of displacements (Figure 9). Hence, the RBMw model results suggest that a range of species with different tensile strength characteristics may more effectively hinder landslide deformation at a range of displacements. In Figure 13, the RBMw model results indicate a contribution from all species except for foxglove in the total contribution to strength. Foxglove roots were both small in diameter and limited in number and as such could be expected to play a minimal role in the total resistance. Hence, results from the RBMw model are more consistent with observations of broken roots of all species along the slide scarp.

Additionally, more sophisticated models also consider root behavior under compression [4,45], a process which is not considered in this paper. In the distal extents of landslides, roots undergo compression, imparting a lower strength than their tensional forces [4,45]. However, remaining evidence following the CB1 landslide did not allow for any estimate of root behavior in the landslide toe where compression would be more pronounced. Such evidence was removed by the passage of the landslide and downslope debris flow (Figures 1 and 2). None of the models applied in this study account for all these processes. Future research directions should continue applying models that account for these processes in addition to pursuing root model validation through alternate means to evaluate actual model robustness.

5. Conclusions

Earlier publications that quantified the contribution of vegetation roots at the CB1 landslide site reported the apparent root cohesion had a spatially averaged, static value of 4.6 kPa over the entire scarp [19,25], without considering the heterogeneity of root cohesion across the failure plane. These analyses were based on the Wu and Waldron model (WWM). We believe that root breakage models that account for progressive root failure better characterize the reinforcement mechanics at the CB1 site, which failed with progressive landslide deformation prior to debris flow mobilization. Hence, the static value of 4.6 kPa determined from the WWM is likely an overestimate and such values should not be used in subsequent numeric landslide susceptibility models. Furthermore, the RBMw results from CB1 indicate that root cohesion may be less than a fifth of the static WWM value (0.8 kPa). Combined with other research suggesting that the WWM can substantially overpredict root cohesion, this result suggests that the vegetation roots contribute far less cohesion to the soil than indicated by earlier investigations at CB1. Additionally, because the vegetation is responsible for nearly all the cohesion in the root–soil composite, and the mineral component of the soil has been shown to have negligible cohesion, this result means that the overall regolith has far less cohesion than previously established by Schmidt et al. [25].

Despite the discrepancies in the magnitude of the apparent root cohesion, the results of all three models consistently show that root cohesion has significant spatial heterogeneity, corroborating the conclusion of Schwarz et al. [17]. This result has important implications for slope stability modeling, which because of constraints on model input parameters have traditionally assumed that root cohesion is a homogeneous, spatially invariant value. When combined with site-specific data on topography, hydrologic response to rainfall, and material properties available for the CB1 site, slope-stability analysis will allow these three

root models to be tested against factors of safety estimated from three-dimensional slope stability models.

Author Contributions: C.C.-R., conceptualization, methodology, formal analysis, investigation, data curation, visualization, writing—original draft, writing—review and editing; K.M.S., conceptualization, investigation, data curation, writing—review and editing, supervision; C.W., conceptualization, methodology, writing—review and editing. All authors have read and agreed to the published version of the manuscript.

Funding: This research was supported by the U.S. Geological Survey Landslide Hazards and National Cooperative Geologic Mapping Programs.

Data Availability Statement: Data used in this study are available in the accompanying data release by Schmidt and Cronkite-Ratcliff [35].

Acknowledgments: The authors would like to thank Jonathan P. Perkins of USGS and five anonymous reviewers for their thoughtful comments which improved the manuscript.

Conflicts of Interest: The authors declare no conflict of interest.

Appendix A

We use the same method of estimating thread tensile strength as Schmidt et al. [25], who used a second-order polynomial regression model to represent maximum tensile load:

$$F_{max}(d) = ad + bd^2, \tag{A1}$$

where F_{max} is the tensile load and a and b are scaling factors.

While Equation (A1) gives the maximum load in units of force, many root breakage models, particularly the FBM, use tensile strength in units of stress. For this reason, we first estimate maximum force at failure using Equation (A1) and then convert to units of stress. Equation (A1) can be converted to negative power-law form by dividing by the cross-sectional area of the root to convert the dependent variable to units of stress. This conversion transforms the relationship to be linear in the reciprocal of the diameter [46]:

$$T_{max}(d) = ud^{-1} + c, \tag{A2}$$

where T_{max} is the tensile strength, u is a scaling factor and c is a constant.

To estimate the tensile load at failure for each species, we use ordinary least squares regression to obtain fits to Equation (A1). We then convert the results to the form of Equation (A2) to obtain results in units of tensile strength. In our specific case, where the tensile force is represented by a load measured in kilograms [25], we first multiply the load by the standard acceleration of gravity to obtain units of force before converting to Equation (A2).

Appendix B

In the RBMw, roots are modeled with linear-elastic deformation that break at a threshold displacement [13]. The average root length L, the average maximum tensile force F, and the average elastic modulus E are modeled as power-law functions of root diameter d [13,30]:

$$L(d) = L_0 d^{\gamma} \tag{A3}$$

$$E(d) = rE_0 d^{\beta} \tag{A4}$$

where L_0 and E_0 are scaling factors for length and elastic modulus, respectively, β and γ are exponents, and r is a scaling factor which accounts for reduction in the elastic modulus due to root tortuosity [13].

Using the above equations, the tensile force sustained by a root as a function of the diameter d and the displacement Δx is:

$$F(d, \Delta x) = \frac{\pi r E_0}{4 L_0} d^{2+\beta-\gamma} \, \Delta x \, , \quad F(d, \Delta x) < F_{max}(d) \tag{A5}$$

where F_{max} represents the maximum tensile force of the root (Equation (A1)). For a given displacement Δx, the force mobilized by the bundle is the sum of the forces on each root at that displacement:

$$F_b(\Delta x) = \sum_{i=1}^{N} F(d, \Delta x) \tag{A6}$$

To represent the variability in the mechanical properties of roots of the same diameter, Schwarz et al. [13] use the two-parameter Weibull survival function defined by the scale parameter λ^* and the shape parameter ω:

$$S(\Delta x^*) = \exp\left[-\left(\frac{\Delta x^*}{\lambda^*} \right)^{\omega} \right] \tag{A7}$$

where Δx^* represents the normalized displacement. The normalized displacement is the ratio of the displacement Δx to the displacement at which the root fails, Δx_{max}:

$$\Delta x^* = \frac{\Delta x}{\Delta x_{max}} \tag{A8}$$

By introducing the Weibull survival function, the force mobilized by roots of the same diameter becomes dependent on displacement as well as the diameter. This additional dependence is achieved by multiplying the force on each root by its probability of survival for a given normalized displacement, giving the term $F(d_i, \Delta x)\, S(\Delta x^*)$. The total strength of the root bundle at a given normalized displacement is the sum of forces mobilized by all roots at that displacement:

$$F_b(\Delta x) = \sum_{i=1}^{N} F(d_i, \Delta x) S(\Delta x^*) \tag{A9}$$

The RBMw requires a range of displacements to be applied to the bundle using Equation (A9), until the maximum applied force is found.

In our model, root length L was calculated using Equation (A3), and the elastic modulus E was calculated using Equation (A4). As no site- nor species-specific values for the scaling factors and exponents were available, we adopted values from Schwarz et al. [30] that fit data for 27 spruce roots: E_0 is 696 MPa mm, L_0 is 335 mm, β is -1, and γ is 0.63. Because the value for E_0 accounts for the effects of tortuosity, the tortuosity coefficient r from Equations (A4) and (A5) is effectively equal to 1 [30]. Root force at failure F_{max} was obtained by Equation (A1) using coefficient values shown in Figure 3.

Because Weibull survival function parameters must be calibrated from the normalized displacement, we estimate the normalized displacement from the experimental data described in Section 2.3. We represent the displacement at which the root fails, Δx_{max}, as the displacement where the applied force equals root force at failure F_{max}. The normalized displacement was estimated as the ratio of the measured displacement to the displacement at failure (Equation (A8)). However, because the displacement is linearly proportional to force, the normalized displacement is equivalent to the ratio of the measured tensile force F_{meas} to the estimated tensile force at failure F_{max}:

$$\Delta x^* = \frac{F_{meas}}{F_{max}} \tag{A10}$$

The estimated normalized displacement values used to calibrate the Weibull functions are therefore equivalent to the multiplicative residuals from the tensile force regression models (Equation (A1); Figure 3). The Weibull survival function shape and scale parameters

(Figure 7) are estimated separately for each species using maximum likelihood estimation (e.g., Lee [47]).

References

1. Sidle, R.C.; Ochiai, H. *Landslides: Processes, Prediction, and Land Use*; American Geophysical Union Water Resources Monograph 18; American Geophysical Union: Washington, DC, USA, 2006.
2. Stokes, A.; Atger, C.; Bengough, A.G.; Fourcaud, T.; Sidle, R.C. Desirable plant root traits for protecting natural and engineered slopes against landslides. *Plant Soil* **2009**, *324*, 1–30. [CrossRef]
3. Stokes, A.; Douglas, G.B.; Fourcaud, T.; Giadrossich, F.; Gillies, C.; Hubble, T.; Kim, J.H.; Loades, K.W.; Mao, Z.; McIvor, I.R.; et al. Ecological mitigation of hillslope instability: Ten key issues facing researchers and practitioners. *Plant Soil* **2014**, *377*, 1–23. [CrossRef]
4. Cohen, D.; Schwarz, M. Tree-root control of shallow landslides. *Earth Surf. Dyn.* **2017**, *5*, 451–477. [CrossRef]
5. Montgomery, D.R.; Schmidt, K.M.; Greenberg, H.M.; Dietrich, W.E. Forest clearing and regional landsliding. *Geology* **2000**, *28*, 311–314. [CrossRef]
6. Iglesias, V.; Balch, J.K.; Travis, W.R. US fires became larger, more frequent, and more widespread in the 2000s. *Sci. Adv.* **2022**, *8*, eabc0020. [CrossRef]
7. Dias, A.S.; Pirone, M.; Urciuoli, G. Review on the Methods for Evaluation of Root Reinforcement in Shallow Landslides. In *Advancing Culture of Living with Landslides*; Mikos, M., Tiwari, B., Yin, Y., Sassa, K., Eds.; Springer: New York, NY, USA, 2017; pp. 641–648. [CrossRef]
8. Mao, Z. Root reinforcement models: Classification, criticism and perspectives. *Plant Soil* **2022**, *472*, 17–28. [CrossRef]
9. Wu, T.H. *Investigation of Landslides on Prince of Wales Island, Alaska*; Alaska Geotechnical Report Issue 5; Department of Civil Engineering, Ohio State University: Columbus, OH, USA, 1976.
10. Waldron, L.J. The shear resistance of root-permeated homogeneous and stratified soil. *Soil Sci. Soc. Am. J.* **1977**, *41*, 843–849. [CrossRef]
11. Wu, T.H.; McKinnell, W.P.; Swanston, D.N. Strength of tree roots and landslides on Prince of Wales Island, Alaska. *Can. Geotech. J.* **1979**, *16*, 19–33. [CrossRef]
12. Pollen, N.; Simon, A. Estimating the mechanical effects of riparian vegetation on stream bank stability using a fiber bundle model. *Water Resour. Res.* **2005**, *41*, W07025. [CrossRef]
13. Schwarz, M.; Giadrossich, F.; Cohen, D. Modeling root reinforcement using a root-failure Weibull survival function. *Hydrol. Earth Syst. Sci.* **2013**, *17*, 4367–4377. [CrossRef]
14. Docker, B.B.; Hubble, T.C.T. Quantifying root-reinforcement of river bank soils by four Australian tree species. *Geomorphology* **2008**, *100*, 401–418. [CrossRef]
15. Zydron, T.; Skorski, L. The effect of root reinforcement exemplified by black alder (*Alnus glutinosa* Gaertn.) and basket willow (*salix viminalis*) root systems—Case study in Poland. *Appl. Ecol. Environ. Res.* **2018**, *16*, 407–423. [CrossRef]
16. Schwarz, M.; Preti, F.; Giadrossich, F.; Lehmann, P.; Or, D. Quantifying the role of vegetation in slope stability: A case study in Tuscany (Italy). *Ecol. Eng.* **2010**, *36*, 285–291. [CrossRef]
17. Schwarz, M.; Cohen, D.; Or, D. Spatial characterization of root reinforcement at the stand scale: Theory and case study. *Geomorphology* **2012**, *171–172*, 190–200. [CrossRef]
18. Ghestem, M.; Cao, K.; Ma, W.; Rowe, N.; Leclerc, R.; Gadenne, C.; Stokes, A. A framework for identifying plant species to be used as 'ecological engineers' for fixing soil on unstable slopes. *PLoS ONE* **2014**, *9*, e95876. [CrossRef]
19. Montgomery, D.R.; Schmidt, K.M.; Dietrich, W.E.; McKean, J. Instrumental record of debris flow initiation during natural rainfall: Implications for modeling slope stability. *J. Geophys. Res.* **2009**, *114*, F01031. [CrossRef]
20. Anderson, S.P.; Dietrich, W.E.; Montgomery, D.R.; Torres, R.; Conrad, M.E.; Loague, K. Subsurface flowpaths in a steep, unchanneled catchment. *Water Resour. Res.* **1997**, *33*, 2637–2653. [CrossRef]
21. Ebel, B.A.; Loague, K.; Borja, R.I. The impact of hysteresis on variably saturated hydrologic response and slope failure. *Environ. Earth Sci.* **2010**, *61*, 1215–1225. [CrossRef]
22. Ebel, B.A.; Godt, J.W.; Lu, N.; Coe, J.A.; Smith, J.B.; Baum, R.L. Field and laboratory hydraulic characterization of landslide-prone soils in the Oregon Coast Range and implications for hydrologic simulation. *Vadose Zone J.* **2018**, *17*, 180078. [CrossRef]
23. Montgomery, D.R.; Dietrich, W.E.; Torres, R.; Anderson, S.P.; Heffner, J.T.; Loague, K. Hydrologic response of a steep, unchanneled valley to natural and applied rainfall. *Water Resour. Res.* **1997**, *33*, 91–109. [CrossRef]
24. Torres, R.; Dietrich, W.E.; Montgomery, D.R.; Anderson, S.P.; Loague, K. Unsaturated zone processes and the hydrologic response of a steep, unchanneled catchment. *Water Resour. Res.* **1998**, *34*, 1865–1879. [CrossRef]
25. Schmidt, K.M.; Roering, J.J.; Stock, J.; Dietrich, W.E.; Montgomery, D.R.; Schaub, T. The variability of root cohesion as an influence on shallow landslide susceptibility in the Oregon Coast Range. *Can. Geotech. J.* **2001**, *38*, 995–1024. [CrossRef]
26. Casadei, M.; Dietrich, W.E.; Miller, N. Controls on shallow landslide size. In *Debris-Flow Hazards Mitigation: Mechanics, Prediction, and Assessment*; Rickenmann, D., Chen, C., Eds.; IOS Press: Amsterdam, The Netherlands, 2003; pp. 91–101.
27. Milledge, D.G.; Bellugi, D.; McKean, J.A.; Densmore, A.L.; Dietrich, W.E. A multidimensional stability model for predicting shallow landslide size and shape across landscapes. *J. Geophys. Res. Earth* **2014**, *119*, 2481–2504. [CrossRef] [PubMed]

28. Thomas, R.E.; Pollen-Bankhead, N. Modeling root-reinforcement with a fiber-bundle model and Monte Carlo simulation. *Ecol. Eng.* **2010**, *36*, 47–61. [CrossRef]
29. Abernathy, B.; Rutherfurd, I.D. The effect of riparian tree roots on the mass stability of riverbanks. *Earth Surf. Process. Landf.* **2000**, *25*, 921–937. [CrossRef]
30. Schwarz, M.; Cohen, D.; Or, D. Root-soil mechanical interactions during pullout and failure of root bundles. *J. Geophys. Res.* **2010**, *115*, F04035. [CrossRef]
31. Preti, F.; Schwarz, M. On root reinforcement modeling. *Geophys. Res. Abstr.* **2006**, *8*, 4555.
32. Arnone, E.; Caracciolo, D.; Noto, L.V.; Preti, F.; Bras, R.L. Modeling the hydrological and mechanical effect of roots on shallow landslides. *Water Resour. Res.* **2016**, *52*, 8590–8612. [CrossRef]
33. Emadi-Tafti, M.; Ataie-Ashtiani, B. A modeling platform for landslide stability: A hydrological approach. *Water* **2019**, *11*, 2146. [CrossRef]
34. Wu, T.H. Root reinforcement of soil: Review of analytical models, test results, and applications to design. *Can. Geotech. J.* **2013**, *50*, 259–274. [CrossRef]
35. Schmidt, K.M.; Cronkite-Ratcliff, C. *Root Thread Strength, Landslide Headscarp Geometry, and Observed Root Characteristics at the Monitored CB1 Landslide, Oregon, USA.*; U.S. Geological Survey Data Release; U.S. Geological Survey: Reston, VA, USA, 2022. [CrossRef]
36. Caplan, J.S.; Yeakley, J.A. *Rubus armeniacus* (Himalayan blackberry) Occurrence and Growth in Relation to Soil and Light Conditions in Western Oregon. *Northwest Sci.* **2006**, *80*, 9–17.
37. Burroughs, E.R.; Thomas, B.R. *Declining Root Strength in Douglas-Fir after Felling as a Factor in Slope Stability*; USDA Forest Service Research Paper INT-190; U.S. Department of Agriculture: Ogden, UT, USA, 1977; 40p.
38. Mao, Z.; Saint-Andre, L.; Genet, M.; Mine, F.X.; Jourdan, C.; Rey, H.; Courbaud, B.; Stokes, A. Engineering ecological protection against landslides in diverse mountain forests: Choosing cohesion models. *Ecol. Eng.* **2012**, *45*, 55–69. [CrossRef]
39. Cohen, D.; Schwarz, M.; Or, D. An analytical fiber bundle model for pullout mechanics of root bundles. *J. Geophys. Res.* **2011**, *116*, F03010. [CrossRef]
40. Giadrossich, F.; Cohen, D.; Schwarz, M.; Ganga, A.; Marrosu, R.; Pirastru, M.; Capra, G.F. Large roots dominate the contribution of trees to slope stability. *Earth Surf. Process. Landf.* **2019**, *44*, 1602–1609. [CrossRef]
41. Vergani, C.; Schwarz, M.; Cohen, D.; Thormann, J.J.; Bischetti, G.B. Effects of root tensile force and diameter distribution variability on root reinforcement in the Swiss and Italian Alps. *Can. J. For. Res.* **2014**, *44*, 1426–1440. [CrossRef]
42. Roering, J.J.; Schmidt, K.M.; Stock, J.D.; Dietrich, W.E.; Montgomery, D.R. Shallow landsliding, root reinforcement, and the spatial distribution of trees in the Oregon Coast Range. *Can. Geotech. J.* **2003**, *40*, 237–253. [CrossRef]
43. Ji, J.; Mao, Z.; Qu, W.; Zhang, Z. Energy-based fibre bundle model algorithms to predict soil reinforcement by roots. *Plant Soil* **2020**, *446*, 307–329. [CrossRef]
44. Schwarz, M.; Lehmann, P.; Or, D. Quantifying lateral root reinforcement in steep slopes—From a bundle of roots to tree stands. *Earth Surf. Process. Landf.* **2010**, *35*, 354–367. [CrossRef]
45. Schwarz, M.; Rist, A.; Cohen, D.; Giadrossich, F.; Egorov, P.; Büttner, D.; Stolz, M.; Thormann, J.J. Root reinforcement of soils under compression. *J. Geophys. Res. Earth* **2015**, *120*, 2103–2120. [CrossRef]
46. Tosi, M. Root tensile strength relationships and their slope stability implications of three shrub species in the Northern Apennines (Italy). *Geomorphology* **2007**, *87*, 268–283. [CrossRef]
47. Lee, E.T. *Statistical Models for Survival Analysis*; Wiley: Hoboken, NJ, USA, 1992.

water

MDPI

Article

Sequence Analysis of Ancient River Blocking Events in SE Tibetan Plateau Using Multidisciplinary Approaches

Yiwei Zhang [1], Jianping Chen [1], Qing Wang [1,*], Yongchao Li [2,3,4], Shengyuan Song [1], Feifan Gu [1] and Chen Cao [1]

[1] College of Construction Engineering, Jilin University, Changchun 130026, China; yiweiz18@mails.jlu.edu.cn (Y.Z.); chenjp@jlu.edu.cn (J.C.); songshengyuan@jlu.edu.cn (S.S.); guff@mails.jlu.edu.cn (F.G.); ccao@mails.jlu.edu.cn (C.C.)
[2] Key Laboratory of Shale Gas and Geoengineering, Institute of Geology and Geophysics, Chinese Academy of Sciences, Beijing 100864, China; liyongchao@mail.iggcas.ac.cn
[3] University of Chinese Academy of Sciences, Beijing 101408, China
[4] Innovation Academy for Earth Science, Chinese Academy of Sciences, Beijing 100864, China
* Correspondence: wangqing@jlu.edu.cn; Tel.: +86-13504321568

Abstract: The temporary or permanent river blocking event caused by mass movement usually occurs on steep terrain. With the increase of mountain population and land use pressure and the construction of water conservancy and hydropower projects, river blocking events have gradually attracted people's attention and understanding. The area in this study is affected by strong tectonic activity in the Jinsha River suture zone and the rapid uplift of the Tibetan Plateau. In the past 6000 years, there have been at least five obvious river blocking events in the reach. The number and density are very rare. Combining field investigation, indoor interpretation, laboratory tests, optically stimulated luminescence (OSL) dating, SBAS-InSAR and previous studies, multidisciplinary approaches are used to systematically summarize the analysis methods and further the understanding of one river blocking event and multiple river blocking events from different perspectives. Especially in multiple river blocking events, we can get the wrong results if interaction is not considered. Through this study, the general method of analyzing the river blocking event and the problems that should be paid attention to in sampling are given, and relatively reliable historical results of river blocking events are obtained. This method has applicability to the identification and analysis of river blocking events and age determination of dams with multiple river blockages.

Keywords: river blocking event; landslide dam; multidisciplinary approaches; dating and SBAS-InSAR

Citation: Zhang, Y.; Chen, J.; Wang, Q.; Li, Y.; Song, S.; Gu, F.; Cao, C. Sequence Analysis of Ancient River Blocking Events in SE Tibetan Plateau Using Multidisciplinary Approaches. *Water* **2022**, *14*, 968. https://doi.org/10.3390/w14060968

Academic Editor: Stefano Morelli

Received: 3 February 2022
Accepted: 14 March 2022
Published: 18 March 2022

1. Introduction

The Qinghai–Tibet Plateau is the highest plateau in the world, and it is still increasing [1–3]. The upper Jinsha River is located on the southeast margin of the Qinghai–Tibet Plateau, significantly affected by tectonic uplift. There are steep slopes, deep valleys, and widely developed mass movement [4]. When geomorphic processes such as landslides cut off the river, they lead to the formation of temporary or permanent stream blockage [5,6] and present the greatest threat to people and property [7,8]. A recent blockage of the Jinsha River occurred on 10 October 2018, and the Baige landslide river blocking event (31°4′51″ N; 98°43′01″ E) was about 200 km upstream of our study area. Then, secondary hazards can be induced when landslide dams form and fail, including dam breach, upstream inundation, and downstream flooding [9]. Jinsha River is one of the rivers with the largest water resource potential in China [10], so it is a relevant area in the development of water conservancy and hydropower projects. In addition, it is of great significance to carry out geological hazard research on this section [11,12].

As a complex geological and geomorphic phenomenon, especially in ancient times, the blocking of Jinsha River provides a lot of information for its development history, quaternary seismic activity, formation and evolution of catastrophic geological disasters

in large valleys, and better understanding of the geological environment caused by earthquakes [13]. In the research area of about 26 km, there are several large landslide bodies, six of which could be identified as river blocking events, named Wangdalong I and II (WDL I and II), Rongcharong (RCR), Suwalong (SWL), Suoduoxi (SDX), Gangda (GD). Geologists are interested in learning ancient information from these events.

In recent years, there have been numerous studies conducted concerned about dammed lakes in the Quaternary, which developed on the major rivers of the Qinghai–Tibet Plateau [2,13–17]. The research methods are becoming more quantitative and systematic, but there are still problems such as the lack of details and theoretical support due to limited information obtainable from Quaternary sediments, which makes it possible to ignore certain information about the river blocking event, and the analysis results are biased, especially in the case of multiple river blocking events in one river section.

Therefore, based on previous studies, we combined field investigation, experimental data and our own analysis methods, hoping to play a complementary role in the research of river blocking events. The goals of this study include: (1) characterizing the geomorphological and sedimentological features of the ancient river blocking events; (2) determining the formation and breaching time of ancient river blocking events in order to contribute to the analysis of paleoclimatic and paleotectonic activity; (3) summarizing key ideas about analysis of multiple river blockages; (4) summarizing of general flow and precautions of river blocking research, providing some further insights in prospective research analysis, experiments, etc.

2. Study Area

2.1. Regional Geologic Setting

The study area is located on the upper reaches of Jinsha River in the southeastern margin of Qinghai–Tibet Plateau (Figure 1a). Tectonically, the structure of the study area is strong and there are many deep faults around (Figure 1b). There are two main groups of active faults in the study area: Yangla–Dongzhulin Fault zone (F_3) and Zeng Datong North–South fault (F_4), which are still active with the estimation of strike slip rates to be 6~7 mm/a and vertical rates to be 2~3 mm/a [18]. The study reach belongs to arid or semiarid climate [3], resulting in serious weathering and poor vegetation development on both sides of the bank slope. Along both sides of the valley, the exposed rocks are mainly schist, granodiorite, marble, limestone and granite (Figure 1c). These conditions lead to the development of jointed fractures in rock mass.

2.2. Geologic Setting of Each Dam

Affected by tectonic activities, there are faults near the dam body in this area, which make the surrounding rock mass more broken and joint fissures to develop, and this is the main reason for the existence of landslide dams in this river section (Figure 2). Except for GD, there are several kinds of lithology around the dam body, and different lithology boundaries are places with poor mechanical properties. The inclined plate rock mass around the dam body is prone to bending and cracking. These are unfavorable factors for the stability of the riverbank slope.

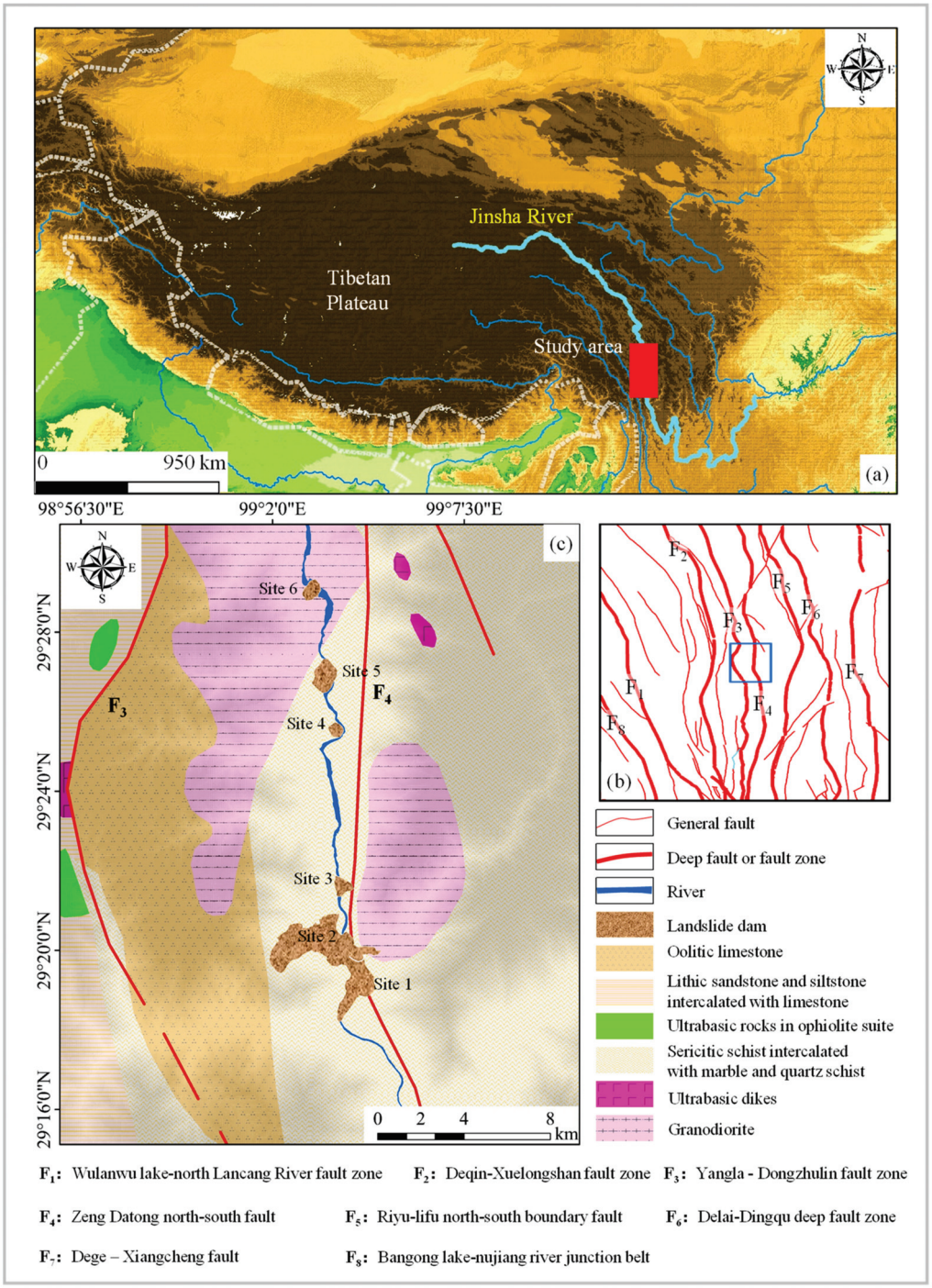

Figure 1. Map showing the locations and regional geologic settings (**a**) located on the southeastern edge of the Tibetan Plateau, (**b**) tectonic outline map (according to 1:1,000,000 geological map), (**c**) regional geological map (according to 1:1,000,000 geological map).

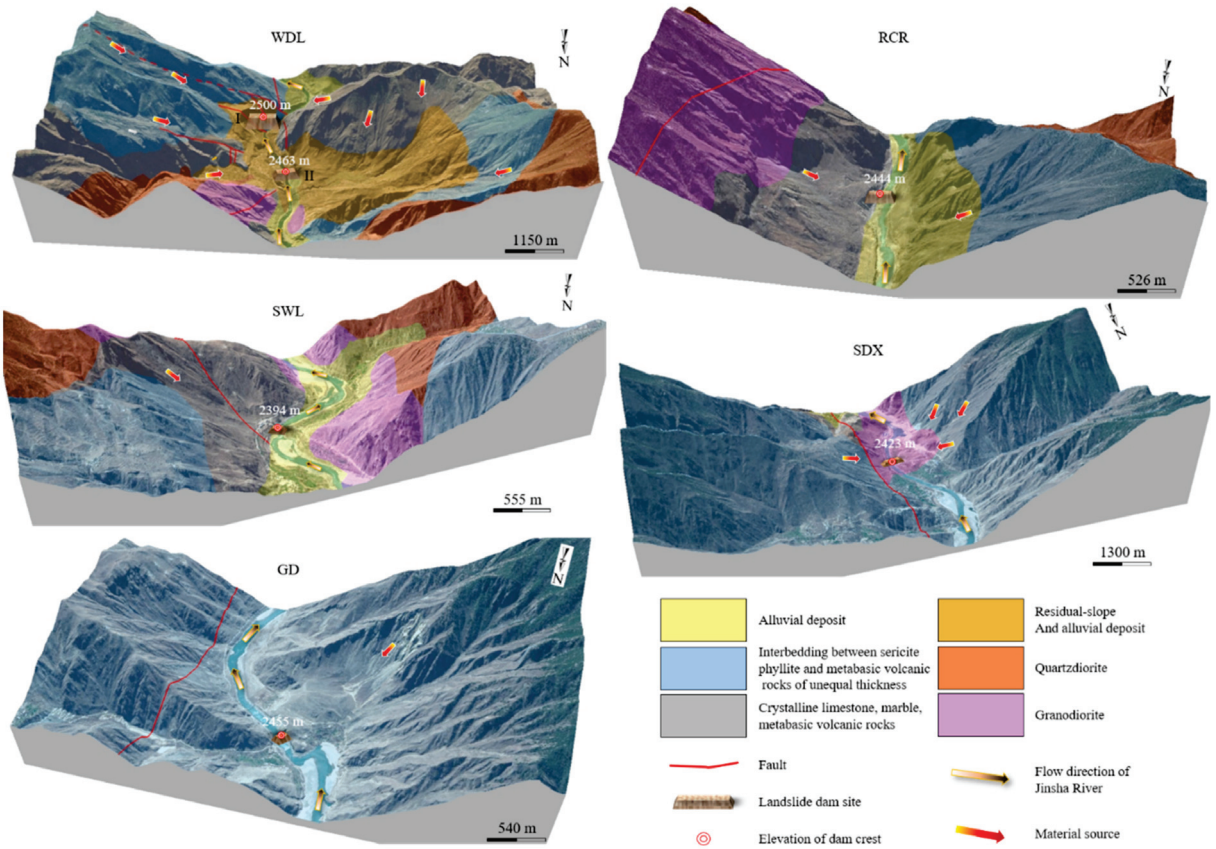

Figure 2. Map showing the specific geological settings of the dam site. Note: Due to the limitations in data collection, WDL, RCR and SWL were generated according to 1:50,000 geological map; SDX and GD were generated according to 1:200,000 geological map. (Note: these figures were created by ArcGIS 10.2).

3. Methodology

Uniformitarianism, also called the comparative–historical method, is an important paradigm in the process of geological research [19,20]. We can deduce the conditions, processes and characteristics of ancient geological events by using the existing laws of geological action, through the geological phenomena and results left over by various geological events. 'The Present is the key to the Past' is the uniformitarian paradigm [19,21] and nature is the best geological museum and laboratory, so field investigation is the premise and foundation of geological research and it is the traditional thinking method of geology. Therefore, a uniformitarian approach with the combination of modern science and technology is applied to improve the analysis of river blocking events.

For an ancient river blocking event, there are many pertinent research methods. A method called the "trinity" combination of residual landslide dams, upstream lacustrine sediments and downstream break-outburst sediments has been proposed [2,22]. In short, the fact that the river is blocked has basically reached a consensus and the method is reliably suitable for landslide dams as classified by Costa and Schuster [23].

3.1. Analysis of an Independent Landslide Damming of River Event

For one landslide damming river event, some traces would be left near the location where the river was blocked. Considering the fact that there would be less key direct information left in some river blocking events, it is necessary to analyze and summarize from different dimensions and perspectives.

3.1.1. Evidence from Remote Sensing Interpretation

The occurrence of the river blocking event requires the joint action of two aspects. The first is the stream channel, the other is blocking dam. For the remaining Quaternary ancient river blocking event, the square is generally large. Therefore, we can search along the river to find the landslide dam body on both sides of the river using remote sensing images (Figure 3), which is the potential evidence of blocking the river. Therefore, there will be greater changes in topography, including the change of bank slope morphology and the phenomenon of river diversion. In Google Earth, we can roughly circle the scope of the remaining dam block to find the source of blocking material. At the same time, we can also use DEM data for 3D modeling in GIS software such as ArcGIS to obtain some relative geometric parameters, such as the accumulation area, the accumulation length along the river, the accumulation width perpendicular to the river direction and the accumulation thickness of the dam body at the collapse.

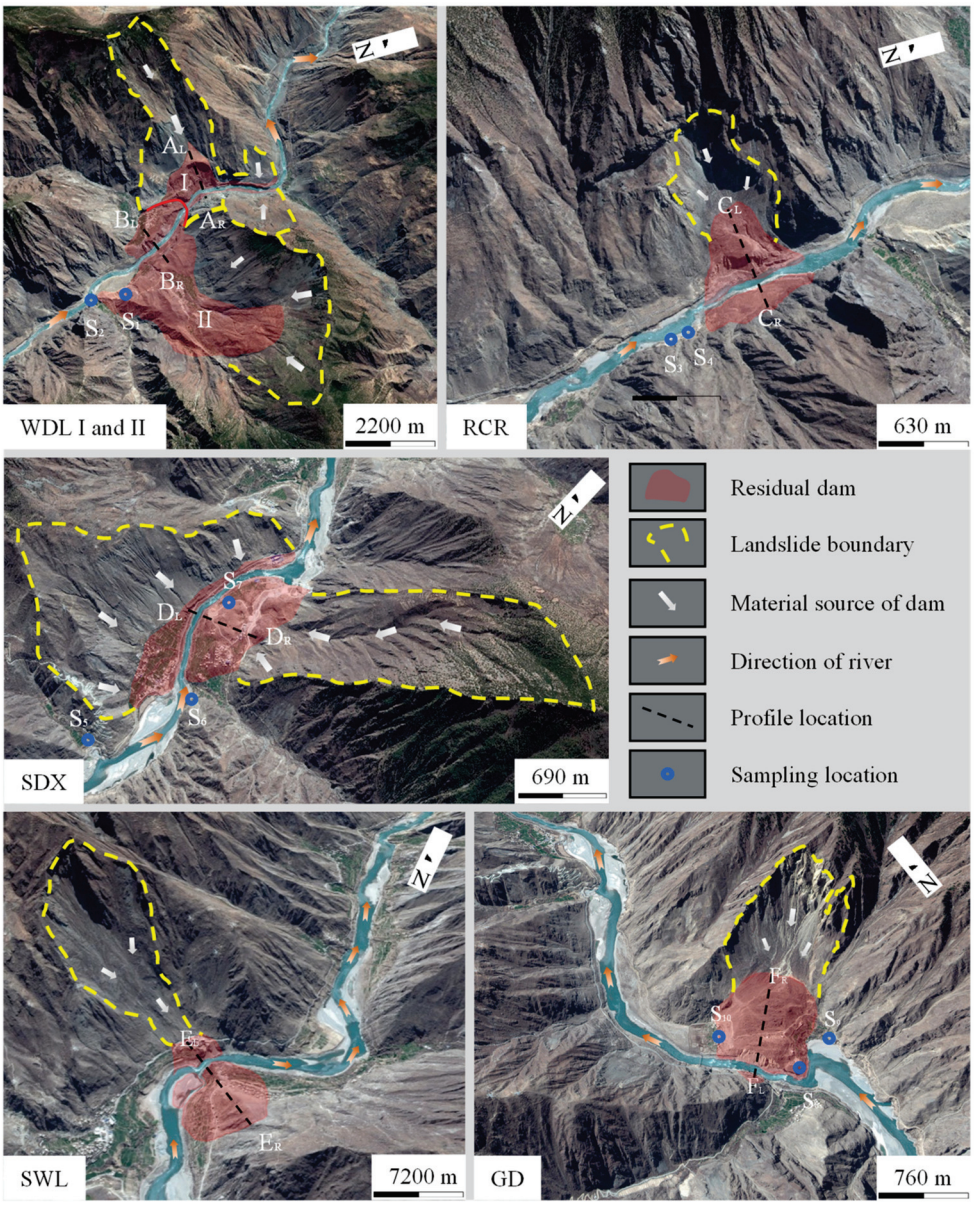

Figure 3. Remote sensing map of river blocking event. (Note: these images are from Google Earth).

3.1.2. Evidence from Morphology

After determining the approximate location of river blocking, the phenomenon of river blocking can be more accurately identified by detailed field investigation. Taking on-site photos of GD as an example (Figure 4), we can see that the dam bodies on both sides of the Jinsha River have geometric continuity and a good curve can be obviously observed by abstracting it into geometry. In the photographs taken, the geometric size of the river blocking body is well identified and recognized. At this time, important information such as the maximum thickness, average thickness of the accumulation body, and the geometric position and size of the breach are recorded, which are of great significance for the verification of the inversion results of the numerical simulation.

Figure 4. Geometry of GD landslide dam.

3.1.3. Evidence from Geology

For a river blocking dam where we can find a source area, geological continuity usually is maintained. That is, the lithology of the dam is consistent with the lithology of the material source area. Similarly, we can look for material sources on this basis. When the lithology of the bank slopes on both sides is inconsistent, and the lithology of the residual dam on both sides is consistent, we can infer the occurrence of river blockage and determine the source of material. However, in turn, when both sides of the bank slope have the same lithology, even if the internal lithology of the residual dam is consistent, it cannot be inferred that the material comes from one bank, which requires further analysis combined with remote sensing interpretation.

3.1.4. Evidence from Sedimentology

In the study section, there are a lot of fine-grained sediments (Figure 5). These lacustrine sediments not only directly reflect the sedimentary environment, but also reflect the hydrodynamic conditions of the transport medium. In order to determine the grain size characteristics of the lake sediments, the samples were taken from the lake sediments during the field investigation. As the lacustrine sediments particles are small, they can be all brought back for grain size analysis to obtain cumulative curve of particle size. In our laboratories, we used a hydrostatic sedimentation experiment to measure the grain size. Then we can get particle size characteristic parameters (Table 1). Firstly, according to Eli law, the diameter of the bed load moving on the riverbed is proportional to the square of the flow velocity (Equation (1)). In this study, we selected the maximum d_{50} value in Table 1 as the calculation data. By the following assignment, $d = d_{50max} = 2.6 \times 10^{-5}$, $r_S = 2700$, $r = 1000$, $g = 9.8$, we calculated $V = 1.73 \times 10^{-2}$ m/s, which is far less than the normal velocity of Jinsha River. Secondly, according to the Stokes formula, similarly, 0.026 mm is chosen as the calculation particle size, and the average temperature of Jinsha River is selected as 9.2 °C (according to the Batang Hydrological Station) to select the particle size calculation coefficient. The sedimentation velocity $v = 8.146 \times 10^{-7}$ m /s is calculated and

the setting time is about 568 days when the settling height is 40 m. Through the above rough calculation, it is concluded that a certain thickness of fine sediment layer on the upstream of landslide body must be formed in a stable still environment where the river is blocked. Therefore, the existence of the lacustrine deposits layer can effectively reveal the river blocking event.

$$d = \frac{rk}{2gf(r_s - r)} \cdot V^2 \quad (1)$$

where V is the velocity acting on the surface of sediment particles, m/s; d is the diameter of sediment particles; mr_S is the density of sediment particles, kg/m^3; r is the density of water, kg/cm^3; f is the coefficient of friction; g is the acceleration of gravity, 9.8 m/s^2.

$$v = \frac{2}{9} \cdot \frac{(\rho_S - \rho_W)g}{\eta} \cdot r^2 \quad (2)$$

where v is the sedimentation velocity of soil particles, cm/s; r is the radius of soil particles, cm; ρ_S is the density of solid particles, g/cm^3; ρ_w is the density of water, g/cm^3; η is the coefficient of dynamic viscosity of water, Pa·s; g is the acceleration of gravity, 980 cm/s^2.

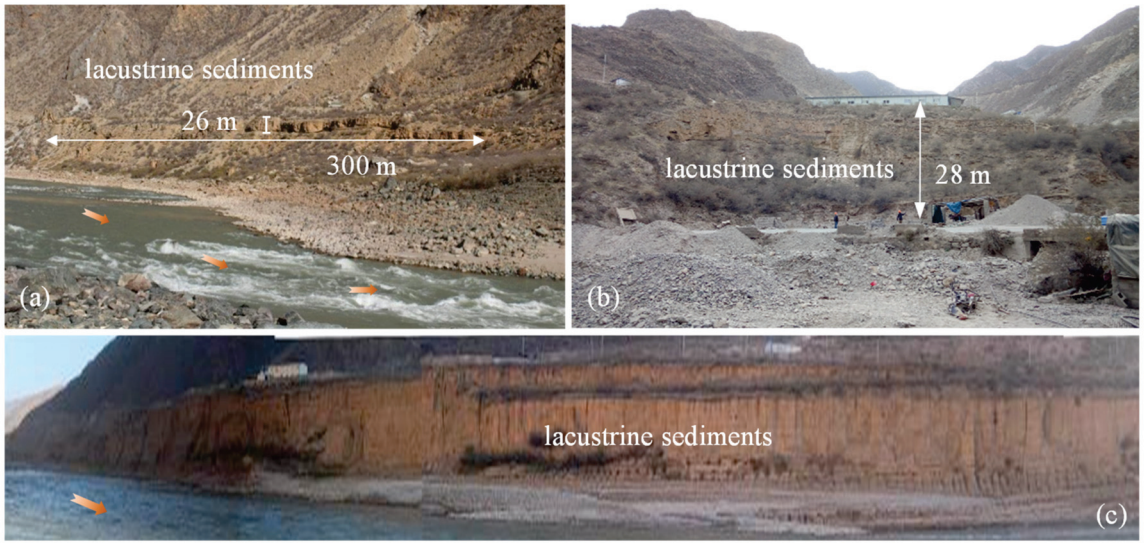

Figure 5. Lake sediments formed in dammed lakes. (**a**) In WDL-RCR reach; (**b**) in WDL-RCR reach; (**c**) in RCR-SWL reach.

Table 1. Characteristic parameters of cumulative percentage curves of lacustrine sediments.

Sample	Effective Size	Mean Size	Control Size	d_{30}/mm
	d_{10}/mm	d_{50}/mm	d_{60}/mm	
S_1	0.0050	0.026	0.032	0.015
S_2	0.0029	0.015	0.019	0.0064
S_3	0.0090	0.03	0.036	0.021
S_4	0.0016	0.01	0.014	0.0043
S_5	0.0043	0.019	0.026	0.012
S_6	0.0027	0.024	0.029	0.0048
S_7	0.0042	0.017	0.018	0.0087
S_8	0.0020	0.009	0.013	0.0045
S_9	0.0015	0.006	0.0088	0.0019
S_{10}	0.0023	0.011	0.014	0.0051

Note: Location of the sample is shown in Figure 2 as S_{number}.

3.1.5. Evidence from Break-Outburst Sediments

The dam break-outburst sediment is also one record of a landslide dammed lake, and it is also an important way to understand the dam-break process, which is usually difficult to find in an old river blocking event. According to the particle size of dam break-outburst sediments, the flood parameters at that time can be obtained by back analysis [22,24]. Furthermore, reasonable analysis of dam break-outburst sediments can also be made to determine the sequence of river blocking events.

In short, for a complete blockage of the river, starting with the blockage of the river by a landslide and ending with a dam failure, we can mainly investigate, describe and summarize from the above five aspects. Among them, many lacustrine deposits is the most critical and convincing evidence for long-term existence of river blocking.

3.2. Analysis of Interdependence Landslide Damming of River Events

The characteristic of the study area is that there have been many river blocking events. Therefore, more data are needed to explain whether these river blocking events interact with each other, which may be inconsistent with or even contrary to the results obtained from a single analysis of river blocking. These problems will mainly affect the judgment of river blocking time and thus affect the order of river blocking events, so more means and evidence are needed to explain the overall process of river blocking events. For example, if the WDL dammed lake formed early and lasted for a long time, then the dating age of the lacustrine sediments is likely to indicate WDL rather than other dams upstream. Besides, considering a long time of dammed lake existence, the effect of water on the genesis of other landslide dams shall be considered in numerical simulation even in such dry and rainy areas.

3.2.1. Elevation Inference

In terms of elevation, there is a rule that E_{dam} (the elevation at stable formation of the dammed lake) $\geq E_{lake}$ (the highest elevation of the dammed lake) $\geq E_{lacustrine}$ (the highest elevation of the lacustrine sediments). Since the ancient barrier lake has disappeared, we can obtain information from the present shape of the dam and the highest retention elevation of the lacustrine sediments. If the lacustrine sediments and landslide dam belong to the same river blocking event, then the highest elevation of the former cannot be higher than that of the latter. If not, the lacustrine sediments would not be formed by the dam. The principle is to rely on the geological boundary.

For E_{dam}, we obtain the profile chart according to the DEM, then the original dam shape is roughly outlined in reference to the form of the Baige landslide which occurred in the upstream according to Feng, et al. [25]. Finally, the reasonable elevation value (Figure 6) is deduced. For $E_{lacustrine}$, we use lacustrine sediments elevation recorded on field investigation by comparing the relatively highest point (Table 2).

Table 2. Elevation of dam crest and maximum elevation of lacustrine deposits upstream from the dam.

Dam	Minimum Elevation of Dam Crest (m)	Maximum Elevation of Lacustrine Deposits Upstream the Dam (m)	Dam	Minimum Elevation of Dam Crest (m)	Maximum Elevation of Lacustrine Deposits Upstream the Dam (m)
WDL I	2500	2426	SWL	2394	2430
WDL II	2463		SDX	2423	2445
RCR	2444	2442	GD	2455	2446

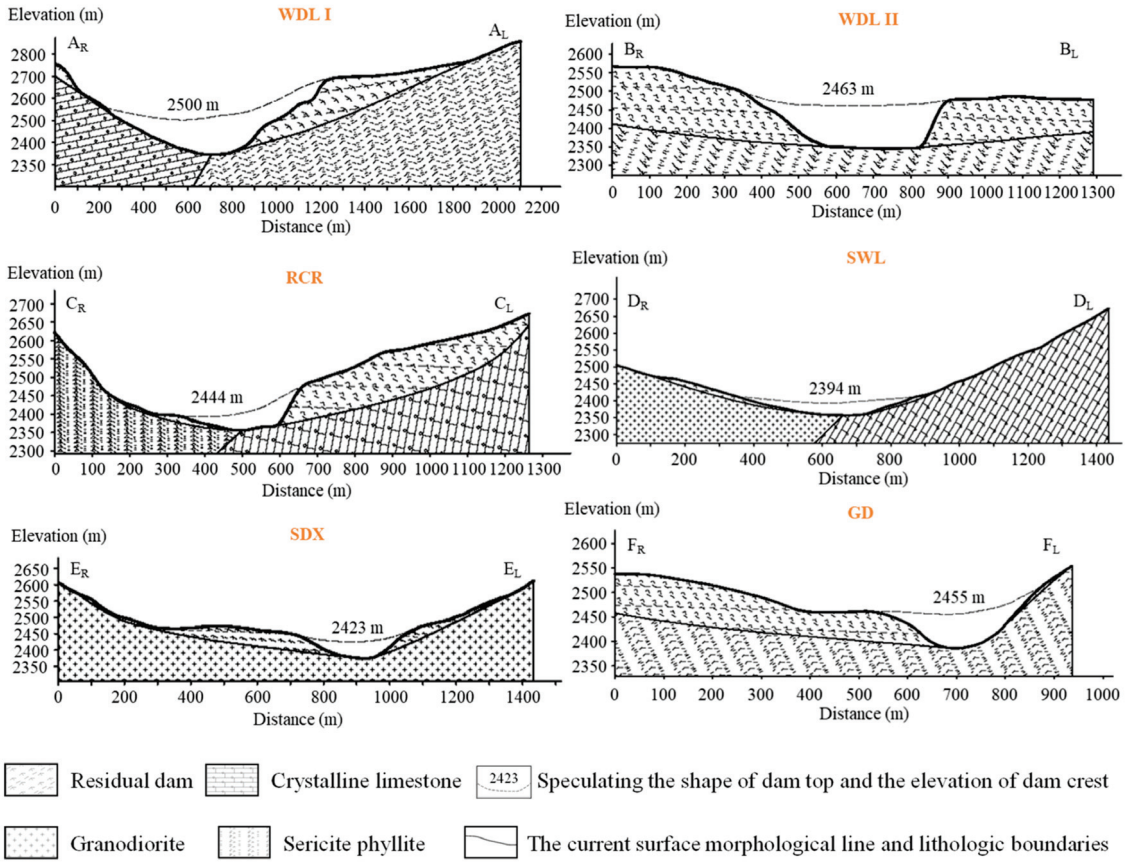

Figure 6. Speculative profile of each dam.

3.2.2. Dating

For several river blocking events, dating is a direct method to determine the sequence and, especially, multi-method dating campaigns enhance our understanding of the beginning and end of the river blocking event. However, due to the limitations of objective conditions, such as the error of test methods, the lack of availability of dating samples, insufficient funds and the uncertainty of whether the obtained samples have been in the accumulation body or later mixed in, it is often necessary to analyze them from multiple aspects using different methods [26]. Although more direct and high precision evidence is the ^{14}C dating age of the dam material, ^{14}C dating requires high wood charcoal samples. First, this section belongs to the dry and hot valley, and there is less vegetation on both sides of the river, so the sample collection is very difficult. Second, the source of samples cannot be guaranteed, so data may be deceptive. Therefore, the dating data of lacustrine sediments can often be used to assist the explanation. At present, the optically stimulated luminescence (OSL) dating method is widely used. In our paper, we commissioned the Institute of Hydrogeology and Environmental Geology to carry out OSL dating of the samples. To enrich the number of samples, we also used sample data from published literature [16,17].

In a single river blocking event, it is reasonable to infer that the normal sequence is formed later in the upper than lower part; in other words, the bottom is older than the top. Through field investigation, there is no sequence inversion caused by tectonic movement. According to the stratigraphic relationships between the dam body and the lacustrine sediments, a relative age for the dam can be concluded.

However, for several river blocking events, due to the influence of river geomorphology (Figure 7), the analysis of the dating results of the lacustrine sediments can be divided into the following situations.

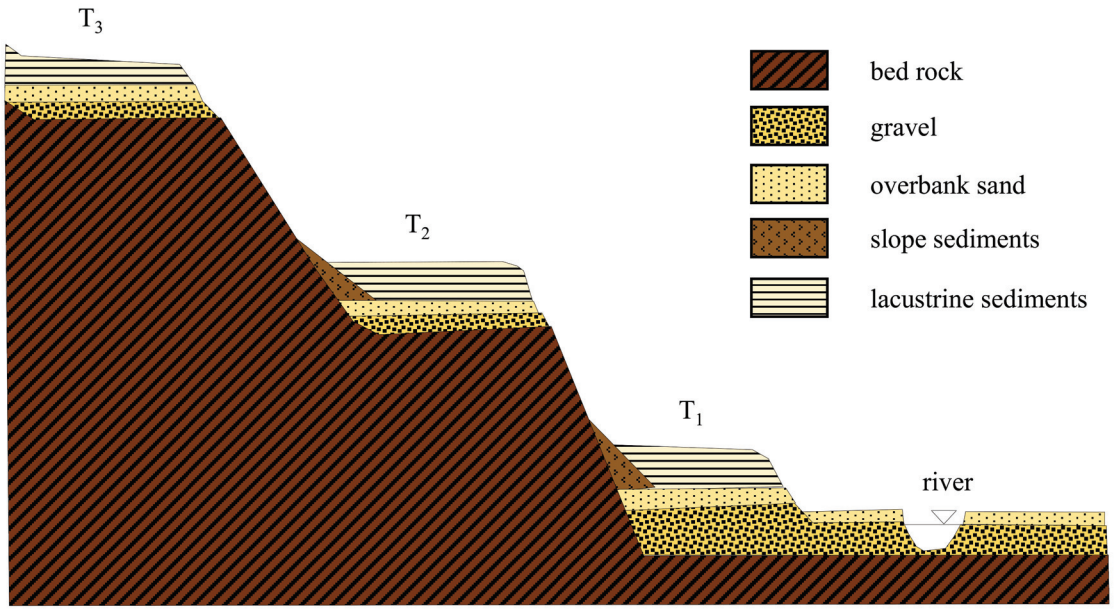

Figure 7. Diagrammatic drawing of river geomorphology.

Situation 1 is the formation of lacustrine sediments in the same river blockage with the same bottom baseline (Figure 8a). In general, through the detailed investigation on the site, the relative bottom and the relative top of the lacustrine sediments are found. Through the time difference between the top and bottom, we can roughly infer the duration of the river blocking.

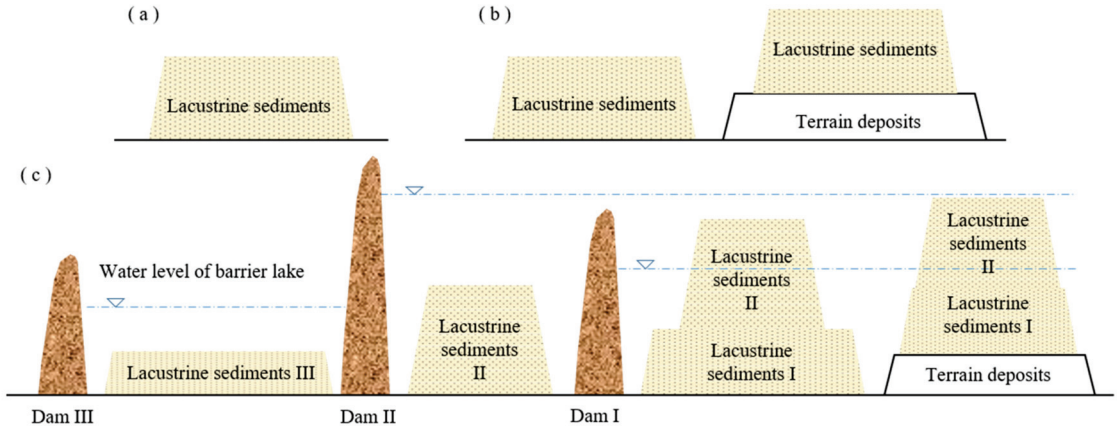

Figure 8. Diagram of the relationship between lacustrine sediments. (**a**) Situation 1; (**b**) Situation 2; (**c**) Situation 3 and Situation 4.

Situation 2 is in the same river blockage with the different bottom baseline (Figure 8b). We find the bottom of the profile of the right-hand sampling point then subtract the bottommost elevation of the left-hand sampling point from the bottommost elevation. Finally, we subtract the difference in elevation obtained above from the right-hand sampling point. The same bottom elevation is obtained according to the above method and then analyzed according to situation 1. When the bottom cannot be determined, the difference can be made by using the elevation of sampling points of the same age.

Situation 3 is in different periods of river blocking events with the same bottom baseline (Figure 8c, Dam II with Dam III). The age of sediments in the bottom is most likely different. Data analysis can often form two series.

Situation 4 is in different periods of river blocking events with the different bottom baseline (Figure 8c, Dam I with Dam II), first according to situation 2, then according to situation 3.

These situations only consider the general case, not all. The specific method will be described below.

We first assume that several river blocking events are independent of each other, and then we make the chart (Figure 9) according to dating data. The analysis results of these data are obviously contrary to the assumption preceding part of the text that there is a negative linear correlation between years and elevation. These data are dependent and need to be processed further. According to the results of dating data and its errors, the frequency statistics are carried out with 100-year intervals, and four peaks are found (Figure 10). Under the guidance of no clear experimental purpose, the results of random sampling are related to the distribution of samples, so it can be considered that these dating data roughly represent the four river blocking events.

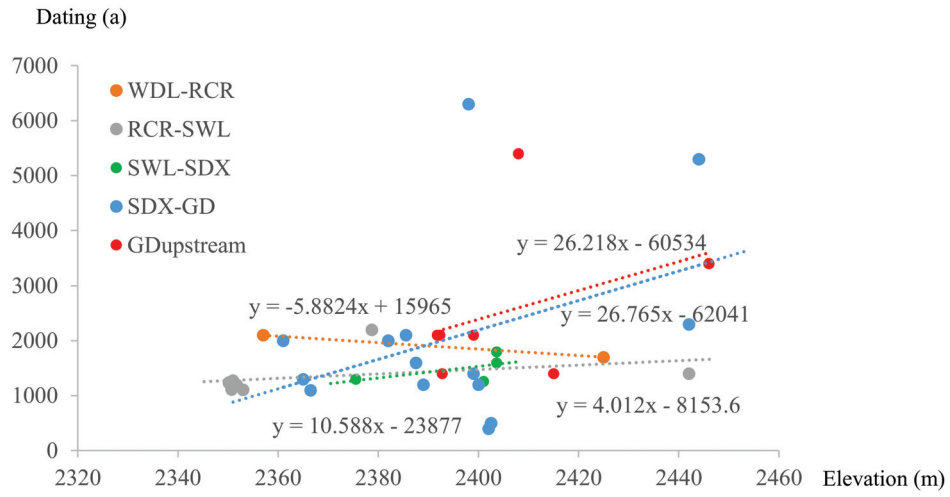

Figure 9. Unprocessed OSL dating data.

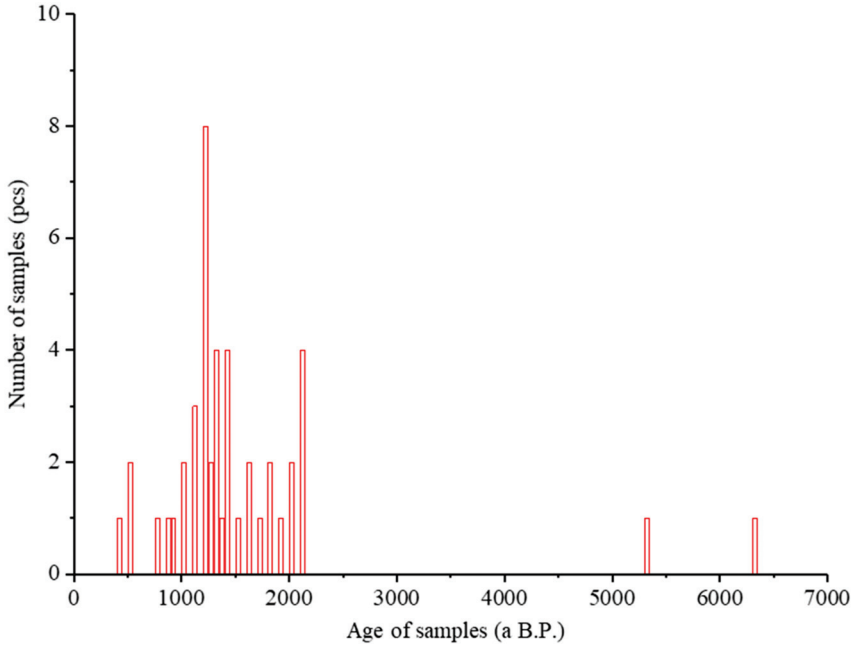

Figure 10. Frequency histogram of OSL dating data.

Therefore, we processed the data as follows:

First, the data were classified by river sections according to their locations.

Then, in each category, the classification was further carried out according to the linear relationship.

Last, the classified data were reasonably segmented combined with the results of the age–frequency histogram, and the classification results were processed into the same baseline to obtain the results (Figure 11).

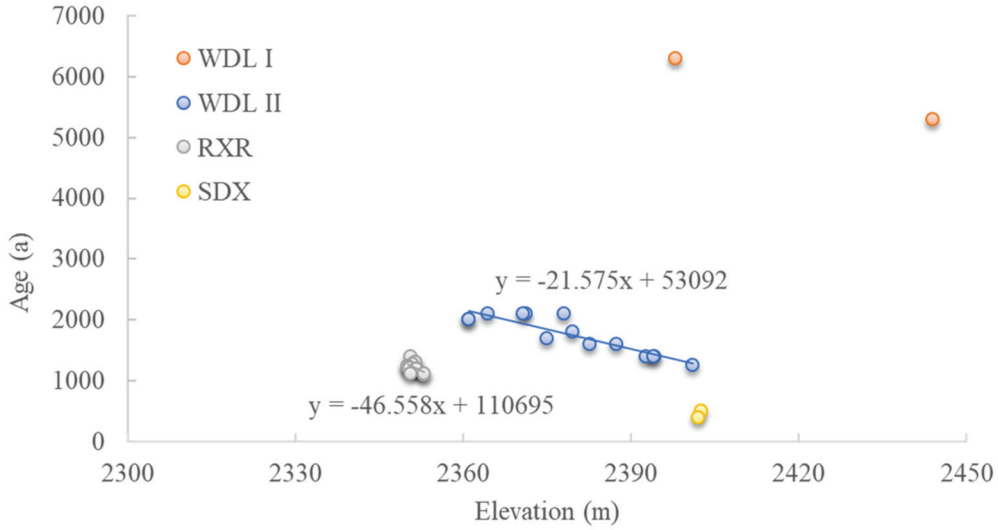

Figure 11. Grouping results of post-processing OSL dating data.

3.2.3. Interpretation of Geological Phenomena

Good analysis results should be able to reasonably explain the observed phenomenon. We explain the field investigation on this basis to show that the above results are correct.

First, considering landslide dam, GD and SDX residual dam body are relatively complete, the distance between the right bank dam and left bank is short, and the collapse occurs at the cross section, which indicates that the dam body exists for a short time.

Second, we consider the characteristics of dam break-outburst sediments. In the upstream of SWL and SDX, the sedimentary layers under different hydrodynamic environments are found, and the maximum number of accumulation layers in SWL (Figure 12) is more than that in SDX. This is because the formation of SWL is earlier than that of SDX and GD, so it is affected by the two river blocking events.

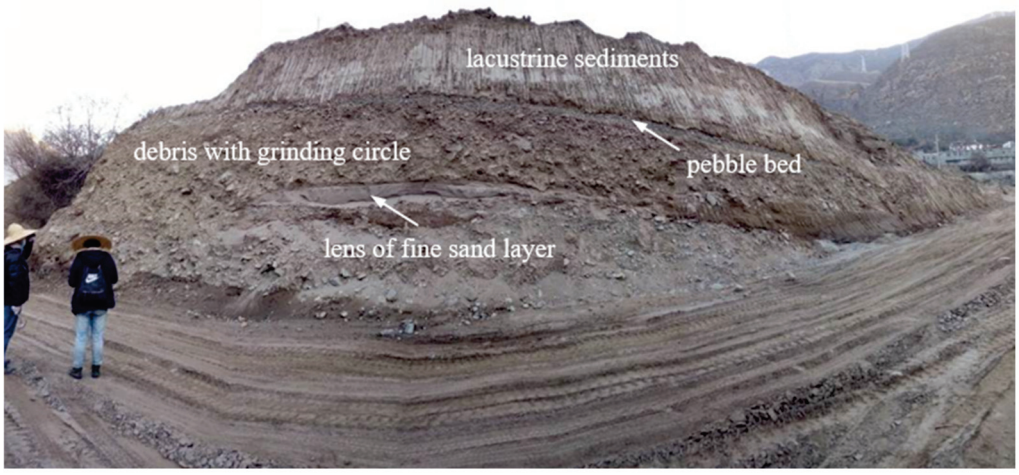

Figure 12. Stratification phenomenon in SWL-SDX reach.

Third, from the point of view of lacustrine sediments, the stratification of lacustrine sediments should be more obvious and nearly horizontal in the general long-term stable water environment, while the stratification of lacustrine sediments found in SWL, SDX and GD deposits is not obvious, indicating that the water environment is not stable in the long-term. It was also found that the bedding of the lacustrine sediments was inclined, indicating that the sediments formed before landslides (Figure 13). The horizontal continuous lacustrine sediments in the WDL-SWL reaching up to hundreds of meters are more obvious than that in the SWL-GD reach. Therefore, according to the results of Section 3.2.2, the sequence of each river blocking is relatively reasonable, which is consistent with the results of field investigation.

Figure 13. Typical geological phenomena. (**a**) Inclined lacustrine sedimentary layer on SDX dam body upstream. (**b**) Horizontal sedimentary layer covers inclined sedimentary layer phenomenon on GD dam body. (**c**) Inclined lacustrine sedimentary layer on SDX dam body downstream. (**d**) Horizontally stratified lacustrine sediments in WDLII-RCR section. (**e**) Horizontally bedding lacustrine deposits layer on RCR dam body upstream.

3.2.4. River Long Profile Morphology

Fluvial response causing by landslide dam may theoretically influence sediment yield, channel planform, cross section, gradient, or bed configuration [27]. Among these potential response variables, researchers are interested in long-term fluvial response, especially in channel gradient (Figure 14). By finding the turning point between the gentle gradient and the steep gradient, knickpoints can be recognized in the river long profile [28]. In our paper, the following steps were used to obtain a profile of the river section:

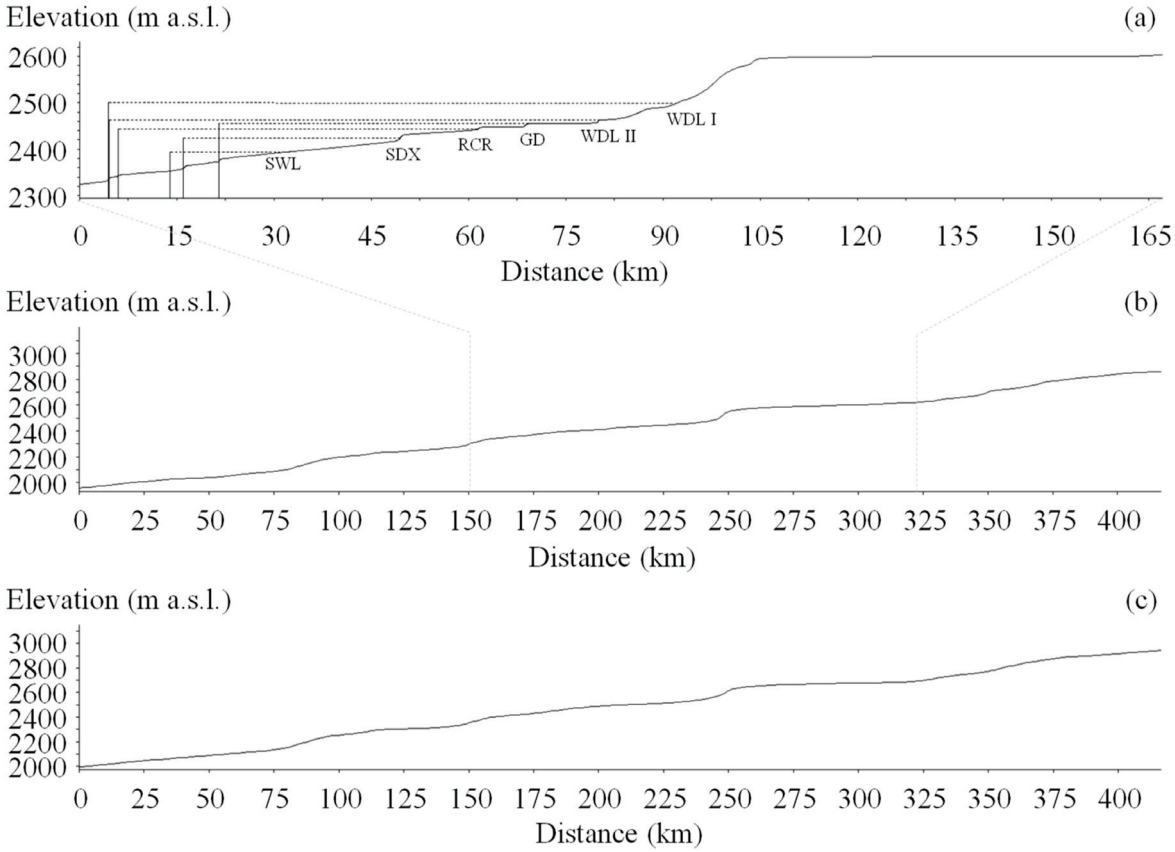

Figure 14. Fluvial response to river blocking dam. (**a**) is generated from ALOS 12.5 m DEM. (**b**) is generated from ALOS 12.5 m DEM in order to determine the scope of (**a**,**c**) which is generated from GDEMV2 30M as the control group of (**b**).

First, generate Jinsha River channel lines; second, generate points every 5 m from the river line; third, extract elevation values to points; fourth, generate a river length profile by using elevation and length; finally, sketch the profile and find the corresponding elevation of the dam. The first four steps were completed by ArcGIS, and the last step was completed by AutoCAD.

3.2.5. Deformation Analysis

Usually, the longer the accumulation body exists, the more tectonic activities it experiences, causing relative instability, vulnerable to erosion, and gradually disappearing. This explains why the longer the time the river blocking event is, the harder we find the remaining dam.

In this paper, the surface deformation of the residual dam body was analyzed through the SARscape module of ENVI 5.3 using remote sensing images from January 2018 to December 2020. Then, the average deformation rate and the response to the flood from Baige barrier lake were obtained of both the whole dam body and part of the whole area along the river (Figure 15).

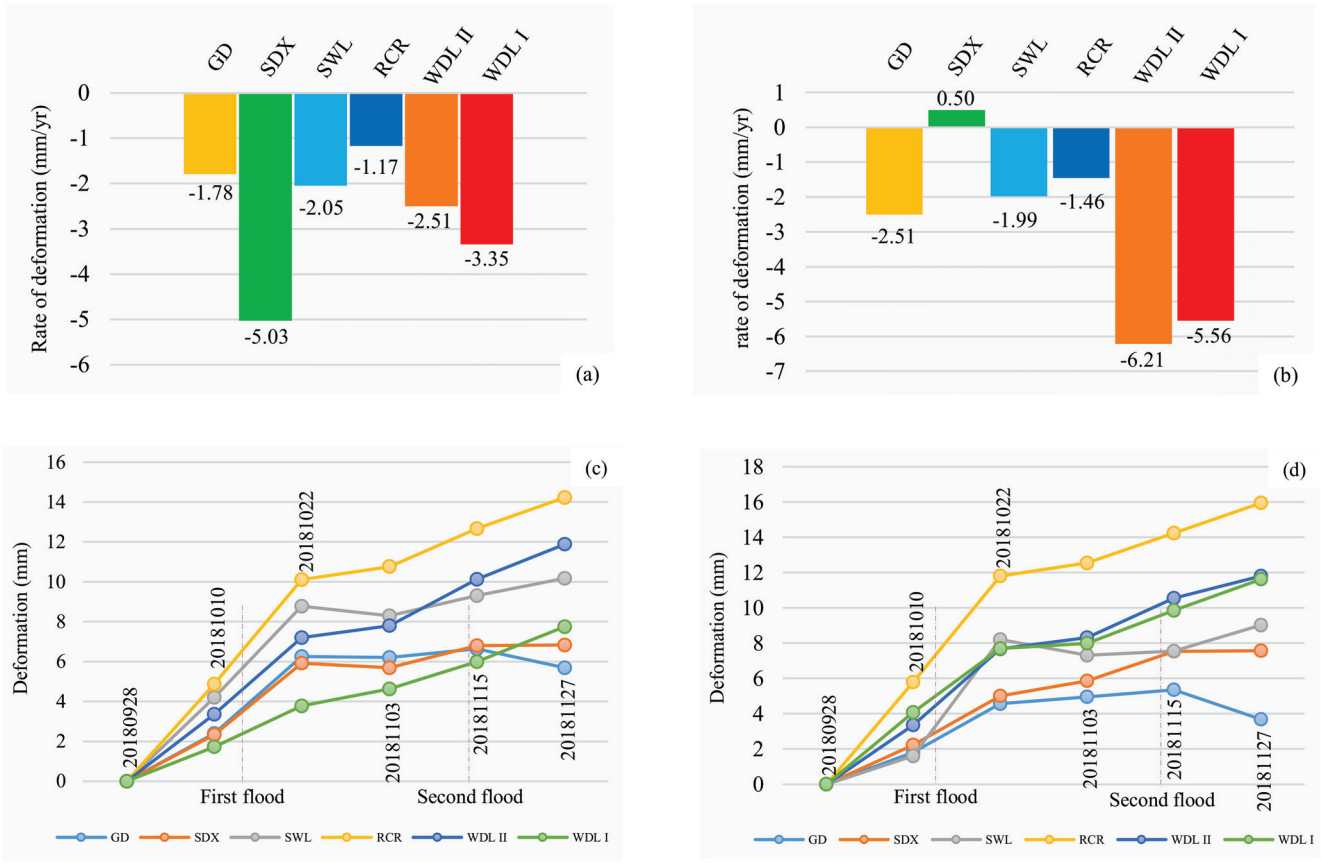

Figure 15. The surface deformation of the residual dam body. (**a**) The average deformation rate of the whole dam body; (**b**) the average deformation rate of part of the whole area along the river; (**c**) the whole dam body response to the flood from Baige barrier lake; (**d**) the response to the flood from Baige barrier lake of part of the whole area along the river.

4. Results and Discussions

Using the proposed analytical approach of multiple river blockages, we derived the evolutionary sequence of the dams blocking the river in this section. Based on Table 2, we can analyze that WDL I, II and RCR river blocking events have a wide range of influence, and other river blocking events might have been affected. Therefore, the influence of each other must be considered in sampling analysis.

On this basis we analyzed the OSL dating data; the fitted data are shown in Figure 11. Compared with the results of ^{14}C dating data [17], the results of WDG II are very close, indicating that the analysis method is suitable. The approximate time of river blocking in this reach can be obtained: the river blocking occurred in WDL I reach about 6300 years ago, and the duration of river blocking is about 1000 years; the river blocking occurred in WDL II reach about 1900 years ago, and the duration is about 400–840 years; the river blocking occurred in RCR reach around 1300–1400 years ago, and the duration is about 190–370 years; the river blocking occurred in SWL reach about 1370 ago, and the river blocking was relatively short; at least two landslides occurred in SDX, the first at 750 a B.P. on the right bank and the second at 510 a B.P. on the left bank. The river blocking duration was about 100–110 years, the GD river blocking time was about 900 years ago, and the river blocking duration was uncertain because of fewer data. The above results can explain many implausible geological phenomena.

Finally, we found further evidence corresponding to the deformation of the dam and the long profile of the river. It can be seen from Figure 14 that the river blocking event not only generates knickpoints at the dam site, but also generates knickpoints at the upstream. Moreover, the results of the points analysis are basically consistent with the above dating

data. The blocking age of WDL I and WDL II is long, and the change of river channel is obvious. The SWL blocking event lasted for a small time and had little effect on the river. In terms of elevation, the height fitted by the profile shape of the dam body seems to be conservative, such that the height of the WDL I may initially reach 2600 m.

By analyzing Figure 15a,b, we can draw a conclusion that the dam bodies are in denudation state, but the denudation rate is small, which is consistent with the situation that the accumulation dam can exist for thousands of years. Comparing GD, SWL, WDL I and WDL II in Figure 15a, the older the age, the greater the deformation rate; SDX is abnormal in Figure 15a because the construction camp of Suwalong Hydropower Station is built on it, and it has been artificially transformed, while in Figure 15b of the control, the part of the whole dam along the river is slightly uplifted mainly due to the uplift of the region with around 5 mm/yr rate [4]. The RCR river section is relatively small because this reach may be a relatively "sedimentary area" in the whole study reach. As can be seen from Figure 15c,d, flood is not the main reason for the disappearance of the dam. After the flood, the dam body is in a state of accumulation rather than erosion, and the accumulation thickness of RCR is the largest in the whole river section of the study area, which may be related to the existence of a large number of continuous lacustrine sediments in the upstream of RCR. Moreover, comparing Figure 15a,b, it can be concluded that the erosion rate along the river section of RCR is lower than the whole erosion rate, because the material on the upper part of the dam body is eroded and stripped from the original position and then deposited in the lower part of the dam body along the river.

If the above deformation can only explain the result of a short time, the landform of the accumulation dam body is the result of long-term evolution. Through the rough measurement of two relatively distant points on both sides of the residual dam body by Google Earth, the erosion section length perpendicular to the river of WDL I is about 1100 m, WDL II is about 500 m, RCR is about 350 m, SDX is about 190 m, and GD is about 200 m; these data are positively correlated with the ages of the accumulation dams.

The paper also summarizes a systematic process for investigating river blocking incidents. The geological environment of the research area breeds a wide range of mass movement, which creates good conditions for the occurrence of the river blocking event. For an ancient river blocking event, whether dammed lakes persist for a short time or a long time [29], there will always be some traces near the river block. Five important aspects of the field investigation of the river blocking event need to be paid attention to. Among this evidence, the dam body on both sides is the most intuitive evidence of ancient river blocking event, because it is one of the necessary conditions for the formation of the river blocking; and the wide range of lacustrine sediments accumulated behind the dam is convincing and abundant evidence (because its existence often indicates longer duration of dammed lake). For example, based on lacustrine sediments located in the same profile, we could roughly predict the age and duration of the river blocking event by calculating the difference between the age of the top layer and the bottom layer; then, we could obtain the average deposition rate by dividing the difference by the thickness of the lacustrine sediments, which is related to the sediment content, fine particle composition and climate; the mineral composition of the sediment; and chemical composition can reveal the source of material and sedimentary environment, etc. In addition, because of its widespread existence and fine-grained sediment with low cementation strength, it makes sampling convenient. Compared with the ^{14}C dating (samples need higher requirements and are not easy to obtain; sometimes we are even unable to find the appropriate test sample), the samples used for OSL dating of lacustrine sediments are easily found and obtained, which can increase efficiency and prevention of accidental errors. However, when multiple river blocking events occur in a river reach interacting with each other, if the sample is not carefully distinguished from which river blocking event, the analysis results from OSL dating will be seriously affected. In this paper, a feasible method for analyzing several river blocking events is proposed. Then, combined with the geological phenomena of field investigation, the relative reasonable sequence of river blocking is obtained, and the age

of some river blocking events that previous researchers did not give clear results for have also been identified. An accurate activity history is of great significance not only for the further study of the tectonic activity and sedimentary climate at that time, but also for the numerical simulation of dam-break and accurate back analysis of the event of landslide blocking river occurrence.

At the same time, our team finds that the error of OSL dating by using lacustrine sediments is within the acceptable range, but the following proposals must be paid attention to: (1) Before sampling, the experimental plan must be made and the samples should be collected purposefully. (2) Light should be avoided when sampling, and timely experiments should be conducted after sampling. Otherwise, the sample needs to be sealed, avoiding light, and stored at room temperature. (3) The determination of moisture content of samples is a very important error factor, which is not only the current moisture content, but also the average moisture content of samples in the historical process. (4) Under money- and time-permitting conditions, parallel samples should be collected around the sample and a profile sequence should be collected for dating in order to reduce accidental errors and improve the accuracy of the results.

Although the research method and research ideas are quite complete, the research is limited because of the complicated geological environment of the reach, the urgent time in the investigation, the inaccessibility of some positions to carry out the field investigation, and the inability to take samples due to the high sampling location. Therefore, the results presented are one of the development processes of river blocking with a greater probability. More discussion is welcome from future researchers. Finally, in order to make the relevant investigation more detailed and efficient, we made a systematic summary based on our team and previous studies, and put forward the following complete investigation and analysis flow chart (Figure 16), so that the relevant investigation can be more scientific and comprehensive, and fully reflect the relevant geological and geomorphic information.

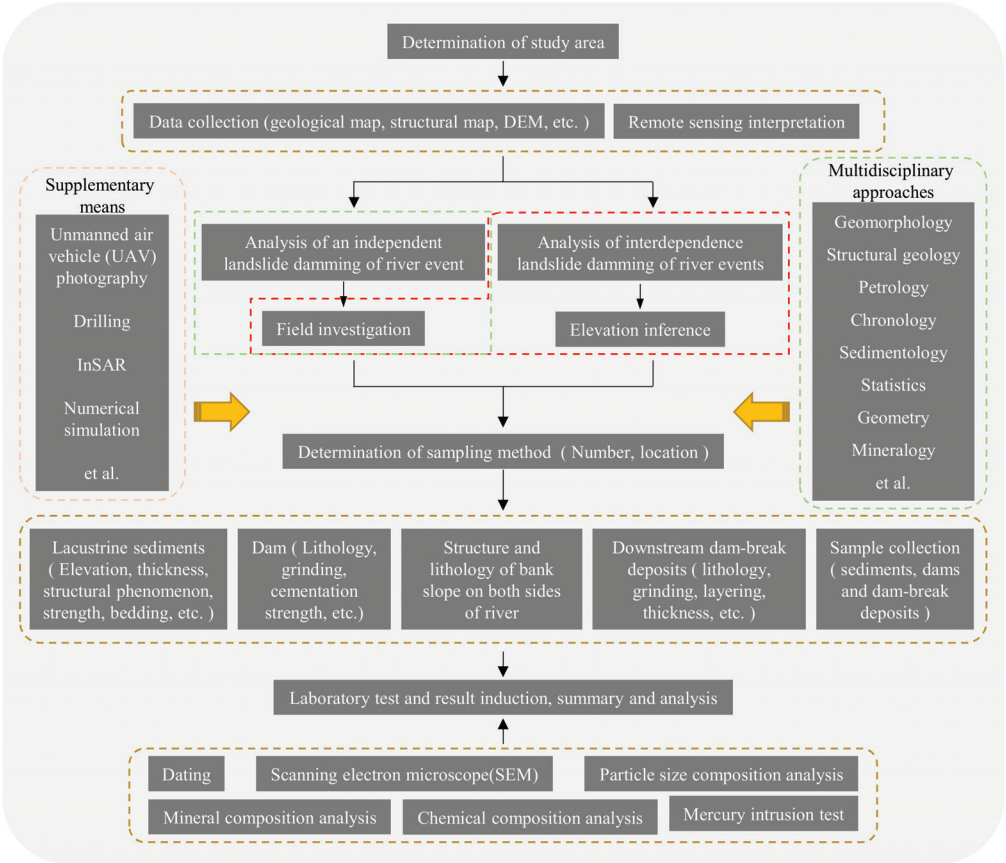

Figure 16. The general flow chart of studying the river blocking event.

5. Conclusions

There are very few studies on the age determination of dams with multiple river blockages. This paper presented an applicable method for investigating river blocking bodies and studying multiple river blocking processes in the same reach. Through this method, the relatively reliable river blocking sequence evolution history of Wangdalong-Gangda reach was scientifically and effectively restored. The results of elevation and dating analysis showed that the river blocking occurred in WDL I reach about 6300 years ago, WDL II reach about 1900 years ago, RCR reach around 1300–1400 years ago, SWL reach about 1370 ago, SDX reach about 750 years ago (a time away from today) and 510 (a time close to today), and the GD river blocking was about 900 years ago. The formation of these barrier lakes led to the decrease of river dynamics and river deposition effect, which may be an important reason for the inhibition of river channel incision and may directly affect the evolution of the local landscape [30]. From this perspective, the above results were also well verified by geological phenomena, river long profile morphology and accumulation deformation. This study is of great significance because it shows that the integrated method can provide a reasonable explanation for the evolution of the history of river closure in this area and provide a reference for future related research.

Author Contributions: Conceptualization, Y.Z., J.C. and Q.W.; methodology, Y.Z. and Y.L.; investigation, Y.Z., J.C., Y.L., F.G. and C.C.; Validation, J.C.; data curation, S.S.; writing—original draft preparation, Y.Z.; writing—review and editing, J.C.; visualization, Y.Z.; supervision, Q.W.; project administration, J.C.; funding acquisition, J.C., Q.W. and S.S. All authors have read and agreed to the published version of the manuscript.

Funding: This research was financially supported by the Key Project of NSFC-Yunnan Joint Fund (Grant no. U1702241), the National Natural Science Foundation of China (Grant No.42177139) and the National Key Research and Development Plan (Grant No. 2018YFC1505301).

Institutional Review Board Statement: Not applicable.

Informed Consent Statement: Not applicable.

Data Availability Statement: Not applicable.

Acknowledgments: The authors would like to thank Yuchao Li, Zhihai Li, Zhaoxi Wang, Jiejie Shen et al. for their contributions, comments and suggestions which helped in making this paper better.

Conflicts of Interest: The authors declare no conflict of interest.

References

1. Li, Y.; Wang, C.; Dai, J.; Xu, G.; Hou, Y.; Li, X. Propagation of the deformation and growth of the Tibetan–Himalayan orogen: A review. *Earth-Sci. Rev.* **2015**, *143*, 36–61. [CrossRef]
2. Li, Y.; Chen, J.; Zhou, F.; Song, S.; Zhang, Y.; Gu, F.; Cao, C. Identification of ancient river-blocking events and analysis of the mechanisms for the formation of landslide dams in the Suwalong section of the upper Jinsha River, SE Tibetan Plateau. *Geomorphology* **2020**, *368*, 107351. [CrossRef]
3. Chen, J.; Li, H. Genetic mechanism and disasters features of complicated structural rock mass along the rapidly uplift section at the upstream of Jinsha River. *J. Jilin Univ. Earth Sci. Ed.* **2016**, *46*, 1153–1167. [CrossRef]
4. Zhan, J.; Chen, J.; Zhang, W.; Han, X.; Sun, X.; Bao, Y. Mass movements along a rapidly uplifting river valley: An example from the upper Jinsha River, southeast margin of the Tibetan Plateau. *Environ. Earth Sci.* **2018**, *77*, 634. [CrossRef]
5. Korup, O. Recent research on landslide dams—A literature review with special attention to New Zealand. *Prog. Phys. Geogr.* **2002**, *26*, 206–235. [CrossRef]
6. Fan, X.; Scaringi, G.; Korup, O.; West, A.J.; Westen, C.J.; Tanyas, H.; Hovius, N.; Hales, T.C.; Jibson, R.W.; Allstadt, K.E.; et al. Earthquake-Induced Chains of Geologic Hazards: Patterns, Mechanisms, and Impacts. *Rev. Geophys.* **2019**, *57*, 421–503. [CrossRef]
7. Bao, Y.; Sun, X.; Zhou, X.; Zhang, Y.; Liu, Y. Some numerical approaches for landslide river blocking: Introduction, simulation, and discussion. *Landslides* **2021**, *18*, 3907–3922. [CrossRef]
8. Chigira, M.; Wu, X.; Inokuchi, T.; Wang, G. Landslides induced by the 2008 Wenchuan earthquake, Sichuan, China. *Geomorphology* **2010**, *118*, 225–238. [CrossRef]
9. Korup, O. Geomorphic hazard assessment of landslide dams in South Westland, New Zealand: Fundamental problems and approaches. *Geomorphology* **2005**, *66*, 167–188. [CrossRef]

10. Immerzeel, W.W.; van Beek, L.P.; Bierkens, M.F. Climate change will affect the Asian water towers. *Science* **2010**, *328*, 1382–1385. [CrossRef]
11. Sigtryggsdóttir, F.G.; Snæbjörnsson, J.T.; Grande, L.; Sigbjörnsson, R. Methodology for geohazard assessment for hydropower projects. *Nat. Hazards* **2015**, *79*, 1299–1331. [CrossRef]
12. Zhang, W.; Li, H.-Z.; Chen, J.-P.; Zhang, C.; Xu, L.-M.; Sang, W.-F. Comprehensive hazard assessment and protection of debris flows along Jinsha River close to the Wudongde dam site in China. *Nat. Hazards* **2011**, *58*, 459–477. [CrossRef]
13. Zhang, Y.; Zhao, X.; Lan, H.; Xiong, T. A Pleistocene landslide-dammed lake, Jinsha River, Yunnan, China. *Quat. Int.* **2011**, *233*, 72–80. [CrossRef]
14. Richardson, S.D.; Reynolds, J.M. An overview of glacial hazards in the Himalayas. *Quat. Int.* **2000**, *65–66*, 31–47. [CrossRef]
15. O'Connor, J.E.; Costa, J.E. *The World's Largest Floods, Past and Present: Their Causes and Magnitudes*; U.S. Geological Survey: Reston, VA, USA, 2004. [CrossRef]
16. Chen, J.; Zhou, W.; Cui, Z.; Li, W.; Wu, S.; Ma, J. Formation process of a large paleolandslide-dammed lake at Xuelongnang in the upper Jinsha River, SE Tibetan Plateau: Constraints from OSL and 14C dating. *Landslides* **2018**, *15*, 2399–2412. [CrossRef]
17. Chen, J.; Dai, F.; Lv, T.; Cui, Z. Holocene landslide-dammed lake deposits in the Upper Jinsha River, SE Tibetan Plateau and their ages. *Quat. Int.* **2013**, *298*, 107–113. [CrossRef]
18. Xu, X.-W.; Zhang, P.-Z.; Wen, X.-Z.; Qin, Z.-L.; Chen, G.-H.; Zhu, A.-L. Features of Active Tectonics and Recurrence Behaviors of Strong Earthquakes in the Western Sichuan Province and Its Adjacent Regions. *Seismol. Geol.* **2005**, *3*, 446–461. [CrossRef]
19. Windley, B.F. Uniformitarianism today: Plate tectonics is the key to the past. *J. Geol. Soc.* **1993**, *150*, 7–19. [CrossRef]
20. Manning, P.M. Charles Lyell's Geological Imagination. *Lit. Compass* **2016**, *13*, 646–654. [CrossRef]
21. Hutton, J.X. Theory of the Earth; or an Investigation of the Laws observable in the Composition, Dissolution, and Restoration of Land upon the Globe. *Trans. R. Soc. Edinb.* **1788**, *1*, 209–304. [CrossRef]
22. Chen, J.; Cui, Z. Discovery of Outburst Deposits Induced by the Xuelongnang Paleolandslide-Dammed Lake in the Upper Jinsha River,China and Its Environmental and Hazard Significance. *Acta Sedimentol. Sin.* **2015**, *33*, 275–284. [CrossRef]
23. Costa, J.E.; Schuster, R.L. The formation and failure of natural dams. *Geol. Soc. Am. Bull.* **1988**, *100*, 1054–1068. [CrossRef]
24. Ma, J.; Chen, J.; Cui, Z.; Zhou, W.; Liu, C.; Guo, P.; Shi, Q. Sedimentary evidence of outburst deposits induced by the Diexi paleolandslide-dammed lake of the upper Minjiang River in China. *Quat. Int.* **2018**, *464*, 460–481. [CrossRef]
25. Feng, W.; Zhang, G.; Bai, H.; Zhou, Y.; Xu, Q.; Zheng, G. A Preliminary Analysis of the Formation Mechanism and Development Tendency of the Huge Baige Landslide in Jinsha River o 11 October 2018. *J. Eng. Geol.* **2019**, *27*, 415–426. [CrossRef]
26. Fan, X.; Dufresne, A.; Whiteley, J.; Yunus, A.P.; Subramanian, S.S.; Okeke, C.A.U.; Pánek, T.; Hermanns, R.L.; Ming, P.; Strom, A.; et al. Recent technological and methodological advances for the investigation of landslide dams. *Earth-Sci. Rev.* **2021**, *218*, 103646. [CrossRef]
27. Korup, O.; Strom, A.L.; Weidinger, J.T. Fluvial response to large rock-slope failures: Examples from the Himalayas, the Tien Shan, and the Southern Alps in New Zealand. *Geomorphology* **2006**, *78*, 3–21. [CrossRef]
28. Safran, E.B.; O'Connor, J.E.; Ely, L.L.; House, P.K.; Grant, G.; Harrity, K.; Croall, K.; Jones, E. Plugs or flood-makers? The unstable landslide dams of eastern Oregon. *Geomorphology* **2015**, *248*, 237–251. [CrossRef]
29. Costa, J.E.; Schuster, R.L. *Documented Historical Landslide Dams from around the World*; US Geological Survey: Vancouver, WA, USA, 1991.
30. Li, Z.; Wang, Q.; Zhou, F.; Li, Y.; Han, X.; Mehmood, Q.; Cao, C.; Gu, F.; Han, M.; Chen, J. Integrating an interferometric synthetic aperture radar technique and numerical simulation to investigate the Tongmai old deposit along the Sichuan-Tibet Railway. *Geomorphology* **2021**, *377*, 107586. [CrossRef]

remote sensing

MDPI

Article

Permafrost Stability Mapping on the Tibetan Plateau by Integrating Time-Series InSAR and the Random Forest Method

Fumeng Zhao [1], Wenping Gong [1,*], Tianhe Ren [1], Jun Chen [2], Huiming Tang [1] and Tianzheng Li [1]

[1] Faculty of Engineering, China University of Geosciences, Wuhan 430074, China
[2] School of Automation, China University of Geosciences, Wuhan 430074, China
* Correspondence: wenpinggong@cug.edu.cn

Abstract: The ground deformation rate is an important index for evaluating the stability and degradation of permafrost. Due to limited accessibility, in-situ measurement of the ground deformation of permafrost areas on the Tibetan Plateau is a challenge. Thus, the technique of time-series interferometric synthetic aperture radar (InSAR) is often adopted for measuring the ground deformation rate of the permafrost area, the effectiveness of which is, however, degraded in areas with geometric distortions in synthetic aperture radar (SAR) images. In this study, a method that integrates InSAR and the random forest method is proposed for an improved permafrost stability mapping on the Tibetan Plateau; to demonstrate the application of the proposed method, the permafrost stability mapping in a small area located in the central region of the Tibetan Plateau is studied. First, the ground deformation rate in the concerned area is studied with InSAR, in which 67 Sentinel-1 scenes taken in the period from 2014 to 2020 are collected and analyzed. Second, the relationship between the environmental factors (i.e., topography, land cover, land surface temperature, and distance to road) and the permafrost stability is mapped with the random forest method based on the high-quality data extracted from the initial InSAR analysis. Third, the permafrost stability in the whole study area is mapped with the trained random forest model, and the issue of data scarcity in areas where the terrain visibility of SAR images is poor or InSAR results are not available in permafrost stability mapping can be overcome. Comparative analyses demonstrate that the integration of the InSAR and the random forest method yields a more effective permafrost stability mapping compared with the sole application of InSAR analysis.

Keywords: permafrost stability; InSAR; random forest method; Tibetan Plateau; data scarcity

Citation: Zhao, F.; Gong, W.; Ren, T.; Chen, J.; Tang, H.; Li, T. Permafrost Stability Mapping on the Tibetan Plateau by Integrating Time-Series InSAR and the Random Forest Method. *Remote Sens.* **2023**, *15*, 2294. https://doi.org/10.3390/rs15092294

Academic Editors: Stefano Morelli, Veronica Pazzi and Mirko Francioni

Received: 20 March 2023
Revised: 19 April 2023
Accepted: 24 April 2023
Published: 27 April 2023

1. Introduction

Global mean surface temperature is increasing at the rate of 0.2 ± 0.1 °C per decade, reaching 1.0 °C above the pre-industrial period (reference period 1850–1900) in 2017. Generally, the burning of fossil fuels is the main source of climate warming [1–3]. Under the influences of global climate warming and human activities, mountain ecosystems and cryosphere systems have changed significantly, especially those at high altitudes and high latitudes [1,4–7]. As the third pole of the Earth, the Tibetan Plateau is sensitive to climate warming. The warming rate in this plateau is about twice as high as the global climate warming rate over the past 40 years [8]. As a result, the permafrost on the Tibetan Plateau has been degraded drastically, manifesting in shrinking of the permafrost extent, change in permafrost types, increase in the thickness of the active layer, emergence of thermokarst lakes, and even soil desertification [9–12]. The degradation of the permafrost will have negative impacts on engineering facilities, ecosystem functions, and hydrogeological processes on the Tibetan Plateau [13,14]. It is worthwhile noting that due to the permafrost warming and degradation, the organic carbon stored in the permafrost will be released into the atmosphere, which can further amplify regional and global climate warming [5]. In addition, the ice in the uppermost permafrost could melt due to climate warming, which causes ground

deformations and related geohazards (e.g., failed slopes and retrogressive thaw slumps). These geohazards may affect the stability and operation safety of highways, railways, and other infrastructure in permafrost areas [6]. Hence, it is particularly important to monitor the deformation and stability of the permafrost on the Tibetan Plateau.

Permafrost stability is often evaluated based on the mean annual ground temperature [13], even though it can be influenced by various factors. Note that the permafrost degradation, manifested by the warming temperatures, could lead to an increase in the annual active-layer thickness and retreat of the permafrost extent [15,16]. The studies in Kovakov and Shvetsov [17] showed that permafrost stability could be assessed by the amount of annual increase in the thickness of the active layer. The thickness of the active layer can be measured directly with grid probing, thaw tubes, and ground penetrating radar [18,19]. Although these measurements are of high quality, they are sparse and the measurement accuracy is site specific [20]. Indeed, similar problems exist in the monitoring of ground temperature. With the aid of an analytical model that is based on the heat conduction equation and the environmental conditions [21], the thickness of the active layer monitored from the point measurement could be extended to that at a regional scale. A potential limitation of this interpolation is that too many environmental factors are involved, and the determination of these factors can be a challenge [22]. Further, permafrost-related disturbances (e.g., retrogressive thaw slumps) can also indicate permafrost stability. Some studies have used deep-learning-based models to map retrogressive thaw slumps [10,23,24]. Though the accuracy of the deep-learning-based models is high, the main limitation is that too many training datasets are needed.

Note that the variation in active-layer thickness can be monitored by the ground deformation [25]. In addition, under warming or local disturbance, the excess ice or ice-rich sediment in the uppermost permafrost can lead to additional long-term ground subsidence, which could be regarded as an indicator of permafrost degradation [14,26]. Thus, the permafrost stability can be assessed based on the ground deformations. For instance, larger ground subsidence indicates permafrost instability or degradation, whereas smaller subsidence indicates permafrost stability. During the past few decades, remote sensing techniques have become an indispensable tool for monitoring the ground deformation and evaluating the permafrost stability in permafrost areas owing to their wide coverage and independence from ground measurements [27–31]. Among the various remote sensing techniques, interferometric synthetic aperture radar (InSAR), the effectiveness of which is not affected by the weather conditions, is quite popular because of its high accuracy in monitoring small ground deformations [6,11]. However, the effectiveness of differential InSAR in monitoring the ground deformation and the permafrost stability is degraded by spatial decoherence and atmospheric distortion. Hence, the techniques of time-series InSAR such as persistent scatterer InSAR (PS-InSAR) and small baseline subset InSAR (SBAS-InSAR) have been developed recently and applied to monitoring the ground deformation and permafrost stability on the Tibetan Plateau [9,14,32]. However, side-view imaging is often adopted to generate SAR images and the terrain visibility of SAR images relies upon the acquisition direction of the adopted satellite radar with respect to the imaged terrain [33,34]. In mountainous areas, the geometric distortions caused by side-view imaging include foreshortening, layover, and shadow, which can degrade the effectiveness of the time-series InSAR [34]. Although a few image pixels with bright reflectivity in the foreshortening areas in the SAR image can be detected and monitored by the time-series InSAR, the monitored ground deformations in foreshortening areas might be inaccurate [34]. In addition, the ground deformation results in layover and shadow areas are also not accurate [34]. Thus, the geometric distortion areas are regarded as poor terrain visibility areas, and the rest are good visibility areas. Further, the ground deformation in areas with dense vegetation and water covering may not be monitored due to decoherence. In other words, the ground deformation points detected by time-series InSAR may not cover the entire study area. In this study, data scarcity can be defined as the area where the terrain visibility is poor or InSAR results are not available.

In the field of landslide susceptibility mapping, the historical landslide information of a region is often collected and adopted for training the relationship between environmental factors and landslide occurrence; the trained relationship is then applied to predict the probability of landslide occurrence in other regions with similar environmental conditions [35,36]. Inspired by the concept of landslide susceptibility mapping, a method that integrates the time-series InSAR and machine learning methods is proposed in this paper for improved permafrost stability mapping on the Tibetan Plateau. The integrated method could have the advantages of the effectiveness of time-series InSAR (in monitoring the ground deformation in areas with good visibility of input SAR images) and the machine learning method (in mapping the relationship between the environmental factors and the ground deformation). With the aid of the trained relationship between the environmental factors and permafrost stability, the permafrost stability in the entire study area can be readily mapped. Thus, the issue of data scarcity can be overcome. Indeed, the method integrating time-series InSAR and machine learning has shown effectiveness in landslide susceptibility mapping [37]. Note that the ground deformation in permafrost areas is correlated with environmental factors [14]; thus, such an integrated method can also be adopted to map permafrost stability.

To illustrate the application and effectiveness of the proposed method, the permafrost stability mapping in a small area located in the central region of the Tibetan Plateau is analyzed. The novelty of this study is the permafrost stability mapping integrating the time-series InSAR and machine learning methods, with which the issue of data scarcity could be overcome. The remainder of this article is organized as follows. First, the study area is briefly introduced in Section 2. Second, the principle of the proposed method and the data processing are provided in Section 3. Third, the ground deformation and permafrost stability mapping results are presented in Section 4. Fifth, the ground deformation and permafrost stability mapping results obtained are validated and discussed in Section 5. Finally, the concluding remarks are provided.

2. Information of the Study Area

The Tibetan Plateau has the largest permafrost area in the middle and low latitude regions of the Earth, with an area underlain by a permafrost of approximately 1.06×10^6 km^2 [38]. According to the permafrost continuity, the duration of frozen ground, and the maximum depth of seasonal frost penetration, the permafrost on the Tibetan Plateau is categorized into six types: predominantly continuous permafrost, predominantly continuous and island permafrost, mountain permafrost, middle-thick seasonally frozen ground, thin seasonally frozen ground, and short-time frozen ground (http://www.ncdc.ac.cn, accessed on 19 March 2023). Figure 1a shows that the distribution of different types of permafrost can be affected by latitude. For example, the predominantly continuous permafrost is mainly located in the central and northwest of the Tibetan Plateau, the predominately continuous and island permafrost is located in the south of the predominately continuous permafrost, the mountain permafrost is mainly located in the north, west, and south of the Tibetan Plateau, and the seasonally frozen ground is primarily scattered in the east of the Tibetan Plateau. Depending on the complex environmental conditions, the responses of these six types of permafrost to climate warming can be different.

To illustrate the application and effectiveness of the integrated method proposed, a small area located in the central region of the Tibetan Plateau, as shown in Figure 1a, is analyzed in this paper. The reasons for selecting this study area are summarized as follows: (1) The permafrost stability in the study area cannot be fully monitored by time-series InSAR due to the terrain visibility and decoherence; thus, the machine learning method is taken as an effective and necessary supplement to the InSAR analysis in the permafrost stability mapping. (2) The time-series InSAR and machine learning method are both effective in the study area; thus, the proposed method is applicable in the study area. (3) This area is predominately occupied by continuous permafrost and the permafrost stability has been studied by many studies [39–41], the results of which indicate that permafrost

degradation occurs frequently in this area under climate warming; thus, this study is significant in assessing the permafrost stability of this area. (4) This area is covered by both ascending and descending SAR data (see Figure 1a), as such, the permafrost stability mapping results obtained can be cross-validated. (5) The Qinghai–Tibet Highway crosses this area; thus, permafrost stability mapping in this area will be significant for the operation of this highway.

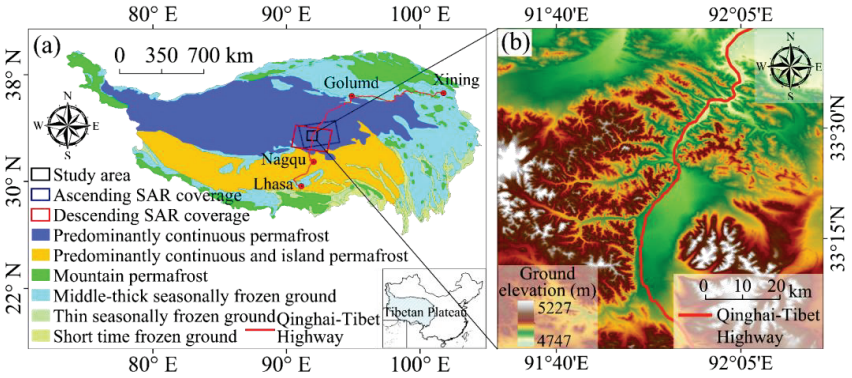

Figure 1. General information of the study area: (**a**) Permafrost types on the Tibetan plateau; (**b**) Ground elevation map of the study area.

As can be seen from Figure 1b, the dimensions of the study area are 80 km by 80 km and the topography mainly consists of mountainous terrain with ground elevations ranging from 4747 to 5227 m. Note that the variation in the ground elevation in the mountainous terrain is relatively small. The bedrock of the study area is red or gray sandstone and mudstone, and lacustrine deposits can also be identified in the study area. The vegetation cover mainly consists of alpine meadow and desert grassland. The climate is cold and dry with the mean annual air temperature of about 4.5 °C, and the annual precipitation ranges from 300 to 400 mm. Note that the precipitation is mainly concentrated in the rainy season (from June to August), and the heavy rainfall in the rainy season often brings about flooding and surface erosion in the study area [42]. Thus, the water content of the soil is fairly low and under the effects of freeze–thaw cycles and surface runoff processes; the study area is prone to suffer from permafrost degradation and desertification [32].

3. Methodology and Data Processing

3.1. Principle of the Integrated Method for Permafrost Stability Mapping

To overcome the data scarcity issue in the InSAR-based permafrost stability mapping, an integrated method that can take advantage of the effectiveness of InSAR analysis (in monitoring the ground deformation in areas with good terrain visibility of SAR images) and that of machine learning (in mapping the relationship between the environmental factors and the permafrost stability) is proposed in this study. The general principle and implementation procedures of this integrated method are illustrated in Figure 2.

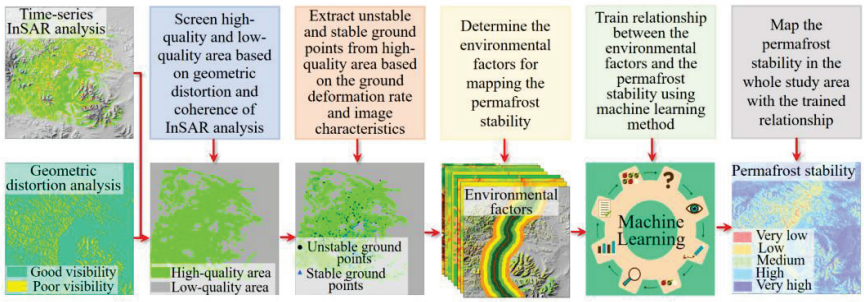

Figure 2. Principle and implementation procedures of the integrated method for permafrost stability mapping.

Within the context of the integrated method, the ground deformation in the concerned region is first studied with the time-series InSAR analysis, through which an initial permafrost stability mapping is obtained. It is noted that the ground deformation in this initial permafrost stability mapping cannot be available in areas with dense vegetation and water covering, due to the temporal decoherence induced in the processing of input SAR images, whereas the permafrost stability obtained in areas with poor visibility (of SAR images) can be problematic. Thus, a screening analysis that is based on the analysis of geometric distortion (in input SAR images) and the coherence of InSAR analysis results is conducted to locate the area with high-quality ground deformation data. The screened area is termed as the high-quality area, whereas the rest of the area is termed as the low-quality area. Then, the high-quality samples (i.e., unstable and stable ground points) for the permafrost stability mapping are extracted from the high-quality area based on the ground deformation rate and Google Earth image characteristics, which are detailed in the results section.

The studies in [14,43] depict that ground deformation and permafrost stability can be closely correlated with environmental factors, including topography, land cover, land surface temperature, and distance to road. Note that although the effectiveness of the time-series InSAR in monitoring the ground deformation in the high-quality area and that in the low-quality area may be different, the mapping relationship between the environmental factors and the permafrost stability in the high-quality area can be applied to the low-quality area; indeed, a similar concept is often employed in landslide susceptibility mapping [35,36]. The machine learning method has been extensively adopted for mapping the relationship between environmental factors and landslide occurrence. Although permafrost stability and landslide susceptibility can follow different physical mechanisms, both are correlated with environmental factors and the relationship between permafrost stability and environmental factors and that between landslide susceptibility and environmental factors can be mapped with similar methods. As such, the relationship between environmental factors and permafrost stability in this study is mapped with the machine learning method. Here, the relationship between the environmental factors and permafrost stability is trained by the data (i.e., permafrost stability and environmental factors) extracted in the high-quality area using the machine learning method and the trained relationship is further adopted to map the permafrost stability in the whole study area. As an outcome, the data scarcity issue in the InSAR-based permafrost stability mapping can be overcome and an improved permafrost stability mapping can be achieved.

3.2. Data Processing with the Proposed Method

3.2.1. Time-Series InSAR Analysis

To analyze the ground deformations and permafrost stability in the study area, 67 scenes of SAR images, acquired by the descending Sentinel-1 from October 2014 to August 2020, were downloaded from the European Space Agency (https://earth.esa.int, accessed on 19 March 2023). Further, 69 scenes of SAR images, acquired by the ascending Sentinel-1 in the same observation period were downloaded to validate the accuracy of the permafrost stability mapping obtained from the integrated method. The boundaries of these SAR images are provided in Figure 1a. Note that although the combination of descending and ascending SAR images can improve the monitoring ability of ground deformation, the reasons for only using the descending SAR images as input to train the permafrost stability mapping model are summarized as follows: (1) the deformation results obtained from ascending SAR images are adopted for the validations of the ground deformations and the permafrost stability mapping, and if the deformation points obtained from descending and ascending SAR images are combined to extract the training samples, such validations would be not convincing and (2) the training samples are extracted from the high-quality area, which is not affected by the geometric distortions; thus, the deformation results of these training samples are reliable. Further, these samples are verified through visual interpretations of Google Earth images to guarantee the accuracy of the training samples and the permafrost stability mapping model. In this study, the SBAS-InSAR

method is employed to reduce the temporal decorrelation caused by the large timespan of the input SAR images. The ground deformation is analyzed with the following steps: (1) The signal-to-noise ratio (SNR) in the interferometric SAR images is improved with the Goldstein radar interferogram filter [44]. (2) The flat-earth phase and the topographic phase in the interferometric SAR images are removed by the precise orbit determination (POD) data and the digital elevation model (DEM) data, respectively. In the InSAR processing, the atmospheric effect is mainly the topography-correlated tropospheric delay. Thus, the tropospheric delay can be estimated from the correlation between the interferometric phase and the topography. However, this method assumes a single relationship between phase and topography over the whole interferogram as it does not account for the spatial variation in the tropospheric properties [45]. In this study, the tropospheric errors are minimized through spatial–temporal filtering, which is based on the assumption of Gaussian distribution of time-series tropospheric delays. This method has been shown effective in reducing the effect of tropospheric delay on the Tibetan Plateau [25,46]. (3) Phase unwrapping (of interferometric SAR images obtained in the previous step) is conducted with the minimum cost flow algorithm (MCF) [47]. (4) The residual phase component and phase ramps (of interferometric SAR images obtained in the previous step) are removed using the ground control points (GCPs). (5) The time-series ground deformation along the line of sight (LOS) direction is retrieved with the inversion model [48]. Note that the GCPs are selected on the flat terrain with minimal ground deformation, and the GCPs are stable in InSAR images over the entire observation period.

The main ground deformation in permafrost areas is thaw subsidence or frost heave, which is manifested in vertical ground deformation. Thus, vertical ground deformation, rather than the LOS deformation, is adopted in this study for analyzing the permafrost stability. As shown in Figure 1b, the study area is relatively flat and homogeneous and no active fault is developed. Thus, the ground deformation in the study area is assumed to be concentrated in the vertical direction. Based on the incidence angle of the satellite LOS, the LOS deformation can be easily converted to vertical ground deformation. This kind of ground deformation transformation is reliable and has been widely adopted [11,19]. Note that the accuracy of the ground deformation obtained from InSAR analysis can be affected by the coherent pixels, the coherence values of which range from 0 to 1. In general, a smaller coherence value indicates that the ground deformation obtained is less reliable, whereas a larger coherence value indicates the ground deformation obtained is more accurate. Thus, the coherence threshold is often adopted in InSAR analyses and the threshold adopted to ranges from 0.4 to 0.9 depending on the topographic complexity [40,49]. In this study, the threshold value is set at 0.8 for screening the InSAR analysis results, which is mainly determined through a preliminary sensitivity analysis; this value can yield accurate and sufficient ground deformation points.

In reference to Daout et al. [9] and Lu et al. [32], the ground deformation of the permafrost on the Tibetan Plateau under climate warming can be decomposed into two elements: long-term deformation (mainly induced by the increase in active-layer thickness under climate warming) and seasonal deformation (mainly induced by the frost heave and thaw settlement within each freeze–thaw cycle). Thus, the ground deformation of the permafrost, denoted as S, can be approximated as follows.

$$S(t) = a \times t + b \times \sin\left(\frac{2\pi}{T} \times t\right) + c \times \cos\left(\frac{2\pi}{T} \times t\right) + d \quad (1)$$

where t represents the time (unit: day); T represents the period of a freeze–thaw cycle, which is usually set at one year (i.e., T = 1 year); and a, b, c, and d represent the model coefficients.

3.2.2. Analysis of Geometric Distortion in Input SAR Images Using the R-Index Model

The quality of the InSAR analysis results (i.e., ground deformation) can be greatly affected by geometric distortions in input SAR images, which can be analyzed from the orientation parameters of the satellite LOS (i.e., incidence angle and azimuth angle) and

the features of the local terrain (i.e., slope and aspect). For example, the effectiveness of the InSAR analysis results can be degraded in areas with poor terrain visibility. To locate the areas with poor visibility (in SAR images) in the study area, the *R-index* model [34,50,51], which has been widely adopted for analyzing geometric distortions, is employed in this paper. This *R-index* is calculated based on the cosine of the angle between the local terrain surface and the radar beam, as follows [44],

$$R - index = sin\{\theta + \arctan[tan\alpha \times \cos(\varphi - \beta)]\} \times La \times Sh \quad (2)$$

where α is the slope of the terrain; β is the aspect of the terrain; θ is the incidence angle of the satellite LOS; φ is the azimuth angle of the satellite LOS; *La* is the layover coefficient; and *Sh* is the shadow coefficient. The coefficients of *La* and *Sh* can be calculated using the hillshade model, with the satellite position representing the sun in GIS software [51]. The geometric distortion areas in the study area can be determined with the following criteria: (1) if the *R-index* is greater than or equal to $sin(\theta)$ (i.e., $R\text{-}index \geq sin(\theta)$), the related area is categorized as an area with good visibility, and no geometric distortion exists; (2) if *R-index* is between 0 and $sin(\theta)$ (i.e., $0 < R\text{-}index < sin(\theta)$), the related area is categorized as a foreshortening region, and geometric distortion exists; and (3) if *R-index* is not positive (i.e., $R\text{-}index \leq 0$), the related area is categorized as a layover or shadow region, and geometric distortion exists. In this study, the areas with geometric distortions (i.e., foreshortening, layover, and shadow) are considered as areas with poor visibility. From there, the high-quality areas, which are defined as the intersection of the areas with InSAR deformation points and good visibility, in the study area can be located, whereas the rest of the areas are categorized as low quality.

3.2.3. Random-Forest-Method-Based Permafrost Stability Mapping

As discussed above, the relationship mapping between the environmental factors and permafrost stability is fairly similar to that between the environmental factors and landslide occurrence. There are various models for mapping the relationship between environmental factors and landslide occurrences, such as neural-network-based deep learning [52,53], decision trees [54], frequency ratios [55], and fuzzy assessment [36]. These methods could be readily adopted for mapping the relationship between environmental factors and permafrost stability. Note that although the deep learning method can achieve high accuracy in landslide susceptibility mapping and permafrost stability mapping, the computational efficiency might be relatively low. In this study, the random forest model [56] is adopted for the relationship mapping between the environmental factors and the permafrost stability, mainly for the following reasons: (1) the random forest method is a non-linear, non-parametric algorithm that can deal with large datasets containing both categorical and numerical data and account for complex interactions and non-linearity between variables; (2) it can handle missing values and maintain accuracy for missing data; (3) compared with other machine learning methods, such as artificial neural network, the random forest method does not require much fine-tuning of hyperparameters; in many cases, using default parameter settings can achieve good performance [57,58]; and (4) compared with other tree-ensemble methods, the random forest method is computationally light. Therefore, the random forest method is commonly used in large-scale mapping and classification applications [58]. Although the random forest method is adopted in this study to map the relationship between permafrost stability and environmental factors, other machine learning methods, which have their specific advantages, can also be adopted for mapping such a relationship. Within the context of the random forest method, the technique of bootstrap resampling is used for extracting bootstrap samples from the original samples; each bootstrap sample is then modeled by a decision tree and the predictions obtained from multiple decision trees are finally combined. As such, the issues caused by the outliers in the prediction, overfitting, and data missing in the training samples can be overcome. In addition, the random forest method adopted has been shown effective in mapping the permafrost degradation-induced thaw settlement susceptibility on the Tibetan Plateau [59].

Note that the selection of the number of decision trees plays a vital role in the prediction accuracy of the trained random forest model. For example, an insufficient number of decision trees may lead to the reduced accuracy of the model prediction, whereas an excessive number of decision trees may cause data redundancy. In this study, the determination of the number of decision trees is based on trial-and-error analysis, and when the number of decision trees is larger than 400, the prediction accuracy does not increase. Thus, based on a tradeoff analysis between prediction accuracy and data redundancy, the number of decision trees in this study is set up as 400.

The analyses by Ran et al. [12] and Chen et al. [60] indicated that permafrost stability can be greatly affected by vegetation coverage (i.e., NDVI) and the topography factors of ground elevation and slope orientation. The report from Deluigi et al. [61] showed that permafrost stability can also be affected by other topographic factors such as slope and curvature, and the analysis in Qin et al. [62] depicted that the land surface temperature might influence the vegetation coverage and soil water content, which could be a good indicator for analyzing the permafrost stability. Further, the land cover plays a vital role in influencing permafrost stability [63]. Apart from the factors discussed above, the permafrost stability might also be degraded by engineering activities. For example, the construction and operation of the Qinghai–Tibet Highway has led to an obvious degradation of the permafrost along this highway [64]; thus, the Qinghai–Tibet Highway is also one of the important environmental factors in assessing permafrost stability.

Under these circumstances, eight environmental factors, including the ground elevation, aspect, slope, curvature, land cover, NDVI, land surface temperature, and distance to the Qinghai–Tibet Highway, are extracted in the study area for mapping the permafrost stability. Here, the topography factors (i.e., ground elevation, aspect, slope, and curvature) are calculated from the ALOS DEM, the land cover is generated from the GlobeLand30 product (http://www.globallandcover.com/, accessed on 19 March 2023), the NDVI and land surface temperature are the annual average NDVI and land surface temperature from 2014 to 2020, which are generated using Landsat 8 Level 2 images on the Google Earth Engine platform (http://earthengine.google.org/, accessed on 19 March 2023), and the distance to Qinghai–Tibet Highway is generated by the Euclidean distance function in GIS software. Plotted in Figure 3 are the environmental factors extracted in the study area, which are resampled into the 100 m by 100 m spatial grids.

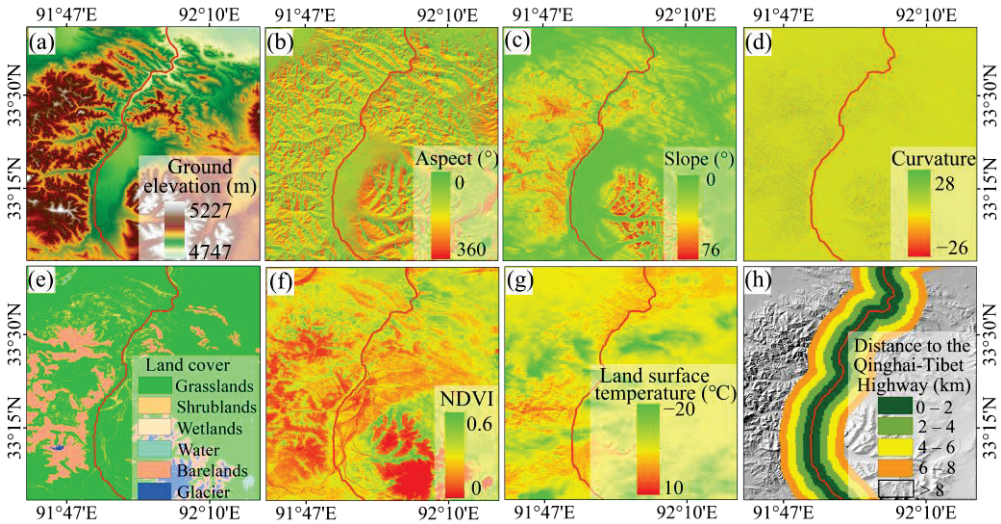

Figure 3. Environmental factors extracted in the study area: (**a**) Ground elevation; (**b**) Aspect; (**c**) Slope; (**d**) Curvature; (**e**) Land cover; (**f**) NDVI; (**g**) Land surface temperature; (**h**) Distance to the Qinghai–Tibet Highway.

A multicollinearity analysis indicates that the environmental factors shown in Figure 3 are independent of each other. For ease of screening stable and unstable ground points

in the initial InSAR analysis results, threshold values for the ground deformation rate are prespecified, and the determination of these threshold values is detailed in the section containing the results. In order to train the relationship between the environmental factors and permafrost stability, 80% of the high-quality samples, which are extracted in the high-quality area and screened according to the threshold values of the ground deformation rate and Google Earth image characteristics, are taken as the training samples, whereas the rest (20%) of the high-quality samples, which are not involved in the model training, are taken as the validation samples to assess the accuracy of the model. In summary, the data adopted for training the random forest model are the high-quality samples extracted in the high-quality area; the inputs to the random forest model are the environmental factors including the ground elevation, aspect, slope, curvature, land cover, NDVI, land surface temperature, and distance to the Qinghai–Tibet Highway, whereas the output of the random forest model is the mapping result in the whole study area, in terms of a probability of permafrost stability ranging from 0 to 1 (where 0 represents permafrost instability and 1 represents permafrost stability).

In this study, except for the validation samples, the receiver operating characteristics (ROC) curve is also employed for evaluating the mapping accuracy of the trained random forest model [65]. The ROC curve plots the true positive rate on the *Y*-axis and the false positive rate on the *X*-axis. The area under the curve (AUC) measures the probability of correct classification, and an AUC value close to 1 indicates high mapping accuracy. In addition, the relative importance of each environmental factor to the permafrost stability is evaluated by the indexes of mean decrease accuracy (MDA) and mean decrease Gini (MDG), which can be calculated according to the reduction in the prediction accuracy when values of this environmental factor in a decision tree are permuted randomly [56].

4. Results

4.1. Results of the Ground Deformation with Time-Series InSAR Analysis

4.1.1. Ground Deformations Obtained in the Study Area

Figure 4a shows the vertical ground deformation rate in the study area obtained from October 2014 to August 2020. As can be seen, the ground deformation rate ranges from −58 mm/year to 29 mm/year, and the regions with permafrost instability, indicated by the area with large deformation rates, are mainly distributed in the valley areas with low altitudes where the water content is relatively high. However, there are areas with high deformation rates that are distributed in high-altitude mountainous areas. The reason may be that permafrost stability is affected by various environmental factors. For example, the land cover type in some high-altitude mountainous areas is bare lands with no vegetation coverage, which is susceptible to ice melting and thaw subsidence. In addition, the ground deformation mainly takes place on the west-facing slopes (see the comparison in Figure 4b,c), partially because the input SAR images are collected by the descending satellite. Note that the terrain visibility of the descending SAR images in east-facing slopes is mainly foreshortening, which means the ground deformation results obtained for east-facing slopes might be not reliable. Further, the visual interpretations of Google Earth images indicate that there may be unstable characteristics in east-facing slopes, as shown in Figure 4d,e. In fact, many studies have shown that the deformation results in foreshortening areas and other poor visibility areas are not accurate [34,66,67]. As such, although there are many deformation points located on east-facing slopes, the related deformation results are not reliable and could not be adopted to indicate permafrost degradation. More deformation points in Figure 4b, compared with Figure 4c, might be attributed to the higher coherence of the interferograms.

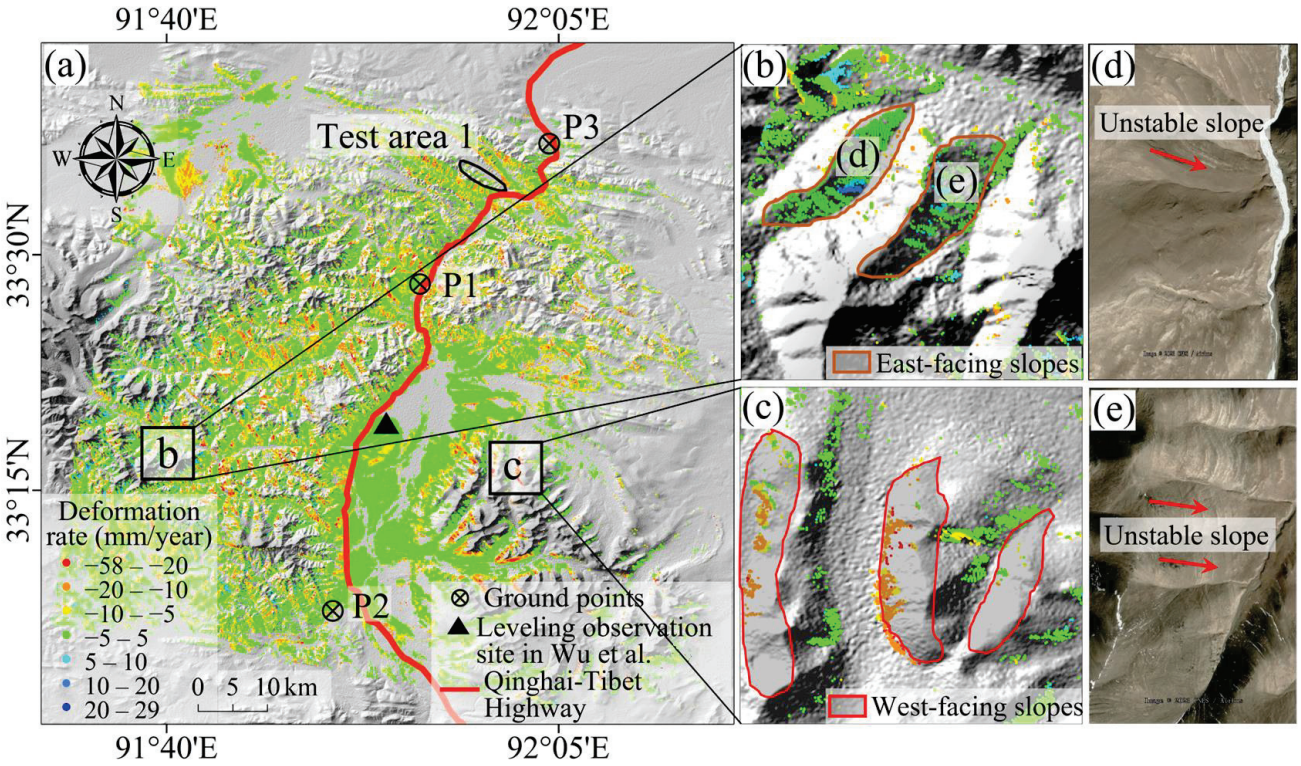

Figure 4. InSAR analysis results of the ground deformation in the study area: (**a**) Vertical ground deformation rate from October 2014 to August 2020 [39]; (**b**) Ground deformation rate in east-facing slopes; (**c**) Ground deformation rate in west-facing slopes; (**d**,**e**) Google Earth images for east-facing slopes (Image from © Google Earth 2020).

As described above, the ground deformation of permafrost areas can be decomposed into two elements: long-term deformation and seasonal deformation. Note that the long-term ground subsidence induced by the thawing permafrost could lead to permafrost instability or degradation. Here, the ground deformations at three points (in terms of points P1, P2, and P3 in Figure 4a) are adopted to analyze the ground deformations using the empirical model established in Equation (1). According to the ground deformations monitored from October 2014 to August 2020, the model coefficients are estimated with the least squares method. Although deviations exist in the estimated deformation trend, and the errors caused by such deviations may come from processing errors (e.g., phase unwrapping errors) and human disturbance that cause the low R-square of P1, the overall trend of the ground deformations is not much affected. For example, the R-squares of P2 and P3 are relatively high (i.e., 0.80 and 0.83), indicating that the ground deformations in the study area can be well captured by the empirical model shown in Equation (1), as shown in Figure 5a. Indeed, such an empirical model has been excessively adopted for the decomposition of ground deformations in permafrost areas [9,32]. Moreover, the decomposition of the ground deformation using the empirical model is mainly conducted to determine the periods of thawing and frozen seasons, and the inputs to the built random forest model are the unstable and stable ground points determined through the ground deformation rate estimated from time-series InSAR analyses and Google Earth images. Thus, the accuracy of the permafrost stability mapping in the study area would not be degraded by the deviations in the empirical models shown in Figure 5a. The plots in Figure 5a indicate that the ground surface exhibits heaves in the frozen season (from September to March, attributed to the freezing of the active layer) and exhibits subsidence in the thawing season (from April to August, attributed to the thaws of the active layer). Hence, the maximum ground settlement of the permafrost each year occurs around the month of August. Figure 5b depicts that the seasonal deformations (calculated as the total deformation minus the long-

term deformation, expressed as $S(t) - a \times t$) tend to be negatively correlated with the air temperature, which confirms that the seasonal deformation is mainly caused by the frost heave and thaw settlement within each freeze–thaw cycle, similar phenomena were also observed by Lu et al. [32] and Zhao et al. [43].

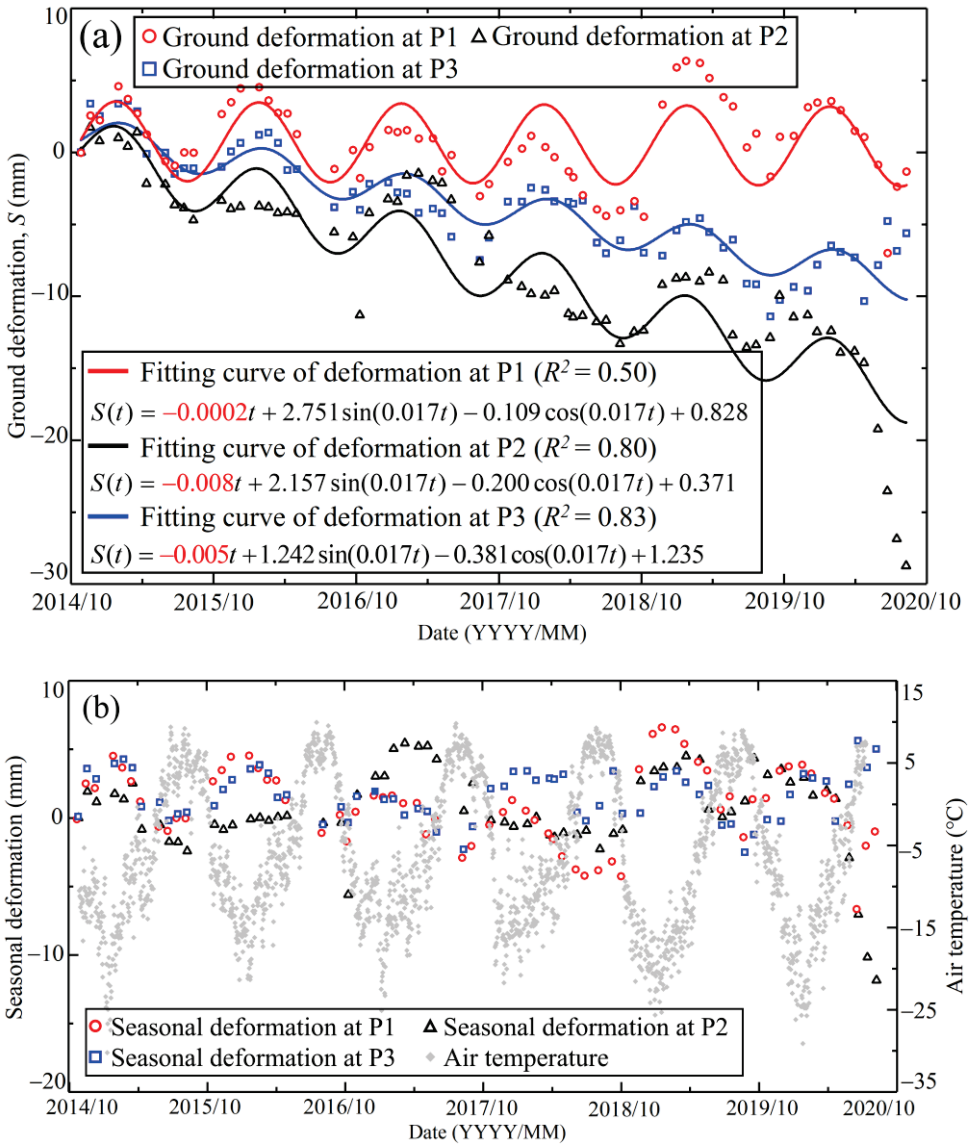

Figure 5. Fitting analysis of the ground deformation in the period from 2014 to 2020: (**a**) Fitting analysis between the ground deformation and the time; (**b**) Correlation analysis between the seasonal deformation and the air temperature (note: the air temperature is from the 2.0 m air temperature dataset from the European Centre for Medium-Range Weather Forecasting—Fifth-Generation Reanalysis (ECMWF ERA5)).

Figure 6 depicts that the maximum ground deformations of the study area occurred during the thawing periods in 2015, 2017, 2018, and 2019. It is found that the magnitude of the maximum seasonal thaw subsidence increases from 2015 to 2019, which is quite evident in the northern region of the study area, though there may be some exceptions due to the accuracy of the ground deformation results. To quantitively assess the subsidence trend, the study area is evenly divided into three regions (i.e., the northern, middle, and southern regions shown in Figure 6), then the average seasonal thaw subsidence of the whole study area and the three regions in 2015, 2017, 2018, and 2019 are estimated; the results are depicted in Figure 7. Note that the seasonal thaw subsidence consists of the

ground deformations that occurred in the thawing season (i.e., from April to August) and the average seasonal thaw subsidence values shown in Figure 7 are estimated in the whole study area, the northern region, the middle region, and the southern region, respectively. It shows that the subsidence in the whole study area and the northern region increases from 2015 to 2019, whereas that in the middle and southern regions is not evident. Note that the ground elevation of this study area tends to decrease from south to north, except along the Qinghai–Tibet Highway, as shown in Figure 1b. Therefore, the regions with a lower altitude have a higher risk of permafrost instability or degradation; this inference is in general agreement with the observations by Huang et al. [10] and Lu et al. [32]. For example, more thermokarst lakes, retrogressive thaw slumps, and failed slopes are detected in regions with low altitudes [10,32].

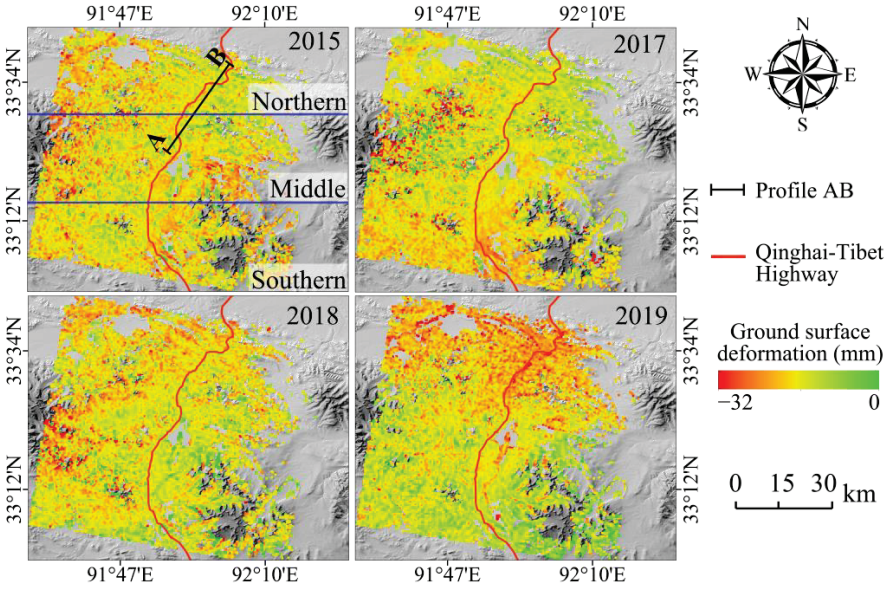

Figure 6. The maximum ground deformations of the study area occurred during the thawing periods in 2015, 2017, 2018, and 2019.

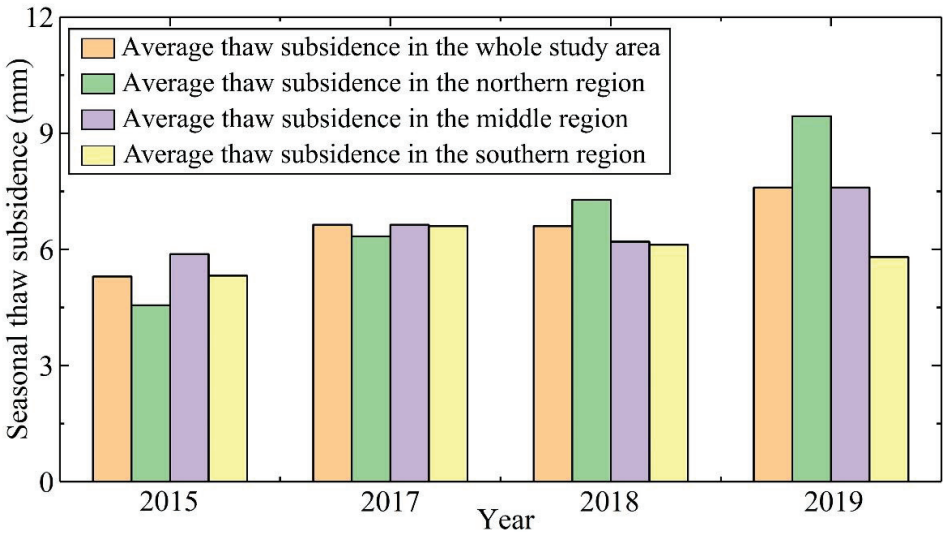

Figure 7. The average seasonal thaw subsidence of the whole study area and the three regions in 2015, 2017, 2018, and 2019.

4.1.2. Influences of Ground Elevation and NDVI on the Seasonal Thaw Subsidence

It is known that the watershed and river network in an area are mainly determined by the topography [60]; thus, the distribution of the water content in the ground can be

strongly affected by the local topography. To analyze the influence of the topography on the seasonal thaw subsidence of the permafrost areas, the river network in the study area is generated from the DEM, which is then superimposed onto the average seasonal thaw subsidence that took place in the period from 2015 to 2019, as shown in Figure 8a. Note that the average seasonal thaw subsidence shown in Figure 8a is the average value of the seasonal thaw subsidence from 2015 to 2019. In addition, in the InSAR processing, the topography-correlated tropospheric delay has been minimized through spatial–temporal filtering; thus, the atmospheric condition could not affect this analysis. As can be seen, the regions with large thaw subsidence are mainly located in the river valleys where the soil is typically fully saturated and the ground ice is rich [60,68], whereas the regions with small thaw subsidence are mainly located in the hill ridges where the water content in the ground is relatively low. Further, the elevation could affect the distribution of water content; thus, the influence of elevation on the seasonal thaw subsidence is also analyzed. To illustrate this analysis more intuitively, a profile, AB, which is along the highway, is delineated (see Figure 8a), and the study results are shown in Figure 8b,c. Figure 8b depicts the relationship between the acquired average seasonal thaw subsidence and the ground elevation. Plotted in Figure 8c are the variations of the seasonal thaw subsidence and the ground elevation along profile AB. As can be seen, a larger ground elevation tends to yield smaller thaw subsidence; however, there are exceptions. For example, the thaw subsidence in Zone I matches the ground elevation well, whereas that in Zone II cannot match the ground elevation. A detailed survey of the topography suggests that Zone I is located in a river valley, whereas Zone II is located on a north-facing slope (see Figure 8d). Although the ground elevation in Zone II is lower than that in Zone I, the solar radiation in Zone II may be much weaker and thus the ice in the ground is more difficult to melt. This phenomenon could also explain the low Pearson's coefficient between the elevation and the ground deformations shown in Figure 8b. Indeed, ground deformation can be affected by many environmental factors, and when other environmental factors are dominant, the impact of the ground elevation may be not significant. Although the Pearson's coefficient is very low, it still indicates that the elevation could have an impact on the ground deformation.

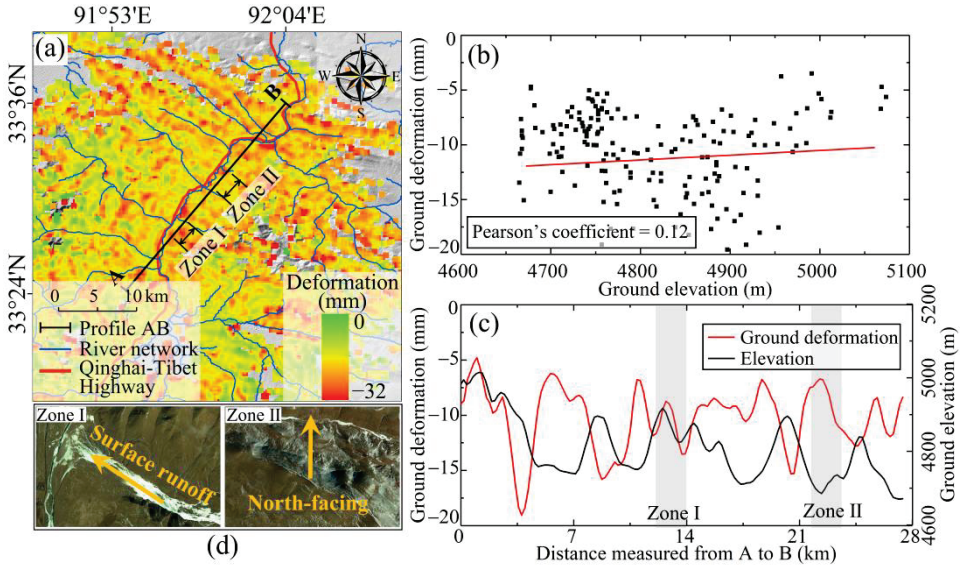

Figure 8. The influence of the topography on the seasonal thaw subsidence of the permafrost: (**a**) Average seasonal thaw subsidence of the study area took place in the period from 2015 to 2019; (**b**) Relationship between the seasonal thaw subsidence and the ground elevation along profile AB; (**c**) Variations in the seasonal thaw subsidence and the ground elevation with the distance measured from A to B along profile AB; (**d**) A detailed survey of the topography (Zone I is located in a river valley; Zone II is located on a north-facing slope).

The vegetation coverage is also taken as an important index of the soil water content [12]. The influence of the vegetation coverage on the seasonal thaw subsidence in the study area is herein investigated. In reference to Figure 9a, the vegetation coverage in the study area is dominated by grasslands and bare lands. The NDVI is employed in this study to represent vegetation coverage, and a larger NDVI value signals denser vegetation coverage. The influence of NDVI on the ground deformation (i.e., the average seasonal thaw subsidence that took place in the period from 2015 to 2019, see Figure 8a) is studied based on the data collected along the profile AB, and the results are illustrated in Figure 9b,c. Similar to that in Figure 8c, the change in the magnitude of the seasonal thaw subsidence is in good agreement with the change in NDVI: a larger NDVI value tends to result in smaller thaw subsidence, partially due to the protective effect of the vegetation coverage (on the ground) in terms of the ice melting (in the ground). The study by Jin et al. [69] confirmed that vegetation coverage has important impacts on the ground thermal regime by influencing the energy transfer between the atmosphere and ground surface and thus affects the seasonal thaw subsidence. Figure 9b,c depict that a smaller NDVI value tends to result in larger thaw subsidence, and the bare lands with smaller NDVI values tend to have larger thaw subsidence; however, the seasonal thaw subsidence can be affected by various factors (e.g., elevation, slope, and ice content), making the relationship between the seasonal thaw subsidence and the NDVI values not statistically significant. As such, the bare lands with smaller NDVI values do not always yield significant deformations.

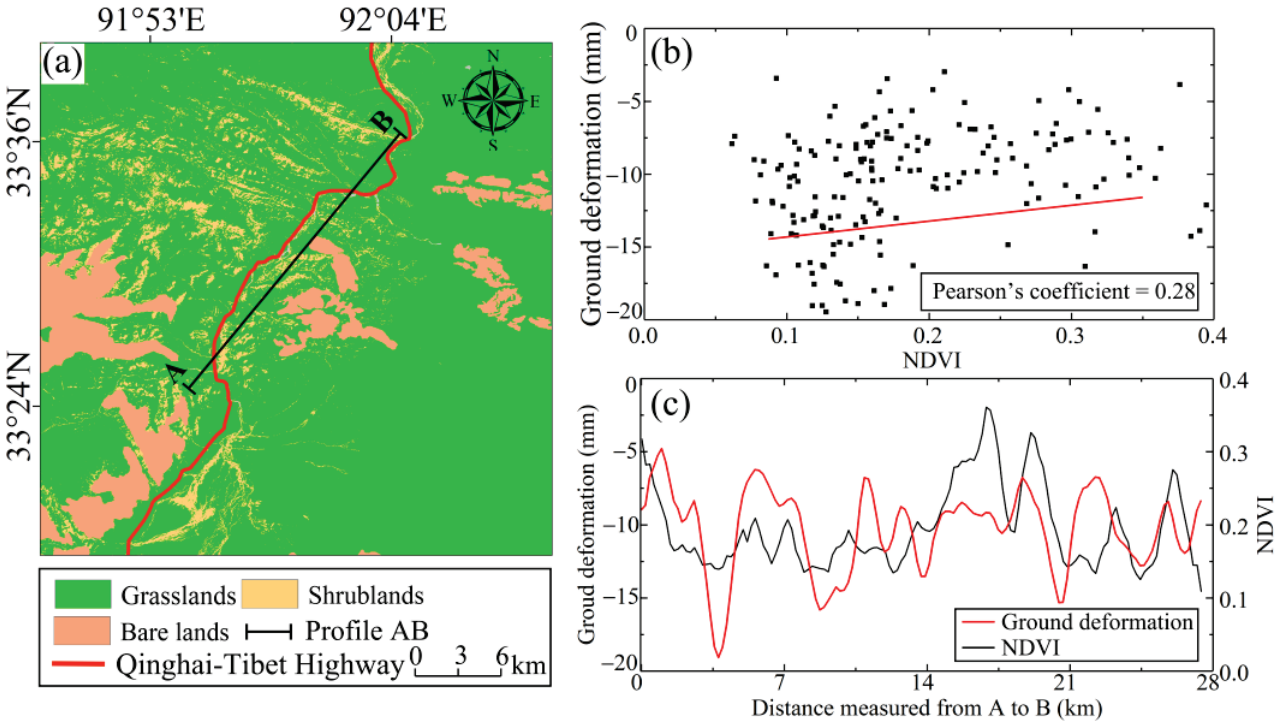

Figure 9. The influence of the vegetation coverage on the seasonal thaw subsidence of the permafrost: (**a**) Vegetation coverage in the study area; (**b**) Relationship between the seasonal thaw subsidence and the NDVI along profile AB; (**c**) Variations in the seasonal thaw subsidence and the NDVI with the distance measured from A to B along profile AB.

4.2. Results of Screening and Permafrost Stability Mapping with the Proposed Method

4.2.1. Screening Results of the High-Quality and Low-Quality Areas

As mentioned previously, the coherence threshold is set at 0.8 in the processing of SAR images. As a result, only the high-quality InSAR deformation points could be kept in the initial InSAR analysis of the ground deformations, whereas the InSAR deformation points where the coherence is less than the threshold value of 0.8 are not displayed. Thus,

the initial map of the obtained ground deformation cannot cover the entire study area, as shown in Figure 4a. Here, the areas that do not have ground deformation are categorized as the low-quality areas.

The geometric distortion analysis results are sketched in Figure 10a. As can be seen, most areas can be categorized as good visibility areas, and the east-facing slopes are mainly located in the regions with geometric distortions (see Figure 10b). The areas with geometric distortions are then categorized as the low-quality areas. From there, the high-quality areas, defined as the intersection of the areas with InSAR deformation points (see Figure 4a) and good visibility (see Figure 10a), can be located. Figure 10c depicts the zonation of the high-quality and low-quality areas in the study area. Here, the ground deformation monitored in the high-quality areas is reliable, whereas that monitored in the low-quality areas can be problematic.

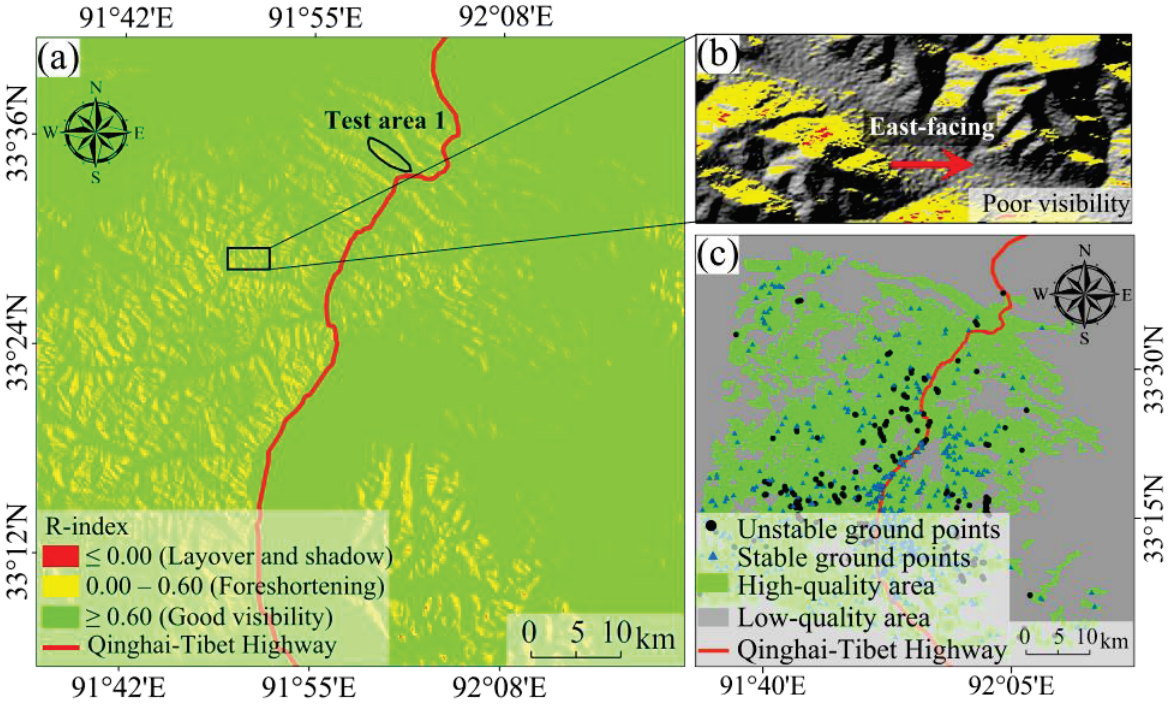

Figure 10. Screening analysis of the InSAR analysis results of ground deformation in the study area: (**a**) Geometric distortion analysis results; (**b**) A detailed survey of the geometric distortions on an east-facing slope; (**c**) Zonation of the high-quality and low-quality areas.

According to the Google Earth images, the permafrost instability areas with obvious unstable characteristics (e.g., retrogressive thaw slumps and failed slopes) are usually located in areas with a ground deformation rate smaller than −40 mm/year. Thus, in this study, the ground points with a deformation rate smaller than −40 mm/year and obvious unstable characteristics are classified as unstable ground points. In reference to Zhang et al. [70], the maximum subsidence rate of the permafrost instability area that is located in the central Tibetan Plateau is about −30 mm/year. In other words, the threshold value of −40 mm/year adopted in this study is relatively conservative. The stable ground points are also determined according to the ground deformation rate and the image characteristics. In general, the areas with a ground deformation rate close to 0 mm/year could be classified as stable, thus the threshold value of the ground deformation rate for stable ground points should be set at a value close to 0 mm/year. Additionally, an equal number of stable ground points should be identified in the high-quality area to avoid potential bias in the selection of samples. Based on these two criteria, the threshold value of the ground deformation rate for the stable ground points is set at ±0.15 mm/year. Thus, the ground points with a deformation rate ranging from −0.15 mm/year to 0.15 mm/year and no obvious unstable

characteristics are classified as stable ground points. Based on these criteria, a total number of 1172 high-quality samples (i.e., 586 unstable ground points and 586 stable ground points) (shown in Figure 10c) are included in the initial InSAR analysis results.

4.2.2. Permafrost Stability Mapping in the Study Area with the Random Forest Method

In order to train the relationship between the environmental factors and permafrost stability, 80% of the 1172 high-quality samples screened above (i.e., 80% of 586 unstable ground points and 80% of 586 stable ground points) are taken as the training samples and the other 20% of the 1172 high-quality samples are taken as the validation samples. The outcome of the permafrost stability mapping by the trained random forest model is a value ranging from 0 to 1, which indicates the probability of permafrost stability. For example, 0 represents permafrost instability whereas 1 represents permafrost stability. For ease of visual interpretation, this value is then categorized into five classes of permafrost stability (i.e., very low, low, medium, high, and very high) with the Jenks optimization method [71], and the resulting values of the five classes are [0, 0.36), [0.36, 0.56), [0.56, 0.72), [0.72, 0.86), and [0.86, 1], respectively.

Figure 11a depicts the results of the permafrost stability mapping in the study area with the trained random forest model. Figure 12 shows the validation of the trained random forest model using the ROC curve based on the descending dataset; the AUC value of the permafrost stability mapping results is 0.975, indicating the high mapping accuracy of the trained random forest model using the descending dataset. Meanwhile, among the 234 validation samples, 82.05% of the unstable ground points are located in areas with very low and low permafrost stability. Therefore, the mapping accuracy of the permafrost stability can be quantitatively validated.

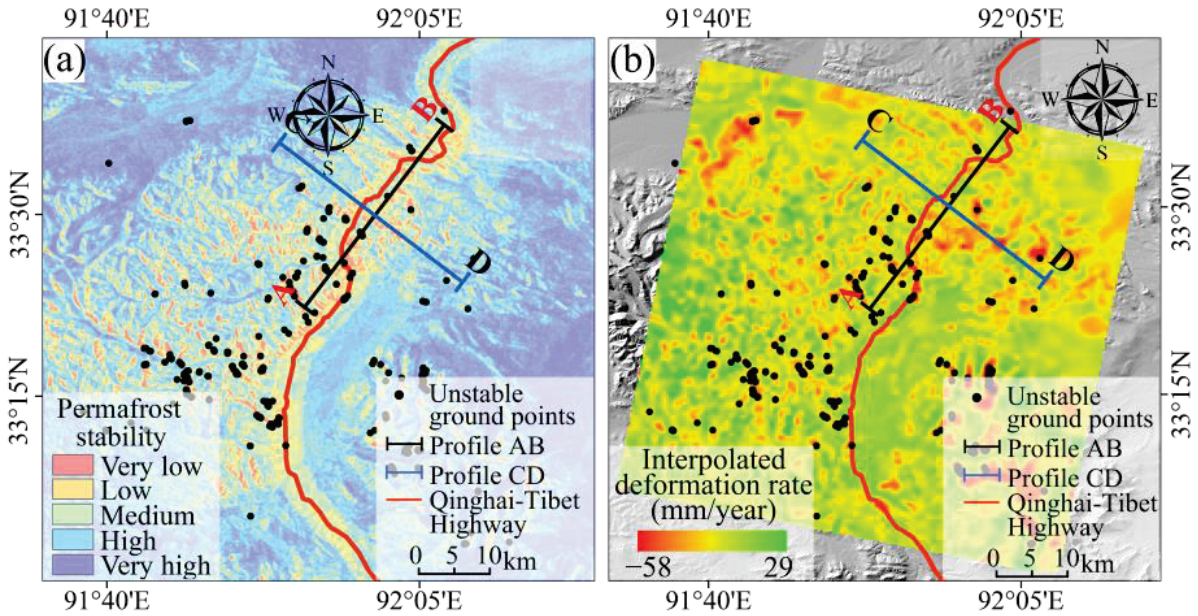

Figure 11. Permafrost stability mapping in the study area: (**a**) Results of the permafrost stability mapping with the trained random forest model; (**b**) Ground deformation rate obtained by the Kriging interpolation of initial InSAR analysis (Note: Profiles AB and CD are delineated to compare the two permafrost stability results).

To illustrate the effects of different classification schemes on permafrost stability classes, other classification schemes including equal intervals and standard deviations are also adopted to categorize permafrost stability; the results are shown in Figure 13. Compared with Figure 11a, although different classification schemes can generate different permafrost stability classes, the spatial distribution of the permafrost stability class is similar. For example, the very low and low permafrost stability is mainly distributed along the highway

and the river valleys. In fact, the Jenks optimization method seeks to reduce the variance within classes and maximize the variance between classes, which can effectively categorize a continuous variable into different classes using natural breaks in the data values. This method has been widely adopted in classification tasks [59,72]. Figure 14 shows the relative importance of the environmental factors for permafrost stability. In general, larger values of these two indexes (i.e., MDA and MDG) could signal the greater importance of the related environmental factor. As can be seen, the permafrost stability is mostly affected by the slope and the aspect, whereas the least impact is from the curvature. The other environmental factors yield similar importance in the permafrost stability mapping. It is noted that although the curvature yields the least impact on permafrost stability, it cannot be ignored in permafrost stability mapping.

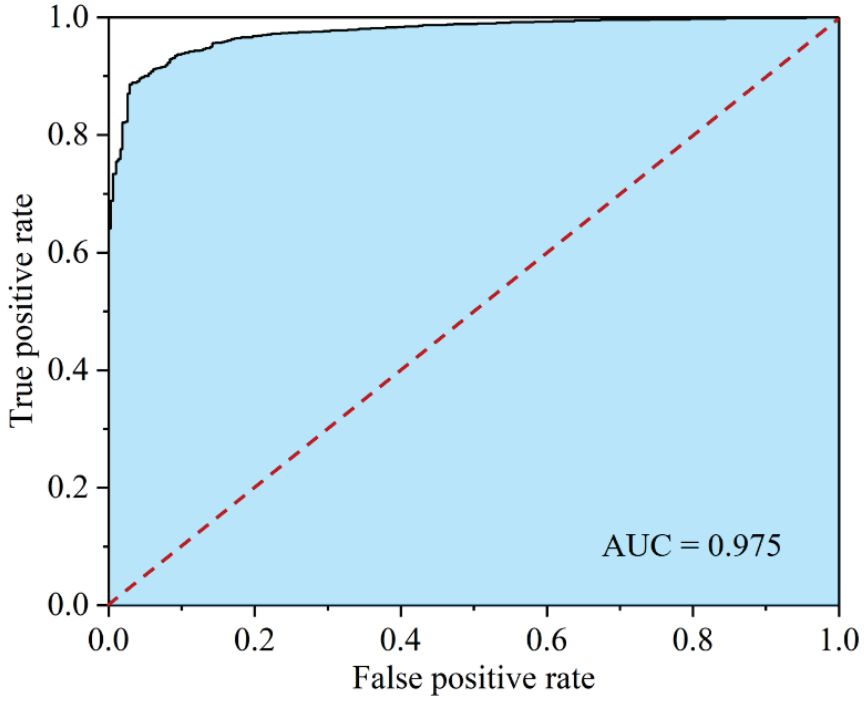

Figure 12. Validation of the trained random forest model using the ROC curve.

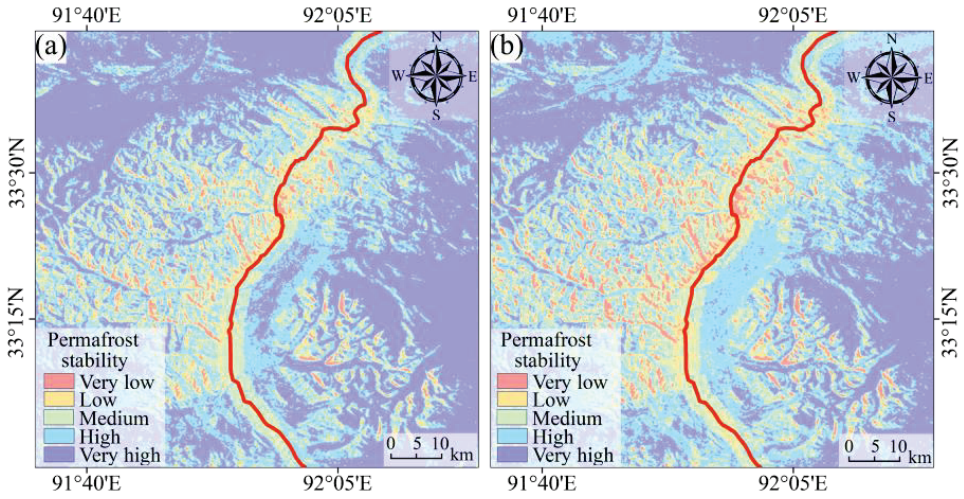

Figure 13. Permafrost stability mapping using different classification schemes: (**a**) Equal intervals; (**b**) Standard deviations.

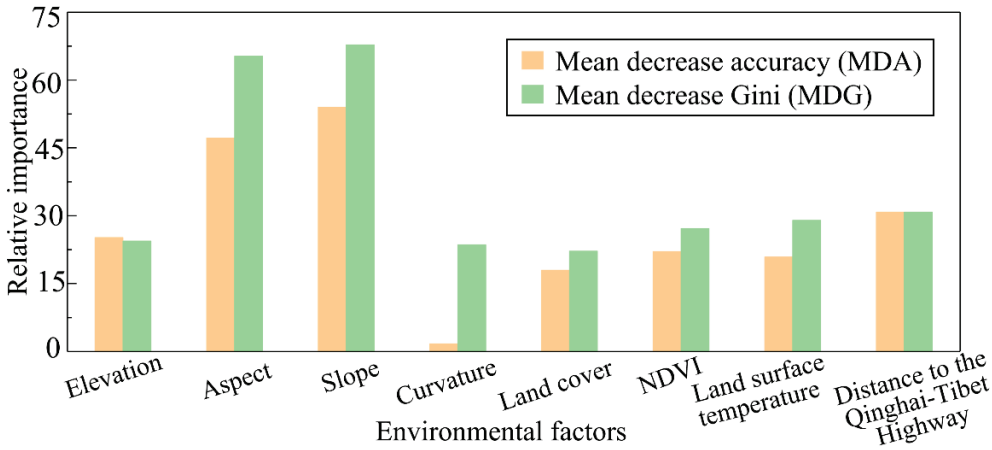

Figure 14. The relative importance of the environmental factors to the permafrost stability.

5. Verifications and Discussions

5.1. Verifications of the Ground Deformations Obtained with InSAR Analysis

As formulated above, the high-quality samples (i.e., the basic inputs to the proposed permafrost stability mapping) are derived from the time-series InSAR analysis. Thus, the verification is vital for the accuracy of the time-series InSAR analysis results. Note that the InSAR analysis results and the field measurements often cover different temporal and spatial scales. Hence, a direct verification by the field measurements might be impossible [60]. Further, ground-based deformation measurement is fairly limited within the study area. In this study, the time-series InSAR analysis results are mainly verified through comparing them with the leveling data and InSAR analysis results outlined by Wu et al. [39]. As only one leveling site is located in the study area, only one leveling datapoint is provided in this study. The location of the leveling observation site is labeled in Figure 4a. Figure 15 shows the InSAR analysis results obtained in this study together with the leveling data and InSAR analysis results obtained by Wu et al. [39]. As can be seen, the InSAR analysis results obtained in this study are in general agreement with the leveling data and InSAR analysis results obtained by Wu et al. [39], even though an inconsistency exists in the frozen season from 2015 to 2016. In our study, frost heave is observed in this frozen season, whereas thaw settlement was detected by Wu et al. [39]. The InSAR analysis results obtained in this study appear to be more consistent with the available knowledge of ground deformations in the study area than those outlined by Wu et al. [39]. In addition, limited by the resolution of the adopted SAR images, the deformation point obtained in this study is only the closest point near the leveling data, and they do not overlap. Further, the leveling site may be disturbed by human activity, which could also cause the inconsistency shown in Figure 15. In general, there are negative correlations between ground deformations and air temperature [43]; thus, the relationships between the ground deformations and the air temperature are analyzed to further verify the effectiveness of the time-series InSAR analysis results obtained in this study. Note that the air temperature is from the 2.0 m air temperature dataset from the European Centre for Medium-Range Weather Forecasting—Fifth-Generation Reanalysis (ECMWF ERA5); this reanalysis data combines model data with observations from across the world into a globally complete and consistent dataset. Here, three ground points (points P1, P2, and P3 in Figure 4a) are studied, and the resulting relationships between the ground surface deformations and the air temperature are plotted in Figure 16a. As expected, the ground deformations in the thawing seasons are large (caused by thaw settlement), whereas those in the frozen seasons are small (caused by frost heave), and the air temperature in the thawing seasons is high, whereas in the frozen season it is low. Figure 16b–d show that the Pearson's coefficients between ground deformation and the air temperature of points P1, P2, and P3 reach −0.53, −0.50, and −0.51, respectively, which quantitatively confirms the

negative correlations between the ground deformations and the air temperature and thus verifies the accuracy of the InSAR analysis results.

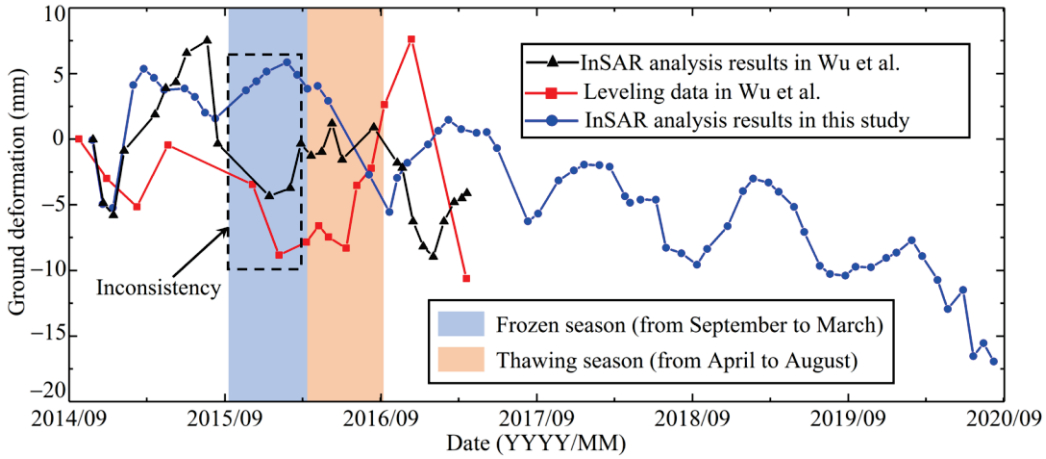

Figure 15. Verifications of the time-series InSAR analysis results with the leveling data and InSAR analysis results obtained by Wu et al. [39] (Reprinted with permission from ref. [39]. Copyright 2018 Copyright Sciences in Cold and Arid Regions).

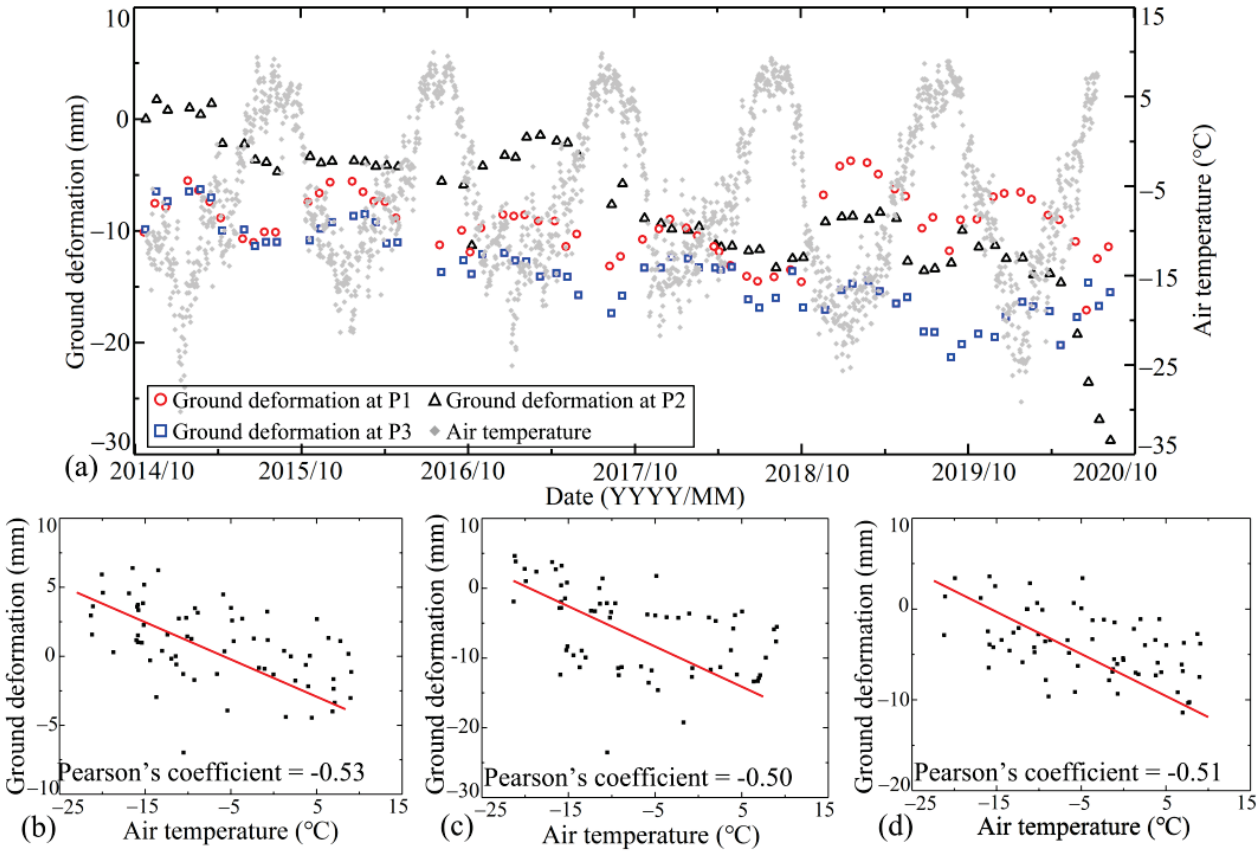

Figure 16. Relationships between the ground deformation and the air temperature: (**a**) Relationships between the ground deformation and the air temperature at points P1, P2, and P3; (**b**–**d**) Correlations between the ground deformation and the air temperature at points P1, P2, and P3.

Note that the comparison of the ground deformations over flat areas obtained from both descending and ascending data can also be adopted for verifying the deformation signals. Thus, the ground deformations in the study area are further analyzed with the

ascending Sentinel-1 SAR images, and the results are illustrated in Figure 17. It is noted that the same procedures are adopted for processing the ascending and descending SAR images. Figure 17a shows the ground deformation rate obtained from the ascending Sentinel-1 SAR images. As can be seen, the ground deformation rates in the study area obtained from the ascending SAR images are in general agreement with those obtained from the descending SAR images (see Figure 4a). To quantitatively compare the two ground deformation results, the vertical ground deformation rates obtained from the ascending and descending SAR images are both extracted from good visibility areas, then the two deformation results are resampled to a grid of 100 × 100 m to avoid spatial mismatch. Figure 18a depicts that Pearson's coefficient reaches 0.84, which confirms the accuracy of the ground deformation results and time-series InSAR processing. Further, Figure 18b shows that the difference in ground deformation rates obtained from the ascending and descending SAR images obeys a normal distribution, with a mean of 0.02 mm/year and a standard deviation of 0.01 mm/year, and that this distribution quantitatively verifies the accuracy of the InSAR analysis results.

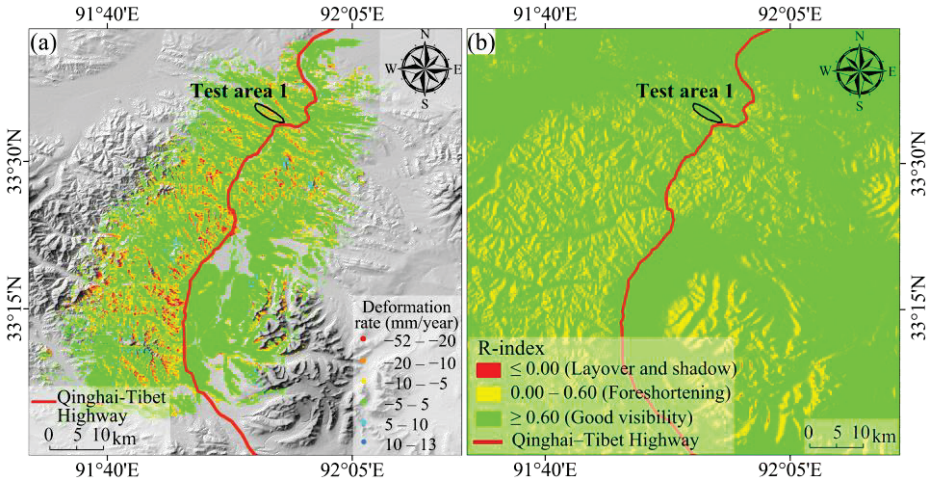

Figure 17. InSAR analysis results in the study area obtained from the ascending Sentinel-1 SAR images: (**a**) Vertical ground deformation rate from October 2014 to August 2020; (**b**) Geometric distortion analysis results.

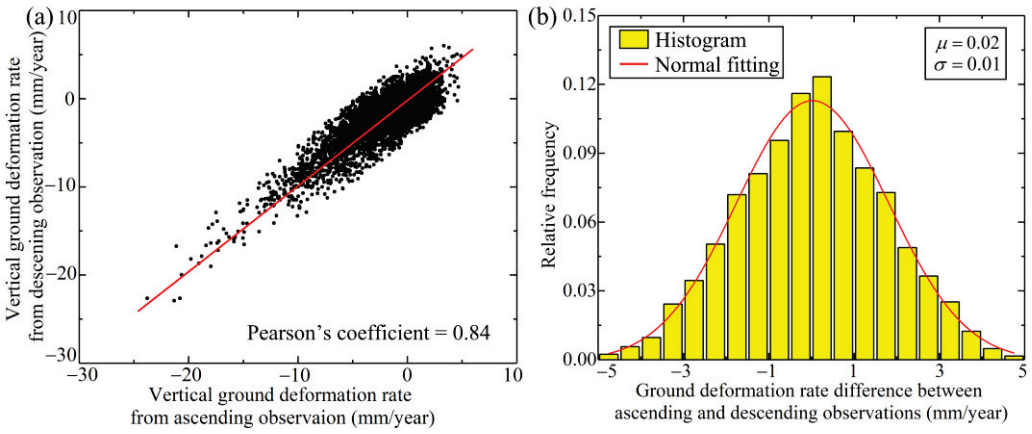

Figure 18. Comparison of the ground deformation rate obtained from ascending and descending SAR images: (**a**) Correlation analysis of the vertical ground deformation rates obtained from ascending and descending SAR images; (**b**) Distribution of the ground deformation rate differences between ascending and descending SAR images.

5.2. Verifications of Permafrost Stability Mapping with Ascending SAR Images

Figure 17b shows the geometric distortion analysis results of the ascending SAR images, which suggests that most regions in the study area can be categorized as having good visibility. To verify the permafrost stability mapping results shown in Figure 11a, the permafrost stability mapping results obtained with the proposed method and the ground deformations obtained from the ascending SAR images (see Figure 17a) are compared in Test Area 1, and the comparison results are illustrated in Figure 19. The permafrost stability in the bottom-right corner of this test area is low and very low (see Figure 19a). Note that this corner is mainly occupied by good visibility areas in the ascending SAR images (see Figure 17b), whereas it is occupied by geometric distortion areas in the descending SAR images (see Figure 10a); thus, the ground deformations in this corner obtained from the ascending SAR images are reliable, whereas those obtained from the descending SAR images might be problematic. Figure 19b shows the ground deformations in this corner obtained from the ascending SAR images, whereas Figure 19c shows those obtained from the descending SAR images. In Figure 19b, the bottom-right corner of Test Area 1 shows a trend of subsidence, which is in general agreement with the low or very low permafrost stability shown in Figure 19a, whereas only limited points with ground deformations could be obtained from the descending SAR images (see Figure 19c). From there, the accuracy of the permafrost stability mapping results obtained with the proposed method could be qualitatively validated based on this visual interpretation. Note that the quantitative comparison between the ground deformation results obtained from the ascending SAR images and the permafrost stability results is not carried out. The reason is that it is difficult to quantitatively measure the correspondence between the ground deformation results and the results of the permafrost stability. In addition, the comparisons in Figure 19 could also indicate that the combination of descending and ascending SAR images can improve the monitoring ability of ground deformation and thus provide an alternative for improving the permafrost stability mapping in some complex areas. However, in regions where the datasets are strongly degraded by terrain visibility, the ground deformation cannot be fully monitored by the combination of ascending and descending datasets. In such situations, the combination of InSAR and the machine learning method for permafrost stability mapping is still a topic worthy of investigation.

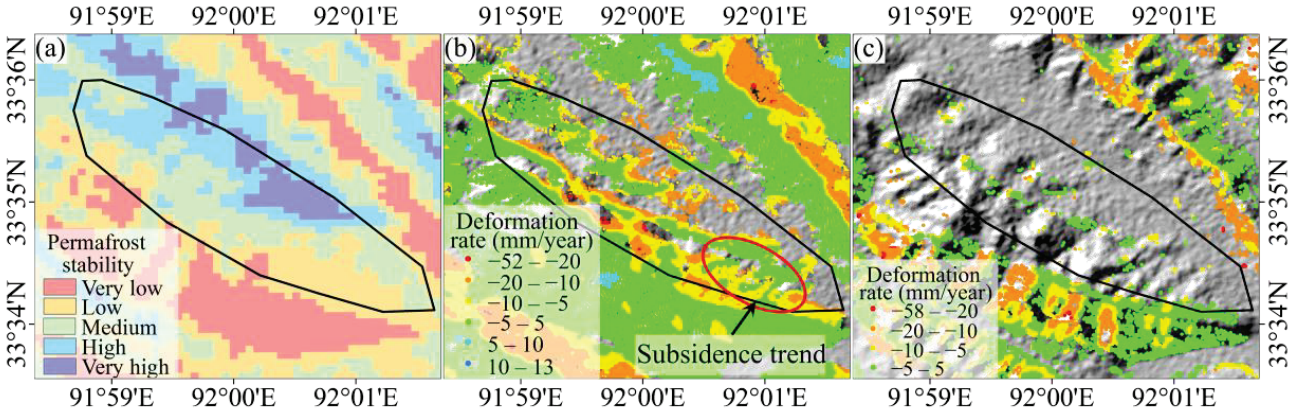

Figure 19. Comparisons between the permafrost stability mapping results in Test Area 1 obtained with the proposed method and the ground deformations obtained from the ascending SAR images: (**a**) Permafrost stability mapping results obtained with the proposed method; (**b**) Vertical ground deformation rates obtained from the ascending SAR images; (**c**) Vertical ground deformation rates obtained from the descending SAR images.

5.3. Superiority of the Proposed Method over the Sole Application of InSAR Analysis

To demonstrate the superiority of the proposed method over the sole adoption of InSAR analysis in permafrost stability mapping, a comparative analysis is carried out

between the permafrost stability zonation obtained by the proposed method and the ground deformation rate obtained from InSAR analyses (with descending Sentinel-1 SAR images as inputs). For ease of comparison, the ground deformation rate in the areas where the InSAR analysis results are not available is interpolated here using the Kriging method [73], and the results of this interpolation are plotted in Figure 11b. Though the interpolated deformation results may have deviations from the real deformation results, this interpolation method has been widely adopted for handling missing data [74,75] and the deviations could not affect the comparative results. As can be seen, the permafrost stability zonation obtained by the proposed method is in general agreement with the ground deformation rate obtained by InSAR analysis (see Figure 11a,b). However, due to the interpolated accuracy of the ground deformations there are exceptions. For example, the permafrost stability zonation is not consistent with the ground deformation rates in Zones III, IV, V, and VI. Figure 20 shows a detailed comparison between the permafrost stability zonation obtained by the proposed method and the ground deformation rate obtained by InSAR analysis along the profiles AB and CD (note: these two profiles are depicted in Figure 11a,b).

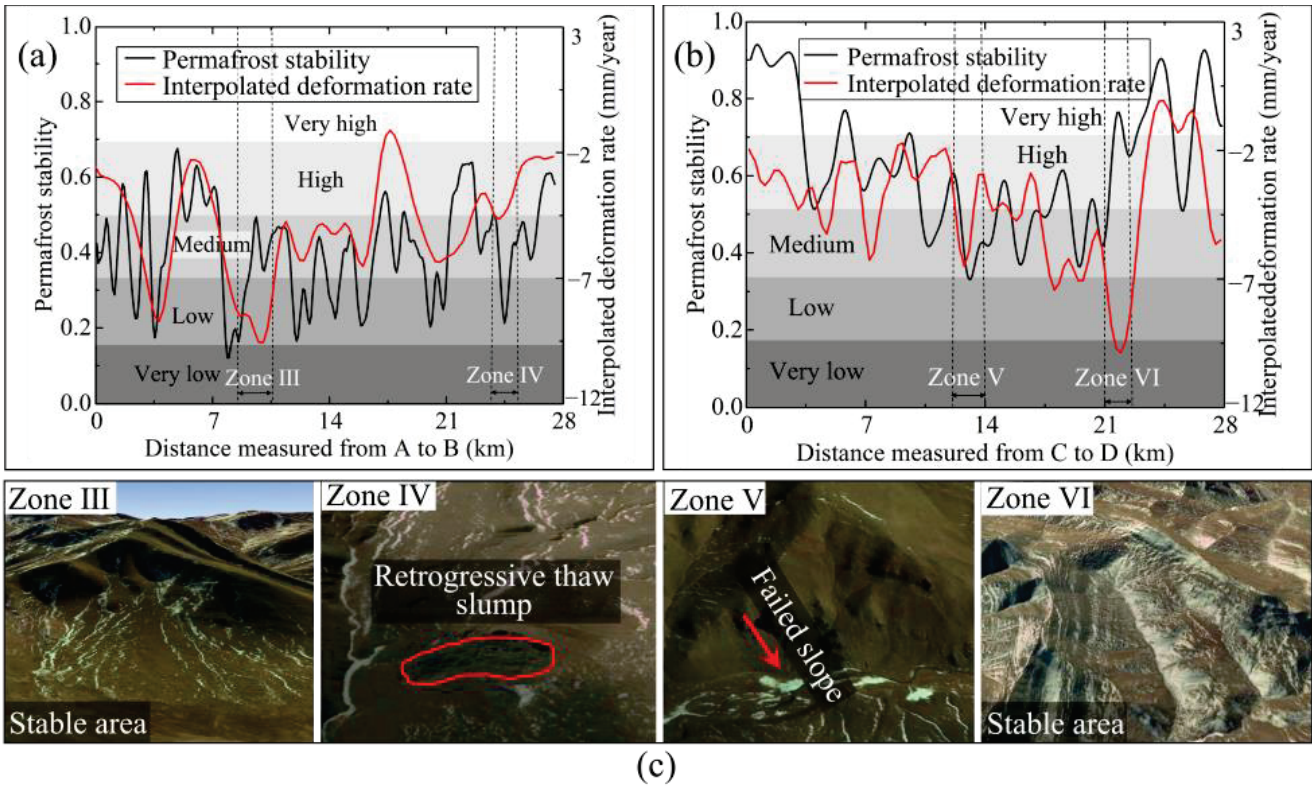

Figure 20. Comparisons between the proposed method and the sole application of InSAR analysis: (**a**) Permafrost stability zonation obtained by the proposed method versus the ground deformation rate obtained by the Kriging interpolation of initial InSAR analysis along profile AB; (**b**) Permafrost stability zonation obtained by the integrated method versus the ground deformation rate obtained by the Kriging interpolation of initial InSAR analysis along profile CD; (**c**) A detailed survey of the permafrost stability in Zones III, IV, V, and VI with the Google Earth images (note: Zones III and VI are located in areas with medium and high permafrost stability and Zones IV and V are located in areas with low permafrost stability. Image from © Google Earth 2019).

It can be seen from Figure 20a,b that Zones III and VI are located in areas with medium and high permafrost stability according to the permafrost stability mapping obtained by the proposed method. The permafrost stability in Zones III and VI can be visually confirmed by the Google Earth images, as depicted in Figure 20c. However, the ground deformation rate (obtained by a combination of InSAR analysis and Kriging interpolation) in Zones

III and VI could reach −10 mm/year, indicating instability of the permafrost. Similarly, according to the permafrost stability zonation obtained by the proposed method, Zones IV and V are located in areas with low permafrost stability. In reference to the Google Earth images shown in Figure 20c, the stability of the permafrost in Zones IV and V is fairly poor, as evidenced by retrogressive thaw slumps and failed slopes. However, the ground deformation rate (obtained by the combination of InSAR analysis and Kriging interpolation) in Zones IV and V is larger than −5 mm/year, indicating stability of the permafrost. Hence, the proposed method is shown to be more effective in permafrost stability mapping than the sole adoption of InSAR analysis and the data scarcity issue of InSAR analysis in the low-quality areas could be surmounted.

5.4. Discussion on the Influence of Environmental Factors on the Permafrost Stability

It is worthwhile mentioning that the transfers of water and heat in the frozen soil could be strongly affected by environmental factors and that the transfers of water and heat can lead to phase changes in the water in the active layer, which consequently affects the permafrost stability [43]. In addition, the seasonal thaw subsidence in permafrost areas is highly related to the distribution of ice or water content in the active layer [60]. However, the ice or water content of the soil in a large area is challenging to monitor. Thus, only the influences of topography and vegetation coverage, which have great impacts on the distribution of the ice or water content in the soil [12,60], on the seasonal thaw subsidence are studied to analyze the influences of the environmental factors on permafrost stability. In this study, the reasons for only analyzing the influence of elevation on the ground deformations among these topography factors are as follows: (1) the occurrence of permafrost on the Tibetan Plateau is mainly affected by the high altitude [76]; thus, the permafrost stability can be more affected by the ground elevation; (2) it is known that the soil water content and the river network could affect the permafrost stability [60] and the river network can be generated from DEM; thus, the ground elevation could be the key parameter to assess permafrost stability.

In addition, the plots in Figure 9c indicate that for the same NDVI value, the seasonal thaw subsidence may vary with the position along the profile AB, implying that the influence of the vegetation coverage on seasonal thaw subsidence can be rather complicated. In most cases, the relationship between permafrost stability and vegetation might be interdependent or symbiotic [30,67]. On one hand, the vegetation coverage could shade from direct sunshine in summer and intercept snowfall in winter, as such, the vegetation could help cool the ground and thus protect the underlying permafrost. On the other hand, the shallow thickness of the active layer and the low temperature of the ground can prevent the growth of vegetation.

It is worthwhile mentioning that the heat flux in permafrost areas is also an important factor affecting permafrost thaw and permafrost stability and that it can be varied over several years. The heat flow can affect the permafrost soil temperature and thus affect permafrost stability [77–79]. However, this study area is only a small area located in the central region of the Tibetan Plateau, and it can be expected that the long-range variation of heat flow is the same over this area. Thus, the physical interpretation of the permafrost stability by considering the effect of heat flux is not achieved in this study.

In summary, this study proposes an integrated permafrost stability mapping method. It can be further applied to other permafrost areas on the Tibetan Plateau. This study is significant in assessing permafrost stability and predicting the potential permafrost degradation-related geohazards on the Tibetan Plateau under climate warming. Further, with the increase in engineering activities on the Tibetan Plateau, the permafrost stability mapping results could provide scientific support for engineering construction.

6. Conclusions

This paper presents a method that integrates InSAR and the random forest method for an improved permafrost stability mapping on the Tibetan Plateau. This method could overcome the problem of the data scarcity of InSAR analysis in low-quality areas (i.e., where InSAR analysis results are not available due to the coherence of InSAR analysis results and geometric distortions in input SAR images). To demonstrate the application of this proposed method, the permafrost stability mapping is studied in a small area located in the central region of the Tibetan Plateau. The results obtained are validated through qualitative and quantitative verifications, and comparative analyses are conducted to illustrate the superiority of this integrated method over the sole adoption of InSAR analysis in permafrost stability mapping. Based upon the results presented, the following conclusions are reached.

1. The initial InSAR analysis of the ground deformation shows that the maximum ground settlement of the permafrost occurs around the month of August each year, due to the frost heave of the active layer in the frozen season and subsidence in the thawing season, and the magnitude of the ground deformations tends to increase from 2015 to 2019, which might be taken as a sign of the degradation of the permafrost. The initial InSAR analysis also confirms that the seasonal thaw subsidence is strongly affected by the ground elevation topography and vegetation coverage.
2. According to the analysis of geometric distortion and coherence of the InSAR results, the high-quality areas could be recognized, in which high-quality samples can be readily located based on the threshold values of the ground deformation rate and Google Earth image characteristics. The permafrost stability and associated environmental factors for these high-quality samples can then be extracted for the permafrost stability mapping of the entire study area. The random-forest-based mapping analysis suggests that the permafrost stability (in the study area) is mostly affected by the slope and aspect, whereas the least impact is from the curvature. The factors of ground elevation, land cover, NDVI, land surface temperature, and distance to the highway yield similar importance in the permafrost stability mapping analysis.
3. The validation analysis of the obtained permafrost stability zonation, which is based on the ROC curve and the unstable ground points in the validation samples, indicates that this integrated method could yield high mapping accuracy in the study area. Through qualitative and quantitative verifications, the ground deformations and the permafrost stability mapping results obtained with the time-series InSAR analysis and the proposed method, respectively, could be validated. Compared with the sole adoption of InSAR analysis, this integrated method is shown to be more effective in permafrost stability mapping of the study area; meanwhile, the issue of data scarcity of InSAR analysis in the low-quality areas could be overcome.

It should be mentioned that although the proposed method has shown to be promising in the permafrost stability mapping of the study area, there is room for improvement. For example, research to further validate the permafrost stability zonation with ground-based measurements is warranted. Moreover, the InSAR analysis in the study is based on the Sentinel-1 C-band SAR images with a 6-day revisiting time, the effectiveness of which is often degraded in mountainous and vegetated areas. Hence, research is also warranted on data fusion methods that could integrate different sources of SAR images.

Author Contributions: Conceptualization, F.Z. and W.G.; methodology, F.Z.; software, T.R.; validation, F.Z., T.R. and J.C.; formal analysis, F.Z. and W.G.; data curation, F.Z.; writing—original draft preparation, F.Z.; writing—review and editing, F.Z. and W.G.; supervision, T.L.; project administration, H.T.; funding acquisition, W.G. and H.T. All authors have read and agreed to the published version of the manuscript.

Funding: This research was funded by the Outstanding Youth Foundation of Hubei Province, China (No. 2022CFA102) and National Natural Science Foundation of China (Grant No. 41977242).

Data Availability Statement: The permafrost classification results are provided by the National Cryosphere Desert Data Center (http://www.ncdc.ac.cn/portal/metadata/16e16d96-482c-4a1a-9345-6f2fa350690e) (accessed on 18 March 2023). The SAR images acquired by Sentinel-1A were downloaded from the European Space Agency (https://scihub.copernicus.eu/dhus/#/home) (accessed on 18 March 2023). The Advanced Land Observing Satellite (ALOS) DEM with a resolution of 12.5 m was downloaded from NASA's Alaska Satellite Facility Distributed Active Archive Center (https://asf.alaska.edu/) (accessed on 18 March 2023).

Acknowledgments: We appreciate the leveling data and InSAR analysis results provided by Wu et al. [39].

Conflicts of Interest: The authors declare no conflict of interest.

References

1. Chapin, F.S.; Iii, F.S.C.; Sturm, M.; Serreze, M.C.; McFadden, J.P.; Key, J.R.; Lloyd, A.H.; McGuire, A.D.; Rupp, T.S.; Lynch, A.H.; et al. Role of Land-Surface Changes in Arctic Summer Warming. *Science* **2005**, *310*, 657–660. [CrossRef]
2. Hoegh-Guldberg, O.; Jacob, D.; Taylor, M.; Bolaños, T.G.; Bindi, M.; Brown, S.; Camilloni, I.A.; Diedhiou, A.; Djalante, R.; Ebi, K.; et al. The human imperative of stabilizing global climate change at 1.5 °C. *Science* **2019**, *365*, eaaw6974. [CrossRef]
3. Fatima, Z.; Ahmed, M.; Hussain, M.; Abbas, G.; Ul-Allah, S.; Ahmad, S.; Ahmed, N.; Ali, M.A.; Sarwar, G.; Haque, E.U.; et al. The fingerprints of climate warming on cereal crops phenology and adaptation options. *Sci. Rep.* **2020**, *10*, 1–21. [CrossRef]
4. Nicholas, P.; Raymond, S.B.; Henry, F.D.; Michel, B. Elevation-dependent warming in mountain regions of the world. *Nat. Clim. Chang.* **2015**, *5*, 424–443.
5. Biskaborn, B.K.; Smith, S.L.; Noetzli, J.; Matthes, H.; Vieira, G.; Streletskiy, D.A.; Schoeneich, P.; Romanovsky, V.E.; Lewkowicz, A.G.; Abramov, A.; et al. Permafrost is warming at a global scale. *Nat. Commun.* **2019**, *10*, 264. [CrossRef]
6. Shan, W.; Zhang, C.; Guo, Y.; Shan, M.; Zeng, X.; Wang, C. Climate Change and surface deformation characteristics in degradation area of permafrost in Lesser Khingan Mountain, China. In *Understanding and Reducing Landslide Disaster Risk: Volume 5 Catastrophic Landslides and Frontiers of Landslide Science 5th*; Springer: Cham, Switzerland, 2021; pp. 209–219.
7. Luo, J.; Yin, G.; Niu, F.; Lin, Z.; Liu, M. High Spatial Resolution Modeling of Climate Change Impacts on Permafrost Thermal Conditions for the Beiluhe Basin, Qinghai-Tibet Plateau. *Remote Sens.* **2019**, *11*, 1294. [CrossRef]
8. Cheng, G.; Zhao, L.; Li, R.; Wu, X.; Sheng, Y. Characteristic changes and impacts of permafrost on Qinghai-Tibet Plateau. *Chin. Sci. Bull.* **2019**, *64*, 2783–2795. (In Chinese)
9. Daout, S.; Doin, M.; Peltzer, G.; Socquet, A.; Lasserre, C. Large-scale InSAR monitoring of permafrost freeze-thaw cycles on the Tibetan Plateau. *Geophys. Res. Lett.* **2017**, *44*, 901–909. [CrossRef]
10. Huang, L.; Luo, J.; Lin, Z.; Niu, F.; Liu, L. Using deep learning to map retrogressive thaw slumps in the Beiluhe region (Tibetan Plateau) from CubeSat images. *Remote Sens. Environ.* **2020**, *237*, 111534. [CrossRef]
11. Lu, P.; Han, J.; Li, Z.; Xu, R.; Li, R.; Hao, T.; Qiao, G. Lake outburst accelerated permafrost degradation on Qinghai-Tibet Plateau. *Remote Sens. Environ.* **2020**, *249*, 112011. [CrossRef]
12. Ran, Y.; Jorgenson, M.T.; Li, X.; Jin, H.; Wu, T.; Li, R.; Cheng, G. Biophysical permafrost map indicates ecosystem processes dominate permafrost stability in the Northern Hemisphere. *Environ. Res. Lett.* **2021**, *16*, 095010. [CrossRef]
13. Ran, Y.; Li, X.; Cheng, G.; Nan, Z.; Che, J.; Sheng, Y.; Wu, Q.; Jin, H.; Luo, D.; Tang, Z.; et al. Mapping the permafrost stability on the Tibetan Plateau for 2005–2015. *Sci. China Earth Sci.* **2020**, *64*, 62–79. [CrossRef]
14. Chen, J.; Wu, T.; Zou, D.; Liu, L.; Wu, X.; Gong, W.; Zhu, X.; Li, R.; Hao, J.; Hu, G.; et al. Magnitudes and patterns of large-scale permafrost ground deformation revealed by Sentinel-1 InSAR on the central Qinghai-Tibet Plateau. *Remote Sens. Environ.* **2021**, *268*, 112778. [CrossRef]
15. Park, H.; Kim, Y.; Kimball, J.S. Widespread permafrost vulnerability and soil active layer increases over the high northern latitudes inferred from satellite remote sensing and process model assessments. *Remote Sens. Environ.* **2016**, *175*, 349–358. [CrossRef]
16. Vasiliev, A.A.; Drozdov, D.S.; Gravis, A.G.; Malkova, G.V.; Nyland, K.E.; Streletskiy, D.A. Permafrost degradation in the Western Russian Arctic. *Environ. Res. Lett.* **2020**, *15*, 045001. [CrossRef]
17. Kovakov, V.P.; Shvetsov, P.F. Problems of integral index stability of ground complex of permafrost. In Proceedings of the 5th International Conference on Permafrost, Trondheim, Norway, 2–5 August 1988; Volume 1, pp. 805–808.
18. Smith, S.L.; Wolfe, S.A.; Riseborough, D.W.; Nixon, F.M. Active-layer characteristics and summer climatic indices, Mackenzie Valley, Northwest Territories, Canada. *Permafr. Periglac. Process.* **2009**, *20*, 201–220. [CrossRef]
19. Liu, L.; Schaefer, K.; Gusmeroli, A.; Grosse, G.; Jones, B.M.; Zhang, T.; Parsekian, A.D.; Zebker, H.A. Seasonal thaw settlement at drained thermokarst lake basins, Arctic Alaska. *Cryosphere* **2014**, *8*, 815–826. [CrossRef]
20. Wu, Q.; Zhang, T. Changes in active layer thickness over the Qinghai-Tibetan Plateau from 1995 to 2007. *J. Geophys. Res. Atmos.* **2010**, *115*, D09107. [CrossRef]
21. Shiklomanov, N.I.; Nelson, F.E. Active-layer mapping at regional scales: A 13-year spatial time series for the Kuparuk region, north-central Alaska. *Permafr. Periglac. Process.* **2002**, *13*, 219–230. [CrossRef]
22. Mishra, U.; Drewniak, B.; Jastrow, J.D.; Matamala, R.M.; Vitharana, U. Spatial representation of organic carbon and active-layer thickness of high latitude soils in CMIP5 earth system models. *Geoderma* **2017**, *300*, 55–63. [CrossRef]

23. Nitze, I.; Heidler, K.; Barth, S.; Grosse, G. Developing and Testing a Deep Learning Approach for Mapping Retrogressive Thaw Slumps. *Remote Sens.* **2021**, *13*, 4294. [CrossRef]
24. Yang, Y.; Rogers, B.M.; Fiske, G.; Watts, J.; Potter, S.; Windholz, T.; Mullen, A.; Nitze, I.; Natali, S.M. Mapping retrogressive thaw slumps using deep neural networks. *Remote Sens. Environ.* **2023**, *288*, 113495. [CrossRef]
25. Li, R.; Li, Z.; Han, J.; Lu, P.; Qiao, G.; Meng, X.; Hao, T.; Zhou, F. Monitoring surface deformation of permafrost in Wudaoliang Region, Qinghai–Tibet Plateau with ENVISAT ASAR data. *Int. J. Appl. Earth Obs. Geoinf.* **2021**, *104*, 102527. [CrossRef]
26. Wagner, A.M.; Lindsey, N.J.; Dou, S.; Gelvin, A.; Saari, S.; Williams, C.; Ekblaw, I.; Ulrich, C.; Borglin, S.; Morales, A.; et al. Permafrost Degradation and Subsidence Observations during a Controlled Warming Experiment. *Sci. Rep.* **2018**, *8*, 10908. [CrossRef] [PubMed]
27. Short, N.; LeBlanc, A.M.; Sladen, W.; Oldenborger, G.; Mathon, V.; Brisco, B. RADARSAT-2 D-InSAR for ground displacement in permafrost terrain, validation from Iqaluit Airport, Baffin Island, Canada. *Remote Sens. Environ.* **2014**, *141*, 40–51. [CrossRef]
28. Widhalm, B.; Bartsch, A.; Leibman, M.; Khomutov, A. Active-layer thickness estimation from X-band SAR backscatter intensity. *Cryosphere* **2017**, *11*, 483–496. [CrossRef]
29. Wang, L.; Marzahn, P.; Bernier, M.; Ludwig, R. Mapping permafrost landscape features using object-based image classification of multi-temporal SAR images. *ISPRS J. Photogramm. Remote Sens.* **2018**, *141*, 10–29. [CrossRef]
30. Anderson, J.E.; Douglas, T.A.; Barbato, R.A.; Saari, S.; Edwards, J.D.; Jones, R.M. Linking vegetation cover and seasonal thaw depths in interior Alaska permafrost terrains using remote sensing. *Remote Sens. Environ.* **2019**, *233*, 111363. [CrossRef]
31. Gao, H.; Nie, N.; Zhang, W.; Chen, H. Monitoring the spatial distribution and changes in permafrost with passive microwave remote sensing. *ISPRS J. Photogramm. Remote Sens.* **2020**, *170*, 142–155. [CrossRef]
32. Lu, P.; Han, J.; Hao, T.; Li, R.; Qiao, G. Seasonal deformation of permafrost in Wudaoliang basin in Qinghai-Tibet Plateau revealed by StaMPS-InSAR. *Mar. Geod.* **2019**, *43*, 248–268. [CrossRef]
33. Colesanti, C.; Wasowski, J. Investigating landslides with space-borne Synthetic Aperture Radar (SAR) interferometry. *Eng. Geol.* **2006**, *88*, 173–199. [CrossRef]
34. Ren, T.; Gong, W.; Bowa, V.M.; Tang, H.; Chen, J.; Zhao, F. An Improved R-Index Model for Terrain Visibility Analysis for Landslide Monitoring with InSAR. *Remote Sens.* **2021**, *13*, 1938. [CrossRef]
35. Guzzetti, F.; Reichenbach, P.; Cardinali, M.; Galli, M.; Ardizzone, F. Probabilistic landslide hazard assessment at the basin scale. *Geomorphology* **2005**, *72*, 272–299. [CrossRef]
36. Gemitzi, A.; Falalakis, G.; Eskioglou, P.; Petalas, C. Evaluating landslide susceptibility using environmental factors, fuzzy membership functions and GIS. *Glob. Nest. J.* **2011**, *13*, 28–40.
37. Ciampalini, A.; Raspini, F.; Lagomarsino, D.; Catani, F.; Casagli, N. Landslide susceptibility map refinement using PSInSAR data. *Remote Sens. Environ.* **2016**, *184*, 302–315. [CrossRef]
38. Mu, C.; Abbott, B.W.; Norris, A.J.; Mu, M.; Fan, C.; Chen, X.; Jia, L.; Yang, R.; Zhang, T.; Wang, K.; et al. The status and stability of permafrost carbon on the Tibetan Plateau. *Earth-Sci. Rev.* **2020**, *211*, 103433. [CrossRef]
39. Wu, Z.; Zhao, L.; Liu, L.; Zhu, R.; Gao, Z.; Qiao, Y.; Xie, M. Surface-deformation monitoring in the permafrost regions over the Tibetan Plateau using Sentinel-1 data. *Sci. Cold Arid Reg.* **2018**, *10*, 114–125.
40. Wang, Z.; Yue, G.; Wu, X.; Zhang, W.; Song, X.; Wang, P.; Wu, J. Surface Deformation over Permafrost Environment of the Tanggula Section in the Qinghai-Tibet Plateau Using Active Microwave Spectral Imagines. *IOP Conf. Ser. Earth Environ. Sci.* **2019**, *384*, 012211. [CrossRef]
41. Zhao, L.; Zou, D.; Hu, G.; Wu, T.; Du, E.; Liu, G.; Xiao, Y.; Li, R.; Pang, Q.; Qiao, Y.; et al. A synthesis dataset of permafrost thermal state for the Qinghai–Tibet (Xizang) Plateau, China. *Earth Syst. Sci. Data* **2021**, *13*, 4207–4218. [CrossRef]
42. Chen, F.; Lin, H.; Zhou, W.; Hong, T.; Wang, G. Surface deformation detected by ALOS PALSAR small baseline SAR interferometry over permafrost environment of Beiluhe section, Tibet Plateau, China. *Remote Sens. Environ.* **2013**, *138*, 10–18. [CrossRef]
43. Zhao, R.; Li, Z.W.; Feng, G.C.; Wang, Q.J.; Hu, J. Monitoring surface deformation over permafrost with an improved SBAS-InSAR algorithm: With emphasis on climatic factors modeling. *Remote Sens. Environ.* **2016**, *184*, 276–287. [CrossRef]
44. Goldstein, R.M.; Werner, C.L. Radar interferogram filtering for geophysical applications. *Geophys. Res. Lett.* **1998**, *25*, 4035–4038. [CrossRef]
45. Bekaert, D.P.S.; Hooper, A.; Wright, T.J. A spatially variable power law tropospheric correction technique for InSAR data. *J. Geophys. Res. Solid Earth* **2015**, *120*, 1345–1356. [CrossRef]
46. Garthwaite, M.C.; Wang, H.; Wright, T.J. Broadscale interseismic deformation and fault slip rates in the central Tibetan Plateau observed using InSAR. *J. Geophys. Res. Solid Earth* **2013**, *118*, 5071–5083. [CrossRef]
47. Costantini, M. A novel phase unwrapping method based on network programming. *IEEE Trans. Geosci. Remote Sens.* **1998**, *36*, 813–821. [CrossRef]
48. Lauknes, T.R.; Zebker, H.A.; Larsen, Y. InSAR Deformation Time Series Using an L_{1}-Norm Small-Baseline Approach. *IEEE Trans. Geosci. Remote Sens.* **2011**, *49*, 536–546. [CrossRef]
49. Wang, C.; Zhang, Z.; Zhang, H.; Zhang, B.; Tang, Y.; Wu, Q. Active layer thickness retrieval of Qinghai-Tibet permafrost using the TerraSAR-X InSAR technique. *IEEE J. Sel. Top. Appl. Earth Observ. Remote Sens.* **2018**, *11*, 4403–4413. [CrossRef]

50. Cigna, F.; Bateson, L.B.; Jordan, C.J.; Dashwood, C. Simulating SAR geometric distortions and predicting Persistent Scatterer densities for ERS-1/2 and ENVISAT C-band SAR and InSAR applications: Nationwide feasibility assessment to monitor the landmass of Great Britain with SAR imagery. *Remote Sens. Environ.* **2014**, *152*, 441–466. [CrossRef]
51. Notti, D.; Herrera, G.; Bianchini, S.; Meisina, C.; López-Davalillo, J.C.G.; Zucca, F. A methodology for improving landslide PSI data analysis. *Int. J. Remote Sens.* **2014**, *35*, 2186–2214. [CrossRef]
52. Huang, F.; Zhang, J.; Zhou, C.; Wang, Y.; Huang, J.; Zhu, L. A deep learning algorithm using a fully connected sparse autoencoder neural network for landslide susceptibility prediction. *Landslides* **2019**, *17*, 217–229. [CrossRef]
53. Azarafza, M.; Azarafza, M.; Akgün, H.; Atkinson, P.M.; Derakhshani, R. Deep learning-based landslide susceptibility mapping. *Sci. Rep.* **2021**, *11*, 24112. [CrossRef] [PubMed]
54. Park, S.J.; Lee, C.-W.; Lee, S.; Lee, M.-J. Landslide Susceptibility Mapping and Comparison Using Decision Tree Models: A Case Study of Jumunjin Area, Korea. *Remote Sens.* **2018**, *10*, 1545. [CrossRef]
55. Shu, H.; Guo, Z.; Qi, S.; Song, D.; Pourghasemi, H.R.; Ma, J. Integrating Landslide Typology with Weighted Frequency Ratio Model for Landslide Susceptibility Mapping: A Case Study from Lanzhou City of Northwestern China. *Remote Sens.* **2021**, *13*, 3623. [CrossRef]
56. Breiman, L. Random forests. *Mach. Learn.* **2001**, *45*, 5–32. [CrossRef]
57. Han, Q.; Gui, C.; Xu, J.; Lacidogna, G. A generalized method to predict the compressive strength of high-performance concrete by improved random forest algorithm. *Constr. Build. Mater.* **2019**, *226*, 734–742. [CrossRef]
58. Taalab, K.; Cheng, T.; Zhang, Y. Mapping landslide susceptibility and types using Random Forest. *Big Earth Data* **2018**, *2*, 159–178. [CrossRef]
59. Li, R.; Zhang, M.; Konstantinov, P.; Pei, W.; Tregubov, O.; Li, G. Permafrost degradation induced thaw settlement susceptibility research and potential risk analysis in the Qinghai-Tibet Plateau. *Catena* **2022**, *214*, 106239. [CrossRef]
60. Chen, J.; Wu, Y.; O'Connor, M.; Cardenas, M.B.; Schaefer, K.; Michaelides, R.; Kling, G. Active layer freeze-thaw and water storage dynamics in permafrost environments inferred from InSAR. *Remote Sens. Environ.* **2020**, *248*, 112007. [CrossRef]
61. Deluigi, N.; Lambiel, C.; Kanevski, M. Data-driven mapping of the potential mountain permafrost distribution. *Sci. Total Environ.* **2017**, *590*, 370–380. [CrossRef]
62. Qin, Y.; Zhang, P.; Liu, W.; Guo, Z.; Xue, S. The application of elevation corrected MERRA2 reanalysis ground surface temperature in a permafrost model on the Qinghai-Tibet Plateau. *Cold Reg. Sci. Technol.* **2020**, *175*, 103067. [CrossRef]
63. Beck, I.; Ludwig, R.; Bernier, M.; Lévesque, E.; Boike, J. Assessing Permafrost Degradation and Land Cover Changes (1986-2009) using Remote Sensing Data over Umiujaq, Sub-Arctic Québec. *Permafr. Periglac. Process.* **2015**, *26*, 129–141. [CrossRef]
64. Yu, F.; Qi, J.; Yao, X.; Liu, Y. Degradation process of permafrost underneath embankments along Qinghai-Tibet Highway: An engineering view. *Cold Reg. Sci. Technol.* **2013**, *85*, 150–156. [CrossRef]
65. Mason, S.J.; Graham, N.E. Areas beneath the relative operating characteristics (ROC) and relative operating levels (ROL) curves: Statistical significance and interpretation. *Q. J. R. Meteorol. Soc.* **2002**, *128*, 2145–2166. [CrossRef]
66. Liu, Y.; Yang, H.; Wang, S.; Xu, L.; Peng, J. Monitoring and Stability Analysis of the Deformation in the Woda Landslide Area in Tibet, China by the DS-InSAR Method. *Remote Sens.* **2022**, *14*, 532. [CrossRef]
67. Guo, R.; Li, S.; Chen, Y.; Li, X.; Yuan, L. Identification and monitoring landslides in Longitudinal Range-Gorge Region with InSAR fusion integrated visibility analysis. *Landslides* **2020**, *18*, 551–568. [CrossRef]
68. Zhang, Z.; Wu, Q. Thermal hazards zonation and permafrost change over the Qinghai–Tibet Plateau. *Nat. Hazards* **2011**, *61*, 403–423. [CrossRef]
69. Jin, X.-Y.; Jin, H.-J.; Iwahana, G.; Marchenko, S.S.; Luo, D.-L.; Li, X.-Y.; Liang, S.-H. Impacts of climate-induced permafrost degradation on vegetation: A review. *Adv. Clim. Chang. Res.* **2020**, *12*, 29–47. [CrossRef]
70. Zhang, X.; Zhang, H.; Wang, C.; Tang, Y.; Zhang, B.; Wu, F.; Wang, J.; Zhang, Z. Active Layer Thickness Retrieval Over the Qinghai-Tibet Plateau Using Sentinel-1 Multitemporal InSAR Monitored Permafrost Subsidence and Temporal-Spatial Multilayer Soil Moisture Data. *IEEE Access* **2020**, *8*, 84336–84351. [CrossRef]
71. Jenks, G.F. The data model concept in statistical mapping. *Int. Yearb. Cartogr.* **1967**, *7*, 186–190.
72. Zhao, F.; Gong, W.; Tang, H.; Pudasaini, S.P.; Ren, T.; Cheng, Z. An integrated approach for risk assessment of land subsidence in Xi'an, China using optical and radar satellite images. *Eng. Geol.* **2023**, *314*, 106983. [CrossRef]
73. Matheron, G. A Simple Substitute for Conditional Expectation: The Disjunctive Kriging. *Adv. Geostat. Min. Ind.* **1976**, *24*, 221–236. [CrossRef]
74. Chen, D.; Chen, H.; Zhang, W.; Cao, C.; Zhu, K.; Yuan, X.; Du, Y. Characteristics of the residual surface deformation of multiple abandoned mined-out areas based on a field investigation and SBAS-InSAR: A case study in Jilin, China. *Remote Sens.* **2020**, *12*, 3752. [CrossRef]
75. Yazici, B.V.; Gormus, E.T. Investigating persistent scatterer InSAR (PSInSAR) technique efficiency for landslides mapping: A case study in Artvin dam area, in Turkey. *Geocarto Int.* **2020**, *37*, 2293–2311. [CrossRef]
76. Yang, M.; Nelson, F.E.; Shiklomanov, N.I.; Guo, D.; Wan, G. Permafrost degradation and its environmental effects on the Tibetan Plateau: A review of recent research. *Earth-Sci. Rev.* **2010**, *103*, 31–44. [CrossRef]
77. Tang, M.; Sun, S.; Zhong, Q.; Wu, S. Energy storage and release of underlying surface and weather change. *Plateau Meteorol.* **1982**, *1*, 24–34.

78. Hinzman, L.D.; Goering, D.J.; Kane, D.L. A distributed thermal model for calculating soil temperature profiles and depth of thaw in permafrost regions. *J. Geophys. Res. Atmos.* **1998**, *103*, 28975–28991. [CrossRef]
79. Zhang, M.; Wen, Z.; Li, D.; Chou, Y.; Zhou, Z.; Zhou, F.; Lei, B. Impact process and mechanism of summertime rainfall on thermal–moisture regime of active layer in permafrost regions of central Qinghai–Tibet Plateau. *Sci. Total Environ.* **2021**, *796*, 148970. [CrossRef]

land

MDPI

Article

Study on the Deformation of Filling Bodies in a Loess Mountainous Area Based on InSAR and Monitoring Equipment

Yuming Wu [1] and Hengxing Lan [1,2,*]

[1] State Key Laboratory of Resources and Environmental Information System, Institute of Geographic Sciences and Natural Resources Research, Chinese Academy of Sciences, Beijing 100101, China
[2] College of Geological Engineering and Geomatics, Chang'an University, Xi'an 710054, China
* Correspondence: lanhx@lreis.ac.cn

Abstract: Several land-creation projects, such as the Lanzhou New Area (LNA), have been undertaken in China as part of the Belt and Road Initiative to bring more living space to the local people in loess areas. However, undisturbed loess and remolded loess have different mechanical characteristics, which may influence the stability of the filling process. Therefore, we monitored the deformation through InSAR and field monitoring to investigate the deformation characteristics and their causes. We obtained the horizontal and vertical displacements, internal deformation, water content, and pressure, according to the air–space–ground integrated monitoring technique. The results show that stress and deformation increase rapidly during construction. Deformation in different places is different during the winter: (1) for vertical displacement, uplift is present in the cut area, settlement is present in the fill area, and heterogeneity is evident in other areas; (2) for horizontal displacement, the expansion state is present in the filling area and the compression state is present at the boundary. Laboratory tests show that the difference in soil compression properties is one of the reasons for these deformation characteristics. Additionally, the difference in volumetric water content and permeability coefficient may trigger different mechanical properties on both sides of the boundary. All the evidence indicates that the boundary region is critical for filling projects. It is also necessary to install monitoring equipment to observe deformation. When abnormal deformations appear, we should take measures to control them.

Keywords: InSAR; loess; in situ; deformation; land creation

Citation: Wu, Y.; Lan, H. Study on the Deformation of Filling Bodies in a Loess Mountainous Area Based on InSAR and Monitoring Equipment. *Land* **2022**, *11*, 1263. https://doi.org/10.3390/land11081263

Academic Editors: Stefano Morelli, Veronica Pazzi and Mirko Francioni

Received: 28 June 2022
Accepted: 5 August 2022
Published: 7 August 2022

1. Introduction

Loess, one of the quaternary sediments, is widely distributed in China, covering approximately 440,000 km^2 [1,2]. The Loess Plateau is a plateau in north-central China formed of loess. It is one of the important agricultural regions in China, covering an area of 624,641 km^2 and supporting 17% of the population [3]. Additionally, there is not enough space for downtown areas to expand in these places. Lanzhou is an important city in western China, but it is located in a valley, which seriously hinders urban development [4]. A total of 57% of the area of Lanzhou comprises unused land such as barren hills, gentle slopes, and gullies; filling gullies to create farmland on the Loess Plateau can help to solve many problems. As part of the strategy of Western Development and the Belt and Road Initiative, several loess projects have been initiated, such as the Lanzhou New Area (LNA) [5], which consists of more than 250 square kilometers of reclaimed land [6]. The maximum annual average expansion rate was about 36 km^2/a from 2012 to 2016 [7]. These projects will give people more new flat land and more ground for agriculture [8], but that comes with risks in the absence of carefully designed engineering controls [6,9].

Loess, a clastic, predominantly silt-sized sediment, has a metastable structure [10–12] and is composed of million-year-old thick deposits of windblown dust and silt. The grain sizes range from 0.005 to 0.05 mm, and the porosity generally ranges from 42% to 55% [13].

The loess structure produces collapsibility, which induces sharp sinking and causes ground deformation when it encounters water. At the micro level, debonding, grain crushing, and fabric transition appear during collapse; at the macro level, creeping and softening appear when the structure changes. According to Wen and Yan [14], the shear strength reduction in loess due to structural characteristics should be attributed to the breaking of cementation bonds between particles. The different physical and mechanical properties make construction difficult, especially for filling and excavation projects; consequently, researchers have designed several experiments to explore such geotechnical properties in order to address these problems [15–17].

Loess, a strongly collapsible soil, easily softens and deforms when it encounters water. The penetration of water into loess is very complicated: after water infiltrates the pores of the undisturbed loess, the moisture content and matric suction of the loess will change, and its shear strength will be reduced significantly [18,19]. In some studies, undisturbed loess is stronger than remolded loess at the same density and water content [20]. The experimental results show that mechanical parameters such as the shear strength, compressive strength, and Young's modulus of undisturbed loess and remolded loess are significantly different. Differential deformation with different properties is one of the factors that trigger geohazards [21–23]; therefore, this variability in soil properties can cause problems in filling projects. However, the deformation process at the boundary is unclear for loess-filling projects.

For displacement monitoring, GPS is the best real-time monitoring technique to monitor surface deformation, especially for landslide displacement [24]. For large-scale monitoring, InSAR observations are the favored tool and have been successfully applied in mountains and plains [25,26], glacier monitoring [27], urban subsidence monitoring [28], and landslide monitoring [29]. Large-scale loess deformation has also been observed using this technique [5,30–32]. From monitoring loess filling projects, it has been found that deformation generally occurs on the edge of the cutting and filling slope; in the LNA, there is significant subsidence after filling from large-scale observations. In addition, the spatial heterogeneity of land creation results in different deformation modes [5]. After land reclamation in loess areas, the stress changes, amounting to hundreds of kilopascals in shallow zones, which, in turn, induce deformations in the filling bodies [33]. Based on monitoring studies, the surface subsidence is mainly located in the filling area [34,35], while uplifting occurs in the excavation area [36].

In this paper, we monitored the surface deformation process in the study area through ascending and descending images during the winter and buried equipment such as displacement meters to monitor the internal deformation. Additionally, we buried moisture meters and earth pressure cells to investigate the reasons for such changes. Based on the space–air–ground integrated monitoring technique, we analyzed the deformation characteristics of loess during the winter.

2. Study Area

Lanzhou city, Gansu, located in northwestern China (Figure 1A), is an important regional commercial center and transportation hub. Due to the U-shaped and V-shaped valleys around the city and the Yellow River that crosses the city, the topography hampers the development of Lanzhou. Lanzhou creates more land for development by filling the loess valley and cutting the loess mountain; in the LNA in particular, hundreds of mountain tops have been flattened.

The LNA, founded in 2012, is a state-level new area that spans 40 km north to south and 16 km east to the west. It is located 30 km from Lanzhou's old city in the Qinwangchuan Plain, which is the largest plateau basin near Lanzhou (Figure 1A). Local governments removed the tops of many high loess mountains to fill the adjacent valleys to create new flat land for living space and agriculture. In this area, it has a typical semiarid continental monsoon climate. The average temperature is approximately 4.1 °C, and the typical annual precipitation is 300–500 mm, with almost 60% of the precipitation occurring in the

summer [5]. There have been many filling projects from 2002 to 2022 (Figure 1B). Our study area is located in the southeast of the LNA, which is set to provide sufficient land for local agriculture in the future.

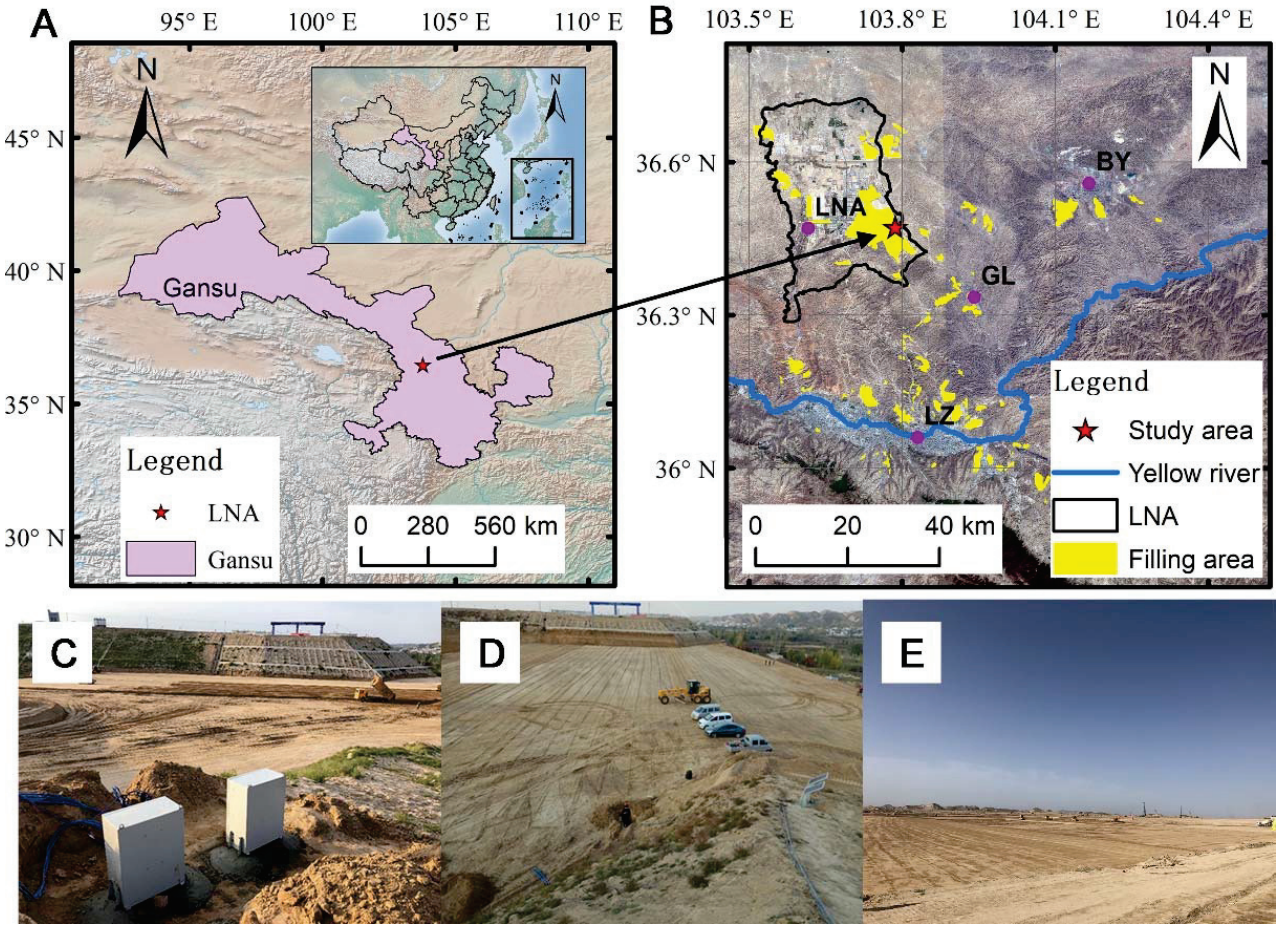

Figure 1. Study area and photos of different stages ((**A**) is the location of the research area, (**B**) is the distribution of the filling areas in Lanzhou, (**C**) is a photo of our research area taken on 12 September 2018, (**D**) is a photo of our research area taken on 16 October 2018, and (**E**) is a photo of our research area taken on 6 June 2019. LZ: Lanzhou city, GL: Gaolan county, BY: Baiyin city).

In this project, the construction process is divided into five steps: (1) cutting the slope into steps; (2) filling 30 cm at a time; (3) watering it to achieve the optimal moisture content; (4) rolling it to achieve the desired compaction degree; and (5) repeating the above steps until the predetermined height is reached. The filling project began on 6 July 2018 and ended on 13 May 2019, according to the construction log. There were 30 layers of landfill from 6 July 2018 to 15 September 2018 (Figure 1C), 35 layers from 11 October 2018 to 14 November 2018 (Figure 1D), and 28 layers from 12 March 2019 to 13 May 2019 (Figure 1E). The winter break lasted from 14 November 2018 to 12 March 2019. During the winter break, the site experienced little human disturbance, thus reflecting the actual site deformation process. Therefore, large-scale loess deformation can be observed thoroughly via InSAR and internal monitoring.

We employed a UAV to conduct terrain mapping before and after the project to measure the surface change after filling and applied Agisoft PhotoScan to create the Digital Surface Model (DSM) [37]. The maximum landfill is 24.91 m, and the maximum excavation thickness is 17.30 m, according to the DSM differences in Figure 2.

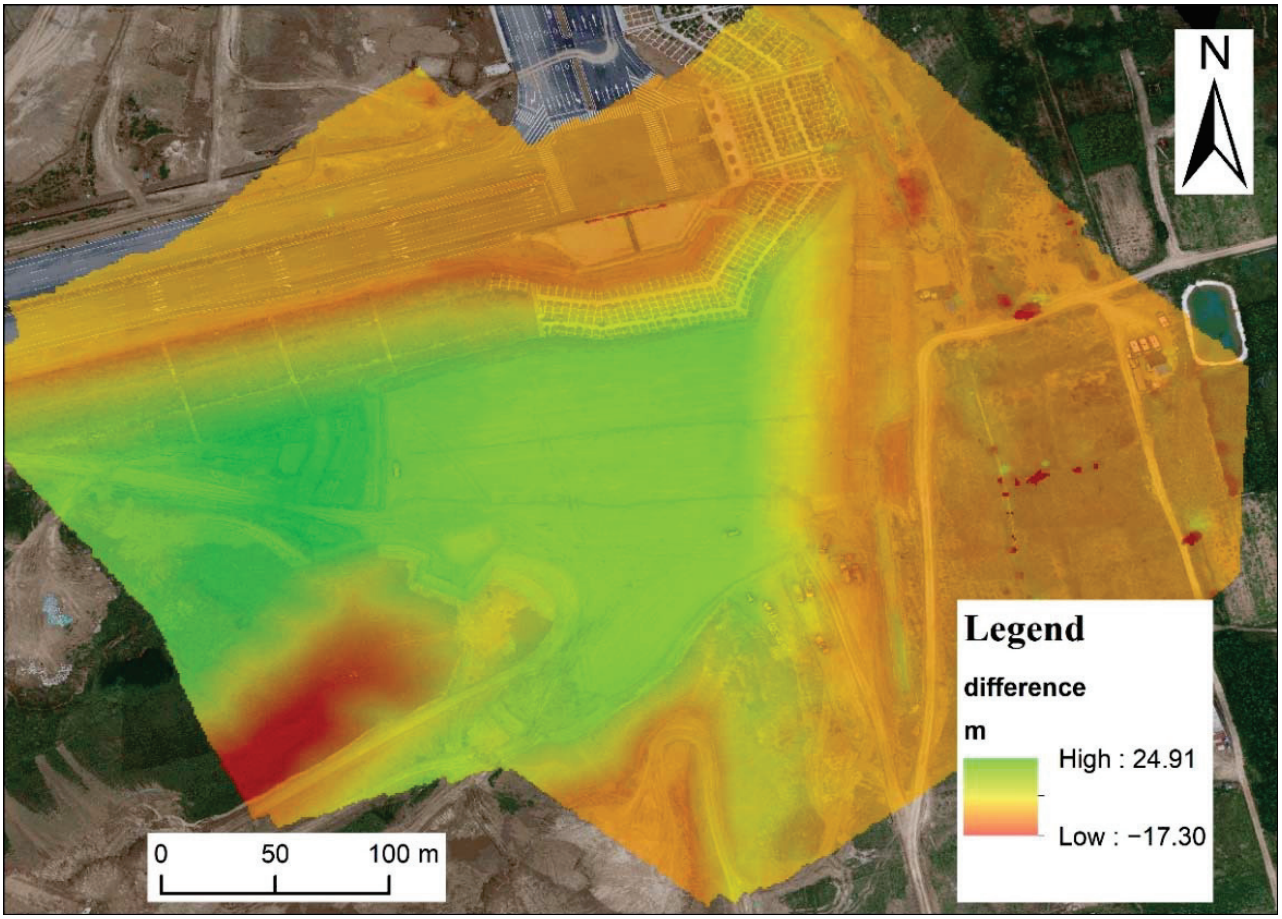

Figure 2. DEM differences before and after filling in the study area (positive value represent filling height and negative values represent excavation depth).

Malan loess is widely distributed in the project area, and the strata are mainly quaternary loose sediments. From the X-ray diffraction, quartz and plagioclase are the main minerals in the Malan loess, which account for 35.2% and 24.0% of minerals, respectively (Table 1). Illite and illite/smectite are the main clay minerals, which account for 41.0% and 35.0% of clays, respectively (Table 2). These characteristics indicate that changes in moisture content can significantly affect the mechanical properties [14,38]. Malan loess is formed by weak cementation between silts, sands, and aggregates. Cementation is provided by crystalline carbonate [39,40]. The Malan loess tensile and shear strengths decrease with water content and increase with dry density, producing a close multi-regression relationship. Differences in tensile strengths between undisturbed loess and remolded loess indicate the significance of its structure [41]. The composition is quaternary alluvial silt, silty clay, sand, and gravel.

Table 1. X-ray diffraction analysis of the relative quantity.

Quartz	Feldspar	Plagioclase	Calcite	Dolomite	Total Clay
35.2	10.9	24.0	11.9	7.6	10.4

Table 2. X-ray diffraction analysis of the relative quantity of clay minerals.

Illite/Smectite	Illite	Kaolinite	Chlorites
41.0	35.0	10.0	14.0

In the study area, we take soil samples and determine the basic parameters in the laboratory (Table 3). According to British Standard (BS 1377) [42], we measured the basic physical property parameters of the samples, while according to the measured volume and mass, the bulk density is 2.03 g/cm^3 for remolded loess, while the density is 1.31 g/cm^3 for undisturbed loess. Subsequently, the samples were dried in an oven until the mass no longer changed (the oven temperature was set to 108 °C). The dry densities of the undisturbed loess and the remolded loess were 1.20 g/cm^3 and 1.80 g/cm^3, and the moisture content was 8.90% and 14.50%. The specific gravity of the loess sample measured by the pycnometer was 2.73. To obtain the void ratio, the equation as follows:

$$e = \frac{(1+\omega)Gs\rho_w}{\rho} - 1 \quad (1)$$

where ω is moisture content, ρ is density, ρ_w is water density, and Gs is specific gravity. Based on the Equation (1), the void ratios of undisturbed loess and remodeled loess are 1.27 and 0.54, respectively. The properties of the loess in the filling area are significantly different from those of the original mountain. These differences in basic properties may result in different deformation characteristics after filling.

Table 3. The basic parameters of the loess in the study area measured by laboratory tests.

Type	Remolded Loess	Undisturbed Loess
Specific gravity	2.73	2.73
Bulk density (g/cm^3)	2.03	1.31
Water content (%)	14.50	8.90
Dry density (g/cm^3)	1.80	1.20
Void ratio	0.54	1.27

3. Methods

3.1. InSAR Process

D-InSAR (differential interferometric synthetic aperture radar) is a technique for mapping ground deformation in the wave phase between two radar images acquired at different times over the same area [43]. PS-InSAR is based on using permanent scatterers to overcome phase decorrelation and atmospheric delay effects in D-InSAR to obtain accurate deformation estimates [44]. Ferretti et al. described the PS-InSAR technique in detail [45]. In the persistent scatterer (PS) targets, the phase includes the deformation phase, atmospheric delay phase, orbit error phase, topographic phase and noise phase as follows:

$$\phi_{int} = \mathrm{W}\left\{\phi_{defo} + \phi_{atmos} + \Delta\phi_{orbit} + \Delta\phi_{topo} + \phi_{noise}\right\} \quad (2)$$

where ϕ_{defo} is the deformation phase, ϕ_{atmos} is the atmospheric delay phase, $\Delta\phi_{orbit}$ is the orbit error phase, $\Delta\phi_{topo}$ is the topographic phase, and ϕ_{noise} is the noise phase. The PS-InSAR method used regression and filtering methods to obtain the real deformation phase.

To date, PS-InSAR has been widely developed. There are many programs for PS-InSAR, such as GAMMA-rs [46], SARPROZ [47], and StaMPS [48]. StaMPS is a software package that allows for the extraction of ground displacements from the time series of synthetic aperture radar (SAR) acquisitions [49,50]. StaMPS applies phase analysis and amplitude to determine the PS probability and calculate displacements on these PSs from the time series of synthetic aperture radar (SAR) acquisitions [44], which it separates into eight steps (Figure 3): (1) data load; (2) phase noise estimation; (3) PS point selection; (4) PS weeding; (5) phase correction; (6) phase unwrapping; (7) estimation of spatially correlated look angle error; and (8) atmosphere filtering [51]. The mean velocity and displacement on each line of sight (*LOS*) can be calculated by StaMPS. Based on the results calculated by StaMPS, we applied our 2-D decomposition method to calculate the displacements.

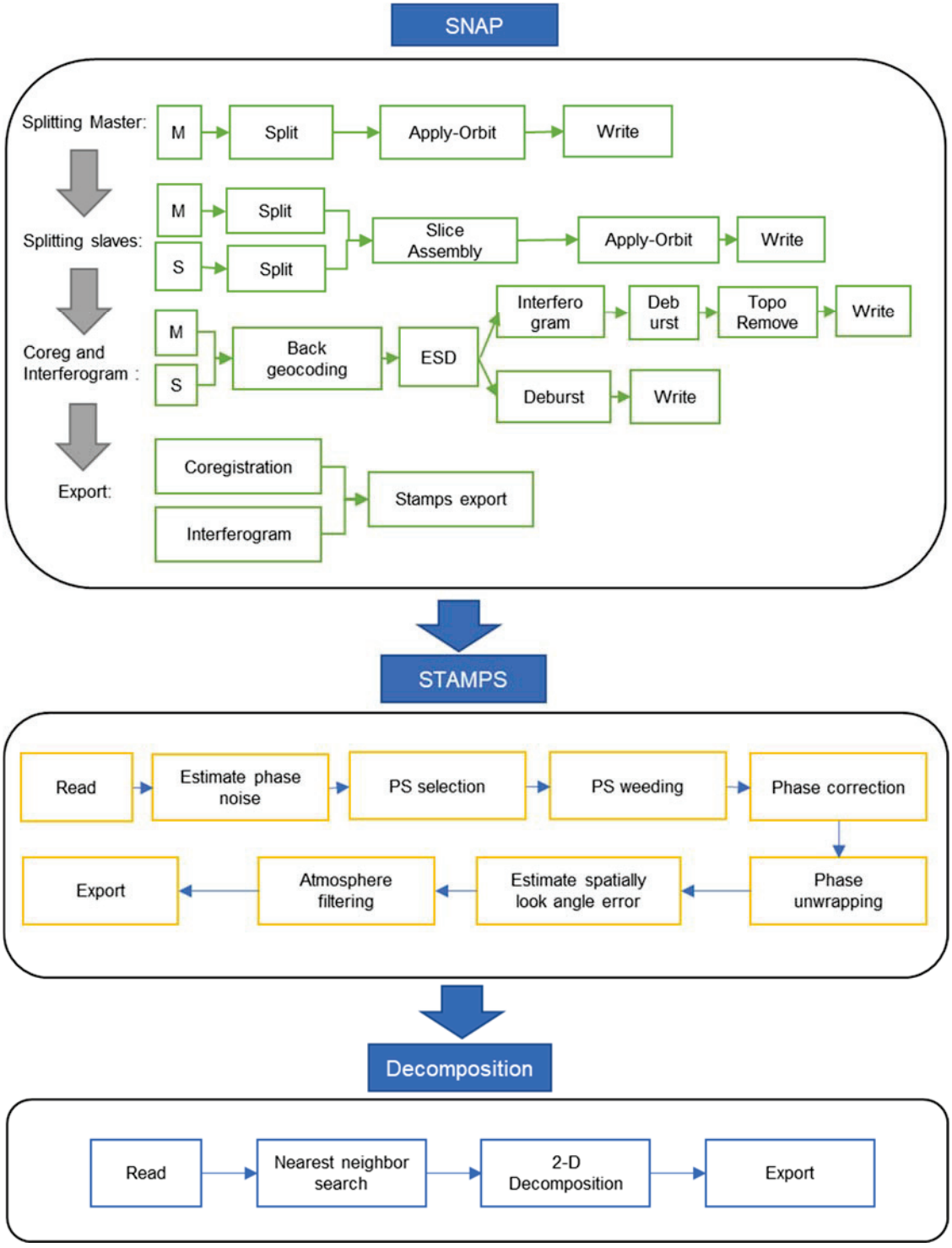

Figure 3. Workflow chart of InSAR.

Sentinel-1 SAR products are free and open access, providing a large number of images to observe deformation around the world. Sentinel Application Platform (SNAP) is the official software for dealing with Sentinel-1 data, which involves coregistration images and the generation of interferograms for data preparation. To integrate SNAP with StaMPS, a free application called snap2stamps [52] was developed and is available on GitHub (https://github.com/mdelgadoblasco/snap2stamps, accessed on 9 May 2022). The workflow for the SNAP–StaMPS approach is shown in Figure 3. In this paper, we used the above method

to deal with the ascending and descending images separately to acquire the deformation on each line of sight (*LOS*) and decomposed them into horizontal and vertical displacements.

3.2. 2-D Decomposition

Based on StaMPS, we can obtain the mean velocity and displacement on each line of sight (*LOS*) through ascending and descending tracks of Sentinel-1 images. SAR is sensitive in the direction perpendicular to its azimuth. Since the Sentinel 1 satellite is in a near-north–south motion, we can obtain the mean velocities and displacements in the vertical and east–west directions based on the ascending and descending images [53–58]. According to the rotation matrix, the east–west motion and vertical motion can be decomposed as follows:

$$\begin{bmatrix} d_{LOS}^{asc} \\ d_{LOS}^{desc} \end{bmatrix} = \begin{bmatrix} \cos\theta_{asc} & -\cos\alpha^{asc}\sin\theta_{asc} \\ \cos\theta_{desc} & -\cos\alpha^{desc}\sin\theta_{desc} \end{bmatrix} \begin{bmatrix} d_v \\ d_e \end{bmatrix} \quad (3)$$

In Equation (3), d_{LOS}^{asc} is the displacement or velocity on the line-of-sight of ascending images, and d_{LOS}^{desc} is the displacement or velocity on the line-of-sight of descending images.

However, the PS in the ascending satellite image and the descending image may not be the same location. Therefore, we cannot decompose the phase on the same PSs. We can assume that the deformation changes in the near region are similar. Then, we estimated the phase and uncertainties according to the PS around the reference and adopted the least squares method. The *LOS* displacement of the ascending and descending images should be included at the same time to prevent equation collinearity (Figure 4). Equation (3) changes to:

$$Y = AX \quad (4)$$

where $X = \begin{bmatrix} d_v \\ d_e \end{bmatrix}$, $Y = \left[d_{LOS_1{}^{asc}}, \ldots, d_{LOS_n{}^{asc}}, d_{LOS_1{}^{desc}}, \ldots, d_{LOS_m{}^{desc}} \right]^T$, and A is:

$$\begin{bmatrix} \cos\theta_1{}^{asc} & \cdots & \cos\theta_n{}^{asc} & \cos\theta_1{}^{desc} & \cdots & \cos\theta_m{}^{desc} \\ -\cos\alpha^{asc}\sin\theta_1{}^{asc} & \cdots & -\cos\alpha^{asc}\sin\theta_n{}^{asc} & -\cos\alpha^{desc}\sin\theta_1{}^{desc} & \cdots & -\cos\alpha^{\mathrm{desc}}\sin\theta_m{}^{desc} \end{bmatrix}^T$$

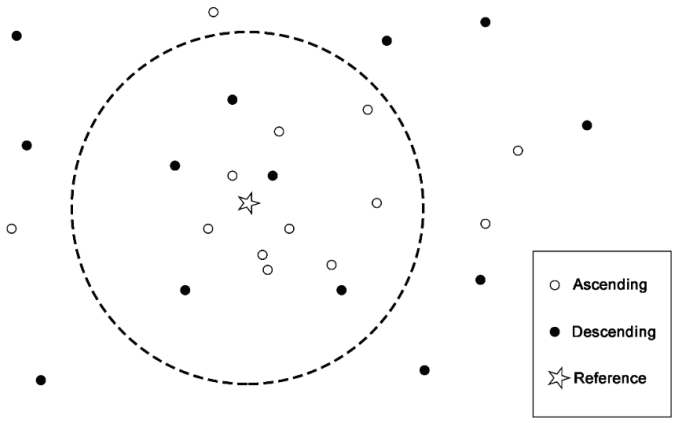

Figure 4. The selection of the PS correction point in the reference PS points.

θ_i^{asc} is the radar incidence angle at the ith PS point through the ascending tracks of Sentinel-1 images, θ_j^{desc} is the radar incidence angle at the jth PS point through the descending tracks of Sentinel-1 images, α^{asc} is the *LOS* azimuth on the ascending tracks, α^{desc} is the *LOS* azimuth on the descending tracks, $d_{LOS^{asc}}$ is the displacement or velocities along the line-of-sight (*LOS*) through the ascending tracks of Sentinel-1 images, $d_{LOS^{desc}}$ is the displacement or velocity along the line-of-sight (*LOS*) through the ascending tracks of the Sentinel-1 images, d_v is the vertical displacement or velocity, and d_e is the displacement or velocity in the east–west direction. Based on the least squares method, X is:

$$X = \left(A^T A\right)^{-1} A^T Y \tag{5}$$

For each PS, we can calculate the east–west displacement and vertical displacement and velocity according to the above method.

3.3. Field Monitoring

We buried instruments in the soil layers to monitor vertical and horizontal stress, deformation, and moisture movements. Three earth pressure cells were buried in this area: two earth pressure cells monitored the horizontal pressure, and one monitored the vertical pressure. Two earth pressure cells were in the landfill at 16 m and 19.4 m relative to the designed elevation to monitor the horizontal pressure. One earth pressure cell was placed at the bottom interface (21 m relative to the designed elevation) to monitor the vertical pressure. For deformation, three extensometers were used to monitor the deformation: two for horizontal deformation and one for vertical deformation. For horizontal deformation, we monitored deformations in the filling area and boundary area. For vertical deformation, the meter monitors the deformation from 16 m to 21 m relative to the designed elevation. For the moisture movement, two moisture meters were located in the filling areas and excavation areas. The schematic layout of the equipment is shown in Figure 5. According to the above monitoring equipment data, the deformation process of the internal landfill area can be measured.

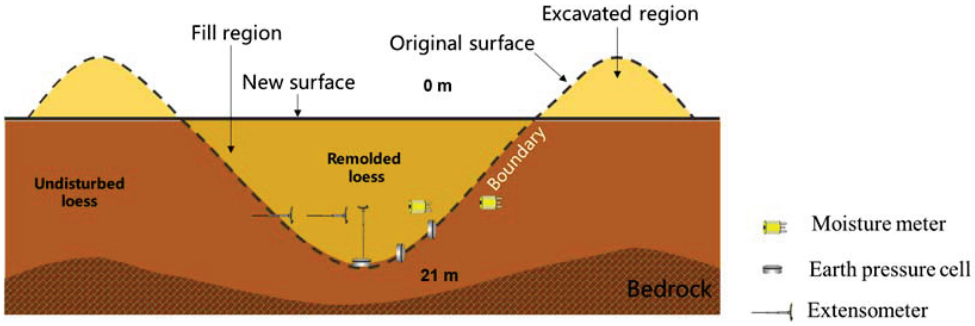

Figure 5. Schematic diagram of buried equipment layout.

4. Results

4.1. Surface Monitoring

Considering Sentinel 1 satellite imagery coverage, we selected nine ascending and nine descending images of this area on the same day during the winter break from 29 November 2018 to 5 March 2019 (Table 4). Then, we adopted the above method to calculate the surface deformation in the vertical and east–west directions. In our method, a positive value in the east–west direction indicates western movement and a positive value in the vertical direction indicates uplift after decomposition.

Table 4. Sentinel data for the LNA.

Ascending		Descending	
No.	**Acquisition Date**	**No.**	**Acquisition Date**
1	29 November 2018	1	29 November 2018
2	11 December 2018	2	11 December 2018
3	23 December 2018	3	23 December 2018
4	4 January 2019	4	4 January 2019
5	16 January 2019	5	16 January 2019
6	28 January 2019	6	28 January 2019
7	9 February 2019	7	9 February 2019
8	21 February 2019	8	21 February 2019
9	5 March 2019	9	5 March 2019

According to the spatial distribution of PS points, they are distributed in the original mountain and cutting areas. There are few PS points in the filling area due to rapid settlement (Figure 6A); therefore, in situ monitoring is required.

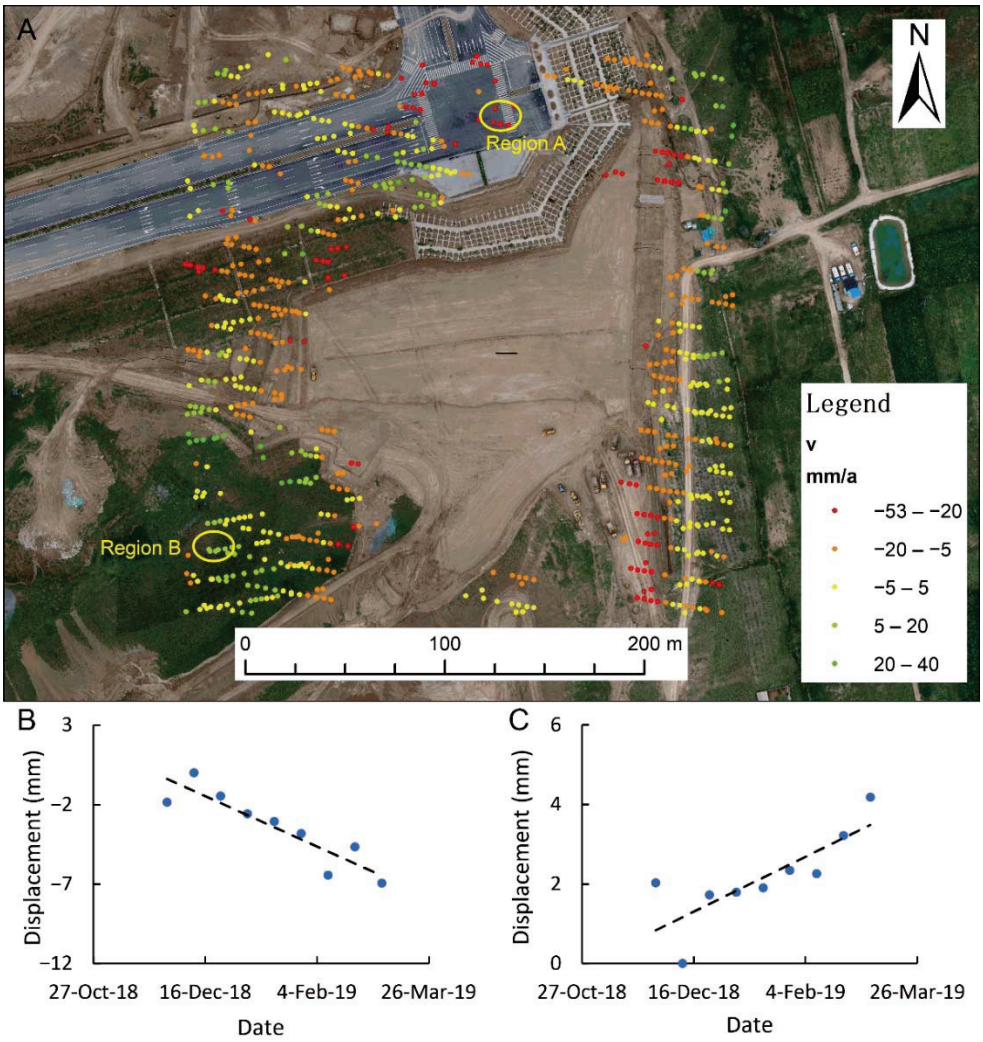

Figure 6. The vertical deformation based on InSAR data ((**A**) is the spatial distribution of vertical deformation, (**B**) is the deformation in region A, and (**C**) is the deformation in region B).

The characteristics of deformation in different areas are different. On the road, there is heterogeneity. There is significant settlement in region A (Figure 6B); however, there is an uplift in the excavation area (Figure 6C) throughout the winter break. The settlement in region A in Figure 6A appears to be more than 20 mm/year, which is affected by the filling projects. In the excavation area, the deformation rate is greater than 5 mm per year, which is related to the cutting process.

According to the horizontal deformation, the movements in the east–west direction show different deformations in the boundary areas and the excavation areas (Figure 7A). Different boundaries show different deformation characteristics. The eastern boundaries (Region A in Figure 7A), i.e., high-fill boundaries, appear to have moved eastwards due to the absence of the original mountain restrictions (>20 mm/a) (Figure 7B), while deformation is relatively low at the western boundary. Additionally, the excavation area appeared to move west (Region B in Figure 7A). The velocity of the excavation area is more than 10 mm/year (Figure 7C). Therefore, the filling procedure will have an impact on the neighboring areas based on these InSAR observations.

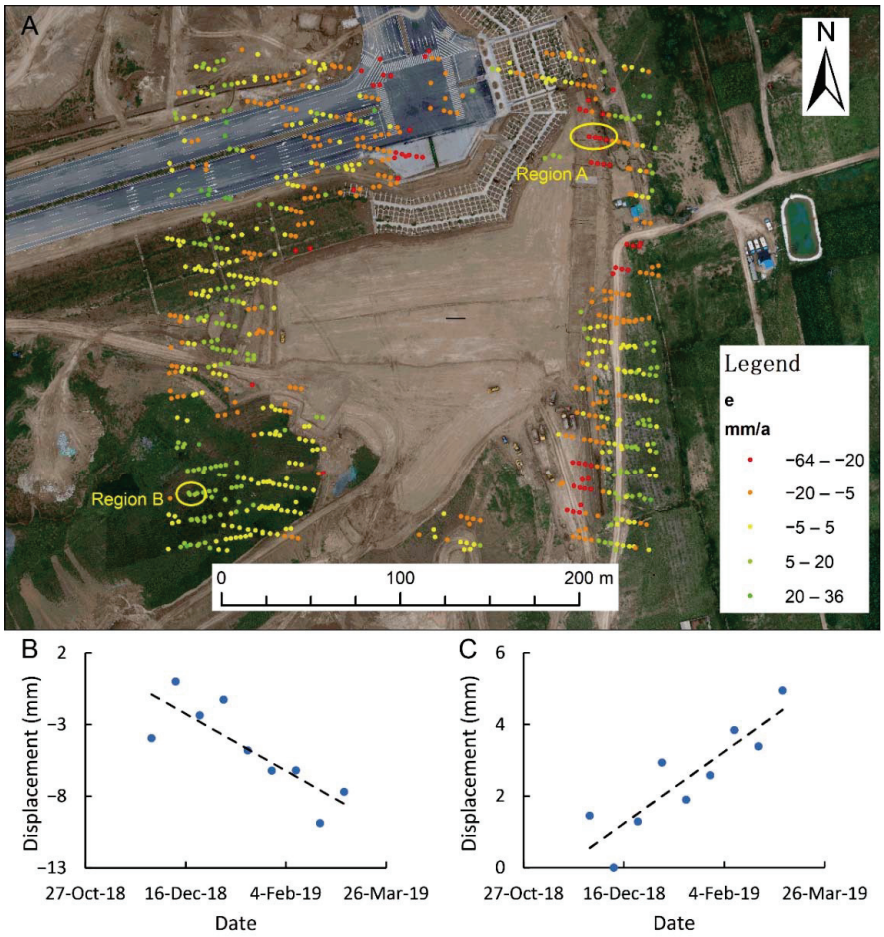

Figure 7. East–west displacement based on InSAR data ((**A**) is the spatial distribution of displacement in the east–west direction, (**B**) is the deformation in region A, and (**C**) is the deformation in region B).

4.2. Internal Monitoring

The geological body is composed of undisturbed loess and remolded loess, which results in complex deformation processes [59]. Based on field monitoring, the deformations during construction are large and range from 16 m to 21 m during the filling process (Figure 8). The pressure at 21 m presents an increase in the filling process (Figure 8A); this pressure is from 125.3 kPa to 172.3 kPa during construction (about 2.14 kPa/day). In terms of vertical deformation, it is about −10.3 mm, and the average velocity is about 0.47 mm/day during construction (Figure 8B).

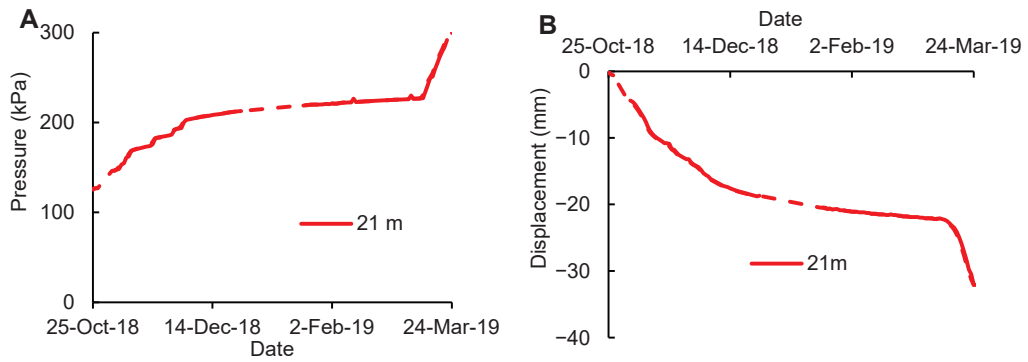

Figure 8. Vertical stress at 21 m and displacement from 16 m to 21 m in the filling areas in the first stage ((**A**) is the pressure over time, and (**B**) is the displacement over time. The solid line is the measured data, and the dashed line is the estimation of missing data due to a lack of data).

During the winter break, the pressure ranged from 172.3 kPa to 227.1 kPa. This process shows that stress in the filling bodies is redistributed (Figure 9A). In addition, the settlement reaches 12 mm from 16 m to 21 m (Figure 9B). The relationship between settlement and time follows logarithmic models during the winter down period, similar to previous studies [60–62].

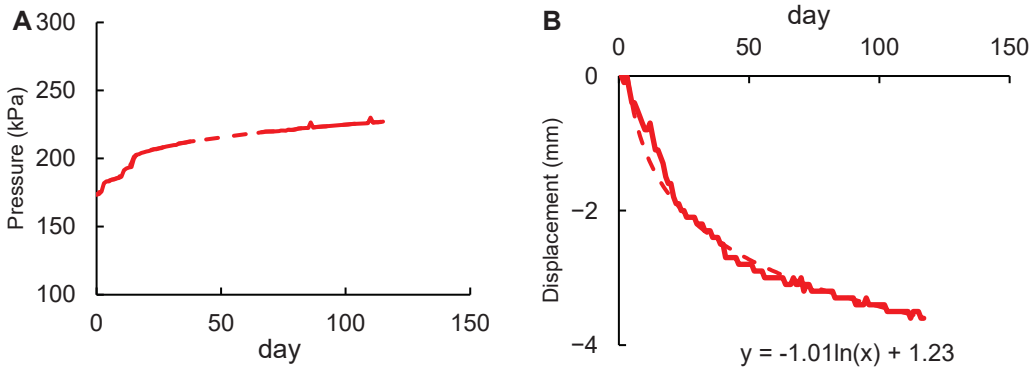

Figure 9. Vertical stress at 21 m and displacement from 16 m to 21 m in the filling areas during winter break ((**A**) is the pressure over time during winter, and (**B**) is the displacement over time during winter. The solid line is the measured data, and the dashed line is the estimation of missing data due to a lack of data).

Compared with vertical deformation, the horizontal deformation is complicated [59]. The horizontal deformation in different areas presents different characteristics: the loess is tense in the filling area and compressed at the boundary (Figure 10A,B). Based on the data measured by the horizontal displacement gauge, the horizontal displacement increased by approximately 2.5 mm in the filling area and decreased by 1 mm at the boundary from 25 October 2018 to 24 March 2019 (Figure 10C). The lateral stress increased rapidly during construction and grew slowly during the winter break (Figure 11). At the same time, this process shows that the filling area is not stable during the winter break. Additionally, the high strength when the undisturbed loess is dry prevents the disturbed loess from moving due to the mechanical characteristics. The results show that the filling body will affect the adjacent areas. According to the above analysis, the internal monitoring results are in good agreement with the surface InSAR measurements. These results show that the filling bodies may squeeze surrounding areas.

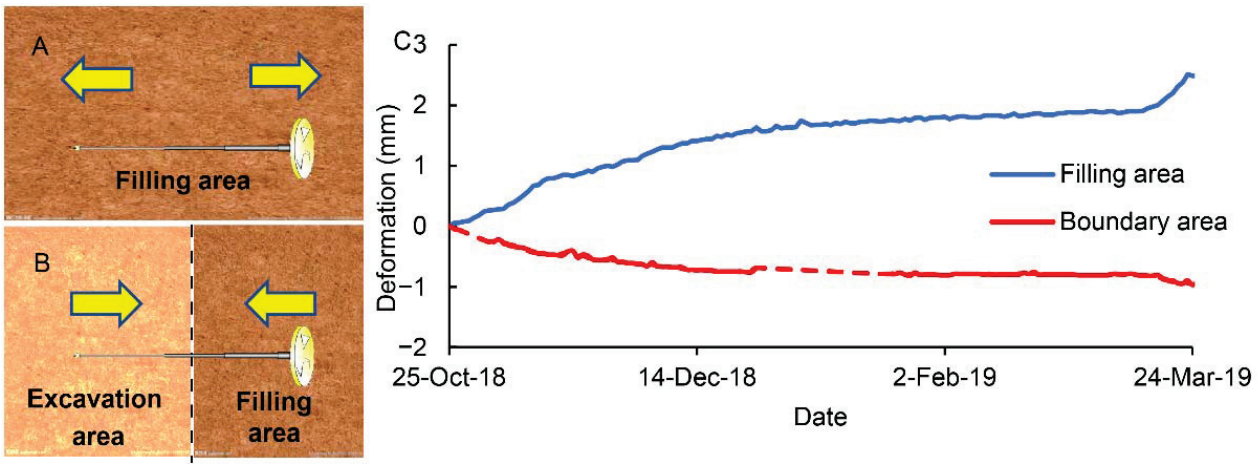

Figure 10. Horizontal displacement ((**A**) is a schematic diagram of the deformation of the landfill area, (**B**) is a schematic diagram of the deformation at the boundary, and (**C**) is the deformation over time).

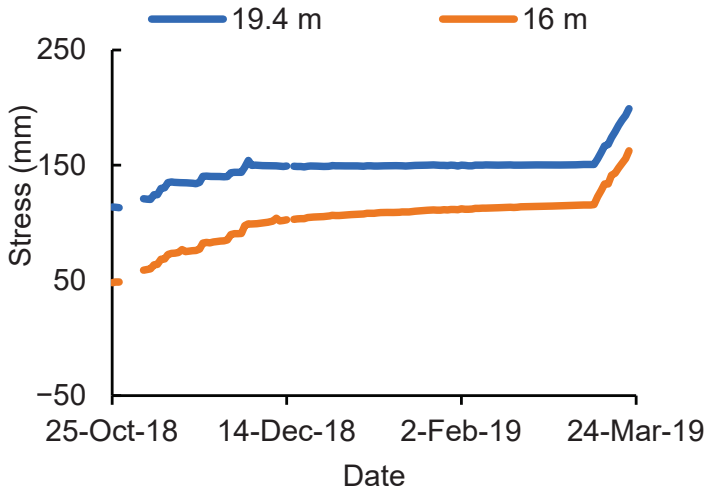

Figure 11. Horizontal stresses (the blue line is at 19.4 m, and the orange line is at 16 m).

5. Discussion

5.1. Effects of Different Compressibilities

The compression tests were conducted on a one-dimensional oedometer apparatus at the College of Geological Engineering and Geomatics, Chang'an University. The Accuracy of this equipment is ±0.001 mm. In this test, we set the pressure to 12.5 kPa, 25 kPa, 50 kPa, 100 kPa, 200 kPa, 400 kPa, 600 kPa, 800 kPa, 1600 kPa, and 3200 kPa on the in situ remolded and undisturbed loess. At each loading step, the settlement of the specimens was measured so that the void ratio could be calculated.

Regarding the results, there are some differences in the compressibility between undisturbed loess and remolded loess (Figure 12). The coefficient of compressibility in undisturbed loess decreases from 0.78 MPa^{-1} to 0.07 MPa^{-1}. For the remolded loess, the curve decreases linearly with pressure in the e-logp plot (Figure 12). The coefficient of compressibility is 1.13 MPa^{-1}, and it gradually decreases to 0.02 MPa^{-1}. Before the load reaches a certain threshold, the compression deformation of undisturbed loess is relatively small, and the compression curve of undisturbed loess is gentler than that of remolded loess. However, when the load exceeds the threshold, the void ratio decreases rapidly. The compression curve of the undisturbed soil after the load exceeds the threshold is steeper than that of the remolded loess, and the compression index of the undisturbed loess is larger than that of the remolded loess. Undisturbed loess has more pores, which provides room for compression. With increasing pressure, the structure of undisturbed loess gradually began to play a role, and the changes in the two curves were also significantly different.

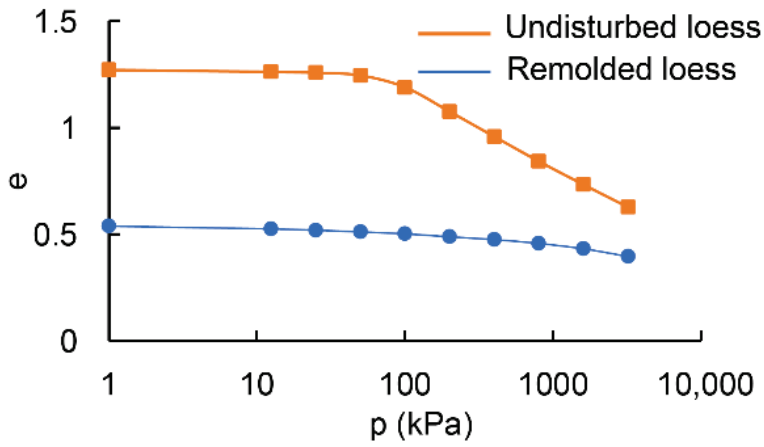

Figure 12. Compression curve shown by *e*-log*p* plots (the orange line is undisturbed loess, and the blue line is remolded loess).

In the filling project, due to the difference in compressibility, the internal deformation of loess produces different characteristics. The compression of undisturbed loess is small compared with that of remolded loess under low pressure. These differences cause the border to appear compressed. The filling body squeezes the adjacent areas. Therefore, different compression properties are one of the reasons that the boundary area becomes a vital area of loess.

5.2. Effects of Different Permeabilities

The volumetric water content (VWC) shows an increasing trend on both sides of the boundary. The process may be related to the groundwater level rising during the filling process. However, there are differences in volumetric water content on both sides of the boundary (Figure 13). According to laboratory tests for in situ loess, remolded loess and undisturbed loess have different hydraulic conductivities: 2.3×10^{-5} m/s for remolded loess and 1.4×10^{-4} m/s for undisturbed loess (Table 5). The hydraulic conductivity of undisturbed loess is an order of magnitude higher than that of remolded loess, which may induce different moisture movements. The difference in the soil properties may lead to different transport processes and cause different moisture concentrations at the boundary [63]. Therefore, the difference in horizontal deformation is related to moisture. In particular, these hydraulic discontinuities may contribute to high pore pressures during intense rainstorms and loading. In the filling project, moisture movement affects the high-fill slope stability, which causes settlement [64].

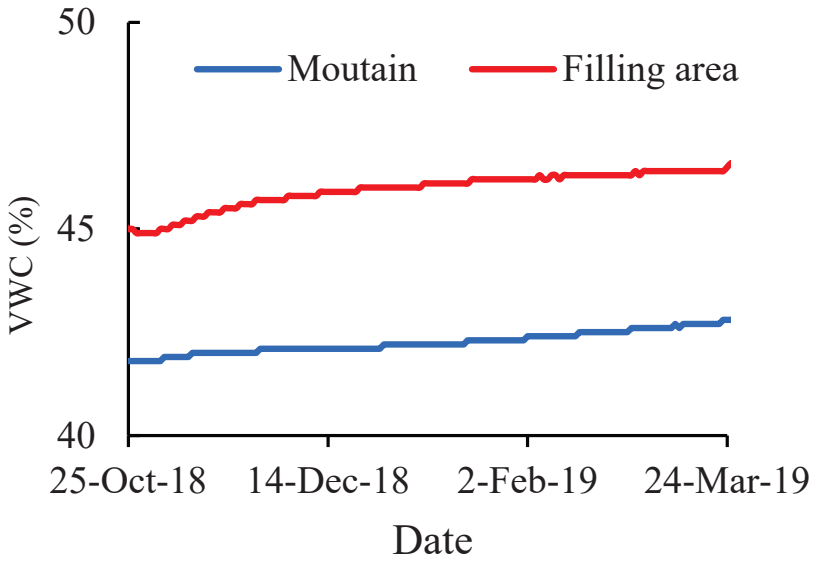

Figure 13. VWC on both sides of the boundary (the blue line is VWC in the original mountain, and the red line is VWC in the filling area).

Table 5. Permeability coefficients of undisturbed loess and remolded loess.

Type of Loess	Sample	Permeability Coefficient	Average Permeability Coefficient
Remolded loess	F01	2.6×10^{-5} m/s	2.3×10^{-5} m/s
	F02	2.2×10^{-5} m/s	
	F03	2.1×10^{-5} m/s	
Undisturbed loess	W01	1.5×10^{-4} m/s	1.4×10^{-4} m/s
	W02	1.4×10^{-4} m/s	
	W03	1.3×10^{-4} m/s	

Based on the above monitoring data, the filling process affects adjacent areas due to having different physical properties and different water contents. The deformation char-

acteristics affected by various factors are not homogeneous. The InSAR results show that the high filling boundary moves outward under the force of gravity. Internal monitoring shows that the boundary region shows a state of compression, while the landfill region shows a state of expansion.

5.3. Lessons from Monitoring

The project has provided new flat land for local agriculture and promoted economic development (Figure 14). This study demonstrates the early deformation characteristics of loess landfill through an air–space–ground integrated monitoring technique. In the excavation area, the deformation characteristics are similar to those of the core of LNA, which uplifts slightly. In the filling areas, due to soil instability in the landfill area, there are few PS points, so it is impossible to measure the deformation through InSAR accurately. From the vertical displacement meter in the filling body, the deformation from 16 m to 21 m reaches about 37.12 mm/a. However, the maximum annual deformation rate in the urban core areas of LNA measured by InSAR was 56.35 mm/a [34]. There are two main reasons for the difference in settlement: (1) different landfill methods and (2) different settling time intervals. Firstly, the study area has only just been landfilled, and the subsidence is relatively fast. In addition, due to this leveled land being intended for agriculture, roller compaction was selected for the landfill process. In general, the deformation in this area after the landfill process is within expectations. In addition, pressure and deformation are related to the filling process. The pressure and deformation increased following the filling process. However, the deformation and stress have some hysteresis according to the monitoring data.

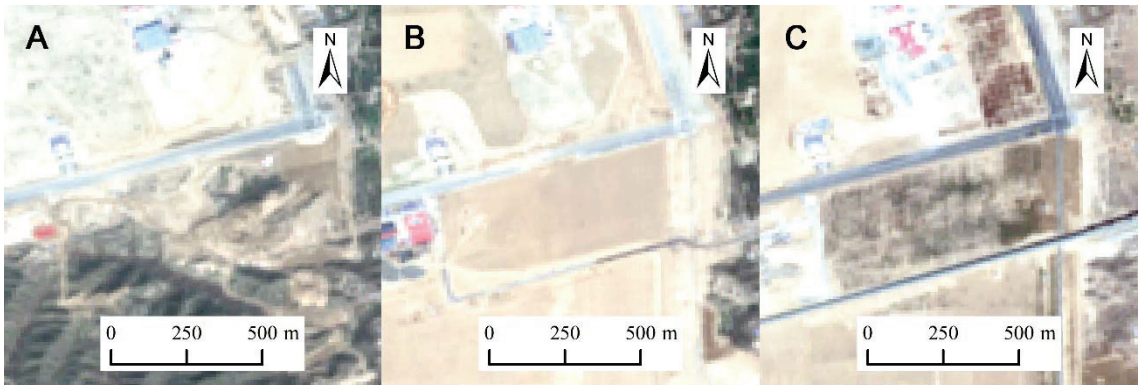

Figure 14. Changes in the research area ((**A**) is on 12 October 2018; (**B**) is on 4 July 2019; (**C**) is on 4 May 2022).

As a result of urban development, filling projects are distributed widely around the world, including projects such as Kansai International Airport in Japan [65], Macau International Airport in China [66], and Treasure Island in the USA [67]. Unreasonable landfill methods may cause geological disasters such as the Shenzhen landslide. Additionally, land subsidence is one of the problems in these areas. This case shows that we can use different landfill methods depending on the purposes and costs. It is also necessary to install monitoring equipment to monitor deformation. When abnormal deformations appear, we should take measures to control them.

6. Conclusions

In this study, we monitored large-scale deformation and investigated the causes using large-scale field monitoring from Sentinel-1 satellite data, in situ monitoring equipment, and laboratory tests. The following conclusions can be drawn:

(1) During the construction, stress and deformation increase rapidly (2.14 kPa/day for vertical stress at 21 m relative to the designed elevation and 0.47 mm/day from 16 m

to 21 m relative to the designed elevation). The loess in the filling area is the state of expansion while the state of compression is at the boundary. The deformation and stress have some hysteresis;

(2) During winter, the deformations in different regions varied. In the horizontal direction, the excavation area exhibits horizontal movement. Some boundaries appear to cause extrusion deformation in adjacent regions. The high filling boundary moves outward under the force of gravity (the deformation velocity in some areas exceeds 20 mm/a). In the vertical direction, there is an uplift in excavated areas and subsidence in the fill region;

(3) The water content on both sides of the boundary gradually increases due to the influence of the filling project. Different permeability properties indicate that the boundary area is critical. The filling and excavation processes have impacted the surrounding area;

(4) The compression characteristics of undisturbed loess and remolded loess are different, which is one of the reasons for their different deformation characteristics. At low pressure, the compressibility coefficient of undisturbed loess (0.78 MPa^{-1}) is lower than that of remolded loess (1.13 MPa^{-1}), but at high pressure, the compressibility coefficient of undisturbed loess (0.07 MPa^{-1}) is higher than that of remolded loess (0.02 MPa^{-1}). Different mechanical properties and hydraulic conductivities may trigger differential soil transfer and cause geohazards. It is also necessary to install monitoring equipment to monitor deformation. When abnormal deformations appear, measures should be taken to control them.

Author Contributions: Conceptualization, Y.W. and H.L.; methodology, Y.W.; validation, Y.W.; formal analysis, Y.W.; investigation, H.L.; resources, H.L.; writing—original draft preparation, Y.W.; writing—review and editing, H.L.; supervision, H.L.; project administration, H.L.; funding acquisition, H.L. All authors have read and agreed to the published version of the manuscript.

Funding: This study was supported by the National Natural Science Foundation of China (Grant NO. 41927806, 42041006 and 41790443) and the Strategic Priority Research Program of the Chinese Academy of Sciences (CAS) (Grant NO. XDA23090301).

Institutional Review Board Statement: Not applicable.

Informed Consent Statement: Not applicable.

Data Availability Statement: Not applicable.

Acknowledgments: We thank Chen Junhui, Lin Gan, and Tian Zhaoyang for burying the equipment and giving their suggestions regarding this paper.

Conflicts of Interest: The authors declare no conflict of interest.

References

1. Li, Y.; Yang, J.; Hu, X. Origin of ground fissures in the Shanxi Graben System, Northern China. *Eng. Geol.* **2000**, *55*, 267–275. [CrossRef]
2. Juang, C.H.; Dijkstra, T.; Wasowski, J.; Meng, X. Loess geohazards research in China: Advances and challenges for mega engineering projects. *Eng. Geol.* **2019**, *251*, 1–10. [CrossRef]
3. Peng, J.; Qi, S.; Williams, A.; Dijkstra, T.A. Preface to the special issue on "Loess engineering properties and loess geohazards". *Eng. Geol.* **2018**, *236*, 1–3. [CrossRef]
4. Li, Y.; Li, Y.; Fang, B.; Qu, L.; Wang, C.; Li, W. Land use change and farmers' sense of place in typical catchment of the Loess hilly and gully region of China. *Land* **2021**, *10*, 810. [CrossRef]
5. Chen, G.; Zhang, Y.; Zeng, R.; Yang, Z.; Chen, X.; Zhao, F.; Meng, X. Detection of Land Subsidence Associated with Land Creation and Rapid Urbanization in the Chinese Loess Plateau Using Time Series InSAR: A Case Study of Lanzhou New District. *Remote Sens.* **2018**, *10*, 270. [CrossRef]
6. Li, P.; Qian, H.; Wu, J. Environment: Accelerate research on land creation. *Nature* **2014**, *510*, 29–31. [CrossRef]
7. Niu, Q.; Bai, J.; Cheng, W.; Dang, X.; Wang, G.; Gao, X.; Wang, Y. Mapping the dynamics of urban land creation from hilltop removing and gully filling Projects in the river-valley city of Lanzhou, China. *J. Indian Soc. Remote Sens.* **2022**, 1–14. [CrossRef]
8. Liu, Y.; Li, Y. China's land creation project stands firm. *Nature* **2014**, *511*, 410. [CrossRef]

9. Jin, Z. The creation of farmland by gully filling on the Loess Plateau: A double-edged sword. *Environ. Sci. Technol.* **2014**, *48*, 883–884. [CrossRef]
10. Assallay, A.M.; Rogers, C.D.F.; Smalley, I.J. Formation and collapse of metastable particle packings and open structures in loess deposits. *Eng. Geol.* **1997**, *48*, 101–115. [CrossRef]
11. Barden, L.; McGown, A.; Collins, K. The collapse mechanism in partly saturated soil. *Eng. Geol.* **1973**, *7*, 49–60. [CrossRef]
12. Dijkstra, T.A.; Smalley, I.J.; Rogers, C.D.F. Particle packing in loess deposits and the problem of structure collapse and hydroconsolidation. *Eng. Geol.* **1995**, *40*, 49–64. [CrossRef]
13. Li, P.; Qian, H. Water in loess. In *Encyclopedia of Sustainability Science and Technology*; Springer: New York, NY, USA, 2018; pp. 1–17.
14. Wen, B.-P.; Yan, Y.-J. Influence of structure on shear characteristics of the unsaturated loess in Lanzhou, China. *Eng. Geol.* **2014**, *168*, 46–58. [CrossRef]
15. Derbyshire, E.; Dijkstra, T.A.; Smalley, I.J.; Li, Y. Failure mechanisms in loess and the effects of moisture content changes on remoulded strength. *Quat. Int.* **1994**, *24*, 5–15. [CrossRef]
16. Lutenegger, A.J.; Hallberg, G.R. Stability of loess. *Eng. Geol.* **1988**, *25*, 247–261. [CrossRef]
17. Yao, Y.; Wang, R.; Yang, J.; Yue, P.; Lu, D.; Xiao, G.; Wang, Y.; Liu, L. Changes in terrestrial surface dry and wet conditions on the Loess Plateau (China) during the last half century. *J. Arid Land* **2013**, *5*, 15–24. [CrossRef]
18. Meng, X.; Liao, H.; Zhang, J. Infiltration law of water in undisturbed loess and backfill. *Water* **2020**, *12*, 2388. [CrossRef]
19. Fredlund, D.; Gan, J. The collapse mechanism of a soil subjected to one-dimensional loading and wetting. In *Genesis and Properties of Collapsible Soils*; Springer: Dordrecht, The Netherlands, 1995; pp. 173–205.
20. Dexter, A.R.; Tanner, D.W. Time Dependence of Compressibility for Remoulded and Undisturbed Soils. *J. Soil Sci.* **1974**, *25*, 153–164. [CrossRef]
21. Shao, S.J.; She, F.T.; Fang, J. Mechanical Behavior of Segmented Lining Structure of Tunnel under Acting Ground Fractures in Xi'an Zone. *Adv. Mater. Res.* **2011**, *261–263*, 1778–1783. [CrossRef]
22. Jiang, M.; Zhang, F.; Hu, H.; Cui, Y.; Peng, J. Structural characterization of natural loess and remolded loess under triaxial tests. *Eng. Geol.* **2014**, *181*, 249–260. [CrossRef]
23. Miao, F.; Wu, Y.; Török, Á.; Li, L.; Xue, Y. Centrifugal model test on a riverine landslide in the Three Gorges Reservoir induced by rainfall and water level fluctuation. *Geosci. Front.* **2022**, *13*, 101378. [CrossRef]
24. Miao, F.; Wu, Y.; Xie, Y.; Li, Y. Prediction of landslide displacement with step-like behavior based on multialgorithm optimization and a support vector regression model. *Landslides* **2018**, *15*, 475–488. [CrossRef]
25. Liu, X.; Zhao, C.; Zhang, Q.; Peng, J.; Zhu, W.; Lu, Z. Multi-Temporal Loess Landslide Inventory Mapping with C-, X- and L-Band SAR Datasets—A Case Study of Heifangtai Loess Landslides, China. *Remote Sens.* **2018**, *10*, 1756. [CrossRef]
26. Shi, X.; Yang, C.; Zhang, L.; Jiang, H.; Liao, M.; Zhang, L.; Liu, X. Mapping and characterizing displacements of active loess slopes along the upstream Yellow River with multi-temporal InSAR datasets. *Sci. Total Environ.* **2019**, *674*, 200–210. [CrossRef]
27. Gray, L. Using multiple RADARSAT InSAR pairs to estimate a full three-dimensional solution for glacial ice movement. *Geophys. Res. Lett.* **2011**, *38*, L05502. [CrossRef]
28. Chen, B.; Gong, H.; Li, X.; Lei, K.; Zhu, L.; Gao, M.; Zhou, C. Characterization and causes of land subsidence in Beijing, China. *Int. J. Remote Sens.* **2017**, *38*, 808–826. [CrossRef]
29. Schlögel, R.; Doubre, C.; Malet, J.-P.; Masson, F. Landslide deformation monitoring with ALOS/PALSAR imagery: A D-InSAR geomorphological interpretation method. *Geomorphology* **2015**, *231*, 314–330. [CrossRef]
30. Zhao, C.; Zhang, Q.; He, Y.; Peng, J.; Yang, C.; Kang, Y. Small-scale loess landslide monitoring with small baseline subsets interferometric synthetic aperture radar technique—Case study of Xingyuan landslide, Shaanxi, China. *J. Appl. Remote Sens.* **2016**, *10*, 026030. [CrossRef]
31. Xue, Y.T.; Meng, X.M.; Li, K.; Chen, G. Loess Slope Instability Assessment Based on PS-InSAR Detected and Spatial Analysis in Lanzhou Region, China. *Adv. Mater. Res.* **2014**, *1065–1069*, 2342–2352. [CrossRef]
32. Zeng, R.Q.; Meng, X.M.; Wasowski, J.; Dijkstra, T.; Bovenga, F.; Xue, Y.T.; Wang, S.Y. Ground instability detection using PS-InSAR in Lanzhou, China. *Q. J. Eng. Geol. Hydrogeol.* **2014**, *47*, 307–321. [CrossRef]
33. Hu, X.; Xue, L.; Yu, Y.; Guo, S.; Cui, Y.; Li, Y.; Qi, S. Remote Sensing Characterization of Mountain Excavation and City Construction in Loess Plateau. *Geophys. Res. Lett.* **2021**, *48*, e2021GL095230. [CrossRef]
34. He, Y.; Chen, Y.; Wang, W.; Yan, H.; Zhang, L.; Liu, T. TS-InSAR analysis for monitoring ground deformation in Lanzhou New District, the loess Plateau of China, from 2017 to 2019. *Adv. Space Res.* **2021**, *67*, 1267–1283. [CrossRef]
35. Wei, Y.; Liu, X.; Zhao, C.; Tomás, R.; Jiang, Z. Observation of Surface Displacement Associated with Rapid Urbanization and Land Creation in Lanzhou, Loess Plateau of China with Sentinel-1 SAR Imagery. *Remote Sens.* **2021**, *13*, 3472. [CrossRef]
36. Wu, Q.; Jia, C.; Chen, S.; Li, H. SBAS-InSAR based deformation detection of urban land, created from mega-scale mountain excavating and valley filling in the Loess Plateau: The case study of Yan'an City. *Remote Sens.* **2019**, *11*, 1673. [CrossRef]
37. Agisoft, L. PhotoScan Python Reference. *Release* **2016**, *1*, 63.
38. Luo, H.; Wu, F.; Chang, J.; Xu, J. Microstructural constraints on geotechnical properties of Malan Loess: A case study from Zhaojiaan landslide in Shaanxi province, China. *Eng. Geol.* **2018**, *236*, 60–69. [CrossRef]
39. Li, Y.; He, S.; Deng, X.; Xu, Y. Characterization of macropore structure of Malan loess in NW China based on 3D pipe models constructed by using computed tomography technology. *J. Asian Earth Sci.* **2018**, *154*, 271–279. [CrossRef]

40. Wei, Y.-N.; Fan, W.; Yu, B.; Deng, L.-S.; Wei, T. Characterization and evolution of three-dimensional microstructure of Malan loess. *Catena* **2020**, *192*, 104585. [CrossRef]
41. Li, Y. A review of shear and tensile strengths of the Malan Loess in China. *Eng. Geol.* **2018**, *236*, 4–10. [CrossRef]
42. Standard, B. *Methods of Test for Soils for Civil Engineering Purposes*; British Standards Institution: London, UK, 1990; BS1377.
43. Botey i Bassols, J.; Vàzquez-Suñé, E.; Crosetto, M.; Barra, A.; Gerard, P. D-InSAR monitoring of ground deformation related to the dewatering of construction sites. A case study of Glòries Square, Barcelona. *Eng. Geol.* **2021**, *286*, 106041. [CrossRef]
44. Sousa, J.J.; Ruiz, A.M.; Hanssen, R.F.; Bastos, L.; Gil, A.J.; Galindo-Zaldívar, J.; de Galdeano, C.S. PS-InSAR processing methodologies in the detection of field surface deformation—Study of the Granada basin (Central Betic Cordilleras, southern Spain). *J. Geodyn.* **2010**, *49*, 181–189. [CrossRef]
45. Ferretti, A.; Prati, C.; Rocca, F. Permanent scatterers in SAR interferometry. *IEEE Trans. Geosci. Remote Sens.* **2001**, *39*, 8–20. [CrossRef]
46. Werner, C.; Wegmüller, U.; Strozzi, T.; Wiesmann, A. Gamma SAR and interferometric processing software. In Proceedings of the Ers-Envisat Symposium, Gothenburg, Sweden, 15–20 October 2000; p. 1620.
47. Perissin, D. SARPROZ Software Manual. 2016. Available online: https://www.sarproz.com (accessed on 12 May 2022).
48. Hooper, A.; Spaans, K.; Bekaert, D.; Cuenca, M.C.; Arıkan, M.; Oyen, A. *StaMPS/MTI Manual*; Delft Institute of Earth Observation and Space Systems Delft University of Technology: Kluyverweg, The Netherlands, 2010; Volume 1, p. 2629.
49. Hooper, A. A multi-temporal InSAR method incorporating both persistent scatterer and small baseline approaches. *Geophys. Res. Lett.* **2008**, *35*, L16302–L16309. [CrossRef]
50. Hooper, A.; Segall, P.; Zebker, H. Persistent scatterer interferometric synthetic aperture radar for crustal deformation analysis, with application to Volcán Alcedo, Galápagos. *J. Geophys. Res. Solid Earth* **2007**, *112*, B07407. [CrossRef]
51. Zhou, S.; Ouyang, C.; Huang, Y. An InSAR and depth-integrated coupled model for potential landslide hazard assessment. *Acta Geotech.* **2022**, *17*, 3613–3632. [CrossRef]
52. Foumelis, M.; Blasco, J.M.D.; Desnos, Y.-L.; Engdahl, M.; Fernández, D.; Veci, L.; Lu, J.; Wong, C. ESA SNAP-StaMPS integrated processing for Sentinel-1 persistent scatterer interferometry. In Proceedings of the IGARSS 2018—2018 IEEE International Geoscience and Remote Sensing Symposium, Valencia, Spain, 4 November 2018; pp. 1364–1367.
53. Bayramov, E.; Buchroithner, M.; Kada, M.; Zhuniskenov, Y. Quantitative Assessment of Vertical and Horizontal Deformations Derived by 3D and 2D Decompositions of InSAR Line-of-Sight Measurements to Supplement Industry Surveillance Programs in the Tengiz Oilfield (Kazakhstan). *Remote Sens.* **2021**, *13*, 2579. [CrossRef]
54. Fuhrmann, T.; Garthwaite, M.C. Resolving three-dimensional surface motion with InSAR: Constraints from multi-geometry data fusion. *Remote Sens.* **2019**, *11*, 241. [CrossRef]
55. Aslan, G.; Cakir, Z.; Lasserre, C.; Renard, F. Investigating subsidence in the Bursa Plain, Turkey, using ascending and descending Sentinel-1 satellite data. *Remote Sens.* **2019**, *11*, 85. [CrossRef]
56. Fialko, Y. Interseismic strain accumulation and the earthquake potential on the southern San Andreas fault system. *Nature* **2006**, *441*, 968–971. [CrossRef]
57. Motagh, M.; Shamshiri, R.; Haghighi, M.H.; Wetzel, H.-U.; Akbari, B.; Nahavandchi, H.; Roessner, S.; Arabi, S. Quantifying groundwater exploitation induced subsidence in the Rafsanjan plain, southeastern Iran, using InSAR time-series and in situ measurements. *Eng. Geol.* **2017**, *218*, 134–151. [CrossRef]
58. Pawluszek-Filipiak, K.; Borkowski, A. Integration of DInSAR and SBAS Techniques to determine mining-related deformations using sentinel-1 data: The case study of Rydułtowy mine in Poland. *Remote Sens.* **2020**, *12*, 242. [CrossRef]
59. Yao, Y.; Zhang, Y.; Ma, C.; Zhao, Y.; Lv, G. Study on deformation of filling composite geological body in loess mountainous area. *Nat. Hazards* **2022**, *110*, 1469–1493. [CrossRef]
60. Sowers, G. Compressibility of broken rock and the settlement of rockfills. In Proceedings of the 6th International Conference on Soil Mechanics and Foundation Engineering, Montreal, QC, Canada, 8–15 September 1965; pp. 561–565.
61. Charles, J. Laboratory compression tests and the deformation of rockfill structures. In *Advances in Rockfill Structures*; Springer: Dordrecht, The Netherlands, 1990; pp. 73–95.
62. Charles, J.; Skinner, H. Compressibility of foundation fills. *Proc. Inst. Civ. Eng. Geotech. Eng.* **2001**, *149*, 145–157. [CrossRef]
63. Wu, Y.; Lan, H.; Huang, W. Relationship between wave velocities and water content of unsaturated loess. *Chin. J. Geophys.* **2021**, *64*, 3766–3773.
64. Mei, Y.; Zhou, D.-B.; Hu, C.-M.; Wang, X.-Y.; Zhang, Y.; Xiao, N.; Shi, W. Study on Deformation Characteristics of Loess Ultrahigh-Fill Slope Based on Large-Scale Undisturbed Soil Centrifugal Model Tests. *Front. Earth Sci.* **2022**, *10*, 848542. [CrossRef]
65. Mesri, G.; Funk, J. Settlement of the Kansai international airport islands. *J. Geotech. Geoenviron. Eng.* **2015**, *141*, 04014102. [CrossRef]
66. Carter, M. Methods used to reduce settlements and shorten construction time at Macau international airport. *HKIE Trans.* **1996**, *3*, 1–8. [CrossRef]
67. Bennett, M.J. *Subsurface Investigation for Liquefaction Analysis and Piezometer Calibration at Treasure Island Naval Station, California*; US Geological Survey: Arcata, CA, USA, 1994; ISSN 2331-1258.

remote sensing

MDPI

Article

Fast Displacement Estimation of Multiple Close Targets with MIMO Radar and MUSICAPES Method

Jian Wang [1,*], Yuming Wang [2], Yueli Li [1] and Xiaotao Huang [1]

[1] College of Electronic Science and Technology, National University of Defense Technology, Changsha 410073, China; liyueli4uwb@nudt.edu.cn (Y.L.); xthuang@nudt.edu.cn (X.H.)
[2] College of Information Science and Engineering, Hunan Normal University, Changsha 410081, China; wangyuming@hunnu.edu.cn
* Correspondence: jianwang_uwb@nudt.edu.cn; Tel.: +86-731-87003353

Abstract: Interferometric radar is a hot research topic in manmade target displacement measuring applications, as it features high precision, a large operation range, and a remote multiple point measuring ability. Most one-dimensional interferometric radars use single-input single-output (SISO) radar architecture to achieve a high repetition measuring rate of more than 200 Hz; however, it cannot resolve multiple targets with the same radial range but different azimuth angles. This paper presents a multiple-input multiple-output (MIMO) radar that adopts a limited number of antennas (usually tens) to simultaneously improve azimuth resolution and achieve a high repetition measuring rate. A MUSICAPES algorithm is proposed, which is cascades the multiple signal classification (MUSIC) algorithm and the amplitude and phase estimation (APES) filter. The MUSIC algorithm is used to further improve the angular resolution of the small array. The APES is used to precisely recover the phases of the multiple close targets by suppressing their mutual interferences. Simulations and experiments with a millimeter-wave radar validate the performance of the proposed method.

Keywords: interferometric MIMO radar; displacement measurement; multiple close targets; millimeter wave; MUSIC; APES

Citation: Wang, J.; Wang, Y.; Li, Y.; Huang, X. Fast Displacement Estimation of Multiple Close Targets with MIMO Radar and MUSICAPES Method. *Remote Sens.* **2022**, *14*, 2005. https://doi.org/10.3390/rs14092005

Academic Editors: Timo Balz and Andrea Monti Guarnieri

Received: 9 February 2022
Accepted: 19 April 2022
Published: 21 April 2022

1. Introduction

Many manmade targets, such as bridges, tunnels, towers, tall buildings, etc., deform slightly under external forces. These external forces are wind, traffic, hydraulic, temperature stress, or a combination of them. The deformation may cause irreversible structural damage if it exceeds the maximum deformation threshold; therefore, it is of great significance to precisely monitor the tiny deformations of these targets. At present, deformation can be measured by contact or non-contact deformation measuring sensors. Conventional contact measurement sensors include displacement gauge, tension gauge, accelerometer, vibration pickup, strain gauge, inclinometer, level gauge, and Beidou/GPS displacement gauge. Non-contact sensors include total station, laser interferometry, high-definition video, interferometric radar, etc. According to the working mode, the most widely used deformation measuring sensors belong to the single-point measurement system; however, they suffer several technical limitations. Interferometric radars are popular for monitoring bridges, towers, slopes, mine pits, dams, and other civil infrastructures.

Interferometric radars receive the echo of an object's backscattering by transmitting microwave radio waves and measuring the displacement of the object by time difference interferometry. They feature high precision, long working range, operational convenience, remote multiple point measuring ability, and good environmental adaptability [1]. They can be further divided into one-dimensional interferometric radars and two-dimensional interferometric radars. The former kind of radars is applied to measure bridges, tall buildings, and towers, which requires a higher repetition measurement rate [2,3], whereas the latter kind is applied to measure slopes and dams, which features a lower repetition rate

but a large coverage requirement [4]. Interferometric radars can be extended to different platforms, such as satellites, airplanes, ships, and rails [5]. These radars would also work at different frequency bands, from the X band up to the W band [6].

One-dimensional interferometric radars generally adopt the single-input signal-output (SISO) radar architecture. The radar can only measure the deformations of objects with different radial distances. It would hinder the radar's application in the case of there being two objects with the same radial distance but different azimuth angles. Most amendments to these radars are to solve displacements with multiple directions [7]. If a one-dimensional interferometric radar adopts multiple-input multiple-output (MIMO) radar architecture, its multiple targets resolving capability can be improved. Traditional MIMO interferometric radars are usually proposed to reduce the data acquisition time of rail-mounted two-dimensional interferometric radars [8,9]. Some improvements to MIMO interferometric radars would involve forming 3-D images and retrieving 3-D displacements [10,11]. Few MIMO radars are capable of even measuring dynamic displacements [12], and many of them find it hard to achieve a high repetition rate similar to that of a one-dimensional radar.

Multiple target imaging algorithms for MIMO interferometric radar include the back projection (BP) algorithm [8], the range migration algorithm, and the far-field pseudo-polar format algorithm (FPFA) [13]. All these algorithms are suitable when the equivalent elements of a MIMO array are large; however, a large repetition rate requires a smaller MIMO array. The imaging algorithm should adapt to the small array while still having a fine multiple-target resolving ability. As the range migration of a target is not prominent for the small array, fast Fourier transformation (FFT) can be used to resolve multiple targets. Although improved methods such as ZOOM-FFT(ZFFT), FFT-FS, and chirp z-transform (CZT) [14], can be used to improve the computation resolution. These FFT-based methods still suffer from a limited angle resolution that is inversely proportional to the array length. Direction of arrival (DOA) estimation methods can achieve a better performance when scatters are independent. These methods include Capon beamforming [15], the amplitude and phase estimation (APES) [16,17], the multiple signal classification (MUSIC) [18,19], and so on. The phases of multiple targets would suffer mutual interferences if they were close. It would cause additional requirements for the DOA methods. None of these methods can achieve azimuth super-resolution and precise phase estimation at the same time.

In this paper, a short MIMO interferometric radar is designed to extract multiple close targets with a high repetition rate. A MUSICAPES algorithm is proposed to resolve multiple targets beyond the angle resolution and suppress the mutual interferences of their side lobes. The algorithm is performed by cascading the root-MUSIC algorithm and an APES filter. The deformations of multiple targets with the same radial distance but different azimuth angles are finally accurately estimated with time differential interferometry. The main contributions of this paper are summarized as follows.

- A MIMO interferometric radar is proposed for a precise, high repetition rate, non-contact, multi-point simultaneous displacement measurement. It has the advantages of both one-dimensional and two-dimensional deformation measuring radars. It can measure multiple close targets such as complex bridges, towers, and buildings, which traditional one-dimensional radars fail to do.
- A MUSICAPES method is proposed to resolve multiple azimuth close targets and precisely extract their displacements. The method first adopts the root-MUSIC algorithm to estimate the azimuth angle of each target. Then, the APES algorithm is used to precisely recover the phases of the targets using the azimuth angles estimated in the former step. The method can improve the displacement measuring precision significantly.
- A millimeter-wave MIMO interferometric radar is designed for multiple target displacement measuring. The radar is composed of a commercial off-the-shelf (COTS) radar front end, an analog to digital (AD) card, and a laptop computer. Experiment results show that the radar can resolve multiple targets beyond the angular resolution

of the MIMO array and can precisely measure their displacements at a repetition rate of more than 100 Hz.

Notation: We denote vectors and matrices by boldface letters. See Table 1 for the main acronyms and symbols and their meanings.

Table 1. Meanings of main abbreviations, acronyms and symbols.

Index	Term	Meaning
1	SISO	single-input signal-output
2	MIMO	multiple-input multiple-output
3	MUSIC	multiple signal classification
4	APES	amplitude and phase estimation
5	CZT	chirp z-transform
6	DOA	direction of arrival
7	MMW	millimeter-wave
8	COTS	commercial off-the-shelf
9	$\mathbf{R}_1$	input covariance matrix for MUSIC
10	$\mathbf{R}_2$	input covariance matrix for APES
11	$\mathbf{U}_S$	signal space by eigen decomposition
12	$\mathbf{U}_N$	noise space by eigen decomposition
13	$\hat{\mathbf{Q}}$	noise covariance matrix for APES
14	$\mathbf{h}$	optimal complex filter coefficients of APES

The rest of this paper is organized as follows. Section 2 briefly describes the architecture of the MIMO interferometric radar and the principles of multiple target discrimination. A MUSICAPES method is proposed in Section 3, to precisely extract the displacements of multiple close targets. Simulations and two-target displacement measuring experiments with an MMW MIMO radar are presented in Section 4. Finally, conclusions are drawn in Section 5.

2. MIMO Interferometric Radar and Multiple Target Discrimination

Conventional one-dimensional interferometric radars adopt one transmitting antenna and one receiving antenna. The azimuth resolution is restricted to the beamwidth of the two antennas. Generally speaking, the radar cannot resolve two targets with the same radial range but different cross-range positions, as target A and target B in Figure 1, for example. The radar can only resolve targets with different radial ranges, as target A and target C in Figure 1, for example.

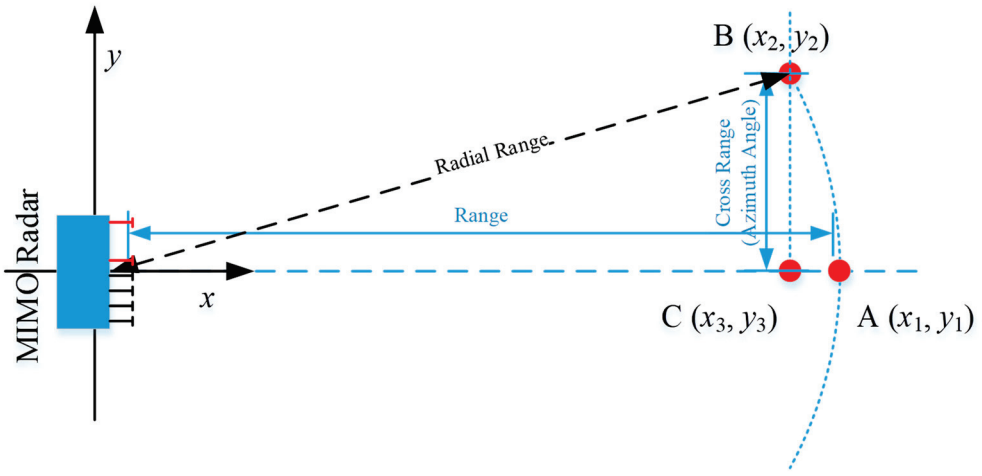

Figure 1. Multiple target deformation measurement with a MIMO interferometric radar.

Azimuth or angle discrimination can be improved by using a SAR or DOA algorithm in traditional radars. Two-dimensional interferometric radars adopt the SAR system and the persistent scatter (PS) algorithm to estimate slow displacement. We use the DOA method to estimate fast displacement. The radar architecture, the principles of range discrimination, and azimuth discrimination are described in this section in detail.

2.1. Basic Architecture of an Interferometric MIMO Radar

To achieve a high repetition measuring rate, all the transmitting and receiving channels of a MIMO radar should work simultaneously. The radar should adopt an orthogonal waveform, multiple transmitters, and multiple receivers to achieve the best performance; however, the overall cost of the radar would be unaffordable in most civil applications. Moreover, we will use the MIMO radar that works in time-division mode.

The MIMO interferometric radar is composed of M transmitting antennas and N receiving antennas, as shown in Figure 2. The space between two receiving antennas is half the wavelength. The interval between two transmitting antennas is N times the half wavelength. As a result, an equivalent transceiving antenna array is formed. The interval between two equivalent antennas is a quarter of the wavelength. In a far-field assumption, the equivalent transceiving antenna TR_{ij} is in the middle of the transmitting antenna T_i and the receiving antenna R_j.

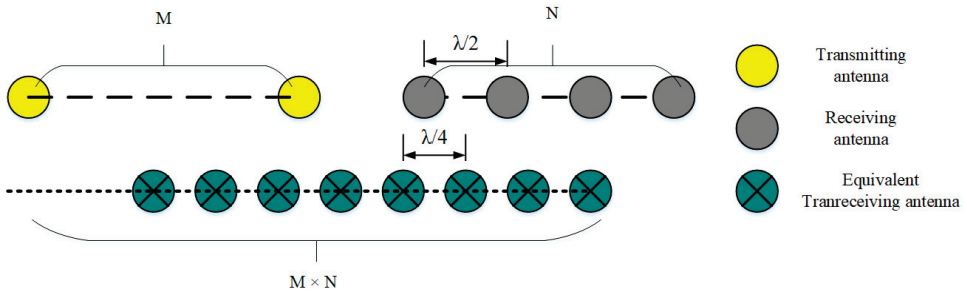

Figure 2. Antenna array layout of the MIMO radar.

$$x_{TR_{ij}} = \left(x_{T_i} + x_{R_j}\right)/2 \qquad y_{TR_{ij}} = \left(y_{T_i} + y_{R_j}\right)/2 \tag{1}$$

where x_{T_i}, x_{R_j}, $x_{TR_{ij}}$ are positions in the x coordinate of the ith transmitting antenna, the jth receiving antenna, and the equivalent transceiving antenna, respectively. y_{T_i}, y_{R_j}, $y_{TR_{ij}}$ are positions in the y coordinate of the ith transmitting antenna, the jth receiving antenna, and the equivalent transceiving antenna, respectively.

The transmitting antenna is connected to an RF switch whose input port is connected to the transmitter. Each receiving antenna is fed to a receiver that performs bandpass filter, low noise amplification, and dechirp demodulation. Then, the outputted echo is fed to an analog-to-digital converter whose output is sent to a laptop computer via Ethernet. A laptop computer controls the radar front end through a serial port, to configure the working frequency range, the sweep duration of a linear frequency modulation (LFM) signal, the pulse repetition frequency, the AD sampling frequency, and the sampling length. The sampled radar echo is streamed out through an LVDS bus to a data acquisition board which formats the echo into standard UDP socket packages. The packages are finally sent to the laptop computer via Ethernet.

2.2. Multiple Target Discriminator from the Range Direction

To distinguish nearby targets, the interferometric MIMO radar has to emit wideband signals. The LFM signal is one of the most widely used waveforms. The frequency of an LFM signal changes linearly with time. It can be formulated as

$$s_t(t) = A \times \mathrm{rect}\left(\frac{t}{T}\right) \exp\left[j\pi\left(2f_0 t + K_f t^2\right)\right] \qquad 0 < t < T \tag{2}$$

where f_0 is the start frequency, T is the sweep period, and K_f is the chirp rate. A is the amplitude, and it is often omitted for simplicity. The function rect is defined as $\mathrm{rect}(x) = \begin{cases} 1, & |x| \le 1 \\ 0, & |x| > 1 \end{cases}$. The received signal of a point target is an attenuated -and time-delayed replica of the transmitting signal. After a dechirp demodulation operation, the received intermediate-frequency signal can be written as

$$s_{\mathrm{IF}}^{(T_i,R_j)}(t) = \exp(j2\pi f_0 \tau) \exp\left(j2\pi K_f \tau t\right) \exp\left(-j\pi K_f \tau^2\right) \tag{3}$$

where the first exponential component indicates the phase delay; the second component is a linear phase term and indicates the range of the target; the last component is the quadratic phase error of the dechirp operation. $\tau = \left(r_{k,T_i} + r_{k,R_j}\right)/c$ is the round trip travelling delay of the electromagnetic wave. r_{k,T_i}, r_{k,R_j} are the distances from the kth target to the transmitting antenna T_i, and the receiving antenna R_j, respectively. c is the electromagnetic wave velocity.

$$\begin{aligned} r_{k,T_i} &= \sqrt{\left(x_k - x_{T_i}\right)^2 + \left(y_k - y_{T_i}\right)^2} \qquad T_i = 1, \cdots M \\ r_{k,R_j} &= \sqrt{\left(x_k - x_{R_j}\right)^2 + \left(y_k - y_{R_j}\right)^2} \qquad R_j = 1, \cdots N \end{aligned} \tag{4}$$

A one-dimensional radar image is obtained by the FFT operation and is expressed as

$$S_{\mathrm{RC}}^{(T_i,R_j)}(n) \approx N_T \exp\left[j2\pi\left(f_0\tau - \frac{1}{2}K_f\tau^2\right)\right] \exp\left[j\pi\left(\frac{K_f\tau}{f_s} - \frac{n}{N_{\mathrm{FFT}}}\right)(N_{\mathrm{FFT}} - 1)\right] \sin c\left[\left(\frac{K_f\tau}{f_s} - \frac{n}{N_{\mathrm{FFT}}}\right)N_{\mathrm{FFT}}\right] \tag{5}$$

where N_{FFT} is the length of the FFT operation. f_s is the sampling frequency of the AD card. The one-dimensional radar image of the target is a peak whose index is $n_{\mathrm{peak}} = \mathrm{round}\left(N_{\mathrm{FFT}}K_f\tau/f_s\right)$. The complex radar response of the target is denoted as $\alpha(n_{\mathrm{peak}}) = \exp\left[j\pi\left(2f_0\tau - K_f\tau^2\right)\right]$. As the second term is far less than the first one, we can obtain the phase of the target as

$$\varphi(T_i, R_j, n_{\mathrm{peak}}) = 2\pi f_0 \tau \tag{6}$$

The range resolution of the radar is proportional to the time duration T-τ. As T is much larger than τ, so is the resolution $\rho_r = 0.886c/(K_f T)$. The coefficient 0.886 is a correction factor that makes the range resolution accurate [20]. If we want to discriminate between target A and target C in Figure 1, ρ_r should be smaller than $\sqrt{(x_1 - x_3)^2 + (y_1 - y_3)^2}$.

2.3. Multiple Target Discriminator from the Cross Range Direction

Each combination of T_i and R_j can output a one-dimensional radar image. The responses of a target in all the images have similar ranges and amplitudes, but they are different in phases. Figure 3 shows the geometry of DOA estimation with the equivalent MIMO array. If the DOA angle of the target is θ, then the phase difference between two adjacent antennas is $\pi \sin\theta$.

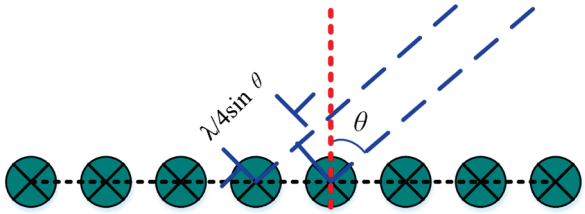

Figure 3. Direction of arrival estimation with an array.

At the discrete time tick t_s, a target response vector can be constructed by using the target's peaks in all the $M \times N$ one-dimensional images.

$$\mathbf{S}(t_s, n_{peak}) = \left[s_{\mathrm{RC}}^{(1,1)}(n_{peak}), s_{\mathrm{RC}}^{(1,2)}(n_{peak}), \cdots, s_{\mathrm{RC}}^{(1,N)}(n_{peak}), \cdots, s_{\mathrm{RC}}^{(M,N)}(n_{peak}) \right]^T \quad (7)$$

The DOA angle θ can be estimated by the traditional FFT operation. An angle response image of the target is famulated as

$$s_{SP}(t_s, k) = Ae^{i\bar{\phi}_0} \frac{\sin[MN\pi(k/(MN) + \sin\theta/2)]}{\sin[\pi(k/(MN) + \sin\theta/2)]} \quad (8)$$

The DOA angle θ coincides with the peak of the angle image. We can find that the angular resolution ρ_θ of an $M \times N$ array is

$$\rho_\theta = \mathrm{asin}\left(\frac{2 \times 0.886}{\mathrm{MN}}\right) \quad (9)$$

where the coefficient 0.886 is a correction factor to make the angular resolution accurate. If we want to discriminate between target A and target B in Figure 1, the resolution ρ_θ should be smaller than $\mathrm{asin}\left[|x_1 - x_3| / \sqrt{(x_1 - x_3)^2 + (y_1 - y_3)^2}\right]$.

3. MUSICAPES for Multiple Close Targets Deformation Estimation

Since the array length of the interferometric MIMO radar is small enough to maintain a high repetition measuring rate, and if the traditional MIMO radar processing method is used to estimate the displacements of multiple targets, it has to face two challenges. One challenge is that the angular resolution of the array is limited. The other one is that the large side lobes of the array would cause prominent phase errors. As a result, the radar would find it difficult to precisely estimate the displacements of multiple close targets. A MUSICAPES is proposed to solve the two problems. Firstly, the method adopts the root-MUSIC algorithm to improve the angular resolution of the short MIMO radar. Then, it employs the APES filter to suppress the interferences of other targets and precisely estimate the complex coefficients, using the DOA angle obtained by the root-MUSIC algorithm. Finally, the displacement is calculated by the traditional time differential operation.

3.1. Multiple Targets Extraction Based on MUSIC

There are many advanced array processing algorithms for DOA estimation, such as Capon beamforming, MUSIC, ESPRIT, IAA [21], and so on. We will adopt the widely used MUSIC algorithm to estimate DOA angles, as the algorithm is famous for its super-resolution performance. The MUSIC algorithm can be incorporated with phase interferometry to improve the performance of DOA estimation [22].

The input to the MUSIC algorithm is one snapshot of the MIMO array, as shown in (7). The length of the observation is $(M \times N)$. Firstly, we have to estimate the covariance of the observation. An estimation of the covariance matrix is usually obtained by (time) averaging several independent snapshots; however, there is only one snapshot, so we have to divide the long snapshot vector into several overlapped shorter subvectors. Supposing the length

of the subvectors is M_{music} ($M_{music} \leq (MN)/2$ generally), then an estimation of the input covariance matrix can be formulated as follows.

$$\mathbf{R}_1 = \sum_{i=0}^{N_{\overline{TR}}-M_{music}} \mathbf{y}_1(i) \times (\mathbf{y}_1(i))^H \tag{10}$$

where $()^H$ is the conjunction transpose operator. The subvector is $\mathbf{y}_1(i) = [s(t_s, n_{peak}, i), s(t_s, n_{peak}, i+1), \cdots s(t_s, n_{peak}, i+M_{music}-1)]^T$. Then, the eigendecomposition is performed, which can be expressed as

$$\mathbf{R}_1 = \mathbf{U}\Lambda\mathbf{U}^H = \mathbf{U}_S\Lambda_S\mathbf{U}_S^H + \mathbf{U}_N\Lambda_N\mathbf{U}_N^H \tag{11}$$

There are M_{music} eigenvalues, among which bigger ones are indicators of targets, and smaller ones are indicators of noise. Supposing there are P bigger eigenvalues, the corresponding eigenvectors in $\mathbf{U}$ span a signal space which is denoted as $\mathbf{U}_S$. The dimensions of $\mathbf{U}_S$ are $M_{music} \times P$. The remaining eigenvectors in $\mathbf{U}$ span the noise space which is expressed as $\mathbf{U}_N$. The dimensions of $\mathbf{U}_N$ are $M_{music} \times (M_{music} - P)$.

The traditional MUSIC algorithm estimates DOA angles by finding peaks of the pseudospectrum. The pseudospectrum estimate is defined as

$$P_{MUSIC}(\theta) = \frac{1}{[\mathbf{a}_1(\theta)]^H\mathbf{U}_N\mathbf{U}_N^H\mathbf{a}_1(\theta)} \tag{12}$$

where $\mathbf{a}_1(\theta) = [1, e^{-j4\pi \sin\theta d/\lambda}, \cdots, e^{-j4\pi \sin\theta M_{music} d/\lambda}]^{\mathbf{T}}$ is the steering vector of DOA angle θ. It is time-consuming to calculate the pseudo spectrum if the number of tested angles is large. The root-MUSIC can reduce the computation load. MUSIC and root-MUSIC have the same asymptotic performances, but the latter one has better performance in small sample situations [23]. The DOA angle can be estimated by solving the equation below [24].

$$z^{M_{APES}-1}p^T(z^{-1})\mathbf{U}_N\mathbf{U}_N^H p(z) = 0 \tag{13}$$

The steering vector $\mathbf{a}_1(\theta)$ is replaced by vector $p(z) = [1, z, \cdots z^{M_{music}-1}]^T$. Where $z = e^{-j4\pi \sin\theta d/\lambda}$. There are $2M_{music}$ solutions for Equation (13). They are symmetrical with respect to the unit circle. We choose the P solutions that are most close to the unit circle. Suppose the solutions are $\theta_1, \theta_2, \cdots \theta_P$.

3.2. Deformation Estimation Based on APES

APES is a maximum likelihood estimation of the complex sinusoidal signal, which is proposed by Li and Stoica. It can obtain more precise phase and amplitude estimations than those of the Capon filter [16]. For a target angle θ_k estimated by the root-MUSIC, a steering vector is formed as $\mathbf{a}_{M_{APES}}(\theta_k) = [1, e^{-j4\pi \sin\theta_k d/\lambda}, \cdots e^{-j(M_{APES}-1)4\pi \sin\theta_k d/\lambda}]^{\mathbf{T}}$. M_{APES} is the length of the APES filter. The complex coefficients are obtained by solving the following problem.

$$\min_{\mathbf{h},\alpha} \frac{1}{L}\sum_{l=0}^{L-1}\left|\mathbf{h}^{\mathbf{H}}\mathbf{y}_2(l) - \alpha(\theta_k)e^{j4\pi l \sin\theta_k d/\lambda}\right|^2, \ \ Subject \quad to \ : \ \ \mathbf{h}^{\mathbf{H}}\mathbf{a}_{M_{APES}}(\theta_k) = 1 \tag{14}$$

where $\mathbf{y}_2(l) = [s\left(t_s, n_{peak}, l\right), s\left(t_s, n_{peak}, l+1\right), \cdots s\left(t_s, n_{peak}, l+M_{APES}-1\right)]^T$; $\mathbf{h}$ is a filter weighting coefficient of length M_{APES}. $L = M \times N - M_{APES}+1$. By some manipulations, the minimization problem is converted into a linear minimization, as shown below

$$\min_{\mathbf{h}} \mathbf{h}^{\mathbf{H}}\hat{\mathbf{Q}}\mathbf{h} \quad subject\ to: \ \mathbf{h}^{\mathbf{H}}\mathbf{a}_{M_{APES}}(\omega) = 1 \tag{15}$$

where $\hat{\mathbf{Q}} = \mathbf{R}_2 - \mathbf{g}(\theta_k)\mathbf{g}^{\mathbf{H}}(\theta_k)$ and $\mathbf{R}_2 = \frac{1}{L}\sum_{l=0}^{L-1}\mathbf{y}_2(l)(\mathbf{y}_2(l))^{\mathbf{H}}$. $\mathbf{g}(\theta_k)$ is the Fourier transformation of $\mathbf{y}_2(l)$. The optimal complex coefficients can be obtained by a Lagrange multiplication [16].

$$\mathbf{h} = \frac{\hat{\mathbf{Q}}^{-1}\mathbf{a}_{\mathrm{M_{APES}}}(\theta_k)}{\mathbf{a}^{\mathrm{H}}_{\mathrm{M_{APES}}}(\theta_k)\hat{\mathbf{Q}}^{-1}\mathbf{a}_{\mathrm{M_{APES}}}(\theta_k)} \tag{16}$$

$$\hat{\alpha}(\theta_k) = \mathbf{a}^{\mathrm{H}}_{\mathrm{M_{APES}}}(\theta_k)\mathbf{h} \tag{17}$$

The matrix inversion operation in APES is computation intensive. It can be reduced by using the matrix inversion lemma. Then a new formulation of $\hat{\mathbf{Q}}^{-1}$ is

$$\hat{\mathbf{Q}}^{-1} = \mathbf{R}_2^{-1} - \frac{\mathbf{R}_2^{-1}\mathbf{g}(\theta_k)\mathbf{g}^{\mathbf{H}}(\theta_k)\mathbf{R}_2^{-1}}{\mathbf{g}^{\mathbf{H}}(\theta_k)\mathbf{R}_2^{-1}\mathbf{g}(\theta_k) - 1} \tag{18}$$

The computation efficiency is improved as direct matrix inversions are prevented. By substituting Equation (18) into Equation (17), a new expression of the coefficients is obtained as follows

$$\hat{\alpha}(\theta_k) = \frac{\mathbf{a}^{\mathrm{H}}_{\mathrm{M_{APES}}}(\theta_k)\mathbf{R}_2^{-1}\mathbf{g}(\theta_k)}{\left(\mathbf{g}^{\mathbf{H}}(\theta_k)\mathbf{R}_2^{-1}\mathbf{g}(\theta_k) - 1\right)\mathbf{a}^{\mathrm{H}}_{\mathrm{M_{APES}}}(\theta_k)\mathbf{R}_2^{-1}\mathbf{a}_{\mathrm{M_{APES}}}(\theta_k) - \left|\mathbf{a}^{\mathrm{H}}_{\mathrm{M_{APES}}}(\theta_k)\mathbf{R}_2^{-1}\mathbf{g}(\theta_k)\right|^2} \tag{19}$$

The phase difference between two coefficients estimated at t_s and t_{s+1} can be written as

$$\Delta\phi(t_s, \theta_k) = phase(\hat{\alpha}(t_{s+1}, \theta_k) \times \hat{\alpha}^*(t_s, \theta_k)) \tag{20}$$

where $phase()$ returns the phase angle in the interval $[-\pi, \pi]$ for a complex number. The time interval between two measurements should be small enough to avoid phase wrapping. Then, the displacement of a target at (n_{peak}, θ_k) can be obtained by summing time differential results from the t_0 to t_s. The displacement can be written as

$$d(t_s, \theta_k) = \sum_{n=t_0}^{t_s} \frac{\lambda}{4\pi}\Delta\phi(t_s, \theta_k) \tag{21}$$

4. Simulation and Experiment Results

The proposed MUSICAPES algorithm is evaluated by simulations and radar experiments. A MIMO interferometric radar is built with a COTS MMW radar frontend, an AD card, and a laptop computer. Main parameters of both tests are the same, which are listed in Table 2.

Table 2. Parameters for simulations and experiments.

Transmitting Antennas	Receiving Antennas	Signal Type	Frequency Slope	Start Frequency	AD Frequency	Sampling Length	PRF
3	4	LFMCW	20 MHz/us	77 GHz	10 MHz	256	100 Hz

4.1. Simulations

One simulation is performed when there is only one target. The other three simulations are conducted to evaluate the performance of the proposed method versus the angle interval between two targets, the length of the MIMO array, and the input SNR.

4.1.1. Single Target Displacement Estimation

Supposing the MIMO radar is composed of three transmitting antennas and four receiving antennas, the angular resolution of the array is 8.46°, according to Equation (9). If one target is located at (20 m, 0°), all the MUSIC, CZT, and root-MUSIC algorithms can

precisely estimate the angle of the target, as shown in Figure 4a. The real displacements of the target are the piecewise linear curves shown in Figure 4b. We can obtain two estimated displacement curves using the MUSICAPES and CZT algorithms. As they are nearly the same as the real value, we further analyze the difference between the estimated curves and the real value. The error curves of the MUSICAPES and CZT algorithms are shown in Figure 4c. The mean errors of the MUSICAPES and CZT algorithms are -0.15 μm and -0.22 μm, respectively. The standard deviations (STD) are 0.40 μm and 0.36 μm for MUSICAPES and CZT, respectively. These errors are far less than 0.1 mm which is a widely used error threshold. The results indicate that the MUSICAPES and CZT algorithms both work well in one-target situations.

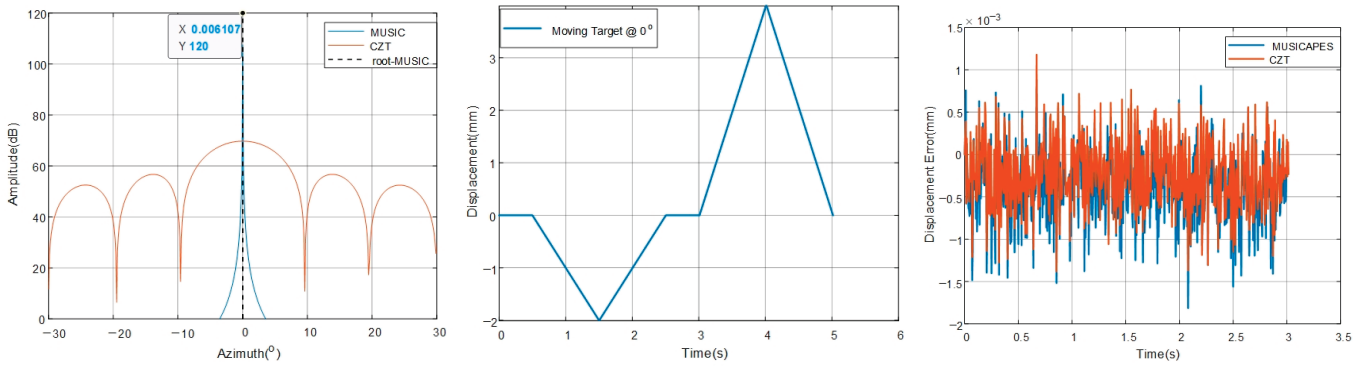

(**a**) (**b**) (**c**)

Figure 4. The simulated displacement curve and the estimated ones by the two algorithms. (**a**) DOA curves in a one-target situation; (**b**) real value of simulated displacement curve; (**c**) errors between the estimated displacements and the simulated one.

4.1.2. Measurement Performance of Two Targets vs. Azimuth Intervals

There are two targets in this simulation case; the 'Target1' is located at (20 m, 0°) and the 'Target2' is located at (20 m, $-8.46°$). The angle interval between the two targets equals the angular resolution of the MIMO radar. The SNR of the input signal is 20 dB. Multiple-target resolving results of the MUSIC, CZT, and root-MUSIC algorithms are shown in Figure 5a. Then, the 'Target2' is moved to (20 m, $-4.23°$), which means the angle interval is half the angular resolution. The multiple-target resolving results are shown in Figure 5b. We can see that the CZT algorithm fails to resolve the two targets when the angle interval is smaller than the angular resolution. Though the CZT algorithm can resolve the two targets when the angle interval is larger than the angular resolution, the estimated angles of the two targets are not precise. This is due to the fact that the side lobes of one target would interfere with the main lobe of the other target. On the contrary, the MUSIC and root-MUSIC algorithms can resolve the two targets and precisely estimate their angles even when the angle interval is smaller than the angular resolution.

The next step is to evaluate the displacement estimation performance in the two-target situation. The angle interval is half the angular resolution of the MIMO radar, namely, 4.23°. This is the same as that of Figure 5b. The real displacement values of the two targets are plotted in Figure 6a. As the CZT algorithm cannot obtain a precise azimuth angle estimation, we use the real angle value for the latter processing. Then, we extract the responses of the CZT and the MUSICAPES and calculate the displacement. The displacement curves are shown in Figure 6b. The blue solid and blue dash curves are the displacements of the 'Target1' estimated by the MUSICAPES and CZT algorithms, respectively. The red solid and red dash curves are the displacements of the 'Target2' estimated by the MUSICAPES and CZT algorithms, respectively. The comparison indicates that the traditional CZT method fails to recover the displacements, but the proposed MUSICAPES can obtain precise results.

The maximum displacement error of the CZT algorithm is 0.42 mm for the 'Target1'. The error is generally unacceptable for normal applications.

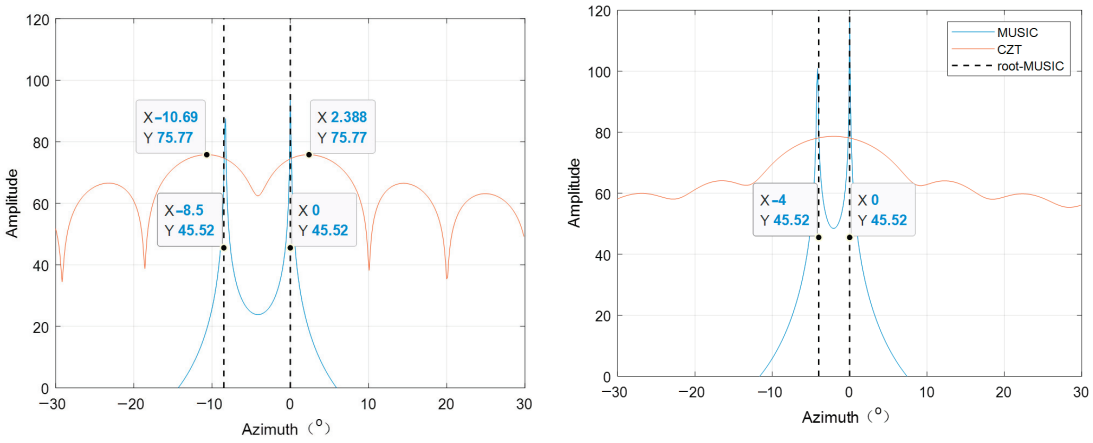

(**a**) (**b**)

Figure 5. Multiple targets resolving ability. (**a**) DOA curves of two targets separated by one angular resolution; (**b**) DOA curves of two targets separated by half the angular resolution.

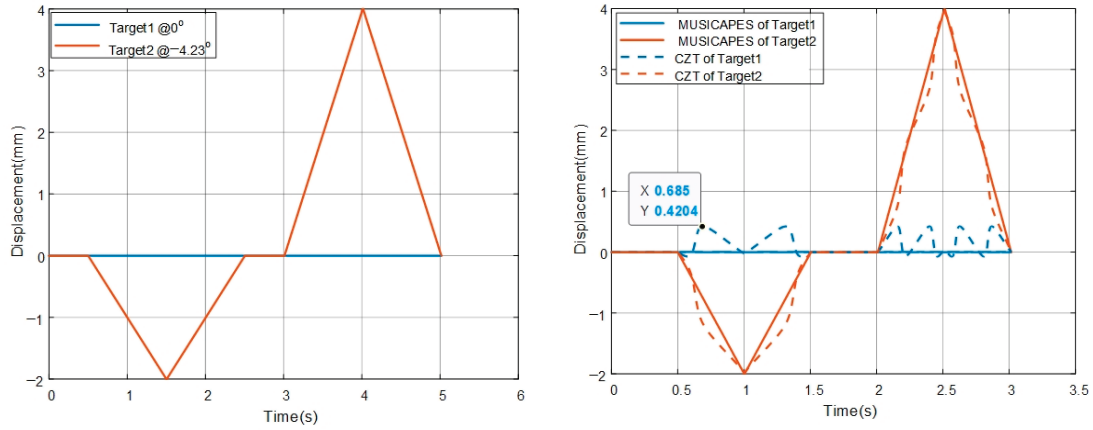

(**a**) (**b**)

Figure 6. Displacement curves of the real value and the estimated ones. (**a**) The real value of displacement; (**b**) the displacement curves estimated by MUSICAPES and CZT.

The performances are further analyzed at different angle intervals between the two targets. 'Target1' is fixed at (20 m, 0°) and the azimuth angle of 'Target2' is variable. The angle interval between them varies exponentially from $10^{-1.5}\ \rho_\theta$ to $10^{0.5}\ \rho_\theta$. The angular resolution ρ_θ is 8.46° in this case. The SNR of the input signal is 20 dB. We use the real angle value to estimate the complex coefficients of the two targets. The displacements of the two targets are subsequently estimated by the MUSICAPES and CZT algorithms. Then, differences between the estimated displacements and the real values (as shown in Figure 6a) are calculated. Finally, the mean and the STD of the differences are measured.

Figure 7 shows the mean error of the difference. The comparison of the curves indicates that the displacement error of the CZT algorithm is much larger than that of the proposed MUSICAPES algorithm. The maximum mean error of the CZT algorithm exceeds 0.2 mm for both targets. On the other hand, the proposed MUSICAPES performs steadily and well, even when the angle interval is a tenth of the angular resolution. If the angle interval further decreases, the performance of MUSICAPES would also deteriorate.

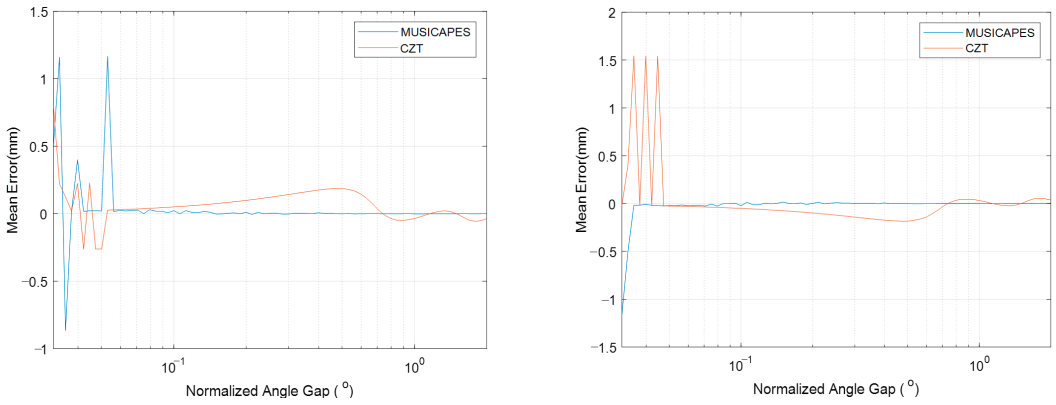

Figure 7. Mean error of displacement difference vs. angle interval. (**a**) The mean error of 'Target1'; (**b**) the mean error of 'Target2'.

Figure 8 shows the STD of the difference. The STD result is similar to the mean error. The CZT algorithm has much larger STD errors. On the other hand, the MUSICAPES works well when the angle interval is larger than a tenth of the angular resolution.

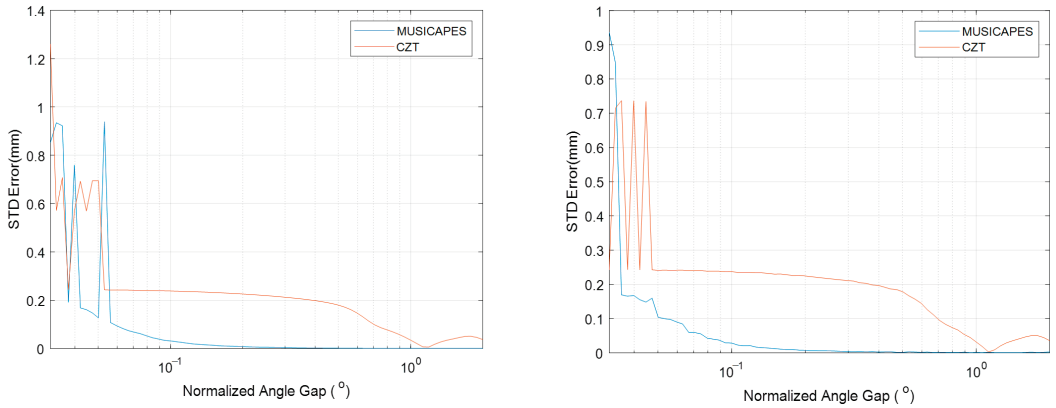

Figure 8. STD of displacement difference vs. angle interval. (**a**) STD of 'Target1'; (**b**) STD of 'Target2'.

4.1.3. Measurement Performance of Two Targets vs. Array Length

We will test the displacement estimation performance versus the number of antennas. In this simulation case, the number of transmitting antennas is set to be 1; the number of receiving antennas varies from 8 to 64 with an incremental step of 2. There are also two targets. 'Target1' is still fixed at (20 m, 0°). 'Target2' is on the right side, 20 m from the radar. The angle interval between the two targets is equal to half the angular resolution of the used array. It is known that the angular resolution is inversely proportional to the number of antenna arrays. As a result, the larger the number of antennas, the smaller the angle interval.

Figure 9 shows the means of the displacement measuring errors of the two targets. Figure 10 shows the STD of the displacement measuring errors of the two targets The proposed MUSICAPES algorithm performs much better than the traditional CZT algorithm. The mean error and STD curve of the MUSICAPES are much smaller than 0.1 mm; however, the STD of the MUSICAPES algorithm would increase as the array gets larger. The reason for this phenomenon is that the input covariance matrix cannot be accurately estimated when the dimensions of the matrix are large, and the input samples are limited.

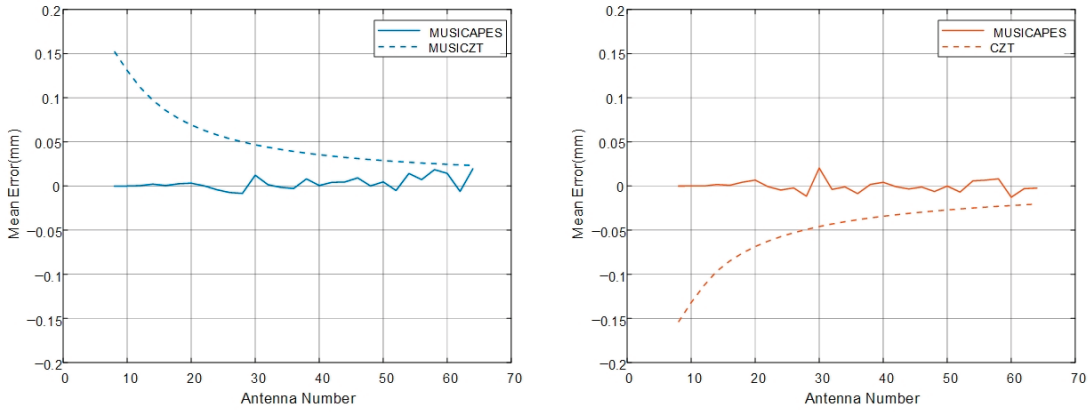

(**a**) (**b**)

Figure 9. Mean error of displacement difference vs. array length. (**a**) The mean error of 'Target1'; (**b**) the mean error of 'Target2'.

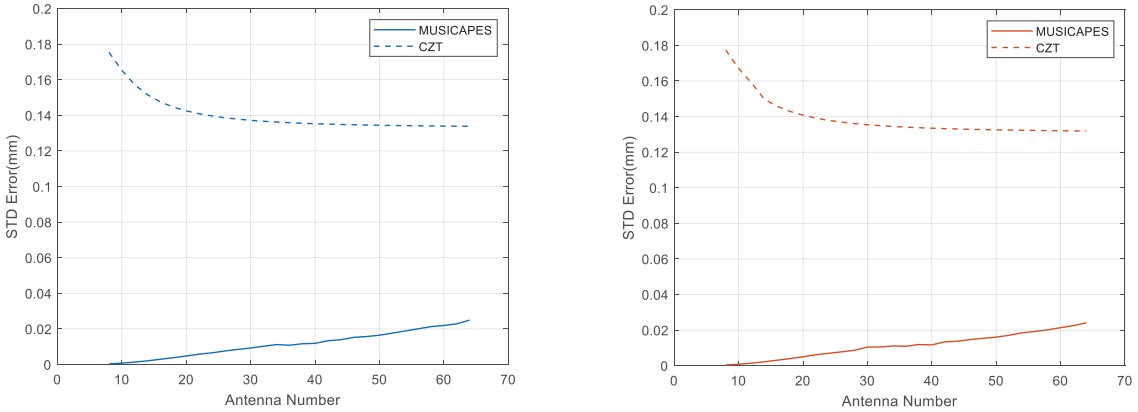

(**a**) (**b**)

Figure 10. STD of displacement difference vs. array length. (**a**) STD of 'Target1'; (**b**) STD of 'Target2'.

4.1.4. Measurement Performance of Two Targets vs. SNR

In this simulation case, the number of transmitting receiving antennas are set as three and four, respectively. There are also two targets. 'Target1' is fixed at (20 m, 0°) and 'Target2' is fixed at (20 m, 4.23°). The angle interval between them is half the angular resolution of the MIMO array. The real displacement curves of the two targets are illustrated in Figure 6a. We will analyze the measuring performance as the input SNR varies from −40 dB to 50 dB with a stride of 3 dB.

Figures 11 and 12 show the results of the two algorithms. We can see that the CZT algorithm performs better than MUSICAPES when the SNR is lower than −30 dB; however, both algorithms cannot give reasonable results in that situation. If the SNR is larger than −25 dB, both algorithms work well. In general, the CZT algorithm is more robust than the MUSICAPES algorithm.

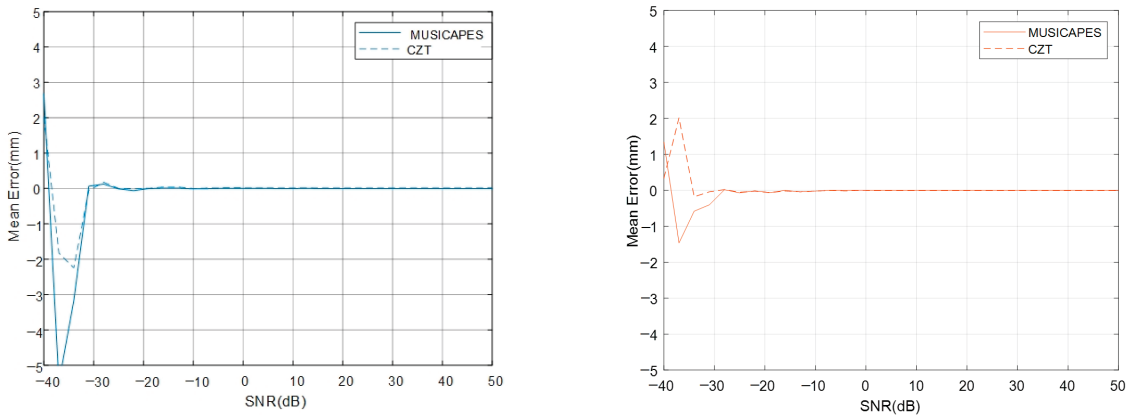

(**a**) (**b**)

Figure 11. Mean error of displacement difference vs. SNR. (**a**) The mean error of 'Target1'; (**b**) the mean error of 'Target2'.

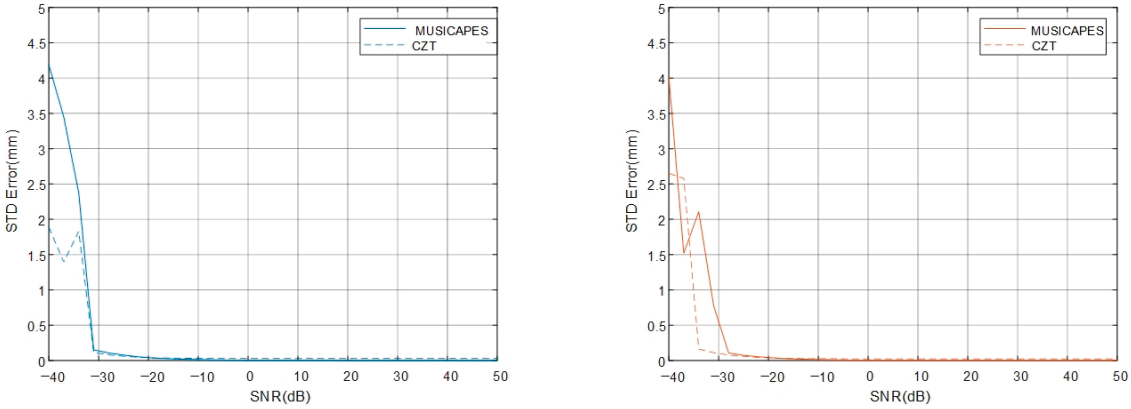

(**a**) (**b**)

Figure 12. STD of displacement difference vs. SNR. (**a**) STD of 'Target1'; (**b**) STD of 'Target2'.

4.2. Experiments

An MMW MIMO radar is designed to measure the displacements of multiple close targets. The MMW MIMO radar is composed of the TI AWR2243BOOST radar front end, the TI DCA1000EVM card, a USB 3.0 hub, and a laptop computer. The experiment is conducted on a table with two trihedral reflectors; one is fixed on the left and the other one is mounted on a sliding platform on the right, as shown in Figure 13. Both ranges of the two trihedral reflectors to the radar are 2.9 m. In the two experiments, the sliding platform stays at 0 mm for several seconds; then it is turned to 1 mm and stays for a while; then it is turned to 2 mm and stays for a moment; finally, it is turned back to 0 mm. The sliding platform operator has to hide beneath the table to eliminate his interference with the trihedral reflectors. The TI AWR2243BOOST has three transmitting antennas and four receiving antennas. The interval between two adjacent receiving antennas is half the wavelength; however, the interval between two adjacent transmitting antennas is one wavelength. So, only the first and the third transmitting antennas can be used to form the required MIMO radar. The angle resolution of the MMW MIMO radar is 12.69°. The maximum repetition rate of the radar can be set to 1 kHz which can satisfy the dynamic displacement measuring requirement.

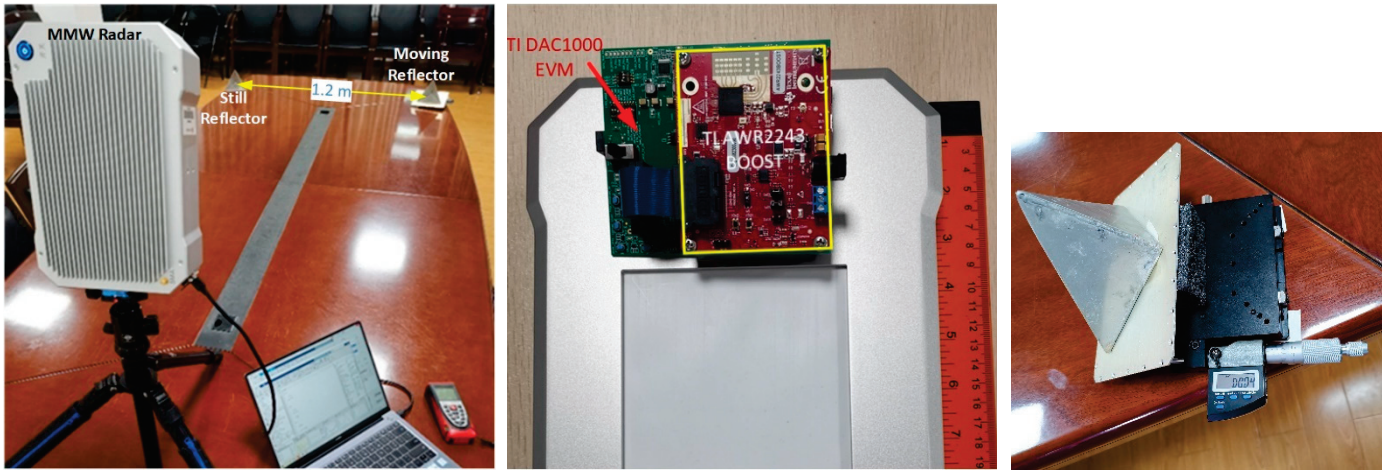

(**a**) (**b**) (**c**)

Figure 13. Multiple close targets displacement measuring experiment with an MMW MIMO radar. The radar is mounted on a tripod and connected to a laptop computer via a USB3.0 hub. (**a**) Two trihedral reflectors are placed at the end of a table. The left one is still and the right one can be moved on a sliding platform. The azimuth distance between them is 1.2 m; (**b**) the TI AWR2243BOOST is mounted on the TI DAC1000 EVM. (**c**) The right reflector is on the sliding platform which can be measured by a micrometer. The platform is stuck onto the desktop to suppress additional displacements caused by manual operations.

4.2.1. Displacement Measurement of Two Targets Separated beyond the Resolution

In the first experiment, the azimuth distance between them is 1.2 m (or 20.1° in angle), which is larger than the angular resolution of AWR2243BOOST. Though a traditional SISO radar cannot resolve the two reflectors, the proposed MIMO radar can successfully resolve them, even with the traditional CZT method. All three methods can resolve the two targets and output the same angle estimations, as shown in Figure 14.

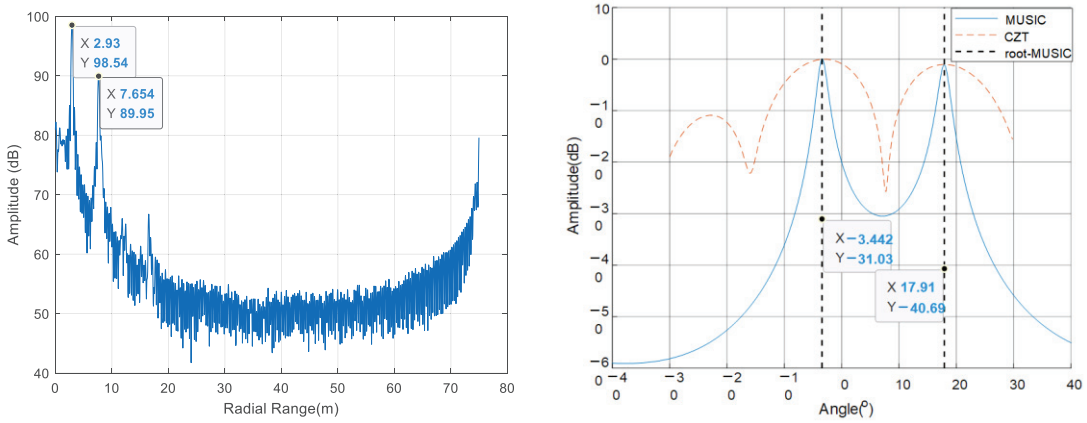

(**a**) (**b**)

Figure 14. One-dimensional image and DOA results of the first experiment. (**a**) High resolution one-dimensional radar image. The first peak is the responses of the two trihedral reflectors separated 1.2 m in azimuth; (**b**) MUSIC, CZT and root-MUSIC can discriminate between the two reflectors.

The estimated displacement curves of the MUSICAPES and CZT methods are shown in Figure 15. When multiple targets present in the same radial range, their side lobes would interfere with the other's main lobe. As a result, even if multiple targets can be resolved, their displacements cannot be precisely estimated by the CZT methods. The

displacement curve of the still reflector fluctuates while the other one moves. The maximum displacement measuring error is about 0.1 mm. The displacement of the moving reflectors is also not precise. As the absolute displacement is large, the relative measuring error is not prominent. On the other hand, the proposed MUSICAPES algorithm can precisely recover the displacements of both reflectors. The mean error and STD error of the still reflector are 0.002 mm and 0.003 mm, respectively. The displacement curve of the moving reflector estimated by MUSICAPES is consistent with the real value. The errors between the measurement and the real value are 0.023 mm and 0.01 mm when the moving reflector stays at 1 mm and 2 mm, respectively. The error is small enough for most applications.

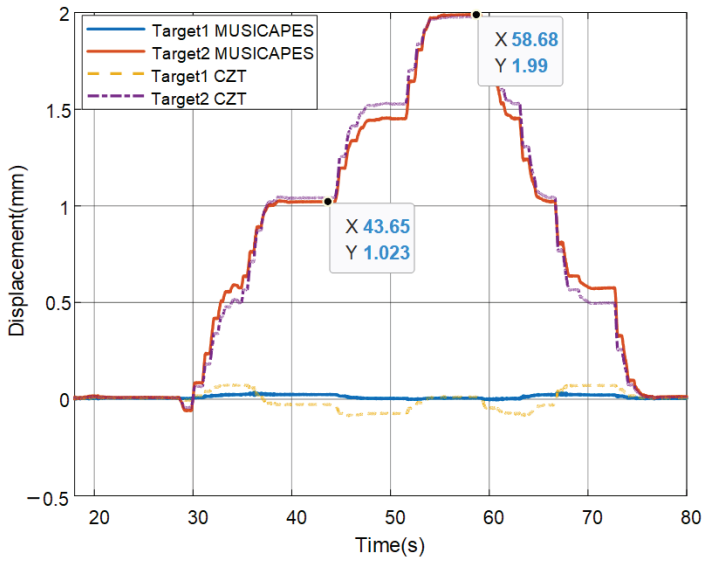

Figure 15. Displacement curves of the two trihedral reflectors estimated by the MUSICAPES and the CZT method. Target 1 is the still reflector and Target 2 is the moving one mounted on the sliding platform.

4.2.2. Displacement Measurement of Two Close Targets

In the second experiment, the azimuth distance between the two reflectors is reduced to 0.7 m (or 11.3° in angle), which is smaller than the angular resolution of AWR2243BOOST. In this situation, both the CZT method and the MUSIC algorithm fail to resolve the two reflectors, but the root-MUSIC works well, as shown in Figure 16. This is due to the fact that the covariance matrix is not accurately estimated from only one snapshot, but root-MUSIC generally has better performance in limited snapshot situations [22].

If we use the angle estimated by root-MUSIC and then estimate the phase by the CZT method, we can obtain the displacement curves of the two reflectors. The estimated displacement curves of the MUSICAPES and CZT methods are shown in Figure 17. We can see that the CZT method fails to estimate the displacements of the reflectors. The maximum displacement error of the moving one is larger than 2 mm. The displacement error of the still one is not prominent, because the interference of the moving one is small. Only the proposed MUSICAPES successfully recovers the displacements of the two close trihedral reflectors. The mean error and STD error of the still trihedral reflector are 0.002 mm and 0.003 mm, respectively. The displacement curve of the moving one estimated by MUSICAPES fits the real value well. The error between the measurement and the real value is 0.042 mm and 0.051 mm when the moving reflector stays at 1mm and 2 mm, respectively. The error is also small enough for most applications.

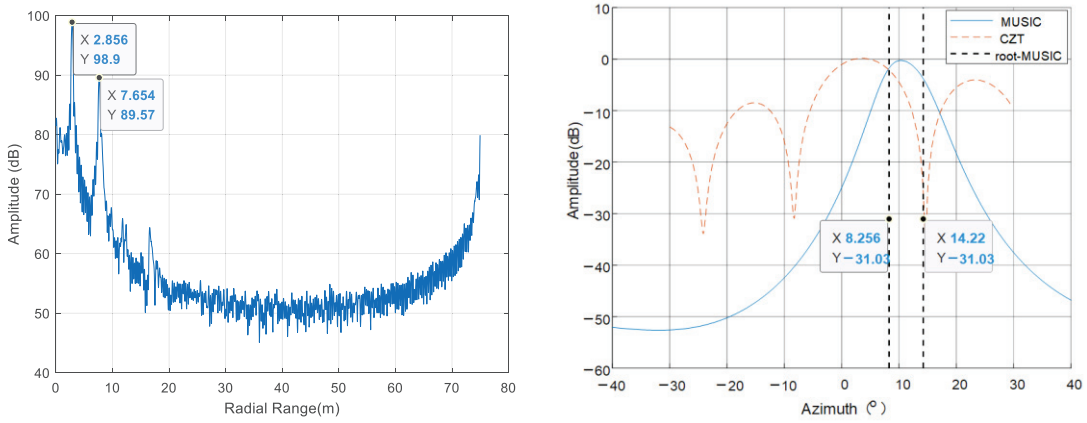

(**a**) (**b**)

Figure 16. One-dimensional image and DOA results of the second experiment. (**a**) High resolution one-dimensional radar image. The first peak is the responses of two trihedral reflectors separated by 0.7 m in azimuth; (**b**) the angle between the two trihedral reflectors is smaller than the angular resolution, root-MUSIC can discriminate between them, but MUSIC and CZT fail.

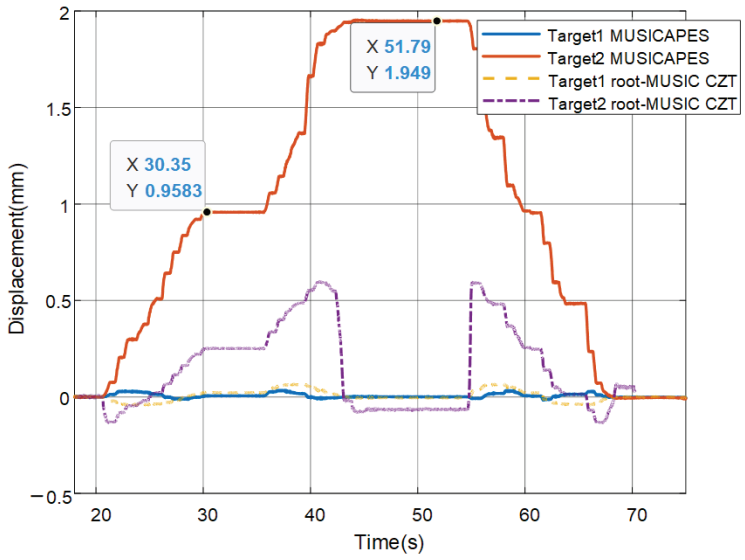

Figure 17. Displacement curves of the two trihedral reflectors estimated by the MUSICAPES and the CZT method. Target 1 is the still reflector and Target 2 is the moving one mounted on the sliding platform.

5. Conclusions

An interferometric MIMO radar and a MUSICAPES algorithm are proposed to precisely estimate the dynamic displacements of multiple close targets. The array length of the MIMO radar is small enough to maintain a high repetition measuring rate; however, the short MIMO radar would face two challenges, which are limited angular resolution and large side lobe interferences. The MUSICAPES method is proposed to resolve the multiple azimuth close targets and precisely extract their displacements. The method firstly adopts the root-MUSIC algorithm to estimate the azimuth angle of each target. Then, the APES algorithm is used to recover the phases of the targets using the azimuth angles estimated in the previous step. The method can improve the displacement measuring precision significantly.

A millimeter-wave MIMO interferometric radar is designed for multiple target displacement measuring. Simulations and experiments with the MMW radar validate the performance of the proposed method.

The proposed radar can be applied to measure dynamic displacements of bridges, towers, and buildings. It is especially useful to solve multiple close-target displacement measuring requirements that traditional one-dimensional interferometric radars fail to do. The proposed method can also be applied to other MIMO radars if both the fine angular resolution and precise phase estimation are the pursuits, such as monitoring the displacements of dams and radar tomography of complex scenes.

Author Contributions: Conceptualization, methodology and writing—original draft preparation, J.W.; software and data curation, Y.W.; validation, Y.L.; writing—review and editing and supervision, X.H. All authors have read and agreed to the published version of the manuscript.

Funding: This research was funded by the National Natural Science Foundation of China (No. 62101562).

Data Availability Statement: The experiment data available on request.

Conflicts of Interest: The authors declare no conflict of interest.

References

1. Wang, Y.; Hong, W.; Zhang, Y.; Lin, Y.; Li, Y.; Bai, Z.; Zhang, Q.; Lv, S.; Liu, H.; Song, Y. Ground-Based Differential Interferometry SAR: A Review. *IEEE Geosci. Remote Sens. Mag.* **2020**, *8*, 43–70. [CrossRef]
2. Zhao, W.; Zhang, G.; Zhang, J. Cable force estimation of a long-span cable-tayed bridge with microwave interferometric radar. *Comput. Aided Civ. Infrastruct. Eng.* **2020**, *35*, 1419–1433. [CrossRef]
3. Dong, H.; Wang, J.; Song, Q. A Way of Cable Force Measurement Based on Interference Radar. In Proceedings of the Electromagnetic Research Symposium (PIERS), Shanghai, China, 8–11 August 2016.
4. Pieraccini, M.; Miccinesi, L. Ground-Based Radar Interferometry: A Bibliographic Review. *Remote Sens.* **2019**, *11*, 1029. [CrossRef]
5. Luo, T.; Li, F.; Pan, B.; Zhou, W.; Chen, H.; Shen, G.; Hao, W. Deformation Monitoring of Slopes with a Shipborne InSAR System: A Case Study of the Lancang River Gorge. *IEEE Access* **2021**, *9*, 5749–5759. [CrossRef]
6. Miccinesi, L.; Consumi, T.; Beni, A.; Pieraccini, M. W-band MIMO GB-SAR for Bridge Testing/Monitoring. *Electronics* **2021**, *10*, 2261. [CrossRef]
7. Miccinesi, L.; Beni, A.; Pieraccini, M. Multi-Monostatic Interferometric Radar for Bridge Monitoring. *Electronics* **2021**, *10*, 247. [CrossRef]
8. Hu, C.; Deng, Y.; Tian, W.; Wang, J. Novel MIMO-SAR system applied for high-speed and high-accuracy deformation measurement. *J. Eng.* **2019**, *2019*, 6598–6602. [CrossRef]
9. Hosseiny, B.; Amini, J.; Safavi-Naeini, S. Simulation and Evaluation of an mm-Wave MIMO Ground-Based SAR Imaging System for Displacement Monitoring. In Proceedings of the 2021 IEEE International Geoscience and Remote Sensing Symposium, Brussels, Belgium, 11–16 July 2021; pp. 8213–8216. [CrossRef]
10. Deng, Y.; Hu, C.; Tian, W.; Zhao, Z. 3-D Deformation Measurement Based on Three GB-MIMO Radar Systems: Experimental Verification and Accuracy Analysis. *IEEE Geosci. Remote Sens. Lett.* **2020**, *18*, 2092–2096. [CrossRef]
11. Feng, W.; Friedt, J.-M.; Nico, G.; Sato, M. 3-D Ground-Based Imaging Radar Based on C-Band Cross-MIMO Array and Tensor Compressive Sensing. *IEEE Geosci. Remote Sens. Lett.* **2019**, *16*, 1585–1589. [CrossRef]
12. Jiao, A.; Han, C.; Huo, R.; Tian, W.; Zeng, T.; Dong, X. A Method of Acquiring Vibration Mode of Bridge Based on MIMO Radar. In Proceedings of the 2019 IEEE International Conference on Signal, Information and Data Processing (ICSIDP), Chongqing, China, 11–13 December 2019; pp. 1–6.
13. Fortuny-Guasch, J. A Fast and Accurate Far-Field Pseudopolar Format Radar Imaging Algorithm. *IEEE Trans. Geosci. Remote Sens.* **2009**, *47*, 1187–1196. [CrossRef]
14. Rabiner, L.R.; Schafer, R.W.; Rader, C.M. The Chirp z-Transform Algorithm and Its Application. *Bell Syst. Tech. J.* **1969**, *48*, 1249–1292. [CrossRef]
15. Li, J.; Stoica, P.; Wang, Z. On robust Capon beamforming and diagonal loading. *IEEE Trans. Signal Process.* **2003**, *51*, 1702–1715. [CrossRef]
16. Li, J.; Stoica, P. An adaptive filtering approach to spectral estimation and SAR imaging. *IEEE Trans. Signal Process.* **1996**, *44*, 1469–1484. [CrossRef]
17. Stoica, P.; Li, H.; Li, J. A new derivation of the APES filter. *IEEE Signal Process. Lett.* **1999**, *6*, 205–206. [CrossRef]
18. Schmidt, R.O. Multiple emitter location and signal parameter estimation. *IEEE Trans. Antennas Propag.* **1986**, *34*, 276–280. [CrossRef]
19. Shang, X.; Liu, J. Multiple Object Localization and Vital Sign Monitoring Using IR-UWB MIMO Radar. *IEEE Trans. Aerosp. Electron. Syst.* **2020**, *56*, 4437–4450. [CrossRef]

20. Wang, J.; Wang, Y.; Zhang, J.; Ge, J. Resolution Calculation and Analysis in Bistatic SAR with Geostationary Illuminator. *IEEE Geosci. Remote Sens. Lett.* **2012**, *10*, 194–198. [CrossRef]
21. Xue, M.; Xu, L.; Li, J. IAA Spectral Estimation: Fast Implementation Using the Gohberg–Semencul Factorization. *IEEE Trans. Signal Process.* **2011**, *59*, 3251–3261.
22. Florio, A.; Avitabile, G.; Coviello, G. Multiple Source Angle of Arrival Estimation through Phase Interferometry. *IEEE Trans. Circuits Syst. II Express Briefs* **2022**, *69*, 674–678. [CrossRef]
23. Rao, B.; Hari, K. Performance analysis of Root-Music. *IEEE Trans. Acoust. Speech Signal Process.* **1989**, *37*, 1939–1949. [CrossRef]
24. Masood, K.F.; Hu, R.; Tong, J.; Xi, J.; Guo, Q.; Yu, Y. A Low-Complexity Three-Stage Estimator for Low-Rank mmWave Channels. *IEEE Trans. Veh. Technol.* **2021**, *70*, 5920–5931. [CrossRef]

MDPI
St. Alban-Anlage 66
4052 Basel
Switzerland
www.mdpi.com

MDPI Books Editorial Office
E-mail: books@mdpi.com
www.mdpi.com/books

Academic Open
Access Publishing

mdpi.com

ISBN 978-3-7258-0324-8